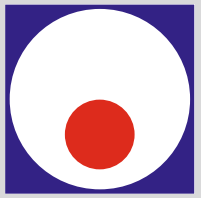




FACULTY OF MECHANICAL AND CIVIL ENGINEERING  
IN KRALJEVO  
UNIVERSITY OF KRAGUJEVAC



X Triennial  
International Conference

# HEAVY MACHINERY HM 2021 Proceedings

VRNJAČKA BANJA, SERBIA  
June 23 - June 25 2021





**FACULTY OF MECHANICAL AND CIVIL ENGINEERING KRALJEVO  
UNIVERSITY OF KRAGUJEVAC  
KRALJEVO – SERBIA**

---

---

**THE TENNTH INTERNATIONAL TRIENNIAL CONFERENCE**

**HEAVY MACHINERY  
HM 2021**

**PROCEEDINGS**

**ORGANIZATION SUPPORTED BY:**

Ministry of Education, Science and Technological Development, Republic of Serbia

**Vrnjačka Banja, June 23–25, 2021**



**PUBLISHER:**

Faculty of Mechanical and Civil Engineering in Kraljevo

**EDITOR:**

Prof. dr Mile Savković

**PRINTOUT:**

TERCIJA d.o.o., Bor

**TECHNICAL COMMITTEE**

Doc. dr Aleksandra Petrović – CHAIRMAN

Bojan Beloica – VICE-CHAIRMAN

Jovana Bojković

Goran Bošković

Vladimir Đorđević

Marina Ivanović

Vladimir Mandić

Mladen Manojlović

Saša Marinković

Stefan Mihajlović

Miloš Nikolić

Đorđe Novčić

Anica Pantić

Vladimir Sindelić

Nenad Stojić

Marko Todorović

Tanja Miodragović

Mladen Rasinac

Dragiša Šimunović

Jovana Perić

Branislav Prokić

Slobodan Bukarica

No. of copies: 80

ISBN 978-86-81412-09-1

**REVIEWS:**

All papers have been reviewed by members of scientific committee



## CONFERENCE CHAIRMAN

Prof. dr Mile Savković, FMCE Kraljevo, Serbia

## INTERNATIONAL SCIENTIFIC PROGRAM COMMITTEE

### CHAIRMAN

Prof. dr Milan Kolarević, FMCE Kraljevo, Serbia

### VICE-CHAIRMAN

Prof. dr Milan Bižić, FMCE Kraljevo, Serbia

### MEMBERS

1. Prof. dr M. Alamoreanu, TU Bucharest, Romania
2. Prof. dr S. Arsovski, FME Kragujevac, Serbia
3. Prof. dr D. Atmadzhova, VTU "Todor Kableskov", Sofia, Bulgaria
4. Prof. dr M. Berg, Royal Institute of Technology-KTH, Sweden
5. Prof. dr H. Bogdevicius, Technical University, Vilnius, Lithuania
6. Prof. dr N. Bogojević, FMCE Kraljevo, Serbia
7. Prof. dr S. Bošnjak, FME Belgrade, Serbia
8. Prof. dr A. Bruja, TU Bucharest, Romania
9. Prof. dr Z. Bučevac, FME Belgrade, Serbia
10. Prof. dr R. Bulatović, FMCE Kraljevo, Serbia
11. Prof. dr S. Ćirić-Kostić, FMCE Kraljevo, Serbia
12. Prof. dr M. Dedić, FMCE Kraljevo, Serbia
13. Prof. dr I. Despotović, FMCE Kraljevo, Serbia
14. Prof. dr R. Durković, FME Podgorica, Montenegro
15. Prof. dr M. Đapić, FMCE Kraljevo, Serbia
16. Prof. dr Z. Đinović, ACMIT, Wiener Neustadt, Austria
17. Prof. dr K. Ehmann, Northwestern University, Chicago, USA
18. Prof. dr I. Emeljanova, HGTUSA Harkov, Ukraine
19. Prof. dr O. Erić Cekić, FMCE Kraljevo, Serbia
20. Prof. dr V. Filipović, FMCE Kraljevo, Serbia
21. Prof. dr D. Golubović, FME East Sarajevo, Bosnia and Herzegovina
22. Prof. dr B. Jerman, FME Ljubljana, Slovenia
23. Prof. dr Z. Jugović, Technical Faculty Čačak, Serbia
24. Prof. dr V. Karamarković, FMCE Kraljevo, Serbia
25. Prof. dr R. Karamarković, FMCE Kraljevo, Serbia
26. Prof. dr M. Karasahin, Demirel University, Istanbul, Turkey
27. Prof. dr I. Kiričenko, HNADU Kiev, Ukraine
28. Prof. dr K. Kocman, Technical University of Brno, Czech Republic
29. Prof. dr S. Kolaković, Faculty of Technical Sciences, Novi Sad, Serbia
30. Prof. dr M. Kostic, Northern Illinois University, DeKalb, USA
31. Prof. dr M. Králik, FME Bratislava, Slovakia
32. Prof. dr M. Krajišnik, FME East Sarajevo, Bosnia and Herzegovina
33. Prof. dr E. Kudrjavcev, MGSU, Moscow, Russia
34. Prof. dr Đ. Lađinović, Faculty of Technical Sciences, Novi Sad, Serbia



35. Prof. dr LJ. Lukić, FMCE Kraljevo, Serbia
36. Prof. dr Z. Marinković, FME Niš, Serbia
37. Prof. dr G. Marković, FMCE Kraljevo, Serbia
38. Prof. dr N. Mešcerin, MGSU, Moscow, Russia
39. Prof. dr A. Milašinović, FME Banja Luka, Bosnia and Herzegovina
40. Prof. dr D. Milković, FME Belgrade, Serbia
41. Prof. dr B. Milošević, FMCE Kraljevo, Serbia
42. Prof. dr G. Minak, University of Bologna, Italy
43. Prof. dr D. Minić, FME Kosovska Mitrovica, Serbia
44. Prof. dr N. Nedić, FMCE Kraljevo, Serbia
45. Prof. dr V. Nikolić, FME Niš, Serbia
46. Prof. dr E. Nikolov, Technical University, Sofia, Bulgaria
47. Prof. dr M. Ognjanović, FME Belgrade, Serbia
48. Prof. dr J. Peterka, FMS&T, Trnava, Slovakia
49. Prof. dr D. Petrović, FMCE Kraljevo, Serbia
50. Prof. dr J. Polajnar, BC University, Prince George, Canada
51. Prof. dr D. Pršić, FMCE Kraljevo, Serbia
52. Prof. dr N. Radić, FME East Sarajevo, Bosnia and Herzegovina
53. Prof. dr V. Radonjanin, Faculty of Technical Sciences, Novi Sad, Serbia
54. Prof. dr M. Rajović, FMCE Kraljevo, Serbia
55. Prof. dr D. Sever, Maribor, Civil Engineering, Slovenia
56. Prof. dr M. Stefanović, FME Kragujevac, Serbia
57. Prof. dr M. A. Stepanov, MGSU, Moscow, Russia
58. Prof. dr I. S. Surovcev, VGSU, Voronezh, Russia
59. Prof. dr S. Šalinić, FMCE Kraljevo, Serbia
60. Prof. dr Z. Šoškić, FMCE Kraljevo, Serbia
61. Prof. dr LJ. Tanović, FME Belgrade, Serbia
62. Prof. dr D. Todorova, VTU “Todor Kableskov”, Sofia, Bulgaria
63. Prof. dr S. Trifunović, FMCE Kraljevo, Serbia
64. Prof. dr J. Vladić, Faculty of Technical Sciences, Novi Sad, Serbia
65. Prof. dr M. Vukićević, FMCE Kraljevo, Serbia
66. Prof. dr K. Weinert, University of Dortmund, Germany
67. Prof. dr N. Zdravković, FMCE Kraljevo, Serbia
68. Prof. dr N. Zrnić, FME Belgrade, Serbia
69. Prof. dr D. Živanić, Faculty of Technical Sciences, Novi Sad, Serbia

## ORGANIZING COMMITTEE

### CHAIRMAN:

Prof. dr Slaviša Šalinić, FMCE Kraljevo

### VICE-CHAIRMAN:

Prof. dr Goran Marković, FMCE Kraljevo, Serbia

### MEMBERS:

Doc. dr M. Bjelić, FMCE Kraljevo, Serbia  
Doc. dr V. Grković, FMCE Kraljevo, Serbia  
Doc. dr Lj. Dubonjić, FMCE Kraljevo, Serbia  
Doc. dr M. Marašević, FMCE Kraljevo, Serbia  
Doc. dr A. Nikolić, FMCE Kraljevo, Serbia  
Doc. dr A. Petrović, FMCE Kraljevo, Serbia

Doc. dr B. Radičević, FMCE Kraljevo, Serbia  
Doc. dr B. Sredojević, FMCE Kraljevo, Serbia  
Doc. dr V. Stojanović, FMCE Kraljevo, Serbia  
Dr N. Pavlović, FMCE Kraljevo, Serbia  
Dr M. Bošković, FMCE Kraljevo, Serbia  
Dr J. Tomić, FMCE Kraljevo, Serbia



## PREFACE

Ladies and gentlemen, dear colleagues,

Welcome to Vrnjačka Banja, to the International Scientific Conference Heavy Machinery.

After postponing the 2020 conference due to the Covid-19 pandemic, this year the Tenth International Conference Heavy Machinery is held by the Faculty of Mechanical and Civil Engineering in Kraljevo, University of Kragujevac, from 23 to 25 June 2021.

It has gained a unique recognizable form for exchange of information, ideas and new scientific researches. The Conference is held in the year when the Faculty of Mechanical and Civil Engineering in Kraljevo celebrates the 61<sup>st</sup> year of university teaching in mechanical engineering, nine years of university teaching in civil engineering and two years of university teaching in occupation safety.

During several decades of existence, it has acquired specific and recognizable form in domestic and foreign scientific circles thanks to its scientific and research results.

The goal of the Conference is to make the research from the fields covered at the Faculty of Mechanical and Civil Engineering in Kraljevo available and applicable both within domestic and foreign frames. Also, our scientists will have the opportunity to learn about results of research done by their colleagues from abroad in the fields of transport design in industry, energy control, production technologies, and civil engineering through the following thematic sessions:

- Earth-moving and transportation machinery,
- Production technologies,
- Automatic control and fluid technique,
- Applied mechanics,
- Railway engineering,
- Thermal technique and environment protection,
- Civil engineering.

Despite the aggravating circumstances due to the Covid-19 pandemic, a high scientific reputation of domestic and foreign participants as well as the number of papers provide guarantees that the Conference will be very successful.

The papers reflect state of the art and deal with the wide spectrum of important topics of current interest in heavy machinery.

I especially want to thank you the Ministry of Education, Science and Technological Development of Republic of Serbia for support of organization of the Conference and our efforts to promote science and technology in the areas of mechanical and civil engineering in Serbia. I would like to express sincere thanks to all members of scientific, organizing and technical committee, reviewers, as well as to all participants including invited speakers for participation in the Conference and presentation of their papers.

Thank you and see you at the next conference.

Kraljevo – Vrnjačka Banja, June 2021

Conference Chairman,

**Prof. dr Mile Savković**



## PLENARY SESSION

|   |           |
|---|-----------|
| <b>MODAL SPACE BASED REAL-TIME FE SIMULATIONS OF COMPLEX AND MULTIFUNCTIONAL STRUCTURES</b> | <b>1</b>  |
| Dragan Marinković   |           |
| <b>INDUSTRY 4.0 CONTEXT OF HEAVY MACHINERY</b>  | <b>9</b>  |
| Vidosav D. Majstorović, Radivoje M. Mitrović, Žarko Z. Mišković                             |           |
| <b>WAYS TO IMPROVE THE EFFICIENCY OF DUMP TRUCKS FOR TRANSPORTING ASPHALT MIX</b>           | <b>17</b> |
| A.I. Dotsenko   |           |

## SESSION A: EARTH-MOVING AND TRANSPORTATION MACHINERY

|  |           |
|--|-----------|
| <b>EXPERIMENTAL STUDY OF THE INFLUENCE OF A COMBINATION OF OPERATING PARAMETERS OF A MOBILE LIFT ON OSCILLATORY PROCESSES OCCURRING AFTER LOCKING THE WORKING PLATFORM</b> | <b>1</b>  |
| Igor Kyrychenko, Oleksandr Reznikov, Dmytro Klets, Anton Kholodov  |           |
| <b>FINITE ELEMENT AND ANALYTICAL MODELLING OF SHIP UNLOADER</b>  | <b>13</b> |
| Zrnić Nenad, Gašić Vlada, Urošević Marko, Arsić Aleksandra   |           |
| <b>THE DEFLECTION OF THE COLUMN-MOUNTED JIB CRANE WITH TAPERED BOOM BY FINITE DIFFERENCE METHOD</b>  | <b>19</b> |
| Nebojša B. Zdravković, Boris Jerman, Mile Savković, Goran Marković, Marko Todorović, Goran Pavlović  |           |
| <b>ANALYSIS OF ELEVATORS DYNAMIC PARAMETERS WITH SOLUTION OF SUMMARY DATA ACQUISITION DURING EXPERIMENTAL RESEARCH</b>   | <b>25</b> |
| Radomir Đokić, Jovan Vladić, Dragan Živanić, Tanasije Jojić, Vesna Jovanović, Nebojša Zdravković   |           |
| <b>LOAD ANALYSIS OF STEERING MECHANISM OF WHEEL LOADER</b>   | <b>33</b> |
| Jovan Pavlović, Dragoslav Janošević, Boban Nikolić, Vesna Jovanović, Nikola Petrović   |           |
| <b>IMPROVEMENT OF CASTING TECHNOLOGY OF CONTINUOUS TRACKS SEGMENT USING CAD/CAE/CAM SOFTWARE TOOLS</b>   | <b>39</b> |
| Aleksandar Jovičić, Nedeljko Dučić, Radomir Radiša, Ivan Milićević, Marko Popović, Vojislav Vujičić  |           |
| <b>STRENGTH OF THE WELDED JOINT WITH IMPROVED MECHANICAL PROPERTIES OF WELD METAL AND HEAT AFFECTED ZONE</b>   | <b>43</b> |
| Miodrag Arsić, Nebojša B. Zdravković, Vencislav Grabulov, Srđan Bulatović, Mladen Mladenović   |           |
| <b>PROJECT OF MODERNIZATION OF LABORATORY MODEL OF TWO-GIRDER OVERHEAD BRIDGE CRANE</b>  | <b>47</b> |
| Dragan Živanić, Nikola Ilanković, Atila Zelić, Radomir Đokić   |           |
| <b>BASIS FOR THE DESIGN OF DRIVE-IN AND DRIVE-THROUGH RACKING</b>  | <b>57</b> |
| Rodoljub Vujanac, Nenad Miloradović, Pavle Živković, Luka Petrović   |           |

|   |    |
|---|----|
| <b>STATISTICAL COMPARISON OF THE EVALUATION PROCESS RESULTS OF LOCATION ALTERNATIVES IN CASE OF FLAT AND HIERARCHY STRUCTURE OF CRITERIA</b><br>Goran Marković, Cătălin Frâncu, Mile Savković, Nebojša Zdravković, Radomir Đokić, Marko Popović | 65 |
| <b>BASIC PARAMETERS OF A TENSILE TESTING DEVICE FOR CONVEYOR BELTS</b><br>Nikola Ilanković, Dragan Živanić, Atila Zelić, Mirko Katona   | 73 |
| <b>APPLICATION OF WATER CYCLE ALGORITHM ON RAMSHORN HOOK OPTIMIZATION PROBLEM</b><br>Goran Pavlović, Mile Savković, Nebojša B. Zdravković   | 81 |
| <b>FINDING THE OPTIMAL SHAPE OF HYDRAULIC SCISSORS LIFT LEGS USING HHO OPTIMIZATION METHOD</b><br>Marko Todorović, Radovan Bulatović, Mile Savković, Goran Marković   | 89 |
| <br><b>SESSION B: PRODUCTION TECHNOLOGIES</b>   |    |
| <b>A SURVEY OF RESEARCH ON INDUSTRY 4.0 IN INTRALOGISTICS</b><br>Nenad Đ. Zrnić, Tamara M. Popović, Goran Z. Milojević, Nenad Ž. Kosanić  | 1  |
| <b>DETERMINATION OF THE PROBABILITY OF A GEAP PUMP FAULT USING THE BAYES NETWORK AND NETICA SOFTWARE</b><br>Jovana Perić*, Mirko Djapić, Tanja Miodragović, Stefan Pajović  | 9  |
| <b>JET LAGGING IN ABRASIVE WATER JET CUTTING OF HIGH-SPEED TOOL STEEL</b><br>Ramiz Kurbegovic, Mileta Janjic  | 15 |
| <b>APPLICATION OF TAGUCHI METHOD TO BEVEL ANGLE OPTIMIZATION DURING PLASMA ARC CUTTING</b><br>Dragoljub Lazarevic, Andjela Lazarevic  | 23 |
| <b>INFLUENCE OF TECHNICAL-TECHNOLOGICAL CHARACTERISTICS OF WORKPIECES ON THE CHOICE OF CNC MACHINE TOOLS</b><br>Marina Ivanović, Mladen Rasinac, Stefan Pajović   | 29 |
| <b>FREQUENCY ANALYSIS OF NOISE AT DIFFERENT MILLING PARAMETERS OF STEEL</b><br>Mladen Rasinac, Branko Radičević, Milan Kolarević, Aleksandra Petrović, Mišo Bjelić  | 35 |
| <b>INFLUENCE OF 3D PRINTING PARAMETERS ON THE GEOMETRY AND SURFACE QUALITY OF MANUFACTURED PARTS ON AN FDM 3D PRINTER</b><br>Petar Đekić, Biljana Milutinović, Mladen Tomić, Saša S. Nikolić  | 39 |
| <b>PREDICTION OF THE STRAIN HARDENING EXPONENT OF HP40-NB ALLOY</b><br>Milica Timotijević, Mišo Bjelić, Dragan Rajnović, Olivera Erić Cekić   | 45 |
| <b>EFFECT OF CHEMICAL COMPOSITION ON THE MICROSTRUCTURE, HARDNESS AND ELECTRICAL CONDUCTIVITY PROFILES OF THE BI-GE-IN ALLOYS</b><br>Dusko Minic, Milena Premovic, Aleksandar Djordjevic, Milan Milosavljevic                                   | 51 |
| <b>EXPERIMENTAL INVESTIGATION AND THERMODYNAMIC DESCRIPTION OF THE TERNARY CU-GE-PB SYSTEM</b><br>Milan Milosavljevic, Milena Premovic, Dusko Minic, Aleksandar Djordjevic  | 63 |

|   |    |
|---|----|
| <b>MECHANICAL AND ELECTRICAL PROPERTIES OF THE BI-GE-SN ALLOYS</b><br>Aleksandar Djordjevic, Dusko Minic, Milena Premovic, Milan Kolarevic, Milan Milosavljevic | 71 |
|---|----|

## **SESSION C: AUTOMATIC CONTROL AND FLUID TECHNIQUE**

|   |    |
|---|----|
| <b>TRAJECTORY TRACKING OF A TWO – LINK GRIPPING MECHANISM</b><br>Radiša Jovanović, Uglješa Bugarić, Lara Laban, Mitra Vesović   | 1  |
| <b>FEEDBACK LINEARIZATION CONTROL OF A TWO – LINK GRIPPING MECHANISM</b><br>Mitra Vesović*, Radiša Jovanović, Lara Laban, Uglješa Bugarić   | 9  |
| <b>A NONLINEAR MODEL PREDICTIVE CONTROL TRACKING APPLICATION FOR A SYSTEM OF CASCADED TANKS</b><br>Guilherme N. G. dos Reis, Marcelo M. Morato, Julio E. Normey-Rico, Vladimir Stojanovic | 17 |
| <b>CONTROL OF A LIQUID LEVEL SYSTEM BASED ON CLASSICAL AND FUZZY PID LIKE CONTROLLER USING THE GREY WOLF OPTIMIZATION ALGORITHM</b><br>Vladimir Zarić, Natalija Perišić, Radiša Jovanović | 23 |
| <b>SYSTEM IDENTIFICATION USING HAMMERSTEIN-WIENER MODEL WITH ORTHOGONAL POLYNOMIALS</b><br>Anđela D. Đorđević, Saša S. Nikolić, Marko T. Milojković, Miodrag D. Spasić, Staniša Lj. Perić | 31 |
| <b>ADAPTIVE DYNAMIC PROGRAMMING BASED OPTIMAL CONTROL FOR HYDRAULIC SERVO ACTUATOR</b><br>Vladimir Djordjevic, Marcelo Menezes Morato, Vladimir Stojanovic                                | 37 |
| <b>SPEED-CONTROLLED HYDRAULIC DRIVE SYSTEMS FOR HEAVY MACHINERY</b><br>Darko Lovrec, Vito Tič   | 43 |
| <b>DESIGN OF PID CONTROLLERS FOR THE SYSTEM OF A PUMP CONTROLLED HYDRO-MOTOR</b><br>Ljubiša Dubonjić, Saša Prodanović, Novak Nedić  | 55 |
| <b>STRUCTURAL LINEAR MODELING OF ELECTROHYDRAULIC ACTUATION SYSTEM WITH HYDRAULIC CYLINDER</b><br>Dragan Nauparac   | 61 |
| <b>TRIBOLOGICAL TEST DEVICES AS HEAVY MACHINERY</b><br>Vito Tič, Darko Lovrec   | 67 |
| <b>THE ANALYSIS OF A SUSTAINED OSCILLATION IN THE HEAT PUMP SYSTEM WITH BUFFER TANK</b><br>Dragan Pršić,, Aleksandar Vičovac, Marko Nešković  | 75 |
| <b>OFFLINE ROBOT PROGRAMMING USING ABB ROBOTSTUDIO</b><br>Vojislav Vujičić , Ivan Milićević, Milan Marjanović, Nedeljko Dučić, Aleksandar Jovičić , Snežana Dragičević                    | 79 |

## **SESSION D: APPLIED MECHANICS**

|  |   |
|--|---|
| <b>NONLINEAR OSCILLATIONS OF A PENDULUM WRAPPED AROUND A CYLINDER</b><br>Anastas Ivanov Ivanov | 1 |
|--|---|

|  |           |
|--|-----------|
| <b>ANALYSIS OF CENTRIFUGAL COMPRESSOR TESTING CAPABILITIES</b><br>Stojko Biočanin, Milica Timotijević  | <b>9</b>  |
| <b>APPLICATION OF DENAVIT-HARTENBERG METHOD TO ROBOT MODEL KUKA IR 161/15.0</b><br>Đorđe Jovanović, Branislav Milenković   | <b>15</b> |
| <b>APPLICATION OF GRASSHOPPER ALGORITHM FOR SOLVING OPTIMIZATION PROBLEMS IN ENGINEERING</b><br>Branislav Milenković, Radovan Bulatović, Ivana Atanasovska   | <b>19</b> |
| <b>CONTRIBUTION TO THE PROBLEM OF IN-PLANE VIBRATION OF CIRCULAR ARCHES WITH VARYING CROSS-SECTIONS</b><br>Slaviša Šalinić, Aleksandar Obradović   | <b>27</b> |
| <b>THE INFLUENCE OF SPATIAL ALIASING TO EXPERIMENTAL DETERMINATION OF DISPERSION RELATIONSHIP OF FLEXURAL WAVES IN BEAMS BY CORRELATION METHOD</b><br>Vladimir Sinđelić, Snežana Ćirić Kostić, Branko Radičević, Zlatan Šoškić | <b>33</b> |
| <b>EXPERIMENTAL DETERMINATION OF DISPERSION RELATIONSHIP OF POLYAMIDE THIN BEAMS</b><br>Jelena Tomić, Vladimir Sinđelić, Aleksandar Nikolić, Nebojša Bogojević   | <b>39</b> |
| <b>FREE VIBRATION OF DOUBLE-CRACKED UNIFORM BEAM</b><br>Aleksandar Nikolić   | <b>47</b> |

## **SESSION E: RAILWAY ENGINEERING**

|   |           |
|---|-----------|
| <b>A METHOD FOR TRANSFORMATION OF BETWEEN THE CRITERIA AGAINST DERAILMENT OF RAIL VEHICLES OF VARIOUS CLASS</b><br>Dobrinka Atmadzhova  | <b>1</b>  |
| <b>RESEARCH AND ANALYSIS OF ELECTRICITY QUALITY PARAMETERS FOR TRACTION OF TRAINS WITH MULTISYSTEM LOCOMOTIVE "SIEMENS VECTRON X4-E-LOC-AB, A26"</b><br>Branislav S. Gavrilović, Zoran Bundalo, Aleksandar B. Blagojević            | <b>11</b> |
| <b>DETERMINATION OF OPTIMAL LAYOUT, NUMBER AND WAY OF CONNECTION OF STRAIN GAUGES ON INSTRUMENTED RAILWAY WHEELSETS</b><br>Milan Bižić, Dragan Petrović   | <b>17</b> |
| <b>FAILURE ANALYSIS IN PASSENGER BOGIES FROM THE RAILWAY SYSTEM OF THE REPUBLIC OF BULGARIA</b><br>Vanio Ralev, Dobrinka Atmadzhova   | <b>23</b> |
| <b>BRAKING – PRECONDITION FOR FASTER MOVEMENT OF RAILWAY VEHICLES</b><br>Dragan Petrović, Milan Bižić   | <b>33</b> |
| <b>NUMERICAL ANALYSIS OF WAGON LEAF SPRING USING ANSYS SOFTWARE PACKAGE</b><br>Mladen Krstić, Branislav Milenković, Đorđe Jovanović   | <b>39</b> |
| <b>EXPERIMENTAL AND NUMERICAL STRENGTH ANALYSIS OF FREIGHT WAGON TYPE SHIMMNS INTENDED FOR THE TRANSPORTATION OF THE SHEET COILS</b><br>Vladimir Milovanović, Miroslav Živković, Snežana Vulović, Aleksandar Dišić, Marko Topalović | <b>45</b> |

|   |           |
|---|-----------|
| <b>INFLUENCE OF THE TRACTION FORCE AND THE SPEED OF MOVEMENT ON THE STRENGTH CHARACTERISTICS OF THE LOCOMOTIVE AXLES</b>                                  | <b>53</b> |
| Vasko Nikolov   |           |
| <b>RESEARCH AND ANALYSIS OF THE WEARING OF THE ELEMENTS OF AXLE ROLLER BEARINGS</b>   | <b>63</b> |
| Lyudmil Paskalev  |           |
| <b>REGARDING REQUIREMENTS FOR THE DESIGN AND INSTALLATION OF ELEMENTS FOR PASSIVE SAFETY OF PASSENGER TRAINS OPERATED BY THE BULGARIAN STATE RAILWAYS</b> | <b>67</b> |
| Venelin Pavlov  |           |
| <b>DETERMINING THE LONGITUDINAL FORCE IN COLLISION OF TWO WAGONS</b>  | <b>77</b> |
| Milica Timotijević  |           |

## **SESSION F: THERMAL TECHNIQUE AND ENVIRONMENT PROTECTION**

|  |           |
|--|-----------|
| <b>THE IMPORTANCE AND BENEFIT OF THE ENERGY MANAGEMENT STANDARD IMPLEMENTATION</b>   | <b>1</b>  |
| Andjela Lazarevic, Ivana Marinovic Matovic   |           |
| <b>SOME ASPECTS OF THE IMPLEMENTATION OF ACTIONS PLANS FOR NOISE PREVENTION AND REDUCTION IN URBAN AREAS</b>                                 | <b>7</b>  |
| Vasile Bacria, Nicolae Herisanu  |           |
| <b>APPLICATION OF BIOLOGICALLY INSPIRED ALGORITHMS FOR DETERMINING THE COEFFICIENTS OF EMPIRICAL MODELS FOR DETERMINING SOUND ABSORPTION</b> | <b>13</b> |
| Kolarević Milan, Radičević Branko, Mišo Bjelić, Tanja Miodragović, Goran Miodragović   |           |
| <b>COMPOSITE MATERIALS THAT ARE GOOD SOUND ABSORBERS</b>   | <b>21</b> |
| Tanja Miodragović, Olivera Erić-Cekić, Branko Radičević, Vladan Grković  |           |
| <b>NON-EXHAUST PM EMISSIONS FROM HEAVY-DUTY VEHICLES</b>   | <b>29</b> |
| Jasna Glišović, Saša Vasiljević, Nenad Miloradović, Nadica Stojanović, Ivan Grujić   |           |
| <b>STANDARDS, REGULATIONS AND LEGISLATION OF USED MOTOR OIL MANAGEMENT AND DISPOSAL – A REVIEW</b>   | <b>37</b> |
| Jelena Mihajlović, Nevena Marković, Goran Petrović, Danijel Marković, Žarko Čojbašić   |           |
| <b>THE USAGE OF SHALLOW GROUNDWATER HEAT BY HEAT PUMPS IN A HIGH-TEMPERATURE DISTRICT HEATING SYSTEM</b>                                     | <b>43</b> |
| Dragiša Šimunović, Rade Karamarković, Miloš Nikolić, Đorđe Novčić, Anđela Lazarević  |           |
| <b>OPTIMIZATION OF COMPACT HEAT EXCHANGERS</b>   | <b>51</b> |
| Miljan Marašević, Nebojša Bogojević, Nenad Stojić, Stefan Adžić, Dragiša Šimunović,  |           |
| <b>GRADUAL COMBUSTION OF WOOD LOGS BY THE USE OF PREHEATED AIR</b>   | <b>57</b> |
| Đorđe Novčić,, Miloš Nikolić, Rade Karamarković, Dragiša Šimunović   |           |

## **SESSION G: CIVIL ENGINEERING**

|   |           |
|---|-----------|
| <b>INTERACTION DIAGRAMS IN LIMIT AND SHAKEDOWN ANALYSIS</b><br>Bojan Milošević, Žarko Petrović, Saša Marinković   | <b>1</b>  |
| <b>THE INFLUENCE OF DIFFERENT TYPE OF AGGREGATE, FLY ASH AND FIBER REINFORCED POLYMER ON SPLITTING RESISTANCE IN PRETENSIONED CONCRETE RAILROAD TIES</b><br>Adrijana Savić, Robert J. Peterman                    | <b>11</b> |
| <b>LOAD-BEARING CAPACITY AND THERMAL CONDUCTIVITY OF AXIALLY LOADED WALLS IN ACCORDANCE WITH EC6</b><br>Iva Despotović, Bojan Milošević, Marina Nikolić – Topalović, Vladimir Mandić, Stefan Mihajlović           | <b>19</b> |
| <b>ANALYSIS OF COST AND TIME REQUIRED FOR THE CONSTRUCTION OF RC DIAPHRAGMS DEPENDING ON THE METHOD OF EXECUTION</b><br>Stefan Mihajlović, Saša Marinković, Vladimir Mandić, Iva Despotović, Marijana Janićijević | <b>25</b> |
| <b>SERVICEABILITY LIMIT STATE ANALYSIS OF A CRACKED CROSS-SECTION IN ACCORDANCE WITH SRPS EN1992-1-1 AND PBAB'87</b><br>Saša Marinković, Bojan Milošević, Stefan Mihajlović, Marijana Janićijević, Žarko Petrović | <b>33</b> |
| <b>EFFICIENCY ANALYSIS OF TWO SPATIAL INTERPOLATION METHODS OF PRECIPITATION ON THE KOLUBARA RIVER BASIN</b><br>Vladimir Mandić, Iva Despotović, Miloš Šešlija, Stefan Mihajlović, Slobodan Kolaković             | <b>43</b> |

# **PLENNARY SESSION**



# Modal Space Based Real-Time FE Simulations of Complex and Multifunctional Structures

Dragan Marinkovic<sup>1,2\*</sup>

<sup>1</sup>Faculty of Mechanical Engineering and Transport Systems, Department of Structural Analysis, Berlin Institute of Technology, Berlin (Germany)

<sup>2</sup>Faculty of Mechanical Engineering, University of Nis, Nis (Serbia)

*The finite element method (FEM) has imposed itself to structural analysts and engineers as the most powerful, highly efficient and quite versatile numerical method. It became a standard method in the field of structural analysis, with very well established and understood procedures of development and application. Numerous FE software packages have been developed offering vast options of numerical analysis to the users. But, so far, all of them have one aspect in common – the conducted computations are the so-called ‘off-line’ computations. This implies that the action of applying the loads onto the model, on one side, and observing the resulting behavior of the model, on the other side, are separated by a substantial amount of time that varies between seconds and hours depending on numerous parameters. However, an incredible pace of both hardware and software developments in recent decades brought the idea of real-time FE computations to life. This paper is focused on this enticing field of work and presents some of the originally proposed solutions to address real-time solutions in FE simulation based on modal superposition technique.*

**Keywords:** Real-time simulation, FEM, Modal superposition, Geometric nonlinearity, Adaptive structures

## 1. INTRODUCTION

In order to deal with real world problems, engineers build models that need to meet two basic requirements. On the one hand, the models must include the most important aspects of the modelled system’s physical behavior so that the real system is suitably represented for the specific purpose of modelling. On the other hand, the models need to be as simple as possible in order to make them mathematically/numerically tractable. Searching for an adequate compromise between these two confronting demands is not an easy task and it needs to account for available modelling tools. More powerful tools allow to move the borders of modelling from simpler to more complex models that account for more details and additional aspects of physical behavior, whereby the computational times are still kept in a reasonable range. In structural engineering, numerical models are typically used because analytical models could not cope with arbitrary geometries and boundary conditions. This is where the Finite Element Method (FEM) comes into play.

FEM has deservedly gained its reputation of being the most powerful method in the fields where solving partial differential equations over arbitrary domains and with arbitrary boundary conditions is required. And this is particularly valid for the field of structural analysis that actually contributed at most to the FEM development. Although relatively new, today FEM is a well-established method. It is a standard tool used in the design of new structures, proof of strength of existing structures, optimization tasks, etc. Typical computations are performed ‘off-line’. Actually, this term appeared only recently as an opposite of ‘on-line’ computation. In this sense, ‘off-line’ implies that the model, together with all the necessary data, is prepared in the preprocessor, while the results are observed and analysed in the postprocessor. Between the two, the solver performs its ‘magic’ in order to transform the input data into the results containing the

displacement, strain and stress fields together with other results at user’s choice. Hence, there is a substantial amount of time between setting the model (preprocessor) and observing the results (postprocessor) and it ranges between seconds and hours, depending on the size of the model, type of analysis, available hardware and software, etc.

However, it is the fast pace of hardware development in the recent years that motivated the idea of real-time FE simulation, i.e. ‘on-line’ FE computations. The idea is of great interest for numerous potential users. Not only would engineers prefer to have the results of their calculations as fast as possible (not necessarily in real-time), but there are also fields where real-time simulation is the most important demand. This pertains to various types of simulators, such as surgery simulators, training simulators, etc.

Various ideas have been addressed in the previous three decades to achieve the objective of real-time simulation. Those ideas reflect the needs and the hardware and software development at that time. As a simplest possible approach, mass-spring systems have been mostly used in the 90’s, but there are also developments of newer date [1, 2, 3]. The simplicity of a mass-spring model is its main advantage – the continuum is replaced by a set of concentrated masses interconnected with springs. Such a model can easily account for geometrically nonlinear effect, because the internal forces of springs are always oriented in the direction defined by the current positions of connected masses (nodes). Also the material nonlinearities can relatively easily be accounted for because otherwise complex strain/stress field is reduced to only one component of strain/stress in the applied rod elements. However, the major problem resides in building the model. One needs to decide how many masses are needed, how they are to be distributed across the continuum, how the topology of interconnections should be defined, what

\*Corresponding author: TU Berlin, Strasse d. 17. Juni 135, 10623 Berlin, Germany, dragan.marinkovic@tu-berlin.de

would be the suitable stiffness of springs/rod elements. Hence, this ambiguity of model building is the major drawback of the approach [4], but there also belongs the fact that no single solution is possible that would produce high accuracy for any set of material parameters and boundary conditions. Despite of that, this approach has been and still is one of the workhorses in many real-time applications, primarily there where only visual effects are of interest and mostly for the background effects, such as in surgery simulators [5].

Another interesting approach may be interpreted as belonging to the group of the model order reduction techniques. Namely, it is a kind of indirect model order reduction. The idea is to use FEM results in order to train the neural networks to produce fast computations for various scenarios with a specific model. A great advantage of this approach resides in the fact that nonlinearities of any kind can be tackled. On the other hand, the major drawback is to be sought in quite demanding and time-consuming FE computations needed for training purposes. Also, changes in kinematic boundary conditions, material parameters and similar would require to perform a new set of computations for training purposes, thus cancelling the positive aspects to a great extent. Despite of that, the idea has already found its application in structural computations [6], virtual reality simulators [7], and particularly in systems for real-time control [8, 9].

It is also possible to perform model order reduction directly in the framework of FEM. This approach has a great potential to reduce the numerical effort by several orders of magnitude. It is a common knowledge that FE models are quite large, often having several 100,000 degrees of freedom (DOFs). Hence, the resulting system of equations contains the same number of equations as there are DOFs in the system. The most time-consuming part in computing the solution is resolving the system of equations. However, there are suitable ways of transforming the problem and thus reducing dramatically the number of DOFs. Typically, one would transform the problem into the modal space, in which each mode represents a degree of freedom [10]. In many cases, a relatively small number of carefully selected modes would produce quite a solid result and this fact is used to produce highly efficient simulations, and even real-time simulations. This fact has been extensively used in Multi-Body-System (MBS) dynamics. Of course, this advantage does not come alone. There is also a drawback in the fact that the modes are valid for one specific structure configuration, thus making the approach suitable for linear computations, which is an important limitation. However, there have been some developments aiming at inclusion geometrically nonlinear effects [11, 12]. This aspect will be addressed in this paper.

Anyway, the most challenging task in FE-based real-time simulation is to keep the full extend FE model (no model reduction) and try to produce a real-time simulation. The level of complexity increases significantly if the demand to cover any type of nonlinearity is included, because this implies changeable structural parameters (primarily the stiffness matrix) which need to be determined again for each new structural configuration. In addition, resolving the system of equations is more time-consuming for nonlinear problems. In such cases,

even with a relatively small number of DOFs, rigorous nonlinear formulations render the problem numerically very demanding and the only way of achieving real-time simulation would be to use extremely powerful hardware and the parallelization possibilities [13]. Most of developments in the fields of virtual reality (VR) and augmented reality (AR) applications were based on linear FE models in the early days of development [14]. The same approach was used in biomedical applications [15, 16]. With the available hardware and software at that time, even the use of linear models was rather challenging.

However, over the course of development, researchers have noticed that various 'tricks' could be applied in order to make a trade-off between the numerical efficiency and achievable accuracy and thus make the inclusion of nonlinear effects mathematically tractable [17, 18]. The 'tricks' mostly consisted in substituting rigorous nonlinear formulations by some simpler formulations that keep the nonlinear effects to a large extent thus producing visually appealing results [19, 20]. Such approaches are mainly used in VR applications.

Marinkovic and Zehn [21] provided a comparative survey of these techniques, in which the major directions of development are discussed and the state-of-the-art in the field of FE-based real-time simulation is represented.

## 2. MEANS OF ACHIEVING FE-BASED REAL-TIME SIMULATION

The first question to be tackled refers to the definition of real-time simulation. Although the term 'real-time simulation' may seem intuitive, the standard definition allows for a wider interpretation. The intuitive comprehension of the term would imply that anything that happens within a certain period of time  $\Delta t$  is computed and presented on the screen within the same period of time  $\Delta t$ . On the other hand, the standard DIN ISO/IEC 2382 [22] states that this term denotes such an operation of a computing system that provides the results within a prescribed period of time. Hence, this definition does not necessarily demand that the computation takes the wall-clock time needed for the process to occur in reality, but could also take a longer time, if this suits the computational requests, or maybe even a shorter time.

At this point, one may note the multidisciplinary of the problem. Namely, it combines the fields of mechanics, numerical computation and computer graphics. Besides the displayed physical behavior of the objects, it is also the quality of the animation and rendering that determines the very first impression about the achieved results.

The question arises: what would be the means to achieve FE-based real-time simulation? The most obvious means are more powerful hardware components and software that is more sophisticated. A less obvious means would be modified formalisms for structural analysis. One could make a nice parallel between the real-time simulation and the objective of setting the fastest time in a F1 car around a racing track. Obviously, more powerful hardware would correspond to a better F1 car in terms of more powerful engine, better aerodynamics, downforce, etc. More sophisticated software corresponds to a better, faster driver. Now, if the hardware would be limited to typical personal computers, whereby the aspect of possible

parallelization is neglected, the achievable gains in computational times would be within several percent. Available software options would even make a smaller difference, although the aspect of software optimization should not be easily neglected. What remains as an interesting option is to play around with formalisms of structural analysis. Again, making a parallel with fastest time around a racing track, this would correspond to the option of reconstructing the track itself. Assuming that the start and finish lines remain the same, one may want to reconstruct the track in order to avoid numerous curvatures so that higher speeds can be used along the track. This would reduce the lap time considerably. And this is exactly the idea used here as it offers the greatest potential of reducing the computational time. It implies that the rigorous formalisms may be suitably modified to account for major effects (but not all the details) so that less computational operations are needed to reach the 'finish line'. Of course, with certain aspects neglected, one would not land exactly at the 'finish line' but somewhere nearby. This is exactly the already mentioned trade-off between the computational effort and achievable accuracy. Depending on the specific application, this trade-off may be either more in the favor of accuracy or more in the favor of computational efficiency.

### 3. MODAL SPACE BASED FE-MODEL REDUCTION

With the objective of reducing the computational burden considerably compared to the approach based on the full extent FE models, a model reduction is performed. Different approaches may be found in the literature, some of which are mentioned in the Introduction, but the most common approach is the modal space based approach. The approach implies that orthogonal mode shapes, determined in a step prior to MBS simulation, become modal degrees of freedom, in terms of which the deformational behavior of a structure is described. Why is this approach so efficient? Not only is the number of degrees of freedom in this manner dramatically reduced (by several orders of magnitude), but the resulting equations are also decoupled. This is due to the property of the eignemodes that are orthogonal with respect to both the mass and stiffness matrices. For this reason, the generalized mass and stiffness matrices are diagonal and the resulting system of equations decoupled. In other words, the structural response in each of the modes is totally independent from the structural response in other modes.

The eigenmodes used in FEM are the result of the modal analysis. The corresponding eigenvalue problem is obtained by assuming free vibrations with damping neglected:

$$[M]\{\ddot{u}\} + [K]\{u\} = \{0\} \quad (1)$$

where  $[M]$  and  $[K]$  are the mass and stiffness matrices of the FE model, and  $\{u\}$  are the nodal displacements with dots above denoting the time derivatives (two dots for acceleration). Upon assuming a harmonic solution, one obtains the following eigenvalue problem:

$$([K] - \omega_i^2 [M])\{\phi_i\} = 0 \quad (2)$$

where  $\{\phi_i\}$  is the  $i^{\text{th}}$  mode shape vector, and  $\omega_i$  the corresponding angular eigenfrequency. The dynamical problem given by the FE system of equations:

$$[M]\{\ddot{u}\} + [C]\{\dot{u}\} + [K]\{u\} = \{f_{\text{ext}}\} \quad (3)$$

where  $[C]$  is the damping matrix and  $\{f_{\text{ext}}\}$  are the external forces. It is then transformed into the modal space:

$$[\tilde{M}]\{\ddot{z}\} + [\tilde{C}]\{\dot{z}\} + [\tilde{K}]\{z\} = \{\tilde{f}\} \quad (4)$$

where

$$[\tilde{M}] = [\Phi]^T [M] [\Phi], \quad [\tilde{C}] = [\Phi]^T [C] [\Phi],$$

$$[\tilde{K}] = [\Phi]^T [K] [\Phi], \quad \{\tilde{f}\} = [\Phi]^T \{f\}$$

with  $[\Phi] = [\{\phi_1\} \{\phi_2\} \dots \{\phi_n\}]$  being the modal matrix (matrix of modal shapes). This is the typical way of transforming the FE equations into the modal space and thus reducing the FE model significantly (easily several orders of magnitude), whereby the resulting system of equations is additionally decoupled.

It is worthwhile to emphasize that the quality of the results obtained with modal approach strongly depends on the quality and number of the mode shapes used in the simulation. The mode shapes determined in the way described above are valid for a specific structural configuration and a specific set of boundary conditions. In MBS problems, one has often to deal with changeable boundary conditions. Hence, the approach used by commercial software package like ADAMS is the Component Mode Synthesis (CMS) technique, particularly the Craig-Bampton method. The method requires to partition the flexible body degrees of freedom (DOFs) into boundary DOFs and interior DOFs, the former belonging to the nodes of the FE-model that the user wants to retain in the simulation model mainly for the purpose of defining (kinematic or dynamic) boundary conditions. In the next step, the method requires to determine two sets of modes: 1) *constraint-modes*, which are static shapes obtained by giving each boundary DOF a unit displacement, while all other boundary DOFs are fixed; 2) *fixed-boundary normal modes*, which are obtained by fixing all boundary DOFs and computing the eigensolution as given above. Now, the so-obtained Craig-Bampton modes are not an orthogonal set of modes. For that reason they are orthonormalized prior to simulation in order to make them more suitable for direct use in MBS dynamics.

As already emphasized, in this manner, FE models can be reduced by several orders of magnitude. An example of a car rear axle, Fig. 1, can be used for obvious demonstration of this advantage.



Figure 1: Car rear axle

Fig. 2 depicts the full extent FE model prepared at the Institute of Mechanics, TU Berlin. It includes 42324 4-node shell elements, 1356 3-node shell elements, 4328 8-node hexahedral elements and 504 6-node wedge

elements. Altogether, there are 50192 nodes, most of which use 6 DOFs as they belong to shell elements and therewith there are nearly 300000 DOFs in the model. Hence, solving the full model in a dynamical analysis would imply solving a great number of equations in each time-step.



Figure 2: FE model of the car rear axle

Upon model reduction, one may decide to keep a number of orthogonal modes. Of course, the choice of modes to be kept has a crucial influence on the final simulation results. There are numerous criteria that will not be addressed here on how to choose a sufficient number of modes and which modes exactly are relevant. In many simulations, it would be sufficient to take 10-20 modes, which implies that the simulation is performed with much less DOFs compared to the full extent FE model, and the accuracy would still be acceptable. Fig. 3 shows two screen-shots of real-time simulation with the car axle. Practically any CPU can perform this real-time simulation. The only difference in the speed of simulation would be determined by the demanding graphics of rendering the faces of nearly 50000 elements.



Figure 3: Screen-shots of real-time simulation with the car rear axle

### 3.1. Inclusion of Geometrically Nonlinear Effects

Modal space based reduction of FE models is an excellent way of reducing the numerical effort greatly. This is practically done by performing a great deal of computation prior to simulation. Namely, the effort resides in the modal analysis needed to obtain the modal degrees of freedom and modal mass and stiffness matrices.

However, the limitation encountered with this approach is in the fact that the modes are valid only for the initial structural configuration and, therewith, the approach is applicable to linear analysis. In order to extend the applicability of the approach to moderate geometrically nonlinear effects, a few approaches have been originally proposed.

The first approach is based on the implementation of the geometric stiffness matrix. The idea is to account only for the stress stiffening effects. This is done through a simplified computation of the geometric stiffness matrix. The stresses are assumed to be linearly proportional to the deformation in each single mode, which is an assumption made in the linear analysis. In this manner, the overall stress is easily approximated as a linear superposition of stresses in single modes. Based on these assumptions, the geometric stiffness matrix is approximated and added to

the linear stiffness matrix over the course of computation. In terms of numerics, the approach is only slightly more expensive than the pure modal superposition technique, and if it is carefully used for the cases to which it is applicable, it offers a highly efficient extension into moderate geometric nonlinearities. This method was presented by Marinkovic and Zehn [11].

Another approach, denoted as warped displacement approach, aims at consideration of geometrically nonlinear effects caused by relatively large rotation of single subdomains of the structure with respect to the structure as a whole. For carefully chosen substructures, the average rigid-body rotation with respect to the whole structure is computed based on the classical modal-space solution. This rotation is further used to rotate the displacement field of the considered substructure, which improves the accuracy of the obtained deformed geometry. More details about the method can be found in Marinkovic and Zehn [11]. The rear car axle is quite a suitable example for this approach. The crank arms are the substructures, to which the approach is to be applied, Fig. 4.



Figure 4: Subdomains for modal displacement warping

In order to test the approach with respect to achievable accuracy of deformed configuration, two load cases suggested by Volkswagen AG are computed. Load case 1 is a vertical force of 1 kN acting upon the wheel, while load case 2 is a side force of 7 kN (see Fig. 5).

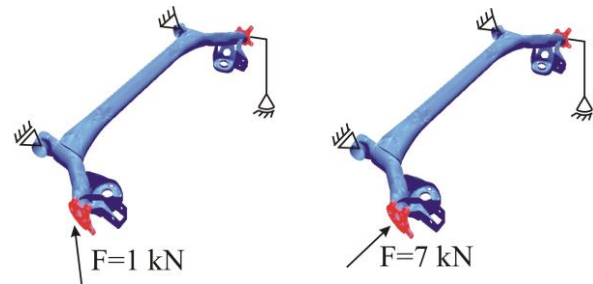


Figure 5: The considered load cases

The deformation is determined by means of presented technique with 10 and 20 modes and compared with the results obtained by rigorous FE results from Abaqus. Diagrams in Figs. 6 and 7 show the results. The suspension travel is given versus toe-angle – hence, two geometric quantities, both of which are of crucial importance for suitable prediction of the car path in a curve. Compared to the linear result, one can easily note the significant improvement of the result obtained with the presented approach. Actually, those results are relatively close to the geometrically nonlinear results from Abaqus, demonstrating the applicability of the approach in this specific case. At the same time, the efficiency of computation remains extremely high as it easily runs in real-time.

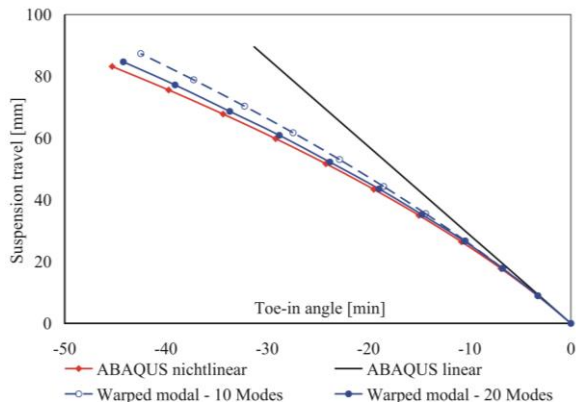


Figure 6: Load case 1: suspension travel vs. toe-in angle

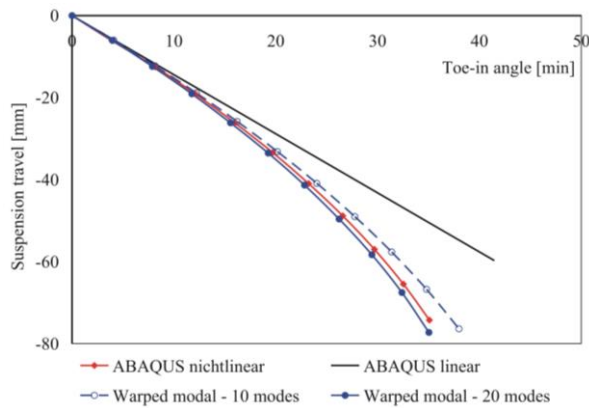


Figure 6: Load case 2: suspension travel vs. toe-in angle

Another interesting approach to account for geometrically nonlinear effects is a combined approach, i.e. a model that combines a modal reduction and the full extent FE model. In many cases, a linear model can adequately describe a large portion of the considered structure, but some structural sub-domains may exhibit nonlinear behavior. In such a case, the modal-space solution can be used for the linear part of the model, whereas the nonlinear sub-domain are to be described by a full geometrically nonlinear FE model. The two parts of the model are then adequately coupled to each other. A simple illustration of this approach is given in Fig. 8 left, where a modal space based model is used for the tower crane, but the steel ropes and the suspended mass remain a separate part of the model, as it exhibits large rotations with respect to the tower crane.

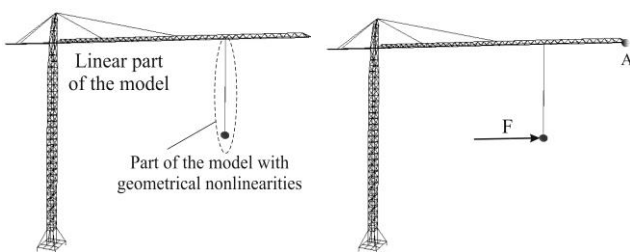


Figure 8: Left: combined model of a tower crane with suspended load; Right: initial configuration with excitation force

A simple example is taken to demonstrate the approach. A load (300 kg) is suspended on the rope and exposed to a short impulse force (5 kN) in duration of  $10^{-3}$  s (Fig. 8, right). The displacements of the working jib tip (point A) is observed. The problem was computed in Abaqus by using the full extend FE model and the rigorous

geometrically nonlinear analysis. Hence, it was a relatively expensive simulation in terms of computational time. The problem was also solved by means of the combined model. The tower crane was considered to be a linear model and the modal reduction was applied to this part of the model in order to reduce the numerical effort as much as possible. However, it was necessary to consider the rope with the suspended load as a nonlinear part of the model, because the rope exhibits significant rotations while swinging, thus constantly changing the direction of the force that acts onto the crane jib. In the conducted analysis, the static computation is done first to determine the statically deformed initial configuration. This is actually the configuration at time  $t=0$  s. In Fig. 9, one may notice the difference in the static deflection of the crane jib computed by the present model and by Abaqus. This is clearly the consequence of the fact that the tower crane model alone determines this response and, in the presented approach, it a linear model, while the Abaqus model employs the rigorous geometrically nonlinear computation based on the updated Lagrange formulation.

The results given in Fig. 9 show a relatively good agreement between the two formulations, particularly having in mind the difference in the initial configurations of both computations. It should be emphasized that the rigorous geometrically nonlinear computation in Abaqus was done with the model containing 1773 DOFs, while the model used with the presented formulation has only 13 degrees of freedom (10 modes and the 3 displacements of the suspended load). In addition, Abaqus must solve the problem incrementally and iteratively, with the coupled system of equations solved in each iteration. Consequently, performing the both computations with the same time-step, the computational time in Abaqus was three orders of magnitude greater (measured in seconds) than the one needed for the presented combined formulation.

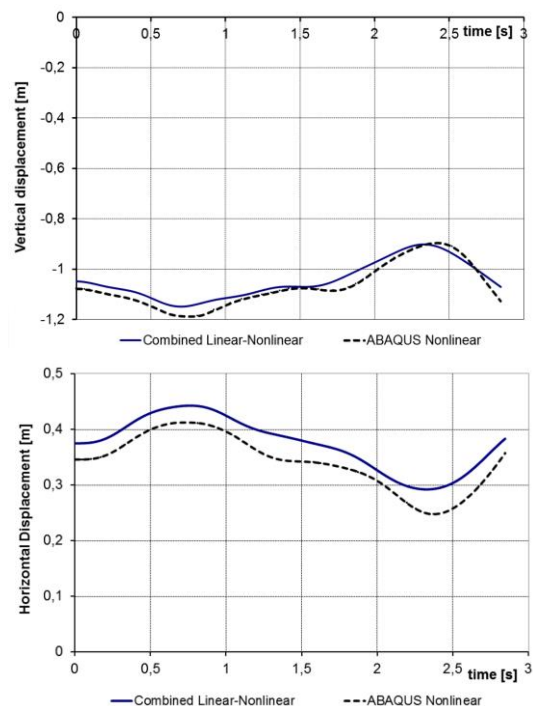


Figure 9: Displacements of the crane jib tip: up - vertical displacement; down - horizontal displacement

### 3.2. Application to Adaptive Structures

The general idea of adaptive/multifunctional structures consists in using advanced multifunctional materials in order to design and integrate active elements, i.e. sensors and actuators, into structures and thus provide the means for their adaptive behavior. The active elements can also be added as additional devices, if such a design suits the structure better. Sensors provide signals that contain information about the state of the structure. The sensor signals are transmitted to a controller that implements the control law, i.e. the desired structural behavior. Hence, the controller processes the sensor signals and determines what action should be performed by actuators in order to produce a desired structural behavior. The corresponding signal is then sent to actuators. In this manner, the active elements, sensors and actuators, are coupled to each other by means of a controller and an active structure becomes adaptive – it can actively react to external excitations in order to adapt its response, mainly with the objective to protect its integrity. In this way, the adaptive systems mimic actually the behavior of natural systems.

The adaptive structural behavior can be used to achieve different objectives. The control of their dynamic behavior belongs to the most common objectives. This approach allows to improve many aspects of their dynamic behavior, such as comfort, robustness and safety. As vibrations in certain regimes of work (e.g. resonance) can give rise to serious structural damage, vibration suppression is quite a common objective of adaptive structural behavior. An example of adaptive structural behavior would be the adaptive car roof depicted in Fig. 10. In this case, the adaptive behavior of the roof is used to suppress its vibrations with the final objective of diminishing noise in the car and thus improving driving comfort of passengers.



Figure 10: Displacements of the crane jib tip: up - vertical displacement; down - horizontal displacement

Control of complex structures with a large number of DOFs would be mathematically a very demanding task. It would be extremely difficult to design algorithms that would efficiently address such problems. Hence, an elegant idea to resolve the problem is needed. There is such an idea and it is closely related to the mode superposition technique discussed above. Its essence is to perform control within a specific frequency range by putting the focus onto the structural vibration modes (eigenmodes). It has been already seen that the structural modes are the DOFs in terms of which the structural response is determined. This fact is massively used in the control of such complex systems. Namely, the eigenmodes are simply regarded as degrees of freedom to be controlled.

The same tower crane already seen above is used as an example. Without getting into details on exactly what kind of effect could be realistically used for this purpose, it is assumed at this point that a truss element can act as both a sensor and an actuator. As a sensor, the element can measure the strain in the element, and as an actuator, it may produce a desired force. Strain rate proportional active damping is implemented in the four active elements at the bottom of the crane (Fig. 11).

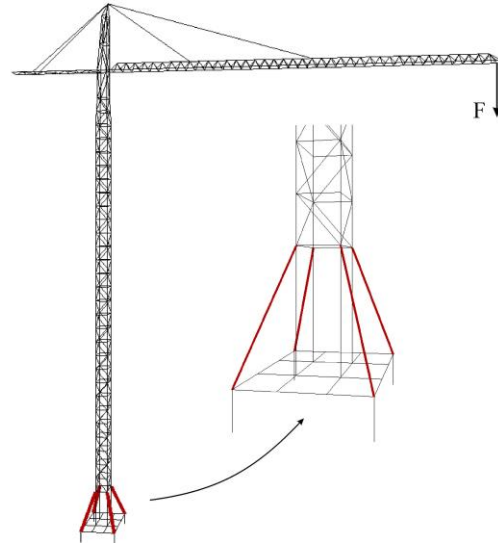


Figure 11: Tower crane with active elements and excitation

From the strains measured by the sensors in the four elements, the strain rate is determined and a force proportional to the strain rate and acting oppositely to the strain rate is induced in each active element. An external force is set to act at the jib tip as an impulse in duration of 0.5 s. The active control is. The diagram in Fig. 12 shows the vertical displacement of the jib tip, with (blue line) and without (red line) active damping turned on after 3 s. The first ten eigenmodes are used for the simulation and such a simulation runs in real-time.

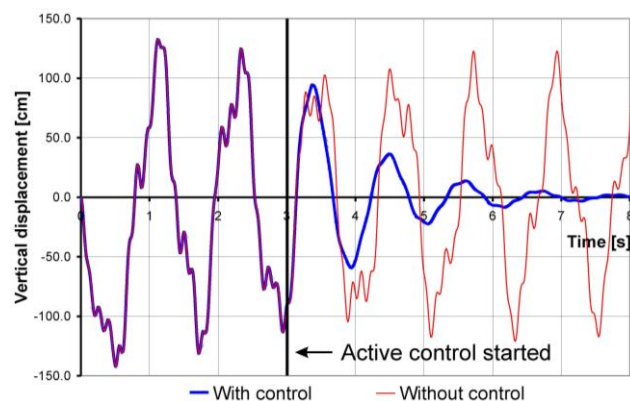


Figure 12: Tower crane – vertical displacement of the jib tip with and without active damping

The same concept is also demonstrated on another simple example, namely a plate structure depicted in Fig. 13. The structure is meshed using 480 recently developed piezoelectric triangular shell elements [23]. Two load cases are considered, in both of which structure is exposed to a concentrated force acting as a short impulse. The load case 1 implies that only the excitation force  $F_1$  acts in the middle of the structure, while in the load case 2, it is only

the force  $F_2$  that acts (Fig. 13). The response is determined using the first 12 eigenmodes for the modal superposition technique. It is straightforward to recognize the motivation for changing the position at which the force acts in the second load case. Namely, in the first case, primarily the first eigenmode (first bending mode) is excited and it dominates the structural response, while the second case excites practically all the considered modes (although some of them to an extremely small extent).

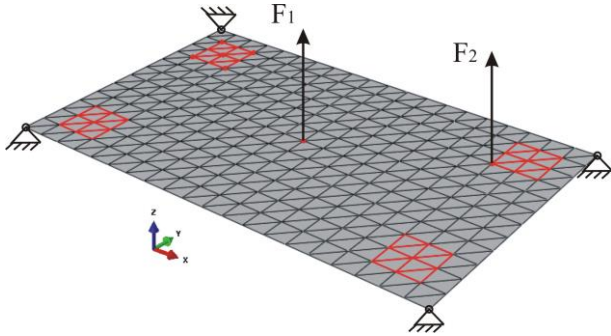


Figure 13: FE model of the plate: position of active elements (red elements) and two considered load cases

The selected position of four pairs of active piezoelements is also depicted in Fig. 13 by red lines. The patches on the lower surface of the structure play the sensor role, while the patches on the upper (visible) surface act as actuators. The vertical displacement at the mid-point is observed during the simulation as a representative result. It is given for the case without active control (thin red line in Figs. 14 and 15) and with the active control started at  $t=5s$  (thick blue line in Figs. 14 and 15). The structural response without active control is characterized by relatively small damping implemented in the model. The active control enhances damping significantly. As already said, in the first case, it is primarily the first eigenmode that is excited, which is also visible from the diagram, while in the second case practically all the considered modes are excited. It is easily recognized in the first response that there is only one frequency, whereas in the second response several frequencies can be noted. But the efficiency of active control is the same in both cases and the simulation runs easily in real-time. This example resembles the case of active noise reduction in a car (Fig. 10). Basically the same approach would be used, with the only difference in the selection of modes to be controlled.

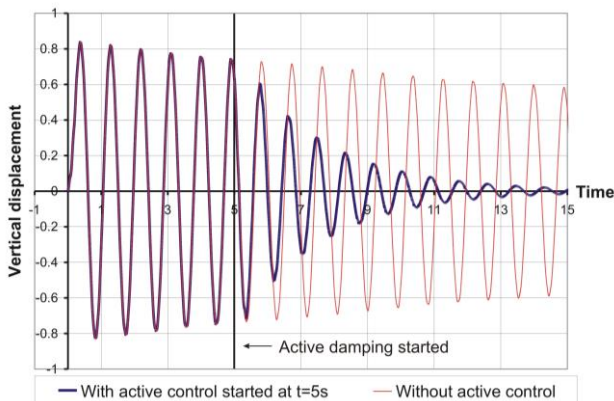


Figure 14: Mid-point deflection in the first load case with and without active control

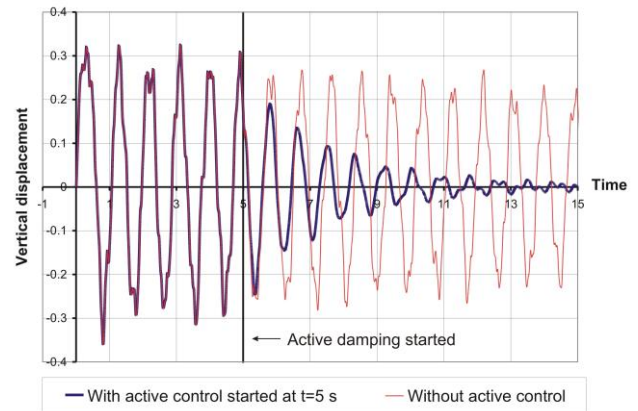


Figure 15: Mid-point deflection in the second load case with and without active control

#### 4. CONCLUSIONS

The idea of physics based real-time simulation has gained in importance in the previous two decades. Besides applications such as various virtual-reality simulators, in which the demand for real-time simulation is crucial, also the classical engineering simulations would benefit from highly efficient, and, should it be possible, even real-time simulations. Among various ideas how to approach and deal with real-time simulations based on the Finite Element Method, the model reduction done by means of the modal superposition technique is addressed in this paper. Transformation to modal space has a great potential in this field. By carefully selecting the modes to be used in the simulation, the numerical effort needed for the simulation is reduced by several orders of magnitude. In this manner, the objective of real-time simulation is easily achieved. However, this nice property comes together with the limitation of the approach to linear analysis.

The paper is further focused on two specific aspects of simulations performed using this technique. The first one is related to the above mentioned limitation to linear analysis. Several originally proposed methods to extend the approach so as to cover moderate geometrically nonlinear effects are briefly explained and demonstrated.

Furthermore, the technique is applied to adaptive structures characterized by the ability to actively react to external excitations in order to produce desired behavior and thus protect their own integrity. By implementing the strain rate proportional active damping, it has been shown that structural vibrations can successfully be reduced, whereby the simulations run in real-time.

The real challenge would be development of FE formulations that would allow real-time simulations based on full extent FE models and that would also cover nonlinear effects. The first steps in this direction have already been done by the author, but this is still a work in progress.

#### REFERENCES

- [1] L.P. Nedel and D. Thalmann, “Real time muscle deformations using mass-spring systems. Proceedings of “Computer Graphics International”, Hannover (Germany), June 1998, pp. 156-165, (1998)
- [2] E. Keeve, S. Girod and B. Girod, “Cranofacial surgery simulation”, Proceedings of the “Visualization in Biomedical Computing”, Lecture Notes in Computer

- Science, vol. 1131, K.H. Bohme and R. Kikinis (Eds.), Springer, Berlin, pp. 541-546, (1996)
- [3] Y. Wang, S. Guo and B. Gao, "Vascular elasticity determined mass-spring model for virtual reality simulators", *International Journal of Mechatronics and Automation*, Vol. 5, pp. 1-10, (2015)
- [4] K. Erlben, J. Sporning, K. Henriksen and H. Dohlmann, "Physics-based animation", Charles river media, Boston (United States), (2005)
- [5] K. Kawamura, Y. Kobayashi and M.G. Fujie, "Basic study on real-time simulation using mass spring system for robotic surgery", *Proceedings of "Medical Imaging and Augmented Reality"*, MIAR 2008, Lecture Notes in Computer Science, vol. 5128, August 2008, T. Dohi, I. Sakuma and H. Liao, (Eds.), pp. 311-319, (2008)
- [6] K. Ordaz-Hernandez, X. Fischer and F. Bennis, "Model reduction technique for mechanical behaviour modelling: efficiency criteria and validity domain assessment", *Proc. IMechE Part C: Journal of Mechanical Engineering Science*, 222, pp. 493-505, (2008)
- [7] K. Morooka, X. Chen, R. Kurazume, S. Uchida, K. Hara, Y. Iwashita and M. Hashizume, "Real-time nonlinear FEM with neural network for simulating soft organ model deformation". *Proceedings of "Medical Image Computing and Computer-Assisted Intervention – MICCAI 2008"*, September 2008, New York (USA), D. Metaxas, L. Axel, G. Fichtinger and G. Székely (Eds.), *Lecture Notes in Computer Science*, vol. 5242, Springer, Berlin, Heidelberg.
- [8] J. Kalkkuhl, K.J. Hunt and H. Fritz, "FEM-based neural-network approach to nonlinear modeling with application to longitudinal vehicle dynamics control", *IEEE Trans. Neural Netw.*, 10, pp. 885-897, (1999)
- [9] G. Runge, M. Wiese and A. Raatz, "FEM-based training of artificial neural networks for modular soft robots", *Proceedings of "2017 IEEE International Conference on Robotics and Biomimetics (ROBIO)"*, Macau, China, December 2017, (2017)
- [10] K.J. Bathe, "Finite element procedures", Prentice Hall, New Jersey (USA), (1996)
- [11] D. Marinković and M. Zehn, "Consideration of stress stiffening and material reorientation in modal space based finite element solutions", *Physical Mesomechanics*, 21, pp. 341-350, (2018)
- [12] M.G. Choi and H.-S. Ko, "Modal warping: real-time simulation of large rotational deformation and manipulation", *IEEE Transactions on Visualization and Computer Graphics*, 11, pp. 91-101, (2005)
- [13] G. Székely, Ch. Brechbühler, R. Hutter, A. Rhomberg, N. Ironmonger and P. Schmid, "Modelling of soft tissue deformation for laparoscopic surgery simulation", *Medical Image Analysis*, 4, pp. 57-66, (2000)
- [14] M. Fiorentino, G. Monno and A.E. Uva, "Interactive 'touch and see' FEM simulation using Augmented Reality", *International Journal of Engineering Education*, 25, pp. 1124-1128, (2009)
- [15] M. Bro-Nielsen and S. Cotin, "Real-time volumetric deformable models for surgery simulation using finite elements and condensation", *Computer Graphics Forum*, 15, pp. 57–66, (1996)
- [16] S. Cotin, H. Delingette and N. Ayache, "A hybrid elastic model for real-time cutting, deformations, and force feedback for surgery training and simulation", *Visual Comp.*, 16, pp. 437-452, (2000)
- [17] D. Marinkovic, M. Zehn and Z. Marinkovic, "Finite element formulations for effective computations of geometrically nonlinear deformations", *Advances in Engineering Software*, 50, pp. 3-11, (2012)
- [18] V.A. Nguyen; M.W. Zehn and D. Marinkovic, "An efficient co-rotational FEM formulation using a projector matrix", *Facta Universitatis-Series Mechanical Engineering*, 14, pp. 227-240, (2016)
- [19] D. Marinkovic and M. Zehn, "Towards real-time simulation of deformable structures by means of co-rotational finite element formulation", *Meccanica*, 53, pp. 3123–3136, (2018)
- [20] M.W. Zehn and D. Marinkovic, "Chances of real-time simulation in FE analyses with conventional hardware", *Proceedings of the "7th International Conference on Structural Engineering, Mechanics and Computation, SEMC 2019"*, September 2019, Cape Town, South Africa, pp. 531-536, (2019)
- [21] D. Marinkovic and M. Zehn, "Survey of finite element method-based real-time simulations", *Applied Sciences*, 9(14), 2775, (2019)
- [22] P. Scholz, „Softwareentwicklung eingebetteter Systeme“, Physica-Verlag – Springer, Heidelberg (Germany), pp. 39-73, (2005)
- [23] D. Marinković and G. Rama, "Co-rotational shell element for numerical analysis of laminated piezoelectric composite structures", *Composites Part B: Engineering*, 125, pp. 144-156. (2017)

## Industry 4.0 Context of Heavy Machinery

Vidosav D. Majstorović<sup>1</sup>, Radivoje M. Mitrović<sup>1</sup>, Žarko Z. Mišković<sup>1\*</sup>

<sup>1</sup>Faculty of Mechanical Engineering, University of Belgrade, Belgrade (Serbia)

*The Industry 4.0 model is based on integration of the Cyber Physical Systems (CPSs) and connection between Internet of Things (IoTs) and Cloud technology (CT). These are high-level methodologies for development of new generation factories, which are more intelligent, flexible and self-adaptable. Those models generate Big Data, horizontally by integration (network of machines, processes and sensors) and vertically by control (usually defined over five levels) which should be analytically processed and managed by the Cyber-Physical Manufacturing (CPM). Industry 4.0 is a new model of technology systems automation, based on the convergence of technologies that make up the concept of intelligent manufacturing, integrated with information and communication technologies that have been applied in a new way (cloud computing, big data analytics and AI), and based on distributed management. This approach has brought unprecedented opportunities to technology systems, from resource levels to supply chains, which are becoming more flexible, responsive to customer demands, and product quality is without defects. On the other hand, planning and control production in this model must have a specific concept that defines it. Also, model has its own development, and the subject of this paper is the analysis and synthesis of the follow two models: Industry 4.0 (I4.0) and enterprise resource planning (ERP) for Heavy Machinery Manufacturing. The paper also provides a research model for the ERP model in SMEs developing the Industry 4.0 concept for Heavy Machinery.*

**Keywords: Heavy machinery, Industry 4.0, Context**

### 1. INTRODUCTION

Industry 4.0 is today and strategic national program of scientific and technological development of the most developed countries around the world, which has been implemented since 2011. Today, thirty-seven countries have this program, whose primary objective is to increase the competitiveness, productivity and efficiency of national industries [1,2]. On the other hand, this model is the basic framework for research, development, designing and implementation of the next generation of technological systems, smart factories. One of the most important elements within them is the ERP model, which is considered in this paper from the following aspects: (i) historical development of the concept of planning and production control in the context of automation of manufacturing systems and the nature, type and volume of data in them, (ii) ERP data management and integration model in I4.0 concept, (iii) structure of the smart manufacturing model I4.0 with the place of the ERP model in it, and (iv) modelling with case studies for SMEs. Finally, some aspects of the future development of the ERP model for the I4.0 concept are given, especially from

the perspective of new paradigms such as designing and production control.

Industry 4.0 concept is so far the best model of technological system for managing the relationships between supply and demand of customers from the following aspects: quantity, variety, time of market appearance, price, quality and design [3,4], because it gives a model of analysis and synthesis the information during product life cycle, using cloud computing and big data analytics. This approach makes it possible to individualize each customer's requests, which has become the smart manufacturing paradigm.

Industry 4.0 model is based on data-driven technology which is networked and decentralized, and realized in cyber space. Therefore, it is very important for the smart manufacturing model to explore nature, the type and size of databases used to plan and manage at the plant, factory and supply chain levels [5-7], from the perspective of the six technologies on which this production is based, and which containing elements of the ERP model. This overview is given in Table 1, with special reference to additional characteristics related to Industry 4.0.

Table 1: Characteristics of data in smart manufacturing, including heavy machinery (adopted according to [6])

|   | Nature of data  | Data type  | Data volume                                     |
|---|---|--|---|
| Automation and manufacturing technology | Prediction technology   | Numerical, string, bits, symbolic                        | Medium. (Very large – big volume) <sup>1)</sup> |
| Data storage technology                 | Status and history of production equipment                        | Numerical, symbolic, string, time series, text           | Very large. (Cloud computing) <sup>1)</sup>     |
| Digitization technology                 | Artifact characterization, status                                 | Numerical, symbolic, text                                | Large. (Digital twin) <sup>1)</sup>             |
| Cloud computing technology              | As-is data, transformed data, integrated data, models, algorithms | Potentially data of types determined by the cloud design | Very large. (SaaS) <sup>1)</sup>                |
| Agent technology                        | Application specific  | Application specific                                     | Low. (AI) <sup>1)</sup>                         |
| Prediction technology                   | Application specific  | Numerical, categorical, time series                      | Medium. (Intelligent Maintenance) <sup>1)</sup> |

\*Corresponding author: Kraljice Marije 16, 11120 Belgrade 35, Serbia, zmiskovic@mas.bg.ac.rs

Information content and level connectivity in smart manufacturing is high and is implemented through 2M (man-machine) - computer communication, which is monitored by AI algorithms. In the smart manufacturing model, information flows are realized through cloud and physical layers. Cloud layer includes models and algorithms related to: operations and configuration management, process and service models and condition monitoring. ERP covers this last layer. The physical layer includes equipment and sensors. In this way, divided

virtual-physical systems through cloud computing perform resource sharing, managed through the ERP model.

The planning of production and technological resources in the production control model (MRP / ERP) has a long history, and this development has taken two directions: (i) business aspect (from stock planning at the plant level to the whole chain (request for offer - delivery of the finished product) at the company level, and (ii) technological aspect (from the software package to the client server architecture). An overview of the development of this model is given in Table 2 [3,8,9].

Table 2: History of ERP model development [3,8,9]

| Year / model / Level               | Characteristics of MRP/ERP model         | Aspects of function                                     |
|------------------------------------|--|---|
| 1960s / IC / I level               | Inventory management and control         | Warehouse control                                       |
| 1970s / MRP I / II level           | Material Requirements Planning           | Bill of product   |
| 1980s / MRP II / III level         | Manufacturing Resources Planning         | Bill of manufacturing process                           |
| 1990s / ERP / IV level             | Enterprise Resource Planning             | Integrate business activities across organization units |
| 2000s / ERP II / V level           | Enterprise Resource Planning by Internet | Services Oriented Architecture (SOA)                    |
| 2010s / Cloud based ERP / VI level | Cloud based ERP                          | ERP as software a service (SaaS) model                  |
| 2020s / I4.0 ERP / VII level       | ERP of Industry 4.0 model                | I4.0 concept introducing                                |

Information system for control the appropriate level of stock in a warehouse (material, spare parts) was been the first level in this area [9]. Material requirement planning (MRP I) used software applications for scheduling manufacturing processes and for operations raw material purchases, level two. Now, for the first time, they are introducing into production planning and control bill of structure, materials (BOM) and quantity. Manufacturing Resource Planning (MRP II) used software for coordinating manufacturing processes from product planning, parts purchasing, inventory control to product distribution, level III. Enterprise resource planning (ERP) uses a multi-module application software system, for improving the performance of the internal business processes, based on integrate business activities (planning, purchasing and distribution) across functional departments (marketing, design, accounting, HR), level IV. ERP II using internet web-browsers, with Services Oriented Architecture (SOA) and mobile devices were made possible, is level V. Cloud ERP, level VI are business applications are delivered as a service (SaaS) model, suitable for SMEs as well. Finally, the last seventh level refers to the ERP model for Industry 4.0. The previous analysis shows that the development of the first four levels of the ERP model was based on the development of information systems, and after that IT technologies involved in the development of this model. The latest model is an internet-oriented networking concept, based on cloud computing and AI tools in Industry 4.0 model.

## 2. ERP MODEL FOR INDUSTRY 4.0 IN HEAVY MACHINERY MANUFACTURING

Digitized and networked technology systems, with Internet of Things as per Industry 4.0 concept, have the ability to assign production control tasks to "intelligent" objects: machines, products and parts [10]. In this way, greater flexibility and adaptability of the manufacturing system itself, through the ERP model, is achieved. This approach defines new paradigms of production planning and control, which is based on a hybrid model of transition at centralized to a decentralized management concept. On the other hand, the optimization of ERP parameters is performed at a centralized (supply chain) and / or distributed (part) control level, which means that decisions regarding production planning and control are made globally or locally, according to Kanban (pull) or Holon model.

Data became the key elements in planning, control and executing all activities along supply chain in I4.0 model. For these reasons, an organization must carefully treat and properly use all data to create an effective basis for decision making [11]. The main challenge is innovative data management on the Industry 4.0 platform, which includes storage, exchange and use of data. The development and implementation of such concepts must be stimulated because only data that is error-free, up-to-date, accessible and usable can contribute to the success of the company, Table 3.

Table 3: Framework of ERP model for Industry 4.0, including Heavy Machinery Manufacturing (extended approach according to [11])

| Characteristics / I4.0 challenge  | Desirable features of an ERP systems | Example  | Goals  | I4.0 approach          |
|---|--------------------------------------|--|--|------------------------|
| Data storage / balance centralized and decentralized approach.                            | Simplification of data model.        | Simple table structures for the logical data model.                                    | Data on time.  | Cloud computing        |
|   | Decentralized data management.       | Distributed storage of data in different systems.                                      | Bidirectional (ERP-MES <sup>1</sup> -PLC <sup>2</sup> ) loading of data. |                        |
| Data flow / the connection of the ERP system in two directions – horizontal and vertical. | Linkage to previous systems.         | Exchange data (vertical and horizontal) and processing of different systems.           | Integration of systems for a flexible planning and control.              | Interoperability       |
|   | Speed of data access                 | ERP system should deliver requested data within short response times.                  | Fast reaction to changes.  |                        |
| Data used / virtual and real models of intelligent products.                              | Visualization                        | The user interface of the ERP systems should display information adequately.           | Improvement of human-machine interaction.                                | Big data analytics, AI |
|   | Integration and Intelligence         | ERP system should connect data from different sources and hence create new information | Generation of new information.   |                        |
|   | Automation                           | ERP system should use the data to trigger automated processes.                         | Reduction of errors and increase in efficiency.                          |                        |

Industry 4.0 is building smart factories in deployment that have four dimensions [12-14]: (i) smart manufacturing based on advanced digital-oriented technologies (Additive manufacturing, Cloud computing and Internet of things). It has automated flexible lines that adapt production processes with changed conditions to the type of product, while sometime maintaining high quality, high productivity and flexibility, as well as production volume, with optimal consumption of resources; (ii) smart products (advanced production mode and new characteristics). They generate and send to the

manufacturer exploitation feedback information, which is used primarily in the field of customer service. On this way increases the value added of the product, and the manufacturer develops a new business model (product + service); (iii) new ways workers perform their activities, based on advanced digital-oriented technologies (smart working), and (iv) smart supply-chain (procurement of raw materials and delivery of finished products). Bidirectional exchange of information in collaborative production, using it exchange also for digital platforms of design of the innovative products, Figure 1.

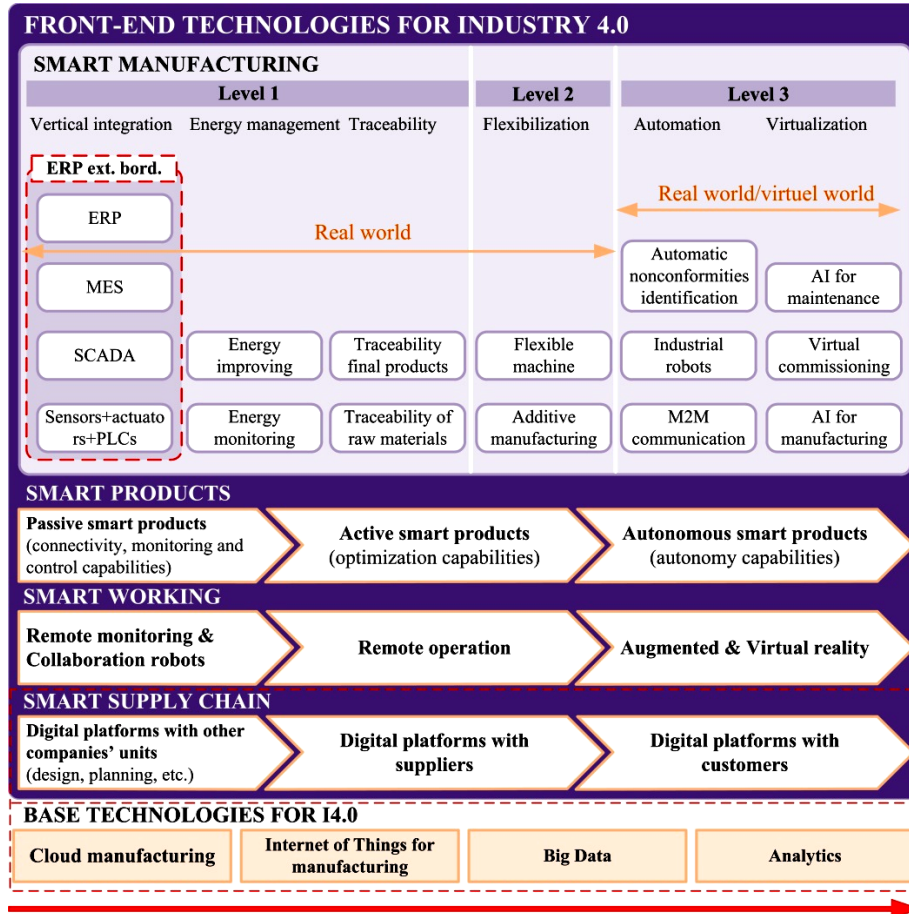


Figure 1: Framework for Industry 4.0 model for Heavy Machinery Manufacturing (adopted according [12])

This framework of a smart factory is also based on four dimensions of basic technologies for Industry 4.0: (i) cloud manufacturing, (ii) internet of things for manufacturing, (iii) big data (for manufacturing), and (iv) analytics (for manufacturing). For our analyses, relate to the ERP model, the dashed line marks elements of both structures. On the other hand, the smart supply chain in the I4.0 concept has a special function - to create added value for the customer, which gives them digital platforms for planning and designing of product and production, procurement and sales, creating a management framework product over the life of the product. This creates a new business model for the organization in the circular economy - eco sustainable smart production [15,16]. In this concept, the ERP model is a key element of the vertical integration model, but is also whole part of the smart chains and core technologies for Industry 4.0, as it is shown in Figure 2. There are three integration concepts in the Industry 4.0 model that apply [7,17,18]: (i) vertical integration (from process - sensor, to organization (corporate planning) - ERP). The center of integration at this level is the cyber-physical system, which production is realized; (ii) horizontal - from request for offer to delivery note of finished product (marketing, designing, production, delivery). Integration center is an intelligent product, with added value; and (iii) supply chains and sustainable production with a customer relationship management (CRM) integration center. Thus, the organization builds a new business model of its Industry 4.0 concept, the center of which is a large database and its reporting. The ERP model plays a key role in this.

### 3. RESEARCH AND DEVELOPMENT OF ERP MODEL FOR SMES IN HEAVY MACHINERY

The Industry 4.0 model currently has forty-five elements that make up its full structure applicable in large

organizations. Our research shows that this model for SMEs should have between fourteen and twenty-two elements depending on the type of production that the SME is engaged. But one of the basic elements without this model cannot be applied is modelling - the virtual part.

Modelling is one of the most important elements of the I4.0 model, especially for the digital twin. This aspect is particularly expressive in the smart manufacturing model, where knowledge modelling is the most important element. In the digital era, the management of technological systems including their elements, encountered in the following forms [19-21]: (i) centralized hierarchical model, where we have an integrated computer system of production and management; (ii) distributed heterarchical model, which builds the symbiosis of the two models (computer-aided manufacturing and management) on the principles of biologically inspired models; (iii) CPS based distributed control [22], and (iv) IoT based distributed control [23,24]. The last two models are important for our research, and they are realized in the I4.0 concepts through the models: agent based, multi-agent based and holonic based, type of control.

The ERP model in these concepts builds as an innovative model on new paradigms, such as: collaborative control, product-driven agents, IoT agents, which makes the infrastructure of the model itself. The ERP model for smart factories is used to manage all business and technology processes in real time across the whole supply chain, based on a fast and flexible response to its customers' requirements. For the first time the Industry 4.0 model allows us do this, and the ERP model permeates the infrastructure of the entire model shown on Figure 2 [25].

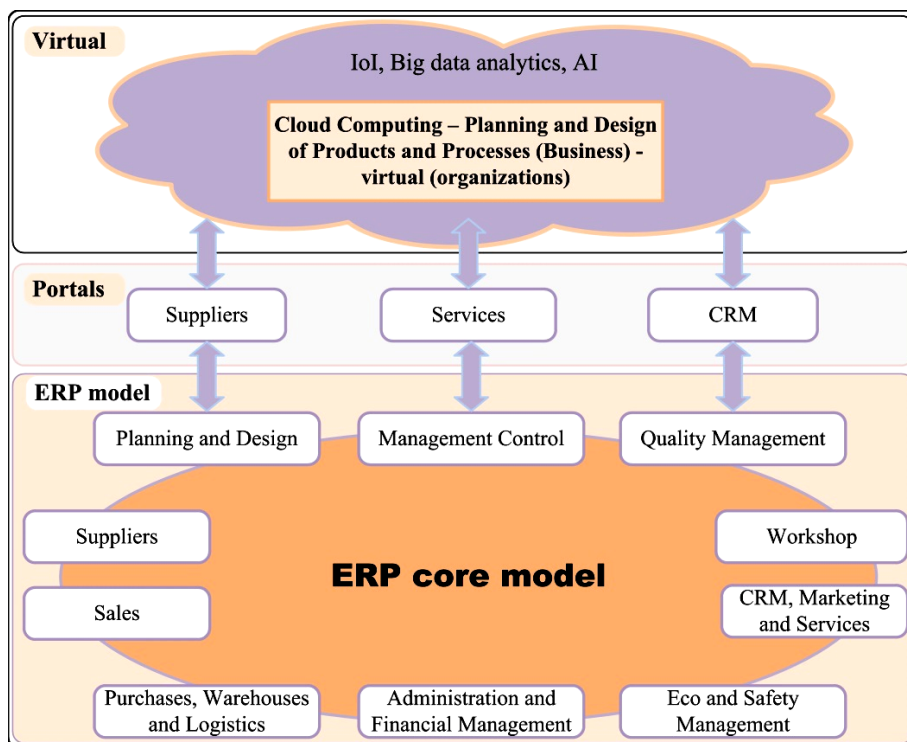


Figure 2: ERP Industry 4.0 model, including Heavy Machinery Manufacturing (adopted according to [25])

The model has three parts: (i) virtual whole, which is based on the cloud computing (SaaS) model. It contains a virtual model of an ERP system, linked through IoT all business (procurement, sales, management, finance), production (workshop) and technological (designing) processes, with large databases that are generating. Their analysis, optimization and decision making are performed using AI and machine learning techniques; (ii) interfaces (suppliers, services and CRM). Their function is to provide to user the on-line user necessary information related to procurement, sales and other services (for example maintenance) that help us track the dynamics of smart manufacturing, and (iii) core model, which includes the business-technological and managerial functions of the organization as well as the production itself, a total of ten units.

In the smart factory model, the following functions are realized using an intelligent ERP system [25,26-29]: (i) management of customer requirements. Real time creating the information content of request or offer using: Electronic Data Interchange (EDI) tools, web portals, forecasts and customer MRPs. Also managing the “Master Production Schedule” (MPS), with open orders and framework agreements, the procurement activities can be scheduled (purchases and production of finished or semi-finished goods); (ii) production planning (MRP 1). The model calculates the needed quantities of raw materials to be procured for the accepted requirements from the previous point, taking into account: accepted offers, existing stock, quantities reserved for production orders in progress and sales plans; (iii) manufacturing scheduling

(MRP 2). Production resource planning for MRP 1 orders, taking into account: machines capacity, labour force, maintenance plans, delivery times. Technology documentation (machining operations, tools and controls plans) are elements of this module; (iv) management production (Manufacturing Execution System – MES). Monitoring and managing the complete work order at all stages of production, both at the manufacturing plant and at the subcontractors, including planned maintenance orders; (v) integration and communication between technical departments and customers. This is related for connecting and integrating about a product (in the factory) – PDM (Product Data Management) and product (along lifecycle) – PLM (Product Lifecycle Management), for all stages of product planning and designing (bills of products) from all aspects of defining and reconsidering; (vi) Quality Management System (QMS), EMS and OH&S. These models manage quality information (quality management and traceability), ecology and health protection; (vii) management warehouses and stock, logistics management. All changes to the storage are monitored online via bar code or RFID, and the ERP model takes care about required / planned quantities. Likewise, internal transport as well as all shipments of finished products, are monitored in the same way, and (viii) administration and financial management. Production accounting management to determine all costs and productivity parameters, by different areas and bases.

In Serbia, intensive work is being done to develop and implement ERP models for SMEs [29], through the national Platform for Industry 4.0 [1], Figure 3.

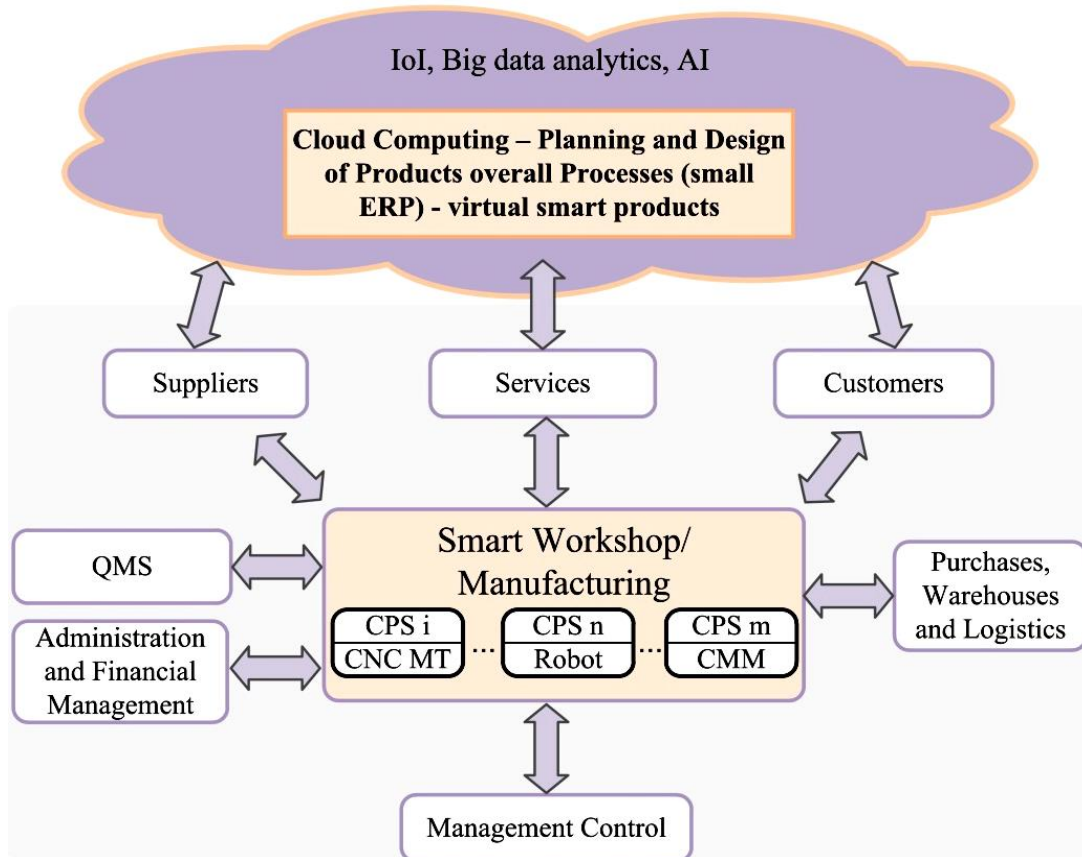


Figure 3: Framework of a smart manufacturing system for Industry 4.0 in SMEs for Heavy Machinery

On the smart workshop where real production takes place as the creating point of manufacturing data. Virtual shop floor of a physical one using agent technology, where each agent has: identification, authorization, configuration, capability, operation and status data, and transmits them and their metadata. Data warehouse is an information hub that stores and exchanges manufacturing data. Data analytics center is the model creation, storage, retrieval and uncertainty which provides machine learning, statistical, or stochastic based models that build on mathematical functions needed to create data driven models. Each agent retrieves such models through a broker agent and decides predictive operations and controls, based on the results that models output. Manufacturing application include applications, such as CAD, CAM, CAQ, ERP systems. These applications communicate with the platform through their application interfaces because they eventually supervise and manage all activities and events occurring on the physical workshop. Agent manager searches adequate agents, and manages them during their lifecycles. Data governor manages master data as well as the lifecycle and quality of raw data. Workflow manager controls workflows to automate the tasks performed on the platform, manages the rules designed to handle workflow appropriately, and engages in model representation. Security controller protects against computer viruses and hacking, and controls electronic authorization and authentication, because data and models that incorporate manufacturing experience and knowledge are valuable and, thus, must be protected.

For SMEs, the integral model of smart manufacturing and ERP is researched and defined, based on the base elements of Industry 4.0: Cyber physical systems (CPS), M2M – Man-machine communication / MMI – Man-machine interaction, Operation management for I4.0, Digital Twins, Horizontal & Vertical Integration, Using Light Signals, Smart / Mobile Maintenance, Condition Monitoring, VR - Virtual Reality, QR Code, Data Security, Open Communication Protocols (OPC-UA), IoT - Internet of Things (IIoT - Industrial Internet of Things) ), Real-Time Communication, Big Data, Cloud, Automation Pyramid, Resource Planning (ERP), Work Order Management (MES), Supplier Relationships, Intelligent Logistics, Customer Relationships, WWW [29]. The SMEs for which this project is implemented are from the field of metal industry and produce parts, subassemblies and assemblies for factories from Italy, Switzerland, Austria, Germany and the Netherlands.

#### 4. CONCLUSIONS

The concept of Industry 4.0 has a special place and role for the design engineer and production planner, which is still irreplaceable, but now has a different role, namely a new paradigm. It is particularly reflected in the construction and management of the digital twin model of the smart factory, and thus of the ERP module. In [30,31], this approach is explored in detail, and a five-level model of the pyramid of the industrial internet is proposed: (i) smart object (physical objects and embedded intelligence), (ii) industrial internet of things (level 1 and network, (iii) cyber-physical production system (level 2 and integration previous levels), (iv) service-oriented digital twin (ubiquitous knowledge and level 3), and (v) smart factory

(manufacturing employees and level 4). From an ERP perspective, the specificities of executives monitoring CPSs, facility managers and engineer resource planners are specifically referenced and used here, as outlined in Levels 4 and 5. One of the future directions of ERP development is the open source model.

Research on the project [29] in the forthcoming period will focus on the development of demonstration models for individual I4.0 segments for SMEs (designing - digital twin, procurement, customers, MES, etc.).

The research presented in this paper will be also very useful for improvement of other heavy machinery systems, such as mining or transportation machinery. Some steps in this direction are already made i.e. an improvement of the maintenance system of auxiliary mining machinery in the energy sector of the Republic of Serbia (JP EPS Company, TE-KO Kostolac) [32].

The improved system can provide more efficient and cost-effective support to the operation of basic mining heavy machinery. More specifically, the level of system reliability, as well as system availability and readiness, will be significantly raised. So far, a process approach and modern technical knowledge, new ICT technologies, as well as specific elements of Industry 4.0 have been applied. The possibilities of further application of Industry 4.0 context in the maintenance and other power production systems in order to address various challenges such as those of productivity, safety, ecology and environmental protection are planned to be analysed in the next period of the presented research.

#### ACKNOWLEDGEMENT

Authors would like to express their sincere gratitude to the Ministry of Education, Science and Technological Development of the Republic of Serbia for their support during the realisation of the project with the contract number 451-03-9/2021-14/200105 (February 5<sup>th</sup> 2021).

#### REFERENCES

- [1] V. Majstorovic, et al., "Industry 4.0 Programs Worldwide", Proceedings of the 4th International Conference on the Industry 4.0 Model for Advanced Manufacturing, AMP 2019, Belgrade, pp. 79-99. [https://doi.org/10.1007/978-3-030-1818-2\\_7](https://doi.org/10.1007/978-3-030-1818-2_7) (2019)
- [2] V. Majstorovic, et al., "Cyber-Physical Manufacturing in Context of Industry 4.0 Model", Proceedings of 3rd International Conference on the Industry 4.0 model for Advanced Manufacturing, AMP 2018, pp. 227-238, Belgrade, <https://doi.org/10.1007/978-3-319-89563-5> (2018)
- [3] Y. Yina, K. E. Steckeb, L. Dongni, "The evolution of production systems from Industry 2.0 through Industry 4.0", International Journal of Production Research, Vol. 56, Nos. 1–2, 848–861, <https://doi.org/10.1080/00207543.2017.1403664> (2018)
- [4] S. Bonnaud, C. Didier, A. Kohler, "Industry 4.0 and Cognitive Manufacturing, Architecture Patterns", Use Cases and IBM Solutions, <https://www.ibm.com/downloads/cas/M8J5BA6R> (Accessed on March 2021)

- [5] J. P. Usuga Cadavid, S. Lamouri, B. Grabot, A. Fortin, “Machine Learning n Production Planning and Control: A Review of Empirical Literature”, Proceedings of 9th IFAC conference on Manufacturing Modelling, Management and Control Berlin, Germany, August 28-30, 2019, IFAC Papers On Line, 52-13, 385–390. <https://doi.org/0.1016/j.ifacol.2019.11.155>. (2019)
- [6] A. Kusiak, “Fundamentals of smart manufacturing: A multi-thread perspective”, Annual Reviews in Control, Volume 47, 214-220, <https://doi.org/10.1016/j.arcontrol.2019.02.001>. (2019)
- [7] L. Monostori, P. Valckenaers, A. Dolgui, H. Panetto, M. Brdys, B. C. Csáji, “Cooperative control in production and logistics”, Annual Reviews in Control, 39, 12–29, <https://doi.org/10.1016/j.arcontrol.2015.02.001>. (2015)
- [8] P. Osterrieder, L. Budde, T. Friedli, “The smart factory as a key construct of industry 4.0: A systematic literature review”, International Journal of Production Economics, 211, 35–51, <https://doi.org/10.1016/j.ijpe.2019.08.011> (2019)
- [9] N., N., “A Brief History of ERP – since 1960 and the future of ERP”, <https://www.erp-information.com/history-of-erp.html> (Accessed on March 2021)
- [10] J. Bendul, H. Blunck, “The design space of production planning and control for Industry 4.0”, Computers in Industry, 105, pp 260-272. <https://doi.org/10.1016/j.compind.2018.10.010> (2019)
- [11] C. A. Hochmuth, C. Bartodziej, C. Schwägler, “Industry 4.0 Is your ERP system ready for the digital era?”, 2017. ([https://www2.deloitte.com/content/dam/Deloitte/de/Documents/technology/Deloitte\\_ERP\\_Industrie-4-0\\_Whitepaper.pdf](https://www2.deloitte.com/content/dam/Deloitte/de/Documents/technology/Deloitte_ERP_Industrie-4-0_Whitepaper.pdf) (Accessed on Feb. 2021).
- [12] A. Frank, L. Dalenogare, N. Ayala, “Industry 4.0 technologies: Implementation patterns in manufacturing”, International Journal of Production Economics, 210, 15–26. <https://doi.org/10.1016/j.ijpe.2019.01.004>. (2019)
- [13] C. Emmanouilidis, P. Pistofidis, L. Bertoncej, V. Katsouros, A. Fournaris, C. Koulamas, C. Ruiz-Carcel, “Enabling the human in the loop: Linked data and knowledge in industrial cyber-physical systems”, Annual Reviews in Control, 47, 249–265, <https://doi.org/10.1016/j.arcontrol.2019.03.004> (2019)
- [14] M. Dassisti, A. Giovannini, P. Merla, M. Chimienti, H. Panetto, “An approach to support Industry 4.0 adoption in SMEs using a core-metamodel”, Annual Reviews in Control, 47, 266–274, <https://doi.org/10.1016/j.arcontrol.2018.11.001> (2019)
- [15] C. Fallera, D. Feldmüllera, “Industry 4.0 Learning Factory for regional SMEs”, The 5th Conference on Learning Factories 2015, Procedia CIRP, 32, 88 – 91. <https://doi.org/10.1016/j.procir.2015.02.117> (2015)
- [16] S. Erola, W. Sihna, “Intelligent production planning and control in the cloud – to-wards a scalable software architecture”, 10th CIRP Conference on Intelligent Computation in Manufacturing Engineering - CIRP ICME '16 Procedia CIRP, 62, 571 – 576, <https://doi.org/10.1016/j.procir.2017.01.003> (2017)
- [17] L.D. Xua, E. L. Xu, L. Lia, “Industry 4.0: state of the art and future trends, International Journal of Production Research”, Vol. 56, No. 8, 2941–2962, <https://doi.org/10.1080/00207543.2018.1444806> (2018)
- [18] D. Ivanov, S. Sethi, A. Dolgui, B. Sokolov, “A survey on control theory applications to operational systems, supply chain management, and Industry 4.0”, Annual Reviews in Control, 46, 134–147, <https://doi.org/10.1016/j.arcontrol.2018.10.014> (2018)
- [19] G. Morel, C.E. Pereira, S.Y. Nof, “Historical survey and emerging challenges of manufacturing automation modelling and control: A systems architecting perspective”, Annual Reviews in Control, 47, 21–34, <https://doi.org/10.1016/j.arcontrol.2019.01.002> (2019)
- [20] D. Zuehlke, “SmartFactory—Towards a factory-of-things”, Annual Reviews in Control, 34, 129–138. <https://doi.org/10.1016/j.arcontrol.2010.02.008> (2010)
- [21] N., N., “Industry 4.0 – Opportunities and Challenges of the Industrial Internet” (2019) (<https://www.pwc.nl/en/assets/documents/pwc-industrie-4-0.pdf> (Accessed on March 2021)
- [22] B. Rodič, “Industry 4.0 and the new simulation modelling paradigm”, Organizacija, 50(3), 193–207. <https://doi.org/10.1515/orga-2017-0017>.
- [23] K.Y.H. Lim, P. Zheng. & Chen, “A state-of-the-art survey of Digital Twin: techniques, engineering product lifecycle management and business innovation perspectives”, J Intell Manuf, <https://doi.org/10.1007/s10845-019-01512-w> (2019)
- [24] P. Barber, “Industry 4.0 and the Digital Factory”, <https://www.weforum.org/agenda/2019/07/factories-lead-fourth-industrial-revolution-automation-jobs/> (Accessed on March 2021).
- [25] N., N., “ERP and Industry 4.0”, <https://www.centrossoftware.com/en/erp-and-industry-4.0> (Accessed on March 2021)
- [26] M. Ahmad, R. Cuenca, “Critical success factors for ERP implementation in SMEs, Robotics and Computer-Integrated Manufacturing”, 29, 104–111. <http://dx.doi.org/10.1016/j.rcim.2012.04.019> (2013)
- [27] U. Cadavid, J.P., Lamouri, S., Grabot, B. et al. “Machine learning applied in production planning and control: a state-of-the-art in the era of industry 4.0”. J Intell Manu, <https://doi.org/10.1007/s10845-019-01531-7> (2020)
- [28] H. Panetto, B. Iung, D. Ivanov, G. Weichhart, X. Wang, “Challenges for the cyber-physical manufacturing enterprises of the future”, Annual Reviews in Control, 47, 200–213, <https://doi.org/10.1016/j.arcontrol.2019.02.002>. (2019)
- [29] V. Majstorovic, et al., “I4.0 for SMEs”, Project, Faculty of Mechanical Engineering, Belgrade, (2019)
- [30] D. Olson, B. Johansson, R. Carvalho, “Open source ERP business model framework”, Robotics and Computer-Integrated Manufacturing, 50, 30–36. <https://doi.org/10.1016/j.rcim.2015.09.007>. (2018)

[31] F. Longo, L. Nicoletti, A. Padovano, "Ubiquitous knowledge empowers the Smart Factory: The impacts of a Service-oriented Digital Twin on enterprises' performance", *Annual Reviews in Control*, Vol. 47, Pages 221-236. <https://doi.org/10.1016/j.arcontrol.2019.01.001> (2019)

[32] V. Simeunović, at all, "Improvement of an auxiliary machinery maintenance system and the concept of smart mining", *Yuinfo 2021, Conference Proceedings -* <http://yuinfo.org/#speakers> (2021)

# Ways to Improve the Efficiency of Dump Trucks for Transporting Asphalt Mix

A.I. Dotsenko<sup>1\*</sup>

<sup>1</sup>Moscow Automobile and Road Construction State Technical University (MADI), Moscow (Russian Federation)

*The system of operational quality control of asphalt concrete road surface during its transportation is considered. The implementation of information technology is carried out with the help of GLONASS / GPS satellite system, which in real time mode allows you to capture the required parameters. Then this information is transferred to the integrated management system of asphalt concrete plant (ACP). The system for monitoring parameters of asphalt concrete mixture is mounted on the basis of dump truck.*

*The developed integral monitoring of quality control of an asphalt-concrete with the use of GLONASS / GPS system provides to increase productivity and quality of work performed, can reduce the influence of the human factor on the quality of finished road surface, provides remote monitoring of main parameters of not only the technical means but also laying material, provides during non standard situation adjustment of system parameters ACP – DUMP TRUCK – ASPHALT CONCRETE.*

**Keywords: Monitoring, GLONASS / GPS, Road-construction machines, Asphaltic concrete, Quality**

## 1. INTRODUCTION

Highways are a complex engineering and technical constructions, one of the most critical elements of which is the road surface. It is the condition of the road surface that determines the quality and service life of the road, and also ensures safe movement of vehicles.

One of the promising areas for improving the quality of roads is the comprehensive monitoring of the parameters of road-construction machines as well as stacked material in the process of performing construction operations.

The concept of monitoring in relation to control systems of road-construction machines includes a remote contactless method of parameter control. In monitoring systems, satellite systems are assigned the function of transmitting information in the forward and reverse direction from operating machines to remote control centers. The monitoring systems allow is accumulation of large volumes of information, which makes it possible to use tools to improve efficiency. To solve the above issues, it is necessary to modernize existing dump trucks or create a new specialized truck.

## 2. THE OBJECT OF THE STUDY

When considering issues related to improving of the quality of asphaltic concrete pavements, it should be taken into account that asphaltic concrete is a multicomponent structure, the final operational properties of which are affected by both factors related to the production of asphaltic concrete mixture at an asphaltic concrete plant (ACP), as well as an external ones, in relation to production factors [1], namely:

*Internal (production) factors*

- Properties of the asphalt mixture components and their types;

- Recipe and structure of the mixture;

- Technology of the production of asphalt mixture;

*External factors*

- The quality of the road cover project;

- Quality of the road base;

- Technology of transportation, laying and compaction of the mixture.

Figure 1 shows a generalized process for the formation of the quality of asphaltic concrete pavement.

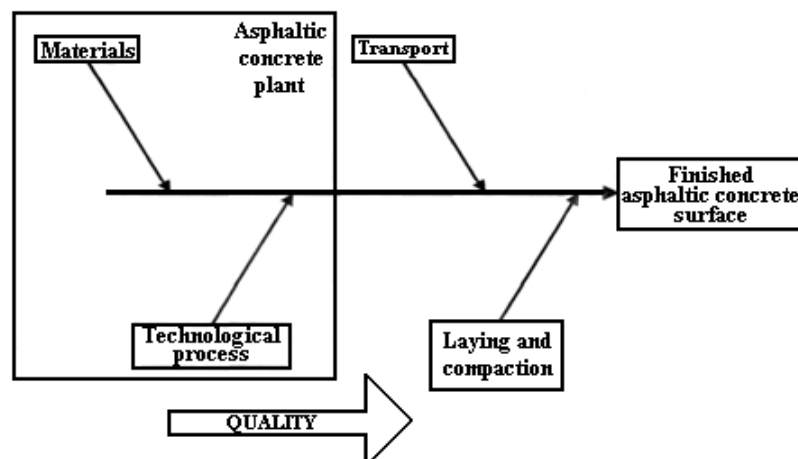


Figure 1: The generalized process of quality formation of an asphaltic concrete pavement

\*Corresponding author: Moscow Automobile and Road Construction State Technical University (MADI), Leningradskiy Prospekt, 64, Moscow, Russia, 125319, dotsenko\_ant@mail.ru

Now consider the individual components of the presented technological chain, significantly affecting the quality of the finished coating.

## MATERIALS.

This part provides the information on the properties of all components of the asphalt mixture. It consists of the information contained in the passports for the components of materials, and the results obtained by the factory laboratory in the course of experimental studies on the actual properties of materials [2].

## TECHNOLOGICAL PROCESS

This part provides information on the actual values of the process parameters [3], among which the most important are:

- Granulometric composition of each components of the asphalt mixture.
- Dosing error.
- Actual mixture composition for each batch.
- Temperature of bitumen, mineral materials, finished mixture at the outlet.
- Accuracy of control.
- Frequency of control.
- Systematic error of the control system.
- Methods and algorithms for processing of measurement results.

## TRANSPORT

During the transportation of asphaltic concrete mixture, the following operations are carried out :

- Monitoring of the vehicle parameters - dump truck (cargo mass, speed and direction of movement);
- Monitoring of the parameters of asphalt mixture (temperature in the upper and lower parts of the dump truck's body, in its side parts);
- The time of loading, delivery and unloading of the mixture;
- The rhythm of supplies;
- Fuel consumption level;
- Environmental conditions.

**LAYING AND COMPACTION** of asphaltic concrete mixture:

- Monitoring of paver's parameters (paving speed, fuel consumption level);
- Monitoring of the parameters of the asphalt mixture during installation (temperature and thickness of the layer to be laid);
- Monitoring of the parameters of the compacting machines (speed of the rollers, amplitude-frequency characteristics, the number of passes on one track, the level of fuel consumption);
- Monitoring of the parameters of the asphalt mixture during compaction (temperature, density);
- Environmental conditions.

To implement the above program, the dump truck must have the following additional equipment:

- Computer control unit
- Falcom F 35-XXL and antenna system Glonass / GPS;
- Dump truck position control subsystem;
- Dump truck identification subsystem;
- Communication subsystem;
- Mixture temperature control subsystem;

- Ambient temperature control subsystem;
- Wind speed sensor;
- Automatic system for covering the mixture with a tarpaulin in the body of a dump truck;
- Memory bloc;
- Manual data entry unit

The collected information from the dump truck is transmitted to the Central computer server of the asphalt concrete plant. This server, taking into account the current situation along the route of vehicle, as well as during the laying and compaction of the mixture, adjusts the operation mode of the factory equipment and ensures that the required quality of asphalt mixture is obtained at the outlet of asphaltic concrete plant. Figures 2 and 3 show the interaction in the process of monitoring of an integrated control system with the subsystems «Transport» and «Laying and compaction».

By means of GLONASS/GPS system, you can determine the coordinates for both moving and stationary vehicles, calculate the maximum and average speed of movement, calculate the time after which the dump truck will be in a given place, find out the distance to the destination.

Currently, GSM cellular networks are an inexpensive alternative to traditional radio communication channels. In addition to reduction of the cost of use due to the absence of a license fee, such a solution simplifies and speeds up the development process, since it uses standard protocols and methods for transmitting information.

Information in GSM cellular networks can be transmitted:

- Via GSM voice channel;
- using GPRS;
- using SMS.

Advantages of GSM technology:

- the ability to quickly deploy the system anywhere with GSM coverage;
- high data rate;
- the principle of payment independence from the time of information transmission in the GPRS mode (payment is carried out not for the time, when the terminal is in the receiving-transmitting state, but for the amount of transmitted or received information).
- low cost when using SMS mode;
- easy customization;
- remote control capability.

There are two types of GSM modems:

- modules that are designed for direct installation in devices.

- modems that have their own enclosure.

If we compare modems with mobile phones, the former have a longer service life, higher reliability and sensitivity to the mobile network. Built-in modules and modems are designed to be embedded in the developer's end systems. In the simplest case, the presence of a built-in microcontroller assumes that the PC board should have only the appropriate circuits for matching with the environment - the power supply system (voltage converter, protection, filtering), transmitters, sensors, actuators, data reception/transmission interfaces (RS232, RS485, CAN). It significantly reduces the cost of the project and time expenditures.

GPRS modems often have a phase of several user inputs and outputs that fully support standard interfaces RS-232, USB, etc., as well as connectors for connecting an external antenna and other devices. In addition, modems have extensive capabilities for remote configuration of parameters and prompt programmed control of their operation. On the other hand, modems are made as easy as possible by eliminating such parts that are not used in this case, such as a microphone, speaker, display, keyboard, etc.

Among the GSM/GPRS/GPS modules and modems currently available on the market, there are several main

series of remote collection and monitoring devices developed by both Russian and foreign specialists. Russian developments are represented by products of OOO Rateos, for example, the navigation controller «Azimut»; sensors for measuring asphalt-concrete mix temperature TSP/1-1288; environmental temperature sensors TSP/1-8045.

Among the foreign equipment, we can name Falcom F35-XXL-SI terminal; the autonomous route recorder «Course GPS»; the GSM/GPRS modem Falcom SAMBA.

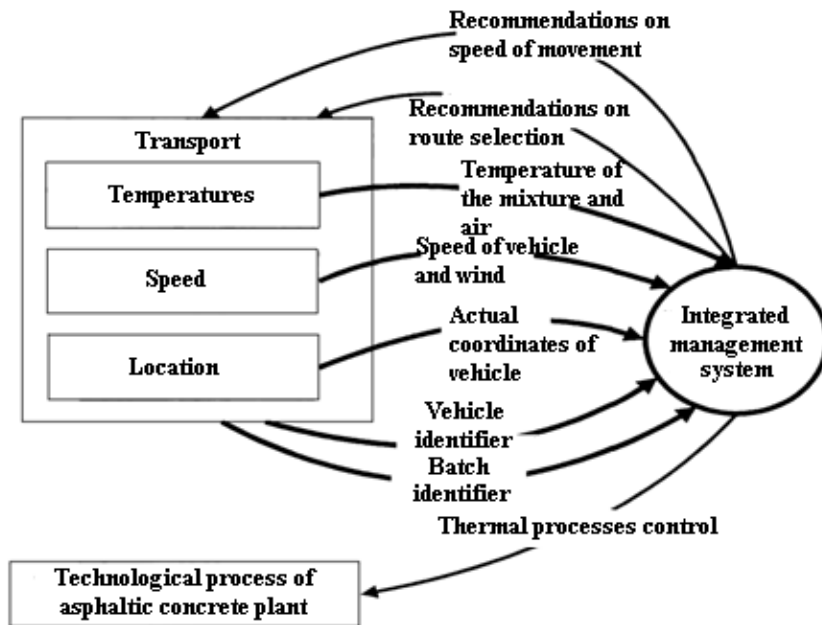


Figure 2: Interaction of an integrated management system with the subsystem «Transport»

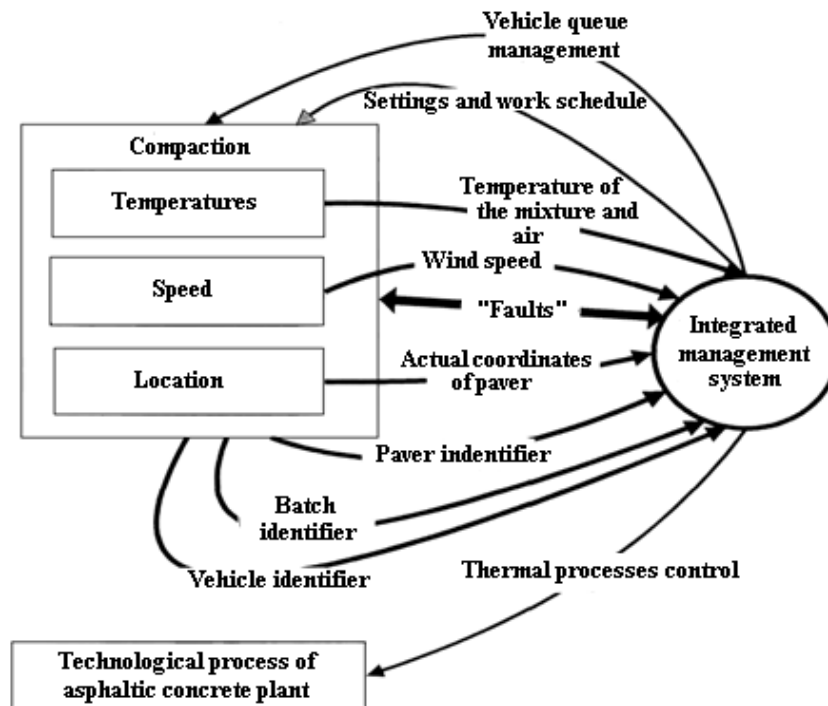


Figure 3: Interaction of an integrated management system with the subsystem «Laying and compaction»

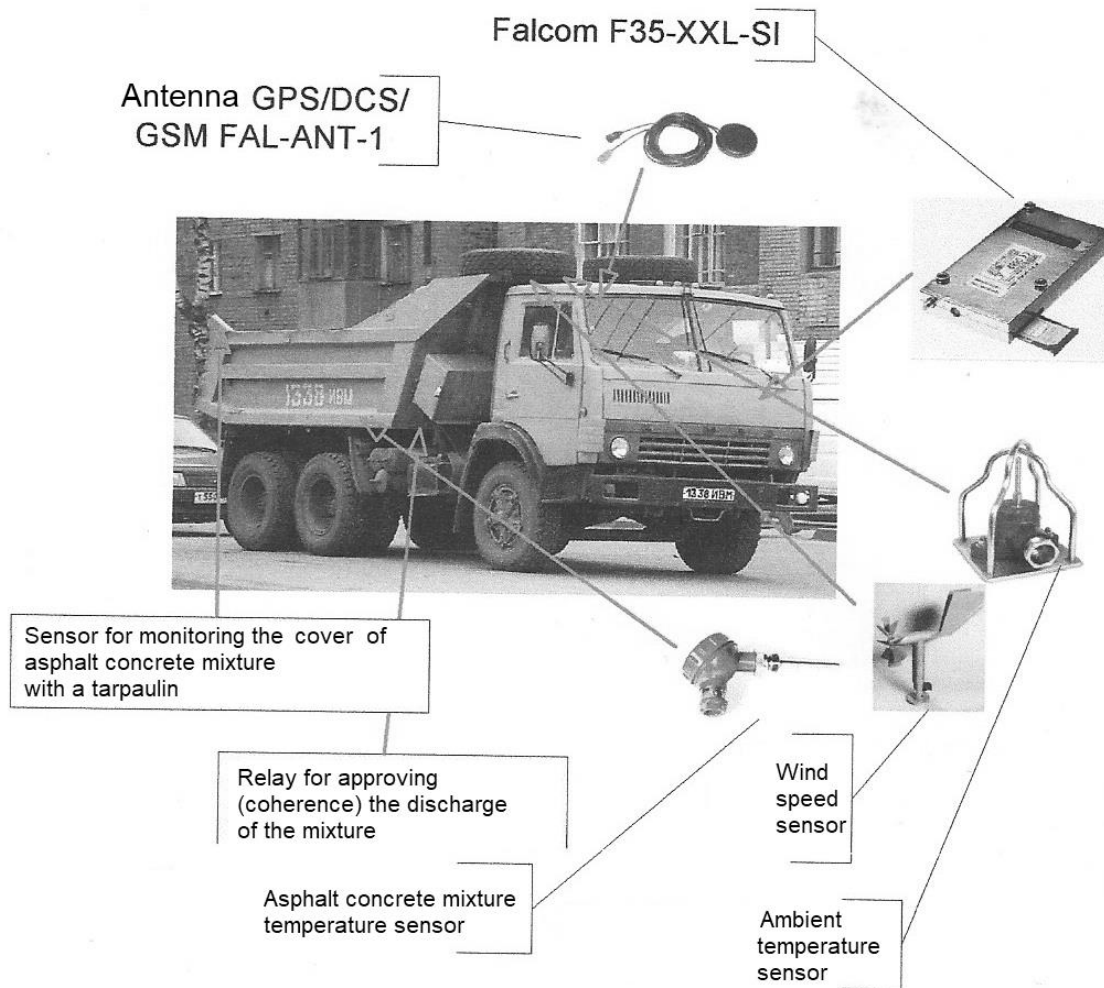


Figure 4: KamAZ 55118 dump truck with a system for monitoring parameters of asphalt concrete mixture during its transportation.

Figure 4 shows a KamAZ 55118 dump truck with a system for monitoring parameters of asphalt concrete mixture during its transportation.

It should be noted that as a result of monitoring, a significant array of data is generated, and its processing requires lengthy computing resources. So, for each truck after receiving its actual coordinates, it is necessary to determine the position on the ground, the average speed in the last segment, the average speed from the start of movement, as well as the presumable total delivery time and temperature fields in the truck body.

Figure 5 presents a generalized algorithm for controlling the transportation of asphalt-concrete mix. This algorithm includes three subroutines:

- mix loading;
- monitoring the parameters of the dump truck and the mix during its transportation;
- monitoring the car parameters during the return to the ACP.

After loading the car in the integrated management system of ACP, a route chart is formed with the following parameters: the car number, the object, the initial characteristics of the asphalt-concrete mix.

The main subroutine in the algorithm is the monitoring of parameters during the movement of the dump truck (Fig. 6). When starting the subroutine, the following parameters are determined: the location coordinates, the readings from the temperature sensors of the mix and the environment. The collected data are formed into a batch and transmitted to the integrated management system of ACP (control point).

Upon receiving these data, the control point sends a confirmation of receipt. The received materials are processed using the TranMaster program. Then the position of the dump truck on the map is determined and the temperature of the asphalt-concrete mix is monitored. If the temperature does not correspond to the set value for this mix grade, the control point corrects the route and parameters of the car movement or may decide to return it to the ACP.

The software allows the user to receive the satellite monitoring data from the «ACP–DUMP TRUCK– ASPHALT CONCRETE» system in the form of visual reports, graphs and tables.

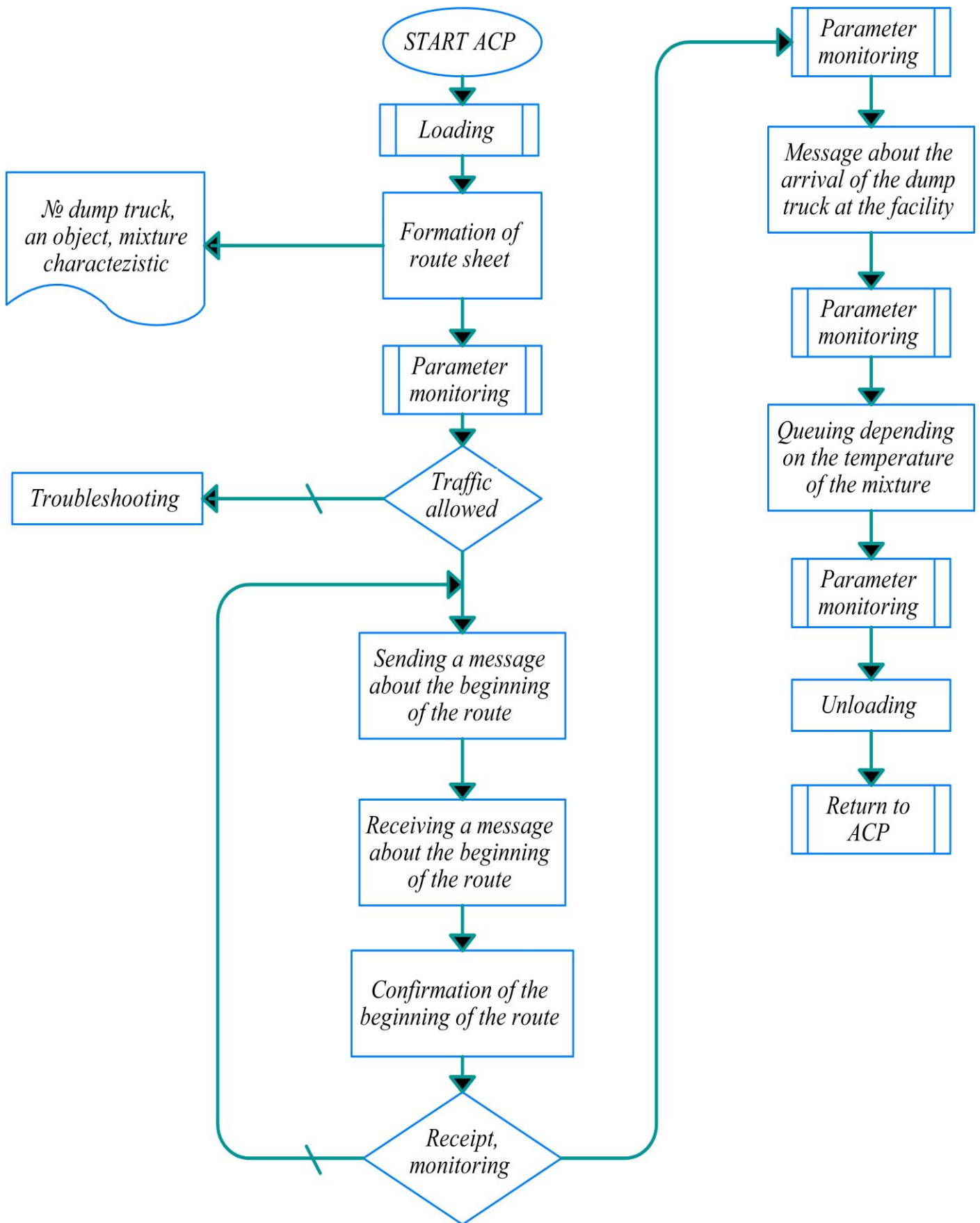


Figure 5: Asphalt mix transportation control algorithm/

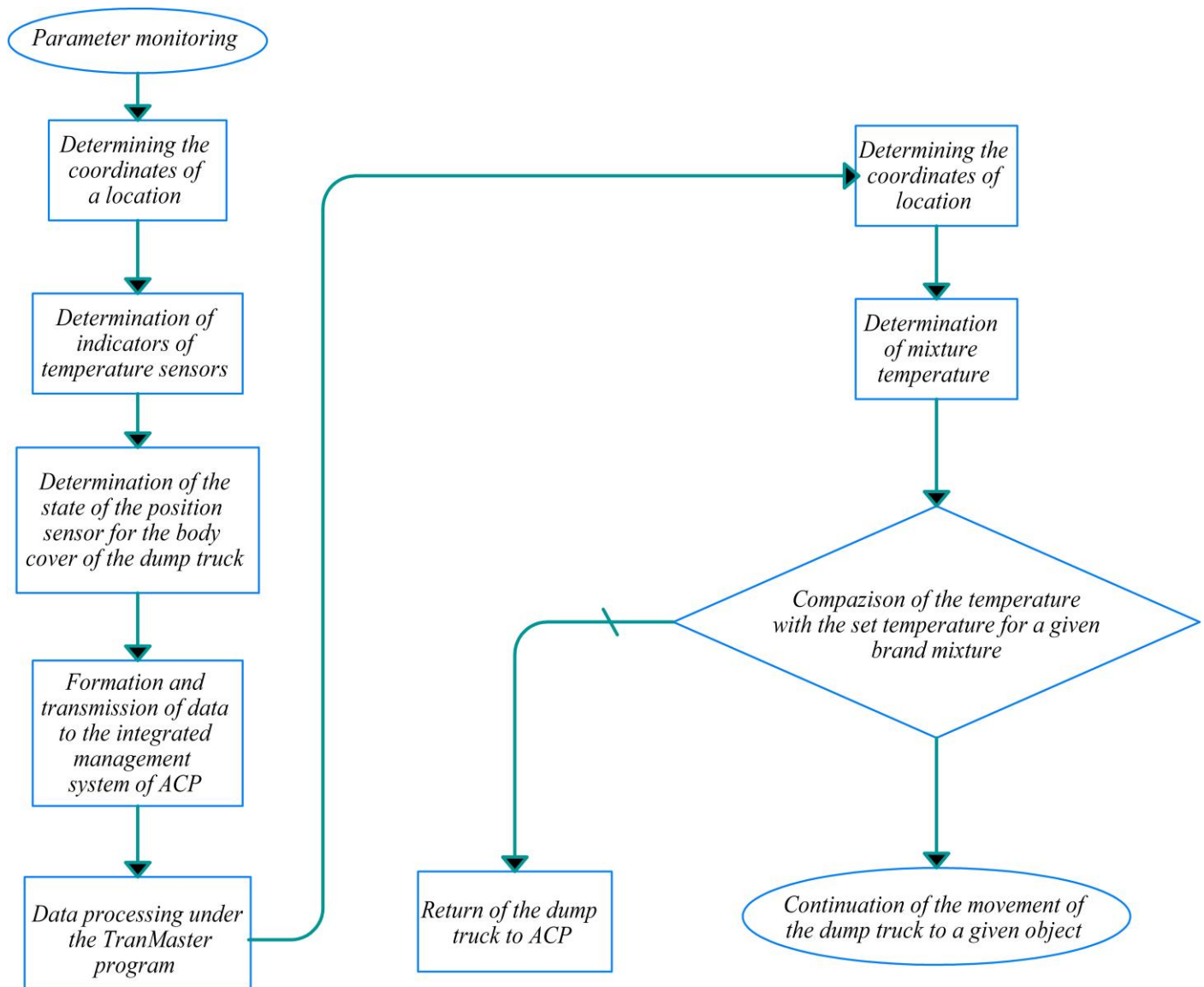


Figure 6: Subroutine of monitoring the parameter of the dump truck and the mix during its transportation.

### 3. CONCLUSION

Integrated monitoring of the parameters of dump truck and asphalt mixtures with using of the GLONASS system provides an increased productivity of the work performance, reduces the influence of the human factor on the quality of the finished road surface, and it becomes possible to carry out the remote control of the main parameters of not only the vehicles, but also the laid material, as well as operational response to the adjustment of the «ACP–DUMP TRUCK–ASPHALT CONCRETE» system parameters in case of emergency.

The system for monitoring parameters of dump truck for transporting asphalt mix, developed at the Moscow Automobile and Road Construction University, is

being successfully implemented at construction sites of Russian Federation.

### REFERENCES

- [1] A.I. Dotsenko, A.V. Rudensky, "The Concept of Integrated Quality Management of Asphaltic Concrete Roads", Mechanization of Construction, Vol. (6), pp. 17-20, (2011)
- [2] N.V. Gorelyshev, "Asphaltic Concrete and Other Materials", Mozhaysk-Tera, Moscow (Russia), (1995)
- [3] V.N. Shestakov, V.B. Permyakov, V.M. Vorozheikin, "Technological Support for the Quality of Construction of Asphaltic Concrete Pavements: Method, Recommendations", SibADI, Omsk (Russia), (1999)

# **SESSION A**

## **EARTH-MOVING AND TRANSPORTATION MACHINERY**



# Experimental Study of the Influence of a Combination of Operating Parameters of a Mobile Lift on Oscillatory Processes Occurring After Locking the Working Platform

Igor Kyrychenko<sup>1\*</sup>, Oleksandr Reznikov<sup>1</sup>, Dmytro Klets<sup>1</sup>, Anton Kholodov<sup>1</sup>

<sup>1</sup>Mechanical engineering faculty, Kharkiv National Automobile and Highway University, Kharkiv (Ukraine)

*Abstract. The article provides a detailed analysis of the influence of the combination of performance indicators of mobile lifts with working platforms (MLWP) at the stage of stopping and the process of vibration damping after stopping the working platform.*

*On the basis of the results of experimental research and processing of the obtained data, an analysis was made of the influence of the angles of inclination of the upper and lower sections of the boom and the mass of the load in the working platform on the maximum amplitude of oscillations of accelerations when the working platform is locked, the period of oscillations and the time of their damping.*

*As a result of the analysis, the spectrum of the response surfaces of the maximum amplitude of acceleration oscillations when the working platform is locked, the period of oscillations and the time of their damping from the working mass and the angles of inclination of the lower and upper boom sections was obtained, on the basis of which it can be concluded that the value of the maximum amplitude of acceleration oscillations in the locking time of the working platform is most influenced by the mass of the load in the working platform.*

**Keywords: Mobile lift, Working platform, Locking, Vibrations, Operational performance, Response surface.**

## 1. INTRODUCTION

During the MLWP operation, oscillatory processes are observed that occur after the working platform is locked. This operating mode is emergency and is observed in the event of a break in the hydraulic drive of the working equipment or an abrupt stop of the working platform.

There is a need for a detailed study of the process of locking the working platform of the MLWP and identifying the performance of the machine and options for their combination, most significantly affect the maximum amplitude of oscillations of accelerations when locking the working platform, the period of oscillations and the time of their damping.

## 2. ANALYSIS OF RECENT RESEARCH AND PUBLICATIONS

In recent years, a large number of studies have appeared aimed at studying the processes observed in MPP during operation. In the works [1-2], the issues of theoretical development of control systems for the movement of the working platform of hydraulic lifters are considered, in addition, a large number of studies are devoted to the study of processes occurring in the volumetric hydraulic drive of machines [3-4]. The analysis and study of the MLWP load modes are given in [5-6], however, there is currently no comprehensive study regarding the appearance of oscillatory modes during operation and stopping of the machine.

In [7], the issues of determining the parameters of motion of an auto-hydraulic lift with a rotary joint are considered, however, insufficient attention is paid to the experimental study of the process of locking the working platform in modern works.

The purpose of the article is to study the influence of the combination of the operating parameters of a mobile lift on the maximum amplitude, period and time of damping of oscillations of the working platform after its locking. To achieve this goal, the following tasks have been identified:

- to carry out a statistical analysis of the experimental data and, on the basis of the data obtained, to construct the response surfaces of the maximum amplitude, period and time of damping of oscillations of the working platform after it is locked from the operational indicators of the working process;
- to determine the degree of influence of the combination of operational parameters of the MP on the oscillatory processes that occur after the working platform is locked;
- based on the data obtained, draw conclusions and make recommendations.

## 3. PRESENTATION OF THE MAIN MATERIAL

For a more detailed study of the locking stage and the process of vibration damping after stopping the working platform, a statistical analysis of the vibrations of the working platform after it stopped was carried out. The analysis was carried out according to the maximum amplitude of the oscillations of the accelerations when the working platform was locked, the period of oscillations and the time of their decay, depending on the performance indicators. As a result, the response surfaces of the maximum amplitude of acceleration oscillations at locking of the working platform, the period of oscillations and the time of their damping from the working mass and the angles of inclination of the lower and upper sections of the boom were obtained.

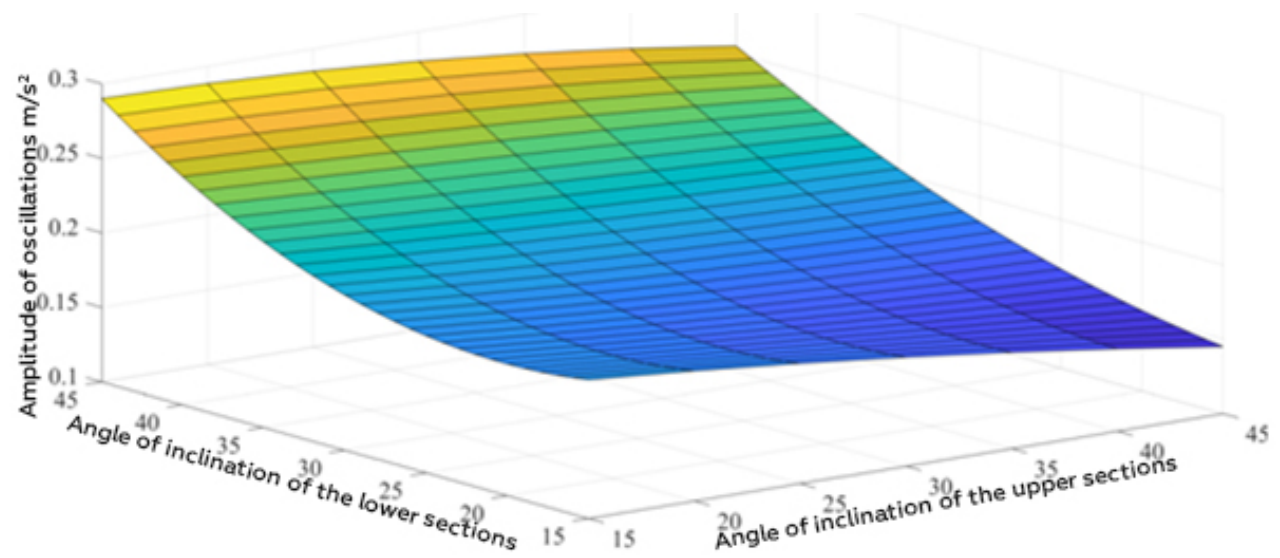
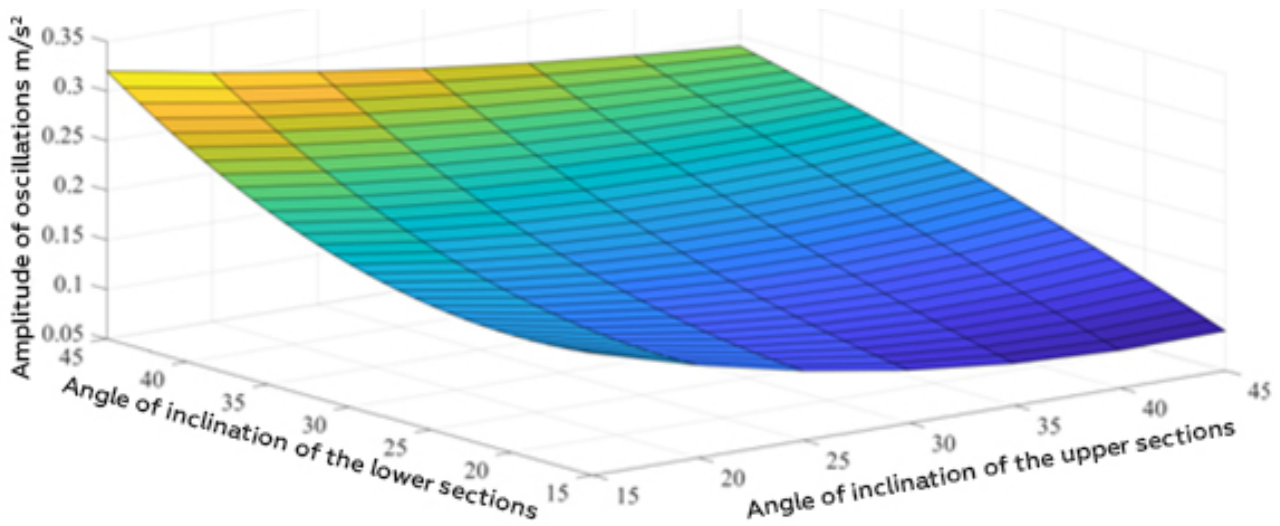
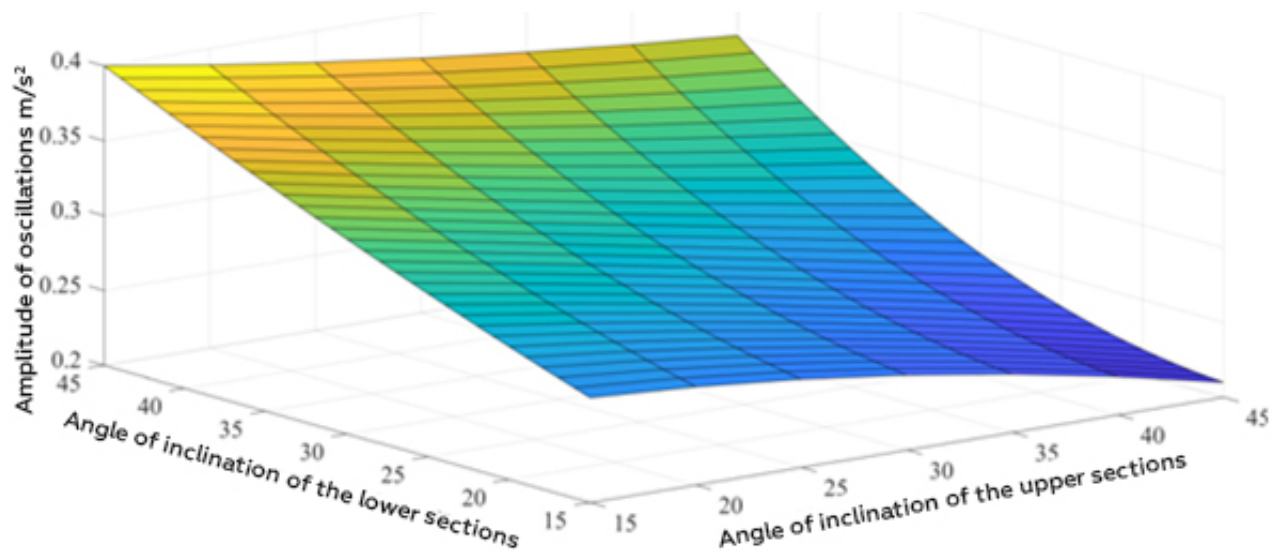
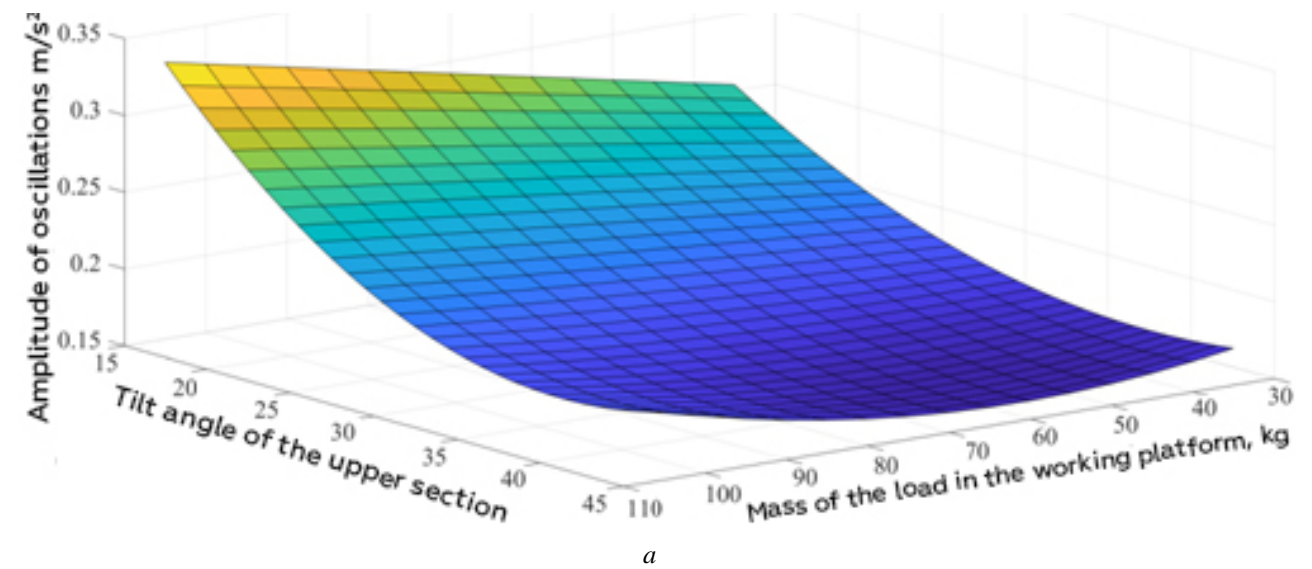
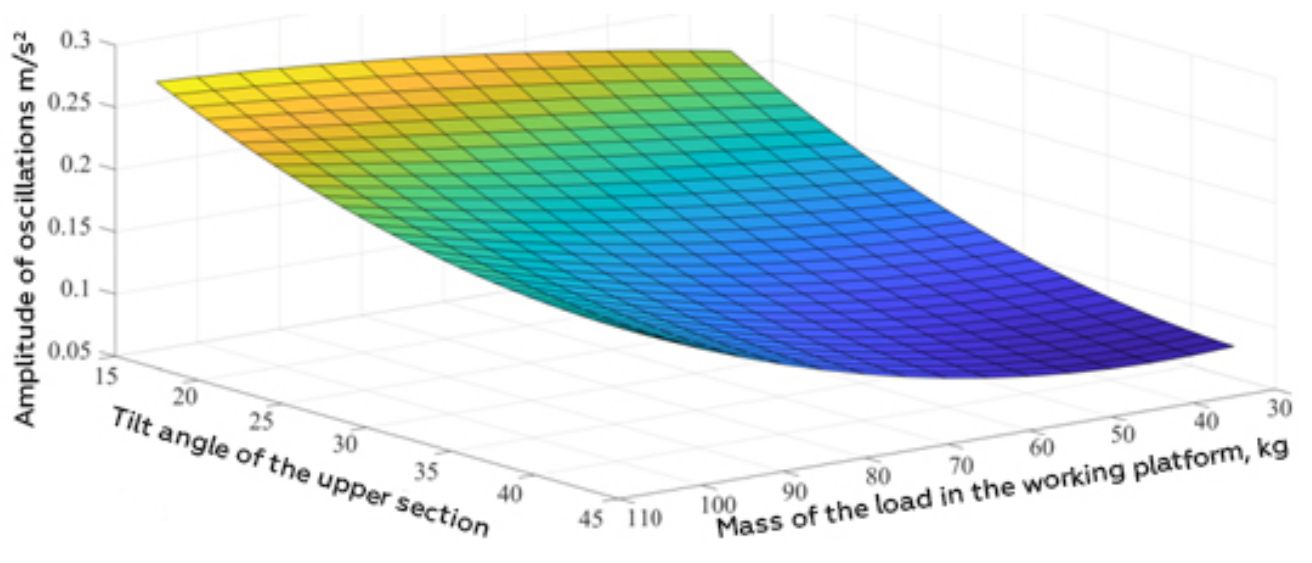
*a**b**c*

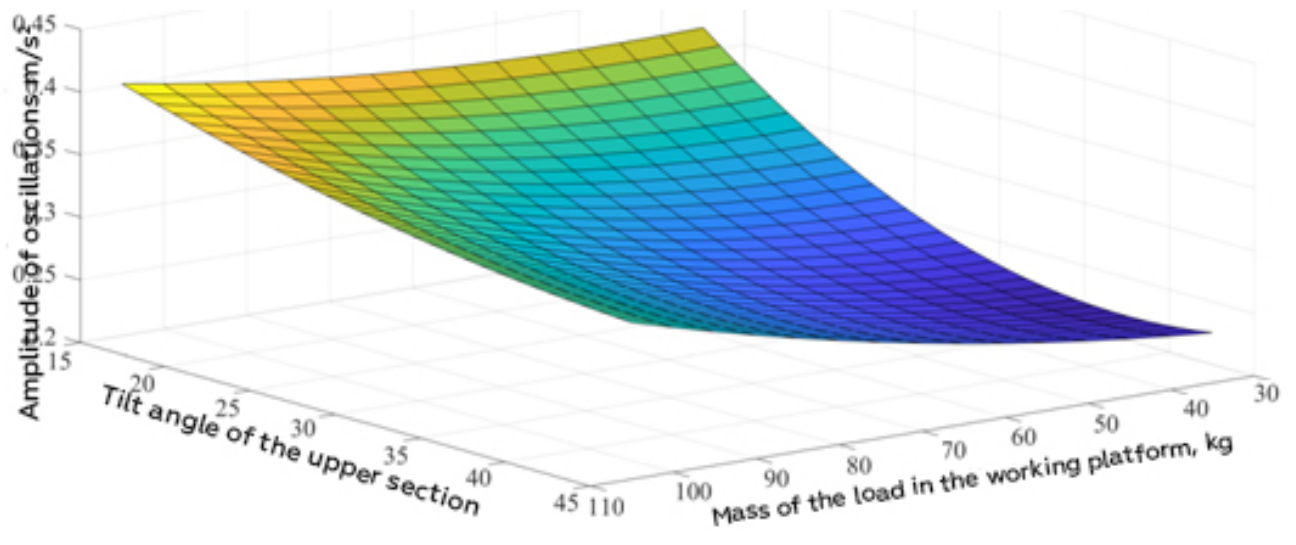
Figure 1: Response surface of the maximum amplitude of oscillations of the working platform from the angles of inclination of the lower and upper sections of the boom: a - with a load mass of 35 kg b - with a load mass of 70 kg c - with a load mass of 105 kg



a



b



c

Figure 2: Response surface of the maximum amplitude of oscillations of the working platform from the angle of inclination of the upper sections of the boom and the mass of the load: a - at an angle of inclination of the lower section of the boom 15 °; b - at an angle of inclination of the lower section of the boom 30 °; c - at an angle of inclination of the lower section of the boom 45 °.

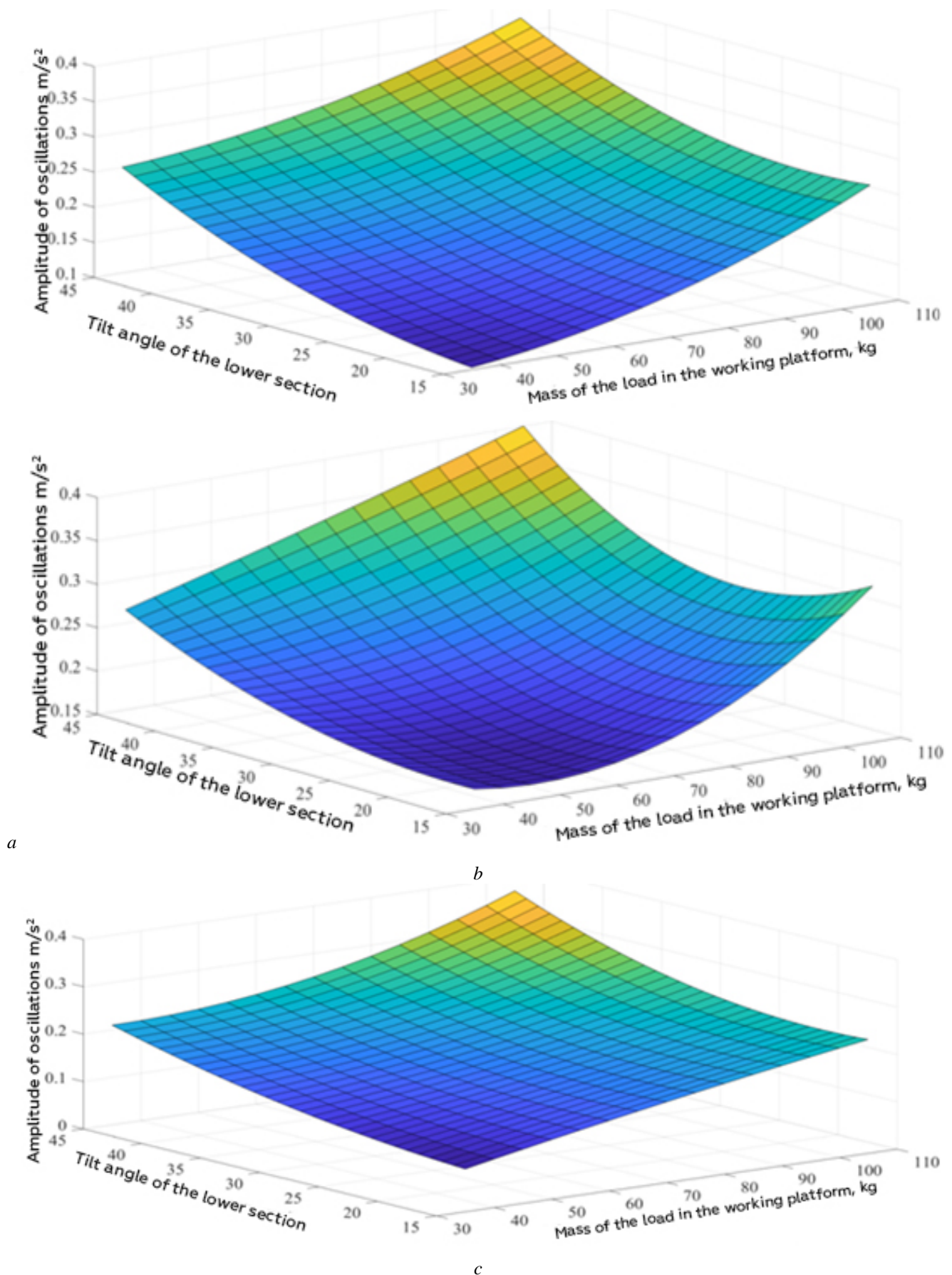
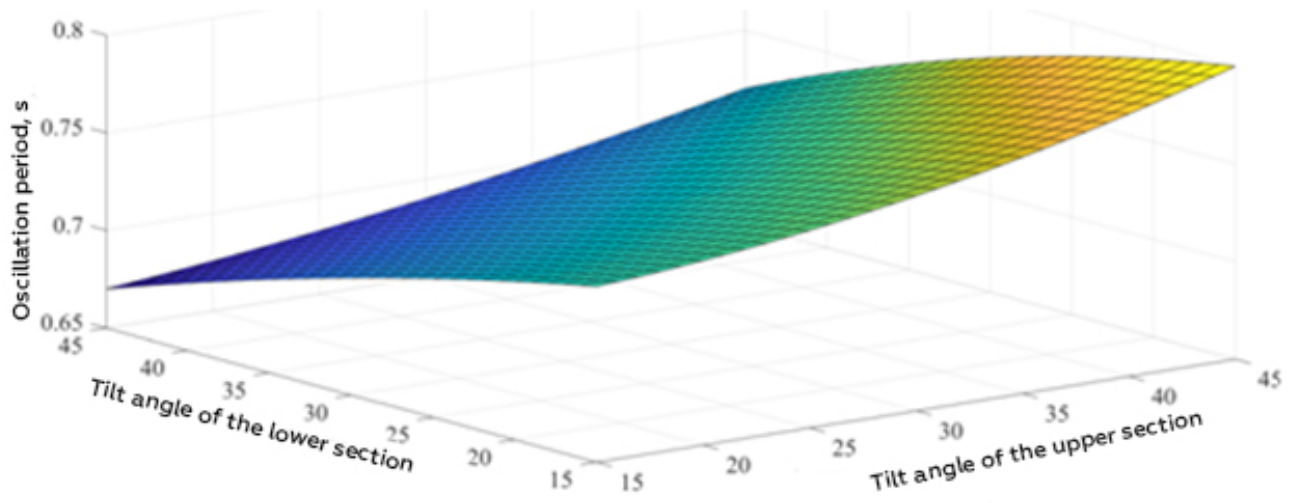
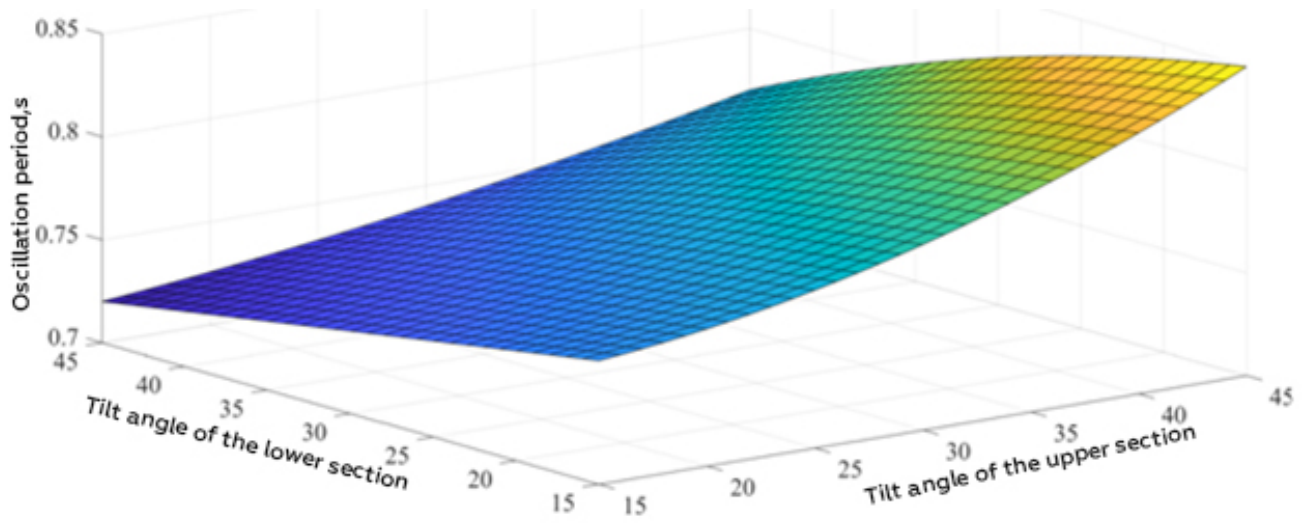


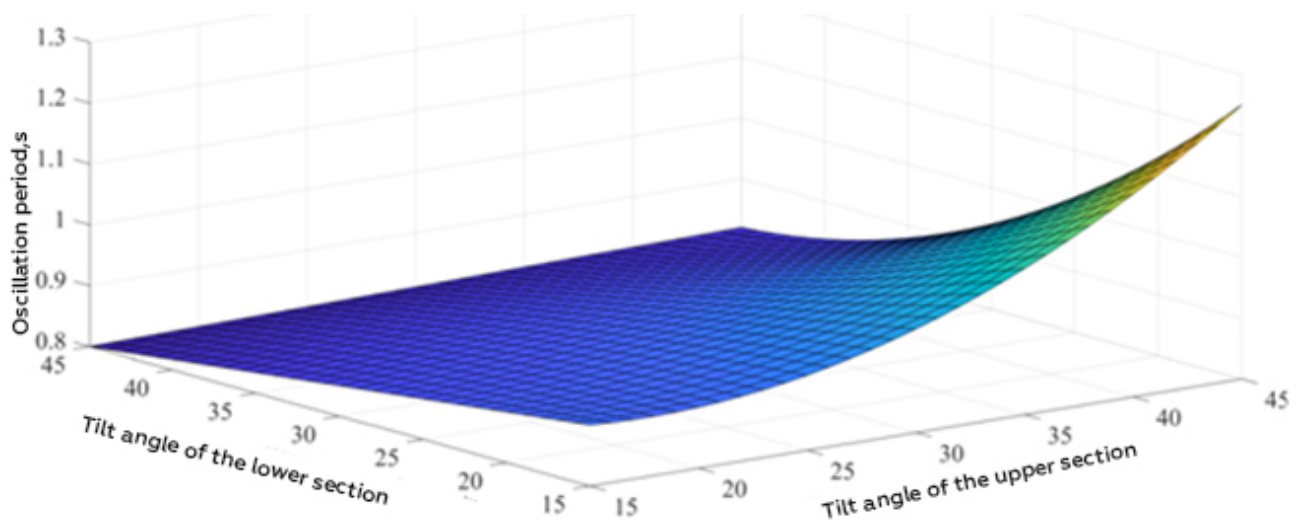
Figure 3: The surface of the response of the maximum amplitude of oscillations of the working platform from the angle of inclination of the lower sections of the boom and the weight of the load: a - at an angle of inclination of the upper section of the boom 15 °; b - at an angle of inclination of the upper section of the boom 30 °; c - at an angle of inclination of the upper section of the boom 45 °.



a

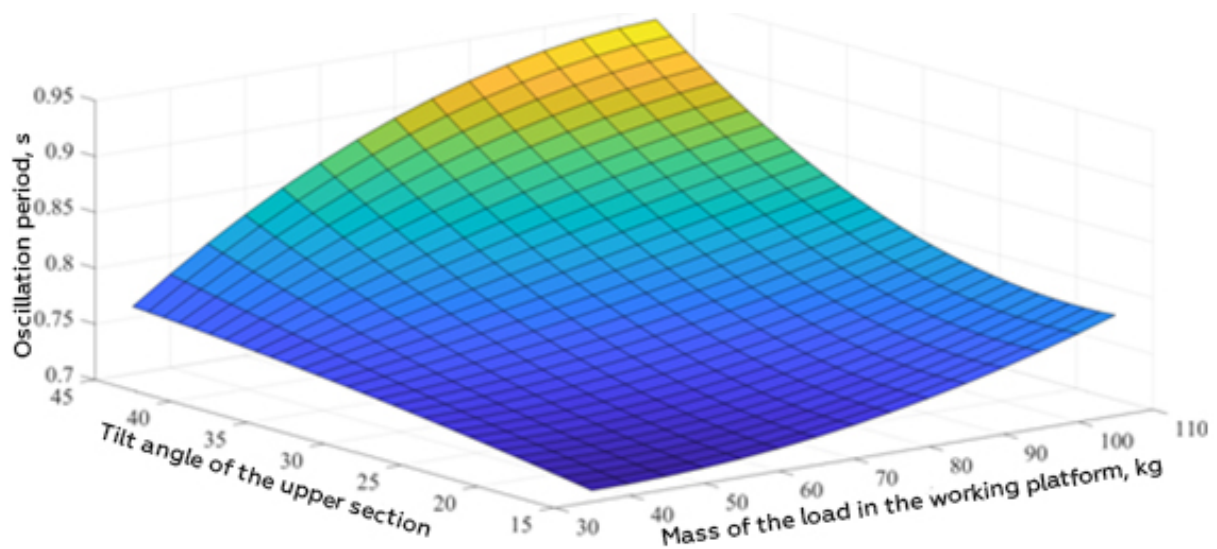


b

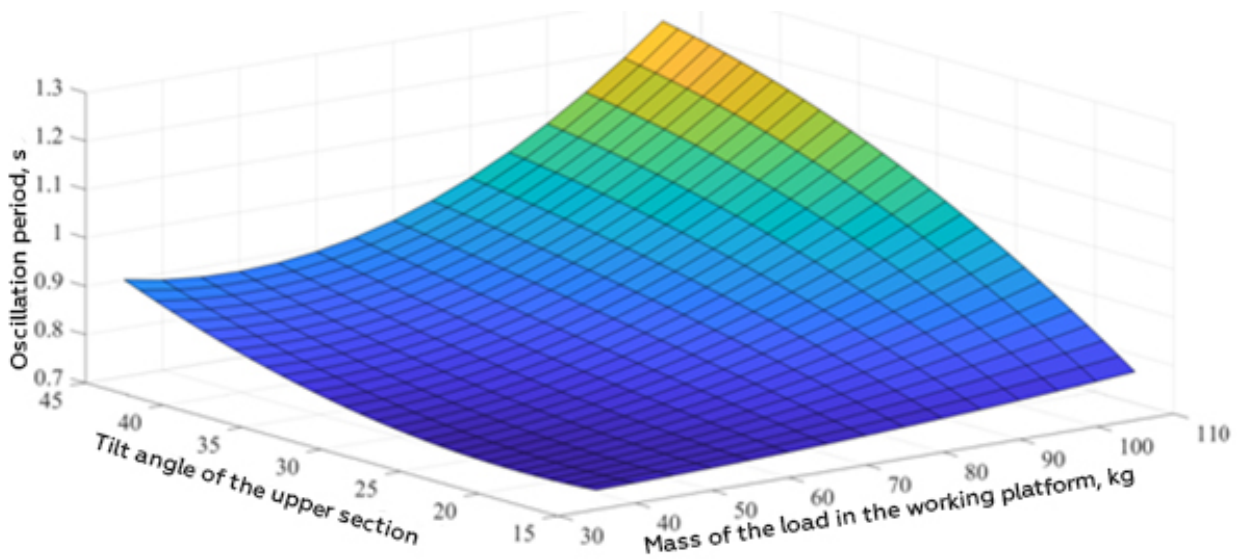


c

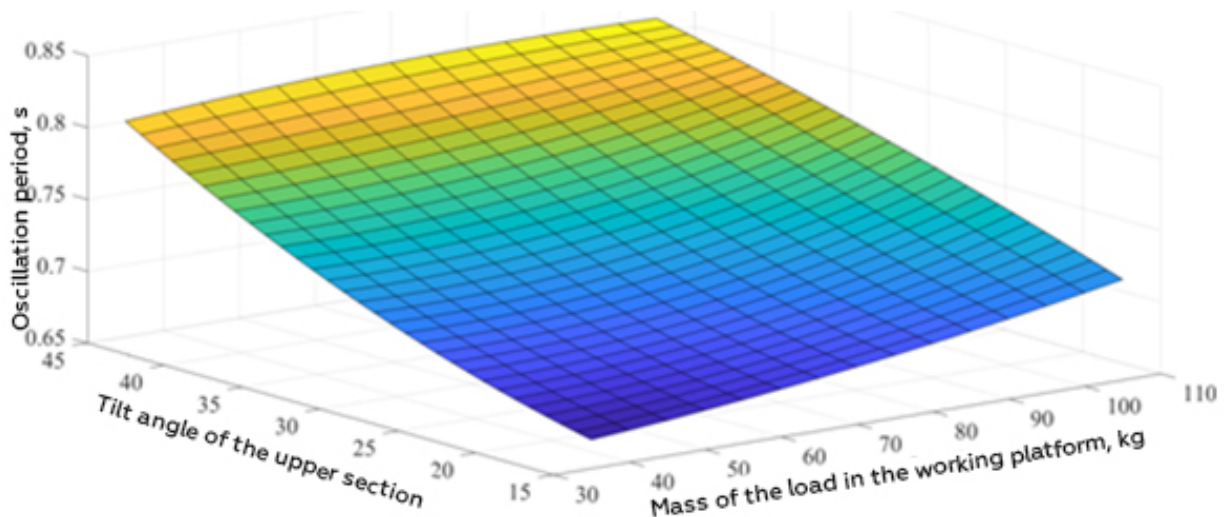
Figure 4: The surface of the response of the oscillation period of the working platform from the angles of inclination of the lower and upper sections of the boom: a - with a load mass of 35 kg b - with a load mass of 70 kg c - with a load mass of 105 kg.



a

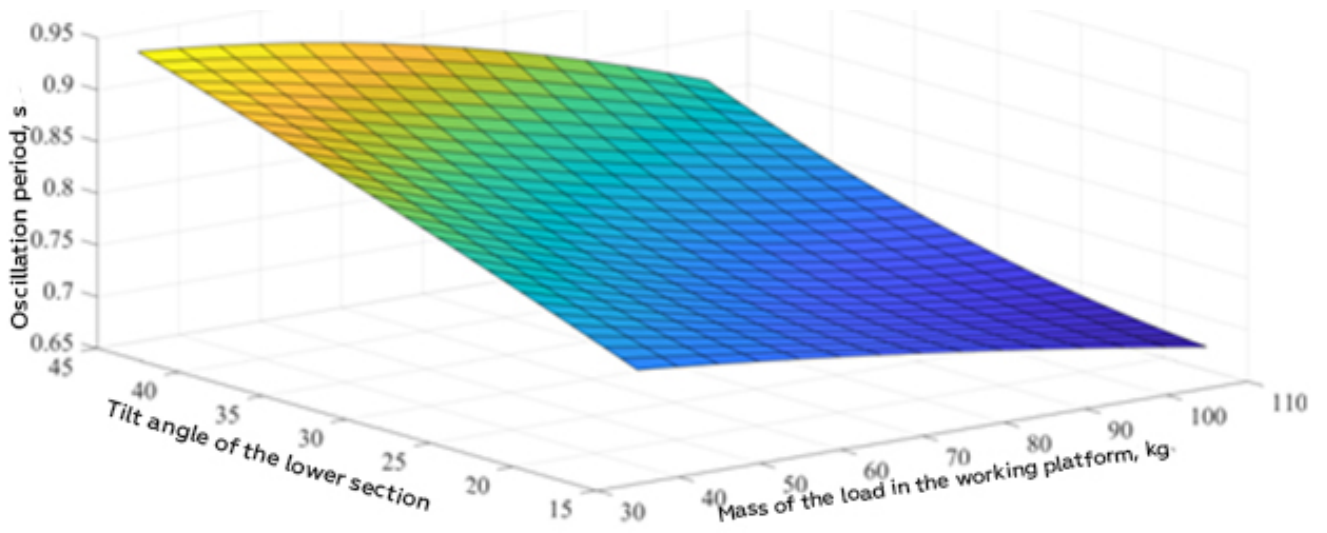


b

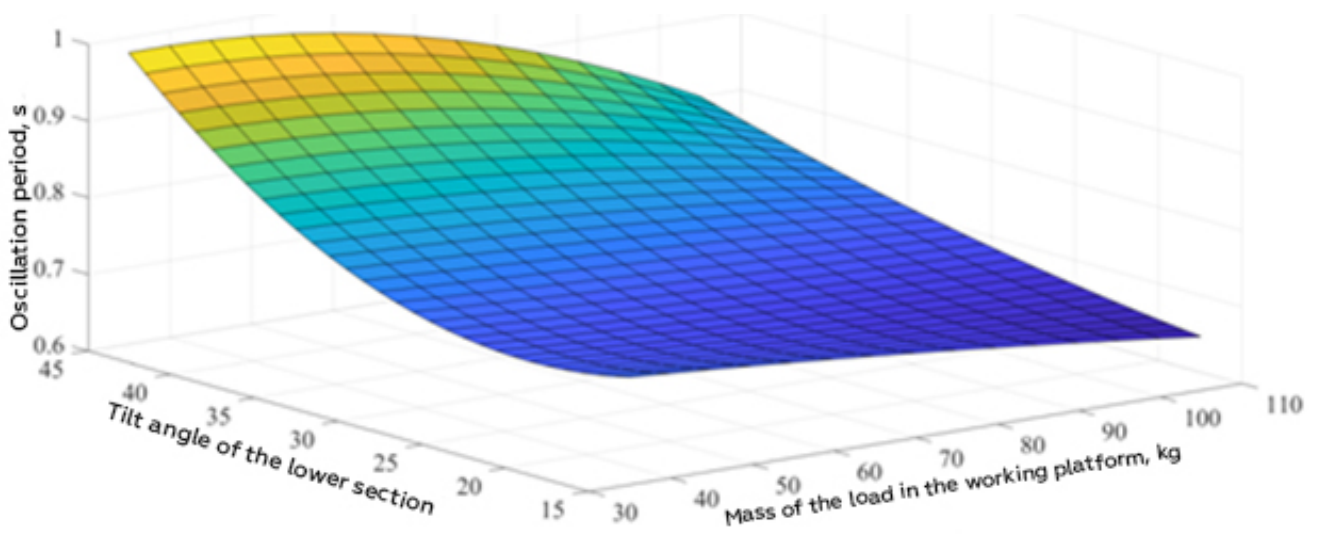


c

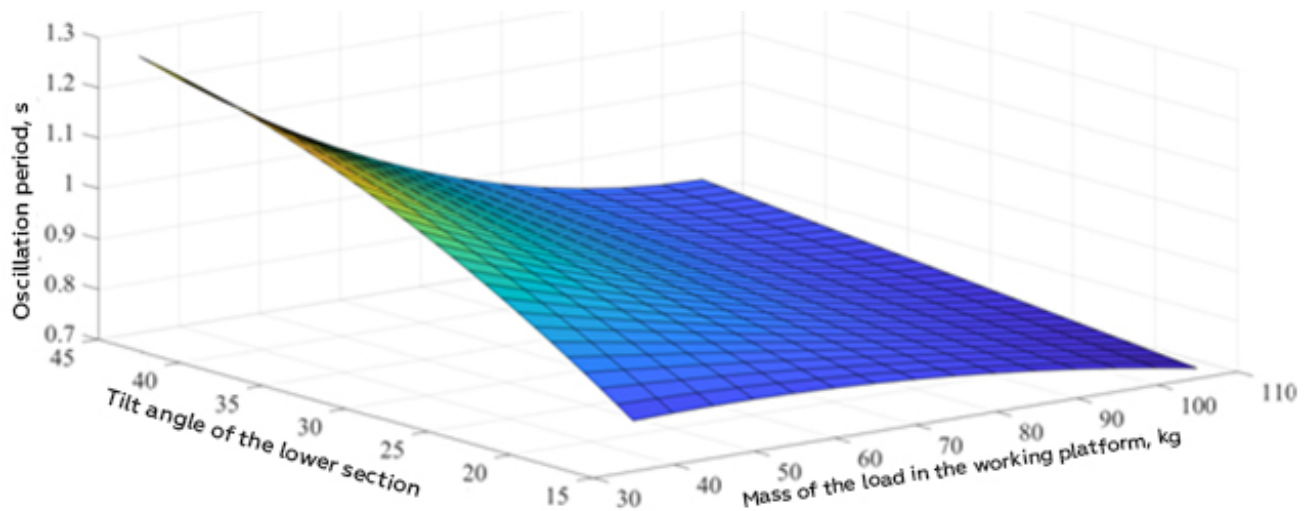
Figure 5: The surface of the response of the oscillation period of the working platform from the angle of inclination of the upper sections of the boom and the weight of the load: a - at an angle of inclination of the lower section of the boom  $15^\circ$ ; b - at an angle of inclination of the lower section of the boom  $30^\circ$ ; c - at an angle of inclination of the lower section of the boom  $45^\circ$ .



a



b



c

Figure 6: The surface of the response of the oscillation period of the working platform from the angle of inclination of the lower sections of the boom and the weight of the load: a - at an angle of inclination of the upper section of the boom 15 °; b - at an angle of inclination of the upper section of the boom 30 °; c - at an angle of the upper lower section of the boom 45 °.

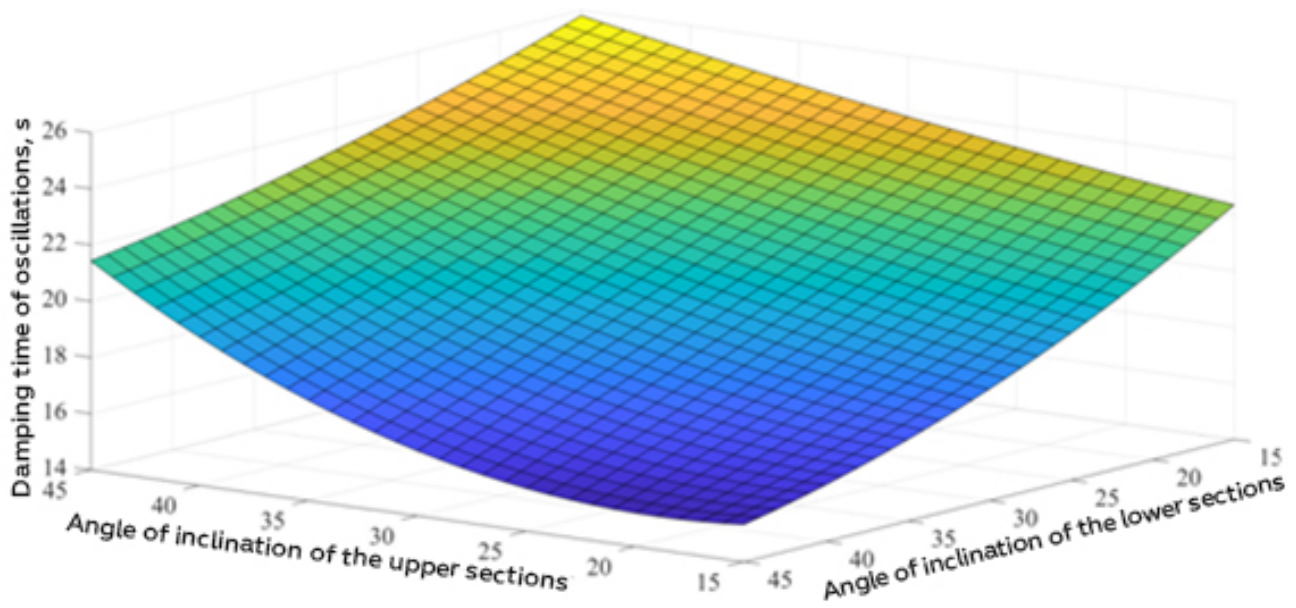
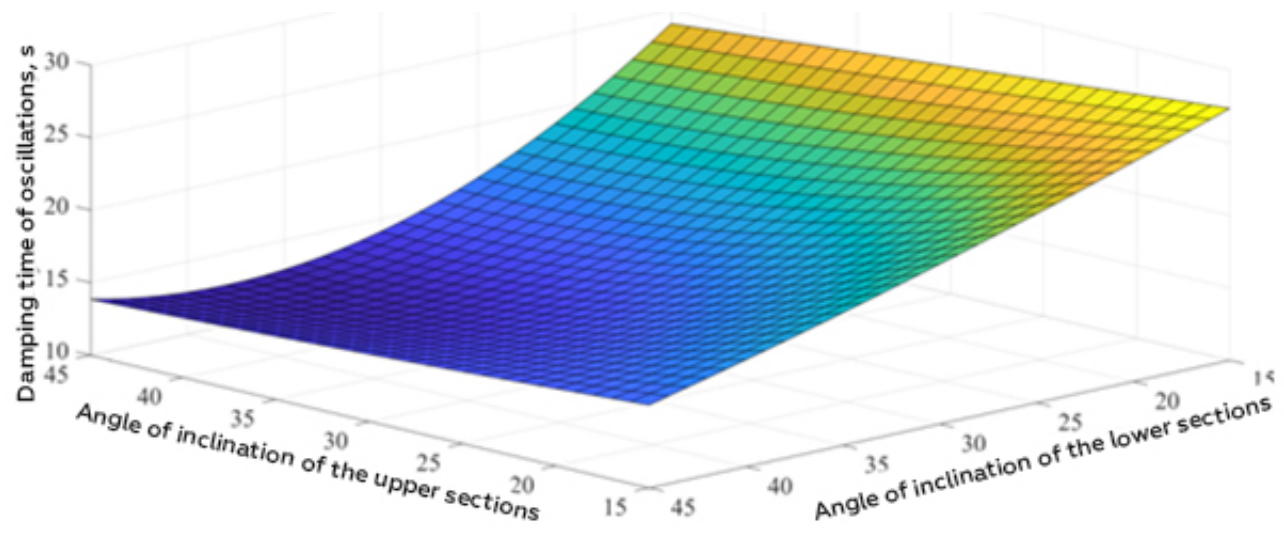
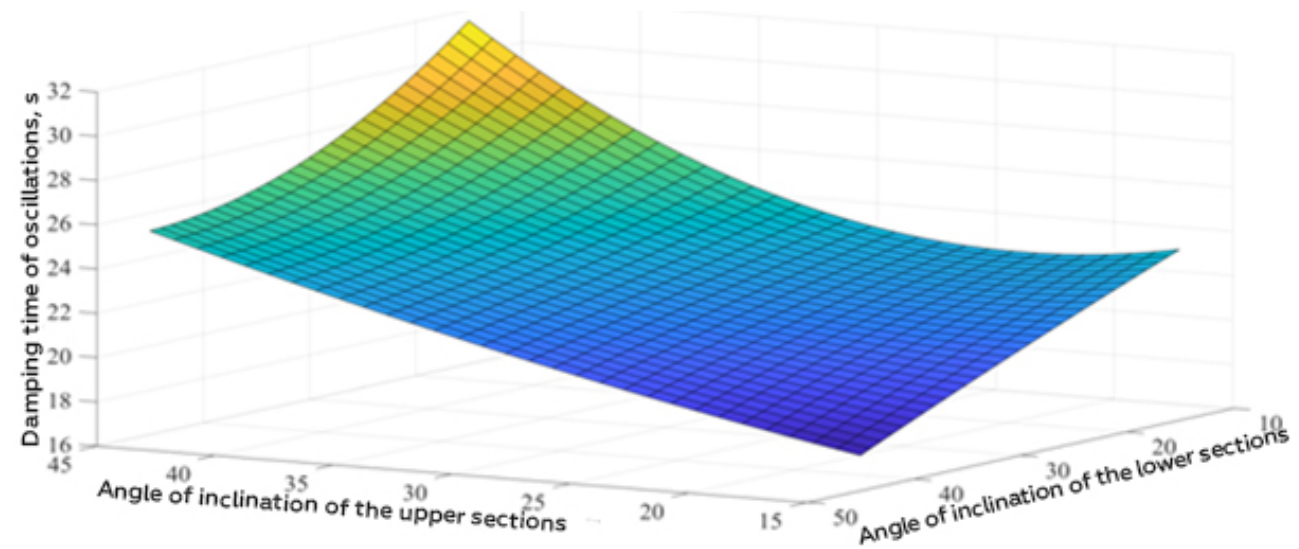
*a**b**c*

Figure 7: The surface of the response of the damping time of oscillations of the working platform from the angles of inclination of the lower and upper sections of the boom: a - with a load mass of 35 kg b - with a load mass of 70 kg c - with a load mass of 105 kg.

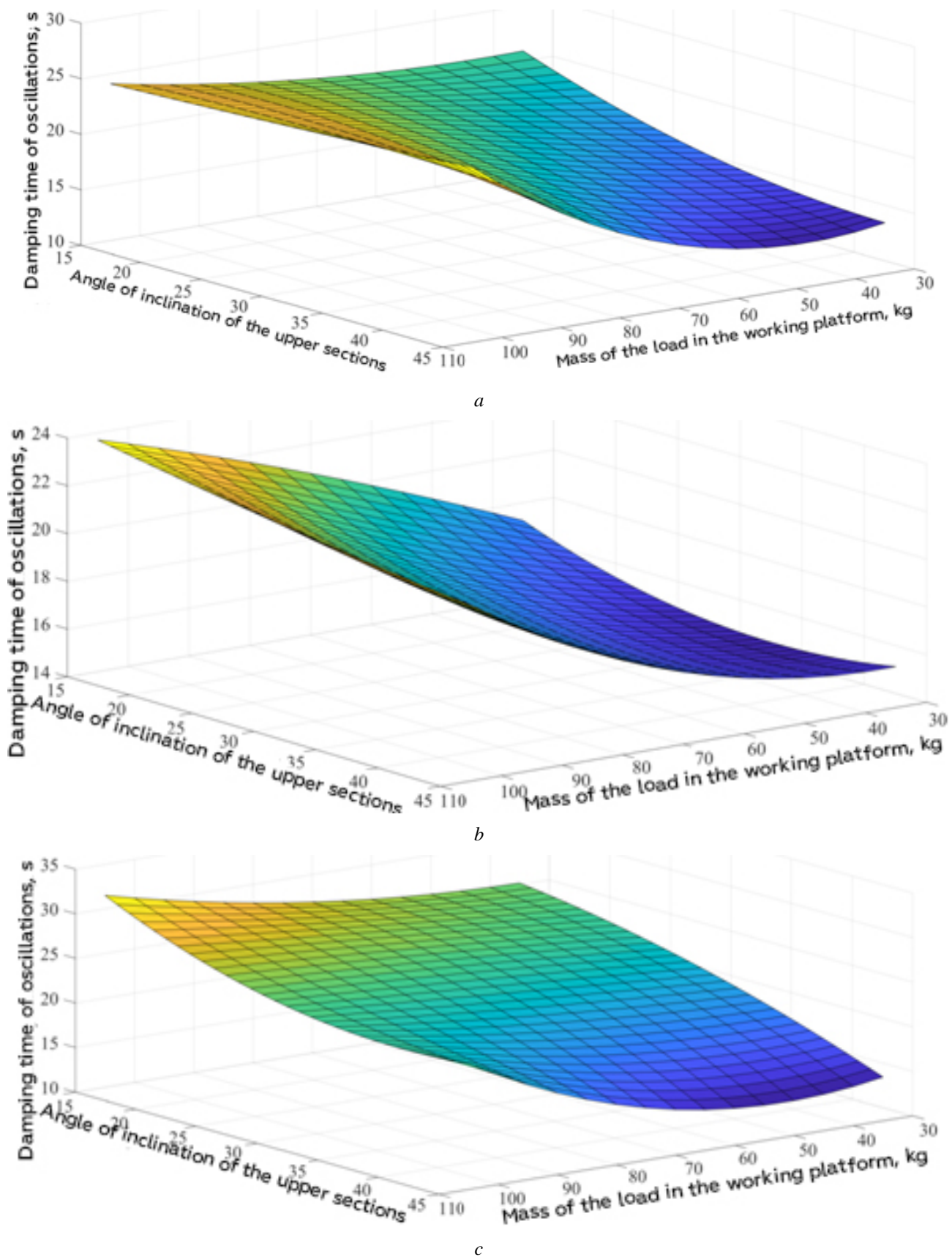
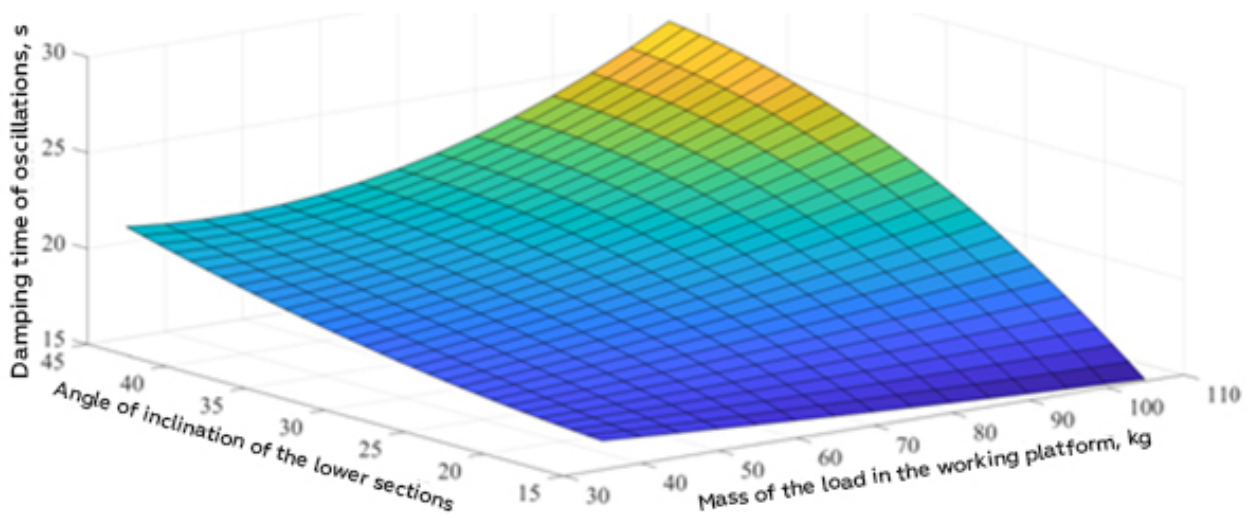
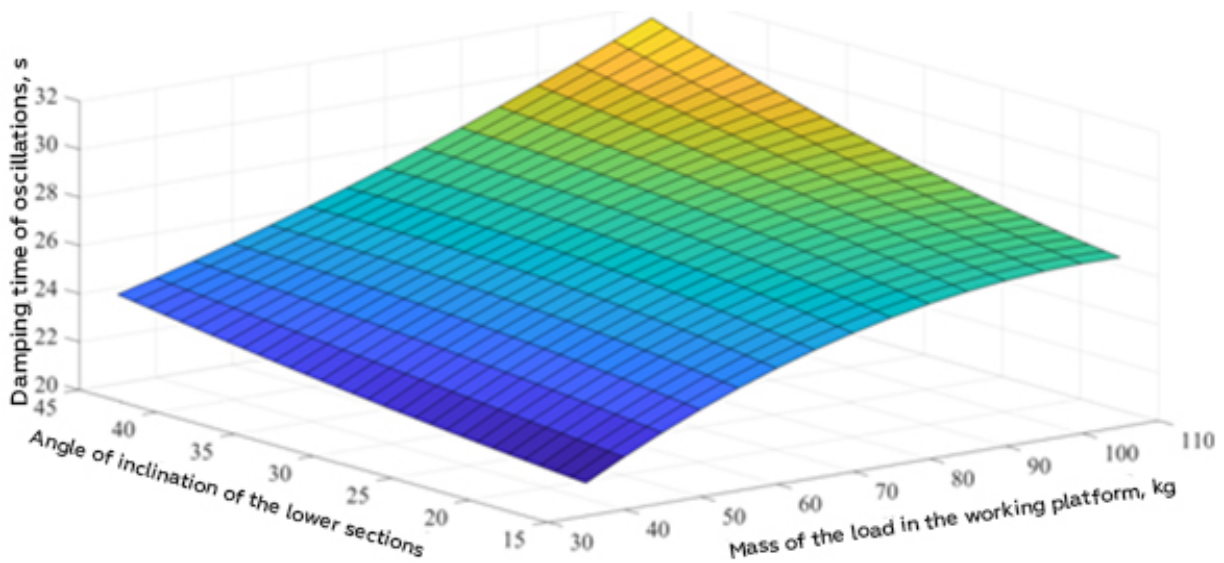


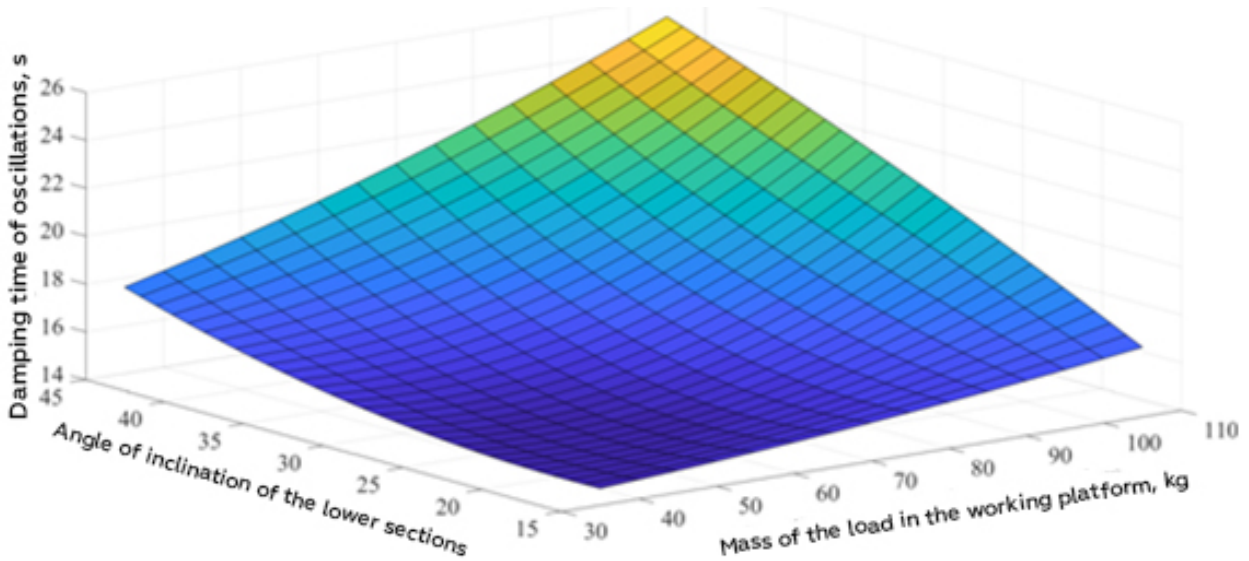
Figure 8: Response surface of the damping time of oscillations of the working platform from the angle of inclination of the upper sections of the boom and the weight of the load: a - at an angle of inclination of the lower section of the boom 15 °; b - at an angle of inclination of the lower section of the boom 30 °; c - at an angle of inclination of the lower section of the boom 45 °.



a



b



c

Figure 9: The surface of the response of the damping time of the oscillations of the working platform from the angle of inclination of the lower sections of the boom and the weight of the load: a - at an angle of inclination of the upper section of the boom  $15^\circ$ ; b - at an angle of inclination of the upper section of the boom  $30^\circ$ ; c - at an angle of the upper lower section of the boom  $45^\circ$

As a result of the analysis of the response surfaces of the maximum amplitude of acceleration oscillations when the working platform is locked, the period of oscillations and the time of their damping from the working mass and the angles of inclination of the lower and upper sections of the boom, it can be concluded that the value of the maximum amplitude of acceleration oscillations when the working platform is locked is most influenced by the weight of the load in the working platform. It should be noted that with a combination of factors such as the angle of inclination of the lower and upper sections of the boom (Fig. 1), the amplitude of oscillations of acceleration when the working platform is locked acquires maximum values at an angle of inclination of the lower section of the boom of  $45^\circ$  and an angle of inclination of the upper section of the boom of  $15^\circ$ . With an increase in the mass of the load, the maximum amplitude of acceleration oscillations when the working platform is locked increases by 28% (from  $0.29 \text{ m/s}^2$  with a load mass of 35 kg to  $0.4 \text{ m/s}^2$  with a load mass of 105 kg).

The response surface of the maximum amplitude of acceleration oscillations when the working platform is locked from the working mass and the angle of inclination of the upper section of the boom acquires maximum values with a weight of 105 kg and an angle of inclination of the upper section of the boom  $15^\circ$  (Fig. 2). With an increase in the angle of inclination of the lower section of the boom, the maximum amplitude of acceleration oscillations when the working platform is locked increases by 35% (from  $0.26 \text{ m/s}^2$  at an angle of inclination of the lower section of the boom  $15^\circ$  to  $0.4 \text{ m/s}^2$  at an angle of inclination of the lower section of the boom  $45^\circ$ ).

With a combination of such factors as the working mass and the angle of inclination of the lower section of the boom, the response surface of the maximum amplitude of oscillations of acceleration when the working platform is locked (Fig. 3) acquires maximum values with a load mass of 105 kg and an angle of inclination of the lower section of the boom of  $45^\circ$ . At the same time, with a change in the angle of inclination of the upper section of the boom from  $15^\circ$  to  $45^\circ$ , the maximum amplitude of oscillations of acceleration when locking the working platform decreases by 10% ( $0.4 \text{ m/s}^2$  at an angle of inclination of the upper section of the boom  $15^\circ$  to  $0.36 \text{ m/s}^2$  at angle of inclination of the upper boom section  $45^\circ$ ).

The period of oscillation of the working platform after stopping with a combination of factors such as the angle of inclination of the lower and upper sections of the boom (Fig. 4) acquires maximum values when the angle of the lower section of the boom is  $15^\circ$  and the angle of inclination of the upper section of the boom is  $45^\circ$ . With an increase in the mass of the load in the working platform from 35 kg to 105 kg, the oscillation period increases by 37% (from 0.79 s with a load mass of 35 kg to 1.25 s with a load mass of 105 kg).

The response surface of the oscillation period of the working platform after locking from the working mass and the angle of inclination of the upper section of the boom acquires maximum values with a weight of 105 kg and an angle of inclination of the upper section of the boom  $45^\circ$  (Fig. 5). With an increase in the angle of inclination of the lower section of the boom from  $15^\circ$  to  $45^\circ$ , the period of

oscillation of the working platform after locking decreases by 36% (from 1.25 s at an angle of inclination of the lower section of the boom  $15^\circ$  to 0.8 s at an angle of inclination of the lower section of the boom  $45^\circ$ ).

With a combination of factors such as the operating mass and the angle of inclination of the lower section of the boom, the response surface of the oscillation period of the working platform after locking (Fig. 6) acquires maximum values with a load weight of 35 kg and an angle of inclination of the lower section of the boom of  $45^\circ$ . At the same time, with a change in the angle of inclination of the upper section of the boom from  $15^\circ$  to  $45^\circ$ , the period of oscillation of the working platform after locking increases by 22% (0.98 s at an angle of inclination of the upper section of the boom  $15^\circ$  to 1.25 s at an angle of inclination of the upper section of the boom  $45^\circ$ ).

The damping time of vibrations of the working platform after stopping with a combination of factors such as the angle of inclination of the lower and upper sections of the boom (Fig. 7) acquires maximum values at an angle of inclination of the lower section of the boom  $15^\circ$  and an angle of inclination of the upper section of the boom  $15^\circ$ . With an increase in the weight of the load in the working platform from 35 kg to 105 kg, the vibration damping time increases by 23% (from 24 s with a load weight of 35 kg to 31 s with a load weight of 105 kg).

The response surface of the damping time of the oscillations of the working platform after stopping from the working mass and the angle of inclination of the upper section of the boom acquires maximum values with a weight of 105 kg and an angle of inclination of the upper section of the boom  $15^\circ$  (Fig. 8). With an increase in the angle of inclination of the lower section of the boom from  $15^\circ$  to  $45^\circ$ , the damping time of oscillations of the working platform after stopping increases by 25% (from 24 s at an angle of inclination of the lower section of the boom of  $15^\circ$  to 31 s at an angle of inclination of the lower section of the boom of  $45^\circ$ ).

With a combination of factors such as the operating mass and the angle of inclination of the lower section of the boom, the response surface of the damping time of oscillations of the working platform after locking (Fig. 9) takes on maximum values with a load mass of 105 kg and an angle of inclination of the lower section of the boom  $45^\circ$ . At the same time, with a change in the angle of inclination of the upper section of the boom from  $15^\circ$  to  $45^\circ$ , the damping time of oscillations of the working platform after locking is reduced by 19% (from 31 s at an angle of inclination of the upper section of the boom of  $15^\circ$  to 25 s at an angle of inclination of the upper section of the boom of  $45^\circ$ ).

## ACKNOWLEDGEMENTS

According to the specified purpose and objectives of the study, the following conclusions can be drawn:

1. Statistical analysis of the results of the experimental study indicates that the operating parameters of the mobile lift significantly affect the indicators of oscillatory processes, such as the amplitude, period and damping time of oscillations occurring in the machine during operation.

2. Analysis of the response surfaces of the maximum amplitude, period and time of damping of

oscillations of the working platform after it is locked from the operational indicators of the working process indicates that the highest indicators of oscillatory processes are observed when the working platform is lowered when the load mass and horizontal reach are maximum.

3. To prevent accidents that may arise during the locking of the MPP working platform, it is advisable to use a proportional hydraulic drive and a number of safety devices, which together will reduce the vibrations of the working platform, significantly increase the safety and ergonomics of the machine.

#### REFERENCES

- [1] Shherbakov V.S. Avtomatizaciya modelirovaniya optimal'noj traektorii dvizheniya rabocheho organa stroitel'nogo manipulyatora: monografiya / V.S. Shherbakov, I.A. Rebrova, M.S. Kory'tov. – Omsk: SibADI, 2009. – 106 s.
- [2] Gurko A. G. Razrabotka sistemy` upravleniya dvizheniem avtogidropod'emnika / A. G. Gurko, I. G. Kirichenko // Budi`vnicztvo. Materi`aloznavstvo. Mashinobuduvannya. Seri`ya: Pi`djomno-transportni`, budi`vel`ni` i` dorozhni` mashini i` obladnannya. – 2014. – S. 210-220.
- [3] Matematicheskoe modelirovanie prozessov v sisteme gidroprivoda lesny`kh manipulyatorov / [P.I. Popikov, P.I. Titov, A.A. Sidorov i dr.] // Nauchny`j zhurnal KubGAU. – 2011. – # 69(5) – S. 1-11.
- [4] Ob`yomny`j gidroprivod v mobil`ny`kh pod`yomnikakh s rabochimi platformami: monografiya / [I.G. Kirichenko, G.A. Avrunin, V.B. Samorodov i dr.]. – Khar`kov : KhNADU, 2018. – 295 s.
- [5] Barkov A.Yu. Rezhimy` nagruzheniya stroitel`ny`kh gruzopassazhirsikh pod`emnikov. Interstrojmekh-2001 / A.Yu. Barkov, M.A. Stepanov // Trudy` Mezhdunarodnoj nauchno-tehnicheskoy konferenczii. – Sankt-Peterburg: Izdatel`stvo SPbGTU, 2001g. – S. 14-18.
- [6] Barkov A.Yu. Analiz rezhimov nagruzheniya privodov stroitel`ny`kh pod`emnikov. Interstrojmekh-2002 / A.Yu. Barkov, M.A. Stepanov // Materialy` Mezhdunarodnoj nauchno-tehnicheskoy konferenczii., Mogilev: Izdatel`stvo MGTU, 2002g. – S.391-394.
- [7] Gurko O. G. Dosli`dzhennya parametri`v rukhu avtogi`dropi`di`jmacha z obertal`nimi zchlenuvannyami / O. G. Gurko, Yu. O. Dolya // Novi` materi`ali i` tekhnologi`yi v metalurgi`yi ta mashinobuduvanni`. – 2016. – #2. – S. 121-127.

# Finite Element and Analytical Modelling of Ship Unloader

Zrnić Nenad<sup>1\*</sup>, Gašić Vlada<sup>1</sup>, Urošević Marko<sup>1</sup>, Arsić Aleksandra<sup>1</sup>

<sup>1</sup>Faculty of Mechanical Engineering, Department of Material Handling Constructions and Logistics, University of Belgrade, Belgrade (Serbia)

The paper deals with the mathematical modelling of the dynamic behaviour of the structure of the ship unloader. It is given the procedure for formulation of the reduced dynamic model which retains the main aspects of the behaviour of the structure and yet is simple enough to be performed with standard engineering tools. The approach is applied on the real bridge-type grab ship unloader but can also be used on similar complex structures. Initially, the complete structure is modelled with finite element software where the natural frequencies were obtained. This 3D model is reduced to an equivalent plane model of the sea-side part of the boom. The postulation of the analytical approach is based on the model of a simple beam with an overhang where dynamic analysis is concerned with the Rayleigh Ritz method for estimating the adopted admissible functions. The results of the modal analysis of the reduced mathematical model showed a small difference from the results of finite element analysis which stands for the verification of the presented approach.

**Keywords:** Ship unloader, FEM analysis, Mathematical modelling

## 1. INTRODUCTION

Ship unloaders are machines located in ports and docks to facilitate bulk material exportation. These cranes are used to transfer, continually, solid bulk material from the ship to the shore and conversely such as iron ore, coal, fertilizers, and grains.

Over time, from 1959 [1] until today, the size, mass, and strength of the crane structures have increased due to the increasing size of ships and the constant growth of goods traffic in ports. However, the structures of the cranes remained relatively slender, i.e. their stiffness did not increase proportionally. Therefore, the movement of the trolley over the boom, as well as the lifting of the grab with material, can cause unacceptable deflection of the structure, especially in the vertical plane, [2]. According to these facts, the dynamic analysis is necessary in process of projecting in order to prevent the occurrence of unwanted stress states and deformations that can greatly reduce the productivity of these systems.

A detailed numerical analysis of the moving load problem for the lifting boom of a ship unloader is given in [3,4]. To analyze the dynamic response of the crane boom structure due to moving mass, the first step should be to create a reliable finite element (FE) model which will give corresponding natural frequencies and the vibration mode shapes of the crane structure, [5].

Creating a mathematical model plays an important role when it is impossible to perform experimental analyzes of the dynamic behaviour of the structure, and can also enable the optimization of the structure by varying the design parameters of the crane while maintaining maximum utilization of its capacity, [6].

In this paper, a numerical and mathematical model of the real construction of a ship unloader for obtaining its natural frequencies is developed. It is a project of the company Ceretti Tanfani S.p.A. Milano [7] for the needs of the Port of Bar. The construction of the boom is made of two girder (double girder boom) and box cross-section, which is connected to the pillar with one forestay and one backstay. Main technical characteristics of this crane is given in Table 1.

Table 1: Main technical characteristics of observed ship unloader

|  |                |
|--|----------------|
| Capacity, ( $Q$ )                              | 400 t/h        |
| Maximum load capacity, ( $M$ )                 | 12 t           |
| Lifting height above the rail level, ( $H_1$ ) | 20 m           |
| Reach from water side leg, ( $L_w$ )           | 32 m           |
| Reach from land side leg, ( $L_l$ )            | 26 m           |
| Span between the legs, ( $L_s$ )               | 28 m           |
| Width between the legs, ( $B$ )                | 14 m           |
| Total height, ( $H$ )                          | $\approx 51$ m |

## 2. NUMERICAL MODEL

In order to perform a modal analysis of the mathematical model of the ship unloader, it is necessary to form its numerical model on the basis of which the natural frequencies will be obtained, which will later be used to verify the results of the mathematical model.

Initially, a 3D FE model – Model 1 of the entire crane was developed (Figure 1). This model is used as a reference for the verification of reduced numerical models. The values of natural frequencies of the structure for the first five modes are given in Table 2.

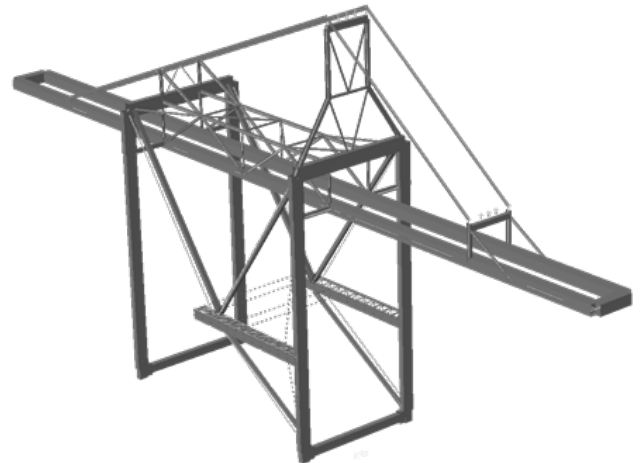


Figure 1: View of the Model 1

Table 2: Values of the natural frequencies for the first five modes

| MODES | Frequencies [Hz] | Periods [s] |
|-------|------------------|-------------|
| I     | 0.5308           | 1.8839      |
| II    | 0.6049           | 1.6532      |
| III   | 1.108            | 0.9025      |
| IV    | 1.7362           | 0.576       |
| V     | 2.1569           | 0.4636      |

Figure 2 shows that in the fifth mode, the boom vibrates practically independently from other parts of the structure. Based on this the part of the boom on the waterside leg can be adopted as a representative to describe the behavior of the entire crane structure, [8].

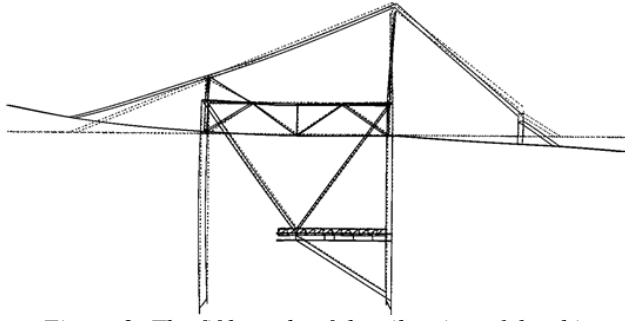


Figure 2: The fifth mode of the vibration of the ship unloader

According to the previous assumption Model 2 was created as an equivalent 2D, non-linear FE model of the boom from the hinge to its end and forestay (Figure 3). Support A is modelled as a hinge and represents the real connection between the boom and the rest of the structure. Table 3 gives all the geometric and physical characteristics of Model 2.

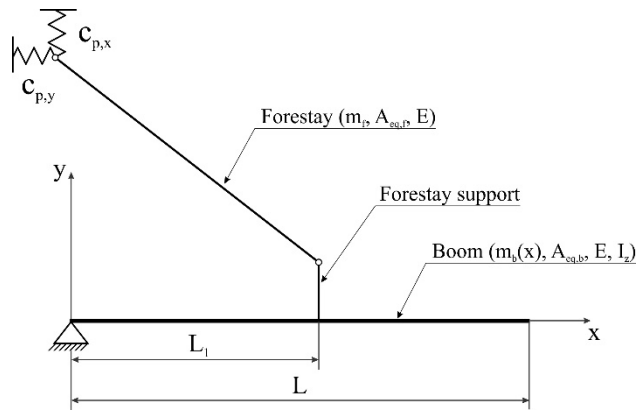


Figure 3: Equivalent 2D FE model of the ship unloader – Model 2

In Figure 1 it can be seen that the stiffness of the pillar in the horizontal and vertical directions is not negligible, so it is taken into account in Model 2 through the springs of the corresponding equivalent stiffnesses  $c_{p,x}$  and  $c_{p,y}$ . By introducing external unit loads (force  $\bar{F}$ ) into the corresponding nodes of Model 1, the displacements of the structure  $\delta_{p,x_1}$ ,  $\delta_{p,y_1}$  and  $\delta_{p,x_2}$ ,  $\delta_{p,y_2}$  in the corresponding directions were obtained. By calculating the arithmetic values (1) and (2) of the obtained displacements, the stiffness values  $c_{p,x}$  and  $c_{p,y}$  (3) and (4) were determined.

$$\delta_{p,x} = \frac{\delta_{p,x_1} + \delta_{p,x_2}}{2} = 6.9351902 \cdot 10^{-8} \text{ m} \quad (1)$$

$$\delta_{p,y} = \frac{\delta_{p,y_1} + \delta_{p,y_2}}{2} = 6.32639674 \cdot 10^{-9} \text{ m} \quad (2)$$

$$c_{p,x} = \frac{\bar{F}}{\delta_{p,x}} = 14419200 \frac{\text{N}}{\text{m}} \quad (3)$$

$$c_{p,y} = \frac{\bar{F}}{\delta_{p,y}} = 158067900 \frac{\text{N}}{\text{m}} \quad (4)$$

Table 3: Geometric and physical characteristics of Model 2

|   |   |
|---|---|
| Boom length, ( $L$ )  | 34.13 m   |
| Distance from support A to support of the forestay, ( $L_1$ ) | 18.464 m  |
| Forestay length, ( $L_f$ )                                    | 25.025 m  |
| Equivalent mass per unit meter of the boom, ( $m_b(x)$ )      | $1007 \frac{\text{kg}}{\text{m}}$               |
| Equivalent mass of the forestay, ( $m_f$ )                    | 4010 kg   |
| Young's modulus of elasticity, ( $E$ )                        | $2.1 \cdot 10^{11} \frac{\text{N}}{\text{m}^2}$ |
| Equivalent section area of the boom, ( $A_{eq,b}$ )           | 0.09504 m <sup>2</sup>                          |
| Equivalent section area of the forestay, ( $A_{eq,f}$ )       | 0.01562 m <sup>2</sup>                          |
| Equivalent axial moment of inertia of the boom, ( $I_z$ )     | 0.0207498 m <sup>4</sup>                        |

The next reduction is the approximation of the forestay by a spring (Model 3) which stiffness is determined by the characteristics of the forestay geometry (5). The forestay mass is reduced to the points of its supports. Model 3 is shown in Figure 4.

$$c_f = \frac{E \cdot A_{eq,f}}{L_f} = 131076923,1 \frac{\text{N}}{\text{m}} \quad (5)$$

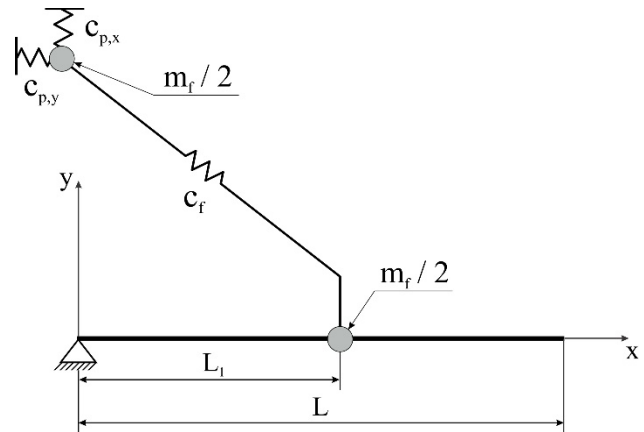


Figure 4: View of the Model 3

Model 4 (Figure 5) is a model in which a three-spring system is replaced by a single spring of equivalent stiffness. Since the stiffness of the springs is a characteristic of the system and does not depend on the mass and stiffness of the boom and the mass of the forestay, all masses are neglected, while the stiffness of the boom is taken as an infinite value. By entering the unit load in the direction of the forestay, the displacement in the same direction  $\delta_{f,F}$  is obtained, on the basis of which the values of equivalent stiffness  $c_{1,eq}$  can be determined by (6).

$$c_{1,eq} = \frac{\bar{F}}{\delta_{f,F}} = 18773134.72 \frac{\text{N}}{\text{m}} \quad (6)$$

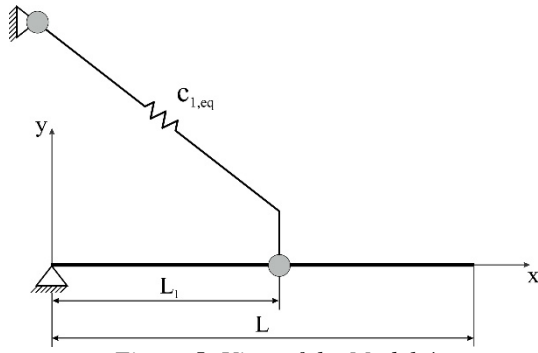


Figure 5: View of the Model 4

Model 5 is a reduced model in which the spring with the stiffness  $c_{1,eq}$  is divided into two springs with the stiffnesses  $c_{1,eq,x}$  and  $c_{1,eq,y}$  in the horizontal and vertical directions, respectively. The concentric mass of the forestay in the upper support is neglected, which is shown in Figure 6. The procedure for determining the stiffnesses of the new springs is the same as in Model 4, while their numerical values are determined according to:

$$c_{1,eq,x} = \frac{\bar{F}_{c_{1,x}}}{|\delta_{31} \cdot \sin \alpha - \delta_{21} \cdot \cos \alpha|} = 50760449.52 \frac{N}{m} \quad (7)$$

$$c_{1,eq,y} = \frac{\bar{F}_{c_{1,y}}}{|\delta_{31} \cdot \cos \alpha + \delta_{21} \cdot \sin \alpha|} = 9181334.46 \frac{N}{m} \quad (8)$$

where  $\bar{F}_{c_{1,x}}$  is projection of the force in the spring on the  $x$ -axis,  $\bar{F}_{c_{1,y}}$  is projection of the force in the spring on the  $y$ -axis,  $\delta_{31} \cdot \sin \alpha$  is projection of the corresponding displacement perpendicular on the forestay direction on the  $x$ -axis,  $\delta_{21} \cdot \cos \alpha$  is projection of the corresponding displacement parallel on the forestay direction on the  $x$ -axis,  $\delta_{31} \cdot \cos \alpha$  is projection of the corresponding displacement perpendicular on the forestay direction on the  $y$ -axis,  $\delta_{21} \cdot \sin \alpha$  is projection of the corresponding displacement parallel on the forestay direction on the  $y$ -axis and  $\alpha$  is an angle between forestay and boom.

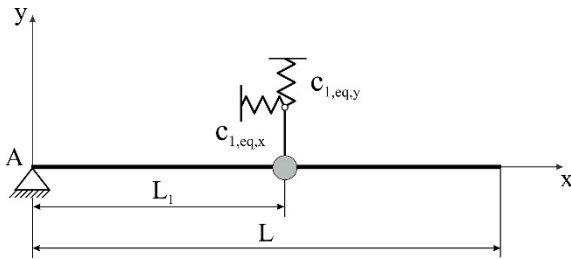


Figure 6: View of the Model 5

By applying a unit force  $\bar{F}$  in the vertical direction at support B, the displacement in the same direction  $\delta_v$  is obtained. This reduces the system of two springs to one equivalent spring whose stiffness  $c_{eq}$  is determined according to (9). The newly made system - Model 6 is shown in Figure 7.

$$c_{eq} = \frac{\bar{F}}{\delta_v} = 11900399.16 \frac{N}{m} \quad (9)$$

Model 6 represents a beam with an overhang of total length  $L = 34.1$  m whose left support A presents a cylindrical joint while at a distance of  $L_1 = 18.5$  m it is supported by a vertical spring.  $M_1 = 8695$  kg is lumped mass originating from the forestay weight and forestay support construction. The boom is modelled as a system with distributed mass where  $m_b$  is mass per unit length and  $EI_z$  is the flexural rigidity of the boom structure.

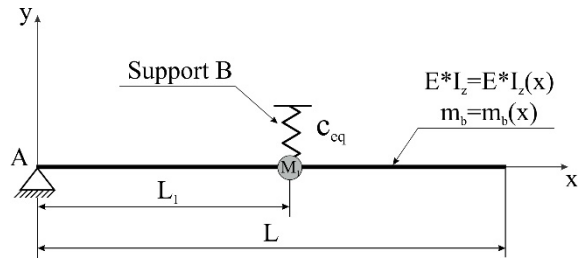


Figure 7: View of the Model 6

Model 2 - Model 6 were verified by comparing the obtained oscillation period of the first mode in the vertical direction with the corresponding mode of Model 1 (mode V from the Table 2). Oscillation period values and relative deviations are shown in Table 4, where relative deviations are obtained according to:

$$\left| \frac{T_n - T_1}{T_1} \right| \cdot 100\%, \quad n = 2,3,4,5,6. \quad (10)$$

where  $T_n$  is oscillation period of corresponding reduced numerical model and  $T_1$  is oscillation period of Model 1.

Table 4: Comparative table of values of the oscillation period for the first mode of oscillation in the vertical plane

| Model | Period [s] | Dev. [%] |
|-------|------------|----------|
| 2     | 0.4405     | 4.98     |
| 3     | 0.4405     | 4.98     |
| 4     | 0.4363     | 5.89     |
| 5     | 0.432      | 6.81     |
| 6     | 0.48       | 3.54     |

As can be seen from Table 4, the relative deviations are acceptable from the aspect of engineering accuracy on the basis of which Model 6 can be adopted as a reference model for forming a mathematical model of ship unloader.

The first mode in the vertical plane of Model 6 is shown in Figure 8, while the higher frequency modes are shown in Figures 9-12.



Figure 8: First mode in vertical plane – Model 6,  $f = 2.0926$  Hz,  $T = 0.48$  s



Figure 9: Second mode,  $f = 4.8963$  Hz,  $T = 0.2042$  s



Figure 10: Third mode,  $f = 13.854$  Hz,  $T = 0.0722$  s

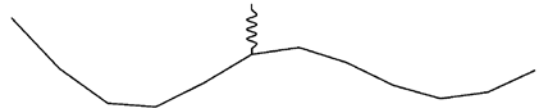


Figure 11: Fourth mode,  $f = 27.357$  Hz,  $T = 0.0365$  s



Figure 12: Fifth mode,  $f = 46.31$  Hz,  $T = 0.0216$  s

### 3. MATHEMATICAL MODEL

As the system shown in Figure 6 is not a "classical" system whose ready-made analytical solutions can be found in the literature, it is necessary to use one of the approximate methods for determining the natural frequencies of the model. In the following text, the procedure for solving this problem using the Rayleigh-Ritz method will be presented.

The Rayleigh-Ritz method is based on solving the equation of the form (11), which also represents the function of moving the points on the structure.

$$y_n(x) = \sum_{i=1}^n a_i \cdot \phi_i \quad (11)$$

In (11)  $a_1, a_2, \dots, a_n$  are unknown coefficients determined from the boundary conditions, and  $\phi_1, \phi_2, \dots, \phi_n$  represent  $n$  linearly independent admissible functions. By this procedure, a continuous system with an infinite number of degrees of freedom (DoF) is reduced to a discretized system with  $n$  DoF.

The Rayleigh-Ritz method is an extension of the Rayleigh method which determines the fundamental frequency of the system. In the first approximation, the Rayleigh method can adopt a test admissible function in the form  $\phi_1(x) = \frac{x}{L}$  which represents the upper limit of the first eigenvalue, as shown in [9]. In the next approximation, the Rayleigh-Ritz method performed an additional reduction of the obtained value of the basic function as well as the formation of a test function that is sufficiently close to the form of the first mode of oscillation of the adopted mathematical model.

$$M = \begin{bmatrix} 1.401 \cdot 10^4 & 1.561 \cdot 10^4 & -6.669 \cdot 10^3 & -709.282 & -421.673 \\ 1.561 \cdot 10^4 & 2.574 \cdot 10^4 & -2.194 \cdot 10^3 & -7.989 \cdot 10^3 & 4.243 \cdot 10^3 \\ -6.669 \cdot 10^3 & -2.194 \cdot 10^3 & 1.776 \cdot 10^4 & 2.05 \cdot 10^3 & -1.089 \cdot 10^3 \\ -709.282 & -7.989 \cdot 10^3 & 2.05 \cdot 10^3 & 2.466 \cdot 10^4 & -3.964 \cdot 10^3 \\ -421.673 & 4.243 \cdot 10^3 & -1.089 \cdot 10^3 & -3.964 \cdot 10^3 & 1.93 \cdot 10^4 \end{bmatrix} \quad (19)$$

$$C = \begin{bmatrix} 3.482 \cdot 10^6 & 6.384 \cdot 10^6 & -1.638 \cdot 10^6 & -5.964 \cdot 10^6 & 3.168 \cdot 10^6 \\ 6.384 \cdot 10^6 & 1.704 \cdot 10^7 & -3.003 \cdot 10^6 & -1.093 \cdot 10^7 & 5.808 \cdot 10^6 \\ -1.638 \cdot 10^6 & -3.003 \cdot 10^6 & 8.616 \cdot 10^7 & 2.805 \cdot 10^6 & -1.49 \cdot 10^6 \\ -5.964 \cdot 10^6 & -1.093 \cdot 10^7 & 2.805 \cdot 10^6 & 4.425 \cdot 10^8 & -5.426 \cdot 10^6 \\ 3.168 \cdot 10^6 & 5.808 \cdot 10^6 & -1.49 \cdot 10^6 & -5.426 \cdot 10^6 & 1.369 \cdot 10^9 \end{bmatrix} \quad (20)$$

The solution of the frequency equation has the form:

$$\Lambda = \omega^2 \quad (21)$$

where  $\omega$  is a circular frequency and has a shape:

$$\omega = \sqrt{\frac{c_{ij}}{m_{ij}}} \quad (22)$$

By further calculation, the following concrete values were obtained for the first five circular frequencies  $\omega$  [ $s^{-1}$ ], natural frequencies  $f$  [Hz] and eigenperiods  $T$  [s]:

$$\omega = \begin{bmatrix} 12.921 \\ 30.006 \\ 84.672 \\ 176.348 \\ 310.909 \end{bmatrix}, \quad f = \begin{bmatrix} 2.056 \\ 4.776 \\ 13.476 \\ 28.067 \\ 49.483 \end{bmatrix}, \quad T = \begin{bmatrix} 0.486292 \\ 0.209395 \\ 0.074206 \\ 0.03563 \\ 0.020209 \end{bmatrix} \quad (23)$$

Eigenvectors which also represent the coefficients  $a_1, a_2, a_3, a_4, a_5$  have the values:

$$EGV1 = \begin{bmatrix} -0.96 \\ 0.28 \\ 3.03 \cdot 10^{-3} \\ -6.679 \cdot 10^{-3} \\ 1.211 \cdot 10^{-3} \end{bmatrix} \quad (24)$$

The determination of higher frequencies of the system is based on the definition of additional permissible functions, which reduces the system to a system with a finite number of DoF. According to [10] from an engineering point of view the number of 5 admissible functions describes the dynamic behavior of the system with sufficient accuracy.

After several iterations, the admissible functions that satisfy all geometric boundary conditions were adopted, while some of them also satisfy the natural boundary conditions in the left support A of the boom and have the following shape:

$$\phi_1(x) = \frac{x}{L} \quad (12)$$

$$\phi_2(x) = \sin \frac{\pi x}{L} \quad (13)$$

$$\phi_3(x) = \sin \frac{2\pi x}{L} \quad (14)$$

$$\phi_4(x) = \sin \frac{3\pi x}{L} \quad (15)$$

$$\phi_5(x) = \sin \frac{4\pi x}{L} \quad (16)$$

It can be shown that the coefficients of mass and stiffness are obtained through the kinetic and potential energy of the system in the form:

$$m_{ij} = \int_0^L m_b \phi_i(x) \phi_j(x) dx + M_1 \phi_i(L_1) \phi_j(L_1) \quad (17)$$

$$c_{ij} = \int_0^L EI_z \frac{\partial^2 \phi_i(x)}{\partial x^2} \frac{\partial^2 \phi_j(x)}{\partial x^2} dx + c_{eq} \phi_i(L_1) \phi_j(L_1) \quad (18)$$

For the specific values of the parameters from Table 3, the following coefficients of mass and stiffness were obtained and presented in matrix form:

$$EGV2 = \begin{bmatrix} 0.628 \\ -0.777 \\ -0.05 \\ 1.152 \cdot 10^{-3} \\ -5.23 \cdot 10^{-4} \end{bmatrix} \quad (25)$$

$$EGV3 = \begin{bmatrix} -0.685 \\ 0.355 \\ -0.629 \\ -0.094 \\ 0.016 \end{bmatrix} \quad (26)$$

$$EGV4 = \begin{bmatrix} 0.691 \\ -0.517 \\ 0.284 \\ -0.415 \\ -0.048 \end{bmatrix} \quad (27)$$

$$EGV5 = \begin{bmatrix} -0.691 \\ 0.506 \\ -0.249 \\ 0.116 \\ -0.437 \end{bmatrix} \quad (28)$$

By substituting the specific values of the coefficients  $a_1 - a_5$  as well as the adopted admissible functions in (11), the following functions  $y_n(x)$  are obtained:

$$y_1(x) = -0.96 \cdot \frac{x}{L} + 0.28 \cdot \sin \frac{\pi x}{L} + 3.03 \cdot 10^{-3} \cdot \sin \frac{2\pi x}{L} - 6.679 \cdot 10^{-3} \cdot \sin \frac{3\pi x}{L} + 1.211 \cdot 10^{-3} \cdot \sin \frac{4\pi x}{L} \quad (29)$$

$$y_2(x) = 0.628 \cdot \frac{x}{L} - 0.777 \cdot \sin \frac{\pi x}{L} - 0.05 \cdot \sin \frac{2\pi x}{L} + 1.152 \cdot 10^{-3} \cdot \sin \frac{3\pi x}{L} - 5.23 \cdot 10^{-4} \cdot \sin \frac{4\pi x}{L} \quad (30)$$

$$y_3(x) = -0.685 \cdot \frac{x}{L} + 0.355 \cdot \sin \frac{\pi x}{L} - 0.629 \cdot \sin \frac{2\pi x}{L} - 0.094 \cdot \sin \frac{3\pi x}{L} + 0.016 \cdot \sin \frac{4\pi x}{L} \quad (31)$$

$$y_4(x) = 0.691 \cdot \frac{x}{L} - 0.517 \cdot \sin \frac{\pi x}{L} + 0.284 \cdot \sin \frac{2\pi x}{L} - 0.415 \cdot \sin \frac{3\pi x}{L} - 0.048 \cdot \sin \frac{4\pi x}{L} \quad (32)$$

$$y_5(x) = -0.691 \cdot \frac{x}{L} + 0.506 \cdot \sin \frac{\pi x}{L} - 0.249 \cdot \sin \frac{2\pi x}{L} + 0.116 \cdot \sin \frac{3\pi x}{L} + -0.437 \cdot \sin \frac{4\pi x}{L} \quad (33)$$

4. RESULTS AND DISCUSSION

The oscillation forms of the mathematical model of the ship unloader obtained by the Rayleigh-Ritz method are presented in Figure 13.

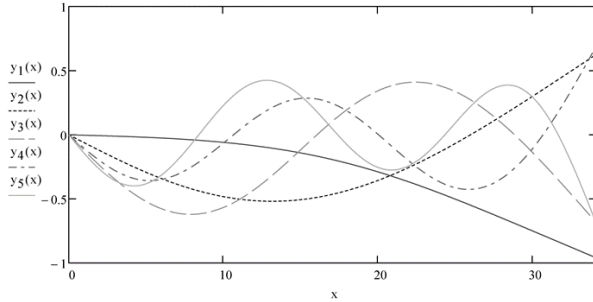


Figure 13: The first five modes of vibration obtained by Rayleigh-Ritz method

Values of eigenperiods for the first five modes of oscillation in the vertical plane obtained by the Rayleigh-Ritz method (23) were verified by their comparing with corresponding periods from the numerical results of FE Model 6 (Figures 8 - 12). Their percentage deviations are given in Table 5, while Figures 14-18 present the graphical comparisons of the corresponding modes of vibration.

Table 5: Percentage deviations of the eigenperiods of Model 6 and mathematical model

| MODES | Eigenperiods [s] |         | Dev. [%] |
|-------|------------------|---------|----------|
|       | Math. model      | Model 6 |          |
| I     | 0.486292         | 0.48    | 1.31     |
| II    | 0.209395         | 0.2042  | 2.54     |
| III   | 0.074206         | 0.0722  | 2.78     |
| IV    | 0.03563          | 0.0365  | 2.38     |
| V     | 0.020209         | 0.0216  | 6.44     |

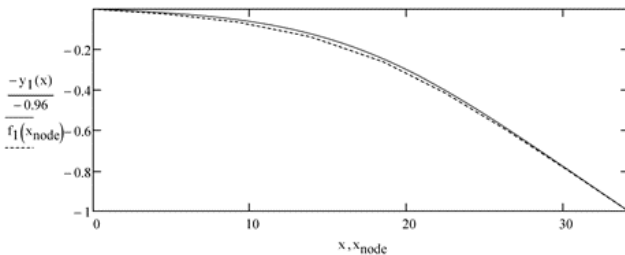


Figure 14: Comparison of the normalized first mode of vibration of the mathematical and FE model

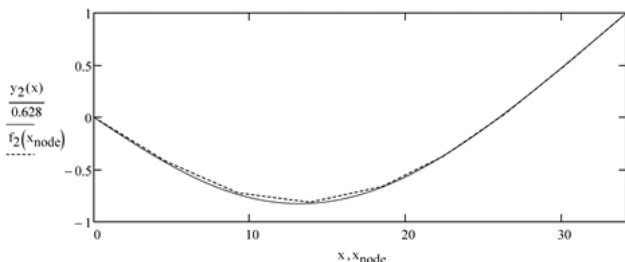


Figure 15: Comparison of the normalized second mode of vibration of the mathematical and FE model

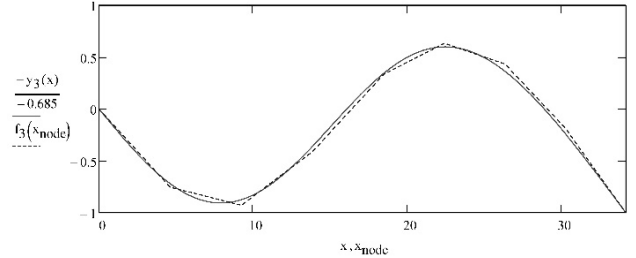


Figure 16: Comparison of the normalized third mode of vibration of the mathematical and FE model

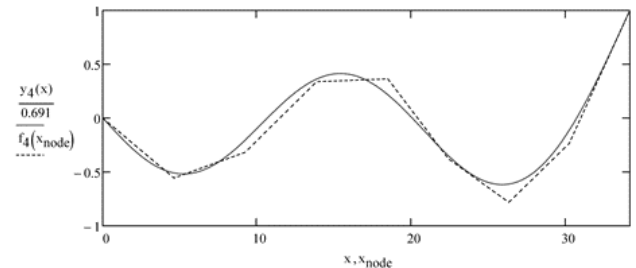


Figure 17: Comparison of the normalized fourth mode of vibration of the mathematical and FE model

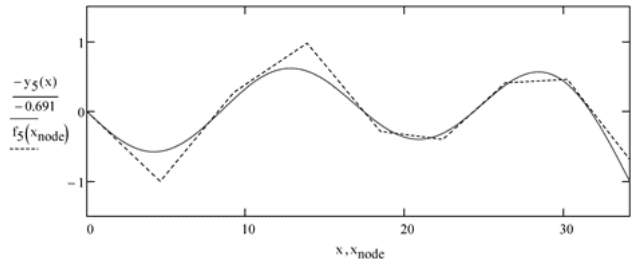


Figure 18: Comparison of the normalized fifth mode of vibration of the mathematical and FE model

As can be observed in Figures 14 - 18, there is very good matching of the first three normalized modes of oscillation between mathematical and numerical model, while slightly larger deviations occur only in the fourth and fifth modes. This shows that the adopted admissible functions can be considered as a sufficiently accurate approximation of the real eigenfunctions of the dynamical system and that the number of 5 adopted admissible functions is sufficient to obtain reliable results from the aspect of engineering accuracy.

5. CONCLUSION

Given that this type of construction is not widely used as, e.g. overhead traveling cranes, the dynamic problems that occur during their exploitation are still not sufficiently examined and discussed in the available literature. The aim of this paper was to present the procedure of modal analysis which gives the first insights into the dynamic behaviour of the structure and as such can be used already in the design phase of these structures.

The paper shows that the complex structure of a ship unloader can be reduced to a relatively simple 2D

system of a beam with an overhang, supported on one fixed and one elastic support, while completely preserving the nature of the behaviour of the real structure. As can be seen from Table 4 and Table 5 numerically and mathematically calculated results are in very close agreement which means that the presented approach can be considered acceptable from the aspect of engineering accuracy.

The mathematical model formed in this way can be used as a basis for further analysis of dynamics problems that occur on structures of this type (moving load problem, fatigue, etc.).

#### ACKNOWLEDGEMENTS

This work is a result of research supported by the Ministry of Education, Science and Technological Development of the Republic of Serbia by Contract 451-03-68/2020-14/200105.

#### REFERENCES

- [1] N. Zrnić and K. Hoffmann, "Development of design of ship-to-shore container cranes: 1959-2004", *History of Machines and Mechanisms*, C. Marco, ed., Kluwer Academic Publishers, Dodrecht, pp. 229–242, (2004)
- [2] N. Zrnić, D. Oguamanam and S. Bošnjak, "Dynamics and modelling of mega quayside container cranes", *FME Trans.*, Vol. 34, pp. 193–198, (2006)
- [3] M. Giulia, K. Banisoleiman and A. Gonzalez, "An investigation into the moving load problem for the lifting boom of a ship unloader", *Eng. Struct.*, Vol. 234, pp. 1–20, (2021)
- [4] M. Giulia, K. Banisoleiman and A. Gonzalez, "Impact of a moving trolley on the dynamic response of a ship unloader boom", *13th International Conference on Steel, Space and Composite Structures (SS18)*, Perth (Australia), 31 January-2 February 2018, pp. 33-38, (2011)
- [5] D. Dinevski, M. Oblak and A. Novak, "Experimental verification of the container crane natural frequencies", *Transactions on Modelling and Simulations*, Vol. 16, WIT Press, pp. 245-254, (1997)
- [6] N. Zrnić, K. Hoffmann and S. Bošnjak, "Modelling of dynamic interaction between structure and trolley for mega container cranes", *Math. Comput. Model. Dyn. Syst.*, Vol. 15, pp. 295–311, (2009)
- [7] Ceretti Tanfani S.p.A. Milano, *Ship unloader 400 t/h*, (1982)
- [8] N. Zrnić, S. Bošnjak and K. Hoffmann, "Parameter sensitivity analysis of non-dimensional models of quayside container cranes", *Math. Comput. Model. Dyn. Syst.*, Vol. 16, pp. 145–160, (2010)
- [9] N. Zrnić, "Uticaj kretanja kolica na dinamičko ponašanje obalskih kontejnerskih dizalica", PhD Thesis, University of Belgrade (Serbia), (2005)
- [10] R.L. Clark, W.R. Saunders and G.P. Gibbs, "Adaptive Structures: Dynamics and Control", John Wiley & Sons, New York (US), (1998)

# The Deflection of the Column-mounted Jib Crane with Tapered Boom by Finite Difference Method

Nebojša B. Zdravković<sup>1\*</sup>, Boris Jerman<sup>2</sup>, Mile Savković<sup>1</sup>, Goran Marković<sup>1</sup>,  
Marko Todorović<sup>1</sup>, Goran Pavlović<sup>3</sup>

<sup>1</sup> Faculty of Mechanical and Civil Engineering in Kraljevo, University of Kragujevac, SERBIA

<sup>2</sup> University of Ljubljana, Faculty of Mechanical Engineering (FME), SLOVENIA

<sup>3</sup> Faculty of Electronic Engineering, University of Niš, SERBIA

*One of the most frequently utilized crane types in industrial applications is the column-mounted jib crane. There are many different designs according to different requirements about lifting height, span, payload capacity, drive options, etc. Within the efforts to optimize the structure's mass, heavy-duty jib cranes with high payload capacity and extended reach often have their boom tapered. Besides strength, deflection is the most considered design criteria, where the crane structure is subjected to the total payload capacity at the tip of the boom. The paper presents the application of the finite difference method (FDM) and MATLAB code for the deflection of the column-mounted jib crane with a tapered boom. Obtained results are very close to the results from the finite element method (FEM) model in Ansys.*

**Keywords:** Jib crane, Tapered boom, Deflection, Finite difference method.

## 1. INTRODUCTION

Jib cranes are one of the most commonly installed crane types in industrial facilities. They are used for frequent load handling within a circular working space. They are suitable for applications requiring repetitive lifting and transferring of loads. The column-mounted jib crane is a piece of highly efficient hoisting equipment. It requires a small space for installation, and it is very safe, energy-efficient and easy to control during operation. The payload capacity usually goes up to 5 tons, while the reach usually goes up to 6 meters.

An adequately designed jib crane should have increased the material handling efficiency and speed up the workflow. Modern industries require versatile, flexible and cost-effective material handling equipment with increased productivity. The requirements are usually related to payload capacity, span/reach, lifting height, drive options, etc. Therefore, there are many designs of jib cranes, depending on various requirements. Nevertheless, the typical column-mounted jib crane consists of the column, the boom or the jib, the boom support leg (optionally) and the hoist mounted on the trolley, which moves along the crane boom. An essential feature of the jib crane is its static and dynamic stability, dependent on the structure's deflection.

Since the jib cranes are the most widespread in industrial facilities, many engineers tried to simplify the model and quickly define these cranes' basic parameters. FEM models of the jib cranes certainly give the results relevant for calculation and dimensioning but also require a longer time to set up the calculation model.

Usually, during the design, the maximum displacement of the jib crane boom tip is critical. So, it is important to determine a simple expression for the boom deflection, based on which it is possible to define the basic parameters of the crane. In such a way, the basic geometric parameters can be defined quickly, which would shorten the design time.

The structural analysis of the jib crane with different cross-sections was performed in the paper [01], where experimental tests and FEM were used to validate the results.

Paper [02] gives a comparative analysis of several concept solutions of jib cranes by implementing the beam, plate and volume finite elements using several software packages. Several parameters (deformation energy over construction elements, kinetic and potential energy over mode shapes of natural frequencies, etc.) were used for local elements optimization. The goal was mass reduction and the increase of the natural frequencies.

The paper [03] presented an analytical model of the lateral-torsional buckling behaviour of steel web tapered tee-section cantilevers when subjected to a uniformly distributed load and/or a concentrated load at the free end. The model check was performed through FEM.

The elastic lateral-torsional behaviour of the cantilever is analysed in [04]. The obtained results in this research can be easily applied in designing the boom of the jib crane. A parametric study is carried out to examine the effectiveness of different types of restraint, the influence of the restraint stiffness and the interplay between these two aspects and the degree of web tapering.

Paper [05] shows the stress and deflection analysis of the jib crane structure for different web thicknesses and heights. The structure locations with maximum deflection and maximum stresses were determined.

The optimization of the jib crane by the evolutionary algorithm was carried out in [06], which enabled significant material savings.

Paper [07] presents the length optimization of the boom support leg, which connects the jib with the column. The authors performed the analysis using FEM. The paper showed the influence of the leg's height on the deflection of the structure.

Based on the effect of self-weight different distribution and large deformation, a mathematical model

\*Corresponding author: Dositejeva 19, 36000 Kraljevo, Serbia, zdravkovic.n@mfv.kg.ac.rs

of telescopic jib displacement was established in [08]. Authors deduced a formula of endpoint displacement of large slenderness ratio telescopic jib structure. Also, the large-deformation finite element method is used as a criterion to evaluate the correctness and precision of the theoretical calculation formula.

The stress and the deflection calculations were performed through finite element analysis (FEA) in [09]. Firstly, after using analytical expressions, the density of the mesh was corrected. In the second phase of the calculation, the height and thickness of the web were varied.

The analysis of stresses and deflections was performed by using FEA in [10]. Also, the analysis of individual parts for the connection with the fundament was carried out.

Using FEA and the direct integration method, the dynamic responses of the jib crane structure in vertical and horizontal directions were considered in [11]. Forced vibration responses of the jib structure due to equivalent moving forces were determined, where the mass matrix was time-dependent.

Integrated FEA of whole jib crane model was established in [12] and arm-side deflection formula for this type of crane structure was derived.

The paper [13] gave a refined expression for the deflection of the jib crane boom tip, taking into account the actual load position at the very end of the boom.

The paper [14] shows the finite difference method (FDM) application procedure for the deflection determination on the simple elastically restrained cantilever beam with continuously varying box-like cross-section and linear change of section height.

This research applies the previous approach for determining the deflection of the column-mounted jib crane with a tapered boom.

## 2. THE MATHEMATICAL MODEL BY FDM

The structures of the heavy-duty cranes are optimized to achieve lighter designs and reduce production and operational costs. The column-mounted jib cranes with high lifting capacity and long reach have optimized booms with a variable cross-section (Fig. 1 [15]).

The main parameters of the model and its cross-sections are depicted in Fig. 2, while the detailed calculation model is presented in Fig. 3.



Figure 1: Heavy-duty column-mounted jib crane with a non-uniform boom [15]

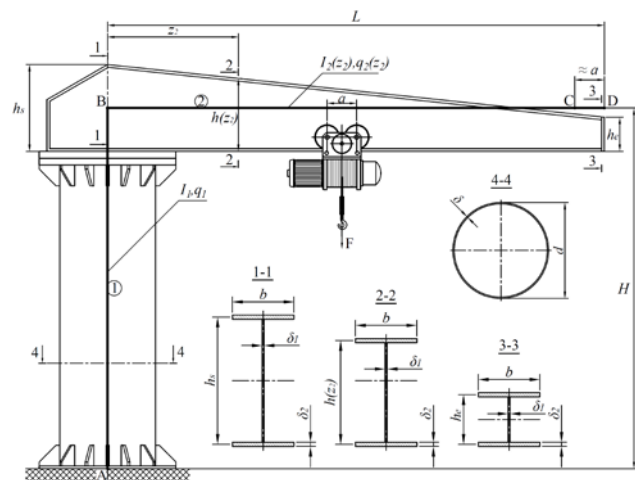


Figure 2: The model and the cross-sections

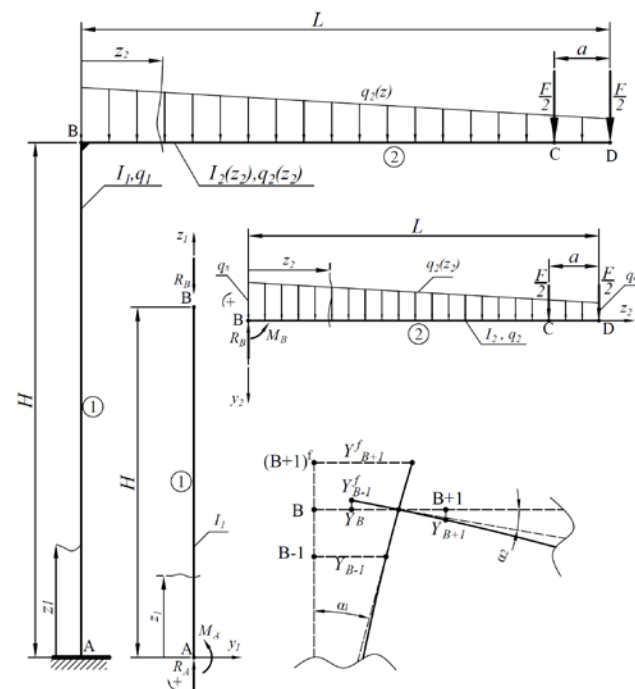


Figure 3: The calculation model with the finite difference scheme at point B

Column 1 is a thin-wall pipe with a diameter of  $D$  and wall thickness  $\delta$ . The non-uniform boom 2 is a web-tapered I-beam with a linear change of its height along its longitudinal coordinate  $z_2$  (Fig. 2). It is better to use the

distance between the flanges' centroids  $h$  than the height to simplify the expressions. In terms of the centroids' distance at the boom start ( $h_s$ ) and centroids' distance at the boom tip ( $h_e$ ), it has the following form:

$$h = h(z_2) = h_s - (h_s - h_e) \frac{z_2}{L} \quad (1)$$

where  $L$  – boom's length.

The web thickness is  $\delta_1$ , while the thickness of the flanges is  $\delta_2$ . The flanges of the I-beam have constant width  $b$  along the longitudinal boom axis.

Hence, the moment of inertia of web-tapered I-beam can be written as follows

$$I_2(z_2) \approx \frac{\delta_1 h^3 + 6b\delta_2 h^2}{12} \quad (2)$$

Further, the approximate but more straightforward expression for its cross-sectional area is

$$A_2(z_2) \approx 2b\delta_2 + \delta_1 h \quad (3)$$

So, the weight per unit length of the boom reads

$$q_2(z_2) \approx \rho g (2b\delta_2 + \delta_1 h) \quad (4)$$

where  $\rho$  – mass per unit volume for steel and  $g$  - gravity.

Hence, the starting and ending weight per unit length of the boom are

$$q_s = q_2(z_2 = 0) = \rho g A_2(z_2 = 0) \approx \rho g (2b\delta_2 + \delta_1 h_s)$$

$$q_e = q_2(z_2 = L) = \rho g A_2(z_2 = L) \approx \rho g (2b\delta_2 + \delta_1 h_e)$$

Static equilibrium of the structure gives the following expressions for forces and bending moments

$$R_B = F + \left( 2b\delta_2 + \delta_1 \frac{h_s + h_e}{2} \right) \rho g L \quad (5)$$

$$M_B = F \left( L - \frac{a}{2} \right) + \left[ (2b\delta_2 + \delta_1 h_s) \frac{L^2}{2} - \delta_1 (h_s - h_e) \frac{L^2}{3} \right] \rho g \quad (6)$$

$$R_A = R_B + q_1 H \quad (7)$$

$$M_A = M_B \quad (8)$$

where

$q_1 = \rho g A_1$  - the weight per unit length of the column

$A_1$  – cross-sectional area of the column

$H$  – the theoretical height of the column (taken along its longitudinal axis from the base plate bottom to the centroid of the boom's cross-section centroid).

Governing differential equation for bending of the column is:

$$\frac{d^2 y_1(z_1)}{dz_1^2} = -\frac{M_1(z_1)}{EI_1} = -\frac{M_1(z_1)}{B_1} = -\frac{M_A}{B_1} = \frac{M_A}{B_1} \quad (9)$$

where

$B_1 = EI_1$  - column bending stiffness,

$M_1(z_1) = -M_A = \text{const.}$  - bending moment.

According to FDM, the axial coordinate becomes  $z_1 = i \cdot s$  and the second derivative of the deflection line has the approximate form:

$$y_1''(z_1) \approx \frac{Y_{i-1} - 2Y_i + Y_{i+1}}{s^2} \quad (10)$$

where

$i$  – the point ordinal,

$s$  – the adopted distance between two adjacent nodes along the neutral axis in an undeformed state of the structure. Hence, Eq.(9) becomes transformed:

$$\frac{Y_{i-1} - 2Y_i + Y_{i+1}}{s^2} \approx \frac{M_A}{B_1} \quad (11)$$

Boundary conditions

$$y_1(z_1 = 0) = 0 \quad (12)$$

$$y_1'(z_1 = 0) = 0$$

after transformation by FDM become

$$Y_0 = 0$$

$$\frac{-Y_{i-1} + Y_{i+1}}{2s} \Big|_0 = \frac{-Y_{-1}^f + Y_1}{2s} = 0 \Rightarrow Y_{-1}^f = Y_1 \quad (13)$$

The superscript index "f" stands for the displacement of a fictitious node (the node out of the curve domain). After introducing designation for characteristic node ordinal  $B = H/s$ , the deflection line of the column can be represented by the following set of algebraic equations:

$$i = 0 \rightarrow 2Y_1 = \frac{M_A s^2}{B_1}$$

$$i = 1 \rightarrow -2Y_1 + Y_2 = \frac{M_A s^2}{B_1} \quad (14)$$

$$i = 2 \div B - 1 \rightarrow Y_{i-1} - 2Y_i + Y_{i+1} = \frac{M_A s^2}{B_1}$$

Governing differential equation for bending of the tapered boom is:

$$\frac{d^2 y_2(z_2)}{dz_2^2} = -\frac{M_2(z_2)}{EI_2(z_2)} \quad (15)$$

where

$$M_2(z_2) = -M_B + R_B z_2 - \rho g \left[ (2b\delta_2 + \delta_1 h_s) \frac{z_2^2}{2} - \delta_1 (h_s - h_e) \frac{z_2^3}{3L} \right] \parallel$$

$$-\frac{F}{2} [z_2 - (L - a)]$$

$$I_2(z_2) = \frac{\delta_1 h^3(z_2) + 6\delta_2 h^2(z_2)}{12}$$

According to FDM, the axial coordinate becomes  $z_2 = (i-B) \cdot s$  and the second derivative of the deflection line has the approximate form:

$$y_2''(z_2) \approx \frac{Y_{i-1} - 2Y_i + Y_{i+1}}{s^2} \quad (16)$$

Boundary conditions

$$y_2(z_2 = 0) = 0 \quad (17)$$

$$y_2'(z_2 = 0) = y_1'(z_1 = H)$$

after FDM transformation yield the expressions for the displacements of the fictitious nodes before and after point B (Fig. 3)

$$Y_{B+1}^f = \frac{M_A}{B_1} s^2 + 2Y_B - Y_{B-1} \quad (18)$$

$$Y_{B-1}^f = Y_{B+1} - \frac{M_A}{B_1} s^2 - 2Y_B + 2Y_{B-1}$$

Hence, the system of algebraic equations (14) now can be continued and complemented with the algebraic equations which are derived from governing differential bending equation for the boom:

$$i = B \rightarrow 2Y_{B-1} - 2Y_B + 2Y_{B+1} = \frac{M_B s^2}{E} \left[ \frac{12}{\delta_1 h_s^3 + 6b\delta_2 h_s^2} + \frac{1}{I_1} \right]$$

$$i = B+1 \rightarrow -2Y_{B+1} + Y_{B+2} = P \frac{Q}{R} \quad (19)$$

$$i = B+2 \div C-1 \rightarrow Y_{i-1} - 2Y_i + Y_{i+1} = P \frac{T}{W}$$

$$i = C \div D-1 \rightarrow Y_{i-1} - 2Y_i + Y_{i+1} = P \frac{T - \frac{F}{2} [(i-B)s - (L-a)]}{W}$$

where

$$P = \frac{12s^2}{E}$$

$$Q = M_B - R_B s + \rho g \left[ (2b\delta_2 + \delta_1 h_s) \frac{s^2}{2} - \delta_1 (h_s - h_e) \frac{s^3}{3L} \right]$$

$$R = \delta_1 \left[ h_s - (h_s - h_e) \frac{s}{L} \right]^3 + 6b\delta_2 \left[ h_s - (h_s - h_e) \frac{s}{L} \right]^2$$

$$T = M_B - R_B (i-B)s + \rho g \left[ (2b\delta_2 + \delta_1 h_s) \frac{(i-B)^2 s^2}{2} - \delta_1 (h_s - h_e) \frac{(i-B)^3 s^3}{3L} \right]$$

$$W = \delta_1 \left[ h_s - (h_s - h_e) \frac{(i-B)s}{L} \right]^3 + 6b\delta_2 \left[ h_s - (h_s - h_e) \frac{(i-B)s}{L} \right]^2$$

$$C = \frac{H+L-a}{s}$$

$$D = \frac{H+L}{s} = N$$

### 3. THE COMPARISON WITH FEM MODEL RESULTS

Based on the system of algebraic equations (14) and (19), a MATLAB code was written, and the displacements for  $Y_j$ ,  $j=1, \dots, N=D$  nodes were calculated for the numerical example with the following data:  $E=2 \cdot 10^4 \text{ kN/cm}^2$ ,  $H=400 \text{ cm}$ ,  $L=600 \text{ cm}$ ,  $F=30 \text{ kN}$ ,  $a=80 \text{ cm}$ ,  $d=50 \text{ cm}$ ,  $\delta=1.2 \text{ cm}$ ,  $b=30 \text{ cm}$ ,  $\delta_1=1.2 \text{ cm}$ ,  $\delta_2=1.6 \text{ cm}$ .

The value of the boom's starting section height  $h_s$  was changed within interval  $400 \div 600 \text{ mm}$ , while its ending section height  $h_e$  took values between  $200 \text{ mm}$  and  $300 \text{ mm}$ , both incremented by a  $50 \text{ mm}$  step. The results for boom tip displacement  $Y_D$  for such input parameters are given in tables 1, 2 and 3. Also, for comparison purposes, the FEM model was built in ANSYS for each test case. The relative error is displayed in the far-right column of the tables.

Fig. 4 presents the test case in ANSYS for  $h_e=200 \text{ mm}$  and  $h_s=500 \text{ mm}$  (bolded cell in table 1), Fig. 5 shows the boom's tip displacement concerning the heights of the start and end section of the boom, while Fig. 6 is the graphical interpretation of results in table 1.

Table 1: Boom tip displacement for  $h_e=200 \text{ mm}$

| $h_e=200 \text{ mm}$ |                   |              |            |
|----------------------|-------------------|--------------|------------|
| $h_s [\text{mm}]$    | $Y_D [\text{mm}]$ |              | rel. error |
|                      | FDM               | FEM          |            |
| 400                  | 69.43             | 71.172       | -2.45%     |
| 450                  | 63.83             | 65.514       | -2.57%     |
| 500                  | 59.66             | <b>61.23</b> | -2.56%     |
| 550                  | 56.47             | 57.888       | -2.45%     |
| 600                  | 53.99             | 55.219       | -2.23%     |

Table 2: Boom tip displacement for  $h_e=250 \text{ mm}$

| $h_e=250 \text{ mm}$ |                   |        |            |
|----------------------|-------------------|--------|------------|
| $h_s [\text{mm}]$    | $Y_D [\text{mm}]$ |        | rel. error |
|                      | FDM               | FEM    |            |
| 400                  | 66.91             | 68.669 | -2.56%     |
| 450                  | 61.88             | 63.535 | -2.60%     |
| 500                  | 58.12             | 59.702 | -2.65%     |
| 550                  | 55.24             | 56.64  | -2.47%     |
| 600                  | 52.99             | 54.208 | -2.25%     |

Table 3: Boom tip displacement for  $h_e=300 \text{ mm}$

| $h_e=300 \text{ mm}$ |                   |        |            |
|----------------------|-------------------|--------|------------|
| $h_s [\text{mm}]$    | $Y_D [\text{mm}]$ |        | rel. error |
|                      | FDM               | FEM    |            |
| 400                  | 64.9              | 66.665 | -2.65%     |
| 450                  | 60.32             | 62.029 | -2.76%     |
| 500                  | 56.89             | 58.476 | -2.71%     |
| 550                  | 54.25             | 55.684 | -2.58%     |
| 600                  | 52.19             | 53.427 | -2.32%     |

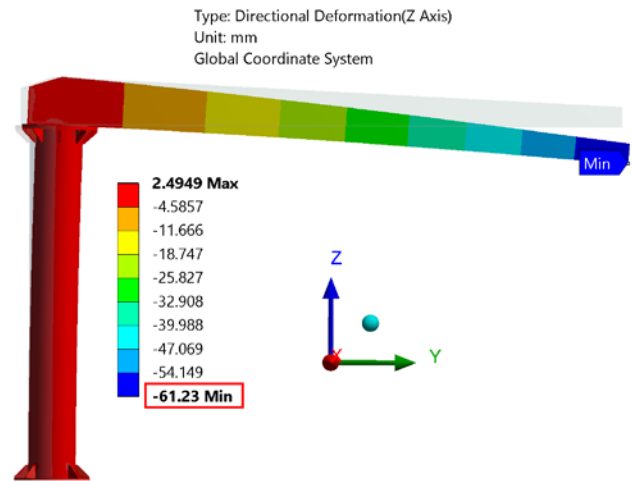


Figure 4: ANSYS test case for  $h_e=200 \text{ mm}$  and  $h_s=500 \text{ mm}$

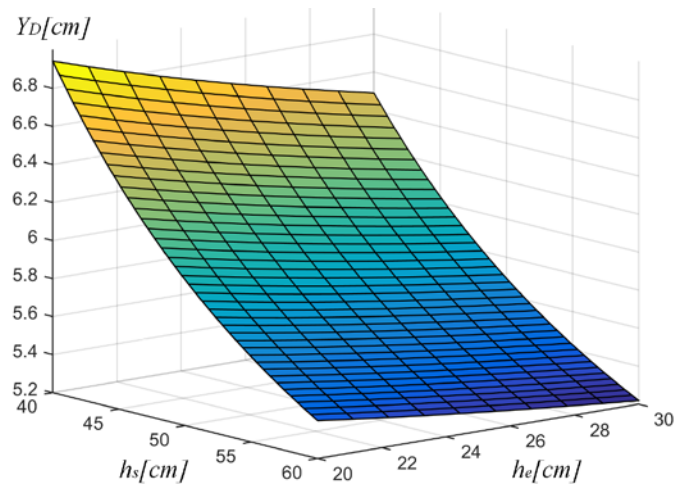


Figure 5: The boom's tip displacement in relation to its start and end section heights

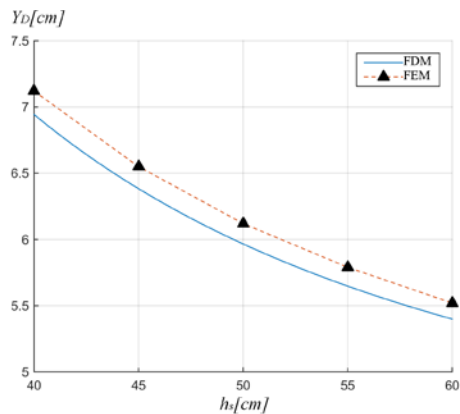


Figure 6: The graphical interpretation of results in table 1

#### 4. THE CONCLUSION

The presented FDM method and applied algorithm yielded a compact system of algebraic equations, convenient for code writing and solving by MATLAB. The results obtained from the FDM model are in very good compliance with the results from the FEM model built in ANSYS. Relative error (less than 3%) is mainly caused by the approximate value for the boom's moment of inertia (Eq. 2). The main advantage of the FDM and the proposed procedure is that it can show the influence of any design parameter on the boom's tip displacement once written and solved, which makes it convenient for crane structure optimization. The presented FDM method is universal and can be applied to other types of cranes in the future.

#### ACKNOWLEDGEMENTS

This paper is supported by the Ministry of Education, Science and Technological Development of the Republic of Serbia through Contract No. 451-03-9/2021-14/200108.

#### REFERENCES

- [1] Chaudhary S. A., Khan N.S., "A review paper on structural analysis of cantilever beam of jib crane", *International Journal of Engineering Research and General Science*, ISSN 2091-2730, Vol. 3, No. 3, pp. 612-615, (2015)
- [2] Hadžikadunić F., Vukojević N., Huseinović S., "An analysis of jib crane constructive solution in exploitation", 12th International Research/Expert Conference "Trends in the Development of Machinery and Associated Technology" - TMT 2008, ISBN 9958-617-41-6, Istanbul, Turkey, 26–30 August 2008, pp. 789-792, (2008)
- [3] Yuan W., Kim B., Chen C., "Lateral-torsional buckling of steel web tapered tee-section cantilevers", *Journal of Constructional Steel Research*, ISSN 0143-974X, Vol 87, pp. 31-37, (2013)
- [4] Andrade A., Providência P., Camotim D., "Elastic lateral-torsional buckling of restrained web-tapered I-beams", *Computers and Structures*, ISSN 0045-7949, Vol 88, pp. 1179-1196, (2010)
- [5] Rajmane S.M., Jadhav A., "Finite element analysis of jib crane", *International journal of innovative research in technology*, ISSN 2321-1156, Volume 2, Issue 6, pp. 404-407, (2015)
- [6] Gandhare K., Thute V., "Design Optimization of Jib Crane Boom Using Evolutionary Algorithm", *International Journal of Scientific Engineering and Research (IJSER)*, ISSN Volume 3, Issue 4, pp. 5-8, (2015)
- [7] Yawale P., Khandare N., "Effect of Length of Boom Support Leg on Free Standing Jib Crane", *International Journal of Scientific Engineering and Research (IJSER)*, ISSN 2319-7064, Volume 4, Issue 5, pp. 19-23, (2016)
- [8] Gening Xu, Guangheng Gao, "Displacement Calculation Method of Super-long Telescopic Jib Structure Considering the Effect of Self Weight and Large Deformation", *Researches and Applications in Mechanical Engineering Vol. 2*, Issue 4, ISSN 2327-1582, pp. 99-104, (2013)
- [9] Kiranalli S.S., Patil N.U., "Jib Crane Analysis using FEM", *IJSRD - International Journal for Scientific Research & Development*, ISSN (online): 2321-0613 Volume 3, Issue 4, pp. 185-189, (2015)
- [10] Khetre S.N., Chaphalkar S. P., Meshram A., "Modelling and stress analysis of column bracket for rotary jib crane", *International Journal of Mechanical Engineering and Technology (IJMET)*, ISSN 0976-6359, Volume 5, Issue 11, pp. 130-139, (2014)
- [11] Gašić V., Zrnić N., Rakin M., "Consideration of a moving mass effect on dynamic behaviour of a jib crane structure", *Technical Gazette*, ISSN 1848-6339, Volume 19, Issue 1, pp. 115-121, (2012)
- [12] Ma, Xiao, and Hui Wang. "Column Jib Crane Based on ANSYS Analysis of Static Stiffness and Improving Measures." *Key Engineering Materials*, ISSN 1662-9795, Vol. 522, pp. 485–89, (2012)
- [13] Pavlović G., Gašić M., Savković M., Zdravković N., Marković G., "Comparative analysis of the models for determination of deflection in the column-mounted jib crane structure", *Mechanics Transport Communications*, ISSN 2367-6620, Vol. 15, No. 3/2, pp. V-5-V11, (2017)
- [14] Nebojša Zdravković, Mile Savković, Goran Marković, Goran Pavlović, "The determination of the deflection of the beam with continuously varying cross-section by the finite difference method", *IMK-14 – Research & Development in Heavy Machinery*, Vol. 26, No. 1, ISSN 0354-6829, pp. EN19-EN 23, (2020)
- [15] <https://jibcranemanufacturer.com/pillar-jib-crane>



# Analysis of Elevators Dynamic Parameters with Solution of Summary Data Acquisition During Experimental Research

Radomir Đokić<sup>1\*</sup>, Jovan Vladić<sup>1</sup>, Dragan Živanić<sup>1</sup>, Tanasije Jojić<sup>1</sup>, Vesna Jovanović<sup>2</sup>, Nebojša B. Zdravković<sup>3</sup>

<sup>1</sup>Faculty of Technical Sciences, University of Novi Sad, Serbia

<sup>2</sup>Faculty of Mechanical Engineering, University of Niš, Serbia

<sup>3</sup>Faculty of Mechanical and Civil Engineering in Kraljevo, University of Kragujevac, Serbia

*Modelling of the dynamic behavior of elevators with high lifting velocities (contemporary elevators in building construction and mine elevators) is a complex task and an important step in the design process and creating conditions for safe and reliable exploitation of these machines. Due to high heights and lifting velocities, the standard procedures for dynamic exploitation are not adequate. With the purpose of identifying the basic parameters of the dynamic model (stiffness and damping), a unique method was applied, based on experimental measures for a concrete elevator. Due to the verification of this procedure, the experiment was conducted on a mine elevator in RTB Bor, Serbia. Simulations of the dynamic behavior of an empty and loaded cage are presented using the obtained computational-experimental results.*

**Keywords:** Mechanical characteristics of steel ropes, Data acquisition, Experimental research

## 1. INTRODUCTION

The elevator quality is estimated according to several important indicators. Safety, comfort, and reliability are especially important features [1]. These indicators depend on, first of all, vibrations occurring while the elevator is in motion. Vibrations are a consequence of driving parameters, inertial characteristics and elasticity of the binding elevator elements.

Judging by the dynamic impact on the vibration values, an elevator can be divided into two basic parts. The first part is a driving mechanism (engine, reductor, brake, and couplings), while the second part is a cabin lifting system, mostly made of steel ropes for lifting the counterweights on one end and cabin (cage) on the other end and their guide rails. The driving mechanism comprises elements that are much more rigid and have smaller mass compared to the cabin lifting system, which in turn causes the oscillations in smaller amplitudes and higher frequencies. As well as that, bearing in mind the oscillations are indirectly transferred to the cabin (cage), via ropes, it can be deduced that the lifting system has a much bigger influence on the comfort during the motion than driving mechanism elements does.

While the elevator is in operation mode, the hoist ropes increase and decrease their free length, so the parameters, such as rope stiffness and damping are constantly being changed [2] and [3]. In high-speed elevators, a dynamic instability may occur during lifting (reduction of free length), due to an increase in relative deformation. This seriously impacts the safety of the passengers. Since classic models are based on elastic body (rope) oscillations with constant dynamic parameters (mass, stiffness and damping), it is necessary to form such dynamic models that will enable the analysis and definition of the dynamic behavior of elevators with variable parameters [4] and [5].

Due to the fact that special attention has to be paid to the accuracy of installing and making of cabin guide rails and counterweight in high-speed elevators, the following conclusion arises. Without the addition of

external influences, it can be concluded that longitudinal oscillations are dominant, as opposed to transversal oscillations.

Taking into consideration that up until this moment the problems in driving mechanism vibrations were the subject of a great number of scientific and research papers, with standard analyses as the most frequently applied method, it seems logical that the main focus of elevator dynamic research should be pointed towards innovative methods for analyzing the longitudinal oscillations with variable parameters [6].

The mine elevators are used to interconnect different mine horizons by using a mine cage (which is moved between at least two firmly set guide rails), whose dimensions and construction enable ore loading and are approachable to people.

The mines use two systems, one with a drum and the other with a driving pulley (Köepe system). Fig. 1 provides a scheme of the most applied lifting system in mine facilities with a friction mechanism (Köepe system).

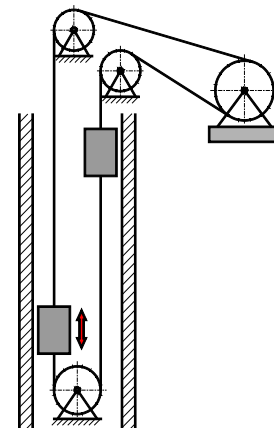


Figure 1: Exploitation facility in the mines with an underground shaft

In the systems with a lifting drum, the carrying ropes are wound and stored on a drum. The drums are located in the machine room which is usually sideways of

the mine shaft, and the ropes go down from it over the deflector pulleys into the shaft next to the cabin.

Friction lifting systems (Köepe) are mostly used in European mines. The drive is set above or sideways to the mine shaft. In the case when it is located sideways (Fig. 1) deflector pulleys are used and they are set above the mine cage (cabin) and the counterweight. The main advantages of the system are decreasing of a driving motor, i.e. necessary torque, a simpler usage of a higher number of steel ropes and the possibility of setting the driving pulley directly above the mine shaft. However, due to the limitations in contact pressure (1.75 MPa) and the limits of slipping ( $S_1/S_2 \leq 1.4$ ) between the ropes and the pulley, the advantages are lost, so in practice both systems are applied almost equally.

2. FORMING A SUITABLE MODEL FOR THE DYNAMIC ANALYSIS OF MINE ELEVATORS

2.1. Standard Models

There has been a large number of researchers interested in studying longitudinal oscillations and their studies have been based on the general theory about the application of oscillation of elastic bars with constant parameters (mass, stiffness, and damping). These are the so-called standard models. Those models are acceptable for analyzing elevators with low lifting velocities and heights. Fig. 2a and 2b show models with one and two degrees of freedom and a rope of constant lengths, represented here as Hook's, i.e. Calvin's body.

A certain improvement has been made with the analysis of high-lift elevators ( $\geq 35$  m) and low velocities (till 3 m/s) by using the model represented in Fig. 2c. The model represents a bar of a constant length with an equally spreaded mass  $q$  (kg/m), i.e. it is a model of an elastic body with an unlimited number of degrees of freedom and a concentrated mass at the bottom end as the boundary condition.

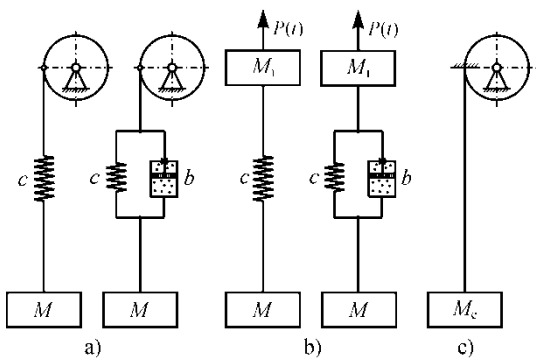


Figure 2: Standard dynamic models; with one degree of freedom (a), with two degrees of freedom (b), and a "heavy" constant length bar (c)

Based on the analysis which was shown in detail in [7] to [9], in the case when the free rope length is small compared to the cabin mass, it is possible to significantly simplify the dynamic model analysis.

In accordance with the above, when it comes to high-lift elevators and low velocities, it is approximately possible to create load oscillation models with one degree of freedom, with a "heavy" spring, which was studied in general literature. Also, it is necessary to replace the total

mass (of both load and rope) with an equivalent mass  $M_e = M + (1/3) \cdot qL$ , reduced in the cabin place, [10] and [11].

2.2. Dynamic Elevator Models with Variable Dynamic Parameters

Fig. 3a shows the most common solutions of the lifting systems for high-speed elevators with a driving pulley, while the corresponding dynamic model is shown in Fig. 3b.

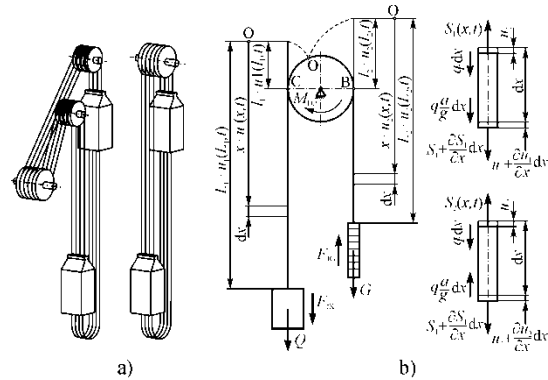


Figure 3: Dynamic model of a high-speed elevator

In order to secure comfort during the motion, control programs are used in contemporary elevators. They define the circumferential velocity of the pulley. Thus, they also define the cabin motion velocity (a kinematic condition), as opposed to the previous period when the motion velocity depended a great deal on the driving electromotor's mechanical characteristics and brake system (the dynamic equilibrium condition). In the earlier periods, a replacement of one-speed engines with two-speed engines was observed as a significant improvement. This bettered the motion comfort in braking instances and aided the accuracy of stopping the cabin. As for the process of a regular elevator, in cases when there is no slipping of the steel rope on the driving pulley and when the driving characteristic is represented via a rope velocity at the meeting point of the rope and pulley, the elevator model can be simplified and represented in the form shown in Fig. 4.

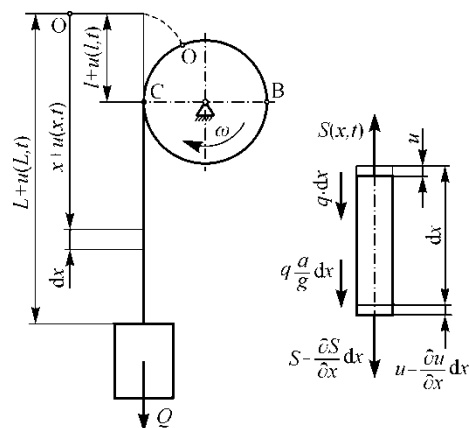


Figure 4: Elevator model with a rope of a variable length with boundary conditions

Upon observing just the upcoming rope end, the model can be represented as a system with an unlimited number of degrees of freedom; at one end it is rolling onto the pulley at a  $v(t)$  velocity, while on the other it is burdened with concentrated mass. Due to the variable rope

length during the motion, the stiffness ( $c=EA/L$ ) changes. This is a characteristic of parametric oscillations and contributes to the possible occurrence of resonance. To this end, it is necessary to complete certain steps in the analysis of dynamic behavior. One needs to determine the critical lifting velocity, during which the unstable motion occurs, i.e. the rope strain is increased when its free length is reduced.

The deformation of an arbitrary cross-section represents the function of the position  $x$ , and the time  $t$ , i.e.:

$$u = f(x, t) \quad (1)$$

Upon observing the equilibrium of the elementary part ( $dx$ ), it can be deduced that:

$$\frac{q \cdot dx}{g} \cdot \frac{\partial^2 u(x, t)}{\partial t^2} = -S(x, t) + S(x, t) + \frac{\partial S}{\partial x} dx + q \cdot dx \pm \frac{q \cdot dx}{g} \cdot a \quad (2)$$

By representing the rope as Calvin's model, where the influence of internal friction can be taken into consideration via the so-called rope resistance force factor ( $b_f$ ), the dependence of the inner force in the rope on its deformation can be noted in this form:

$$S(x, t) = E \cdot A \cdot \frac{\partial}{\partial x} \left[ u(x, t) + b_f \cdot \frac{\partial u(x, t)}{\partial t} \right] \quad (3)$$

If the Eq. (2) is divided with  $\frac{q \cdot dx}{g}$  and a replacement for  $S(x, t)$ , this is obtained:

$$\frac{\partial^2 u(x, t)}{\partial t^2} = \frac{g \cdot E \cdot A}{q} \cdot \frac{\partial^2}{\partial x^2} \left( u(x, t) + b_f \cdot \frac{\partial u(x, t)}{\partial t} \right) + g \pm a \quad (4)$$

By using the differential equation, (Eq. (4)) and the equilibrium condition of moments on the driving pulley, it is possible to form a system of equations that describes a dynamic equilibrium on the driving pulley in the case of a model shown in Fig. 4b in this form [12]:

$$\frac{q}{g} \cdot \frac{\partial^2 u_1(x, t)}{\partial t^2} = E \cdot A \cdot \frac{\partial^2}{\partial x^2} \left[ u_1(x, t) + b_f \cdot \frac{\partial u_1(x, t)}{\partial t} \right] + q \cdot \left( 1 \pm \frac{a}{g} \right) \quad (5)$$

$$\frac{q}{g} \cdot \frac{\partial^2 u_2(x, t)}{\partial t^2} = E \cdot A \cdot \frac{\partial^2}{\partial x^2} \left[ u_2(x, t) + b_f \cdot \frac{\partial u_2(x, t)}{\partial t} \right] + q \cdot \left( 1 \pm \frac{a}{g} \right) \quad (6)$$

$$M_m = \frac{R}{i \cdot \eta} \cdot E \cdot A \cdot \frac{\partial}{\partial x} \left[ u_1(l_1, t) - u_2(l_2, t) + b_f \frac{\partial}{\partial t} [u_1(l_1, t) - u_2(l_2, t)] \right] - J_r \cdot \frac{a \cdot i}{R} \quad (7)$$

with:

- $u_1, u_2$  - elastic deformation of the rope on the incoming and outgoing rope end,
- $E$  - rope elasticity modulus,
- $A$  - rope's cross-section area,
- $a$  - acceleration of the driving mechanism,
- $M_m$  - driving motor torque
- $i$  - gear ratio,
- $\eta$  - driving mechanism efficiency,
- $J_r$  - moment of inertia of rotational masses, reduced to the shaft of a driving pulley,
- $R$  - driving pulley radius,
- $q$  - rope weight per meter.

### 3. DYNAMIC PARAMETERS DETERMINATION BY SUMMARY DATA ACQUISITION

Experimental studies shown in this paper represent the sequel of the research in [8]. The measuring was done on a mine elevator in RTB Bor, Serbia; the maximum projected cage lifting velocity was 16 m/s and the

projected lifting height was 523 m in the first phase and 763 m in the second phase of mining. The driving mechanism is shown in Fig. 5. The other significant characteristics of this exploitation machine can be seen in Tab. 1.

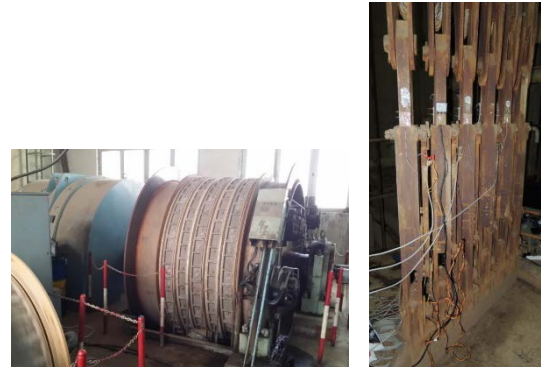


Figure 5: Driving machine of a mine elevator and the connecting tools for connecting the hoist ropes and the cage

Table 1: Mine elevator technical characteristics

|                        |  |
|------------------------|--|
| Driving electric motor | Power: 1500/2860 kW, number of revolutions: 122.2 rpm, torque: 117.2/233.4 kNm   |
| Cage (cabin)           | Mass: 13 t (it includes the cage and the connecting tools for connecting the hoist ropes), Fig. 8  |
| Counterweight          | Mass: 21 t   |
| Hoist ropes            | $z = 6$ pieces,<br>$d = 27$ mm (150 wires per cross section).<br>Lang's lay ropes, three right hand lang's lay ropes, and three left hand lang's lay ropes.<br>Breaking force: 561 kN, tensile strength of the wires: 1700 MPa.<br>Unit mass: 3.02 kg/m. |
| Compensation ropes     | $z = 2$ pieces,<br>$d = 50$ mm (222 wires per cross section).<br>Connected with the cage via rotating hooks to prevent unwinding. Unit mass: 9.64 kg/m.  |

A mine shaft is like a round cross-section, with a 10 m diameter. The transfer of the driving moment to the hoist ropes is done through friction (Köepe system) from the grooved drum with a 2.5 m diameter.

#### 3.1. Equipment Used and the Method for Measuring Data Acquisition

The following measuring equipment was used for the mine elevator experiment:

- Universal 8-channel measuring amplifier (2 pieces), QUANTUM X MX480B, pos. 10a and 10b (Fig. 6),
- A computer for storing the measuring signals, pos. 13 (Fig. 6),
- Antennas for the wireless transfer of the measuring signal (2 pieces) NanoStation loco NS2L, made by IBIQUITI NETWORKS; 5 km range with the antennas optical visibility, pos. 12a and 12b (Fig. 6),

- Incremental encoder - the number of revolutions sensor AINS 41, made by Meyer Industrie-Electronic GmbH – MEYLE; measuring range up to 6000 rpm and with an allowed axial/radial load at the output shaft of 30/20 N, pos. 9 (Fig. 6),
- Optical measuring device for the number of revolutions ROS type, made by Monarch Instrument; measuring range varies from 1 to 250 000 rpm, pos. 1 (Fig. 6),
- Accelerometer HBM B12, pos. 2 (Fig. 6),
- Strain gauges HBM LY41-6/120, pos. 3 to 8 (Fig. 6),
- Software for acquisition and processing of measuring signals, HBM catmanEasy-AP.

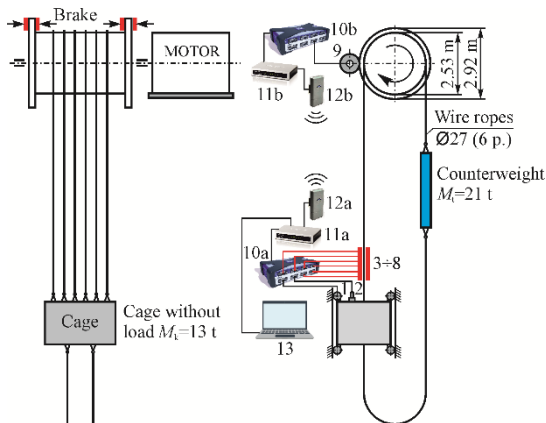


Figure 6: Schematic layout of the measuring places

The experiment was done according to the principle of summary data acquisition via a wireless data transfer, by using the NanoStation loco NS2L antennas (pos. 12a and 12b, Fig. 6). This way, a complete synchronization of the collected data on the cage roof and machine room was achieved. The drum number of revolutions was measured with an AINS 41 incremental encoder (pos. 9, Fig. 6). It was set on the adaptive carrier with a 127 mm diameter measuring wheel, which was directly leaned onto the rim of the brake disc, Fig. 7a. The encoder measuring signal was led to the amplifier (pos. 10b, Fig. 6), and then via a LAN switch (pos. 11b, Fig. 6) and the antenna (pos. 12b, Fig. 6) wirelessly connected to the other radio antenna positioned on the cage (pos. 12a, Fig. 6). The measuring signal was stored in a common computer file (pos. 13, Fig. 6) placed on the cage. It was done via another LAN switch (pos. 11a, Fig. 6).



Figure 7: The incremental encoder connected with the measuring wheel positioned on the rim of the brake disc (a), and the optical sensor (number of revolutions sensor) positioned on the cage (b)

The lifting and lowering velocity of the cage was measured via a roller guide, whose change in the number of revolutions was registered with an optical sensor (pos. 1, Fig. 6), positioned on a small magnet table, Fig. 7b. The change in the cage's acceleration during the measuring process was registered by an HBM B12 accelerometer

(pos. 2, Fig. 6), set on the connecting tools of the cage through a magnetic holder, Fig. 8a. The force changes in the hoist ropes were monitored by measuring the deformation of the connecting tools (pos. 3 to 8, Fig. 6). The deformations were measured on each connecting tool (out of 6 in total), by using the HBM LY41-6/120 strain gauges, Fig. 8b



Figure 8: Measurements of acceleration (a) and deformations (b) on the cage connections tools

All measuring signals were led to the other eight-channel measuring amplifier (pos. 10a, Fig. 6) and they were recorded on the computer (pos. 13, Fig. 6) via an LAN switch (pos. 11a, Fig. 6).

### 3.2. Results of the Experiment

Experiment results and determination of the dynamic model parameters in this paper are shown in four characteristic motion cases (lifting and lowering) of the cage, with and without load. A significantly higher number of measurements was completed for different cases (different positions for starting and stopping the cage motion etc.) and the results are presented in [7]. Here, the results of lowering and lifting of an empty cage and a loaded cage (traction machine) are presented.

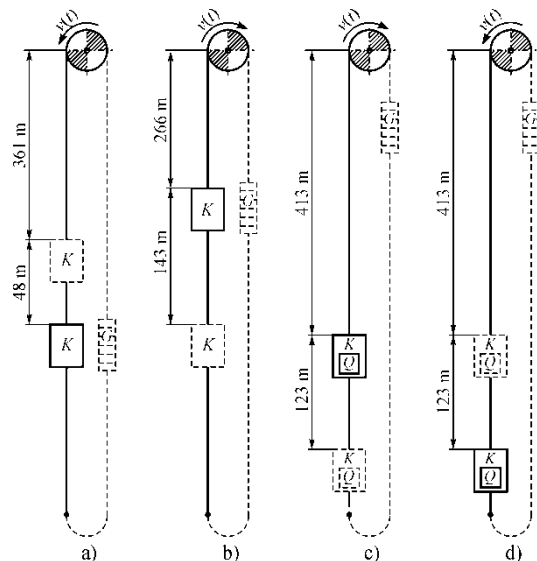


Figure 9: Mine elevator parameters that are relevant for the analysis

According to those, the system oscillation parameters are defined. The characteristics of experimental cases are as follows:

**I)** Lowering an empty cage from position +104 m to position +56 m (48 m). The action of stopping the cage was performed by suddenly switching off the driving electromotor (at a high velocity, Fig. 9a).

**II)** Lifting of an empty cage from position +56 m to a position +199 m (143 m). Stopping the cage was done just like in the case above, with the sudden switching off

the power to the driving electromotor, at a high velocity, Fig. 9b.

**III)** Lifting a loaded cage (the traction machine for wagons, mass ~9.35 t) from position a -71 m, to position +52 m (123 m). Stopping the cage was done at a low speed, Fig. 9c.

**IV)** Lowering the loaded cage (the traction machine for wagons, mass ~9.35 t) from position +52 m to -71 m (123 m). Stopping the cage was done at a low speed, Fig. 9d.

The results of the conducted experimental research can be seen in the following figures, which are showing the changes in the winding velocities of hoist ropes that were wound onto the drum; cage acceleration and changes in the forces in the hoist ropes, i.e. on the elements for connecting the ropes to the cage. The results are valid for all four chosen examples of motion. The diagram shows the character of the changes of the said parameters. It shows the cage oscillation amplitudes that occur after stopping the driving machine. This part of the diagram (after stopping the driving machine) is used to set the mechanical characteristics of steel ropes (harmonic oscillations).

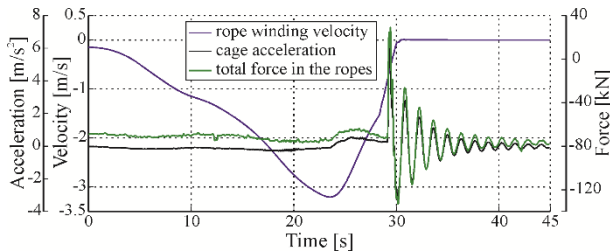


Figure 10: Diagram with the results obtained during lowering an empty cage and sudden stopping, at a "high" velocity (I motion case)

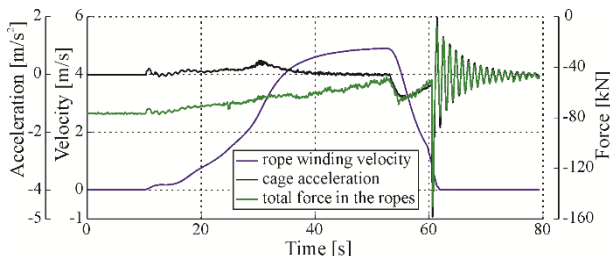


Figure 11: Diagram with the results obtained during lifting the empty cage and sudden stopping, at a "high" velocity (II motion case)

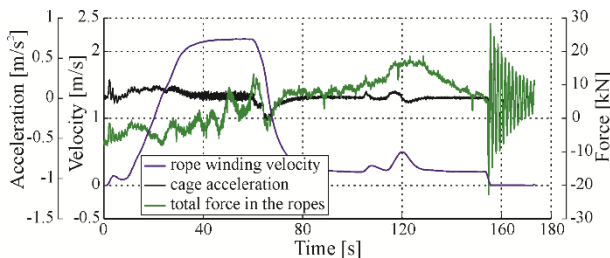


Figure 12: Diagram with the results obtained during the loaded cage lifting process (III motion case)

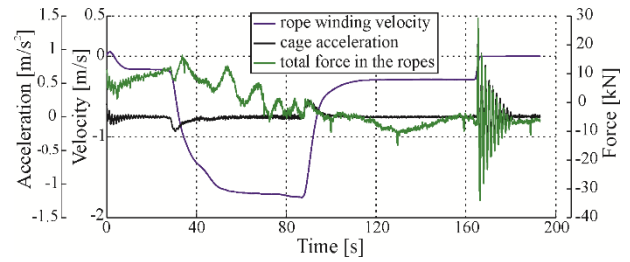


Figure 13: Diagram with the results obtained during loaded cage lowering process (IV motion case)

### 3.3. Main dynamic parameters

**Stiffness** is the basic parameter of oscillatory processes and it represents a feature of a material that defines the ratio between load and deformation. It is viewed as a constant matter in most oscillatory processes with small amplitudes and elements made of steel and similar materials [13]. On the other hand, it is a case with some materials also used in mechanical engineering that the feature is not linear, which brings to the occurrence of the so-called non-linear oscillations whose analysis is more complex on numerous levels. A specific case of non-linearity happens at the lifting machines with steel ropes and it refers to the fact that the stiffness changes together with the change in the ropes' free lengths in the following relation:

$$c(t) = \frac{E \cdot A}{L - l(t)} \quad (8)$$

Apart from the variable stiffness, attention should be paid to the **elasticity modulus (E)**, which is much more difficult to define in comparison with the homogenous bodies since the steel rope is a complex structure, consisting of a large number of wires layered into strands, while the strands are stranded into a rope with the core made of steel or fibre.

There are different expressions mentioned in the literature, for its calculation depending on the wire elasticity modulus and the angles at which the wires lay into a strand, and strands into a rope. These expressions only give approximate data because the real magnitudes of the elasticity modulus, apart from the above mentioned parameters, depend on the stress magnitude, core material, time spent in service (the number of load cycles), types of wire connections etc.

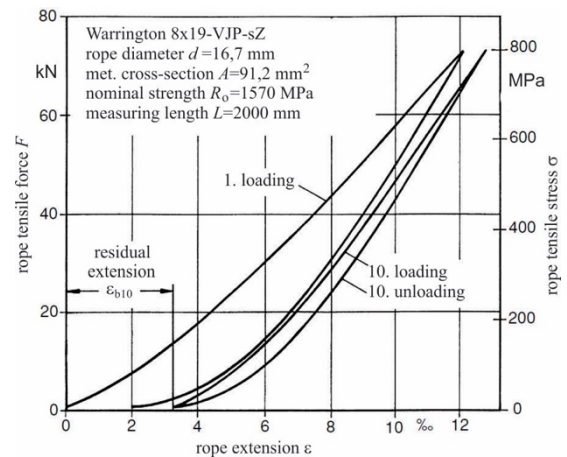


Figure 14: Stress-extension curves for new stranded wire ropes with fibre core, after 10 loadings, [14]

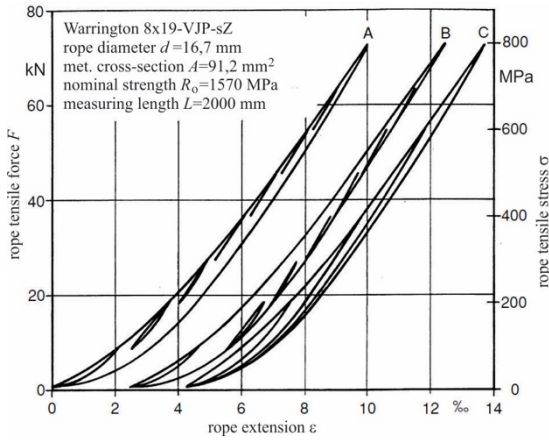


Figure 15: Stress-extension curves for new stranded wire ropes with fibre core, after 10 loadings for the difference stress levels, [14]

Fig. 14 and 15 show the experimental results [14] which show a noticeable difference in the results between the first loading of the rope (new rope), and after 10 loadings (Fig. 14), and also the effect of the stress level with the loading and unloading in Fig. 15.

Nevertheless, the application of the results generated in this way is disputable when it comes to dynamic processes. Adequate elasticity modulus values for the ropes in exploitation can be gained through direct measuring in the real working conditions of the elevator facilities.

**Damping.** In a lot of practical systems, oscillation energy is gradually transformed into heat or sound, the effect mostly known as damping. Despite the fact that the quantity of such energy is relatively small, it is important to dedicate some attention to damping in order to predict the oscillatory systems response, such as the elevator systems considered in this paper.

Damping at the elevator is complex and it happens because of the rope inner friction (viscous and hysteretic damping), Coulomb's friction on guide rails and damping due to the air flow around the cabin (cage) in the elevator shaft [8] and [10].

Since the presented experiment results (Tab. 2) refer to the moment of stopping the cage ( $v=0$ ), damping as a consequence of air flow around the cage can be neglected.

The friction on the elevator guide rails creates the damping force (Coulomb's friction) which is constant in its magnitude, but it is of the opposite direction compared to the motion of the oscillating load. Since this type of elevator requires special attention to be paid to the guiding accuracy and reducing the guide rails friction, in the example with central cabin load, the friction forces can be neglected in relation to the total load. Nevertheless, the influence can be of importance for cabin oscillation analyses.

The size of the impact caused by rope damping and damping due to guide rails friction is possible to define via "overlapping" of the diagram measurement results and simulation results, as presented in Fig. 16.

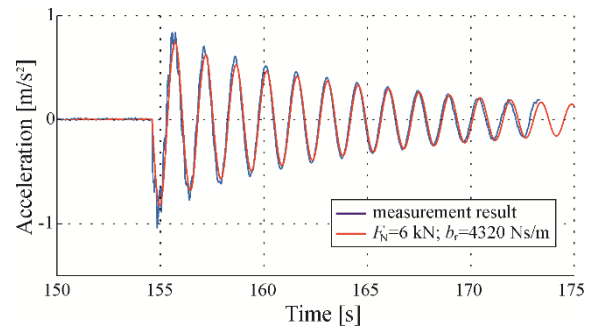


Figure 16: The impact of inner and Coulomb's friction on oscillating systems when  $b=5161$  Ns/m (Table 2)

Based on the theory about free harmonic damping oscillations, it is concluded that for determining the dynamic parameters, one should take the part of the cage oscillation diagram after the driving machine is stopped.

By measuring the amplitudes and oscillating periods of free damping oscillations (changes in cage acceleration), the damping coefficient ( $\delta$ ) can be determined via a logarithmic decrement, and based on this, a resistance force coefficient ( $b$ ):

$$D = \ln \frac{x_i}{x_{i+1}} = \frac{1}{n} \ln \frac{x_i}{x_{i+n}} = \delta \cdot \tilde{T} \rightarrow \delta = \frac{D}{\tilde{T}} \quad (9)$$

$$b = 2 \cdot \delta \cdot M_e \quad (10)$$

with:

$x_i, x_{i+1}$  and  $x_{i+n}$  - measured oscillating amplitudes,

$\tilde{T}$  - measured oscillating period of free damping oscillations,

$M_e = M + q \cdot \frac{1}{3} L(t)$  - reduced oscillating mass,

$M$  - total mass hanging on hoist ropes (loaded cage and compensation ropes),

$L(t) = L - \int v(t) dt$  - hoist ropes' free length

$v(t)$  - circumferential velocity of the pulley (drum).

Determining the stiffness coefficient ( $c$ ) and elasticity modulus ( $E$ ) of hoist ropes can be performed with the measured oscillation parameters (oscillating period, oscillating amplitudes, etc.):

$$c = M_e \cdot \omega^2 \quad (11)$$

$$E = \frac{c \cdot L}{A} \quad (12)$$

with:

$\omega = \sqrt{\tilde{\omega}^2 + \delta^2}$  - circular frequency of free oscillations,

$\tilde{\omega} = \frac{2\pi}{\tilde{T}}$  - damping oscillation frequency

Fig. 17 is an illustration of determining the said mechanical characteristics of hoist ropes based on the cage acceleration changes diagram (after the driving machine was stopped) in the III motion case.

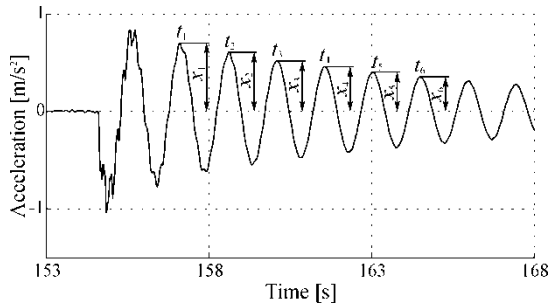


Figure 17: The measured values of cage acceleration for III motion case

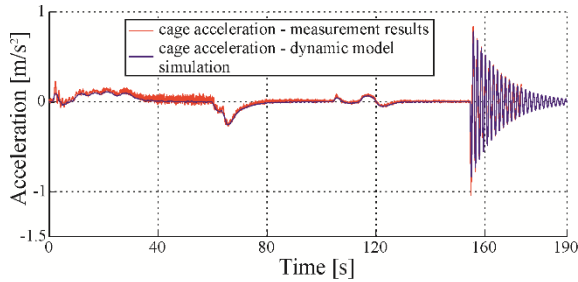
Based on the diagram in Figs. 10 to 13 and the expressions (Eq. (9) and (12)), mechanical characteristics

Table 2: Values obtained by measuring and parameters of hoist ropes

|                 | $L$ [m] | $M_e$ [kg] | $\delta$ [s <sup>-1</sup> ] | $\omega$ [rad/s] | $c$ [N/m] | $b$ [Ns/m] | $E$ [MPa] | $\delta/\omega$ |
|-----------------|---------|------------|-----------------------------|------------------|-----------|------------|-----------|-----------------|
| I (Fig. 9a) ↓   | 409     | 18 797     | 0.33                        | 4.67             | 409 163   | 12 222     | 98 440    | 0.070           |
| II (Fig. 9b) ↑  | 266     | 20 525     | 0.21                        | 5.69             | 663 329   | 8718       | 103 792   | 0.037           |
| III (Fig. 9c) ↑ | 413     | 28 099     | 0.09                        | 4.26             | 510 803   | 5161       | 124 095   | 0.022           |
| IV (Fig. 9d) ↓  | 536     | 26 613     | 0.18                        | 3.88             | 401 206   | 9639       | 126 498   | 0.047           |

### 3.4. Computer simulations results

In order to simulate the mine elevator operation process, the study has set the change in hoisting rope velocity at the point of winding onto the driving drum as the change (diagram), obtained by direct measuring on the driving machine via an incremental encoder (pos. 9, Fig. 6).



Slika 18: Cage acceleration diagrams in the motion case III (Fig. 9c)

An oscillation diagram was separated with the purpose of verifying the dynamic model during the whole period while the cage was moving, as well as after the complete stop in the driving machine moving. The acceleration diagram in the III motion case is shown, “overlapping” the diagram with the measured results, Fig. 18.

Judging by the diagram in Fig. 18, it can be concluded that the dynamic model with dynamic parameters, determined by the measuring with satisfactory accuracy, shows the real behavior of a mine elevator. As a result, this makes computer simulations possible, which will analyze the real loads of the exploitation facility [7]. The described method is a new approach that will ensure the analysis of dynamic behavior in systems for vertical hoisting, which can be found in exploitation.

As an illustration of the possibility of dynamic analysis, the following section shows diagrams that represent changes in individual values. They were created in specialized software for dynamic analysis, MSC ADAMS, using the experimental data shown in Table 2.

of steel ropes are defined, as shown in Table 2. Upon analyzing the measured results, it can be concluded that the data for elasticity modulus are in agreement with the data from the literature [14]. The higher values of elasticity modulus for loaded cabins are seen as a consequence of the rope that was constructed by putting the lays of wires in strands, and strands into a rope. This confirms the validity of the applied procedure, enabling us to define the real (exploitation) values in mine elevators. The damping coefficient values, for which there is no significant comparative data, are not constant in size, but appear to be different in the analyzed experiments.

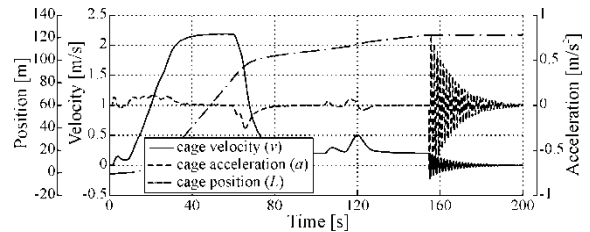


Figure 19: Diagram showing the changes in cage position, velocity, and acceleration, for III motion case

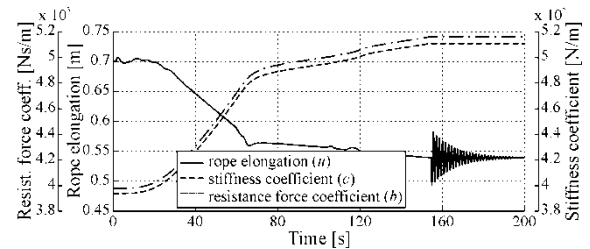


Figure 20: Comparative diagrams showing the changes in the elongation, stiffness coefficient, and resistance force coefficient of hoist ropes, for III motion case

## 4. CONCLUSION

The paper presents an experimental method that can be used to determine dynamic parameters such as stiffness, elasticity modulus, and damping in exploited elevator steel ropes. Certain elasticity modulus values that are presented in Tab. 2 reveal the noticeable dependence on the load, i.e. rope stress. In addition, the damping coefficient in ropes is not a constant size, but it depends on the position of a cage. It can be deduced that ropes experience a combination of viscous damping and hysteretic damping, which should be further investigated in these systems.

Mine elevators are used in the mines with underground exploitation at the depths as deep as 2000 m with the carrying capacity of maximum 30 t and the lifting velocities up to 20 m/s. Therefore, their analysis is of special interest because they define the quality basis for optimal projecting and their maintenance in relatively heavy working conditions.

Apart from the mentioned extreme parameters, the complexity of the dynamic analysis of these facilities is primarily due to these facts:

- The basic model is an oscillatory problem with an infinite number of DOF and it is influenced by a large number of factors.
- The driving torque is a variable value (the function of the pulley rotational speed and the operating load).
- The stiffness of the wire rope varies with the changes in the cage position, causing parametric oscillations.
- Steel rope elasticity modulus is not a constant value, as it is the case with homogenous bodies. It depends on rope structure, stress level and how long the rope was in service.
- Damping in the wire rope is a feature which has not been sufficiently examined. It is a consequence of the inner friction of a hysteretic type, depending on the construction of the rope, stress in the rope, contact type and friction between the wires, then lubrication, oscillation amplitudes etc.
- The influence of friction in the guide rails on the damping of the whole system cannot be ignored.

#### REFERENCES

- [1] Q. Peng, P. Xu, H. Yuan, H. Ma, J. Xue, Z. He, S. Li, „Analysis of Vibration Monitoring Data of Flexible Suspension Lifting Structure Based on Time-Varying Theory“, *Sensors*, Vol. 20(22), pp. 6586, (2020)
- [2] Q. Zhang, Y. Yang, T. Hou, R. Zhang, „Dynamic analysis of high-speed traction elevator and traction car-rope time-varying system“, *Noise & Vibration Worldwide*, Vol. 50(2), pp. 37-45, (2019)
- [3] J. Bao, P. Zhang, C. Zhu, „Modeling of Rope Longitudinal Vibration on Flexible Hoisting System with Time-Varying Length“, *Applied Mechanics and Materials*, Vol. 130-134, pp. 2783-2788, (2011)
- [4] X. Arrasate, S. Kaczmarczyk, G. Almandoz, J. M. Abete, I. Isasa, „The modelling, simulation and experimental testing of the dynamic responses of an elevator system“, *Mechanical Systems and Signal Processing*, Vol. 42(1-2), pp. 258-282, (2014)
- [5] I. Herrera, H. Su, S. Kaczmarczyk, „Investigation into the damping and stiffness characteristics of an elevator car system“, *Applied Mechanics and Materials*, Vol. 24-25, pp. 77-82, (2010)
- [6] S. Watanabe, T. Okawa, „Vertical vibration of elevator compensating sheave due to brake activation of traction machine“, *Journal of Physics: Conference Series*, Vol. 1048(012012), (2018)
- [7] R. Đokić, „Dynamics researching and development of vertical transport machines using numerical-experimental procedures“, PhD thesis, University of Novi Sad (Serbia), (2016)
- [8] J. Vladić, M. Jovanović, R. Đokić, M. Kljajin, M. Karakašić, „Theoretical and experimental analysis of elevator dynamic characteristics“, *Tehnički vjesnik / Technical Gazette*, Vol. 22(4), pp. 1011-1020, (2015)
- [9] J. Vladić, R. Đokić, M. Kljajin, M. Karakašić, „Modelling and simulations of elevator dynamic behaviour“, *Tehnički vjesnik / Technical Gazette*, Vol. 18(3), pp. 423-434, (2011)
- [10] S. S. Rao, „Mechanical vibrations“, Prentice Hall, Upper Saddle River (USA), (2011)
- [11] A. Sinha, „Vibration of Mechanical Systems“, Cambridge University Press, Cambridge (England), (2010)
- [12] O. A. Goroshko, „Evolution of the dynamic theory of hoist ropes“, *International Applied Mechanics*, Vol. 43(1), pp. 64-67, (2007)
- [13] J. Vladić, R. Đokić, M. Jovanović, „Steel wire rope and computational-experimental procedures for the analysis of specific transport machines“, University of Novi Sad, Faculty of Technical Sciences, Novi Sad (Serbia), (2019)
- [14] K. Feyrer, „Wire Ropes“, University of Stuttgart, Stuttgart (Germany), (2007)

## Load Analysis of Steering Mechanism of Wheel Loader

Jovan Pavlović<sup>1\*</sup>, Dragoslav Janošević<sup>1</sup>, Boban Nikolić<sup>1</sup>, Vesna Jovanović<sup>1</sup>, Nikola Petrović<sup>1</sup>

<sup>1</sup>Faculty of Mechanical Engineering, University of Niš, Niš (Serbia)

*The paper presents, in the first part, a mathematical model for determination of the load components of a rotating joint of a hydraulic steering mechanism for controlling the motion of a wheel loader. In the second part of the paper, results of research are given, of the steering mechanism load obtained by the numerical simulation of working cycle of the loader which has in mass 15000 kg.*

**Keywords:** Wheel loader, Mobile hydraulic, Steering mechanism

### 1. INTRODUCTION

A wheel loader is mobile machine mainly used to load and unload bulk materials and for light excavation work. The general configuration of wheel loader kinematic chain consists of: the rear  $L_1$  (Fig. 1) and front  $L_2$  moving mechanism and the manipulator with arm  $L_3$  and bucket  $L_4$ . The rear and front moving mechanism are connected by vertical joint thus forming articulated vehicle. Wheel loaders do not have axle suspension, the front wheels are attached directly to the front body, and the rear axle is allowed to oscillate around the longitudinal axis, thus allowing all wheels to maintain contact with the ground.

Steering of the wheel loaders and other vehicles of large capacity requires great physical effort from the operator and therefore are large number of different types of steering system. One of the most important requirements of easily steering is the reduction of control effort and less transmission of shock loads from wheels to the steering wheel and therefore to the body of operator. In order to enable easy steering of a large capacity vehicles in the steering system are included power systems with a particular source of energy whose main task is to reduce the force required on the steering wheel, where by the energy parameters of power steering systems, controlled by the input signal, performs the activation of valve-regulating members of the hydrostatic system.

Compared with other types of steering system, two hydraulic cylinders arranged symmetrically on a frame has become a major form of steering mechanism for articulated wheel loaders. Articulated steering mechanism provides higher steering torque than conventional pivot steering systems of vehicles of the same weight [1]. A major disadvantage of off-road vehicles with articulated steering system is low maximum velocity. This is made by snaking phenomena considered as self-path changing and the steering of the vehicle is completed by the push and pull of the steering hydraulic cylinders.

Research of steering mechanism of wheel loader and other articulated vehicle is related to design optimization of steering mechanisms with objective function to minimize pressure fluctuation, vibration noise, and a waste of torque during the process of steering due to the difference of stroke between two cylinders and the difference arm. The differences of stroke and arm are reduced based on a genetic algorithm and optimization validation is done

by software package MSC Adams [2].

In a paper [3] dynamic model and validation of an articulated steering wheel loader on slopes and over obstacles is given. A scale wheel loader was designed and manufactured to validate the dynamic model in three conditions (turning on level ground, turning on slopes, and passing over obstacles). The developed dynamic model was found to be useful and could serve as an important tool for analysing the stability of wheel loaders.

In a paper [4] mathematical model of steering kinematics is given. Turning resistance torque have been obtained experimentally and it was concluded that depends on geometrical parameters, mass distribution and a type of suspension system of an articulated body steer vehicle with a combination of a ground type. It is important how does a driving system is designed because of its influences on wheels torque while turning.

The development and testing of a novel steering concept for vehicles with articulated steering are presented and explained in paper [5]. The opportunities are offered with respect to energy consumption, replacement of the hydraulic steering system, and stability of the angle of articulation are emphasized.

In paper [6] analysis of a loads acting on steering mechanism during turning of an articulated vehicle is given. Load analysis is necessary for optimization of steering mechanisms and represent input parameter for optimal selection of hydrostatic steering drive mechanism.



Figure 1: Physical model of wheel loader

\*Corresponding author: Faculty of Mechanical Engineering, University of Niš, Niš (Serbia), jovan.pavlovic@masfak.ni.ac.rs

## 2. HYDROSTATIC STEERING MECHANISM OF ARTICULATED WHEEL LOADER

The function of the movement control system of mobile machines is reflected in the mobility of the machine, which is characterized by: manoeuvrability, agility and possibility of the machine.

Manoeuvrability is the ability to change the direction of the machine. Manoeuvrability is characterized by the ability of the machine to achieve curvilinear movement along the path of the largest possible curvature with a minimum overall surface area of movement, regardless of external movement restrictions. The possibility determines the conformity of the minimum overall surface of the machine movement with the external restrictions of the given path of movement. Mobility (manoeuvrability) of machines is achieved by its movement control system, which, in principle, consists of a mechanism and drive control.

Kinematic chain of moving mechanism of articulated wheel loaders consists of rear moving mechanism  $L_1$  (Fig. 2) and a front moving mechanism  $L_2$  which are connected with vertical joint  $O_2$ .

The general power steering hydrostatic system of mobile machines build the following basic components: hydraulic pump 2 (Fig. 2), the rotary control valve 3 with a steering wheel 3.1 and steering pillar 3.2 and hydraulic cylinders 4. The system components are connected to an open hydraulic circuit. The drive of the rotary control valve is performed directly with a hydraulic pump 2 or from the priority valve 2.1 (Fig.2), with a hydraulic pump 2 which is used to drive some other system of the machine, for example, the brake system or drive system of the manipulator.

**Rotary control valves.-** At the hydrostatic steering system, rotary control valves has a dual function: a) as a rotary valve for the distribution of oil to the chamber of hydrocylinder of steering mechanism and b) as a hand pump in the case of failure of the main hydraulic pump, during spraying running lines or other malfunction of the steering system. The rotary control valve is powered by the operator with the steering wheel of the machine by which, depending on the installation space, it can be directly connected with rotary valve, or via a rigid or an articulated steering pillar

It has been developed power steering systems with the closed and open center. The power steering system of open center with non reaction (OC/NR) has the hydraulic pump which is in the neutral position connected with a tank P-T. Wherein L and R lines of the power steering system blocked so that the external loads of wheels are transferred to the power steering system but the operator via the steering wheel does not feel.

The rotary control valve in power steering has working lines indicated with L (left) and R (right) and does not like the rest of control valves A and B. The power steering systems with the closed-center in hydrostatic control system mainly is driven by the hydraulic pump with the constant specific flow.

At the power steering system of the open center with reaction (OC/R) in the neutral position lines L-R are connected to hydraulic cylinders of the steering mechanism. External forces that are acting on the hydraulic cylinder, the operator feels as reaction forces on

the steering wheel. If the operator lets go the steering wheel after the rotation of machine in a road curve, the wheels and steering wheel correct themselves and the machine continues to move in a linear trajectory.

## 3. LOAD ANALYSIS OF STEERING MECHANISM

For the articulated steering mechanism of the loader during the movement and loading operation of the machine, the steering resistance torque  $M_o$  is determined according to the equation (Fig. 2):

$$M_o = W_{max} \frac{B_4}{2} \left( \frac{l-l_2}{l} \right) \quad (1)$$

where:  $W_{max}$  – resistance that in intensity is equal to the maximum traction force of the machine,  $B_4$  - width of the bucket,  $l$  – wheelbase distance,  $l_2$  – distance from front axis to axis of articulated joint the moving mechanism.

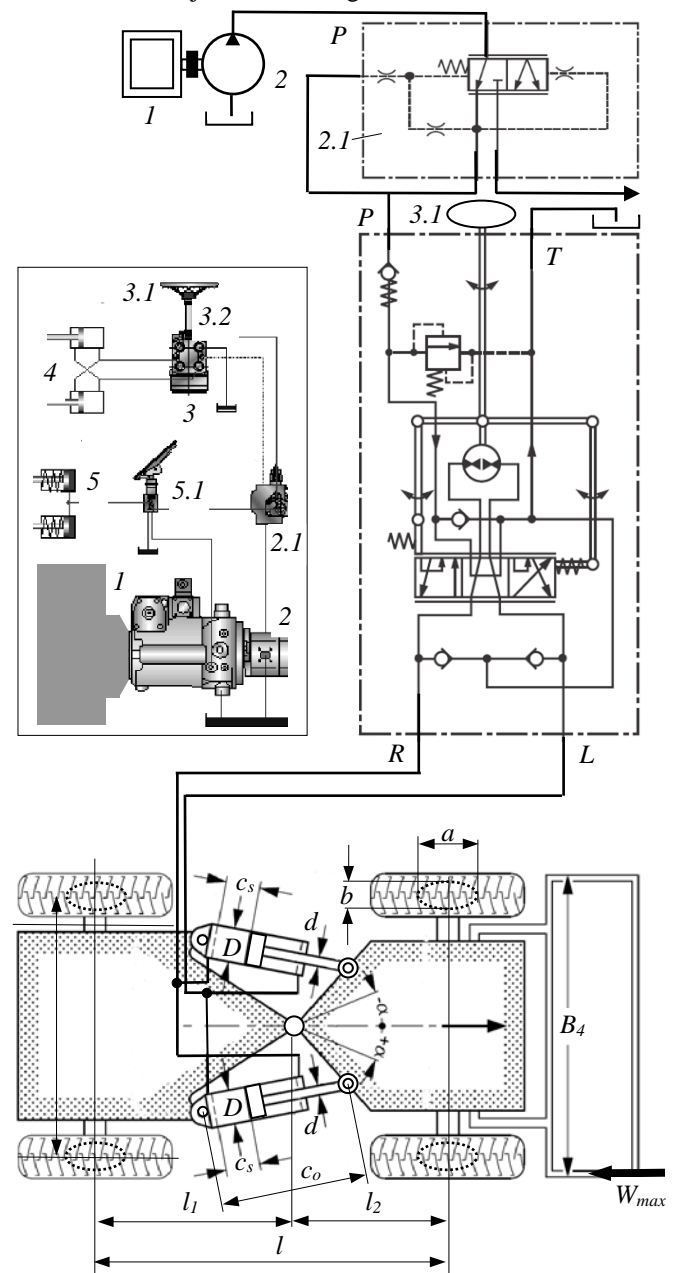


Figure 2: Hydrostatic steering system of articulated moving mechanism of wheel loader [8]

For practical use, companies that manufacture components of hydrostatic steering mechanism have developed empirical formulas for determination of articulated steering loads:

$$M_o = \frac{F_t \cdot \mu}{4} (\sqrt{a_r^2 + b_r^2} + \sqrt{a_r^2 + 4b_r^2}) + F_t \cdot f \cdot (l_1 + l_2) \quad (2)$$

where:  $F_t$  - static load of one tire of the wheel loader under load:

$$F_t = \frac{g \cdot m}{n_t} \quad (3)$$

$n_t$  - number of tires,  $\mu$  - tire and ground friction coefficient,  $f$  - rolling resistance coefficient,  $a_r, b_r$  - reduced tire contact surface of tire and ground:

$$a_r = \frac{a_e}{2} \sqrt{\pi}; \quad b_r = \frac{b_e}{2} \sqrt{\pi} \quad (4)$$

where:  $a_e = (0,4 \div 0,45) \cdot D$  - the length of the contact surface of the tire with the ground,  $b_e = (0,55 \div 0,6) \cdot b$  - the width of the contact surface of the tire with the ground [7].

Authors in paper [2] have been concluded that steering resistance torque of pivot steering is usually 2–3 times that of driving, thus, the pivot steering torque is taken as the calculated load. The following equation describes empirical formula for steering torque that comes from the test curve:

$$M_o = \frac{G \cdot \mu^n}{\eta} (0,1 \cdot L + 0,6) (0,3b^2 + 0,1b + 2,6) \quad (5)$$

where:  $G$  - vertical load on the tire,  $\eta$  - steering mechanism efficiency,  $\mu$  - friction coefficient,  $L$  - wheelbase of the vehicle,  $b$  - tire width.

When the wheel loader is fully loaded, the load of the front axle is greater than that of the rear axle. When the wheel loader is moving and steering, the wheels of the front axle, at same time, are rolling and slipping, and the rear axle wheels only have drag torque caused by the opposite rotation of the left and right wheels. During steering, the machine has to overcome three resistances due to:

- wheel alignment,
- wheel rolling,
- wheel dragging.

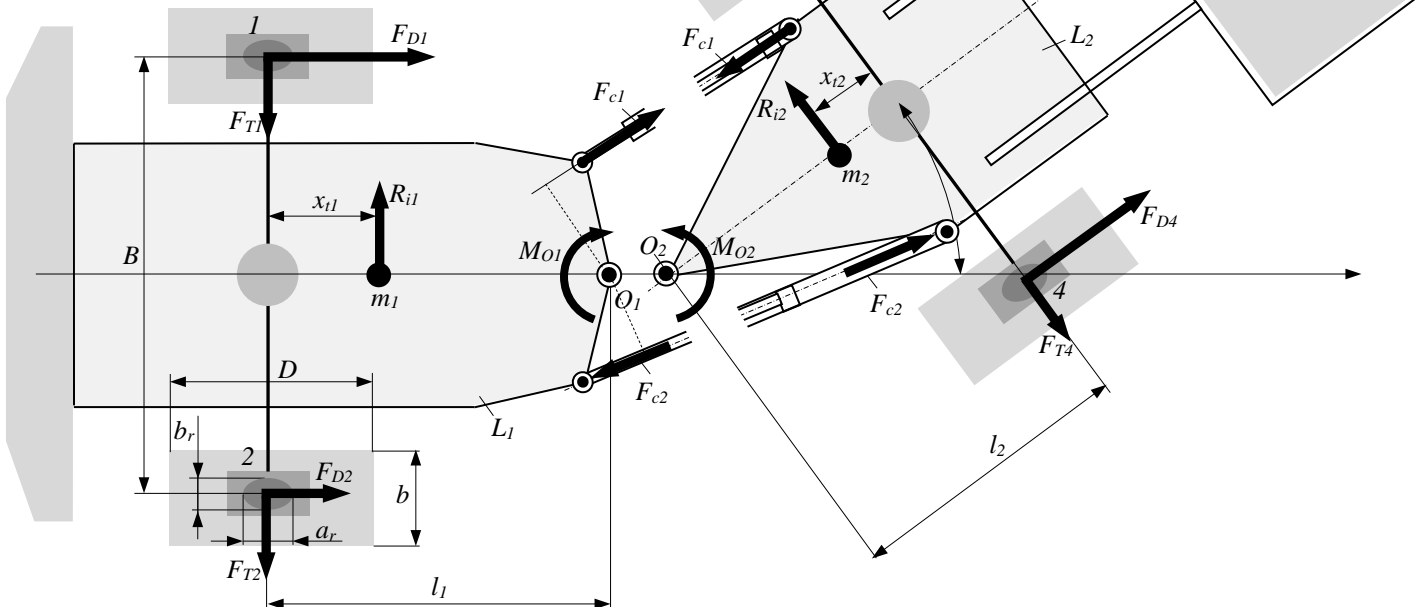


Figure 3: Model of loader steering analysis

A mathematical model of wheel loader steering is shown in Fig. 3. The model takes in consideration forces that acts on loader when is turning, neglecting wheel and air resistance, friction in the joint and rotating inertia forces.

Firstly, is observed rear then front part of moving mechanism. For the correct selection of the components of the steering hydrostatic system, one of the conditions is that the drive torque  $M_p$  is greater than the load torque  $M_o$ :

$$M_p \geq M_o \quad (6)$$

Based on force analysis, the load torque of rear moving mechanism  $L_1$  is [3]:

$$M_{o1} = (F_{D1} - F_{D2}) \cdot \frac{B}{2} - (F_{T1} + F_{T2}) \cdot l_1 + F_{i1} \cdot (l_1 - x_{i1}) \quad (7)$$

The load torque of front moving mechanism  $L_2$  is:

$$M_{o2} = (F_{D4} - F_{D3}) \cdot \frac{B}{2} - (F_{T3} + F_{T4}) \cdot l_2 + F_{i2} \cdot (l_2 - x_{i2}) \quad (8)$$

where:  $F_{D1}, F_{D2}, F_{D3}, F_{D4}$  - driving forces,  $F_{T1}, F_{T2}, F_{T3}, F_{T4}$  - lateral forces,  $F_{i1}, F_{i2}$  - inertial forces of wheel loader,  $B$  - track width,  $l_1, l_2$  - wheelbase of the wheel loader,  $x_{i1}, x_{i2}$  - center of mass coordinates of rear and front part.

Drive torque of hydrostatic steering mechanism is obtained by:

$$M_p = F_{c1} \cdot r_1 + F_{c2} \cdot r_2 \quad (9)$$

where:

$$F_{c1} = \left[ \frac{D_i^2 - d_i^2}{4} \pi \cdot p - \frac{D_i^2}{4} \pi \cdot p_o \right] \eta_{cm} \quad (10)$$

$$F_{c2} = \left[ \frac{D_i^2 \pi}{4} p - \frac{D_i^2 - d_i^2}{4} \pi \cdot p_o \right] \eta_{cm} \quad (11)$$

where:  $F_{c1}$  - the retraction force of hydraulic cylinder,  $F_{c2}$  - the extraction force of hydraulic cylinder,  $D, d$  - diameter of the piston and the piston rod of hydraulic cylinder,  $p, p_o$  - pressure in the main and return lines of the hydraulic cylinder,  $\eta_{cm}$  - mechanical efficiency of hydraulic cylinder  $r_1, r_2$  - transmission lengths of the hydraulic cylinders in relation to the vertical axis of the articulated joint.

One factor of significant importance in articulated steering of a vehicle is the track width  $B$ . Different driving forces  $F_{Di}$  acting on a driven axle produce a torque around the vertical axis of each vehicle section. As both sections of a vehicle are connected by an articulated joint, opposite torques acting on the front and the rear section are required. The consequence is that steering requires to apply the driving force differences on an axle conversely in front and rear section. For instance, if higher traction forces exist on the right hand front side and the left hand rear side, the vehicle will buckle to the left. Fig. 3 shows the steering principle and the forces acting on the vehicle.

Dynamic considerations show that lateral forces acting on the centers of mass of the two vehicle sections create a self-reinforcing or self-stabilizing characteristic, depending on the position of the center of mass. If the centers of mass of the two vehicle sections, compared to the respective axle, are located between this axle and the link, the vehicle tends to continue buckling on its own.

#### 4. SIMULATION OF WHEEL LOADER STEERING

In this part of the paper, the results of the numerical simulation of loader steering within the entire working cycle are presented. The general cyclic manipulation task of the loader consists of operations: loading (Fig.4) transfer and unloading of material or cargo and return to the beginning of a new cycle. During loading and unloading operations, the direction of movement of the loader is normal to the position of the gripping material or load, ie to the longitudinal axis of the vehicle into which the unloading is performed. Depending on the position of the place and the method of unloading, the paths of the loader during the transfer and return operations to the beginning of the new cycle are usually in the form of the letters V or Y.

The numerical simulation was done in the software package *MSC ADAMS (Automated Dynamic Analysis of Mechanical Systems)* and firstly is simulated steering process of a loader which have in mass  $15000 \text{ kg}$  and a bucket volume of  $2.3 \text{ m}^3$ , from a given  $\theta_{min}=45^\circ$  to  $\theta_{max}=-45^\circ$  which does not move and which is loaded with a full bucket. The tire and ground friction coefficient is  $\mu=0,7$ .

Steering the wheel loader from  $\theta=0^\circ$  to  $\theta=45^\circ$  takes  $2.5 \text{ s}$  ( $8-10.5 \text{ s}$  in simulation), while turning from  $\theta=45^\circ$  to  $\theta=-45^\circ$  takes  $5 \text{ s}$  ( $10.5-15.5 \text{ s}$  in simulation) And such a duration of the turning cycle is an ergonomic requirement to turn the loader from  $\theta_{min}$  to  $\theta_{min}$  for  $5 \text{ s}$  making 4 turns of the steering wheel.

Force components that are acting on articulated joint are given on Fig. 5a.

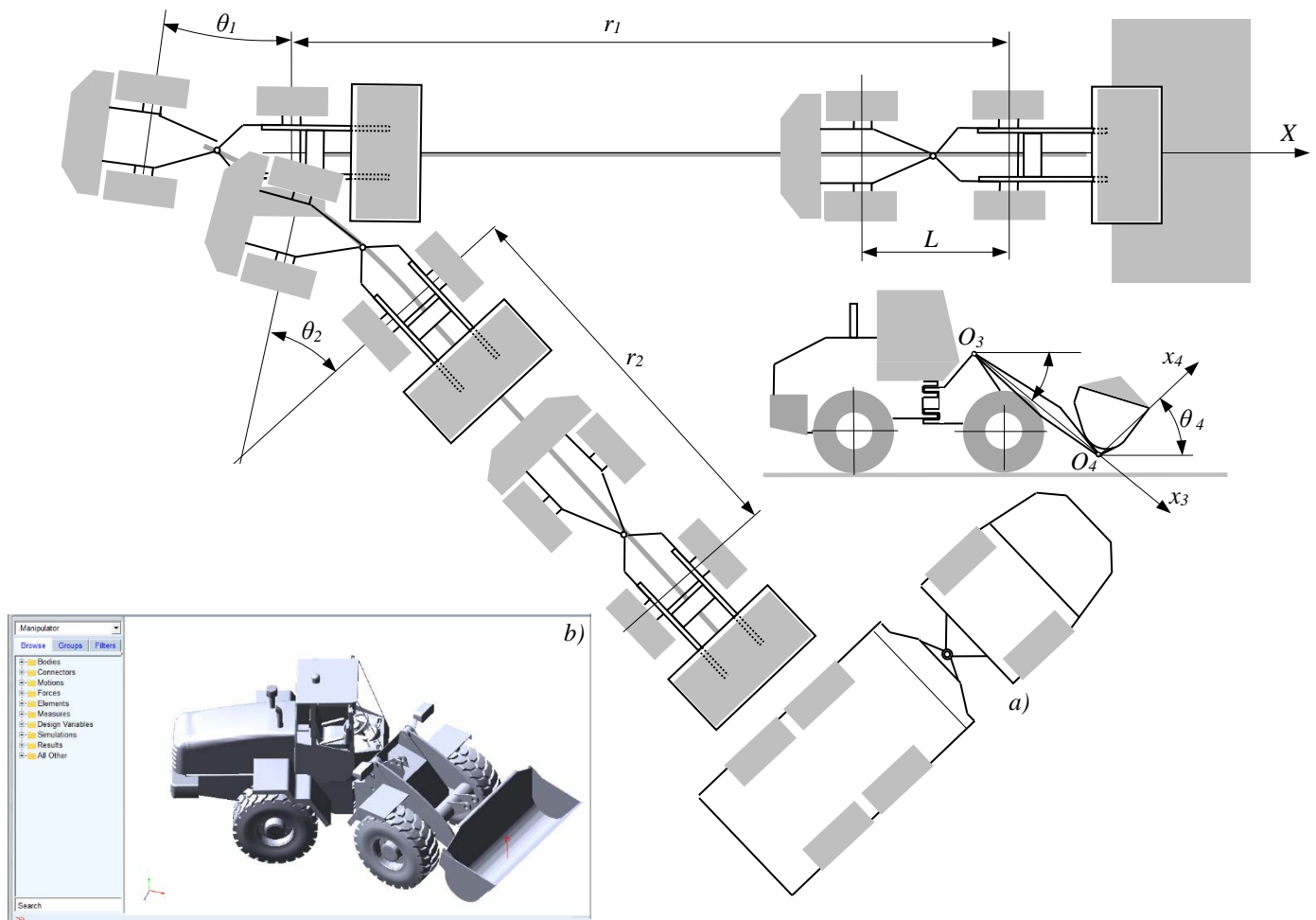


Figure 4: Working cycle of wheel loader: a) cycle in the form of letter V, b) 3D model of loader in ADAMS

The results of the loader rotation simulation are given by the diagram in Figure 6a and it can be seen that the highest value of the steering torque resistance is  $M_{oz1}=70000 Nm$ .

As another way of steering, the real working cycle (Fig. 6b) of the loader in the shape of the letter V is given, which after loading and moving backwards for the length  $r_1$ , rotate by the angle  $\theta_1=20^\circ$ . The diagram in Figure 6b shows that then the steering torque resistance is  $M_{oz2}=60 kNm$ .

After that, the loader rotates by an angle of  $\theta=60^\circ$ , in oposit direction, where it rotates and at the same time moves in a straight line forward to the place of unloading. Then the loader also achieves a steering torque resistance of  $M_{oz2}=60 kNm$ . It can be noticed that by moving and simultaneously steering, the loader achieves lower steering resistances then on stationary steering.

CONSLUSION

The load analysis of steering mechanism of wheel loader represents input of optimal synthesis of steering mechanism and right choice of hydrostatic system components.

The analysis defined the components of the hydrostatic transmission with the most important component - rotary control valve. Two types of power steering systems have been developed with the closed and open center.

For optimal synthesis and load analysis of steering system it has been developed a general mathematical model of wheel loader with rear and front part of moving mechanism which are connected with vertical joint forming thus articulated vehicle.

Using force analysis, the model has been developed which take in consideration forces that acts on loader when is turning, neglecting wheel and air resistance, friction in the joint and rotating inertia forces. Firstly, is observed rear then front part of moving mechanism. For practical use, companies and researchers have developed empirical formulas for determination of articulated steering loads.

In the last chapter of the paper, the results of the numerical simulation of loader steering have been presented. The results of obtained simulation are given for two case of wheel loader steering: stationary steering with full loaded bucket and for whole working cycle of loader in the V-shape path

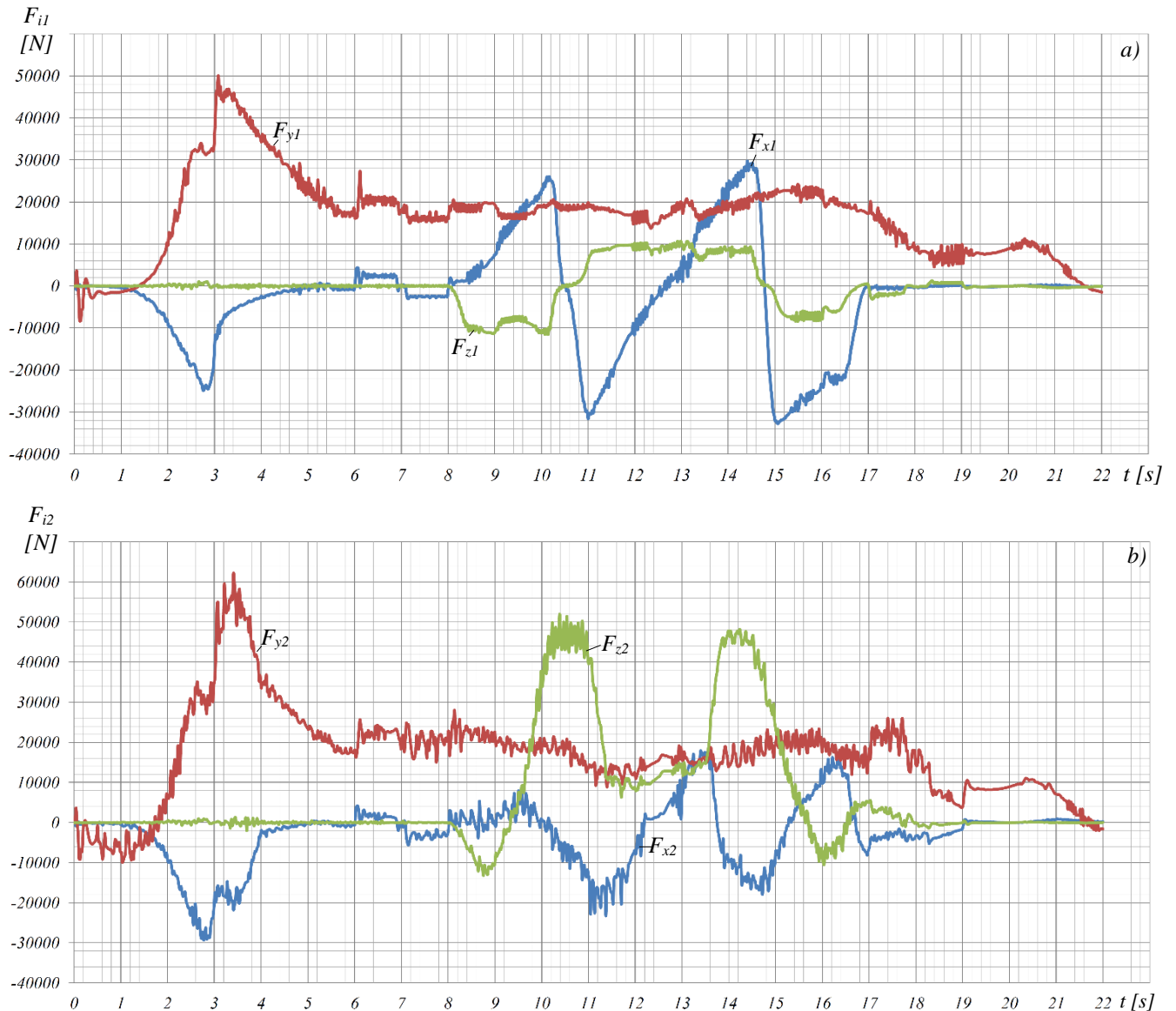


Figure 5: Force components acting on articulated joint: a) stationary steering, b) steering in cycle with V-shape path

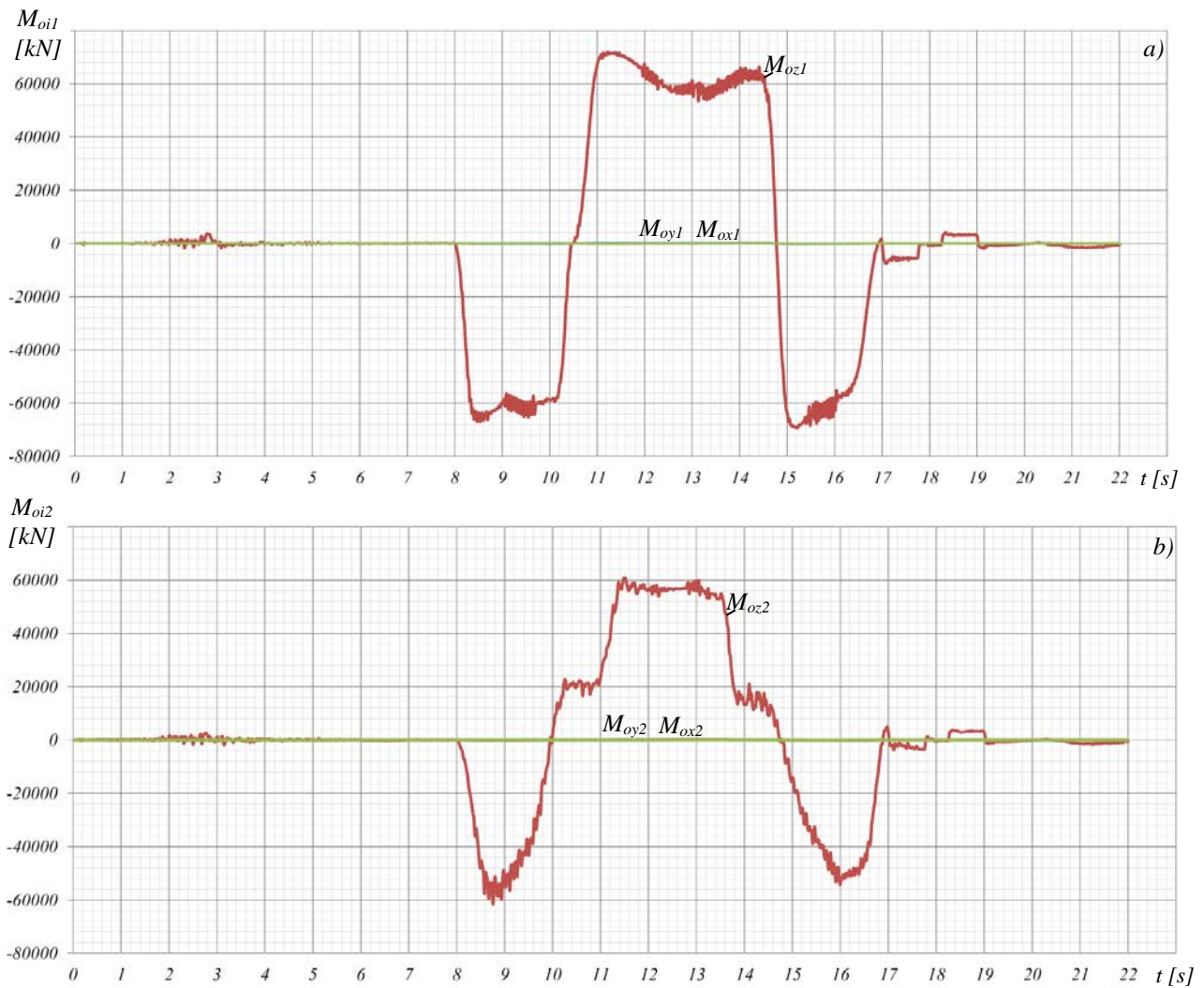


Figure 6: Torque components acting on articulated joint: a) stationary steering, b) steering in cycle with V-shape path

#### ACKNOWLEDGEMENTS

This research was financially supported by the Ministry of Education, Science and Technological Development of the Republic of Serbia (Contract No. 451-03-9/2021-14/ 200109)

#### REFERENCES

- [1] Wadephul, J., Engelmann, D., Kautzmann, P. et al. Development of a Novel Steering Concept for Articulated Vehicles. *ATZ high world* 11, 54–61 (2018). <https://doi.org/10.1007/s41321-018-0039-6>
- [2] Zhou, C.; Liu, X.; Xu, F. Design Optimization of Steering Mechanisms for Articulated Off-Road Vehicles Based on Genetic Algorithms. *Algorithms* 2018, 11, 22. <https://doi.org/10.3390/a11020022>
- [3] Li, X., Wang, G., Yao, Z., Qu, J.: Dynamic model and validation of an articulated steering wheel loader on slopes and over obstacles, *Vehicle System Dynamics*, Vol. 51, No. 9, 1305-1323, 2013. <http://dx.doi.org/10.1080/00423114.2013.800893>
- [4] Skurjat, A.: Steering Kinematics and Turning Resistance Experimental Investigation of Articulated Rigid Body Vehicles, *Experimental Mechanics of Solids, Materials Research Proceedings*, Vol. 12, pp. 131-138, 2019. <https://doi.org/10.21741/9781644900215-19>
- [5] Lopatka MJ, Rubiec A.: Concept and Preliminary Simulations of a Driver-Aid System for Transport Tasks of Articulated Vehicles with a Hydrostatic Steering System, *Applied Sciences*, Vol. 10(17), pp. 1-16, 2020. <https://doi.org/10.3390/app10175747>
- [6] Pavlović, J., Janošević, D., Jovanović, V., Petrović G., Spasović N.: Development of the power steering system in mobile machines, In *Proceedings of the sixth international conference transport and logistics - TIL 2017*, Niš, Serbia, pp. 145-151, 2017. (M33)
- [7] Danfoss: *Hydraulische Lenkungscomponenten, Vollhydraulisch und mechanisch-hydraulische Lenksysteme*, 1989.
- [8] Јаношевић, Д.: *Пројектовање мобилних машина (Design of mobile machines)*, Машински факултет Ниш, Универзитет у Нишу, Ниш. 2018.

# Improvement of Casting Technology of Continuous Tracks Segment Using CAD/CAE/CAM Software Tools

Aleksandar Jovičić<sup>1\*</sup>, Nedeljko Dučić<sup>1</sup>, Radomir Radiša<sup>2</sup>, Ivan Milićević<sup>1</sup>, Marko Popović<sup>1</sup>, Vojislav Vujičić<sup>1</sup>

<sup>1</sup>Faculty of Technical Sciences Čačak, Department of Mechatronics and Department of Mechanical Engineering, University of Kragujevac, Čačak (Serbia)

<sup>2</sup>Lola institute Ltd, Belgrade (Serbia)

*The casts of continuous track segments, used in the continuous track assembly, are very responsible components of the tanks drive system. Continuous track segments, are made by casting process, where casting can be considered an unsurpassed technological process for these parts. As a solution in such cases, the use of specialized CAD/CAE/CAM tools for simulation, optimization and geometric modelling of products and casting tools is imposed. By applying the mentioned tools, the time of development of a new product and its production process is shortened in relation to traditional methods with prototype testing. In this paper, the improvement of the casting process of continuous track segments, was carry out by using the software MAGMASoft. The concept applied in this paper, includes virtual production, practical realization of the defined technological process, improvement of the existing technology with final check of the casting quality, through mechanical and metallographic tests.*

**Keywords:** Casting, Continuous track segment, CAD/CAE/CAM, Simulation

## 1. INTRODUCTION

Continuous track segments are the main parts of continuous track assembly, which is the component of tanks propulsion and drive system [1]. For the production of continuous track segments, is used casting technology with high-alloy wear-resistant manganese steel.

Metal casting is probably the oldest production technology, whose roots go back to the time when the first metals and metallurgy were discovered. Casting technology is constantly improving through the research process in the field of applied sciences and engineering. In the previous period, the basic source of innovation in casting technology has been primarily in multidisciplinary.

The defence industry, ie production of weapons, tools and armoured vehicles for military needs, cannot exist without casting technology. From 30 to 70% of the mass of these products are parts made by casting technology. Many of them, are very important parts, and they can't be manufactured in rationally way by using alternative production technologies [1].

## 2. FORMATING PAGES MODERN TECHNOLOGY FOR DESIGN A PRODUCT AND MANUFACTURING PROCESSES

Modern technology for design a product and manufacturing processes include:

- a) Specialized CAE tools (MAGMASOFT and similar) intended for the simulation and optimization of casting processes (casting, hardening, cooling etc.)
- b) CAD tools for geometric modelling of a products and casting molds (model, mold cavity, etc.)
- c) CAE tools for analysis and simulation of the mechanical behaviour of castings in the static and dynamic domains, by using the FEM
- d) CAM tools for design of manufacturing process of the molds and models [1].

The development of the casting process is increasingly based on scientific results, obtained through the use of specialized modern software tools. This software enables virtual production based on simulations, in order to optimize process parameters, improve the quality of castings and reduce production costs.

Nimbulkar and Dalu (2016) presented the application of Auto-CAST X1 software to simulate the casting process. In this paper, the authors emphasized the importance of the design of the infusion system and feeding system, for the correctness of the casting, using different simulations in the mentioned software [2]. Jie and co-authors (2014), applied the Pro Cast software to improve the aluminium alloy casting process. The general conclusion drawn by the authors, is that by increasing the casting temperature and casting speed, can solve problems of porosity [3]. Dabade and his associates (2013) used MAGMASoft software to analyze various defects in the casting process. They detected the causes of casting defects, through simulations of different variants of casting and gating systems [4].

Dučić and others (2017) presented a methodology for optimization of the gating system for sand casting, using a genetic algorithm. The subject of optimization was the geometry of the gating system, ie, the cross section of the pouring cup and the sprue height, while the goal of optimization was to minimize the casting time. In this case, the simulation was used to verify and evaluate the optimized inflow system geometry [5].

### 2.1. Casting in the sand molds

For the production of continuous track segments, the casting in sand molds is used as the main technology. Casting in the sand molds, is suitable for production of continuous track segments, because this parts have complex geometry with high geometrical and dimensional accuracy.

After the breakup of Yugoslavia, most of the technological knowledge disappeared, especially those that

\*Corresponding author: Faculty of Technical Sciences Čačak, Svetog Save 65, Čačak, aleksandar.jovicic@ftn.kg.ac.rs

existed in the former republics of Yugoslavia. The production of continuous track segments, was initially realized in Slovenia (Ravne), and then in Bosnia and Herzegovina (Jelšingrad). After that, this production was developed and continued in the former machine tool factory "Ivo-Lola-Ribar", but with limited success. For none of the mentioned production units, data on the applied technological production processes have been saved. During the search of the warehouse of the Serbian Army, only samples of continuous track segments were found [1].

### 3. CASTING DEFECTS

Verification of the proposed casting technology can be done by applying the simulation and optimization tool MAGMASOFT. This software is specialized in modelling and simulation of all phases of the metal casting process. For the imported CAD model (Figure 1), a simulation of the casting process was performed and the CO<sub>2</sub> mold was made. On the base of this CO<sub>2</sub> mold and in according to the previously given technological parameters, continuous track segment was cast.

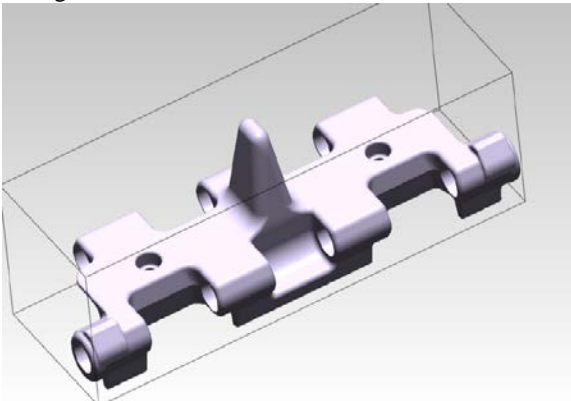


Figure 1: CAD model of continuous track segment

The analysis of the sample casting part, which is obtained in according to the previously defined technology, revealed significant and visible casting defects. The criteria of porosity and microporosity, obtained by simulation on the model, with great reliability coincide with the real situation.

For the simulation of the casting process, by using MAGMASoft, was create CAD 3D model of all elements of the mold cavity: gating system (pouring cup, sprue, choke, runner, and ingates), casting with cores, risers and gas vents and more. A properly designed gating system should ensure that the liquid metal pours into the mold cavity quickly and without turbulence [6].

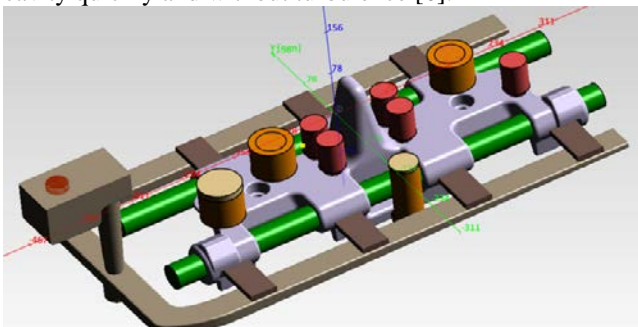


Figure 2: Simulation model of casting technology applied in previous phases of development of continuous track segment

The proposed solution showed an inadequate feeding system (Figure 2) (topology, position, geometry, etc.) and filtration. Williams' risers are obviously, oversized and dysfunctional in the critical phase of hardening. The Military Technical Institute, this technology declared as unsuccessful, because this technology didn't give the casting part with required geometric and metallurgical characteristics.

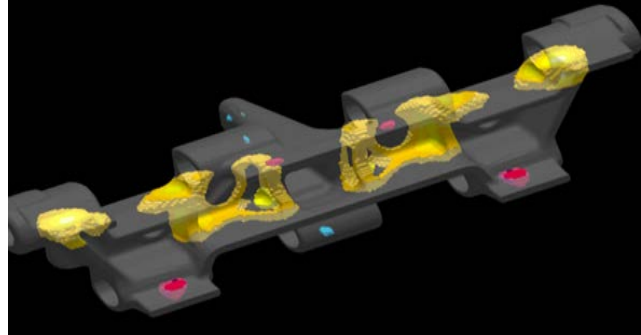


Figure 3: Hot spots in the casting part without influence of gating system and riser

Auxiliary risers were also dysfunctional due to poor location - they were far from hot spots (Figure 3). By analyzing the simulation, it can be noticed vortex motion and level oscillations of the metal filling (multiple filling and subsequent melting of the metal that has already started to harden in the filling phase). Due to the long casting time, a cold zone appeared before the end of the casting process. Also, the fluidity of the molten metal in the final stage is very poor. Cold shuts and the final porosity appeared on the model of the casting part. Those phenomena also was confirmed in the selected characteristic cross section of the real casting part (Figure 4).

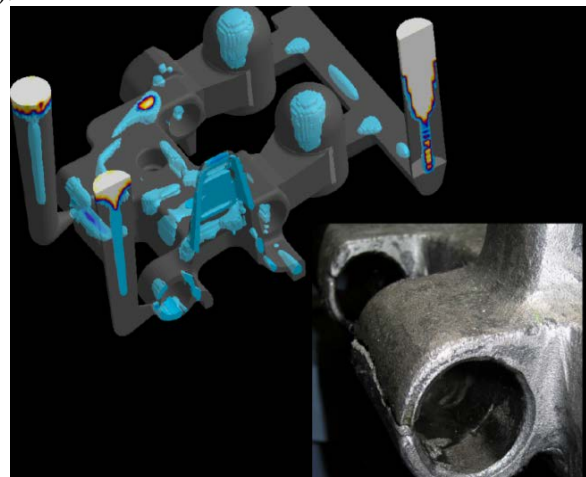


Figure 4: The final porosity and cold shuts

From all the above, it can be concluded that it is necessary to define the new casting parameters. The new casting parameters will be obtained on the base of the knowledge gained in previous activities and through the casting process simulation and optimization of the new gating system (filling, hardening and cooling).

### 4. CASTING TECHNOLOGY FOR PRODUCTION OF CONTINUOUS TRACK SEGMENT

In order to improve the casting technology of continuous track segment, test casting of continuous track segment members was performed in foundry IKL Guča. Using decades of experience in casting manganese steels

(steel X120Mn12 (DIN), or Hetfield steel of chemical composition: C = 1.1–1.25, Si = 0.30–0.50, Mn = 11.5–13, Cr<sub>max</sub> = 0.20, S<sub>max</sub> ≤ 0.02, P<sub>max</sub> ≤ 0.035), in the foundry of IKL Guča with the application of modern CAE tools for simulation and optimization of the casting process (MAGMASOFT), a new solution of the casting system was proposed, after which a continuous track segment was cast from the mentioned material. Hatfield steel is characterized by the fact that in the process of exploitation, its surfaces become harder when in contact with other material, which significantly improves the performance of the casting part, in this case the continuous track segment. Through this improvement of the casting process, emphasis is placed on the casting of the casting without internal defects (porosity and the appearance of gas bubbles), as well as the mechanical and metallographic characteristics of the casting. If the mentioned characteristics are satisfactory, the geometric harmonization of the casting is performed. Based on the casting technological parameters given during the simulation process, a continuous track segment was cast in the sand molds (Figure 5). From the characteristic cross-sections (Figure 6) it can be seen that the casting part has no internal defects.



Figure 5: Sand mold and casting part after removal of the pouring system



Figure 6: Characteristic cross-sections of continuous track segment as confirmation that there are no internal defects

#### 4.1. Mechanical - metallographic characteristics of the continuous track segment

The mechanical characteristics of the casting part after the technological process of normalization are: tensile strength: R<sub>m</sub> = 600 N / mm<sup>2</sup>, elongation (l = 5d<sub>0</sub>) %: A = 20. It can be stated that an austenitic polygonal and uniform cross-sectional structure has been achieved

(Figure 7), expected for Hatfield steel, which should be transformed into martensite during exploitation under stress, which provides the steel with hardness and wear resistance. The carbides are small and evenly distributed so that their network is not noticeable anywhere. The presence of non-metallic inclusions is also negligible.

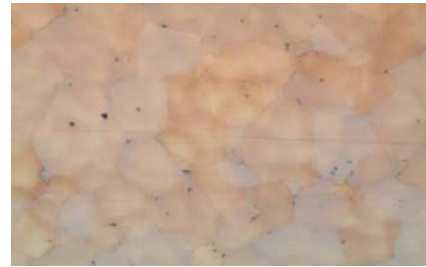


Figure 7: Microstructure of continuous track segment material

##### 4.1.1. Hardness of castings after thermal treatment

In order to transfer the load that appears on the components of the caterpillar, the caterpillar members (continuous track segment) must, after thermal treatment, have the appropriate mechanical characteristics determined by the hardness, which must be in the range of 170 HB to 207 HB.

##### 4.1.2. The bending force of the casting part

A parameter that is also an indicator of the mechanical characteristics of continuous track segment is the bending resistance. When bending the castings of continuous track segment after thermal treatment, according to the schemes presented in Figures 8 and 9, forces of not less than 300 kN, 320 kN and 240 kN, respectively, must be obtained. In the event that the continuous track segment break during bending, the specified force values must be obtained before the fracture occurs.

Based on the testing of cast samples performed at the Military Technical Institute in Belgrade, the bending test loads were met, and the obtained microstructure of the material corresponds to the required structure so that further tests and harmonization of geometric characteristics of castings can be continued.

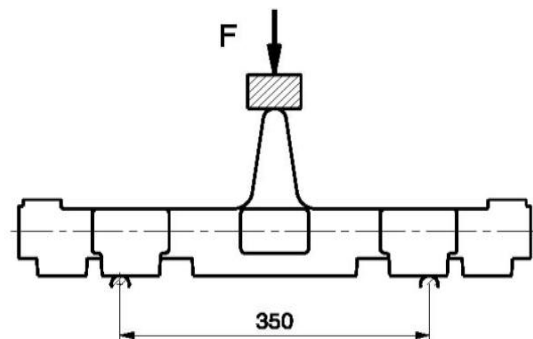


Figure 8: Bending the continuous track segment with the ridge upwards

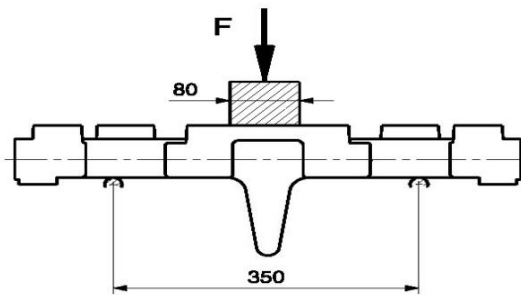


Figure 9: Bending the continuous track segment with the ridge down

## 5. CONCLUSION

Continuous track segment used to form a caterpillar assembly (caterpillars), as a component of the caterpillar moving tank are responsible components and from the aspect of their production, casting technology can be considered an unsurpassed technological process. As solutions in such cases, specialized CAE tools for simulation and optimization of the casting process (very often internal cracks and residual stresses occur during casting cooling) and CAD tools for geometric modeling of casting parts, elements of gating system, cores, etc.) are imposed. For many metal foundries, the simulation of the casting process has become a standard tool for designing the casting system, feeders and studying thermal processes in order to obtain the desired characteristics of the casting part. Also, simulation has become one of the instruments in quality assurance and process optimization systems. The improvement of the casting process for production of continuous track segment was carried out using the MAGMASoft software package. The application of the methodology presented in the paper shortens the development time of a new product and its production in relation to traditional methods of trial and error.

Verification and final quality control was performed by mechanical - metallographic tests.

## ACKNOWLEDGEMENTS

The research presented in this paper is partially funded by the Ministry of Education, Science and Technological Development of RS, contract no. 451-03-9 / 2021-14 / 200132 whose implementer is the Faculty of Technical Sciences in Čačak - University of Kragujevac.

## REFERENCES

- [1] P. Petrović, R. Radiša, V. Petrović, N. Lukić, I. Danilov, Tehničko rešenje, Nova tehnologija livenja guseničnog članka, Beograd, CMSysLab 2016-01.
- [2] S.L. Nimbalkar, R.S. Dalu: Design optimization of gating and feeding system through simulation technique for sand casting of wear plate, Perspectives in Science, Vol. 8, pp. 39-42, 2016.
- [3] Z. Jie, Z. Dongqi, W. Pengwei, W. Gang, L. Feng, D. Penglong: Numerical simulation research of investment casting for TiB<sub>2</sub>/A356 aluminum base composite, Rare Metal Materials and Engineering, Vol. 43, pp. 47-51, 2014.
- [4] U.A. Dabade, R.C. Bhedasgaonkar: Casting defect analysis using design of experiments (DoE) and computer aided casting simulation technique, Procedia CIRP, Vol. 7, pp. 616-621, 2013.
- [5] N. Dučić, Ž. Čojbašić, S. Manasijević, R. Radiša, R. Slavković, I. Milićević, Optimization of the gating system for sand casting using genetic algorithm, International Journal of Metalcasting, Vol. 11, pp. 255–265, 2017.
- [6] R., Slavković, S., Dragičević, I., Milićević, A., Jovičić, N., Dučić, M., Popović, Integrisan proces proizvodnje abrazivnih reznih elemenata bagera u rudarskoj industriji, IMK-14 – Istraživanje i razvoj u teškoj mašingradnji 24(2018)2, SR35-41 UDC 621 ISSN 0354-6829.

# Strength of the Welded Joint with Improved Mechanical Properties of Weld Metal and Heat Affected Zone

Miodrag Arsić<sup>1\*</sup>, Nebojša B. Zdravković<sup>2</sup>, Vencislav Grabulov<sup>1</sup>, Srđan Bulatović<sup>1</sup>, Mladen Mladenović<sup>1</sup>

<sup>1</sup> Institute for materials testing, Belgrade (Serbia)

<sup>2</sup> Faculty of Mechanical and Civil Engineering in Kraljevo, University of Kragujevac, Kraljevo (Serbia)

*Selection of steel, dimensions and fabrication technology for the welded structure are all parts of the design process, because they are in close connection with the function of the structural whole under certain conditions of exploitation for the predicted service life. Quality of welded joints in the process of production of the welded structure is being defined by properties that the structure has to possess in order to fulfill certain requirements, which is being accomplished by the selection of the adequate welding procedure and welding parameters, implementation of inspection programs for all technological operations, as well as by performing mechanical and technological tests in order to determine the magnitude of strength and deformation of base material and welded joints. Constituent parts of a welded joint are base material, heat affected zone and weld metal. Heat affected zone of structural steels is being characterized by the fusion zone, overheating zone, zone of complete normalization and zone of incomplete normalization.*

*In this paper the effect of change in hardness of weld metal and heat-affected zone on mechanical properties of welded joints when base material is quenched and tempered steel C45 is being considered. Test results showed that the application of welded structures made of quenched and tempered steels with hardness HV10 > 400 and tensile strength UTS > 600 MPa is useful only when the stress concentration is low ( $\alpha_s \leq 2$ ) and when there are no residual stresses due to welding.*

**Keywords:** Supply quenched and tempered steel, Mechanical properties, Hardness of the welded joint, Heat affected zone

## 1. INTRODUCTION

Safety of welded structures depends on the simultaneous influence of technological, metallurgical, structural and exploitation factors, or in other words on the welding procedure and shape of welded joints, stress concentration and heterogeneity of structural and mechanical properties of constituent parts of welded joints (base material, heat affected zone, weld metal). Increase or decrease of endurance of welded joints under exploitation conditions, apart from the presence of stress concentrators and residual stresses that occur due to welding, is also being affected by the heterogeneity of mechanical properties of base material, heat affected zone and weld metal, as well as by the width of heat affected zone and weld metal, Fig. 1

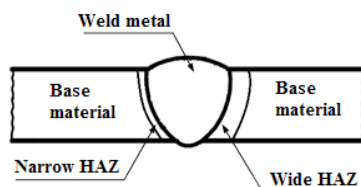


Figure 1: Appearance of a welded joint

Structure and mechanical properties of individual constituent parts of welded joints depend on the welding regime and chemical composition of base and filler material. With the increase of the cooling rate within the subcritical temperature range, strength and yield stress for weld metal and heat affected zone grow and, depending on the chemical composition of steel, are 1.5–2 times larger than for base material [1].

Numerous researches have been carried out around the world in order to determine the effect of various

welding procedures on mechanical properties of quenched and tempered steels. Researches regarding the effect of laser welding parameters on geometry, mechanical properties and structure of weld metal and heat affected zone, showed that large increase of hardness in the area of the welded joint does not necessarily affect the mechanical properties in a negative way [2]. Experimental researches regarding the friction welding of steel C45 (DIN EN 10083) and tests that were carried out in order to determine the mechanical properties of weld metal and heat affected zone enabled the defining of optimum welding parameters for this procedure [3]. Predictions of temperature fields for quenched and tempered steels subjected to the effect of double elliptical heat sources were considered by Goldak and his associates, through the use of modelling and finite element method [4], while analyses of microstructures contributed in defining of geometry coefficient of a welded joint [5,6].

## 2. EFFECT OF THE WELDING THERMAL CYCLE ON MECHANICAL NON-HOMOGENEITY OF THE WELDED JOINT

The presence of non-homogeneous zones is characteristic for welded joints. There are soft layers – zones with lower hardness value than that of the base material and hard layers - zones with higher hardness value than that of the base material. Those layers could exist in weld metal, diffusion zone, which is located in near proximity of the fusion zone, and in the heat affected zone, especially for thermally or thermo-mechanically hardened metals. Causes of occurrence of these non-homogeneous layers are diffusion of alloying elements from weld metal into base material, larger amount of

\*Corresponding author: Bulevar vojvode Mišića 43, 11000 Belgrade, Serbia, miodrag.arsic@institutims.rs

hardened material in weld metal, near the fusion line, and presence of a thermal gradient.

Examples of distribution of hardness, measured transversely on macro strips of two samples, are presented in Fig. 2. When the martensite steel sample, prone to softening aging, is concerned, soft layer is located in weld metal, Fig.2b. As far as the other sample, taken from thermally hardened steel, is concerned, soft layer is located in the heat affected zone. As can be seen in Fig. 2b and 2c, hardness sharply changes from a minimum value, caused by structural and technological properties of a welded joint, to a maximum value characteristic for base material.

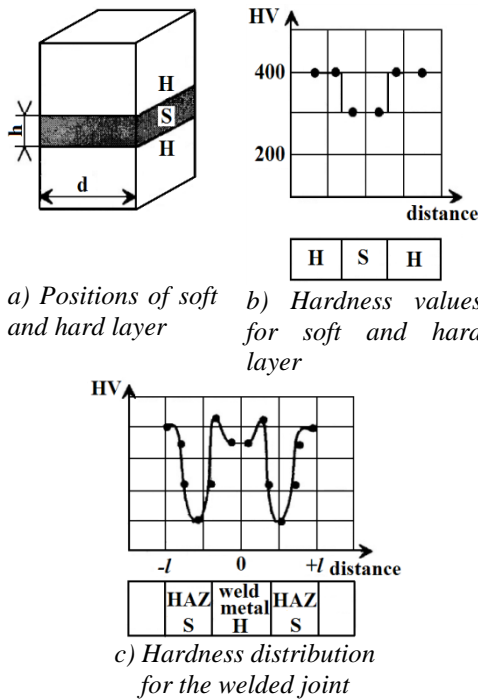


Figure 2: Examples of distribution of hardness

Relative thickness of the soft layer  $\kappa$  is being obtained through the use of the following equation [1]:

$$\kappa = \frac{h}{d} \quad (1)$$

where:  $h$  – width of the soft layer, mm

$d$  – thickness or diameter of the sample, mm.

Static endurance of welded joints ( $\sigma$ ) with variable mechanical properties of the soft or hard layer, subjected to pure shear or to tension, is being obtained as follows [7]:

– pure shear

$$\sigma_{SS} = 2 \cdot R_{SS} \cdot k_{\kappa}$$

$$\sigma_{SH} = 2 \cdot R_{SH} \cdot k_{\kappa} \quad (2)$$

– tension

$$\sigma_{TS} = R_{TS} \cdot k_C$$

$$\sigma_{TH} = R_{TH} \cdot k_C \quad (3)$$

where:  $R_{TS}$  - yield stress of the soft layer,  $R_{TH}$  - yield stress of the hard layer,  $k_C$  - coefficient of mechanical non-homogeneity (coefficient of contact strengthening).

### 3. EXPERIMENTAL TESTS

Steel C45 is hardly weldable due to a large amount of carbon ( $CE > 0.45$ ). It is necessary to perform preheating of sheets before welding in order to create a reliable welded joint. Nevertheless, welding was performed without preheating, in order to avoid the effect of heat treatment on hardness values.

Analysis of parameters that greatly influence the selection of the welding procedure (weldability of the material, energetic possibilities of welding procedures, geometrical complexity, economic indicators) enabled the determination of the most adequate procedure – 111 and filler material - E 51 5B 262 (electrode diameter  $d_e = 3.25$  mm), with welding parameters  $I = 130A$ ,  $U = 25V$ , direct current (=), polarity (+), idle voltage of 70 V in all welding positions, except when welding vertically downwards.

Tensile and hardness testing have been performed on  $250 \times 10 \times 5$  (20) mm specimens with a butt weld, Fig. 3, while the hardness testing has been performed on  $200 \times 90 \times 10$  mm specimen with a cruciform welded joint, Fig. 4. Plate with the butt joint and dimensions of samples which were used for the fabrication of specimens, depending on the type of testing, are presented in Fig. 5. Tensile tests were performed on butt welds in case when  $d > B$  – axisymmetric deformation and when  $d \ll B$  – planar deformation, Fig. 3. Plate with the butt weld and dimensions of samples from which the specimens were taken, depending on type of testing, are presented in Fig. 5. On specimens taken from samples 1, 2 and 3 grooves with stress concentration  $\alpha_s \leq 2$  have been machined in the soft layer, while on specimens taken from samples 1', 2', 3' grooves were machined in the hard layer (width of specimens is 5 mm), according to Fig. 2 (details A and C). Notches have been machined in the soft layer of specimens taken from samples 4, 5 and 6 (width of samples is 20 mm). Hardness testing has been performed on sample no. 7, as presented in Fig. 3 (details A and C).

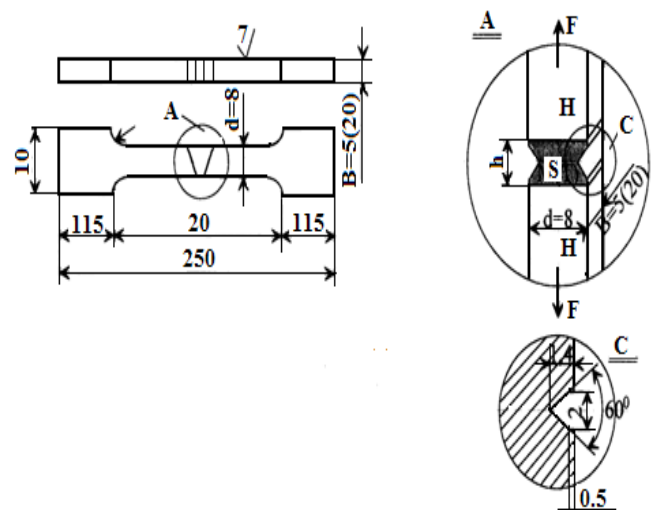


Figure 3: Specimens for tensile and hardness testing

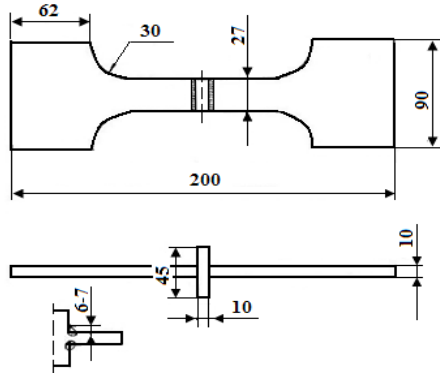


Figure 4: Specimen for hardness testing

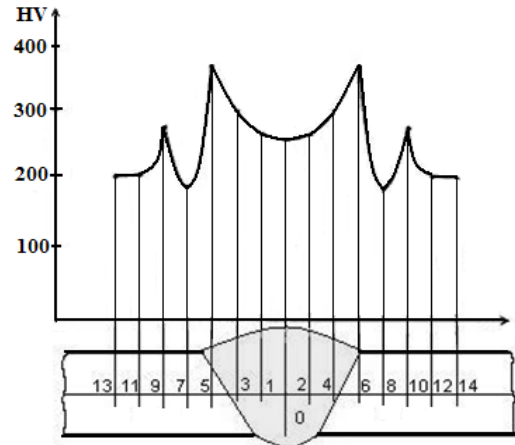
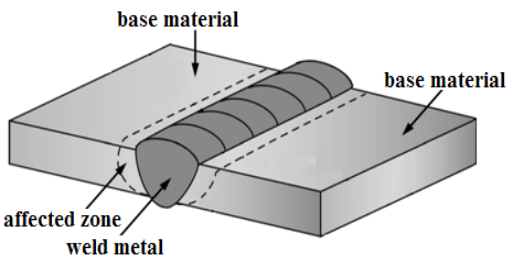
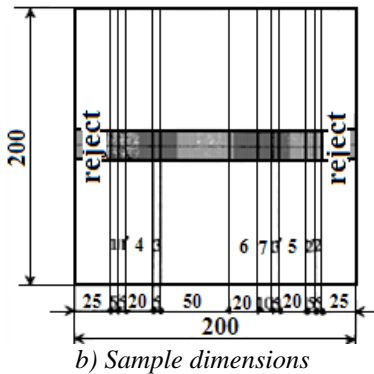


Figure 6: Hardness distribution diagram for the butt weld



a) Plate with the butt joint from which the samples were taken



b) Sample dimensions

Figure 5: Plate with the butt joint and dimensions of samples from which the specimens were taken depending on type of testing

#### 4. RESULTS AND DISCUSSION

Hardness results, according to Vickers HV10, are presented in Fig.6 and 7, while comparative tensile strength results for specimens 1, 2, 3 and 1', 2', 3' with notches in the soft and hard layer are presented in Table 1.

Hardness results for butt and fillet welds showed that highest values of hardness occur in transition zones between weld metal and the heat affected zone.

Analysis of fracture surfaces of specimens on which tensile strength tests were performed showed that the strength of the soft layer has a greater effect on static endurance of welded joints than the strength of the hard layer.

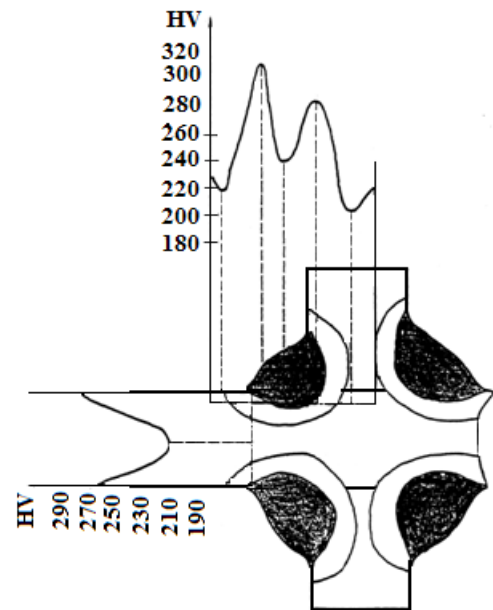


Figure 7: Hardness distribution diagram for the fillet weld

Table 1: Tensile strength results for specimens with a notch in the soft and hard layer

| Specimens   | Groove in the soft layer | 1   | 2   | 3   | Mean value |
|---|--------------------------|-----|-----|-----|------------|
|   | Groove in the hard layer | 1'  | 2'  | 3'  |            |
| Tensile strength for the axisymmetrical deformation $d > B$                         | Soft layer, UTS [MPa]    | 550 | 540 | 542 | 544        |
|   | Hard layer, UTS [MPa]    | 670 | 675 | 680 | 675        |
| Tensile strength of the soft layer for the planar deformation $d \ll B$ , UTS [MPa] |                          | 650 | 590 | 620 | 620        |

## 5. CONCLUSION

Lower hardness of the soft layer of the welded joint has a greater effect on tensile strength of the welded joint under conditions of static axisymmetrical loading. Also, based on performed tests, it can be concluded that deformation and strength of the welded joint under conditions of planar loading increase tensile strength under static load.

It can be generally concluded that the use of welded structures made of quenched and tempered steel C45 with hardness HV10 > 400 and tensile strength UTS > 600 MPa is purposeful only if the stress concentration is low ( $\alpha_s \leq 2$ ) and if there are no residual stresses due to welding.

## ACKNOWLEDGMENT

This work was supported by the Ministry of Education, Science and Technological Development of the Republic of Serbia (Contracts No. 451-03-9/2021-14/200012 and No. 451-03-9/2021-14/200108).

## REFERENCES

- [1] М.В. Шахматов, В.В. Ерофеев, "Напряженное состояние и прочность сварных соединений с переменными механическими свойствами металла мягкого участка," Сварочное производство, Vol. 3, pp. 6–7, (1982)
- [2] S.Kralj, B. Bauer, Z. Kožuh, "Laser welding of steels with higher carbon content," Proc. of 4<sup>th</sup> international conference EUROJOIN 4, Cavtat (Croatia), May, (2001)
- [3] E. Machedon Pisu, T. Machedon Pisu, "Experimental research on friction welding superalloys technique used vehicles," Metalurgia international, Vol. 15 (4), pp. 40-45, (2010)
- [4] J. Goldak, A. Chakravarti, M. Bibby, "A new finite element model for welding heat source," Metall. Trans. B, 15B, pp. 299–305, (1984).
- [5] D. Iordachescu, D. Lavric, "Contributions to increasing of 3 o'clock mechanized welding efficiency," The Annals of "Dunarea de Jos" University from Galati, Vol. XII, pp. 33-40, (1990)
- [6] D. Iordachescu, E. Constantin, V. Georgescu, M. Iordachescu, "Antigravity arc welding processes and the weld geometry," The Annals of "Dunarea de Jos" University of Galati, Vol. XII, pp. 15-18, (1999-2000)
- [7] О.А Бакши, Н.Л. Зајцев, Л.А. Вайсман, "Прочност на статическом растяжении сварных соединений с наружной трещиной в мягкой прослойке," Сварочное производство, Vol. 3, pp. 3–6, (1982)

# Project of Modernization of Laboratory Model of Two-girder Overhead Bridge Crane

Dragan Živanić<sup>1</sup>, Nikola Ilanković<sup>1\*</sup>, Atila Zelić<sup>1</sup>, Radomir Đokić<sup>1</sup>

<sup>1</sup>Faculty of Technical Sciences/Department of Mechanization and Design Engineering, University of Novi Sad, Novi Sad (R. Serbia)

*The document also contains defined quick-styles that may be used for fast formatting of the submitted papers. Overhead bridge cranes are intermittent transport devices that are exposed to dynamic loads during load transport. Experiments with cranes and their runways for dynamic phenomena requires great preparation and represents dangerous experiments. Therefore, according to the theory of similarity in mechanical engineering, it is possible to perform experiments on scaled laboratory models of cranes. The results obtained from such experiments are completely equal to the results obtained during the testing of real cranes. The topic of this paper is the project of modernization of the laboratory model of a two-girder overhead bridge crane from 1970, which is located in the laboratory of the Department of Mechanization and Design Engineering at the Faculty of Technical Sciences in Novi Sad. At the beginning, a brief history of the crane model is given and similar models used at other faculties are presented. Then the installed crane drives are shown - the drive of the bridge and trolley, as well as the lifting drive. The scheme of crane drive control is given. At the end, the design of the runway for the crane model is presented and its construction is shown.*

**Keywords:** Laboratory crane model, Crane drives, Crane runway

## 1. INTRODUCTION

Each phenomenon in technics can be viewed as a set of influencing factors, each of which participates in the course of the phenomenon with certain associations. If a construction is presented as a model in a certain scale, every phenomenon on that construction can be observed on the model, but it will also be in the scale of the model. In this way, the behavior of the construction due to the action of a phenomenon can be predicted. In other words, this is also called model testing.

Model testing is applied when it is impossible to perform the test in time or if there is an economic or technical advantage of testing on the model in relation to the actual construction. Testing time is much shorter and a much deeper understanding of the phenomenon is gained. The best examples of this can be found in aeronautics. In addition to numerous economic and technical requirements, aviation technology is characterized by a high risk to human life. Therefore, key tests are performed on prototype models of new aircraft. With today's advancement of computer technology, modelling technique still has its very important place in the development process.

The model technique should not be viewed competitively in relation to the computer technique, but both techniques should be viewed as mutually complementary. Sometimes it is impossible or very difficult to analytically describe a phenomenon on a computer without prior experimental testing on the model.

## 2. THEORY OF SIMILARITY

To study mechanical phenomena, numerous terms such as force, stress, deformation, weight, velocity, acceleration and frequency were introduced. These terms are derived from basic units: length, time and mass. In order for model testing to be used in the construction of a real machine, there must be some relationship between the

model and the original, or in other words the model and the original must be similar. The conditions of similarity are set by the theory of similarity and they are such that the differential equations of the problem for the original and the model coincide [1].

There are several types of similarities: geometric, kinematic, dynamic, static, thermodynamic, etc. [2].

### 2.1. Geometric Model Similarity

Two bodies (original and the downsized model) are similar if there is a relationship between their lengths  $L$  and  $L'$ :

$$\frac{L}{L'} = \lambda \quad (1)$$

where:

- scale coefficient –  $\lambda$ .

If  $A$  is a piece of the original body surface and  $A'$  is the corresponding body surface of the downsized model, then between those surfaces a relationship exists:

$$\frac{A}{A'} = \lambda^2 \quad (2)$$

This also stands for the relationship between corresponding volumes:

$$\frac{V}{V'} = \lambda^3 \quad (3)$$

If there is a correlation between the length, surface and volume of the original model in the form of:

$$f = (L_1, L_2, \dots, A_1, A_2, \dots, V_1, V_2, \dots) = 0 \quad (4)$$

there is the same correlation if a  $\lambda$  times smaller unit of length is taken into consideration:

$$f = (\lambda L_1', \lambda L_2', \lambda^2 A_1', \lambda^2 A_2', \lambda^3 V_1', \lambda^3 V_2', \dots) = 0 \quad (5)$$

Concerning (4), it implies:

$$f = (L_1', L_2', \dots, A_1', A_2', \dots, V_1', V_2', \dots) = 0 \quad (6)$$

which means that the same correlation can be applied to the downsized model.

## 2.2. Static Model Similarity

Concerning the Hooke's law, between forces which act on two geometrically similar bodies with elastic modulus  $E$ , a relationship can be established:

$$f = (\lambda L_1', \lambda L_2', \lambda^2 A_1', \lambda^2 A_2', \lambda^3 V_1', \lambda^3 V_2', \dots) = 0 \quad (7)$$

because the dilatation due to the geometric similarity is  $\frac{\epsilon'}{\epsilon} = \frac{\Delta l'/l'}{\Delta l/l} = 1$ .

## 2.3. General Remarks

The absolute similarity of the phenomenon requires that at all times in all appropriate points of space, process parameters and elements of one system must be proportional to the corresponding parameters of another system. When applying the theory of similarity in technical and physical tasks, they differ in terms of complete, incomplete or approximate similarity. In the case of complete similarity, there is a dependence of the corresponding parameters of the model and the original, which is expressed by the ratio coefficient  $\lambda$  and it is usually adopted as a constant, but in special cases it can be variable depending on mode, time or spatial coordinates. In the case of incomplete similarity, the changes in all basic parameters that characterize the studied phenomenon are partially similar (either only in time or only in space). In the case of approximate similarity, some factors that do not significantly affect the course of the phenomena are modelled approximately or not taken into account at all. This introduces an error that can be assessed in some way. This means that this similarity is related to some adopted or additional simplifications, which were assessed as possible on the basis of analytical or experimental tests.

## 2.4. Model Testing Methodology

In static testing of constructions, there are generally three concepts with differences in testing methods and objectives [3].

According to the first conception, the model serves as a computer. This means that model testing replaces complex static calculations of constructions, which change with many simplifications. The model is loaded so that it remains in the domain of elastic deformations. Based on that, the hypotheses on which the calculation is based can be evaluated. According to the second conception, the model should show everything that happens in the original model or can happen in nature. Therefore, the load can go beyond the calculation, i.e., individual parts of the downsized model can be loaded beyond the limit of proportionality, and even up to the failure of the construction. According to the third conception, model testing does not serve as a computer, but as a control of individual parameters that are obtained or uncertainly estimated by analytical method (size or sign of voltage, shape of elastic lines, etc.). Which concept will be applied depends on the problem being studied. In other words, the model testing methodology is adapted to the needs of the problem being tested. In any case, the downsized model must be made according to certain conditions in relation to the original model, and these conditions are dictated by the law of similarity - The events and states on the original model and the downsized model are physically similar if the influences acting on both causes relatively the same consequences on them [3].

## 2.5. Material for Model Creating and Modelling Scale Selection

Models can be made of materials other than the material of the actual construction and this depends on the phenomenon being studied on the model. Various metal materials can be used to make the model, such as steel, brass and aluminium.

When modelling metal constructions, it is most favourable to use the same type of metal on the model and the original, since they are approximately homogeneous and isotropic and behave approximately according to Hooke's law. The disadvantage of using metal models is the need to apply relatively high loads due to the high strength of the material, which can create difficulties in laboratory tests. Metal models often have problems related to the manufacturing technology, due to small sheets with thicknesses that can be below 1 mm. If technological similarity is required, welding in this case can be difficult. In such situations, the use of aluminium can be considered because at relatively lower loads, sufficient deformations can be obtained for measurement. The use of brass, which has twice the modulus of elasticity of steel, can also be considered, so the same deformations can be obtained with a lower load, and in addition, brass is easier to process.

The use of plastic materials for model making can be applied when the loads are not examined on the model, but the influence of the shape of the model on the manifestation of a certain phenomenon is examined. When considering any material, however, its specific weight should also be taken into account. It is possible to add mass in the form of weights in precisely defined places in order to simulate a higher specific weight.

The scale in the case of the application of metal models usually ranges from 1:5 to 1:15, while in the case of the application of plastic materials it ranges from 1:100 to 1:25 [4].

## 3. THE ANALYSED MODEL OF TWO-GIRDER OVERHEAD BRIDGE CRANE

The laboratory model of two-girder overhead bridge crane was primarily intended for static testing. The development of this model and the procedure of its testing are discussed in [4]. The model was made in the scale of 1:10, based on the existing real bridge crane located in the Bajina Basta Hydroelectric Power Plant. The original version of the model was not equipped with electric motor drives, figure 1.



Figure 1: Authentic photograph of the bridge crane model

Based on figure 2, the following elements of the laboratory model of a two-girder bridge crane can be seen: 1 – crane bridge, 2 - trolley, 3 - test weight carrier, 4 - test weights and 5 - stand for static tests. On the static test stand, there is a rail track segment on which the crane rests over four wheels. In its original state, the crane could move only a few centimetres along the segment of the rail track. The trolley could move freely on the bridge on both sides. Test weights could be hung on the trolley via a bar carrier as a free-hanging load. By moving the trolley, it was possible to examine the load of the supporting structure along the entire length of the bridge.

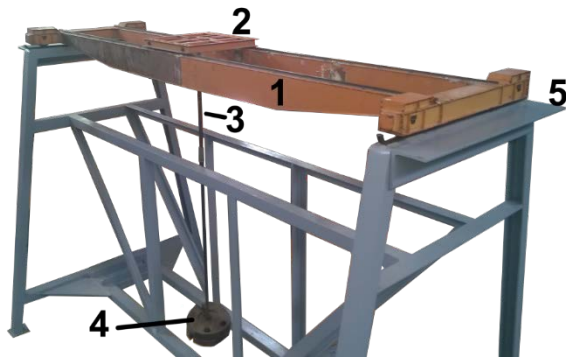


Figure 2: Basic elements of the laboratory model of a two-girder bridge crane

Figure 3 shows the components of the two-girder bridge crane model. The crane bridge consists of two main girders (2) and two side girders (1) which are interconnected by a screw connection, while the elements of the supporting construction are obtained by soldering steel sheets. The screw connection is made with miniature screws M 1.8x0.35 5 mm long. In this way, an exceptional similarity with the actual construction was achieved, and thanks to that, much greater accuracy of all calculations of the supporting structure was obtained.



Figure 3: Components of the laboratory model of a two-girder bridge crane

Two papers have dealt with different topics related to this bridge crane model so far. The first paper [4] included the following:

- Analysis of the occurrence of dynamic load in bridge cranes;
- Review of methods for calculating the dynamic load of constructions;
- Review of methods for determining the stress state by model testing;
- Calculation of stress under dynamic load of the bridge crane;
- Determination of stress using model testing on a bridge crane model;
- Analysis of the conformity of the results of the model test with the existing test data of the actual construction of the bridge crane.

Within the paper [4], the development of drive mechanisms for the movement of the crane model is

proposed, because in that way the kinematic similarity of the model with the actual construction could be achieved.

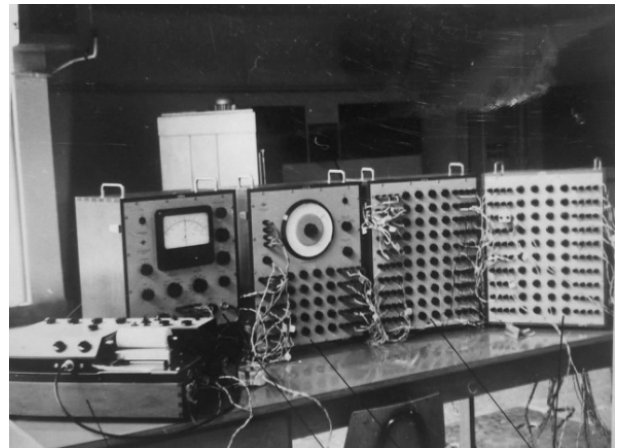


Figure 4: Authentic photograph of crane model testing instruments [4]

Another paper [5] dealing with this model of a bridge crane included the determination of the stress-strain state by calculation and experiment. An overview of procedures and procedures for the analysis of stress-strain state required for the design and dimensioning of a bridge crane was given. A comparative analysis of experimental and computational results was also given.

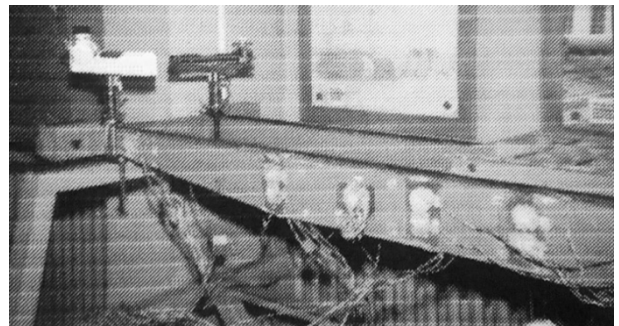


Figure 5: Authentic photograph of determination of stress-strain state of laboratory model of bridge crane [5]

#### 4. EXISTING MODELS IN THE WORLD

In the meantime, from the preparation of the paper [4] to the preparation of this paper, various models of bridge cranes have appeared in the world literature, some of which are presented below.

##### 4.1. University of Technology in Tallinn, Estonia



Figure 6: Model of the bridge crane of the University of Technology in Tallinn [6]

A paper [6] from the University of Technology in Tallinn describes how to operate bridge cranes without the use of sensors. For these needs, a laboratory model of a bridge crane was made, figure 6. The disadvantage of this work is the construction of the bridge crane, which does not correspond to actual crane constructions because the control of the crane is greatly influenced by the dynamic loads from the inertia of the moving parts.

#### 4.2. Yantai University of China and Chinese Academy of Sciences

The paper [7] describes the mathematical approach of bridge crane control where a prototype model of a bridge crane for the application of the mentioned control was made for that purpose, figure 7.



Figure 7: Model of a bridge crane of Yantai University of China and Chinese Academy of Sciences [7]

The disadvantage of this bridge crane model is also the construction that does not correspond to the actual crane constructions. The model is more reminiscent of a CNC (Computer Numerically Controlled) machine tool.

#### 4.3. Busan National University, South Korea

The paper [8] describes the adaptive control scheme of container cranes. A laboratory model was developed to test the described control method, figure 8. The disadvantage of this model is the same as in the previous examples, a construction that does not correspond to the actual crane construction.

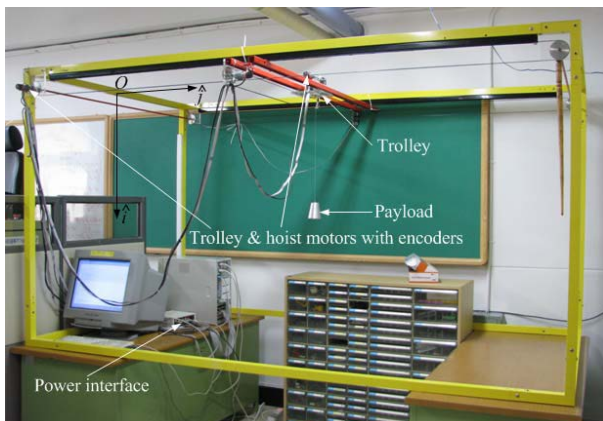


Figure 8: Container crane model of Pusan National University [8]

#### 4.4. Kranbau Köthen, Germany

Kranbau Köthen from Germany is one of the top crane manufacturers in the world. They manufacture special, process and automated cranes. For marketing

purposes, they made an identical model of a bridge crane for transporting foundry pots. The crane on which the model is made has a total weight of 450 t. The model that can be seen in figure 9 is made similarly to the smallest details. It moves on a segment of the track with its own drive and is controlled by wireless commands.



Figure 9: Model of a foundry bridge crane [9]

This is one of the best examples in the world when it comes to bridge crane models. The exact parameters of the crane drive and calculations related to this model or its actual construction are not known, so conclusions can be made only on the basis of photographs and a short report on the manufacturer's website [9].

#### 4.5. Cukurova University, Turkey

Figure 10 shows a laboratory model of the crane support structure intended for testing control and safety systems to prevent side effects during crane operation in order to increase the performance of the crane operator as well as greater safety in the crane operating area [10]. Also, the flaw of the model is the fact that does not correspond to actual crane designs.

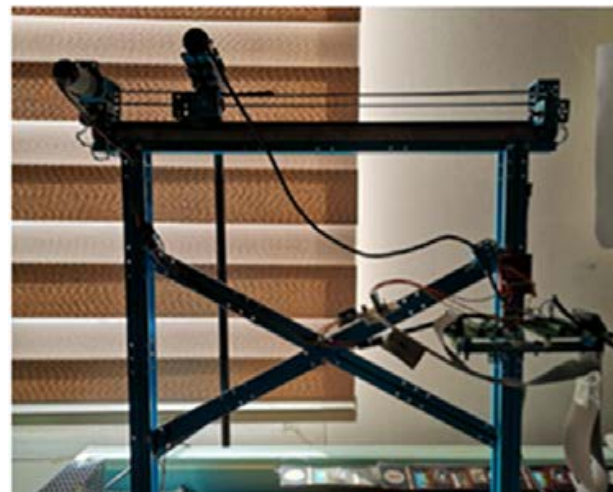


Figure 10: Model of the crane support structure [10]

#### 4.6. Pavia University, Italy

Figure 11 shows a model of the supporting structure with a crane bridge for testing saturation zones and dead zones at the actuator [11]. The flaw is the fact that the crane bridge does not have its own drive mechanism, it is driven by a belt system.

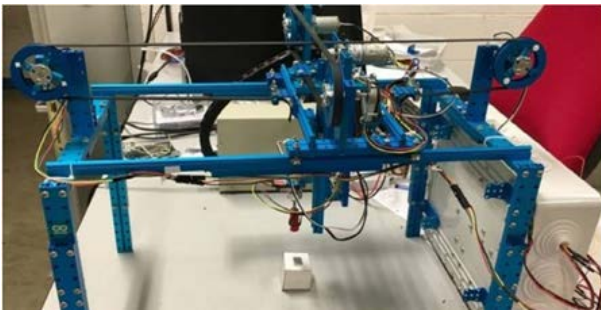


Figure 11: Model of a crane bridge for actuator testing

### 5. THE DRIVE MECHANISM OF THE CRANE MODEL

For practical reasons, a DC electric motor was chosen. A large number of different DC electric motors types are available, and two basic types will be compared.

#### 5.1. DC electric motors with brushes

These DC motors are characterized by internal commutation via graphite brushes. The disadvantage of this type of motor is the need for a reducer on the motor output shaft in order to increase the torque and reduce the rotational speed. In addition, graphite brushes wear out, which shortens the lifespan.

Electric motors with reducers (with multistage gear or planetary gearbox) are extremely expensive, so the available electric motors with a built-in worm gearbox are chosen, figure 13. The worm gearbox is self-braking, but self-braking is an advantage in this case because it is not necessary to install a mechanical brake in the drive mechanism.

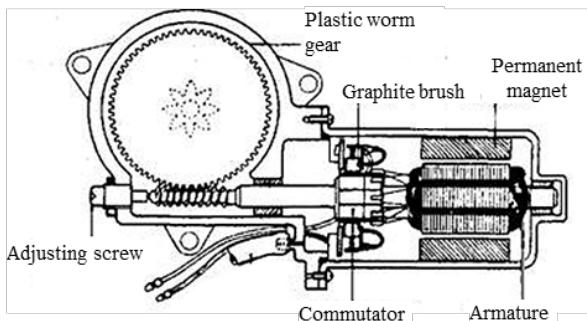


Figure 13: Cross section of DC motor with graphite brushes and worm gear [12]

#### 5.2. DC electric motors with brushes

This type of Brushless DC motor is characterized by electronic commutation, figure 15, most often performed by inverters, in the case of robotics and hobby modelling via ESC (Electronic Speed Controller), figure 14. The advantages of this type of electric motor are higher power per unit mass, and it is also geometrically more suitable for the bridge crane model. The disadvantage of using this type of DC motor is the high cost of the electric motor itself and its controller. Also, a disadvantage in the use of ESC is the limited possibility of adjusting the parameters of the electric motor such as acceleration and deceleration. The controller itself does not provide the ability to connect to another microcontroller. However, ESC as such is quite sufficient for the needs of hobby modelling.

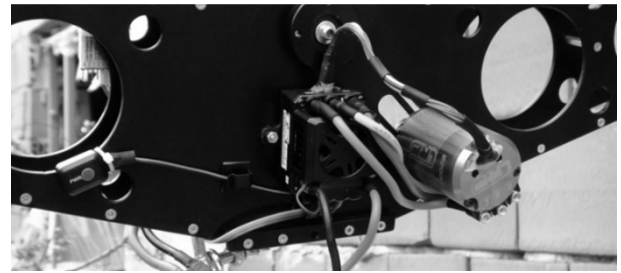


Figure 14: Example of DC motor with electronic commutation and control (black box) for driving the movement of a film camera on a rope

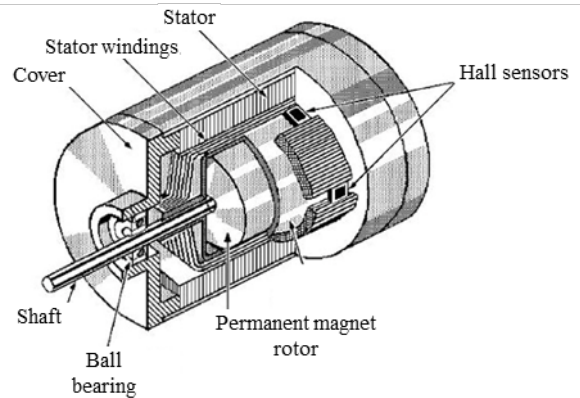


Figure 15: Cross section of DC motor with electronic commutation [13]

#### 5.3. DC electric motors with brushes

Based on the previously presented examples of DC electric motors, a DC motor with a built-in worm gearbox was chosen, figure 16. This selection satisfies economic conditions, but also technical conditions from the aspect of drive control. The chosen electric motor has rated voltage of 12 V, rated current 2.5 A and rated power 30 W. This electric motor also has 2 speeds, one of 60 min<sup>-1</sup> and one of 40 min<sup>-1</sup>. The weight of the electric motor with the reducer is 1.3 kg. The gear ratio of the worm gearbox is 50. As a reminder, a total of two electric motors are used to drive both sides of the bridge crane.



Figure 16: Selected DC motor with worm gearbox

During the work on the drive mechanism of the bridge crane, restoration was done by removing corrosion and applying new paint layers on the model construction. In free wheels of the crane, bearings were placed in order to reduce resistance during crane movement.

The model of the bridge crane with built-in electric motor drives and movement mechanisms, after the restoration of crane model, is shown in figure 17. The electric motor supports are connected to side girders of the crane via a screw connection on the upper side of side girders. The connection was made with the help of two M6 screws, 5 mm long, on both sides of the girders.



Figure 17: Restored model of a bridge crane with a built-in electric drive

The speed of rotation of the DC motor depends on the interaction of two magnetic fields in the motor, one field is inside the stator whose source is permanent magnets, and the other field is electromagnetic, inside the rotor armature, which is obtained by establishing current in the motor, figure 18. If this interaction of magnetic fields is controlled, the speed of rotation of the motor can also be controlled. Since the stator magnetic field is permanent, only the electromagnetic field in the rotor armatures can be controlled. If the strength of the electromagnetic field is changed by regulating the flow of current through the rotor windings, more or less magnetic flux will be produced, which results in a stronger or weaker interaction between the magnetic and electromagnetic fields. This results in a higher or lower motor speed.

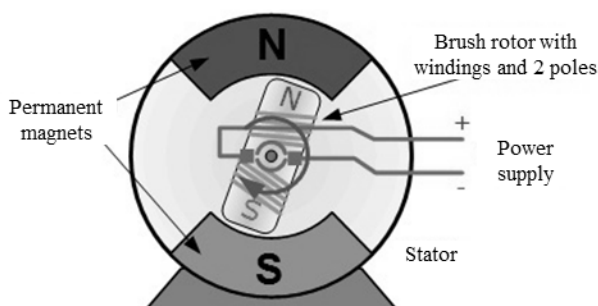


Figure 18: Working principle of DC motor with graphite brushes [13]

#### 5.4. The control unit of the DC motor

A typical way of DC motor control is the application of PWM (Pulse Width Modulation) control, i.e., pulse-width modulation of the motor power supply.

In other words, the voltage level at the motor input is regulated. Therefore, pulse-width modulation switches the electric motor on and off in pulses with a constant frequency. By changing the time between these pulses, the motor speed also changes. In electronics, this is achieved

by using transistors. A transistor-based driver was selected as a mediator between the motor and the microcontroller.

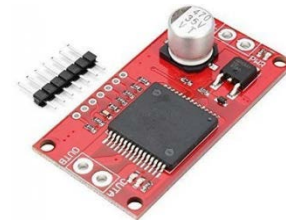


Figure 19: VNH2SP30 DC Motor Driver [14]

An electric motor controller with the following characteristics is used for the chosen electric motor, figure 19:

- Name: VNH2SP30 DC Motor Driver;
- Maximum voltage: 16 V;
- Maximum current: 30 A (at times);
- Continuous current: 14 A (with additional cooling);
- Continuous current: 6 A (without additional cooling);
- Maximum PWM frequency: 20 kHz;
- Overheat protection;
- Keeping the voltage within operating limits.

The microcontroller represents the so-called PLC (Programmable Logic Controller), which means that it can be programmed for a large number of different applications. It is used in industry wherever it is necessary to somehow control machines, production lines or collect certain measurement data. The microcontroller used in this case is the Arduino ATmega 2560 Rev. 3, figure 20.



Figure 20: Arduino ATmega 2560 Rev3 microcontroller [15]

The bridge crane model drive control scheme is given in Figure 21.

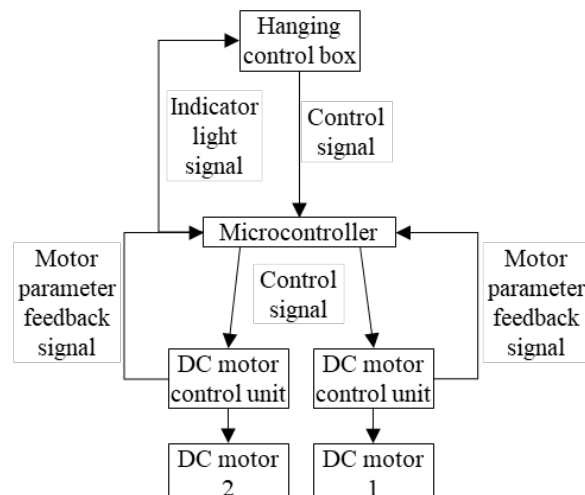


Figure 21: Block diagram of bridge crane model control

### 5.5. Hanging control box



Figure 22: Created control box and its 3D model

The hanging control box of the crane is made with 8 buttons and 2 signal lights, figure 22. The red light indicates whether a button is activated, and the green light indicates whether the electrical cabinet is on. Buttons are made in pairs to drive the bridge, trolley and the lift. The hanging control box was made on a 3D printer with FFF technology (Fused Filament Fabrication) using ABS plastic. A label with markings for each key is provided on the back of the control box.

### 6. THE DRIVE MECHANISM OF THE TROLLEY

Electric motors with worm gearboxes, which are used to drive the bridge, have a nominal voltage of 12VDC, power of 30W and a speed of rotation at the output of the gearbox of 60 min-1. Therefore, the current of an individual electric motor is approximately 2.5A. In the event of a shaft blockage, the current is approximately 10A. These electric motors can work in both directions of rotation. A total of two electric motors with a gear drive are used for the crane model and one electric motor with gear drive for the trolley. The difference in the electric motor for the trolley drive in relation to those for the crane drive is the constructive design of the housing, figure 23.



Figure 23: Electric motor with worm gearbox for trolley drive

The electric motor of the trolley drive is mounted perpendicular to the central shaft, Fig. 24. The worm gear

is made of plastic and is fixed to the shaft by means of a pin. The electric motor of the trolley drive is mounted for the construction of the trolley by means of a bearing plate 1.5 mm thick, on its lower side. The material of the supporting plate is steel S235JR, and the plate itself is painted. The plate is connected to the trolley construction by means of several M3 screws. A lifting drive mechanism is also mounted on this plate.

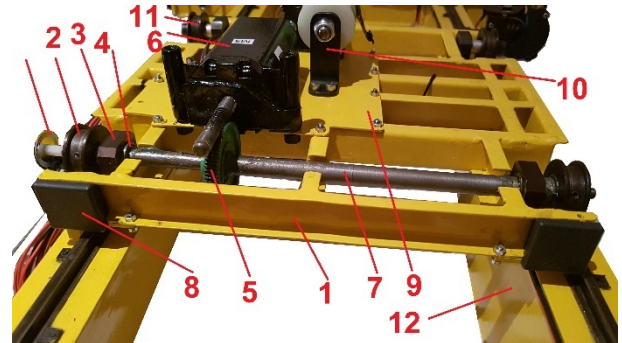


Figure 24: Assembled trolley drive mechanism (appearance of the trolley from the bottom)

Figure 24. shows the positions of elements of the drive mechanisms on the trolley: the supporting construction of the trolley (1), the drive wheel (2), the bearing housing (3), the bearing (4), the worm gear (5), the drive electric motor (6), the central drive shaft (7), bumper (8), support plate (9), lifting drive assembly (10), free wheel (11) and crane support construction (12).

### 7. LIFTING DRIVE MECHANISM

The lifting mechanism on this crane model is designed for lifting smaller and lighter, demonstration loads, figure 25. Therefore, this mechanism can be fitted into a compact form. The provided electric motor is made with a combination of worm and gear reducer, as a whole. To connect the output shaft of this gearbox to the rope pulley, it is necessary to use a gear pair with a gear ratio of 1: 1 in order to transfer the rotational movement to the pulley. The pulley is mounted on the shaft by means of two bearings. The pulley itself is designed with a coil at the beginning of which the end of the rope is fixed. Under the pulley, the installation of sliders for guiding the rope along the coil is planned.

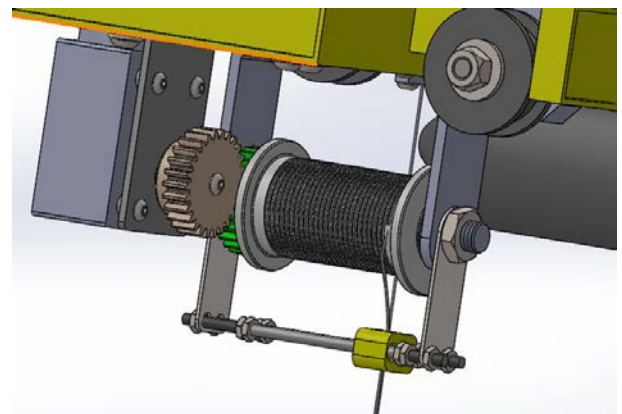


Figure 25: Final concept of the lifting drive mechanism

Figure 26. shows positions of the elements of the lifting drive mechanism: the supporting construction of the trolley (1), the driving electric motor of the trolley movement (2), the driving electric lifting motor with the

reducer (3), the driving gear of the electric motor (4), the driven gear pulley (6), self-locking nut (7), rope winding pulley (8) and the steel wire rope (9).

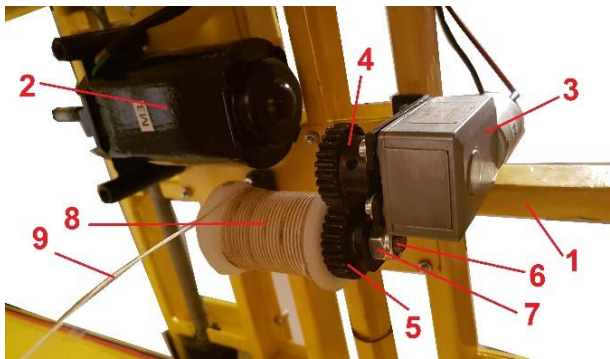


Figure 26: Mounted drive mechanism for lifting on the trolley

The electric motor for the lifting drive, figure 27, is made with a worm gearbox and gear ratio  $i = 588$ . The nominal voltage is 12VDC (6-15V), and the speed of rotation on the output shaft of the reducer at a nominal torque of 78 Ncm is  $10 \text{ min}^{-1}$ . The current without load is 35mA, and with load of 180mA. The torque blocking the motor is 314 Ncm and in that case the current is 1A.



Figure 27: Electric motor with worm gearbox for the lifting drive

8. ELECTRONICS ON THE CRANE MODEL

The layout of the electronics on the crane model is done according to figure 28. The markings are as followed: EO – electric cabinet, KI1-KI4 – bridge end switches, KI5-KI8 – trolley end switches, M1 and M2 – DC motors of the crane model, M3 – DC motor of the trolley, M4 – DC motor of the lifting mechanism, RE1 – rotary crane encoder, RE2 – rotary trolley encoder, SV – vibration sensor in the middle of the trolley, SU2 – acceleration sensor in the middle of the trolley and S - siren.

There are end switches at all four ends of the runway. There is a rotary encoder on one drive electric motor of the crane. Additionally, there are strain gauges on the bridge of the crane model for monitoring the stress in the supporting construction of the crane. A vibration and acceleration sensor are mounted on the trolley in the geometric center of the trolley, and a rotary encoder is located on the drive shaft of the trolley. The steel wire rope is tightened between the side girders of the bridge and allows free sliding of the trolley electric cables during the movement of the trolley. There is also a warning siren on the bridge. The end switches of the bridge are placed separately from the model crane, at the ends of the runway. These switches are mounted by means of support plates on the runway.

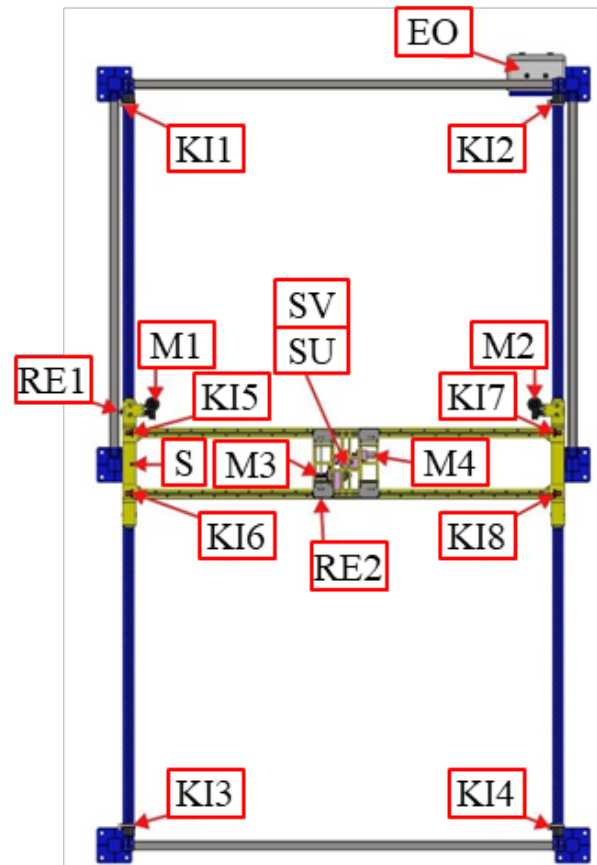


Figure 28: Positions of electronic components on the crane model and on the runway

9. CRANE MODEL CONTROL SCHEME

Figure 29 shows the crane control scheme with all important elements.

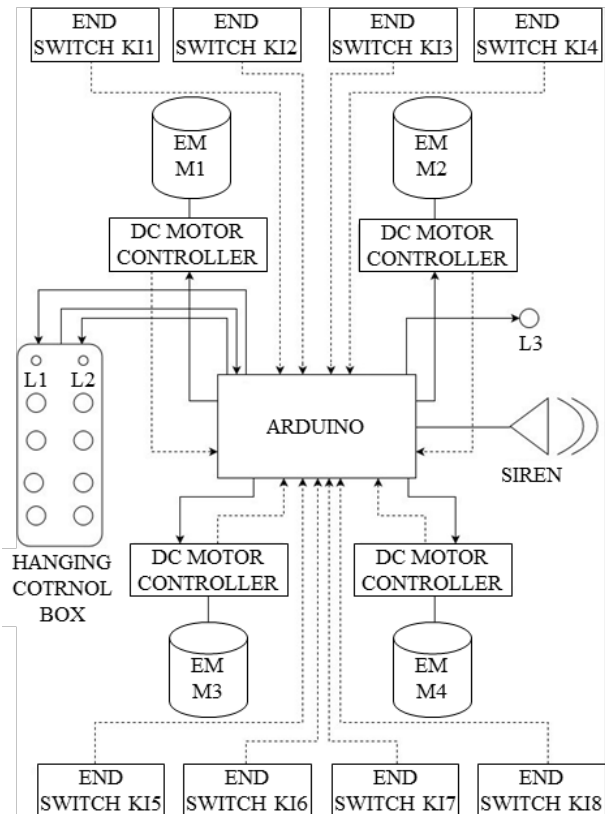


Figure 29: Crane model control scheme

## 10. DESIGN AND CONSTRUCTION OF THE RUNWAY

In order to complete the model of the two-girder bridge crane, the design and construction of the runway was done.

The basic parameters of the runway are:

- crane load capacity: 320 kg;
- runway span: 1,837 m;
- runway height: 1,4 m;
- runway length: 3,2 m;
- runway profile: IPE 80;
- material of used profiles: Steel S235.

The runway design was performed in Autodesk Inventor Professional software, the Dynamic Simulation module in the same software was used for dynamic analysis, while the Autodesk Inventor Nastran software was used for FEM analysis. The CAD model of the runway and crane is shown in figure 30.

It is important to note that the complete construction of the runway took place at the Faculty of Technical Sciences in Novi Sad - preparation of profiles, joining profiles with screw connections and MIG / MAG welding and final painting.

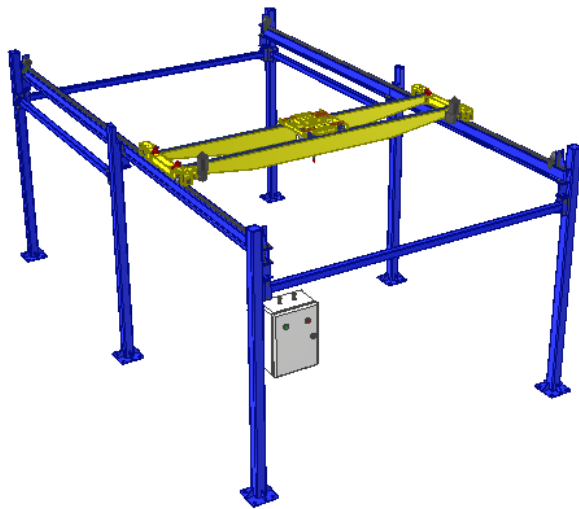


Figure 30: CAD model of the runway and crane

In the pictures that follow, it is possible to see the process of manufacturing and assembling of the runway.

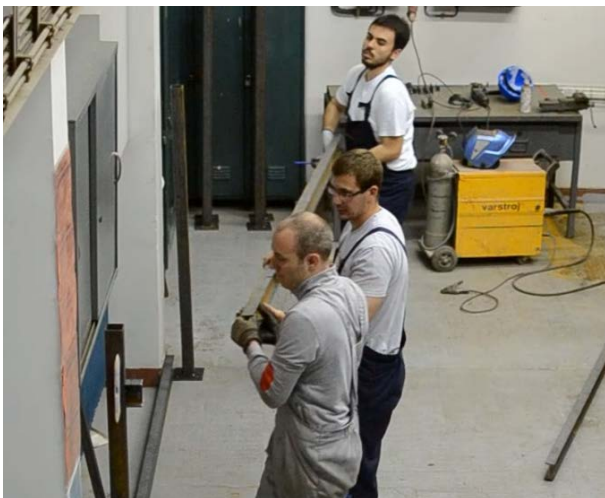


Figure 31: Assembling of IPE 80 profile on vertical columns



Figure 32: Welding of cross stiffeners



Figure 33: Precise mounting of the square rail



Figure 34: Welding of the square rail on the IPE 80 profile

Figure 35 shows the final appearance of the assembled runway and with the crane model on it in the Laboratory for Mechanical Structures, Transport and Construction Machinery, Chair of Machine Design, Transport Systems and Logistics, Department of Mechanization and Design Engineering, Faculty of Technical Sciences, University in Novi Sad, R. Serbia.



Figure 35: Final appearance of the runway with the crane model

## 11. CONSLUSION

The process of creating the model of a two-girder bridge crane began half a century ago with the idea whose main goal was to give future generations of students the opportunity to get acquainted with this type of transport machine through experiments with it and to acquire additional knowledge and skills they will need in the future.

The modernization of the crane model, which was realized by introducing electric drives for the crane, the trolley and lifting mechanism, led to bringing the 50-year-old teaching equipment to a modern level through a symbiosis of two sciences that were completely separate at the time when the model was created - mechanical engineering and electrical engineering. An example is given through which future generations of students can understand that a modern mechanical engineer must know the basics of electrical engineering and machine control in order to be successful in his career.

On the other hand, design and construction of the runway has shown that a good engineer must also possess practical skills in addition to theoretical knowledge. The use of design software, dynamic and static analysis software demonstrated the importance of the skill of using CAD software, while the construction of the runway emphasized the need for good practice of students during their studies in order to better prepare for the job waiting for them after graduation.

Finally, it is necessary to express the desire for further improvement of this teaching equipment so that half a century does not pass again until some next modernization.

## ACKNOWLEDGEMENTS

This research (paper) has been supported by the Ministry of Education, Science and Technological Development through project no. 451-03-9/2021-14/200156: "Innovative scientific and artistic research from the FTS (activity) domain".

## REFERENCES

- [1] R. Emori and D. Schuring, "Scale Models in Engineering - Fundamentals and Applications", Pergamon Press, Oxford (England), (1977)
- [2] D. Rašković, "Mehanika III Dinamika", Naučna knjiga, Beograd (R. Serbia), (1962)
- [3] M. Radojković, "Ispitivanje konstrukcija", Građevinski fakultet Univerziteta u Beogradu, Beograd (R. Serbia), (1974)
- [4] N. Babin, "Mogućnost određivanja ukupne nosivosti nosača mostovskog kрана na temelju modelskog ispitivanja, statičkim simuliranjem dinamičkog opterećenja", Master Thesis, University of Belgrade (R. Serbia), (1970)
- [5] A. Anđušić, "Računsko i eksperimentalno određivanje naponsko-deformacijskog stanja na modelu laboratorijske mosne dizalice", Bachelor Thesis, University of Novi Sad (R. Serbia), (1997)
- [6] A. Aksjonov, V. Vodovozov and E. Petlenkov, "Sensorless control of the three-dimensional crane using the Euler-Lagrange approach with a built-in state-space model", Proceedings of 56th International Scientific Conference on Power and Electrical Engineering of Riga Technical University (RTUCON), Riga (Latvia), pp. 1-4, DOI: 10.1109/RTUCON.2015.7343138, (2015)
- [7] D. Liu, J. Yi, D. Zhao and W. Wang, "Swing-free transporting of two-dimensional overhead crane using sliding mode fuzzy control" Proceedings of the 2004 American Control Conference, Boston (USA), pp. 1764-1769, DOI: 10.23919/ACC.2004.1386835, (2004)
- [8] Q. C. Nguyen, H. Q. Le and K. Hong, "Improving control performance of a container crane using adaptive friction compensation", Proceedings of the 14th International Conference on Control, Automation and Systems (ICCAS 2014), Gyeonggi-do, (S. Korea), pp. 157-162, DOI: 10.1109/ICCAS.2014.6987978, (2014)
- [9] <https://www.kranbau.de/de/pressemitteilungen/24-presse-media/pressearchiv-2016/126-abschlussbericht-kranbau-koethen-auf-der-cemat-2016>
- [10] S. Beller and H. Yavuz, "Crane automation and mechanical damping methods" AEJ - Alexandria Engineering Journal. Vol. 60(3), pp. 3275–3293, DOI: 10.1016/j.aej.2021.01.048, (2021)
- [11] G. Galuppini, L. Magni and D. M. Raimondo, "Model predictive control of systems with deadzone and saturation", Control Engineering Practice, Vol. 78, pp. 56-64, DOI: 10.1016/j.conengprac.2018.06.-010, (2018)
- [12] <http://what-when-how.com>
- [13] <http://emadrlc.blogspot.com>
- [14] [www.polulu.com](http://www.polulu.com)
- [15] [www.arduino.cc](http://www.arduino.cc)

## Basis for the Design of Drive-In and Drive-Through Racking

Rodoljub Vujanac<sup>1\*</sup>, Nenad Miloradović, Pavle Živković, Luka Petrović<sup>2</sup>

<sup>1</sup>Faculty of Engineering/Mechanical Construction and Mechanization, University of Kragujevac, Kragujevac (Serbia)

<sup>2</sup>Faculty Engineering/Mechanical Construction and Mechanization, University of Kragujevac, Kragujevac (Serbia)

*Drive-in and drive-through accumulation racking systems are recommended for great amounts of goods with few various units. According to the "First In, Last Out" - FILO and "First-In, First-Out" - FIFO principle, the palletized load unit are stored into deep tunnels accessible by forklift trucks for handling operations. This allows exploiting as much room as possible and eliminating the aisles traditionally required for manipulating purposes. This paper provides basic information on the requirements, design and use of drive-in an Improvement of casting technology of continuous tracks segment using CAD/CAE/CAM software tools d drive-through racking systems in accordance with current regulations and standards. Minimum required clearances and tolerances due to all influencing parameters for manually operated systems are discussed.*

**Keywords:** Pallet racking, Drive-In, Drive-Through, Regulation, Standard

### 1. INTRODUCTION

Within the most popular adjustable pallet racking configuration each pallet is accessible from an operating aisle. Conventional pallet racking tunnels systems connected in the block with loadable aisles are static accumulation system recommended for great amounts of goods with only few various units [1]. The main principle of this racks structure is to store pallets on deep rail beams, one after the other. The forklift truck drives into the rack aisle to position and reposition the pallet units. According to the "First-In, Last-Out" - FILO or "First-In, First-Out" - FIFO principle there are two types of the rack configuration as shown on the layout in Fig. 1; Drive-In Rack (DIR) and Drive-Through Rack (DTR) [2]. DIR and/or DTR racks are systems of racking that provide blocks of storage where pallets are stored two or more deep and where access is gained by driving a forklift truck into a lane with pallets supported along their sides on beam rails supported from the uprights. In DIR system which provides FILO principle of functioning, the forklift truck drives into a lane and reverse out, allows loading and unloading from the same face of the rack structure. This method for storage products does not require monitoring of deadlines and therefore not necessarily the first pallet stored is the first taken. DTR system is very similar to DIR actually identical in the structure, but in functioning the forklift truck could drive through the line if there are no pallets in the line. DTR configuration which follows FIFO method for storage is mainly used in food and pharmaceuticals field. This method of storage allows loading of pallets from a front storage system and the discharge from the opposite side. For both types racking configuration can be typically four pallets in height, minimum two but usually three or more pallets in depth (recommended up to seven due to monitoring) and can be numerous bays wide. Drive-in & drive-through racking can store up to 75% more pallets in the same space than adjustable racking - depending on the application [3]. The aim of this paper is to specify the basic on the requirements, design and use of drive-in and drive-through

racking systems in accordance with current FEM regulations and EN standards.

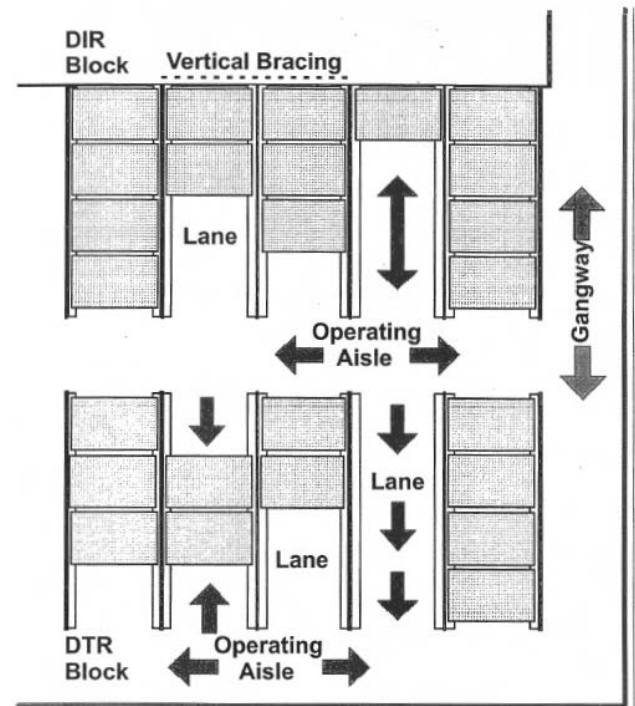


Figure 1: Layout of a Drive-In / Drive-Through Rack [2]

### 2. RACK CONFIGURATION

A typical DIR or DTR configuration is shown in Fig. 2 and Fig. 3. Both systems can be braced or unbraced. The upright frames (1) and/or mono post (2) connected with top-tie beams (3) form a basic spatial structure of the bloc of tunnels, i.e. group of interconnected lanes. The lane shown in Fig. 1 is the space between adjacent rows of uprights, perpendicular to the operating aisle shown in Fig. 1 too, allowing the forklift truck to enter the space and to pick and deposit unit loads (4) in depth and height. Spacer (5) is structural component joining a mono-post or upright frames with another upright frame in the down-line direction. Unit load, i.e. individual loaded pallet lies on the beam rails (6). Bracket (7) is an element with hooks which

engage in holes or slots in the upright and supporting the beam rail and connecting it to the upright. Sometimes the beam rail may be bolted directly to the upright. Vertical bracing (8) as bracing structure in the vertical plane provides the rack stability in cross-line direction. Plane bracing (9) as top horizontal bracing structure provide down-line stability. In the down-line direction upright frame bracing (10) provides stability too. For an unbraced structure the cross-line stability is provided by the restraining effect of the top-tie beam to upright connection and of the upright to floor-tie connection. Ground rails (11) fixed to the ground or directly to the uprights provides visual and mechanical guidance to help the operator to centre the forklift truck at the lane entry. Pallet entry guides (12) are elements positioned in front of each beam rail to help the operator to centre the unit load at the lane entry. Rear pallet stopper (13) mechanically prevents falling of the unit load at the end of line. Upright protector (14) is usually integral part of the baseplate on the entry uprights.

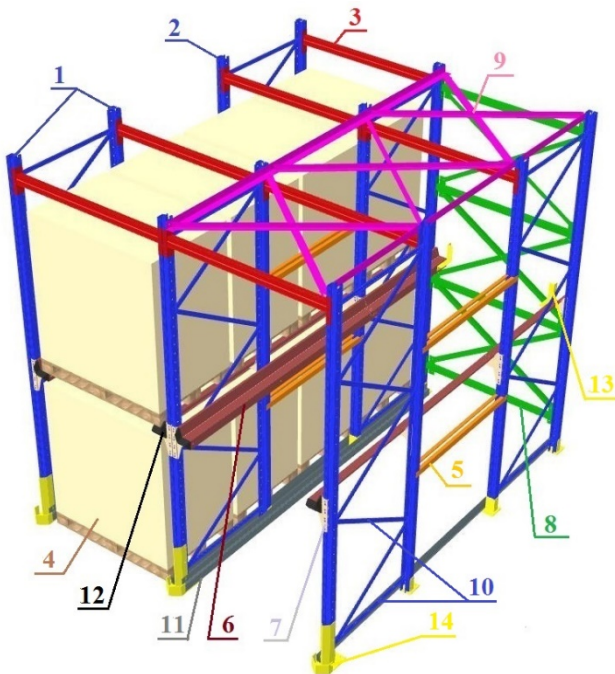


Figure 2: Drive-in rack configuration without bracing tunnel

In some unbraced configuration without vertical and plan bracing, especially for the DTR structures, extra stability of the system is provided by the "blind line" (15) where storage is prevented as shown in Fig. 3. In that case system must have at least one bracing tunnel [4]. The minimum width of the bracing tower should be:

$$I_c = H / 10 \quad (1)$$

where is:

$I_c$  – bracing tunnel width, i.e. uprights distance;

$H$  – drive-through height.

The horizontal action  $T$  to be considered at the top to design the bracing is:

$$T = F_h / N \quad (2)$$

$$F_h = N_p \cdot N_l \cdot N_t \cdot P / 200 \quad (3)$$

$$N = 2 \cdot N_{sp} \cdot N_c \quad (4)$$

where is:

$F_h$  – total horizontal action at the top of the drive in;

$N$  – total amount of vertical bracing;

$N_p$  – number of levels (brackets) in height;

$N_l$  – number of pallets in depth;

$N_t$  – number of tunnels;

$P$  – maximum pallet weight;

$N_{sp}$  – number of frames in depth;

$N_c$  – number of bracing tunnels.

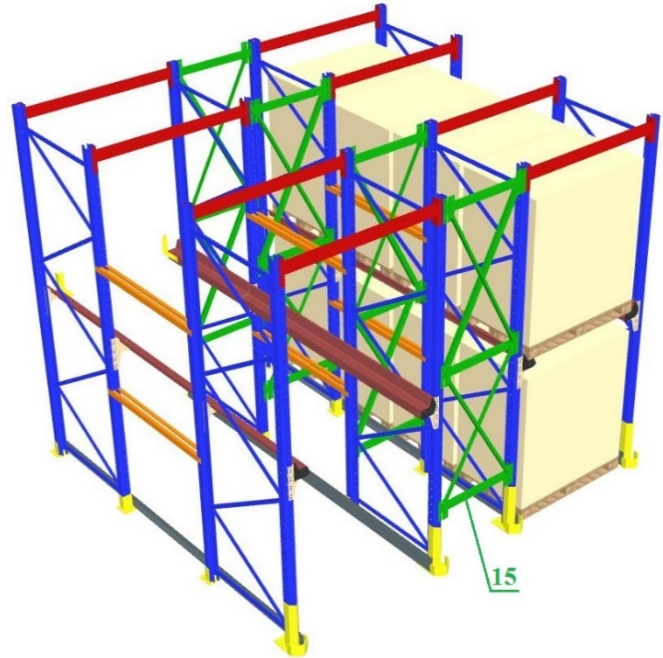


Figure 3: Drive-through rack configuration with bracing tunnel

### 3. PARAMETERS INFLUENCING THE MINIMUM REQUIRED CLEARANCES

Clearances are required to ensure safe operation condition in placing and picking by operators with the storage system environment concerned and with the intended manually operated mechanical equipment [2]. Parameters influencing the minimum required clearances are as following:

- Floor flatness;
- Rack production tolerance;
- Rack installation tolerance;
- Rack deformation.
- Pallet tolerance;
- Lift truck properties;

#### 3.1. Floor Flatness

For the system levels up to 6 m the floor flatness is not a critical parameter in the effective use of DIR or DTR provided that the floor flatness satisfies at least class FM3 according to EN 15620 [5] or DIN 182020 group 3 as an alternative. For the storage levels over 6 m the floor flatness should satisfy at least class FM3 according to EN 15620 or DIN 182020 group 4.

#### 3.2. Rack production and installation tolerances

Rack production and installation tolerances are given in Table 1 and shown in Fig. 4 [2].

Table 1: Tolerance limit values for the installed rack [2]

| Type of tolerance            | Description   | Limit value         |
|------------------------------|---|---------------------|
| <b>Horizontal tolerances</b> |   |                     |
| $\delta A_{TOP}$             | Maximum variation in width of individual lane (at top) (mm)                             | $\pm 1.5$           |
| $\delta A_{BOTTOM}$          | Maximum variation in width of individual lane (at bottom) (mm)                          | $\pm 5.0$           |
| $\delta A_T (n)$             | Total deviation in rack length cumulative at top or bottom (mm). n- number of lines     | $\pm 2.0 n$         |
| $\delta E$                   | Frame alignment in the down-line direction (measured separately at top and bottom) (mm) | $\pm 3.0$           |
| $C_z$                        | Maximum out-of-plumb upright in the cross-line direction                                | 1/500               |
| D                            | Rack depth (mm)   | $\pm 5.0$ per frame |
| $J_x, J_z$                   | Maximum bow imperfection of upright   | 1/1000              |
| $C_x$                        | Maximum out-of-plumb upright in the down-lane direction                                 | 1/500               |
| <b>Vertical tolerances</b>   |   |                     |
| L                            | Maximum deviation of bracket level with regard to the top of baseplate level (mm)       | $\pm H/250$         |
| M                            | Maximum deviation of pallet support level between both sides of the pallet (mm)         | 6.0                 |

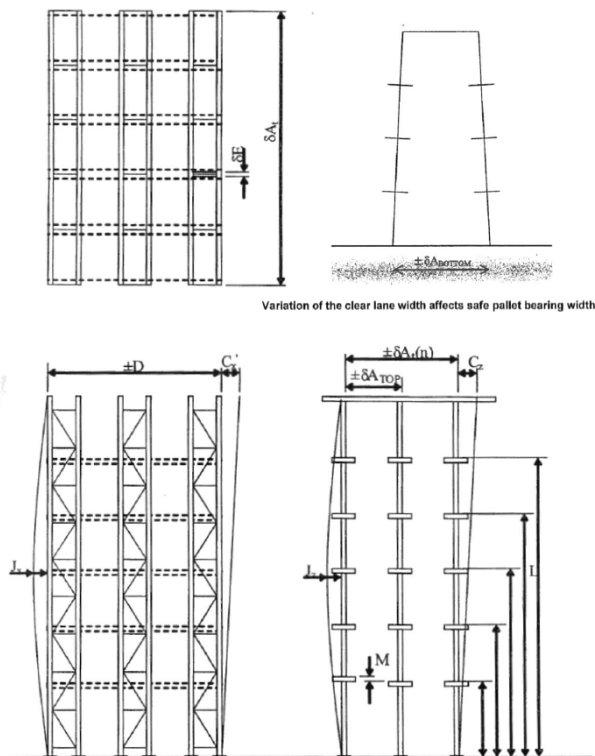


Figure 4: Relevant rack production and installation tolerances [2]

3.3. Rack deformations

The deformation limits and clearances are based on the operational method for placing pallets in DIR/DTR given in FEM 10.2.04 [6] and EN 15635 (2008) [7]. When a pallet is being placed into a drive-in rack, the following sequential loading activities take place as shown in Fig. 5 [6]:

- The fork lift truck drives with a pallet to the pallet storage location, Fig. 5 (a).
- The driver raises and manoeuvres the pallet into the racking lane, clear of the rack uprights, with the no forward tilt on the forks, at the required storage level and with the pallet load positioned centrally between the uprights, Fig. 5 (b).
- The truck is then driven forward to the set down position keeping the pallet and truck mast clear of contact with the beam rails or other parts of the drive-in rack structure, Fig. 5 (c).
- The driver lowers the pallet carefully onto the beam rails, releasing the load from the forks. Once in contact with the beam rails the pallet must not be slid or dragged along or across these supporting members.
- The driver takes the forks out of the pallet, reverses the truck carefully back out of the lane and then lowers the forks.

In DIR or DTR racking the sequence of placement of loads shown in Figure 6 (a) and 6 (b) should be followed [6-7]. On the input cycle the first pallet is placed at position 1 and the rack is loaded from the bottom upwards and from the back outwards. On the output cycle the procedure is the exact reverse, from the top down working in towards the back of the drive-in rack. Beam rails of DIR / DTR racking fitted with integral or non-integral sloping side guards should be loaded as shown in the sequence illustrated in Fig. 5.

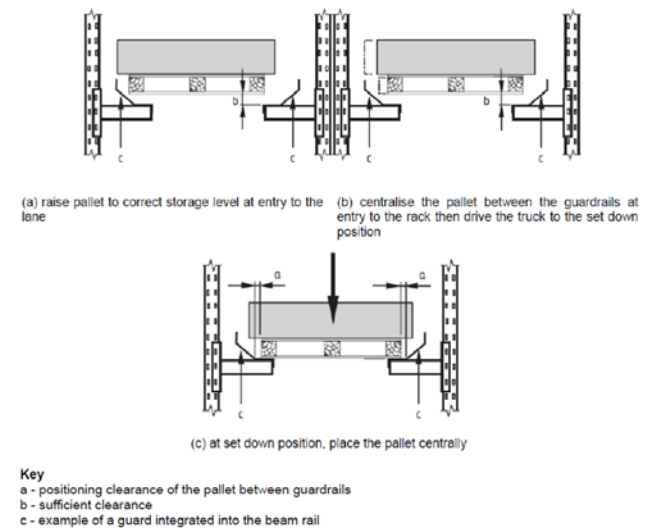


Figure 5: Correct sequence of loading for types of drive-in systems with guardrails [6-7]

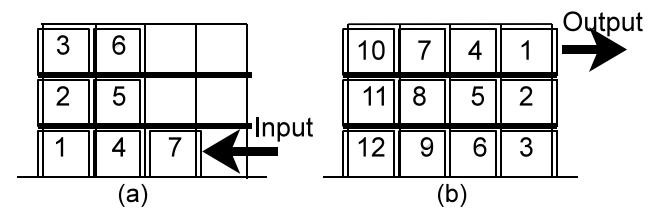


Figure 6: Loading (a) - Unloading (b) sequence for drive in racking [6-7]

The pallet shall be centralised between the selected lane uprights by first using the fork side shift, if

necessary, to centralise the pallet in relation to the truck mast and then by steering the truck before the pallet enters the lane. The racking structure is not designed to provide pallet or truck mast guidance. Therefore minimum safe bearing of pallet on rails must be foreseen as show in Fig. 7 [6].

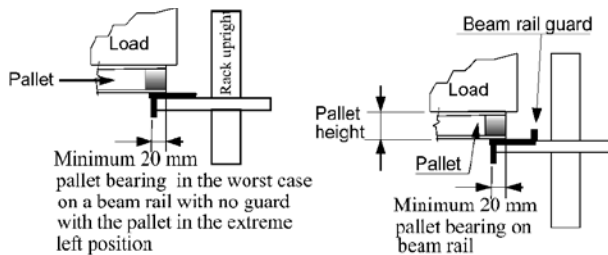


Figure 7: Minimum safe bearing of a pallet on DIR/DTR beam rails with the pallet in the extreme left position [6]

### 3.4. Pallet specification for DIR/DTR racking

The specification of pallets used in drive-in racking shall include for a quality of pallet that when loaded with the specified goods to be stored shall not deflect more than the *pallet span/100* when supported on the beam rails with a minimum bearing on one side of 20 mm, see Fig. 7. The pallet span is the nominal clear dimension between the beam rails. Timber pallet quality is extremely important for the safe operation of pallet racking and particularly drive-in racks. Weak pallets or damaged pallets (e.g., with broken bottom boards) should not be used neither should incorrect types of pallets. Advice on suitable pallet types can be obtained from prospective suppliers.

### 3.5. Lift truck properties

Lift truck shall be equipped with side-shift for operation at storage levels above 6 m [2]. This assists to correctly deposit the pallet on the pair of beam rails and it is recommended for all applications. Mast stiffness shall be in accordance with EN 15635 clause 8.7 [7]. The maximum lifting height shall be sufficient to allow driving down lane without touching the pallet rail. The lane width and detailing of the baseplate connection shall ensure that the lift truck can enter and drive in a lane adequate clearances. Relevant truck dimensions are given in Fig. 8 as following:

- 1 - Between the outer tyre edges;
- 2 - Overall width;
- 3a - Width of cabin (standard);
- 3b - Width of cabin (special for DIR / DTR);
- 4 - Width of lower mast (including and attached equipment);
- 5 - Width of middle mast (if any, and including any attached equipment);
- 6 - Width of upper mast (including any attached equipment);
- 7 - Ground clearance;
- 8 - Height of overhead guard (cabin);
- 9 - Height of lower mast;
- 10 - Height of middle mast;
- 11 - Lift height.

The speed at which the lift truck is driven in the rack storage lanes is critical to the safe operation of the

storage system [6]. To prevent the mast from flexing and swaying excessively on uneven floors and striking the beam-rails, the truck speed must be regulated by the driver to suit the floor flatness and the mast flexibility.

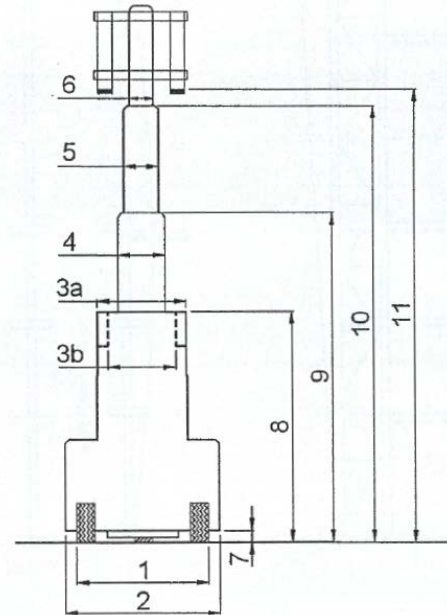


Figure 8: Relevant truck dimensions for the cross line direction [2]

## 4. CLEARANCES

The clearances detailed should be considered in relation to the overall measurements of the pallet and load (i.e. including any pallet load overhang) and the type of beam rail, with or without a pallet guide element [8]. With regard to the clearance consideration there are five potential critical positions as shown in Fig. 9 [2]:

- Pallet or truck body with respect to the baseplate, upright and floor rail (if present) (Item 1; clearances  $a_7$  and  $a_8$  in Fig. 10),
- Truck cabin in relation to the beam rail outer side (Item 2; clearance  $a_9$  in Fig. 10),
- Truck mast in relation to the beam rail (Item 3; clearance  $a_{10}$  in Fig. 10)
- Pallet edge with regards to the pallet beam rail guard, if any (Item 4; clearance  $\frac{1}{2} a_5$  in Fig. 11)
- Pallet load with regard to the upright (Item 5; clearance  $a_1$  in Fig. 11).

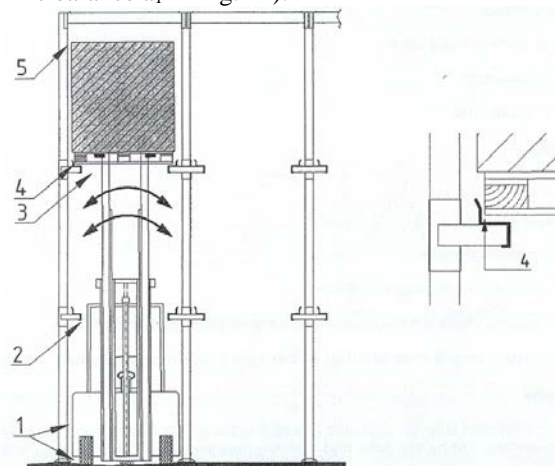


Figure 9: Relevant positions for the specification of minimum clearances [2]

The spacing between the sides of the pallet (including the pallet load) and the uprights should at least be in accordance with the following (see Fig. 11 (a), dimensions  $a_1$  and  $a_2$ ) [8]:

- High drive-in racks (top bracket level higher than about 5 m) and/or relatively high turnover, 100 mm;
- Other cases 75 mm.

The spacing between a pair of beam rails shown in Fig. 10,  $a_{11}$ , in a drive-in rack should be so chosen, that the bearing width, dimension  $a_6$  (see Fig. 11) of the pallet bearer on the beam rail is at least 20 mm [8].

Account must be taken of the most unfavourable placement of the pallet (pallet on one side against an upright or side guide rail) and the maximum lateral bowing deflection,  $\Delta a_{11}$ , of the uprights (see Fig. 11 (a) and (b) and the width tolerance,  $W_t$ , of the bay (see Fig. 12).

The spacing between the pallet load and the upright during placement of the pallet should be at least 45 mm (see Fig. 11, dimension  $a_3$ ) when the pallet is positioned 25 mm above the horizontal support surface of the beam rail.

The spacing between the side guide rail, when present, and the uprights should be at least 45 mm at the point of contact of the pallet and beam rail guide element when the pallet is positioned 25 mm above the horizontal support surface of the beam rail in Fig. 11, dimension  $a_4$ .

The spacing between the wheels of the fork lift truck and the side of the base plates should be at least 75 mm (see Fig. 10, dimensions  $a_7$ ).

The spacing between the wheels or body of the fork lift truck and the side of the uprights should be at least 75 mm (see Fig. 10, dimension  $a_8$ )

The following minimum clearance dimensions each side must be taken for the spacing between the fork lift truck and the side of the pallet beam rails.

- At the lowest bracket level, 75mm (see Fig. 10, dimension  $a_9$ );
- Other bracket levels, 100 mm (see Fig. 10, dimension  $a_{10}$ ).

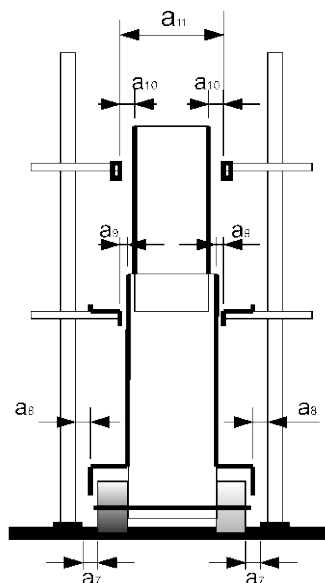


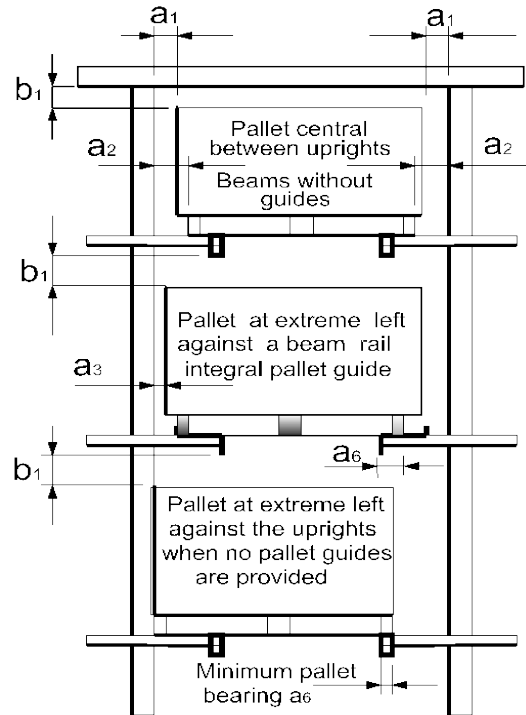
Figure 10: Truck aisle clearances and pallet rail spacing dimensions with respect to fork lift truck [8]

The spacing,  $a_5$ , between the pallet and a side guide rail should be at least 50 mm when the pallet is positioned 25 mm above the horizontal support surface of the beam rail and touching one of the guide rail elements, see Fig. 11(b).

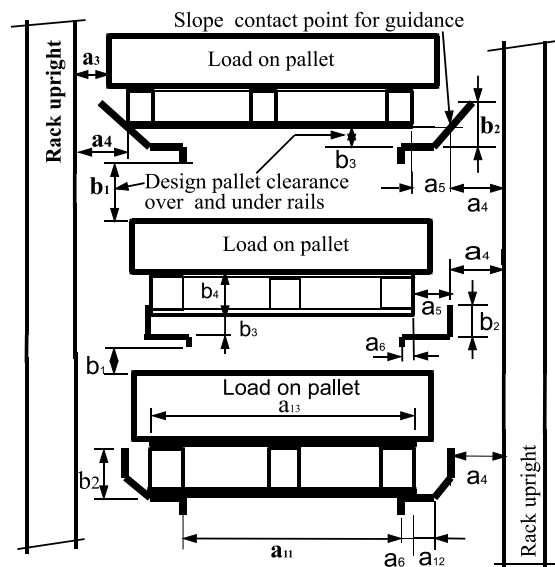
The spacing,  $b_1$ , between the top of the pallet load and bottom surface of the rack cantilever bracket or beam rail when the pallet is seated on the horizontal support surface of the beam rail, should be as for dimension  $Y_3$  for APR Class 400 [8].

The spacing between pallets in determining the overall rack bay depth should be at least 25 mm [8].

The pallet span  $a_{11}$  is the nominal clear dimension between the beam rails, see Fig. 10.

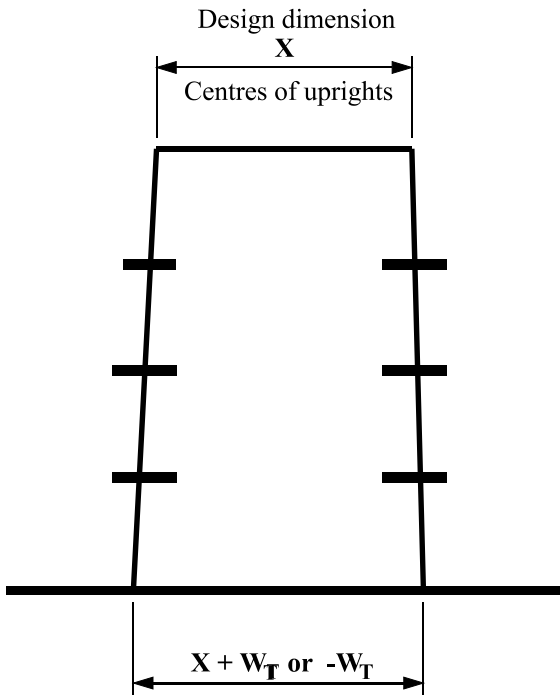


(a) Placement of pallets



(b) Beam rail guide details

Figure 11: Vertical and horizontal clearances for drive in racking with regard to the unit load [8]



$W_T$  = Erection tolerance  
 If  $W_T < +5 \text{ mm}$  then  $\Delta_T = 0$   
 If  $W_T > +5 \text{ mm}$  then  $\Delta_T = W_T$

Figure 12: Truck aisle clearances and pallet rail spacing dimensions with respect to erection tolerance [8]

For drive-in racks, the maximum lateral bending of the uprights as a consequence of pallets already in place should be considered. It is necessary to determine the sum of the bending deflections  $\Delta a$  of adjacent uprights towards each other, (dimension  $\Delta a$  according to the FEM recommendations in preparation for drive-in racks). This dimension  $\Delta a_{11}$  (see Fig. 13) can assume a value of up to  $\pm 30 \text{ mm}$ , depending upon the rack upright properties, overall height, bracket length and pallet load.

The width tolerance  $W_T$  between consecutive uprights together with  $\Delta a$  should also be considered in assessing the horizontal beam rail pallet support dimensions  $a_5$  and  $a_6$ .

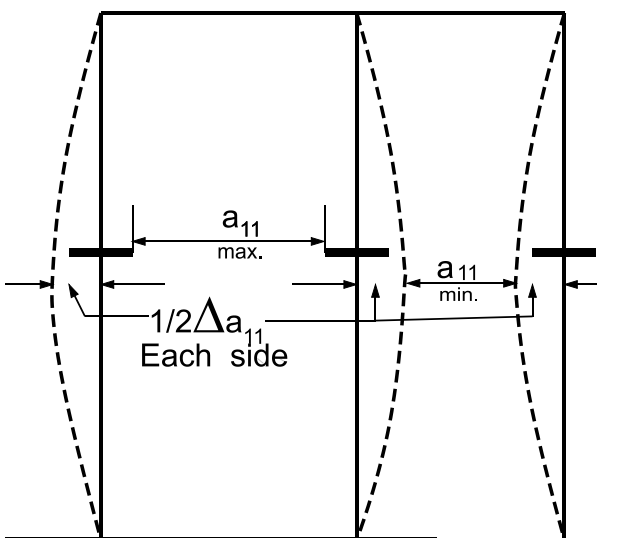


Fig 13: Measurement of upright bending deflection [8]

The minimum bearing of the pallet on the right hand rail with the pallet hard over to the left side is shown in Fig. 14 as 20 mm.

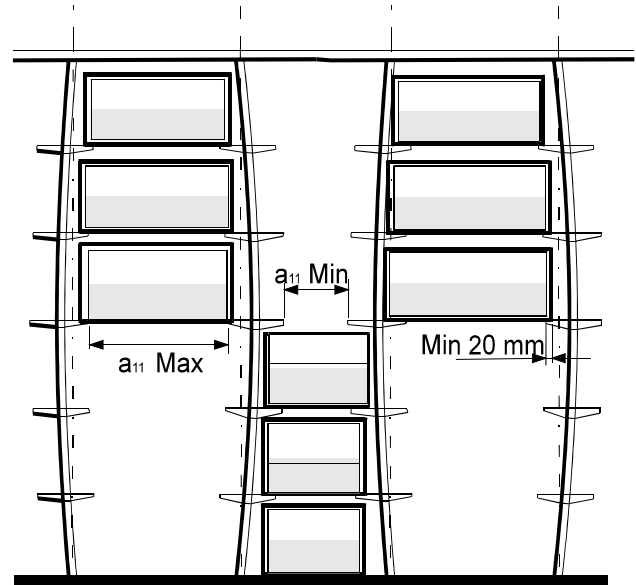


Figure 14: Uprights Lateral bending deflection [8]

5. CONCLUSIONS

Drive-in and or drive-through racking system is strongly represented high density storage solution especially in refrigerated chambers, food warehouses, water and drink manufacturers and distribution centres. The palletized load units usually are stored into deep tunnels accessible by forklift trucks for handling operations. This allows exploiting as much space as possible and eliminating the aisles traditionally required for service purposes in adjustable pallet racking configurations. The configuration chosen must be right for the realistic product movement through the warehouse. Firstly, adequate principle of functioning FIFO or FILO must be satisfied referring to the stored goods. Then, some logistic consideration must be taken into account because if the system is much too deep, or much too high, it will increase operating costs, because of the time required to take load from the storage, or to put load in the storage. This is simply because operation of a forklift truck within a rack system must be done carefully and relatively slowly in comparison to the lift trucks normal operating speed. After the proper configuration is selected, unit load characteristics determine the required design of the components used. Most common materials used in the rack structures are light cold-formed profiles or hot-rolled steel in standard structural shapes. At the end the functionality of DIR and/or DTR systems can be additionally improved with automatization of handling process where adequate systems can better achieve results instead of traditional fork lift truck. Introduction of radio shuttle as standard equipment and its improvement with shuttle carriage together with vertical reciprocating conveyors brings to the fully automatization of the system. Beside of faster handling thsi system allow further increases in productivity, reduced damages, improved safety and ergonomics.

## REFERENCES

- [1] R. Vujanac, "Razvoj metodologije za projektovanje i proračun nosećih elemenata skladišnih sistema", In Serbian, MSc Thesis, University of Kragujevac, (2007)
- [2] FEM 10.2.07, "Drive-in and Drive-Through Racking Drive-in Design Code", European Racking Federation. Hitchin (England), (2012)
- [3] R. Vujanac, R. Slavković and N. Miloradović, "Automatization of Multi-Depth High-Density Storage System," *Metalurgia International*, Vol. 18 (8), p. 49-55, (2013)
- [4] Dalmine Logistics Solutions, "DRIVE IN" Technical Manual, Piacenza, (2015)
- [5] EN 15620, "Steel static storage systems – Adjustable pallet racking – Tolerances, deformation and clearances", European Committee for Standardization. Brussels (Belgium), (2008)
- [6] FEM 10.2.04, "Guidelines for the Safe Use of Static Steel Racking and Shelving - User's Code", Fédération Européenne de la Manutention (FEM), Section X. Brussels (Belgium), (2000)
- [7] EN 15635, "Steel static storage systems - Application and maintenance of storage equipment", European Committee for Standardization. Brussels (Belgium), (2008)
- [8] FEM 10.2.03, "Guidelines for Specifier's of Static Steel Racking and Shelving - Specifier's Code", Fédération Européenne de la Manutention (FEM), Section X. Brussels (Belgium), (2000)



# Statistical Comparison of the Evaluation Process Results of Location Alternatives in Case of Flat and Hierarchy Structure of Criteria

Goran Marković<sup>1,\*</sup>, Cătălin Frâncu<sup>2</sup>, Mile Savković<sup>1</sup>, Nebojša B. Zdravković<sup>1</sup>, Radomir Đokić<sup>3</sup>, Marko Popović<sup>4</sup>

<sup>1</sup>Faculty of Mechanical and Civil Engineering in Kraljevo, University of Kragujevac, Kraljevo (Serbia)

<sup>2</sup>Faculty of Technological Equipment, Technical University of Civil Engineering, Bucharest, (Romania)

<sup>3</sup>Faculty of Technical Sciences, University of Novi Sad, Novi Sad (Serbia)

<sup>4</sup>Faculty of Technical Sciences Čačak, University of Kragujevac, Čačak (Serbia)

*The main directions in this research are focused mainly on the peculiarity and nature of the decision-making process. The desire is to develop and improve a multi-criteria approach to solve logistics and many real problems. The most common issues in the standard multi-criteria decision-making (MCDM) technique are obtaining criteria weights, the possibility to work with a large number of criteria and alternatives, and ranking and selecting the most desirable alternative. Generally, the produced ranks obtained by different techniques would have different levels of similarities. Kendall's tau-b was selected to analyse the similarities of the produced ranks by proposed approach in a case with a flat and hierarchy structure of criteria. The study demonstrates the robustness of the proposed approach by changing a criteria number and highlights the significance of sensitivity analysis in assessing the reliability of MCDM outcomes.*

**Keywords:** Decision-making, Logistics, Location, Criteria, Kendall's tau-b, Sensitivity analysis

## 1. INTRODUCTION

The location problems have an interdisciplinary character and could be solved with the application of complex procedures in the selection of solutions [1], [2], [3], [4]. MCDM methods are the most common approach applied for the evaluation process of location alternatives. The ranking, sorting, and selecting the most desirable alternative with the obtaining of criteria weight and the possibility to work with a large number of criteria [7] and alternatives are the most common issues in the standard MCDM techniques.

Generally, solving various tasks [5,6] and multi-criteria location problems uses the methodology of comparing alternatives pairwise to discover if they are indifferent or incomparable [8].

Also, not all MCDM problems present evaluation criteria simultaneously, so a hierarchical structure of criteria can exist. For example, at the first level, they intuitively combine them (e.g., economical alternative characteristic combines the following features (sub-criteria): costs of location activation, the average cost of infrastructure (water/sewerage system), investment in the construction of access routes, and infrastructure, period of return on funds, etc.). The consequences of this approach (flat structure of criteria) may be many criteria, the problems of determining the relative weight of each criterion, and insufficient information provided by the dominance relation, which makes many alternatives incomparable.

This paper used and compared a modified and extended outranking method with the flat and hierarchical structure of criteria. The modified algorithm with the development of an appropriate software tool simplifies the process of ranking, provides a more objective comparison of various individual criteria to rank the alternatives, and finally reduces the influence of experience and subjective evaluation of the decision-maker (DM) [9].

The developed algorithm, through several stages of iteration, relatively easy and quick made unique solutions. The proposed procedure recommends that the number of criteria at the 1-st level of ranking and sub-criteria on the  $r$ -the level does not exceed 12. The level of significance criteria or the levels of decomposing should be limited to 3 [10].

The influence of experience and subjective assessment of the DM is reduced to a minimum by changing the existing generalized criterion and implementing the new one, by changing the procedure selecting generalized criteria and transforming the mean values of the outranking flow in case of hierarchy structure of criteria.

The statistical significances of the differences between the obtained ranks in the case with and without a hierarchy structure are calculated using Kendall's tau-b test. The robustness of the proposed approach is demonstrated by changing a criteria number and sensitivity analysis in assessing the reliability of MCDM outcomes.

This study provides efforts to create an effective decision-making process and is organized in the following way: Section 2 gives basic concepts of the proposed approach with provided a hierarchy structure of criteria; Section 3 is provided a numerical example of the selection process with or without hierarchy structure of criteria; Section 4 gives a statistical comparing of the obtained results and sensitivity analysis; Section 5 collects conclusions.

## 2. THE PRINCIPLES OF EVALUATING ALTERNATIVES BY MODIFIED APPROACH

In operational research, theorists and practitioners have developed many methods and approaches to multi-criteria decision-making. The MCDM method is used for ranking a finite number of alternatives by considering multiple criteria. By combining methods [11,12] for determining the relative importance of criteria and classical methods of ranking alternatives, an optimal decision on a

specific problem is made, regardless of the nature of the parameters that describe it. The proposed selection methodology in domain logistics and transport systems combines experiences in applying known decision-making methods and modifications.

### 2.1. The process of evaluating alternatives with flat structures of criteria

The outranking methods [13] construct a binary relation which reads: alternative  $a$  is at least as good as alternative  $b$ , which means  $a$  outranks  $b$ . PROMETHEE method [14] is well adapted to the decision problems and is based on pairwise comparisons of alternatives for each criterion. This study is focused on a modified PROMETHEE approach based on improving the family of methods for multi-criteria ranking through a change of the existing generalized criteria and introducing the new ones (for a detailed description in case of the flat structure of criteria see [9]). The proposed approach introduces a preference function to describe DM preference. The type III of preference function (V-shape criterion) and type V (V-shape with indifference criterion) are replaced with the linear criterion whose parameters are calculated through linear regression. The type V and VI of preference function are calculated by regression analysis [9].

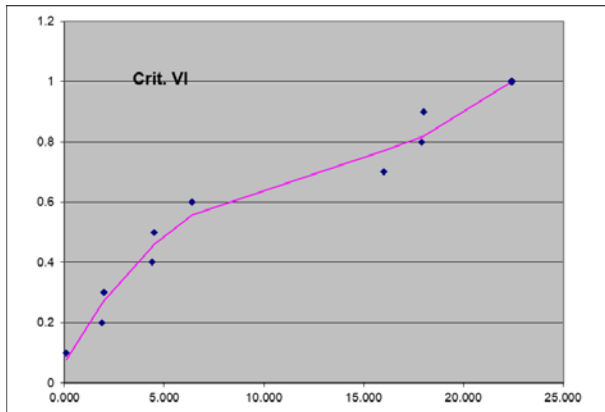


Figure 1: The chosen generalized criterion based on the method of least squares (type VI) [9]

The generalized criterion in which the sum of squares of deviations of experimental points from the theoretical curve is the least is chosen based on the method of least squares by the developed appropriate software tool (Fig.1).

### 2.2. The process of evaluating alternatives in case of hierarchy structure of criteria

In the multi-criteria hierarchy process, criteria decomposition can go to a certain ( $r$ -th) level [10]. The relative weight of criteria or sub-criteria must be determined at each level. A formal record of such problems is given in Table 1, where are:

- $m$  - number of alternatives;
- $n$  - number of criteria functions at  $r$ -th level;
- $s$  - number of criteria functions at  $(r-1)$ -th level;
- $l$  - number of criteria functions at 2-nd level;
- $k$  - number of criteria functions at the 1-st level.

Table 1: A formal record of the problem of multi-criteria analysis with hierarchy structure of criteria [10]

| Criterion level |             |             |             | Alternatives |          |       |          | Relative weights |     |              |     |
|-----------------|-------------|-------------|-------------|--------------|----------|-------|----------|------------------|-----|--------------|-----|
| 1               | 2           | ...         | $r-1$       | $r$          | $A_1$    | $A_2$ | ...      | $A_m$            | $r$ | ...          | 1   |
| $K_1^2$         | $K_1^{r-1}$ | ...         | $K_1^r$     | $C_{11}$     | $C_{21}$ | ...   | $C_{m1}$ | $\omega_1^r$     | ... | $\omega_1^l$ |     |
|                 |             |             |             | $C_{12}$     | $C_{22}$ | ...   | $C_{m2}$ | $\omega_2^r$     |     |              |     |
|                 |             |             |             | $C_{13}$     | $C_{23}$ | ...   | $C_{m3}$ | $\omega_3^r$     |     |              |     |
|                 |             |             |             | $C_{14}$     | $C_{24}$ | ...   | $C_{m4}$ | $\omega_4^r$     |     |              |     |
| $K_2^2$         | ...         | $K_2^{r-1}$ | $K_2^r$     | ...          | ...      | ...   | ...      | $\omega_5^r$     | ... | $\omega_5^l$ |     |
|                 |             |             |             | ...          | ...      | ...   | ...      | ...              |     |              |     |
| ...             | ...         | ...         | ...         | ...          | ...      | ...   | ...      | ...              | ... | ...          | ... |
| $K_k^1$         | $K_k^2$     | ...         | $K_k^{r-1}$ | $C_{1n}$     | $C_{2n}$ | ...   | $C_{mn}$ | $\omega_n^r$     | ... | $\omega_k^l$ |     |
|                 |             |             |             | $C_{1n}$     | $C_{2n}$ | ...   | $C_{mn}$ | $\omega_n^r$     |     |              |     |
|                 |             |             |             | $C_{1n}$     | $C_{2n}$ | ...   | $C_{mn}$ | $\omega_n^r$     |     |              |     |
|                 |             |             |             | $C_{1n}$     | $C_{2n}$ | ...   | $C_{mn}$ | $\omega_n^r$     |     |              |     |

The primary criterion (first level of observation) could be expressed with criterion function at 1-st level  $K_k^l$ , i.e., the sub-criterion function at the 2-nd level could be expressed with  $K_l^2$ , etc. We assume that for each criterion, DM has determined its importance (weights)  $\omega_n^r$ . The sub-criteria functions of a certain level don't need to have equal requirements (type min or max).

The algorithm of the procedure proposed for solving multi-criteria optimization with the hierarchy structure of criteria is shown in Fig. 2 (for a detailed description of the hierarchy structure of criteria, see [9]).

The following phases can describe the implementation procedures:

**Phase 1:** Definition of the matrix of criterion values for specific alternatives and standard deviation for each criterion

**Phase 2:** Ranking of alternatives based on sub-criteria functions at a  $k$ -level which is carried out in several steps:

**Step 2.1:** Selection of the preference function

**Step 2.2:** Calculation of the preference index for each pair of alternatives ( $\Pi$ )

For each pair of alternatives ( $a_i, a_k$ ), the preference index is determined by the expression:

$$\Pi(a_i, a_k) = \frac{\sum_{j=1}^n \omega_j P_j(a_i, a_k)}{\sum_{j=1}^n \omega_j}, \quad (1)$$

where:  $\omega_j$  - the assigned relative weight of criterion.

**Step 2.3:** Calculation of the values of flows ( $\Phi$ )

Following the preference index, the input, output, and outranking (pure) flows of action are defined for each alternative. The mean values transformation of the net outranking flow from a  $k$ -th level, which are used to rank the alternatives at a  $(k-1)$ -th level, is performed by the expression:

$$e_i = \frac{\bar{\Phi}(a_i) - \min \bar{\Phi}}{R}, \quad (2)$$

where is:

$$R = \max \bar{\Phi} - \min \bar{\Phi}, \quad (3)$$

The "range" -  $R$  represents the difference between maximum and minimum values of the net outranking flow.

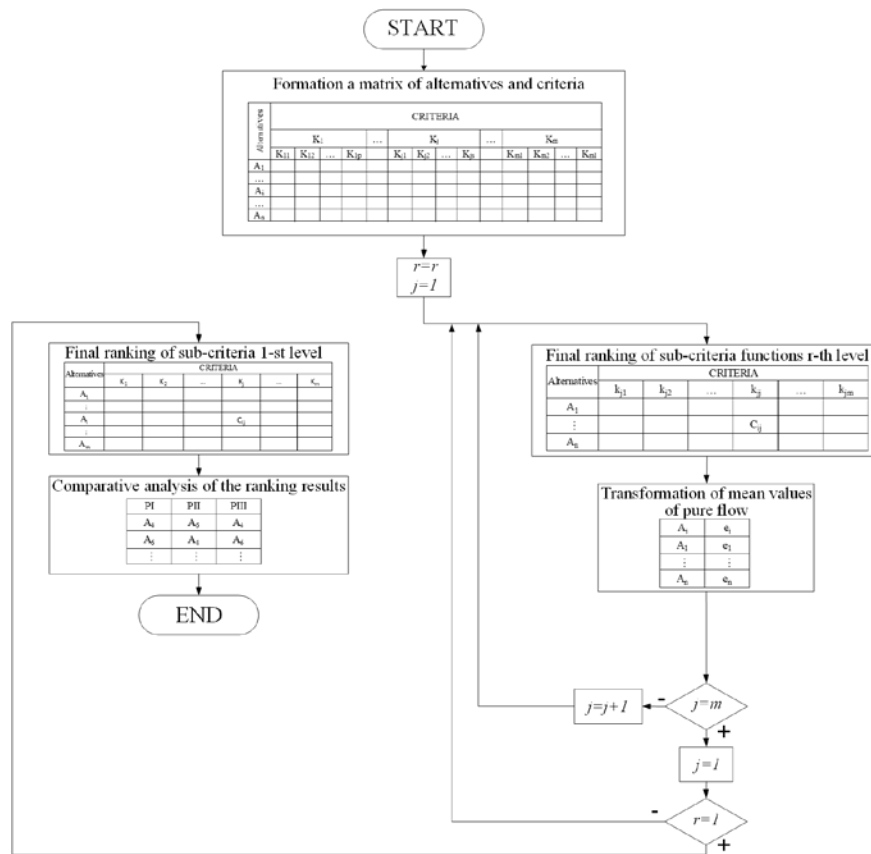


Figure 2: The proposed algorithm for solving multi criteria hierarchy process [10]

Therefore, in the first iteration, the multi-criteria analysis starts from the last  $r$ -th level, where the criterion functions accurate values are used. In the next iteration with criteria functions at an  $r-1$  level, the transformed values of the net outranking flow  $\Phi$  obtained in the previous stage are used. Thus, calculated results represent the new matrix of alternatives and the criteria by which the criteria are decomposed down into  $r-1$  levels. Finally, the procedure is repeated until the 1-st (primary) level.

**Phase 3:** Generation of the final ranking

The ranking procedure on the 1-st level is performed by forming the table of partial ranking according to the PROMETHEE I method, creating the table of complete ranking according to the PROMETHEE II method, and forming the table of interval ranking according to the PROMETHEE III method [11].

3. AN ILLUSTRATIVE EXAMPLE

In this section, an illustrative example shows strategic decision-making by ranking potential alternative locations of a new logistics warehouse and implementing the proposed approach in case of a hierarchy structure of criteria. Let us assume that the DM must analyse potential locations (zones)  $A_1$  to  $A_5$ .

Tables 2 and 3 presents a list of criteria and sub-criteria for evaluation [10]. Again, the decomposition of criteria is performed only up to the second level.

3.1. Evaluation model with the flat structure of criteria

At this stage, pre-defined alternatives are evaluated based on the adopted criteria and their relative weights.

After defining the given criteria for each alternative and the corresponding transformation of criterion type min in the type max (Table 4), the standard deviation values for each criterion are given in Table 5.

The results of the multi-criteria analysis are displayed in the form of a report presenting a final order of the alternatives PROMETHEE I, PROMETHEE II, and PROMETHEE III, and a graph of the interval order of alternatives (Fig.3).

Table 2: Criteria for evaluating the alternatives

| Criteria                   | Label of criteria | Relative weights | Label of sub-criteria | Relative weights of sub-criteria |
|----------------------------|-------------------|------------------|-----------------------|----------------------------------|
| Technological              | $K_I$             | 20%              | $K_{11}$              | 40%                              |
|                            |                   |                  | $K_{12}$              | 40%                              |
|                            |                   |                  | $K_{13}$              | 20%                              |
| Social/ labor              | $K_{II}$          | 20%              | $K_{21}$              | 20%                              |
|                            |                   |                  | $K_{22}$              | 35%                              |
|                            |                   |                  | $K_{23}$              | 45%                              |
| Legal-regulatory framework | $K_{III}$         | 10%              | $K_{31}$              | 35%                              |
|                            |                   |                  | $K_{32}$              | 35%                              |
|                            |                   |                  | $K_{33}$              | 30%                              |
| Economical                 | $K_{IV}$          | 25%              | $K_{41}$              | 40%                              |
|                            |                   |                  | $K_{42}$              | 40%                              |
|                            |                   |                  | $K_{43}$              | 20%                              |
| Technical                  | $K_V$             | 25%              | $K_{51}$              | 20%                              |
|                            |                   |                  | $K_{52}$              | 40%                              |
|                            |                   |                  | $K_{53}$              | 40%                              |

Table 3: Sub-criteria for evaluating the alternatives

| Label           | Sub-criteria – 2nd level  |
|-----------------|---|
| K <sub>11</sub> | Road transport system-distance from the highway - (km)  |
| K <sub>12</sub> | Effective railway transport system - (points)   |
| K <sub>13</sub> | Airport access-min distance - (km)  |
| K <sub>21</sub> | Unemployment rate - (points)  |
| K <sub>22</sub> | Alleviate unemployment - (%)  |
| K <sub>23</sub> | Availability of specialized technicians - (points)  |
| K <sub>31</sub> | Availability of land - (points)   |
| K <sub>32</sub> | Possibility of regulating ownership over land and facility - (points)                               |
| K <sub>33</sub> | Coordination with the spatial and urban plans - (points)  |
| K <sub>41</sub> | Costs of location activation - (euro/m <sup>2</sup> )   |
| K <sub>42</sub> | Average cost of infrastructure (water/sewerage system) - (euro/m <sup>3</sup> )                     |
| K <sub>43</sub> | Period of return on funds - (months)  |
| K <sub>51</sub> | Geological characteristics of the location - (points)   |
| K <sub>52</sub> | Technical possibilities for connection with the infrastructure of railway transportation - (points) |
| K <sub>53</sub> | Technical possibilities for connection with the infrastructure of road transportation - (points)    |

3.2 Evaluation model with hierarchy structure of criteria

According to the proposed procedure for pre-defined criteria, the multi-criteria analysis should be conducted in two phases:

**Phase 1:** Multi-criteria analysis of the criteria functions at a 2-nd level by the PROMETHEE III method. Table 7 shows the input data related to these sub-criteria functions.

After defining a matrix of criteria values for specific alternatives and with appropriate transformation so that the criteria of minimum type are transformed to type max, the values of standard deviation value for each criterion are determined. In the next step of this phase, a preference function  $P_j(a_i, a_k)$  should be assigned to each criterion to compare two alternatives. Based on the preference functions, the generalized criterion in which the sum of squares of deviations of experimental points from the theoretical curve of the generalized criterion is least is chosen [10].

Table 4: Input data for multi-criteria analysis

| Criteria         | Alternatives    |                |                |                |                | $\omega_j$ | max/min |     |
|------------------|-----------------|----------------|----------------|----------------|----------------|------------|---------|-----|
|                  | A <sub>1</sub>  | A <sub>2</sub> | A <sub>3</sub> | A <sub>4</sub> | A <sub>5</sub> |            |         |     |
| K <sub>I</sub>   | K <sub>11</sub> | 26             | 75             | 164            | 80             | 24         | 0.08    | min |
|                  | K <sub>12</sub> | 4              | 5              | 2              | 3              | 3          | 0.08    | max |
|                  | K <sub>13</sub> | 60             | 10             | 109            | 35             | 70         | 0.04    | min |
| K <sub>II</sub>  | K <sub>21</sub> | 23             | 21.1           | 39             | 16.6           | 21         | 0.04    | min |
|                  | K <sub>22</sub> | 0.6            | 0.65           | 0.8            | 0.65           | 0.6        | 0.07    | max |
| K <sub>III</sub> | K <sub>23</sub> | 4              | 3              | 2              | 3              | 2          | 0.09    | max |
|                  | K <sub>31</sub> | 4              | 3              | 2              | 2              | 2          | 0.035   | max |
|                  | K <sub>32</sub> | 3              | 2              | 2              | 3              | 3          | 0.035   | max |
| K <sub>IV</sub>  | K <sub>33</sub> | 4              | 3              | 2              | 3              | 3          | 0.03    | max |
|                  | K <sub>41</sub> | 54             | 60             | 56             | 55.2           | 40.8       | 0.1     | min |
|                  | K <sub>42</sub> | 0.82           | 0.93           | 0.64           | 0.36           | 1.3017     | 0.1     | min |
| K <sub>V</sub>   | K <sub>43</sub> | 60             | 84             | 120            | 72             | 72         | 0.05    | min |
|                  | K <sub>51</sub> | 3              | 3              | 2              | 3              | 3          | 0.05    | max |
|                  | K <sub>52</sub> | 4              | 4              | 2              | 4              | 4          | 0.1     | max |
|                  | K <sub>53</sub> | 4              | 3              | 2              | 4              | 3          | 0.1     | max |

Table 8 shows the procedure for selecting generalized criteria functions for the criteria K<sub>11</sub>, K<sub>12</sub>, and K<sub>13</sub>.

Generating the final ranking of alternatives based on the criteria K<sub>11</sub>, K<sub>12</sub> and K<sub>13</sub> requires calculating preference index values by Eq. (1) (Table 9) and flows for each pair of alternatives. It is automated by the developed software tool.

Table 5: Standard deviation of criteria

| Criteria        | $\sigma$ | S-the sum of squares of the generalized criterion function |         |          |         |         |         |          |
|-----------------|----------|--|---------|----------|---------|---------|---------|----------|
|                 |          | Type I   | Type II | Type III | Type IV | Type V  | Type VI | Type VII |
| K <sub>1</sub>  | 50.8739  | 2.8500   | 2.0500  | 0.06302  | 0.2500  | 0.0568  | 0.0426  | 0.0873   |
| K <sub>2</sub>  | 1.01980  | 2.5185   | 0.8518  | 0.1599   | 0.5185  | 0.1482  | 2.5185  | 0.1774   |
| K <sub>3</sub>  | 33.39101 | 2.8500   | 2.0500  | 0.0405   | 0.3000  | 0.0221  | 0.01237 | 0.0133   |
| K <sub>4</sub>  | 7.72103  | 2.8500   | 1.0500  | 0.0738   | 1.0500  | 0.05561 | 0.0237  | 0.4389   |
| K <sub>5</sub>  | 0.07348  | 2.8500   | 1.0500  | 0.0738   | 1.0500  | 0.0556  | 0.0237  | 0.4389   |
| K <sub>6</sub>  | 0.74833  | 2.1875   | 1.4375  | 0.28125  | 0.3125  | 2.1875  | 2.1875  | 0.4241   |
| K <sub>7</sub>  | 0.8      | 1.8571   | 0.7142  | 0.1428   | 0.2857  | 2.8571  | 4.0000  | 0.3091   |
| K <sub>8</sub>  | 0.48989  | 1.5277   | 1.5277  | 2.5277   | 1.5277  | 2.5277  | 2.5277  | 0.9982   |
| K <sub>9</sub>  | 0.63245  | 1.8571   | 1.8571  | 0.3571   | 0.3571  | 1.8571  | 1.6442  | 0.6306   |
| K <sub>10</sub> | 6.518895 | 2.8500   | 1.0500  | 0.0573   | 1.0500  | 0.0398  | 0.0164  | 0.3360   |
| K <sub>11</sub> | 0.312303 | 2.8500   | 2.0500  | 0.0364   | 0.4500  | 0.0127  | 0.0059  | 0.0114   |
| K <sub>12</sub> | 20.64558 | 2.5185   | 1.1851  | 0.0755   | 0.4629  | 0.0724  | 0.0691  | 0.1651   |
| K <sub>13</sub> | 0.4      | 0.87500  | 0.8750  | 1.8750   | 0.8750  | 1.8750  | 1.8750  | 0.7509   |
| K <sub>14</sub> | 0.8      | 0.87500  | 0.8750  | 1.8750   | 0.8750  | 1.8750  | 1.8750  | 0.7509   |
| K <sub>15</sub> | 0.748331 | 2.1875   | 1.4375  | 0.2812   | 0.3125  | 2.1875  | 2.1875  | 0.4240   |

Table 6: The values of the index of preference

| The values of the index of preferences P(a,b) |                |                          |                |                |                |                |             |
|---|----------------|--------------------------|----------------|----------------|----------------|----------------|-------------|
|   |                | relative to alternatives |                |                |                |                | Output flow |
|   |                | A <sub>1</sub>           | A <sub>2</sub> | A <sub>3</sub> | A <sub>4</sub> | A <sub>5</sub> |             |
| Examined                                      | A <sub>1</sub> | 0                        | 0.26800        | 0.68360        | 0.17998        | 0.28394        | 1.4155      |
|   | A <sub>2</sub> | 0.08487                  | 0              | 0.50329        | 0.09722        | 0.21666        | 0.9021      |
|   | A <sub>3</sub> | 0.08504                  | 0.12859        | 0              | 0.04813        | 0.15620        | 0.4180      |
|   | A <sub>4</sub> | 0.11841                  | 0.23604        | 0.57424        | 0              | 0.23973        | 1.1684      |
|   | A <sub>5</sub> | 0.09959                  | 0.18244        | 0.51090        | 0.11864        | 0              | 0.9116      |
| Input flow                                    |                | 0.38791                  | 0.81507        | 2.27205        | 0.44397        | 0.89654        |             |

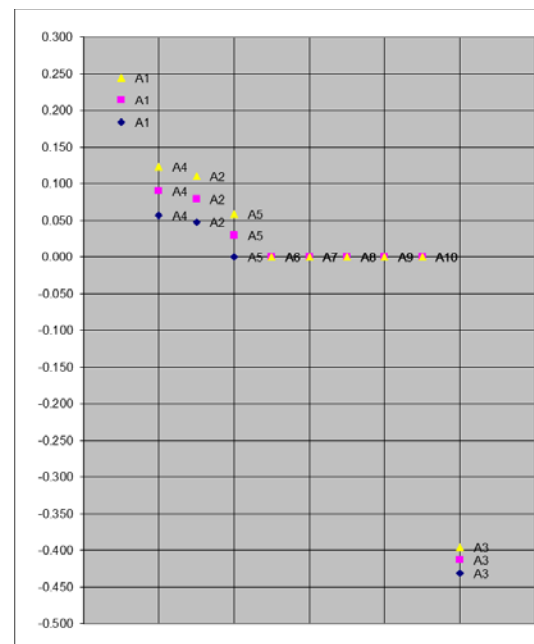


Figure 3: The final order of alternatives for flat structure of criteria

Table 7: Input data for ranking the alternatives based on sub-criteria functions  $K_{11}$ ,  $K_{12}$ , and  $K_{13}$

| Criteria       | Alternatives    |                |                |                |                |    | $\omega_j$ | max/min |
|----------------|-----------------|----------------|----------------|----------------|----------------|----|------------|---------|
|                | A <sub>1</sub>  | A <sub>2</sub> | A <sub>3</sub> | A <sub>4</sub> | A <sub>5</sub> |    |            |         |
| K <sub>I</sub> | K <sub>11</sub> | 26             | 75             | 164            | 80             | 24 | 0.4        | min     |
|                | K <sub>12</sub> | 4              | 5              | 2              | 3              | 3  | 0.4        | max     |
|                | K <sub>13</sub> | 60             | 10             | 109            | 35             | 70 | 0.2        | min     |

Table 8: Standard deviation and the chosen generalized criterion for criteria  $K_{11}$ ,  $K_{12}$  and  $K_{13}$

| Sub-criteria    | $\sigma$ | S - the sum of squared deviations for generalized criterion |         |          |         |        |         |          | Chosen gen. criterion |
|-----------------|----------|---|---------|----------|---------|--------|---------|----------|-----------------------|
|                 |          | Type I  | Type II | Type III | Type IV | Type V | Type VI | Type VII |                       |
| K <sub>11</sub> | 50.874   | 2.850   | 2.050   | 0.06302  | 0.250   | 0.0568 | 0.0426  | 0.0874   | Type VI               |
| K <sub>12</sub> | 1.0198   | 2.5185  | 0.8519  | 0.1599   | 0.5185  | 0.1482 | 2.5185  | 0.1774   | Type V                |
| K <sub>13</sub> | 33.391   | 2.850   | 2.050   | 0.0405   | 0.300   | 0.0220 | 0.0123  | 0.0133   | Type VI               |

Table 9: Preference index values with input and output flows

| Preference index values P(a,b) |                |                |                |                |                |             |         |
|--------------------------------|----------------|----------------|----------------|----------------|----------------|-------------|---------|
| Compared to alternative        |                |                |                |                |                |             |         |
|                                | A <sub>1</sub> | A <sub>2</sub> | A <sub>3</sub> | A <sub>4</sub> | A <sub>5</sub> | Output flow |         |
| Alternatives                   | A <sub>1</sub> | 0              | 0.16656        | 0.81871        | 0.31803        | 0.15015     | 1.45345 |
|                                | A <sub>2</sub> | 0.26212        | 0              | 0.90982        | 0.42359        | 0.46777     | 2.06329 |
|                                | A <sub>3</sub> | 0              | 0              | 0              | 0              | 0           | 0.00000 |
|                                | A <sub>4</sub> | 0.05377        | 0              | 0.61532        | 0              | 0.08323     | 0.75232 |
|                                | A <sub>5</sub> | 0.05686        | 0.17375        | 0.60825        | 0.19208        | 0           | 1.03094 |
| Input flow                     | 0.37275        | 0.34030        | 2.95210        | 0.93370        | 0.70114        |             |         |

The order of alternatives is obtained based on interval order using the PROMETHEE III method. The transformed values of net outranking flow for the K<sub>I</sub> criterion are obtained using Eq. (2) and (3) and given in Table 10. In the same way, the values of net outranking flow are obtained for the remaining criteria functions at the 1-st level of K<sub>II</sub>, K<sub>III</sub>, K<sub>IV</sub>, and K<sub>V</sub>. The values are shown in Tables 11, 12, and 13.

Table 10: Transformed values of the net outranking flows of criteria  $K_I$  obtained in Phase 1

| A <sub>i</sub> | C <sub>ij</sub> |
|----------------|-----------------|
| A <sub>1</sub> | 0.86262         |
| A <sub>2</sub> | 1.00000         |
| A <sub>3</sub> | 0.00000         |
| A <sub>4</sub> | 0.59266         |
| A <sub>5</sub> | 0.70200         |

**Phase 2:** Multi-criteria analysis of the criteria functions at the 1-th level, where the input data are transformed values of the net outranking flows obtained in the previous stage (Table 14).

The determined values of standard deviation value for each criterion (K<sub>I</sub>, K<sub>II</sub>, K<sub>III</sub>, K<sub>IV</sub>, and K<sub>V</sub>) and chosen generalized criterion functions are shown in Table 15. Generating the final ranking of alternatives based on the criteria K<sub>I</sub>, K<sub>II</sub>, K<sub>III</sub>, K<sub>IV</sub>, and K<sub>V</sub> is done with the family of methods PROMETHEE I, II, and III (A<sub>1</sub> > A<sub>4</sub> > A<sub>2</sub> > A<sub>5</sub> > A<sub>3</sub>).

Based on the comparative analysis of the ranking of a potential location of the logistics warehouse, by the proposed procedures, the DM makes the final decision - a conceptual solution (alternative 1-A<sub>1</sub>) exceeds all present constraints and represents the best solution.

Table 11: Input data and transformed values of the net outranking flows of criteria  $K_{II}$ ,  $K_{III}$ ,  $K_{IV}$  and  $K_V$  obtained in Phase 1

| Criteria        | Alternatives    |                |                |                |                | $\omega_j$ | max/min |     |
|-----------------|-----------------|----------------|----------------|----------------|----------------|------------|---------|-----|
|                 | A <sub>1</sub>  | A <sub>2</sub> | A <sub>3</sub> | A <sub>4</sub> | A <sub>5</sub> |            |         |     |
| K <sub>II</sub> | K <sub>21</sub> | 23             | 21.1           | 39             | 16.6           | 21         | 0.20    | min |
|                 | K <sub>22</sub> | 0.6            | 0.65           | 0.8            | 0.65           | 0.6        | 0.35    | max |
|                 | K <sub>23</sub> | 4              | 3              | 2              | 3              | 2          | 0.45    | max |

| Criteria         | Alternatives    |                |                |                |                | $\omega_j$ | max/min |     |
|------------------|-----------------|----------------|----------------|----------------|----------------|------------|---------|-----|
|                  | A <sub>1</sub>  | A <sub>2</sub> | A <sub>3</sub> | A <sub>4</sub> | A <sub>5</sub> |            |         |     |
| K <sub>III</sub> | K <sub>31</sub> | 4              | 3              | 2              | 2              | 2          | 0.35    | max |
|                  | K <sub>32</sub> | 3              | 2              | 2              | 3              | 3          | 0.35    | max |
|                  | K <sub>33</sub> | 4              | 3              | 2              | 3              | 3          | 0.30    | max |

| Criteria        | Alternatives    |                |                |                |                | $\omega_j$ | max/min |     |
|-----------------|-----------------|----------------|----------------|----------------|----------------|------------|---------|-----|
|                 | A <sub>1</sub>  | A <sub>2</sub> | A <sub>3</sub> | A <sub>4</sub> | A <sub>5</sub> |            |         |     |
| K <sub>IV</sub> | K <sub>41</sub> | 54             | 60             | 56             | 55.2           | 40.8       | 0.4     | min |
|                 | K <sub>42</sub> | 0.82           | 0.93           | 0.64           | 0.36           | 1.3017     | 0.4     | min |
|                 | K <sub>43</sub> | 60             | 84             | 120            | 72             | 72         | 0.2     | min |

| Criteria       | Alternatives    |                |                |                |                | $\omega_j$ | max/min |     |
|----------------|-----------------|----------------|----------------|----------------|----------------|------------|---------|-----|
|                | A <sub>1</sub>  | A <sub>2</sub> | A <sub>3</sub> | A <sub>4</sub> | A <sub>5</sub> |            |         |     |
| K <sub>V</sub> | K <sub>51</sub> | 3              | 3              | 2              | 3              | 3          | 0.2     | max |
|                | K <sub>52</sub> | 4              | 4              | 2              | 4              | 4          | 0.4     | max |
|                | K <sub>53</sub> | 4              | 3              | 2              | 4              | 3          | 0.4     | max |

Table 12: Preference index values with input and output flows

| Preference index values P(a,b) |                |                |                |                |                |             |         |
|--------------------------------|----------------|----------------|----------------|----------------|----------------|-------------|---------|
| Compared to alternative        |                |                |                |                |                |             |         |
|                                | A <sub>1</sub> | A <sub>2</sub> | A <sub>3</sub> | A <sub>4</sub> | A <sub>5</sub> | Output flow |         |
| Alternatives                   | A <sub>1</sub> | 0              | 0.19688        | 0.57613        | 0.19687        | 0.42187     | 1.39176 |
|                                | A <sub>2</sub> | 0.16224        | 0              | 0.35988        | 0              | 0.3062      | 0.82837 |
|                                | A <sub>3</sub> | 0.32813        | 0.24063        | 0              | 0.24062        | 0.32812     | 1.13750 |
|                                | A <sub>4</sub> | 0.22085        | 0.09193        | 0.39687        | 0              | 0.39696     | 1.10662 |
|                                | A <sub>5</sub> | 0.05467        | 0.01553        | 0.163560       | 0              | 0           | 0.23377 |
| Input flow                     | 0.76589        | 0.54497        | 1.496450       | 0.4375         | 1.45321        |             |         |

Table 13: Input data for multi-criteria optimization in Phase 2

| Criteria         | Alternatives   |                |                |                |                | $\omega_j$ | max/min |
|------------------|----------------|----------------|----------------|----------------|----------------|------------|---------|
|                  | A <sub>1</sub> | A <sub>2</sub> | A <sub>3</sub> | A <sub>4</sub> | A <sub>5</sub> |            |         |
| K <sub>I</sub>   | 0.86262        | 1              | 0              | 0.59266        | 0.702          | 0.20       | max     |
| K <sub>II</sub>  | 0.9771         | 0.79576        | 0.45563        | 1              | 0              | 0.20       | max     |
| K <sub>III</sub> | 1              | 0.31793        | 0              | 0.50916        | 0.50916        | 0.10       | max     |
| K <sub>IV</sub>  | 0.74526        | 0              | 0.33817        | 1              | 0.66863        | 0.25       | max     |
| K <sub>V</sub>   | 1              | 0.80823        | 0              | 1              | 0.80823        | 0.25       | max     |

Table 14: Transformed values of the net outranking flows obtained in the previous stage – Phase 1

| Transformed values of the net outranking flows |                |                |                |                |                |
|--|----------------|----------------|----------------|----------------|----------------|
|  | A <sub>1</sub> | A <sub>2</sub> | A <sub>3</sub> | A <sub>4</sub> | A <sub>5</sub> |
| K <sub>I</sub>                                 | 0.862615       | 1.000000       | 0.000000       | 0.592656       | 0.701998       |
| K <sub>II</sub>                                | 0.928637       | 0.853619       | 0.000000       | 1.000000       | 0.430345       |
| K <sub>III</sub>                               | 1.000000       | 0.450924       | 0.000000       | 0.613741       | 0.613741       |
| K <sub>IV</sub>                                | 1.000000       | 0.000000       | 0.047434       | 0.933870       | 0.958466       |
| K <sub>V</sub>                                 | 0.870650       | 0.960054       | 0.000000       | 1.000000       | 0.845921       |

Table 15: Standard deviation and chosen generalized criterion for  $K_I, K_{II}, K_{III}, K_{IV}$ , and  $K_V$ .

| Sub - Criteria | $\sigma$ | S - the sum of squared deviations for generalized criterion |         |          |         |        |         |          | Chosen gen. criterion |
|----------------|----------|---|---------|----------|---------|--------|---------|----------|-----------------------|
|                |          | Type I  | Type II | Type III | Type IV | Type V | Type VI | Type VII |                       |
|                |          | $K_I$   | 0.3448  | 2.8500   | 1.4500  | 0.0405 | 0.6500  | 0.0176   |                       |
| $K_{II}$       | 0.3771   | 2.8500  | 1.4500  | 0.0242   | 0.2500  | 0.0170 | 0.0161  | 0.6593   | Type VI               |
| $K_{III}$      | 0.3249   | 2.5185  | 1.7407  | 0.0865   | 0.2963  | 0.0651 | 0.0553  | 0.0865   | Type VI               |
| $K_{IV}$       | 0.3470   | 2.8500  | 1.4500  | 0.0582   | 0.4000  | 0.0516 | 0.0485  | 0.0589   | Type VI               |
| $K_V$          | 0.3717   | 2.188   | 0.6875  | 0.1066   | 0.6875  | 0.0938 | 2.1875  | 0.3329   | Type V                |



Figure 4: The final order of alternatives with hierarchy structure of criteria

3.3 Comparative results

By ranking the alternatives with different criteria numbers (Tables 16 - 20), it is possible to notice a significant correlation and the stability of the final rank of five alternatives by proposed procedure with hierarchy structure of criteria for 10, 12, and 15 criteria (5A-10C, 5A-12C and 5A-15C).

Table 17: Input data for multi-criteria optimization in Phase 2 – decision matrix 5A-10C

| Criteria  | Alternatives   |                |                |                |                | $\omega_j$ | max/min |
|-----------|----------------|----------------|----------------|----------------|----------------|------------|---------|
|           | A <sub>1</sub> | A <sub>2</sub> | A <sub>3</sub> | A <sub>4</sub> | A <sub>5</sub> |            |         |
| $K_I$     | 0.981681       | 1              | 0              | 0.536289       | 0.803354       | 0.20       | max     |
| $K_{II}$  | 0              | 0.583250       | 0.605392       | 1              | 0.2245253      | 0.20       | max     |
| $K_{III}$ | 1              | 0.226350       | 0              | 0.513765       | 0.5137654      | 0.10       | max     |
| $K_{IV}$  | 0.606200       | 0              | 0.632908       | 1              | 0.632960       | 0.25       | max     |
| $K_V$     | 1              | 1              | 0              | 1              | 1              | 0.25       | max     |

Table 19: Input data for multi-criteria optimization in Phase 2 – decision matrix 5A-12C

| Criteria  | Alternatives   |                |                |                |                | $\omega_j$ | max/min |
|-----------|----------------|----------------|----------------|----------------|----------------|------------|---------|
|           | A <sub>1</sub> | A <sub>2</sub> | A <sub>3</sub> | A <sub>4</sub> | A <sub>5</sub> |            |         |
| $K_I$     | 0.862615       | 1              | 0              | 0.592656       | 0.701997       | 0.20       | max     |
| $K_{II}$  | 0.977096       | 0.795760       | 0.455633       | 1              | 0              | 0.20       | max     |
| $K_{III}$ | 1              | 0.226350       | 0              | 0.513765       | 0.513765       | 0.10       | max     |
| $K_{IV}$  | 0.606200       | 0              | 0.632908       | 1              | 0.63296        | 0.25       | max     |
| $K_V$     | 1              | 1              | 0              | 1              | 1              | 0.25       | max     |

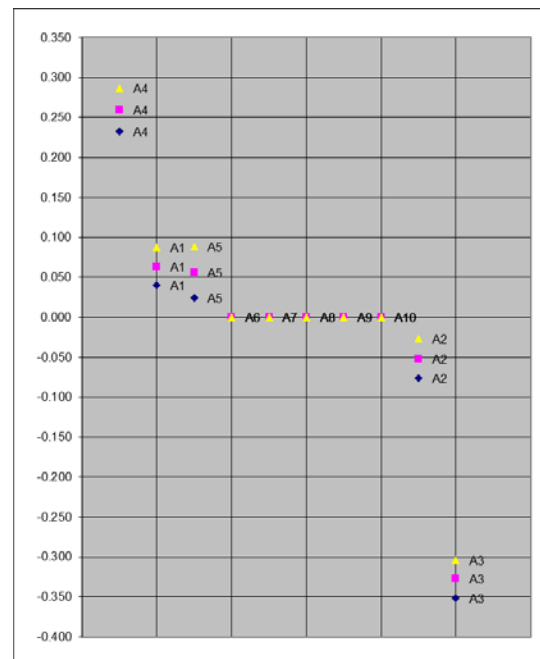
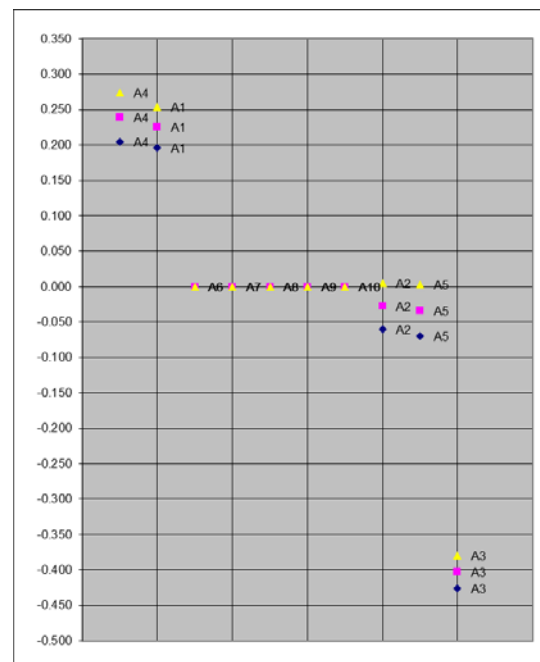


Figure 5: The final order of alternatives – decision matrix 5A-10C



| PROMETHEE I |                | PROMETHEE II |                | PROMETHEE III |                |
|-------------|----------------|--------------|----------------|---------------|----------------|
| Rang        |                | Rang         |                | Rang          |                |
| 3           | A <sub>1</sub> | 4            | A <sub>4</sub> | 3             | A <sub>1</sub> |
| 3           | A <sub>4</sub> | 3            | A <sub>1</sub> | 3             | A <sub>4</sub> |
| 1           | A <sub>2</sub> | 2            | A <sub>2</sub> | 1             | A <sub>2</sub> |
| 1           | A <sub>5</sub> | 1            | A <sub>5</sub> | 1             | A <sub>5</sub> |
| 0           | A <sub>3</sub> | 0            | A <sub>3</sub> | 0             | A <sub>3</sub> |

Figure 6: The final order of alternatives – decision matrix 5A-12C

4. STATISTICAL COMPARISON OF RESULTS

Kendall's tau-b test was selected to analyse the produced ranks by the proposed approach through different criteria numbers in terms of their pairwise correlations.

These non-parametric tests are used to test for associations in hypothesis testing. The null hypothesis (H<sub>0</sub>) is that there is no association between the variables under study or no correlation.

#### 4.1. Kendall's tau-b test

The main advantages of using Kendall's tau-b test are as follows: the better statistical properties and the interpretation of Kendall's tau-b in terms of the probabilities of observing the agreeable (concordant) and non-agreeable (discordant) pairs is straightforward.

Kendall's tau-b coefficient is calculated using Eq. (4) as follows [16]:

$$\tau_B = \frac{n_C - n_D}{\sqrt{(n_0 - n_1)(n_0 - n_2)}} \quad (4)$$

where are:

$$n_0 = n(n-1)/2, n_1 = \sum_i t_i(t_i - 1) / 2, n_2 = \sum_j u_j(u_j - 1) / 2,$$

and  $n_C$  is the number of concordant pairs;  $n_D$  is the number of discordant pairs;  $t_i$  is the number of tied values in the  $i$ -th group of ties for the first quantity, and  $u_j$  is the number of tied values in the  $j$ -th group of relations for the second quantity. This formulation yields  $\tau_B$  between  $-1$  and  $+1$ . The value of  $-1$  stands for 100% negative association, and the value of  $+1$  stands for 100% positive associations. The value of zero stands for the absence of any association.

#### 4.2. Statistical comparison of results

The final, sorted ranks obtained by modified approach with hierarchy structure of criteria were statistically analysed by Kendall's tau-b test using a specific macro written in Excel. Table 20 gives a statistical result of Kendall's tau-b test for decision matrix with five alternatives and 10, 12, 15, and 20 criteria [analysed in 10]. The results obtained for  $\alpha$ -level = 0.05 shows the similarity of performances between two statistical tests for criteria number larger than ten. Cases B, C, and D provide the exact ranking. The rank difference increased when the criteria number is decreased (case A).

The problem is also analysed using standard methods for multi-criteria analysis. The obtained results are the same:  $A_1 > A_4 > A_2 > A_5 > A_3$ . In all cases, the most optimal variant remains unchanged, which indicates the robustness of the proposed approach in resolving these types of multi-criteria tasks. The detailed comparison of the proposed method using the third level of criteria decomposition on a better way should be giving information about applicability and robustness.

#### 4.3 Sensitivity analysis

It is often difficult to get a robust result due to the relative importance of a given criterion [17]. Therefore, an interactive tool called walking weights is used to check the sensitivity of the results. In our case, the four criteria,  $k_{10}$ ,  $k_{11}$ ,  $k_{14}$ , and  $k_{15}$ , have the most impact on the alternatives (Fig. 7).

Table 20: Analysis of differences using rank correlation test

| Alternatives                           | Set of ranks obtained with specific criteria number |          |          |         |
|--|---|----------|----------|---------|
|  | A (C10)   | B (C12)  | C (C15)  | D (C20) |
| A <sub>1</sub>                         | 4   | 1        | 1        | 1       |
| A <sub>2</sub>                         | 1   | 4        | 4        | 4       |
| A <sub>3</sub>                         | 5   | 2        | 2        | 2       |
| A <sub>4</sub>                         | 2   | 5        | 5        | 5       |
| A <sub>5</sub>                         | 3   | 3        | 3        | 3       |
| Compared groups of ranks               | A-D   | B-D      | C-D      |         |
| P-value                                | 0.058592  | 0.004511 | 0.004511 |         |
| Statistical significance value Z-score | -1.566698   | 2.611164 | 2.611164 |         |
| Kendall's tau-b test                   | -0.6  | 1        | 1        |         |

The criteria weights were changed in increments: -50%, -25%, -10%, +10%, +25%, +50%, while the values of other criteria are customized so that the total of their weights is always 1 (Fig.7). Thus, it can be seen that the weight changes of observed criteria for the different values do not lead to changes in the final rank of alternatives.

In all cases, the most optimal variant remains unchanged, which indicates the robustness of the proposed approach in resolving these types of multi-criteria tasks.

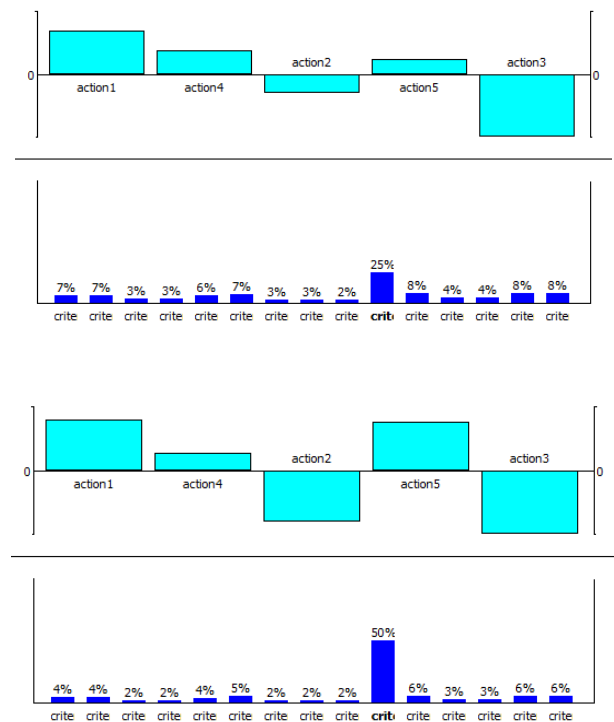


Figure 7: Sensitivity analysis

## 5. CONCLUSION

An MCDM problem with a hierarchy structure of criteria could be solved by conventional multi-criteria optimization methods by the developed algorithm. Through several stages of iteration, it is relatively easy and quick to make unique solutions. The proposed procedure is based on the transformation of mean values of the pure flow sub-criteria functions obtained by PROMETHEE III by introducing new types of generalized criteria for expressing decision-makers criteria selection. The power of the algorithm lies in the simplification of ranking while respecting all the characteristics and parameters of an alternative, more objective comparison of the impact of various individual criteria for ranking alternatives, and reducing them to a common goal function.

The study demonstrates the robustness of the proposed approach by changing criteria numbers and highlights the significance of sensitivity analysis in assessing the reliability of MCDM outcomes. The MCDM outcomes depend on the distribution of the weighting amongst criteria. The detailed comparison of the proposed approach with more decomposition level or with the Robust Ordinal Regression approach [8] and detailed sensitive analysis (e.g., identifying tolerable change) are directions for future research. The desire is to develop and improve a multi-criteria approach to solve logistics and many real problems and allow the DM to obtain comprehensive preference relation concerning all criteria and sub-criteria at different times levels of hierarchy.

## ACKNOWLEDGEMENTS

This paper is supported by the Ministry of Education, Science and Technological Development of the Republic of Serbia through Contract No. 451-03-9/2021-14/200108.

## REFERENCES

- [1] Avittathur, B., Shah, J. and Gupta, O. K., "Distribution center location modeling for differential sales tax structure", *European Journal of Operations Research*, 162, pp. 191–205, (2005).
- [2] Farahani, R. Z., Steadie Seifi, M., & Asgari, N., "Multiple criteria facility location problems: a survey. *Applied Mathematical Modelling*", 34 (7), pp.1689–1709, (2010), doi:10.1016/j.apm.2009.10.005.
- [3] Sawicka, H., Węgliński, S., & Witort P., "Application of multiple criteria decision aid methods in logistic systems". *Electronic Scientific Journal of Logistics*, 6 (3), pp.99-110, (2010)
- [4] Tabari, M., Kaboli, A., Arzaneyhad, M. B., Shahanaghi, K., & Siadat, A., "A new method for location selection: A hybrid analysis", *Applied Mathematics, and Computation*, 206, pp.598–606, (2008), doi:10.1016/j.amc.2008.05.111
- [5] Afshari, A., Vatanparast, M., & Ćoćkalo, D., "Application of multi-criteria decision-making to urban planning - a review", *Journal of Engineering Management and Competitiveness*, 6 (1), pp.46-53, (2016),doi:10.5937/jemc1601046A.
- [6] Vaysilova E., "Sensitivity analysis as a tool for a management decision-making in condition of risk", *International Scientific Conference Management 2012*, Mladenovac, 20-21 April 2012, pp.117, (2012)
- [7] Liu, Jian, Zhao, Hong-Kuan., Li, Zhao-Bin, & Liu, Si-Feng, "Decision process in MCDM with a large number of criteria and heterogeneous risk preferences", *Operations research Perspectives*, 4, pp.106-112, (2017), <http://dx.doi.org/10.1016/j.orp.2017.07.00>
- [8] Corrente, S., Greco, S., & Sowinski, R., "Multiple Criteria Hierarchy Process with ELECTRE and PROMETHEE", *Omega*, 41, pp.820–846, (2013), [dx.doi.org/10.1016/j.omega.2012.10.009](http://dx.doi.org/10.1016/j.omega.2012.10.009)
- [9] Marković, G., Gašić M., Kolarević, M., Savković, M. & Marinković, Z., "Application of the MODIPROM method to the final solution of logistics center location", *Transport*, 28 (4), pp.341-351, (2013). doi: 10.3846/16484142.2013.864328
- [10] G. Marković, N. Zdravković, M.Karakašić, M. Kolarević: "Modified PROMETHEE Approach for Solving Multi-Criteria Location Problems with Complex Criteria Functions", *Tehnički vjesnik -Technical Gazette*, Volume 27(1): 8 pages, (2019), doi: 10.17559/TV-20190225151515,.
- [11] Brans, J. P., Mareschal, B., & Vincke, P., "PROMETHEE: A new family of outranking methods in MCDM". *Operational research*, pp.477–490, (1984).
- [12] Dagdeviren, M., "Decision Making in equipment selection: an integrated approach with AHP and PROMETHEE", *Journal of Intelligent Manufacturing*, 19, pp. 397-406, (2008)
- [13] Taha, Z. and Rostam, S., "A hybrid AHP-PROMETHEE decision support system for machine tool selection in a flexible manufacturing cell", *J. Intell. Manuf.* (2012), 23, pp.2137-2149, (2012)
- [14] Greco, A., Figuera, J., & Ehrgott, M., "Multiple Criteria Decision Analysis: State of the Art Surveys". Berlin: Springer, (2016).
- [15] Behzadian, M., Kazemzadeh, R. B., Albadvi, A. & Aghdasi, M., "PROMETHEE: A comprehensive literature review on methodologies and applications". *European Journal of Operations Research*, 200 (1), pp.198-215, (2010). <https://doi.org/10.1016/j.ejor.2009.01.021>
- [16] Sabzi H.Y., King J.P., Gard C.C., Abudu S., "Statistical and analytical comparison of multi-criteria decision-making techniques under fuzzy environment", *Operations Research Perspectives*, 3(19), pp. 92-117, (2016)
- [17] Vida Maliene, Robert Dixon-Gough, Naglis Malys, "Dispersion of relative importance values contributes to the ranking uncertainty: Sensitivity analysis of Multiple Criteria Decision-Making methods", *Applied Soft Computing*, Volume 67, pp. 286-298, (2018), <https://doi.org/10.1016/j.asoc.2018.03.003>.

## Basic Parameters of a Tensile Testing Device for Conveyor Belts

Nikola Ilanković<sup>1</sup>, Dragan Živanić<sup>1\*</sup>, Atila Zelić<sup>1</sup>, Mirko Katona<sup>1</sup>

<sup>1</sup>Faculty of Technical Sciences/Department of Mechanization and Design Engineering, University of Novi Sad, Novi Sad (R. Serbia)

The most important element of belt conveyors is the belt, both in terms of construction and economic reasons, because it has the largest share in the investment cost. As it is both a load-bearing and a pulling element, it is very important to choose and maintain the belt correctly in order to maximize its service life. Belt manufacturers specify in the specification the tensile strength of the belt, which is the basic size used when calculating the belt conveyor and selecting the belt. However, there is not much research regarding the behaviour of the belt during exploitation, i.e., whether and to what extent it loses tensile strength over time. In this paper, the design of a device for testing conveyor belts is presented. At the beginning, an overview of existing research in the area is given and the types of axial belt tests performed according to the standards are listed. Then, the construction of the device for testing conveyor belts is shown, an overview of the measuring equipment that will be used is given, and their connection scheme is shown. Finally, the need for a detailed study of the fatigue of the carcass of the belt was emphasized in order to obtain a clearer picture of the behaviour of the belt during operation.

**Keywords:** Belt conveyors, Belt carcass, Axial test device

### 1. INTRODUCTION

Material handling plays a major role in the industry. Mass production mainly depends on transport systems and it can be said that conveyors are a component without which modern products could not be found in stores in appropriate quantities. The most important conveyor is the belt conveyor, which consists of a large number of elements. However, no element is economically more important than a conveyor belt. The belt has a large share in the initial investment and therefore its construction must be chosen with great care. It consists of three basic parts - the upper and lower protective rubber layer and the middle load bearing layer. Protective layers have the role of protecting the load bearing layer from the material being transported. The role of the load bearing layer is to accept the tensile force required to move the belt with the material and to absorb the impact energy that is released as the material is loaded on the belt. It consists of one or more layers of fabric that can be made of natural or artificial materials. The strength of the belt depends on the type of material and the number of load bearing layers of the belt, i.e., depends on the tensile strength of the belt [N/mm]. According to [1], manufacturers are obliged to clearly mark on each belt information about who the manufacturer is, what material the bearing layers are made of and how many there are, the tensile strength of bearing layers, whether the belt has special properties and to indicate on each belt the serial number. In order for manufacturers to be able to guarantee the characteristics of the belt, it is necessary to test the belt samples through several experiments, the largest and most significant of which are performed by axial testing of the samples.

### 2. OVERVIEW OF STANDARDS APPLICABLE IN THE FIELD OF TESTING OF CONVEYOR BELTS

As stated in the introduction, conveyor belts are the most important component of belt conveyors and therefore there are a number of standards governing this area.

#### 2.1. Belt sampling and required environmental conditions

Sampling is performed on the basis of a precisely determined sampling technique defined in [1]. The sampling scheme is shown in figure 1.



Figure 1: Sampling scheme on the conveyor belt

The number of samples to be taken depends on the length of the belt and is determined in [2]. Table 1 shows the required number of samples in relation to the total length of the belt.

Table 1. Number of samples depending on the total length of the belt

| Total length of the conveyor belt [m] | Number of samples |
|---------------------------------------|-------------------|
| $L \leq 500$                          | 1                 |
| $500 < L \leq 1000$                   | 2                 |
| $1000 < L \leq 2000$                  | 3                 |
| $2000 < L \leq 3500$                  | 4                 |
| $3500 < L \leq 5000$                  | 5                 |
| $5000 < L \leq 7000$                  | 6                 |
| $7000 < L \leq 10\ 000$               | 7                 |

Note: It is necessary to take one additional sample for each 5000 m if the length of the belt is over 10 000 m.

In order for the testing of belt samples to be adequate, it is necessary to comply with the defined weather conditions in [3], as well as a certain time interval that should pass between sampling and the testing itself. There are 5 combinations of weather conditions during which testing is possible and they are shown in table 2.

Table 2. Required atmospheric conditions

|   |   | Temperature<br>[°C]      | Relative<br>humidity<br>[%] |
|---|---|--------------------------|-----------------------------|
| 1 | Atmospheric conditions A                                | $20 \pm 2$               | $65 \pm 5$                  |
| 2 | Atmospheric conditions B                                | $23 \pm 2$               | $50 \pm 5$                  |
| 3 | Atmospheric conditions C (tropical)                     | $27 \pm 2$               | $65 \pm 5$                  |
| 4 | Atmospheric conditions D (only temp. control)           | $23 \pm 2$ or $20 \pm 2$ | /                           |
| 5 | Atmospheric conditions E (only temp. control, tropical) | $27 \pm 2$               | /                           |

## 2.2. The testing device

The device for axial testing of samples of conveyor belts should work on the principle of CRE - constant speed of elongation of the sample, or on the principle of CRT - constant speed of movement of the jaws. The device must be capable of stretching the belt sample at a speed of  $100 \pm 10$  mm / min. It needs to be designed according to [4].

Jaws of the device should be designed to prevent movement of the belt sample during the test and therefore it is necessary to use jaws with a serrated surface shown in figure 2.

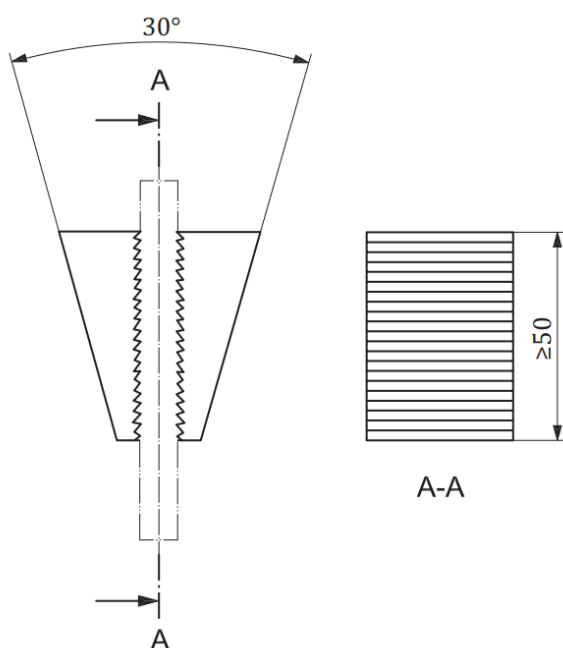


Figure 2: Recommended design of serrated jaws

Before using the device, it is necessary to calibrate the force and displacement measuring system for each force and displacement range which will be used. The calibration of the force and displacement measuring system is performed using instruments to confirm the specified values. Calibration of the displacement measuring system is performed using the etalon, while calibration of the force measuring system is performed according to [5]. It is possible to use weights of known masses or instruments to exercise known forces. The class of the instrument for realizing the known force must be of a better accuracy class than the device being calibrated.

An example of a device for testing samples of conveyor belts is given in figure 3, where 1 indicates the measuring force transmitter, 2 is the upper jaw, while 3 indicates the belt sample.



Figure 3: INSTRON 5960 series device

## 2.3. Types of axial tests of conveyor belt samples

There are 4 types of axial tests of conveyor belts samples:

- determination of tensile strength and elongation of the belt sample;
- determination of elastic and permanent deformation of the belt sample and modulus of elasticity;
- determining the resistance to separation of the belt sample layers;
- determining the maximum force that can be withstood by the connection of the ends of the belt sample.

The tensile strength and elongation of the belt sample are determined according to [6]. This test is used to determine the tensile strength of the belt sample in the longitudinal and transverse direction of the sample and elongation of the sample under the action of the reference

force - one tenth of the nominal tensile strength of the belt multiplied by the width of the belt sample in the narrowest part expressed in millimeters. The tensile strength of the belt [N / mm] is a quantity that shows how much force the belt can withstand before it breaks. It is calculated by dividing the maximum force [N] recorded during the test by the width [mm] of the test sample in the narrowest part. The test is performed by placing the belt sample in jaws of the testing device and stretching it to the desired limits depending on the type of test. An example of a belt sample elongation test at the breaking point is shown in figure 4.



Figure 4: Belt sample test procedure

There are four types of samples that depend on the tensile strength of the belt, i.e., of the nominal tensile strength of the sample. Samples A, B and C are used arbitrarily when the tensile strength of the belt is less than 2000 N/mm, while sample D is used when the tensile strength of the belt is greater than 2000 N/mm.

Testing of elastic and permanent deformation of the belt sample and modulus of elasticity is performed according to [7]. As for light conveyor belts, they are tested according to [8]. The test is performed by stretching the belt sample. The force with which the sample is stretched depends on the tensile strength of belt sample plies. The elastic deformation test of a belt sample is shown in figure 5.



Figure 5: Elastic deformation test of a belt sample

Determination of the resistance of the belt sample to separation of belt layers is performed according to [9]. It is not possible to use this test on light conveyor belts as described in [10]. There are two ways in which this test can be performed - methods A and B. According to method A, it is necessary to separate the upper protective rubber layer from the rest of the sample at one end of the sample so that the jaw can accept the sample, Figure 10. It is necessary for one jaw to grab the rubber layer and the other jaw to grab the rest of the sample. The sample is then stretched and the force required to separate the layers by an additional 100 mm is recorded. It is then necessary to repeat the procedure for each subsequent ply until the middle of the sample is reached. Next, it is necessary to put another sample in the jaw and start from the lower

protective rubber layer and repeat the procedure until the middle of the sample is reached. Separation of the layers should occur between them, if it happens that during the separation a layer begins to split inwards, such a phenomenon should be noted because it is an indicator of the inadequate connection between the layers. According to method B, the same steps are performed at the beginning as with method A. The difference is that the individual plies are not separated, but 2 by 2 plies are separated. In both methods, it is necessary to find the mean value of the force at which layers separate. Also, it is necessary to note the minimum value of the force at which the separation occurs. Obtained results are evaluated according to [11]. The mean adhesion [N/mm] is obtained as the quotient of the mean force [N] recorded and the sample width [mm]. The minimum adhesion is obtained as the quotient of the minimum value of the force [N] that was recorded and the width of the sample [mm].

According to [1], the value of adhesion (resistance to separation) should be close to the values shown in table 3:

Table 3. Adhesion values

| Adhesion [N/mm] |                                 |           |
|-----------------|---------------------------------|-----------|
| Between plies   | Between plies and rubber covers |           |
|                 | Cover thickness [mm]            |           |
|                 | 0,8 - 1,5                       | above 1,5 |
| 5               | 3,5                             | 4,5       |

The testing procedure of the belt sample to separation of belt layers is shown in figure 6:



Figure 6: Test of resistance to layer separation of a belt sample

Concerning the determination of the maximum force that can be withstood by the connection of ends of the belt sample, there are three ways to connect ends of the belt:

- vulcanization (hot joining) - used for belts with textile or synthetic plies, with one, two

or more plies, as well as for belts where steel ropes are used as plies;

- adhesive (cold bonding) - used for belts with textile or synthetic plies, with two or more plies;
- mechanical – it is considered as a temporary connection.

First two ways of connecting belt ends are tested according to [12], while the third way of connecting belt ends is tested according to [13]. When testing connections formed by vulcanization and adhesion, the tensile strength of the joint, the delamination strength of an adhesive joint and the shear strength of an adhesive joint are examined. The belt sample is placed in jaws of the test device and the sample is stretched until the joint breaks. Then the tensile strength of the joint is calculated as the quotient of the measured force [N] and the width of the sample [mm]. It is not necessary to prepare a sample for this test, i.e., it is possible to test rectangular samples with a minimum width of 100 mm. According to [1], the percentage of loss of tensile strength of joints in relation to the tensile strength of the belt is shown in table 4.

Table 4. Percentage of loss of tensile strength of joints in relation to the tensile strength of the belt

| Number of plies  | The loss of tensile strength at joints of belt ends [%] |
|--|---|
| 1  | 0,2   |
| 2  | 0,2 <sup>1)</sup> 0,5 <sup>2)</sup>                     |
| 3  | 0,33  |
| 4  | 0,25  |
| 5  | 0,2   |
| <sup>1)</sup> combination with reinforcement interlayer and 2-step joint |   |
| <sup>2)</sup> without reinforcement interlayer                           |   |

Testing of the vulcanized joint of the belt sample is shown in figure 7.



Figure 7: Vulcanized belt joint test

### 3. PREVIOUS RESEARCH IN THE FIELD OF TESTING OF SAMPLES OF CONVEYOR BELTS

In [14], a device of small dimensions for axial testing of conveyor belt samples is presented. Its structure is presented and the construction of a system for measuring forces in a belt sample is described - 3 sensors consisting of a full bridge of strain gauges. The sensors are

placed in a plane with an angle between them of 120 °, which achieves better linearity and repeatability of measurements. The device scheme is shown in figure 8.

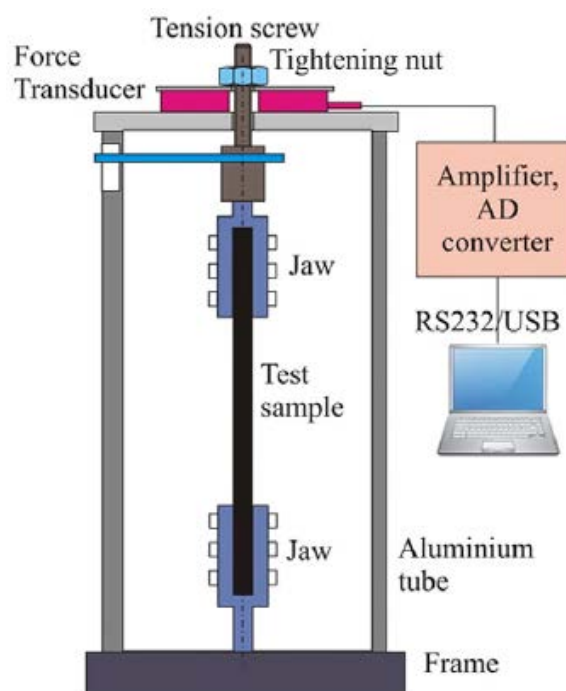


Figure 8: The scheme of the testing device [14]

Furthermore, [15] shows how the belt sample behaves during axial testing. Two tests were performed - continuous loading of the belt sample to the breaking point and step loading of the belt sample with periods of relaxation. During the experiment, a belt sample was monitored in metro-tomography to determine the behavior of the load bearing layer, which is a novelty in this field.

Fatigue testing of a polymer composite material sample is presented in [16]. The sample was tested with a ratio of minimum and maximum voltage, R, defined to be 0.1. The test frequency was 4 Hz. It has been shown that the damage that occurs during the fatigue test manifests initially as cracks in the sample which then spread transversely and lead to layer delamination.

In [17], the examination of the connection of two ends of the belt is presented. It was determined that there is a decrease in the tensile strength of the belt at the joint. The belt sample was statically tested, but was also tested for fatigue. It is shown that the tensile strength of the sample, the modulus of the belt elasticity, the modulus of the rubber cover have an influence on the bond strength and the correlation between the stated parameters and the maximum tensile strength of the joint is given. In fatigue testing, a correlation was given between the number of fatigue cycles after which the splice was delaminated and the tensile belt strength, the elasticity modulus of the belt and the adhesive strength of the joint.

### 4. DESIGN OF THE DEVICE FOR AXIAL TESTING OF SAMPLES OF CONVEYOR BELTS

Input data for device design:

- maximum tension force: 50.000 N;
- stroke of the jaw: min. 127,5 mm;
- sample tensioning speed: 100 mm/min  $\pm$  10 mm/min;

- constant tensioning speed;
- possibility of achieving a longer sample loading period.

The scheme of the device is shown in figure 9. It is consisted of the worm gear screw jack (1), connecting shaft (2), helical geared motor (3), supporting construction (4), upper jaw (5), belt sample (6), lower jaw (7), tension load cell (8) and potentiometric displacement sensor (9).

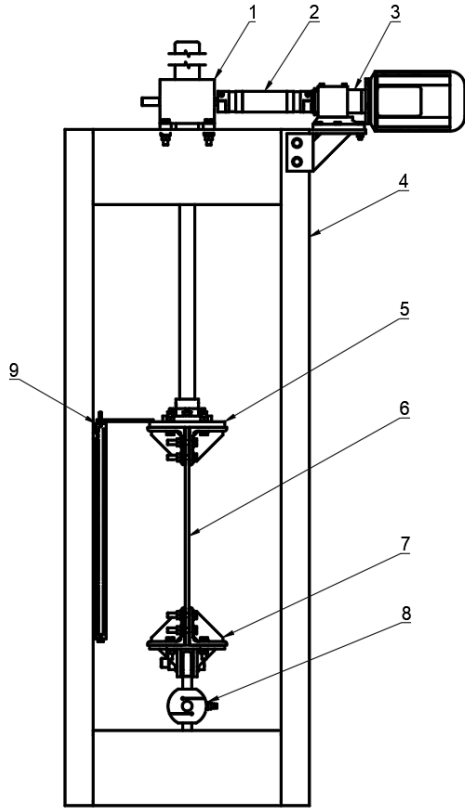


Figure 9: The scheme of the testing device

The worm gear screw jack, connecting shaft and helical geared motor are chosen from the catalogue [18]. The worm gear screw jack has an anti-rotation guide, figure 10. The thread size of the spindle is 40x7 and the material is C45. Stroke pro full rotation of the input shaft is 1 mm.



Figure 10: Worm gear screw jack [18]

In order to achieve the desired tensile force of 50.000 N with the screw jack, the required torque is 34 Nm [18]. Because of that, the chosen helical geared motor has the rated torque of 47 Nm, rated power of 0,55 kW and rated output rpm of 107 min<sup>-1</sup>, figure 11.



Figure 11: Helical geared motor [18]

The connecting shaft was chosen for drive transfer from the motor to the screw jack. It can transfer 78 Nm and can compensate large shaft misalignments – axial, radial and angular. The shaft is shown in figure 12.



Figure 12: Connecting shaft [18]

The tension load cell was chosen from the catalogue [19] and it is shown in figure 13. It has the capacity of 7.500 kg which is exactly 73.575 N – it provides enough reserve for testing. The load cell is equipped with ball-and-socket joints that provide only force transmission to the load cell.



Figure 13: Tension load cell [19]

The potentiometric displacement sensor was chosen from the catalogue [20]. The measuring range of the sensor is 0 ÷ 500 mm with the measuring resolution of 0,01 mm. The measuring range overpasses the required range for testing of belt samples and the reason for that is to provide a possibility for different usage of the sensor in the future. It is shown in figure 14.



Figure 14: Potentiometric displacement sensor [20]

In order to automate the device, electrical components are needed to control the electric motor. Also, in order to get results from the load cell and displacement sensor, an acquisition device that reads signals from sensors is needed, and a computer is needed to display these results. Figure 15 shows control components required to operate the testing device and shows their connection.

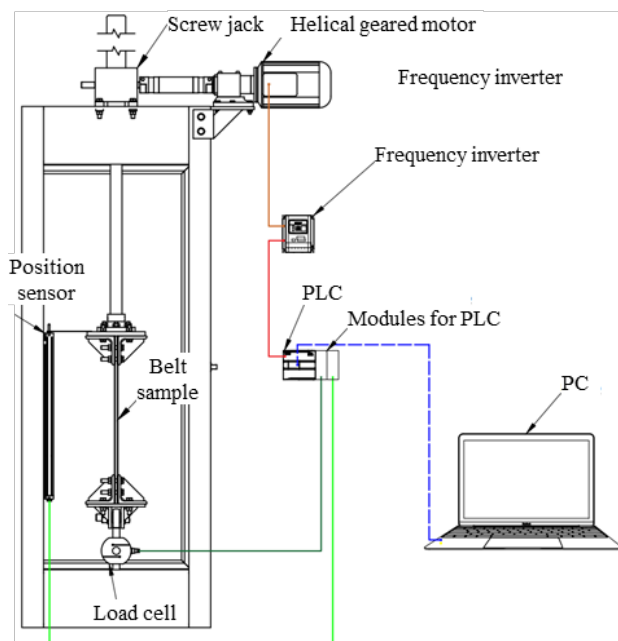


Figure 15: Device control components and the connection diagram

PLC model FBs - 32MA, figure 16, is selected from the catalog [21] with following characteristics:

- 20 connectors for digital input lines 24 V DC (2 high speed lines 100 kHz, 6 medium speed lines 20 kHz, 8 medium speed lines total 5 kHz);
- 12 lines of relay or transistor output (2 lines of high speed 100 kHz, 6 lines of medium speed 20 kHz);
- 1 RS232 or USB port.



Figure 16: Programmable logic controller FBs - 32MA [21]

The electric motor is a very complex control object and the PLC is not designed to control it directly [22]. Therefore, when controlling an electric motor with a PLC, a frequency inverter is also required. The three-phase model NES1 - 007 HBE, figure 17, from the catalog [23], with a nominal power of 0.75 kW, was selected.



Figure 17: Frequency inverter NES1 - 007 HBE [23]

The supporting structure of the testing device was calculated according to [24]. The chosen profile is U200, material Steel S355.

The final appearance of the testing device is shown in figure 18.



Figure 18: CAD model of the testing device

### 5. SAFETY PRECAUTIONS AT WORK WITH THE DEVICE FOR TESTING SAMPLES OF CONVEYOR BELTS

On both sides of the device, doors are planned for protection from parts of the belt sample that can break out and injure the operator of the device as well as the personnel who are nearby when the sample is torn. When working with the device, it is recommended that the device be used by one operator who will set up the belt sample and manage the test. In the case where the device would be used by two operators, it could happen that one operator sets the belt sample and the other accidentally starts the belt sample test. Although safety doors are planned, the operator and staff (students observing the test) who are near the device are required to wear goggles and safety shoes, figure 19. The device operator is required to wear protective gloves while placing the sample in the jaw device.



Figure 19: Device operator with protective equipment

Before starting the test, the operator needs to perform a visual inspection of the device, as well as the environment of the device to determine whether the device is in good condition and safe to use. In case he notices some machine elements in the vicinity of the device, it is necessary to determine whether those elements belong to the device or not. If the elements belong to the device, the test is postponed until the fault of the device is rectified.

In case the operator notices some dirt such as oil around the device or on the device itself, it is necessary to determine the cause of the dirt. When the cause of the dirt is a malfunction of the device, the test is postponed until the fault is rectified. Before starting the test, it is necessary to check whether the belt sample is properly clamped between the clamping surfaces of the jaws. When the sample is properly clamped, it is necessary to close the protective door and after that it is possible to start the test safely. After the test, the movable jaw must be returned to its initial position and then the device must be turned off. When the jaw is in the initial position and the power supply to the device is stopped, the operator can open the protective door and remove the tested belt sample.

After the test, it is necessary to clean the device for testing conveyor belts, and dispose of the tested belt sample in a safe place.

### 6. CARCASS FATIGUE

Cycling loading and offloading generally leads to fatigue failures. However, the cyclic action is not limited to tensile or compressive modes where lateral tension or compression eventually leads to failure. Repetitive bending (flexural) and twisting (torsional) are other means by which fatigue failures occur [25].

Figure 20. shows the principal differences between straight tensile failures and that of a tensile fatigue failure.

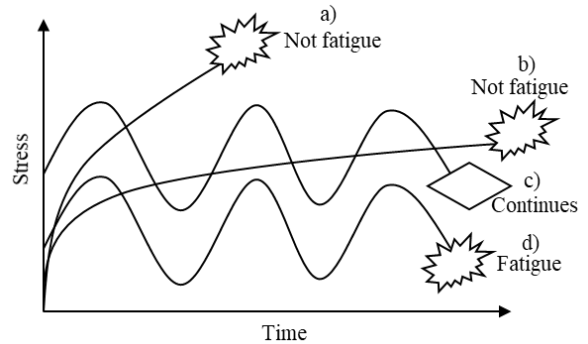


Figure 20: The principal differences between straight tensile failures and tensile fatigue failure

When a single fibre is stressed at a relatively fast speed, tensile failure eventually occurs as shown by curve a). When stress is applied at relatively slow speed, the fibre undergoes gradual extension or creep and reaches the breaking point at lower stress level over a longer period, curve b). When cyclic loading in form of reduction and increase in the applied load is experienced, as shown by the sinusoidal profile, curve c), failure never occurs. Fatigue-resistant structures, i.e., suspension bridges specialised conveyor belts and so forth, are designed and erected based on this principle. However, when cyclic loading and off loading is applied, failure occurs rather quickly. This is indeed what is commonly referred to as fatigue failure.

Fibre fatigue is relatively new concept compared to metal fatigue where unforeseen disastrous accidents in the early days of engineering led to serious consideration of metal fatigue. Since only small cyclic forces lead to fatigue failures, failure always occurs within the elastic or fully reversible regions of materials, i.e., along the Hookean region not far from the origin of stress-strain axis. Fibres differ from metals in one major way and that is fibres can not undergo compression as they tend to buckle under compressive stresses, thus giving the rather desirable aesthetic property of flexibility and drape, which is absolutely unacceptable in metals.

Fibres being semi-crystalline materials display visco-elastic behaviour, i.e., a bit of viscous liquid and a bit of elastic behaviour. This translates into a classical stress-strain curve that is common to most fibres. Elastic and plastic regions in visco-elastic materials are not clearly defined in fibrous materials.

Fibres are also anisotropic in nature, which means that there are directional restrictions for molecular alignments and thus crystallinity within a fibre. This inherent property directly influences the failure mode of the fibre depending on the directional application of the cyclic stresses. Hence fibre fatigue failures can be far more complex than metal failures. Furthermore, given the

inherent flexibility of fibres, under normal practical conditions and use, no single failure mode could be held responsible as the sole cause of the ultimate failure. Under these circumstances the fibrous materials, like conveyor carcass, could be undergoing tensile stretch/failure as well as tensile/flexural and/or torsional failures whilst also experiencing some form of abrasion and this is not even taking temperature and humidity variations into account. Hence a very confused and complex state of affairs could be the outcome of what might otherwise credulously be taken as a straightforward failure.

Where once individual experiences and trial and error methodologies were the dominant approach in design and product development, today almost exclusively all performance materials are designed and manufactured on their functional requirements and their predictive behaviour supported by in-depth understanding of their failure characteristics. Although mathematical modelling and accurate theoretical predictions masterminding performance criteria continues to remain an ongoing challenge.

## 7. CONCLUSION

The design of the device for testing conveyor belts is used to make a device that will be used for testing various conveyor belts in the laboratory of the Department of Mechanization and Design Engineering at the Faculty of Technical Sciences, University of Novi Sad, Novi Sad, R. Serbia.

Since conveyor belts are among the most responsible elements of belt conveyors, their testing before use is very important. In order to obtain the value of the force that the conveyor belt can withstand before the occurrence of its permanent deformation as well as before the occurrence of tearing of the belt, it is necessary to test the belt by applying tension.

When calculating belt conveyors for a certain material, the force that occurs in the belt is calculated. However, in practice, there are materials whose parameters are not constant values but change.

During the transport of gravel, the density of which changes due to the content of water and sludge during transport and therefore in the conveyor belt may occur forces that are greater than the value of the force obtained by the calculation. The action of such forces leads to improper operation of the conveyor, and in more extreme cases it can also lead to the failure of certain elements of the belt conveyor.

Using a belt sample testing device, it is possible to simulate the action of a force greater than the force obtained by the calculation and thus come to the conclusions of what consequences this leaves on the belt.

To obtain such data, further research is needed, which could be the topic of some future work, and in the implementation of that research, a designed device for testing conveyor belts is necessary.

## ACKNOWLEDGEMENTS

This research (paper) has been supported by the Ministry of Education, Science and Technological Development through project no. 451-03-9/2021-14/200156: "Innovative scientific and artistic research from the FTS (activity) domain".

## REFERENCES

- [1] Standard DIN 22102, (2014)
- [2] Standard ISO 282, (1992)
- [3] Standard ISO 18573, (2012)
- [4] Standard ISO 7500-1, (2018)
- [5] Standard ISO 376, (2011)
- [6] Standard ISO 283, (2015)
- [7] Standard ISO 9856, (2016)
- [8] Standard EN 873, (1996)
- [9] Standard ISO 252, (2011)
- [10] Standard ISO 21183, (2018)
- [11] Standard ISO 6133, (2015)
- [12] Standard PN-C-94147, (1997)
- [13] Standard ISO 1120, (2012)
- [14] G. Fedorko, V. Molnar, P. Michalik, M. Dovica, T. Toth and T. Klemenova, "Extension of inner structures of textile rubber conveyor belt – Failure analysis", *Engineering Failure Analysis*, Vol. 70, pp. 22-30, DOI: 10.1016/j.engfailanal.2016.07.006, (2016)
- [15] G. Fedorko, V. Molnar, P. Michalik, M. Dovica, T. Klemenova and T. Todor, "Failure analysis of conveyor belt samples under tensile load", *Journal of Industrial Textiles*, Vol. 48(8), pp. 1364-1383, DOI: 10.1177/1528083718763776, (2018)
- [16] P. R. Vieira, E. M. Lopes Carvalho, J. Domingos Vieira and R. Dias Toledo Filho, "Experimental fatigue behaviour of pultruded glass fibre reinforced polymer composite materials", *Composites Part B: Engineering*, Vol. 146, pp. 69-75, DOI: 10.1016/j.compositesb.2018.03.040, (2018)
- [17] R. Blazej, M. Hardygora, H. Komander and L. P. Jurdziak, "Method of predicting the fatigue strength in multiplies splices of belt conveyors", *Eksplatacja i Niezawodnosc - Maintenance and Reliability*, Vol. 14(2), pp. 171-175, (2013)
- [18] Mädler: Catalogue 42, Stuttgart, Germany, (2019)
- [19] Laumas: Tension (compression) load cells, Italy, (2020)
- [20] Bruster: Potentiometric Displacement Sensor, Germany, (2020)
- [21] Fatek: FBs Series Programmable Logic Controller, Taiwan, (2020)
- [22] D. Marčetić, M. Gecić and B. Marčetić, "Programabilni logički kontroleri i komunikacioni protokoli u elektroenergetici", *Fakultet tehničkih nauka Univerziteta u Novom Sadu, Novi Sad (R. Serbia)*, (2016)
- [23] Hitachi: NE-S1 Series Inverter, Japan, (2020)
- [24] Z. Petković, D. Ostrić, "Metalne konstrukcije u mašingradnji 1", *Mašinski fakultet Univerziteta u Beogradu, Beograd (R. Serbia)*, (1996)
- [25] M. Miaftab, "Fatigue failures of textile fibres", *Woodhead Publishing, Cambridge (England)*, (2009)

# Application of Water Cycle Algorithm on Ramshorn Hook Optimization Problem

Goran Pavlović<sup>1\*</sup>, Mile Savković<sup>2</sup>, Nebojša B. Zdravković<sup>2</sup>

<sup>1</sup> Faculty of Electronic Engineering, University of Niš, Niš (Serbia)

<sup>2</sup> Faculty of Mechanical and Civil Engineering in Kraljevo, University of Kragujevac, Kraljevo (Serbia)

*This research presents the problem of optimization of the most critical cross-sectional area of Ramshorn hook, where the geometric parameters of the trapezoidal and T cross-sections were taken as optimization variables. The minimization of the area of the cross-section of the Ramshorn hook was set as the main goal in this research. The stresses at the inner and outer fibers of the hook cross-section were taken according to the DIN standard, and they represented the constraint functions for the optimization model.*

*As a method of optimization, two nature-inspired metaheuristic algorithms were applied for this optimization problem, using MATLAB software: Water Cycle Algorithm (WCA) and its modified version Evaporation Rate based Water Cycle Algorithm (ER-WCA). The optimization results for both types of cross-sections were compared to show which one achieves the best results. The comparison of the applied optimization algorithms was performed, too.*

**Keywords:** Ramshorn hook, Optimization, Water cycle algorithm, Evaporation rate based water cycle algorithm

## 1. INTRODUCTION

Ramshorn hook is a very important component for lifting and hanging of heavy load capacities for heavy-duty cranes and the marine industry. Ramshorn hook should be designed and manufactured in such a way that it delivers the best performance under all working conditions without function cancellation, failure and accident. The failure depends on various factors such as material properties, geometry and overload.

The design of a crane hook involves the determination of parameters such as type of material, the cross-sectional area, and shape, the radius of curvature, etc. For this reason, the problem of analysis and optimization design of a crane hook is the subject of research in many publications.

The analysis of these types of equipment is mainly done by applying FEM. In the paper [1], an analysis of one standard hoist hook with a capacity of 20 tons was carried out using Autodesk Simulation software. The paper [2] presents the FEM analysis of Ramshorn hook using ANSYS software package, where a comparison of circular cross-section with T and I cross-sections was performed.

In the research [3], the design of a hoisting mechanism of an EOT crane is presented, with the FEM analysis of the crane hook in the ANSYS software package. The cross-section of one standard hook was modified, and other different cross-sectional shapes were also observed, such as circular, square, trapezoidal and triangular cross-sections. In the paper [4], the design and validation of the hook with T cross-section, used in double spring balancers are given. CREO and ANSYS software packages were used for the 3D model and FEM analysis.

Recently, laminated crane hooks have become increasingly used. The review paper [5] gives an overview of the literature about the design, analysis and optimization of this type of equipment.

The paper [6] presents an analysis of the fracture of a hook-shaped steel rod from a lifting beam, resulting from the torsional overload of the hook body, where

microstructural, fractographic, and strength evaluation were used as analytical techniques.

In addition to FEM, analysis can also be done analytically. In the paper [7], the stresses at the characteristic points of the critical cross-section of one standard crane hook were calculated using an approximate method and using two exact methods, where these values were compared with the critical stresses according to DIN standard. The recommendations are given in the case where the stresses are calculated by an approximate method.

Numerical optimization methods are of great use for engineering problems, especially metaheuristic optimization algorithms. In the paper [8], the optimization of different cross-sections of a crane hook was performed using several metaheuristic algorithms. In the paper [9], the optimization and comparison for two cases of T and I cross-sections of a crane hook were performed, using two physics-inspired optimization algorithms.

Based on the above publications, it can be seen the importance of the analysis and optimization of these types of equipment. This research will be carried out the optimization of the trapezoidal cross-section of Ramshorn hook, as well as T cross-section of one standard hook capacity. It also will be carried out and a comparison of results for both cross-sections.

## 2. OPTIMIZATION PROBLEM

### 2.1. Optimization model:

The next figure shows one standard Ramshorn hook, according to [11], as well as the static model for calculation (Fig. 1).

Also, Fig. 1 shows the critical place (A–A) where the analysis and optimization of the cross-section are performed, which is the topic of this research.

The goal of the research for this optimization problem is to minimize the objective function (cross-sectional area) subjecting the constraint functions, which are composed of critical stresses.

\*Corresponding author: Aleksandra Medvedeva 14, 18000 Niš, Serbia, goran.pavlovic@elfak.ni.ac.rs

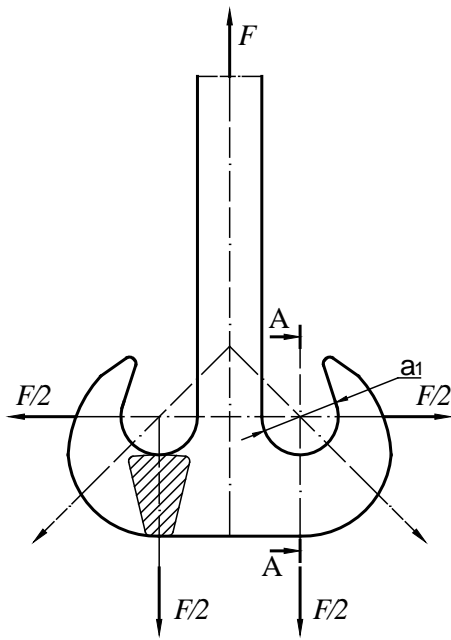


Figure 1: Ramshorn hook

The mathematical formulation of the objective function is:

$$f(X) = A(X) = A(x_1 \dots x_n), \quad (1)$$

where the parameters from  $x_1$  to  $x_n$  present the optimization variables.

The input parameters for this optimization problem are:

$F$  - the lifting force, according to [10],

$a_1$  - inner diameter (Fig. 1), according to [11],

$\sigma_{z,g}$ ,  $\sigma_{d,g}$  - critical stresses, according to [10].

Below will be present the objective functions for both profiles and the constraint functions.

### 2.2. Objective function for trapezoidal cross-section:

The objective function is represented by the area of trapezoidal cross-section of Ramshorn hook at the most critical location (A – A, Fig. 1).

The cross-sectional area (Fig. 2), the objective function, is:

$$A = A_r = \frac{b_1 + b_2}{2} \cdot h \quad (2)$$

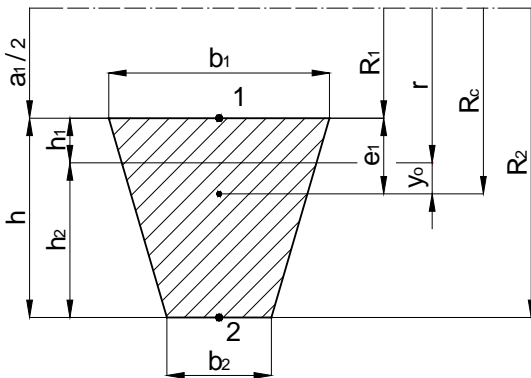


Figure 2: Trapezoidal cross-section

The previous figure shows the geometric relationships between parameters that are required for the calculation, where:

$e_1$  - the position of the center of the cross-section (Fig. 2),

$R_1$  - the radius of inner fiber (Fig. 2),

$R_2$  - the radius of outer fiber (Fig. 2),

$R_c$  - the radius of the centroidal axis (Fig. 2),

$r$  - the radius of the neutral axis (Fig. 2),

$y_o$  - the distance between the centroidal axis and the neutral axis (Fig. 2).

Other geometrical parameters and variables that are the subject of optimization, are shown in Fig. 2.

The radius of the neutral axis is defined in the following way, (3) and (4):

$$r = \frac{A_r}{\int_{A_r} \frac{dA}{\rho}} \quad (3)$$

$$\int_{A_r} \frac{dA}{\rho} = b_1 \cdot \left( e_o + \frac{a_1 + 2 \cdot h}{2} \cdot \frac{1 - e_o}{h} \right) \cdot \ln \frac{a_1 + 2 \cdot h}{a_1} - b_1 \cdot (1 - e_o), \quad e_o = b_2 / b_1 \quad (4)$$

### 2.3. Objective function for T cross-section:

The objective function is represented by the area of T cross-section of Ramshorn hook at the most critical location (A – A, Fig. 1).

The cross-sectional area (Fig. 3), the objective function, is:

$$A = A_r = b \cdot t + h \cdot s \quad (5)$$

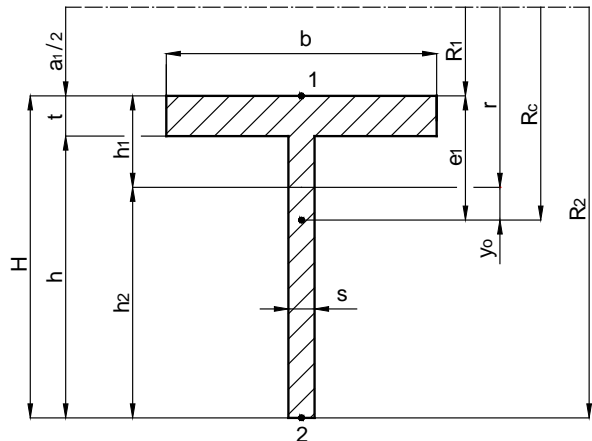


Figure 3: T cross-section

The previous figure shows the geometric relationships between parameters that are required for the calculation, and their meaning is the same as in the previous case.

The radius of neutral axis is defined in following way, (6) and (7):

$$r = \frac{A_r}{\int_{A_r} \frac{dA}{\rho}} \quad (6)$$

$$\int_{A_r} \frac{dA}{\rho} = b \cdot \ln \frac{a_1 + 2 \cdot t}{a_1} + s \cdot \ln \frac{a_1 + 2 \cdot (h + t)}{a_1 + 2 \cdot t} \quad (7)$$

### 2.4. Constraint functions:

The optimization process is based on critical stresses, according to [10], where crane hook is treated as a curved beam.

The maximum values for normal stresses in the characteristic points (point 1 and point 2, Fig. 2 and Fig. 3) are:

$$\sigma_z = \frac{F}{2 \cdot A} + \frac{M}{S_x} \cdot \frac{h_1}{R_1} \quad (8)$$

and

$$\sigma_d = \frac{F}{2 \cdot A} - \frac{M}{S_x} \cdot \frac{h_2}{R_2} \quad (9)$$

$$M = \frac{F}{2} \cdot R_c \quad (10)$$

$$S_x = A \cdot y_o \quad (11)$$

where:

$M$  - the bending moment,

$S_x$  - the static moment of the area.

The maximum values for shear stress is:

$$\tau = \frac{F}{2 \cdot A} \quad (12)$$

Finally, the mathematical formulation of the constrain functions are:

$$g_1 = \sigma_1 = \sqrt{\sigma_z^2 + 3 \cdot \tau^2} \leq \sigma_{z,g} \quad (13)$$

and

$$g_2 = \sigma_2 = \sqrt{\sigma_d^2 + 3 \cdot \tau^2} \leq \sigma_{d,g} \quad (14)$$

Also, this analysis is adopted that the minimum value of the thickness of the profile is  $0.5 \text{ cm}$  (for T cross-section).

### 3. APPLIED OPTIMIZATION ALGORITHMS

In this paper, the optimization procedure was performed using two metaheuristic algorithms based on nature: Water Cycle Algorithm (WCA) and its modified version Evaporation Rate based Water Cycle Algorithm (ER-WCA). Both algorithms are simulated in the MATLAB software.

The Water Cycle Algorithm (WCA) as an optimization method is introduced in [12]. The fundamental concepts and ideas which underlie the WCA are inspired by nature and based on the observation of the water cycle process and how rivers and streams flow to a sea in the real world. Similarly to other metaheuristic algorithms, the proposed method begins with an initial population, the so-called raindrops. The best individual (best raindrop) is chosen as a sea. Then, a number of good raindrops are chosen as a river and the rest of raindrops are considered as streams which flow to the rivers and the sea. The paper [13] provides a detailed open source code for the WCA, of which the performance and efficiency has been demonstrated for solving engineering constrained optimization problems.

The Evaporation Rate based Water Cycle Algorithm (ER-WCA) is a modified version of the WCA, [14]. In order to define this concept, in the ER-WCA, the evaporation process is modified by adding the concept of evaporation rate, which offers improvement in search. Furthermore, the evaporation condition is also applied for the streams that directly flow to the sea based on the new approach. The ER-WCA shows a better balance between exploration and exploitation phases compared to the standard WCA. The ER-WCA was able to find the global

minimum in multi-criteria optimization problems with a minimum possibility of getting trapped in the local minimum.

The source codes for both algorithms are present on the website [15].

### 4. OPTIMIZATION RESULTS

The optimization process was performed using the mentioned algorithms WCA and ER-WCA. The source codes were taken from the website [15], written for MATLAB software.

The optimization variables are  $b_1$ ,  $h$ , and  $b_2$  for trapezoidal cross-section (Fig. 2) and  $b$ ,  $t$ ,  $h$  and  $s$ , for T cross-section (Fig. 3). Input parameters for optimization, according to [10] are:  $F=80 \text{ kN}$  (for the hook capacity:  $Q=8 \text{ t}$ , drive group: 3m, strength class: S) and  $a_1=6.3 \text{ cm}$ . The permissible stresses are taken according to [10], and their values are:  $\sigma_{z,g}=15 \text{ kN/cm}^2$  – tensile critical stress and  $\sigma_{d,g}=6.3 \text{ kN/cm}^2$  – compressive critical stress.

The cross-sectional area of standard crane hook [11], in comparison to which the optimal results are compared is:  $A_s=24.857 \text{ cm}^2$ . Some geometrical constraints (height and width) were taken, too.

For both algorithms, population size is: 200, number of rivers+sea: 4 and number of iterations: 1000 (control parameters for optimization).

The following tables show the results of optimization for trapezoidal cross-section (optimal cross-sectional geometric parameters and areas, convergence characteristics and savings in material) for both algorithms, (Table 1÷Table 3).

Table 1: Results of optimization for trapezoidal cross-section

| Method                   | WCA              | ER-WCA        |
|--------------------------|------------------|---------------|
| $b_1$ (cm)               | 2.641352         | 2.645896      |
| $h$ (cm)                 | 15.243012        | 15.216829     |
| $b_2$ (cm)               | 0                | 0             |
| time (s)                 | <b>13.848421</b> | 16.549830     |
| Best (cm <sup>2</sup> )  | <b>20.131</b>    | <b>20.131</b> |
| Mean (cm <sup>2</sup> )  | 20.148           | <b>20.134</b> |
| Worst (cm <sup>2</sup> ) | 27.668           | <b>21.842</b> |
| Std                      | 0.324            | <b>0.057</b>  |
| Saving (%)               | 19.01            | 19.01         |

Table 2: Results of optimization for trapezoidal cross-section with constraint ( $H_{max}=6.7 \text{ cm}$ )

| Method                   | WCA              | ER-WCA        |
|--------------------------|------------------|---------------|
| $b_1$ (cm)               | 4.616152         | 4.616152      |
| $h$ (cm)                 | 6.7              | 6.699999      |
| $b_2$ (cm)               | 2.678085         | 2.678086      |
| time (s)                 | <b>14.078390</b> | 14.361893     |
| Best (cm <sup>2</sup> )  | <b>24.436</b>    | <b>24.436</b> |
| Mean (cm <sup>2</sup> )  | <b>24.445</b>    | 24.458        |
| Worst (cm <sup>2</sup> ) | <b>27.290</b>    | 32.798        |
| Std                      | <b>0.141</b>     | 0.318         |
| Saving (%)               | 1.69             | 1.69          |

Table 3: Results of optimization for trapezoidal cross-section with constraint ( $H_{max}=10$  cm)

| Method                   | WCA           | ER-WCA           |
|--------------------------|---------------|------------------|
| b <sub>1</sub> (cm)      | 3.454282      | 3.454283         |
| h (cm)                   | 10            | 10               |
| b <sub>2</sub> (cm)      | 0.776428      | 0.776428         |
| time (s)                 | 16.587225     | <b>16.122742</b> |
| Best (cm <sup>2</sup> )  | <b>21.154</b> | <b>21.154</b>    |
| Mean (cm <sup>2</sup> )  | 21.167        | <b>21.157</b>    |
| Worst (cm <sup>2</sup> ) | 25.513        | <b>23.850</b>    |
| Std                      | 0.233         | <b>0.086</b>     |
| Saving (%)               | 14.90         | 14.90            |

The following tables show the results of optimization for T cross-section (optimal cross-sectional geometric parameters and areas, convergence characteristics and savings in material) for both algorithms, (Table 4÷Table 7).

Table 4: Results of optimization for T cross-section

| Method                   | WCA           | ER-WCA           |
|--------------------------|---------------|------------------|
| b (cm)                   | 6.070106      | 6.070106         |
| t (cm)                   | 0.5           | 0.5              |
| h (cm)                   | 18.978059     | 18.978059        |
| s (cm)                   | 0.5           | 0.5              |
| time (s)                 | 17.216509     | <b>15.875222</b> |
| Best (cm <sup>2</sup> )  | <b>12.524</b> | <b>12.524</b>    |
| Mean (cm <sup>2</sup> )  | 12.558        | <b>12.543</b>    |
| Worst (cm <sup>2</sup> ) | 30.619        | <b>26.777</b>    |
| Std                      | 0.685         | <b>0.458</b>     |
| Saving (%)               | 49.62         | 49.62            |

Table 5: Results of optimization for T cross-section with constraint ( $H_{max}=6.7$  cm)

| Method                   | WCA           | ER-WCA           |
|--------------------------|---------------|------------------|
| b (cm)                   | 11.340956     | 11.339729        |
| t (cm)                   | 0.5           | 0.5              |
| h (cm)                   | 6.2           | 6.2              |
| s (cm)                   | 2.405889      | 2.405988         |
| time (s)                 | 18.525694     | <b>16.721073</b> |
| Best (cm <sup>2</sup> )  | <b>20.587</b> | <b>20.587</b>    |
| Mean (cm <sup>2</sup> )  | 20.967        | <b>20.648</b>    |
| Worst (cm <sup>2</sup> ) | <b>32.519</b> | 44.314           |
| Std                      | 1.562         | <b>1.025</b>     |
| Saving (%)               | 17.18         | 17.18            |

Table 6: Results of optimization T cross-section with constraints ( $b_{max}$ ,  $H_{max}=6.7$  cm)

| Method                   | WCA              | ER-WCA        |
|--------------------------|------------------|---------------|
| b (cm)                   | 6.7              | 6.7           |
| t (cm)                   | 0.607912         | 0.588040      |
| h (cm)                   | 6.092088         | 6.111960      |
| s (cm)                   | 2.821345         | 2.834086      |
| time (s)                 | <b>15.932656</b> | 16.322639     |
| Best (cm <sup>2</sup> )  | <b>21.261</b>    | 21.262        |
| Mean (cm <sup>2</sup> )  | <b>21.562</b>    | 21.568        |
| Worst (cm <sup>2</sup> ) | 33.245           | <b>29.585</b> |
| Std                      | 1.256            | <b>1.236</b>  |
| Saving (%)               | 14.47            | 14.46         |

Table 7: Results of optimization for T cross-section with constraint ( $H_{max}=10$  cm)

| Method                   | WCA       | ER-WCA           |
|--------------------------|-----------|------------------|
| b (cm)                   | 9.276761  | 9.176871         |
| t (cm)                   | 0.5       | 0.5              |
| h (cm)                   | 9.5       | 9.5              |
| s (cm)                   | 1.189075  | 1.194284         |
| time (s)                 | 18.112465 | <b>16.886159</b> |
| Best (cm <sup>2</sup> )  | 15.935    | <b>15.934</b>    |
| Mean (cm <sup>2</sup> )  | 16.012    | <b>15.950</b>    |
| Worst (cm <sup>2</sup> ) | 31.315    | <b>22.507</b>    |
| Std                      | 0.680     | <b>0.281</b>     |
| Saving (%)               | 35.89     | 35.90            |

The following figures show the convergence diagrams for the mentioned methods of optimization and cross-sectional types (Fig. 4÷Fig. 10).

## 5. CONCLUSION

It can be noted that the optimization task was successfully realized, as can be seen from the values of savings in material, shown in the previous tables (Table 1÷Table 7). In this case, a saving of 19% was achieved for trapezoidal cross-section, while for T cross-section, savings of as much as 49% were achieved.

For both types of cross-section profiles, the optimum height values are significantly higher than the standard height (6.7 cm) for the observed example (Table 1 and Table 4). In the case of the trapezoidal cross-section, for optimal geometric values, a triangular cross-section was obtained (Table 1). For this reason, additional geometric constraints are included.

With the height restriction ( $H_{max}=6.7$  cm), for the trapezoidal cross-section, very small savings are obtained (Table 2), which means that the standard hook for the observed example is designed optimally since the cross-section of the standard hook is a trapezoidal shape. With increasing height ( $H_{max}=10$  cm), the value of the optimum cross-sectional area decreases (Table 3).

In the case of T cross-section, with height restriction ( $H_{max}=6.7$  cm), an enviable value of material savings was achieved, but the width of the profile base was much larger (Table 5). For this reason, the width restriction of the profile base was also observed, so that there was a slight increase in the optimum cross-sectional area, which was expected (Table 6). With increasing height ( $H_{max}=10$  cm), the value of the optimum cross-sectional area decreases (Table 7). Finally, it should be noted that this cross-sectional shape gives a much lower value of the optimum cross-sectional area in comparison to the trapezoidal cross-section.

Regarding the applied optimization algorithms, it should be said that in most cases both algorithms gave the same values of optimal surfaces. In most cases, the ER-WCA algorithm achieves better values of the convergence diagram parameters, and especially for the standard deviation value (Table 1÷Table 7).

Regarding the time it takes to perform the optimization process, in some cases the first optimization method performed better time, and in some cases the second method (Table 1÷Table 7).

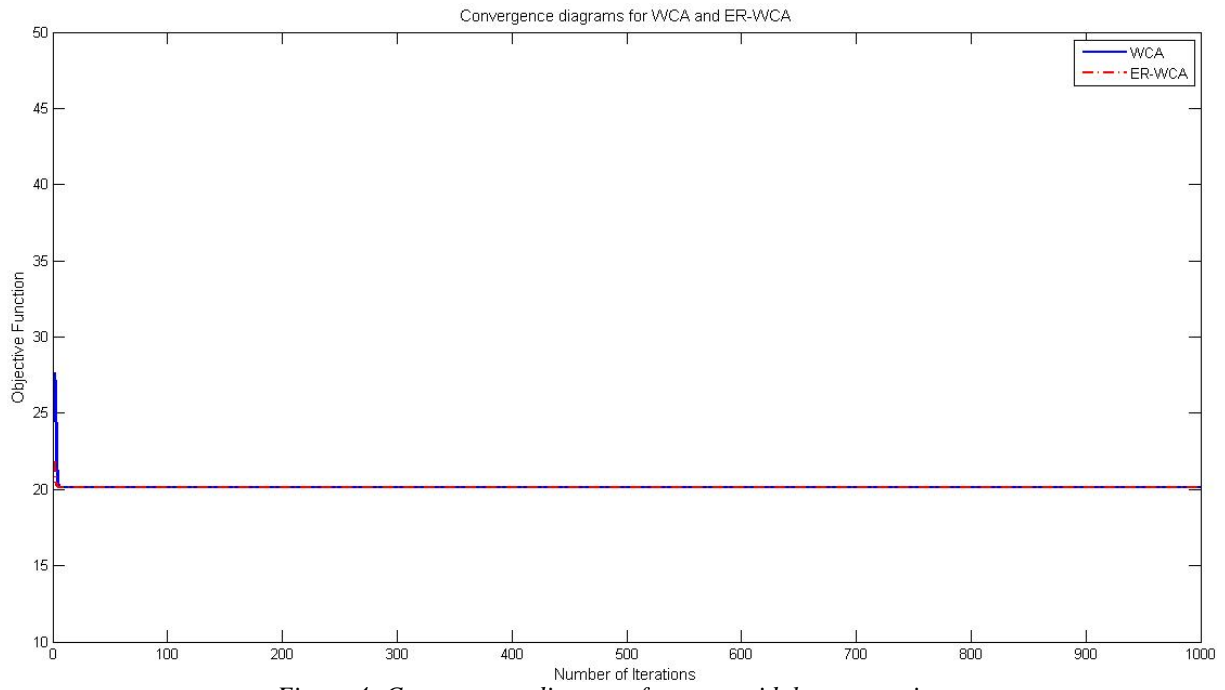


Figure 4: Convergence diagrams for trapezoidal cross-section

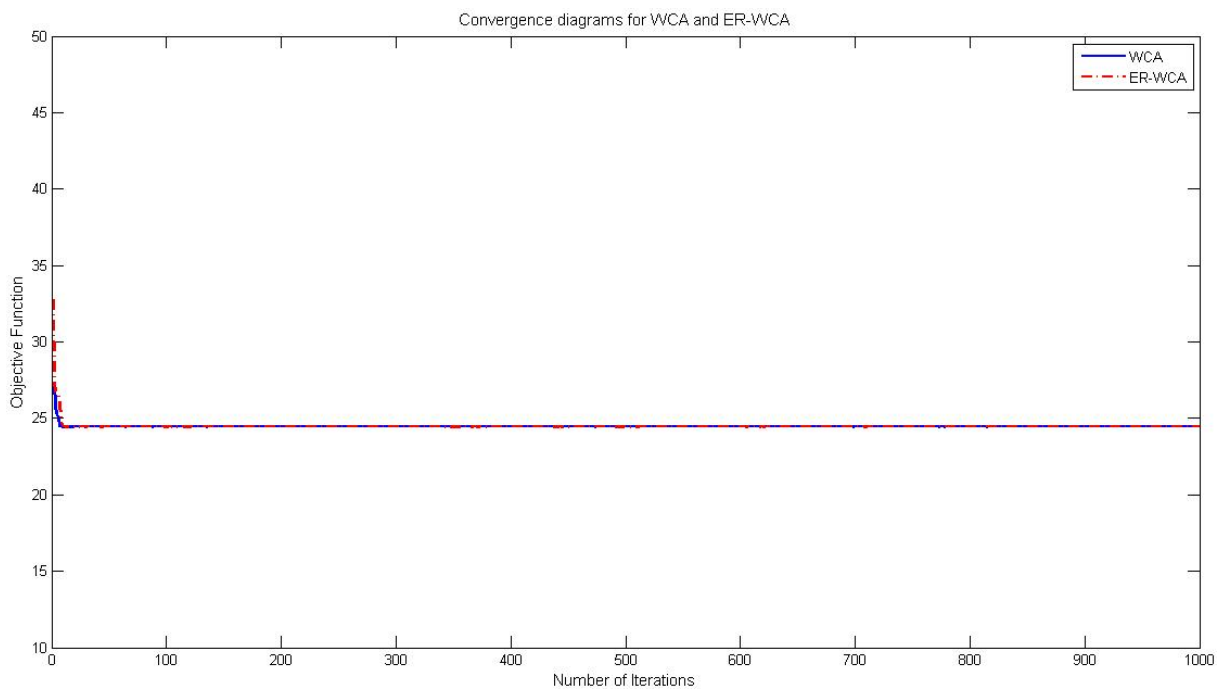


Figure 5: Convergence diagrams for trapezoidal cross-section with constraint ( $H_{max}=6.7$  cm)

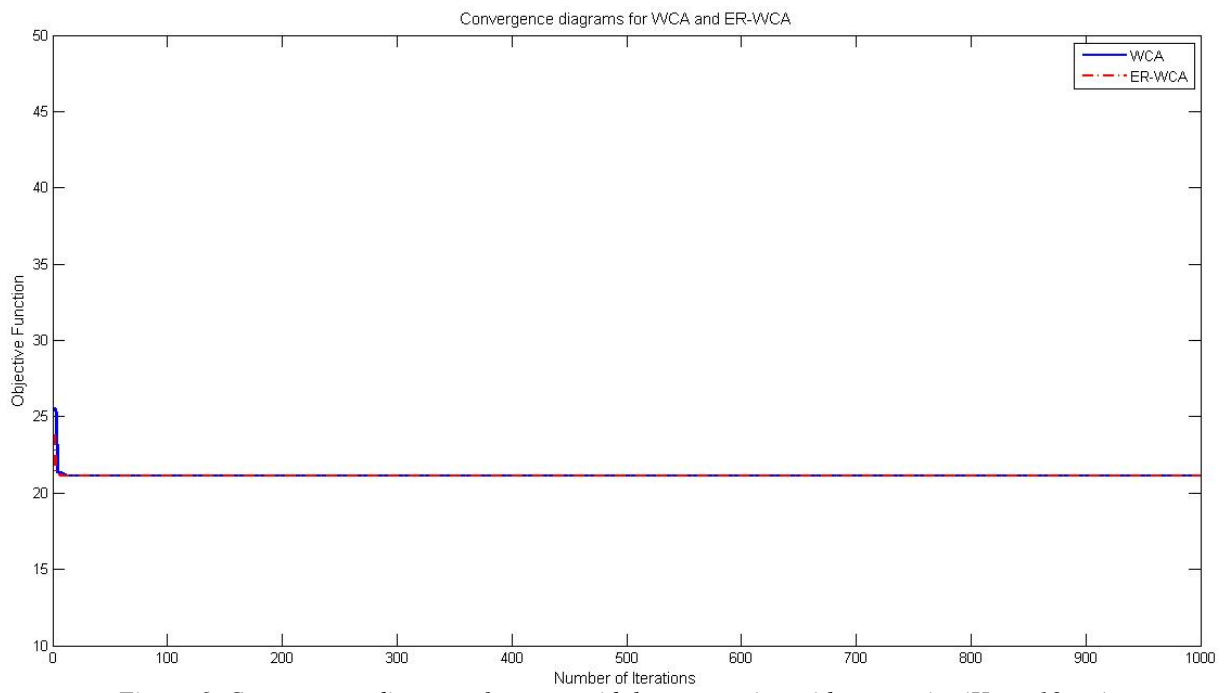


Figure 6: Convergence diagrams for trapezoidal cross-section with constraint ( $H_{max}=10$  cm)

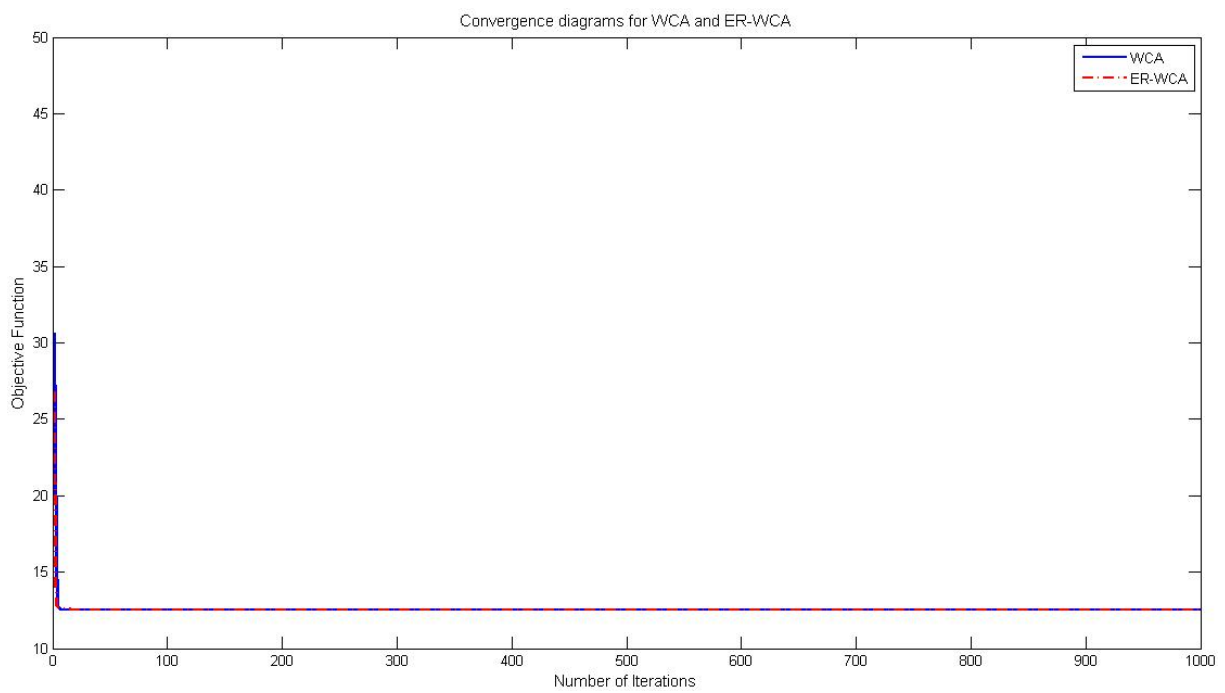


Figure 7: Convergence diagrams for T cross-section

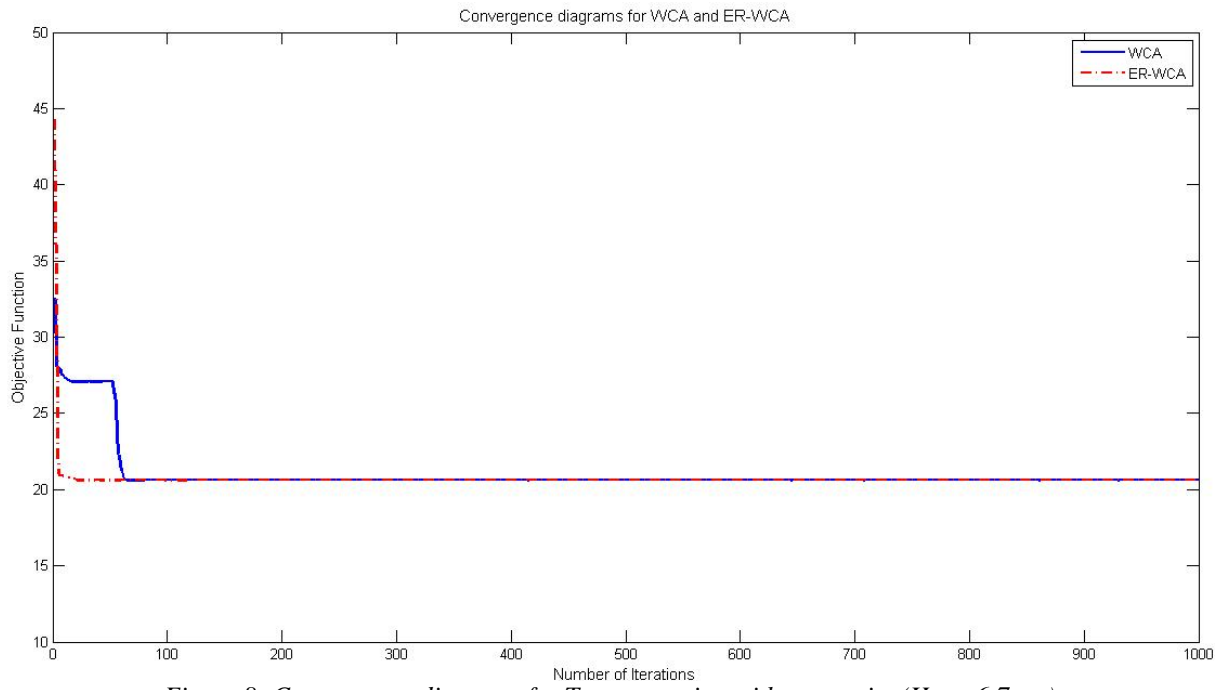


Figure 8: Convergence diagrams for  $T$  cross-section with constraint ( $H_{max}=6.7$  cm)

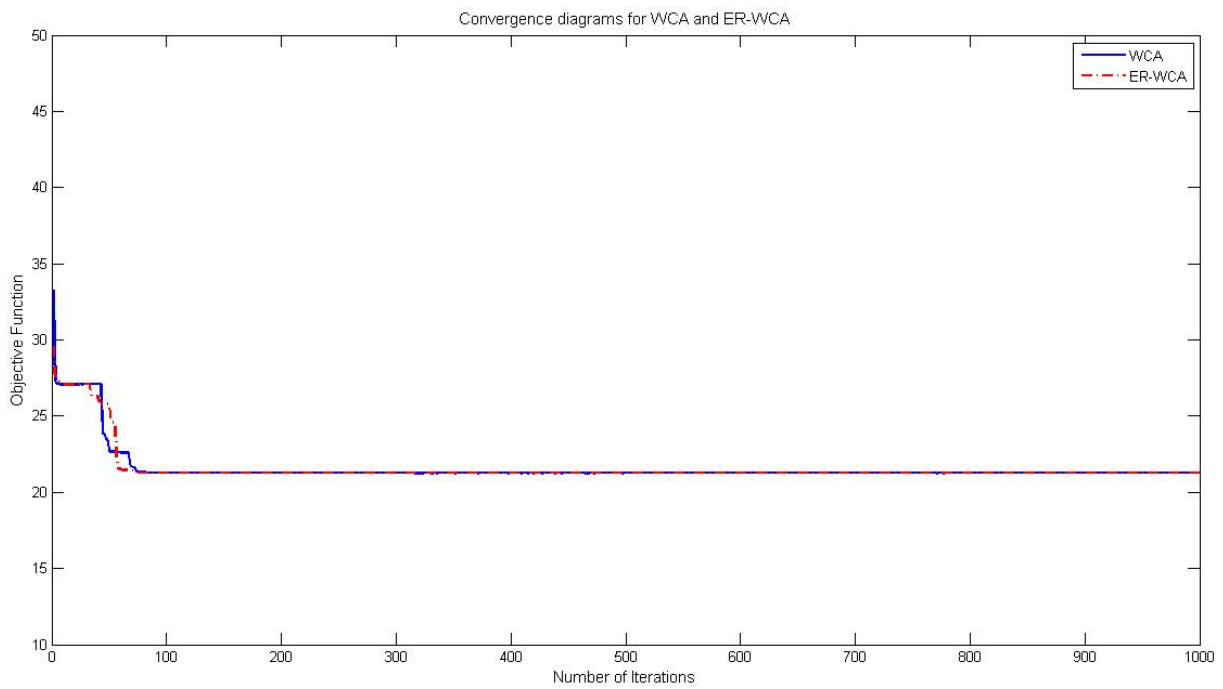


Figure 9: Convergence diagrams for  $T$  cross-section with constraints ( $b_{max}, H_{max}=6.7$  cm)

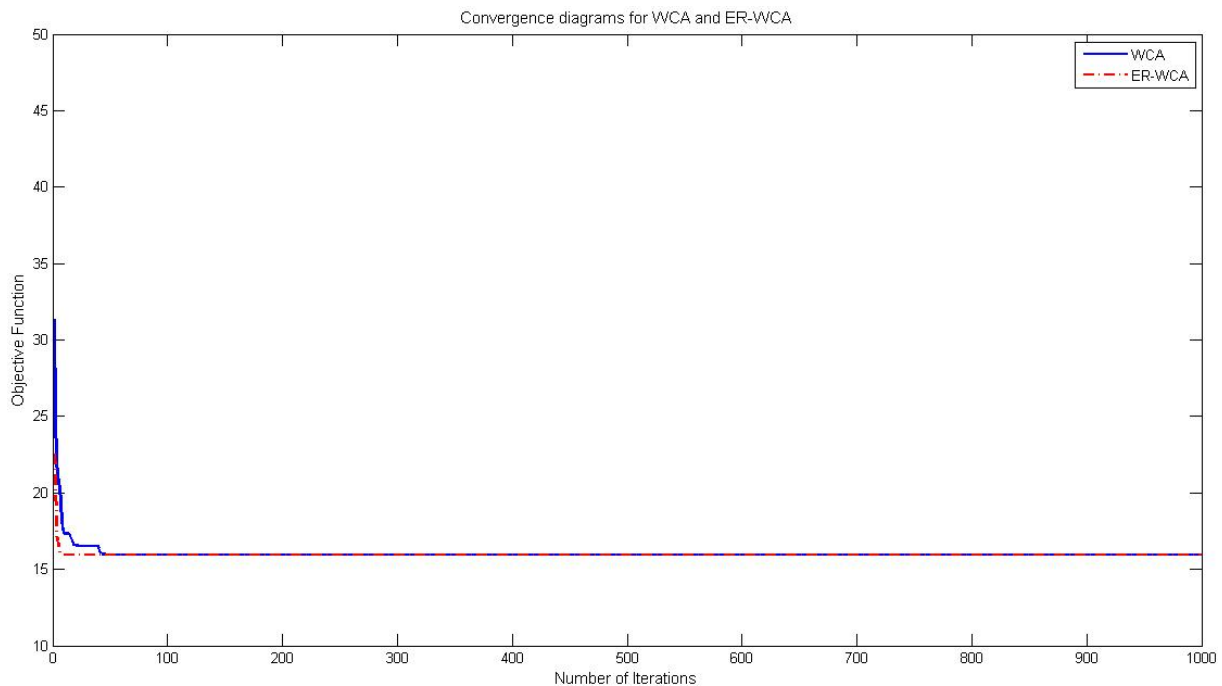


Figure 10: Convergence diagrams for T cross-section with constraint ( $H_{max}=10$  cm)

#### ACKNOWLEDGEMENTS

This work has been supported by the Ministry of Education, Science and Technological Development of the Republic of Serbia, through the Contract for the scientific-research activity realization and financing in 2021, 451-03-9/2021-14/200108.

#### REFERENCES

- [1] C. Xu and B. Luo, "Finite Element Analysis of Hook Structure Based on Autodesk Simulation", *Advances in Computer Science Research*, Vol. 75, pp. 201–204, (2018)
- [2] N. Khan, G. Bhushan and P. Chandna, "Design and Stress Analysis of Ramshorn Hook with Different Cross Section using CAE Tools", *IJETS*, Vol. 4(1), pp. 1-8, (2017)
- [3] P.K. Maharanain, "Computer Aided Analysis and Design of Hoisting Mechanism Of an EOT Crane", BSc Thesis, National Institute of Technology Rourkela (India), (2012)
- [4] S.S. Sampath, S. Sawan and P.S.M. Chithirai, "Design and Validation of Hook Used in Double Spring Balancer for the Suspension of Weight using FEA Technique", *International Journal of Energy Science and Engineering*, Vol. 1(4), pp. 141-147, (2015)
- [5] S.J. Tiwari and V. Padole, "Design, Analysis and Material Optimization of Laminated Crane Hook: A Review," *IJAEEFA*, Vol. 2(3), pp. 109-111, (2015)
- [6] G.A Pantazopoulos, "Failure Analysis of a Fractured Hook-Shaped Steel Rod from a Lifting Weight Bridge Beam," *J Fail. Anal. and Preven.*, Vol. 10, pp. 18-22, (2010)
- [7] D. Ozer, A.B. Erdil and I. Gerdemeli, "Finite Element Approach to 3-D Modelling and Stress Analysis for Crane Lifting Hooks", 11<sup>th</sup> International Research/Expert Conference "Trends in the Development of Machinery and Associated Technology" TMT 2007, Hammamet (Tunisia), 05–09 September, pp. 1007-1010, (2007)
- [8] G. Pavlović, M. Savković, N. Zdravković, G. Marković and M. Gašić, "Optimization of Crane Hooks Considered as Curved Beams with Different Cross-sections – A Comparative Study Using MATLAB", *XXIII International Conference on Material Handling, Construction and Logistics "MHCL'19"*, Vienna (Austria), 18–20 September, pp. 59-64, (2019)
- [9] G. Pavlović, M. Savković, N. Zdravković, and G. Marković, "Comparative analysis and optimization of T and I cross sections of crane hook using by two physics-inspired algorithms", *IMK – 14, Research&Development in Heavy Machinery*, Vol. 25(3), pp. 87-95, (2019)
- [10] DIN 15 400: Lifting hooks – Materials, mechanical properties, lifting capacity and stresses, Deutsches Institut für Normung, Berlin (Germany), (1990)
- [11] DIN 15 402: Lifting hooks for lifting appliances – Ramshorn hooks - Unmachined parts, Deutsches Institut für Normung, Berlin (Germany), (1982).
- [12] H. Eskandar, A. Sadollah, A. Bahreininejad and M. Hamdi, "Water cycle algorithm – A novel metaheuristic optimization method for solving constrained engineering optimization problems", *Computers and Structures*, Vols. 110-111, pp. 151–166, (2012)
- [13] A. Sadollah, H. Eskandar, H.M. Lee, D.G. Yoo and J.H. Kim, "Water cycle algorithm: A detailed standard code", *SoftwareX*, Vol. 5, pp. 37-43, (2016)
- [14] A. Sadollah, H. Eskandar, A. Bahreininejad and J.H. Kim, "Water cycle algorithm with evaporation rate for solving constrained and unconstrained optimization problems", *Applied Soft Computing Journal*, Vol. 30, pp. 58-71, (2015)
- [15] <https://ali-sadollah.com/water-cycle-algorithm-wca/>

# Finding the Optimal Shape of Hydraulic Scissors Lift Legs Using HHO Optimization Method

Marko Todorović<sup>1\*</sup>, Radovan Bulatović<sup>1</sup>, Mile Savković<sup>1</sup>, Goran Marković<sup>1</sup>

<sup>1</sup>Faculty of Mechanical and Civil Engineering in Kraljevo, University of Kragujevac, SERBIA

*By analysing the forces in legs of the hydraulic scissors lift using symbolic variables, the expressions for stress have been derived. Novel Harris hawks optimization algorithm had been used in order to get the optimal values of variables that present geometrical characteristics of the cross section of the hydraulic scissors legs, for the given scissors lift. By connecting the optimal cross sections across the length of the scissors lift legs, optimal geometric shape of the scissors lift legs had been acquired, and displayed in this paper.*

**Keywords:** Harris hawks optimization, hydraulic scissors lift, optimal shape of scissors lift legs

## 1. INTRODUCTION

Lifting platforms that employ the scissors mechanism are very commonly used in various situations where it is needed for load that contains objects, people, or both at the same time to be transferred across the vertical plane. They can be installed permanently in which case they cannot be easily moved to different locations without disassembling them. There are also mobile lifting platforms with scissors mechanism where the mechanism is installed on some kind of carts or trailers.

The mechanism itself is consisted of one pair of beams on each side that are connected in the middle, making one pair of scissors. Multiple pairs of scissors can be stacked on top of each other which enables the platform to be lifted to higher altitude with shorter beams.

Lifting is usually accomplished by hydraulic or pneumatic cylinders that are connected to the beams of the scissors mechanism, so the whole mechanism can be illustrated as presented in figure 1.

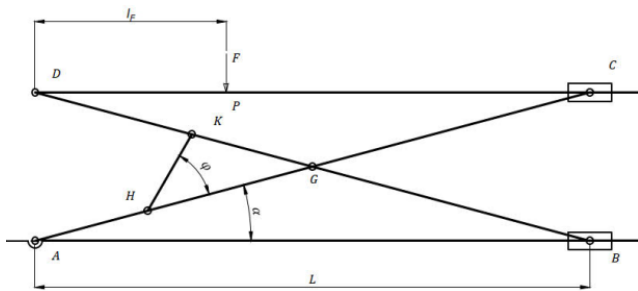


Figure 1: Illustration of the lifting platform with scissors mechanism

By elongating the hydraulic or pneumatic cylinder, the angle between the beams changes which, as one end of each beam is fixed, leads to platform changing the altitude and load being lifted.

During the design process of any piece of machinery or mechanism, the goal is to achieve the best performance and stability, while lowering the amount of material used for construction. That is a good practice because, not only it makes the final product cheaper, but it makes it lighter which reduces the dead load, hence the energy needed for the mechanism to work is lower.

The dead load reduction can be accomplished by using the optimal geometrical shape of the beams, and the optimal shape can be derived using different optimization methods.

In papers [1] and [2] the kinetic analysis of hydraulic scissor lifts with a single set of scissors is being represented, while in the article [3] more general expressions were derived for lifting platforms with multiple sets of scissors stacked on each other. Using similar mathematical model, kinetic analysis will be done in such way that it can be used as starting point for the optimization algorithm.

Optimization represents a process where the most superior values of the parameters (variables) are obtained based on the given constraint functions, for the observed objective function. [4] There are many optimization methods that can be used for successfully completing this task. In past decades, many new p-metaheuristic methods have been developed, and one of them, the novel Harris Hawk optimization method that was purposed in the article [5], will be used for performing the optimization.

## 2. HARRIS HAWK OPTIMIZATION

Harris hawk optimization, described in detail in the article [5] is metaheuristic, population based optimization method. Its creation is inspired by the specific ways Harris hawks hunt in groups.

Initial population in this method is consisted of randomly generated positions of hawks in set boundaries which represent hunting area. The best solution in each iteration represents the prey which escapes within the searching area. Based on prey's energy, hawks change the way they attack the prey. Energy of the prey represents the value of the objective function for the values of parameters that are being stored inside of the prey's location.

As the hawks hunt the prey, the location of the hawks evolves through the iterations until the set number of iterations has been completed following this rule:

$$X(t+1) = \begin{cases} X_{rand}(t) - r_1 |X_{rand}(t) - 2r_2 X(t)| & q \geq 0.5 \\ (X_{rabbit}(t) - X_m(t)) - r_3 (LB + r_4 (UB - LB)) & q < 0.5 \end{cases} \quad (1)$$

...where the  $X_{rand}(t)$  represents location of random hawk in the previous iteration  $t$ ,  $X(t)$  represents the location of each hawk in iteration  $t$ ,  $X_{rabbit}(t)$  is the location of the prey in the iteration,  $LB$  and  $UB$  are limits of the searching area,  $q$  is the chance for hawks to choose each perching

strategy, and  $X_m(t)$  is the average position of all hawks in the current iteration.

Energy of the prey is modelled in the way that it decreases through iterations, as the prey, mostly rabbit gets more and more tired as it is being chased by the hawks. If the value of the energy of the prey is less than 1, it means the rabbit is weak enough for hawks to attack it. This means that the optimization algorithm switches from the phase of exploration to the phase of exploitation. The energy of the prey is being calculated using the following rule:

$$E = 2E_0 \left(1 - \frac{t}{T}\right) \quad (2)$$

In the equation (2),  $E_0$  is the number that randomly changes its value in the interval (-1,1),  $t$  is the number of the current iteration, while  $T$  is the total number of iterations. Different phases of the optimization process are being illustrated in the figure 2.

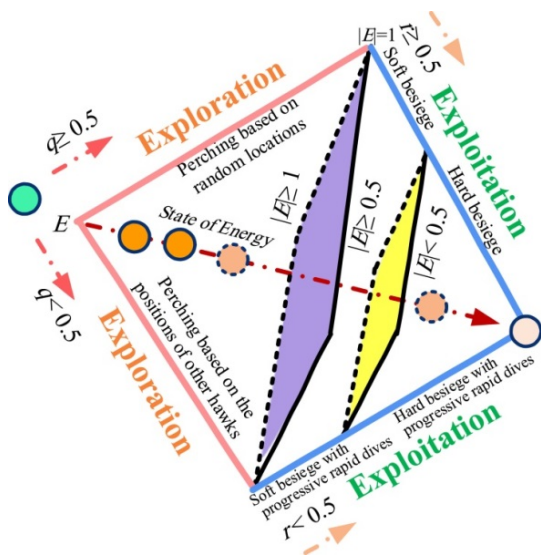


Figure 2: Different phases of Harris Hawks optimization algorithm [6]

The source code provided with the article [5] is consisted of four scripts written in MathWorks Matlab programming languages: *main.m*, *initialization.m*, *HHO.m*, *Get\_Function\_details.m*.

The “*main.m*” script is the script where the number of members of initial population (number of hawks) is being defined, the name of the object function that is addressing the function with the exact name from the “*Get\_Function\_details.m*” file, as well as the total number of iterations the optimization algorithm is supposed to complete. This script is the script that starts the optimization process, and it calls all other scripts and functions. The first script that is being called is the “*Get\_Function\_details.m*” script which contains all the needed information about the object function: lower and upper boundaries of the searching area, the dimension of the problem, and it calculates the value of the object function. This is the file that is usually being modified for the purpose of performing custom optimization.

When the needed parameters are defined as output from the previous script, the script “*HHO.m*” is being called. Input for this script contains all of the previously defined variables: number of members of the initial population, total number of iterations, limits of the

searching area, as well as the value of the object function. This script first calls the “*initialization.m*” script which then creates the initial population following the rules defined in previous steps, after which the optimization process begins. The initial population evolves through iterations until the maximum number of iterations is completed. The outputs from the “*HHO.m*” are the “*Rabbit\_Location*” (optimal values of the optimized variables) and the “*Rabbit\_Energy*” (value of the object function for the values of optimized variables). Illustration of the algorithm is shown in the figure 3.

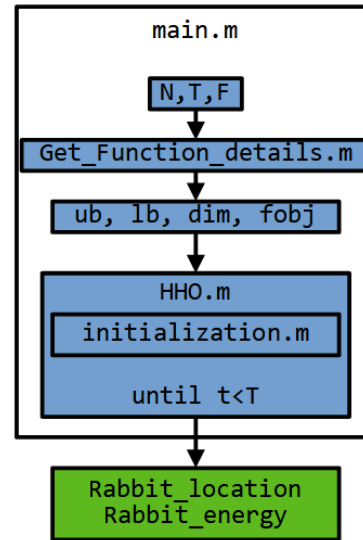


Figure 3: Illustration of the source code of the HHO algorithm:  $N$  – number of hawks,  $T$  – total number of iterations,  $F$  – name of the function,  $ub$ ,  $lb$  – boundaries of the searching interval,  $dim$  – dimension of the problem,  $fobj$  – value of the object function,  $t$  – current iteration

### 3. KINETIC ANALYSES

In order to perform the optimization, it is required to define the object function as well as the constraints, which is why it is necessary to perform kinetic analyses. Since these platforms usually carry the load that often can be humans, the speed of lifting is usually not high, so dynamic changes of load in the components of the platform can be neglected, therefore the platform can be observed as static structure.

The structure of the platform is consisted of two legs of equal length, AC and AB, hydraulic cylinder GH that is usually placed in the plain behind the mechanism itself, but for the purpose of performing the kinetic analyses it can be represented as shown in the figure 1. Cylinder is connected to the leg AB over pin support G which is placed on a distance  $a$  from the pin E, and it is connected to the leg BD over the pin H that is placed on a distance  $b$  from the pin G, forming the triangle GEH. The ends of the legs, A and D are fixed with pin supports, while B and C are connected to pinned collar on smooth rod which enables them to move in horizontal direction as the platform is lifting or lowering. The angle between the leg AC and ground is labelled as the angle  $\alpha$ , the angle EGH is labelled as the angle  $\varphi$ , while the angle GHE is labelled as the angle  $\beta$ . Since the pin E is located in the middle of both legs, the angle GEH equals  $2\alpha$ . On the

horizontal metal sheet CD the load  $T$  is being placed on distance  $l_f$  from the pin C.

When disassembled, directions of the forces in the pins of individual components can be assumed as it is represented in the figure 4.

Based on the assumed directions of forces in figure 3, system of equations can be formed.

Static equations for the member DE:

$$\Sigma X_i = 0: X_D = 0 \quad (3)$$

$$\Sigma Y_i = 0: Y_D - T + Y_C = 0 \quad (4)$$

$$\Sigma M_{i(D)} = 0: Y_C L - T l_f = 0 \quad (5)$$

Static equations for the member AC:

$$\Sigma X_i = 0: X_A - F_{cil} \cos(\alpha + \varphi) + X_E = 0 \quad (6)$$

$$\Sigma Y_i = 0: Y_A - F_{cil} \sin(\alpha + \varphi) + Y_E - Y_C = 0 \quad (7)$$

$$\Sigma M_{i(E)} = 0: -\frac{Y_A L}{2} + F_{cil} \sin(\varphi) a - \frac{Y_C L}{2} + \frac{X_A \sin(\alpha)}{2} = 0 \quad (9)$$

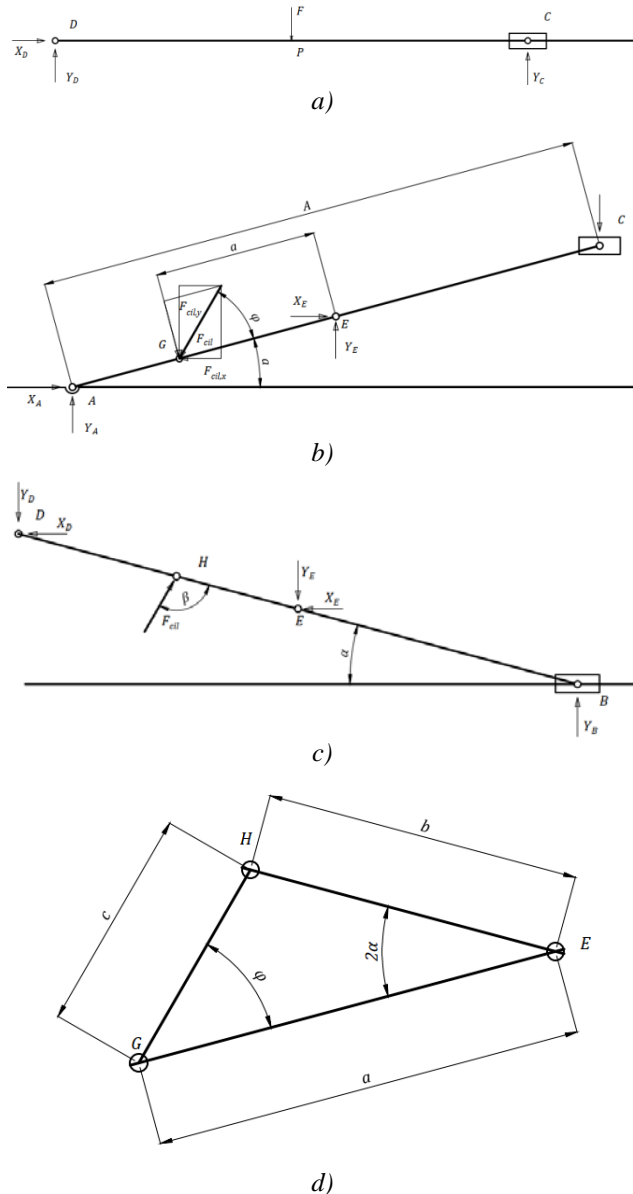


Figure 4: Free body diagram of the lifting platform: a) horizontal metal sheet, b) leg AC, c) leg BD, d) triangle GEH

Static equations for the member BD:

$$\Sigma X_i = 0: -X_D + F_{cil} \cos(\alpha + \varphi) - X_E = 0 \quad (10)$$

$$\Sigma Y_i = 0: -Y_D + F_{cil} \sin(\alpha + \varphi) - Y_E + Y_B = 0 \quad (11)$$

$$\Sigma M_{i(E)} = 0: \frac{Y_B L}{2} + \frac{Y_D L}{2} - F_{cil} \sin(\beta) b + \frac{X_D A \sin(\alpha)}{2} = 0 \quad (12)$$

Solutions of this system of nine equations are:

$$F_{cil} = \frac{LT}{2a \sin(\varphi)} \quad (13)$$

$$Y_D = T - \frac{T l_f}{L} \quad (14)$$

$$Y_C = \frac{T l_f}{L} \quad (15)$$

$$X_E = F_{cil} \cos(\alpha + \varphi) \quad (16)$$

$$X_A = 0 \quad (17)$$

$$Y_A = \frac{2}{L} \left( F_{cil} \sin(\varphi) a - \frac{Y_C L}{2} \right) \quad (18)$$

$$Y_E = \frac{2LY_C + F_{cil}(\sin(\alpha + \varphi)L - 2a \sin(\varphi))}{L} \quad (19)$$

$$Y_B = \frac{L(Y_D + 2Y_C) - 2a \sin(\varphi) F_{cil}}{L} \quad (20)$$

...where  $L$  represents the horizontal projection of the length of the platform leg  $A$ , and  $F_{cil}$  is the force withing the hydraulic cylinder.

The mass of the scissors lift itself was not accounted in the previous system of equations because, as it is stated in the article [3], the weight of the scissors lift itself can be added to the active load:

$$T = Q \cdot g + \frac{m_p \cdot g}{2} = \frac{2Q + m_p}{2} \cdot g \quad (21)$$

For the purpose of this paper, the mass of the scissors lift will be neglected.

#### 4. OBJECT FUNCTION AND CONSTRAINTS

It was assumed that for the scissors platform legs would be used a beam with the cross section that is shown in figure 5.

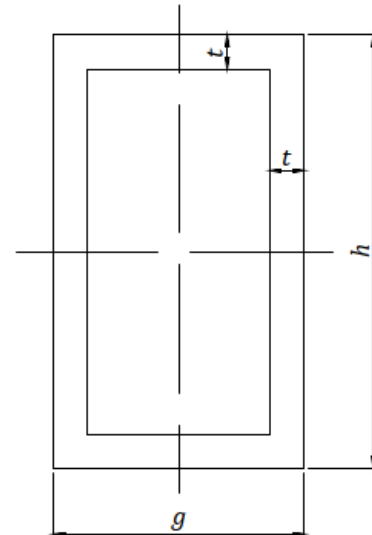


Figure 5: The cross section of the beam:  $t$  – thickness of the box,  $h$  – height of the box,  $g$  – width of the box

By knowing the shape of the cross section, the geometrical properties and the load in each point across the length of the legs, the diameter of pins  $A, B, C, D, E, G$  and  $H$  can be calculated. Considering that the attack

force on the pins is making shear stress within it, the diameter of the minimal diameter of the pin can be determined in the following way:

$$d = \sqrt{\frac{4 \cdot F_s}{m \cdot \pi \cdot \tau_{dop}}}; d_0 = d + 0.1 \text{ (cm)} \quad (22)$$

...where  $d$  is the diameter of the pin,  $m$  is the number of shear surfaces,  $\tau_{dop}$  is allowed shear stress in the pin for the given material, and  $F_s$  is the shear force that is attacking the pin, and it is equal to:

$$F_s = \sqrt{T(z)^2 + A(z)^2} \quad (23)$$

Putting the pins in the beam that makes a leg of the scissors lift platform weakens the beam, so the cross section at those places have the shape that is represented in figure 6.

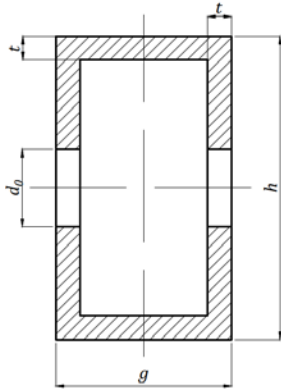


Figure 6: The weakend cross section of the beam

#### 4.1. Object function

The goal of the optimization is to find the optimal ratio between the height and width of the cross section of the beam for the given static load. In order for that to be accomplished, the shear stress, normal stress and combined stress in the beam should not exceed the allowed values for the material from which the beam was made, but it should be close to that limit.

The minimal area of the cross section, or the minimal moment of inertia can be calculated, but the question that remains is if the cross section should have higher height or width, and by how much should one dimension be larger than the other. The optimization algorithm such as HHO can help in the search for the answer to the question.

Since the load of the beam changes along its length, the optimal height and width of the profile in the cross section changes accordingly. The thickness  $t$ , on the other hand, will be taken as constant in every point of the beams.

In order to perform the optimization, appropriate object function must be set within the code. Considering the expressions for calculating the shear  $\tau$  and normal stress  $\sigma$  are:

$$\sigma(z) = \sigma_M(z) + \sigma_A(z) = \frac{M(z)}{I_x(z)} y_{max}(z) + \frac{A(z)}{S(z)} \quad (24)$$

$$\tau(z) = \frac{T(z) \cdot S_x(z)}{I_x(z) \cdot t} \quad (25)$$

...the combined stress can be calculated with the following expression:

$$\sigma_u(z) = \sqrt{\sigma(z)^2 + 3 \cdot \tau(z)^2} \quad (26)$$

...where the variables are:

- $\sigma_M(z), \sigma_A(z)$  – normal stress from the bending moment and axial force at the point  $z$ ;
- $\tau(z)$  – shear stress from the shear force at the point  $z$ ;
- $M(z), T(z), A(z)$  – bending moment, shear force and axial force at the point  $z$ ;
- $S_x(z), I_x(z), S(z)$  – the first moment area, moment of inertia and area of cross section at the point  $z$ :

$$S_x(z) = g(z)t \frac{h(z) - t}{2} + t \left( \frac{h(z)}{2} - t \right)^2 - \frac{d_0(z)^2}{4} t \quad (27)$$

$$I_x(z) = 2 \cdot \left[ \frac{g(z)t^3}{12} + g(z)t \left( \frac{h(z) - t}{2} \right)^2 + \frac{t(h(z) - 2t)}{12} - \frac{td_0(z)^3}{12} \right] \quad (28)$$

$$S(z) = 2t(g(z) + h(z) - 2t - d_0(z)) \quad (29)$$

Since the optimization algorithm searches for the optimal values of the variables in such way that the object function has minimal value, and the combined stress in this situation should as high as it is allowed, then the optimization algorithm has to minimize this function:

$$\sigma_u(z) = -\sqrt{\sigma(z)^2 + 3 \cdot \tau(z)^2}. \quad (30)$$

#### 4.2. Limits of the searching area

The cross section of the beams has a shape of a box, as presented in the figure 5 and the figure 6. Considering that the thickness of the wall of the box is constant across the length of the beam, the only two variables are height and width of the box.

If either the height or the width of the cross section is equal to  $2 \cdot t$ , then the shape of the cross section is not a box, but rather a rectangle. In order to keep the shape of the cross section a box, the minimal height and width of the cross section of the beams should be  $2 \cdot t$ . The lower boundary in the script "Get\_function\_details.m" is defined as the vector, and it has the following form:

$$lb = [2 \cdot t, 2 \cdot t] \quad (31)$$

The maximum values of the height and the width are not as important. Lower upper boundary should result in faster convergence to the optimal solutions, but this should be taken with precaution, because it still has to be high enough so the possible optimal solutions would not be cut out by setting the upper limit too low.

#### 4.3. Constrains

In order to get the shape of the structure that can safely endure the given load, normal stress, shear stress, as well as combined stress must not exceed the limits for the given material. Following that thought, the four limits can be set:

$$g_1 = \sqrt{\sigma(z)^2 + 3 \cdot \tau(z)^2} - \sigma_{dop} \leq 0; \quad (32)$$

$$g_2 = \frac{A(z)}{S(z)} - \sigma_{dop} \leq 0; \quad (33)$$

$$g_3 = \frac{M(z)}{I_x(z)} \cdot \frac{h(z)}{2} - \sigma_{dop} \leq 0; \quad (34)$$

$$g_4 = \frac{T(z)S_x(z)}{I_x(z)t} - \tau_{dop} \leq 0. \quad (35)$$

Additional two constraints can be applied so the width would not be too bigger then height, and the other way around. This behaviour can be constrained in the following way:

$$g_5 = \frac{g(z)}{h(z)} - 3 \leq 0; \quad (36)$$

$$g_6 = \frac{h(z)}{g(z)} - 3 \leq 0. \quad (37)$$

One additional constraint should be applied in the places where the pins pass through the beams:

$$g_7 = 4 \cdot d_0 - h \leq 0 \quad (38)$$

#### 4.4. Source code modification

The optimal shape of the hydraulic scissors lift legs can be acquired by doing multiple optimizations across the length of the legs. Each of the legs has been divided into three sections and each section is divided into ten equidistant subsections, as it is shown in figure 7, where the optimization is performed for each of them individually. Hence, the leg AC has been divided into sections: AG, GE, EC, and the leg DB has been divided into sections: DH, HE and EB.

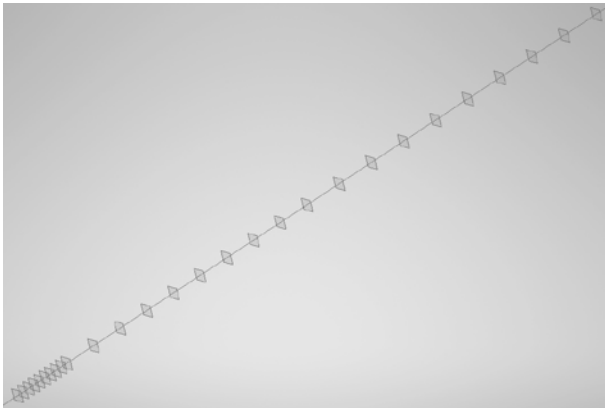


Figure 7: Graphical representation of the leg AC with its subsections

The fastest way to perform thirty optimizations in a row is to write a script that would call the "main.m" script which starts the optimization process for different locations on the scissor legs. The created "start.m" script is erasing content of the files that contain the location and energy of the prey, then it resets the counter and enters the for loop until the total number of optimizations has been completed. The counter provides the needed progression of the z parameter (position of the section for which the optimization is being performed) through optimizations, and it saves the value of the counter in the separate file.

The value of the counter then enters the "main.m" script that runs either the "AC.m" or "BD.m" script, depending on which leg is being optimized. Those two scripts contain geometrical characteristics of the scissors lift (such as the position of the hydraulic cylinder, total length of the legs, etc.), the formulas derived in the third chapter of this paper, and they are being executed before the "Get\_Function\_details.m" script because the values of the axial and shear force, and bending moment are needed for calculating the levels of stress. The reason why these scripts need to be run separately rather than within "Get\_Function\_details.m" script is because it shortens the

time needed for performing each iteration within the optimization process. Considering that there could be thousand iterations in single optimization, and that there would be thirty optimizations like that one, the creation of additional script and placing the calculations of the forces and bending moment in it is justified as considerable amount of time is being saved.

The last change in the "main.m" file represents adding the two lines of code where each saves the values of the prey's location and energy at the end of each optimization, so when the whole process is finished, and all thirty optimizations are done, the optimal results for each subsection can be found in one text file.

After applying the purposed changes, the illustration shown in figure 3 takes the form represented in the figure 8.

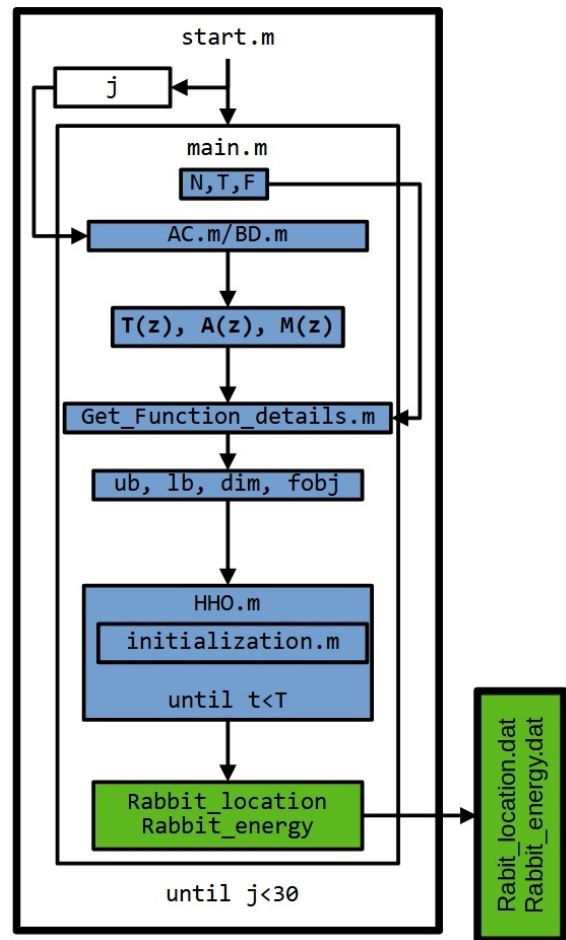


Figure 8: Illustration of the source code with modifications applied

## 5. RESULTS

For the platform that lifts the 1000 kg of load with centre of gravity located on  $l_f = 0.5 \text{ m}$  distance from the pin D, in the lowest position of the platform, when the angle  $\alpha = 7.5^\circ$ , and the parameters that define the position of the hydraulic cylinder:  $a = 0.4 \cdot A \text{ m}$ ,  $b = 0.3 \text{ m}$ , axial, shear, and bending moment diagrams for both AC and BD legs are shown in figures 9 and 10. Diagrams for the same platform when it is in the position where  $\alpha = 75^\circ$  are shown in figure 11 and figure 12.

By comparing the diagrams, it can be concluded that the load in the scissors lift legs is highest in the lowest

position of the platform, making it the only relevant position of the platform for the optimization.

The thickness of the walls of the profile is set to  $t = 6 \text{ mm}$ . Boundaries of the searching area, according to the equation 37 are:

$$lb = [2 \cdot 0.6, 2 \cdot 0.6] = [1.2, 1.2] \quad (39)$$

$$ub = [100, 100] \quad (40)$$

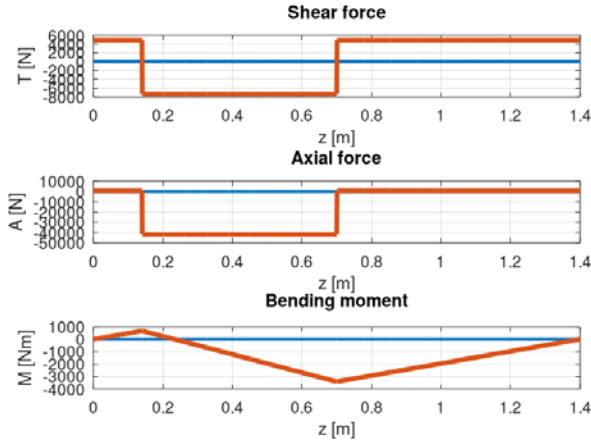


Figure 9: Static diagrams for the AC platform leg in the  $\alpha = 7.5^\circ$  position

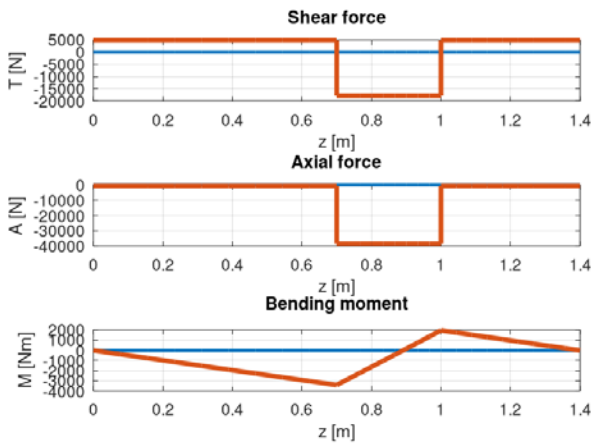


Figure 10: Static diagrams for the BD platform leg in the  $\alpha = 7.5^\circ$  position

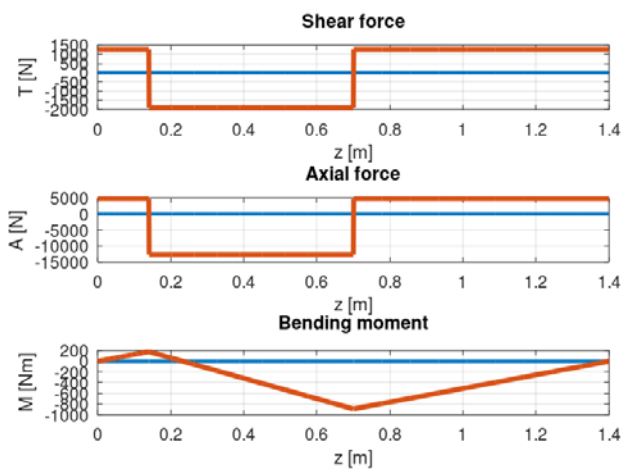


Figure 11: Static diagrams for the AC platform leg in the  $\alpha = 75^\circ$  position

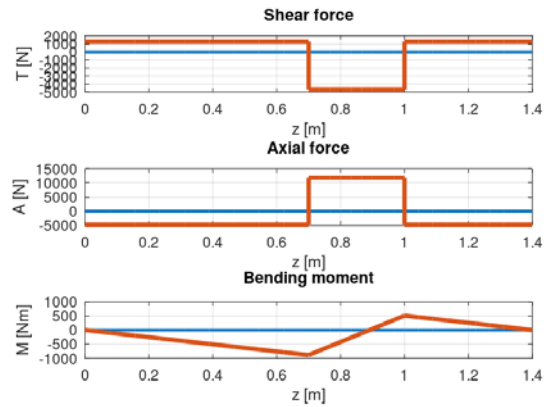


Figure 12: Static diagrams for the BD platform leg in the  $\alpha = 75^\circ$  position

If the material of the scissors legs are being made from structural steel S235, and safety factor is  $\nu = 1.50$ , allowed limits for both normal and tangential stress are:

$$\sigma_{dop} = 16 \frac{kN}{cm^2}$$

$$\tau_{dop} = 9 \frac{kN}{cm^2}$$

The number of hawks (size of initial population) was set to  $N = 60$ , and the maximum number of iterations was set to  $T = 500$ . These parameters represent the needed input information for the optimizer. After the optimization process is being completed, optimal values of the scissors legs, height and width are being shown in the table 1 and table 2.

Table 1. Results of the optimization process for the leg AC

| $z$ [m] | $h$ [cm] | $g$ [cm] | $\sigma_u$ $\left[\frac{kN}{cm^2}\right]$ |
|---------|----------|----------|---|
| 0       | 1.68     | 1.20     | 16  |
| 0.0156  | 1.99     | 1.59     | 16  |
| 0.0311  | 1.79     | 4.88     | 16  |
| 0.0467  | 2.03     | 4.25     | 16  |
| 0.0622  | 2.21     | 4.39     | 16  |
| 0.0778  | 2.41     | 4.40     | 16  |
| 0.0933  | 3.43     | 2.37     | 16  |
| 0.1089  | 2.84     | 4.25     | 16  |
| 0.1244  | 4.63     | 1.59     | 16  |
| 0.14    | 3.54     | 5.25     | 16  |
| 0.2022  | 4.10     | 2.56     | 16  |
| 0.2644  | 2.32     | 3.40     | 16  |
| 0.3267  | 1.64     | 4.06     | 16  |
| 0.3889  | 2.02     | 5.84     | 16  |
| 0.4511  | 2.48     | 5.96     | 16  |
| 0.5133  | 3.45     | 4.24     | 16  |
| 0.5756  | 3.28     | 6.48     | 16  |
| 0.6378  | 3.19     | 8.77     | 16  |
| 0.7     | 4.88     | 5.98     | 16  |
| 0.7778  | 6.88     | 2.45     | 16  |
| 0.8556  | 3.73     | 7.12     | 16  |
| 0.9333  | 3.61     | 6.38     | 16  |
| 1       | 2.88     | 7.75     | 16  |
| 1.0889  | 4.94     | 2.10     | 16  |
| 1.1667  | 2.99     | 4.24     | 16  |
| 1.2444  | 3.85     | 1.54     | 16  |
| 1.3222  | 2.63     | 1.65     | 16  |
| 1.4     | 2.39     | 1.20     | 6.32                                      |

Table 2. Results of the optimization process for the leg BD

| $z$ [m] | $h$ [cm] | $g$ [cm] | $\sigma_u$ [ $\frac{kN}{cm^2}$ ] |
|---------|----------|----------|----------------------------------|
| 0       | 2.40     | 1.20     | 6.32                             |
| 0.0778  | 2.27     | 2.25     | 16                               |
| 0.1556  | 3.17     | 2.39     | 16                               |
| 0.2333  | 2.81     | 4.69     | 16                               |
| 0.3111  | 3.78     | 3.72     | 16                               |
| 0.3889  | 3.06     | 6.93     | 16                               |
| 0.4667  | 5.36     | 2.99     | 16                               |
| 0.5444  | 4.27     | 5.62     | 16                               |
| 0.6222  | 3.70     | 8.28     | 16                               |
| 0.7     | 6.96     | 2.60     | 16                               |
| 0.7333  | 4.31     | 7.90     | 16                               |
| 0.7667  | 4.58     | 4.14     | 16                               |
| 0.8     | 3.72     | 8.96     | 16                               |
| 0.8333  | 3.85     | 4.40     | 16                               |
| 0.8667  | 4.41     | 3.85     | 16                               |
| 0.9     | 5.10     | 4.26     | 16                               |
| 0.9333  | 6.97     | 2.71     | 16                               |
| 0.9667  | 5.34     | 7.48     | 16                               |
| 1       | 4.49     | 7.29     | 16                               |
| 1.0444  | 3.79     | 8.60     | 16                               |
| 1.0889  | 5.02     | 4.45     | 16                               |
| 1.1333  | 5.36     | 3.21     | 16                               |
| 1.1778  | 3.00     | 8.09     | 16                               |
| 1.2222  | 3.10     | 6.00     | 16                               |
| 1.2667  | 3.21     | 4.15     | 16                               |
| 1.3111  | 3.28     | 5.87     | 16                               |
| 1.3556  | 2.11     | 3.70     | 16                               |
| 1.4     | 1.68     | 1.20     | 16                               |

The values from table 1 and 2, as well as the ratio between the height and width of the profile across the length of the legs are being visualised in the figure 13 and figure 14.

The three-dimensional models of the scissors lift legs AC and BD made using the parameters from tables 1 and 2 are being shown in figures 15 and 16.

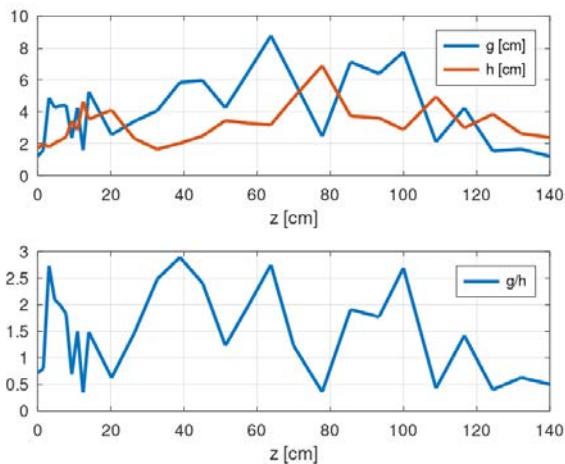


Figure 13. Visual representation of the values from the table 1

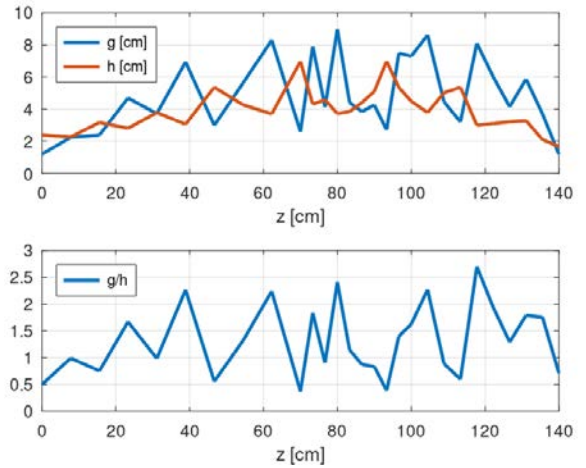
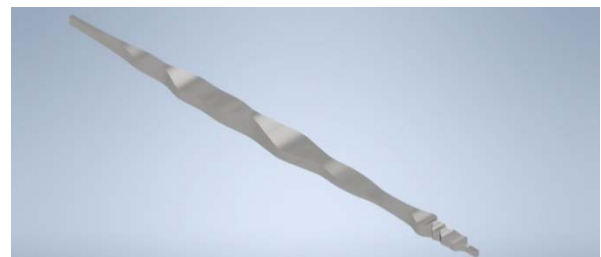


Figure 14. Visual representation of the values from the table 2

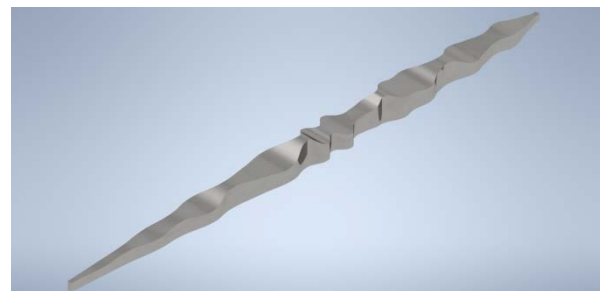


a)



b)

Figure 15: Three-dimensional model of the scissors lift leg AC: a) isometric view, b) cross section view



a)



b)

Figure 16: Three-dimensional model of the scissors lift leg BD: a) isometric view, b) cross section view

## 6. CONCLUSION

Comparing the results of the optimization represented on graphs displayed in figure 13 and figure 14 with the static diagrams displayed in figure 9 and figure 10, it can be concluded that the width of the profile  $g(z)$  tends to be larger than the height  $h(z)$  as the  $z$  gets further from the pins in both AC and BD leg.

Due to the constraint  $g_7$  in the places where the pins pass through the legs, the height of the profile increases, while the width is getting shorter.

## ACKNOWLEDGEMENTS

This paper is supported by the Ministry of Education, Science and Technological Development of the Republic of Serbia through Contract No. 451-03-9/2021-14/200108.

## REFERENCES

- [1] AT. Dang, DN. Nguyen and DH. Nguyen, "A Study of Scissor Lifts Using Parameter Design", *Advances in Engineering Research and Application. ICERA 2020. Lecture Notes in Networks and Systems, Vol 178*, pp. 75-85, Springer, Cham. DOI: 10.1007/978-3-030-64719-3\_10
- [2] T.Liu, J. Sun, "Simulative Calculation and Optimal Design of Scissor Lifting Mechanism", *2009 Chinese Control and Decision Conference*, 2009, pp. 2079-2082, DOI: 10.1109/CCDC.2009.5192393.
- [3] A. Saxena, "Deriving a Generalized, Actuator Position-Independent Expression for the Force Output of a Scissor Lift", *ArXiv abs/1611.10182* (2016): n. pag.
- [4] G. Pavlović, M. Savković, G. Marković, N. Zdravković and J. Stanojković, "Optimal design of welded I-beam of slewing pillar jib crane", 2018, *IMK-14 - Istraživanje i razvoj*, vol. 24, no. 3, pp. 75-82
- [5] A.A. Heidari, S. Mirjalili, H. Faris, I. Aljarah, M. Mafarja, H. Chen, "Harris hawks optimization: Algorithm and applications", *Future Generation Computer Systems* 97(2019), pp. 849-872, DOI:10.1016/j.future.2019.02.028
- [6] E. H. Houssein, M. E. Hosney, D. Oliva, W. M. Mogamed, M. Hassaballah, "A novel hybrid Harris hawks optimization and support vector machines for drug design and discovery", *Computers & Chemical Engineering*, vol. 133, DOI: 10.1016/j.compchemeng.2019.10665

**SESSION B**

**PRODUCTION TECHNOLOGIES**



## A Survey of Research on Industry 4.0 in Intralogistics

Nenad Đ. Zrnić<sup>1\*</sup>, Tamara M. Popović<sup>1</sup>, Goran Z. Milojević<sup>1</sup>, Nenad Ž. Kosanić<sup>1</sup>

<sup>1</sup> Faculty of Mechanical Engineering, Department of Material Handling Constructions and Logistics, University of Belgrade, Belgrade (Serbia)

*This paper presents the research, development and application of Industry 4.0 in Intralogistics in the last five years. The progress made in Intralogistics, using Industry 4.0, is presented. An overview of the basic principles and elements of Industry 4.0 as well as its impact in the field of Intralogistics is given. Intralogistics is a field that is still being researched and has great potential for further development. Finally, the aim of this paper is to focus on sustainability parameters, technology and elements that still need to be worked on.*

**Keywords: Industry 4.0, Intralogistics, Sustainability parameters, technology and elements**

### 1. INTRODUCTION

For humanity, continuous development and progress is necessary in all fields, including industry. Modern societies have higher expectations, so continuous development is essential. Throughout centuries, the industry has developed by applying scientific knowledge and achievements. So far, the industry has gone through four different revolutions:

- 1<sup>st</sup> Industrial Revolution (Ca. 1750),
- 2<sup>nd</sup> Industrial Revolution (Ca. 1900),
- Digital Revolution (Ca. 1970),
- Industry 4.0 (today).

The new technology that will be applied in the industry must be sustainable in order to be successful and applicable worldwide. Sustainability and implementation means that economic, social and environmental aspects must be fulfilled. This is possible through further research and better utilization of these aspects and contributions of Industry 4.0 in the field of Intralogistics. Smart intralogistics will lead to increased flexibility and productivity in the future. All possibilities must be taken into account when accepting the changes brought by (Intra) Logistics 4.0.

A certain group of scientific papers, journals and catalogs dealing with this topic was analyzed. These scientific papers provide us with a complete insight into previous research.

The following is an overview of published works in the previous five years (Figure 1), covered by this paper.

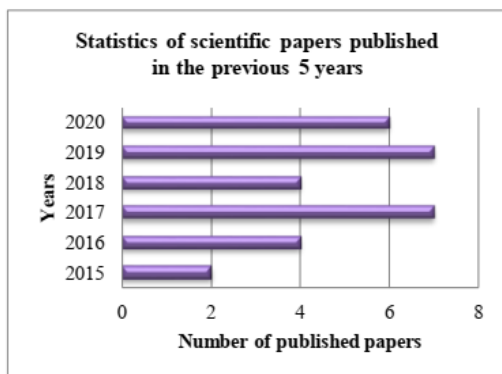


Figure 1: Statistics of scientific papers published in the previous 5 years (which are covered in this paper)

Below is an overview of the countries in which the paper was published, according to the main author (Figure 2). Statistics are given according to papers from references.

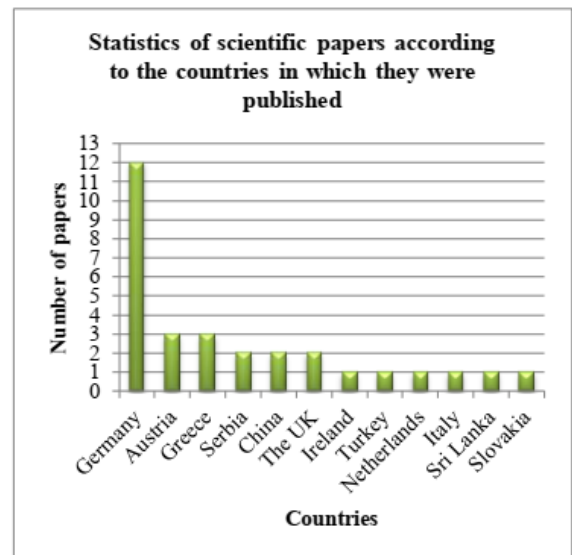


Figure 2: Statistics of scientific papers according to the countries in which they were published

### 2. INDUSTRY 4.0

Industry 4.0 is coined as the Fourth Industrial Revolution, hence the '4.0'. To understand this terminology, a brief summarization on the earlier three revolutions is necessary (Figure 3).

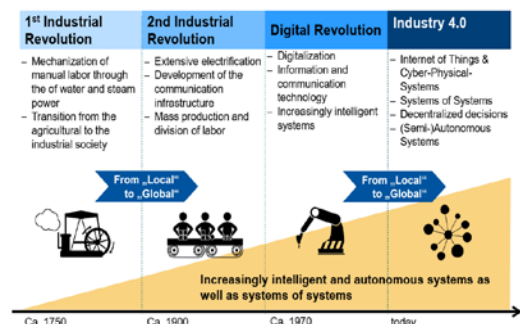


Figure 3: Illustration of Industrial Revolutions (adapted from [2])

The first Industrial revolution was characterized by the introduction of the steam engine, which provided mechanical motion for labor activities and resulted in the transition from hand production to machine production. The second revolution was characterized by the mobilization of people and information due to improvements of infrastructure facilities as railroads and telephone lines. Technological innovations, as the factory electrification and the development of the production line, enabled mass production. In the Third revolution, the rise of computers and communication systems occurred. [1]

This has improved the collection, processing and analysis of information, as well as enabled automated production.

It should be noted that accelerated development in all fields is yet to come, so expectations for the future are high.

The term Industry 4.0 was first introduced in 2011 in Germany, but in the same time other European countries began to make major changes. Then came the terms "Smart Factory", "Industrial Internet of Things (IIoT)" or "Smart Industry" that we use today.

The concept of Industries 4.0 implies connecting machines, products, systems and people that can share information and manage themselves and each other. In such a model, all objects are smart entities that have the ability to autonomously manage, control and communicate with the environment. Industry 4.0 understands complete automation and digitalization of business systems and their connections with the environment. This leads to the existence of a virtual reality model in which it is possible to monitor and manage all processes and activities. ICT, software applications and information platforms have the biggest role in the concept of Industry 4.0 because they provide connecting the virtual and physical business system. [3]

In [4] the concept of Industry 4.0 is presented using a theoretical framework with the application of technology and its functionality.

The main elements of Industry 4.0 are Cyber-Physical Systems (CPS), Internet of Things (IoT), Industrial Internet (Industrial Internet of Things), Internet of Services (IoS), Cloud Computing, Internet of Energy (IoE), Big Data, Artificial Intelligence (AI), Augmented Reality (AR), 3D printing, Blockchain. Each of these elements is presented in [5].

The Industry 4.0 distinguishes four key principles [1].

- **Interoperability between cyber physical systems**, which emphasized the collaboration between the different cyber-physical systems via the Internet of Things
- **Information transparency**, which accentuates the large amounts of data that are processed into information and are shared, in order to establish an open and transparent business environment
- **Technical assistance to humans**, is providing the user with systems that are able to assist in the performance of complex tasks within for example production activities
- **Autonomous decision-making of the cyber-physical systems**, through the increasing quality of transparent information available for these

systems, and their improving programming, autonomous decision making by cyber physical systems is becoming more developed.

The fields in which the influence of 4.0 Industry may bring improvement [6]:

- **Productivity improvement:** Industry 4.0 provides several improvements such as automation, real-time inventory management, and continuous optimization that lead to productivity enhancement.
- **Increased quality:** ongoing monitoring and control of production allows for improved quality of products and services.
- **Increased flexibility:** with a customer-centric approach, Industry 4.0 allows manufacturing flexibility through automation and robotics.
- **Increased speed:** with enhanced product life cycle management and physical-digital integration, the speed of production is enhanced.
- **Safer and better working conditions:** with increased automation, real-time monitoring of incidents, better-designed workstations, and enhanced work structuring, workers have safer and better working conditions.
- **Improved collaboration:** as the availability of data is enhanced, and digital layer and physical layer are integrated the intra- and inter-organization collaboration is improved.
- **Sustainability:** optimized use of resources, reduction in defects, and other environmental improvements make operations more sustainable.
- **Innovation:** Industry 4.0 leads to new ways of creating value and new forms of employment, for example through downstream services.

### 3. LOGISTICS 4.0

The term Logistics 4.0 appeared in 2011 within Industry 4.0. Everything within Industry 4.0 related to logistics (Transportation, Warehousing, Packaging, Distribution, Loading/Unloading and Information service) will be now Logistics 4.0.

A feature of Logistics 4.0 is smart process management.

The most important technologies and applications used in Logistics 4.0 are Wireless Sensors Networks, Internet of Things, Automatic Guided Vehicle, 3D Printing, Drones, Cloud Computing, Big Data, Blockchain, Robotics and Automation, Augmented Reality. Each of these elements and technologies is presented in [3]. We can see that there is an overlap of elements in Industry 4.0 with Logistics 4.0, which is logical considering that Logistics 4.0 comes from Industry 4.0.

Table 1 provides an overview of the applied technologies and applications used in Logistics 4.0 as well as the personal impression of the authors on their importance and contribution.

Table 1: The applied technology and the corresponding elements with the sources in which they are processed as well as their use

| Technologies and elements | Source  | Utilization |
|---------------------------|---|-------------|
| Wireless Sensors Networks | [3], [5], [7], [8]                            | ++          |
| Internet of Things        | [1], [3], [5], [6], [7], [8], [9], [10], [11] | +++         |
| Automatic Guided Vehicle  | [1], [3], [7], [8], [12], [13], [14]          | +++         |
| 3D Printing               | [1], [3], [5], [10], [15]                     | ++          |
| Drones                    | [3]   | n/d         |
| Cloud Computing           | [3], [5], [7], [8], [9], [10], [11], [13]     | +++         |
| Big Data                  | [3], [5], [8], [10], [11]                     | +           |

|                         |                                      |     |
|-------------------------|--------------------------------------|-----|
| Blockchain              | [1], [3], [5], [16]                  | +   |
| Robotics and Automation | [3], [9], [13], [1], [10], [5], [8], | +++ |
| Augmented Reality       | [3], [9], [10], [5], [8]             | ++  |

Utilization: n/d not enough data yet, + less / bad, ++ moderate, +++ high / excellent

#### 4. INTRALOGISTICS

Intralogistics is a subset of Logistics 4.0. The history of Intralogistics dates back to the immediate post-war period, when economic and industrial development was mainly driven by manufacturing. Transportation at the factory initially relied on simple equipment such as bag carts, other trolleys and overhead cranes. The goods were stored at ground level, as stacking the blocks in height led to poor visibility and accessibility. [17]

Since 1950, Intralogistics has been evolving. In Figure 4, we can see significant features in Intralogistics shown according to years of development.

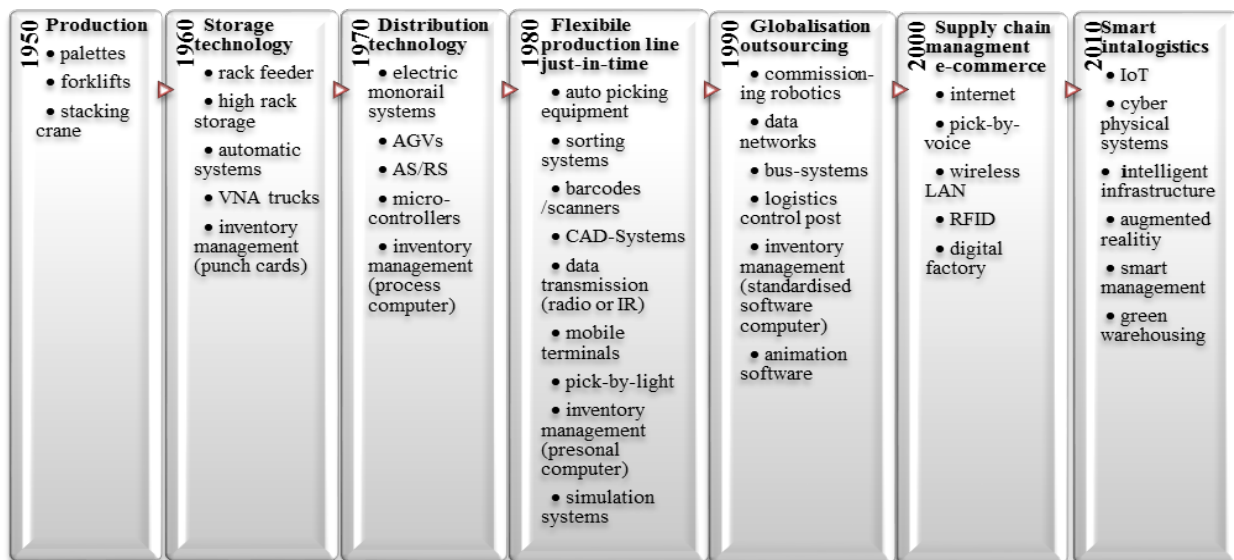


Figure 1: History of Intralogistics (the paper [17] complemented)

Definitions of Intralogistics [18]:

The new term "Intra-Logistics" describes the organization and optimization of internal material flow and logistic technologies as well as the goods transshipment in industry, trade and in public institutions by means of technical components, partial and full systems and services.

- Intralogistics as a brand describes the organization, realization and optimization of internal material flows in industrial and trading companies as well as in public institutions by means of technical systems and services.

- Under "Supply Chain Management", Intralogistics controls the flow of materials along the entire value chain.
- Intralogistics describes the internal flow of materials between different "logistics hubs" - from the flow of materials in production, distribution centres, airports and seaports - as well as the associated flow of information.
- Intralogistics is part of a trend-setting industry which consists of thousands of companies in Germany (e.g. from manufacturers of lifting and crane devices, forklifts and storage technology, to

developers and suppliers of complete systems).

Megatrends will determine the development of Intralogistics in the future.

In order to get acquainted with the subject of research and examination in Intralogistics, an overview of the fields with a description and the corresponding reference is given, Table 2.

Table 2: The subject of application in Intralogistics is presented in the papers

| Subject of applying   | Description   | Source |
|---|---|--------|
| Logistics 4.0 Application and DB Schenker Application Results     | <ul style="list-style-type: none"> <li>Blockchain</li> <li>AVs</li> <li>Electronic market platforms</li> <li>3D printing - reduction of storage space</li> <li>Interview with DB Schenker</li> </ul>  | [1]    |
| Autonomous mobile robots in smart Intralogistics                  | <ul style="list-style-type: none"> <li>Ability to maintain flexibility</li> <li>The role of AMR application</li> <li>Connection, automation and fast information exchange</li> <li>Comparison of AMR and AGV</li> <li>Impact of AMR application</li> </ul>  | [13]   |
| Automated Storage and Retrieval Systems (AS/RS)                   | <ul style="list-style-type: none"> <li>Solution of the collection problem using Shuttle vehicle</li> <li>Mechanical solutions, technical characteristics, design and specification of Shuttle vehicle</li> <li>Requirements and problem improvement</li> <li>Creating a subsystem</li> </ul>                                  | [19]   |
| Smart Warehouse   | <ul style="list-style-type: none"> <li>Better information exchange</li> <li>Sensors</li> <li>Wireless communication</li> <li>New design warehouse and fewer workers</li> <li>Smart management systems</li> <li>Efficiency that contributes to reducing mistakes</li> <li>Opportunities and challenges in Sri Lanka</li> </ul> | [20]   |
| Application of AGV and other technologies to increase flexibility | <ul style="list-style-type: none"> <li>Flexibility - a variety of assessments, tasks and resources</li> <li>Assessment and dimensions of flexibility</li> <li>Application schemes</li> </ul>  | [21]   |
| Smart Conveyor  | <ul style="list-style-type: none"> <li>Control of conveyor belts</li> <li>Conveyor belts as cyber -</li> </ul>  | [22]   |

|   |   |      |
|---|---|------|
|   | <ul style="list-style-type: none"> <li>physical systems</li> <li>Roller as a source of information</li> <li>Controller drum drive unit</li> </ul>   |      |
| Intelligent infrastructure, Sensor system at the forklift truck, Celluveyor - Omnidirectional Cellular Conveyor | <ul style="list-style-type: none"> <li>Production combination</li> <li>Forklifts with tablet</li> <li>Increasing security</li> <li>Design and application of Celluveyor - Omnidirectional Cellular Conveyor</li> </ul>  | [23] |
| AGVs in industrial environments   | <ul style="list-style-type: none"> <li>Impact of AGV and increase productivity</li> <li>Operation plans</li> <li>AGV Ecosystem</li> <li>Software for AGV</li> <li>Proposed layout of the warehouse and the path for the movement of vehicles</li> <li>Eco-indicators</li> </ul> | [24] |

As mentioned in the introduction, sustainability will justify the application of Industry 4.0 in Intralogistics. It consists of the following factors: economic, social and environmental aspects (Figure 5).

As already stated, these aspects represent sustainability.

Sustainability should reflect the following:

- **Economic:** An affordable system that works efficiently, offers common solutions, is financially stable and supported. Selects and supports the local economy.
- **Social:** The basic needs of individuals / communities to be met in a safe way and to support good living conditions as well as safety at work, on an equal footing within the collective.
- **Environment:** Reducing the consumption of non-renewable resources, reduced greenhouse gas emissions, as well as taking into account pollution and waste. Use of technology that reuses energy and recycles certain components.

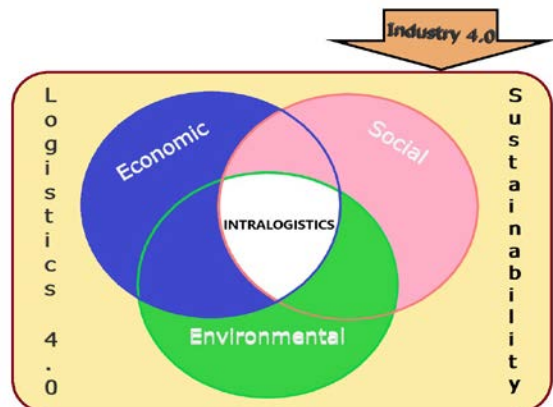


Figure 5: Illustration of interrelationship in Intralogistics

To indicate the importance of sustainability factors in the field of Intralogistics, Table 3 provides an overview of scientific papers in which this factor is (more or less) described.

Table 3: Assessment of fulfilment of Sustainability factors described by papers

| Source | Description   | Sustainability factors     |   | Level of meeting criteria |
|--------|---|----------------------------|---|---------------------------|
| [1]    | <ul style="list-style-type: none"> <li>Reduction of storage space and problematic supply of raw materials in 3D printing</li> <li>Company DB Schenker efficiency and safety</li> </ul>  | Economic                   | ✓ | +                         |
|        |   | Social                     |   | /                         |
|        |   | Ecological (Environmental) | ✓ | +                         |
| [5]    | <ul style="list-style-type: none"> <li>Application in various industries</li> <li>Man-centered management model</li> </ul>  | Economic                   | ✓ | ++                        |
|        |   | Social                     | ✓ | ++                        |
|        |   | Ecological (Environmental) |   | /                         |
| [6]    | <ul style="list-style-type: none"> <li>Real-time progress monitoring, enhanced quality and safety, and improved communication between stakeholders is the contribution of the application</li> </ul>  | Economic                   | ✓ | +                         |
|        |   | Social                     | ✓ | +                         |
|        |   | Ecological (Environmental) |   | +                         |
| [10]   | <ul style="list-style-type: none"> <li>Contributes to Sustainability Factors</li> <li>Perspective for customers, production, employees</li> <li>Opportunities, threats and the biggest problems</li> </ul>  | Economic                   | ✓ | +                         |
|        |   | Social                     | ✓ | ++                        |
|        |   | Ecological (Environmental) |   | /                         |
| [13]   | <ul style="list-style-type: none"> <li>Comparison from an economic and technical perspective</li> <li>Price chart analysis and impact of flexibility and productivity</li> <li>Direct impact of AMR</li> </ul>  | Economic                   | ✓ | +++                       |
|        |   | Social                     |   | /                         |
|        |   | Ecological (Environmental) |   | /                         |
| [15]   | <ul style="list-style-type: none"> <li>Industry 4.0 and its impact on ecological sustainability</li> <li>Resources, Recycling - Extending the product life cycle, 3D printing</li> <li>Energy – Smart management, Smart Meter</li> <li>Reduction of costs</li> <li>Environmental Protection</li> </ul>  | Economic                   | ✓ | ++                        |
|        |   | Social                     |   | /                         |
|        |   | Ecological (Environmental) | ✓ | +++                       |
| [17]   | <ul style="list-style-type: none"> <li>New environmental challenges for ports and terminals</li> <li>Environmental aspects</li> <li>Forms of environmental impacts</li> </ul>   | Economic                   | ✓ | +                         |
|        |   | Social                     |   | /                         |
|        |   | Ecological (Environmental) | ✓ | +++                       |
| [21]   | <ul style="list-style-type: none"> <li>Analysis of the novelty of the method relies in the possibility of evaluating the virtual systems of systems, equipped with the needed functionalities, before its actual development (process requirements, assessing factors: feasibility, development costs, market potential and effective impact on the current processes)</li> </ul> | Economic                   | ✓ | ++                        |
|        |   | Social                     |   | /                         |
|        |   | Ecological (Environmental) |   | /                         |
| [23]   | <ul style="list-style-type: none"> <li>Intelligent infrastructure</li> <li>Sensor system at the forklift truck</li> </ul>   | Economic                   |   | /                         |
|        |   | Social                     | ✓ | +                         |
|        |   | Ecological (Environmental) |   | /                         |
| [24]   | <ul style="list-style-type: none"> <li>Increase productivity and reduce environmental impact</li> <li>Reduction of energy consumption</li> <li>Eco - indicators (AGV emission measurement)</li> </ul>   | Economic                   | ✓ | +                         |
|        |   | Social                     |   | /                         |
|        |   | Ecological (Environmental) | ✓ | +++                       |

|      |   |                            |   |     |
|------|---|----------------------------|---|-----|
| [26] | <ul style="list-style-type: none"> <li>Smart factory production system opposite Traditional production line</li> <li>Beneficial Outcomes, Flexibility, Productivity, Resource and Energy Efficiency, Transparency, Promoting Integration, Profitable, Friendly to Staff with application demonstration</li> </ul> | Economic                   | ✓ | ++  |
|      |   | Social                     | ✓ | +   |
|      |   | Ecological (Environmental) | ✓ | +   |
| [27] | <ul style="list-style-type: none"> <li>Market offer with faster, safer (less damage) equipment</li> <li>Safe handling</li> <li>Optimization of consumption of raw materials, resources, energy</li> <li>E - sales</li> </ul>  | Economic                   | ✓ | +   |
|      |   | Social                     | ✓ | +   |
|      |   | Ecological (Environmental) | ✓ | +   |
| [28] | <ul style="list-style-type: none"> <li>Reduction: transport costs, resources, energy consumption</li> <li>Green Warehousing</li> <li>Investments and recommendations</li> <li>Numerical experiments</li> </ul>  | Economic                   | ✓ | +++ |
|      |   | Social                     |   | /   |
|      |   | Ecological (Environmental) | ✓ | +++ |
| [29] | <ul style="list-style-type: none"> <li>Lean management</li> <li>Supplier factors, Customer factor, Process factors, Control and human factors</li> </ul>  | Economic                   |   | /   |
|      |   | Social                     | ✓ | +   |
|      |   | Ecological (Environmental) | ✓ | +   |
| [30] | <ul style="list-style-type: none"> <li>Life cycle assessment of all parts</li> <li>Climate change</li> <li>Graphical display of results</li> </ul>  | Economic                   |   | /   |
|      |   | Social                     |   | /   |
|      |   | Ecological (Environmental) | ✓ | +++ |

*Level of fulfillment of criteria: / unexplored, + less/poor, ++ moderate, +++ high/excellent*

From the previous table (Table 3) and the mentioned scientific papers, it is noticeable that the economic factor is most represented in as many as thirteen papers, then the environmental factor in ten, while the social factor is represented in seven papers. Thus, it is concluded that the greatest importance was given to the economic factor, while other factors gained less importance. Therefore, we came to the conclusion that it is necessary to identify other factors in order to achieve adequate representation.

The level of fulfilment of the criteria is a personal assessment of the author of this paper and gives us an insight into the importance that the author has given to a certain factor in his work.

## 5. CONCLUSION

The idea of this paper is to provide an overview of the research, development and application of Industry 4.0 in Intralogistics.

By developing the industry over the years, i.e. centuries, we come to today: Industries 4.0.

In the introduction, the authors give a statistical overview of the processed papers by years and countries of publication, in order to get the best possible impression of the time and places of research that are described. At the beginning we can get acquainted with the origin of Industry 4.0 and its concept.

The most significant elements that define Industry 4.0 at its core are:

- Big Data,
- Smart Factory,
- Cyber Physical Systems,
- Internet of Things (IoT),
- Interoperability.

This paper provides references that deal with each of these elements. Four key principles of development are given, as well as the area of application in which Industry 4.0 can bring improvement.

To understand the concept of Intralogistics, we need to get acquainted with Logistics, of which it is a subset.

In this particular case, Logistics 4.0 (which was created by the implementation of Industry 4.0), has its own technologies and related elements that it applies, Table 1. The given table shows the use of technologies and related elements in the mentioned scientific papers. All of the above technologies and elements must be further developed in the future in order to make progress. Intralogistics has developed gradually, throughout history, in accordance with the development of storage technology, market needs, as well as the needs of distributors and customers (users). That's how 'Smart Intralogistics' came about.

In this paper, new definitions of Intralogistics are presented. Emphasis is placed on monitoring megatrends and the current method of application.

In order to better understand mentioned term, a table with paper dealing with the application of "Smart Intralogistics" of its elements and technologies is given, Table 2. We notice that in the last 5 years the list of published scientific papers on a given topic is deficient (30 papers in the period from 2015 to 2020), but also that in recent years that has changed for the better (13 papers in the period from 2019 to 2020). We emphasize what has already been mentioned in Industry 4.0 and what is important for this part: Sustainability.

The factors that make up Sustainability are:

- Economic,
- Social and
- Ecological (Environmental).

Since the paper is based on research, a table is given describing the presence of these significant factors, Table 3.

After processing the collected data, we can conclude that Intralogistics with the application of Industry 4.0 is still in development, not only in practice, but also in scientific research.

In the future, intralogistics will continue to monitor and apply scientific knowledge. This will result in opportunities for improvement during development. Consideration would be reduced not only to a scientific basis, but also to its application in the industry practice.

Countries around the world understand the benefits of switching to "Smart Intralogistics", while countries in the region, including Serbia, will need more time to embrace and implement it.

#### ACKNOWLEDGEMENTS

This work was supported by the MPNTR RS under Grant 451-03-9/2021-14/200105 from 05.02.2021.

#### REFERENCES

- [1] D. Horenberg, "Applications with Logistics 4.0 - A research conducted on the visions of 3PL service providers", D. Horenberg, "9th IBA Bachelor Thesis Conference", 5 July 2017, Enschede (The Netherlands), (2017)
- [2] M. Haberstroh, T. Meisen and S. Jeschke "Logistics 4.0 – The impact of IoT and Big, Data on the industry", "ECTA Annual Meeting", Düsseldorf (Germany) 10th November 2016, (2016)
- [3] G. Radivojević, and L. Milosavljević, "The Concept Of Logistics 4.0", "4th Logistics International Conference", Belgrade (Serbia), 23 – 25 May 2019, pp. 283-292, (2019)
- [4] C. J. Bartodziej, "The Concept Industry 4.0 - An Empirical Analysis of Technologies and Applications in Production Logistics", Springer Nature, Berlin (Germany), (2017)
- [5] M. Stankovic, R. Gupta, J. E. Figueroa, B. Calzadilla-Sarmiento and O. Memedovic, "Industry 4.0 – Opportunities Behind The Challenge", Background Paper, "Unido General Conference 17", Vienna (Austria), 27 Nov -1 Dec 2017, (2017)
- [6] A. Sawhney, M. Riley and J. Irizarry, "Construction 4.0", Routledge - Taylor & Francis Group, London and New York, pp. 12-13, (2020)
- [7] S. T. Ponis and O. K. Efthymiou, "Cloud and IoT Applications in Material Handling Automation and Intralogistics", *Logistics* 2020, (2020)
- [8] O. K. Efthymiou, S. T. Ponis, "Current Status of Industry 4.0 in Material Handling Automation and In-house Logistics", *World Academy of Science, Engineering and Technology, International Journal of Industrial and Manufacturing Engineering* Vol.13, pp. 1370-1374 (2019)
- [9] S. Vaidyaa, P. Ambadb and S. Bhoslec, "Industry 4.0 – A Glimpse", "2nd International Conference on Materials Manufacturing and Design Engineering", *Procedia Manufacturing* 20, pp. 233–238, (2018)
- [10] S. Saniuk, S. Grabowska, B. Gajdzik, "Social Expectations and Market Changes in the Context of Developing the Industry 4.0 Concept", *Sustainability* 2020, (2020)
- [11] S. Winkelhaus and E. H. Grosse, "Logistics 4.0: a systematic review towards a new logistics system", *International Journal of Production Research*, Vol. 58, pp. 18–43, (2020)
- [12] J. Yan, M. Zhang and Z. Fu, "An intralogistics-oriented Cyber-Physical System for workshop in the context of Industry 4.0", "2nd International Conference on Sustainable Materials Processing and Manufacturing (SMPM 2019)", *Procedia Manufacturing* 35, pp. 1178–1183, (2019)
- [13] G. Fracapane, D. Ivanov, M. Peron, F. Sgarbossa and J. O. Strandhagen, "Increasing flexibility and productivity in Industry 4.0 production networks with autonomous mobile robots and smart intralogistics", S.I.: *Artificial Intelligence In Operations Management, Annals of Operations Research*, Springer, 7 February 2020, (2020)
- [14] A. Z. Benleulmi and T. Blecker, "Investigating the Factors Influencing the Acceptance of Fully Autonomous Cars", Part I - Innovation and Technology Management, *Digitalization in Supply Chain Management and Logistics - Smart and Digital Solutions for an Industry 4.0 Environment*, "Proceedings of the Hamburg International Conference of Logistics (HICL)", Berlin (Germany), (2017)
- [15] M. Gabriel and Pessl E., "Analysis Of Environmental Potential By Implementing Industry 4.0", *International Scientific Journal "Industry 4.0"*, pp. 141-144, (2016)
- [16] N. Hackius and M. Petersen, "Blockchain in Logistics and Supply Chain: Trick or Treat?", Part I - Innovation and Technology Management, *Digitalization in Supply Chain Management and Logistics - Smart and Digital Solutions for an Industry 4.0 Environment*, "Proceedings of the Hamburg International Conference of Logistics (HICL)", Berlin (Germany), (2017)
- [17] G. Kartnig, B. Grösel and N. Zrnić, "Past, State-of-the-Art and Future of Intralogistics in Relation to Megatrends", "FME Transactions", Vol. 40, No 4, pp. 193-200, (2012)
- [18] <https://www.logistics-journal.de/about/intralogistics>
- [19] J. Fernandes, F. J. G. Silva, R. D. S. G. Campilho, G. F. L. Pinto, A. Baptista, "Intralogistics and industry 4.0: designing a novel shuttle with picking system", "29th International Conference on Flexible Automation and Intelligent Manufacturing (FAIM2019)", Limerick, (Ireland), June 24-28 2019, *Procedia Manufacturing* 38 pp. 1801–1832 (2019)

- [20] N. Karunaratna, R. Wickramarachchi and K. Vidanagamachchi, "A Study of the Implications of Logistics 4.0 in Future Warehousing: A Sri Lankan Perspective", "Proceedings of the International Conference on Industrial Engineering and Operations Management" Bangkok (Thailand), pp.1024–1035, 5-7 March 2019, (2019)
- [21] M. Bonini, A. Urru, S. Steinau, S. Ceylan, M. Lutz, J. Schuhmacher, K. Andrews, H. Halfar, S. Kunaschk, A. Haque, V. Nair, M. Rollenhagen, N. Shaik, M. Reichert, N. Bartneck, C. Schlegel, V. Hummel and W. Echelmeyer, "Automation of Intralogistic Processes through Flexibilisation A - Method for the Flexible Configuration and Evaluation of Systems of Systems", "In Proceedings of the 15th International Conference on Informatics in Control, Automation and Robotics (ICINCO 2018)", Volume 2, pp. 380-388, (2018)
- [22] G. Fedorko, "Implementation of Industry 4.0 in the belt conveyor transport", "MATEC Web of Conferences 263, 01001", VVaPOL 2018, (2019)
- [23] M. Freitag, "Prospects for Intralogistics through Industry 4.0", BIBA, University of Bremen, Bremen Research Cluster for Dynamics in Logistics, Paderborn (Germany), 15 June 2016, (2016)
- [24] D. Bechtsis, N. Tsolakis, M. Vouzas and D. Vlachosa, "Industry 4.0: Sustainable material handling processes in industrial environments", "Proceedings of the 27th European Symposium on Computer Aided Process Engineering – ESCAPE 27", Barcelona (Spain), October 1 - 5th October 2017, (2017)
- [25] Y. Kayikci, "Sustainability impact of digitization in logistics", "15th Global Conference on Sustainable Manufacturing (GCSM)", Procedia Manufacturing 21, pp. 782–789, (2018)
- [26] S. Wang, J. Wan, D. Li and C. Zhang, "Implementing Smart Factory of Industrie 4.0: An Outlook", Hindawi Publishing Corporation, "International Journal of Distributed Sensor Networks", Volume 2016, (2016)
- [27] [https://www.researchandmarkets.com/reports/347936/material\\_handling\\_equipment\\_global\\_market?utm\\_source=dynamic&utm\\_medium=CI&utm\\_cod...](https://www.researchandmarkets.com/reports/347936/material_handling_equipment_global_market?utm_source=dynamic&utm_medium=CI&utm_cod...)
- [28] R. Carli, M. Dotoli, S. Digiesi, F. Facchini and G. Mossa, "Sustainable Scheduling of Material Handling Activities in Labor-Intensive Warehouses: A Decision and Control Model", Sustainability 2020, (2020)
- [29] K. Ejsmont , B. Gladysz , D. Corti , F. Castaño, W. M. Mohammed and J. L. M. Lastra, "Towards 'Lean Industry 4.0' – Current trends and future perspectives", Cogent Business & Management, (2020)
- [30] C. Scharpenberg, E. Pohl, L.-P. Lauven and J. Geldermann, "Ecological Assessment of Port Equipment for Container Terminals", Part I - Maritime and Port Logistics, Logistics 4.0 and Sustainable Supply Chain Management - Innovative Solutions for Logistics and Sustainable Supply Chain Management in the Context of Industry 4.0, "Proceedings of the Hamburg International Conference of Logistics (HICL)", Berlin (Germany), (2018)

# Determination of the Probability of a Geap Pump Fault Using the Bayes Network and Netica Software

Jovana Perić\*, Mirko Djapić<sup>1</sup>, Tanja Miodragović<sup>1</sup>, Stefan Pajović<sup>1</sup>

<sup>1</sup>The Faculty of Mechanical and Civil Engineering in Kraljevo, University in Kragujevac, Kraljevo (Serbia)

*The literature dealing with risk analysis and finding an adequate solution in the mechanical engineering sector shows that the use of the Bayesian network as one of the methods for risk assessment in this context is well known. Therefore, the authors of this paper use the Bayesian network, while accordingly, for the purpose of simpler work with Bayesian networks, special software has been developed, one of them being Netica, as the most commonly used method for determining an adequate solution, and in this case determining the probability of malfunction. gear pumps if the probabilities of variables that directly affect the correctness of the pump are known. The procedure for determining the probability of malfunction of the gear pump in the specific example shown in this paper is obtained first by designing the Bayesian network, and then by creating the same network in Netica software, where pre-defined nodes (variables) to which assigned values are entered in program, after which the arrows show the dependences of the given variables, and then enter the conditional probabilities of these variables and form a network on the basis of which the probability of malfunction of the gear pump is determined.*

**Keywords:** Bayesian networks, Netica software, conditional probabilities, variables, adequate solution, faulty operation of the steam pump.

## 1. INTRODUCTION

Bayesian networks represent directed, acyclic graphs where nodes play the role of variables and branches represent their interconnectedness. Linking variables is a basic problem, because it is necessary to clearly determine the relationship between each of the two variables that are observed. This is followed by the assignment of conditional probabilities, which also requires a lot of knowledge in the field that is the subject of the examination. From the model thus formed, it is possible to draw a conclusion about each of the variables, taking into account the influences that other variables have on it. Also, the Bayesian network provides the ability to model the interdependence of a large number of variables. When it comes to the relationship of two dependent variables, inference is simple. In this case, the answer is given by Bayes' theorem. However, a much more complicated case arises when there are several dependent variables for which the required conditional probabilities due to complexity cannot be calculated using Bayes' theorem but using Bayesian networks [1], [2].

As an adequate solution is one of the key segments in the machine system, this paper shows how to obtain a probability that shows the percentage of non-correctness of the gear pump operation if the probabilities of variables that directly affect the correct operation of the pump are known. One of the variables that directly affects the correct operation of the gear pump, which is performed using Bayesian networks and Netica software, is oil overheating.

Overheating of the oil as one of the consequences can be due to excessive friction or elevated ambient temperature or insufficient amount of oil. Furthermore, the presence or absence of excessive friction can lead to shock

loads or pump overload or excessive speed. While elevated ambient temperature or insufficient oil or shock loads or pump overload or excessive speed has a direct impact on the correct operation of the gear pump. From the given example, it is easy to conclude that each of the variables affects another variable or depends on some variable. This would further mean that the variables can be chained in a certain way, which is the first step in forming a Bayesian network. For variables that are directly related, it is necessary to determine the conditional probabilities, this is done on the basis of previous experience and theoretical knowledge of the person making the conclusion. So the first step in determining the probability that shows the percentage of non-operation of the gear pump is the process of designing a Bayesian network where each variable is defined in detail, and then creating a Bayesian network in Netica software in which predefined variables are entered into the program and formed a network.

## 2. THE PROCEDURE FOR DESIGNING A BAYES NETWORK

In order to design a Bayesian network, it is first necessary to define the following:

- nodes in the network (variables to be solved),
- possible outcome of each node (values received by each of the variables),
- branches in the network (interdependence of variables),
- the probability distribution of each of the variables depending on the probability distribution of their parents in the network.

The next step is to assign probabilities. They represent the initial probabilities assigned to the variables,

\*Corresponding author: Jovana Perić, The Faculty of Mechanical and Civil Engineering in Kraljevo of the University in Kragujevac, Dositejeva 19, 36000 Kraljevo, peric.j@mfkv.kg.ac.rs

and they are arrived at on the basis of some previous research. When it comes to the Bayesian network, probability would imply anticipating the outcome of each of the variables when no evidence is known for any node in the network.

A variable that is not affected by any other variable in the network is called a parent or root. They are placed first in the network. Then the parents connect the branches with the variables on which they have a direct influence and they are called children. This procedure continues until the final variables are reached, those that do not have children, ie they do not affect any of the variables. A similar procedure is used when assigning probabilities. It is first necessary to assign probabilities to the variables that represent the root in the network.

This is the probability in the observed example of a malfunction of the gear pump, overheating of the oil. Then, for each variable that has parents, a conditional probability table is formed. So for each variable it is necessary to take into account all combinations of probabilities of its parents. The number of parents of a variable determines the dimensionality of the table.

Figure 1 shows the analysis of the interdependence of nodes (variables) in the network. The presence of excessive friction, elevated ambient temperature and insufficient oil depends on whether the oil is overheated or

not. So, this variable overheating oil has three children. Furthermore, impact loads, pump overload, excessive speed depend on whether there is too much friction or not. Well, this variable also has three children. While the variable malfunction of the gear pump, which is also the question that arises in order to reach an adequate solution to the problem, has five parents, depends on elevated ambient temperature, insufficient oil, shock loads, pump overload and excessive speed. In order for this model to be complete, it is necessary to associate each variable with the corresponding conditional probability, Figure 2.

Each of the variables that has parents is accompanied by tables of conditional probabilities that will be taken into account by each of the outcomes of her parents. As the number of parents increases, so does the number of conditional probabilities that will be associated with the mentioned variable. For example, a node that has two parents will be associated with a total of 4 probabilities, because each parent has two states in which it can be. Thus, the total number of conditional probabilities joining the node, which has  $n$  parents, is  $2^n$ . This procedure performs the design of the Bayesian network, which is further entered into the Netica program, which leads to a percentage probability of failure of the gear pump.

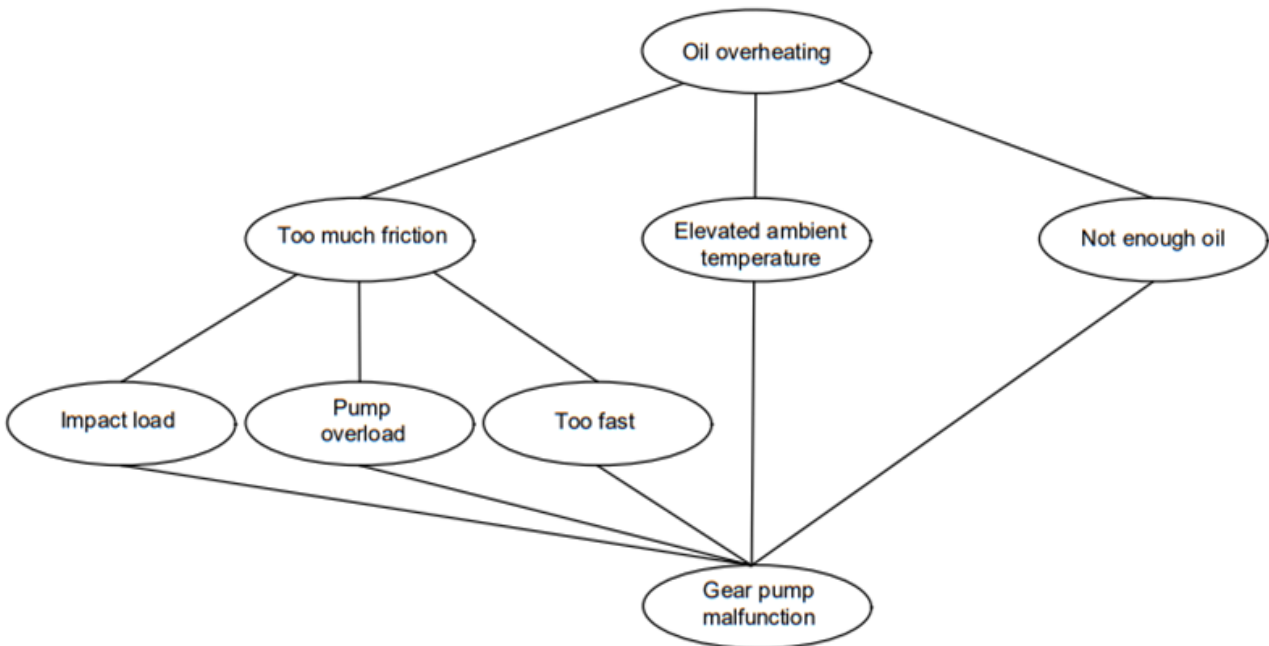


Figure 1: Bayesian network

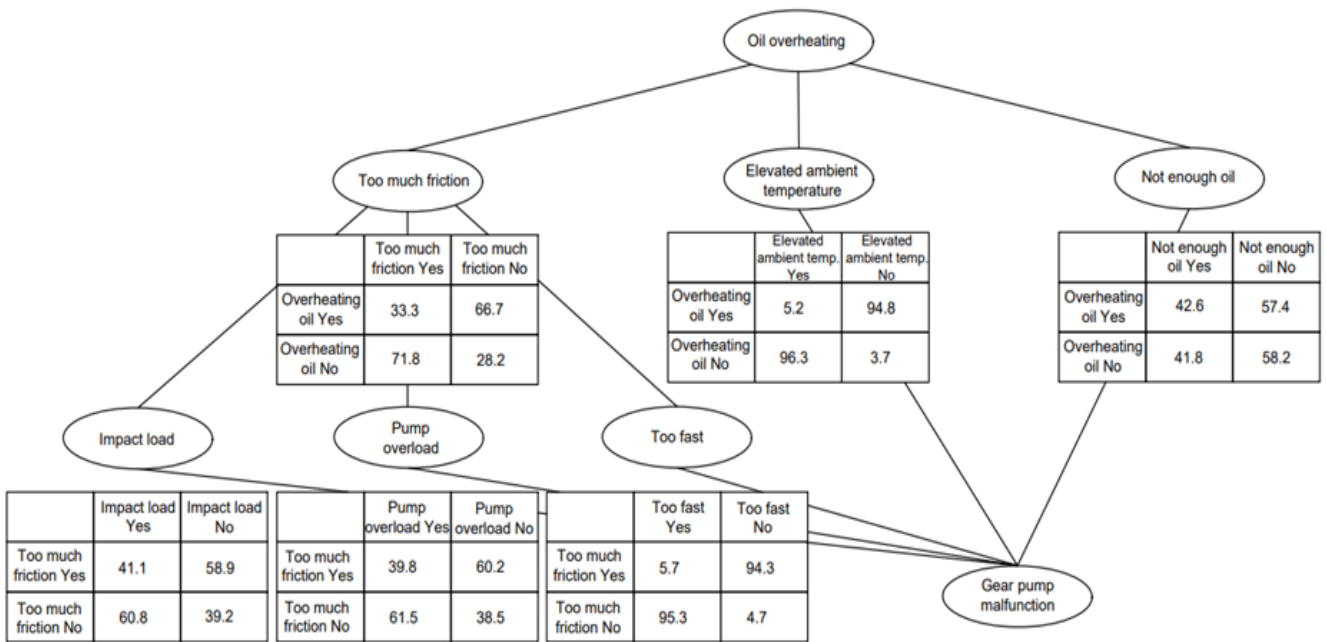


Figure 2: Bayesian network with conditional probabilities

### 3. CREATING A BAYES NETWORK USING NETICA SOFTWARE

Calculating probabilities in Bayesian networks that have a large number of nodes can be very complicated if the probabilities were calculated "on foot". In order to make working with Bayes' networks as simple as possible, several software tools have been developed, one of which is used in this work is Netica.

The principle of operation of this program is extremely simple. It is necessary to enter nodes (variables), values that variables can receive, conditional probabilities, more precisely everything that is defined by the formatting procedure. After that, the arrows show the dependence of the given variables and a network is formed. Figure 3 shows the appearance of the working window of the running Netica program.

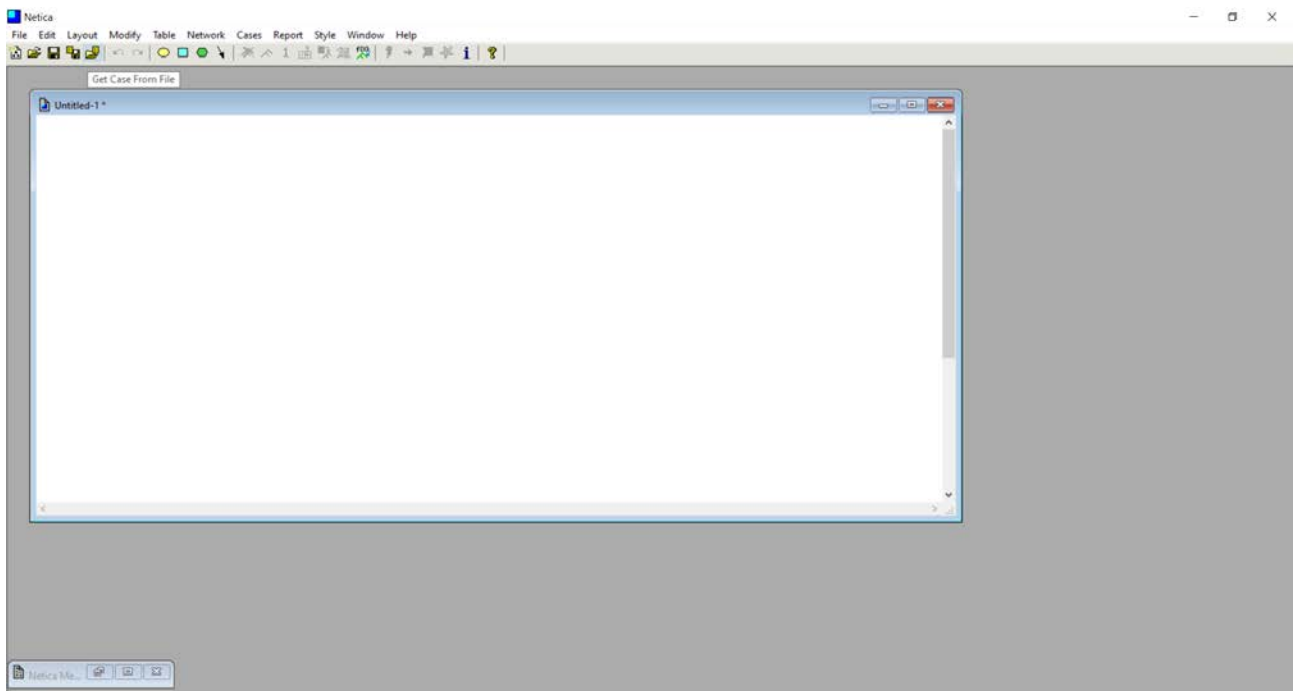


Figure 3: Appearance of the Netica program window

In the following text, it will be briefly explained how the Bayesian network is created with the help of Netika software, through the determination of the probability that shows the percentage of non-operation of the gear pump.

Creating a network in software begins with selecting defined nodes that represent variables. Netica software provides the ability to draw three types of nodes,

arranged respectively in the form: circle, square and hexagon. These are, respectively: nodes of "nature", nodes of "decisions" and nodes of "values". Nature nodes are variables that can be influenced by the decision maker. They are used to represent empirical or calculated parameters and the probabilities of occurrence of different states. Decision nodes are management variables that can be directly implemented by the decision maker. These

nodes represent a set of available management actions. They are closely related to value nodes, which are used to estimate the correct optimal decision on the network that will maximize the sum of the expected values of the value nodes. Next to the nodes, there is also an arrow that is used to establish the dependencies between the nodes. Relationships between nodes can be entered as individual probabilities, in the form of equations, or they can be downloaded from a data file.

In the concrete example of the network in Netica, the network will be drawn over the nodes of nature, and the relations will be entered as probabilities. When a sufficient number of nodes are displayed in the Netica software workspace, determined whether they are of

discrete or continuous type, then the values that the variable can receive are entered, Figure 4, the next step is to connect the nodes to establish dependency and provide the ability of Netica to recognize who the parents of each of the variables are and thus enable easier entry of predetermined conditional probabilities, Figure 5. A further step is to enter the conditional probabilities that are known, Figure 6. Now, when all probabilities have been entered by clicking on the Compile Net option, the probabilities for all variables in the network are obtained Figure 7, after the check, based on previously defined and entered probabilities, the probability is determined, which shows the percentage of gear pump failure.

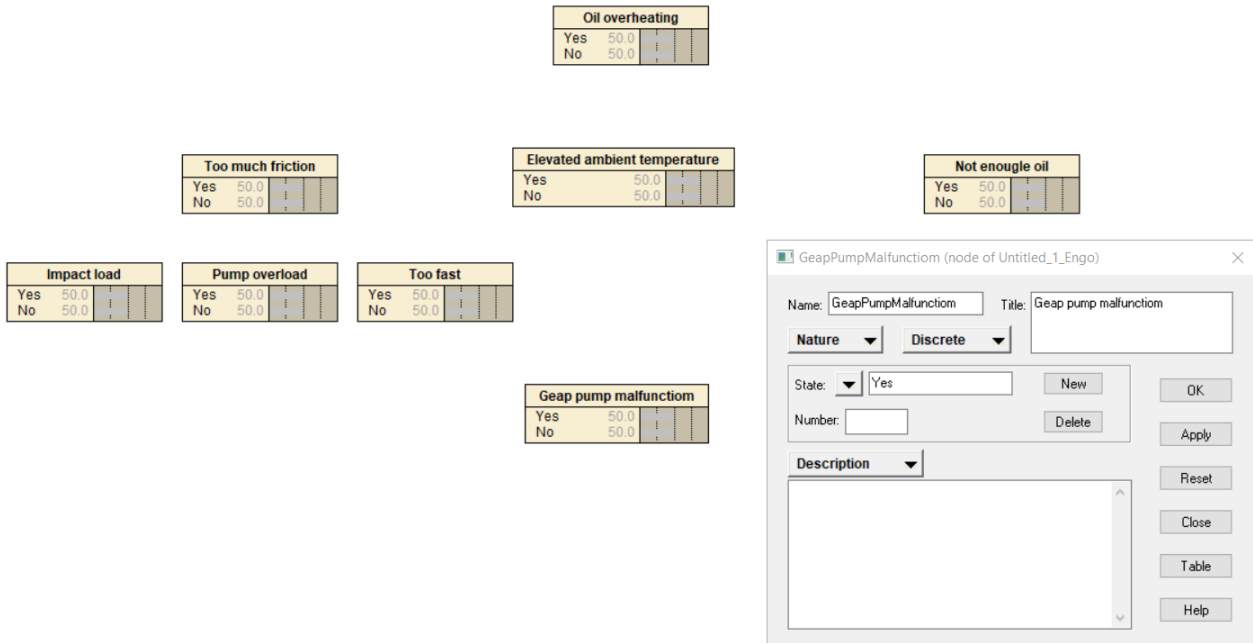


Figure 4: Node naming, input of node type and values that node receives

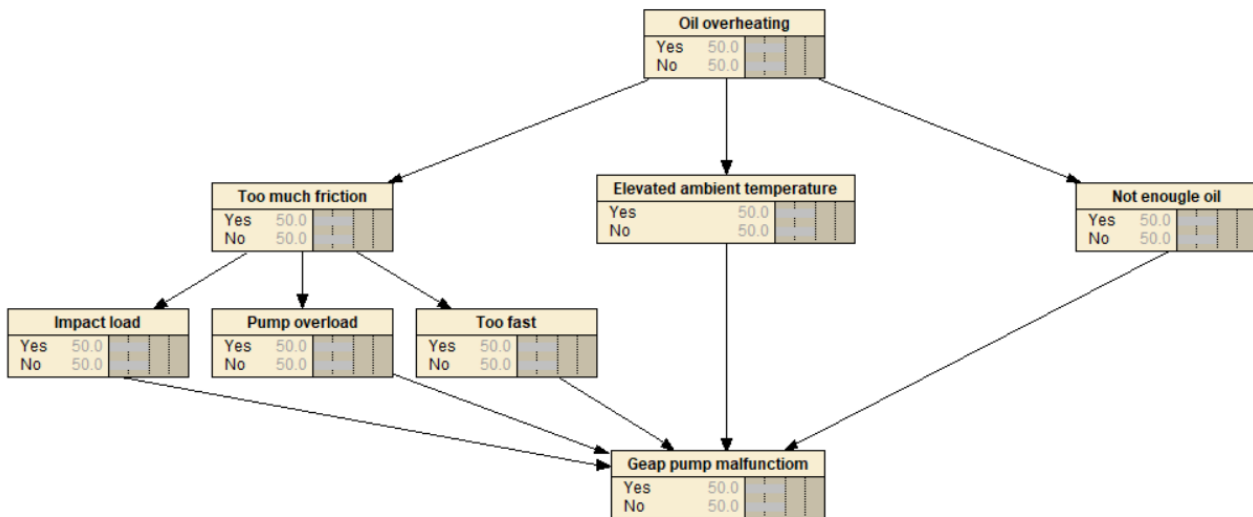


Figure 5: Connecting nodes

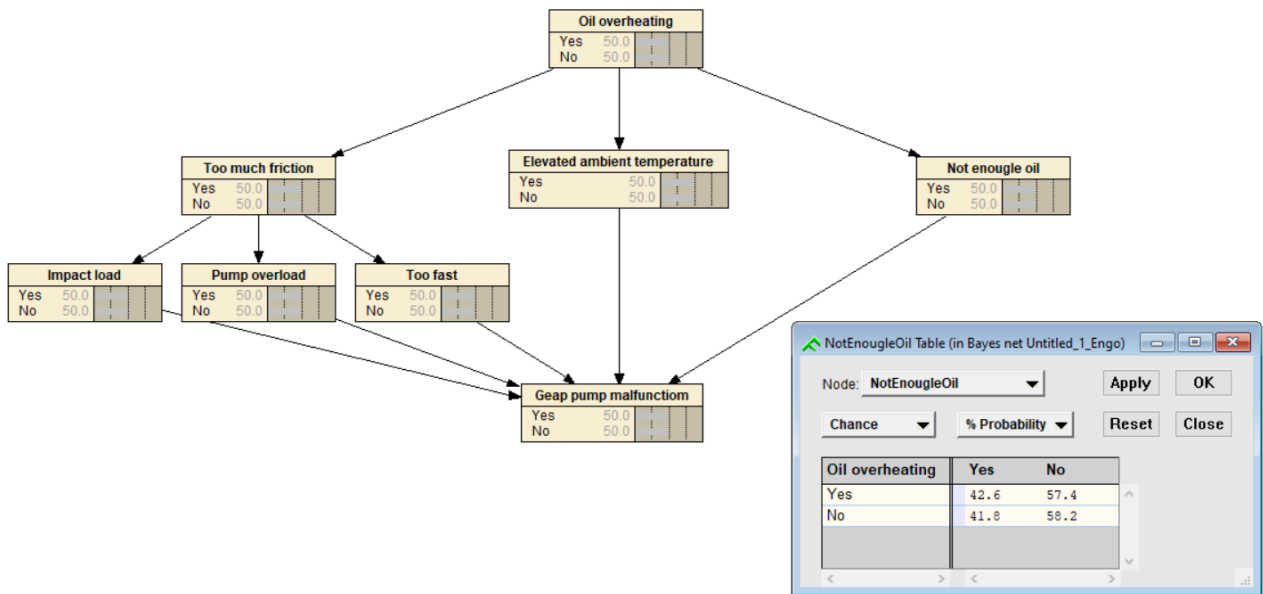


Figure 6: Entering conditional probabilities

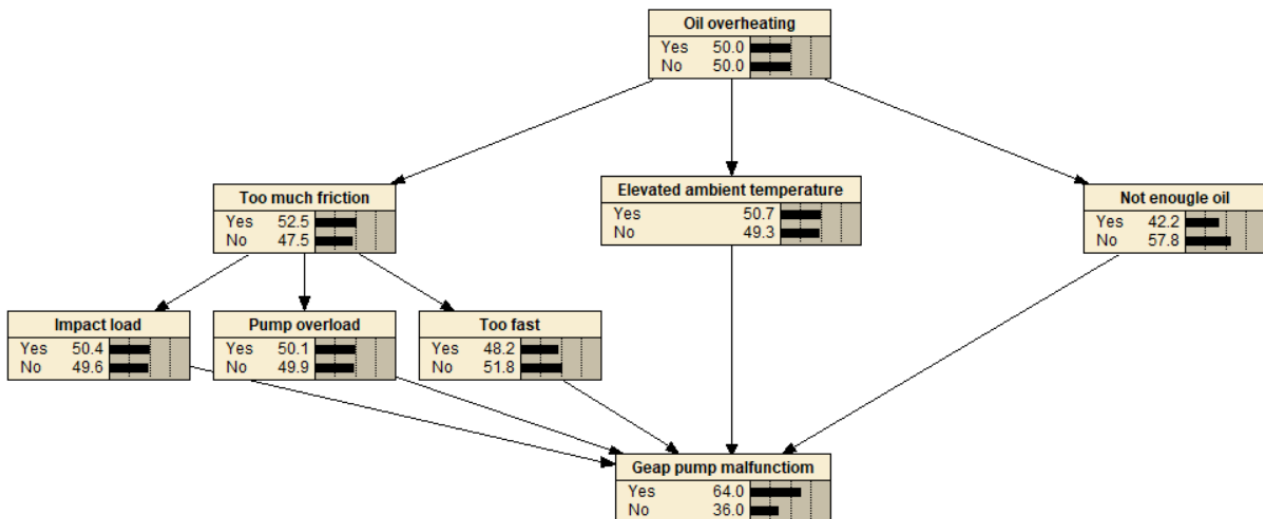


Figure 7: Assigned probabilities to all nodes

4. POSSIBILITY OF CHANGE OF PROBABILITY ON THE CORRESPONDING NODE (VARIABLE) IN THE FORMED NETWORK

In the finished Bayesian network, Netica offers the possibility of changing conditional probabilities, if there is a need for that, more precisely if there is evidence for a variable, ie it is known what value the given variable takes. In order to change the probability of the corresponding variable, it is necessary to set its probability to the appropriate one, after which the program will

change the probabilities of other nodes that depend on that node (variable).

Modification within the given network for malfunction of the gear pump was performed on the node (variable) pump overload, where the problem observer set the probability for the selected node (variable) is 100, after which the program automatically adjusted the conditional probabilities of all other variables with to which it is related and in this way it is easy to calculate the percentage of malfunction of the gear pump when there is a change in the probability of the corresponding variable, Figure 8.

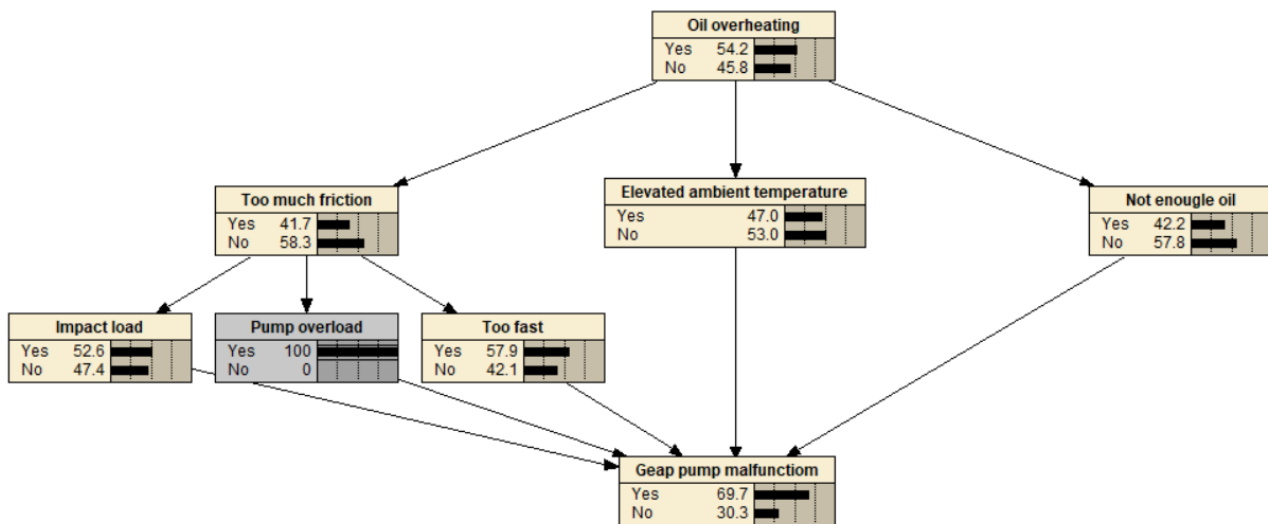


Figure 8: Probability change on the selected node

## CONCLUSION

In the last few decades, new methods have been developed for mechanical engineering that enable faster and more efficient solving of problems that designers encounter when making decisions. Before solving any problem, the most important thing is to determine the exact cause of the problem. This involves a series of actions, observations and interpretations of the very cause of the problem that would lead to the presence of a suspected problem. In almost all areas of mechanical engineering, the exact cause of the problem can be solved by experience, intuition, knowledge or skill, but also by using programs that enable faster and more efficient problem solving. One such program is the Netica software, the principle of operation, design process and creation of the network is presented in this paper. The whole procedure performed to create a Bayesian network in the given example provides the possibility to determine the percentage values of gear malfunction if variables (causes) are known that directly affect the correct operation of the pump.

The paper also provides an opportunity for the problem observer to adjust the probability of a variable depending on his problem after the network is created, after which the modified Bayesian network can be easily adapted to the new data, no matter how many variables there are. This actually means that if one probability changes on one of the variables, it is possible to automatically adjust the conditional probabilities of all

other variables to which it is related, which further provides the possibility of easily calculating the probability of malfunction of the gear pump.

## ACKNOWLEDGEMENTS

This work is co-financed by the Ministry of Education, Science and Technological Development of the Republic of Serbia on the base of the contract whose record number is 451-03-9/2021-14/200108. The authors thank the Ministry of Education, Science and Technological Development of the Republic of Serbia for supporting this research.

## REFERENCES

- [1] R. Neapolitan, "Learning Bayesian Networks", Northeastern Illinois University, Chicago, (2000)
- [2] Norman Fenton, Martin Neil, "Decision Analysis with Bayesian Networks", Second Edition, (2019)
- [3] Scott Ferson, "Bayesian methods in risk assessment", (New York, USA)
- [4] T. Aven, J.T. Kvaløy, "Implementing the Bayesian paradigm in risk analysis", Stavanger University College, P.O. Box 8002, 4068 Stavanger, Norway
- [5] [https://www.norsys.com/tutorials/netica/nt\\_toc\\_C.htm](https://www.norsys.com/tutorials/netica/nt_toc_C.htm).

# Jet Lagging in Abrasive Water Jet Cutting of High-Speed Tool Steel

Ramiz Kurbegovic<sup>1\*</sup>, Mileta Janjic<sup>1</sup>

<sup>1</sup>Faculty of Mechanical Engineering, University of Montenegro, Podgorica (Montenegro)

*Abrasive water jet machining is a very efficient unconventional method for contour cutting of different types of materials. As one of the main characteristics of the quality of surfaces machined with this method is curved lines that appear during machining. These lines are a consequence of the deviation of the abrasive water jet from its ideal vertical line, jet lagging, which are the cause of machining errors.*

*The aim of this work is to investigate the influence of machining parameters on jet lagging. The samples of high-speed steel EN HS6-5-2 (JUS c.7680) were machined with an abrasive water jet under varying working pressure, traverse speed, abrasive mass flow rate, and stand-off distance. The jet lagging was measured at twenty places along with the depth of cut, and based on these results, the relationship between the jet lagging and machining parameters has been formed.*

*In order to correctly select the process parameters, an empirical model for the prediction of jet lagging in abrasive waterjet cutting of high-speed steel EN HS6-5-2 was developed using regression analysis. This developed model has been verified with the experimental results that reveal high applicability of the model within the experimental range used.*

**Keywords:** Jet lagging, Abrasive waterjet, Empirical model, High speed tool steel, Regression analysis

## 1. INTRODUCTION

Abrasive Waterjet Cutting [AWJC] has various distinct advantages over the other non-conventional cutting technologies, such as no thermal distortion, high machining versatility, minimum stresses on the work piece, high flexibility and small cutting forces and has been proven to be an effective technology for processing various engineering materials [1]. It is superior to many other cutting techniques in processing variety of materials and has found extensive applications in industry [2]. However, AWJC has some drawbacks and limitations. It creates tapered edges on the kerf, especially when cutting at high traverse rates [3,4], generate loud noise and a messy working environment.

In the abrasive water jet cutting, the tool is the abrasive water jet, Figure 1.

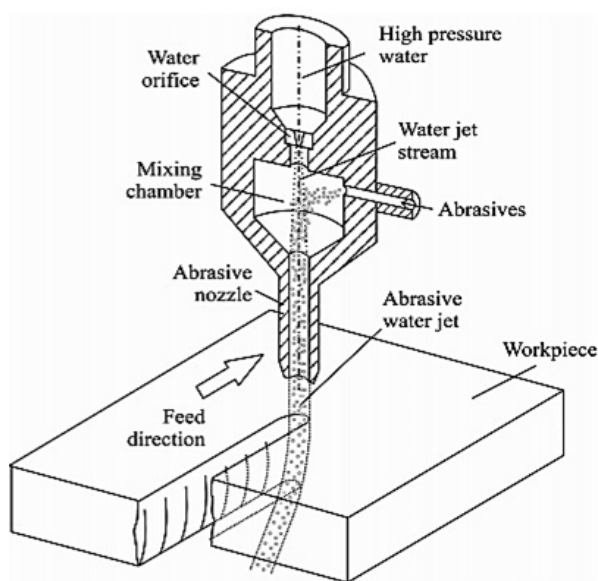


Figure 1: Schematic view of abrasive water jet cutting [5]

The abrasive water jet is a narrow, high-speed water jet stream, formed by highlighting the small diameter water orifice. Downstream from the orifice, in the mixing chamber, abrasive particles are added in the high-speed water jet. They are accelerated by momentum exchange with the high-speed water jet in an abrasive nozzle. From there, the abrasive water jet is directed to the work piece.

The principles on which the abrasive water jet machining process is based on is erosion. Some authors explain the process of erosion as a kind of abrasive wear, at which abrasive particles and water jet repeatedly impact the surface, resulting in flushing of the material from that surface [2,6].

There are several papers dealing with the formation of cut front geometry and the factors that influence its final appearance. Mostly, the cutting front geometry of the workpiece machined by the abrasive water jet is influenced by machining parameters such as operating pressure, stand-off distance, traverse speed, abrasive flow rate [2,7].

Defining the geometry of the cutting front, is in fact, the determination of the deviation - lagging,  $Y_{lag}$ , of the abrasive water jet from the vertical line. Momber and Kovačević [2] explained the deviation of the cut front geometry from ideal as a consequence of energy loss during the cutting process, Figure 2.

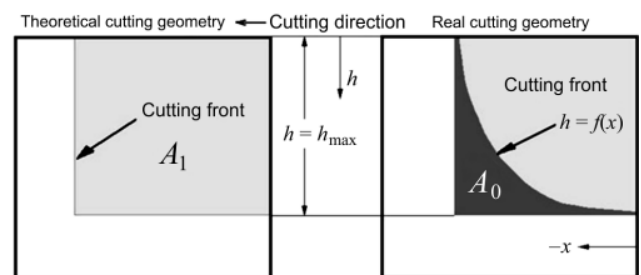


Figure 2: Deviation of the cut front geometry from ideal [2]

The line that defines the lagging of abrasive water jet is described by Zeng, Heines and Kim [8] as a parabola.

The aim of this work is to investigate the influence of machining parameters, such as operating pressure,  $p$ , standoff distance,  $Sd$ , traverse speed,  $U$ , and abrasive mass flow rate,  $Ma$ , on jet lagging and to make an empirical model for the prediction of jet lagging in abrasive waterjet cutting of high-speed steel EN HS6-5-2.

M. Chithirai Pon Selvan i N. Mohana Sundara Raju [9] observed the maximum cutting depth,  $h_{max}$ , as a main parameter for evaluating the applicability of the abrasive water jet machining process for a particular material. They found that water pressure has the most effect on the depth of cut and surface roughness. An increase in water pressure is associated with an increase in depth of cut but a decrease in surface roughness. Depth of cut constantly increases and surface roughness decreases as mass flow rate increases. As nozzle traverse speed increase, surface roughness increases but depth of cut decreases. This means that low traverse speed should be used to have more depth of cut and surface smoothness but is at the cost of sacrificing productivity. This experimental study has resulted that standoff distance has no apparent effect on depth of cut. Nevertheless, surface smoothness increases as stand-off distance decreases. Using regression analysis, they developed a model for predicting the depth of cut of stainless steel. During the development of the model, various parameters of the abrasive water jet machining process were taken into account. Their model is represented by a formula:

$$h_{max} = 678 \cdot \frac{p^{0,339} \cdot Ma^{0,107} \cdot d_a^{1,795} \cdot \rho_a^{0,878}}{E^{0,324} \cdot U^{0,137} \cdot Sd^{0,009} \cdot \rho_w \cdot d_j} \quad (1)$$

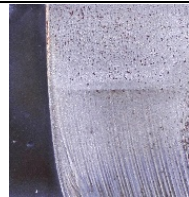
where  $p$  is the working pressure,  $Ma$  is the abrasive mass flow rate,  $d_a$  is the mean value of the abrasive particle diameter,  $\rho_a$  is the density of the abrasive particles,  $E$  is the material modulus of elasticity,  $U$  is the traverse speed,  $Sd$  is the stand-off distance of the cutting head from the workpiece,  $\rho_w$  is the density of the water and  $d_j$  is the diameter of the water jet.

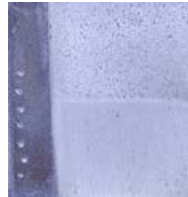
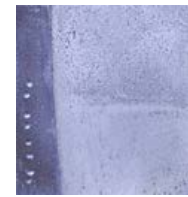
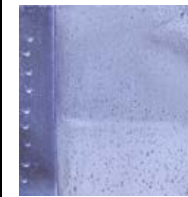
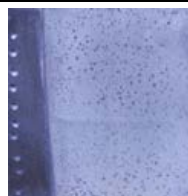
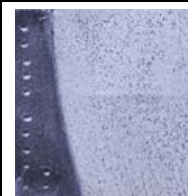
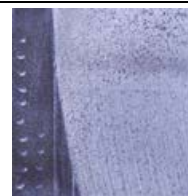
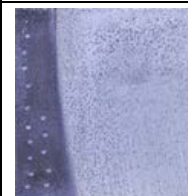
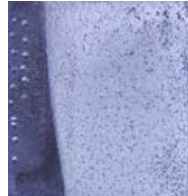
This model showed a good correlation with the experimentally obtained results and will be used as a basis for experimental analysis of the influence of the machining process parameters on the jet lagging.

## 2. EXPERIMENTAL WORK

Samples presented by Kurbegovic, Janjic, Vukcevic and Durovic [10], Table 1, concerning the influence of the water pressure ( $p$ ), traverse speed ( $U$ ), abrasive flow rate ( $Ma$ ) and stand-off distance ( $Sd$ ) on the abrasive water jet lagging, were used for creating relationships and adopting a mathematical model of influence of the machining process parameters on the jet lagging.

Table 1: Samples and its machining parameters [10]

| Sample 1  | Sample 2  | Sample 3  |
|---|---|---|
|  |  |  |
| $p_1 = 199,9$ MPa<br>$U = 20$ mm/min<br>$Ma = 395$ g/min<br>$Sd = 2$ mm             | $p_2 = 251,7$ MPa<br>$U = 20$ mm/min<br>$Ma = 395$ g/min<br>$Sd = 2$ mm             | $p_3 = 299,9$ MPa<br>$U = 20$ mm/min<br>$Ma = 395$ g/min<br>$Sd = 2$ mm             |

| Sample 4   | Sample 5  | Sample 6  |
|--|---|---|
|    |    |    |
| $p_4 = 351,6$ MPa<br>$U = 20$ mm/min<br>$Ma = 395$ g/min<br>$Sd = 2$ mm              | $p_5 = 413,7$ MPa<br>$U = 20$ mm/min<br>$Ma = 395$ g/min<br>$Sd = 2$ mm               | $p = 413,7$ MPa<br>$U = 20$ mm/min<br>$Ma = 395$ g/min<br>$Sd_1 = 3$ mm               |
| Sample 7   | Sample 8  | Sample 9  |
|    |    |    |
| $p = 413,7$ MPa<br>$U = 20$ mm/min<br>$Ma = 395$ g/min<br>$Sd_2 = 4$ mm              | $p = 413,7$ MPa<br>$U = 20$ mm/min<br>$Ma = 395$ g/min<br>$Sd_3 = 6$ mm               | $p = 413,7$ MPa<br>$U = 5$ mm/min<br>$Ma = 395$ g/min<br>$Sd = 2$ mm                  |
| Sample 10  | Sample 11   | Sample 12   |
|   |   |   |
| $p = 413,7$ MPa<br>$U_2 = 10$ mm/min<br>$Ma = 395$ g/min<br>$Sd = 2$ mm              | $p = 413,7$ MPa<br>$U_3 = 30$ mm/min<br>$Ma = 395$ g/min<br>$Sd = 2$ mm               | $p = 413,7$ MPa<br>$U_4 = 40$ mm/min<br>$Ma = 395$ g/min<br>$Sd = 2$ mm               |
| Sample 13  | Sample 14   | Sample 15   |
|  |  |  |
| $p = 413,7$ MPa<br>$U_5 = 60$ mm/min<br>$Ma = 395$ g/min<br>$Sd = 2$ mm              | $p = 413,7$ MPa<br>$U = 20$ mm/min<br>$Ma_1 = 166,5$ g/min<br>$x = 2$ mm              | $p = 413,7$ MPa<br>$U = 20$ mm/min<br>$Ma_2 = 229$ g/min<br>$Sd = 2$ mm               |
| Sample 16  | Sample 17   |   |
|  |  |   |
| $p = 413,7$ MPa<br>$U = 20$ mm/min<br>$Ma_3 = 274,5$ g/min<br>$Sd = 2$ mm            | $p = 413,7$ MPa<br>$U = 20$ mm/min<br>$Ma_4 = 331,5$ g/min<br>$Sd = 2$ mm             |   |

The system used for machining the samples is the product of WJS, model NCX 4020, Sweden. The diameter of the water orifice was 0,254 mm and the abrasive nozzle

(focusing tube) diameter was 0,768 mm (ROCTEC 100). The abrasive material was Garnet mesh 80.

The material used for the experiment is high-speed tool steel EN HS6-5-2 (JUS c.7680, AISI M2), produced with the Electro Slag Remelting (ESR) method in a round-shaped ingot, normalized, bandsawed to 42 mm thick discs and lathe cut to 40±0,05 mm. Material is then water jet machined to a 40x40x110±0,05 mm specimens. The side which is water jet machined is milled and flattened to 38±0,05 mm for distinction purposes. The material was cut to a length of 30 mm. Then the flow of abrasives was stopped and then the machine was stopped. After that, the specimens were cut till the end with Wire Electric Discharge Machining (WEDM). Cutting with WEDM was done to avoid damaging the cut front line and that it could be possible to measure the jet lagging.

Measurements for determining water jet lagging were performed in twenty places (at the same distance) along the sample thickness using an optical microscope. Measurement principle of jet lagging is shown on Figure 3.

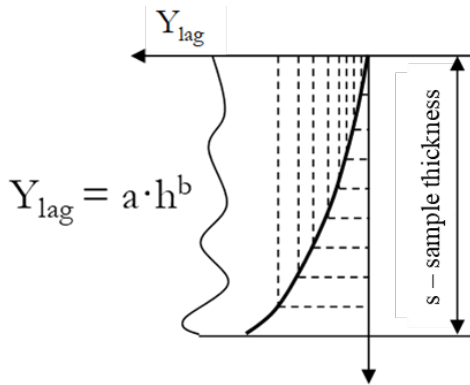


Figure 3: Measurement of jet lagging [11]

Measured values of jet lagging for samples shown in Table 1, are shown in Table 2.

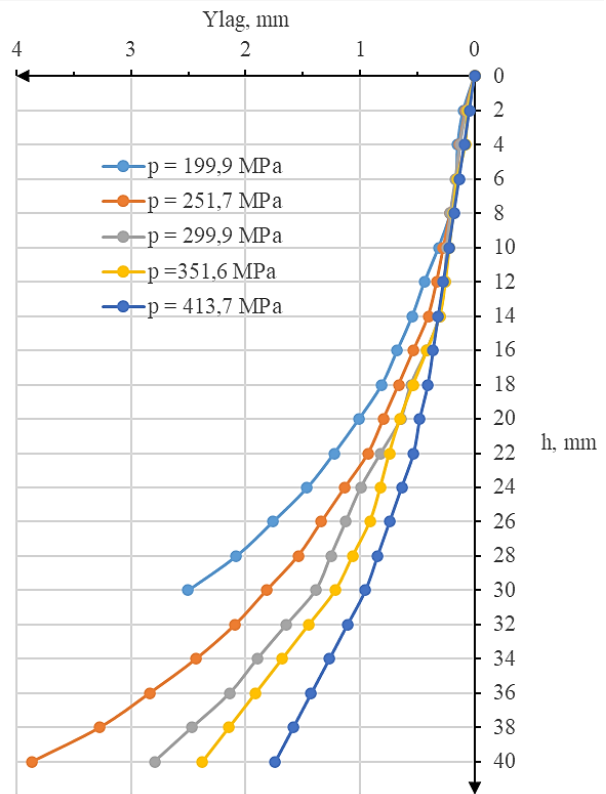
Table 2: Measured values of jet lagging [10]

|              | Sample 1                   | Sample 2 | Sample 3 | Sample 4 |
|--------------|----------------------------|----------|----------|----------|
| <b>h, mm</b> | <b>Y<sub>lag</sub>, mm</b> |          |          |          |
| 0            | 0                          | 0        | 0        | 0        |
| 2            | 0,0978                     | 0,0774   | 0,0693   | 0,0590   |
| 4            | 0,1473                     | 0,1294   | 0,1277   | 0,0804   |
| 6            | 0,1554                     | 0,1534   | 0,1661   | 0,1531   |
| 8            | 0,2108                     | 0,2133   | 0,2104   | 0,1865   |
| 10           | 0,3152                     | 0,2726   | 0,2436   | 0,2198   |
| 12           | 0,4381                     | 0,3314   | 0,2608   | 0,2537   |
| 14           | 0,5450                     | 0,4058   | 0,3066   | 0,3042   |
| 16           | 0,6765                     | 0,5350   | 0,4178   | 0,4162   |
| 18           | 0,8117                     | 0,6642   | 0,5569   | 0,5385   |
| 20           | 1,0111                     | 0,7969   | 0,6451   | 0,6536   |
| 22           | 1,2282                     | 0,9297   | 0,8191   | 0,7461   |
| 24           | 1,4628                     | 1,1341   | 0,9932   | 0,8241   |
| 26           | 1,7640                     | 1,3384   | 1,1247   | 0,9159   |
| 28           | 2,0834                     | 1,5427   | 1,2561   | 1,0661   |
| 30           | 2,5039                     | 1,8170   | 1,3876   | 1,2163   |
| 32           | -                          | 2,0914   | 1,6424   | 1,4484   |
| 34           | -                          | 2,4332   | 1,8973   | 1,6805   |
| 36           | -                          | 2,8380   | 2,1376   | 1,9127   |
| 38           | -                          | 3,2731   | 2,4666   | 2,1448   |
| 40           | -                          | 3,8638   | 2,7958   | 2,3769   |

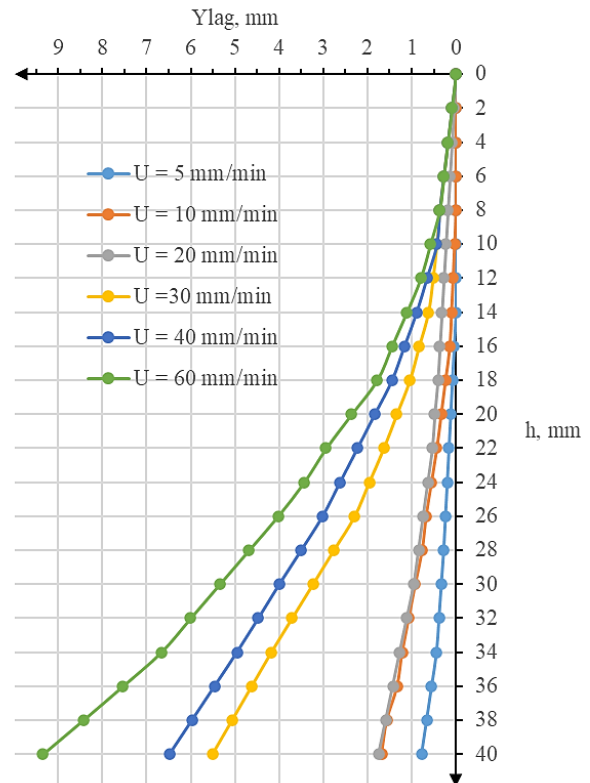
|              | Sample 5                   | Sample 6  | Sample 7  | Sample 8  |
|--------------|----------------------------|-----------|-----------|-----------|
| <b>h, mm</b> | <b>Y<sub>lag</sub>, mm</b> |           |           |           |
| 0            | 0                          | 0         | 0         | 0         |
| 2            | 0,0453                     | 0,0651    | 0,0709    | 0,0703    |
| 4            | 0,0906                     | 0,1303    | 0,1418    | 0,1407    |
| 6            | 0,1359                     | 0,1954    | 0,2126    | 0,2110    |
| 8            | 0,1811                     | 0,2309    | 0,2571    | 0,2813    |
| 10           | 0,2264                     | 0,2754    | 0,3016    | 0,3517    |
| 12           | 0,2717                     | 0,3198    | 0,3329    | 0,4220    |
| 14           | 0,3170                     | 0,3643    | 0,3708    | 0,4923    |
| 16           | 0,3623                     | 0,4087    | 0,4087    | 0,5627    |
| 18           | 0,4076                     | 0,4624    | 0,5130    | 0,6330    |
| 20           | 0,4786                     | 0,5160    | 0,6173    | 0,7033    |
| 22           | 0,5329                     | 0,6443    | 0,7217    | 0,8407    |
| 24           | 0,6382                     | 0,7726    | 0,8260    | 0,9782    |
| 26           | 0,7434                     | 0,9107    | 0,9803    | 1,1337    |
| 28           | 0,8487                     | 1,0489    | 1,1346    | 1,2892    |
| 30           | 0,9539                     | 1,1871    | 1,2890    | 1,4448    |
| 32           | 1,1120                     | 1,3642    | 1,5121    | 1,6671    |
| 34           | 1,2701                     | 1,5414    | 1,7351    | 1,8894    |
| 36           | 1,4282                     | 1,7185    | 1,9582    | 2,1116    |
| 38           | 1,5863                     | 1,8957    | 2,1813    | 2,3339    |
| 40           | 1,7445                     | 2,0729    | 2,4045    | 2,5563    |
|              | Sample 9                   | Sample 10 | Sample 11 | Sample 12 |
| <b>h, mm</b> | <b>Y<sub>lag</sub>, mm</b> |           |           |           |
| 0            | 0                          | 0         | 0         | 0         |
| 2            | 0                          | 0         | 0,0926    | 0,0926    |
| 4            | 0                          | 0         | 0,1852    | 0,1852    |
| 6            | 0                          | 0         | 0,2777    | 0,2777    |
| 8            | 0                          | 0         | 0,3703    | 0,3703    |
| 10           | 0                          | 0,0329    | 0,4351    | 0,4351    |
| 12           | 0                          | 0,0658    | 0,5232    | 0,6626    |
| 14           | 0                          | 0,1023    | 0,6245    | 0,8925    |
| 16           | 0,0393                     | 0,1389    | 0,8342    | 1,1718    |
| 18           | 0,0786                     | 0,2365    | 1,0439    | 1,4512    |
| 20           | 0,1179                     | 0,3342    | 1,3387    | 1,8412    |
| 22           | 0,1572                     | 0,4319    | 1,6336    | 2,2312    |
| 24           | 0,1965                     | 0,5532    | 1,9633    | 2,6259    |
| 26           | 0,2359                     | 0,6744    | 2,2930    | 3,0207    |
| 28           | 0,2752                     | 0,7631    | 2,7636    | 3,5046    |
| 30           | 0,3289                     | 0,9202    | 3,2342    | 3,9984    |
| 32           | 0,3826                     | 1,0672    | 3,7047    | 4,4723    |
| 34           | 0,4363                     | 1,2141    | 4,1753    | 4,9562    |
| 36           | 0,5485                     | 1,3298    | 4,6183    | 5,4635    |
| 38           | 0,6608                     | 1,5612    | 5,0612    | 5,9708    |
| 40           | 0,7730                     | 1,6769    | 5,5042    | 6,4779    |
|              | Sample 13                  | Sample 14 | Sample 15 | Sample 16 |
| <b>h, mm</b> | <b>Y<sub>lag</sub>, mm</b> |           |           |           |
| 0            | 0                          | 0         | 0         | 0         |
| 2            | 0,0926                     | 0,0926    | 0,0926    | 0,0834    |
| 4            | 0,1852                     | 0,1852    | 0,1852    | 0,1668    |
| 6            | 0,2777                     | 0,2777    | 0,2777    | 0,2503    |
| 8            | 0,3703                     | 0,3703    | 0,3703    | 0,3439    |
| 10           | 0,5809                     | 0,4715    | 0,4715    | 0,4175    |
| 12           | 0,7997                     | 0,6278    | 0,6278    | 0,4691    |

|              |                            |        |        |        |
|--------------|----------------------------|--------|--------|--------|
| 14           | 1,1137                     | 0,8224 | 0,7458 | 0,5187 |
| 16           | 1,4497                     | 1,0830 | 0,9277 | 0,7437 |
| 18           | 1,7856                     | 1,4235 | 1,0865 | 0,9907 |
| 20           | 2,3621                     | 1,7762 | 1,3359 | 1,2030 |
| 22           | 2,9387                     | 2,1288 | 1,5853 | 1,4153 |
| 24           | 3,4368                     | 2,5145 | 1,8378 | 1,7352 |
| 26           | 4,0273                     | 2,8689 | 2,0485 | 2,0485 |
| 28           | 4,6854                     | 3,2476 | 2,3667 | 2,3667 |
| 30           | 5,3470                     | 3,6263 | 2,6848 | 2,6848 |
| 32           | 6,0086                     | 4,0051 | 3,0029 | 3,0029 |
| 34           | 6,6703                     | 4,3838 | 3,321  | 3,3210 |
| 36           | 7,5399                     | 4,9571 | 3,8172 | 3,6890 |
| 38           | 8,4366                     | 5,5929 | 4,3531 | 3,9815 |
| 40           | 9,3471                     | 6,1071 | 4,8004 | 4,1935 |
|              | Sample 17                  |        |        |        |
| <b>h, mm</b> | <b>Y<sub>lag</sub>, mm</b> |        |        |        |
| 0            | 0                          |        |        |        |
| 2            | 0,0410                     |        |        |        |
| 4            | 0,0820                     |        |        |        |
| 6            | 0,1229                     |        |        |        |
| 8            | 0,1639                     |        |        |        |
| 10           | 0,2962                     |        |        |        |
| 12           | 0,4284                     |        |        |        |
| 14           | 0,5606                     |        |        |        |
| 16           | 0,6928                     |        |        |        |
| 18           | 0,8251                     |        |        |        |
| 20           | 0,9999                     |        |        |        |
| 22           | 1,1748                     |        |        |        |
| 24           | 1,3876                     |        |        |        |
| 26           | 1,7095                     |        |        |        |
| 28           | 2,0332                     |        |        |        |
| 30           | 2,3569                     |        |        |        |
| 32           | 2,6806                     |        |        |        |
| 34           | 3,0043                     |        |        |        |
| 36           | 3,3133                     |        |        |        |
| 38           | 3,6340                     |        |        |        |
| 40           | 3,9440                     |        |        |        |

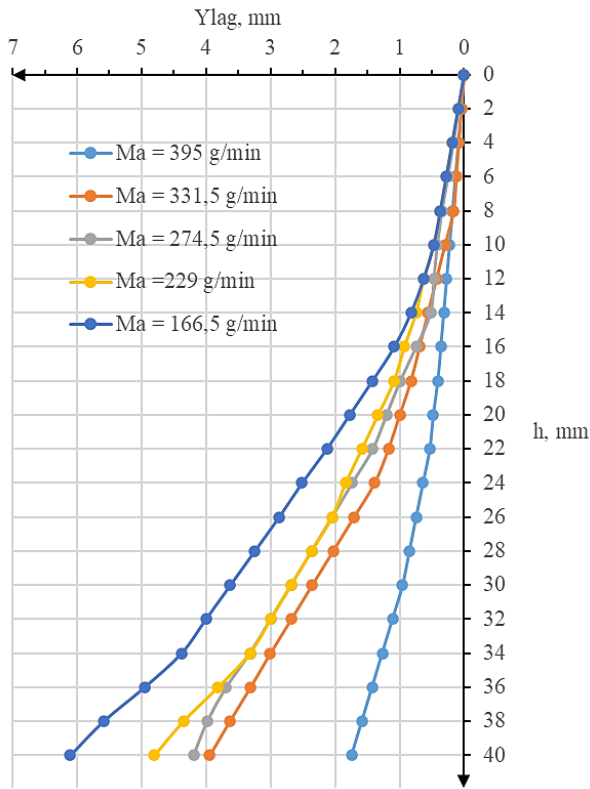
It was concluded in [10] and shown on figure 2 that as the cutting depth increases, the deviation of the front cutting line from its ideal line, jet lagging, also increases. The increase in traverse speed and the distance of the cutting head from the machining material, stand-off distance, results in an increase of the jet lagging. As the values of the abrasive flow and working pressure processing parameters increase, the jet lagging decreases. This clearly demonstrates the strong correlation between the jet lagging and the applied machining parameters.



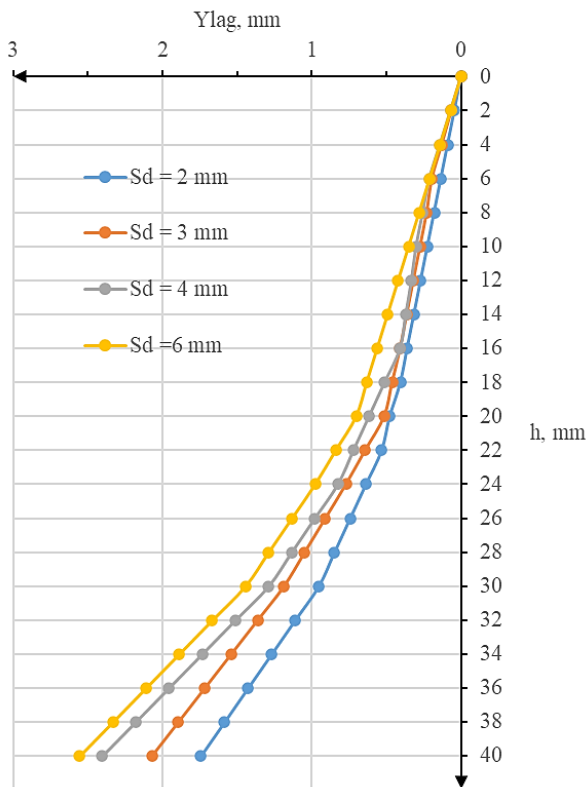
(a)



(b)



(c)



(d)

Figure 4: Influence of (a) operating pressure, (b) traverse speed, (c) abrasive mass flow rate and (d) stand-off distance on jet lagging [10]

### 3. PREDICTIVE MODEL FOR JET LAGGING

AWJC process involves a large number of variables that affect the cutting performance. Dimensional analysis is a powerful analytical technique in describing the relationship between physical engineering quantities (such as jet lagging) and independent variables. This technique is used to develop mathematical model for the jet lagging based on the experimental data for high-speed tool steel. The constants in the models were obtained by the regression analysis technique. These constants were statistically determined at minimum 95 % confidence level. This model relates the jet lagging to four process variables, namely water pressure, nozzle traverse speed, abrasive mass flow rate and nozzle stand-off distance.

Mathematical model adopted for this research work will be as follows:

$$Y_{lag} = a \cdot h^b \cdot p^c \cdot U^d \cdot Ma^e \cdot Sd^f \quad (2)$$

where **a**, **b**, **c**, **d**, **e**, **f** are regression analysis coefficients.

The above model is valid for the operating parameters in the following range for practical purposes and machine limitations:

- Water pressure: 199,9 MPa < p < 413,7 MPa,
- Traverse speed: 5 mm/min < U < 60 mm/min,
- Abrasive mass flow rate: 166,5 g/min < ma < 395 g/min and
- Stand-off distance: 2 mm < Sd < 6 mm.

The mathematical model that describes the impact of the corresponding machining parameters on the jet lagging was given for each diagram.

$$Y_{lag} = 1.347 \cdot h^{2.132} \cdot p^{-1.251} \quad (3)$$

Standard deviation of (3) is R = 0.9948869.

$$Y_{lag} = 0.0001017 \cdot h^{1.945} \cdot U^{1.046} \quad (4)$$

Standard deviation of (4) is R = 0.986002.

$$Y_{lag} = 1.022 \cdot h^{1.821} \cdot Ma^{-0.9575} \quad (5)$$

Standard deviation of (5) is R = 0.9948869.

$$Y_{lag} = 0.001864 \cdot h^{1.789} \cdot Sd^{0.352} \quad (6)$$

Standard deviation of (6) is R = 0.9943339.

It is shown that the model predictions are in good agreement with the experimental data with the deviations less than 3 %. Also, using the MATLAB software package, multiple regression analysis was performed on the measured values of jet lagging, Ylag, and given in a 3D representations in figure 5, within the experimental range.

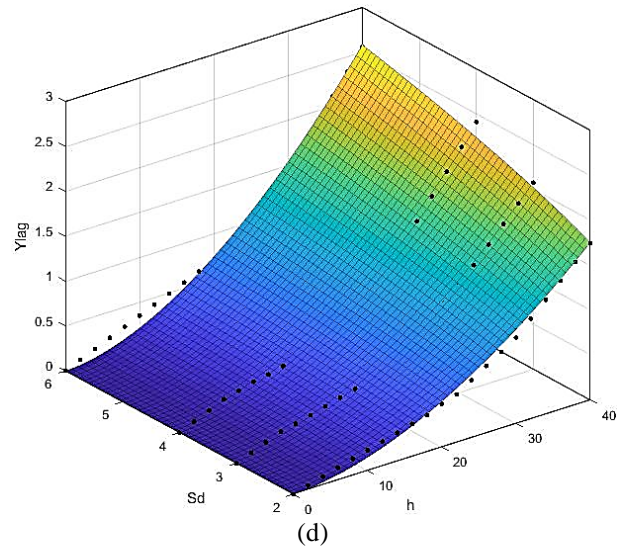
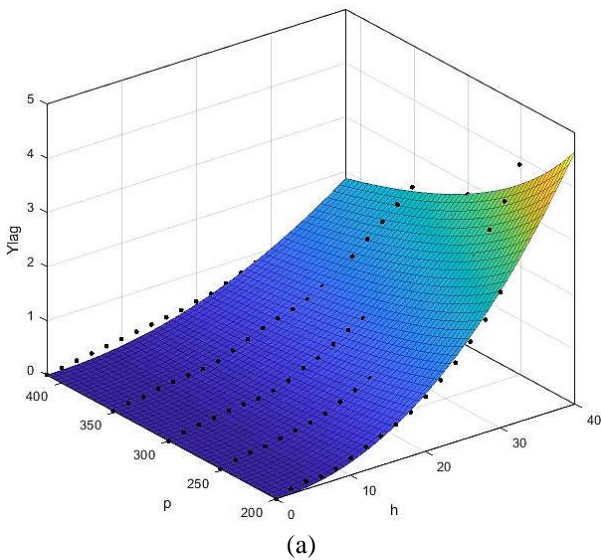
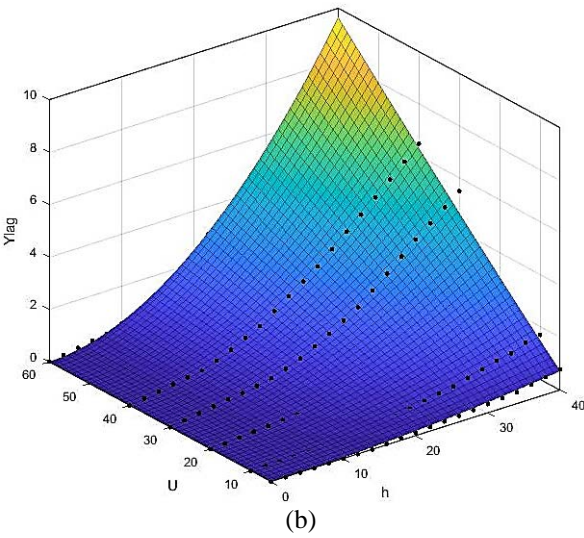


Figure 5: Influence of (a) operating pressure, (b) traverse speed, (c) abrasive mass flow rate and (d) stand-off distance on jet lagging



Based on the measured values in Table 2, the relationship between the jet lagging and operating pressure, stand-off distance, traverse speed, abrasive mass flow rate and depth of cut, is formed. This relationship is represented by a mathematical model described in (2).

$$Y_{lag} = 3.4656 \cdot \frac{h^{1.4008} \cdot Sd^{0.1086} \cdot U^{1.1424}}{p^{0.4053} \cdot Ma^{1.1316}} \quad (7)$$

Standard deviation of (7) is  $R = 0.9702062$ .

Figure 6 shows the observed values of the jet lagging versus the values of the jet lagging predicted by the model presented in (7).

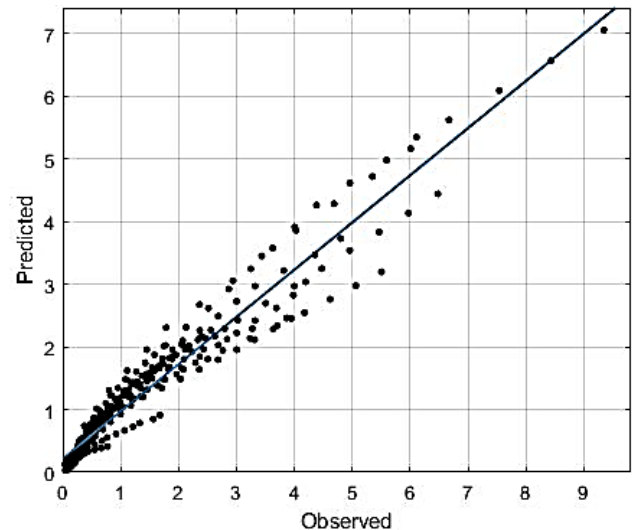
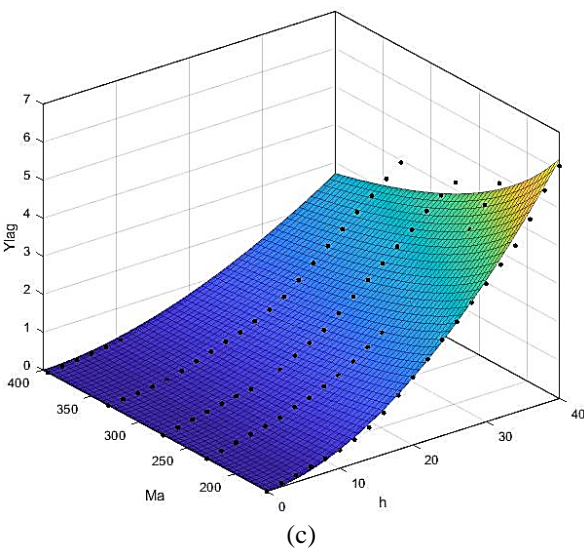


Figure 6: Observed versus predicted values of the jet lagging

#### 4. CONCLUSIONS

Experimental investigations have been carried for the jet lagging in abrasive waterjet cutting of high-speed tool steel. The effects of different operational parameters such as: pressure, abrasive mass flow rate, traverse speed and nozzle stand-off distance on jet lagging have been investigated.

The change of the jet lagging as the function of operating pressure, stand-off distance, traverse speed, and abrasive mass flow rate can be noted. With the increase of the traverse speed, there is an increase in the jet lagging. Furthermore, it can be observed that the increase of operating pressure and abrasive flow rate causes the decrease of the water jet lagging. This clearly suggests a firm correlation between the water jet lagging and the referred machining parameters. The influence of the depth of cut on the jet lagging is also significant. With the increasing depth of cut, the jet lagging also increases.

It is interesting that the exponent associated with the depth of cut, in all Equations (3, 4, 5 and 6), has a value of about 2.

As a result of this study, it is observed that these operational parameters have a direct effect on jet lagging. It has been found that traverse speed has the most effect on jet lagging. An increase in traverse speed is associated with an increase in jet lagging. These findings indicate that the use of low traverse speed is preferred to obtain overall good cutting performance, but at the cost of productivity. Jet lagging constantly decreases as the mass flow rate increases. It is recommended to use a more mass flow rate to decrease jet lagging. Among the process parameters considered in this study traverse speed and abrasive mass flow rate have a similar effect on jet lagging, but one opposite from another. Stand-off distance has no apparent effect on jet lagging, but to achieve an overall cutting performance, a low stand-off distance should be selected.

From the experimental results, an empirical model for the prediction of jet lagging in the AWJC process of high-speed tool steel has been developed using regression analysis. Also, verification of the developed model for using it as a practical guideline for selecting the parameters has been found to agree with the experiments. Therefore, the need for extensive experimental work in order to select the magnitudes of the most influential abrasive waterjet cutting parameters on jet lagging of high-speed tool steel can be eliminated.

Based on the model from (7), it can be concluded that with the proper selection of the machining parameters, the desired values of the jet lagging can be achieved. The entire length of the cut does not need to be machined with such selected machining parameters, but only the parts of the path that make the curve, because major mistakes occur there.

From the (7), we can conclude that an increase of the depth of cut, stand-off distance and traverse speed leads to an increase of the jet lagging, and with an increase of operating pressure and abrasive mass flow rate jet lagging decreases.

The experiments were carried out on only one material, EN HS6-5-2, so that the obtained models are only valid for this material. It is necessary to carry out the experiments on different materials or the same material with different heat treatments to determine the effects of the mechanical properties of materials on the jet lagging.

It would also be interesting to carry out the experiments on the same material with different thicknesses and other mechanical properties, and to investigate this phenomenon and its dependencies.

## NOMENCLATURE

|                    |                                     |
|--------------------|-------------------------------------|
| $d_a$              | Mean diameter of abrasive particles |
| $d_j$              | Diameter of water jet               |
| $h$                | Depth of cut                        |
| $Ma$               | Abrasive mass flow rate             |
| $p$                | Working pressure                    |
| $U$                | Traverse speed                      |
| $S_d$              | Stand-off distance                  |
| $E$                | Materials Young's modulus           |
| $Y_{lag}$          | Jet lagging                         |
| $\rho_a$           | Abrasives density                   |
| $\rho_w$           | Density of water                    |
| $s$                | Sample thickness                    |
| $a, b, c, d, e, f$ | Coefficients of regression analysis |

## ACKNOWLEDGEMENTS

This paper presents the results of research conducted on the doctoral research project "Investigation of Abrasive Water Jet Machining Parameters" which is financially supported by the Ministry of Science of Montenegro.

## REFERENCES

- [1] A. Hascalik, U. Caydas and H. Gurun, "Effect of Traverse Speed on Abrasive Waterjet Machining of Ti-6Al-4V Alloy," *Materials and Design*, Vol. 28(6), pp. 1953-1957, (2007)
- [2] A.W. Mombar and R. Kovacevic, "Principles of abrasive water jet machining", Springer, London, (1998)
- [3] M.A. Azmir, A.K. Ahsan, "Investigation on glass/epoxy composite surfaces machined by abrasive waterjet machining". *Journal of Materials Processing Technology*, Vol.198, pp 122-128, (2008)
- [4] C. Ma, R.T. Deam. "A correlation for predicting the kerf profile from abrasive waterjet cutting". *Experimental Thermal and Fluid Science*, Vol.30, pp 337-343, (2006)
- [5] P. Jankovic, M. Radovanovic, J. Baralic and B. Nedic, "Prediction model of surface roughness in abrasive water jet cutting of aluminum alloy", *Balkan Tribology*, Vol.19(4), pp 618-628, (2013)
- [6] D. Arola and M. Ramulu, "Mechanism of material removal in abrasive waterjet machining", *Proceedings of the 7th Water Jet Conference*, pp. 46-64, (1993)
- [7] M. Hasish, "A modeling study of metal cutting with abrasive waterjets", *Journal of Engineering Materials and Technology*, Vol. 106, pp. 88-100, (1984)
- [8] J. Zeng, R. Heines and T.J. Kim, "Characterization of energy dissipation phenomena in abrasive water jet cutting", *Proceedings of the 6th American Water Jet Conference*, pp. 163-177, (1991)

[9] M. Chithirai Pon Selvan and N. Mohana Sundara Raja, "A Machinability Study of Stainless Steel Using Abrasive Waterjet Cutting Technology", International Conference on Mechanical, Automobile and Robotics Engineering, Penang, Malaysia, (2012)

[10] R. Kurbegovic, M. Janjic, M. Vukcevic and D. Durovic, "Effect of abrasive water jet machining process parameters on jet lagging", 42. Jupiter conference, Belgrade, Serbia, pp. 3.81-3.87, (2020)

[11] V. Marušić, J. Baralić, B. Nedić i ostali, "Effect of machining parameters on jet lagging in abrasive water jet cutting", Technical Gazette, Vol. 20(4), pp. 677-682, (2013)

# Application of Taguchi method to bevel angle optimization during plasma arc cutting

Dragoljub Lazarevic<sup>1</sup>, Andjela Lazarevic<sup>1,\*</sup>

<sup>1</sup>Faculty of Mechanical Engineering, University of Nis (Serbia)

*Increasing machinability is usually a challenging issue, thus represents an often-explored topic. Many useful tools and methodologies were developed to support engineers and researchers in their effort to optimize production and find good trade-off between competitive priorities in manufacturing. Taguchi optimization method represents experimental methodology that allows engineers to obtain information about the process factors' effects on the selected outcome, with the minimum number of experiments. In this paper one element of the plasma cut quality was investigated, namely bevel angle in terms of the combination of plasma cutting process input factors: cutting current, cutting speed and material thickness. The orthogonal array L9 was developed, therefore nine experiments were conducted while each experiment was repeated 3 times under the same conditions. Signal-to-noise ratio, analysis of means and analysis of variance were undertaken to estimate the factor effects on the process output, optimal combination of the input factor levels, as well as these factors significance with the 95% of confidence. Finally, the confirmation testing was done in order to verify the expected response of the obtained optimal combination of the input factor levels.*

**Keywords:** Plasma cutting, Taguchi method, bevel angle, optimization

## 1. INTRODUCTION

Plasma arc cutting is non-conventional machining process that employs thermal energy for removing material from the kerf zone, as well as the high kinetic energy of the plasma jet. Plasma arc is formed by heating pressurized plasma gas, which is supplied in a gap between the cutting nozzle and the electrode of the plasma torch (cathode). The ionization of constricted plasma gas begins with the ignition high frequency spark, forming a pilot arc. When the cutting torch is sufficiently close to the workpiece, the pilot arc is transferred to the material, acting as an anode. Thus, the main arc is established between the cathode and the workpiece material [1]. Passing through the nozzle, outside toward the workpiece material, plasma arc maintains gas ionization of the plasma jet, containing heated partially ionized gas, with high kinetic energy. Plasma jet heats the workpiece's surface in the kerf zone, which melts and partially vaporize material at a localized area of workpiece. Melted material is expelled out of the kerf by the kinetic energy of plasma jet. After initial piercing of material, plasma arc is moved across the workpiece's surface to produce required cut [2, 3].

The electrode is usually made of water-cooled copper, which melts fast. Therefore, its durability was improved by using a tungsten or hafnium inserts at the top of each electrode, which is the point where the arc attaches. The selection of plasma gases is wide, starting from the compressed air or oxygen, toward nitrogen, carbon dioxide, argon and different argon mixtures (hydrogen-argon ...). For cooling the torch components and consumables, the shield gas is employed. If plasma cutting process involves cutting with transferred arc materials that could be cut are aluminium, brass, carbon steel, mild steel, stainless steel, cast iron, copper, copper alloys, high nickel, magnesium etc [4].

Plasma arc cutting has wide range of applications in various manufacturing processes, intended either for final products or further processing. Plasma arc cutting is also a fascinating process that provokes researchers to undertake different kind of experimental investigations, metering, statistical analysis, modelling, simulations and optimizations. In this process researchers are facing high quantities of energy and intense temperatures and velocities in plasma jet, that impact significantly to the cutting quality. High temperatures of ionized gas lead also to the significant changes in plasma jet depending of the distance from the workpiece, or the position in the kerf area during cutting. Finally, high temperatures during this process influence considerably working conditions and environment, therefore, a special attention should be assigned to the safety issues at the work floor [5,6].

In the past years, researches focused on the plasma arc cutting process could be classified into several groups. Although the technology is getting more and more advanced and the precision is increased, the phenomena that follow intense phase transformations of material during plasma cutting are very often subject of different investigations and challenges in research. Cutting quality is still subject of interest for many researchers, especially in application of different artificial and computational intelligence methods or advanced statistical methods for process modelling and optimization, with respect to the various elements of plasma cut quality [7].

Number of studies is devoted to the investigation of the relationship between plasma cutting parameters and desired cut quality characteristics. Some of them do not investigate relations between cutting parameters and their interrelations in terms of finding mathematical or other models of the processes abstracted as black box. They present the metering results, varying one or more parameters, using the graphical representation as one of the most explicatory ways of data representation. These

\*Corresponding author: Andjela Lazarevic, Aleksandra Medvedeva 14, 18.000 Nis, andjela.lazarevic@gmail.com

studies could be important from the empirical point of view, since it is useful to have as many data as it could be obtained in order to reach the appropriate conclusions of the plasma arc cutting process [8-10].

Each investigation of the plasma cutting process aimed to understand process mechanisms and effects of the plasma cutting parameters on the quality characteristics, gave special attention to the experimental investigation. Although many types of designs of experiment were used for plasma cutting process modelling and optimization (Box-Behnken design, Box-Wilson design etc.) [11-14], in recent years the application of Taguchi orthogonal arrays dominated.

Salonitis investigated the effects of cutting power, cutting speed, cutting height and plasma and gas pressure on the kerf taper angle, surface roughness and the size of heat affected zone (HAZ) by Taguchi L<sub>9</sub> orthogonal array, which was followed by the empirical regression model development [15]. Bhuvnesh used Taguchi method to achieve the optimum condition for material removal rate and surface roughness, while its study revealed that the surface roughness is inversely proportional to the material removal rate [16]. Plasma arc surface hardening was also explored using Taguchi design, while the significance of process parameters and its interactions was investigated [17]. Plasma surface hardening was also investigated by Yang, while the Taguchi L<sub>9</sub> orthogonal array was used. One research included the study of the effect of specimen thickness on the maximum hardness obtained in plasma surface hardening, while the other one is related to the process optimization to achieve maximum hardened depth of ASSAAB 760 Steel [18,19]. It could be concluded that the surface roughness and material removal rate are the most investigated output process parameters, while usual input process parameters are cutting speed, material thickness, cutting current and gas pressure.

Standard for thermal cutting, including plasma arc cutting, provided the methodology and evaluation criteria for the cut quality classification SRPS EN ISO 9013:2017 (Thermal cutting – Classification of thermal cuts – Geometrical products specification and quality tolerances). These standard defined terms related to the cutting process, as well as finished workpiece and specified the determination of the quality of cut surface, including the definition of bevel cut [20]. Bevel angle is angle of the cut edge. When bevel angle is 0° for vertical cut, the cut surface is under 90° comparing to the both upper and lower side of the workpiece (the torch position is perpendicular to the workpiece surface during cutting). However, this cut characteristic is not always easy to reach, therefore bevel angle is measured to assess the quality of the cut. Bevel angle is influenced by cutting speed, cutting current, material thickness, torch movement direction, standoff distance (distance between the nozzle and workpiece) [21]. Bevel angle, as one element of the plasma cut quality, was previously explored by experimental research and application of artificial neural network to model the impact of plasma cutting current, cutting speed and material thickness on the bevel angle [22].

However, the purpose of this research was to investigate the impact of cutting current, cutting speed and material thickness on the bevel angle during plasma arc

cutting. The experiment was based on the L<sub>9</sub> orthogonal array, in which three factors are varied at three levels. Based on the observed experimental results, the analysis of means (ANOM) and analysis of variance (ANOVA) was done (ANOVA) was done in order to determine process parameter significance and to find the optimal setting of the plasma cutting input parameters with respect to as small as possible bevel angle.

## 2. TAGUCHI DESIGN AND EXPERIMENTAL SETUP

Taguchi method is closely related to the quality engineering, as a research procedure for improving functionality by taking advantages of measurement methods in functional, multidimensional space. It introduced the idea of robust design which is design of a product that causes no trouble under any conditions (especially uncontrollable environmental conditions) or which are insensitive to component variation. This could be reached if the product functions could be evaluated under known and unknown conditions, by experimentally manipulating its design parameters, with the objective to find product design configuration insensitive or less sensitive to variation [23]. Taguchi methodology proposed to conduct the design of experiment using special set of orthogonal arrays, which stipulates full information out of as low as possible number of experiments, by choosing adequate level combinations of the input process parameters. Therefore, this Taguchi approach significantly reduces the time and cost of the experiments since it uses various types of fractional designs to study the entire experimental hyperspace.

In this paper, the Taguchi methodology was used to find optimal setting of the plasma cutting input parameters to make this process as less sensitive as possible. The considered process parameters were cutting current, cutting speed and material thickness. The observed output parameter was bevel angle, as an angle of the cut edge, in the cases when the cut edge is not perfectly squared to the surface of the workpiece.

Therefore, three input parameters were selected, each having three levels (low, medium and high). Based on parameter factors and levels, L<sub>9</sub> (3<sup>3</sup>) orthogonal array was developed, followed by the experimental setup in accordance with orthogonal array variable factor layout. For the same experimental setup, each experiment was repeated three times. Table 1 shows low, medium and high level of the input process parameters of the cutting current, cutting speed and material thickness.

Table 1. Input parameters and their levels

| Cutting parameter       | Level      |               |             |
|-------------------------|------------|---------------|-------------|
|                         | 1<br>(low) | 2<br>(medium) | 3<br>(high) |
| Cutting current [A]     | 80         | 100           | 130         |
| Cutting speed [mm/min]  | 800        | 1,200         | 1,900       |
| Material thickness [mm] | 8          | 10            | 15          |

The experiment was performed on the CNC machine HPm Steel Max 6.25 (High Performance Machinery). Plasma cutting unit used on this machine was Hypertherm HPR130. The workpiece material was X10CrNiMn-16-10-2 (EN 10025), with the following

chemical composition: 0.1 % C; 16 % Cr; 10 % Ni and 2 % Mn [4].

Taguchi method parameter design converts the output (response) parameter to the signal-to noise ratio. This ratio combines the mean (signal) and the standard deviation (noise) of the output process parameter at each setting of input parameters in orthogonal array into a single performance measure. Basically, it compares the level of a desired signal to the level of background noise. There could be distinguished three types of this ration, depending on the criterion for the quality characteristic to be optimized: smaller-the-better, larger-the-better, and nominal-the-better. In this paper smaller-the-better ration

was used since the objective is to make output as small as possible.

$$\eta_i = S / N = -10 \log \left( \frac{1}{n} \sum_{j=1}^n y_{ij}^2 \right) \quad (1)$$

Where  $\eta_i$  is signal-to-noise ratio of the  $i^{\text{th}}$  trial,  $y_{ij}$  is  $j^{\text{th}}$  observed value of the response in  $i^{\text{th}}$  trial.

Design of experiment, together with the response value, as well as calculated signal-to-noise ration are shown at figure 2.

Table 2. Design of experiment and experimental results (signal-to-noise ration)

| Trial no. | Cutting current | Cutting speed | Material thickness | Bevel angle |           |           | Signal to noise |
|-----------|-----------------|---------------|--------------------|-------------|-----------|-----------|-----------------|
|           | I [A]           | v [mm/min]    | s [mm]             | $\beta_1$   | $\beta_2$ | $\beta_3$ | $\eta$          |
| 1         | 80              | 800           | 8                  | 3.32        | 3.40      | 3.78      | -10.896         |
| 2         | 80              | 1,200         | 10                 | 2.8         | 3.40      | 3.25      | -9.995          |
| 3         | 80              | 1,900         | 15                 | 2.7         | 2.67      | 3.03      | -8.958          |
| 4         | 100             | 800           | 10                 | 3.6         | 3.74      | 4.06      | -11.607         |
| 5         | 100             | 1,200         | 15                 | 3.35        | 3.60      | 3.25      | -10.638         |
| 6         | 100             | 1,900         | 8                  | 2.5         | 2.26      | 2.44      | -7.612          |
| 7         | 130             | 800           | 15                 | 3.4         | 3.35      | 3.45      | -10.630         |
| 8         | 130             | 1,200         | 8                  | 2.45        | 2.50      | 2.85      | -8.320          |
| 9         | 130             | 1,900         | 10                 | 2.18        | 2.40      | 2.32      | -7.241          |

### 3. ANALYSIS OF THE RESULTS AND DISCUSSION

#### 3.1. Analysis of means (ANOM)

ANOM is the average response for each combination of input process parameters levels in a

statistic Taguchi method and is used to estimate factor of the process parameters. Figure 1 represents average response at each process parameter level, where it could be seen which parameter affects more on the bevel angle.

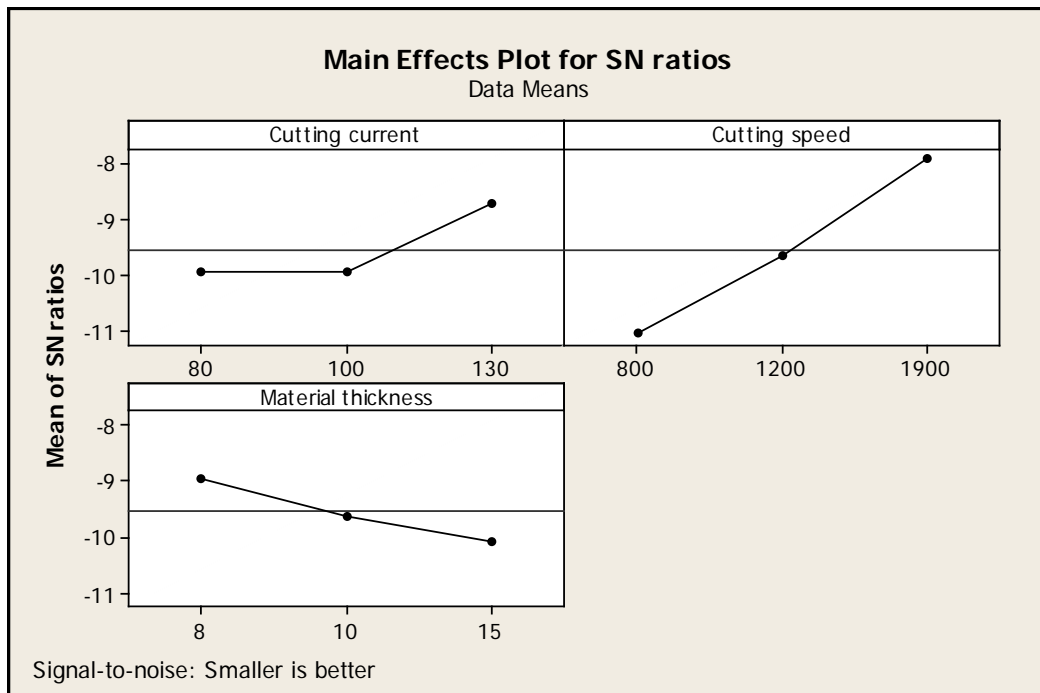


Figure 1. ANOM – response diagram for S/N ratio

Figure 1 reveals the optimal combination of input plasma cutting parameters and their levels that yield to the optimum bevel angle with minimum variance around the target value. This combination includes cutting current at the high level (130 A), cutting speed at high level as well (1,900 mm/min) and material thickness at low level (8mm) ( $A_3B_3C_1$ ).

Table 3 shows ANOVA for signal-to-noise ratio

| Source             | Degrees of freedom | Sum of squares | Mean square | Fisher's ratio (F) |
|--------------------|--------------------|----------------|-------------|--------------------|
| Cutting current    | 2                  | 2.978          | 1.489       | 37.194             |
| Cutting speed      | 2                  | 14.532         | 7.266       | 181.477            |
| Material thickness | 2                  | 1.947          | 0.974       | 24.314             |
| Error              | 2                  | 0.080          | 0.040       |                    |
| Total              | 8                  | 19.538         |             |                    |

In order to perform ANOVA, the total sum of squared deviations was calculated, which was then decomposed into sum of squared deviations due to each input process parameter and sum of squared error.

F test was then applied to assess the which input process parameter have significant effect on the bevel angle. The mean of squared deviations due to each process parameter was calculated, which is equal to the sum of squared deviations due to each input process parameter divided by the number of degrees of freedom associated with each process parameter. Finally, Fisher's ratio (or F value) represents the ratio between the mean of squared deviations (variance) of the input cutting parameter and the mean of error squared (error variance). F test value of the individual process parameter is compared with the standard F table value at the 5% significance level. If the F test value is greater than table value, the cutting parameter can be considered significant. Table F value is 19, therefore, it could be concluded that all three input process parameters represent significant input parameter for the observed quality characteristic.

Table 3 also enabled to measure percentage contribution of each input process parameter on the bevel angle.

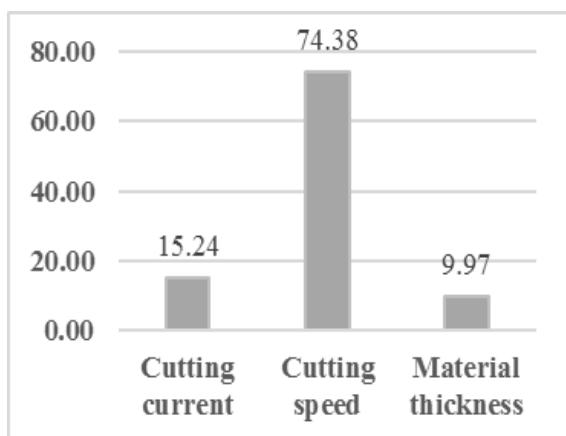


Figure 2. Percentage contribution of each input process parameter

### 3.2. Analysis of variances (ANOVA)

ANOVA for the S/N ratios was carried out in order to assess the effect and significance of each process parameter. Table 3 shows the result of ANOVA for signal-to-noise ratio for bevel angle.

From figure 2 it could be observed that the change of all input process parameters, for the given experimental hyperspace, affects the bevel angle significantly. From the parameter contributions, it is obvious that the most influential plasma cutting process parameter with respect to the bevel angle is cutting current (74.38%). The second-high parameter contribution is cutting current (15.24%), while the material thickness has the least impact although not neglecting (9.97%).

### 3.3. Confirmation test

Since the optimal combination of input process parameters and their levels ( $A_3B_3C_1$ ) does not match any experimental observation carried out in Taguchi orthogonal array from table 2, the verification of the estimated result against experimental value was needed.

Once again, the experiment carried out for the cutting current of 130A, cutting speed of 1,900 mm/min and material thickness of 8mm. After three experimental runs and bevel angle measuring, its average level, as well as signal-to noise ratio was calculated.

To predict signal-to-noise ratio of the bevel angle obtained with optimal conditions the following equation was applied:

$$\eta_{opt} = \eta_m + \sum_{i=1}^8 (\bar{\eta}_i - \eta_m) \quad (2)$$

where  $\eta_m$  is the overall mean of the signal-to-noise ratio and  $\eta_i$  is the mean of the signal-to-noise ratio at the optimal level of each factor i.

Since the experimental signal-to-noise ratio was -6.418, while estimated signal-to-noise ratio was -6.522 it could be concluded that the estimated value is very close to the experimental value, therefore, the optimal combination of input process parameters by could be confirmed.

## 4. CONCLUSIONS

In this paper, Taguchi method was used to find the optimal combination of the input process parameters that yield to the optimum bevel angle with minimum variance around the target value. The experimental investigation

was performed in accordance with the Taguchi  $L_9$  orthogonal array, for the selected number of three input process parameters and their levels. The investigation showed that the optimal combination of the process input parameters is as follows: high level cutting current (130 A), high level cutting speed (1,900 mm/min) and low level material thickness (8mm) -  $A_3B_3C_1$ . This conclusion could be supported by the consideration of the named parameters impact on the cut surface quality from the theory, practice and experience. Namely, when cutting current increase more energy is transferred to the workpiece, therefore the plasma jet needs to spend less time in the kerf zone. This is the reason why cutting speed should increase when using higher cutting current. Increasing the cutting current increase the plasma cutting unit ability to cut, especially if thicker materials are about to be cut. However, for the particular material thickness range, the increase in cutting current and speed will not significantly impact the quality, as it was confirmed also by this investigation. However, it should be stated that material thickness is influential parameter for wide ranges of thicknesses, and it represents one of the first parameters to be considered during the selection of the plasma cutting unit.

The confirmation test led to the conclusion that experimental results obtained after repeating the experiment by setting input process parameters at optimal levels ( $A_3B_3C_1$ ) are very close to the estimated results, therefore the optimal machine setting can be verified for the considered experimental hyperspace.

This paper also investigates the effects and significance of input process parameters cutting current, cutting speed and material thickness on bevel angle. F test was used to determine whether each input process parameter has significant effect on the bevel angle. The analysis has showed that all considered process parameters are significant. The cutting speed was identified as the most significant process parameter followed by the cutting current and finally material thickness.

As it was suggested by many researches for various machining processes, Taguchi approach was proved as powerful methodology for plasma cutting process optimization. The design of experiment was simplified comparing to the potential full factorial experimental design, where 27 combinations of the input process parameters were needed to perform the experimental investigation. The number of 9 performed experiments, with three repetition each, was three times lower than if the full factorial design was carried out. This considerably decreased the time and cost of the experimentations, while the optimum input process parameter combination at specified levels can be simultaneously discovered for the bevel angle with minimum variance.

## REFERENCES

- [1] D.J. Osterhouse, J.W. Lindsay and J.V.R. Heberlein, "Using arc voltage to locate the anode attachment in plasma arc cutting", *Journal of Physics D: Applied Physics*, Vol.46, (2013)
- [2] V. Nemchinsky, "Plasma flow in a nozzle during plasma arc cutting", *Journal of Physics D: Applied Physics*, Vol. 31, pp. 3102-3107, (1998)
- [3] G. Cantoro, V. Colombo, A. Concetti, E. Ghedini, P. Sanibondi, F. Zinzani, F. Rotundo, S. Dallavalle and M. Vancini, "Plasma arc cutting technology: simulation and experiments", *Journal of Physics: Conference Series* Vol. 275, (2011)
- [4] A. Lazarevic, „Modelling of the parameters correlations of the plasma arc cutting process and analysis of the process energy balance by applying artificial intelligence methods”, Doctoral dissertation, Faculty of Mechanical Engineering, University of Nis, (2010)
- [5] D. Begic, M. Kulenovic, A. Cekic and E. Dedic, "Some experimental studies on plasma cutting quality of low alloy steel", *Annals of DAAM for 2012 & Proceedings of the 23<sup>rd</sup> International DAAM symposium*, Vol. 23, No. 1, pp. 183-186, (2012)
- [6] C.C. Fagarasan, M.S. Popa and A. Tirla, "Theoretical and experimental contributions on the use of plasma arc installations in cutting different types of materials – Part 1", *Annals of DAAM for 2010 & Proceedings of the 21st International DAAM symposium*, Vol. 21, No. 1, (2010)
- [7] B. R. Hendricks, "Simulation of plasma arc cutting", Ms Thesis, Faculty of Engineering Peninsula Technikon, Center for Research in Applied Technology (1999)
- [8] M. I. Ojovan, "Handbook of Advanced Radioactive Waste Conditioning Technologies", Woodhead Publishing Series in Energy (United Kingdom), (2011)
- [9] J. Kechagias, M. Pappas, S. Karagiannis, G. Petropoulos, V. Iakovakis and S. Maropoulos, "An ANN Approach on the Optimization of the Cutting Parameters During CNC Plasma-Arc Cutting", *Conference proceedings on ASME 2010 10th Biennial Conference on Engineering Systems Design and Analysis, Istanbul (Turkey)*, 12-14 July 2010, pp. 643-649, (2010) <https://doi.org/10.1115/ESDA2010-24225>
- [10] D. K. Naik and M. Kalipada, "Predictive modeling of surface roughness, material removal rate and kerf using multiple regression analysis in plasma arc cutting process of hardox and abrex steel", *Surface Review and Letters*, Vol. 27 (9): 1950206 (12 pages), (2020) <https://doi.org/10.1142/S0218625X19502068>
- [11] K. Dehnad, "A Geometric Interpretation of Taguchi's Signal to Noise Ratio", *Quality Control, Robust Design, and the Taguchi Method*, Springer (Boston, MA) (1989) <https://doi.org/10.1007/978-1-4684-1472-1>
- [12] V. Colombo, A. Concetti, E. Ghedini, F. Rotundo, P. Sanibondi, M. Boselli, S. Dallavalle, M. Gherardi, V. Nemchinsky and M. Vancini, "Advances in Plasma Arc Cutting Technology: The Experimental Part of an Integrated Approach", *Plasma Chem Plasma Process*, Vol. 32, pp.411–426, (2012)
- [13] K. Kadirgama, M.M. Noor, W.S.W. Harun, K.A. Aboue-El-Hosseini, "Optimisation of heat affected zone by partial swarm optimization air plasma cutting operation", *Journal of Scientific & Industrial Research* Vol. 69, pp. 439-443, (2010)
- [14] C. Özek, U. Çaydas, E. Ünal, "A Fuzzy Model for Predicting Surface Roughness in Plasma Arc Cutting of

AISI 4140 Steel", Materials and Manufacturing Processes  
Vol. 27, pp. 95-102, (2012)

[15] K. Salonitis and S. Vatousianos, "Experimental Investigation of the Plasma Arc Cutting Process", Procedia 45th CIRP Conference on Manufacturing Systems 2012, pp.287-292, (2012)

[16] R. Bhuvanesh, M.H. Norizaman and M.S. Abdul Manan, "Surface Roughness and MRR Effect on Manual Plasma Arc Cutting Machining", World Academy of Science, Engineering and Technology, Vol. 6, (2012)

[17] M.I.S. Ismail and Z. Taha, "Experimental Design and Performance Analysis in Plasma Arc Surface Hardening", World Academy of Science, Engineering and Technology, Vol. 5, (2011)

[18] L.J. Yang, "Plasma surface hardening of ASSAB 760 Steel specimens with Taguchi optimization of the processing parameters", Journal of materials processing technology, Vol. 113, pp. 521-526, (2001)

[19] L.J. Yang, "The effects of specimen thickness on the hardness of plasma surface hardened ASSAB 760steel specimens", Journal of materials processing technology, Vol. 185, pp. 113-119, (2007)

[20] SRPS EN ISO 9013:2017 "Thermal cutting – Classification of thermal cuts – Geometrical products specification and quality tolerances" International Standards Organization/ Institute for Standardization of Serbia, (2017)

[21] V.V. Frolov, V.A. Vinokurov and V.N. Volčenkov, "Teoretičeskie osnov svarki", Высшая школа (Россия), (1979)

[22] A. Lazarevic, D. Lazarevic and N. Dabic, "Prediction of the Workpiece Bevel Angle during Plasma Cutting Process", Proceedings on the third international conference Mechanical Engineering in XXI century, Nis (Serbia), 17-18 September 2015, (2015)

[23] G. Taguchi, S. Chowdhury and Y. Wu, "Taguchi's quality engineering Handbook", John Wiley & Sons (Canada), (2005)

# Influence of technical-technological characteristics of workpieces on the choice of CNC machine tools

Marina Ivanović<sup>1\*</sup>, Mladen Rasinac<sup>1</sup>, Stefan Pajović<sup>1</sup>

<sup>1</sup>Faculty of Mechanical and Civil Engineering in Kraljevo, University of Kragujevac, Kraljevo (Serbia)

*The largest number of influences of the metal processing industry and the machine tool industry must be analyzed in defining the strategy, research and development of new products and technologies. The development of the industry and a large number of different products have conditioned certain requirements in terms of different structures of machining systems. One of the important conditions for the selection of CNC machine tools are the technical and technological characteristics of the workpieces. In this paper, prismatic workpieces will be considered. According to the technologies needed for the processing of a certain family of prismatic workpieces, it is necessary to define the structure of CNC machine tools. One of the ways to form the structure of CNC machine tools is from the appropriate library of standard machine modules. The goal is to increase productivity in production and reduce the number of machines, tools and accessories for their production.*

**Keywords: Workpiece, Machining system, CNC machine tools, Modules of machine tool**

## 1. INTRODUCTION

Machining of workpieces on machine tools is achieved by the relative movement of the tool and the workpiece. The path of relative contact between the tool and the workpiece depends on the shape of the workpiece being machined.

The path of relative contact is composed of elementary translational and rotational movements, which are realized by rectilinear and circular movement of the working organs of the machine tool. Each trajectory of the relative contact of the tool and the workpiece can theoretically be realized by a maximum of six elementary movements:

- Three translational movements along orthogonal coordinate axes,
- Three circular motions around these coordinate axes.

For the operation of machine tools, in addition to the movements that form the trajectory of the relative contact of the tool and the workpiece, additional movements are often required. These movements are most often related to the manipulation of tools and workpieces [1].

Modern machine tools and multi-position special machines have one, two or more main movements, several auxiliary movements and several additional movements.

Therefore, the total number of elementary movements of the formation of forms and additional movements can reach more than ten of movements, such as transfer lines. These elementary movements are highly predetermined by the technologies and morphology of the work items for which the machine tool is selected or designed. Hence, the influence of workpiece and technologies on the elementary movements of the education of form and on the structure of kinematic connections is of decisive importance.

## 2. DEVELOPMENT OF MACHINE TOOLS

Previously, machine tools specialized in a particular production process or a set of several such processes. With the development that eliminated all technological shortcomings, there was a significant re-examination of functionality. A "machining centers" has been developed capable of providing several functions that have

traditionally been performed by different groups of machines such as milling machines, drills, lathes, etc. With the development of such machining centers, and the ability to get to know the possibilities of machine tools by simply looking at the name, it has become a thing of the past. Although the names of processes such as scraping, final milling, etc. used to describe the process, the structure and appearance of the machines performing these operations can be completely different.

The main improvement of the machine tool came from the development of controllers that controlled functions such as movement, spindle, flow, fault diagnosis, coolant, tool changers, pallet changers, memory storage, etc. This almost eliminated the need for qualified machine operators and significantly reduced idle time in machine tools.

Many motion functions are integrated and controlled on a single CNC machine tool providing great flexibility, and the trend is to incorporate multiple functions. Technological advances have created a trend of "adding more features to an already complex machine tool for producing more complex components." This created the need for a systematic methodology for presenting current and future machine tools.

### 2.1. Application in industrial practice

Metal processing companies have a range of machine tools, from traditional lathes and milling machines to CNC machining centers, and perform the contracted work on these machines. Before they earn, they charge an hourly rate for the machine, the operator and the general cost of the job. The hourly rate for a machine depends on the price of the machine, so the rate charged by different companies may vary depending on which machine they intend to use for production.

Therefore, the method for quickly adjusting the capabilities of the machine tool, depending on the complexity of the component being processed, is basic for the customer and engineers for economical and high-quality production.

\*Corresponding author: Marina Ivanović, Dositejeva 19, Kraljevo, Serbia, ivanovic.m@mfkv.kg.ac.rs

Within special industrial sectors such as pharmaceutical, aerospace and food there is a group of specific workpieces. These workpieces have different weights, are machined outside the standard dimensions and have special characteristics.

A large number of characteristics present in such treatments cause high costs for their production. They are often produced once and with the help of code generated by CAD / CAM software [2].

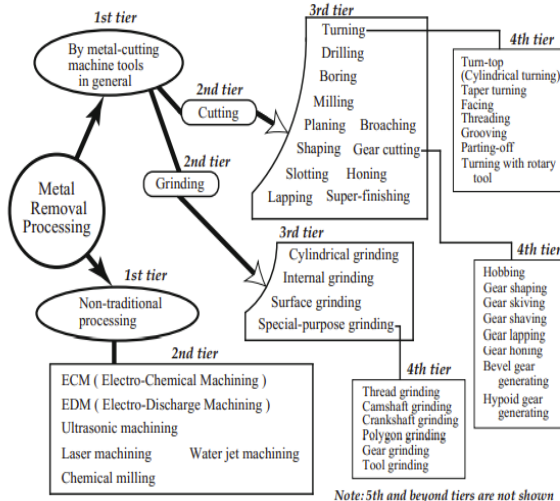


Figure 1: classification of different types of metal processing

Figure 1 shows the classification of basic types of metal processing

A study of the literature about machine tools identified the following basic points [3]:

- Advances in machining technology have reached a point where high-quality tools have been developed, coolants have been designed, control systems and controllers have been developed, technologies have been improved and better design methods have been applied. CNC machine tools capable of performing several processes that are traditionally performed on different machine tools have been developed. An analysis of some commercially available machine tools has indicated that there are machines that have widely different functions of movement and degrees of freedom.
- The block structure of the machine tool is divided into two parts as the main flow of forces and the flow of forces. This laid the foundations for the method of describing machine tools by an alphanumeric sequence.
- Shino and Ito presented the machine tool design methodology. They said the primary step was to provide a motion function in the block structure, which was then improved by structural design methods for mechanical properties. This shows that future machine tools can have more blocks that provide more complex motion functions. This was useful for developing alphanumeric code.

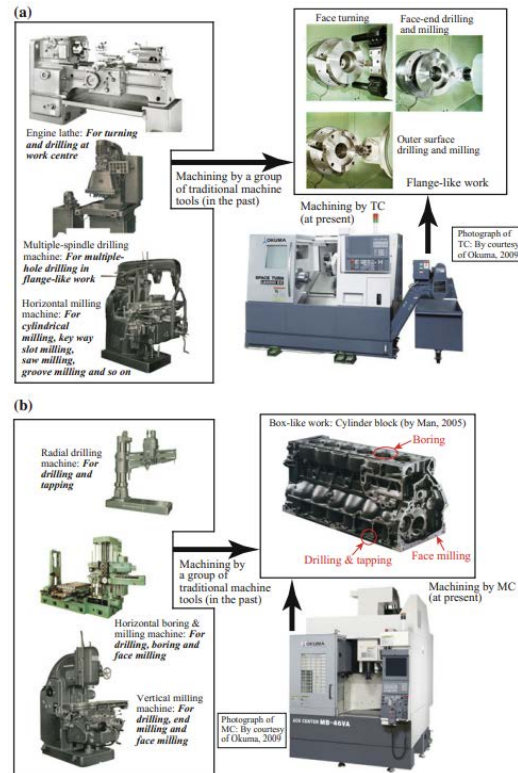


Figure 2: Integration of machining on traditional machine tools with machining centers (TC-turning centre, MC-machining centre)

Figure 2.A, B show that CNC machine tools can effectively replace various processing methods performed by a group of traditional machine tools. It is therefore natural that CNC machine tools now play a leading role in metalworking.

### 3. CHARACTERISTICS OF WORKPIECES

The basic division of workpieces is: cylindrical (axisymmetric) and prismatic. In this paper, will be considered prismatic workpieces due to their characteristics.

The processing of non-rotating (prismatic) workpieces is of special importance for any metal processing industry, because:

- they are of special importance for the functions of the machines in which they are installed,
- high percentage of the cost of machine structure waste on these parts (minimum 50%),
- production cycle and processing times are the longest.

Of the total number (100%) of prismatic workpieces, which appear in the metal processing industry, 35% belong to the group of plate-shaped objects and about 65% to the group of housing-shaped objects. Of the total number of prismatic parts, 80% do not exceed a volume of 650x650x650, which means that 80% of prismatic workpieces can be processed on machine tools with a working volume of 800x800x800 and smaller than these.

Prismatic workpieces can in principle be machined on three-coordinate drill-milling machines of different degrees of automation, with the proviso that workpieces with curved surfaces cannot be machined on machine tools with manual control [4].

Certainly, the results of workpiece processing are not the same, neither in terms of quality, productivity, nor in terms of price per workpiece. These and similar factors have a decisive influence on the orientation of work items on the available CNC machine tools, ie on the investment in new machines.

3.1. Characteristics of workpieces

Some of the basic characteristics of workpieces are:

- D - dimensional characteristics

The dimensions of the workpiece are directly related to the volume of the working space of the machine. In order to satisfy all the necessary processing operations, it is necessary that the workpiece corresponds to the working volume of the machine.

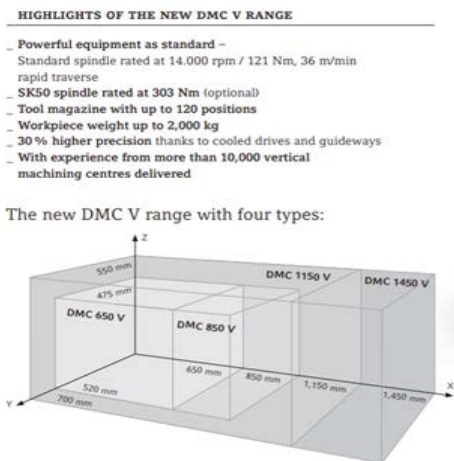


Figure 3: Dimensions of the workspace different types of machining centers from Deckel Maho DMC

- M - mass - weight

Workpiece classification by weight:

- light weight workpiece (up to 5 kg)
- medium weight workpiece (from 5 kg to 500 kg)
- high weight processing (up to several tons)

Some of the characteristics according to the working space of the machine is that the maximum workpiece weight for the DMC650 machine is 800 kg, and the maximum workpiece weight for the DMU 270 FD machine tool (5-axis milling machine) is 7 tons.

- $M_t$  – Material

Some of the most common processing materials are: aluminum alloys, cast iron, copper alloys, magnesium alloys, insoluble alloys, stainless steels, carbon steels, titanium alloys.

Depending on the machining material and the tool material (high-speed steel or hard metal), machining parameters such as cutting speed, pitch, cutting forces, etc. are defined.

- K –Construction characteristics

In terms of construction characteristics, it can be considered what type of surfaces are being processed, whether they are flat surfaces or have cylindrical, conical depressions or protrusions, whether the surfaces are stepped, whether they have certain grooves or pockets, whether the surfaces are from the outside sides of the workpiece or also internal, which require tool movement (linear or contour machining in several axes).

- T - technological (types of processing)

According to the technical drawing of the treatment, the following may be required: rough and / or fine treatment of a surface. Depending on the required type of processing (extensive milling, face milling, groove milling, hole milling, thread cutting, ...), it is necessary to take into account the choice of machine and tools with appropriate parameters.

- Q - quality / measure accuracy

Processing accuracy includes:

- accuracy of measures
- surface shape accuracy, and
- the accuracy of the relationship between two or more surfaces.

The accuracy of the measures represents the degree of concordance achieved with the nominal measure.

The accuracy of the shape of the surface represents the degree of concordance of the treated surface with the corresponding geometric surface.

The accuracy of the mutual relation of surfaces is defined by the appropriate deviation from the given nominal position, such as the deviation from parallelism, directness, coaxiality of cylindrical surfaces, etc.

- O – processing operations (coarse, fine, ...)

For each machining operation, it is necessary to define whether it is rough or fine machining. The sequence of operations is also defined in order to make optimal use of available tools and processing modes.

The field of computer-aided modeling workpieces has developed a number of techniques for unambiguous three-dimensional representations of objects. Characteristics recognition is a sub-discipline of modeling that focuses on the design and application of algorithms for detecting production data from manufactured solid models to computer-aided design (CAD) systems [5].

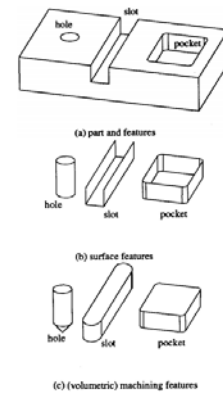


Figure 4: Basic shapes of surfaces on the workpiece

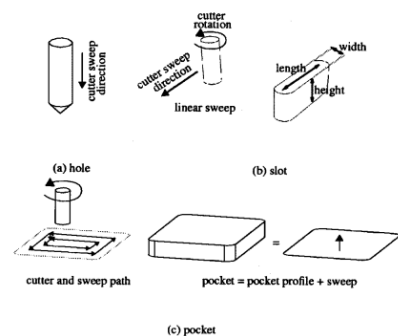


Figure 5: Procedure for obtaining surfaces during processing

Examples of this production information include functions such as holes, slots, pockets and other shapes that can be machined on modern CNC machine tools, Figures 4 and 5. Automated feature recognition has been an active research area in solid modeling for many years.

4. MODULAR DESIGN

The modular principle is a very popular method in the design of cars, diesel engines, household appliances, information devices, industrial equipment, etc. This trend can be considered as one of the great contributions of modular machine tool design to those working in other industries. Modular design can be classified into a significant number of variants, depending on the idea, goals and scope of application, areas of application, expected advantages, etc. In addition, the terminology of modular design itself has changed along with hierarchical changes in its meaning. Therefore, it is very difficult to present modular design in a simple sentence. Currently, the presence of modular design in the production sphere ranges from tools, templates and clamping accessories, through machine tools, to the production system [6].

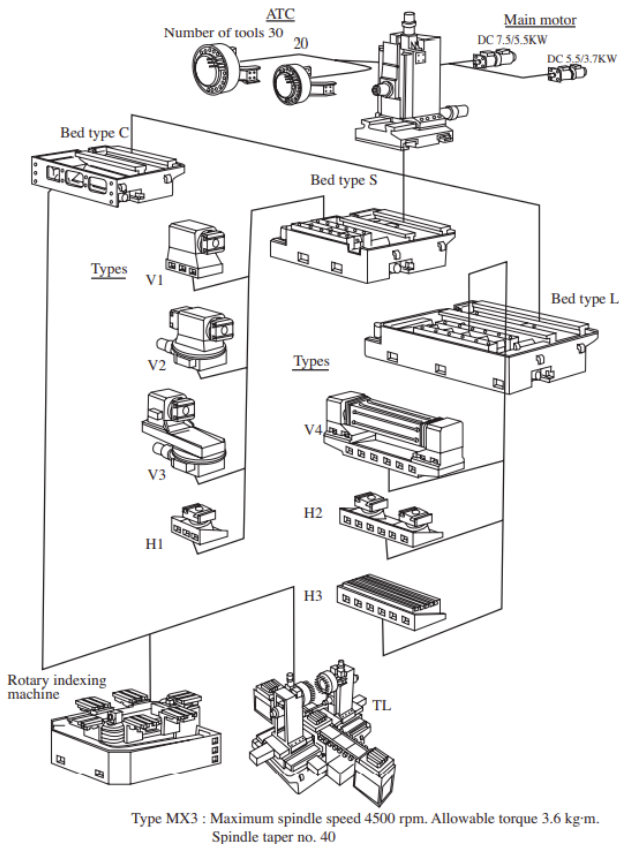


Figure 6: Modular design of the machining center (MC- machining center, courtesy of Ikegai Iron Works)

Figure 6 shows an advanced version of the MC-machining center of the Japanese company Ikegai Iron Works (type MX3) in the early 1980s. As can be seen, modular design is preferably used to produce 10 variants, ranging from a flexible pallet-type FMC (flexible manufacturing cell), through flexible transfer lines FTL (flexible transfer line), to a five-axis processing machine. In this case, the leading modules are the pole, the stand, the worktable, the tool magazine, the main spindle, etc. This

machine is a typical precursor to today's five-axis CNC machine tools.

Once the group of modules has been determined, a CNC machine tool with the required dimensional and performance specifications can be designed and manufactured as needed by selecting and combining the required modules from a predetermined group. In this case, the module must be standardized so that it has functionality or appropriate performance, including interchangeability with other modules. Figure 7 shows the hierarchical structure of a machining center (MC). For example, a machine consists of a unit assembly, a unit consists of functional assemblies, and a functional assembly is a combination of several parts - modules. Therefore, the question arises as to how to determine the module fully taking into account the hierarchical attributes of the product.

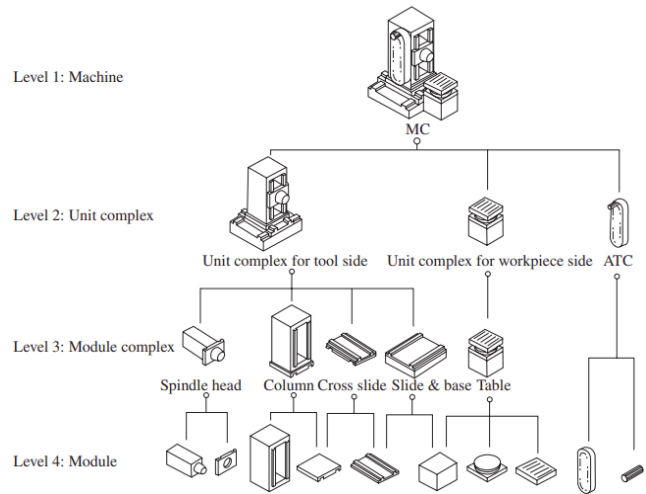


Figure 7: Modular structure of design machining center (MC- Machining center)

The following principles must be observed in modular design:

1. Modules must be replaceable without the use of measuring equipment.
2. The module must be self-contained with its own drive system, return voltage and lubrication systems or design accessories for easy expansion of such systems.
3. Each unit must have its own servo package with electronic connection to the digital input.
4. Modules must be usable in any orientation.
5. Modules must be replaceable within about half an hour.
6. The machining operations that are allowed in the first stage are scraping, drilling, grinding and milling.

It has been observed that modular design for conventional machine tools can provide economic benefit to the manufacturer and user, together with a wide range of choices according to production requirements.

4.1. Application of modular design for CNC machine tools

Modular design has been applied to CNC machine tools, with the aim of enabling machine flexibility from a hardware aspect. When the required machine tool flexibility is far greater than that possessed, the machine tools must be reconfigured to strengthen the machine flexibility by modular design, Figure 8.

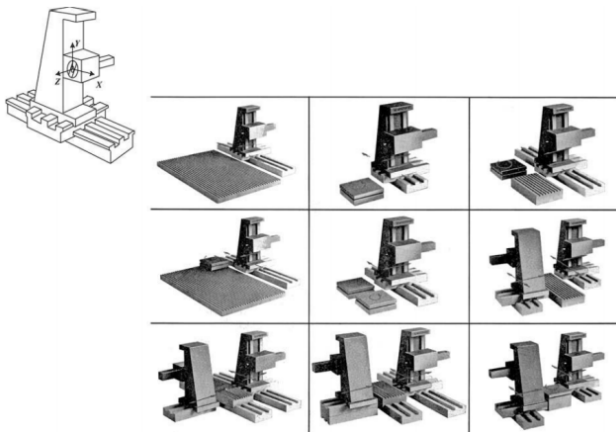


Figure 8: Horizontal machine tool with modular design (Scharmnn Co.)

For a given family of parts, as shown in the first block in Figure 9, the processing characteristics for each part will be extracted as shown in the second block and compared with the processing characteristics library shown in the third block to find the desired motion modules shown in the fourth. block through matching the corresponding movements. Different types of workpieces will lead to different sets of modules shown in the fifth block [7].

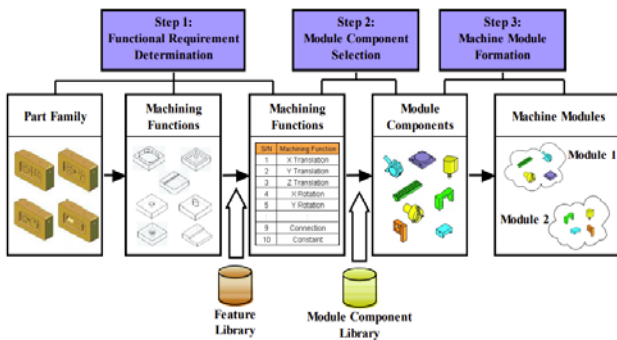


Figure 9. Diagram of module selection

As an illustrative example of the industrial application of mold making, Table 1 lists the processing characteristics that are allocated according to the STEP standard for a family of four given workpieces.

Part 1 includes five processing features: (i) two general pockets; (ii) 10 protrusions (and depressions) inside the pocket - cylindrical; (iii) two slots - rectangular profile; (iv) two blind holes - drilled; and (c) seven blind holes - cylindrical. Parts 2 and 3 contain six machining characteristics each, and part 4 contains four machining characteristics.

All these functions can be fitted with seven machining features (MF - machining features) as noted in Table 1: MF1— “General Pocket”; MF2— “Pocket bulges - cylindrical”; MF3— “Slot - rectangular profile”; MF4— “Blind hole - oppositely drilled”; MF5— “Blind hole - cylindrical”; MF6— “Bulge - general profile”; MF7— “Staircase”; MF8— “Rotated Profile - Removed Material Within Profile”.

Table 1: Machining features extraction

| Part 1   | Part 2  | Part 3  | Part 4  |
|--|---|---|---|
|  |   |   |   |
| Machining Features:<br>(1) General Pocket (2)<br>(2) Boss within a Pocket—Cylindrical (10)<br>(3) Slot—Rectangular Profile (2)<br>(4) Blind Hole—Counter-Bored (2)<br>(5) Blind Hole—Cylindrical (7) | Machining Features:<br>(1) Boss—General Profile (3)<br>(2) Boss within a Pocket—Cylindrical (3)<br>(3) Slot—Rectangular Profile (2)<br>(4) Blind Hole—Counter-Bored (2)<br>(5) Blind Hole—Cylindrical (7) | Machining Features:<br>(1) General Pocket (1)<br>(2) Boss—General Profile (1)<br>(3) Boss within a Pocket—Cylindrical (5)<br>(4) Step (1)<br>(5) Hole—Counter-Bored (2)<br>(6) Blind Hole—Cylindrical (7) | Machining Features:<br>(1) General Pocket (1)<br>(2) Boss—General Profile (1)<br>(3) Revolved Feature—Volume Removal (1)<br>(4) Blind Hole—Cylindrical (14) |

Table 2: Corresponding motion requirements

| Machining Feature | Spindle Axis | Motion Requirement                          |
|-------------------|--------------|---|
| MF1               | z            | x-Translation, y-Translation, z-Translation |
| MF2               | z            | x-Translation, y-Translation, z-Translation |
| MF3               | z            | x-Translation, y-Translation, z-Translation |
| MF4               | z            | z-Translation                               |
| MF5               | z            | z-Translation                               |
| MF6               | z            | x-Translation, y-Translation, z-Translation |
| MF7               | z            | x-Translation, y-Translation                |
| MF8               | y            | z-Translation                               |

Note: MF1—“General Pocket”; MF2—“Boss within a Pocket—Cylindrical”; MF3—“Slot—Rectangular Profile”; MF4—“Blind Hole—Counter-Bored”; MF5—“Blind Hole—Cylindrical”; MF6—“Boss—General Profile”; MF7—“Step”; MF8—“Revolved Feature—Volume Removal”.

Table 2 shows how these processing characteristics are related to the corresponding movement requirements. For example, MF1 (general pocket) is processed by placing the spindle in the z-axis and moving it in the x, y and z-axes. For MF2 to MF8, their movement requirements are detailed in Table 2.

### 5. CRITERIA FOR SELECTION OF THE MACHINE TOOL

The selection of workpieces for machining on CNC machine tools is often guided by the following criteria:

- Small and medium series with multiple repetitions,
- Complex geometry of workpieces with high processing requirements,
- High cost of production and long time of possible procurement or production in case of scrap,
- Work items with a long production cycle.

When describing the structural characteristics of CNC machine tools, the following are important [8]:

- position of the axis of the main working spindle,
- working stroke length (X, Y, Z),
- desk surfaces,
- maximum weight of the workpiece,
- positioning accuracy,
- installed power,
- speed and translational movements,
- time required to change tools,
- time required to change the work item,
- ways to change tools and work items and more.

### 6. CONCLUSION

All possible combinations of modules in the structural model of the CNC machine tool give many variant solutions, each of which is not adequate for realization from the production point of view. A large number of variant solutions are only theoretical possibilities, because the production of such structural

models of CNC machine tools would be very complex, and the functional characteristics would not meet the necessary requirements in terms of the possibility of upgrading the automatic pallet change system. In addition, modularity would not be satisfied, as some structural models of CNC machine tools would be suitable only for machining smaller and lighter workpieces, and some only for machining large and heavy machine parts.

The optimal structural solution of the CNC machine tool must be adapted to the technical and technological requirements of the cutting process when processing prismatic workpieces.

#### ACKNOWLEDGEMENTS

The authors wish to express their gratitude to the Serbian Ministry of Education, Science and Technological Development for supporting this paper (451-03-9/2021-14/200108).

#### REFERENCES

- [1] Y. Ito, T. Matsumura, "Theory and Practice in Machining Systems", Springer International Publishing, Switzerland,(2017), DOI 10.1007/978-3-319-53901-0
- [2] L.Chen, F.(Jeff) Xi, A. Macwan, „Optimal Module Selection for Preliminary Design of Reconfigurable

Machine Tools“, Journal of Manufacturing Science and Engineering, vol. 127(1), pp.104–115 (2005)

[3] S. Gao and J. J. Shah, Automatic recognition of interacting machining features based on minimal condition subgraph, Computer-Aided Design, Vol. 30, No. 9, pp. 727–739, (1998)

[4] M. Milojević, Lj. Lukić, „Modularno projektovanje“, Monografija, Lola Institut, Beograd (1996)

[5] E. Kumar „Optimal choice of a machine tool for a machining job in CAE environment“, PhD Thesis, School of Engineering and Design, Brunel University, (2010)

[6] J. Hyun Han, M. Pratt, W. C. Regli, Manufacturing Feature Recognition from Solid Models: A Status Report, IEEE Transactions on Robotics and Automation, VOL. 16, NO. 6, DECEMBER (2000)

[7] Y.Ito, „Modular Design for Machine Tools“, McGraw Hill: New York, NY, USA (2008), DOI: 10.1036/0071496602

[8] Z. Xu, F. Xi, L. Liu and L. Chen, „A Method for Design of Modular Reconfigurable Machine Tools“, Machines 2017, 5, 5; doi:10.3390/machines5010005

## Frequency Analysis of Noise at different Milling Parameters of Steel

Mladen Rasinac<sup>1\*</sup>, Branko Radičević<sup>1</sup>, Milan Kolarević<sup>1</sup>, Aleksandra Petrović<sup>1</sup>, Mišo Bjelić<sup>1</sup>

<sup>1</sup>Faculty of Mechanical and Civil Engineering, University of Kragujevac, Kraljevo (Serbia)

The aim of this paper was to experimentally analyse dependency between level of noise in octave band at various standardized central frequencies (31.5, 63, 125, 250, 500, ..., 16000 Hz) and different cutting parameters of milling. Based on data from our previous research we analyzed dependency between level of noise in octave band, at standard frequency 500 Hz, and axial and radial depth of cut. In Design-Expert<sup>®</sup> software we have found adequate models and equations that describes these dependencies. The experimental results obtained can be used for future investigations in this field.

**Keywords:** Milling, Noise, Frequency analysis

### 1. INTRODUCTION

In the literature it is usual to compare noise levels in milling process with respect to the spindle speed, feed rate, axial and radial depth of the cut. Purpose of those comparisons is to gain insight in effects of cutting parameters on occurrence of noise and vibrations. [1,2,3]

In addition to measuring noise levels, it is often useful to search characteristic patterns in acoustic spectra of certain technological process (milling, welding, grinding,...).

We have employed the acoustic spectra in analysis of sound emission caused by milling in a series of experiments with different technological parameters.

In [1,2] are explained in detail experiments that were conducted in our previous research. Based on the data obtained in the first set of experiments [1] we have done analysis of level of noise in octave band at different standardized central frequencies.

### 2. EXPERIMENT

As was mentioned above, in [1,2] are explained in detail experiments that were performed. Here are the most important data. Machine was CHARNOA CNC SYSTEMS (vertical milling machine). We used the milling cutter of diameter of 40 mm and with four APKT inserts and tool holder SANDVIK. For measurements of the sound pressure level (SPL) microphone Bruel & Kjaer 2270 was used. The distance between the centre of the cutter and the microphone was 200 mm. Material of the workpiece was carbon steel S355. The dimensions of the workpiece were: 80x55x55 mm. [1]

In Table 1 are given values of the cutting parameters for each of the experiments of the first set.

Table 1: Values of cutting parameters in first set of experiments [1]

| Cutting parameters |                  |                    |                     |                   |
|--------------------|------------------|--------------------|---------------------|-------------------|
| Experiment no.     | Axial depth [mm] | Feed rate [mm/min] | Spindle speed [rpm] | Radial depth [mm] |
| 1.1                | 0.5 – 3          | 150                | 800                 | 5                 |
| 1.2                | 1                | 375 - 900          | 1000                | 5                 |
| 1.3                | 1                | 300                | 600 - 1300          | 5                 |
| 1.4                | 1                | 150                | 1000                | 5 - 40            |

### 3. FREQUENCY ANALYSIS

In [1] we have done analysis of maximum sound pressure level  $L_{F_{max}}$ , dBA and equivalent sound pressure level  $L_{eq}$ , dBA on cutting parameters (axial depth of cut, feed rate, spindle speed and radial depth of cut).

There were performed analysis of time variations of sound pressure level. Here, the goal was to do a frequency analysis of noise levels for different cutting parameters.

By frequency analysis of noise levels for all mentioned cutting parameters, it is noticed that the maximum noise level occurs at a frequency of 500 Hz. On Figures 1 and 2 are given values of level of noise in octave band for all standard central frequencies for 8 passes in experiment 1.1. and 1.4.

From the given diagrams it can be clearly seen that the maximum level of noise occurs at a frequency of 500 Hz. The same was obtained for other experiments (1.2, 1.3).

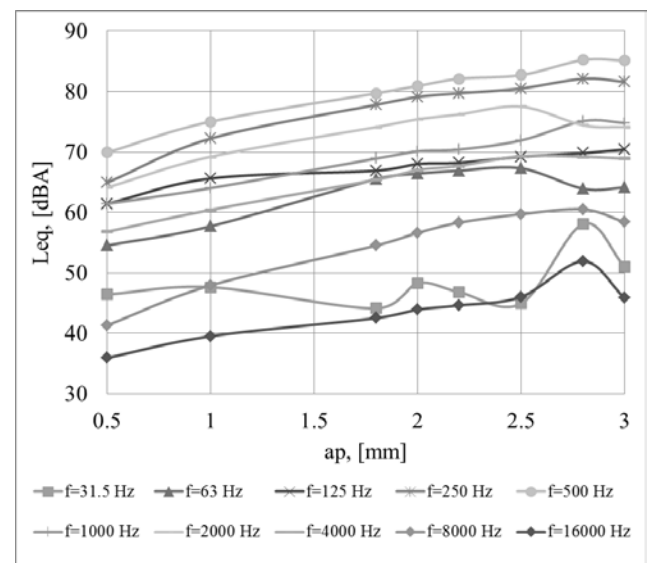


Figure 1: Equivalent sound pressure level at standard central frequencies for 8 passes in experiment 1.1.

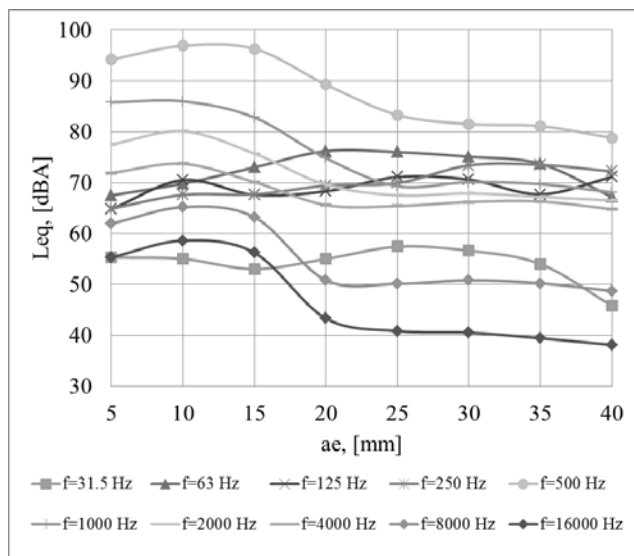


Figure 2: Equivalent sound pressure level at standard central frequencies for 8 passes in experiment 1.4.

Below we will focus on the frequency of 500 Hz.

On Figures 3 and 4 are given values of noise level at standard central frequency of 500 Hz.

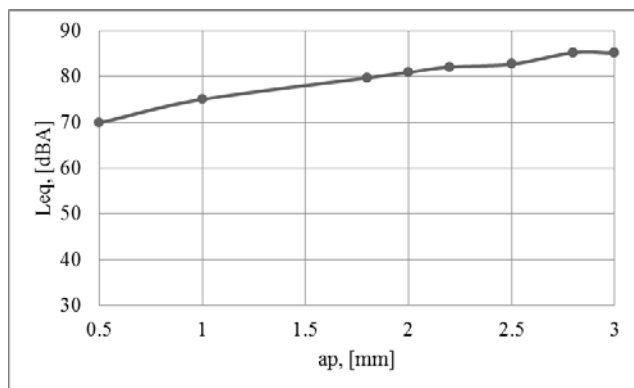


Figure 3: Equivalent sound pressure level at 500 Hz for 8 passes in experiment 1.1.

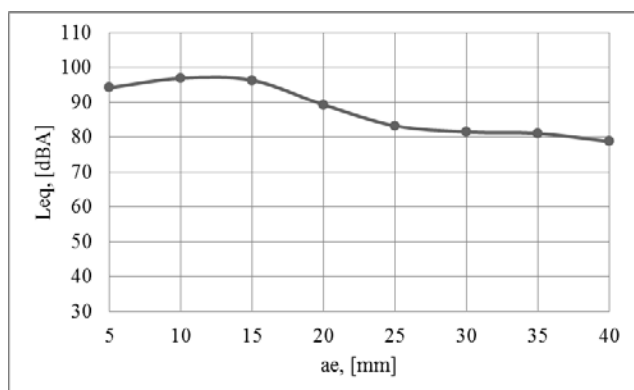


Figure 4: Equivalent sound pressure level at 500 Hz for 8 passes in experiment 1.4.

In Tables 2 and 3 are given values of equivalent sound pressure level at standard frequency of 500 Hz for different values of axial and radial depth of cut (for all 8 passes).

Table 2: Equivalent sound pressure level at 500 Hz for different values of axial depth of cut

| 500 Hz           |      |      |      |      |      |      |      |      |
|------------------|------|------|------|------|------|------|------|------|
| Pass             | 1    | 2    | 3    | 4    | 5    | 6    | 7    | 8    |
| Axial depth [mm] | 0.5  | 1.0  | 1.8  | 2.0  | 2.2  | 2.5  | 2.8  | 3.0  |
| $L_{eq}$ dBA     | 69.9 | 75.0 | 79.7 | 80.9 | 82.1 | 82.7 | 85.2 | 85.1 |

Table 3: Equivalent sound pressure level at 500 Hz for different values of radial depth of cut

| 500 Hz            |      |      |      |      |      |      |      |      |
|-------------------|------|------|------|------|------|------|------|------|
| Pass              | 1    | 2    | 3    | 4    | 5    | 6    | 7    | 8    |
| Radial depth [mm] | 5    | 10   | 15   | 20   | 25   | 30   | 35   | 40   |
| $L_{eq}$ dBA      | 94.2 | 96.9 | 96.3 | 89.3 | 83.3 | 81.5 | 81.1 | 78.8 |

#### 4. DEPENDENCE BETWEEN LEVEL OF NOISE AND PARAMETERS OF MILLING

In Design-Expert® v.9.0.6.2 software we have entered the data obtained from experiment, in order to find a suitable mathematical model that describes the relationship between level of noise and axial depth of cut, and level of noise and radial depth of cut, at frequency of 500 Hz.

The obtained mathematical model in the form of a polynomial of n-th degree represents the response function.

##### 4.1. Dependence between level of noise and axial depth of cut

Of the mathematical models available has been proposed quadratic model. In Table 4 are given ANOVA analysis of the proposed quadratic model.

After analysis of variance (ANOVA) the adequacy of the proposed mathematical model was confirmed. F value of the model ( $F=338.71$ ) implies the model is significant and there is only a 0.01% chance that an F-value could occur due to noise. Low probability value ( $p=0.00000459 < 0.0500$ ) confirms that the model parameters are also significant. Coefficient of determination (R-squared) and other statistics have good values which confirms the justification for choosing a mathematical model, Table 5.

The final equation of the mathematical model, with real coefficients, which adequately describes the dependence between equivalent sound pressure level, at frequency of 500 Hz, and axial depth of cut is as follows:

$$L_{eq} = 65.47268 + 10.09477 \cdot a_p - 1.17185 \cdot a_p^2 \quad (1)$$

A graphical representation of the mathematical model described by (1) and the arrangement of the experimental points is given in Figure 5.

Table 4: ANOVA analysis for the quadratic model

| ANOVA for Response Surface Quadratic model                     |                |    |             |          |                  |             |
|--|----------------|----|-------------|----------|------------------|-------------|
| Analysis of variance table [Partial sum of squares - Type III] |                |    |             |          |                  |             |
| Source   | Sum of Squares | df | Mean Square | F Value  | p-value Prob > F |             |
| Model  | 191.2038       | 2  | 95.6018777  | 338.7148 | 4.59E-06         | significant |
| A-ap   | 187.3202       | 1  | 187.3202349 | 663.6703 | 1.65E-06         |             |
| A^2  | 3.883521       | 1  | 3.883520509 | 13.7592  | 0.013864         |             |
| Residual   | 1.411245       | 5  | 0.282248918 |          |                  |             |
| Cor Total  | 192.615        | 7  |             |          |                  |             |

Table 5: Computational values of statistics for the evaluation of a quadratic model

|           |          |                |          |
|-----------|----------|----------------|----------|
| Std. Dev. | 0.531271 | R-Squared      | 0.992673 |
| Mean      | 80.075   | Adj R-Squared  | 0.989743 |
| C.V. %    | 0.663467 | Pred R-Squared | 0.972526 |
| PRESS     | 5.291962 | Adeq Precision | 46.05464 |

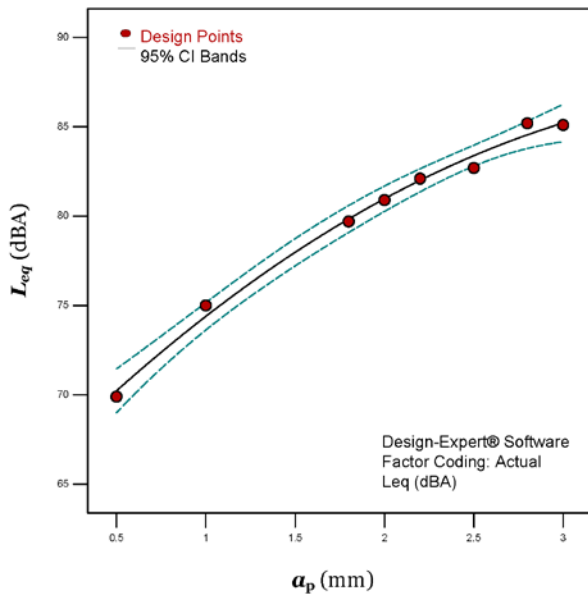


Figure 5: 2D response of the noise level

4.2. Dependence between level of noise and radial depth of cut

Here, of the mathematical models available a sixth degree model is proposed. In Table 6 are given ANOVA analysis of the proposed sixth degree model.

After analysis of variance (ANOVA) the adequacy of the proposed mathematical model was confirmed. F value of the model (F=7003.46) implies the model is significant and there is only a 0.91% chance that an F-value could occur due to noise. Low probability value (p=0.009147<0.0500) confirms that the model parameters are also significant. Coefficient of determination (R-squared) and other statistics have good values which confirms the justification for choosing a mathematical model, Table 7.

Table 7: Computational values of statistics for the evaluation of a sixth degree model

|           |          |                |          |
|-----------|----------|----------------|----------|
| Std. Dev. | 0.09559  | R-Squared      | 0.999976 |
| Mean      | 87.675   | Adj R-Squared  | 0.999833 |
| C.V. %    | 0.109028 | Pred R-Squared | 0.832819 |
| PRESS     | 64.19342 | Adeq Precision | 202.5326 |

The final equation of the mathematical model, with real coefficients, which adequately describes the dependence between equivalent sound pressure level, at frequency of 500 Hz, and radial depth of cut is as follows:

$$L_{eq} = 124.5 - 14.7371 \cdot a_e + 2.546904 \cdot a_e^2 - 0.19554 \cdot a_e^3 + \dots + 0.007273 \cdot a_e^4 - 0.00013 \cdot a_e^5 + 8.98 \cdot 10^{-7} \cdot a_e^6 \quad (2)$$

Table 6: ANOVA analysis for the sixth degree model

| ANOVA for Response Surface Sixth model                         |                |    |             |          |                  |             |
|--|----------------|----|-------------|----------|------------------|-------------|
| Analysis of variance table [Partial sum of squares - Type III] |                |    |             |          |                  |             |
| Source   | Sum of Squares | df | Mean Square | F Value  | p-value Prob > F |             |
| Model  | 383.9659       | 6  | 63.99431041 | 7003.459 | 0.009147         | significant |
| A-ae   | 59.91608       | 1  | 59.91608272 | 6557.143 | 0.007861         |             |
| A^2  | 4.83933        | 1  | 4.839330035 | 529.6104 | 0.027646         |             |
| A^3  | 7.767073       | 1  | 7.767073306 | 850.019  | 0.021827         |             |
| A^4  | 2.60352        | 1  | 2.60351976  | 284.926  | 0.037671         |             |
| A^5  | 3.386447       | 1  | 3.386446886 | 370.6086 | 0.033039         |             |
| A^6  | 1.545606       | 1  | 1.545606061 | 169.1492 | 0.048853         |             |
| Residual   | 0.009138       | 1  | 0.009137529 |          |                  |             |
| Cor Total  | 383.975        | 7  |             |          |                  |             |

A graphical representation of the mathematical model described by (2) and the arrangement of the experimental points is given in Figure 6.

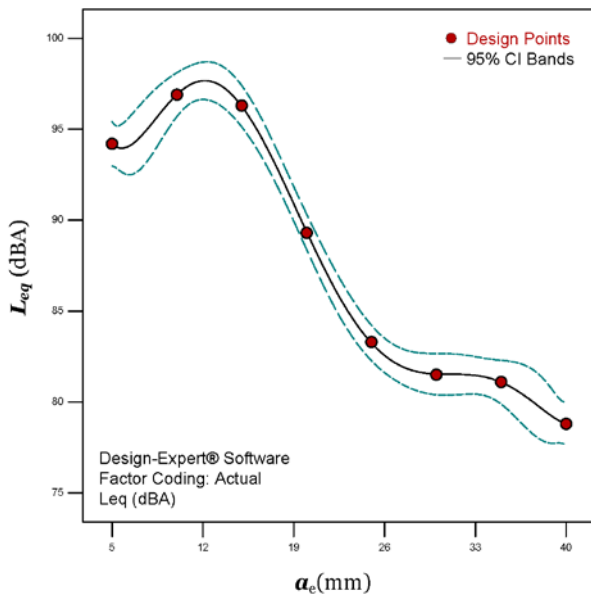


Figure 6: 2D response of the noise level

## 5. CONCLUSIONS

Measurements of noise reveal the maximum and equivalent values of sound pressure level, allowing studies of the influence of the cutting parameter to the generated noise. [1] In addition to measuring noise levels, it is often useful to search characteristic patterns in acoustic spectra of certain technological process.

The analysis performed in this study have shown that the maximum level of noise occurs at a frequency of 500 Hz for each value of the selected parameters.

Because the maximum noise level is observed at that frequency, we focused our analysis on finding the dependence between level of noise and axial depth of cut, and level of noise and radial depth of cut, at frequency of 500 Hz. Mathematical models that describe these dependencies were found in the software Design-Expert® v.9.0.6.2. By Analysis of variance (ANOVA) adequacy of the proposed mathematical models was confirmed.

More reliable results can certainly be obtained by performing a larger number of experiments.

The described methodology can serve as a basis for further research in this direction.

## ACKNOWLEDGEMENTS

This research is co-financed by the Ministry of Education, Science and Technological Development of the Republic of Serbia on the base of the contract whose record number is 451-03-9/2021-14/200108.

The authors express their gratitude to the Ministry of Education, Science and Technological Development of the Republic of Serbia for supporting this research.

## REFERENCES

- [1] M. Rasinac, A. Petrović, B. Radičević, V. Grković, M. Ivanović, "Experimental Analysis of Noise and Chatter Detection in Milling Depending on the Cutting Parameters", Proceedings of the 15th AVMS Conference, Timisoara (Romania), May 30-31, 2019 - Springer Proceedings in Physics, Vol. 251, pp. 333-342, ISBN 978-3-030-54136-1, DOI 10.1007/978-3-030-54136-1\_33, (2019)
- [2] A. Petrović, M. Rasinac, V. Grković, M. Ivanović, "An Experimental Plan for Noise Analysis and Chatter Detection in Milling Depending on the Cutting Parameters", Proceedings of the 26th International Conference Noise & Vibration – Serbia, Niš (Serbia), December 6-7, pp. 41-44, ISBN 978-86-6093-088-2, (2018)
- [3] G. Quintana, J. Ciurana, "Chatter in Machining Process: A review", International Journal of Machine Tools and Manufacture, Vol. 51, pp. 363-376 (2011)
- [4] M. J. Anderson, P. J. Whitcomb, "RSM Simplified, Optimizing Processes Using Response Surface Methods for Design of Experiments", Second Edition, CRC Press, Taylor & Francis Group (2017)
- [5] G. E. P. Box, N. R. Draper, "Response Surfaces, Mixtures, and Ridge Analyses", Second Edition, Wiley, (2007)
- [6] R. H. Myers, D. C. Montgomery, C. M. Anderson-Cook, "Response Surface Methodology, Process and Product Optimization Using Designed Experiments", Fourth Edition, Wiley (2016)
- [7] Stat-Ease, "Handbook for Experimenters", Version 11.01, Stat-Ease, Inc. (2019)  
www.statease.com/pubs/handbk\_for\_exp\_sv.pdf

## Influence of 3D printing parameters on the geometry and surface quality of manufactured parts on an FDM 3D printer

Petar Đekić<sup>1\*</sup>, Biljana Milutinović<sup>1</sup>, Mladen Tomić<sup>2</sup>, Saša S. Nikolić<sup>3</sup>

<sup>1</sup>The Academy of Applied Technical and Preschool Studies, Niš (Serbia)

<sup>2</sup> Faculty of Technical Sciences, University of Novi Sad, Novi Sad (Serbia)

<sup>3</sup>Faculty of Electronic Engineering, University of Niš, Niš (Serbia)

*The application and development of additive technologies has led to a significant change in production technologies. The application of these technologies significantly accelerates the development and shortens the production time of new products. In the product development process, the first step is to create a product model in order to eliminate the shortcomings of the final product. However, the creation of a physical model can be very complicated and expensive, so in recent times, the creation of a virtual product model is performed, using the appropriate CAD software. By applying 3D printing, physical models, prototypes or finished products are quickly obtained from a virtual product model. However, the quality of these products depends on many factors (type of 3D printer, print speed, print temperature, layer thickness, etc.). In this paper, the influence of the printing parameters on the FDM 3D printer at accuracy of the geometry of the created mode is presented. The material from which the parts were printed is ABS plastic, and the following parameters were varied: printing speed, layer thickness, extrusion speed, printing temperatures, etc. The paper presents the optimal printing parameters in which the appropriate surface quality and the exact geometry of the part are obtained.*

**Keywords:** Heavy machinery, Mechanical engineering, Civil engineering

### 1. INTRODUCTION

The term additive technology can be explained by the following definition "adding material in the form of layers, which is in contrast to conventional technologies to subtractive manufacturing in order to obtain the desired product" [1-4]. The application of these technologies significantly accelerates the development and shortens the production time of new products. Additive technologies make it possible to make parts from just a few millimetres to entire residential buildings. The goal of additive technologies is to quickly and accurately create a three-dimensional object, based on CAD models, with the goal of significant cost reduction compared to traditional technologies. [3-5]

Additive technologies are also called 3D printing. These technologies can be divided into several groups based on the principle of operation:

- Binder jetting
- Sheet lamination
- Material extrusion
- Direct energy deposition
- Material jetting
- Powder bed fusion
- Vat photo polymerisation [5, 6]

The processes also differ according to the type of material from which the part is made:

- Polymers,
- Ceramics,
- Metal

Process of 3D printing consists of several steps. The first step is to create a 3D model and adjust the print parameters; this process is called pre-printing preparation. The next step is the production of the part, i.e. 3D printing. The last step is to remove the excess material and, if necessary, to correct the product and this process is called post processing. [6].

Fuse deposition Modelling (FDM) is a typical representative of additive technologies and consists in the fact that the product is manufactured by building layer by layer of thermoplastic materials. The material is used in the form of a wire and is wound on a spool; the wire can be of different diameters, as follows: 1.75 mm; 2.85mm and 3mm. The group of materials most commonly used includes for 3D printing:

- Acrylonitrile butadiene styrene - ABS
- Polylactic acid - PLA
- Polyethylene terephthalate glycol - PET-G
- Polyvinyl Alcohol - PVA

Typical FDM printer is shown in figure 1. The printing process consists in drawing a wire filament (fig. 1 position 1) through the hot extruder (fig. 1 position 2) set to melting temperature of the filament. In the extruder, the solid material turns into a liquid state and is applied layer by layer to the hot working bed (fig.1 position3), until the finished product is obtained.[7]



Figure 1: Typical FDM printer [7]

Pre-printing preparation is one of the most important processes in FDM printing. During this process, a CAD model with the appropriate extension STL, OBJ, etc. needs to be processed by a piece of software called a "slicer," which converts the model into a series of thin layers and produces a G-code file. In this step it is necessary to set the following parameter:

- Working parameters
- Printing speed
- Layer thickness
- Infill pattern
- Infill density

Working parameters mainly depend on the type of material, so the manufacturer's recommendations for extruder and work bed temperatures are mainly used.

Printing speed represents the speed of movement of the nozzle and the following speeds are distinguished: printing speed, infill speed and travel speed.

Layer thickness denotes the height of layer which is stacked over other 3d printing is carried out by the addition of filament over layer. [6-9]

Infill pattern presents outer coated part of plastic which is inside the print. In 3D printing, different infill patterns can be used lines, concentric, zigzag, etc. [6-9]

Infill density is an amount of plastic whichever is incorporated inside the printing, usually ranging from 20 to 80 percent, rarely 100 percent is used.

## 2. EXPERIMENTAL

### 2.1. Material and device

For the purposes of this research, ABS thermoplastic with the following characteristics was used:

- Density 1.04g / cm<sup>3</sup>;
- Filament diameter 3 mm;
- Extruder temperature: 220-240 ° C;
- Bed temperature: 100-110 ° C.

The samples were made on a Pangu I3 printer with a nozzle diameter of 0.3 mm, and with a print space size of 150x150x150mm.

### 2.2. Dimensions and shapes of samples

All Samples for this research were modelled in Solid Works and then post processed in software called "Repetier-Host".

For the purpose of testing the influence of printing speed on dimensional stability and roughness, a test tube of the following dimensions was made: width 15 mm; length 15mm and height 20mm; wall thickness 1mm. The appearance of the CAD model and the real sample "1" are shown in Figure 2.

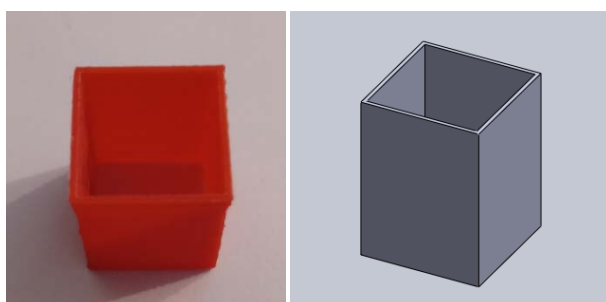


Figure 2: Real model and CAD model of sample "1"

The influence of the layer thickness of 0.1 mm; 0.2 mm; and 0.3 mm was first determined. After that printing speed was varied 15mm/s, 20mm/s, 30mm/s, 40mm/s and 60 mm / s, while travel speed was constant at 100 mm/s and infill speed was also constant at 60 mm / s.

For the purpose of testing the influence of infill pattern and infill density on dimensional stability and roughness, a test tube of the following dimensions was made: width 10 mm; length 80mm and height 4mm. The appearance of the CAD model and the real sample "2" are shown in Figure 3.

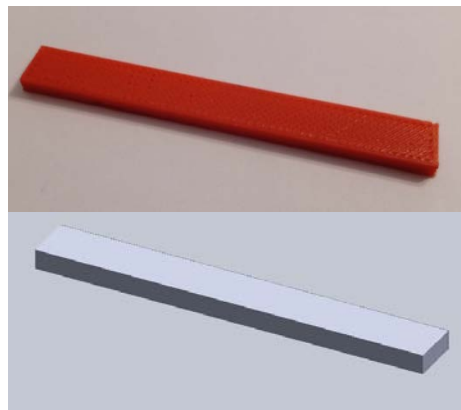
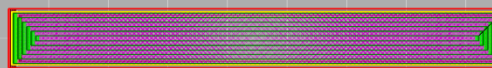
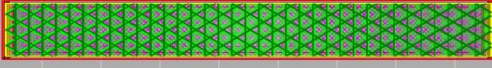


Figure 3: Real model and CAD model of sample "2"

Once the optimal layer thickness and print speed were determined, the effect of infill pattern on dimensional stability and surface roughness at constant infill density of 30 percent was determined. The following cases of infill patterns which are considered are shown in Table 1

Table 1: Different types of infill patterns

| Sample Name | Infill pattern   |
|-------------|--|
| Grid        |  |
| Line        |  |
| Concetric   |  |
| Crstal      |  |
| ZigZag      |  |

After that, the infill density was changed from 20 percentages to 80 percentages, by 10 percentages, at the optimal printing parameters that were previously determined.

The influence of optimal printing parameters, which were determined previously, on circularity were observed at the sample "3" with dimensions are inner diameter 25mm; outer diameter 40mm and high 15mm, whose appearance and CAD model is shown at figure 4.



Figure 4: Real model and CAD model of sample "3"

The influence of optimal printing parameters, on alignment were observed at the sample "4" with dimensions are diameter 20mm and high 40mm, whose appearance and CAD model is shown at figure 5.

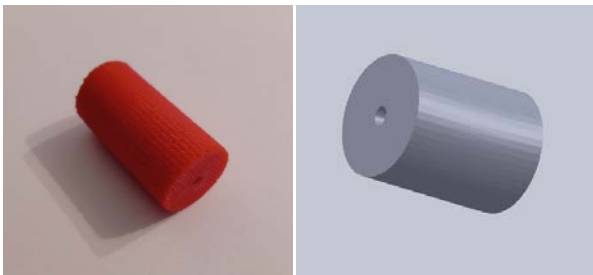


Figure 5: Real model and CAD model of sample "4"

### 2.3. Measuring of the samples

Dimension control of all samples were performed by using Digital Calipers type "Mitutoyo" from 0 to 150mm, with accuracy of 0.01mm. During the control, three consecutive measurements were performed, where the average value of the measurement was taken as the measured value. For each type of test, three samples were made and then controlled.

Surface roughness of all samples was measured with the device SurfTest "Mitutoyo" type SJ410. The appearance of the measuring point with the samples is shown in Figure 6.



Figure 6: Surface roughness measuring point

The measurement of the inner diameter (circularity) was performed on the sample "3" using a micrometer for internal measurement with a clock; the accuracy of the device is 0.01 mm.

The measurement procedure and the appearance of the measuring point are shown in Figure 7.



Figure 7: Measuring point of inner diameter

The alignment check was performed on samples "4" using a device with an accuracy of 0.01 mm, which is shown in Figure 8.



Figure 8: Alignment measuring point

### 3. RESULT AND DISCUSSION

At a default printing speed of 30mm/s and by varying the layer thickness of the material, it was found that with increasing layer thickness there is an increase in roughness, the measurement results are shown in the diagram at figure 9.

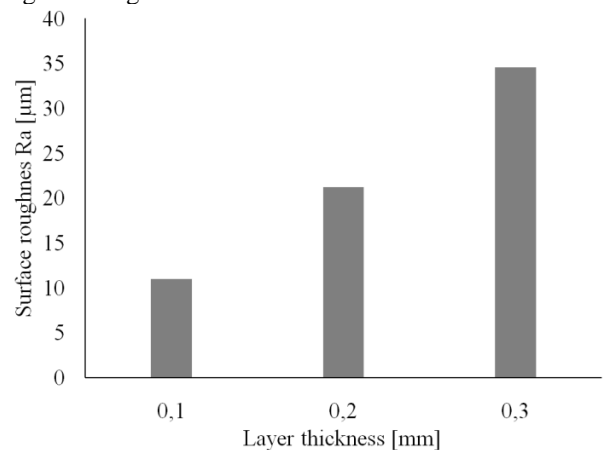


Figure 9: Influence of layer thickness on surface roughness

This is obvious because the thickness of the applied layer increases. However, when it comes to dimensions, all dimensions are reduced, which is shown in Table 2.

Table 2: Different types of layer thickness

| Layer thickness | Nominal dimensions  | Real dimensions   |
|-----------------|---|---|
| 0.1 mm          | width - 15 mm;<br>length - 15mm<br>height - 20mm;<br>w. thickness - 1mm | width - 13.9 mm;<br>length - 14.1mm<br>height - 18.34mm;<br>w. thickness 0,9mm    |
| 0.2 mm          | width - 15 mm;<br>length - 15mm<br>height - 20mm;<br>w. thickness 1mm   | width - 14,1 mm;<br>length - 13.8 mm<br>height - 18.75mm;<br>w.thickness - 0.91mm |
| 0.3 mm          | width - 15 mm;<br>length - 15mm<br>height - 20mm;<br>w. thickness - 1mm | width - 14.1 mm;<br>length - 14mm<br>height - 18.9mm;<br>w. thickness - 0.91mm    |

This is due to the reduction of the material and not the printing parameters. The largest dimension reduction is about 8 percentages.

However, changing the printing speed over 40mm / s up to 60 mm/s not only increases the roughness but also the effects to loss of flatness. In this case it is around 4.15 degrees. What can be seen in Figure 10, ImageJ software was used to process the image.



Figure 10: Deviation from flatness of planes

When it comes to testing samples "2", the samples were made with a layer thickness of 0.1 mm and printing speed was 30 mm / s, while travel speed was constant at 100 mm / s and infill speed was also constant at 60 mm / s.

This phenomenon can be explained by the fact that with increasing printing speed, the lower layers of the material cannot be cooled, so the material is smeared, i.e. there is an irregular and uneven application of the material.

The appearance of the layers of material at a printing speed of 30 mm / s is shown in Figure 11. The magnification on the microscope was 50x.

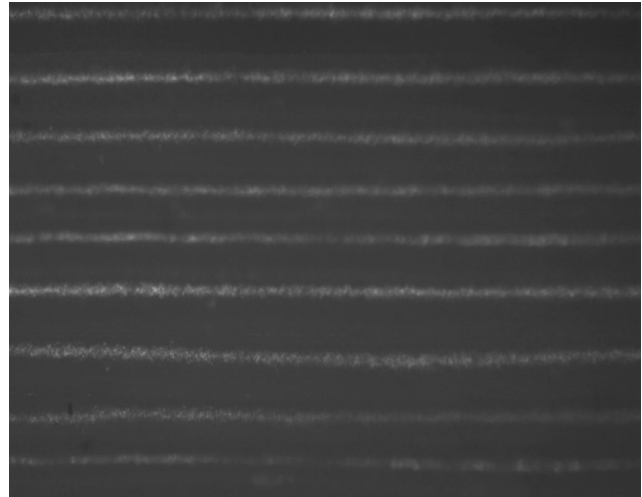


Figure 11: Shape of printing layers at printing speed of 30 mm/s

The appearance of the layers of material at a printing speed of 60 mm/s is shown in Figure 12. The magnification on the microscope was 50x



Figure 12: Shape of printing layers at printing speed of 60 mm/s

When measuring the dimensions of the samples, it was determined that the largest deviation occurred in the thickness of the sample, and this led to a decrease in height by about 17 percent. Deviation of dimension of sample "2" is shown in table 3.

Table 3: deviation of dimensions of sample "2"

| Nominal dimension | Real dimension   |
|-------------------|------------------|
| width - 10 mm;    | width – 8.mm;    |
| length - 80 mm    | width – 74.4 mm; |
| height - 4mm      | width – 3.32 mm; |

This is probably a consequence of the constant pressure of the nozzle on the material, which compresses it and fills the cavities between the layers, which did not cool down completely during the application of the next layer. What can be seen on a microscopic image of the structure Figure 13. The magnification of the stereo microscope is 50x.



Figure 13: Deformation of layers

Based on the measurement of surface roughness, the best results are obtained by applying a line-infill pattern, while the worst results are obtained by zigzag infill pattern, which is shown in the diagram in Figure 14.

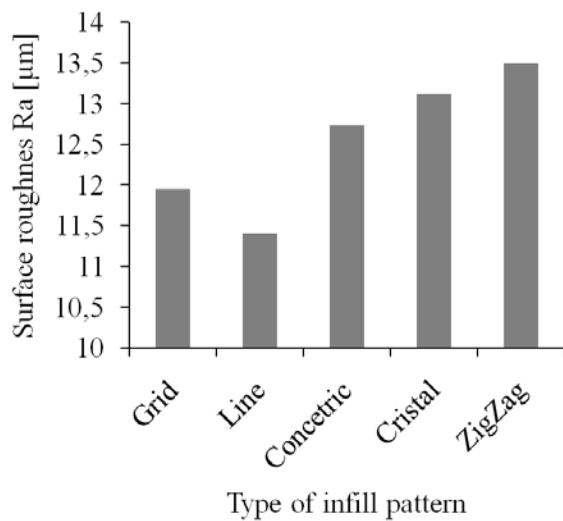


Figure 14: Influence of infill pattern on surface roughness

This phenomenon can be explained by the lack and uneven distribution of layers of material and cavities under the final layer of material.

If you look in more detail at the central layers in the samples, you can see that they are most densely distributed in the line and grid infill patterns, while in zigzag they are literally randomly distributed. This is shown in figure 15. Layer arrangement in zigzag infill pattern:

- position 1- outer layer (red)
- position 2 – cavity (grey)
- position 3 - one random layer (black)

- position 4 - second random layer (green)

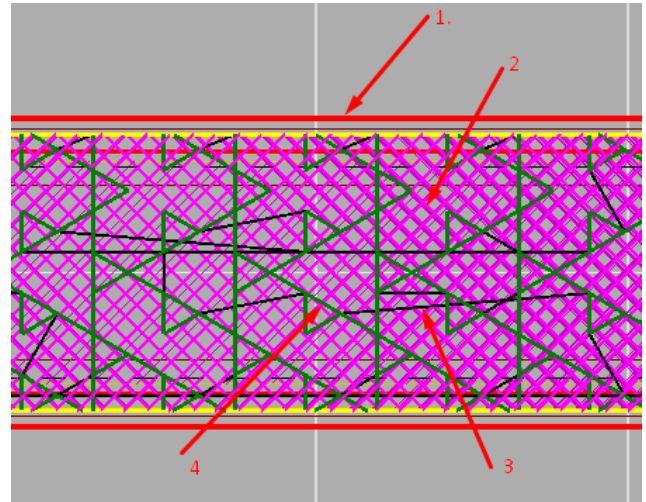


Figure 15 Layer arrangements in zigzag infill pattern

As the layers are applied during printing, the material penetrates into the cavities with a certain pressure and the roughness of the final layer increases.

As it was determined that the infill pattern *Line* has the lowest surface roughness, with the previously obtained optimal printing parameters, the infill density variation was approached, from 20 percentages to 80 percentages with a gap of 10 percentages. The influence of infill density on surface roughness is shown in the diagram in Figure 16.

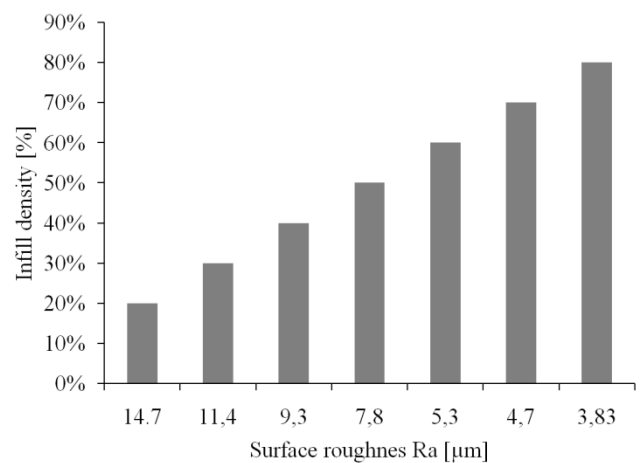


Figure 16: The influence of infill density on surface roughness

Based on the diagram, it can be noticed that with the increase of infill density there is a decrease of surface roughness. The reason for this phenomenon lies in the fact that the amount of air cavities is reduced and the material cannot penetrate into them. I.e. the layers of material are applied evenly so that there are no deviations in roughness when the finishing layer is applied. Also, it can be concluded that the smallest deviations in terms of dimensions at infill density are at infill density of 80%.

Influents of printing parameters at dimensions of sample "3" are shown in table 4.

Table 4: Deviation of dimensions of sample "2"

| Nominal dimension      | Real dimension           |
|------------------------|--------------------------|
| inner diameter - .25mm | inner diameter - 23,96mm |
| outer diameter - 40mm  | width - 38,46 mm;        |
| high - 15mm            | width - 13,44 mm;        |

This change in dimensions is a consequence of material shrinkage. Regarding the circularity, no significant deviations of the measured values of the inner and outer diameters were observed.

Influents of printing parameters at dimensions of sample "4" are shown in table 4.

Table 4: deviation of dimensions of sample "4"

| Nominal dimension | Real dimension           |
|-------------------|--------------------------|
| diameter - 20mm   | inner diameter - 19.33mm |
| high - 15mm       | width - 38.74 mm;        |

This change in dimensions is a consequence of material shrinkage. Regarding the alignment, no significant deviations of the measured values of the inner and outer diameters were observed. The measured deviations were less than two hundredths of a millimetre.

#### 4. CONCLUSIONS

Although additive technologies are considered advanced technologies in terms of material consumption and speed of workmanship, there are still a number of constrains.

Based on the experiments, it is concluded that the parts which were made, are within the tolerance of position and shape, but is not the case with the dimensions. According to the performed tests, it was determined that the material is being shrinkage. The degree of material shrinkage depends on the layer height, infill pattern and infill density. In essence, the shrinkage of material mostly depends on the cavities in the material created by printing. With a decrease in the thickness of the printing layer and an increase in infill density, there is a decrease in dimensional deviations.

Also, it was found that the surface roughness also depends on the above mentioned parameters. But in this case, the dominant role is also played by the infill pattern. The more even and denser the infill pattern is, the lower the surface roughness is. With increasing infill density there is a significant decrease in surface roughness. Best surface quality can be achieved by maximum infill density.

#### REFERENCES

- [1] N. Dixit, P. K. Jain, "3D printed carbon fiber reinforced thermoplastic composites: A review" *Materials Today: Proceedings* 43 pp. 678–681, (2021)
- [2] T. Singh, S. Kumar, S. Sehgal, "3D printing of engineering materials: A state of the art review," *Materials Today: Proceedings* 28 , pp. 1927–1931, (2020)
- [3] M. M. Prabhakar, A.K. Saravanan, A.Lenin, I. Jerinleno, K. Mayandi, P. S. Ramalingam "A short review on 3D printing methods, process parameters and materials", *Materials Today: Proceedings* (2020)
- [4] L. Safai, J. S. Cuellar, G. Smit, A. A. Zadpoor, "A review of the fatigue behavior of 3D printed polymers", *Additive Manufacturing Vol:28,pp. 87–97* (2019)
- [5] B. Sandeep, T.T.M. Kannan, J. Chandradass, M. Ganesan, A. J. Rajan, "Scope of 3D printing in manufacturing industries-A review", *A short review on 3D printing methods, process parameters and materials*, *Materials Today: Proceedings*, (2021)
- [6] M. R. Khosravanian, F. Bertob, M. R. Ayatollahic, T. Reinickea, "Fracture behavior of additively manufactured components: A review "Theoretical and Applied Fracture Mechanics Vol. 109, (2020)
- [7] <https://www.prusa3d.com/>
- [8] P. Morampudi, V.S.N. Ramana, K. A. Prabha , S. Swetha, A.N. Brahmeswara Rao," 3D-printing analysis of surface finish", *Materials Today: Proceedings* 43, pp. 587–592 (2021)
- [9] A. Ouballouch, R. El Alaiji, S. Ettiqa, M. Sallaoua, A. Bouayad, L. Lasri "Evaluation of dimensional accuracy and mechanical behavior of 3D printed reinforced polyamide parts ", *Procedia Structural Integrity Vol. 19, pp. 433–441* (2019)
- [10] R. Srinivasan, T. Pridhar, L.S. Ramprasath, N. Sree Charan, W. Ruban, "Prediction of tensile strength in FDM printed ABS parts using responsesurface methodology (RSM)", *Materials Today: Proceedings, Vol 27, pp. 1827–1832* (2020)
- [11] C. Abeykoon, P. Sri-Amphorn, A. Fernando, "Optimization of fused deposition modeling parameters for improved PLA and ABS 3D printed structures", *International Journal of Lightweight Materials and Manufacture, Vol. 3, pp 284-297* (2020)

## Prediction of the Strain hardening exponent of HP40-Nb alloy

Milica Timotijević<sup>1\*</sup>, Mišo Bjelić<sup>1</sup>, Dragan Rajnović<sup>2</sup>, Olivera Erić Cekić<sup>1</sup>

<sup>1</sup>Faculty of Mechanical and Civil Engineering, University of Kragujevac, Kraljevo (Serbia)

<sup>2</sup>Department of Production Engineering, Faculty of Technical Science, University of Novi Sad, Novi Sad (Serbia)

*This paper investigate the reliability of the strain hardening exponent calculation methods in the case of HP40-Nb class material. The approach was to analyse which one of the mathematical models (Hollomon, Swift, and Ludwik) could be applied and which provides the most accurate results to obtain the strain hardening exponent of centrifugally cast steel alloy HP40-Nb. The modelling was performed using the values of stress and strain obtained in the experiment by uniaxial tension. It was found that using the Hollomon and Swift methods the best approximation of the strain hardening exponent with theoretical values could be obtained.*

**Keywords: Mathematical Models, Strain hardening exponent, alloy HP40-Nb**

### 1. INTRODUCTION

The strain-hardening exponent ( $n$ ) and the strength coefficient are basic mechanical behaviour performance parameters of metallic materials. The exponent  $n$  can be determined from a tension test through appropriate transformations of stress-strain data and least-squares fitting of a straight line. Procedures for the computation of exponent  $n$  have been standardized by ASTM International and ISO. There are various mathematical models that were developed to represent the stress- strain behaviour of the materials [1].

Many researchers have carried out studies on the modelling of flow curves of materials. Sener et al. [2] have compared different constitutive equations for austenitic stainless 304 and ferritic 430 stainless steel sheets and have recommended the most suitable model for these materials. The models applicable are the Hollomon, Ludwik, Swift and El-Magd, model. Uniaxial tensile tests were carried out to obtain the material constants (strength coefficient and strain hardening coefficient) of the models. Afterwards, the applicability of these models was evaluated by comparing nonlinear regression parameter  $R^2$  and the most suitable model was determined for the tested materials. It was concluded that the maximum plastic strain value of the austenite 304 stainless steel sheet (0.35) is higher than that of the 430 ferritic stainless steel sheet (0.11) in the uniform plastic deformation region. This is expected due to the higher value of the strain hardening coefficient  $n$  in austenite stainless steel. From the value of statistical parameters  $R^2$ , it was concluded that the El-Magd model is highly effective for predicting the stress-strain curve, compared to the other three models. Ludwig model showed the worst performance for both materials.

Samuel et al. [3] have investigated suitability of the different constitutive equations for 316 stainless sheet steels which were prior deformed to 7.5%, 16.2% and 24.7% true plastic strain in uniaxial tension at room temperature. They found that behaviour could be adequately described by Ludwigs type and Swift equation. Further, they concluded that the strain hardening parameters at a given strain rate and temperature show that the strain hardening coefficient is weakly dependent on

yield strength while the strain hardening index shows a strong dependence on yield strength.

The results of tensile tests on AISI 1004 steel, AISI 1020 steel, and copper were used for a computer simulation by applying the finite element analysis (FEA) in work of Samuel and Rodriguez [4]. The values of the strength coefficient and the strain hardening exponent were obtained by linear regression using a power function. The results were very similar to those determined in accordance with the ASTM E646-07 standard. Finally, the good correlation between the simulations and the physical tests in the plastic region suggests that the simulation method adopted in this work has significant potential for quick and precise application to the drawing process.

D.F Pinto et al. [5] carried out the transformation of nominal voltage deformation curve into true voltage deformation dependency curve by math method. For the calculation, diagrams of dependency of eight different materials were used: nickel alloy 75, 12% Mn steel, steel S355, stainless steel 316L, aluminium tin alloy AA 1050, aluminum alloy sheet AA 5182, steel sheet dx56, and steel sheet of ZStE. The values for strain hardening coefficient were calculated based on three definitions of strains: true strain, conventional definition of true plastic strain, and true plastic strain according to ISO formula. After that, the values for the strain hardening coefficient were compared and it proposed an alternative formulation in which the strength coefficient and the strain-hardening exponent are functions of true-plastic deformation.

In this paper, a comparative study was carried out on Hollomon, Ludwik and Swift models to describe the flow behaviour of HP40-Nb alloy and validate it through ASTM E 646-16 [6] with the experimental data from the literature.

### 2. EXPERIMENTAL DETAILS

The materials in this study were machined out of one tube, made of the centrifugally cast alloy HP-40 alloy containing 1.5 wt.% Nb. Chemical composition of the tube samples supplied for investigation was analysed through standard analytical method of optical emission spectrophotometry at Spark 8860.

\*Corresponding author: Milica Timotijević, timotijevic.milica93@gmail.com

The catalytic tubes coming from the hydrogen plant are conventionally labelled as F-1A in this paper. The tube segments with 350 mm in length, were cut from the furnace regions which has been in exploitation for 20 years. Operating condition of the tubes was 870 °C under the maximum internal pressure of 2.5 bars (250 kPa). The exact locations where the sections were cut on the reformer columns in the respective plants were unreported and remain unknown. The tensile test of standard specimens (ISO 6892-1:2009) with a gauge length of 50 mm were carried out at room temperature using universal testing machine Schenck Trebel (1000 kN) under the constant crosshead speed mode with a nominal strain rate of 2 mm/min.

The specimens for microstructural investigation were polished following standard metallographic procedure and etched using a solution of 15 ml HCl, 10 ml Glycerol, and 5 ml HNO<sub>3</sub>. The microstructure was examined using scanning electron microscope JOEL JSM 6460 LV. The phases observed were analysed using an energy dispersive x-ray analyser system (EDS) INCA Oxford Instruments in conjunction with a SEM.

### 3. RESULTS

The chemical composition of the tube samples is presented in Table 1.

Table 1: Chemical composition (mass. %) of the tube samples

|       | C    | Mn    | Si   | P    | Ni    | Cr    | Mo   | Nb   |
|-------|------|-------|------|------|-------|-------|------|------|
| HP 40 | 0.45 | 0.984 | 1.45 | 0.04 | 33.47 | 25.04 | 0.03 | 1.50 |

The mechanical properties of the experimental samples are shown in Table 2.

The service tube tensile tests demonstrate that the tensile strength decreased from 450 MPa to 358 MPa, the yield strength increased from 240 MPa to 308 MPa, and the elongation decreased from 10% to 4.5%, respectively.

Table 2: The mechanical properties of samples measured by the tensile tests

| Material     | Ultimate tensile strength [MPa] | 0.2%Proof stress [MPa] | Elongation [%] | Hardness HB |
|--------------|---------------------------------|------------------------|----------------|-------------|
| As-cast      | 450                             | 240                    | 10             | 215         |
| Service tube | 358                             | 308                    | 4.5            | 185         |

Results of microstructural analysis are given in Figure 1. The microstructure consists of an austenitic matrix and a continuous network of primary eutectic carbides of two types: one rich in Nb (bright particles in Fig.1b) and one rich in Cr (dark particles in Fig.1b). These carbides are NbC and M7C3 (M= Cr, Ni, Fe) type.

The schematic illustration of tensile testing specimen is shown in Figure 2. The uniaxial tensile test is performed on a universal testing machine (Schenck Trebel), in displacement control mode, Figure 3.

The illustration of a True- Stress versus True-Strain curve for the material analysed is shown on Figure 4.

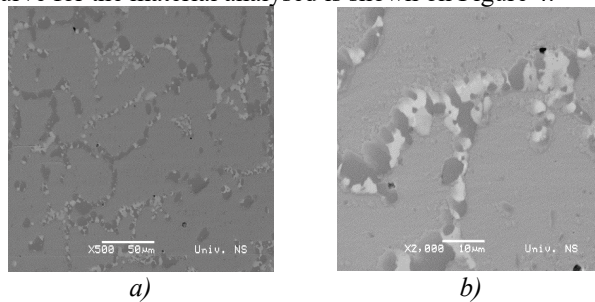


Figure 1: Microstructure of the HP heat resistant alloy SEM BSE images illustrating cross sections of samples from tube HP at different magnifications

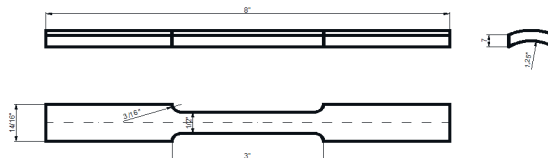


Figure 2: Schematic illustration of a tensile specimen



Figure 3: Photograph of the universal testing machine Schenck Trebel 1000 kN

The illustration of a True- Stress versus True-Strain curve for the material analysed is shown on Figure 4.

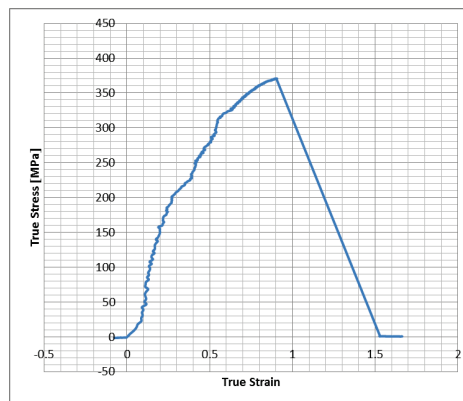


Figure 4: True Stress vs. True Strain Curve of the material analysed

The strain-hardening exponent n was calculated using the standard test method for tensile strain-hardening

exponents of metallic sheet materials (ASTM standard E646-16 [6]).

The equation for calculating  $n$  from a linear regression using five points taken in geometrical progression between true strain values of  $\epsilon = 0.010$  and  $0.032$  is as follows:

$$n = \frac{5 \sum_{i=1}^5 (\log \epsilon_i \log \sigma_i) - (\sum_{i=1}^5 \log \epsilon_i \sum_{i=1}^5 \log \sigma_i)}{5 \sum_{i=1}^5 (\log \epsilon_i)^2 - (\sum_{i=1}^5 \log \epsilon_i)^2} \quad (2)$$

where  $\sigma_i$  is the true stress and  $\epsilon_i$  is the true strain.

The equation for calculating the logarithm of the strength coefficient,  $K$ , is as follows:

$$\log K = \frac{\sum_{i=1}^N (\log \sigma_i) - n \sum_{i=1}^N \log \epsilon_i}{N} \quad (3)$$

The calculation of the standard deviation of the strain-hardening exponent,  $SD_n$ , is based upon the variance of the slope of the regression line.

$$SD_n = \left[ \frac{N \sum_{i=1}^N (\log \sigma_i - \log K - n \log \epsilon_i)^2}{(N - 2) \left( N \sum_{i=1}^N (\log \epsilon_i)^2 - \left( \sum_{i=1}^N \log \epsilon_i \right)^2 \right)} \right]^{1/2} \quad (4)$$

An example of a worksheet for manually calculating these values is found in Appendix 1.

The logarithmized yield stress curve for test tubes is provided in Figure 5.

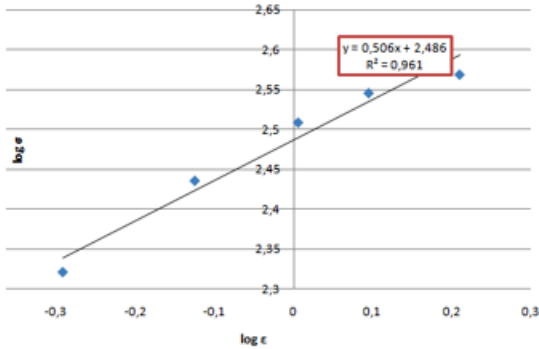


Figure 5: Log  $\sigma$  versus log  $\epsilon$  for  $n$  and  $k$  calculation

The trend line in Figure 5 is linear, i.e., of the type  $y=ax + b$ , where the coefficient (slope of the line)  $a$  and the intercept  $b$  represent the hardening exponent  $n$  and the strength coefficient  $K\sigma$ , respectively.

The theoretical value for the strain hardening coefficient for the material is  $n = 0.45-0.55$  [10.].

In the logarithmic curve of experimental values ( $\log \sigma - \log \epsilon$ ) the value of the strain hardening coefficient is obtained:  $n = 0,48$  for the material analysed.

Based on the presented, it can be concluded that the obtained values of the strain hardening coefficient with the experiment are within the boundaries of theoretical values.

Mathematical modelling on the experimental values of yield stress for the analysed material (numeric and logarithmic) are provided in Table 3.

Table 3: Experimental values of yield stress for the investigated material

| point | $\sigma$ [MPa] | $\epsilon$ [%] |
|-------|----------------|----------------|
| 1     | 209.10         | 0.5105         |
| 2     | 272.50         | 0.7501         |
| 3     | 322.63         | 1.0137         |
| 4     | 351.43         | 1.2452         |
| 5     | 370.77         | 1.6228         |

Mathematical modelling of yield stress ( $\sigma - \epsilon$ ) was performed using three equations of considered quasi-static models:

- Hollomon equation  $\sigma(\epsilon) = K\epsilon^n$  [7] (5)

- Ludwik equation  $\sigma(\epsilon) = \sigma_y + K\epsilon_p^n$  [8] (6)

- Swift equation  $\sigma(\epsilon) = K(\epsilon_0 + \epsilon_p)^n$  [9] (7)

Here  $\sigma$  is true stress,  $\sigma_y$  is the yield stress,  $\epsilon$  is true plastic strain,  $K$  is the strength coefficient,  $\epsilon_p$  plastic strain,  $\epsilon_0$  is initial strain,  $n$  is the strain hardening exponent.

Five different yield stress values  $\sigma$  were used to model yield stress curve  $\sigma - \epsilon$ , as recommended in ASTM E646-16

In the MATLAB program, a simulation of yield stress curve was performed using the specified models (empirical equations).

Three different constitutive models (Hollomon, Ludwik and Swift) are evaluated in this paper. The parameters for such models are identified from experimentally determined flow curves of material by curve fitting techniques.

Comparisons of predicted flow curves by different models with experimental data for the material analysis are shown in Figure 6-8.

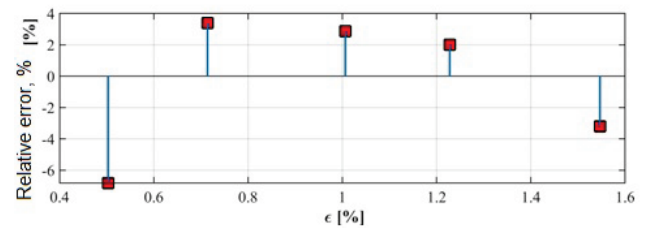
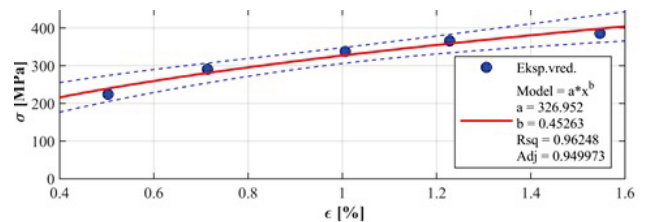


Figure 6: Comparison between the experimentally measured and calculated  $K$  and  $n$  ( $a$  and  $b$  in legend) values obtained by Hollomon method

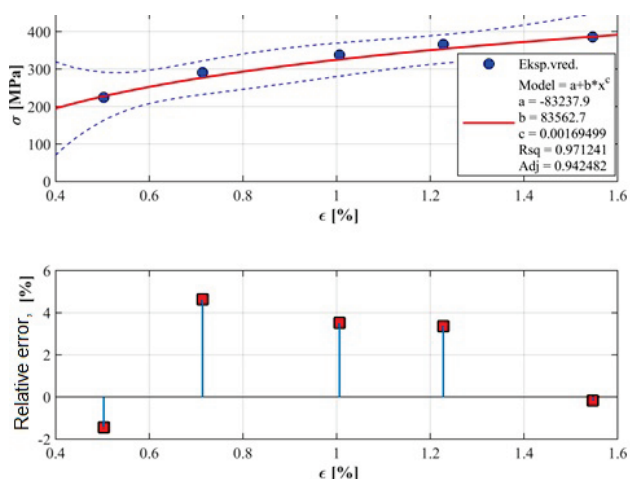


Figure 7: Comparison between the experimentally measured and calculated  $a$  ( $K$ ) and  $b$  ( $n$ ) values obtained by Ludwik method

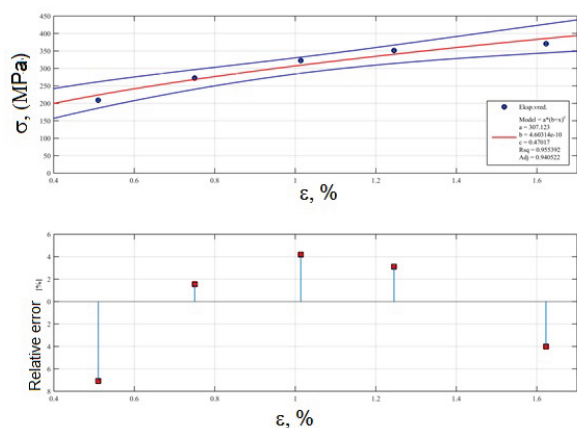


Figure 8: Comparison between the experimentally measured and calculated  $a$  ( $K$ ) and  $b$  ( $n$ ) values obtained by Swift method

Comparing the values of Adj from the legend in Figures 6-8 for the Hollomon, Ludwik and Swift models for the investigated material, we notice that the accuracy of the obtained values for all three models is  $\approx 94\%$ .

The  $R^2$  values of the models for HP40+Nb alloy are shown in Figure 6-8. It can be seen that Swift model is the best model for the prediction of flow curve in the uniform plastic deformation region for the material analysed. In another hand, the Ludwik model although had the highest  $R^2$  values among gives unrealistic values  $K$  and  $n$  (Table 4) compared to the other models (Hollomon and Swift). This parameter ( $R^2$ ) is the square of the correlation between the response values and the predicted response values [10].

Total review of theoretical values, experimental values, and strain hardening coefficient values obtained by the simulation in MATLAB, are given in Table 4.

The lowest  $n$  values were obtained for the HP40+Nb alloy using Ludwik model.

Table 4: Parameters obtained for the constitutive equations and methodology with ASTM E-646[6], during the characterization of the HP40+Nb alloy

| Model         | $K$ [MPa] | $n$   | $\sigma_y$ | $\epsilon_0$ |
|---------------|-----------|-------|------------|--------------|
| Hollomon [7]  | 326.96    | 0.47  |            |              |
| Ludwik [8]    | 83562.70  | 0.002 | -          |              |
| Swift [9]     | 307.12    | 0.46  |            | 4.60314E-10  |
| ASTM E 646[6] | 2503.78   | 0.530 |            |              |

It can be seen from Table 4, that applying Hollomon and Swift models, the most approximate value to the theoretical value of strain hardening coefficient could be obtained.

#### 4. CONCLUSION

Based on the analysis done and the experimental results, the following conclusions can be made:

- The values of strain hardening coefficient for tested samples obtained using the Hollomon model and Swift model are in c with theoretical values of strain hardening. These two methods proved to be satisfactory for mathematical modelling of the material tested.
- The Ludwik method has shown the worst performance for the material analysed.
- For the material tested it can be concluded that yield stress curve is best described by Hollomon and Swift mathematical models.

#### ACKNOWLEDGEMENTS

This work is co-financed by the Ministry of Education, Science and Technological Development of the Republic of Serbia on the base of the contract whose record number is 451-03-9/2021-14/200108. The authors thank the Ministry of Education, Science and Technological Development of the Republic of Serbia for supporting this research.

For the continuous support in our experimental work at Military Technical Institute in Belgrade in the Laboratory for Construction and Technical Materials, my thanks go to dr Z. Burzic and dr S. Perkovic.

#### REFERENCES

- [1] A.E. Matusевич, R.Mancini, J. Massa: "Computation of Tensile Strain-Hardening Exponents through the Power-Law Relationship", Journal of Testing and Evaluation, pp. 1-29, (2012)
- [2] B, Sener, M.E.Yurci: "Comparison of Quasi-Static Constitutive Equations and Modeling of Flow Curves for Austenitic 304 and Ferritic 430 Stainless Steels", Special Issue of the 6<sup>th</sup> International Congress & Exhibition

(APMAS2016),, Istanbul, Turkey, Vol. 131, pp. 605-607 (2017)

[3] K. G. Samuel: "Limitations of Hollomon and Ludwigson stress-strain relations in assessing the strain hardening parameters", Journal of Physics S: Applied Physics, Vol. 39, pp. 203-212 (2016)

[4] K.G.Samuel, P. Rodriguez: "On power-law type relationships and the Ludwigson explanation for the stress-strain behaviour of AISI 316 stainless steel",Journal od materials science,Vvol. 40, pp. 5727-5731 (2005)

[5] D.F. Pinto, M.A. Pinto, P.R. Pinto, A. Rodrigues da Costa: "Validation of a simplified computer simulation method for plastic forming of metals by conventional tensile tests", REM International Engineering Journal, Vol. 70, no 4, pp. 437-443 (2017)

[6] ASTM Standard E 646-16: Standard Test Method for Tensile Strain-Hardening Exponents (n -Values) of Metallic Sheet Materials, ASTM International, West Conshohocken, PA, (2016).

[7] J. Hollomon, Tensile Deformation, Trans AIME, Vol. 32, pp. 268–290 (1945).

[8] . P. Ludwik, Elemente der Technologischen Mechanik, (Verlag Von Julius Springer, Leipzig), p. 32 (1909).

[9] H. J. SWIFT, J. Mech. Phys. Solids **1** p.1 (1952).

[10] D.G. Kleinbaum, L.L. Kupper, Applied Regression Analysis and Other Multivariable Methods, Cengage Learning, Belmont (2007).

**APPENDIX**

Table X1.1

|           | A                    | <b>B = A x (1+D)</b> |                       | <b>C= log B</b>       |                |
|-----------|----------------------|----------------------|-----------------------|-----------------------|----------------|
|           | Load F               | Engineering Stress   | True Stress           | Y=log <sub>10</sub> □ | Y <sup>2</sup> |
|           | kN                   | MPa                  | MPa                   |                       |                |
| 1         | 18.150               | 209.10               | 211.23                | 2.324759              | 5.404504       |
| 2         | 23.653               | 272.50               | 276.59                | 2.441835              | 5.962559       |
| 3         | 28.004               | 322.63               | 329.17                | 2.517417              | 6.337389       |
| 4         | 30.504               | 351.43               | 360.18                | 2.556522              | 6.535803       |
| 5         | 32.183               | 370.77               | 382.80                | 2.582974              | 6.671756       |
|           | <b>D=G/50</b>        | <b>E = ln (1+D)</b>  |                       |                       |                |
|           | D                    | E                    | <b>X=logE</b>         | X <sup>2</sup>        | X*Y            |
| Extension | Engineering Strain ε | True Strain ε        | X=log <sub>10</sub> ε |                       |                |
|           | mm                   |                      |                       |                       |                |
| 0.511     | 0.010                | 0.010158             | -1.993182             | 3.972774              | -4.633668      |
| 0.750     | 0.015                | 0.014891             | -1.827088             | 3.338252              | -4.461449      |
| 1.014     | 0.020                | 0.020071             | -1.697426             | 2.881256              | -4.273130      |
| 1.245     | 0.025                | 0.024599             | -1.609083             | 2.589150              | -4.113657      |
| 1.623     | 0.032                | 0.031940             | -1.495659             | 2.236997              | -3.863249      |
| <b>N=</b> | <b>5</b>             |                      | <b>ΣY=12.423507</b>   | <b>12.423507</b>      |                |

$$\Sigma X = -8.622439; \quad \Sigma Y^2 = 30.912012;$$

$$\Sigma X^2 = 15.018428$$

$$\Sigma XY = -21.345152$$

A- Values are obtained from Fig.2

B- Area =  $0.504 \times 0.1045 = 0.052668 \text{ in}^2$ .

C = log B

C- True stress = (engineering stress)  $\times$  (1 + engineering strain)  
 $B = A \times (1 + D)$

D- Engineering strain = (extension) / gage length

E- True strain =  $\ln(1 + \text{engineering strain})$

E =  $\ln(1 + D)$

Where: X denotes  $\epsilon$ ; Y denotes  $\sigma$ , n denotes strain hardening exponent, and b denotes log K

Data operated upon this example are taken from Fig. 2 and evaluated in Table X1.1

The number of data-pairs N is 5

All logarithms used in the example area base 10

**From Table X1.1. :**

$$\Sigma X = \Sigma(\log \epsilon) = -8.622439$$

$$\Sigma Y = \Sigma(\log \sigma) = 12.423507$$

$$\Sigma X^2 = 15.018428$$

$$\bar{X} = \frac{\Sigma X}{N} = -1.724488$$

$$\Sigma Y = \Sigma(\log \sigma) = 12.4223507$$

$$\Sigma Y^2 = 30.912012$$

$$\bar{Y} = \frac{\Sigma Y}{N} = 2.484701$$

$$\Sigma XY = -21.345152$$

**The calculations for n and b**

$$\frac{\Sigma X * \Sigma Y}{N} = -21.424187$$

**Step 1**

$$S_{XY} = \Sigma XY - \frac{\Sigma X * \Sigma Y}{N} = \Sigma XY - \text{Step 1} = 0.079035$$

Step 2

$$\frac{(\Sigma X)^2}{N} = 14.869292$$

**Step 3**

$$S_{XX} = \Sigma X^2 - \frac{(\Sigma X)^2}{N} = \Sigma X^2 - \text{Step 3} = 0.149136$$

**Step 4**

$$n = \frac{S_{xy}}{S_{xx}} = \frac{\text{Step 2}}{\text{Step 4}} = 0.529951$$

**n = 0,530**

**Step 5**

$$n * \bar{X} = -0.913895$$

**Step 6**

$$b = \bar{Y} - n * \bar{X} = \bar{Y} - \text{Step 6} = 3.398596$$

**b = log<sub>10</sub> K**

**Step 7**

$$K = 10^b = 2503.779385$$

**K = 2503.78**

**Step 7a**

**X1.1.3 The calculations for the standard deviation:**

$$\frac{(S_{xy})^2}{S_{xx}} = \text{Step 5} * \text{Step 2} = 0.041885 \quad \text{see X1.3}$$

**Step 8**

$$S_{yy} = \Sigma Y^2 - \frac{(\Sigma Y)^2}{N} = 0.043305$$

Step 9

$$S_y^2 = \frac{\text{Step 9} - \text{Step 8}}{N-2} = 4.73E-04$$

**Step 10**

$$S_n^2 = \frac{\text{Step 10}}{\text{Step 4}} = 3.17E-03$$

**Step 11**

$$S_n = \sqrt{\text{Step 11}} = 5.63E-02 \quad \text{Standard Deviation}$$

$$S_n = \sqrt{\text{Step 11}} = 5.63E-02 \quad \text{Standard Deviation}$$

$$S_b^2 = S_y^2 \left( \frac{1}{N} + \frac{\bar{X}^2}{S_{xx}} \right) = \text{Step 10} \left( \frac{1}{N} + \frac{\bar{X}^2}{\text{Step 4}} \right) = 0.009535838$$

**Step 12**

$$S_b = \sqrt{\text{Step 12}} = 9.77E - 02 \quad \text{Standard Deviation}$$

# Effect of chemical composition on the microstructure, hardness and electrical conductivity profiles of the Bi-Ge-In alloys

Dusko Minic<sup>1</sup>, Milena Premovic<sup>1,\*</sup>, Aleksandar Djordjevic<sup>1</sup>, Milan Milosavljevic<sup>1</sup>

<sup>1</sup>University of Priština in Kosovska Mitrovica, Faculty of Technical Science, Department of Technological engineering Kneza Milosa 7, 38220 Kos. Mitrovica, Serbia

*In this study, the microstructure, hardness and electrical properties of selected ternary Bi-Ge-In alloys were investigated. Isothermal sections of the Bi-Ge-In system at 25, 200, and 300 °C were extrapolated using optimized thermodynamic parameters from the literature. The experiments which were used were optical microscopy, X-ray powder diffraction (XRD), scanning electron microscopy (SEM) and energy dispersion spectrometry (EDS), Brinell hardness measurements and electrical conductivity measurements. Good overall agreement between experimental and calculated values was obtained. EDS results were compared with predicted phase equilibria and good overall agreement between experimental and calculated values was obtained. Results of the XRD were also in line with the predicted phase balance. By using obtained results for properties and ANOVA analysis it is suggested mathematical model for calculation properties for every composition of alloys. By using appropriated mathematical model hardness and electrical conductivity were predicted throughout the whole composition range.*

**Keywords:** Phase equilibrium, Mathematical model, Hardness, Electrical conductivity

## 1. INTRODUCTION

The ternary Bi-Ge-In system have been previously investigated by our group [1]. In our previous study, a reliable thermodynamic data set was proposed and experimentally confirmed. For Bi-Ge-In system three vertical sections Bi-GeIn, Ge-BiIn and In-BiGe and three isothermal sections at 50, 75 and 100 °C were experimentally tested [1]. The same thermodynamic parameters obtained by a previous study [1] were used in the current study to calculate three isothermal sections at 25, 200 and 300 °C for ternary system. Thermodynamic calculations of isothermal sections were performed by using Pandat software [2]. Experimental results were obtained using scanning electron microscopy (SEM) with energy dispersive spectrometry (EDS), X-ray powder diffraction (XRD) analysis and inverted metallographic microscope. In addition, important properties such as hardness and electrical conductivity were measured. The reason for testing these properties is due to the contribution to the further development of the field of application, because Bi-Ge based alloys have applications in industry for making different optical and electronic devices [3-5]. Germanium-based alloys have special application in modern technology for making optical disks, blue disks, flash memory etc. [6-8]. Very limited number of studies carried out on Bi-Ge-X alloy systems is available in literature. Premović et al. [9] experimentally investigated phase equilibria of the ternary Bi-Ge-Sb system. The phase diagram of ternary Bi-Ge-Ag system has been experimentally examined and calculated by Milisavljević et al. [10]. The results presented in this study should benefit to the industry for development of new alloys.

## 2. MATERIALS AND METHODS

High-purity (99.999 wt. %) Bi, Ge and In metals produced by Alfa Aesar (Germany) were used for preparation of investigated alloy samples. Total mass of each sample was 4 g. Weighed masses of the samples were arc-melted and re-melted five times under a high purity argon atmosphere using a non-consumable tungsten electrode. The average weight loss of the samples during melting was about 1 mass %. After melting samples were divided into three series (first series annealed at 200 °C, second series annealed at 300 °C and third series for electrical conductivity and hardness measurements). Samples for investigation of isothermal sections at 200 °C and 300 °C were sealed in evacuated quartz tubes and then heated to a temperature that is 50 °C higher than the melting temperature of Ge. The alloy samples were then cooled down to 200 °C (first series) and 300 °C (second series) at the cooling rate of 5 °Cmin<sup>-1</sup>. The samples were kept at 200 °C for four weeks and six weeks at 300 °C and then quenched in the water and ice mixture to preserve desired equilibrium at 200 and 300 °C. Those samples were prepared and used for SEM-EDS and XRD analysis.

The compositions of the alloy samples were determined using a JEOL JSM-6460 scanning electron microscope (SEM) and TESCAN VEGA3 scanning electron microscope, which were both equipped with an EDS system (Oxford Instruments X-act). The samples for SEM-EDS analysis were first ground using sand paper, polished with diamond paste, and then cleaned in an ultrasonic bath. The overall compositions of the annealed samples were determined by mapping the entire polished surfaces of the samples. By contrast, the compositions of the observed coexisting phases were determined examining the surface of the same phase at different parts of the sample (at least five different positions of the same phase were examined per phase). The chemical compositions of the phases determined in this study

\*Corresponding author: M. Premovic, milena.premovic@pr.ac.rs

represented the mean values based on at least five individual analyses.

Powder XRD data for the phase analysis of the alloy samples were recorded with a D2 PHASER (Bruker, Karlsruhe, Germany) powder diffractometer equipped with a dynamic scintillation detector and ceramic X-ray Cu tube (KFL-Cu-2K) in the  $2\theta$  range from  $10^\circ$  to  $75^\circ$  with a step size of  $0.02^\circ$ . Before the XRD analysis, the selected samples were first powdered using ball mill (YKT-04 machine) and the powders obtained were then placed in special holders and pressed to obtain compact samples. The recorded XRD patterns were subsequently analyzed using TOPAS 4.2 software and the International Centre for Diffraction Data (ICDD) Powder Diffraction Files (PDF2) database (2013). The lattice parameters were determined using TOPAS software and by performing full Rietveld refinement.

Third group of samples were used for light optical microscopy, XRD analysis, electrical conductivity and hardness measurements. These samples were again melted in an electric furnace under high-purity argon atmosphere and slowly cooled to the room temperature using a cooling rate of  $2^\circ\text{C min}^{-1}$  in a way to achieve equilibrium at room temperature for the hardness and electrical conductivity measurements. Obtained microstructure has been checked with XRD analysis. Samples were prepared by classic metallographic procedure. Microstructures of the samples were recorded on a light microscopy using (LOM) OLYMPUS GX41 inverted metallographic microscope. Electrical conductivity measurements were carried out using Foerster SIGMATEST 2.069 eddy instrument. Hardness of the samples was measured using Brinell hardness tester INNOVATEST, model NEXUS 3001.

### 3. RESULTS AND DISCUSSION

Constitutive binary systems of the ternary Bi-Ge-In system were extensively studied in the past. Reliable thermodynamic datasets for these binary systems are available in literature [11-13]. Based on the literature information for binary sub-systems considered phase, their crystallographic data and database names for the solid phases are summarized in Table 1.

Table 1: Considered phase, their crystallographic data and database names for the solid phases of the ternary Bi-Ge-In system

| Thermodynamic database name | Common name              | Space group symbol | Struktural designation | Pearson's symbol |
|-----------------------------|--------------------------|--------------------|------------------------|------------------|
| LIQUID                      | Liquid                   | -                  | -                      | -                |
| RHOMBO_A7                   | (Bi)                     | $R\bar{3}mH$       | A7                     | <i>hR2</i>       |
| DIAMOND_A4                  | (Ge)                     | $Fm\bar{3}m$       | A4                     | <i>cF8</i>       |
| TETRAG_A6                   | (In)                     | $I4/mmm$           | A6                     | <i>tI2</i>       |
| BIIN                        | BiIn                     | $P4/nmms$          | B10                    | <i>tP4</i>       |
| BI3IN5                      | $\text{Bi}_3\text{In}_5$ | $I4/mcm$           | D8 <sub>1</sub>        | <i>tI32</i>      |
| BIIN_BRASS                  | $\text{BiIn}_2$          | $P6_3/mmc$         | B8 <sub>2</sub>        | <i>hP6</i>       |
| TET_ALPHA1                  | $\epsilon$               | $I4/mmm$           | A6 <sub>mod</sub>      | <i>tI2</i>       |

In ternary Bi-Ge-In system should appear as stable phases liquid phase, four solid solution phases (Bi), (Ge), (In) and  $\epsilon$  and three binary intermetallic compounds BiIn,  $\text{Bi}_3\text{In}_5$  and  $\text{BiIn}_2$ .

#### 3.1. Isothermal section at $200^\circ\text{C}$

Five ternary samples were annealed at  $200^\circ\text{C}$  for four weeks and then analyzed by using SEM-EDS and XRD techniques. Obtained results are summarized in Table 2.

Table 2: Combined results of SEM-EDS and XRD analyzes of the selected Bi-Ge-In alloys annealed at  $T=200^\circ\text{C}$

| N. | Composition of samples (at. %)   | Determined phases |              | Compositions of phases (at. %)     |                                   |                                   | Lattice parameters ( $\text{\AA}$ ) |                |
|----|----------------------------------|-------------------|--------------|------------------------------------|-----------------------------------|-----------------------------------|-------------------------------------|----------------|
|    |                                  | EDS               | XRD          | Bi                                 | Ge                                | In                                | <i>a=b</i>                          | <i>c</i>       |
| 1. | 9.36 Bi<br>51.42 Ge<br>39.22 In  | L<br>(Ge)         | (Ge)         | 73.55±0.4<br>0.83±0.1              | 1.42±0.5<br>98.45±0.3             | 25.03±0.8<br>0.72±0.9             | 5.6557±0.0004                       |                |
| 2. | 23.69 Bi<br>53.21 Ge<br>23.10 In | L<br>(Ge)         | (Ge)         | 81.38±0.8<br>0.14±0.2              | 1.18±0.1<br>99.05±0.2             | 17.44±0.2<br>0.81±0.2             | 5.6585±0.0006                       |                |
| 3. | 26.84 Bi<br>17.93 Ge<br>55.23 In | L<br>(Ge)         | (Ge)         | 87.91±0.6<br>0.67±0.7              | 0.88±0.3<br>98.71±0.5             | 11.21±0.4<br>0.62±0.2             | 5.6456±0.0003                       |                |
| 4. | 44.35 Bi<br>49.17 Ge<br>6.48 In  | L<br>(Ge)<br>(Bi) | (Ge)<br>(Bi) | 69.32±0.8<br>0.50±0.4<br>98.18±0.3 | 3.18±0.1<br>98.28±0.1<br>0.98±0.8 | 27.50±0.2<br>1.22±0.8<br>0.84±0.6 | 5.6578±0.0001<br>4.5565±0.0004      | 11.8143±0.0004 |
| 5. | 70.18 Bi<br>10.85 Ge<br>18.97 In | L<br>(Ge)<br>(Bi) | (Ge)<br>(Bi) | 71.98±0.4<br>1.26±0.4<br>97.87±0.7 | 2.36±0.9<br>98.25±0.6<br>1.23±0.3 | 25.66±0.4<br>0.49±0.9<br>0.90±0.7 | 5.6821±0.0009<br>4.5378±0.0002      | 11.8345±0.0006 |

Within five investigated samples, two different phase regions were detected. One is L+(Ge) two-phase regions and one is L+(Ge)+(Bi) three phase region. Samples 1, 2 and 3 belong to the same phase region L+(Ge). It is detected that liquid phase is rich with bismuth and indium, while phase (Ge) solid solution is rich with germanium. Samples 4 and 5 have same three phases in microstructure. Detected phases are L, solid solution (Ge) and solid solution (Bi). It is noticeable that for the samples 1-5, content of the bismuth increases, from

9,36 at. % (sample 1) to 70,18 at. % (sample 5). Increase in bismuth content leads to the microstructural changes, so in microstructures of samples 1, 2 and 3 L and (Ge) solid solution are detected. In the samples 4 and 5, and beside L and (Ge) phases, (Bi) solid solution is detected. In all samples L phase is stable, as well as the (Ge) solid solution. Stability of (Bi) solid solution changes. So, in samples 4 and 5, (Bi) solid solution is stable. Determined lattice parameters of the (Ge) and (Bi) solid solutions are compared with literature values [14,15]. Both solid

solutions dissolve some amount of other two elements, and determined lattice parameters are very slightly changed in relation to the literature.

SEM micrographs of microstructures of the two samples annealed at 200 °C are presented in Figure 1 as an illustration.

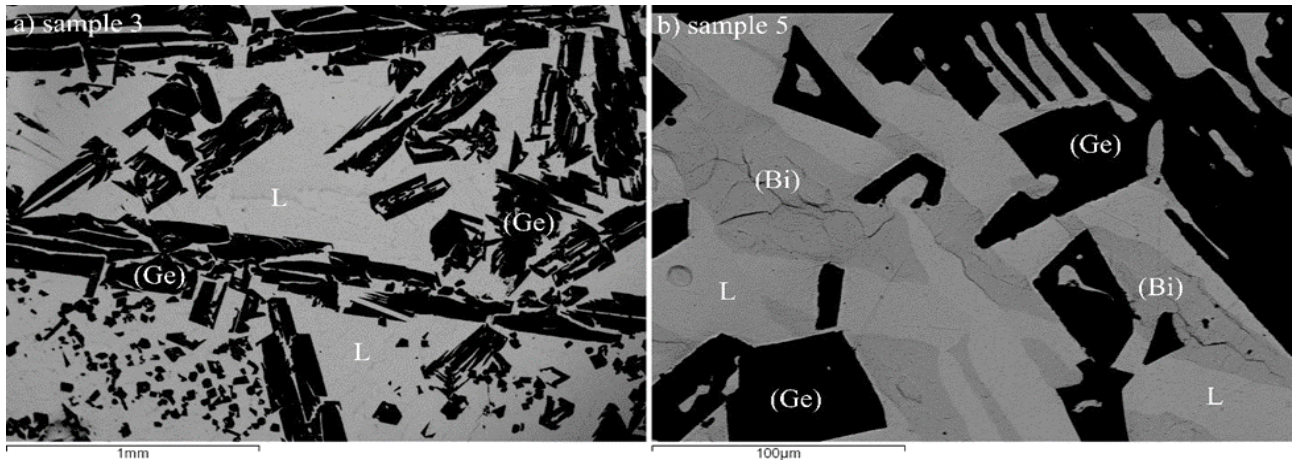


Figure 1: SEM micrographs of the samples annealed at 200 °C a) sample 3 and b) sample 5

Phases detected by EDS and XRD analysis are marked on the given micrographs. Microstructure of sample 3 have two phases: L as a gray phase and (Ge) solid solution as a dark phase. Sample 5 have three phases in microstructure: L as a gray phase, (Ge) solid solution as a dark phase and solid solution (Bi) as a dark gray phase.

isothermal section at 200 °C. Figure 2 shows comparison of EDS results and calculated isothermal section at 200 °C. The obtained experimental results are marked with the same symbol but in different color in way to distinguished results of different samples.

Experimentally obtained results of EDS analysis summarized in Table 2 are compared with calculated

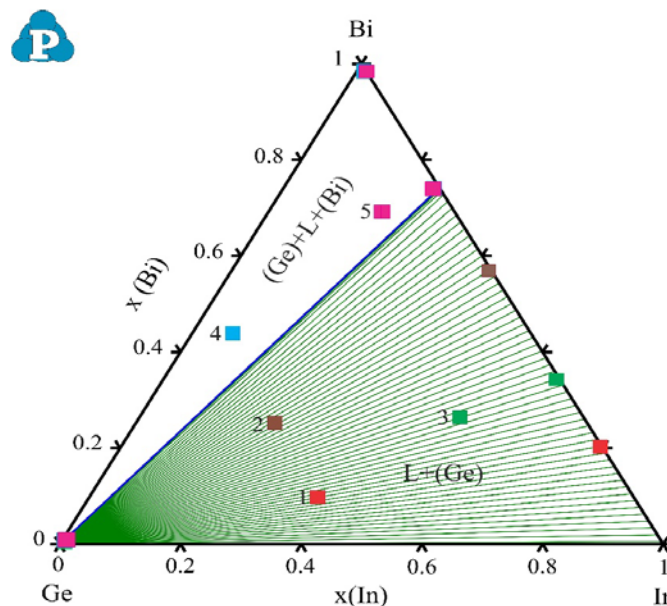


Figure 2: Calculated isothermal section at 200 °C compared with EDS results given in Table 2

The calculated isothermal section at 200 °C consists of two different phase regions, one is two phase region L+(Ge) and one is three phase region (Ge)+L+(Bi). Both are experimentally confirmed by analysis of the samples annealed at 200 °C. Samples 1, 2 and 3 are located in L+(Ge) two-phase region, samples 4 and 5 are located in (Ge)+L+(Bi) three-phase region, in the same phase regions as experimentally proved.

### 3.2. Isothermal section at 300 °C

For second selected isothermal section of Bi-Ge-In system at 300 °C, five ternary samples annealed at 300 °C were experimentally analyzed and the obtained results (SEM-EDS and XRD) are summarized in Table 3.

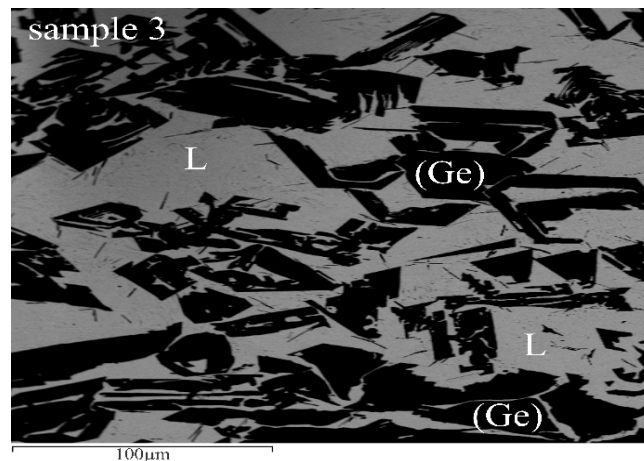
Table 3: Combined results of SEM-EDS and XRD analyzes of the selected Bi-Ge-In alloys annealed at  $T=300\text{ }^{\circ}\text{C}$ 

| N. | Composition of samples (at. %)   | Determined phases |      | Compositions of phases (at. %) |                       |                       | Lattice parameters ( $\text{\AA}$ ) |
|----|----------------------------------|-------------------|------|--------------------------------|-----------------------|-----------------------|-------------------------------------|
|    |                                  | EDS               | XRD  | Bi                             | Ge                    | In                    | $a=b=c$                             |
| 1. | 11.41 Bi<br>65.14 Ge<br>23.45 In | L<br>(Ge)         | (Ge) | 56.32±0.4<br>1.65±0.6          | 2.76±0.2<br>97.66±0.1 | 40.92±0.8<br>0.69±0.8 | 5.6556±0.0002                       |
| 2. | 9.65 Bi<br>39.84 Ge<br>50.51 In  | L<br>(Ge)         | (Ge) | 66.67±0.6<br>0.52±0.6          | 0.83±0.5<br>98.43±0.3 | 32.50±0.2<br>1.05±0.2 | 5.6512±0.0005                       |
| 3. | 29.96 Bi<br>17.49 Ge<br>52.55 In | L<br>(Ge)         | (Ge) | 45.78±0.1<br>0.80±0.8          | 1.24±0.7<br>99.07±0.3 | 52.98±0.2<br>0.13±0.1 | 5.6435±0.0002                       |
| 4. | 46.45 Bi<br>40.50 Ge<br>13.05 In | L<br>(Ge)         | (Ge) | 72.78±0.6<br>0.98±0.7          | 1.65±0.2<br>98.08±0.1 | 25.57±0.1<br>0.94±0.6 | 5.6587±0.0006                       |
| 5. | 58.81 Bi<br>10.85 Ge<br>26.18 In | L<br>(Ge)         | (Ge) | 83.34±0.7<br>1.47±0.2          | 0.78±0.6<br>97.25±0.6 | 15.88±0.5<br>1.28±0.8 | 5.6556±0.0005                       |

As it is given in Table 3, in all tested samples same two phases are detected. Detected phases are L and (Ge) solid solution. From EDS results it is detected that (Ge) solid solution is rich with germanium and can dissolve neglected amount of indium and bismuth. EDS result shows that L phase have different composition

depending on composition of the samples. L phase is rich in bismuth and indium and dissolves a negligible amount of germanium.

One SEM micrographs of the sample annealed at  $300\text{ }^{\circ}\text{C}$  are presented in Figure 3.

Figure 3: SEM micrographs of the samples annealed at  $300\text{ }^{\circ}\text{C}$  of sample 3

From microstructure it is visible that (Ge) solid solution appears as a dark phase and L phase a gray phase.

Since tested samples are annealed at  $300\text{ }^{\circ}\text{C}$ , EDS results of tested samples (Table 3) are compared with

calculated isothermal section at  $300\text{ }^{\circ}\text{C}$ . Figure 4, presents calculated isothermal section at  $300\text{ }^{\circ}\text{C}$  compared with EDS results.

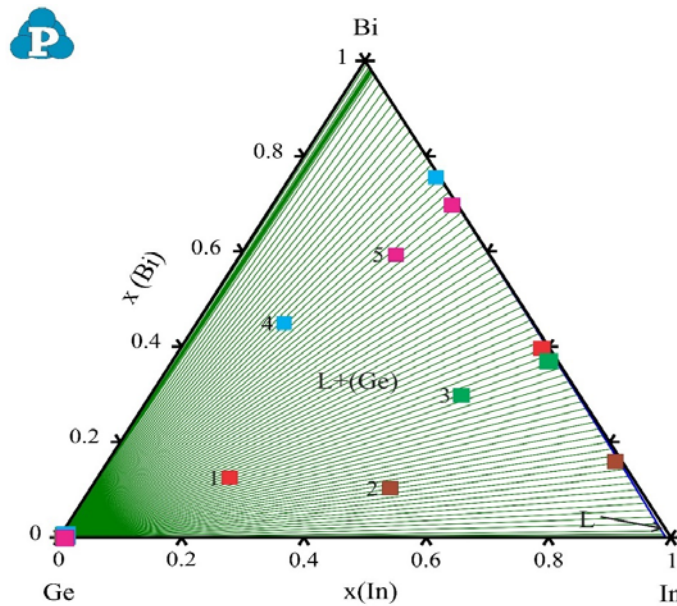


Figure 4: Calculated isothermal section at 300 °C compared with EDS results given in Table 3

Calculated isothermal section at 300 °C consists of two phase regions. One is single phase region L and other is two-phase region L+(Ge). By comparing EDS composition of the tested samples it is located that all samples are from two-phase region L+(Ge) same phases as experimentally detected. EDS compositions of the phases are in good agreement with calculated compositions of the phases.

### 3.3. Microstructural analysis of slowly-cooled samples

Twelve ternary samples are observed with light optical microscope. The compositions of ternary samples are positioned along three vertical sections Bi-GeIn, Ge-BiIn and In-BiGe. From each section four samples were prepared and marked with numbers from 1 to 12. First four samples are from Bi-GeIn section, another four samples are from Ge-BiIn section and samples 9-12 are from In-BiGe section. Figure 5 presents calculated isothermal section at 25 °C with marked composition of prepared samples.

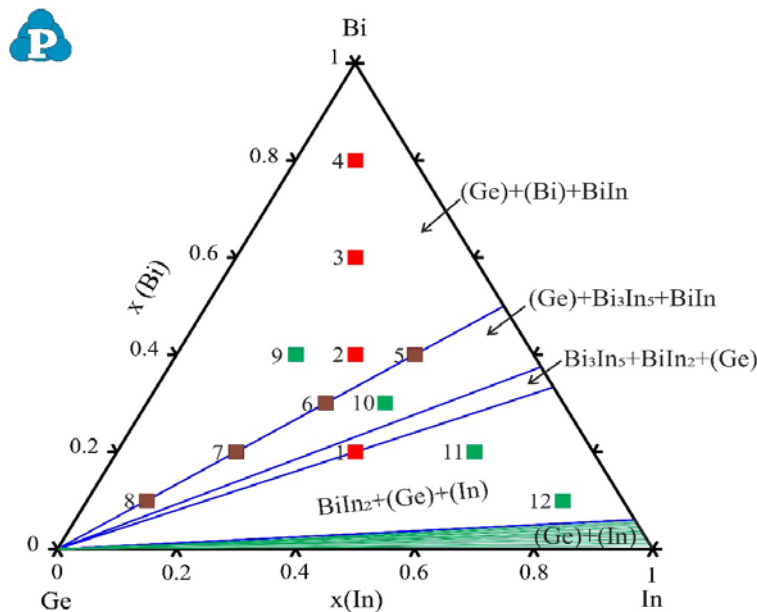


Figure 5: Predicted isothermal section at 25 °C with marked compositions of tested alloys

According to the calculation, sample 1 belong to the BiIn<sub>2</sub>+(Ge) region, samples 2-4 and 9 to the (Ge)+(Bi)+BiIn region, samples 5-8 to the (Ge)+BiIn, sample 10 to the (Ge)+Bi<sub>3</sub>In<sub>5</sub>+BiIn region, samples marked with numbers 11 and 12 belong to the BiIn<sub>2</sub>+(Ge)+(In) three-phase region. By comparing XRD

results and calculation same phase regions are calculated and experimentally determined.

These samples were used for measurements of mechanical and electrical properties. Two microstructures of samples 2 and 11 are given in Figure 6.

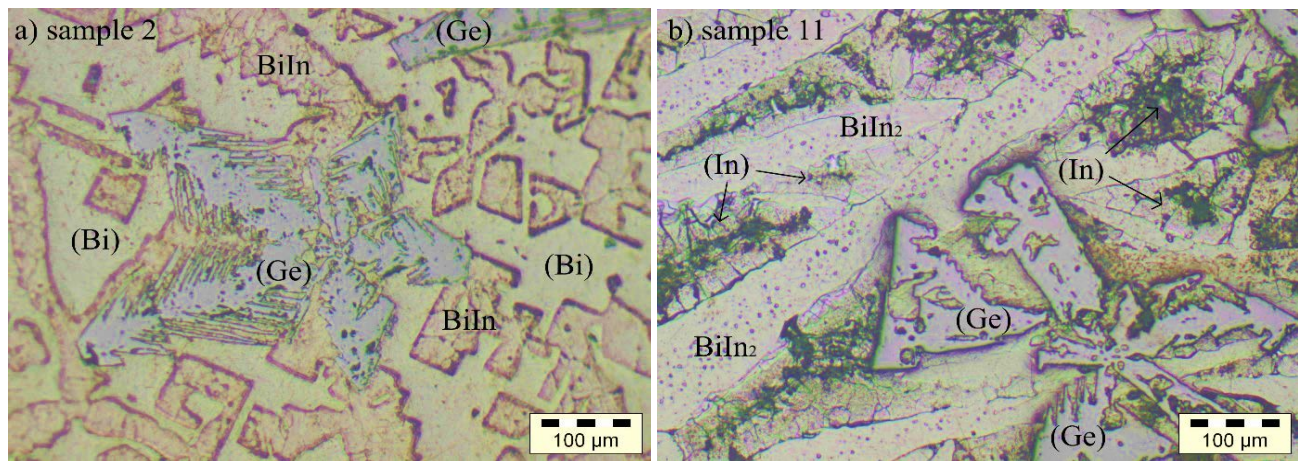


Figure 6: LOM micrographs of a) sample 2 and b) sample 11

Phases which appear in microstructures are marked at presented micrographs.

### 3.3.1. Brinell hardness measurements

Twelve ternary samples and three binary samples were subjected to the Brinell hardness measurements. Based on repeated measurements, mean values of Brinell

hardness were calculated and presented in Table 4. Literature values of hardness for pure elements [16] are also shown in Table 4 for comparison.

Table 4: Compositions of the investigated samples at room temperature and related Brinell hardness values

| N. | Alloy nominal composition (at.%) |            |            | Measured value (MN/m <sup>2</sup> ) |        |        | Mean value (MN/m <sup>2</sup> ) |
|----|----------------------------------|------------|------------|-------------------------------------|--------|--------|---------------------------------|
|    | x(Bi)                            | x(Ge)      | x(In)      | 1                                   | 2      | 3      |                                 |
| B1 | <b>0</b>                         | 0.5        | 0.5        | 243.80                              | 249.60 | 246.30 | 246.43                          |
| 1  | <b>0.2</b>                       | 0.4        | 0.4        | 7.30                                | 7.10   | 7.20   | 7.20                            |
| 2  | <b>0.4</b>                       | 0.3        | 0.3        | 8.20                                | 7.30   | 9.60   | 8.36                            |
| 3  | <b>0.6</b>                       | 0.2        | 0.2        | 9.60                                | 10.10  | 9.30   | 9.66                            |
| 4  | <b>0.8</b>                       | 0.1        | 0.1        | 10.40                               | 10.30  | 10.50  | 10.40                           |
| Bi | <b>1</b>                         | 0          | 0          |                                     |        |        | 94.20 [16]                      |
| B2 | 0.5                              | <b>0</b>   | 0.5        | 93.20                               | 94.10  | 92.30  | 93.20                           |
| 5  | 0.4                              | <b>0.2</b> | 0.4        | 1.60                                | 1.80   | 2.30   | 1.90                            |
| 6  | 0.3                              | <b>0.4</b> | 0.3        | 4.80                                | 3.60   | 3.30   | 3.90                            |
| 7  | 0.2                              | <b>0.6</b> | 0.2        | 4.80                                | 5.30   | 4.70   | 4.93                            |
| 8  | 0.1                              | <b>0.8</b> | 0.1        | 9.80                                | 10.00  | 11.60  | 10.46                           |
| Ge | 0                                | <b>1</b>   | 0          |                                     |        |        | 973.40 [16]                     |
| B3 | 0.5                              | 0.5        | <b>0</b>   | 213.20                              | 215.60 | 217.40 | 215.40                          |
| 9  | 0.4                              | 0.4        | <b>0.2</b> | 9.30                                | 7.80   | 8.30   | 8.46                            |
| 10 | 0.3                              | 0.3        | <b>0.4</b> | 7.80                                | 4.90   | 5.60   | 6.10                            |
| 11 | 0.2                              | 0.2        | <b>0.6</b> | 4.90                                | 4.60   | 4.50   | 4.66                            |
| 12 | 0.1                              | 0.1        | <b>0.8</b> | 4.10                                | 3.80   | 3.70   | 3.86                            |
| In | 0                                | 0          | <b>1</b>   |                                     |        |        | 8.83 [16]                       |

In addition to the tabular presentation, the obtained values for hardness are also presented graphically.

Figure 7 shows a graphical representation of the relationship between the hardness of the tested alloys and the composition of the alloys.

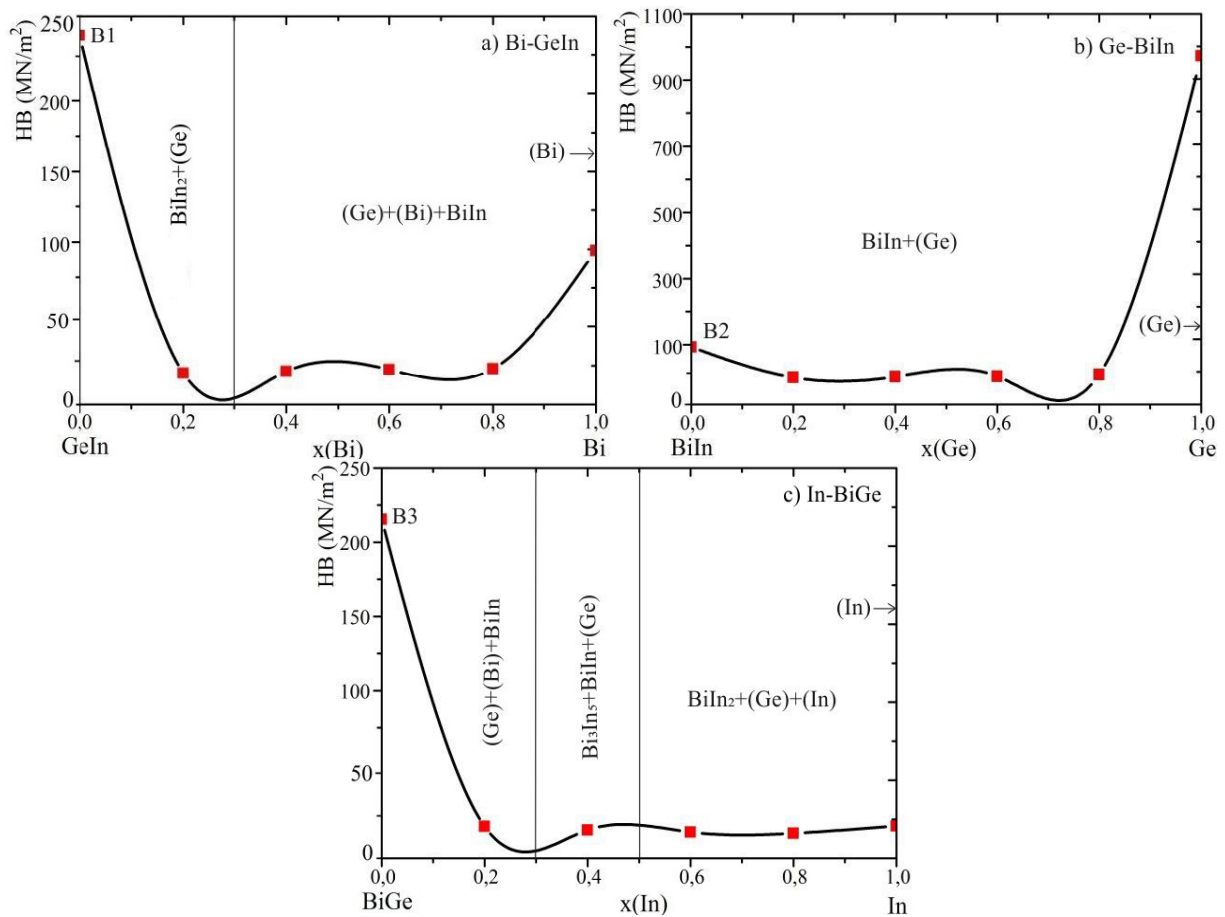


Figure 7: Graphical presentation of Brinell hardness dependence of composition and phase fraction: a) vertical section Bi-GeIn, b) vertical section Ge-BiIn and c) vertical section In-BiGe

Based on the obtained results, shown in Table 4, as well as graphically shown in Figure 7, it can be seen that the binary samples  $Ge_{50}In_{50}$  and  $Bi_{50}Ge_{50}$  have the highest hardness values. Among other ternary tested samples, the highest hardness value was recorded on the  $Bi_{10}Ge_{80}In_{10}$  sample of  $10.46 \text{ MN/m}^2$ , which is understandable due to the presence of high Ge content in the alloy. The lowest value of hardness was measured on the sample  $Bi_{40}Ge_{20}In_{40}$ , of  $1.90 \text{ MN/m}^2$  due to the low content of Ge, as well as on the sample  $Bi_{10}Ge_{10}In_{80}$  of  $3.86 \text{ MN/m}^2$  due to the high content of In. Also, it can be seen that with increasing Bi and Ge in ternary alloys, the hardness also increase slightly, while increasing In in ternary samples leads to a slight decrease in the hardness of the alloys. Response Surface Methodology - RSM was used to quantify the relationship between independent

input parameters and the dependent variable (response) [17-21]. Data processing was done in the software package Design Expert v.9.0.6.2. By utilizing experimentally determined values of hardness given in Table 4 mathematical model of the dependence of the Brinell hardness on composition for the Bi-Ge-In alloys was developed. Using all possible canonicals or Scheffe models, Special Cubic model has been suggested. The diagnosis of the statistical properties of the assumed model found that the distribution of residuals is not normal and that it is necessary to transform the mathematical model in order to meet the conditions of normality. The Box-Cox diagnostics recommends the "Inverse Square Root" transformation for the variance stabilization.

The final equation of the predictive model in terms of real components is (1):

$$\begin{aligned} 1/\text{Sqrt}(\text{HB}+1.00) = & 0.130602071 \cdot (\text{Bi}) + 0.102462155 \cdot (\text{Ge}) + 0.370110518 \cdot (\text{In}) \\ & - 0.05470384 \cdot (\text{Bi}) \cdot (\text{Ge}) - 0.31283672 \cdot (\text{Bi}) \cdot (\text{In}) - 0.44269865 \cdot (\text{Ge}) \cdot (\text{In}) \\ & + 9.202504558 \cdot (\text{Bi}) \cdot (\text{Ge}) \cdot (\text{In}) \end{aligned} \quad (1)$$

The repeated analysis for Inverse Square Root model transformation confirms the significance of the Transformed Special Cubic model. In this case, ANOVA

confirms the adequacy of the Reduced Special Cubic Mixture model (Table 5).

Table 5: ANOVA for Special Cubic Mixture model

| Source         | Sum of Squares | df | Mean Square | F Value | p-value<br>Prob > F |
|----------------|----------------|----|-------------|---------|---------------------|
| Model          | 0.2976         | 6  | 0.0496      | 4.3057  | 0.0177              |
| Linear Mixture | 0.0626         | 2  | 0.0313      | 2.7185  | 0.1098              |
| AB             | 0.0001         | 1  | 0.0001      | 0.0115  | 0.9167              |
| AC             | 0.0043         | 1  | 0.0043      | 0.3747  | 0.5529              |
| BC             | 0.0086         | 1  | 0.0086      | 0.7504  | 0.4048              |
| ABC            | 0.1338         | 1  | 0.1338      | 11.6180 | 0.0058              |
| Residual       | 0.1267         | 11 | 0.0115      |         |                     |
| Cor Total      | 0.4243         | 17 |             |         |                     |

The F-value of the Model is 4.30 and it implies that the model is significant. In this case, all model terms are significant. R-squared and other statistics after the ANOVA have appropriate values which confirm the justification of the choice of the adopted mathematical model (Table 6).

Table 6: R-squared and other statistics after the ANOVA

|           |          |                |         |
|-----------|----------|----------------|---------|
| Std. Dev. | 0.10733  | R-Squared      | 0.70137 |
| Mean      | 0.29367  | Adj R-Squared  | 0.53847 |
| C.V. %    | 36.54931 | Pred R-Squared | 0.36179 |
| PRESS     | 0.68656  | Adeq Precision | 5.24704 |

The diagnosis of the statistical properties of the assumed model found that the distribution of residuals are normal. After the applied *Box-Cox* procedure, the value of  $\lambda$  is -0.5, the optimum value of  $\lambda$  is -0.37 and the 95% confidence interval for  $\lambda$  (Low C.I.=-0.76, High C.I.=-0.01) contains the value -0.5, thus proving the justification of the model transformation (Figure 8).

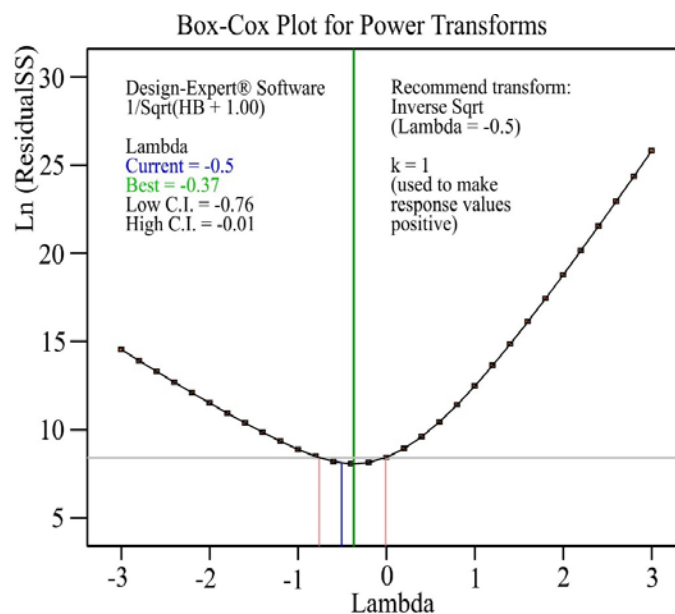


Figure 8: The Box-Cox plot for power transforms

Iso-lines contour plot for Brinell hardness of alloys defined by equation 1 is shown in Fig. 9.

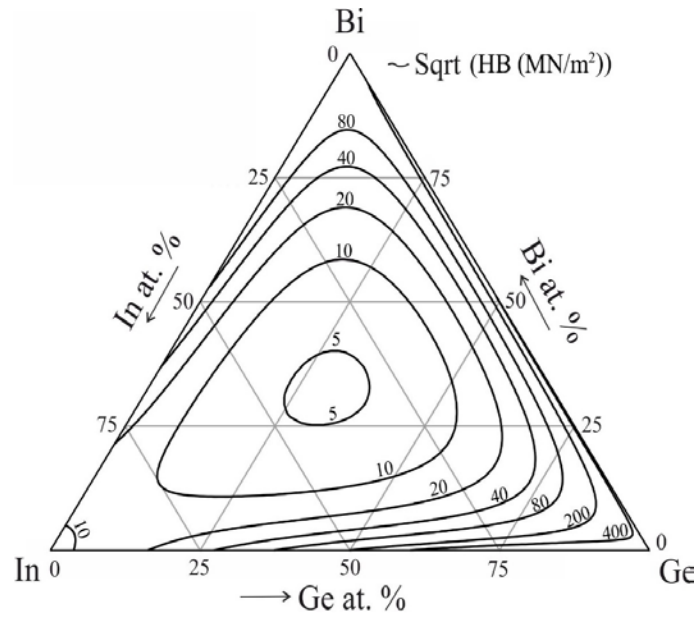


Figure 9: Calculated iso-lines of Brinell hardness in ternary Bi-Ge-In system with  $R2 = 0.701$

3.3.2. Electrical conductivity measurements

Measurements of electrical conductivity were performed on the same group of samples used for hardness test. For all investigated samples electrical conductivity measurement were repeated four times at different positions

and obtained values for each measured point are given in Table 7. Beside measured values, Table 7 also includes calculated mean values and literature values of electrical conductivity for pure elements [22].

Table 7: Compositions of the investigated samples at room temperature and related electrical conductivity values

| N. | Alloy nominal composition (at.%) |            |            | Value (MS /m) |        |        |        | Mean value (MS/m) |
|----|----------------------------------|------------|------------|---------------|--------|--------|--------|-------------------|
|    | x(Bi)                            | x(Ge)      | x(In)      | 1             | 2      | 3      | 4      |                   |
| B1 | <b>0</b>                         | 0.5        | 0.5        | 3.6362        | 3.8328 | 3.4332 | 3.5983 | 3.6251            |
| 1  | <b>0.2</b>                       | 0.4        | 0.4        | 0.3169        | 0.3200 | 0.3098 | 0.3182 | 0.3162            |
| 2  | <b>0.4</b>                       | 0.3        | 0.3        | 0.3233        | 0.3180 | 0.3193 | 0.3158 | 0.3191            |
| 3  | <b>0.6</b>                       | 0.2        | 0.2        | 0.3222        | 0.3193 | 0.3281 | 0.3233 | 0.3232            |
| 4  | <b>0.8</b>                       | 0.1        | 0.1        | 0.3396        | 0.3289 | 0.3401 | 0.3395 | 0.3370            |
| Bi | <b>1</b>                         | 0          | 0          |               |        |        |        | 0.77 [22]         |
| B2 | 0.5                              | <b>0</b>   | 0.5        | 0.2630        | 0.2840 | 0.2990 | 0.2380 | 0.2710            |
| 5  | 0.4                              | <b>0.2</b> | 0.4        | 0.2935        | 0.3159 | 0.3269 | 0.3278 | 0.3160            |
| 6  | 0.3                              | <b>0.4</b> | 0.3        | 0.3385        | 0.3289 | 0.3258 | 0.3188 | 0.3280            |
| 7  | 0.2                              | <b>0.6</b> | 0.2        | 0.3366        | 0.3419 | 0.3313 | 0.3487 | 0.3396            |
| 8  | 0.1                              | <b>0.8</b> | 0.1        | 0.3596        | 0.3623 | 0.3496 | 0.3554 | 0.3567            |
| Ge | 0                                | <b>1</b>   | 0          |               |        |        |        | 0.002 [22]        |
| B3 | 0.5                              | 0.5        | <b>0</b>   | 0.3430        | 0.3410 | 0.3530 | 0.3440 | 0.3452            |
| 8  | 0.4                              | 0.4        | <b>0.2</b> | 0.3555        | 0.4189 | 0.4266 | 0.3999 | 0.4002            |
| 10 | 0.3                              | 0.3        | <b>0.4</b> | 0.6540        | 0.6799 | 0.6702 | 0.6635 | 0.6669            |
| 11 | 0.2                              | 0.2        | <b>0.6</b> | 0.9630        | 0.9562 | 0.9988 | 1.1023 | 1.0050            |
| 12 | 0.1                              | 0.1        | <b>0.8</b> | 1.4530        | 1.6140 | 1.5030 | 1.6483 | 1.5545            |
| In | 0                                | 0          | <b>1</b>   |               |        |        |        | 12 [22]           |

Figure 10 presents graphical presentation of results (mean value) given in Table 7 for a easier overview of the results.

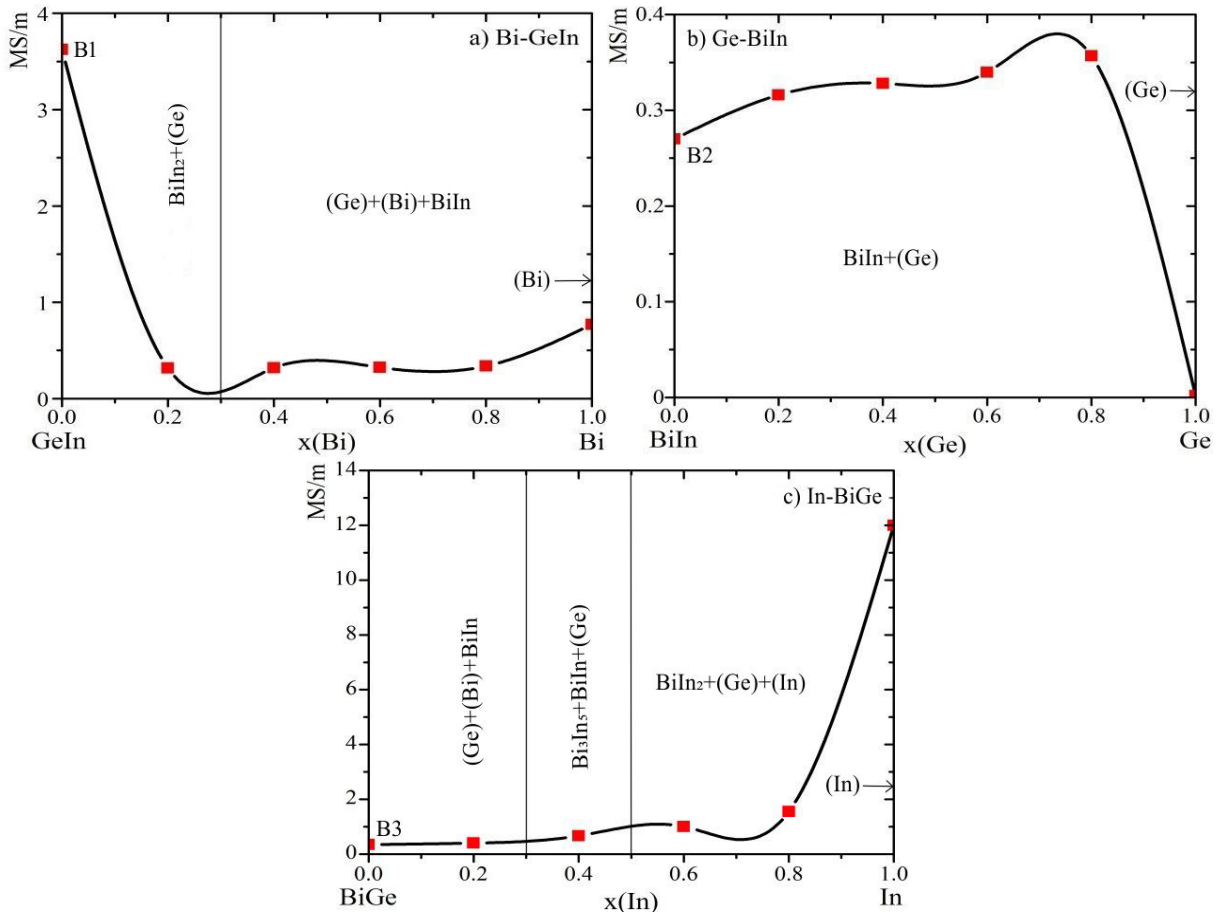


Figure 10: Graphical presentation of electrical conductivity dependence of composition and phase fraction  
 a) vertical section Bi-GeIn, b) vertical section Ge-BiIn and c) vertical section In-BiGe

It is known that the chemical composition of alloys has a strong influence on electrical conductivity. Electrical conductivity mainly increases with the growth of indium content as the element. In the studied ternary samples, the highest electrical conductivity was obtained with the Bi10Ge10In80 alloy of 1.5545 MS/m. However, in addition to the composition of the alloy, the phase components and their amount can also significantly affect the electrical conductivity. We can conclude that with increasing Bi and Ge content in alloys, the values of electrical conductivity change in small ranges, while with

increasing In in alloys we have a trend of a increasement in electrical conductivity.

Quadratic Mixture model was suggested as a final equation for prediction of electrical conductivity. The diagnosis of the statistical properties of the assumed model found that the distribution of residuals is not normal and that it is necessary to transform the mathematical model in order to meet the conditions of normality. The Box-Cox diagnostics recommends the "Natural Log" transformation for the variance stabilization.

The final equation of the predictive model in terms of Real components is:

$$\ln(\sigma+0.10)=-0.0125953 \cdot(\text{Bi})-1.9440351 \cdot(\text{Ge})+2.2392631 \cdot(\text{In})-9.6950768 \cdot(\text{Bi}) \cdot(\text{In})+2.8577311 \cdot(\text{Ge}) \cdot(\text{In}) \tag{2}$$

The repeated analysis for Natural Log model transformation confirms the significance of the Transformed Quadratic Mixture model. In this case,

ANOVA confirms the adequacy of the Quadratic Mixture model (Table 8).

Table 8: ANOVA for Quadratic Mixture model

| Source         | Sum of Squares | df | Mean Square | F Value  | p-value Prob > F |
|----------------|----------------|----|-------------|----------|------------------|
| Model          | 16.56761       | 4  | 4.1419      | 32.93354 | 0.000001         |
| Linear Mixture | 10.58847       | 2  | 5.2942      | 42.09611 | 0.000002         |
| AC             | 5.79625        | 1  | 5.7962      | 46.08778 | 0.000013         |
| BC             | 0.50360        | 1  | 0.5036      | 4.00429  | 0.066712         |
| Residual       | 1.63495        | 13 | 0.1258      |          |                  |
| Cor Total      | 18.20256       | 17 |             |          |                  |

The F-value of the Model is 32.93 and it implies that the model is significant. R-squared and other statistics after the ANOVA have good values which confirm the justification of the choice of the adopted mathematical model (Table 9).

The diagnosis of the statistical properties of the assumed model found that the distribution of residuals are normal. After the applied Box-Cox procedure, the value of  $\lambda$  is 0.0, the optimum value of  $\lambda$  is -0.14 and the 95% confidence interval for  $\lambda$  (Low C.I.=-0.42, High C.I.=0.13) contains the value 0.0, thus proving the justification of the model transformation (Figure 11).

Table 9: R-squared and other statistics after the ANOVA

|           |          |                |          |
|-----------|----------|----------------|----------|
| Std. Dev. | 0.35463  | R-Squared      | 0.91018  |
| Mean      | -0.41859 | Adj R-Squared  | 0.88254  |
| C.V. %    | 84.72114 | Pred R-Squared | 0.72134  |
| PRESS     | 5.07231  | Adeq Precision | 22.38151 |

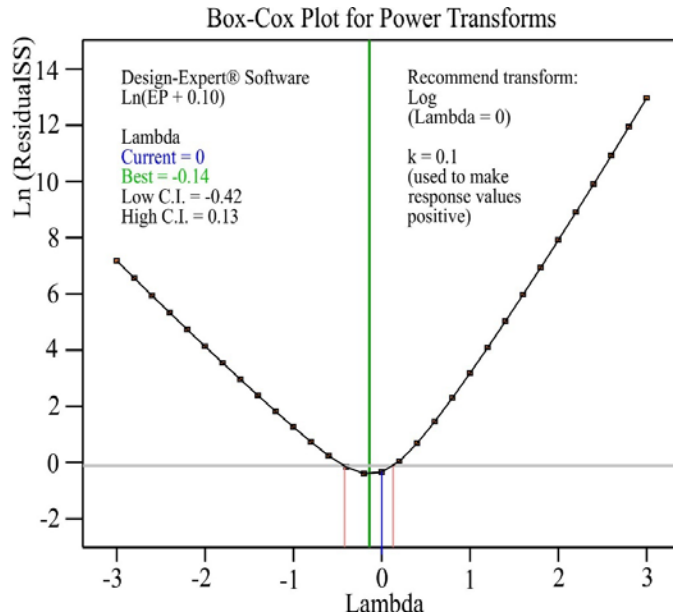


Figure 11: The Box-Cox plot for power transforms.

Iso-lines contour plot for Electrical conductivity of Bi-Ge-In alloys defined by equation 1 is shown in Fig. 12.

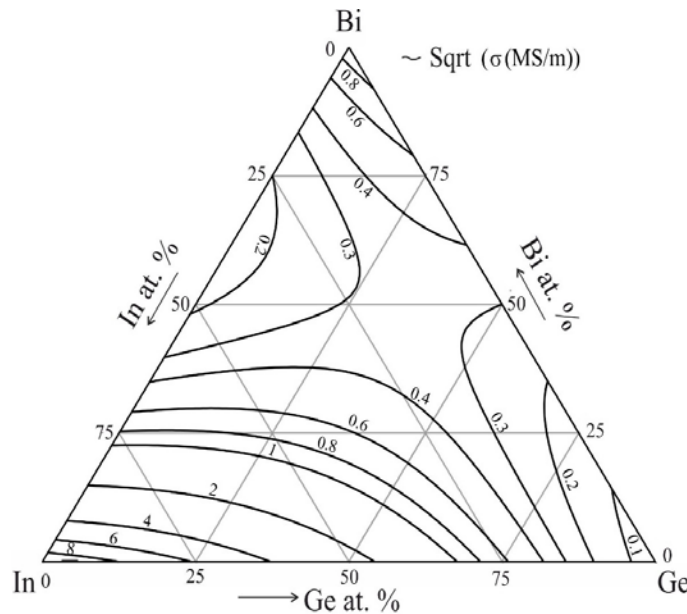


Figure 12: Calculated iso-lines of Electrical conductivity in ternary Bi-Ge-In system with  $R^2 = 0.91$

#### 4. CONCLUSION

The ternary Bi-Ge-In system have been experimentally investigated by using appropriate experimental techniques. The EDS results were matched to the calculated isothermal sections at 200 °C and 300 °C and a close agreement was observed. By EDS it is not detected ternary compound or large solubility of elements. Microstructural, hardness, electrical conductivity tests were performed on twelve ternary alloys and three binary alloys slowly-cooled samples. Experimentally determined phases by XRD analysis were compared with calculated isothermal section at 25 °C and agreement between the results was reached. On same samples Brinell hardness and electrical conductivity were measured. Results of Brinell hardness and electrical conductivity were used for prediction of those properties along all composition of the ternary Bi-Ge-In system. By using obtained results for properties and ANOVA analysis it is suggested mathematical model for calculation properties for every composition of alloys.

#### ACKNOWLEDGEMENTS

This work has been supported by the National Nature Science Foundation of China (project No.51950410600) and the Ministry of Education, Science and Technological Development of the Republic of Serbia (Grant No. OI172037).

#### REFERENCES

- [1] A. Djordjević, D. Minić, M. Premović, D. Manasijević, V. Čosović, Experimental Examination and Thermodynamic Description of the Ternary Bi-Ge-In and -Sn Systems, *JPED*, 2019, 40(4), p 623-637
- [2] W. Cao, S.L. Chen, F. Zhang, K. Wu, Y. Yang, Y.A. Chang, R. Schmid-Fetzer and W.A. Oates, PANDAT Software With Panengine, Panoptimizer And Panprecipitation For Multicomponent Phase Diagram Calculation And Materials Property Simulation, *Calphad*, 2009, 33(2), p 328–342
- [3] G.W. Burr, B.N. Kurdi, J.C. Scott, C.H. Lam, K. Gopalakrishnan, and R.S. Shenoy, Overview of candidate device technologies for storage-class memory, *IBM J. Res. Dev.*, 2008, 52(4-5), p 449–464
- [4] T.C. Chong, X. Hu, L.P. Shi, P.K. Tan, X.S. Miao, and R. Zhao, Multispeed Superlattice-Like Phase Change Optical Disk, *Jpn. J. Appl. Phys.*, 2003, 42 (2B), p 824–827
- [5] J. Solis, C.N. Afonso, J.F. Trull, and M.C. Morilla, Fast crystallizing GeSb alloys for optical data storage, *J. Appl. Phys.*, 1994, 75 (12), p 7788–7793
- [6] S. Raoux and T.J. Ibm, Phase Change Memory (PCM) Materials and Devices, 2nd ed., Y. Nishi, Ed., *Advances in Nonvolatile Memory and Storage Technology*, 2014, p 161–199
- [7] T. Siegrist, P. Jost, H. Volker, M. Woda, P. Merkelbach, C. Schlockermann and M. Wuttig, Disorder-induced localization in crystalline phase-change materials, *Nat. Mater.*, 2011, 10, p 202–208
- [8] N. Yamada, E. Ohno, N. Akahira, K. Nishiuchi, K. Nagata and M. Takao, High speed over writable phase change optical disk material, *Jpn. J. Appl. Phys.*, 1987, 26, p 61–66
- [9] M. Premović, D. Minić, V. Cosović, D. Manasijević, and D. Živković, Experimental investigation and thermodynamic calculations of the Bi-Ge-Sb phase diagram, *Metall. Mater. Trans A*, 2014, 45A, p 4829-4841
- [10] D. Milisavljević, D. Minić, M. Premović, D. Manasijević, V. Čosović, and N. Košanin, Combined thermodynamic description and experimental investigation of the ternary Ag-Bi-Ge system, *Int J Thermophys.*, 2019, 40(3), p 29
- [11] D. Boa, and I. Ansara, Thermodynamic assessment of the ternary system Bi–In–Pb, *Thermochim. Acta.*, 1998, 314, p 79-86
- [12] P.Y. Chevalier, A Thermodynamic Evaluation of the Ge-In, Ge-Pb, Ge-Sb, Ge-Tl, and Ge-Zn Systems, *Thermochim. Acta*, 1989, 155, p 227-240.
- [13] P.-Y. Chevalier, Thermodynamic evaluation of the Bi-Ge system, *Thermochim. Acta*, 1988, 132, p 111–116.
- [14] A. S. Cooper, Precise Lattice Constants of Germanium, Aluminum, Gallium Arsenide, Uranium, Sulphur, Quartz and Sapphire. *Acta Cryst.*, 1962, 15, p 578-582
- [15] P. Cucka, and C. S. Barrett, The crystal structure of Bi and of solid solutions of Pb, Sn, Sb and Te in Bi, *Acta Cryst.*, 1962, 15, p 865-875
- [16] <http://periodictable.com/Properties/A/BrinellHardness.al.html>, access 29.11.2018
- [17] M. J. Anderson, P. J. Whitcomb, RSM Simplified, Optimizing Processes Using Response Surface Methods for Design of Experiments, Second Edition, CRC Press, Taylor & Francis Group, 2017
- [18] G. E. P. Box, N. R. Draper, Response Surfaces, Mixtures, and Ridge Analyses, Second Edition, Wiley, 2007
- [19] Stat-Ease, Handbook for Experimenters, Version 11.00, Stat-Ease, Inc. 2018
- [20] D. C. Montgomery, Design and Analysis of Experiments, Ninth Edition, Wiley, 2017
- [21] R. H. Myers, D. C. Montgomery, C. M. Anderson-Cook, Response Surface Methodology, Process and Product Optimization Using Designed Experiments, Fourth Edition, Wiley, 2016
- [22] <http://periodictable.com/Properties/A/ElectricalConductivity.an.html>, access 25.12.2018

# Experimental investigation and thermodynamic description of the ternary Cu-Ge-Pb system

Milan Milosavljevic<sup>1</sup>, Milena Premovic<sup>1,\*</sup>, Dusko Minic<sup>1</sup>, Aleksandar Djordjevic<sup>1</sup>

<sup>1</sup>University of Priština in Kosovska Mitrovica, Faculty of Technical Science, Department of Technological engineering Kneza Milosa 7, 38220 Kos. Mitrovica, Serbia

*Decades of scientific work dedicated to the investigation of phase diagrams gave significant benefit to industry and science. After all those years of phase diagram investigation still there is missing information about phase diagram of some ternary systems. One of those systems is Cu-Ge-Pb.*

*It is known importance of Cu-based alloys and Ge-based alloys in electro industry. Since such combination is not tested before this work will provide information about phase diagram of ternary Cu-Ge-Pb system. In this work ternary Cu-Ge-Pb system has been tested experimentally and analytically by using Calphad model. Two isothermal sections at 600 and 400 °C and three vertical sections are experimentally tested and results were compared with calculated corresponding phase diagrams. None of the ternary compound and large solubility of third element in binary compound is not confirmed.*

**Keywords:** Experiments, Modeling, Cu-Ge-Pb alloys

## 1. INTRODUCTION

Importance of phase diagram is known for decades. Due to the fact that alloy is combination of two and more elements, leads to the conclusion that a huge number of systems combination from binary to the multicomponent should be tested. Since binary systems [1,2] are tested for a long and almost all combination are well known and reliable thermodynamic dataset are established. Some of the ternary systems are still not known and future test should be done. Chose system for this work is Cu-Ge-Pb. Chosen combination of elements is due to the fact that Pb-Zn ores contain various valuable metals, such as Cu, Ge, In, Ag, Au, Bi [3]. For improvement of separation and purification process knowledge of relevant multicomponent phase diagrams is necessary. Systems such as Cu-In-Pb [3], In-Pb-Zn [4], Au-Cu-Ge [5], Au-Ag-Ge [6] and other are tested earlier. In our group we were focused on Ge-based systems and Ag-Ge-In [7], Bi-Ge-Zn [8], Bi-Ge-In [9] and other were tested earlier. Beside this fact that Cu-Ge-Pb is not tested before and system is important for understanding multicomponent Pb-Zn ores selected system is interesting for electro industry [10,11] and potential phase change memory material [12,13].

For this work three group of samples were selected for experimental work. Experiments were performed by using differential thermal analysis (DTA), scanning electron microscopy (SEM) with energy dispersive spectrometry (EDS), and X-ray powder diffraction (XRD). Selected samples are from three vertical sections (Cu-GePb, Ge-CuPb and Pb-CuGe) and two isothermal sections at 400 and 600 °C. Experimental results of selected alloys were compared with corresponding calculated phase diagrams and reasonable agreement between the calculated phase diagrams and experimental data have been obtained.

## 2. LITERATURE INFORMATION

Up to now according to the literature survey the ternary Cu-Ge-Pb system has not been studied before. Information related to the ternary system is based on available sub-binary phase diagrams.

The binary Cu-Ge system consists of seven phases and eight reactions. One liquid phase L, and six solid phases (Cu),  $\xi$ ,  $\varepsilon$ ,  $\theta$ ,  $\eta$  and (Ge). From eight reactions two are peritectic, two eutectic, one peritectoid and three eutectoid reactions. Figure 1, presents calculated binary Cu-Ge system by using optimized thermodynamic parameters by Wang et al. [14].

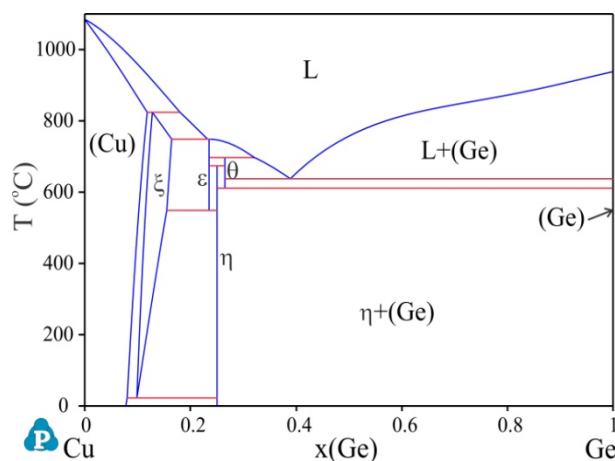


Figure 1. Calculated Cu-Ge phase diagram by using thermodynamic data established by Wang et al. [14].

The binary Cu-Pb system, consist of three phases with miscibility of gap in the liquid phase (L' and L'') and two reactions. One phase is liquid L with miscibility of gap in the liquid phase (L' and L'') and two solid phases (Cu) and (Pb). From two reactions one is mono eutectic reaction at higher temperature and second is eutectic reaction. Figure

\*Corresponding author: M. Premovic, milena.premovic@pr.ac.rs

2, presents calculated binary phase diagram of Cu-Pb system by using thermodynamic parameters from Jantzen and Spencer [15].

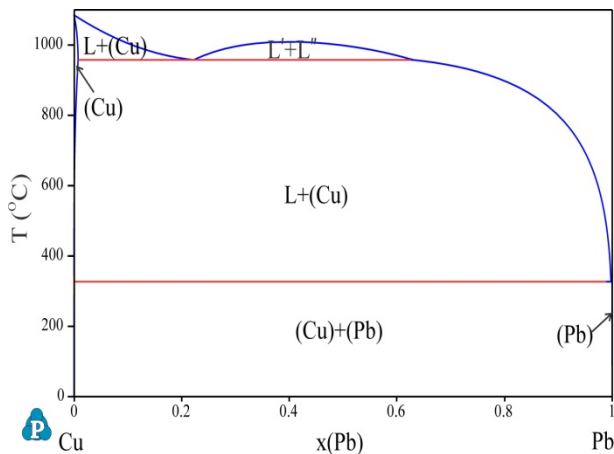


Figure 2. Calculated Cu-Pb phase diagram by using thermodynamic data established by Jantzen and Spencer et al. [15].

The binary Ge-Pb system consists of three phases and one eutectic reaction. One phase is liquid L phase and two are solid phases (Ge) and (Pb). Figure 3, presents calculated binary Ge-Pb system by using thermodynamic data published by Chevalier [16].

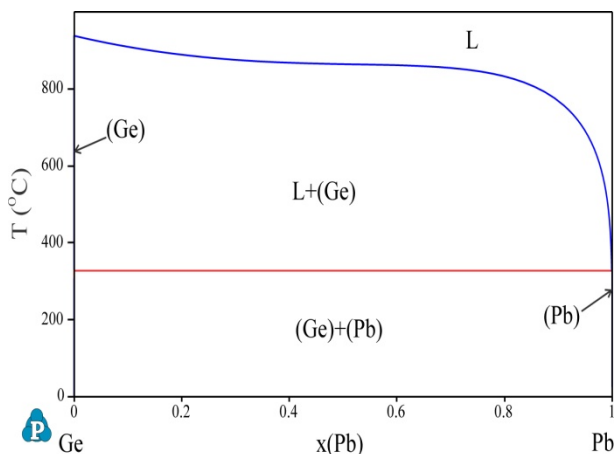


Figure 3. Calculated Ge-Pb phase diagram by using thermodynamic data by Chevalier [16].

Solid phase and their crystallographic information are used from literature [17-23].

### 3. EXPERIMENTAL PART

Three groups of ternary Cu-Ge-Pb alloys samples were prepared. Prepared alloys were from high purity Cu, Ge and Pb (99.999 %) produced by Alfa Aesar. All samples were melted and re-melted five times in an induction furnace, to preserve homogeneity. The compositions of all samples were determined by using scanning electron microscopy (SEM) with energy dispersive spectrometry (EDS).

One group of samples (six samples) were selected for testing of phase equilibria at 600 °C. Six samples (each sample in separate tube) were evacuated in quartz tube under vacuum and such prepared samples were annealed at 600 °C for five weeks. After annealing samples were quenched in ice-water. Such samples were tested with scanning electron microscopy (SEM) with energy dispersive spectrometry (EDS) and X-ray powder diffraction (XRD). One part of samples used for SEM-EDS were grinded, polished and clean in ultrasonic bath. Other parts of samples used for XRD test were finely ground.

Second group of samples were used for testing of phase equilibria at 400 °C. Same procedure as described in previous paragraph were apply for samples in second group except annealing time which was 400 °C.

Third group of samples were used for testing of temperature phase transition. Twelve ternary samples were prepared and tested by using differential thermal analysis (DTA).

### 4. RESULTS AND DISCUSSION

Six ternary samples annealed at 600 °C, were prepared for phase equilibria test of isothermal section at 600 °C. Those six samples were tested with same method and same procedure was applied on each sample. First samples were tested with XRD and detected phase are summarized in Table 1. Second used techniques were SEM-EDS, by which composition of sample and composition of present phases in microstructure were determined. Summary results of both techniques are given in Table 1.

Table 1. Combined results of SEM-EDS and XRD analyzes of the selected Cu-Ge-Pb alloys annealed at T=600 °C.

| No. | Composition of samples (at.%) | Determined phases |      | Compositions of phases (at.%) |           |           | Lattice parameters (Å)                            |
|-----|-------------------------------|-------------------|------|-------------------------------|-----------|-----------|---|
|     |                               | EDS               | XRD  | Cu                            | Ge        | Pb        |   |
| 1   | 9.38 Cu                       | L                 | -    | 1.01±0.5                      | 3.17±0.1  | 95.82±0.7 | -<br>a=b=c=5.6550<br>a=5.2911, b=4.1983, c=4.5487 |
|     | 59.44 Ge                      | (Ge)              | (Ge) | 1.56±0.3                      | 98.03±0.5 | 0.41±0.2  |   |
|     | 31.18 Pb                      | η                 | η    | 73.57±0.2                     | 26.25±0.8 | 0.18±0.2  |   |
| 2   | 15.24 Cu                      | L                 | -    | 1.10±0.1                      | 3.79±0.2  | 95.11±0.1 | -<br>a=b=c=5.6558<br>a=5.2918, b=4.1980, c=4.5482 |
|     | 33.07 Ge                      | (Ge)              | (Ge) | 0.55±0.7                      | 99.24±0.3 | 0.21±0.2  |   |
|     | 51.69 Pb                      | η                 | η    | 72.95±0.5                     | 25.67±0.1 | 1.38±0.3  |   |
| 3   | 33.62 Cu                      | L                 | -    | 1.89±0.2                      | 3.06±0.7  | 96.05±0.2 | -<br>a=b=c=5.6559<br>a=5.2913, b=4.1982, c=4.5485 |
|     | 39.87 Ge                      | (Ge)              | (Ge) | 0.58±0.3                      | 99.24±0.6 | 0.18±0.1  |   |
|     | 26.51 Pb                      | η                 | η    | 73.46±0.1                     | 26.13±0.2 | 0.41±0.5  |   |
| 4   | 50.73 Cu                      | L                 | -    | 1.60±0.2                      | 0.51±0.1  | 97.89±0.1 | -<br>a=b=4.1685, c=7.4981<br>a=b=2.6137, c=4.2305 |
|     | 12.19 Ge                      | ε                 | ε    | 76.33±0.4                     | 22.80±0.2 | 0.87±0.2  |   |
|     | 37.08 Pb                      | ξ                 | ξ    | 83.88±0.5                     | 15.71±0.4 | 0.41±0.5  |   |
| 5   | 40.26 Cu                      | L                 | -    | 2.25±0.1                      | 0.32±0.3  | 97.43±0.3 | -<br>a=b=c=3.6672<br>a=b=2.6073, c=4.2311         |
|     | 4.81 Ge                       | (Cu)              | (Cu) | 89.32±0.7                     | 10.50±0.2 | 0.18±0.3  |   |
|     | 54.93 Pb                      | ξ                 | ξ    | 87.5±0.3                      | 12.34±0.1 | 0.16±0.1  |   |

|   |                                 |           |           |                       |                      |                       |                     |
|---|---------------------------------|-----------|-----------|-----------------------|----------------------|-----------------------|---------------------|
| 6 | 74.22 Cu<br>4.81 Ge<br>20.97 Pb | L<br>(Cu) | -<br>(Cu) | 2.35±0.5<br>92.02±0.2 | 0.44±0.3<br>7.10±0.3 | 97.21±0.5<br>0.88±0.7 | -<br>$a=b=c=3.6618$ |
|---|---------------------------------|-----------|-----------|-----------------------|----------------------|-----------------------|---------------------|

From results it is noticeable that four different phase regions were detected.

In microstructures of samples 1, 2 and 3 same three phases L, (Ge) and  $\eta$  were detected. EDS results of phase composition in each samples shows that L phase is rich with Pb and have 95.11 to the 96.05 at. % of Pb while leftover belongs to the 3.06 to the 3.79 at. % of Ge and 1.01 to the 1.89 at. % of Cu. For (Ge) solid solution it is noticeable that this phase is rich with germanium 98.03 to the 99.24 at. % of Ge, while rest part is 0.55 to the 1.56 at. % of Cu and 0.18 to the 0.41 at. % of Pb. Last detected phase in samples 1, 2 and 3 is  $\eta$  intermetallic compound with composition of 72.95 to the 73.56 at. % Cu, 25.67 to the 26.25 at. % of Ge and leftover is Pb, 0.18 to the 1.56 at. % of Pb.

In microstructure of sample 4, three phases were detected L,  $\epsilon$  and  $\xi$ . Liquid phase is rich with Pb and dissolve 1.6 at. % of Cu and 0.51 at. % of Ge. Phase  $\epsilon$  and  $\xi$  are rich with Cu while  $\xi$  dissolve 83.33 at. % of Cu and  $\epsilon$  76.33 at. % of Cu.

Sample 5, detected another three phases L, (Cu) and  $\xi$ . As detected in previous cases L phase is rich with lead 97.43 at. % of Pb. Next phase (Cu) is copper solid solution rich with copper 89.32 at. % while high solubility of germanium 10.50 at. % and small amount of lead 0.18 at. %. Next phase in this sample is  $\xi$  which also can dissolve high amount of copper 87.50 at. % and 12.34 at. % of Ge and small amount of Pb. Since (Cu) and  $\xi$  phase have similar phase composition XRD result help to distinguished phases.

Sample 6, detected two phase region L+(Cu). Liquid phase L is rich with lead while (Cu) solid solution is rich with (Cu) and can dissolve 7.10 at. % of Ge and 0.88 at. % of Pb. Also XRD result in this sample help to detect (Cu) phase.

Two microstructures of samples annealed at 600 °C are given on figure 4.

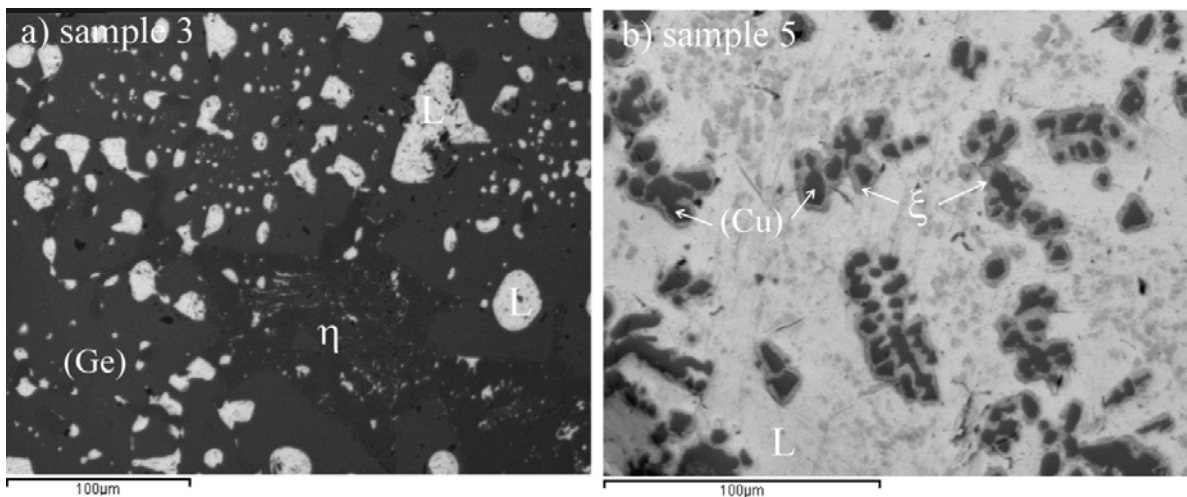


Figure 4. SEM microstructure of samples 3 and 5 annealed at 600 °C for five weeks.

Microstructure of sample 3 and 5 are used as representative. Sample 3 have three phases in microstructure, while L phase is grey oval phase trapped between (Ge) and  $\eta$  phase. (Ge) and  $\eta$  phase appears as a dark phase while  $\eta$  phase is a little darker. Sample 5, have three phases in microstructure L as a light gray phase,  $\xi$  as a gray phase and (Cu) solid solution as a dark phase.

Since the samples were annealed at 600 °C, EDS results of phase compositions were compared with calculated isothermal section at 600 °C. Calculated isothermal section compared with EDS result is given on Figure 5.

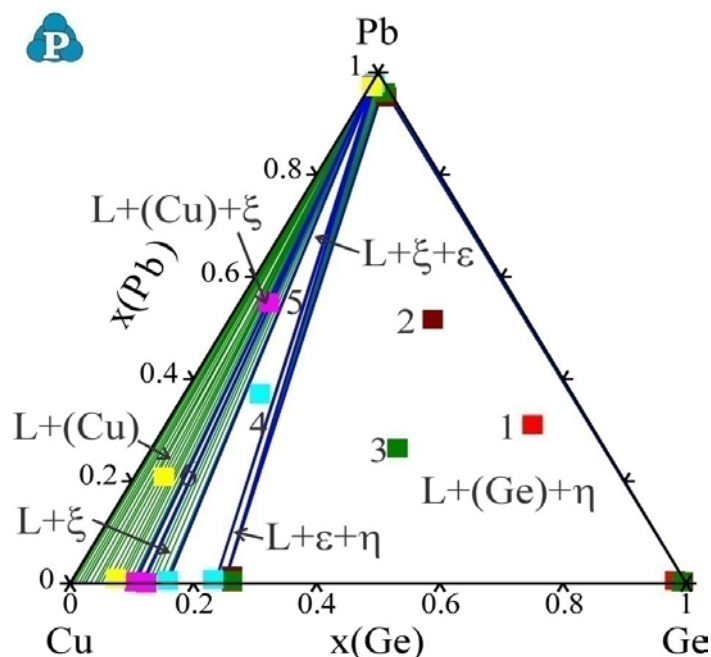


Figure 5. Calculated Cu-Ge-Pb isothermal section at 600 °C compared with EDS results given in Table 1.

Seven different phase regions were predicted on isothermal section at 600 °C while four are experimentally confirmed. Largest region on isothermal section at 600 °C belongs to the three-phase region  $L+(Ge)+\eta$ , beside it there is other three-phase regions  $L+\varepsilon+\eta$ ,  $L+\xi+\varepsilon$  and  $L+(Cu)+\xi$  and three two-phase regions  $L+\eta$ ,  $L+\xi$  and  $L+(Cu)$ . Four experimentally confirmed phase regions are  $L+(Ge)+\eta$  with three samples 1, 2 and 3,  $L+\xi+\varepsilon$  with

sample 4,  $L+(Cu)+\xi$  with sample 5 and two-phase region  $L+(Cu)$  with sample 6. EDS composition of each phase detected in observed samples are in agreement with calculated phase composition.

In a next part six experimental results of ternary alloys annealed at 400 °C are summarized in Table 2. Similar procedure as applied for samples annealed for 600 °C was applied for those annealed at 400 °C and obtained results are given in Table 2.

Table 2. Combined results of SEM-EDS and XRD analyzes of the selected Cu-Ge-Pb alloys annealed at  $T=400$  °C.

| No. | Composition of samples (at.%) | Determined phases |        | Compositions of phases (at.%) |           |           | Lattice parameters (Å)  |
|-----|-------------------------------|-------------------|--------|-------------------------------|-----------|-----------|---|
|     |                               | EDS               | XRD    | Cu                            | Ge        | Pb        |   |
| 7   | 30.28 Cu                      | L                 | -      | 0.26±0.5                      | 1.61±0.4  | 98.13±0.5 | -<br>$a=b=c=5.6549$<br>$a=5.2915, b=4.2032, c=4.5511$         |
|     | 44.13 Ge                      | (Ge)              | (Ge)   | 1.15±0.2                      | 98.13±0.5 | 0.72±0.1  |   |
|     | 25.59 Pb                      | $\eta$            | $\eta$ | 74.97±0.1                     | 24.38±0.1 | 0.65±0.6  |   |
| 8   | 18.40 Cu                      | L                 | -      | 0.73±0.3                      | 0.45±0.3  | 98.82±0.4 | -<br>$a=b=c=5.6559$<br>$a=5.2951, b=4.2012, c=4.5508$         |
|     | 46.31 Ge                      | (Ge)              | (Ge)   | 0.46±0.7                      | 99.13±0.3 | 0.41±0.3  |   |
|     | 35.29 Pb                      | $\eta$            | $\eta$ | 73.77±0.1                     | 26.05±0.4 | 0.18±0.3  |   |
| 9   | 26.10 Cu                      | L                 | -      | 0.46±0.2                      | 1.41±0.6  | 98.13±0.1 | -<br>$a=b=c=5.6547$<br>$a=5.2897, b=4.1987, c=4.5523$         |
|     | 27.05 Ge                      | (Ge)              | (Ge)   | 1.83±0.4                      | 98.02±0.7 | 0.15±0.7  |   |
|     | 46.85 Pb                      | $\eta$            | $\eta$ | 73.76±0.4                     | 25.53±0.2 | 0.71±0.5  |   |
| 10  | 67.92 Cu                      | L                 | -      | 1.07±0.3                      | 0.79±0.1  | 98.14±0.5 | -<br>$a=5.2913, b=4.1992, c=4.5512$<br>$a=b=2.6069, c=4.2318$ |
|     | 19.43 Ge                      | $\eta$            | $\eta$ | 73.79±0.7                     | 25.79±0.3 | 0.42±0.5  |   |
|     | 12.65 Pb                      | $\xi$             | $\xi$  | 85.90±0.2                     | 13.23±0.5 | 0.87±0.4  |   |
| 11  | 56.90 Cu                      | L                 | -      | 0.69±0.1                      | 0.48±0.5  | 98.83±0.3 | -<br>$a=5.2909, b=4.2012, c=4.5513$<br>$a=b=2.6052, c=4.2307$ |
|     | 10.81 Ge                      | $\eta$            | $\eta$ | 73.47±0.3                     | 25.92±0.2 | 0.61±0.2  |   |
|     | 32.29 Pb                      | $\xi$             | $\xi$  | 84.95±0.1                     | 14.37±0.7 | 0.68±0.1  |   |
| 12  | 50.51 Cu                      | L                 | -      | 1.69±0.5                      | 0.28±0.2  | 98.03±0.5 | -<br>$a=b=c=3.6653$   |
|     | 2.88 Ge<br>46.61 Pb           | (Cu)              | (Cu)   | 95.64±0.2                     | 4.18±0.4  | 0.18±0.7  |   |

Six ternary samples annealed at 400 °C were used for test of phase equilibria at same temperature. By experiment three different phase regions are detected. Samples 7, 8 and 9 detected three-phase region  $L+(Ge)+\eta$ , samples 10 and 11 detected another three-phase region  $L+\eta+\xi$  and sample 12 detected two-phase region  $L+(Cu)$ . In samples 7, 8 and 9 three phases L, (Ge) and  $\eta$ . Detected L which is rich with lead 98.13 to the 98.82 at. % of Pb and leftover is copper and germanium. Next phase is (Ge) rich with germanium 98.02 to the 99.13 at. % and rest is other two elements. Third phase is intermetallic compound

$\eta$  which is by literature line compound  $Cu_3Ge$ , with composition 75 at. % of Cu and 25 at. % of Ge, while in our experimental study this compound has composition 73.76 to the 74.97 at. % of copper, 24.38 to the 26.05 at. % of germanium and small amount of lead 0.18 to the 0.71 at. %. Experimental composition of  $\eta$  phase is close to literature one.

In samples 10 and 11, three phases L,  $\eta$  and  $\xi$  are detected. As in previous case detected L phase is rich with Pb 98.14 and 98.83 at. % of Pb, while leftover is another two elements. Next phase is  $\eta$  phase with 73.79 and 73.47 at. % of Cu, 25.79 and 25.92 at. % of Ge and 0.42 and

0.61 at. % of Pb. Last phase is  $\xi$  phase with composition 85.90 and 94.95 at. % of Cu, 13.23 and 14.37 at. % of Ge and leftover is Pb.

In sample 12 two phases are detected L and (Cu) solid solution. L phase is rich with lead 98.03 at. %, while composition of other two elements are 1.69 at. % of Cu

and 0.28 at. % of Ge. (Cu) solid solution is rich with copper with amount of 95.64 at. % and 4.18 at. % of Ge and leftover is 0.18 at. % of Pb.

Two microstructures of samples annealed at 400 °C are given on Figure 6.

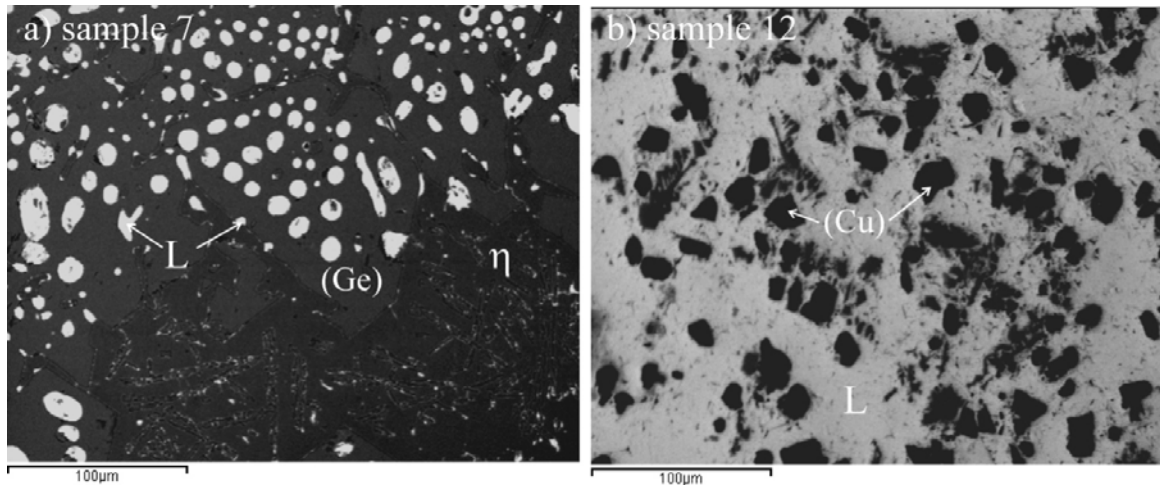


Figure 6. SEM microstructure of samples 7 and 12 annealed at 400 °C for five weeks.

Microstructures of samples 7 and 12 are presented as one representative microstructures of samples annealed at 400 °C. In microstructure of sample 7, three phases are visible L, as a light gray phase, (Ge) as a gray phase and  $\eta$  as a dark gray phase. In microstructure of

sample 12, two phases are visible L phase as a light gray phase and (Cu) solid solution as a dark phase.

Experimental result of EDS test given in Table 2 are compared with calculated isothermal section at 400 °C and given on Figure 7.

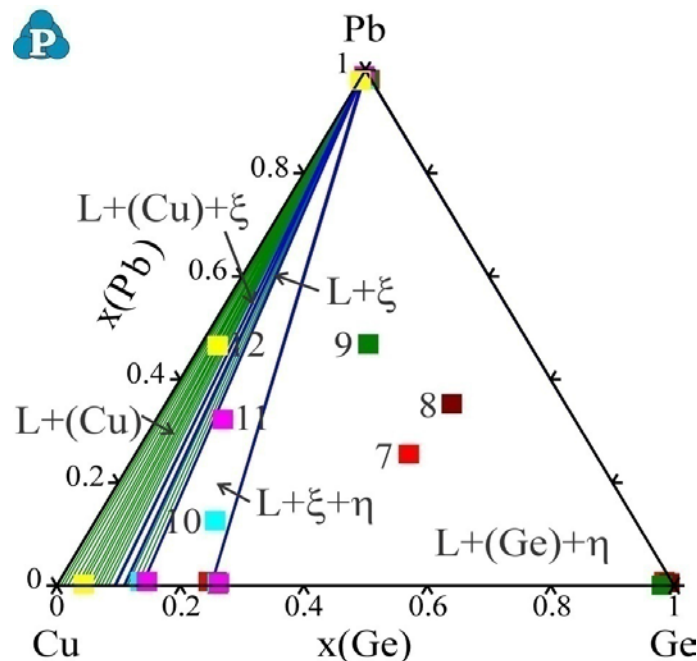


Figure 7. Calculated Cu-Ge-Pb isothermal section at 400 °C compared with EDS results given in Table 2.

Calculated isothermal section at 400 °C consists of five different phase regions, three three-phase regions and two two-phase regions. Large phase region is three-phase region  $L+(Ge)+\eta$  and in this region three samples are located. Samples 7, 8 and 9 are located in this phase region  $L+(Ge)+\eta$  and detected phases of those three samples are same predicted. EDS results of each samples

are marked with color square and it can be notice good agreement between calculated phase composition and experimental one. Next phase region is  $L+\xi+\eta$ , in this region samples 10 and 11 are located. Same phases which are predicted are experimentally confirmed. EDS compositions marked with corresponding color square are close to the calculated composition.

Last tested sample 12 is located in two-phase region L+(Cu) same phase region as experimental predicted. In general good agreement between experimental and calculated phase composition is reached.

Twelve ternary samples were prepared for DTA tests. Prepared samples were from three vertical sections Cu-GePb, Ge-CuPb and Pb-CuGe. From each vertical section four samples were selected as representative ones. In Table 3, are summarized DTA results.

Table 3. Phase transition temperatures of the studied alloys from the ternary Cu-Ge-Pb system determined by DTA at pressure  $p = 0.1$  MPa.

| Number                   | Composition (at. %)                          |   | Identified phase transition temperature in °C |                             |          |
|--------------------------|--|---|---|-----------------------------|----------|
|                          | nominal                                      | EDS   | Ternary eutectic reaction                     | Ternary transition reaction | Liquidus |
| Vertical section Cu-GePb |  |   |   |                             |          |
| 13                       | $\text{Cu}_{10}\text{Ge}_{45}\text{Pb}_{45}$ | $\text{Cu}_{10.83}\text{Ge}_{44.87}\text{Pb}_{44.3}$      | 327.8/614.9/642.1                             | 803.5                       | 967.4    |
| 14                       | $\text{Cu}_{30}\text{Ge}_{35}\text{Pb}_{35}$ | $\text{Cu}_{30.08}\text{Ge}_{35.61}\text{Pb}_{34.3}$<br>1 | 320.1/611.2/630.9                             | 750.8                       | -        |
| 15                       | $\text{Cu}_{50}\text{Ge}_{25}\text{Pb}_{25}$ | $\text{Cu}_{49.92}\text{Ge}_{25.11}\text{Pb}_{24.9}$<br>7 | 321.8/618.9/640.1                             | 700.9                       | -        |
| 16                       | $\text{Cu}_{70}\text{Ge}_{15}\text{Pb}_{15}$ | $\text{Cu}_{69.93}\text{Ge}_{14.89}\text{Pb}_{15.1}$<br>8 | 329.3/555.3/740.7                             | 809.3                       | -        |
| Vertical section Ge-CuPb |  |   |   |                             |          |
| 17                       | $\text{Cu}_{45}\text{Ge}_{10}\text{Pb}_{45}$ | $\text{Cu}_{44.92}\text{Ge}_{10.19}\text{Pb}_{44.8}$<br>9 | 329.8/557.2/747.9                             |                             |          |
| 18                       | $\text{Cu}_{35}\text{Ge}_{30}\text{Pb}_{35}$ | $\text{Cu}_{35.73}\text{Ge}_{29.83}\text{Pb}_{34.4}$<br>4 | 330.9/620.1/636.9                             | 705.8                       | -        |
| 19                       | $\text{Cu}_{25}\text{Ge}_{50}\text{Pb}_{25}$ | $\text{Cu}_{25.81}\text{Ge}_{49.98}\text{Pb}_{24.2}$<br>1 | 323.1/615.9/639.9                             | 777.9                       | 941.7    |
| 20                       | $\text{Cu}_{10}\text{Ge}_{80}\text{Pb}_{10}$ | $\text{Cu}_{10.32}\text{Ge}_{79.81}\text{Pb}_{9.87}$      | 321.9/620.9/638.1                             | 795.7                       | 880.9    |
| Vertical section Pb-CuGe |  |   |   |                             |          |
| 21                       | $\text{Cu}_{40}\text{Ge}_{40}\text{Pb}_{20}$ | $\text{Cu}_{39.81}\text{Ge}_{40.05}\text{Pb}_{20.1}$<br>4 | 327.8/616.8/636.9                             | 735.1                       | 1120.1   |
| 22                       | $\text{Cu}_{30}\text{Ge}_{30}\text{Pb}_{40}$ | $\text{Cu}_{30.15}\text{Ge}_{29.92}\text{Pb}_{39.9}$<br>3 | 336.1/606.9/625.9                             | 720.9                       |          |
| 23                       | $\text{Cu}_{20}\text{Ge}_{20}\text{Pb}_{60}$ | $\text{Cu}_{19.83}\text{Ge}_{20.18}\text{Pb}_{59.9}$<br>9 | 320.9/619.5/633.1                             | 714.5                       |          |
| 24                       | $\text{Cu}_{10}\text{Ge}_{10}\text{Pb}_{80}$ | $\text{Cu}_{10.07}\text{Ge}_{9.87}\text{Pb}_{80.06}$      | 327.1/609.3/636.5                             | 681.2                       |          |

Detected temperatures of phase transformation summarized in Table 3 are compared with corresponding vertical section. For better understanding phase transformation calculated vertical sections are plotted together and presented on figure 8.

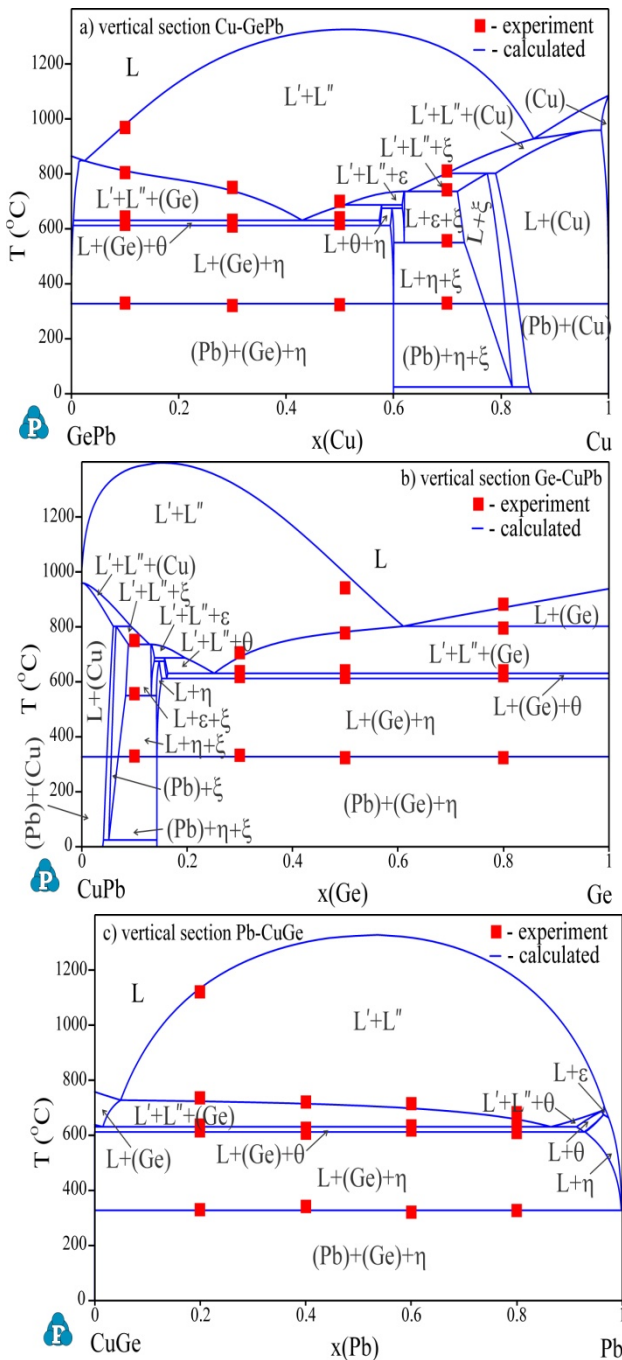


Figure 8. Calculated vertical sections of the ternary Cu-Ge-Pb system compared with DTA experimental results: a) Cu-GePb, b) Ge-CuPb and c) Pb-CuGe.

Samples 13 to 16 are used for testing phase transformation of vertical section Cu-GePb. By comparing results (Fig. 8a)) it is clear that first transformation temperature detected with samples 13, 14 and 15 is related to the reaction  $L \rightarrow \eta + (Ge) + (Pb)$ . Experimentally this is detected at temperature in range from 320.1 to the 327.8 °C while calculated one is at 326.82 °C. On same samples next detected temperature is related to the reaction  $\theta \rightarrow L + \eta + (Ge)$  which is calculated at temperature 611.64 °C while experimental one is in range from 611.2 to the 618.9 °C. Third detected temperature on all samples is related to the same reaction  $L \rightarrow \theta + (Ge) + L$ . This reaction is experimentally determined at temperatures 640.1, 630.9 and 639.1 °C, respectively while calculated one is at 630.40 °C. Next detected temperature on all samples is

described as a temperature of primary solidification. On sample 13 one more temperature is detected and it is related to the liquid curve. From same vertical section sample 16 was selected for tests. By this sample four temperatures were detected. First one is related to the reaction  $L + \eta \rightarrow \xi + (Pb)$  calculated at 326.75 °C, next one is to the reaction  $L + \epsilon \rightarrow \xi + \eta$  calculated at 549.31 °C, third one to the  $L \rightarrow L + \epsilon + \xi$  calculated at 735.72 °C, while last temperature is related to the temperature of primary solidification. Experimentally determined temperatures respectively are 329.3, 555.3, 740.7 and 809.3 °C.

Four samples marked with number from 17 to 20 are used for testing temperature of phase transformation of vertical section Ge-CuPb. By sample 17, three temperatures were detected at 329.8, 557.2 and 747.9 °C. By comparing detected temperatures with calculated vertical section is clear that detected temperatures are related to the reactions  $L + \eta \rightarrow \xi + (Pb)$ ,  $L + \epsilon \rightarrow \xi + \eta$  and  $L \rightarrow L + \epsilon + \xi$ , respectively. By samples 18, 19 and 20 first three temperatures on each samples detected temperature of three reactions. Detected temperatures of reactions are  $L \rightarrow \eta + (Ge) + (Pb)$ ,  $\theta \rightarrow L + \eta + (Ge)$  and  $L \rightarrow \theta + (Ge) + L$ . By comparing experimental results and calculated temperatures reasonable agreement is visible and difference between temperatures are less than 10 °C. On same samples at high temperature are detected temperatures of primary crystallization and liquid.

Samples 21 to 24 are selected for checking temperatures of phase transformation of Pb-CuGe vertical section. In all four samples first four detected temperatures are detected same transformation. First three temperatures are related to the reaction calculated at 326.82, 611.64 and 630.40 °C. Fourth temperature on each sample is related to the temperature of (Ge) primary crystallization. On sample 21 five temperatures are detected and this temperature is related to the liquid.

## 5. CONCLUSION

Two isothermal sections and three vertical sections are experimentally tested. Results of experiments are compared with calculated corresponding phase diagrams. By comparison it is clear that good agreement between results is reached. Phase composition shows similar composition with calculate compositions also experimental temperatures of phase transformation shows close value with calculated one. This led to the conclusion that thermodynamic dataset made from three constitutive binary systems is satisfactory for description of ternary system without introducing ternary parameters.

## ACKNOWLEDGEMENTS

This work has been supported by the National Nature Science Foundation of China (project No.51950410600) and the Ministry of Education, Science and Technological Development of the Republic of Serbia (Grant No. OI172037).

## REFERENCES

- [1] Y.-Y. Huang, B. Wu, F. Li, L.-L. Chen, Z.-X. Deng, K. Chang, First-principles and CALPHAD-type study of the Ir-Mo and Ir-W systems, *J. Min. Metall. Sect. B-Metall.*, 56 (1) (2020) 109-118. DOI:10.2298/JMMB190211001H
- [2] Z. Hu, C. Huang, J. Tu Y. Huang, A. Dong, Thermodynamic modeling of the In-Sc and In-Y systems supported by first-principles calculations, *J. Min. Metall. Sect. B-Metall.* 54 (2) B (2018) 161-167. DOI:10.2298/JMMB171121004
- [3] V.P. Vassiliev, V.A. Lysenko, Thermodynamic assessment of the Cu-In-Pb system, *Journal of Alloys and Compounds*, 629, (2015), 326-331. <https://doi.org/10.1016/j.jallcom.2014.12.217>
- [4] V.P. Vassiliev, V.A. Lysenko, W.P. Gong, New EMF measurements and thermodynamic evaluation of the In-Pb-Zn system, *J. Alloys Comp.*, 564 (2013), pp. 49-54
- [5] Shan Jin, Liliana I. Duarte, Christian Leinenbach, Experimental study and thermodynamic description of the Au-Cu-Ge system, *Journal of Alloys and Compounds*, 588, (2014), 7-16. <https://doi.org/10.1016/j.jallcom.2013.11.054>
- [6] J. Wang, Y.J. Liu, C.Y. Tang, L.B. Liu, H.Y. Zhou, Z.P. Jin, Thermodynamic description of the Au-Ag-Ge ternary system, *Thermochimica Acta*, 512(1-2), (2011), 240-246.
- [7] Dušan Milisavljević, Duško Minić, Milena Premović, Dragan Manasijević, Nebojša Košanin, Experimental examination and thermodynamic description of the ternary Ag-Ge-In system, *Thermochimica Acta*, 665, (2018) 1-10.
- [8] A. Djordjevic, M. Premovic, D. Minic, V. Cosovic, D. Manasijevic, Experimental examination and thermodynamic description of the ternary Bi-Ge-Ga,Zn systems, *Journal of Chemical Thermodynamics*, 2020, 142, 106000.
- [9] A. Djordjević, D. Minić, M. Premović, D. Manasijević, V. Čosović, Experimental Examination and Thermodynamic Description of the Ternary Bi-Ge-In and -Sn Systems, *Journal Of Phase Equilibria And Diffusion*, 40(4), (2019), 623-637.
- [10] S. Semboshi, S. Sato, A. Iwase, T. Takasugi, Discontinuous precipitates in age-hardening Cu-Ni-Si alloys. *Materials Characterization*. 2016;115:39-45.
- [11] J. Lei, H. Xie, S. Tao, R. Zhang, Z. Lu, Microstructure and Selection of Grain Boundary Phase of Cu-Ni-Si Ternary Alloys. *Rare Metal Materials and Engineering*. 2015;44(12):3050-3054
- [12] S.L. Ou, C.P. Cheng, C.Y. Yeh, C.J. Chung, K.S. Kao, R.C. Lin Characteristics of In-Ge-Sb-Sn-Te thin film used for phase change optical recording media, *Adv. Mater. Res.*, 189 193 (2011), pp. 4430-4433.
- [13] P. Nemeč, V. Nazabal, A. Moreac, J. Gutwirth, L. Benes, M. Frumar Amorphous and crystallized Ge-Sb-Te thin films deposited by pulsed laser: local structure using Raman scattering spectroscopy, *Mater. Chem. Phys.*, 136 (2012), 935-941.
- [14] J. Wang, S. Jin, C. Leinenbach, A. Jacot, Thermodynamic assessment of the Cu-Ge binary system, *J. Alloys Compd.* 504 (2010) 159-165.
- [15] T. Jantzen, P. J. Spencer, Thermodynamic assessments of the Cu-Pb-Zn and Cu-Sn-Zn systems, [https://doi.org/10.1016/S0364-5916\(98\)00040-6](https://doi.org/10.1016/S0364-5916(98)00040-6)
- [16] P. Chevalier, A thermodynamic evaluation of the Ge-In, Ge-Pb, Ge-Sb, Ge-Ti and Ge-Zn systems, *Thermochemica Acta*, 155 (1989), 227-240.
- [17] H. E. Swanson, E. Tatge, Standard X-ray diffraction powder patterns, *Natl. Bur. Stand. (U.S.), Circ.* 539 (1953) 539, 1.
- [18] S. K. Halder, G. Sen, An X-ray determination of the thermal expansion of silver and copper-base alloys at high temperature. II. Cu-Ga, *Acta Crystallogr. A*, 31 (1975) 158-159.
- [19] A.S. Cooper, Precise lattice constants of germanium, aluminum, gallium arsenide, uranium, sulphur, quartz and sapphire, *Acta Crystallogr.* 15 (1962) 578-582.
- [20] K. Schubert, G. Brandauer, Zum Aufbau des Systems Kupfer-Germanium, *Z. Met.* 43 (1952) 262-268.
- [21] V.M. Glasov, A.Y. Potemkin, Interaction between copper and antimony in a solid solution based on germanium with the formation of a charged complex, *Semiconductors* 34 (5) (2000) 495-501.
- [22] K. Schubert, H. Breimer, W. Burkhardt, E. Gunzel, R. Haufler, H.L. Lukas, H. Vetter, J. Wegst, M. Wilkens, Einigestructurelle Ergebnisse an metallischen Phasen II, *Naturwissenschaften* 44 (7) (1957) 229-230.
- [23] J. Lenz, K. Schubert, Uebereinige Leerstellen- und Stapelvarianten der Beta-Messing Strukturfamilie, *Z. Met.* 62 (1971) 810-816.

## Mechanical and electrical properties of the Bi-Ge-Sn alloys

Aleksandar Djordjevic<sup>1</sup>, Dusko Minic<sup>1</sup>, Milena Premovic<sup>1\*</sup>, Milan Kolarevic<sup>2</sup>, Milan Milosavljevic<sup>1</sup>

<sup>1</sup>University of Priština in Kosovska Mitrovica, Faculty of Technical Science, Department of Technological engineering  
Kneza Milosa 7, 38220 Kos. Mitrovica, Serbia

<sup>2</sup>University of Kragujevac, Faculty of Mechanical Engineering, Kraljevo, Serbia

*Mechanical and electrical properties of the ternary Bi-Ge-Sn alloys were investigated in this study. Calculation of isothermal section at 200, 300 and 25 °C was carried out by using optimized thermodynamic parameters for the constitutive binary systems. Microstructures of alloys were observed by using optical microscopy and scanning electron microscopy (SEM). Phases in microstructures have been detected by x-ray diffraction (XRD) analysis and compositions of the phasis by energy dispersive spectrometry (EDS). ANOVA analysis and using obtained results an appropriate mathematical model is proposed for every composition of alloys. The Brinell hardness and electrical conductivity of selected alloys were measured and obtained results were analyzed with respect to their overall compositions and phase constituents. Based on all the obtained experimental and calculated results, it was concluded that a general good agreement was obtained between them.*

**Keywords:** Ternary Bi-Ge-Sn system, Microstructures, Hardness properties, Electrical properties

### 1. INTRODUCTION

As the properties of the material can be changed with the addition of other elements, the testing of other alloys is always current, in a way to obtain alloys with new properties. Due to the technical importance of germanium-based systems, our group has previously tested germanium-based systems [1-3]. Experimental examination and thermodynamic description of the ternary Bi-Ge-Sn system have been investigated by Aleksandar et al. [4]. Electrical and mechanical properties of ternary Bi-Ge-Sn system have not been investigated before. Germanium-based alloys are mainly used as memory materials [5-8]. Because of all that, in this study is shown experimental investigation of electrical and mechanical properties of the ternary Bi-Ge-Sn alloys at room temperature ( $\approx 25$  °C), as well as isothermal sections on 200 and 300 °C. Thermodynamic data proposed by Aleksandar et al. [4] has been used in our study for the calculation of selected isothermal sections. Alloys of the tested ternary system tested with Brinell hardness test and test for electrical conductivity. Too, have been investigated phase equilibria of the isothermal sections at 200, 300 and 25 °C using scanning electron microscopy (SEM) with energy dispersive spectrometry (EDS) and x-ray diffraction (XRD). The results obtained in this paper were intended to provide a better insight into the properties of the test alloys.

### 2. MATERIALS AND METHODS

All tested samples (ternary and binary) with total masses of about 5 g were prepared from elements high purity (99.999 at. %) Bi, Ge, and Sn. Samples were melted in an induction furnace under high purity argon atmosphere and slowly cooled. The average weight loss of the samples during induction melting was about 1 mass %.

Samples for investigation of isothermal sections at 200 °C and 300 °C, were sealed in evacuated quartz tubes and then heated to the appropriate temperatures. Then they were extinguished in the water and ice mixture to preserve desired equilibrium at appropriate temperatures (200 and 300 °C). Prepared samples in this way were examined SEM-EDS and XRD analysis. Samples cooled to room temperature were tested Brinell hardness and electrical conductivity.

The compositions of samples and coexisting phases were determined by using JEOL JSM-6460 scanning electron microscope with energy dispersive spectroscopy (EDS) (Oxford Instruments X-act). Powder XRD data for phase identification of samples were recorded on a D2 PHASER (Bruker, Karlsruhe, Germany) powder diffractometer equipped with a dynamic scintillation detector and ceramic X-ray Cu tube (KFL-Cu-2K) in a  $2\theta$  range from  $10^\circ$  to  $75^\circ$  with a step size of  $0.02^\circ$ . The patterns were analyzed using the Topas 4.2 software, ICDD databases PDF2. Microstructures of the samples were recorded on a light microscopy using (LOM) OLYMPUS GX41 inverted metallographic microscope. Hardnesses of the samples were measured using Brinell hardness tester INNOVATEST, model NEXUS 3001. Electrical conductivity measurements were carried out using Foerster SIGMATEST 2.069 eddy current instrument.

### 3. RESULTS AND DISCUSSION

Constitutive binary systems of the ternary Bi-Ge-Sn system were extensively studied in the past. Reliable thermodynamic datasets for these binary systems are available in literature [9-11]. Based on the literature information for binary sub-systems considered phase, their crystallographic data and database names for the solid phases are summarized in Table 1.

\*Corresponding author: M. Premovic, milena.premovic@pr.ac.rs

Table 1: Considered phase, their crystallographic data and database names for the solid phases of the ternary Bi-Ge-Sn system

| Thermodynamic database name | Common name    | Space group symbol | Struktural designation | Pearson's symbol |
|-----------------------------|----------------|--------------------|------------------------|------------------|
| LIQUID                      | Liquid         | -                  | -                      | -                |
| RHOMBO_A7                   | (Bi)           | $\bar{R}3mH$       | A7                     | <i>hR2</i>       |
| DIAMOND_A4                  | (Ge)           | $\bar{Fm}3m$       | A4                     | <i>cF8</i>       |
| DIAMOND_A4                  | ( $\alpha$ Sn) | $\bar{Fd}3m$       | A4                     | <i>cF8</i>       |
| BCT_A5                      | ( $\beta$ Sn)  | $I4_1/amd$         | A5                     | <i>tI4</i>       |

In ternary Bi-Ge-Sn system, should appears liquid phase and four solid solution phases: (Bi), (Ge), ( $\alpha$ Sn) and ( $\beta$ Sn).

### 3.1. Isothermal section at 200 °C.

For investigation of the phase equilibria at 200 °C, five samples were analyzed by SEM-EDS and XRD methods. Experimental results are summarized in Table 2.

Table 2: Combined results of SEM-EDS and XRD analyzes of the selected Bi-Ge-Sn alloys annealed at  $T=200$  °C

| N. | Composition of samples (at. %)   | Determined phases |              | Compositions of phases (at. %)     |                                   |                                   | Lattice parameters (Å)         |                |
|----|----------------------------------|-------------------|--------------|------------------------------------|-----------------------------------|-----------------------------------|--------------------------------|----------------|
|    |                                  | EDS               | XRD          | Bi                                 | Ge                                | Sn                                | <i>a=b</i>                     | <i>c</i>       |
| 1. | 10.90 Bi<br>55.27 Ge<br>33.83 Sn | L<br>(Ge)         | (Ge)         | 27.01±0.7<br>0.33±0.4              | 1.82±0.2<br>98.87±0.1             | 71.17±0.4<br>0.80±0.7             | 5.6545±0.0002                  |                |
| 2. | 22.28 Bi<br>19.14 Ge<br>58.58 Sn | L<br>(Ge)         | (Ge)         | 30.21±0.6<br>0.65±0.7              | 2.63±0.5<br>99.12±0.4             | 67.16±0.1<br>0.23±0.2             | 5.6589±0.0007                  |                |
| 3. | 33.97 Bi<br>33.67 Ge<br>32.36 Sn | L<br>(Ge)         | (Ge)         | 27.02±0.3<br>0.82±0.7              | 3.03±0.6<br>98.99±0.1             | 69.95±0.7<br>0.19±0.9             | 5.6536±0.0004                  |                |
| 4. | 45.96 Bi<br>44.53 Ge<br>9.51 Sn  | L<br>(Ge)<br>(Bi) | (Ge)<br>(Bi) | 10.87±0.7<br>0.57±0.7<br>99.12±0.7 | 5.01±0.4<br>98.25±0.8<br>0.18±0.9 | 84.12±0.8<br>1.18±0.7<br>0.70±0.2 | 5.6512±0.0006<br>4.5367±0.0004 | 11.8124±0.0006 |
| 5. | 63.79 Bi<br>13.61 Ge<br>22.60 Sn | L<br>(Ge)<br>(Bi) | (Ge)<br>(Bi) | 7.53±0.9<br>1.07±0.2<br>98.76±0.1  | 5.27±0.7<br>98.12±0.7<br>0.62±0.8 | 87.20±0.8<br>0.81±0.1<br>0.62±0.9 | 5.6578±0.0005<br>4.5398±0.0006 | 11.8179±0.0003 |

As can be seen from the presented EDS and XRD results, the all studied alloy samples have the same L and (Ge) solid solution phase in microstructure. In addition to the liquid phase and (Ge) solid solution phase, in the samples 4 and 5 occur an (Bi) solid solution phase. The EDS results show that (Ge) solid solution phase is rich

with germanium with neglected solubility of other two elements. (Bi) solid solution phase is rich with bismuth and with neglected solubility of germanium and tin. Liquid phase is rich with Bi and Sn.

SEM micrograph of one sample annealed at 200 °C is presented in Figure 1 as an illustration.

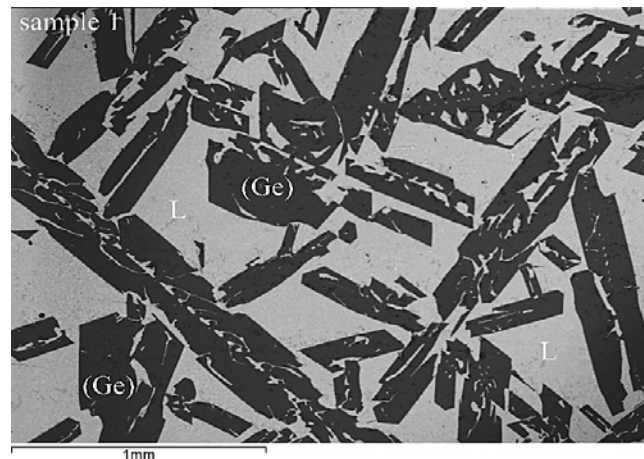


Figure 1: SEM micrographs of the sample 1 annealed at 200 °C

On the given micrograph, (Ge) solid solution phase appears as a dark phase and L phase as a light phase.

Since the samples were annealed at 200 °C, compositions of the phases determined by EDS analysis

were compared with the calculated isothermal section at 200 °C. Figure 2 shows comparison of the EDS results (Table 2) and the calculated isothermal section at 200 °C.

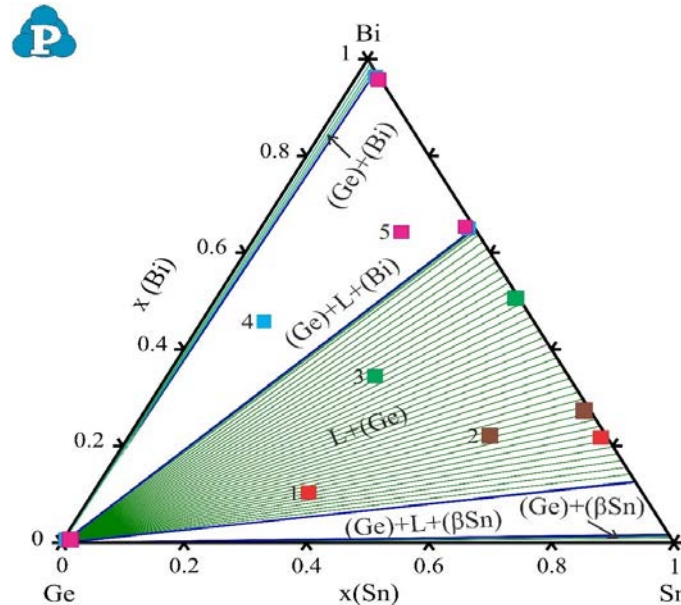


Figure 2: Calculated isothermal section at 200 °C compared with EDS results given in Table 2

From Figure 2 it can be seen that the calculated isothermal section has five phase regions. Three of them are L+(Ge), (Ge)+(βSn) and (Ge)+(Bi) two-phase regions, two are (Ge)+L+(Bi) and (Ge)+L+(βSn) three-phase regions. Two of the three phase regions have been experimentally proven. Tested alloy samples 1, 2 and 3 belong to L+(Ge) two-phase region. Samples 4 and 5 belong (Ge)+L+(Bi) three-phase region.

3.2. Isothermal section at 300 °C

As a next step, five alloys annealed at 300 °C were used for checking phase equilibria at 300 °C. Results of SEM-EDS and XRD analysis for the alloys annealed at 300 °C are summarized in Table 3.

Table 3: Combined results of SEM-EDS and XRD analyzes of the selected Bi-Ge-Sn alloys annealed at T=300 °C

| N. | Composition of samples (at. %)   | Determined phases |      | Compositions of phases (at. %) |                       |                       | Lattice parameters (Å)<br><i>a=b=c</i> |
|----|----------------------------------|-------------------|------|--------------------------------|-----------------------|-----------------------|--|
|    |                                  | EDS               | XRD  | Bi                             | Ge                    | Sn                    |  |
| 1. | 13.03 Bi<br>22.91 Ge<br>64.06 Sn | L<br>(Ge)         | (Ge) | 23.98±0.7<br>0.78±0.7          | 0.24±0.4<br>98.78±0.2 | 75.78±0.2<br>0.44±0.4 | 5.6523±0.0006                          |
| 2. | 36.75 Bi<br>16.77 Ge<br>46.48 Sn | L<br>(Ge)         | (Ge) | 24.91±0.6<br>0.42±0.8          | 1.92±0.3<br>98.21±0.1 | 73.17±0.8<br>1.37±0.5 | 5.6568±0.0001                          |
| 3. | 16.29 Bi<br>60.83 Ge<br>22.88 Sn | L<br>(Ge)         | (Ge) | 38.63±0.2<br>0.28±0.4          | 1.52±0.3<br>99.07±0.7 | 59.85±0.1<br>0.65±0.9 | 5.6561±0.0007                          |
| 4. | 60.18 Bi<br>23.01 Ge<br>16.81 Sn | L<br>(Ge)         | (Ge) | 41.87±0.3<br>0.82±0.1          | 0.24±0.6<br>98.91±0.7 | 57.89±0.3<br>0.27±0.2 | 5.6569±0.0002                          |
| 5. | 53.36 Bi<br>23.30 Ge<br>23.34 Sn | L<br>(Ge)         | (Ge) | 21.13±0.3<br>0.47±0.8          | 0.62±0.2<br>99.11±0.4 | 78.25±0.9<br>0.42±0.5 | 5.6530±0.0006                          |

Detected phases are L and (Ge) solid solution. (Ge) solid solution is rich with germanium and can dissolve neglected amount of tin and bismuth. EDS result shows that L phase have different composition depending on composition of the samples. In general L phase is rich in

tin and bismuth and dissolves a negligible amount of germanium.

SEM micrographs of the sample 2 annealed at 300 °C present at Figure 3.

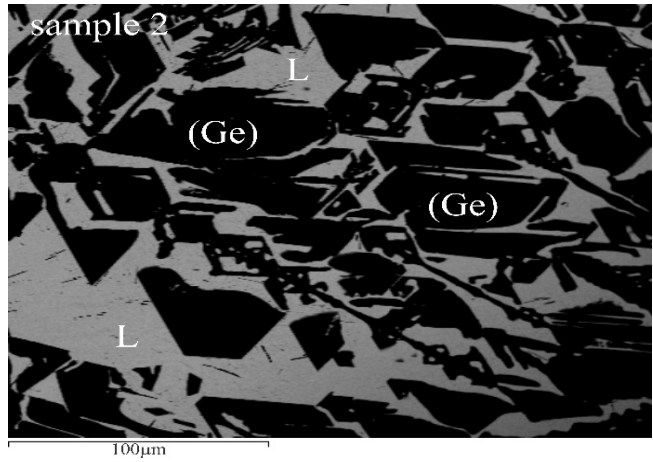


Figure 3: SEM micrographs of the sample 2 annealed at 300 °C

From microstructure it is visible that (Ge) solid solution appears as a dark phase and L phase a gray phase.

The EDS results obtained for the samples annealed at 300 °C are given in Table 3 and compared with the

calculated isothermal section at 300 °C. Figure 4 presents comparison of the calculated phase diagram and the EDS results.

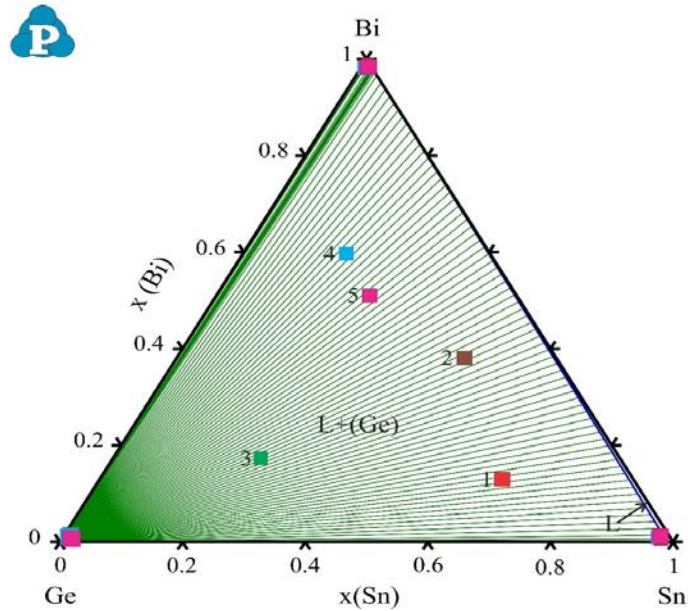


Figure 4: Calculated isothermal section at 300 °C compared with EDS results given in Table 3

The calculated isothermal cross section at 300° C consists of two phase regions. One is a single-phase region L, and the other is a two-phase region L+(Ge). By comparing the EDS composition of the tested samples, it is determined that all samples are from the two-phase L+(Ge) region, the same region as the experimentally detected samples. The EDS phase compositions agree well with the calculated phase compositions.

### 3.3. Microstructural analysis of slowly-cooled samples

Twelve slowly cooled ternary samples, marked with numbers from 1 to 12, were subjected to the tests of mechanical and electrical properties. Overall compositions of samples were situated along three vertical sections (samples 1 to 4, along Bi-GeSn vertical section, samples 5 to 8 along Ge-BiSn vertical section and samples from 9 to 12 along Sn-BiGe vertical section). Figure 5 presents calculated isothermal section at 25 °C with marked nominal composition of tested ternary alloys.

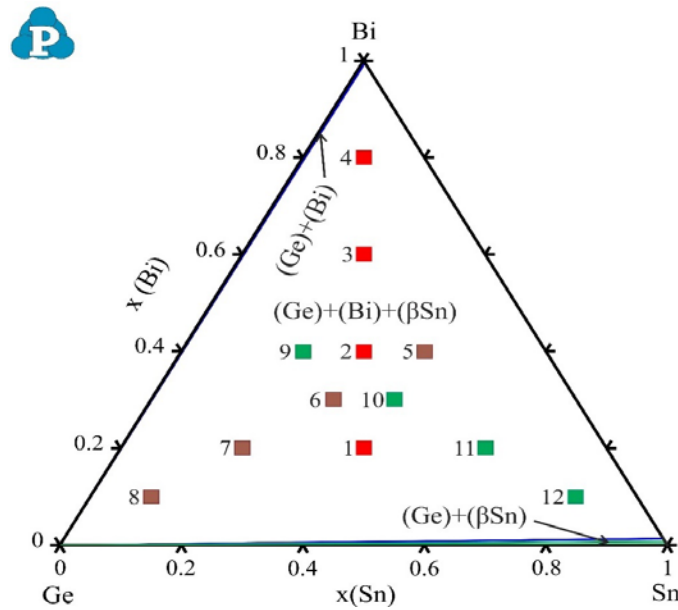


Figure 5: Predicted isothermal section at 25 °C with marked compositions of tested alloys

Before determination of hardness and electrical conductivity samples were analyzed using XRD and their microstructure was observed with light optical microscopy. Results of XRD analysis of all samples

revealed that all samples have (Ge), (Bi) and (βSn) phases in microstructure. Three microstructures of samples 1, 4 and 7 are given in Figure 6.

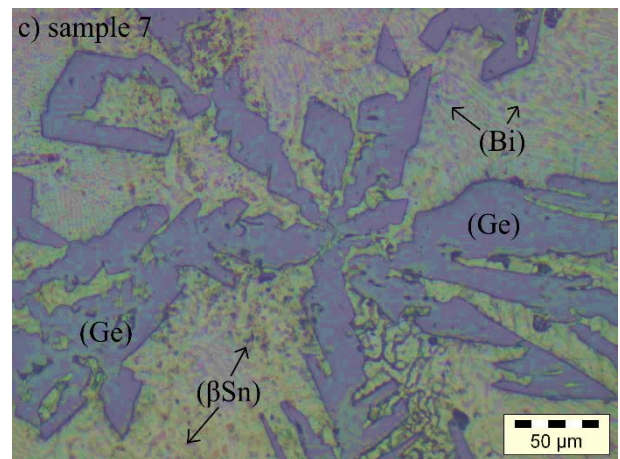
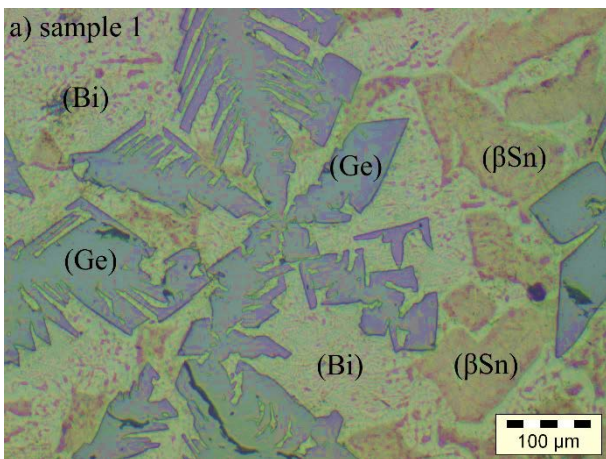
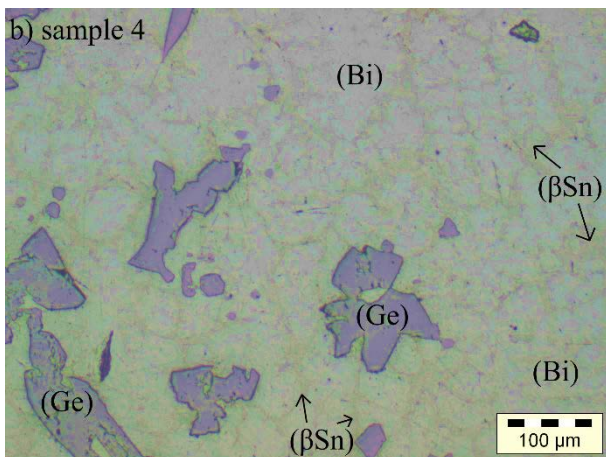


Figure 6: LOM micrographs of a) sample 1, b) sample 4 and c) sample 7



Phases which appear in microstructures are marked at presented micrographs.

### 3.3.1. Brinell hardness measurements

Twelve ternary samples and three binary samples were subjected to the Brinell hardness measurements. Based on repeated measurements, mean values of Brinell hardness were calculated and presented in Table 4. Literature values of hardness for pure elements [12] are also shown in Table 4 for comparison.

Table 4: Compositions of the investigated samples at room temperature and related Brinell hardness values

| N. | Alloy nominal composition (at. %) |            |            | Measured value (MN/m <sup>2</sup> ) |        |        | Mean value (MN/m <sup>2</sup> ) |
|----|-----------------------------------|------------|------------|-------------------------------------|--------|--------|---------------------------------|
|    | x(Bi)                             | x(Ge)      | x(Sn)      | 1                                   | 2      | 3      |                                 |
| B1 | <b>0</b>                          | 0.5        | 0.5        | 19.40                               | 24.20  | 18.60  | 20.73                           |
| 1  | <b>0.2</b>                        | 0.4        | 0.4        | 27.80                               | 28.00  | 28.30  | 28.03                           |
| 2  | <b>0.4</b>                        | 0.3        | 0.3        | 23.90                               | 26.20  | 24.80  | 24.96                           |
| 3  | <b>0.6</b>                        | 0.2        | 0.2        | 22.60                               | 22.00  | 24.40  | 23.00                           |
| 4  | <b>0.8</b>                        | 0.1        | 0.1        | 23.60                               | 19.10  | 20.20  | 20.96                           |
| Bi | <b>1</b>                          | 0          | 0          |                                     |        |        | 94.20 [12]                      |
| B2 | 0.5                               | <b>0</b>   | 0.5        | 15.40                               | 12.30  | 16.20  | 14.63                           |
| 5  | 0.4                               | <b>0.2</b> | 0.4        | 31.90                               | 32.70  | 32.30  | 32.30                           |
| 6  | 0.3                               | <b>0.4</b> | 0.3        | 38.80                               | 43.10  | 42.80  | 41.56                           |
| 7  | 0.2                               | <b>0.6</b> | 0.2        | 41.60                               | 46.20  | 44.80  | 44.20                           |
| 8  | 0.1                               | <b>0.8</b> | 0.1        | 63.30                               | 58.50  | 56.20  | 59.33                           |
| Ge | 0                                 | <b>1</b>   | 0          |                                     |        |        | 973.40 [12]                     |
| B3 | 0.5                               | 0.5        | <b>0</b>   | 213.20                              | 215.60 | 217.40 | 215.40                          |
| 9  | 0.4                               | 0.4        | <b>0.2</b> | 37.30                               | 38.00  | 39.00  | 38.10                           |
| 10 | 0.3                               | 0.3        | <b>0.4</b> | 35.50                               | 36.80  | 34.90  | 35.73                           |
| 11 | 0.2                               | 0.2        | <b>0.6</b> | 43.40                               | 42.10  | 42.80  | 42.76                           |
| 12 | 0.1                               | 0.1        | <b>0.8</b> | 39.90                               | 42.30  | 41.20  | 41.13                           |
| Sn | 0                                 | 0          | <b>1</b>   |                                     |        |        | 51.00 [12]                      |

In addition to the tabular presentation, the obtained values for hardness are also presented graphically. Figure 7 shows a graphical representation of the relationship

between the hardness of the tested alloys and the composition of the alloys.

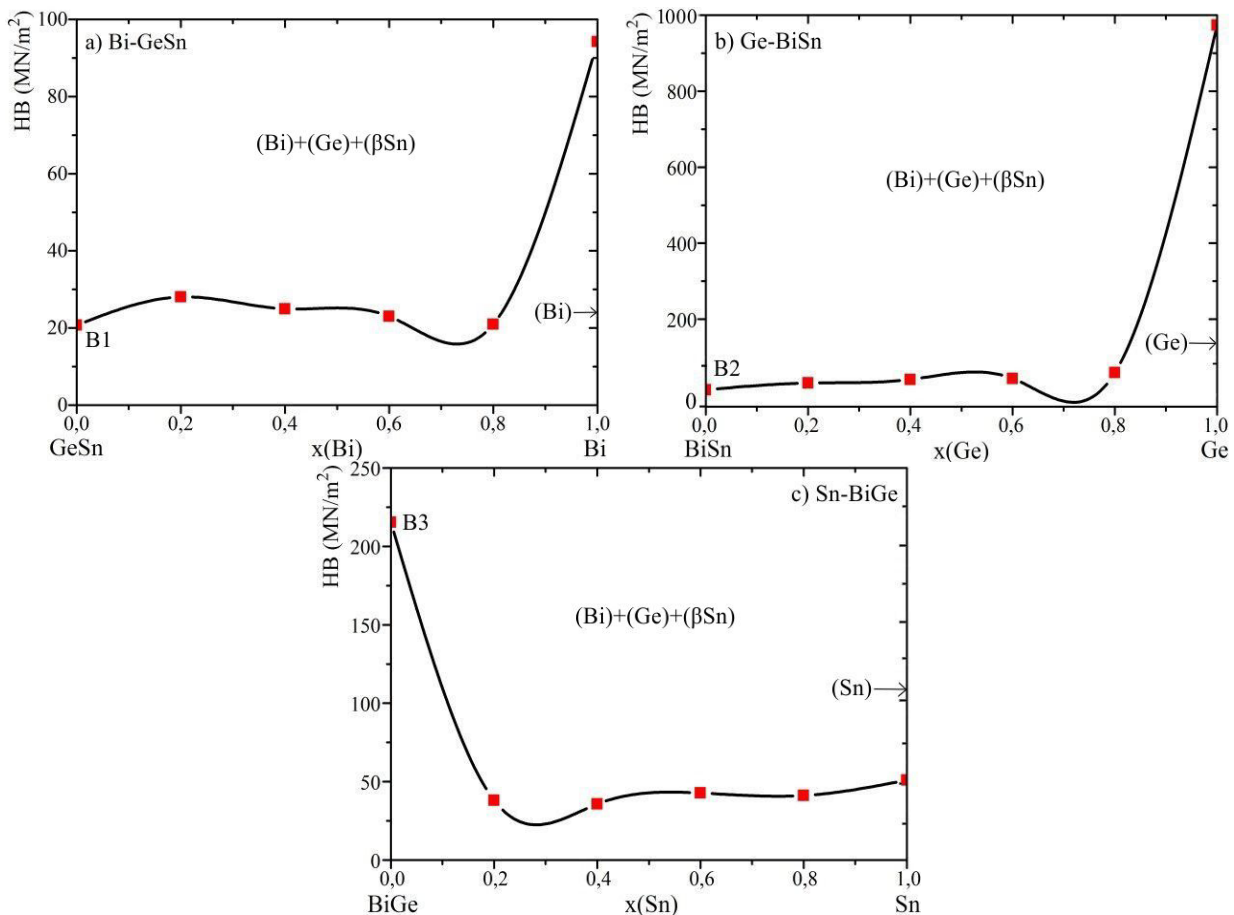


Figure 7: Graphical presentation of Brinell hardness dependence of composition and phase fraction: a) vertical section Bi-GeSn, b) vertical section Ge-BiSn and c) vertical section Sn-BiGe

The highest value of hardness for ternary alloys was measured on the sample Bi10Ge80Sn10 of 59.33 MN/m<sup>2</sup>, which is understandable due to the high amount of germanium.

As none of the S-models (Scheffe-model) met the adequacy requirements, the so-called SV-models (Slack-Variable mixture models) were used [13,14]. The Quartic Slack Mixture model was selected. By utilizing experimentally determined values of hardness given in

Table 5 mathematical model of the dependence of the Brinell hardness on composition for the Bi-Ge-Sn alloys was developed. The diagnosis of the statistical properties of the assumed model found that the distribution of residuals is not normal and that it is necessary to transform the mathematical model in order to meet the conditions of normality. The Box-Cox diagnostics recommends the

”Inverse Square Root“ transformation for the variance stabilization.

The final equation of the predictive model in terms of Real components is:

$$1/\text{Sqrt}(\text{HB})=0.0317625+0.07459893 \cdot (\text{Bi})+1.39074537 \cdot (\text{Sn})-3.14882 \cdot (\text{Bi}) \cdot (\text{Sn})-0.0033572 \cdot (\text{Bi}^2)-2.7651581 \cdot (\text{Sn}^2)+4.02037782 \cdot (\text{Bi}^2) \cdot (\text{Sn})+3.92451675 \cdot (\text{Bi}) \cdot (\text{Sn}^2)+1.48355978 \cdot (\text{Sn}^3)-3.2914706 \cdot (\text{Bi}^2) \cdot (\text{Sn}^2) \tag{1}$$

The repeated analysis for Inverse Square Root model transformation confirms the significance of the Transformed Quartic Slack Mixture model. In this case,

ANOVA confirms the adequacy of the Reduced Quartic Slack Mixture model (Table 5).

Table 5: ANOVA for Reduced Quartic Slack Mixture model

| Source                        | Sum of Squares | df | Mean Square | F Value  | p-value Prob > F |
|-------------------------------|----------------|----|-------------|----------|------------------|
| Model                         | 0.05065        | 9  | 0.00563     | 35.49194 | 0.00002          |
| A-Bi                          | 0.00022        | 1  | 0.00022     | 1.40959  | 0.26918          |
| C-Sn                          | 0.00593        | 1  | 0.00593     | 37.37938 | 0.00029          |
| AC                            | 0.00362        | 1  | 0.00362     | 22.82148 | 0.00140          |
| A <sup>2</sup>                | 0.00000        | 1  | 0.00000     | 0.00310  | 0.95699          |
| C <sup>2</sup>                | 0.00286        | 1  | 0.00286     | 18.04155 | 0.00281          |
| A <sup>2</sup> C              | 0.00597        | 1  | 0.00597     | 37.62949 | 0.00028          |
| AC <sup>2</sup>               | 0.00175        | 1  | 0.00175     | 11.06407 | 0.01044          |
| C <sup>3</sup>                | 0.00185        | 1  | 0.00185     | 11.65229 | 0.00917          |
| A <sup>2</sup> C <sup>2</sup> | 0.00118        | 1  | 0.00118     | 7.44329  | 0.02592          |
| Residual                      | 0.00127        | 8  | 0.00016     |          |                  |
| Cor Total                     | 0.05191        | 17 |             |          |                  |

The F-value of the Model is 35,49 and it implies that the model is significant. In this case, all model terms are significant. R-squared and other statistics after the ANOVA have appropriate values which confirm the justification of the choice of the adopted mathematical model (Table 6).

The diagnosis of the statistical properties of the assumed model found that the distribution of residuals are normal. After the applied Box-Cox procedure, the value of λ is -0.5, the optimum value of λ is -0.26 and the 95% confidence interval for λ (Low C.I.= -0.79, High C.I.=0.11) contains the value -0.5, thus proving the justification of the model transformation (Figure 8).

Table 6: R-squared and other statistics after the ANOVA

|           |         |                |          |
|-----------|---------|----------------|----------|
| Std. Dev. | 0.01259 | R-Squared      | 0.97557  |
| Mean      | 0.16054 | Adj R-Squared  | 0.94808  |
| C.V. %    | 7.84322 | Pred R-Squared | 0.78256  |
| PRESS     | 0.01129 | Adeq Precision | 24.09909 |

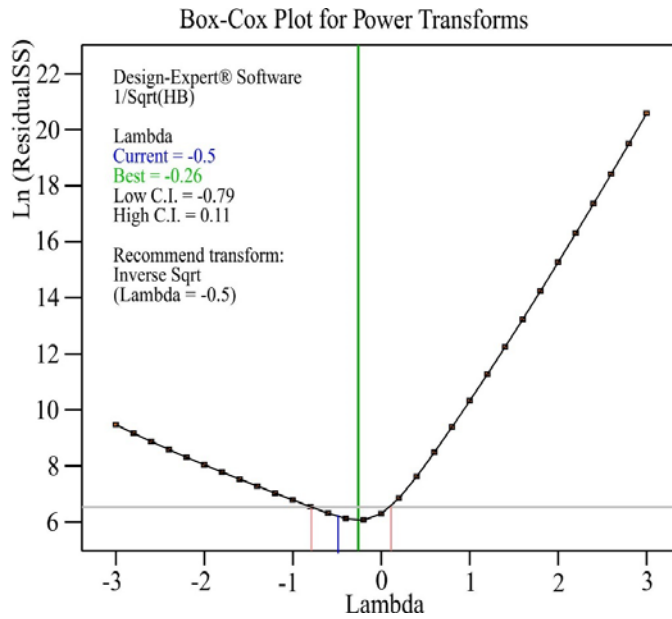


Figure 8: The Box-Cox plot for power transforms

Iso-lines contour plot for Brinell hardness of alloys defined by equation 1 is shown in Figure 9.

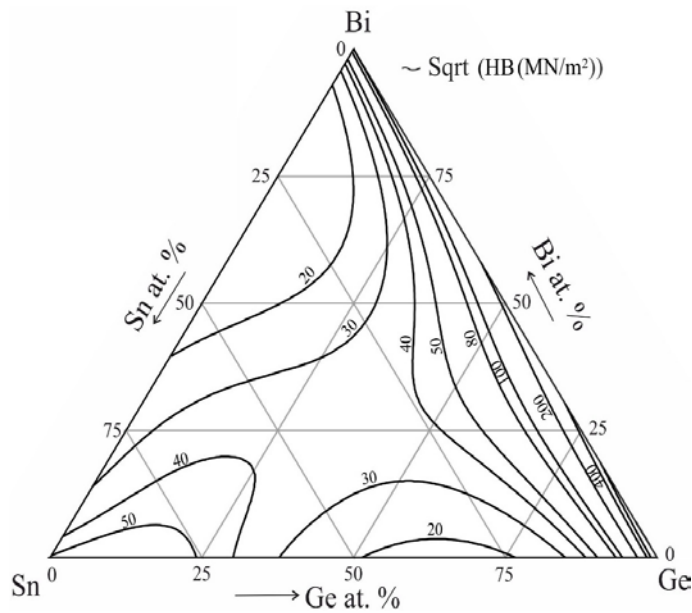


Figure 9: Calculated iso-lines of Brinell hardness in ternary Bi-Ge-Sn system with  $R^2 = 0.976$

3.3.2. Electrical conductivity measurements

Measurements of electrical conductivity were performed on the same group of samples used for hardness test. For all investigated samples electrical conductivity measurements were repeated four times at different

positions and obtained values for each measured point are given in Table 7. Beside measured values, Table 7 also includes calculated mean values and literature values of electrical conductivity for pure elements [15].

Table 7: Compositions of the investigated samples at room temperature and related electrical conductivity values

| N. | Alloy nominal composition (at. %) |            |       | Value (MS/m) |        |        |        | Mean value (MS/m) |
|----|-----------------------------------|------------|-------|--------------|--------|--------|--------|-------------------|
|    | x(Bi)                             | x(Ge)      | x(Sn) | 1            | 2      | 3      | 4      |                   |
| B1 | <b>0</b>                          | 0.5        | 0.5   | 2.8010       | 2.7370 | 2.7800 | 2.7680 | 2.7710            |
| 1  | <b>0.2</b>                        | 0.4        | 0.4   | 0.5323       | 0.7698 | 0.6397 | 0.7885 | 0.6825            |
| 2  | <b>0.4</b>                        | 0.3        | 0.3   | 0.4978       | 0.4757 | 0.5042 | 0.4989 | 0.4941            |
| 3  | <b>0.6</b>                        | 0.2        | 0.2   | 0.8899       | 0.6365 | 0.7895 | 0.6325 | 0.7371            |
| 4  | <b>0.8</b>                        | 0.1        | 0.1   | 0.9636       | 0.9800 | 0.9993 | 0.8998 | 0.9606            |
| Bi | <b>1</b>                          | 0          | 0     |              |        |        |        | 0.77 [15]         |
| B2 | 0.5                               | <b>0</b>   | 0.5   | 1.3699       | 1.0236 | 1.3698 | 1.0233 | 1.1966            |
| 5  | 0.4                               | <b>0.2</b> | 0.4   | 0.8161       | 0.8317 | 0.8561 | 0.8383 | 0.8355            |

|    |     |            |            |        |        |        |        |        |            |
|----|-----|------------|------------|--------|--------|--------|--------|--------|------------|
| 6  | 0.3 | <b>0.4</b> | 0.3        | 0.7896 | 0.6356 | 0.7853 | 0.6669 | 0.7193 |            |
| 7  | 0.2 | <b>0.6</b> | 0.2        | 0.3168 | 0.3156 | 0.3147 | 0.3158 | 0.3157 |            |
| 8  | 0.1 | <b>0.8</b> | 0.1        | 0.3695 | 0.2225 | 0.2314 | 0.2323 | 0.2639 |            |
| Ge | 0   | <b>1</b>   | 0          |        |        |        |        |        | 0.002 [15] |
| B3 | 0.5 | 0.5        | <b>0</b>   | 0.3430 | 0.3410 | 0.3530 | 0.3440 | 0.3452 |            |
| 8  | 0.4 | 0.4        | <b>0.2</b> | 0.3080 | 0.3068 | 0.3091 | 0.3087 | 0.3081 |            |
| 10 | 0.3 | 0.3        | <b>0.4</b> | 0.3889 | 0.4545 | 0.5232 | 0.4999 | 0.4666 |            |
| 11 | 0.2 | 0.2        | <b>0.6</b> | 2.0450 | 1.9999 | 2.0050 | 2.0254 | 2.0188 |            |
| 12 | 0.1 | 0.1        | <b>0.8</b> | 3.1232 | 3.1252 | 2.9362 | 2.9316 | 3.0290 |            |
| Sn | 0   | 0          | <b>1</b>   |        |        |        |        |        | 9.1 [15]   |

Figure 10 presents graphical presentation of results (mean value) given in Table 7 for easier overview of the results.

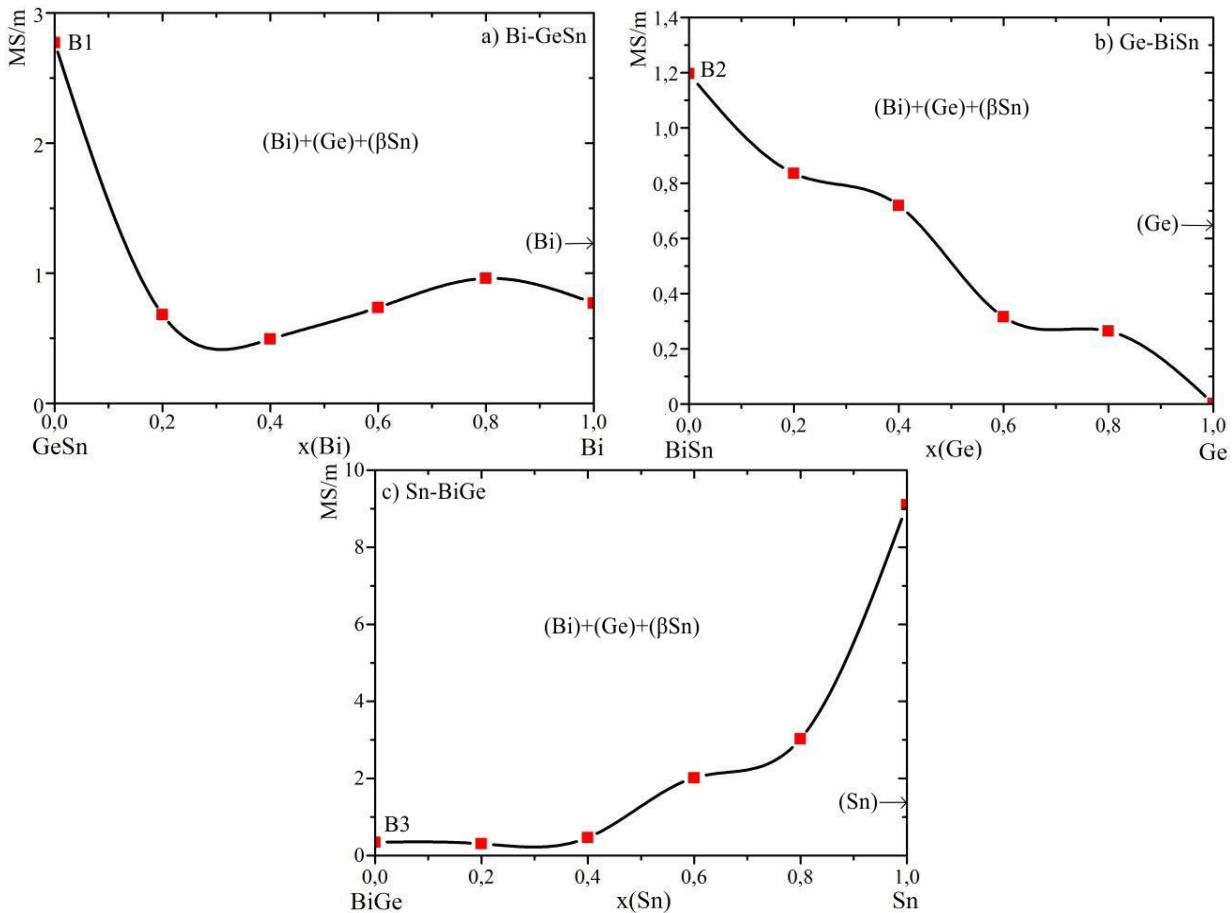


Figure 10: Graphical presentation of electrical conductivity dependence of composition and phase fraction a) vertical section Bi-GeSn, b) vertical section Ge-BiSn and c) vertical section Sn-BiGe

According to the obtained results, the triple alloy Bi10Ge10Sn80 has the highest value of electrical conductivity, 3.0290 MS/m, which is expected because in this combination of bismuth, germanium and tin, tin has the highest electrical conductivity compared to the other two components.

Special Quartic Mixture model was suggested as a final equation for prediction of electrical conductivity. The

diagnosis of the statistical properties of the assumed model found that the distribution of residuals is not normal and that it is necessary to transform the mathematical model in order to meet the conditions of normality. The Box-Cox diagnostics recommend the "Square Root" transformation for the variance stabilization.

The final equation of the predictive model in terms of Actual components is:

$$\begin{aligned} \text{Sqrt}(\sigma) = & 0.976127 \cdot (\text{Bi}) + 0.0501598 \cdot (\text{Ge}) + 2.8830787 \cdot (\text{Sn}) + 0.4271847 \cdot (\text{Bi}) \cdot (\text{Ge}) \\ & - 3.0859792 \cdot (\text{Bi}) \cdot (\text{Sn}) + 0.514126 \cdot (\text{Ge}) \cdot (\text{Sn}) - 26.711332 \cdot (\text{Bi}) \cdot (\text{Ge}) \cdot (\text{Sn}^2) \end{aligned} \quad (2)$$

The repeated analysis for Square Root model transformation confirms the significance of the Transformed Special Quartic Mixture model. In this case,

ANOVA confirms the adequacy of the Special Quartic Mixture model (Table 8).

Table 8: ANOVA for Special Quartic Mixture model

| Source           | Sum of Squares | df | Mean Square | F Value   | p-value<br>Prob > F |
|------------------|----------------|----|-------------|-----------|---------------------|
| Model            | 6.97359        | 6  | 1.16227     | 48.75690  | 0.00000027          |
| Linear Mixture   | 5.68286        | 2  | 2.84143     | 119.19764 | 0.00000004          |
| AB               | 0.00972        | 1  | 0.00972     | 0.40762   | 0.53624788          |
| AC               | 0.43643        | 1  | 0.43643     | 18.30800  | 0.00130137          |
| BC               | 0.01211        | 1  | 0.01211     | 0.50815   | 0.49078544          |
| ABC <sup>2</sup> | 0.18397        | 1  | 0.18397     | 7.71754   | 0.01796658          |
| Residual         | 0.26222        | 11 | 0.02384     |           |                     |
| Cor Total        | 7.23581        | 17 |             |           |                     |

The F-value of the Model is 48.76 and it implies that the model is significant. R-squared and other statistics after the ANOVA have good values which confirm the justification of the choice of the adopted mathematical model (Table 9).

Table 9: R-squared and other statistics after the ANOVA

|           |          |                |          |
|-----------|----------|----------------|----------|
| Std. Dev. | 0.15440  | R-Squared      | 0.96376  |
| Mean      | 0.99388  | Adj R-Squared  | 0.94399  |
| C.V. %    | 15.53469 | Pred R-Squared | 0.81299  |
| PRESS     | 1.35317  | Adeq Precision | 29.42299 |

The diagnosis of the statistical properties of the assumed model found that the distribution of residuals are normal. After the applied Box-Cox procedure, the value of  $\lambda$  is 0.5, the optimum value of  $\lambda$  is 0.32 and the 95% confidence interval for  $\lambda$  (Low C.I.=0.10, High C.I.=0.55) contains the value 0.5, thus proving the justification of the model transformation (Figure 11).

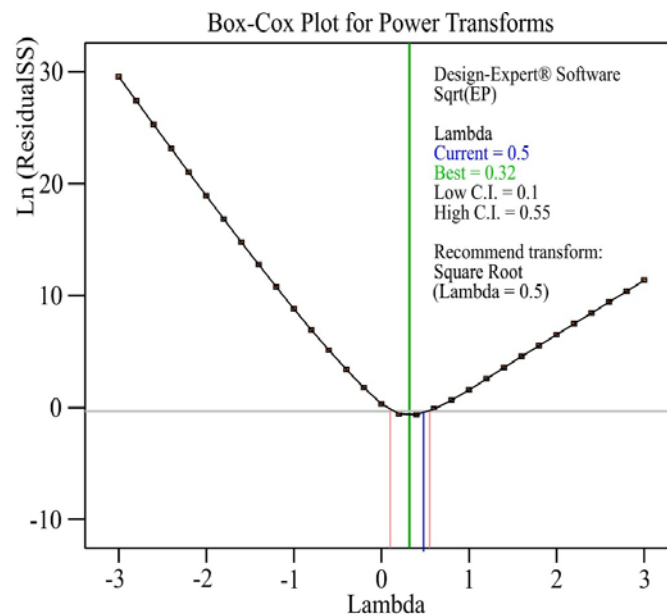


Figure 11: The Box-Cox plot for power transforms

Iso-lines contour plot for Electrical conductivity of Bi-Ge-Sn alloys defined by equation 2 is shown in Figure 12.

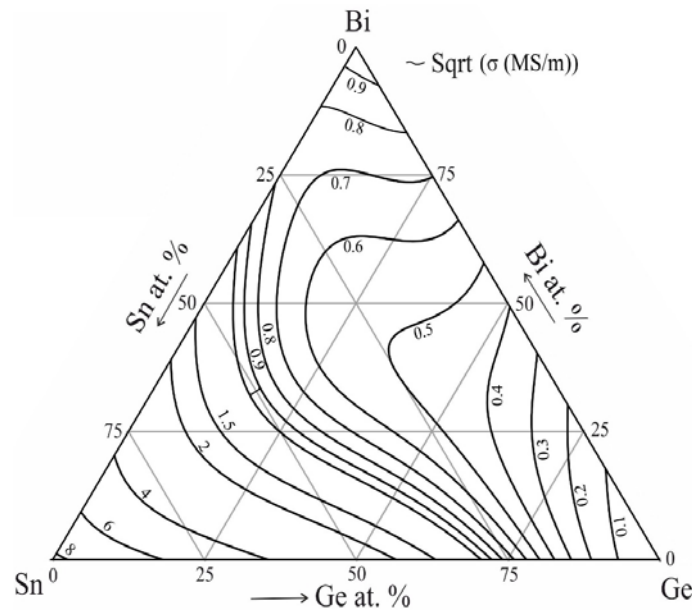


Figure 12: Calculated iso-lines of Electrical conductivity in ternary Bi-Ge-Sn system with  $R2 = 0.964$

#### 4. CONCLUSION

In this study, for ternary Bi-Ge-Sn system are experimentally investigated three isothermal sections at 200, 300 and 25 °C. SEM-EDS and XRD analysis were applied for analysis of the chosen ternary samples after long-term annealing. Experimental results SEM-EDS and XRD techniques were compared with calculated phase diagrams at 200 and 300 °C and good agreement between data is reached. By using thermodynamic data set, isothermal section at 25 °C was calculated and three different phase fields were predicted. One of three phase region were confirmed with EDS and XRD results. On twelve ternary alloys and three binary alloys were performed tests microstructural, hardness and electrical conductivity. With SEM and LOM microstructures of tested alloys were observed. On 25 °C detected phases with XRD method are (Ge), (Bi) and ( $\beta$ Sn) solid solutions. All results from Brinell hardness test and electrical conductivity were used for predicting a mathematical model for calculation of properties along all composition range.

#### ACKNOWLEDGEMENTS

This work has been supported by the National Nature Science Foundation of China (project No.51950410600) and the Ministry of Education, Science and Technological Development of the Republic of Serbia (Grant No. OI172037).

#### REFERENCES

- [1] Premovic, M., Minić, D., Kolarevic, M., Manasijevic, D., Živković, D., Djordjevic, A., Milisavljevic, D., 2017. *Rev Metal.* 53(3), p. e098
- [2] Premović, M., Manasijević, D., Minić, D., Živković, D., 2016. *Kovové Mater.* 54(1), p. 45
- [3] Premovic, M., Du, Y., Minic, D., Zhang, C., Manasijevic, D., Balanovic, Lj., Markovic, I., 2017. *J. Alloy Compd.* 726, p. 820

- [4] Djordjević A., Minić D., Premović M., Manasijević D., Čosović V., *JPED*, 2019, 40(4), p 623-637
- [5] Lacaíta, A.L., Wouters, D.J., 2008. *Phys. Status Solidi A Appl. Mater.*, 205, p. 2281
- [6] Ou, S. L., Cheng, C. P., Yeh, C. Y., Chung, C. J., Kao, K. S., Lin, R. C., 2011. *Adv. Mater. Res.*, 189, p. 4430
- [7] Ielmini D., Lacaíta, A. L., 2011. *Mater. Today*, 14(12), p. 600
- [8] Nemeč, P., Nazabal, V., Moreac, A., Gutwirth, J., Benes, L., Frumar, M., 2012. *Mater. Chem. Phys.*, 136, p. 935
- [9] Chevalier P.-Y., *Thermochim. Acta*, 1988, 132, p. 111–116
- [10] Vizdal J., Braga M. H., Kroupa A, Richter K. W., Soares D., Malheiros L. F., Ferreira J., *Calphad*, 2007, 31, p. 438–448
- [11] Feutelais Y, Legendre B, and Fries S.G., *Calphad*, 1996, 20(1), p. 109-123
- [12] <http://periodictable.com/Properties/A/BrinellHardness.al.html>, access 29.11.2018
- [13] Cruz-Salgado Javier, *Selecting the Slack Variable in Mixture Experiment*, *Ingeniería Investigación y Tecnología*, 2015, 14 (4), p 613-623
- [14] G. F. Piepel, D. C. Hoffmann, S. K. Cooley, *Slack-Variable versus Mixture Modeling for Mixture Experiments: A Definitive Comparison*, 2018.
- [15] <http://periodictable.com/Properties/A/ElectricalConductivity.an.html>, access 25.12.2018



# **SESSION C**

## **AUTOMATIC CONTROL AND FLUID TECHNIQUE**



# Trajectory Tracking of a Two – Link Gripping Mechanism

Radiša Jovanović<sup>1\*</sup>, Uglješa Bugarić<sup>2</sup>, Lara Laban<sup>1</sup>, Mitra Vesović<sup>1</sup>

<sup>1</sup>Faculty of Mechanical Engineering/Department of Control Engineering, University of Belgrade, Serbia

<sup>2</sup>Faculty of Mechanical Engineering/Department of Industrial Engineering, University of Belgrade, Serbia

*The manufacturing industry frequently deals with the problem of gripping mechanism and their movement optimization. This paper presents an optimization methodology based on the whale optimization algorithm to design an optimal fuzzy PD controller of a two - link gripping mechanism (robot arm) as a part of mobile robot working cycle. The dynamical analysis of gripping mechanism investigates a coupling relation between the joint torques applied by the actuators and the position and acceleration of the robot arm. The proposed fuzzy controller optimizes the trajectory of the robot's end effector. Additionally, a simulation study was done for the specific initial case and the trapezoidal velocity profile was generated. Based on the predefined acceleration, movement of the robot arm is shown to be smooth and without an abrupt braking.*

**Keywords:** Gripping mechanism, Trajectory tracking, Fuzzy controller, Whale optimization algorithm

## 1. INTRODUCTION

Robots take part in an important role in the current manufacturing industry. Per se, an essential feature of the Industry 4.0 are the autonomous production methods powered by robots that can complete tasks intelligently, with a focus on safety, flexibility, versatility, and collaboration [1].

Intelligent mobile robots can be used for many different purposes, for example, in the production process, one of them is internal transport – material handling. In that case we can consider an intelligent mobile robot as sort of a transportation machine – device. The main characteristic of all transportation machines is their working cycle (single or complex). Moreover, we will be considering intelligent mobile robot as „a single position machine“ with a discontinuous working regime. Single-position machine is a type of machine that will handle only one piece – product at a time and during handling it is on the machine the whole time [2].

Single working cycle of an intelligent mobile robot consists of: 1) Robot movement – from the starting point, to the position in front of the production machine, in reach of the gripping mechanism from where the transportation unit can be captured from the production machine; 2) Movement of the gripping mechanism - from starting (transport) position to the position needed for capturing the transportation unit; 3) Capturing of the transportation unit; 4) Reverse movement of the gripping mechanism with the transportation unit on it – from the position where the transportation unit is captured all the way to the starting (transport) position; 5) Reverse robot movement – from the position in front of the production machine to the starting point. 6) Activity 2), 3) and 4) are repeated, with the transportation unit releasing instead of capturing. However, if reverse robot movement is not finished at the same point i.e. starting point, then the working cycle is called complex.

Generally, the robot's motion in the environment is realized according to the predefined optimal path based on a defined criterion, and the current state of the robot is determined using preprocessed images obtained by a stereo vision system. In this paper, only a part of

intelligent robot working cycle, which refers to movement of the gripping mechanism, will be considered and optimized.

Many different techniques can be and are utilized to control the trajectory of the robot: traditional feedback controls (proportional integral derivative (PID) like controls), adaptive control, robust control, sliding mode control, optimal control, fuzzy control, and many others, as well as, a combinations of previous techniques.

Fuzzy logic controller (FLC) is only one of the intelligent controllers and represents a widespread control technique since it has a satisfactory performance for nonlinear and complex systems. The advantages of a fuzzy PID controller for trajectory tracking control of a mobile robot, and its gripping mechanism are paramount in its rapidity, stability, anti-interference and tracking precision [3-5]. The fuzzy PID controller can be designed with a trial-and-error approach and the optimization can be done by using the cross-entropy method [6]. The varying fuzzy PID and proportional-derivative (PD) controllers tend to use either the Mamdani or Takagi-Sugeno type of the fuzzy systems [7]. Implementation of metaheuristic algorithms can deal with nonconvex, nonlinear, and multimodal problems subjected to linear or nonlinear constraints with continuous or discrete decision variables as global optimization algorithms. Differential evolution and genetic algorithms have been utilized to conduct the optimum design of a fuzzy controller for mobile robot trajectory tracking [8-10]. A 2 DOF planar robot was controlled for a given trajectory where the parameters of Mamdani type FLC were tuned with the particle swarm optimization [11]. The genetic algorithm is applied to improve the performance of the PID controller in terms of control precision and speed of convergence in paper [13]. A fuzzy sliding mode tracking controller for robot manipulators with uncertainty in the kinematic and dynamic models is designed and analyzed in paper [14]. Further, a sliding mode controller, an adaptive fuzzy approximator, is designed in such way that it controls the position tracking of a robot manipulator with two degrees of freedom. Initially, by utilizing an inverse dynamic method, it reduces the uncertainties bound and finally,

\*Corresponding author: Kraljice Marije 16, Belgrade, Serbia and rjovanovic@mas.bg.ac.rs

sliding mode control eliminates the influence of the remaining uncertainties in closed-loop system stability [15]. In another paper a multiple-input multiple-output (MIMO) fuzzy logic unit was applied to the robot to track the desired trajectory with high accuracy. Moreover, in order to assess the performance of the proposed MIMO fuzzy sliding mode controller in the presence of parameter variations and external disturbances, a sudden load variation and noise were introduced to the robot system [16]. Feedback linearization controller is used to compute the required arm torque using the nonlinear feedback control law for a robotic manipulator with three degree of freedom. In addition, when all dynamic and physical parameters are known the FLC works remarkably, but given that a large amount of systems have uncertainties and the fuzzy FLC can reduce this kind of limitation [17]. However, various different approaches are included when combating the problem of the robotic arm, including the new methods using the neuro-fuzzy approach to estimate system uncertainties in paper [18].

The main goal of this paper is to design a fuzzy PD controller of a two-link gripping mechanism as a part of mobile robot working cycle. The whale optimization algorithm (WOA), as a novel optimization technique for solving optimization problems defined in [19], is used to determine the proper parameters of FLC in the trajectory tracking control of robot arm with two degrees of freedom (2-DOF).

## 2. DYNAMICS OF A TWO-LINK GRIPPER

Figure 1 shows the real object - mobile robot with gripping mechanism. As the desired task is to optimize the motion of this mechanism with two link and two degrees of freedom, it can be approximated with the scheme as

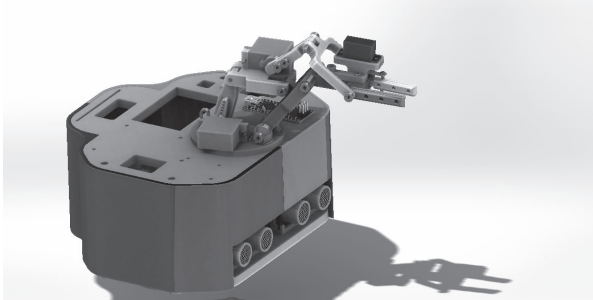


Figure 1: Real object: mobile robot with gripping mechanism

shown in Figure 2, where  $\theta_i$ , and  $m_i$  are respectively the link angle, the length and the mass of the  $i$ -th link,  $i = 1, 2$ . Without considering the friction and the disturbances, the dynamic model of a rigid two-link robot can be written as follows [20]:

$$M(\mathbf{q})\ddot{\mathbf{q}} + C(\mathbf{q}, \dot{\mathbf{q}})\dot{\mathbf{q}} + G(\mathbf{q}) = \boldsymbol{\tau} \quad (1)$$

where  $\mathbf{q}$ ,  $\dot{\mathbf{q}}$  and  $\ddot{\mathbf{q}} \in \mathbb{R}^{2 \times 1}$  are the robotic link position, the velocity and the acceleration vector, respectively;  $\boldsymbol{\tau} \in \mathbb{R}^{2 \times 1}$  is the torque input vector;  $M(\mathbf{q}) \in \mathbb{R}^{2 \times 2}$  is the positive definite inertia matrix;  $C(\mathbf{q}, \dot{\mathbf{q}}) \in \mathbb{R}^{2 \times 2}$  is the centripetal Coriolis force matrix; and  $G(\mathbf{q}) \in \mathbb{R}^{2 \times 1}$  is the gravitational vector.

Assuming that the centres of masses are in the middle of the levers, the elements  $M_{ij}(\mathbf{q})$  ( $i = 1, 2$ ) of the inertia matrix  $M(\mathbf{q})$  are as follows [20]:

$$M_{11} = \frac{1}{3}m_1l_1^2 + \frac{1}{3}m_2l_2^2 + m_2l_1^2 + m_2l_1l_2 \cos q_2 \quad (2)$$

$$M_{12} = M_{21} = \frac{1}{3}m_2l_2^2 + \frac{1}{2}m_2l_1l_2 \cos q_2, \quad M_{22} = \frac{1}{3}m_2l_2^2$$

In the case of robot from Figure 2,  $\mathbf{q}$  is the vector of angular displacements  $\theta_1$  and  $\theta_2$ ,  $\mathbf{q} = [\theta_1 \quad \theta_2]^T$ .

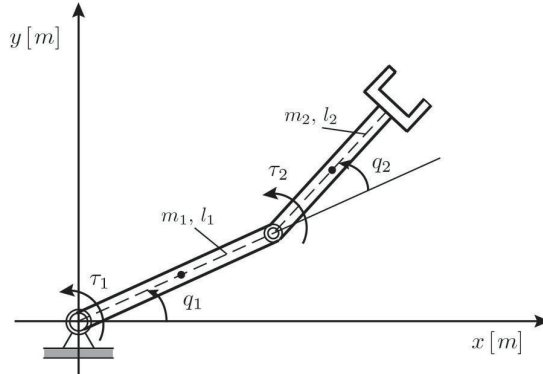


Figure 2: Scheme of the robotic gripper

The elements  $C_{ij}(\mathbf{q}, \dot{\mathbf{q}})$  ( $i, j = 1, 2$ ) of the matrix  $C(\mathbf{q}, \dot{\mathbf{q}})$  are presented as,

$$C_{11} = -\frac{1}{2}m_2l_1l_2\dot{q}_2 \sin q_2$$

$$C_{12} = -\frac{1}{2}m_2l_1l_2 \sin q_2 (\dot{q}_1 + \dot{q}_2) \quad (3)$$

$$C_{21} = -\frac{1}{2}m_2l_1l_2\dot{q}_1 \sin q_2, \quad C_{22} = 0$$

Finally, the elements of the gravitational torque vector  $G(\mathbf{q})$  are given by:

$$G_1 = \left( \frac{1}{2}m_1l_1 + m_2l_1 \right) g \cos q_1 + \frac{1}{2}m_2l_2g \cos(q_1 + q_2) \quad (4)$$

$$G_2 = \frac{1}{2}m_2l_2g \cos(q_1 + q_2)$$

## 3. TRAJECTORY PLANING

In view of practical implementation, the trapezoidal velocity profile is one of the simplest motion profiles. It is composed of the ability to be accelerating to a constant velocity and decelerating to a rest state, and can therefore achieve fast motions. Its advantages are primarily that the time necessary to reach a constant speed is used and distributed so that the movement is smooth, without abrupt starting and stopping i.e. braking. The setting of this movement is actually done by setting the acceleration so that the speed decreases slightly until it reaches zero.

According to the time, the profile divides into three regions and outputs: the maximum acceleration, deceleration, or zero value as acceleration. As shown in Figure 3, in the constant acceleration region the acceleration is the maximum positive value  $\ddot{q}_{\max}$  until the velocity reaches the maximum value,  $\dot{q}_{\max}$ . After that the constant velocity region where the acceleration and

velocity are zero, and the maximum value as well, respectively, the velocity decreases to a zero with the maximum deceleration,  $-\ddot{q}_{max}$ .

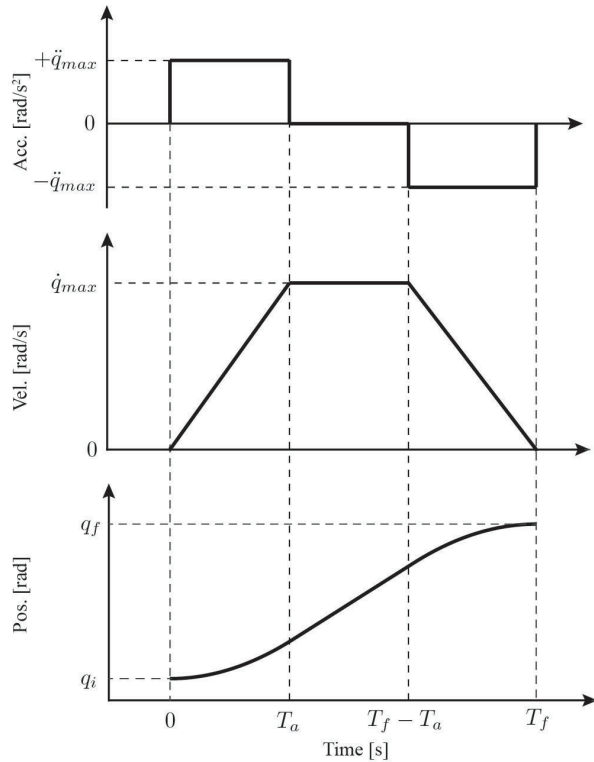


Figure 3: The trapezoidal velocity profile: the acceleration, velocity and position profiles

Using the following important parameters: the initial  $q_i$  and the final  $q_f$ , the total duration of the movement  $T_f$  and the time provided for acceleration  $T_a$ , the acceleration, velocity and position profiles can be described as:

$$\ddot{q}(t) = \begin{cases} +\ddot{q}_{max} & 0 < t \leq T_a \\ 0 & T_a < t \leq T_f - T_a \\ -\ddot{q}_{max} & T_f - T_a < t \leq T_f \end{cases} \quad (5)$$

$$\dot{q}(t) = \begin{cases} \ddot{q}_{max} \cdot t & 0 < t \leq T_a \\ \ddot{q}_{max} \cdot T_a & T_a < t \leq T_f - T_a \\ \ddot{q}_{max} \cdot (T_f - t) & T_f - T_a < t \leq T_f \end{cases} \quad (6)$$

$$q(t) = \begin{cases} q_i + 0.5 \cdot \ddot{q}_{max} \cdot t^2 & 0 < t \leq T_a \\ q_i + \ddot{q}_{max} \cdot T_a \left( t - \frac{T_a}{2} \right) & T_a < t \leq T_f - T_a \\ q_f - 0.5 \cdot \ddot{q}_{max} \cdot (T_f - t)^2 & T_f - T_a < t \leq T_f \end{cases} \quad (7)$$

Clearly, from the acceleration output, the velocity and position profiles are generated by integration operations, while taking into account the initial conditions.

Maximum speed, maximum acceleration and the time provided for acceleration have the following relationship:

$$\dot{q}_{max} = \ddot{q}_{max} T_a \quad (8)$$

Using the following equation:

$$q_f - q_i = (\ddot{q}_{max} \cdot T_a) \cdot (T_f - T_a) \quad (9)$$

the only unrevealed variable (maxima acceleration  $\ddot{q}_{max}$ ) can be obtained:

$$\ddot{q}_{max} = \frac{q_f - q_i}{T_a (T_f - T_a)} \quad (10)$$

In all previous expressions it is logically assumed that  $T_a \leq T_f / 2$ , that is, the acceleration period is shorter than half of the total time. In the case of equality, the shape of the function becomes a triangle [21].

#### 4. FUZZY LOGIC CONTROLLER

In the following section, we will be using the fuzzy control technique in order to design a fuzzy controller which is able to move a two link robot to track a desired trajectory. Consequentially, we will be designing two fuzzy controllers, one for each separate link. Some of the essential elements when designing a fuzzy controller include, first and foremost, defining the input and output variables, secondly the choice of fuzzification and defuzzification process, and most importantly determining the rule-base of the controller.

In this paper, a proportional derivative (PD) type of FLC is utilized. The inputs of this type of controller are the error and the change in error, whilst the output is the control signal. Nevertheless, in the considered robot trajectory control, the input variables of the FLC are the error and error derivation of link position. The output variable of the fuzzy controller is the link control input, i.e. torque. All membership functions for the controller inputs and outputs are defined on the common normalized interval  $[-1, 1]$ . For all of the membership functions we use symmetric triangular functions (except for the two membership functions at the ends, which are trapezoidal) with an equal base and 50% overlap with neighbouring membership functions as shown in Figure 4 and Figure 5.

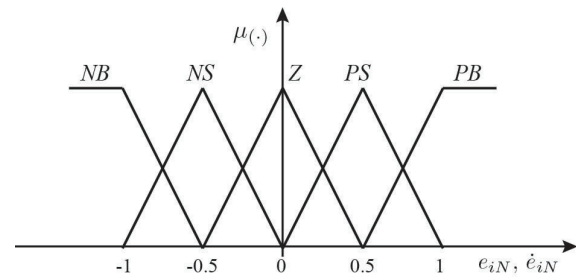


Figure 4: The input membership functions

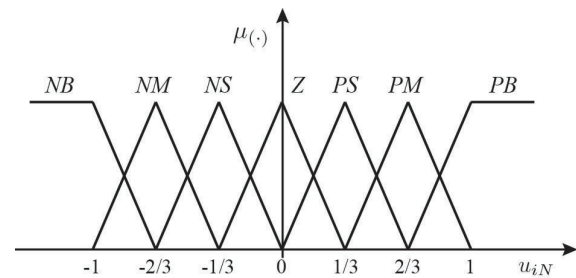


Figure 5: The output membership functions

Further, fuzzy controllers both of the links share a common membership function, where  $e_{iN}$  and  $\dot{e}_{iN}$ , for all  $i=1,2,\dots$  represent the normalized error and the normalized derivative of the error, respectively. The normalized control signals are represented by  $u_{iN}$ , for all  $i=1,2$  respectively, for the link 1 and link 2.

Table 1: Fuzzy IF-THEN rules for the robot trajectory control

| $e_N \backslash \dot{e}_N$ | NB | NS | Z  | PS | PB |
|----------------------------|----|----|----|----|----|
| NB                         | NB | NB | NM | NS | Z  |
| NS                         | NB | NM | NS | Z  | PS |
| Z                          | NM | NS | Z  | PS | PM |
| PS                         | NS | Z  | PS | PM | PB |
| PB                         | Z  | PS | PM | PB | PB |

In a standard fuzzy partition, each fuzzy set determines the value of the linguistic variable. The fuzzy linguistic variables NB, NM, NS, Z, PS, PM and PB

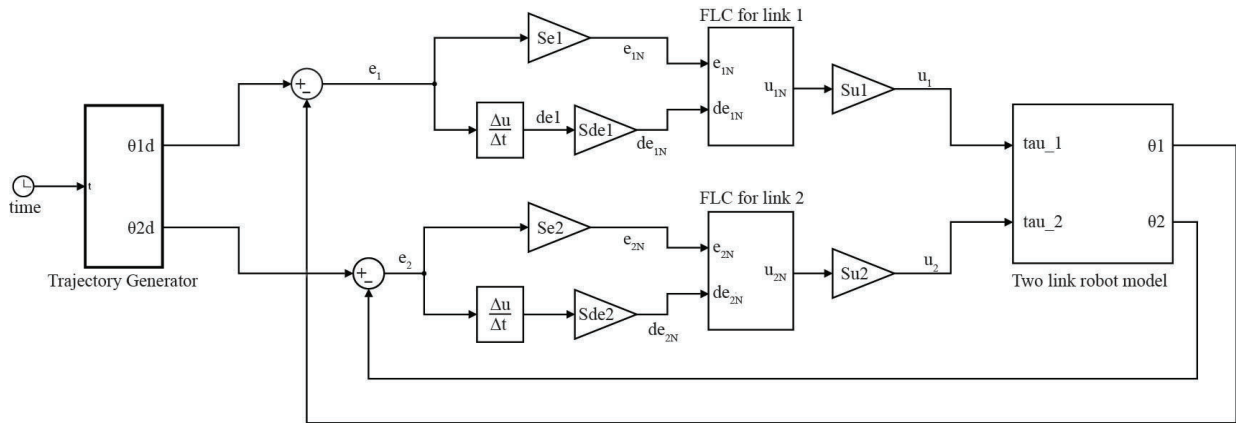


Figure 6: Simulink model of the 2-DOF gripping mechanism with fuzzy control

## 5. OPTIMIZATION OF FLC

### 5.1. Whale optimization algorithm

The highly utilised and implemented WOA was first suggested by Seyedali Mirjalili and Andrew Lewis in their paper [19]. The WOA has proven to be outstanding at resolving a variety of modes, multimodal and problems that are not linear. The foremost supremacies of this algorithm, and all metaheuristic algorithms in general, are that it has random distribution, which avoids getting stuck in the local minimum. The hunting method which they deeply rely on is the bubble-net feeding method. Using this method they dive deep, a couple of meters deep into the ocean and then start swimming upwards to the surface creating a bubbles in a spiral shape while encircling the prey.

#### 5.1.1. Encircling the prey

Since the whales can recognize the location of the prey, the WOA algorithm assumes that the current best solution is the target prey, or very close to it. Stressing this, after the best search agent is defined the other search

agents will try to update their position towards it. The mathematical model of encircling the prey is proposed using the following equations (where  $\mathbf{D}$  is the distance vector and  $\mathbf{X}$  is the vector utilized to update the position):

$$\mathbf{D} = |\mathbf{CX}^*(t) - \mathbf{X}(t)| \quad (12)$$

$$\mathbf{X}(t+1) = \mathbf{X}^*(t) - \mathbf{AD} \quad (13)$$

where  $t$  indicates the current iteration,  $\mathbf{A}$  and  $\mathbf{C}$  are coefficient vectors,  $\mathbf{X}^*$  is the position vector of the best solution obratined so far,  $\mathbf{X}$  is the position vector [19].

5.1.2. Exploitation phase: Hunting using the Bubble-net method

Moreover when stating the mathematical modeling of the exploitation phase it is found that there are two diverse approaches to it; the shrinking encircling mechanism and spiral updating position. An universal assumption suggests that there is a 50% chance that the whale will chose between one of these two approaches, when updating the position. The first approach is related to decreasing linearly the value of  $a$  from 2 to 0 over the

course of iterations. Hence, the random values for  $\mathbf{A}$  are between  $[-1,1]$ , where the new position of the agent is located between the current best agent and the original position. The second approach is based on the calculations of the position of the prey and the whale.

The mathematical model for these approaches is henceforward, depicted as the following equation:

$$\mathbf{X}(t+1) = \begin{cases} \mathbf{X}^*(t) - \mathbf{A}\mathbf{D} & \text{if } p < 0.5 \\ \mathbf{D}' \cdot e^{bl} \cdot \cos(2\pi l) + \mathbf{X}^*(t) & \text{if } p > 0.5 \end{cases} \quad (14)$$

where  $p$  is a random number in  $[0,1]$ ,  $b$  is a constant for defining the shape of the logarithmic spiral,  $l$  is a random number in  $[-1,1]$  and  $\mathbf{D}' = |\mathbf{X}^*(t) - \mathbf{X}(t)|$  indicates the distance of the  $i$ -th whale from the prey [19].

### 5.1.3. Exploitation phase: Search for the prey

The whales search for the prey randomly according to the position of each others locations. The parameter  $\mathbf{A}$  is used to force the search agent to move far away from a reference whale. The position update here is based on the position of a randomly chosen search agent, instead of the best agent so far. The mechanism and  $|\mathbf{A}| > 1$  emphasizes the exploration and allows the WOA algorithm to perform a global search, henceforward it favors exploration and local optima avoidance. In other words the agent is diverging and moving away from the prey, unlike the converging and the best solution selection when using  $|\mathbf{A}| < 1$  [19]. The mathematical model is as ensuing:

$$\mathbf{D} = |\mathbf{C}\mathbf{X}_{rand} - \mathbf{X}| \quad (15)$$

$$\mathbf{X}(t+1) = \mathbf{X}_{rand} - \mathbf{A}\mathbf{D} \quad (16)$$

### 5.2. Optimization of FLC using the whale optimization algorithm

In a general sense, fuzzy controllers have a large number of parameters that can be adjusted in an attempt to gain an optimal dynamical response. Those parameters are the shape of the membership functions, the number of the linguistic variables for input and output values of the set of rules, scaling factors, etc. Moreover, in using the predetermined membership functions for the input and output values defined in section 4, and on Figure 4 and Figure 5, as well as, the set of rules (Table 1), it becomes obvious that the performance of the fuzzy PD controller depends on the input and output scaling factors, in turn the design of the fuzzy controller can be simply be attributed to the choice of the input/output scaling factors.

In this paper we have been focused only on the tuning of the scaling factors, considering that is correspondent to the gains of the controller. Further, for the design of the optimal fuzzy PD controller the WOA optimization algorithm was used. Moreover, the mentioned parameters are all coded into one whale, i.e. one agent, that is presented with a vector which contains, in our case, six parameters. For the objective function we utilized the algebraic sum of ITAE (integral of time-weighted absolute error) performance criterion of both links, as defined in the ensuing equation:

$$J = \int_0^{\infty} t \cdot [|e_1(t)| + |e_2(t)|] dt \quad (17)$$

## 6. EXPERIMENTAL RESULTS

Finally, in order to demonstrate the methodology previously discussed, a 2-DOF robot, that is depicted in Figure 2, is used in order to perform the following simulation. The physical parameters for the gripping mechanism are  $m_1 = 0.00799$  kg,  $m_2 = 0.00521$  kg,  $l_1 = 0.05831$  m and  $l_2 = 0.0422$  m.

The desired end-effector trajectory of the 2-DOF manipulator is specified according to trapezoidal velocity profile defined in Section 3. The initial position of the robotic gripper is determined by the mechanism itself. In our case, the initial link configuration is defined as  $q_0 = [1.3963 \quad -0.5236]^T$  rad and lastly, the initial end-effector position is  $x_0 = 0.0373$  m,  $y_0 = 0.0898$  m.

The control task is to move that point from its initials to the finals coordinates defined by angles  $q_f = [0.7854 \quad -0.7854]^T$  rad, and the end-effector position  $x_f = 0.0834$  m,  $y_f = 0.0412$  m.

The time required to reach this position is set to be  $T_f = 6$  s, the maximum acceleration  $\ddot{q}_{max}$  and the time provided for acceleration  $T_a$  are calculated based on the equation (10) and the following,

$$T_a = \frac{T_f}{3} = 2 \text{ s}, \quad |\ddot{q}_{max1}| = 0.0763 \frac{\text{m}}{\text{s}^2}, \quad |\ddot{q}_{max2}| = 0.0330 \frac{\text{m}}{\text{s}^2}$$

In the proposed WOA algorithm the population is set to 10, while the total number of iterations is set to 30. Furthermore, in this optimization method, one agent represents one potential optimal fuzzy controller. All of the parameter values that were used in the implementation of the WOA were taken from the original paper [19]. The convergence curve of the objective function value is depicted in Figure 7.

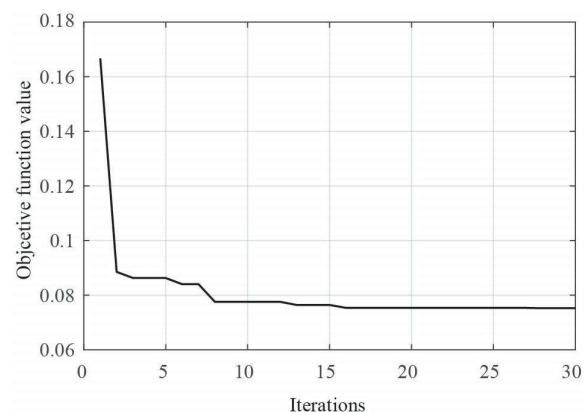


Figure 7: The convergence curve of the objective function value

In addition, after the optimization the obtained parameters for the scaling factors are:

$$S_{e_1} = 1.8505, \quad S_{d_{e_1}} = 0.0784, \quad S_{u_1} = 0.9218$$

$$S_{e_2} = 1.5, \quad S_{d_{e_2}} = 0.0025, \quad S_{u_2} = 1.4385$$

In the following two pictures, we have shown the comparison between the real trajectory and the desired trajectory of the link 1 (Figure 8) and link 2 (Figure 9).

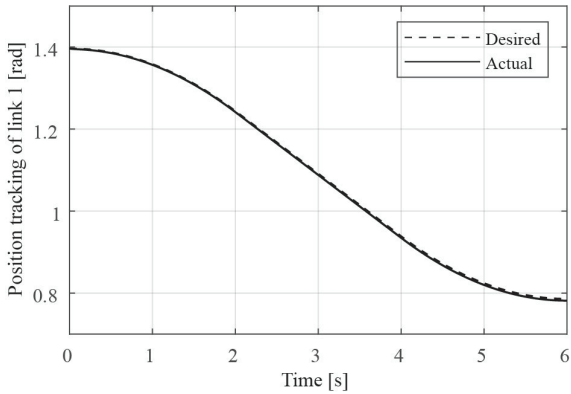


Figure 8: A comparison between the desired and real trajectory of link 1

There we can also observe that the real and desired trajectory curves both almost match, with very slight deviations, nearly neglectable.

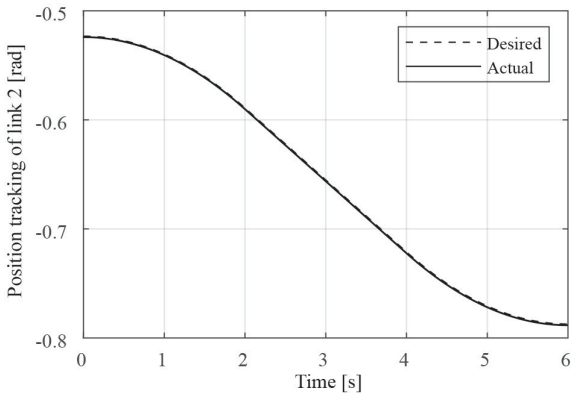


Figure 9: A comparison between the desired and real trajectory of link 2

Moreover, the errors of position tracking for link 1 and link 2, are given in Figure 10 and Figure 11, respectively.

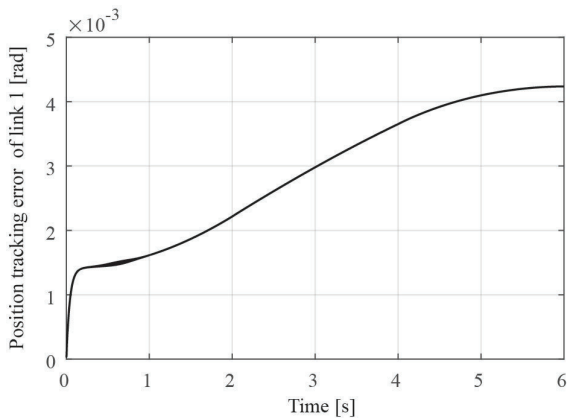


Figure 10: Position tracking error of link 1

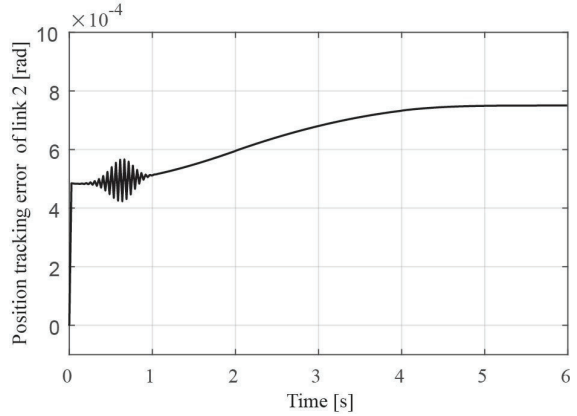


Figure 11: Position tracking error of link 2

The error for the position tracking of the first link is less than 0.005 rad, while for the second link it is less than 0.001 rad. Finally, in Figure 12 and Figure 13 we have depicted the control torque of both link 1 and link 2.

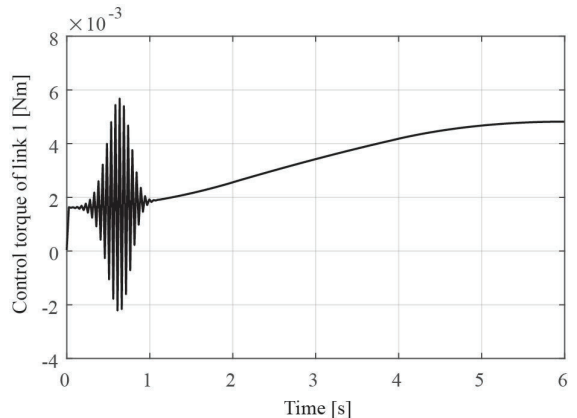


Figure 12: Control torque of link 1

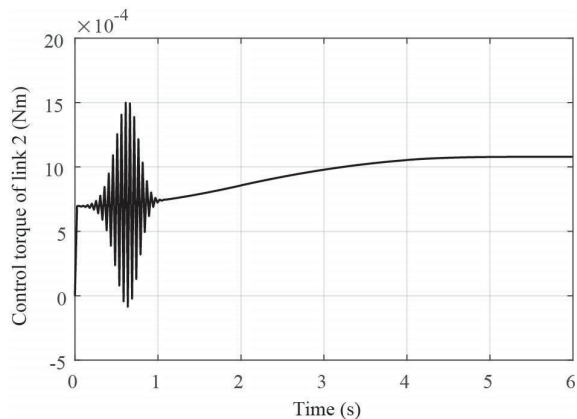


Figure 13: Control torque of link 2

Furthermore, the robustness of the designed fuzzy controllers is tested, as follows. Hence, in order to test the robustness, the mass of the robotic arm of each link is increased three times, as in [11].

The parameters of the fuzzy controller, which were optimized using the WOA algorithm, have remained unchanged, and comparisons of real and desired trajectories are given in Figure 14 and Figure 15.

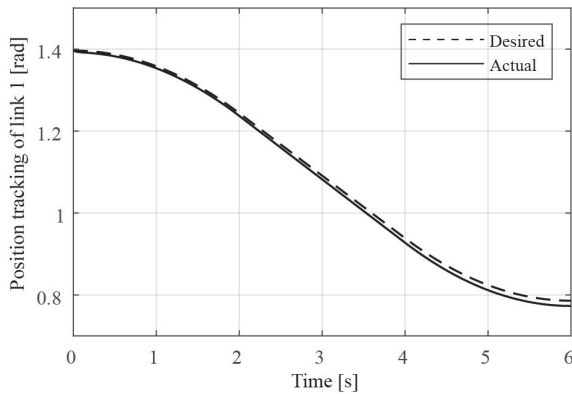


Figure 14: A comparison between the desired and real trajectory of link 1 (increased mass of links three times)

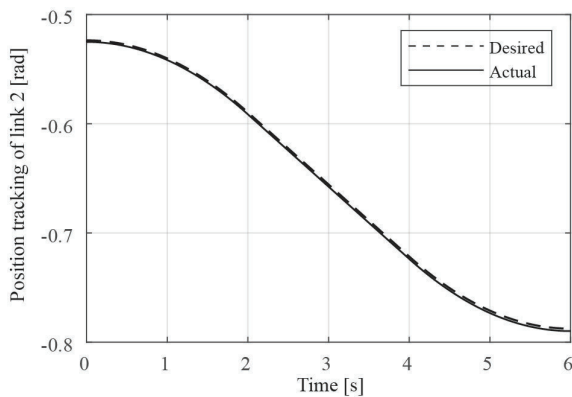


Figure 15: A comparison between the desired and real trajectory of link 2 (increased mass of links three times)

In the pictures above we can clearly notice that even though we enlarged the mass of link 1 and link 2, the optimized algorithm works exceptionally well.

In addition, the errors of position tracking for link 1 and link 2, where the given links have a mass that has been increased three times in order to test the robustness, are given in Figure 16 and Figure 17, respectively.

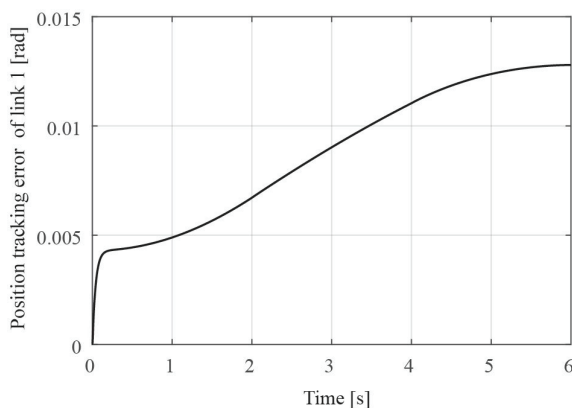


Figure 16: Position tracking error of link 1 (increased mass of links three times)

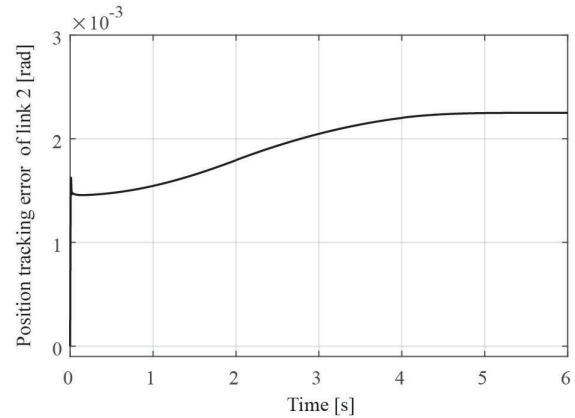


Figure 17: Position tracking error of link 2 (increased mass of links three times)

Here the error for the position tracking of the first link is about 0.015 rad, while for the second link it is about 0.001 rad.

## 7. CONCLUSION

In this paper, fuzzy controllers were proposed for the trajectory tracking control of a two-link gripping mechanism as a part of mobile robot working cycle. The whale optimization algorithm was used to optimize the scaling factors of the proposed fuzzy PD controller. Namely, optimal input/output gains for the fuzzy PD controller were generated according to ITAE performance criterion. Numerical simulations were done to analyze the trajectory tracking performance of the designed controller. Moreover, the robustness of the controllers was tested in the case of the mass changes. The simulation results have shown that the proposed controller was capable of dealing with the nonlinearities of the robot and the changing of its parameters. One possible area of the future work can be simultaneous optimization of the scaling factors as well as parameters of input and output membership functions.

## ACKNOWLEDGEMENTS

This research was supported by the Science Fund of the Republic of Serbia, grant No. 6523109, AI-MISSION4.0, 2020-2022.

This work was financially supported by the Ministry of Education, Science and Technological Development of the Serbian Government, MPNTR RS under contract 451-03-9/2021-14/200105, from date 05.02. 2021.

## REFERENCES

- [1] M.A.K. Bahrin, M.F. Othman, N.H.N. Azli and M.F. Talib, "Industry 4.0: A review on industrial automation and robotic," *Journal Teknology*, Vol. 8(6-13), pp. 137–143, (2016)
- [2] U. Bugarić, D. Popović and S. Tošić, "Methodology for analysis of working cycle," XVII International Conference on "Material Flow, Machines and Devices in Industry", Belgrade (Serbia), pp. 4–5, (2002)
- [3] Q. Xu, J. Kan, S. Chen and S. Yan, "Fuzzy PID Based Trajectory Tracking Control of Mobile Robot and its Simulation in Simulink," *International Journal of Control and Automation*, Vol. 7(8), pp. 233–244, (2014)

- [4] M. Tong, W. Lin, X. Huo, Z. Jin and C. Miao, "A model-free fuzzy adaptive trajectory tracking control algorithm based on dynamic surface control," *International Journal of Advanced Robotic Systems*, Vol. 17(1), pp. 1–11, (2020)
- [5] M. S. Abood, I. K. Thajeel, E. M. Alsaedi, M. M. Hamdi, A. S. Mustafa and S. A. Rashid, "Fuzzy Logic Controller to control the position of a mobile robot that follows a track on the floor," *4th International Symposium on Multidisciplinary Studies and Innovative Technologies*, Istanbul (Turkey), 22-24 October 2020, pp. 1–7, (2020)
- [6] T.A. Mai, T.S. Dang, D.T. Duong, V.C. Le and S. Banerjee, "A combined backstepping and adaptive fuzzy PID approach for trajectory tracking of autonomous mobile robots," *Journal of the Brazilian Society of Mechanical Sciences and Engineering*, Vol. 43, (2021)
- [7] B. Jiang, H. R. Karimi, S. Yang, C. Gao and Y. Kao, "Observer-Based Adaptive Sliding Mode Control for Nonlinear Stochastic Markov Jump Systems via T-S Fuzzy Modeling: Applications to Robot Arm Model," *IEEE Transactions on Industrial Electronics*, Vol. 68(1), pp. 466–477 (2021)
- [8] H. Nejat Pishkenari, S.H. Mahboobi and A. Alasty, "Optimum synthesis of fuzzy logic controller for trajectory tracking by differential evolution," *Scientia Iranica*, Vol. 18 (2), pp. 261–267, (2011)
- [9] R.M. da Silva, M.A de Souza Leite Cuadros and D.F.T. Gamarra, "Comparison of a Backstepping and a Fuzzy Controller for Tracking a Trajectory with a Mobile Robot," *Intelligent Systems Design and Applications*, Vol. 941, pp. 212–221, (2019)
- [10] J. Zhao, L. Han, L. Wang and Z. Yu, "The fuzzy PID control optimized by genetic algorithm for trajectory tracking of robot arm," *12th World Congress on Intelligent Control and Automation*, Guilin (China), 12 June-15 June 2016, pp. 556–559, (2016)
- [11] Z. Bingul and O. Karahan, "A Fuzzy Logic Controller tuned with PSO for 2 DOF robot trajectory control," *Expert Systems with Applications* Vol. 38, pp. 1017–1031, (2011)
- [12] H. Feng, Cb. Yin, Ww. Weng, W. Ma, Jj. Zhou, Wh. Jia and Zl. Zhang, "Robotic excavator trajectory control using an improved GA based PID controller," *Mechanical Systems and Signal Processing*, Vol. 105, pp. 153–168 (2018)
- [13] A. Alouache and Q. Wu, "Genetic Algorithms for Trajectory Tracking of Mobile Robot Based on PID Controller," *14th International Conference on Intelligent Computer Communication and Processing*, Cluj-Napoca (Romania), 6-8 September 2018, pp. 237–241, (2018)
- [14] F. Piltan, A.R. Nabae, M.M. Ebrahimi and M. Bazregar, "Design Robust Fuzzy Sliding Mode Control Technique for Robot Manipulator Systems with Modeling Uncertainties," *International Journal Information Technology and Computer Science*, Vol. 8, pp. 123–135, (2013)
- [15] M.R. Soltanpour, P. Otadolajam and M.H. Khooban, "Robust control strategy for electrically driven robot manipulators: adaptive fuzzy sliding mode," *IET science measurement and technology*, Vol. 9 (3), pp. 322–334, (2015)
- [16] Y. Hacioglu, Y.Z. Arslan and N. Yagiz, "MIMO fuzzy sliding mode controlled dual arm robot in load transportation," *Journal of the Franklin Institute*, Vol. 348 (8), pp. 1886–1902, (2011)
- [17] F. Piltan, M.H. Yarmahmoudi, M. Mirzaie, S. Emamzadeh and Z. Hivand, "Design Novel Fuzzy Robust Feedback Linearization Control with Application to Robot Manipulator," *International Journal of Intelligent Systems and Applications*, Vol. 5(5), pp. 1–10, (2013)
- [18] D.C. Theodoridis, Y. Boutalis and M.A. Christodoulou, "A New Adaptive Neuro-Fuzzy Controller for Trajectory Tracking of Robot Manipulators," *International Journal of Robotics and Automation*, Vol. 26(1), pp. 64–75, (2011)
- [19] S. Mirjalili and A. Lewis, "The Whale Optimization Algorithm," *Advances in engineering software*, Vol. 95, pp. 51–67, (2016)
- [20] L. Sciavicco and B. Siciliano, "Modeling and control of robot manipulators," Springer-Verlag, London (England), (2000)
- [21] [https://www.ucg.ac.me/skladiste/blog\\_13269/objava\\_8796/fajlovi/35\\_industrijska781.pdf](https://www.ucg.ac.me/skladiste/blog_13269/objava_8796/fajlovi/35_industrijska781.pdf), University of Montenegro, pp. 87-102, (last accessed 30/05/21)

# Feedback Linearization Control of a Two – Link Gripping Mechanism

Mitra Vesović<sup>1\*</sup>, Radiša Jovanović<sup>1</sup>, Lara Laban<sup>1</sup>, Uglješa Bugarić<sup>2</sup>

<sup>1</sup>Faculty of Mechanical Engineering/Department of Control Engineering, University of Belgrade, Serbia

<sup>2</sup>Faculty of Mechanical Engineering/Department of Industrial Engineering, University of Belgrade, Serbia

*This paper presents a feedback linearization controller for trajectory tracking of two degrees of freedom (2DOF) gripping mechanism. To reach this goal, after deriving the dynamical equations of the gripping mechanism, the feedback linearization approach is utilized to change the nonlinear dynamics to a linear one. Classical proportional-derivative controller with feedback linearization is applied for positioning and tracking control. Furthermore, in order to achieve movement of the mechanism without the sudden stopping at the desired point, a trapezoidal velocity profile is used to obtain desired trajectory. Numerical simulations using Matlab/Simulink successfully demonstrate the effectiveness of the proposed method.*

**Keywords:** Gripping mechanism, Robotics, Feedback linearization, Control engineering

## 1. INTRODUCTION

A robot gripping mechanism is a device that enables the capturing, handling, releasing and tightening of an object that is manipulated. Modern robotics and their grippers use integrated mechanisms and controls to simulate movements of human hands. Robotic grippers are only one component of an automated system, that has been around for more than fifty years ever since the development of the first Stanford arm, an early robot that would come to be known as the first readily controllable gripper. Many of its design and control elements are used in grippers of today [1]. The focal point of this paper is on the implementation of feedback linearization for trajectory tracking of a robot gripping mechanism with two degrees of freedom. Furthermore a proportional integral-derivative (PID) controller is used along with the feedback linearization. The PID controller uses a control loop feedback mechanism, to control process variables and to keep the actual output from a process as close to the target as possible, hence it is to this day the cheapest and the most accurate and stable controller.

Since, it is necessary to implement feedback linearization control (FLC), nonlinear feedback terms are utilized and a mathematical model for the two-link robot is of the essence if this technique is applied. An exact mathematical models cannot be easily obtained, particularly for the system parameters of a two-link gripping mechanism. One way to battle this kind of problem was introduced in the paper which used real coded genetic algorithm with a multiple-crossover in order to estimate the unknown system parameters. In order to later on incorporate the resulted system model to the feedback linearization control such that the nonlinear robotic system can be transferred to a linear model with a nonlinear bounded time-varying uncertainty [2]. FLC is used to compute the required arm torque using nonlinear feedback control law. In addition, when all dynamic and physical parameters are known the FLC works remarkably. Given that a large amount of systems have uncertainties and the fuzzy FLC can reduce this kind of limitation. A robotic manipulator with three degree of freedom is controlled by a novel fuzzy sliding feedback

linearization controller. In this paper the work outline uses soft computing in order to increase the stability and robustness new mathematical switching sliding mode methodology is applied to the fuzzy FLC [3]. Additionally, a new optimal proportional-derivative (PD) feedback linearization controller is employed to achieve the finest trajectory tracking for nonholonomic wheeled mobile robots. In this paper a teaching-learning-based optimization is utilized in order for the proposed controller to handle the difficulty of the integrated kinematic and dynamic tracking [4]. In the ensuing paper a numerical algorithm, based on the Newton–Euler dynamic equations, is used in order to compute the inverse dynamics of robot manipulators with an arbitrary number of joints. Furthermore, a variant of the algorithm is used for implementing a FLC law for the accurate tracking of desired link and stiffness trajectories. Considering that the algorithm does not use numerical approximations, it grows linearly in complexity with the number of joints and is therefore suitable for online feed forward and real-time feedback control [5]. In the next paper utilizing a systematic method to build a kinematic model and dynamic model of a nonholonomic wheeled mobile robot with a longitudinal and lateral slip, a control law is used with the input-output feedback linearization method to drive the mobile robot to track a given trajectory while longitudinal, and lateral slip simultaneously exist. The asymptotical stability of the system is corroborated by solving second-order differential linear equations [6]. Moreover, a variety of control methods were used to control the space robots attitude to obtain time response in order to minimize the eulerint criterion. The PD controller was used, as well as, other control methods including LQR, pole placement and adaptive feedback linearization. All of this was conducted using the quaternion kinematics to determine which method yields the lowest value, control effort and simulation elapsed time [7]. Furthermore, the integration of a cable-driven parallel Robot with a wheeled mobile robot is proposed to overcome some of the issues related to each of these robots. In order to derive the dynamic equations the Gibbs–Appel formulation is used. Howbeit, based on some conditions, the equations are input–output linearizable via

\*Corresponding author: Kraljice Marije 16, Belgrade, Serbia and mvesovic@mas.bg.ac.rs

a static feedback. The platform trajectory is designed based on the given end-effector trajectory tests [8]. Ensuing all the following, in one of the papers the trajectory tracking problem is addressed of the end-effector of a single link flexible arm in which the gravity forces and the joint friction forces are taken into account. As an overall approach, a double loop cascade control is used to deal with the joint friction, while in its outer loop an input-state feedback linearization-based controller is implemented to suppress the vibrations and track an end-effector trajectory [9]. Similarly, a paper that develops a simple learning strategy for the FLC algorithm for uncertain nonlinear systems is proposed. Here, the strategy uses desired closed-loop error dynamics to update the controller coefficients and the disturbance term in the feedback control law, whilst the traditional feed forward control law is designed based on the nominal model by using FLC method [10]. Moreover, in a different paper an optimal super-twisting algorithm with time delay estimation is designed based on input/output feedback linearization for uncertain robot manipulators. Lyapunov theory is used to prove the finite-time convergence of the sliding surface and its derivative, into the bargain this structure is used to estimate unknown dynamics and to reduce the control effort and the chattering phenomenon [11]. A predictor-based controller for a high-DOF manipulator to compensate a time-invariant input delay during a pick-and-place task is proposed in this paper. The controller is formulated in the presence of input delay, in order to track desired trajectories later on being able to investigate the effects of input delays in the absence of a robust predictor. In due course this reveals a robustness of the formulated algorithm [12].

As the construction industry frequently deals with the problem of robot's movements and gripping optimization, the main goal of this paper is to apply some of the more conventional techniques like the PID with feedback linearization, so as to achieve the movement of the mechanism without the sudden stopping at the desired point. In those purposes, a trapezoidal velocity profile will be used to obtain a desired trajectory.

This study proposes only a fragment of intelligent machine working cycle, which refers to movement of the gripping mechanism.

## 2. MATHEMATICAL MODEL OF THE OBJECT

Real object is shown in the Figure 1. Robot has a gripper that can be represented as link mechanism with two degrees of freedom (2DOF), which is approximated with the scheme as shown in Figure 2.

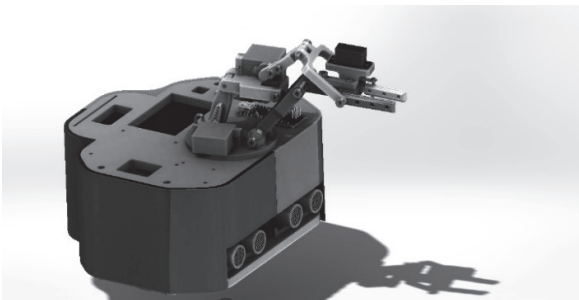


Figure 1: Mobile robot with gripping mechanism

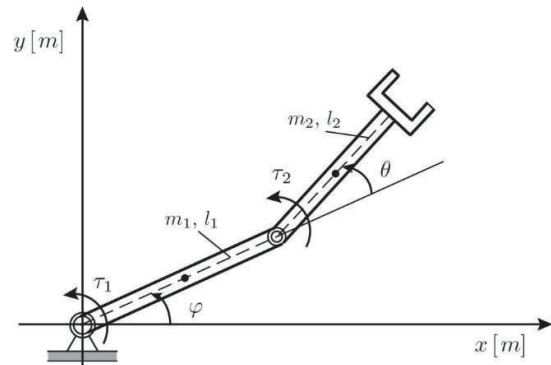


Figure 2: Scheme of the robotic gripper

It is assumed that the centers of masses are in the middle of levers.

From the Figure 2 coordinates of centers of masses for the first:  $x_{1CM}, y_{1CM}$ , and the second link:  $x_{2CM}, y_{2CM}$  are:

$$\begin{aligned} x_{1CM} &= \frac{l_1}{2} \cos \varphi \\ y_{1c} &= \frac{l_1}{2} \sin \varphi \\ x_{2CM} &= l_1 \cos \varphi + \frac{l_2}{2} \cos(\varphi + \theta) \\ y_{2CM} &= l_1 \sin \varphi + \frac{l_2}{2} \sin(\varphi + \theta), \end{aligned} \quad (1)$$

where  $l_1$  and  $l_2$  are lengths of links and  $\varphi$  and  $\theta$  are angles, taken to be generalized coordinates. Potential energy  $\Pi$  can be easily calculated:

$$\begin{aligned} \Pi &= \frac{1}{2} m_1 g l_1 \sin \varphi + m_2 g l_1 \sin \varphi \\ &\quad + \frac{1}{2} m_2 g l_2 \sin(\varphi + \theta), \end{aligned} \quad (2)$$

where  $m_1, m_2$  are the masses of the links.

Kinetic energy of the system can be found as:

$$\begin{aligned} E_k &= \dot{\varphi}^2 \left( \frac{1}{6} m_1 l_1^2 + \frac{1}{6} m_2 l_2^2 + \frac{1}{2} m_2 l_1^2 \right. \\ &\quad \left. + \frac{1}{2} m_2 l_1 l_2 \cos \theta \right) + \dot{\theta}^2 \left( \frac{1}{6} m_2 l_2^2 \right) \\ &\quad + \dot{\varphi} \dot{\theta} \left( \frac{1}{3} m_2 l_2^2 + \frac{1}{2} m_2 l_1 l_2 \cos \theta \right) \end{aligned} \quad (3)$$

Energy is conserved, so the Lagrangian of the system is described as:

$$L = E_k - \Pi \quad (4)$$

and the Euler - Lagrange equations for the two - link rotary system are:

$$\begin{aligned} \frac{\partial^2 L}{\partial t \partial \dot{\varphi}} - \frac{\partial L}{\partial \varphi} &= Q_1 \\ \frac{\partial^2 L}{\partial t \partial \dot{\theta}} - \frac{\partial L}{\partial \theta} &= Q_2 \end{aligned} \quad (5)$$

where  $Q_i, i = 1, 2$  are the generalized forces.

For:

$$Q_i = \tau_i \quad (6)$$

where  $\tau_i$  are torques. The Euler-Lagrange equations is a systematic method of finding the equations of motion, i.e., EOMs, of a system. Once the kinetic and potential energy are obtained and the Lagrangian is found, then the task is to compute various derivatives to get the EOMs. By introducing generalized coordinates and abbreviations:

$\varphi = q_1$ ,  $\theta = q_2$ ,  $S_1 = \sin q_1$ ,  $S_2 = \sin q_2$ ,  $S_{12} = \sin(q_1 + q_2)$ ,  $C_1 = \cos q_1$ ,  $C_2 = \cos q_2$ ,  $C_{12} = \cos(q_1 + q_2)$  and after going through this process, the nonlinear equations of motion i.e. dynamic model for the rotary two – linked gripping mechanism is:

$$\mathbf{M}\ddot{\mathbf{q}} + \mathbf{C}\dot{\mathbf{q}} + \mathbf{G} = \boldsymbol{\tau} \quad (7)$$

$$\mathbf{Y} = \mathbf{q}$$

where:

$$\mathbf{M} = \begin{bmatrix} M_{11} & M_{12} \\ M_{21} & M_{22} \end{bmatrix} \quad (8)$$

$$M_{11} = \frac{1}{3}m_1l_1^2 + \frac{1}{3}m_2l_2^2 + m_2l_1^2 + m_2l_1l_2C_2$$

$$M_{12} = M_{21} = \frac{1}{3}m_2l_2^2 + \frac{1}{2}m_2l_1l_2C_2$$

$$M_{22} = \frac{1}{3}m_2l_2^2$$

is the inertia matrix,

$$\mathbf{q} = \begin{bmatrix} q_1 \\ q_2 \end{bmatrix} \quad (9)$$

is vector of generalized coordinates,

$$\mathbf{C} = \begin{bmatrix} C_{11} & C_{12} \\ C_{21} & C_{22} \end{bmatrix} \quad (10)$$

$$C_{11} = -\frac{1}{2}m_2l_1l_2\dot{q}_2S_2$$

$$C_{12} = -\frac{1}{2}m_2l_1l_2S_2(\dot{q}_1 + \dot{q}_2)$$

$$C_{21} = -\frac{1}{2}m_2l_1l_2\dot{q}_1S_2$$

$$C_{22} = 0$$

is vector of Coriolis and centrifugal forces,

$$\mathbf{G} = \begin{bmatrix} G_1 \\ G_2 \end{bmatrix} \quad (11)$$

$$G_1 = \left(\frac{1}{2}m_1l_1 + m_2l_1\right)gC_1 + \frac{1}{2}m_2l_2gC_{12}$$

$$G_2 = \frac{1}{2}m_2l_2gC_{12}$$

is a vector of gravity torques,

$$\boldsymbol{\tau} = \begin{bmatrix} \tau_1 \\ \tau_2 \end{bmatrix} \quad (12)$$

is the vector of torque and it will be considered as the control (input signal);  $\mathbf{Y}$  is the output.

### 3. VELOCITY PROFILE OF THE GRIPPING MECHANISM

#### 3.1. Trapezoidal velocity profile

The trapezoidal velocity profile is a realistically feasible implementation of motion at a constant speed. Namely, since the robot starts from a state of rest it takes some time to reach that constant speed. Also, stopping does not happen abruptly. Instead it include braking in a controlled manner at the end of the movement, and the

speed decreases to zero. This movement can be described from the mathematical aspect. Important parameters are: the initial  $q_i$  and the final  $q_f$  generalized coordinates, as well as the total duration of the movement  $T_f$  and the time provided for acceleration, i.e. deceleration  $T_a$ . The position, velocity and acceleration profiles are shown in Figure 3.

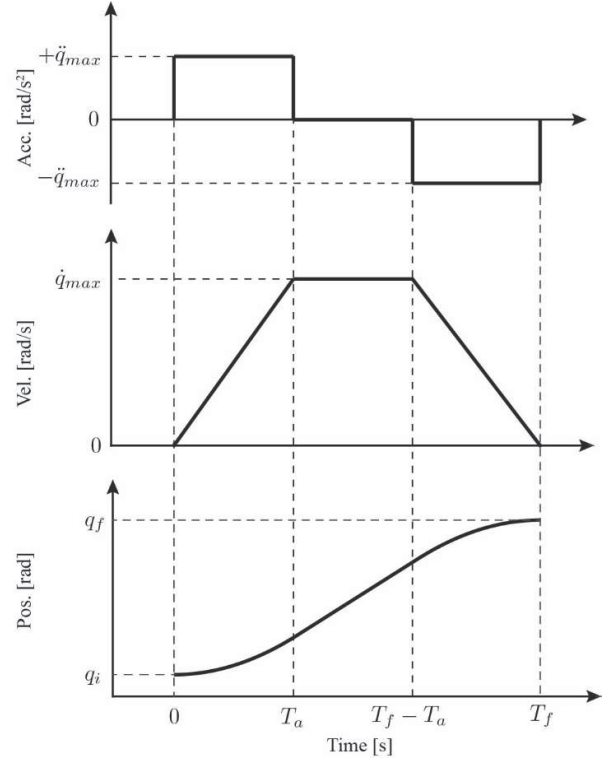


Figure 3: The trapezoidal velocity profile: the acceleration, velocity and position profiles

From Figure 3 it can be seen that, in the time interval from the initial moment to the moment  $T_a$ , acceleration is positive, constant and equal to  $\ddot{q}_{max}$ . It is clear that body moves with uniformly accelerated rectilinear motion, so the speed of movement increases linearly, from the value of zero, i.e. rest, to the value of  $\dot{q}_{max}$ , while the position changes according to smooth curve. This interval represents robot acceleration period.

From the moment  $T_a$  to the moment  $T_f - T_a$ , the acceleration is equal to zero, so the body moves at a constant speed  $\dot{q}_{max}$ . In this period, the change of position is a linear function of time.

Finally, from the moment  $T_f - T_a$  to the end of the motion, body has the negative constant acceleration  $-\ddot{q}_{max}$ , i.e. deceleration, so the movement is uniformly decelerated. Therefore the velocity is linearly decreases from  $\dot{q}_{max}$  cruising speed to zero when the robot stops. Change of position in this interval is again a squared function of time. This interval of movement is called the period robot braking. Due to the appearance of the velocity graph, this movement was called trapezoidal movement speed profile. Maximum velocity, maximum acceleration and the time provided for acceleration are not of independent magnitude:

$$\dot{q}_{max} = \ddot{q}_{max} T_a \quad (13)$$

From the Figure 3. acceleration is given with the equation:

$$\ddot{q}(t) = \begin{cases} +\ddot{q}_{max} & 0 < t \leq T_a \\ 0 & T_a < t \leq T_f - T_a \\ -\ddot{q}_{max} & T_f - T_a < t \leq T_f \end{cases} \quad (14)$$

The velocity can be determined by integrating equation (14), taking into account the initial conditions and connection given by expression (13), in the following form:

$$\dot{q}(t) = \begin{cases} \ddot{q}_{max} \cdot t & 0 < t \leq T_a \\ \ddot{q}_{max} \cdot T_a & T_a < t \leq T_f - T_a \\ \ddot{q}_{max} \cdot (T_f - t) & T_f - T_a < t \leq T_f \end{cases} \quad (15)$$

The expression for the position can be obtained by integrating the expression for velocity (15) and taking into account o again initial conditions:

$$q(t) = \begin{cases} q_i + 0.5 \cdot \ddot{q}_{max} \cdot t^2 & 0 < t \leq T_a \\ q_i + \ddot{q}_{max} T_a \left(t - \frac{T_a}{2}\right) & T_a < t \leq T_f - T_a \\ q_f - 0.5 \ddot{q}_{max} (T_f - t)^2 & T_f - T_a < t \leq T_f \end{cases} \quad (16)$$

Since that assumption is made that the important parameters are the given range of position change from  $q_i$  to  $q_f$ , total movement execution time  $T_f$ , as well as acceleration or braking time  $T_a$ , the only unknown quantity in expressions (13) - (16) is the maximum value of acceleration  $\ddot{q}_{max}$ , which, obviously, must depend on the initial parameters. The required value of maximum acceleration is determined as follows. The change of the position from the beginning to the end, i.e. the distance, must be equal to the area below speed chart. Given the fact that the graph has the shape of a trapezoid, it is easy to establish connection:

$$q_f - q_i = (\ddot{q}_{max} \cdot T_a) \cdot (T_f - T_a), \quad (17)$$

where, according to the (15) expression  $\ddot{q}_{max} \cdot T_a$  represents trapezoid height, while the expression  $T_f - T_a$  stands for the length of the trapezoid midsegment. With all of these expression it is easy to obtain unknown parameter of the maximum acceleration as:

$$\ddot{q}_{max} = \frac{q_f - q_i}{T_a(T_f - T_a)} \quad (18)$$

In all previous expressions it is logically assumed that:

$$T_a \leq \frac{T_f}{2} \quad (19)$$

that is, the acceleration or braking periods cannot be longer than half of the total time. In the special case, when  $T_a = \frac{T_f}{2}$  the acceleration and deceleration periods last per half of the total time, as soon as the speed  $q_{max}$  is reached the braking starts. Trapezoidal velocity profile from Figure 3 is then deformed because the central part is lost for the

movement with the constant speed, this kind of movement is called a triangle speed profile. The other way for obtaining the trapezoidal velocity profile is taking into the account the robot's movements, from the point of view of velocity and acceleration, which are limited by the applied actuators. In other words, there is a maximum acceleration given by the actuator, so time parameters can be obtained according to it. Therefore, sometimes in practice, it is common, instead of setting the duration of the movement and acceleration or deceleration periods, setting the maximum acceleration, and to calculate the time parameters [13].

## 4. FEEDBACK LINEARIZATION

### 4.1. Introduction

One of the major engineering problems is finding a mathematical model that is good enough to describe the system, and at the same time easy enough to treat mathematically and analytically. Depending on the design goals, there are several formulations of the control problem. The task of stabilization, tracking, and disturbance rejection or attenuation (and various combination in them) lead to a number of control problems. There are many control tasks that require the use of feedback [14]. That is why feedback linearization is a very useful technique that strikes a great balance between a good model and simple nonlinear control algorithm. Precisely because of these features, this method has found wide usage in research and applied engineering. It has been successfully implemented in many applications of control, such as industrial robots, high performance aircraft, helicopters and biomedical engineering. The central idea of the approach is to algebraically transform a nonlinear system dynamics into a (fully or partly) linear one, so that linear control techniques can be applied. [15]. Feedback linearization requires extremely precise measurements of system parameters to eliminate the effect of nonlinearity from the system and thereby achieve the anticipated effects [16] – [19].

### 4.2. Conditions

Feedback linearization approach differs from the classical linearization (about the desired equilibrium point) in that no approximation is used; it is exact [14]. This differs entirely from conventional linearization in that feedback linearization is achieved by exact state transformations and feedback, rather than by linear approximations of the dynamics [15].

In this section, the theoretical basis for the application of the proposed method will be presented Also, the conditions for applying this algorithm on the 2DOF gripping mechanism will be checked.

Of specific concern will be creating the control approach in the sense of the feedback algorithm law which will bring the annulment of nonlinearity in the equations that describe the system.

For the single input – single output nonlinear SISO system [14]:

$$\begin{aligned} \dot{\mathbf{x}} &= \mathbf{f}(\mathbf{x}) + \mathbf{g}(\mathbf{x})u \\ y &= h(\mathbf{x}) \end{aligned}$$

where  $\mathbf{f}(\mathbf{x})$ ,  $\mathbf{g}(\mathbf{x})$  and  $h(\mathbf{x})$  are sufficiently smooth in a domain  $D \subset R^n$   $\dot{\mathbf{x}} = [x_1, x_2, \dots, x_n]^T$  is a state vector. It is necessary to find a state feedback control  $u$ , that transforms the nonlinear system into an equivalent linear system. Clearly, generalization of this idea is not possible in every nonlinear system: there must be a certain structural property that allows performing in such a manner of cancellation. There are four conditions that must be met to enable this type of control.

A. State equation of the system has to be in the following form:

$$\dot{\mathbf{x}} = \mathbf{A}\mathbf{x} + \mathbf{B}\gamma(\mathbf{x})[u - \alpha(\mathbf{x})]$$

Note: If the system is not in this form, in some cases it is possible to transform it by transforming the coordinates. All functions has to be smooth enough.

B. Pair  $(\mathbf{A}, \mathbf{B})$  must be controllable, i.e. there has to be a controllability matrix whose rank is equal to the order of the system:  $\text{rank}(\mathbf{U}) = n$ .

C.  $\gamma(\mathbf{x})$  must be nonsingular, or if it is a scalar value then it has be different from zero.

D. All functions i.e. functions has to be differentiable (smooth enough).

In order to determine form of the control law new term relative degree of the system will be explained.

The relative degree of a linear system is defined as the difference between the poles (degree of the transfer function's denominator polynomial number) and zeros (degree of its numerator polynomial) [20].

*Relative degree*, in notation  $r$ , of the system which can be described at a point  $x_0$  is defined if:

1.  $L_g L_f^k h(\mathbf{x}) = 0$  for all  $x$  in a neighbourhood of  $x_0$  and all  $k < r - 1$

2.  $L_g L_f^{r-1} h(\mathbf{x}) \neq 0$

$$\mathbf{U} = \begin{bmatrix} \frac{M_{22}}{\#2} & -\frac{M_{12}}{\#2} & \frac{-C_{11}M_{22}^2}{\#2^2} - \#1 & \frac{C_{21}M_{11}M_{12} + C_{11}M_{12}M_{22}}{\#2^2} \\ -\frac{M_{21}}{\#2} & \frac{M_{11}}{\#2} & \frac{C_{22}M_{11}M_{21} + C_{21}M_{21}M_{22}}{\#2^2} & \frac{-C_{22}M_{11}^2}{\#2^2} - \#1 \end{bmatrix} \quad (24)$$

where the following substitution was made:  $\#1 = \frac{C_{21}M_{11}M_{12}}{\#2^2}$ ,  $\#2 = M_{11}M_{22} - M_{12}M_{21}$

C.  $\gamma(\mathbf{x})$  is a scalar value, equal to 1

D. All functions are differentiable (since in them are only sine and cosine functions), so this condition is met.

It is obvious from (7) that the second derivative of the output  $\mathbf{Y}$  will be the first derivative that will be equal to the function, which depends on the input signal ( $\boldsymbol{\tau}$ ). It is clear from the definition of relative degree that:  $r=2$  - relative degree of the system is two:

$$\ddot{\mathbf{Y}} = \ddot{\mathbf{q}} = \mathbf{M}^{-1}(-\mathbf{C}\dot{\mathbf{q}} - \mathbf{G} + \boldsymbol{\tau}) \quad (25)$$

The terms  $L_g$  and  $L_f^k$  represent the Lie derivative of  $h(\mathbf{x})$  taken along  $\mathbf{g}(\mathbf{x})$  and  $k$ -times along  $\mathbf{f}(\mathbf{x})$ , respectively.

Now finally, using these theoretical definitions, a control law can be formed by annulling nonlinearities in order to obtain linear equations:

$$u = \frac{1}{L_g L_f^{r-1} h(\mathbf{x})} [-L_f^r h(\mathbf{x}) + z] \quad (20)$$

This control signal will reduce the input – output map to:

$$y^r = z, \quad (21)$$

So this kind of linearization is called Input – Output Linearization, and  $z$  is called ‘new control signal’. The control signal given in (22) has a more general form:

$$u = \alpha(\mathbf{x}) + \frac{1}{\gamma(\mathbf{x})} z \quad (22)$$

The equation (20) has the same constrains as it is in C. and that is  $L_g L_f^{r-1} h(\mathbf{x})$  has to be different from zero.

#### 4.3. Control law synthesis

One of the first steps in the synthesis of a feedback linearizing controller is to check all of the constraints from the previous section.

A. State equation of the system could be easily transformed into a suitable form:

$$\begin{aligned} \dot{\mathbf{v}} &= -\mathbf{M}^{-1}\mathbf{C}\mathbf{v} + \mathbf{M}^{-1}(-\mathbf{G} + \boldsymbol{\tau}) \\ \mathbf{A} &= -\mathbf{M}^{-1}\mathbf{C} \\ \mathbf{B} &= \mathbf{M}^{-1} \\ \gamma(\mathbf{x}) &= 1, \alpha(\mathbf{x}) = \mathbf{G} \end{aligned} \quad (23)$$

B. Controllability matrix has the following form:

In order to fulfil (20) the control signal  $\boldsymbol{\tau}$  is chosen to be in the form:

$$\boldsymbol{\tau} = \mathbf{C}\dot{\mathbf{q}} + \mathbf{G} + \mathbf{M}\mathbf{z}, \quad (26)$$

and new linear system is in the form:

$$\begin{aligned} \ddot{q}_1 &= z_1 \\ \ddot{q}_2 &= z_2 \end{aligned} \quad (27)$$

The new control signal  $z$  is chosen to be in the form of proportional derivative controller:

$$z = \begin{bmatrix} K_P \varepsilon + K_D \dot{\varepsilon} \\ K_P \varepsilon + K_D \dot{\varepsilon} \end{bmatrix} \quad (28)$$

Coefficient of the PD controller has been chosen as:

$$\begin{aligned} K_P &= \omega_0^2 \\ K_D &= 2\zeta\omega_0 \end{aligned} \quad (29)$$

where  $\omega_0$  is a natural frequency and  $\zeta$  is a damping factor and they were calculated with the respect of the overshoot and settling time:  $\zeta = 0.9815$  and  $\omega_0 = 9.3731$ , so the parameters of PD controllers are (they have same values):

$$K_P = 87.8555, K_D = 18.4000$$

### 5. EXPERIMENTAL RESULTS

#### 5.1. The desired shape of the trajectory

The initial position of the robotic gripper is determined by the mechanism itself. The initial generalized coordinates are equal to:  $q_{10} = \varphi_0 = 80^\circ \approx 1.396260$  rad and  $q_{20} = \theta_0 = -30^\circ \approx -0.523599$  rad. This means that the gripping mechanism (end effector) from the Figure 2 has the coordinates:  $x_0 = 0.0373$  and  $y_0 = 0.0898$ .

Main goal of this study was to move that point from its initials to the finals coordinates. In order to do so, the feedback control system with the proportional derivative gains was developed. It is important to notice that its algorithm is convenient for any reference, i.e. it allows tracking of a given path to any endpoint with the desired velocity (and therefore with the desired position and acceleration) profile. For example, in this paper task will be to achieve angles (or in the Cartesian coordinates, end effector should be in):

$$\begin{aligned} q_{1f} &= \varphi_f = 45^\circ \approx 0.785398 \text{ rad} \\ q_{2f} &= \theta_f = -45^\circ \approx -0.785398 \text{ rad}, \\ x_f &= 0.0834 \\ y_f &= 0.0412 \end{aligned}$$

Additionally, the time required to reach this position is set to be  $T_f = 6s$ .

Maximum acceleration  $\ddot{q}_{max}$  and the time provided for acceleration, i.e. deceleration  $T_a$  are calculated according to (18) and Section 3 as:  $T_a = \frac{T_f}{3} = 2s$ ,  $|\ddot{q}_1| = 0.0763 \frac{m}{s^2}$  and  $|\ddot{q}_2| = 0.0330 \frac{m}{s^2}$ .

The parameters for the gripper are given in Table 1.

Table 1: Gripping mechanism parameters

|             | mass [kg] | length [m] |
|-------------|-----------|------------|
| first link  | 0.00799   | 0.05831    |
| second link | 0.00521   | 0.0422     |

Comparisons between the desired trajectory signals and the output signals are shown on the following Figures. All Figures were obtained from Matlab and Simulink

graphical programming environment for modelling, simulating and analyzing dynamical systems.

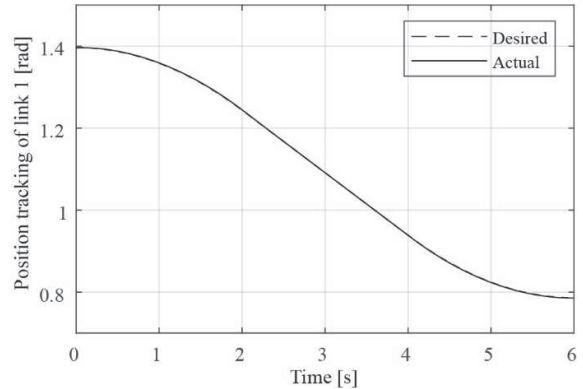


Figure 4: Comparison: Desired and simulated position for link 1

As it is very difficult to see, from the previous Figure (4), the difference between the desired and the output signal, the next one (Figure 5) shows an enlarged detail from it.

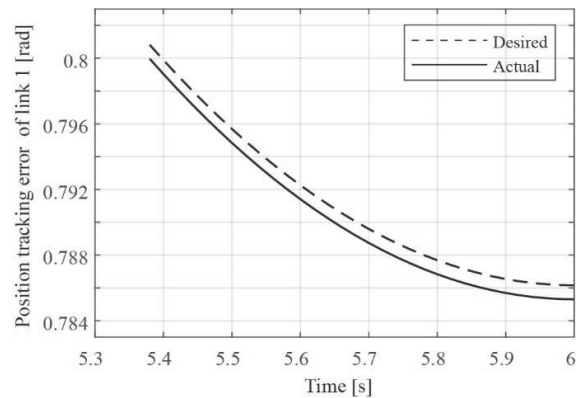


Figure 5: Increased detail from Figure 4

Velocity profile is given as trapezoidal function of maxima acceleration, time, and specific moments in time, as shown on Figure 6.

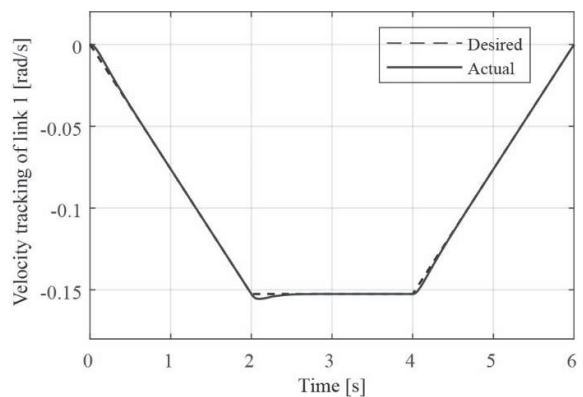


Figure 6: Comparison: Desired and simulated velocity for link 1

For constant velocity, the acceleration will be zero, Figure 7.

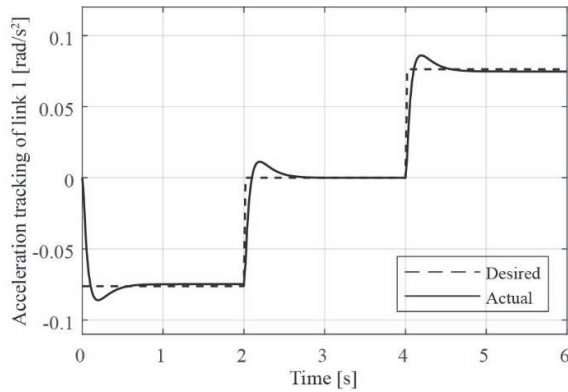


Figure 7: Comparison: Desired and simulated acceleration for link 1

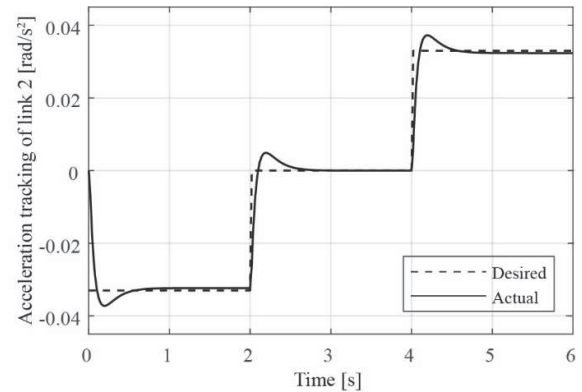


Figure 10: Comparison: Desired and simulated acceleration for link 2

Same conclusion can be drawn for Figures 8 – 11.

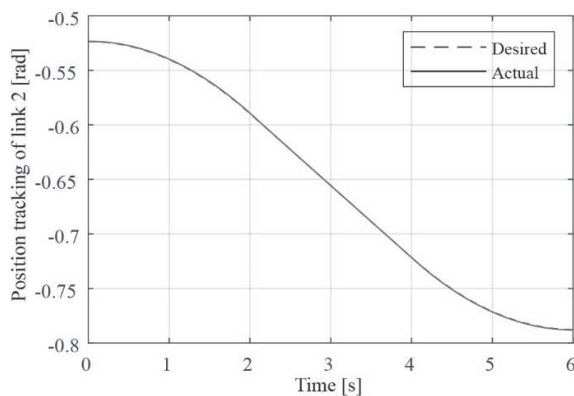


Figure 8: Comparison: Desired and simulated position for link 2

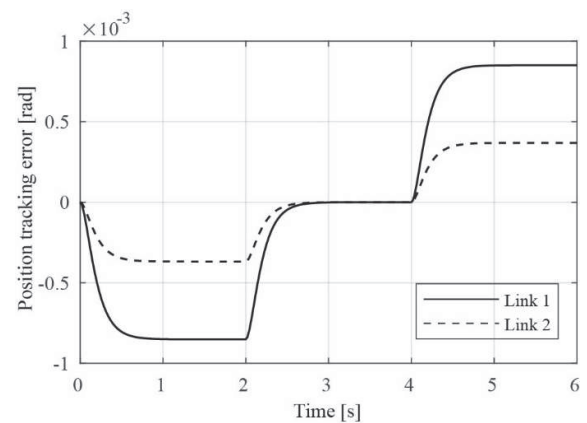


Figure 11: Position tracking errors

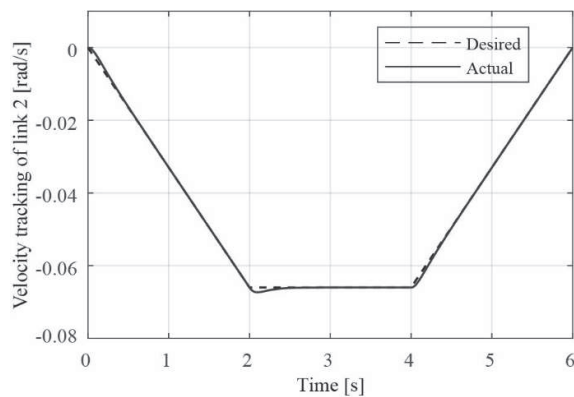


Figure 9: Comparison: Desired and simulated velocity for link 2

## 6. CONCLUSION

As a means to give an insight into the navigation and to obtain satisfying examination of the mobile robot's arm before the fabrication, this paper proposed detailed solution to the specific control problem for the two degrees of freedom (2DOF) gripping mechanism. Firstly, mathematical model has been obtained using Lagrange's approach and an evaluation of the theoretical bases was made. The nonlinear mathematical model has been derived using the positions and velocities of the points, along with the moments of inertia and energies of the system. Due to the existing nonlinearities that occur in the system, the feedback linearization with proportional derivative controller method was chosen. For the given trajectory controller parameters were chosen based on the new linear model, which was obtained using nonlinearities cancellation. Additionally, a simulation study was done for the specific initial case and the trapezoidal velocity profile was generated. This profile was used to obtain referent signal so the motion of the robot is shown to be flat and without an abrupt braking. Obtained experimental results are provided and they have verified the effectiveness of the proposed performance. The control algorithm has been validated using Matlab/Simulink software. Finally, by applying this approach satisfying results are achieved and the reasonableness of each assumption has been proven.

## ACKNOWLEDGEMENTS

This research was supported by the Science Fund of the Republic of Serbia, grant No. 6523109, AI- MISSION4.0, 2020-2022.

This work was financially supported by the Ministry of Education, Science and Technological Development of the Serbian Government, MPNTR RS under contract 451-03-9/2021-14/200105, from date 05.02.2021.

## REFERENCES

- [1] Stanford Artificial Intelligence Laboratory: <http://infolab.stanford.edu/pub/voy/museum/pd/Calculus.htm> (last accessed 25/05/2021).
- [2] J.L. Chen and W.D. Chang, "Feedback linearization control of a two-link robot using a multi-crossover genetic algorithm," *Expert Systems with Applications*, Vol. 36(2), pp. 4154–4159, (2009)
- [3] F. Piltan, M.H. Yarmahmoudi, M. Mirzaie, S. Emamzadeh and Z. Hivand, "Design Novel Fuzzy Robust Feedback Linearization Control with Application to Robot Manipulator," *International Journal of Intelligent Systems and Applications*, Vol. 5(5), pp. 1–10, (2013)
- [4] M.H. Khooban, "Design an intelligent proportional-derivative PD feedback linearization control for nonholonomic-wheeled mobile robot," *International Journal of Intelligent and Fuzzy Systems*, Vol. 26(4), pp. 1833–1843, (2014)
- [5] G. Buondonno and A. De Luca, "Efficient Computation of Inverse Dynamics and Feedback Linearization for VSA-Based Robots," *IEEE Robotics and Automation Letters*, Vol. 1(2), pp. 908–915, (2016)
- [6] N. V. Tinh, N. T. Linh, P. T. Cat, P. M. Tuan, M. N. Anh and N. P. T. Anh, "Modeling and feedback linearization control of a nonholonomic wheeled mobile robot with longitudinal, lateral slips," *IEEE International Conference on Automation Science and Engineering*, Fort Worth, TX (USA), 21 August-24 August 2016, pp. 996–1001, (2016)
- [7] M. Navabi and S. Hosseini, "Adaptive feedback linearization control of space robots," *IEEE 4th International Conference on Knowledge-Based Engineering and Innovation*, Tehran (Iran), 22 December 2017, pp. 0965–0970, (2017)
- [8] M.H. Korayem, M. Yousefzadeh and S. Manteghi, "Dynamics and input–output feedback linearization control of a wheeled mobile cable-driven parallel robot," *Multibody System Dynamics*, Vol. 40, pp. 55–73, (2017)
- [9] J.C. Cambera and V. Feliu-Batlle, "Input-state feedback linearization control of a single-link flexible robot arm moving under gravity and joint friction," *Robotics and Autonomous Systems*, Vol. 88, pp. 24–36, (2017)
- [10] M. Mehndiratta, E. Kayacan and E. Kayacan, "A Simple Learning Strategy for Feedback Linearization Control of Aerial Package Delivery Robot," *IEEE Conference on Control Technology and Applications*, Copenhagen (Denmark), 21 August-24 August 2018, pp. 361–367, (2018)
- [11] Y. Kali, M. Saad and K. Benjelloun, "Optimal super-twisting algorithm with time delay estimation for robot manipulators based on feedback linearization," *Robotics and Autonomous Systems*, Vol. 108, pp. 87–99, (2018)
- [12] M. Bagheri, P. Naseradinmousavi and M. Krstić, "Feedback linearization based predictor for time delay control of a high-DOF robot manipulator," *Automatica*, Vol. 108, (2019)
- [13] [https://www.ucg.ac.me/skladiste/blog\\_13269/objava\\_8796/fajlovi/35\\_industrijska781.pdf](https://www.ucg.ac.me/skladiste/blog_13269/objava_8796/fajlovi/35_industrijska781.pdf), University of Montenegro, pp. 87-102, (last accessed 30/05/21)
- [14] H. K. Khalil, "Nonlinear Systems"; 3rd ed. New Jersey, United States: Prentice Hall, (2002)
- [15] W. Ghazlane, J. Knani, "Nonlinear Control via Input-Output Feedback Linearization of a Robot Manipulator," *Advances in Science, Technology and Engineering Systems Journal*, vol. 3, October, (2018)
- [16] Farzin, P.; Yarmahmoudi, M.H.; Mirzaie, M.; Emamzadeh, S.; Hivand, Z. "Design novel fuzzy robust feedback linearization control with application to robot manipulator" *J. Intell. Syst. Appl.*, Vol. 5, pp. 1–10, (2013)
- [17] Lin, C.-H. Precision Motion Control of a Linear Permanent Magnet Synchronous Machine Based on Linear Optical-Ruler Sensor and Hall Sensor. *Sensors*, 18, 3345. (2018)
- [18] Su, W.-T.; Liaw, C.-M. Adaptive positioning control for a LPMSM drive based on adapted inverse model and robust disturbance observer. *IEEE Trans. Power Electron.*, 21, pp. 505–517, (2006)
- [19] Yung-Te Chen & Chi-Shan Yu & Ping-Nan Chen, "Feedback Linearization Based Robust Control for Linear Permanent Magnet Synchronous Motors," *Energies*, MDPI, Open Access Journal, vol. 13(20), pp. 1-17, (2020)
- [20] M. Vesović, R. Jovanović, L. Laban, V. Zarić, "Modelling and Control of a Series Direct Current (DC) Machines Using Feedback Linearization Approach," *7th International Conference on Electrical, Electronic and Computing Engineering IcETRAN*, 28 September – 29 September, pp. 191 – 197, (2020)

# A Nonlinear Model Predictive Control Tracking Application for a System of Cascaded Tanks

Guilherme N. G. dos Reis<sup>1\*</sup>, Marcelo M. Morato<sup>1</sup>, Julio E. Normey-Rico<sup>1</sup>, Vladimir Stojanovic<sup>2</sup>

<sup>1</sup>Dept. de Automação e Sistemas, Univ. Fed. de Santa Catarina, Florianópolis (Brazil)

<sup>2</sup>Faculty of Mechanical and Civil Engineering, Univ. of Kragujevac, Kraljevo (Serbia)

*Nonlinear Model Predictive Control (NMPC) formulations through quasi-Linear Parameter Varying (qLPV) embeddings have been brought to focus in recent literature. In this brief paper, we evaluate the application of this kind of control strategy to the reference tracking problem of a cascaded tank system. This benchmark application has four states and two control inputs, which represent the fluid inlets to the upper tanks. The levels of each of the four tanks dependent not only on these input flows, but also on bounded disturbance variables. The system exhibits nonlinearities due to the fluid dynamics, which are incorporated as state-dependent qLPV variables. This case study serves to illustrate how a Sequential Quadratic Program (SQP) is an elegant solution to NMPC design: the qLPV realisation of the nonlinear dynamics yields linear predictions at each sampling instant, which can be refined through sequential operations of a single QP. The resulting numerical toughness is much smaller than the Nonlinear Programs generated with "regular" NMPC design, which is very convenient. Moreover, the SQP solution provides estimates of the future scheduling parameters, with convergence properties. Using realistic simulations, we demonstrate the effectiveness of this control approach with respect to piecewise constant reference tracking and disturbance rejection, which are assessed using standard performance indexes.*

**Keywords:** Nonlinear Model Predictive Control, Cascaded Tanks, Linear Parameter Varying Systems

## 1. INTRODUCTION

Model Predictive Control (MPC) represents a family of advanced control techniques, derived in the late 1980's for industrial processes subject to with constraints [1], since then, they have been intensively studied by academics and used by engineers. With thousands of industrial applications [2], some of the problems still open for research are nonlinear applications and their particularities. Nonlinear Model Predictive Control (NMPC) may, among other problems, bring real-time obstacles, given that the resulting numerical complexity increases.

The key step of MPC algorithms, solving an optimization problem, gets complicated in the majority of nonlinear systems: this procedure is not trivial and is frequently avoided through approximations. One possible solution explored more recently is the use of sophisticated tools for solving Nonlinear Programming (NP), as [3-5].

Linear Parameter Varying (LPV) framework has been, concurrently, expanded lately, as a way to circumvent these nonlinear issues. For a large class of nonlinear systems, it is possible to make use of a quasi-LPV (qLPV) embedding in order to redesign state equations by the means of linear maps parametrized by known and bounded scheduling variables, denoted  $p$ .

Nevertheless, qLPV embedding are not compatible with linear MPC techniques, since these realisations are based on the availability of the scheduling parameters, which depend on endogenous variables of the process. As the future process variables are unknown, qLPV model-

based predictions are of uncertain computation, these are based on scheduling variables. The usual solution for this kind of problem would be Robust MPC (RMPC), but it usually implies excessive conservativeness.

Recent methods have provided alternative options to the robust design, considering qLPV embedding, [6-8]. Bearing in mind this context, a NMPC solution based on Sequential Quadratic Programming (SQP) is presented in this work. This approach contrasts with full nonlinear MPCs, making real-time applications possible, as well as with RMPCs, since the method does not imply in conservative results. The method is applied to a benchmark quadritank process [9], for which we demonstrate the effectiveness of the method in terms of reference tracking and disturbance rejection.

This paper is organized as follows: Section 1 introduces briefly the subject studied; Section 2 lays down the problem setup, passing through qLPV framework, qLPV MPC and SQP problems; Section 3 describes the process used as case study; and finally, on Section 4, results derived from a numerical simulation are shown.

## 2. PROBLEM SETUP

Consider the following discrete-time nonlinear system:

$$\begin{cases} x[k+1] = f(x[k], u[k]) \\ y[k] = g(x[k], u[k]) \end{cases} \quad (1)$$

\*Corresponding author: Guilherme N. G. dos Reis, Dept. de Automação e Sistemas, Univ. Fed. de Santa Catarina, Florianópolis (Brazil)

where  $x \in \mathbf{R}^{n_x}$ ,  $u \in \mathbf{R}^{n_u}$  and  $y \in \mathbf{R}^{n_y}$  are, respectively, state, input and output variables, all constrained to sets  $\mathbf{X}$ ,  $\mathbf{U}$  and  $\mathbf{Y}$ . Functions  $f: \mathbf{R}^{n_x+n_u} \rightarrow \mathbf{R}^{n_x}$  and  $g: \mathbf{R}^{n_x+n_u} \rightarrow \mathbf{R}^{n_y}$  are called the state and output maps, respectively.

### 2.1. qLPV-embedding

Consider that the Linear Differential Inclusion property is satisfied [10], which means that

$$\exists G(x, u): \mathbf{R}^{n_x+n_u} \rightarrow \mathbf{R}^{(n_x+n_y) \times (n_x+n_u)} \text{ such that}$$

$$\begin{bmatrix} f(x, u)^T & g(x, u)^T \end{bmatrix}^T = G(x, u) \begin{bmatrix} x^T & u^T \end{bmatrix}^T.$$

Then, there exists a qLPV realization for the considered nonlinear system, as follows:

$$\begin{cases} x[k+1] = A(\rho[k])x[k] + B(\rho[k])u[k] \\ y[k] = C(\rho[k])x[k] + D(\rho[k])u[k] \\ \rho[k] = h(x[k], u[k]) \end{cases} \quad (2)$$

where  $\rho \in \mathbf{P} \subseteq \mathbf{R}^{n_\rho}$  is called scheduling variable vector and  $h: \mathbf{R}^{n_x+n_u} \rightarrow \mathbf{R}^{n_\rho}$ , scheduling map. As all four matrix functions  $A: \mathbf{R}^{n_\rho} \rightarrow \mathbf{R}^{n_x \times n_x}$ ,  $B: \mathbf{R}^{n_\rho} \rightarrow \mathbf{R}^{n_x \times n_u}$ ,  $C: \mathbf{R}^{n_\rho} \rightarrow \mathbf{R}^{n_y \times n_x}$  and  $D: \mathbf{R}^{n_\rho} \rightarrow \mathbf{R}^{n_y \times n_u}$  derive from LDI matrix,

$$X_{k_0} = \begin{bmatrix} x[k_0+1|k_0] \\ x[k_0+2|k_0] \\ \vdots \\ x[k_0+N_p|k_0] \end{bmatrix} \quad U_{k_0} = \begin{bmatrix} u[k_0|k_0] \\ u[k_0+1|k_0] \\ \vdots \\ u[k_0+N_p-1|k_0] \end{bmatrix} \quad Y_{k_0} = \begin{bmatrix} y[k_0+1|k_0] \\ y[k_0+2|k_0] \\ \vdots \\ y[k_0+N_p|k_0] \end{bmatrix} \quad (5)$$

are the prediction vectors for, respectively, states, inputs and outputs. Also,

$$P_{k_0} = \begin{bmatrix} \rho[k_0]^T & \rho[k_0+1|k_0]^T & \dots & \rho[k_0+N_p-1|k_0]^T \end{bmatrix}^T \quad (6)$$

represents the predictions for scheduling variables, which parametrizes all matrix functions  $A: \mathbf{R}^{N_p n_\rho} \rightarrow \mathbf{R}^{N_p (n_x \times n_x)}$ ,  $B: \mathbf{R}^{N_p n_\rho} \rightarrow \mathbf{R}^{N_p (n_x \times n_u)}$ ,  $C: \mathbf{R}^{N_p n_\rho} \rightarrow \mathbf{R}^{N_p (n_y \times n_x)}$  and  $D: \mathbf{R}^{N_p n_\rho} \rightarrow \mathbf{R}^{N_p (n_y \times n_u)}$ , and map  $H: \mathbf{R}^{N_p (n_x+n_u)} \rightarrow \mathbf{R}^{N_p n_\rho}$  defines it. Previous vectors take values from instant  $k_0$  to instant  $k_0+N_p$ , thus comprising the full prediction horizon of  $N_p$  steps.

Accordingly, we consider the following quadratic cost function:

$$J_k = E_k^T Q E_k + \Delta U_k^T R \Delta U_k \quad (7)$$

$$\begin{bmatrix} f(x[k], u[k]) \\ g(x[k], u[k]) \end{bmatrix} = \begin{bmatrix} A(\rho[k]) & B(\rho[k]) \\ C(\rho[k]) & D(\rho[k]) \end{bmatrix} \quad (3)$$

Note that Eq. (1) and Eq. (2) are equivalent, with the upper part of Eq. (2) is outsourcing the nonlinearities through the scheduling parameter interconnection  $\rho = h(x, u)$ , which depends on the endogenous variables  $x$  and  $u$ . Hence, we emphasize the quasi(-LPV) prefix given that  $\rho$  is not exogenous.

### 2.2. qLPV MPC Problem

As an intrinsically discrete-time technique, MPC solves, at each sampling instant, an optimization problem, which attempts to minimize a cost function subject to a set of constraints, with respect to a vector of decision variables. It does so by making use of a model of the system to be controlled in order to predict future values for the output vector and utilizing these predictions to evaluate performance.

Consecutively applying state equation from some initial condition  $x_{k_0}$  yields

$$\begin{cases} X_{k_0} = A(P_{k_0})x_{k_0} + B(P_{k_0})U_{k_0} \\ Y_{k_0} = C(P_{k_0})x_{k_0} + D(P_{k_0})U_{k_0} \\ P_{k_0} = H(X_{k_0}, U_{k_0}) \end{cases} \quad (4)$$

where

as a performance index, where  $E_k = R_k - Y_k$  is a reference tracking prediction vector and  $\Delta U_k$  is the input variation prediction vector, weighted by matrices  $Q$  and  $R$ , implies on a nonlinear cost function for the problem  $P(x_{k_0}, R_k)$ :

$$\begin{aligned}
 & \min_{\Delta U_{k_0}} J_{k_0} \\
 & \left\{ \begin{array}{l} X_{k_0} = \mathbf{A}(P_{k_0})x_{k_0} + \mathbf{B}(P_{k_0})U_{k_0} \\ Y_{k_0} = \mathbf{C}(P_{k_0})x_{k_0} + \mathbf{D}(P_{k_0})U_{k_0} \\ P_{k_0} = \mathbf{H}(X_{k_0}, U_{k_0}) \end{array} \right. \quad (8) \\
 & \text{s.t.} \left\{ \begin{array}{l} X_{k_0} \in \mathbf{X} \\ U_{k_0} \in \mathbf{U} \\ Y_{k_0} \in \mathbf{Y} \\ P_{k_0} \in \mathbf{P} \end{array} \right.
 \end{aligned}$$

Since a qLPV embedding was used to rewrite Eq. (1) as Eq. (2), all state nonlinearities were reallocated to the definition of the scheduling variable. Yet, problem  $\mathbf{P}$  still has to include its nonlinear dynamics, which implicates a NP problem.

### 2.3 Sequential Quadratic Programming

In this paper, we follow the method from [6]. Accordingly, we solve a Sequential Quadratic Program, which is operated as follows: we solve the original optimization problem (6) by iterating a sequence of QPs, all parametrized by a scheduling vector  $P$ . Starting with some suitable initial guess  $P^0$ , the MPC optimization problem is solved as a QP, given that Eq. (4) based on  $P^0$  is linear. Then, with the optimal values resulted from previous QP,  $P$  is updated to  $P^1 = h(X_k, U_k)$  and this process is iterated until a convergence threshold is reached:  $\|P^l - P^{l-1}\| \leq \varepsilon$ . This SQP is able to approximate the NP problem form, Eq. (6), very well, for any arbitrarily small positive scalar  $\varepsilon$  and can be solved more quickly.

However, equality constraint  $P_k = \mathbf{H}(X_k, U_k)$  is the only nonlinear aspect of  $\mathbf{P}$ . Thus, employing a SQP algorithm to solve it transposes a NP problem into a number of QP problems. This means any commercial QP solver would handle  $\mathbf{P}_{SQP}(x_{k_0}, \mathbf{R}_k, P^l)$  on a reasonable time.

$$\begin{aligned}
 & \min_{\Delta U_{k_0}} J_{k_0} \\
 & \left\{ \begin{array}{l} X_{k_0} = \mathbf{A}(P^l)x_{k_0} + \mathbf{B}(P^l)U_{k_0} \\ Y_{k_0} = \mathbf{C}(P^l)x_{k_0} + \mathbf{D}(P^l)U_{k_0} \end{array} \right. \quad (9) \\
 & \text{s.t.} \left\{ \begin{array}{l} X_{k_0} \in \mathbf{X} \\ U_{k_0} \in \mathbf{U} \\ Y_{k_0} \in \mathbf{Y} \\ P^l \in \mathbf{P} \end{array} \right.
 \end{aligned}$$

### Algorithm 1: SQP qLPV MPC

```

k ← k0
x[k-1] ← xk0
u[k-1] ← uk0
ρ[k-1] ← h(xk0, uk0)
while control condition
  Measure x[k]
  l ← 0
  Pl ← α-1
  while converge condition
    Solve PSQP(xk0, Rk, Pl)
    Pl+1 ← h(Xkl, Ukl)
    l ← l+1
  Apply u[k|k]
    
```

### 3. CASCADED

In order to test the SQP method, we use the case study from [9]. Consider the scheme of four cascaded tanks as shown in Fig. 1. This system is an educational benchmark for illustration of performance limitations, with a focus on the adjustable multivariable zeros.

Consisting of four tanks, two valves, two pumps and a reservoir, it is shown in Fig. 1. Fed by the reservoir, both pumps fill crossed lower and upper tanks, regulated by the valves. Each tank has an outlet hole that either fills another tank or the reservoir, this way there is no loss of liquid.

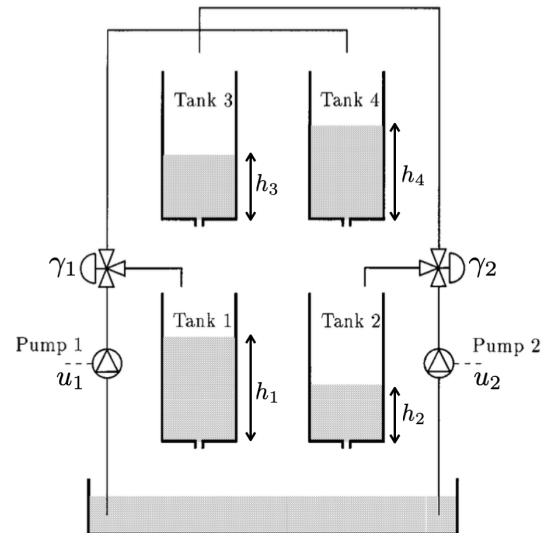


Figure 1: Cascade Tanks Process. Fig. from Johansson (2000)

From mass balance and Bernoulli's law, it is possible to model this process, yielding nonlinear ordinary differential equations, Eq. (8),

$$\frac{d}{dt} \begin{bmatrix} h_1(t) \\ h_2(t) \\ h_3(t) \\ h_4(t) \end{bmatrix} = \begin{bmatrix} -\frac{a_1}{A_1} \sqrt{2gh_1(t)} + \frac{a_3}{A_1} \sqrt{2gh_3(t)} + \frac{k_1 \gamma_1(t)}{A_1} v_1(t) \\ -\frac{a_2}{A_2} \sqrt{2gh_2(t)} + \frac{a_4}{A_2} \sqrt{2gh_4(t)} + \frac{k_2 \gamma_2(t)}{A_2} v_2(t) \\ -\frac{a_3}{A_3} \sqrt{2gh_3(t)} + \frac{k_2(1-\gamma_2(t))}{A_3} v_2(t) \\ -\frac{a_4}{A_4} \sqrt{2gh_4(t)} + \frac{k_1(1-\gamma_1(t))}{A_4} v_1(t) \end{bmatrix} \quad (10)$$

where  $h_i$ ,  $i = 1, 2, 3, 4$ , is the water level on the  $i$ -th tank,  $v_i$ ,  $i = 1, 2$ , is the voltage applied on the  $i$ -th pump and, lastly,  $\gamma_i$ ,  $i = 1, 2$ , is the position of the  $i$ -th valve. Parameters  $a_i$  and  $A_i$ ,  $i = 1, 2, 3, 4$ , are, respectively, the area of the outlet hole of the  $i$ -th tank and the bottom area of the  $i$ -th tank. Also,  $k_i$ ,  $i = 1, 2$ , is the proportionality coefficient of flow per voltage of the  $i$ -pump.

This system is clearly a nonlinear model, which can be put in state-space by taking the following state, input and output vectors, respectively:

$$\begin{aligned} x(t) &= [h_1(t) \quad h_2(t) \quad h_3(t) \quad h_4(t)]^T \\ u(t) &= [v_1(t) \quad v_2(t) \quad \gamma_1(t) \quad \gamma_2(t)]^T \\ y(t) &= [h_1(t) \quad h_2(t)]^T \end{aligned} \quad (11)$$

$$A(\rho(t)) = \begin{bmatrix} \frac{-a_1 \sqrt{2g} \rho_1(t)}{A_1} & 0 & \frac{a_3 \sqrt{2g} \rho_3(t)}{A_1} & 0 \\ 0 & \frac{-a_2 \sqrt{2g} \rho_2(t)}{A_2} & 0 & \frac{a_4 \sqrt{2g} \rho_4(t)}{A_2} \\ 0 & 0 & \frac{-a_3 \sqrt{2g} \rho_3(t)}{A_3} & 0 \\ 0 & 0 & 0 & \frac{-a_4 \sqrt{2g} \rho_4(t)}{A_4} \end{bmatrix}$$

$$B(\rho(t)) = \begin{bmatrix} \frac{k_1 \rho_7(t)}{2A_1} & 0 & \frac{k_1 \rho_5(t)}{2A_2} & 0 \\ 0 & \frac{k_2 \rho_8(t)}{2A_2} & 0 & \frac{k_2 \rho_6(t)}{2A_2} \\ 0 & \frac{(1-k_2/2) \rho_8(t)}{A_3} & 0 & \frac{-k_2 \rho_6(t)}{2A_3} \\ \frac{(1-k_1/2) \rho_7(t)}{A_4} & 0 & \frac{-k_1 \rho_5(t)}{2A_4} & 0 \end{bmatrix} \quad (13)$$

Since this model satisfied the LDI property, we can obtain a qLPV realization by considering the scheduling variables vector as

$$\rho(t) = [\rho_x(t) \quad \rho_u(t)]^T, \quad \text{with}$$

$$\rho_x(t) = \left[ \frac{1}{\sqrt{h_1(t)}} \quad \frac{1}{\sqrt{h_2(t)}} \quad \frac{1}{\sqrt{h_3(t)}} \quad \frac{1}{\sqrt{h_4(t)}} \right]^T \quad \text{and}$$

$$\rho_u(t) = [v_1(t) \quad v_2(t) \quad \gamma_1(t) \quad \gamma_2(t)]^T,$$

$$\begin{cases} \frac{dx(t)}{dt} = A(\rho(t))x(t) + B(\rho(t))u(t) \\ y(t) = C(\rho(t))x(t) + D(\rho(t))u(t) \end{cases} \quad (12)$$

where

This qLPV model is discretized in order for it to be presented in the form of Eq. (2). It is noteworthy the fact that  $A(\rho(t))$  depends affinely only on  $\rho_x(t)$ ,  $B(\rho(t))$  depends affinely only on  $\rho_u(t)$  and  $C$  and  $D$  are constant matrices.

#### 4. SIMULATION RESULTS

A simulation scenario is carried out to validate the SQP qLPV MPC algorithm in practice and it is described in detail in the sequence.

Starting with the model itself, it is used Eq. (1) to reproduce the process, as it is a numerical simulation, and Eq. (8) for MPC predictions, both normalized, with sampling period  $t_s = 0.1s$ . Table 1 displays all model parameters.

Table 1: Model Parameters

|   |   |
|---|---|
| $a [cm^2]$                                    | $[0.5 \ 0.5 \ 0.5 \ 0.5]^T$             |
| $A [cm^2]$                                    | $[1 \ 1 \ 1 \ 1]^T$                     |
| $k \left[ \frac{cm^3}{s} \frac{1}{V} \right]$ | $[1.4 \ 1.4]^T$                         |
| $h_{k_0} [cm]$                                | $[5 \ 5 \ 5 \ 5]^T$                     |
| $u_{k_0} [V/\%]$                              | $[5\sqrt{0.5} \ 5\sqrt{0.5} \ 0 \ 0]^T$ |

Additionally, state, inputs and outputs constraint sets  $\mathbf{X}$ ,  $\mathbf{U}$  and  $\mathbf{Y}$  are given by

$$\mathbf{X} = \left\{ x \in \square^{n_x} : \begin{bmatrix} 0 \\ 0 \\ 0 \\ 0 \end{bmatrix} \leq x \leq \begin{bmatrix} 10 \\ 10 \\ 10 \\ 10 \end{bmatrix} \right\}$$

$$\mathbf{U} = \left\{ u \in \square^{n_u} : \begin{bmatrix} 0 \\ 0 \\ 0 \\ 0 \end{bmatrix} \leq u \leq \begin{bmatrix} 5 \\ 5 \\ 1 \\ 1 \end{bmatrix} \right\} \quad (14)$$

$$\mathbf{Y} = \left\{ y \in \square^{n_y} : \begin{bmatrix} 0 \\ 0 \end{bmatrix} \leq y \leq \begin{bmatrix} 10 \\ 10 \end{bmatrix} \right\}$$

as the scheduling variables constraint set can be derived from there, on an abuse of notation,  $\mathbf{P} = h(\mathbf{X}, \mathbf{U}) \subseteq \square^{n_p}$ .

Now, on the control system scheme, Algorithm 1 is employed. All states are considered to be available, by measurement or estimation. Initialization for  $P^l$  is taken as a constant vector,  $P^0 = \rho[k] \otimes \bar{1}$ , and convergence condition is a limit on the number of iterations,  $l \leq n_{iter}$ , and a lower bound on the variation of  $P$ ,  $\left\| (P^l - P^{l-1})^T (P^l - P^{l-1}) \right\|_{\infty} \leq \varepsilon$ .

Cost function  $J_k$  is the same from Eq. (5), where  $\mathbf{Q} = 10I$  and  $\mathbf{R} = I$ , both of appropriate dimensions, meaning it is 10 times more important to track reference than to have constant input signals. Also, the prediction horizon is chosen to be  $N_p = 20$  samples or  $N_p = 2s$ .

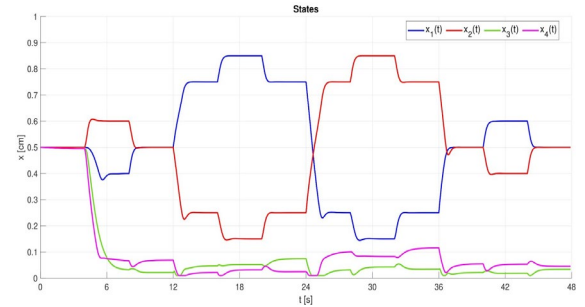


Figure 2: Cascaded Tanks: States - in blue is  $x_1(t)$ ; in red is  $x_2(t)$ ; in green is  $x_3(t)$ ; in pink is  $x_4(t)$ ;

Fig. 2 depicts, starting on  $h_{k_0}$ , all four state's trajectories: in order, on blue, red, green and pink. On Fig. 3, upper graph shows first output  $y_1(t)$  and its reference signal  $r_1(t)$  and lower graph, second output  $y_2(t)$  and its reference signal  $r_2(t)$ . It is evident, by the first 12 seconds, this approach can maintain the process on stationary regime, as the pair  $(h_{k_0}, u_{k_0})$  is an equilibrium point. Likewise, as reference changes its value, both outputs can achieve a zero-error steady-state after just a few seconds. Nor first, nor second outputs do it with oscillations, although they present small overshoots when descending. Assessing disturbance rejection, every 12 seconds, starting on  $t = 4s$ , it is applied 4 seconds long step-like signals with 10% of max level amplitude as additive disturbances, and MPC takes just a few seconds to completely reject them, implying a zero-error steady-state.

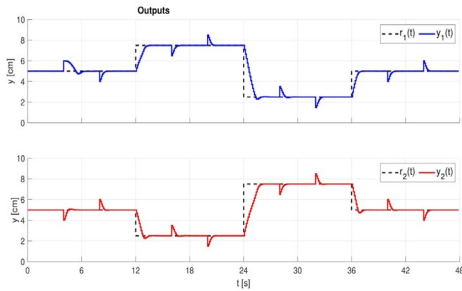


Figure 3: Cascaded Tanks: Outputs - (a) in black dashed is  $r_1(t)$ ; in blue is  $y_1(t)$ ; (b) in black dashed is  $r_2(t)$ ; in red is  $y_2(t)$ ;

Fig. 4 exhibits all four input signals, both pump voltages and valves positions. It is clear that when it is necessary, such as during reference changes, there are significant inputs variations.

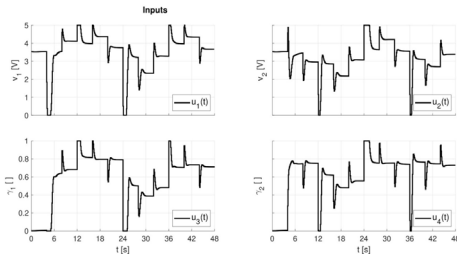


Figure 4: Cascaded Tanks: Inputs

As a way to quantify how well SQP qLPV MPC works, three indexes are proposed: integral squared error (ISE), integral average control variation (IACV) and mean value of cost function  $J_k$ . The first is an already established performance index and comprises of 
$$ISE = \frac{1}{k_\infty - k_0} \int_{k_0}^{k_\infty} (r(\tau) - y(\tau))^2 d\tau$$
. The second is defined by 
$$IACV = \frac{1}{k_\infty - k_0} \int_{k_0}^{k_\infty} |u(\tau)| d\tau$$
. The third is calculated by Eq. (5) divided by the number of samples. All indexes are presented in Table 2.

Table 2: Performance Indexes

|                          |                                 |
|--------------------------|---------------------------------|
| $ISE(\times 10^{-3})[]$  | $[3.6 \ 3.9]^T$                 |
| $IACV(\times 10^{-3})[]$ | $[14.9 \ 17.1 \ 14.7 \ 18.0]^T$ |
| $J_k(\times 10^{-3})[]$  | 6.2                             |
| $t_{comp}[s]$            | 0.3072                          |

### 5. CONCLUSION

This paper offered validation through numerical simulation of an MPC algorithm for the nonlinear benchmark process Cascaded Tanks. Combining the qLPV framework and a SQP approach, the method showed satisfactory results for the tracking and rejection problems. And it does so because predictions for the scheduling variables converge to its nonlinear dynamics after a few iterations of QP optimization.

### ACKNOWLEDGEMENTS

The authors thank CNPq for supporting project 304032/2019-0 and Serbian Ministry of Education, Science and Technological Development (No. 451-03-9/2021-14/200108).

### REFERENCES

- [1] E.F.Camacho, and C. Bordons, “Model Predictive Control”. Springer Science & Business Media, (2013)
- [2] M. Alami, “A Pragmatic Story of Model Predictive Control: Self Contained Algorithms and Case-studies”. CreateSpace Independent Publishing Platform, (2013)
- [3] S. Gros, M. Zanon, R. Quirynen, A. Bemporad, and M. Diehl, “From linear to nonlinear MPC: bridging the gap via the real-time iteration”. International Journal of Control, 93(1), pp. 62–80. (2020)
- [4] K.M.M. Rathai, “Synthesis and real-time implementation of parameterized NMPC schemes for automotive semi-active suspension systems”. Theses, Université Grenoble Alpes.(2020).
- [5] R. Quirynen, M. Vukov, M. Zanon, and M. Diehl, “Autogenerating microsecond solvers for nonlinear MPC: A tutorial using ACADO integrators”. Optimal Control Applications and Methods, 36(5), pp. 685–704. (2015)
- [6] P.S.G. Cisneros, S. Voss, and H. Werner, “Efficient nonlinear model predictive control via quasi-LPV representation”, In 2016 IEEE 55th Conference on Decision and Control (CDC), pp. 3216–3221, (2016)
- [7] M.M. Morato, J.E. Normey-Rico, and O. Sename, “Model predictive control design for linear parameter varying systems: A survey”. Annual Reviews in Control, 49, pp. 64–80. (2020)
- [8] P.S. Gonzalez Cisneros, and H. Werner, “Nonlinear model predictive control for models in quasi-linear parameter varying form”. International Journal of Robust and Nonlinear Control, 30(10), pp. 3945–395, (2020)
- [9] K.H. Johansson, “The quadruple-tank process: A multivariable laboratory process with an adjustable zero”. IEEE Transactions on control systems technology, 8(3), 456–465. (2000)
- [10] J.S. Shamma, “An Overview of LPV Systems”, pp. 3–26. Springer US, Boston, MA. (2012)

# Control of a Liquid Level System Based on Classical and Fuzzy PID Like Controller Using the Grey Wolf Optimization Algorithm

Vladimir Zarić<sup>1\*</sup>, Natalija Perišić<sup>1</sup>, Radiša Jovanović<sup>1</sup>

<sup>1</sup>Faculty of Mechanical Engineering/Control Engineering, University of Belgrade, Belgrade (Serbia)

*This paper deals with liquid level control as one of the frequent problems in industry. Several classical methods for tuning a PID like controller were applied. Furthermore, parameters for the controller were optimized using grey wolf optimizer. In addition to the classical controller, fuzzy PID like controller has also been designed and optimized using the same optimization algorithm. Experimental results obtained on the tank system are provided.*

**Keywords:** grey wolf optimizer, fuzzy control system, liquid level control

## 1. INTRODUCTION

Different types of liquid tank plants have wide application in various industries such as chemical, petrochemical, food & beverage industry, etc. Consequently, the liquid level control is an open question that is always relevant and constantly requires optimal solution.

Classical Ziegler-Nichols (ZN) [1] and Cohen-Coon (CC) [2] methods are often used for tuning PID like controllers and obtained results are frequently compared with the results of newer methods. This is exactly done in [3] where the authors compared ZN, CC and Takahashi's tuning method in order to obtain optimal parameters for PI controller for liquid flow process and in [4], on coupled tank system, where performance comparison was made between ZN, CC and Ciancone tuning methods for PI and PID. Another available control technique for nonlinear systems is feedback linearization. Paper [5] proposed feedback linearization control method for level control of coupled tanks system. It concluded that achieved benefit was reducing chattering and lowering control effort with better control results. A new approach in automatic control theory appeared when Lotfi A. Zadeh laid the foundations of fuzzy logic [6]. The basis of fuzzy logic is that right value of variables can be any value from [0,1] set. Applied fuzzy logic controller (FLC) can be found in [7]. There, authors studied and implemented PID controller and FLC using Arduino for the experiment of liquid level control. The results showed that FLC can be easily formed and dominates over PID controller in removing the overshoot and steady state oscillations. The conducted research in [8] offers a comparison between ZN, CC, Chien-Hrones-Reswick (CHR) PID tuning method and tuning PID controller using fuzzy logic. Obtained overcome on four-coupled tank system showed that applied decentralized fuzzy PID controller could be used in industrial process as it provides an optimal solution. In paper [9] researchers made comparative study of fuzzy PI + fuzzy PD controller and conventional PID in feedback and cascade system configuration. In both configurations fuzzy PI + fuzzy PD controller achieved better results in liquid-level control process, especially in cascade loop configuration. Another strategy for solving this problem is finding an optimal solution in field of artificial intelligence. On coupled tanks system, neural network NARX model was used for

identification and control of a non-linear process in [10]. It was proven that neural network identified model achieved sufficient accuracy. Additionally, achieved improvements in control process using neural network control scheme compared to conventional PI controller were presented. Succeeding, fuzzy logic and neural network were combined in order to improve control of non-linear process. Paper [11] demonstrated superiority of application Neuro Fuzzy Controller over the FLC for control process of coupled tank system. Further, used strategies found basis in nature process. Natural selection and genetics gave ideas for development of Genetic Algorithm (GA), that led to generation of high-quality solutions to optimization problems. The article [12] researched optimal PID controller for coupled tank liquid level control. ZN method has been applied for tuning PID and optimized with bat algorithm in various time domain. In [13] authors proposed Takagi-Sugeno fuzzy model optimized with the whale optimization algorithm for control of a liquid level system. Paper [14] presented comparison of ZN, CC, minimum effort criteria (ISE, IAE, IATE) and GA tuning method of PID controller for three tank liquid level process. Research [12-14] concluded that GA provided superior solution and gave better results of output signal characteristic such as decreased pick overshoot, rise and settling time.

In this study liquid level control system was conducted using classical and fuzzy PI controller optimized with grey wolf optimization (GWO) algorithm.

## 2. SYSTEM DESCRIPTION

Physical values and parameters, that describe system used in the study are given in Table 1.

*Table 1: System parameters*

|                                  |   |
|----------------------------------|---|
| Pump Flow Constant, $K_p$        | $5.39 \cdot 10^{-6} \text{ m}^3/\text{s/V}$ |
| Out 1 Orifice Diameter, $D_{o1}$ | $0.47625 \cdot 10^{-2} \text{ m}$           |
| Out 2 Orifice Diameter, $D_{o2}$ | $0.47625 \cdot 10^{-2} \text{ m}$           |
| Tank 1 Inside Diameter, $D_1$    | $4.445 \cdot 10^{-2} \text{ m}$             |
| Tank 2 Inside Diameter, $D_2$    | $4.445 \cdot 10^{-2} \text{ m}$             |
| Gravitational constant, $g$      | $9.81 \text{ m/s}^2$                        |

System consists of two identical cylindrical tanks placed one above another, water pump and reservoir. Water from reservoir is pumped vertically through pumping system into water tank in higher position. The

water level of the second tank needs to be controlled. Fig. 1 represents diagram of the used system.

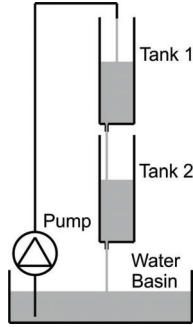


Figure 1: Liquid level system

### 3. SYSTEM MODELLING

#### 3.1. Nonlinear model

System of the study is consisted of two subsystems, tank 1 and tank 2. The input value in tank 1 is pump voltage  $V_p$ , and the output is water level in tank 1,  $H_1$ . The flow into tank 1 can be expressed as

$$Q_{i1} = K_p V_p. \quad (1)$$

The outflow from tank 1 is a product of outflow velocity,  $V_{o1}$  and the cross-sectional opening area of the first tank,  $A_{o1}$ ,

$$Q_{o1} = A_{o1} V_{o1}. \quad (2)$$

Finally, mass balance equation for the first subsystem is

$$A_1 \frac{dH_1}{dt} = Q_{i1} - Q_{o1} = K_p V_p - A_{o1} \sqrt{2gH_1}, \quad (3)$$

where  $A_1$  is cross-sectional area of the first tank. Outflow from the tank 2 is a product of outflow velocity  $V_{o2}$  and the cross-sectional opening area of the second tank  $A_{o2}$ ,

$$Q_{o2} = A_{o2} V_{o2}. \quad (4)$$

The second subsystem mass balance equation is determined as

$$A_2 \frac{dH_2}{dt} = Q_{i2} - Q_{o2} = A_{o1} \sqrt{2gH_1} - A_{o2} \sqrt{2gH_2}. \quad (5)$$

By choosing state variables  $X_1 = H_1$ ,  $X_2 = H_2$ , output variable  $Y = H_2$  and control variable  $U = V_p$  nonlinear state space model is obtained as,

$$\dot{X}_1 = \frac{K_p}{A_1} U - \frac{A_{o1}}{A_1} \sqrt{2gX_1}, \quad (6)$$

$$\dot{X}_2 = \frac{A_{o1}}{A_2} \sqrt{2gX_1} - \frac{A_{o2}}{A_2} \sqrt{2gX_2}, \quad (7)$$

$$Y = X_2. \quad (8)$$

#### 3.2. Linearized model

For a steady state condition it is considered that water level in tank 2 has constant nominal value, and therefore, water level in tank 1 and pump voltage have constant values as well.

$$H_1 = H_{1N}, \quad H_2 = H_{2N}, \quad V_p = V_{pN}. \quad (9)$$

The following step is approximating nonlinear functions (10), (11) using Taylor's series representation at nominal values (9).

$$f_1 = \frac{dH_1}{dt} = \frac{K_p V_p}{A_1} - \frac{A_{o1} \sqrt{2gH_1}}{A_1}, \quad (10)$$

$$f_2 = \frac{dH_2}{dt} = \frac{A_{o1} \sqrt{2gH_1}}{A_2} - \frac{A_{o2} \sqrt{2gH_2}}{A_2}. \quad (11)$$

The result is polynomials of the following form

$$\dot{h}_1 = a_1 h_1 + b_1 v_p, \quad \dot{h}_2 = a_2 h_2 + b_2 h_1. \quad (12)$$

In equations (12) variables  $h_1, h_2, v_p$  represent deviations from a nominal values,

$$h_1 = H_1 - H_{1N}, \quad h_2 = H_2 - H_{2N}, \quad v_p = V_p - V_{pN}, \quad (13)$$

and coefficients  $a_1, a_2, b_1, b_2$  are determined as in the following expressions,

$$a_1 = -\frac{A_{o1} \cdot g}{A_1 \sqrt{2gH_{1N}}}, \quad b_1 = \frac{K_p}{A_1}, \quad (14)$$

$$a_2 = -\frac{A_{o2} \cdot g}{A_2 \sqrt{2gH_{2N}}}, \quad b_2 = \frac{A_{o1} \cdot g}{A_2 \sqrt{2gH_{1N}}}. \quad (15)$$

Thus, taking into account the defined state variables and (13), from (12) follows linear state space model:

$$\dot{x}_1 = a_1 x_1 + b_1 u, \quad (16)$$

$$\dot{x}_2 = a_2 x_2 + b_2 x_1, \quad (17)$$

$$y = x_2. \quad (18)$$

Based on the previous equations, the transfer functions of each subsystem can be easily obtained, which will be discussed in more detail in the next section.

#### 3.3. Identified model

The identification method was used based on the plant's step response. In this study, system transfer function was obtained based on measured input output data using MATLAB 'System Identification Toolbox'. In the Table 2 all nominal values and transfer functions of linearized and identified model, for tank 1 and tank 2 can be found.

Table 2: Nominal values and transfer functions

|                     | Tank 1                                   | Tank 2                                  |
|---------------------|--|---|
| Nominal water level | $H_{1N} = 0.1273$ m                      | $H_{2N} = 0.13$ m                       |
| Linearized model    | $G_1(s) = \frac{0.0034734}{s + 0.07126}$ | $G_2(s) = \frac{0.071258}{s + 0.07051}$ |
| Identified model    | $G_1(s) = \frac{0.002577}{s + 0.04471}$  | $G_2(s) = \frac{0.06278}{s + 0.05793}$  |
| $V_{pN} = 5.32$ V   |  |   |

Figure 2 represents comparison of measured open loop system output signal, with nonlinear, linearized and identified model of the system when deviation from a nominal pump voltage equals  $v_p = 0.3$  V. In order for the results to be observed better, the filtered measured response (labeled as "Experiment") is shown in Fig. 2. The same moving average filter with a span of 100 data points has been used for every measured signal in this paper.

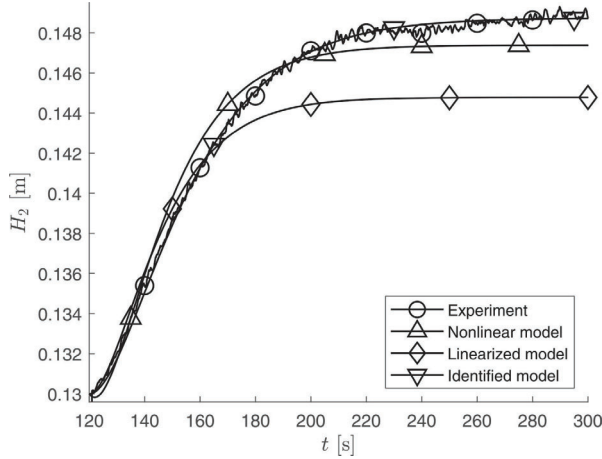


Figure 2: Comparison of measured open loop system output with nonlinear, linearized and identified model

4. CLASSICAL PI CONTROLLER

Block diagram of control system with PID like controller is shown on Fig. 3.

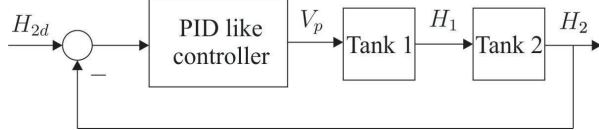


Figure 3: Block diagram of liquid level control system

Controller input is error signal

$$e(t) = H_{2d}(t) - H_2(t) \quad (19)$$

and output is control signal expressed with

$$u(t) = K_p \left( e(t) + \frac{1}{T_I} \int_0^t e(\tau) d\tau \right) = K_p e(t) + K_I e_I(t) \quad (20)$$

PI controller transfer function equals

$$G_{PI}(s) = K_p \left( 1 + \frac{1}{T_I s} \right) \quad (21)$$

Proportional gain and integral time constant are determined by  $K_p$  and  $T_I$ , respectively. Parameters of PID like controllers could be tuned by many different methods. In this research, well known Ziegler-Nichols and Cohen-Coon tuning methods will be applied for comparison with the methods described below.

4.1. Ziegler-Nichols tuning method

Observed system is the second order and stable that implies utilization of ZN open-loop tuning technique [15]. Primarily, step response of the open-loop is obtained.

Table 3: Ziegler-Nichols formula

|     | $K_p$       | $T_I$  | $T_D$  |
|-----|-------------|--------|--------|
| P   | $T / KL$    | -      | -      |
| PI  | $0.9T / KL$ | $3.3L$ | -      |
| PID | $1.2T / KL$ | $2L$   | $0.5L$ |

Further, the response is used for finding parameters necessary for tuning, as dead time  $L$ , time constant  $T$  and process gain  $K$ , as it is shown on Fig. 4. Table 3 gives insight in ZN formula for determination P, PI and PID parameters.

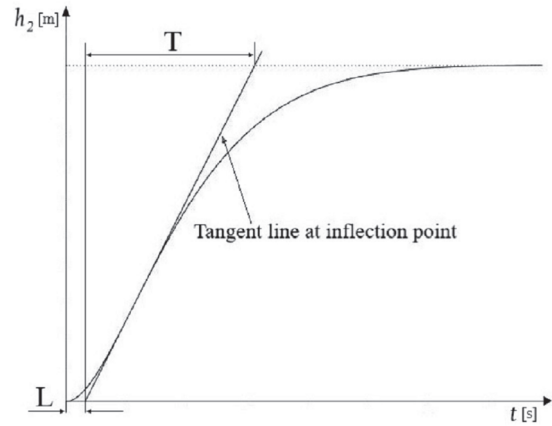


Figure 4: Tangent method

4.2. Cohen-Coon tuning method

For CC tuning method typical process reaction curve was used in the same way as in Fig. 5.

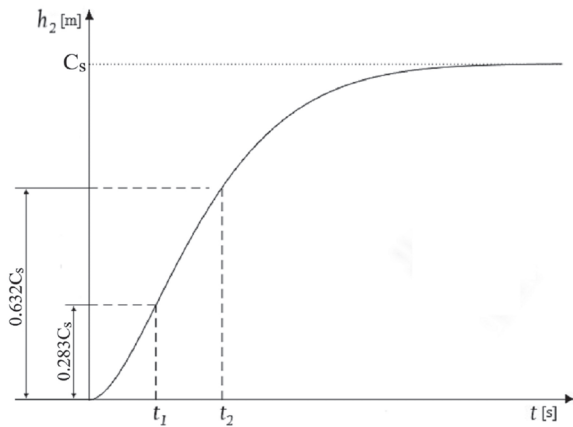


Figure 5: Process reaction curve

CC tuning formula [14] is given in Table 4.

Table 4: Cohen-Coon formula

|     | $K_p$  | $T_I$   | $T_D$                                     |
|-----|--|---|---|
| P   | $\frac{\theta}{K\tau} \left( 1 + \frac{\tau}{3\theta} \right)$           | -   | -   |
| PI  | $\frac{\theta}{K\tau} \left( 0.9 + \frac{\tau}{12\theta} \right)$        | $\frac{\tau \left( 30 + \frac{3\tau}{\theta} \right)}{9 + \frac{20\tau}{\theta}}$ | -   |
| PID | $\frac{\theta}{K\tau} \left( \frac{4}{3} + \frac{\tau}{4\theta} \right)$ | $\frac{\tau \left( 32 + \frac{6\tau}{\theta} \right)}{13 + \frac{8\tau}{\theta}}$ | $\frac{4\tau}{11 + \frac{2\tau}{\theta}}$ |

Values from Table 4 are

$$\theta = \frac{3}{2}(t_2 - t_1), \quad (22)$$

$$\tau = t_2 - \theta. \quad (23)$$

Finally, the calculated values for identified model from Table 2 are given in Table 5.

Table 5: Parameters for PI controller

|    | Ziegler-Nichols |       |       | Cohen-Coon |        |       |
|----|-----------------|-------|-------|------------|--------|-------|
|    | $K_p$           | $T_I$ | $T_D$ | $K_p$      | $T_I$  | $T_D$ |
| PI | 140.4           | 18.19 | -     | 48.989     | 20.226 | -     |

5. FUZZY PI LOGIC CONTROLLER

Fuzzy logic controllers are designed in order to avoid using complicated mathematical models that are crucial in conventional control. Fuzzy logic is inspired by human intelligence and knowledge where defining value of variable is not numerically strict and precise. Input sets in fuzzy controller are linguistic variables. Values that can be used in fuzzy rules for fuzzy PI controller as inputs are error (19) and integral of error, that from (20) can be defined as

$$e_I(t) = \int_0^t e(\tau) d\tau . \tag{24}$$

Membership functions for error, derivative of error and control are defined on the normalized domain [-1, 1]. Input and output membership functions and depicted in Fig. 6 and Fig. 7, respectively.

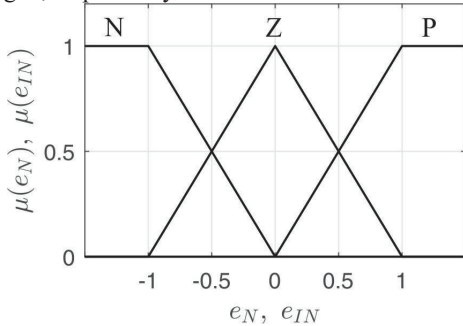


Figure 6: Input membership functions

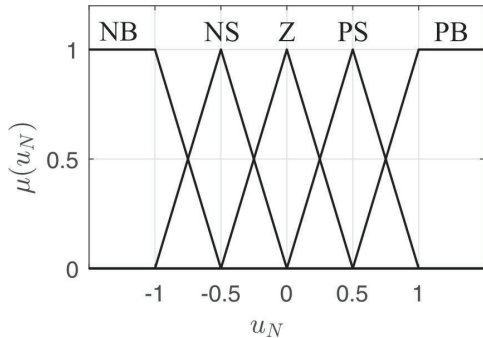


Figure 7: Output membership functions

Rules for PI controller are given in Table 6. Linguistic values from Table 6 have usual meaning NB – negative big, PB – positive big, NS – negative small, PS – positive small, Z – zero.

Table 6: Rules for PI controller

| $e_N \setminus e_{IN}$ | N  | Z  | P  |
|------------------------|----|----|----|
| N                      | NB | NS | Z  |
| Z                      | NS | Z  | PS |
| P                      | Z  | PS | PB |

Centre of area (COA) is used as defuzzification method. Fig. 8 shows the fuzzy PI controller that will be used later in this paper. It is important to realize that the scaling factors  $K_{pf}$ ,  $K_{if}$  and  $K_f$  are not the only parameters that

can be tuned to improve the performance of the fuzzy control system. Sometimes, what is needed is a more careful consideration of how to specify better membership functions or additional rules.

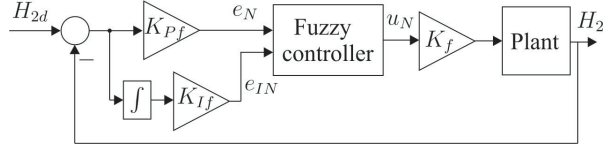


Figure 8: Fuzzy PI controller for liquid level system

The problem with this could be that there are too many parameters to tune (e.g., membership function shapes, positioning, type and number of rules) and often there is no clear connection between design objectives (e.g., smaller overshoot) and method that should be used to tune parameters.

Increasing scaling factors  $K_{pf}$  will often make the system respond faster. Increasing  $K_{if}$  leads to reducing error but increases overshoot. In addition to these two parameters, the fuzzy PI controller has one more parameter  $K_f$  that provides the possibility of finer settings.

6. THE GREY WOLF OPTIMIZER

The GWO algorithm represents type of metaheuristic optimization technique whose characteristic such as simplicity, applicability to different types of a problem and derivation-free mechanisms allow application on constrained and unconstrained problems of nonlinear systems. GWO algorithm was first proposed in [17]. Inspiration for developing this optimization algorithm was found in hierarchical organization of a pack of grey wolves and their hunting way. Pack of grey wolves can be divided into four hierarchical levels,  $\alpha$ ,  $\beta$ ,  $\delta$ ,  $\omega$  where  $\alpha$  represents the most dominant wolves that lead the pack. Next,  $\beta$  level is consisted of subordinate wolves that help alpha in making decisions and replace alpha in case of dead or oldness. The  $\omega$  level wolves have to submit to the will of all others more dominant pack members, and wolves from  $\delta$  level submit to wolves from first two levels and dominates over omega wolves. Capturing prey takes place through several phases. In the first phase wolves that participate in hunt encircle prey. Grey wolf can change its position depending on position of the prey in any random location. Mathematical description of this phase is given by the following equations

$$\mathbf{D} = |\mathbf{C} \cdot \mathbf{X}_p(t) - \mathbf{X}(t)|, \tag{25}$$

$$\mathbf{X}(t+1) = \mathbf{X}_p(t) - \mathbf{A} \cdot \mathbf{D}. \tag{26}$$

Vector  $\mathbf{X}_p$  indicates the position vector of the prey,  $\mathbf{X}$  is the position vector of a wolf and  $t$  indicates the current iteration. Equations for calculating coefficient vectors  $\mathbf{A}$  and  $\mathbf{C}$  are

$$\mathbf{A} = 2a \cdot \mathbf{r}_1 - a, \tag{27}$$

$$\mathbf{C} = 2 \cdot \mathbf{r}_2. \tag{28}$$

In equations (27) and (28) components of vector  $\mathbf{a}$  are linearly decreasing from 2 to 0 during the iterations and vectors  $\mathbf{r}_1$  and  $\mathbf{r}_2$  are random vectors from [0,1]. Following phase is hunting. Assuming that alpha, beta and delta participate in hunting and that alpha leads the hunt it is possible to suppose that they know potential location of

the prey, especially alpha. Three best solutions of potential location of the prey are saved and rest of the search agents are obligated to change their positions according to position of agent that is the nearest to the prey. This phase can be described mathematically by following equations,

$$\mathbf{D}_\alpha = |\mathbf{C}_1 \cdot \mathbf{X}_\alpha - \mathbf{X}|, \quad (29)$$

$$\mathbf{D}_\beta = |\mathbf{C}_2 \cdot \mathbf{X}_\beta - \mathbf{X}|, \quad (30)$$

$$\mathbf{D}_\delta = |\mathbf{C}_3 \cdot \mathbf{X}_\delta - \mathbf{X}|, \quad (31)$$

$$\mathbf{X}_1 = \mathbf{X}_\alpha - \mathbf{A}_1(\mathbf{D}_\alpha), \quad (32)$$

$$\mathbf{X}_2 = \mathbf{X}_\beta - \mathbf{A}_2(\mathbf{D}_\beta), \quad (33)$$

$$\mathbf{X}_3 = \mathbf{X}_\delta - \mathbf{A}_3(\mathbf{D}_\delta), \quad (34)$$

$$\mathbf{X}(t+1) = \frac{\mathbf{X}_1 + \mathbf{X}_2 + \mathbf{X}_3}{3}. \quad (35)$$

When the prey stops moving grey wolves begin attacking and then starts exploitation phase. Decreasing the value of  $\mathbf{a}$  from 2 to 0 is mathematical approach related to lowering the distance between grey wolves and prey. It is possible to conclude that vector  $\mathbf{A}$  can be any value in  $[-2\mathbf{a}, 2\mathbf{a}]$  and when  $\mathbf{A}$  takes value in  $[-1, 1]$  search agent can change its position into any position between position of the prey and its momentary position. In other words, when  $|\mathbf{A}| < 1$  wolves start to attack. The last phase is exploration phase which implies searching for prey. When  $|\mathbf{A}| > 1$  grey wolves are forced to search for the prey and then wolves split up in order to complete the task which mathematically means that  $\mathbf{A}$  consists of random values. Also, vector  $\mathbf{C}$  of random values is used to provide weights for prey in order to point up exploration process during all iterations.

In the proposed GWO algorithm the total number of iterations is set to 30 while the population is set to 20. The number of iterations and the population size are determined based on a series of experiments with different values. In this optimization method one agent represents one potential optimal controller. Additional optimization requirement is that the value of control signal should be in the allowable range of 0-12V. The integral of squared

errors (ISE) is taken as an objective function and it can be calculated as

$$J = \int_0^t (H_{2d}(t) - H_2(t))^2 dt. \quad (36)$$

### 6.1. Optimization of classical PI controller

In order to achieve better performance of the plant a more adequate control signal, relative to classical PI controllers, is achieved by adjusting the parameters of the controller gains. The mentioned parameters are all coded into one wolf, per say one agent that is presented with a vector which has two parameters ( $K_p$  and  $T_i$ ) in case of optimized classical PI controller. As a result of optimization, the following values were obtained.

Table 7: Parameters for optimized classical PI controller

| PI GWO |        |
|--------|--------|
| $K_p$  | $T_i$  |
| 298.45 | 294.59 |

### 6.2. Optimization of fuzzy PI controller

When it comes to optimization of fuzzy PI controller, there are three parameters which are all coded into one wolf. Optimized parameters  $K_{pf}$ ,  $K_{if}$  and  $K_f$  from Fig. 8 are given in Table 8.

Table 8: Parameters for optimized fuzzy PI

| Fuzzy PI GWO |          |        |
|--------------|----------|--------|
| $K_{pf}$     | $K_{if}$ | $K_f$  |
| 200          | 0.17832  | 10.481 |

## 7. SIMULATION RESULTS

In this section, the simulations show the behavior of the plant controlled by different controllers that were designed in the previous sections. Simulation results for change in level  $H_2$  controlled by four different PI controllers are given in Fig. 9. Change in control signals for all implemented controllers is shown in Fig. 10.

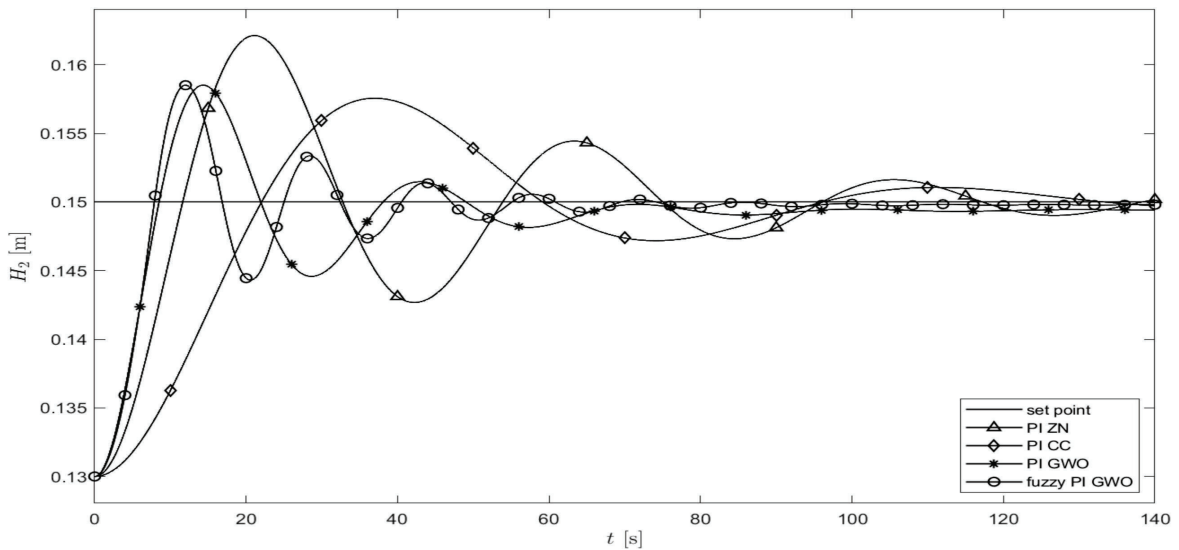


Figure 9: Simulation results of level  $H_2$  controlled by different PI controllers

According to the values from Table 9, it can be expected that optimized fuzzy PI controller achieve the best result on the experiment as its ISE was the lowest. Numerical ISE values from Table 9, were calculated based on the operation of the system for 200 seconds, while in order to achieve better visibility, only the first 140 seconds are shown in the figures. The same goes for Table 10 and

experimental results. Comparative display of overshoot, rise time and settling time is given in the same Table 9.

Table 9: Simulation step response characteristics

|            | PI ZN   | PI CC   | PI GWO  | fuzzy PI GWO |
|------------|---------|---------|---------|--------------|
| ISE        | 0.00462 | 0.00513 | 0.00235 | 0.00215      |
| Overs.[%]  | 60.6    | 37.8    | 42.5    | 42.5         |
| Rise t.[s] | 11.6    | 22.0    | 8.5     | 7.9          |
| Set. t.[s] | 115.1   | 112.0   | 64.0    | 52.6         |

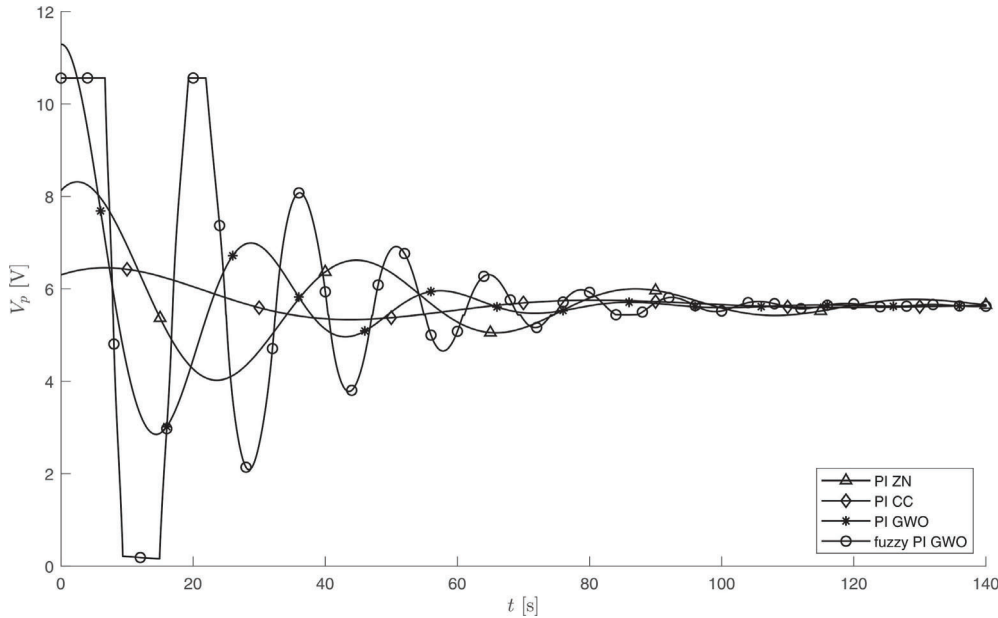


Figure 10: Control signals for PI controllers obtained by simulation

8. EXPERIMENTAL RESULTS

This section presents the results of the experiments performed for the PI controller parameters determined in

the previous sections. Change in level  $H_2$  controlled by all four PI controllers is shown in Fig. 11.

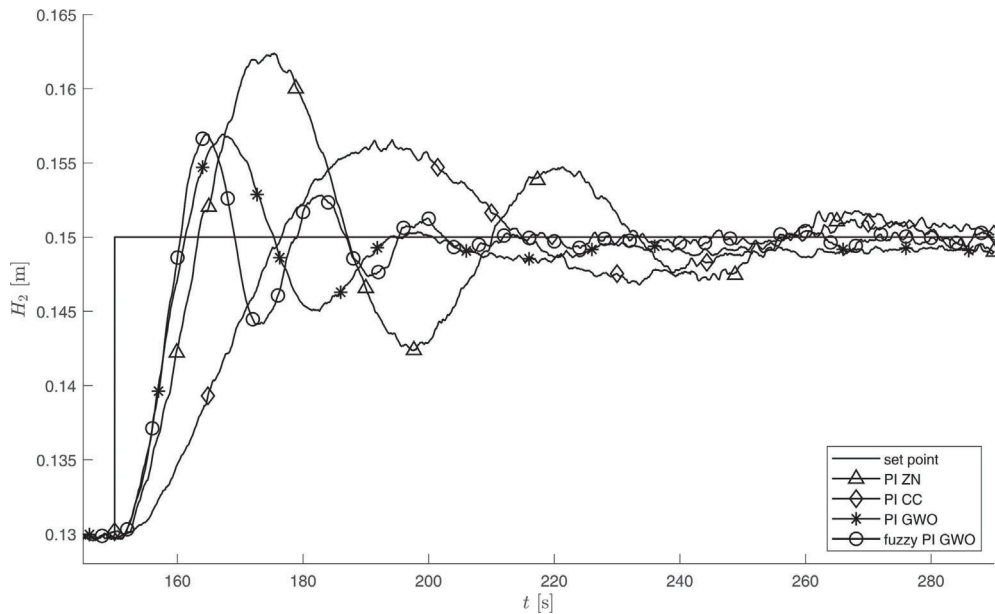


Figure 11: Experimental results of level  $H_2$  controlled by different PI controllers

To explicitly see the improvement caused by the optimization, the numerical values of an ISE calculated using (36), are given. Mentioned values for four different

controllers (PI ZN, PI CC, PI GWO, fuzzy PI GWO) are given in Table 10. Step response characteristics are in the

similar relationship to that previously given for simulation responses and are also shown in Table 10.

Table 10: Experimental step response characteristics

|             | PI ZN   | PI CC   | PI GWO  | fuzzy PI GWO |
|-------------|---------|---------|---------|--------------|
| ISE         | 0.00527 | 0.00547 | 0.00269 | 0.00247      |
| Overs.[%]   | 62      | 33      | 34.7    | 34.7         |
| Rise t. [s] | 13.3    | 26.6    | 11.2    | 10.5         |
| Set. t. [s] | 129     | 129     | 75.1    | 50.4         |

Taking into account minimum integral of squared errors as the criterion for comparison, the results show that the lowest value is obtained when using an optimized fuzzy PI controller (fuzzy PI GWO) and the highest when using a Ziegler Nichols PI controller (PI ZN). According to this criterion the optimized classical PI controller (PI GWO) performed worse than the optimized fuzzy PI controller (fuzzy PI GWO).

A comparison of control signals obtained by using different PI controllers is given in Fig. 12.

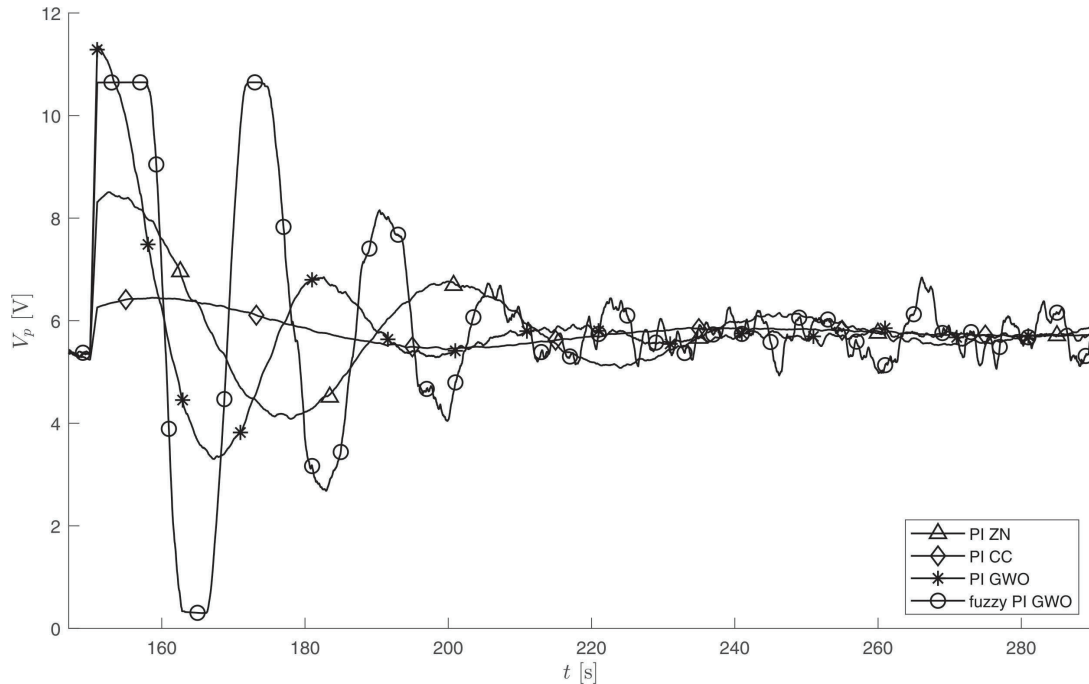


Figure 12: Control signals for PI controllers obtained by experiment

## 9. CONCLUSION

This research concerned optimization of classical and fuzzy controllers using GWO algorithm and its impact on the liquid level control of coupled tanks as one of the current problems in industry.

Firstly, analytical nonlinear, linearized and identified model were compared to obtained experimental results for noncontrolled system. It was shown that identified model was suitable for describing real system.

This paper covers process control using PI controllers. GWO algorithm was used for optimization of classical and fuzzy PI controller. In order to verify effectiveness of their performance a comparison was made with two different classical tuning methods.

All of the designed controllers were tested in simulation and experimentally and all obtained results were analyzed and compared to each other using minimum integral of squared errors criteria. Experiment confirmed expectations from simulations, but ISE had higher values in the experiment. Nevertheless, the difference between values was not drastic.

The best result in general was obtained by applying optimized fuzzy PI controller, according to the mentioned criteria. Also, its result achieved better step response characteristics that is an argument more for the application of this type of controller in liquid level process control.

## ACKNOWLEDGEMENTS

This work was financially supported by the Ministry of Education, Science and Technological Development of the Serbian Government, under contract 451-03-9/2021-14/200105, Grant TR-35029 (2021) and Grant TR-35004 (2021).

## REFERENCES

- [1] J.G. Ziegler and N.B. Nichols, "Optimal Settings for Automatic Controllers," *Trans. ASME*, Vol. 64, pp. 759-768, (1942)
- [2] G.H. Cohen and G.A. Coon, "Theoretical Consideration of Retarded Control," *Trans. ASME*, Vol. 75, p. 827, (1953)
- [3] N.H. Sabri, N. H. A. Rani, M. I. Kamarulzaman and M. Arbanah, "Optimal PI Tuning Rules for Liquid Flow Process Control System Using Cohen-Coon's (C-C), Ziegler-Nichols's and Takahashi's Tuning Method," *MJIT*, Vol. 4, pp. 1-6, (2020)
- [4] A. Kumar, R. Morya and M. Vashishath, "Performance Comparison Between Various Tuning Strategies: Ciancone, Cohen Coon & Ziegler-Nicholas Tuning Methods," *IJCT*, Vol. 5, pp.60-68, (2013)
- [5] M.T. Alam, Z. H. Khan, P. Charan and M.A. Ansari, "Level Control of Coupled Tanks System using Feedback

- Linearization Control Theory," IJSRD, Vol.3, pp. 60-63, (2015)
- [6] L.A.Zadeh, "Fuzzy sets," IC, vol.8, pp. 338-353, (1965)
- [7] M. Alotaibi, M.Balabid, W. Albeladi and F. Alharbi "Implementation of Liquid Level Control System," 2019 IEEE International Conference on Automatic Control and Intelligent Systems, pp. 311-314, (2019)
- [8] O.H. Adigun, "Decentralized Fuzzy-PID Based Control Model for a Multivariable Liquid Level System," JACET, Vol. 4, pp. 247-254, (2018)
- [9] V. Kumar, K.P.S. Rana and V. Gupta, "Real-Time Performance Evaluation of a Fuzzy PI + Fuzzy PD Controller for Liquid-Level Process," IJICS, Vol. 13, pp. 89-96, (2008)
- [10] J.B. Gomm, J.T. Evans and D. Williams, "Development and Performance of a Neural-Network predictive controller," CEP, Vol. 5, pp. 49-59, (1997)
- [11] S. Rajan and S. Sahadev, "Performance Improvement of Fuzzy Logic Controller using Neural Network", Procedia Technology 24, pp. 704-714, (2016)
- [12] N. Katal, P. Kumar and S. Narayan, "Optimal PID Controller for Coupled-Tank Liquid-Level Control System using Bat Algorithm," 2014 International Conference on Power, Control and Embedded Systems, pp. 1-4, (2014)
- [13] R. Jovanovic, V. Zaric, M. Vesovic and L. Laban, "Modeling and Control on the Takagi-Sugeno Fuzzy Model Using the Whale Optimization Algorithm", 64 National Conference on Electronics, Telecommunication, Computing, Automatic Control and Nuclear Engineering, pp. 197-202, (2020)
- [14] P. Srinivas, K.V. Lakshmi and V.N. Kumar, "A Comparison of PID Controller Tuning Methods for Three Tank Level Process," IJAREEIE, vol. 3, pp.6810-6820, (2014)
- [15] A.G. Brito "On the Misunderstanding of the Ziegler-Nichols's Formulae Usage," JAS, vol. 6, pp. 142-147, (2019)
- [16] R. Jovanovic, "Fuzzy logic, modelling and control," Akademska misao, Belgrade (Serbia), (2020) (in Serbian)
- [17] S. Mirjalili, S.M. Mirjalili and A. Lewis, "Grey Wolf Optimizer," AES, vol. 69, pp. 46-61, (2014)

# System Identification Using Hammerstein-Wiener Model with Orthogonal Polynomials

Anđela D. Đorđević<sup>1\*</sup>, Saša S. Nikolić<sup>1</sup>, Marko T. Milojković<sup>1</sup>, Miodrag D. Spasić<sup>1</sup>, Staniša Lj. Perić<sup>1</sup>  
<sup>1</sup>Faculty of Electronic Engineering/Department of Control Systems, University of Niš, Niš, Serbia

*Abstract: Hammerstein-Wiener systems can be described with a structure consisting of three cascade blocks, two of which represent static nonlinearities with a linear dynamical block laying between them. Some of the common linear model structures include rational transfer function, FIR, ARX, ARMAX, Box-Jenkins and Output-Error model structure. In this article a new improvement is proposed, which is consisted in the basic structure of HW models with a new class of the orthogonal polynomials applied. The newly proposed structure was used to identify the hydraulic system.*

**Keywords: Hammerstein-Wiener models, orthogonal polynomials, system identification, hydraulic multitank system**

## 1. INTRODUCTION

Throughout the years, Hammerstein-Wiener models have proved to be an adequate tool for nonlinear systems representation. They have a wide range application: from the use for control systems to medical purposes. In the last years, some of the examples of Hammerstein-Wiener models application can be found in [1] where Hammerstein-Wiener model was used for identification of precision motion stage, and in [2] where the application for robotic bone biopsy procedures has been proposed.

Hammerstein-Wiener systems can be described with a structure consisting of three cascade blocks, two of which represent static nonlinearities with a linear dynamical block laying between them. The first and the last blocks are usually referred to as input and output nonlinearity, respectively. Some of the common linear model structures are mentioned in [3] and include rational transfer function, FIR, ARX, ARMAX (also used in [4, 5]) and Box-Jenkins model structure (used in [6]) and Output-Error model. The nonlinearity blocks can be continuous and discontinuous (such as death-zone, saturation [1], etc.) [3]. Continuous nonlinearities can be represented using function expansion, with polynomial representation as a simple case [3, 5]. Splines can also be used for continuous nonlinearity representation [6]. The application of neural networks has also been explored by some authors. Authors in [7] used two independent single-hidden layer feedforward networks, whose parameters were identified by extreme learning machines (ELM) algorithm. Commonly, the output nonlinearity is supposed to be invertible [6, 9, 11]. However, this is not always the case. For example, the work of Wills *et al.* considered a Hammerstein-Wiener system with no such constraint if the derivatives of the input and the output nonlinearity function with respect to their parameter vectors exist [10].

Identification algorithms have been proposed for Hammerstein-Wiener model estimation by many authors, some of which are presented in [3, 4, 6-12]. Bai proposed an identification algorithm which is divided in two stages: recursively calculating the least square estimate of the parameter vector and singular value decomposition of fixed size matrices [8]. The Hammerstein-Wiener structure studied in the previously mentioned paper [8], was

reformulated in [9]. In [9], the authors applied and compared the performances of over-parameterization and iterative approach for the identification of the proposed model. A blind approach, where the structure of the input nonlinearity does not necessarily have to be known, is presented in [11]. Guo introduces adaptive recursive pseudo-linear regression method where smoothing techniques are employed in [3]. Relaxation iteration scheme was proposed and studied as an optimization method for SISO Hammerstein-Wiener model estimation in [6]. Maximum likelihood approach with the expectation-minimization algorithm employed is suggested for very general model estimation by Schoukens *et al.* in [10]. For Hammerstein-Wiener ARMAX models, Wang D. *et al.* developed an extended stochastic gradient algorithm [4]. Wang Y. *et al.* proposed two algorithms: recursive generalized extended least squares and generalized extended stochastic gradient algorithm [12]. A forgetting factor was introduced for additional optimization of the second algorithm in [12]. Authors in [3, 4, 12] achieved the acceleration of convergence by using the forgetting factor.

An interesting approach can be found in [13], where Aljamaan *et al.* proposed using Hermite polynomials to represent nonlinearity, and global orthogonal basis functions for the representation of linear block of a Wiener system.

In this paper, the authors consider the application of orthogonal polynomials of Legendre type [14-15] for the representation of input and output nonlinearities of a Hammerstein-Wiener system. In [16, 17] authors proposed a new class of almost orthogonal polynomials with application in modeling of dynamical systems. Papers [18-21] presented some possibility applications in orthogonal endocrine adaptive neuro-fuzzy systems. Also, authors in [22-27] proposed a new classes of quasi-orthogonal polynomials and their applications in modeling, neural networks, sliding mode control and control of dynamical systems. The proposed structure of HW is used to identify a hydraulic multitank system.

This paper is organized as follows. In Section 2 the basic structure of Hammerstein-Wiener models is described. Section 3 gives a short mathematical background of orthogonal, almost orthogonal and quasi-

\*Corresponding author: Aleksandra Medvedeva 14, 18000 Nis, Serbia, andjela.djordjevic@elfak.ni.ac.rs

orthogonal polynomials of Legendre type. The description of multitank system is given in Section 4, while simulation results are presented in Section 5. The last section consists of concluding remarks.

## 2. HAMMERSTEIN-WIENER MODEL

As it has been mentioned previously, Hammerstein-Wiener model structure is formed of two nonlinear blocks and a linear block between them. This structure is a combination of Hammerstein (Fig. 1. a) and Wiener model structures (Fig. 1. b). Hammerstein model is presented using input nonlinearity and then a linear model of the system, while Wiener model consists of linear block followed by output nonlinearity. Depending on the way this models are combined, Hammerstein-Wiener (HW) or Wiener-Hammerstein (WH) structure can be formed. HW model structure is presented in Fig. 1. c) and Fig. 2, while WH structure is presented in Fig. 1. d).

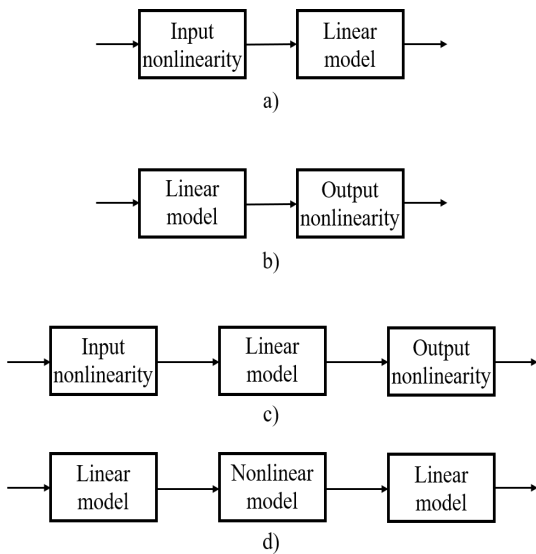


Figure 1: a) Hammerstein model structure; b) Wiener model; c) Hammerstein-Wiener model; d) Wiener-Hammerstein model.

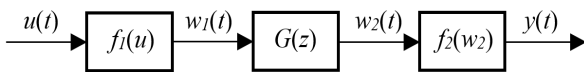


Figure 2: HW model structure

In Fig. 2.  $u(t)$  is denoting the system input and  $y(t)$  the output. Nonlinear functions  $f_1$  and  $f_2$  are representing the input and the output nonlinearity, respectively. The linear block can be described using various model structures [3]. The output signal of the structure presented in Fig. 2 can be determined using equations (1) to (5).

$$w_1(t) = f_1(u(t)) \quad (1)$$

$$w_2(t) = G(z)f_1(u(t)) \quad (2)$$

$$y(t) = f_2(w_2(t)) = f_2(G(z)f_1(u(t))) \quad (3)$$

One of the commonly used models for the representation of the linear block is the ARMAX model (Fig. 3.) [3].

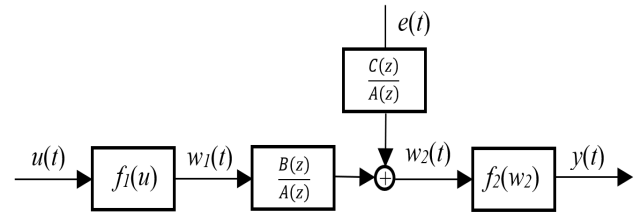


Figure 3: HW ARMAX system

The linear part of the system can be described with the following equation [3, 5]:

$$w_2(t) = \frac{B(z)}{A(z)} w_1(t) + \frac{C(z)}{A(z)} e(t) \quad (4)$$

where  $e(t)$  represents the disturbance term, and  $A(z)$ ,  $B(z)$  and  $C(z)$  are polynomials of order  $n_a$ ,  $n_b$  and  $n_c$ , respectively [3, 5]:

$$A(z) = 1 + \sum_{i=1}^{n_a} a_i z^{-i} \quad (5)$$

$$C(z) = 1 + \sum_{i=1}^{n_c} c_i z^{-i} \quad (6)$$

$$B(z) = \sum_{i=1}^{n_b} b_i z^{-i} \quad (7)$$

Substituting (1) and (4) in (3), the term for the output signal is derived:

$$y(t) = f_2 \left( \frac{B(z)}{A(z)} f_1(u(t)) + \frac{C(z)}{A(z)} e(t) \right) \quad (8)$$

The influence of measurement noise  $\varepsilon$  on the output signal can also be considered [3, 10, 12]:

$$y(t) = f_2(w_2(t)) + \varepsilon(t) \quad (9)$$

In this paper, Output-Error (OE) model has been used for the parametrization of the linear part of the system [3].

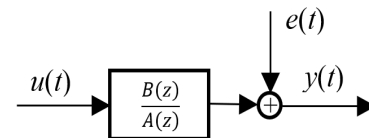


Figure 4: Output-Error model structure

OE model structure can be described using following equation:

$$y(t) = \frac{B(z)}{A(z)} u(t - n_k) + e(t) \quad (10)$$

where  $n_k$  is an input delay.

The advantages of the Wiener system with orthogonal Hermite polynomials used for nonlinearity representation have been presented in the work by Aljamaan et al. [13]. In this paper a class of orthogonal

polynomials of Legendre type is proposed for the nonlinearity functions’  $f_1$  and  $f_2$  representation.

### 3. ORTHOGONAL POLYNOMIALS

Authors of this article developed several new types of orthogonality. In this paper we give mathematical background for almost and quasi-orthogonal polynomials.

Almost orthogonal system [14, 15, 28-30] is a sequence of polynomials  $\{P_n^{(\varepsilon)}(x)\}$  such that:

$$\begin{aligned} (P_n^{(\varepsilon)}(x), P_m^{(\varepsilon)}(x)) &= \int_a^b P_n^{(\varepsilon)}(x) P_m^{(\varepsilon)}(x) w(x) dx = \\ &= \begin{cases} \varepsilon, & n \neq m \\ \|P_n^{(\varepsilon)}\|^2, & n = m \end{cases} \end{aligned} \quad (11)$$

where  $\varepsilon$  is a very small positive real number ( $0 < \varepsilon \ll 1$ ).

$\lim_{\varepsilon \rightarrow 0} P_n^{(\varepsilon)}(x) = P_n(x)$ , i.e., when  $\varepsilon$  strives to zero, sequence of almost orthogonal polynomials becomes a sequence of orthogonal polynomials. We should also notice that because of the presence of additional  $\varepsilon$ , the property of distributivity of inner product no longer applies. Because of that, majority of rules that apply to the classical orthogonal polynomials, do not apply to the almost orthogonal polynomials.

Since monic polynomials  $\{P_k^{(\varepsilon)}(x)\}_{k=0}^n$  form basis in the space of polynomials with order not greater than  $n$ , the following two relations, which give the connection between orthogonal and almost orthogonal polynomials, are valid [14, 15]:

$$P_n^{(\varepsilon)}(x) = P_n(x) + \sum_{k=0}^{n-1} \frac{b_k^{(n)}(\varepsilon)}{\|P_k\|^2} P_k(x), \quad (12)$$

$$P_n(x) = \sum_{k=0}^n c_k^{(n)}(\varepsilon) P_k^{(\varepsilon)}(x) \quad (c_n^{(n)} = 1) \quad (13)$$

Coefficients  $b_j^{(n)}$  can be calculated as:

$$b_j^{(n)}(\varepsilon) = \varepsilon_n \sum_{i=0}^j c_i^{(j)}(\varepsilon) \quad (j = 0, 1, \dots, n-1) (\forall n \in N_0), \quad (14)$$

and they do not depend on  $n$ .

An example of sequence (first three members) of almost orthogonal polynomials is (almost orthogonal Legendre monic polynomials  $\{P_n^{(\varepsilon)}(x)\}$  derived from shifted monic Legendre polynomials orthogonal over interval  $(0, 1)$  with weight function  $w(x) = 1$ ):

$$\begin{aligned} P_0^{(\varepsilon)} &= 1, P_1^{(\varepsilon)} = 2x - (1 - 2\varepsilon), \\ P_2^{(\varepsilon)} &= 6x^2 - 6(1 - 12\varepsilon + 12\varepsilon^2)x + (1 - 30\varepsilon + 36\varepsilon^2), \dots \end{aligned} \quad (15)$$

Now, we give a short mathematical background for quasi-orthogonal polynomials of Legendre type.

Concept of quasi-orthogonality was introduced in [30] as a mathematical tool for solving problem of moments in mechanics. Quasi-orthogonal functions, and,

especially, quasi-orthogonal polynomials, were later explored in several papers [20, 22, 23, 27, 29, 32].

Quasi-orthogonal system is a sequence of polynomials  $\{P_n^k(x)\}$  such that:

$$\begin{aligned} (P_n^k(x), P_m^k(x)) &= \int_a^b P_n^k(x) P_m^k(x) w(x) dx = \\ &= \begin{cases} 0, & 0 \leq m \leq n - k - 1 \\ N_{n,m}^k \neq 0, & n \geq k + 1 \end{cases} \end{aligned} \quad (16)$$

where  $k$  represents the order of quasi-orthogonality,  $a$  and  $b$  are the boundaries of quasi-orthogonality interval, and  $w(x)$  is the weight function.

Complete mathematical background for quasi-orthogonal polynomials can be found in [23, 27].

An example of sequence (first three members) of Legendre first order ( $k=1$ ) quasi-orthogonal polynomials are given as:

$$\begin{aligned} P_1^1(x) &= -x + 1, \\ P_2^1(x) &= -2x^2 + 3x - 1, \\ P_3^1(x) &= -5x^3 + 10x^2 - 6x + 1, \dots \end{aligned} \quad (17)$$

For the purposes of this paper, functions have been performed as ( $e^{-t} = x$ ):

$$P_1^{(\varepsilon)}(t)^{-1} = \frac{1}{2e^{-t} - (1 - 2\varepsilon)}, \quad \text{and} \quad P_1^1(t)^{-1} = \frac{1}{-e^{-t} + 1}.$$

### 4. MULTITANK SYSTEM – DESCRIPTION

For the purpose of analysis of HW and orthogonal HW models, we used a multitank system shown in Fig. 5. The multitank system [33] comprises a number of separate tanks fitted with drain valves. The separate tank mounted in the base of the set-up acts as a water reservoir for the system. Some of the tanks have a constant cross section, while others are spherical or conical, and so have a variable cross section. This creates the main nonlinearities of the system. A variable speed pump is used to fill the upper tank. The liquid flows out of the tanks due to gravity. The tank valves act as flow resistors. The area ratio of the valves is controlled and can be used to vary the outflow characteristic. Each tank is equipped with a level sensor based on hydraulic pressure measurement.

The multitank system relates to liquid level control problems commonly occurring in industrial storage tanks. For example, steel producing companies around the world have repeatedly confirmed that substantial benefits are gained from accurate mould level control in continuous bloom casting. Mould level oscillations tend to stir foreign particles and flux powder into molten metal, resulting in surface defects in the final product.

The multitank system given in Fig. 5. can be described using the well-known “mass balance” equations:

$$\begin{aligned}\frac{dH_1}{dt} &= \frac{1}{\beta_1(H_1)}q - \frac{1}{\beta_1(H_1)}C_1H_1^{\alpha_1} \\ \frac{dH_2}{dt} &= \frac{1}{\beta_2(H_2)}C_1H_1^{\alpha_1} - \frac{1}{\beta_2(H_2)}C_2H_2^{\alpha_2} \\ \frac{dH_3}{dt} &= \frac{1}{\beta_3(H_3)}C_2H_2^{\alpha_2} - \frac{1}{\beta_3(H_3)}C_3H_3^{\alpha_3}\end{aligned}\quad (18)$$

where  $q$  represents the inflow to the upper tank,  $H_i$  is the fluid level in the  $i$ -th tank ( $i=1, 2, 3$ ),  $C_i$  is the resistance of the output orifice of  $i$ -th tank,  $\alpha_i$  represents the flow coefficient for the  $i$ -th tank.  $\beta_1(H_1)$  represents the cross sectional area of  $i$ -th tank at the level  $H_i$ . These values for the single tanks are the following:  $\beta_1(H_1) = aw$  is the constant cross sectional area of the upper tank;  $\beta_2(H_2) = cw + \frac{H_2}{H_{2\max}}bw$  is the variable cross sectional area for the middle tank, and  $\beta_3(H_3) = w\sqrt{R^2 - (R - H_3)^2}$  is the variable cross sectional area of the lower tank.

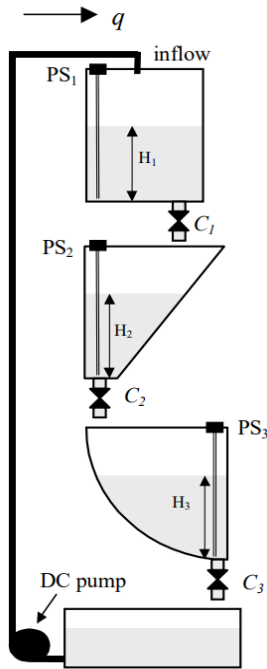


Figure 5. The multitank system by Inteco

The specified parameter values are the following:

$a = 0.25m$ ,  $b = 0.345m$ ,  $c = 0.1m$ ,  $w = 0.035m$ ,  $R = 0.364m$  and  $H_{1\max} = H_{2\max} = H_{3\max} = 0.35m$ .

Rewrite the right sides of (19) in the form  $F(x, q) = [F_1, F_2, F_3]$ , where:

$$\begin{aligned}F_1(q, H_1) &= \frac{1}{\beta_1(H_1)}q - \frac{1}{\beta_1(H_1)}C_1H_1^{\alpha_1} \\ F_2(H_1, H_2) &= \frac{1}{\beta_2(H_2)}C_1H_1^{\alpha_1} - \frac{1}{\beta_2(H_2)}C_2H_2^{\alpha_2} \\ F_3(H_2, H_3) &= \frac{1}{\beta_3(H_3)}C_2H_2^{\alpha_2} - \frac{1}{\beta_3(H_3)}C_3H_3^{\alpha_3}\end{aligned}\quad (19)$$

For the model (19), for fixed  $q=q_0$  we can define an equilibrium state (steady-state points) given by  $q_0 = C_1H_{10}^{\alpha_1} = C_2H_{20}^{\alpha_2} = C_3H_{30}^{\alpha_3}$ .

The linearized model is obtained by the Taylor expansion of (19) around the assumed equilibrium state:

$$\frac{dh}{dt} = J_H h + J_q u \quad (20)$$

where:  $h = H - H_0$  is the modified state vector (deviation from the equilibrium state  $H_0$ ),  $u = q - q_0$  is deviation of the control, relative to  $q_0$ ,  $J_p$  and  $J_q$  are Jacobians of the function

$$J_H = \left[ \frac{\partial F(H, q)}{\partial H} \right]_{H=H_0, q=q_0}, \quad J_q = \left[ \frac{\partial F(H, q)}{\partial q} \right]_{H=H_0, q=q_0} \quad \text{i.e.:$$

$$J_H = \begin{bmatrix} \frac{-C_1\alpha_1}{(H_{10})^{1-\alpha_1}\beta_1(H_{10})} & 0 & 0 \\ \frac{C_1\alpha_1}{(H_{10})^{1-\alpha_1}\beta_2(H_{20})} & \frac{-C_2\alpha_2}{(H_{20})^{1-\alpha_2}\beta_2(H_{20})} & 0 \\ 0 & \frac{C_2\alpha_2}{(H_{20})^{1-\alpha_2}\beta_3(H_{30})} & \frac{C_3\alpha_3}{(H_{30})^{1-\alpha_3}\beta_3(H_{30})} \end{bmatrix}, \quad (21)$$

$$J_q = \begin{bmatrix} 1 \\ \beta_1(H_{10}) \\ 0 \\ 0 \end{bmatrix}$$

This linear model (21) can be used for the sensitivity analysis, for the stability analysis, and for the design of local controllers of the pump-controlled system.

## 5. SIMULATION RESULTS

The proposed improvement in HW structure was tested through simulations in Matlab. Firstly, the input-output dataset has been formed using the model of multitank system Eq. (21). The dataset used for this purpose is presented in Fig. 6.

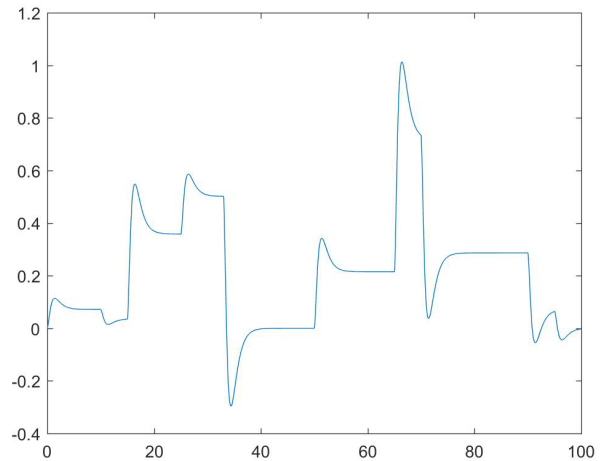


Figure 6: Generated dataset used for system identification and validation of the results.

We then applied the proposed HW structure to identify the system. For this purpose, the first half of the generated dataset has been used to determine HW model parameters. Afterwards, the second half of the dataset has been used to test the performance of the obtained structure.

The HW structure proposed in this paper consists of nonlinear blocks presented by orthogonal functions performed as ( $e^{-t} = x$ ). In order to implement orthogonal functions as HW model nonlinearities, Matlab function *customnet* has been used [34]. Two cases were explored:

the first case in which input nonlinearity has been represented using function  $P_1^{(\varepsilon)}(t)^{-1}$  and the output nonlinearity has been represented using  $P_1^l(t)^{-1}$ , and the second case in which both the input and output nonlinearities have been represented with  $P_1^{(\varepsilon)}(t)^{-1}$  function.

The comparison of simulated response of multitank system and proposed HW structure, used to identify it, is shown in Figs. 7 and 8.

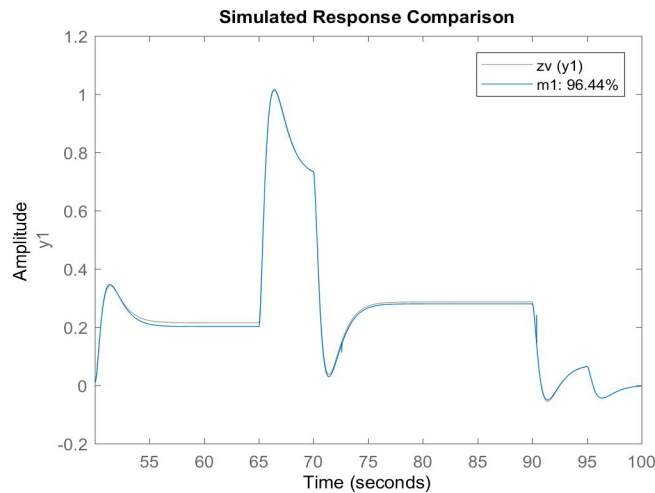


Figure 7: Comparison of simulated response of the multitank system (zv signal) and of HW model of the system (m1). The input and output nonlinearities of a HW model have been represented using  $P_1^{(\varepsilon)}(t)^{-1}$  and  $P_1^l(t)^{-1}$  functions.

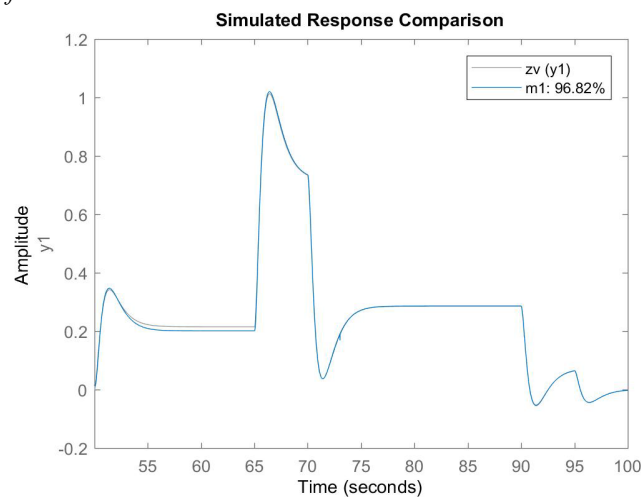


Figure 8: Comparison of simulated response of the multitank system (zv signal) and of HW model of the system (m1). Both the input and output nonlinearities of a HW model have been represented using  $P_1^{(\varepsilon)}(t)^{-1}$  function.

The results in Fig. 7 show that the proposed HW structure with  $P_1^{(\varepsilon)}(t)^{-1}$  as input nonlinearity and  $P_1^l(t)^{-1}$  as output nonlinearity is able to capture the behavior of the multitank system.

Fig. 8 shows the results obtained when both the input and output nonlinearities are represented using  $P_1^{(\varepsilon)}(t)^{-1}$  function.

In this case, the proposed structure is also able to capture the behavior of the multitank system. It can be noticed that the structure with both input and output nonlinearities realized using  $P_1^{(\varepsilon)}(t)^{-1}$  gives slightly better results and follows the multitank system response with slightly higher precision. Based on the results, it can be concluded that HW models with orthogonal polynomials implemented as nonlinearities are very robust.

## 6. CONCLUSION

During the last fifteen years, Hammerstein-Wiener models have proved to have a wide application: from medical purposes to their use in control systems. They have especially shown their potential for nonlinear systems representation. In this paper, we considered the application of orthogonal polynomials for the representation of nonlinearities of a Hammerstein-Wiener system. For this purpose, the application of almost orthogonal and quasi-orthogonal polynomials has been addressed. The functions used have been performed as  $(e^{-t} = x)$ . We used the proposed structure to identify a multitank system. The simulated results of our research have shown that Hammerstein-Wiener models with proposed orthogonal functions implemented in nonlinear blocks effectively capture the behavior of the system. The proposed structure is very robust.

## ACKNOWLEDGEMENTS

This work has been supported by the Ministry of Education, Science and Technological Development of the Republic of Serbia.

## REFERENCES

- [1] Z. Zhang, D. Zhang, H. Zheng, T. Huang and Y. Xie, "Identification of a precision motion stage based on the Hammerstein-Wiener model," Proceedings of the 38th Chinese Control Conference (CCC), Guangzhou (China) 27-30 July 2019, pp. 1637-1642, IEEE, (2019)
- [2] E. Shokrollahi, A. A. Goldenberg, J. M. Drake, K. W. Eastwood and M. Kang, "Application of a Nonlinear Hammerstein-Wiener Estimator in the Development and Control of a Magnetorheological Fluid Haptic Device for Robotic Bone Biopsy," Actuators, Vol. 7(4), p. 83, (2018)
- [3] F. Guo, "A new identification method for Wiener and Hammerstein systems," PhD Thesis, Karlsruhe, University of Karlsruhe (Germany), (2004).
- [4] D. Wang and F. Ding, "Extended stochastic gradient identification algorithms for Hammerstein-Wiener ARMAX systems," Computers & Mathematics with Applications, Vol. 56(12), pp. 3157-3164, (2008)
- [5] F. Ding and T. Chen, "Identification of Hammerstein nonlinear ARMAX systems," Automatica, Vol. 41(9), pp. 1479-1489, (2005)
- [6] Y. Zhu, "Estimation of an N-L-N Hammerstein-Wiener model," Automatica, Vol. 38(9), pp. 1607-1614, (2002)

- [7] K. K. Xu, H. D. Yang and C. J. Zhu, "A novel extreme learning machine-based Hammerstein-Wiener model for complex nonlinear industrial processes," *Neurocomputing*, 358, pp. 246-254, (2019)
- [8] E. W. Bai, "An optimal two-stage identification algorithm for Hammerstein-Wiener nonlinear systems," *Automatica*, Vol. 34(3), pp. 333-338, (1998)
- [9] M. Schoukens, E. W. Bai and Y. Rolain, "Identification of Hammerstein-Wiener systems," *IFAC Proceedings Volumes*, Vol. 45(16), pp. 274-279, (2012)
- [10] A. Wills, T. B. Schön, L. Ljung and B. Ninness, "Identification of Hammerstein-Wiener models," *Automatica*, Vol. 49(1), pp. 70-81, (2013)
- [11] E. W. Bai, "A blind approach to the Hammerstein-Wiener model identification," *Automatica*, Vol. 38(6), pp. 967-979, (2002).
- [12] Y. Wang and F. Ding, "Recursive least squares algorithm and gradient algorithm for Hammerstein-Wiener systems using the data filtering," *Nonlinear Dynamics*, Vol. 84(2), pp. 1045-1053, (2016).
- [13] I. Aljamaan, D. T. Westwick and M. Foley, "Non-iterative identification of iir wiener systems using orthogonal polynomial," *IFAC Proceedings Volumes*, Vol. 47(3), pp. 487-492, (2014).
- [14] D. Antić, B. Danković, S. Nikolić, M. Milojković, and Z. Jovanović, "Approximation Based on Orthogonal and Almost Orthogonal Functions", *Journal of the Franklin Institute*, Vol. 349(1), pp. 323-336, (2012)
- [15] D. Antić, S. Nikolić, M. Milojković, N. Danković, Z. Jovanović, and S. Perić, "Sensitivity Analysis of Imperfect Systems Using Almost Orthogonal Filters", *Acta Polytechnica Hungarica*, Vol. 8(6), pp. 79-94, (2011)
- [16] D. Antić, Z. Jovanović, V. Nikolić, M. Milojković, S. Nikolić, and N. Danković, "Modeling of Cascade-Connected Systems Using Quasi-Orthogonal Functions", *Electronics and Electrical Engineering*, Vol. 18(10), pp. 3-8, (2012)
- [17] B. Danković, S. Nikolić, M. Milojković, and Z. Jovanović, "A Class of Almost Orthogonal Filters", *Journal of Circuits, Systems, and Computers*, Vol. 18(5), pp. 923-931, (2009)
- [18] M. Milojković, D. Antić, M. Milovanović, S. Nikolić, S. Perić, and M. Almawlawe, "Modelling of Dynamic Systems Using Orthogonal Endocrine Adaptive Neuro-Fuzzy Inference Systems", *Journal of Dynamic Systems, Measurement, and Control*, Vol. 137(9), (2015)
- [19] M. Milojković, D. Antić, S. Nikolić, Z. Jovanović, and S. Perić, "On a New Class of Quasi-Orthogonal Filters", *International Journal of Electronics*, Vol. 100(10), pp. 1361-1372, (2013)
- [20] M. Milojković, S. Nikolić, B. Danković, D. Antić, and Z. Jovanović, "Modelling of Dynamical Systems Based on Almost Orthogonal Polynomials", *Mathematical and Computer Modelling of Dynamical Systems*, Vol. 16(2), pp. 133-144, (2010)
- [21] M. Milojković, M. Milovanović, S. S. Nikolić, M. Spasić, and A. Antić, "Designing Optimal Models of Nonlinear MIMO Systems Based on Orthogonal Polynomial Neural Networks", *Mathematical and Computer Modelling of Dynamical Systems*, Vol. 27(1), pp. 242-262, (2021)
- [22] S. Nikolić, D. Antić, S. Perić, N. Danković, and M. Milojković, "Design of Generalized Orthogonal Filters: Application to the Modelling of Dynamical Systems", *International Journal of Electronics*, Vol. 103(2), pp. 269-280, (2016)
- [23] S. Nikolić, D. Antić, M. Milojković, M. Milovanović, S. Perić, and D. Mitić, "Application of Neural Networks With Orthogonal Activation Functions in Control of Dynamical Systems", *International Journal of Electronics*, Vol. 103(4), pp. 667-685, (2016)
- [24] S. Nikolić, D. Antić, B. Danković, M. Milojković, Z. Jovanović, and S. Perić, "Orthogonal Functions Applied in Antenna Positioning", *Advances in Electrical and Computer Engineering*, Vol. 10(4), pp.35-42, (2010)
- [25] S. Perić, D. Antić, D. Mitić, S. Nikolić, and M. Milojković, "Generalized Quasi-Orthogonal Polynomials Applied in Sliding Mode Based Minimum Variance Control of ABS", *Acta Polytechnica Hungarica*, Vol. 17(4), pp. 165-182, (2020)
- [26] S. Perić, D. Antić, M. Milovanović, D. Mitić, M. Milojković, and S. Nikolić, "Quasi-Sliding Mode Control With Orthogonal Endocrine Neural Network-Based Estimator Applied in Anti-Lock Braking System", *IEEE/ASME Transactions on Mechatronics*, Vol. 21(2), pp. 754-764, (2016)
- [27] M. Milojković, D. Antić, S. Nikolić, Z. Jovanović, and S. Perić, "On a New Class of Quasi-Orthogonal Filters", *International Journal of Electronics*, Vol. 100(10), pp. 1361-1372, (2013)
- [28] I. Ben-Yaacov and F. Wagner, "On Almost Orthogonality in Simple Theories", *Journal of Symbolic Logic*, Vol. 69(2), pp. 398-408, (2004)
- [29] M. Alfaro and L. Moral, "Quasi-Orthogonality on the Unit Circle and Semi-Classical Forms", *Portugaliae Mathematica*, Vol. 51(1), pp. 47-62, (1994)
- [30] A. Beny and R.H. Torres, "Almost Orthogonality and a Class of Bounded Bilinear Pseudodifferential Operator", *Mathematical Research Letters*, Vol. 11(1), pp. 1-11, (2004)
- [31] Riesz, M. "Sur le Probleme des Moments", *Troisième Note*, *Arkiv för Matematik, Astronomi och Fysik*, Vol. 17(16), pp. 1-52, (1923)
- [32] T.S. Chihara, "On Quasi-Orthogonal Polynomials", in *Proceedings of the American Mathematical Society*, Vol. 8, pp. 765-767, (1957)
- [33] Inteco, "The multitank system", available at <http://www.inteco.com.pl/products/multi-tank/>, (2009)
- Math Works, available at <https://ch.mathworks.com/help/ident/ref/customnet.html>, (2021)

# Adaptive dynamic programming based optimal control for hydraulic servo actuator

Vladimir Djordjevic<sup>1</sup>, Marcelo Menezes Morato<sup>2</sup>, Vladimir Stojanovic<sup>1\*</sup>

<sup>1</sup>Faculty of Mechanical and Civil Engineering in Kraljevo, University of Kragujevac, Kraljevo (Serbia)

<sup>2</sup>Departamento de Automação e Sistemas, Universidade Federal de Santa Catarina, Florianópolis, (Brazil)

*This paper considers optimal tracking control for hydraulic servo actuator with unknown dynamics. The aim is to achieve asymptotic tracking and disturbance rejection by minimizing some predefined performance index. Through the combination of adaptive dynamic programming (ADP) and internal model principle, an approximate optimal controller is iteratively learned online using measurable input/output data. Unmeasurable states are also reconstructed from input/output data. The discrete-time algebraic Riccati equation is iteratively solved by ADP approach. Simulation results demonstrate the feasibility and effectiveness of the proposed approach.*

**Keywords:** Adaptive dynamic programming, Optimal control, Hydraulic servo actuator, Unknown dynamics, Algebraic Riccati equation

## 1. INTRODUCTION

The performance of hydraulic servo systems strongly depends on the control valve and spool geometry as well as their manufacturing tolerances. Without a proper model, accurate analysis of hydraulic system performance is not possible. It is well known that it is very difficult to determine a large number of physical parameters which are integral part of complex systems. Despite the fact that many system parameters are available with some reasonable accuracy, a large number of parameters are known within a certain range, while some parameters are entirely unknown because manufacturers consider these data as proprietary information. For example, precise determination of system parameters such as dimensions of certain components, leakage and friction coefficients, as well as static and dynamic friction forces due to impossibility of direct measurement or calculation causes great difficulty in control of servo actuators [1]. More precise knowledge of the system parameters increases the model quality, which causes better control performances. Recent reviews dedicated to the influence of disturbances, modeling errors, various uncertainties in the control systems in the real systems[2-3].

Adaptive dynamic programming (ADP) provides a feasible and effective way to achieve optimal control performance based on traditional or intelligent control methods. It combines the theories of dynamic programming and neural networks, trying to solve optimal control problems in dynamic programming problems using the approximating characteristic of neural networks [4-5]. Recent years the ADP also has been extended and applied to many different areas, such as robots, spacecraft and so on [6-7].

For the reason that ADP not only has unique algorithm and structure, but also overcomes the disadvantage that classical variational theory cannot deal with the optimal control problem of control variables with closed-set constraints, and also solves the curse of dimensionality problems, more and more research and application attentions have focused on it.

When the state of a system is not directly measurable and the system matrices are unknown, it is thus meaningful to resort to output feedback based ADP. An output feedback ADP methodology for discrete-time linear systems is proposed in [8]. The measurable input/output data are used to describe the state of the discretized model, and then use policy iteration (PI) and value iteration (VI) to obtain optimal control policy. Nevertheless, in order to get the unique solution in each iteration step, some exploration noise need to be added, which may influence the accuracy of solutions.

It is usually too expensive to measure directly the system states. Self-applied state estimation methods assume that the system parameters are constant. In the real world, these parameters can't know exactly (e.g., friction coefficients, temperature, pressure, or flow). It's also known that the dynamic behavior of complex systems can be described by a linear stochastic state-space model with online estimated dynamics [9]. Precise knowledge of system parameters and states is crucial for successful realization of many control techniques. Many modern engineering applications such as intelligent vehicles[10], microphone sensing[11], maintaining security of cyber-physical systems[12], robotic manipulation tasks[13], 2-degree-of-freedom helicopter[14], require real-time control based on linear models.

In this paper, the continuous-time linear plant is discretized due to easier practical implementation, and then, the optimal control problem is considered. An adaptive optimal output feedback strategy for the discretized model is applied for optimal control of hydraulic actuator with unknown dynamics. Simulation results demonstrate the validity and effectiveness of the proposed control approach, in which the exploration noise does not affect accuracy of the solution of discrete Riccati equation.

## 2. HYDRAULIC SERVO ACTUATOR

Hydraulic systems are often employed in high performance applications that require fast response and high power. These applications include high bandwidth

\*Corresponding author: Dositejeva 19, Kraljevo, Serbia, e-mail: [vladostojanovic@mts.rs](mailto:vladostojanovic@mts.rs)

control position and force. The problem is that these systems contain non-smooth nonlinearities caused by variable geometry and variable working conditions. The external load consists of the mass of external mechanical elements connected to the piston and a force produced by an environmental interaction. Schematic view of double acting, asymmetric hydraulic cylinder with connected four-way spool valve is shown on Figure 1.

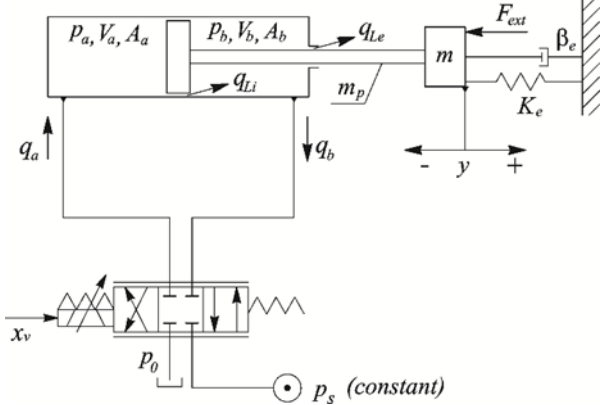


Figure 1: Schematic representation of the valve-controlled asymmetric piston

The total mass of the piston  $m_i$  includes the mass of piston rod  $m_p$  and the mass of the load  $m$  referred to the piston.

A detailed mathematical model derivation of the hydraulic servo actuator is given in [1]. Using this model, we can express the system model in the state space.

### 2.1. Force balance equation for piston

Applying Newton's second law to the forces on the piston, the resulting force equation is:

$$A_a p_a - A_b p_b = m_i \ddot{y} + F_f(\dot{y}) + K_e y + F_{ext} \quad (1)$$

The spool valve displacement is denoted as  $x_v$ . Pressures  $p_a$  and  $p_b$  denote the forward and the return pressure, respectively, the corresponding flows are  $q_a$  and  $q_b$ ,  $y$  is the piston displacement,  $K_e$  denotes the load spring gradient,  $p_s$  is the supply pressure, and  $p_0$  is the tank pressure. The piston displacement depends on the action of fluid pressures as well as on the load referred to the piston. This load can be seen as summing effects of inertia which comes from the total piston mass  $m_i$ , friction forces  $F_f$ , spring load forces  $K_e y$  and disturbance forces  $F_{ext}$ . The total mass of the piston  $m_i$  in addition to the mass of piston rod  $m_p$  also includes the mass  $m$  of the load referred to the piston. The mass of the piston is considered together with the load mass due to the fact that, in every moment, the load directly affects on the piston. The term  $F_f$  in equation (1) describes the summing nonlinear effects of viscous, static and Coulomb friction forces of the system. The detailed analysis for the influences of friction forces can be found in [15]. The area ratio of the asymmetric piston is  $\alpha = A_b/A_a$ , where  $A_b$  is the effective area of the head side of the piston, and  $A_a$  is the effective area of the rod side of the piston, see Figure 1.

### 2.2. Pressure dynamics in cylinder chamber

Applying the continuity equation to each of the cylinder chambers yields:

$$q_a - q_{Li} = \dot{V}_a + \frac{V_a}{\beta_e} \dot{p}_a \quad (2)$$

$$q_b + q_{Li} - q_{Le} = \dot{V}_b + \frac{V_b}{\beta_e} \dot{p}_b \quad (3)$$

where  $\beta_e$  is the bulk modulus of the fluid,  $q_{Li}$  and  $q_{Le}$  denote the internal leakage flow and the external leakage flow, respectively. The internal leakage flow can be calculated by:

$$q_{Li} = c_{Li}(p_a - p_b) \quad (4)$$

where  $c_{Li}$  is the internal leakage flow coefficient. External leakage (leakage from each cylinder chamber to case drain or to tank) is usually neglected,  $q_{Lea} = q_{Leb} = 0$ .

The total fluid volumes of two cylinder sides,  $V_a$  and  $V_b$ , are given as:

$$V_a = V_{a0} + y A_a \quad (5)$$

$$V_b = V_{b0} + (L - y) \alpha A_a \quad (6)$$

where  $L$  is the piston stroke and  $V_{a0}$  and  $V_{b0}$  represent initial chamber volumes. Equations (2) and (3) can be rearranged to yield the pressure dynamics equations

$$\dot{p}_a = \frac{\beta_e}{V_a(y)} (q_a - A_a \dot{y} - q_{Li} - q_{Lea}) \quad (7)$$

$$\dot{p}_b = \frac{\beta_e}{V_b(y)} (q_b + \alpha A_a \dot{y} + q_{Li} - q_{Leb}) \quad (8)$$

### 2.3. Valve flow equations

The flow through the  $i$ th valve orifice  $q_{svi}$  is described by next relation, which takes the direction of the pressure drop into account:

$$q_{svi} = q(x_v, \Delta p) = c_{vi} \operatorname{sg}(x_v) \operatorname{sign}(\Delta p) \sqrt{|\Delta p|} \quad (9)$$

where  $i = 1, 2, \dots, 4$ .

The function  $\operatorname{sg}(x)$  is defined by:

$$\operatorname{sg}(x) = \begin{cases} x, & x \geq 0 \\ 0, & x < 0 \end{cases} \quad (10)$$

where  $i = 1, 2, \dots, 4$ .

Discharge coefficients of valve orifices  $c_{vi} > 0$ ,  $i = 1, 2, 3, 4$  represent valve constants, which will be equal if all orifices are identical. Consider the four-way spool valve as shown in Figure 2.

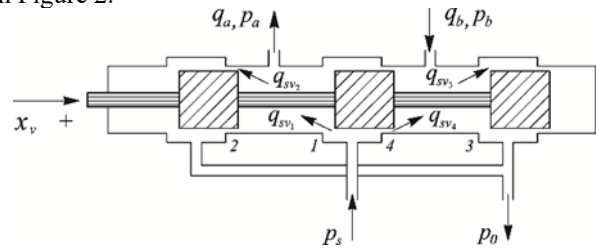


Figure 2: Four-way spool valve

The corresponding flow equations for two valve chambers can be written as:

$$q_a = q_{sv1} - q_{sv2} = c_{v1} \operatorname{sg}(x_v) \operatorname{sign}(p_s - p_a) \sqrt{|p_s - p_a|} - c_{v2} \operatorname{sg}(-x_v) \operatorname{sign}(p_a - p_0) \sqrt{|p_a - p_0|} \quad (11)$$

$$q_b = q_{sv3} - q_{sv4} = c_{v3} \operatorname{sg}(-x_v) \operatorname{sign}(p_s - p_b) \sqrt{|p_s - p_b|} - c_{v4} \operatorname{sg}(x_v) \operatorname{sign}(p_b - p_0) \sqrt{|p_b - p_0|} \quad (12)$$

$$\dot{x}_1 = x_2$$

$$\dot{x}_2 = \frac{1}{m_t} (A_a x_3 - \alpha A_a x_4 - F_f(x_2) - K_e x_1),$$

$$\dot{x}_3 = \frac{\beta_e}{A_a x_1 + V_{a0}} (c_{v1} \operatorname{sg}(u) \operatorname{sign}(p_s - x_3) \sqrt{|p_s - x_3|} - c_{v4} \operatorname{sg}(-u) \operatorname{sign}(x_3 - p_0) \sqrt{|x_3 - p_0|} - A_a x_2 - c_{Li}(x_3 - x_4)) \quad (15)$$

$$\dot{x}_4 = \frac{\beta_e}{\alpha A_a (L - x_1) + V_{b0}} (c_{v3} \operatorname{sg}(-u) \operatorname{sign}(p_s - x_4) \sqrt{|p_s - x_4|} - c_{v2} \operatorname{sg}(u) \operatorname{sign}(x_4 - p_0) \sqrt{|x_4 - p_0|} + \alpha A_a x_2 + c_{Li}(x_3 - x_4))$$

It is known that there are coefficients with random characters in the nonlinear state space model of a hydraulic servo system [16]. Taking into account that some parameter changes have random character, as well as the possibility of approximation of nonlinear models with a model with time-varying parameters, see [17], this paper proposes a linear stochastic model with time-varying parameters.

It is now more convenient to define the pressure drop across the load, or simply the load:

$$p_L = p_a - \alpha p_b \quad (16)$$

which can be seen as the "virtual" pressure required to counterbalance the friction and load forces.

Finally, after linearization of nonlinear equations (15), using previous notation which allows us to present the hydraulic servo system in more compact form, with new state vector  $[x_1 \ x_2 \ x_3]^T \square [\Delta y(k) \ \Delta \dot{y} \ \Delta p_L]^T$ , the continuous time state-space description of the reduced order, can be obtained as [16]:

$$\dot{x}(t) = Ax(t) + Bu(t) \quad (17)$$

$$y(t) = Cx(t) \quad (18)$$

$$\text{where } A = \begin{bmatrix} 0 & 1 & 0 \\ 0 & -\frac{1}{T_m} & \frac{A_a}{m_p} \\ 0 & -K_d & -\frac{1}{T_h} \end{bmatrix}, B = [0 \ 0 \ K_Q]^{-T}.$$

The damping of the resonance frequency is determined by the viscous friction ( $-1/T_m = -B_C/m_p$ ) and the leakage ( $-1/T_h$ ), where  $T_m = m_t/B_C$ . Other useful quantities are the

hydraulic capacitance  $C_h = \left( \frac{\beta_e}{V_A} + \alpha^2 \frac{\beta_e}{V_B} \right)$ ,  $K_d = \frac{A_1}{C_h}$ ,

valve flow-pressure coefficients  $K_{Qp}$ , valve flow gains  $K_{Qx}$ , as well as pressure sensitivities  $K_{px} = K_{Qx}/K_{Qp}$  and damping ratio:

$$K_j = (R + B_d^T P_{j-1} B_d)^{-1} B_d^T P_{j-1} A_d \quad (19)$$

## 2.4. Dynamic model of the hydraulic servo actuator

If state variables and input variables are defined as:

$$x = [x_1 \ x_2 \ x_3 \ x_4]^T \square [y \ \dot{y} \ p_a \ p_b]^T \quad (13)$$

$$u = x_v \quad (14)$$

then a completely nonlinear model of the hydraulic system, can be expressed in a state-space form as:

## 3. OPTIMAL PROBLEM FORMULATION

For practical implementation in the hydraulic actuator control system, we will consider the discretized system described by:

$$x_{k+1} = A_d x_k + B_d u_k \quad (20)$$

$$y_k = C x_k \quad (21)$$

in which  $A_d = e^{Ah}$ ,  $B_d = \int_0^h (e^{A\tau} d\tau) B$  and  $h > 0$  is the

sampling period, assuming  $\omega_h = 2\pi/h$  is non-pathological sampling frequency [18]. In other words, one cannot find any two eigenvalues of  $A$  with equal real parts and imaginary parts that differ by an integral multiple of  $\omega_h$ .

The state, input, and output vector at the sampled instant  $kh$  are  $x_k$ ,  $u_k$ ,  $y_k$ , respectively. Then, both  $(A_d, C)$  and  $(A_d, Q^{1/2}C)$  are observable and  $(A_d, B_d)$  is controllable.

Cost for (20)-(21) is:

$$J_d(x_0) = \sum_{j=0}^{\infty} y_j^T Q y_j + u_j^T R u_j \quad (22)$$

The optimal control law minimizing (un) is

$$u_k = -K_d^* x_k \quad (23)$$

where discrete optimal feedback gain matrix is  $K_d^* = (R + B_d^T P_d^* B_d)^{-1} B_d^T P_d^* A_d$ , and  $P_d^*$  is the unique symmetric positive definite solution to

$$A_d^T P_d^* A_d - P_d^* + C^T Q C - A_d^T P_d^* B_d K_d^* = 0 \quad (24)$$

Up to now, this known optimal control design method is mainly applicable to low order simple linear systems. In fact, for high order large scale systems, it is usually difficult to directly solve  $P_d^*$  from (24), which is nonlinear in  $P_d$ . Nevertheless, many efficient algorithms have been developed to numerically approximate the solution of (24). One of such algorithms was developed by Hewer [19]. By iteratively solving the Lyapunov equation

$$(A_d - B_d K_j)^T P_j (A_d - B_d K_j) + C^T Q C + K_j^T R K_j = 0 \quad (25)$$

which is linear in  $P_j$ , and updating  $K_j$  by

$$K_j = (R + B_d^T P_{j-1} B_d)^{-1} B_d^T P_{j-1} A_d \quad (26)$$

the solution to the nonlinear equation (24) is numerically approximated. It has been concluded that sequences  $\{P_j\}_{j=0}^{\infty}$  and  $\{K_j\}_{j=0}^{\infty}$  computed from this algorithm converge to  $P_d^*$  and  $K_d^*$ , respectively. Moreover, for  $j = 0, 1, \dots, A_d - B_d K_j$  is a Schur matrix.

It should be noted that Hewer's algorithm is model based policy iteration (PI) algorithm which cannot be implemented when the system matrices are all unknown, since it is an offline algorithm relying on system parameters. In order to implement it online, we will develop an adaptive optimal control algorithm for the discretized system (20)-(21) via output feedback which does not rely on the knowledge of the system matrices.

#### 4. ADAPTIVE OPTIMAL CONTROLLER DESIGN

Just like in [8] the extended state equation using input/output sequences on time horizon can be written as  $[k - N, k - 1]$ :

$$\begin{aligned} x_k &= A_d^N x_{k-N} + V(N) \bar{u}_{k-1, k-N} \\ \bar{y}_{k-1, k-N} &= U(N) x_{k-N} + T(N) \bar{u}_{k-1, k-N} \end{aligned} \quad (27)$$

where

$$\begin{aligned} \bar{u}_{k-1, k-N} &= [u_{k-1}^T \quad u_{k-2}^T \quad \dots \quad u_{k-N}^T]^T \\ \bar{y}_{k-1, k-N} &= [y_{k-1}^T \quad y_{k-2}^T \quad \dots \quad y_{k-N}^T]^T \\ V(N) &= [B_d \quad A_d B_d \quad \dots \quad A_d^{N-1} B_d] \\ U(N) &= [(CA_d^{N-1})^T \quad (CA_d)^T \quad \dots \quad C^T]^T \\ T(N) &= \begin{bmatrix} 0 & CB_d & CA_d B_d & \dots & CA_d^{N-2} B_d \\ 0 & 0 & CB_d & \dots & CA_d^{N-3} B_d \\ \vdots & \vdots & \ddots & \ddots & \vdots \\ 0 & 0 & \dots & 0 & CB_d \\ 0 & 0 & \dots & 0 & 0 \end{bmatrix} \end{aligned}$$

and  $N = \max(\rho_u, \rho_v)$  is the observability index, where  $\rho_u$  is the minimum integer which can make  $U(\rho_u)$  full column rank,  $\rho_v$  is the minimum integer which can make  $V(\rho_v)$  full row rank.

A lemma about the uniqueness of state reconstruction is shown below.

**Lemma 1.** Given a controllable and observable system (20)-(21), the system state is obtained uniquely in terms of measured input/output sequences by

$$x_k = \Theta z_k \quad (28)$$

where  $M_u = V(N) - M_y T(N)$ ,  $M_y = A_d^N U^+(N)$ ,

$\Theta = [M_u \quad M_y]$ ,  $z_k = [\bar{u}_{k-1, k-N}^T \quad \bar{y}_{k-1, k-N}^T]^T \in \mathbb{R}^q$ , where  $q = N[\dim(u) + \dim(y)]$ .

Now, based on (25)-(26) online output feedback learning strategy for linear discretized system (20)-(21) can be derived. The discrete model (20) can be rewritten as

$$x_{k+1} = A_j x_k + B_d (K_j x_k + u_k) \quad (29)$$

where  $A_j = A_d - B_d K_j$ . Letting  $\bar{K}_j = K_j \Theta$  and  $\bar{P}_j = \Theta^T P_j \Theta$ , from (25) and (29) it follows that,

$$\begin{aligned} z_{k+1}^T \bar{P}_j z_{k+1} - z_k^T \bar{P}_j z_k &= \\ \phi_k^1 \text{vec}(\bar{H}_j^1) + \phi_k^2 \text{vec}(\bar{H}_j^2) - (y_k^T Q y_k + z_k^T \bar{K}_j^T R \bar{K}_j z_k) \end{aligned} \quad (30)$$

in which  $\bar{H}_j^1 = B_d^T \bar{P}_j B_d$ ,  $\bar{H}_j^2 = B_d^T \bar{P}_j A_d \Theta$ ,

$$\phi_k^1 = u_k^T \otimes u_k^T - (z_k^T \otimes z_k^T) (\bar{K}_j^T \otimes \bar{K}_j^T),$$

$$\phi_k^2 = 2[(z_k^T \otimes z_k^T) (I_q \otimes \bar{K}_j^T) + (z_k^T \otimes u_k^T)]$$

This assumption is related to the condition of persistent excitation in adaptive control theory [20]. Then,  $\bar{K}_{j+1}$  can be computed as

$$\bar{K}_{j+1} = (R + \bar{H}_j^1)^{-1} \bar{H}_j^2. \quad (31)$$

Here, (30) is called policy evaluation, which is used to uniquely solve  $\bar{P}_j$ , and (31) is policy improvement (PI), which is used to update control gain  $\bar{K}_{j+1}$ . Then, we present our output feedback adaptive optimal control algorithm.

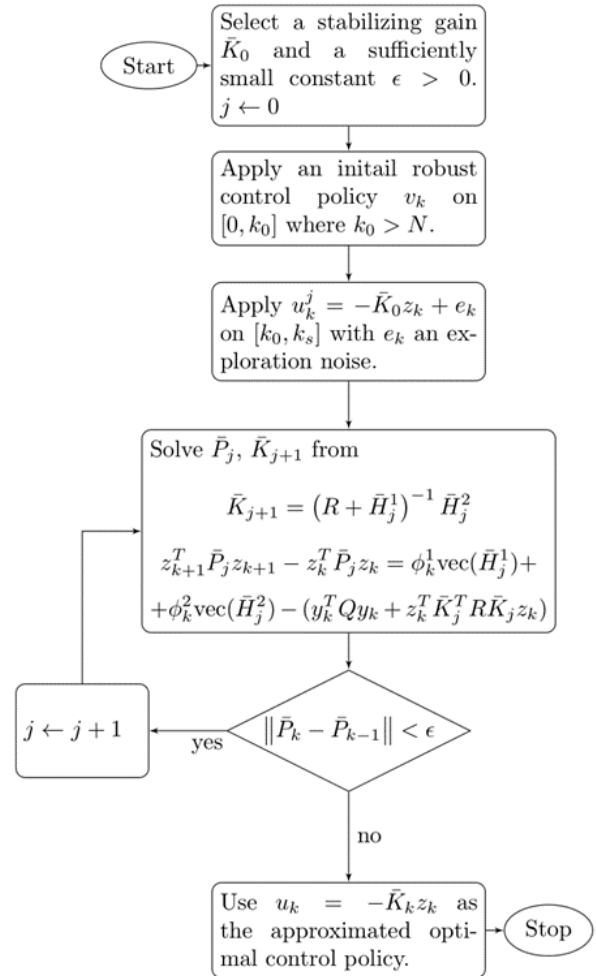


Figure 3: Flowchart of adaptive optimal controller design

#### 5. SIMULATION RESULTS

A basic prerequisite for energy savings in processes of production, transportation, and energy consumption is a

high-quality synthesis of optimal control algorithm. In this section, we conduct simulations on the valve-controlled hydraulic actuator to show the effectiveness of the output-feedback ADP control algorithm in the case with unknown system matrices and unmeasurable states.

Through iterative calculation, the approximated optimal control gain and performance index for the discrete-time system can be obtained. Furthermore, the discrete control policy is implemented on the continuous plant by zero-order holder. Adopted sampling time is  $h = 0.1s$ .

The model parameters are:  $\beta_e = 2.1 \cdot 10^8 Pa$  is the bulk modulus of the fluid,  $K_e = 10^{-1}$  denotes the load spring gradient,  $F_{ext}$  represents the load force disturbance on the piston,  $p_s = 40bar$  is the supply pressure, and  $p_0 = 1.7bar$  is the tank pressure,  $V_{a0} = V_{b0} = 8 \cdot 10^{-6} m^3$

$$\bar{P}_d^* = \begin{bmatrix} 269.1657 & -377.7014 & 139.5220 & 7.7063 & -276.6863 & 293.3140 \\ -377.7014 & 535.9737 & -199.3177 & -10.0756 & 387.6731 & -419.0086 \\ 139.5220 & -199.3177 & 74.4521 & 3.7667 & 3.7667 & 156.5180 \\ 7.7063 & -10.0756 & 3.7667 & 1.5862 & -7.2146 & 7.9186 \\ -276.6830 & 387.6731 & -142.9420 & -7.2146 & 284.9547 & -300.5013 \\ 293.3140 & -419.0086 & 156.5180 & 7.9186 & -300.5013 & 329.0404 \end{bmatrix} \quad (32)$$

$$\bar{K}_d^* = [3.3615 \quad -4.4696 \quad 1.6358 \quad 0.3700 \quad -3.3307 \quad 3.4388] \quad (33)$$

The input/output data are collected from 0.8 to 4 seconds, and the PI is started from  $t = 4s$ . The online information of input and output are collected in the whole process and the

$$\bar{P}_6^* = \begin{bmatrix} 269.1659 & -377.7057 & 139.5221 & 7.7082 & -276.6863 & 293.3106 \\ -377.7057 & 535.9646 & -199.3158 & -10.0757 & 387.6722 & -419.0119 \\ 139.5221 & -199.3158 & 74.4526 & 3.7667 & -142.9427 & 156.5181 \\ 7.7082 & -10.0757 & 3.7667 & 1.5861 & -7.2146 & 7.9186 \\ -276.6863 & 387.6722 & -142.9427 & -7.2146 & 284.9548 & -300.5016 \\ 293.3106 & -419.0119 & 156.5181 & 7.9186 & -300.5016 & 329.0404 \end{bmatrix} \quad (34)$$

$$\bar{K}_6^* = [3.3615 \quad -4.4695 \quad 1.6358 \quad 0.3700 \quad -3.3306 \quad 3.4387] \quad (35)$$

Figures 4-6 depict the plots of input, output and states of the hydraulic actuator. At  $t = 4s$ , the approximated optimal control gain is thus obtained by applied optimal ADP and is implemented online.

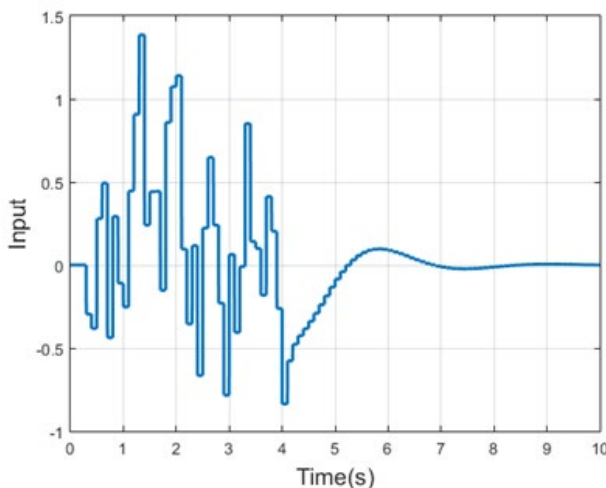


Figure 4: Trajectory of input

represent initial chamber volumes,  $L = 1m$  is the piston stroke,  $m = 20kg$  is the piston mass.

The area ratio of the asymmetric piston is  $\alpha = A_b/A_a$ , where  $A_b = 2.36 \cdot 10^{-4} m^2$  is the effective area of the head side of the piston, and  $A_a = 4.91 \cdot 10^{-4} m^2$  is the effective area of the rod side of the piston. Discharge coefficients of valve orifices  $c_{vi} > 1.14$ ,  $i = 1, 2, 3, 4$  represent valve constants, and  $c_{Li} = 5 \cdot 10^{-14}$  is the internal leakage coefficient.

Behavior of the control algorithm will be considered on discretized continuous linear model (17)-(18). For the purpose of simulation,  $Q$  and  $R$  are chosen to be identity matrices. The observability index is  $N = 3$  and the stopping criterion is  $\varepsilon = 0.1$ . By solving of the discrete-time Riccati equation (24), we get the optimal values  $\bar{P}_d^*$ ,  $\bar{K}_d^*$ . More precisely

adaptive optimal controller is also computed iteratively. After 6 iterative iterations, we obtain the derived approximate optimal values as shown below:

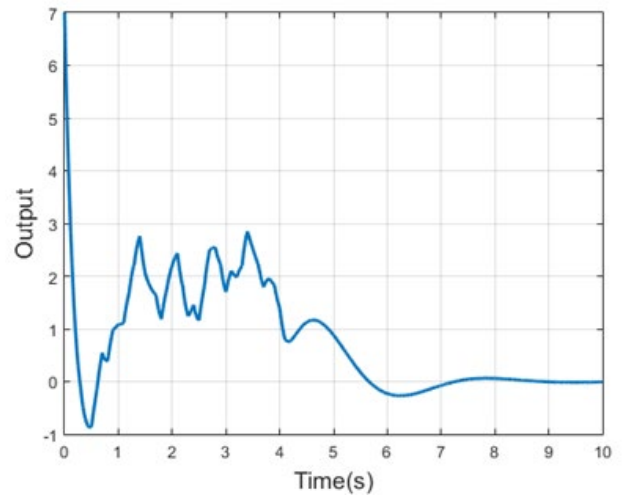


Figure 5: Trajectory of output

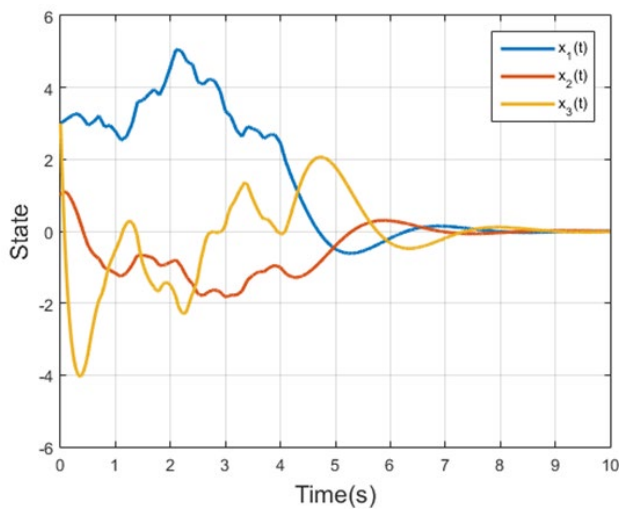


Figure 6: Trajectory of states

## 6. CONCLUSION

In this paper, ADP based optimal controller design has been considered for the hydraulic servo actuator with completely unknown dynamics. Applied sampled-data adaptive optimal control strategy based on the discretized model and output feedback has been shown as useful tool in this cases. It should be noted that exploration noise does not affect accuracy of the solution of discrete Riccati equation. Simulation results demonstrate the validity and effectiveness of the proposed control approach.

## ACKNOWLEDGEMENTS

This research has been supported by the Serbian Ministry of Education, Science and Technological Development under grant No. 451-03-9/2021-14/200108 and CNPq under grant No. 304032/2019-0.

## REFERENCES

- [1] N. Nedic, V. Stojanovic and V. Djordjevic, "Optimal control of hydraulically driven parallel robot platform based on firefly algorithm", *Nonlinear Dynamics*, Vol. 82(3), pp. 1457–1473, (2015)
- [2] D. Peng, X. Li, R. Rakkiyappan and Y. Ding, "Stabilization of stochastic delayed systems: Event-triggered impulsive control", *Applied Mathematics and Computation*, Vol 401 (2021) pp. 126054, (2021)
- [3] Y. Zhao, X. Li and J. Cao, "Global exponential stability for impulsive systems with infinite distributed delay based on flexible impulse frequency", *Applied Mathematics and Computation*, Vol. 386 (2020) pp. 125467, (2020)
- [4] R.S. Sutton and A.G. Barto, "Reinforcement Learning: An Introduction", MIT Press (USA), (1988)
- [5] B. Tao and Z.P. Jiang, "Value iteration and adaptive dynamic programming for data-driven adaptive optimal control design", *Automatica*, Vol. 71, pp. 348-360, (2016)
- [6] M. Roozegar, M.J. Mahjoob and M. Jahromi, "Optimal motion planning and control of a nonholonomic spherical robot using dynamic programming approach: simulation

and experimental results", *Mechatronics*, Vol. 39, pp. 174-184, (2016)

[7] J.H. Zhu, X.S. Ge and M.Z. Wang, "Adaptive dynamic programming method for attitude control of three-axis spacecraft", *Journal of Beijing University of information science and technology: natural science edition*, (2018)

[8] F.L. Lewis and K.G. Vamvoudakis, "Reinforcement learning for partially observable dynamic processes: adaptive dynamic programming using measured output data", *IEEE Trans. Syst. Man Cybern. B, Cybern*, Vol. 41(1), pp. 14–25, (2011)

[9] M.T. Rodriguez and S.P. Banks, "Linear, Time-Varying Approximations to Nonlinear Dynamical Systems", Berlin Springer (Germany), (2010)

[10] M. Mynuddin and W. Gao, "Distributed Predictive Cruise Control Based on Reinforcement Learning and Validation on Microscopic Traffic Simulation", *IET Intelligent Transportation Systems*, Vol. 14(5), pp. 270-277, (2020)

[11] A. Walle, F. Naets and W. Desmet, "Virtual microphone sensing through vibro-acoustic modelling and Kalman filtering", *Mech. Syst. Signal Process*, Vol. 104, pp. 120–133, (2018)

[12] Y.H. Chang, Q. Hu, C.J. Tomlin, "Secure estimation based Kalman filter for cyber-physical systems against sensor attacks", *Automatica*, Vol. 95, pp. 399–412, (2018)

[13] A. Cavallo, G. de Maria, C. Natale and S. Pirozzi, "Slipping detection and avoidance based on Kalman filter", *Mechatronics* Vol. 24(5), pp. 489–499, (2014)

[14] W. Gao, M. Huang, Z.P. Jiang and T. Chai, "Sampled-data-based adaptive optimal output-feedback control of a 2-degree-of-freedom helicopter" *IET Control Theory & Applications*, Vol. 10, pp. 1440-1447, (2016)

[15] J.F. Blackburn, G. Reethof and J.L. Shearer, "Fluid Power Control", Massachusetts, The MIT Press Cambridge (USA), (1960)

[16] M. Jelali and A. Kroll, "Hydraulic Servo-systems: Modelling", Identification and Control, Berlin: Springer (Germany), (2003)

[17] M.T. Rodriguez and S.P. Banks, "Linear, time-varying approximations to nonlinear dynamical systems", Berlin: Springer (Germany), (2010)

[18] T. Chen and B.A. Francis, "Optimal Sampled-data Control Systems", New York (USA) Springer-Verlag; (1995)

[19] G. Hewer, "An iterative technique for the computation of the steady state gains for the discrete optimal regulator", *IEEE Transactions on Automatic Control*, Vol. 16(4), pp. 382–384, (1971)

[20] K.J. Astrom and B. Wittenmark B, "Adaptive control", Addison-Wesley Longman Publishing Co., (1994)

# Speed-controlled hydraulic drive systems for heavy machinery

Darko Lovrec<sup>1\*</sup>, Vito Tič<sup>1</sup>

<sup>1</sup>Faculty of Mechanical Engineering, University of Maribor, Maribor (Slovenia)

*The paper discusses electrohydraulic variable supply systems in different design concepts. In the forefront of discussion are design concepts with constant and speed-controlled electric motor in combination with constant and variable pumps, implemented within different control strategies.*

**Keywords:** Hydraulic supply system, Variable pump flow, Control concepts

## 1. INTRODUCTION

Reductions in energy consumption and noise reduction regarding drive systems, as well as cost-effectiveness, are increasingly important factors in modern machinery design. All of the above requirements are especially important for machines equipped with hydraulic supply and drive systems. Application areas are heavy tool and metal shaping and forming machines, presses, and extruders, machines in the steel processing industry and all machines with a large installed power in many other areas. In some applications, rational energy use is more important than drive dynamics, while in other cases it is important to both. [1-2]

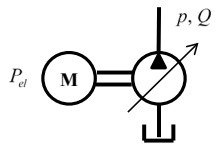
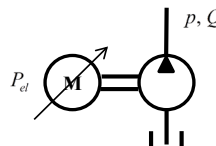
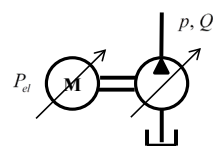
Adapting to the energy needs of the actuator, to the current load of the actuator or actuators, can be achieved with an adaptive hydraulic power supply system and an appropriate strategy for adjusting the power of the hydraulic actuator or actuators. For example, the Load-Sensing, LS system, has long been known as one such system, as well as the Flow-Matching system and many other variants, which represent larger or smaller upgrades of these and similar systems of this kind. What these systems have in common is that adjustable, variable hydraulic pump flow is used to adapt to the needs of the actuators – volumetrically pump control. Only the principle of volumetrically-controlled hydraulic energy (variable supply systems e.g. with the use of variable pumps), has proved satisfactory for the above requirements and solutions. In some cases, adaptation can be achieved with both hydraulic-mechanical and electro-hydraulic variant of the pump control, whereby the latter

variant providing a number of additional advantages, especially in terms of the use of appropriate adaptive control concepts – electro-hydraulic adaptive control concepts. In this regard, electro-hydraulic solutions in particular, make it possible to use all the advantages of modern electrical signal transmission and controller designs. [3-6]

In the electro-hydraulic version hydraulic variable supply systems of the pump control can be, in principle, controlled on hydraulically (pump control) or electrically (electric motor control) site. Constant-speed electric motors in combination with a variable displacement volume pump are commonly used solutions, in order to control flow, or consequently, the pressure of the fluid. The second concept represents the drive design using a constant displacement volume pump in combination with variable rotational speed electric motor. The latter concept is extremely interesting in praxis due to the affordable price and robustness of the complete drive. This is especially true in cases where a conventional, speed-controlled asynchronous electric motor and a suitable gear pump are used to perform the drive. In the third case, a speed-controlled hydraulic variable pump can be used. [7-10]

All three mentioned examples of variable drive design concept: variable pump and constant electric motor (hydraulic pump variable system), constant pump and variable speed electric motor drive (electric variable hydraulic system) as well as variable pump and variable speed electric motor drive (electric and hydraulic variable system), are shown schematically in Table 1.

Table 1: Different electrohydraulic variable drive concepts

|                         | Design concept CV<br>Asynchronous motor<br>Variable axial piston pump               | Design concept VC<br>Variable frequency drive controller<br>Asynchronous motor<br>Constant gear pump | Design concept VV<br>Variable frequency drive controller<br>Asynchronous motor<br>Variable axial piston pump |
|-------------------------|---|--|--|
| Pump's rotational speed | <u>C</u> onstant  | <u>V</u> ariable   | <u>V</u> ariable   |
| Pump's displacement     | <u>V</u> ariable  | <u>C</u> onstant   | <u>V</u> ariable   |
| Scheme                  |  |                  |                         |

\*Corresponding author: Smetanova ulica 17, Maribor, Slovenia; darko.lovrec@um.si

The paper discusses in more detail two design concepts for speed-controlled hydraulic drives. In the first case, a simpler example of a speed-controlled constant hydraulic pump is presented, using a cost-effective frequency-controlled asynchronous electric motor. A press-brake machine served as an example of the application of this concept. In the second case, the concept of a speed-controlled variable pump is presented. This concept involves the simultaneous control of the rotational speed of the drive electric motor combined with simultaneously adjusting the variable axial piston pump. This concept of cascade-control, with two controllers, enables the control of the drive with the highest efficiency, at the same time with higher dynamics.

2. VARIABLE PUMP FLOW WITH CONSTANT PUMP

The use of a constant pump driven by a speed-controlled asynchronous electric motor is one of the most cost-effective variants. In the case of a robust gear pump with internal gears, the entire design is additionally very robust and less sensitive to solid contaminants in hydraulic fluids. Using a low noise gear pumps (so-called silence pump), the noise level of the hydraulic drive is lower.

In a variant with a speed controlled asynchronous electric motor and the constant pump, the question often arises about the dynamics of the drive and its efficiency. “What are the characteristic properties and comparative advantages or disadvantages of this concept, particularly in regard to dynamic behaviour?” and “Is it possible to replace an existing hydraulic supply system powered by a hydraulic-mechanically controlled variable pump, with a speed-controlled constant pump?” The main concern is the high inertia of electro motors’ rotational parts, compared to the swash-plate of a variable pump.

In order to answer the above questions, the real application of an industrial press-brake was considered, which is used for cast product finishing in the automotive industry. Part of the hydraulic scheme of the discussed hydraulic press brake with its existing hydraulic-mechanically controlled axial piston pump needing to be replaced with speed controlled constant pump, is shown in Figure 1 (for more details see [4]).

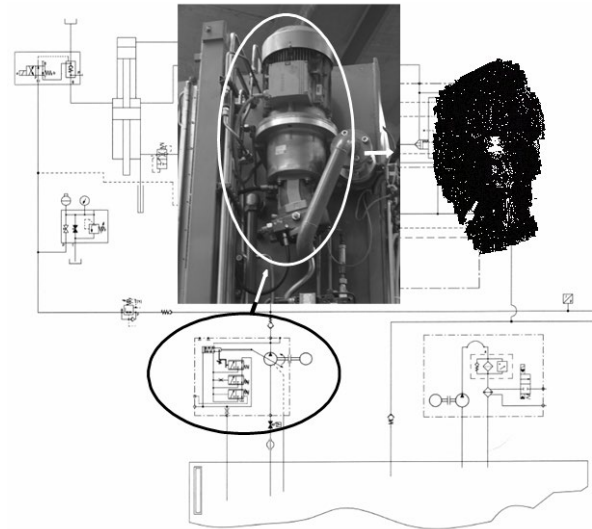


Figure 1: Hydraulic press brake with a variable pump replaced with a speed controlled constant pump

Each machine has its own working cycle – the duration of each working phase and the dynamics of speed changes between phases. In the case of replacing one type of drive with another, special care must be taken to ensure the same dynamics. This is even more important in the case of speed control with an electric motor, which is characterized by a large inertia mass of the rotor.

For the purpose of using a different drive concept, it is therefore first necessary to check the drive dynamics: to know the exactly profile of the working cycle. In the next step, it makes sense to build a test facility where we can practically check the dynamics of the new drive concept and give a statement on the suitability of the drive.

In order to carry-out the intended drive replacement, it was necessary to establish a real working-profile of the machine and its pressure characteristics over the whole working cycle and adapt it for testing purposes. The actual course of pressure changes in regard to more dynamically demanding machining is presented in Figure 2. It was used as a starting point for further studies.

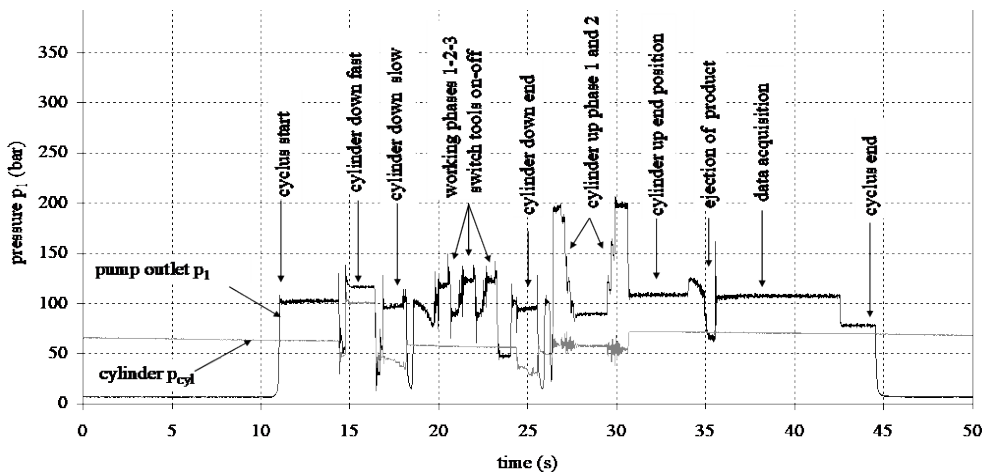


Figure 2: Real pressure profile over the working cycle with working phases

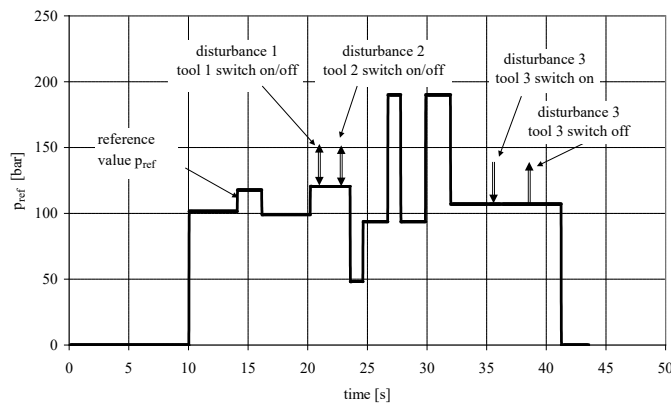


Figure 3: Adapted pressure profile for testing purposes

An adapted, but dynamically comparable pressure profile was generated, to be achieved by using a speed-controlled constant pump in load-sensing control concept. The adapted profile is presented in Figure 3.

### 2.1. Testing the speed-controlled constant pumps concept

In the first step, it was necessary to determine the difference in the dynamics of the response in the pressure control, performed once with a conventional variable pump and a second time with a speed-controlled constant pump. For this purpose and for the purposes of further research, a multi-purpose test facility was built, as shown in Figure 4. The drive capacity of the existing power unit was considered. A selection of those components to be used on the suggested drive concept was introduced for the test-rig. Cost-effective industrial components, available on the market, were used intentionally to build the rig.

A commonly used variable axial piston swash-plate pump (A10VSO NG30, Bosch-Rexroth), driven by a 15 kW asynchronous electric motor was used for the variable pump principle. Due to the constant drive speed ( $1500 \text{ min}^{-1}$ ) the flow depends solely on the pump swash-plate angle. Control of the swash-plate system is done by a proportional valve. The swash-plate control system is internally supplied from the pressure control pipeline system. Consequently, additional disturbance is introduced, but no additional supply system is needed.

For the concept of speed-controlled constant pump, axial piston pump was replaced by a constant internal gear pump (PGF3 31/032RE07VE4, Bosch-Rexroth) driven by the same 15 kW, but now speed-controlled asynchronous electric motor. The electric motor is driven by a frequency converter (Midimaster vector 6SE32, Siemens). The pump supplies a hydraulic pipeline system of equivalent length and dimensions (comparable hydraulic capacity and inductivity [4]), and corresponds to the existing pipeline systems of the press-brake, or different design variant (variation of pipeline lengths).

Overloading of the system is prevented by an additional pressure relief-valve. The remaining components of the test-rig are the loading unit, pressure sensors, and the control and signal acquisition system.

The loading unit consists of two throttle valves  $TV_1$  and  $TV_2$  which, used together with a proportional pressure valve, make-up the load – hydraulic cylinder of the press. The components of the loading units enable realistic simulation of the real system's workloads. Disturbances of

the control, such as switching on/off the additional actuators, was simulated by a directional-valve mounted in front of the throttle valve  $TV_2$ , enabling an almost instant change in the hydraulic flow.

Two additional pressure sensors were applied at the pump outlet port ( $p_1$ ), and at the end of the pipeline system ( $p_2$ ), for pressure variation acquisition.

All the devices needed for control of the constant pump and variable-speed electric motor (setting of control structure, controllers...) were integrated into the frequency converter. The setting of reference values, data acquisition, monitoring, and graphical interfacing were performed using a personal computer.

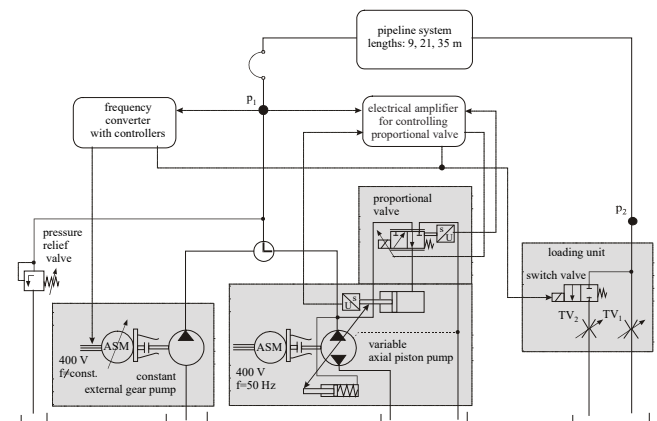


Figure 4: Structure of the test-rig

### 2.2. Features of both control concept

The conceptual design of such complex systems, including the interference of hydraulics, electronics, control techniques and sensor technology is a very demanding task. Application of a suitable block scheme can be a very helpful tool.

The special features of both concepts must be considered in order to understand and clearly describe the actual state and, consequently, specific behavior of the discussed control systems. [4]

For instance, in the case of the variable pump, it is reasonable to consider a specific type of supplying swash-plate system. An internally supplied 3/2-proportional control valve was used in our case. Such a design solution is simpler than a valve with additional external supply, but has certain disadvantages: any change in the disturbance value or reference values, influences the control loop's properties. A variable amount of fluid

needed for internal valve supply is taken from the controlled pipeline system, with the additional influence of the current pressure level. Consequently, inferior dynamic and static performance can be expected.

The principal simple block scheme of pressure control with a variable pump within a single control loop, and including the above specific features as used on our test rig, is presented in Figure 5 above.

When constant pump and speed-controlled asynchronous motor are used for pressure (or for flow as well as power) control, there are two active control loops: the speed control loop of the asynchronous motor as a secondary (internal) control loop, and the pressure control as a primary control loop. Such a solution is known as cascade-control [13].

In the case of cascade-control, two variables, pressure  $p$  and electric motor turning speed  $n$  are monitored. Both values are measured and controlled. A

principal block diagram of pressure control in the case of a constant pump is shown in Figure 5, below. The control system structure is typical example of cascade-control.

In the case of cascade-control, special attention should be paid to choosing an appropriate type of controller (see e.g. [13]). It is important to ensure that the selected secondary controller provides sufficient control loop dynamics, which must be as fast and stable as possible, over whole the expected operating range. The primary controller must allow for optimal pressure control behaviour. In the case under consideration, a P-controller was used in the secondary loop, and a PID-controller was used in the primary control-loop. When both secondary and primary controllers are applied, more appropriate dynamic behaviour can be expected. The application of a secondary controller allows for faster disturbance handlings in the secondary loop.

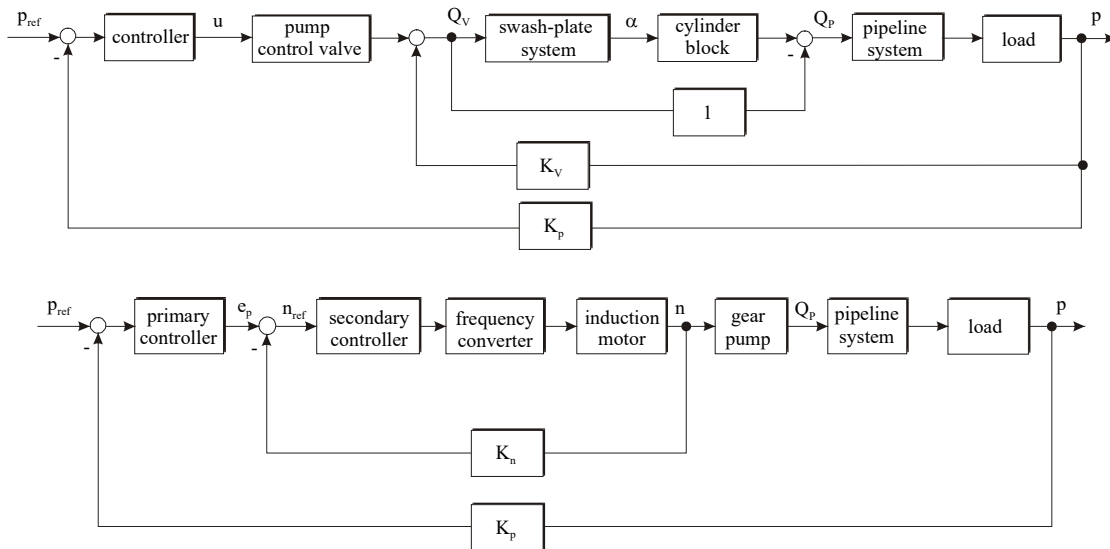


Figure 5: Principal block diagram of discussed control concepts; with a variable pump (above) and constant pump (below)

For the testing purposes regarding the dynamic behaviour of both pressure control concepts a principal pressure profile of the combined reference-disturbance behaviour, for the equal pipeline length, was designed – Figure 6. The assumed ratio of dynamic responses corresponds to the ratio of inertia of the electric motor’s rotational parts, compared to the swash-plate of the variable pump. Consequently, due to a higher electric motor, the inertia speed-controlled concept is expected to react more slowly.

The reference behaviour of the control (following the prescribed reference pressure profile) is presented by a step change of the reference value up to 140 bars. The disturbance behaviour is afterwards simulated by switching the additional load (throttle valve TV<sub>2</sub>) on/off. Throttle valves are adjusted in such manner that at the working point OP<sub>1</sub> the pump flow tilts in order to deliver 35 % of maximum flow and approximately 70 % in OP<sub>2</sub>.

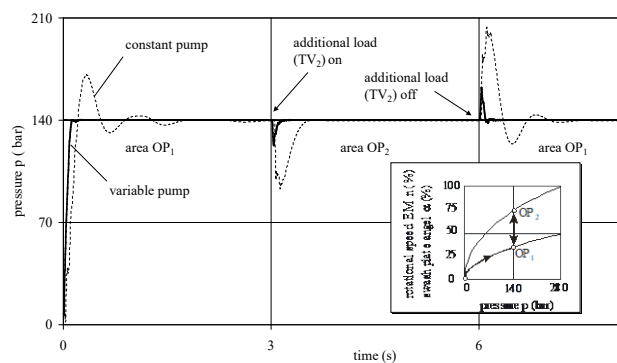


Figure 6: Expected responses to the reference and disturbance steps for both drive concepts

Rapidly opening of the throttle valve causes a substantial drop in pressure. Consequently, fluid flow changes according to the components characteristics. Due to control error, the swash-plate angle is increased, in the case of speed-controlled motor, and turning speed is increased, respectively. Until the flow through the throttle valves is higher than the pump flow, the pressure decreases. In order to sustain the required pressure, the pump must replace the missing volume. The swash-plate

angle, or electric motor turning speed, respectively, increases until the pressure exceeds the required value. When the required pressure is reached, both the increasing values remain fixed. Analogous, but inverse behaviour is present when closing the same throttle valve.

It is necessary to perform both control concepts under equal conditions: the same operating conditions, same change of operational points, same pipeline lengths and same loads.

A satisfactory answer to the question: "What is the actual difference between the dynamic responses of both pressure control concepts?" can only be obtained by experimental comparison of both. A comparison of the concepts is shown here only for the case of a 33 m long pipeline and for equal control requirements.

The main objective of the control was to achieve a quality pressure profile as a controlled quantity, regarding reference and disturbance actions: small or no steady state errors, acceptable overshoot, appropriate dynamics and a short-time of disturbance compensation. The control responses achieved by the variable and constant pump are presented in Figure 7.

The Figure 7 shows the dynamic responses to typical steps in the reference value achieved with the variable pump in a test the configurations for 33 m long pipeline. Any influence on the operating points and corresponding pressure losses can be noticed. The pressure losses (difference between  $p_1$  and  $p_2$ ) are due to a relatively smaller pump flow in OP<sub>1</sub> (see value of the swash-plate angle  $\alpha$ ) smaller than in OP<sub>2</sub>.

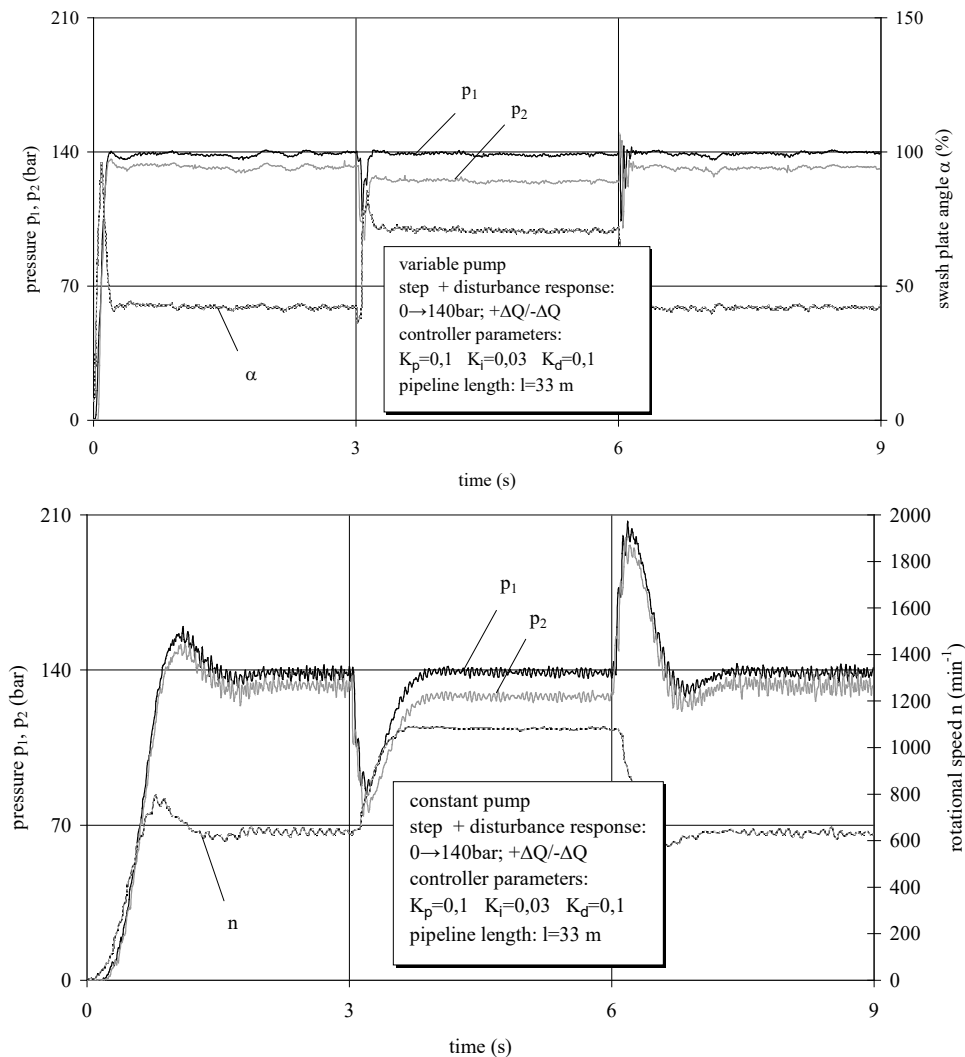


Figure 7: Experiment; pressure, rotational speed and power distribution in the case of a variable pump (above) and a speed-controlled constant pump (below)

Comparison of the dynamics regarding the reference behavior of pressure between variable and constant pump concepts gives the ratio 1 : 4.7. In the case of disturbance behavior when switching on the load, the obtained ratio is approximately 1 : 3 and by switching the load off 1 : 4.4. Based on the obtained experimental results, the general ratio of dynamic responses (variable pump versus constant pump principle) can be estimated at between 1 : 4 and 1 : 5. In other words, the variable pump

control, CV-concept responds 4 to 5 times faster than the constant pump VC-concept, in spite of the much higher rotating masses inertia ratio (swash-plate versus electric motor rotor).

Besides the known dynamic ratio of both compared control concepts, it is reasonable to consider some other features like the necessity of pressure signal conditioning, choice of appropriate electric motor and frequency converter to be applied in hydraulic systems and,

nevertheless, to choose an appropriate constant pump and to be familiar with the operational regime that is to be applied in such a concept. This complex and interdisciplinary know-how is needed to assure faultless and maintenance-free operation.

In the case of constant pump VC-concept, much higher pressure pulsation can be noticed than in the case of the variable pump. Such behavior can be ascribed to the applied signal conditioning.

In the case of variable pump flow and, consequently, pressure pulsation corresponds to the turning speed, the number of pump pistons, and is constant. Signal filtering can be set regarding the above known frequency. This is not the case when pressure control is realized with a constant pump and variable electric motor turning speed. Frequency changes according to the value of the product: number of gear teeth times turning speed.

In the case with speed-controlled pump, it is possible to filter the controlled value with a filter of constant settings, whereas it is inapplicable in the second case. An adaptive filter (see e.g. [14]) should be used or a turning speed (operating point) should be chosen, where the signal filtering is optimal. Consequently, signal filtering will not be optimal at every other turning speed. The latter type of filtering was applied in order to preserve a simple design for the suggested control concept. Consequently, it results in higher pulsation of the pressure at every non-optimal rotation speed, and a corresponding influence on the control of the electric motor's rotation speed. For more information regarding pressure control with both concepts and different influencing factors, modelling the system is given in the literature [12], [13], [15], [16].

### 2.3. Load-sensing pressure control concept

In our case, the implementation of a speed-controlled constant pump, the pressure control was performed according to the load-sensing (LS) control concept. When supplying a number of independent valve-controlled actuators with different loads and with a single pump, in the load-sensing concept, the supply pressure is adjusted to suit the actuator's highest pressure value.

In a load-sensing concept, the supply pressure is variable. It changes to accommodate the highest load pressure. It lies at a value  $\Delta p_{LS}$  above the highest load pressure. When the LS-system with variable pump is used, the pressure and flow dependent losses are reduced. Pressure is measured at the most loaded actuator  $p_2$ , (see Figure 4), while the pump is controlled according to the pressure increased by a certain  $\Delta p_{LS}$  (actual pump control pressure is:  $p_2 + \Delta p_{LS}$ ), needed to cover the losses in a hydraulic pipeline system. The use of a variable displacement pump in a load-sensing operation presents the most economical energy supply type for several valve-controlled actuators (for more details see [12]).

LS-control concept is, in fact, a pressure control approach where the controlled value is not 'given from outside' but generated inside the controlled system,

depending on the actual load. The required pressure level corresponds to the current level of load increased for the value of the pressure difference due to the load  $\Delta p_{LS}$ . To reduce power losses,  $\Delta p_{LS}$  should be as small as possible, then again big enough to ensure the expected dynamic.

In the following, the LS-pressure control concept using a variable speed motor and constant pump was tested experimentally for a previously presented operational profile of a metal forming machine. Such a strategy was chosen due to the fact that the hydraulic cylinder of the press for most of the working cycle operates as the most loaded actuator with variable load (except in the initial and final phases during product manipulation – see Figure 2). Above all, the main purpose of the presented work was to check the feasibility of the LS-control concept with a variable speed motor and constant pump in the case of a real operational profile for metal-forming machine.

Application of such concept was motivated by scepticism regarding the dynamic properties of control systems using variable pumps with higher inertia of rotational parts. It could be even slower in combination with the LS-control concept where the controlled value is generated inside the controlled system.

The existing controllers in the used frequency converter were used for realization of cascade-control. It was necessary to configure the control structure and set appropriate controller parameters, to meet the requirements of the described cascade control. Definition and optimisation of both controllers was carried out, in accordance with the principles of the control technique: always in a stable and optimally steady-state, and with dynamic behaviour. The above-mentioned necessary tasks were also done in compliance with the manufacturer's instructions for the applied frequency converter.

A PI-controller was used, as a secondary controller, to control speed, whereas the integral parameter was set as low as possible (to achieve behaviour similar to the suggested simple P-controller). A PID-controller was used, as primary controller, to control the pressure, whereas a higher integral parameter was set to achieve pressure control without steady-state error.

An actual profile of the achieved control-values, using the suggested LS-control concept, is shown in Figure 8. The actual profile is in accordance with a simplified pressure profile as shown in Figure 3. The variable flow of the constant pump and power is presented, in addition to the pump pressure profile. The latter two profiles were calculated from the actual turning speed and geometrical volume of the pump, regarding the influence of compressibility and temperature of the media.

The pressure, rotational speed and calculated power of the driven electrical motor are achieved using load-sensing reference value  $\Delta p_{LS,ref} = 10$  bar. As mentioned before it must be sufficient to cover all pressure losses in the system and to enable expected dynamics.

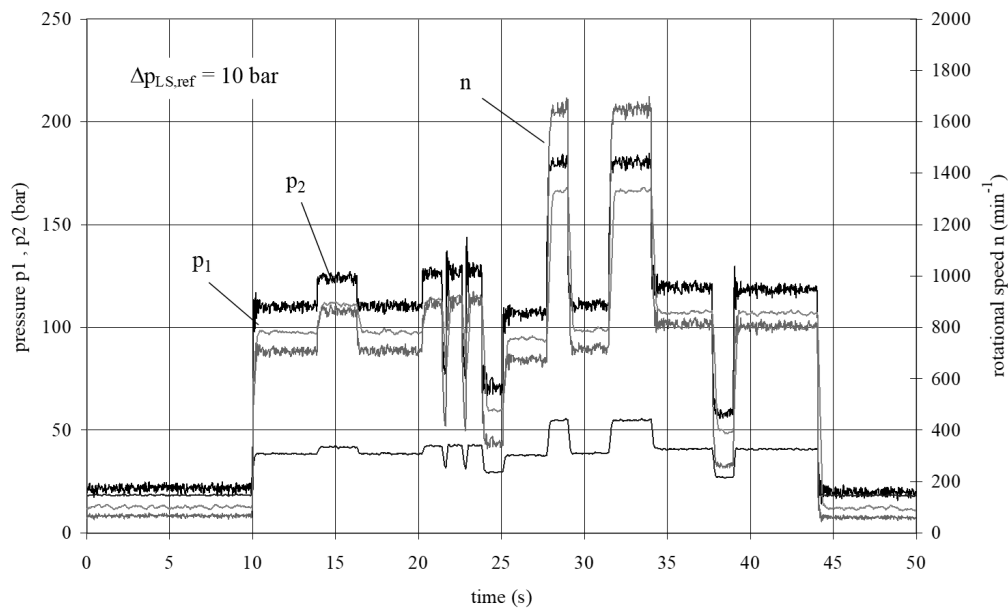


Figure 8: Experiment; pressure, rotational speed and power distribution in the case of a speed-controlled motor and internal gear pump  $\Delta p_{LS,ref} = 10$  bar

As it can be seen from Figure 8,  $\Delta p_{LS,ref} = 10$  bar enables suitable dynamics of the actuator  $p_{load} = p_2$  – press cylinder to follow pressure changes during the working cycle.

Choosing a suitable  $\Delta p_{LS,ref}$  is very important for achieving adequate dynamics. This system will provide very good control dynamics if too high a value is selected, but will operate at higher pressure than needed. Consequently energy consumption and power losses will be increased. In the case of  $\Delta p_{LS,ref}$  set too low (e.g.  $\Delta p_{LS,ref} = 6$  bar), power losses will decrease but it will be impossible to achieve the required control dynamics. To satisfy general power-loss reduction efforts, it certainly must be taken into account. [4]

As can be seen from the experimental results, the suggested LS-control concept using variable speed motor and constant pump enables low energy losses and reasonably priced solutions. It can be used for metal forming machines, despite some doubt regarding dynamics.

### 3. VARIABLE PUMP FLOW WITH SPEED CONTROLLED VARIABLE PUMP

The fact is, that the most machines are still using the classic drive concept: A constant volume pump or, as a better solution, the usage of a variant variable displacement pump, in both cases driven at constant speed. The requirement for greater robustness, taking into account the reasonable price, has led to usage of the speed controlled constant pumps. However, such a concept cannot meet the dynamic requirements of the classic drive concept.

The more effective approach, to adapt the supply energy to the actual needs of the actuator(s) or load, offers the combination of a variable pump and a speed-controlled electric motor. Within this drive concept, two parameters need to be adjusted: The rotational speed of the electric motor and the displacement volume of the used variable

pump as well. All three mentioned adaptive supply principles with main properties are shown in Table 1.

More information regarding the detailed drive design, including the specified type and characteristics of used components, along with its efficiency, reliability, robustness, operating costs, purchase price, has been the subject of various researches e.g. [17] – [22]. The same applies to studies related to the use of a wide range of control concepts and control strategies, from classical to non-linear approaches that have proven to be effective on hydraulic or other types of drives, e.g. [23] – [29]. In studies, the focus was on efficiency of a specified drive concept, at different operating points, but with less attention to its dynamics.

In this control concept (VV-concept), two aspects are in the forefront of interest. The first is achievable dynamics, as in this case we have two options to "speed up" the response: by changing the setting of the variable pump (for example, the angle of the swash-plate of the axial piston pump) and at the same time by changing the speed of the electric drive motor above the nominal speed characteristic for mains voltage frequency.

Another aspect is to achieve the best possible efficiency of the entire electric motor-pump drive unit. For both the electric motor and the pump, the value of the total efficiency of each component depends on the operating parameters. Thus, e.g. the value of the total efficiency of the variable pump depends on the operating speed of the pump, the height of the operating pressure and the setting of the variable pump (of course at a certain viscosity of the hydraulic fluid). Similarly applies to the efficiency of the electric motor. In the case that the maximum efficiency of the entire drive is at the forefront as a control strategy, the speed of the electric motor and the pump setting can be adjusted so that at each operating point, the total efficiency is always in the area of the highest values. Similarly, we can set a strategy for achieving the fastest system response.

In the case of using a variable pump, a fourth concept can be used: the variable pump can be used as a constant pump, by setting it to the maximum flow quantity, or even to a smaller one. This variant corresponds in principle to the use of a constant pump, e.g. gear pumps, only in this case we use another type of pump, e.g. axial piston pump (APP), which has a higher efficiency than the gear pump. In the case of a speed-controlled variable APP set to a constant maximum value, this concept could be termed VC-APP-concept.

3.1. Comparison of dynamics and efficiencies

To compare different drive concepts, the comparison criteria need to be chosen. The most sensible is to compare the efficiency. However, since all the drive concepts do not follow the pressure set-point the same way, it is necessary to compare the included control error - the difference between the pressure set-point and the actual pressure. This can best be done by calculating the root mean squared error according Eq. (1), since it eliminates the influence of the sign of the error.

$$RMSE = \sqrt{\frac{\sum_{i=1}^n (p^*(i) - p(i))^2}{n}} \quad (1)$$

- RMSE [bar] root mean square error
- n [-] number of pressure measurements
- p\*(i) [bar] pressure set-point of i<sup>th</sup> measurement
- p(i) [bar]...actual pressure of i<sup>th</sup> measurement

Because the pressure waveform is different, supplied hydraulic energy is also not the same for all concepts, so it makes sense to add the consumed electrical and supplied hydraulic energy to the list. A lot of information of the dynamics of each concept is hidden in overshoot and setup time of the step change. Overshoot is defined as the maximum excess of the desired value of; set-time as the time that elapses from the initiation until the actual value reaches and remains within 5 % of the desired value. The comparison will include both parameters at a step change from 50 bars to 150 bars.

To increase ease of comparison, all the criteria will be combined using weighted average, which will result in a numeric score. All the criteria, including weights, are shown in Table 2.

The best scores in each category are indicated in Table 3. The percentages for all criteria are weighted, summed and displayed in the last column of Table 3.

The consumed electricity and the supplied hydraulic energy have been measured over 50 consecutive cycles, which improves the accuracy of the measurements, as a cycle lasts for only 5 s. The average yield was calculated as the quotient between the produced and consumed energy. Both form of energies quoted in Table 4 refer to one cycle. RMSE was calculated for the entire cycle and only sinusoidal change (3 s to 5 s). For the second step, settling time and overshoot were calculated. A close-up view of step changes of all the concepts is presented in Figure 9.

Table 2: Weights and criteria for comparing different drive concepts

| Category                | Energy             |                      |                           | Dynamics   |           |               |           |
|-------------------------|--------------------|----------------------|---------------------------|------------|-----------|---------------|-----------|
| Category weight         | 60 %               |                      |                           | 40 %       |           |               |           |
| Criterion               | Average efficiency | Consumed electricity | Supplied hydraulic energy | Total RMSE | Sine RMSE | Settling time | Overshoot |
| Weights inside category | 50 %               | 30 %                 | 20 %                      | 60 %       | 20 %      | 10 %          | 10 %      |
| Final weights           | 30 %               | 18 %                 | 12 %                      | 24 %       | 8 %       | 4 %           | 4 %       |

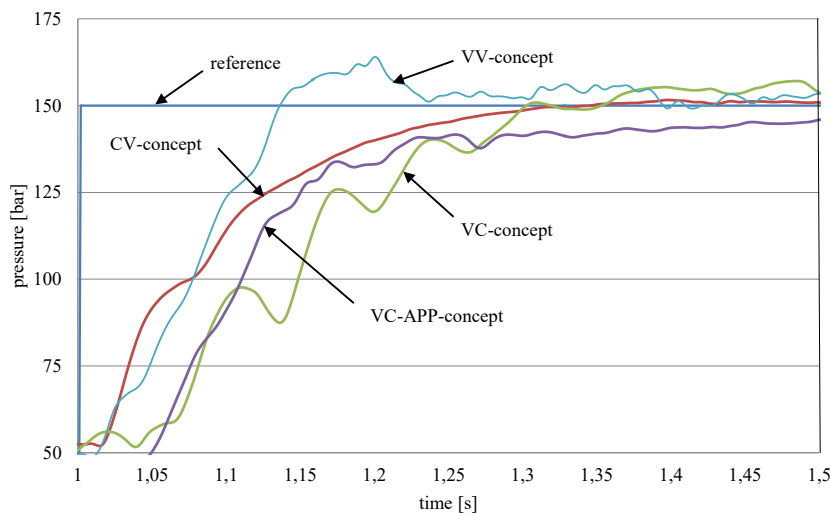


Figure 9: Comparison of step responses (from 50 bars to 150 bars) for different drive concepts

Table 3: Measurement results of dynamics of different drive concepts

| Concept        | Average efficiency | Consumed electricity [kJ] | Supplied hydraulic energy [kJ] | Total RMSE [bar] | Sine RMSE [bar] | Settling time [s] | Over-shoot [bar] | Total  |
|----------------|--------------------|---------------------------|--------------------------------|------------------|-----------------|-------------------|------------------|--------|
| CV-concept     | 57,7 %             | 46,2                      | 26,7                           | 12,55            | 8,10            | 0,22              | 1,63             | 94,0 % |
| VC-concept     | 56,9 %             | 45,4                      | 25,8                           | 21,22            | 14,42           | 0,28              | 7,07             | 79,7 % |
| VC-APP-concept | 57,5 %             | 46,0                      | 26,5                           | 19,79            | 12,56           | 0,36              | 0                | 83,1 % |
| VV-concept     | 53,6 %             | 47,5                      | 25,5                           | 14,49            | 4,45            | 0,13              | 14,00            | 89,3 % |

Based on the average efficiency all the drive concepts perform similarly. The least efficient was the VV-concept with PID<sup>2</sup>-controller. The smaller average efficiency is due to non-optimal setting of the pump setting, and the unneeded acceleration and braking of the rotating parts. Although the desired pressures for all the concepts are the same, the produced hydraulic energy differs throughout different concepts, due to different control strategies. Concepts with lower dynamics produced less hydraulic power.

The ability to trace the desired profile is higher when using a variable displacement pump. RMSE is there more than 3-times lower. The dynamics of the systems are similar; VV-concept, which has for one-third the shortest settling time times with little higher overshoot. We were surprised that the dynamics (short settling time) of the drive concepts using a variable displacement pump were approximately 3-times higher, compared to those using a constant pump, whereas the literature states approximately 4-times higher dynamics. The case for this difference could be noise on the pressure signal, which prevented us from attenuating the controller parameters further.

#### 4. CONCLUSION

Using a constant speed electric motor and variable pump (CV-concept) is the concept with a fairly high dynamic but a lower overall efficiency, (when also considering the electric motor efficiency at the pump's operating point), and less robust than a constant pump and variable speed drive (VC-concept).

VC-concept was asserted mainly due to good efficiency and a wide operating range [31]. It also excels at lower operating costs and a consecutively smaller effect on the environment. Lower operating costs and higher efficiency come mainly from the more efficient connection of the motor to the electrical grid via a variable-frequency drive controller. However, VC-concept also has one major drawback: a slow system response that occurs due to the moments of inertia of the rotating parts (motor rotor and rotary parts of the pump). The response of CV-concept is up to 5 times faster than the response of VC-concept [30] but both responses are good enough for most hydraulic applications.

If we look for the highest efficiency of the entire drive train at high responsiveness, the third concept (VV-concept) is promising drive concept. The biggest drawback of VV-concept is the highest purchase price amongst all the concepts because a variable frequency drive controller and a variable displacement pump are needed, where the variable displacement pump is the more expensive component of the required components. Additionally is also necessary to pay attention to the hydraulic fluid

cleanliness level and, of course, to know the values of the efficiencies of each component within the entire field regarding all operating parameters.

A principle comparison of the characteristics of each type of drive design concept is summarized in Table 4.

One of the disadvantages of the speed variable drive concepts, based on the use of an asynchronous electric motor, is motor acceleration and deceleration for short pressure bursts. If a valve opens for 1 second, for example, the motor starts to accelerate to increase pressure and, after 1 second, has to decelerate again as the pressure is too high because the valve has closed again.

Every acceleration and deceleration using asynchronous electromotors results in higher current, which yields higher copper losses, where energy from decelerating rotating masses can be regenerated when using a state-of-the-art variable frequency drive controller. It is easily avoidable by adding a hydraulic accumulator to the hydraulic circuit, which smooths short pressure bursts and aids the motor and pump in their battles with rapid pressure changes.

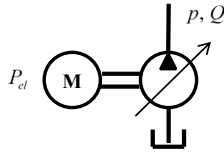
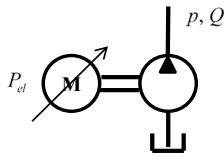
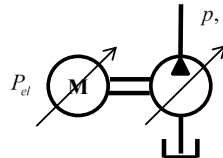
From the drive component point of view, instead of usage of a frequency controlled asynchronous motor, a much better variant represents the usage of a speed-controlled electric servo motor. Due to its smaller inertia, its responsiveness is much better. This was also the reason why the VV-concept did not show even better dynamics than was achieved with the currently used "slow" asynchronous electric motor.

On the signal side, in respect to the control concept, the further improvement in regard to the energy efficiency is the implementation of an advanced control strategy, e.g. the usage of the s.c.  $\eta$ -drive concept or maximum efficiency drive concept, which is based on the VV-concept [31].

The heart of the  $\eta$ -drive concept is a maximum efficiency controller. The maximum efficiency controller controls the pump's displacement and rotational speed of the asynchronous motor using the variable frequency drive controller.

The maximum efficiency controller is based on a combination of a Look-up Table and a classic PID controller. The PID-controller is used to control the displacement of the axial piston pump. The advantages of using a PID-controller for displacement control are elimination of steady state error, fast response to rapid pressure changes and the ability to track pressure when the rotational speed of the motor is changing to the optimum. [32]

Table 4: Considered variable electrohydraulic supply concepts in comparison

|                         | <b>Design concept CV</b>  | <b>Design concept VC</b>   | <b>Design concept VV</b>  |
|-------------------------|---|--|---|
|                         | Asynchronous motor<br>Variable axial piston pump                                  | Variable frequency drive controller<br>Asynchronous motor<br>Constant gear pump    | Variable frequency drive controller<br>Asynchronous motor<br>Variable axial piston pump |
| Pump's rotational speed | Constant  | Variable   | Variable  |
| Pump's displacement     | Variable  | Constant   | Variable  |
| Scheme                  |  |  |      |
| Efficiency              | Lower   | Higher   | Highest   |
| Reliability             | High  | High   | High  |
| Robustness              | Less  | More   | Less  |
| Operating costs         | Highest   | Higher   | Lower   |
| System dynamics         | Highest<br>4.4  | Low<br>1.0   | Control principle<br>dependent (approx. 4)  |
| Purchase price          | Higher  | Lower  | Highest   |

The next limitation when implementing the variable drive concept is at those operating points where the best efficiencies are achieved at pump settings close to 100 %. A Look-up Table that reports the best rotational speed at which a pump setting of higher than 100 % would be needed to reach the pressure set-point. This error can arise due to fluid changes, temperature changes, wear or Look-up Table smoothing during calculation. To avoid this limitation, a feedforward loop for rotational speed should be added to increase rotational speed further if the desired pressure set-point cannot be reached with a 100 % pump setting.

Further improvement can be made for machines with cyclic operational cycles, where the pressure cycle or load demands are repeating throughout the machines' operations. The pressure changes in this case can be predicted in advance. Therefore, it would be reasonable to couple the maximum efficiency controller with the Model Predictive Controller (MPC), which has already proved to be very useful for machines with repeating operation cycles.

#### REFERENCES

- [1] S. Helduser, "Improved Energy Efficiency in Plastic Injection Molding Machines", 8<sup>th</sup> Scandinavian International Conference on Fluid Power, SICFP'03, Tampere, Finland, (2003)
- [2] A. Helbig, "Injection Molding Machine with Electric-Hydrostatic Drives", 3. International Fluid Power colloquium, Aachen, Volume I, pp. 67-81, (2002)
- [3] H. Esders, "Elektrohydraulisches Load Sensing für Mobile Anwendungen" (in German), O+P Ölhydraulik und Pneumatik 36, Nr.8, (1994)
- [4] D. Lovrec, M. Kastrevc, S. Ulaga, "Electro-hydraulic load sensing with a speed-controlled hydraulic supply system on forming-machines", The International Journal of Advanced Manufacturing Technology, Vol. 41, No. 11-12, pp. 1066-1075, doi: 10.1007/s00170-008-1553-y, (2009)
- [5] W. Huang, L. Quan, J. Huang, "Flow Matching with combined control of the pump and the valves for the independent metering swing system of a hydraulic excavator", Proceedings of the Institution of Mechanical Engineers Part D Journal of Automobile Engineering, Vol. 232, Iss.10 (1):095440701772884, pp. 1310-1322, doi:10.1177/0954407017728848, (2017)
- [6] Z. Quan, L. Gei, Z. Wei, Y.R. Li, "A survey of powertrain technologies for energy-efficient heavy-duty machinery, Proceedings of the IEEE PP(99), DOI:10.1109/JPROC.2021.3051555, (2021)
- [7] I. Rühlicke, "Elektrohydraulische Antriebssysteme mit drehzahlveränderbarer Pumpe," PhD Thesis, TU Dresden, (in German), (1997)
- [8] T. Neubert, "Untersuchungen von drehzahlveränderbaren Pumpen (Eng.: Research of speed controlled pumps)", PhD Thesis, TU Dresden, (2002)
- [9] R. Bonefeld, R., Ch. Lebert, "Adaptive pressure control using variable speed pump", 6<sup>th</sup> International Fluid Power Conference Dresden, Workshop Proceedings, pp. 151-164, (2008)
- [10] M. Ristic, M., "Conversant technology – New key aspects: Development of variable speed drives", 6<sup>th</sup> International Fluid Power Conference, Conference Dresden, Proceedings, pp. 93-108, (2008)
- [11] D. Lovrec, M. Kastrevc, "Modelling and simulating a controlled press-brake supply system", International journal of simulation modelling, ISSN 1726-4529, Vol.

- 10, No. 3, pp. 133-144, doi: 10.2507/IJSIMM10(3)3.184, (2011)
- [12] D. Lovrec, E. Detiček, F. Faber, "Electro hydraulic load-sensing with closed-loop controlled actuators - theoretical background", *Advances in production engineering & management*, ISSN 1854-6250, Vol. 4, No. 3, pp. 93-104. [http://maja.uni-mb.si/files/APEM/APEM4-3\\_093-104.pdf](http://maja.uni-mb.si/files/APEM/APEM4-3_093-104.pdf), (2009)
- [13] D. Lovrec, S. Ulaga, "Pressure control in hydraulic systems with variable or constant pumps?", *Experimental techniques*, ISSN 0732-8818. [Print ed.], Mar./Apr. 2007, Vol. 31, No. 2, pp. 33-41. <http://dx.doi.org/10.1111/j.1747-1567.2007.00146.x>, (2007)
- [14] A. H., Sayed, "Fundamentals of Adaptive Filtering", John Wiley & Sons, NY, p. 1168, (2003)
- [15] D. Lovrec, F. Faber, "Electrohydraulic pressure control by a self-adjusting proportional derivative controller", *Experimental techniques*, ISSN 0732-8818. [Print ed.], May/June 2006, Vol. 30, No. 3, pp. 57-63. <http://dx.doi.org/10.1111/j.1747-1567.2006.00044.x>, (2006)
- [16] D. Lovrec, E. Detiček, "Improvement of the statical behaviour of pressure controlled axial piston pumps", *Strojniški vestnik*, ISSN 0039-2480, 2009, Vol. 55, No. 12, pp. 766-774, [http://www.sv-jme.eu/scripts/download.php?file=/data/upload/2009/SV-12-09/5\\_2009\\_069\\_Lovrec\\_zl\\_p766\\_774.pdf](http://www.sv-jme.eu/scripts/download.php?file=/data/upload/2009/SV-12-09/5_2009_069_Lovrec_zl_p766_774.pdf), (2009)
- [17] M. Xu, B. Jin, G. Chen, J. Ni, "Speed-Control of Energy Regulation Based Variable-Speed Electrohydraulic Drive", *Journal of Mechanical Engineering*, Vol. 59, No. 7-8, pp. 433-442, doi:10.5545/sv-jme.2012.91, (2013)
- [18] F.J.T.E. Ferreira, J. Fong, A. De Almeida, "Ecoanalysis of variable-speed drives for flow regulation in pumping systems", *IEEE Transactions on Industrial Electronics*, Vol. 58, No. 6, pp. 2117-2125, (2011)
- [19] W. Wang, B. Wang, "An energy-saving control strategy with load sensing for electro-hydraulic servo systems", *Journal of Mechanical Engineering*, Vol.62, No 12, pp. 709-716, doi:10.5545/sv-jme.2016.3685, (2016)
- [20] J. Huang, Z. Zan, L. Quan, Y. Lan, "Characteristics of delivery pressure in the axial piston pump with combination of variable displacement and variable speed", *Proceedings of the Institution of Mechanical Engineers, Part I: Journal of Systems and Control Engineering*, Vol. 229, No. 7, pp. 573–586, (2015)
- [21] T. Tašner, K. Les, V. Tič, D. Lovrec, "Energy efficiency of different electrohydraulic drives", 9<sup>th</sup> International Fluid Power Conference, RWTH University, IFAS, pp.14-25, (2014)
- [22] M. Man, F. Ding, C. Ding, S. Liu, S. "Study of an Energy Regeneration System with Accumulator for Hydraulic Impulse Testing Equipment", *Journal of Mechanical Engineering*, Vol. 61, No. 3, pp. 196-206, doi:10.5545/sv-jme.2014.2138, (2015)
- [23] E. Detiček, M. Kastrevc, "Design of Lyapunov based nonlinear position control of electrohydraulic servo systems", *Journal of Mechanical Engineering*, Vol. 62, No. 3, 163-170, doi: 10.5545/sv-jme.2015.2921, (2016)
- [24] T. Žilić, J. Kasać, M. Essert, B. Novaković, Ž. Šitum, "Performance Comparison of Different Control Algorithms for Robot Manipulators", *Strojjarstvo – Journal for the theory and application in mechanical engineering*, Vol. 54, No. 5, pp. 399-407, (2012)
- [25] H. Zupan, N. Heraković, M. Starbek, J. Kušar, "Hybrid algorithm based on priority rules for simulation of workshop production", *International journal of simulation modelling*, ISSN 1726-4529, Vol. 15, No. 1, pp. 29-41, doi: 10.2507/IJSIMM15(1)3.319, (2016)
- [26] J.F. Wang, W.L. Kang, J.L. Zhao, K.Y. Chu, "A simulation approach to the process planning problem using a modified particle swarm optimization", *Advances in Production Engineering & Management*, Vol. 11, No. 2, pp. 77-92, <http://dx.doi.org/10.14743/apem2016.2.211>, (2016)
- [27] T. Tašner, V. Tič, D. Lovrec, "Advanced control concepts suitable for energy efficient hydraulic systems", *SIMULTECH 2013, 3<sup>rd</sup> International Conference on Simulation and Modeling Methodologies, Technologies and Applications*, Reykjavik, pp. 3-11, (2013)
- [28] I. Petrović, T. Pavlic, A. Čikić, "The approach to stability determination of single axis positioning regulation for the model of TTT manipulator", *Technical gazette*, Vol. 21, No. 5, pp.1041-1046, (2014)
- [29] B. Mohd, A. Mohd, K.A. Danapalasingam, A.R. Husain, "Design and optimization of backstepping controller for an under actuated autonomous Quadrotor unmanned aerial vehicle", *Transaction of FAMENA*, Vol. 38, No. 3, pp. 27-44, (2014)
- [30] P. Casoli, N. Pompini, L. Riccò, "Simulation of an Excavator Hydraulic System Using Nonlinear Mathematical Models", *Journal of Mechanical Engineering*, Vol. 61, No. 10, pp. 583-593 doi:10.5545/sv-jme.2015.2570, (2015)
- [31] D. Lovrec, V. Tič, T. Tašner, "Simulation-aided determination of an efficiency field as a basis for maximum efficiency-controller design", *International journal of simulation modelling*, ISSN 1726-4529, Vol. 14, No. 4, pp. 669-682, doi: 10.2507/IJSIMM14(4)9.324, (2015)
- [32] D. Lovrec, T. Tašner, V. Tič, "Dynamic behaviour of different hydraulic drive concepts – comparison and limits", *International journal of simulation modelling*, ISSN 1726-4529, Sep. 2017, Vol. 16, No. 3, pp. 448-457, (2017)



# Design of PID Controllers for the System of a Pump Controlled Hydro-Motor

<sup>1</sup>\*Ljubiša Dubonjić, <sup>2</sup>Saša Prodanović, <sup>1</sup>Novak Nedić

<sup>1</sup>Faculty of Mechanical and Civil Engineering Kraljevo, University of Kragujevac, Serbia

<sup>2</sup>University of East Sarajevo, Faculty of Mechanical Engineering, East Sarajevo, Bosnia and Herzegovina

**Abstract:** This paper presents design of a PID controller for the system of a pump-controlled motor with a long transmission line. By using possibilities offered by computers and software the graphical method is used in the design of PID controllers. The D-decomposition method including system performances, damping and settling time was applied. This type of controllers frequently satisfies practical needs because the feedback loop system is fast, and the static error is reduced to 0. The proposed method allows easy design of PID controllers in significant modifications of lengths of the transmission line. The system performances are included in a new manner without the need for calculation of Chebyshev functions for every change of the damping coefficient thanks to strong software support.

**Keywords:** PID controller, D-decomposition, relative stability, settling time, robustness

## 1. INTRODUCTION

Increasingly strict and wide requirements regarding displacement hydrostatic power transmitters have recently appeared in the sense of simultaneous accomplishment of high power exploitation degrees, high speed of response with the reduction of price [1-4]. This particularly refers to high power systems and systems with variable load (building and mining machines, agricultural machines, transportation machines, machine tools, etc). It is obvious that these requirements result in the need for more intense development of systems with displacement control in relation to the systems with damping control. It is obvious that these requirements result in the need for more intense development of systems with displacement control in relation to the systems with damping control. One of the main preconditions for quality and reliable operation of a high power system is the stable and quality operation of the system for automatic control of hydrostatic power transmitter, the pump-controlled motor with long transmission lines (Figure 1). The existence of a long transmission line in this system makes its dynamics rather complex because the physical values, pressure and flow, which characterize the transfer of energy along the long transmission line depend both on the time coordinate and the space coordinate. Dependence of these physical values on the space coordinate, too, conditions that in the mathematical description of the long transmission line the space distribution cannot be neglected, so that it is described by a model with distributed parameters. Models with distributed parameters are described by partial differential equations and the model obtained is of an infinitesimally high order [5-9]. In addition to mathematical modeling of the long transmission line by means of the model with distributed parameters, it is possible to describe the long transmission line by common differential equations, i.e. models with lumped parameters [1-4] because solving common differential equations makes considerably fewer difficulties in comparison with solving partial differential equations. The authors of this paper considered the problem of modelling and dynamic behaviour of such systems in a very systematic way, and the results are presented in several papers, the most significant of which are [4], [10] and [12]. Reference [10] gives a complete mathematical model of the system of a

pump-controlled motor with a long transmission line by means of a model with lumped parameters where the long transmission line is divided into  $n$  equal "II" segments. The mathematical model thus obtained is of high order but by applying the appropriate methodology its order is reduced, which considerably increases its use value. From the aspect of control, reference [10] presents design of a P controller by applying the Nyquist criterion, including system performances, damping and settling time. The P controller designed in this way, for the described system, eliminates the occurrence of oscillations of the transfer characteristic due to the existence of the long transmission line. However, design of the P controller could not eliminate the error, so that a PI controller was designed in order to solve that problem.

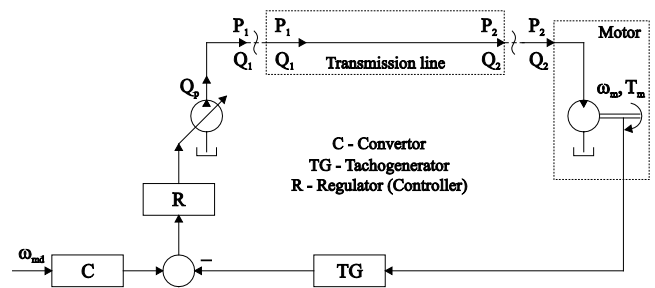


Figure 1: Symbolic diagram of the closed automatic control system of a pump-controlled motor with a long transmission line

This paper proposes the procedure for design of the PID controller for systems of a pump-controlled motor. The starting point is a requirement which establishes a direct relation between the IE criterion and the integral gain (the higher the integral gain, the smaller the value of the IE criterion). The result is extended by introducing engineering specifications (settling time and relative stability). It results in a simple and efficient procedure for design of the PID controller for systems of a pump-controlled motor.

## 2. DESIGN PROCEDURE OF PID CONTROLLER

Since the problem of disturbance load rejection is reduced to the minimization of IE criteria, it is also considered in this paper, but engineering constraints are introduced on:

- i) relative stability
- ii) settling time

This is the basis for development of a simple graphical method based on D-decomposition [11-16].

The transfer function of the PID controller is:

$$W_R = K_p + \frac{K_i}{s} + K_d \cdot s \quad (1)$$

$$W_R = K_p \left(1 + \frac{1}{T_i s} + T_d \cdot s\right) \quad (2)$$

Based on (1) and (2), we can get:

$$K_i = \frac{K_p}{T_i}, K_d = K_p T_d \quad (3)$$

$$T_i = n T_d \quad (4)$$

Based on equations (3) i (4), the relation between  $K_d$  and  $K_i$  is obtained in the following form:

$$K_d = \frac{K_p^2}{n \cdot K_i} \quad (5)$$

The transfer function of the process is represented in the form:

$$W_P(s) = \frac{N(s)}{M(s)} = \frac{\sum_{k=0}^m b_k s^k}{\sum_{k=0}^n a_k s^k}, \quad m \leq n \quad (6)$$

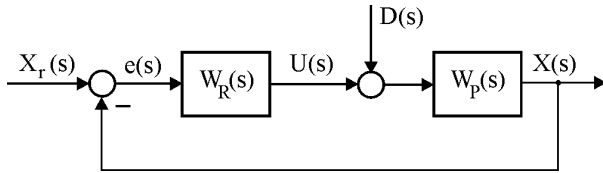


Figure 1: Automatic control system

The characteristic equation of the automatic control system from Fig1 is determined by the equation:

$$f(s) = 1 + W_R(s)W_P(s) = 0 \quad (7)$$

Putting  $K_d = 0$  in the equation (1), the problem is reduced to PI controller design.

$$f(s) = 1 + \left(K_p + \frac{K_i}{s}\right) \cdot \frac{N(s)}{M(s)} = 0 \quad (8)$$

$$f(s) = s \cdot M(s) + (K_p s + K_i) \cdot N(s) = 0 \quad (9)$$

$$f_1(s) = s \cdot M(s) = \sum_{k=0}^n a_k s^{k+1} \quad (10)$$

By connecting (9) and (10), the final expression for the characteristic equation of the automatic control system in the complex domain is obtained as follows:

$$f(s) = f_1(s) + (K_p s + K_i) \cdot N(s) = 0 \quad (11)$$

Taking into account (11), it is necessary to express the complex number  $s$  in a suitable form and use it for establishing the relation between the damping degree  $\xi$  and the variable parameters of the controller  $K_p$  and  $K_i$  contained in the characteristic equation (11) for the automatic control system. This is how the area from the

" $s$ " plane below the straight line  $\xi = \text{const.}$  (Fig. 2), is mapped in the area of the corresponding damping coefficient represented by the curve  $\xi = \text{const.}$ , in the parameter plane of tuning parameters of the controller ( $K_p$ ,  $K_i$ ) with the condition for observation of the integral gain  $K_i$  as a parameter that fulfills the condition of minimum of IE criteria for the corresponding level of the damping coefficient  $\xi$ .

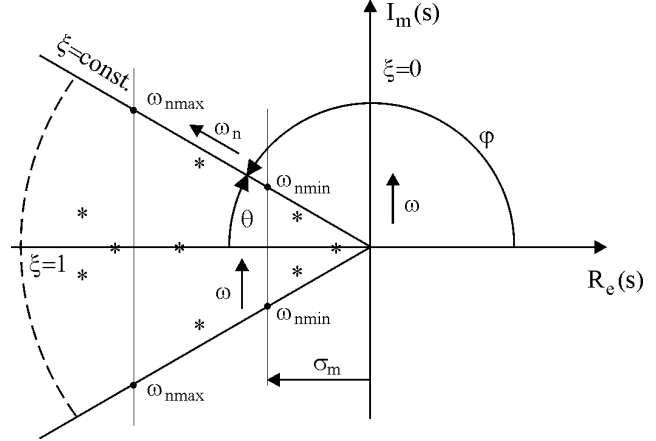


Figure 2: Area with the required settling time and relative stability

Since:

$$s = -\omega_n \xi + j\omega_n \sqrt{1-\xi^2} \quad (12)$$

By connecting (11) with (12) the characteristic equation of the automatic control system obtains the form:

$$f_1(\xi, \omega_n) + \left[ K_p (-\xi \omega_n + j\omega_n \sqrt{1-\xi^2}) + K_i \right] \cdot N(\xi, \omega_n) = 0 \quad (13)$$

$$f_1(\xi, \omega_n) = \alpha(\xi, \omega_n) + j\beta(\xi, \omega_n) \quad (14)$$

where  $\alpha(\xi, \omega_n)$  and  $\beta(\xi, \omega_n)$  represent the real and imaginary parts of the polynomial  $f_1(\xi, \omega_n)$ .

$$\alpha(\xi, \omega_n) = \sum_{k=1}^n a_{k-1} (-1)^k \omega_n^k T_k(\xi) \quad (15)$$

$$\beta(\xi, \omega_n) = \sqrt{1-\xi^2} \sum_{k=1}^n a_{k-1} (-1)^{k+1} \omega_n^k U_k(\xi) \quad (16)$$

$$\beta(\xi, \omega_n) = \sqrt{1-\xi^2} B(\xi, \omega_n) \quad (17)$$

where  $T_k$  and  $U_k$  are Chebyshev functions of the first and second types for which the following recurrent equations hold:

$$T_{k+1} = 2\xi T_k - T_{k-1}, U_{k+1} = 2\xi U_k - U_{k-1} \quad (18)$$

$$T_0 = 1, T_1 = \xi, U_0 = 0, U_1 = 1. \quad (19)$$

$$N(\xi, \omega_n) = \gamma(\xi, \omega_n) + j\delta(\xi, \omega_n) \quad (20)$$

where  $\gamma(\xi, \omega_n)$  and  $\delta(\xi, \omega_n)$  represent the real and imaginary parts of the polynomial  $N(\xi, \omega_n)$  and they are determined based on the following equations:

$$\gamma(\xi, \omega_n) = \sum_{k=0}^m b_k (-1)^k \omega_n^k T_k(\xi) \quad (21)$$

$$\delta(\xi, \omega_n) = \sqrt{1-\xi^2} \sum_{k=0}^m b_k (-1)^{k+1} \omega_n^k U_k(\xi) \quad (22)$$

$$\delta(\xi, \omega_n) = \sqrt{1-\xi^2} D(\xi, \omega_n) \quad (23)$$

By connecting the equation (13) with equations from (14) to (23), after appropriate mathematical transformations

and separating the real and imaginary parts, the following system of equations is obtained:

$$\begin{aligned} K_p \left[ \xi \cdot \omega_n \cdot \gamma(\xi, \omega_n) + \sqrt{1-\xi^2} \cdot \omega_n \cdot \delta(\xi, \omega_n) \right] - K_i \cdot \gamma(\xi, \omega_n) &= \alpha(\xi, \omega_n) \\ K_p \left[ \xi \cdot \omega_n \cdot \delta(\xi, \omega_n) - \sqrt{1-\xi^2} \cdot \omega_n \cdot \gamma(\xi, \omega_n) \right] - K_i \cdot \delta(\xi, \omega_n) &= \beta(\xi, \omega_n) \end{aligned} \quad (24)$$

By solving the system of equations at  $\omega_n \neq 0$ ,  $0 \leq \xi < 1$ , the expressions for the parameters  $K_p$  and  $K_i$  of the PI controller are obtained.

$$K_i = \omega_n \left[ \xi + \sqrt{1-\xi^2} \cdot \frac{\beta(\xi, \omega_n) \cdot \delta(\xi, \omega_n) + \alpha(\xi, \omega_n) \cdot \gamma(\xi, \omega_n)}{\beta(\xi, \omega_n) \cdot \gamma(\xi, \omega_n) - \alpha(\xi, \omega_n) \cdot \delta(\xi, \omega_n)} \right] \cdot K_p \quad (25)$$

### 3. CONTROL OF A PROCESS WITH A LONG TRANSMISSION LINE

In order to show the efficiency of the proposed method for PID controller design we have performed simulations in MATLAB program for transfer function of the process  $W_P(s)$ :

$$W_P(s) = \frac{1}{5.2 \cdot 10^{-25} s^{10} + 9.23 \cdot 10^{-22} s^9 + 9.677 \cdot 10^{-19} s^8 + 7.838 \cdot 10^{-16} s^7 + 4.592 \cdot 10^{-13} s^6 + 2.072 \cdot 10^{-10} s^5 + 7.257 \cdot 10^{-8} s^4 + \dots + 1.755 \cdot 10^{-5} s^3 + 2.962 \cdot 10^{-3} s^2 + 0.243s + 1.248} \quad (26)$$

The transfer function described by (26), represents a mathematical model of a pump controlled hydromotor, where the variable flow pump and the hydromotor of constant flow are connected by means of a long transmission line [17].

Based on the programme created in MATLAB, according to the proposed procedure, the parameters of the PI controller can be determined for the transfer function of the process described by (26), so that the closed loop of the system could possess the required damping coefficient ( $\xi \geq 0.6$ ).

Figure 3 shows the parameter plane ( $K_p$ - $K_i$ ) for values of damping coefficient  $\xi = 0.6$ . From the boundary curve, it can be selected the maximum value of the integral gain and the corresponding value of the proportional gain. This value of integral gain enables a minimum of IE criteria. The area under the curve represents the area with the damping coefficient  $\xi \geq 0.6$ .

On figure 5 it is shown the comparative response of the system between PI and PID controller. PID controller is designed in such a way that the value of the gain  $K_d$  is determined based on equation (5). In this, care should be taken to be satisfied the condition  $n \geq 4$  [18-20]. In this determination of differential gain  $K_d$ , it was taken into account that the system constantly maintains the value of the damping coefficient  $\xi \geq 0.6$ , while at the same time the minimum IE criteria is satisfied. From Figure 5, it can be shown that increasing the number  $n$  from 4 to 10 in the designed PID controller, leads to significant reduction in the settling time from 216 ms to 130 ms. Also compared to the PI regulator we can see that there has been a reduced jump from 43% to 28%. An overview of all these performances is given in detail in Table 1. Figure 6 shows how the designed PID controller for  $n = 10$  suppresses the load disturbance in relation to the PI controller.

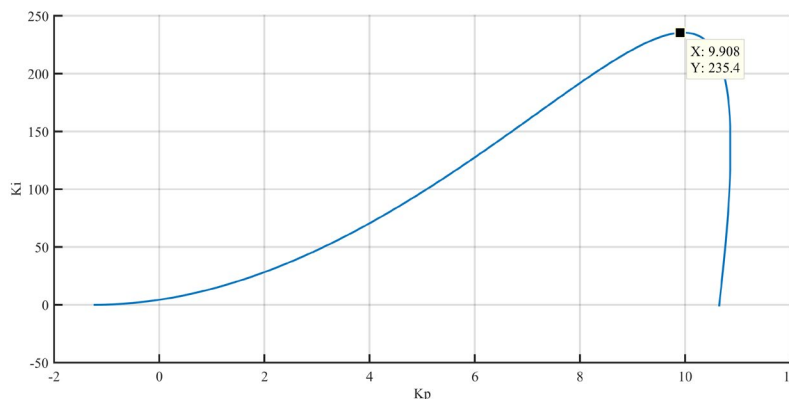


Figure 3: Parameter plane for damping coefficient  $\xi = 0.6$

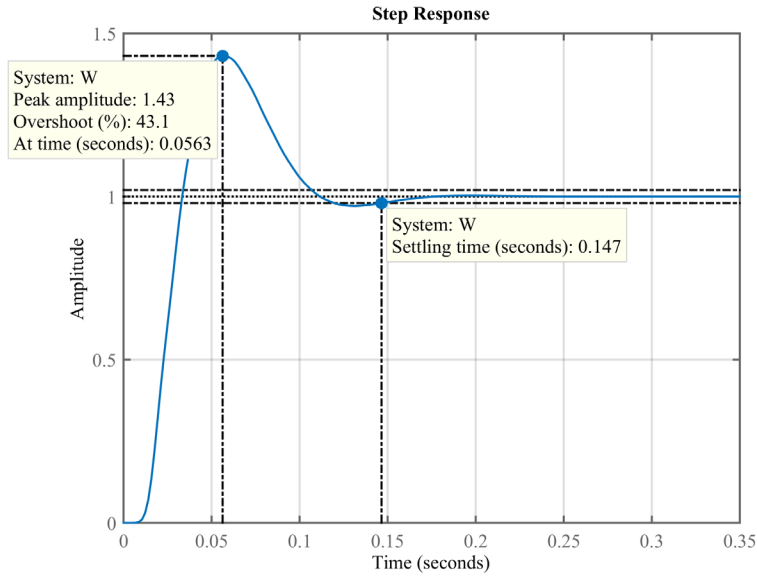


Figure 4: System response regulated by PI controller for  $\xi=0.6$

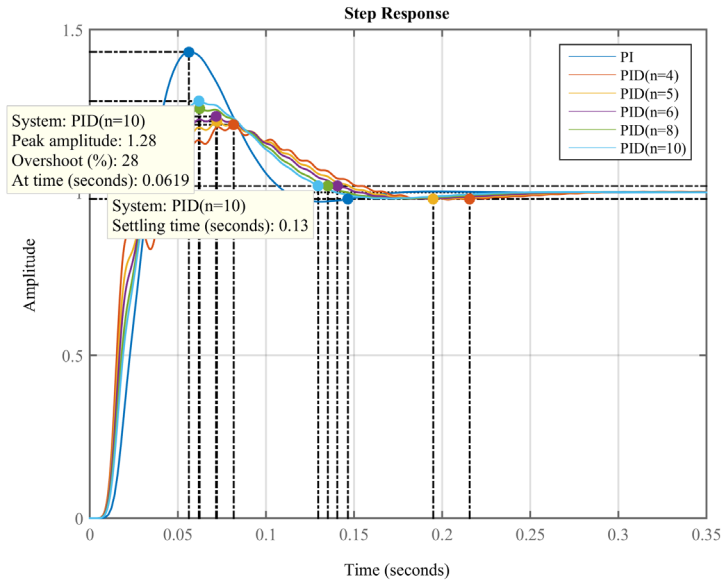


Figure 5: Comparative response of a system regulated by PI and PID controller for different value of number n

Table 1: Comparative presentation of the results of design of the PI controller with PID controller

| Method     | $K_p$ | $K_i$ | $K_d$  | Overshoot (%) | Settling time $t_s$ (ms) | Phase margin $\phi_m$ (degrees) |
|------------|-------|-------|--------|---------------|--------------------------|---------------------------------|
| PI         | 9.908 | 235.4 | -      | 43.1          | 147                      | 35.7                            |
| PID (n=4)  | 9.908 | 235.4 | 0.1043 | <b>20.8</b>   | 216                      | 60.7                            |
| PID (n=5)  | 9.908 | 235.4 | 0.0834 | <b>21.9</b>   | <b>195</b>               | 55.7                            |
| PID (n=6)  | 9.908 | 235.4 | 0.0695 | <b>23.3</b>   | <b>140</b>               | 52.5                            |
| PID (n=8)  | 9.908 | 235.4 | 0.0521 | <b>25.7</b>   | <b>135</b>               | 48.4                            |
| PID (n=10) | 9.908 | 235.4 | 0.0417 | <b>28</b>     | <b>130</b>               | 45.9                            |

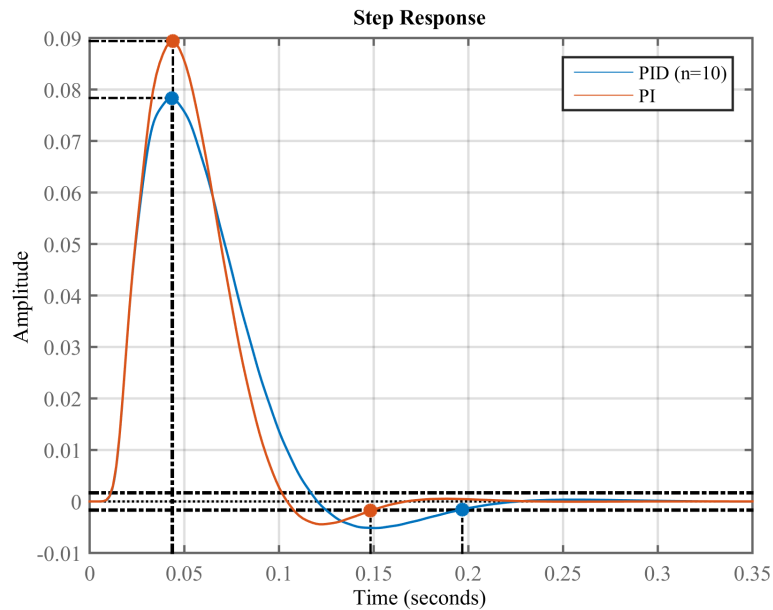


Figure 6: Comparative response of a system regulated by PI and PID controller in relation to suppression of load disturbance

#### 4. CONCLUSION

Based on everything said, we can conclude that it has been developed an efficient and simple graphical methods for design of the PID controller, which achieves high performances for a broad range of linear processes. The process of high order has been considered, in which the variable flow pump controls the hydromotor, where a connection between the pump and the hydromotor is realized by a long transmission line. In comparison with the procedures for tuning of the PID controller proposed in literature, the method described in this paper is characterized by great simplicity and clear engineering specifications. The results of simulations show good robustness in relation to unmodelled dynamics as well as superiority over some other methods of tuning of controllers. The proposed method is suitable for on line real-time realization and for auto tuning of the PID controller.

#### ACKNOWLEDGEMENTS

This research has been supported by the Serbian Ministry of Education, Science and Technological Development under grant No. 451-03-9/2021-14/200108

#### REFERENCES

- [1] Watton J., "Fluid Power Systems", Prentice Hall, 1989.
- [2] Watton J., "The dynamic performance of an electrohydraulic servovalve /motor system with transmission line effects", ASME Journal Dynamic Systems, Measurement and Control, 109, pp. 14-18, 1987.
- [3] Watton J., Tadmori M., "A comparison of techniques for the analysis of transmission line dynamics in electrohydraulic control systems", Journal of Applied Mathematical Modelling, 12, pp. 457-466. 2001.
- [4] N.N. Nedić, L.J.M. Dubonjić, "The Stability and Response of the Electrohydraulic Valve Controlled Hydromotor with Long Transmission Flow Line", VIII International SAUM Conference, Belgrade, pp. 186-193, 2004.
- [5] Stecki J.S., Davis D.C., "Fluid transmission lines – distributed parameter models" Part 1: a review of the state of the art. Proc IMechE, 200, Part A, pp. 215-228, 1986.
- [6] Stecki J.S., Davis D.C., "Fluid transmission lines – distributed parameter models" Part 2: comparison of models. Proc IMechE, 200, Part A, pp. 229-236, 1986.
- [7] Hullender D.A., Healey A.J., "Rational Polynomial approximation for fluid transmission models" Fluid Transmission line dynamics, published by ASME, pp. 33-56, 1981.
- [8] Hsue C.Y., Huulender, D.A., "Modal approximations for the fluid dynamics of hydraulic and pneumatic transmission lines", Fluid Transmission line dynamics, published by ASME, pp. 51-77, 1983.
- [9] Hullender D.A., Woods R. Hsue C., "Time Domain Simulation of fluid Transmission Lines using Minimum Order State Variable Models" Fluid Transmission Line Dynamics, published by ASME, pp. 78-97, 1983.
- [10] Nedić N., Filipović V., Dubonjić L.J., "Design of Controllers With Fixed Order for Hydraulic Control System With a Long Transmission Line", FME Transactions (2010) Vol. 38 No. 2, pp. 79-86, 2010.
- [11] Y.I. Neimark Search for the parameter values that make automatic control system stable, Automatica i Telemekhanika, 9 (3), pp. 190–203 (1948).(in Russian)

- [12] D. Mitrovic, Graphical analysis and synthesis of feedback control systems. I-Theory and analysis, II-Synthesis, III-Sampled-data feedback control systems, AIEE Transactions (Application and Industry), 77, pp. 476–496 (1959).
- [13] D. Siljak, "Analysis and synthesis of feedback control systems in the parameter plane. I—Linear continuous systems, II—Sampled-data systems", AIEE Transactions (Application and Industry), 83 pp. 449–466 (1964).
- [14] D. Siljak, "Generalization of the parameter plane method", IEEE Transactions on Automatic Control, AC-11 (1), pp. 63–70 (1966).
- [15] Dubonjić LJ, Nedić N, Filipović V, Pršić D. Design of PI controllers for hydraulic control systems. Math. Probl. Eng. 2013; 2013: 1–10.
- [16] Lj. M. Dubonjić, V. Ž. Filipović, N. N. Nedić, V. Đorđević, Design of an H(lemniscate) PI controller with given relative stability and its application to the CSTR problem, Hem. Ind., (2018), 72(3), pp.115-127, ISSN: 0367-598X
- [17] Nedić N, Dubonjić LJ, Filipović V (2011) Design of constant gain controllers for the hydraulic control system with a long transmission line. Forschung im Ingenieurwesen 75(4):231–242
- [18] Filipović V. Industrial Controllers, Kraljevo, University of Kragujevac, 2016
- [19] Astrom KJ. Limitations on control systems performance. European J. of Control. 2000; 6: 2-20
- [20] Diaz-Rodriguez I.D., Han S., Bhattacharyya S.P., Analytical Design of PID Controllers, Springer, (2019), USA, ISBN:978-3-030-18227-4

# Structural linear modeling of electrohydraulic actuation system with hydraulic cylinder

Dragan Nauparac <sup>1</sup>

<sup>1</sup>PPT-Engineering, Belgrade (Serbia)

*The basic structure of the model based on the classical approach to linearization, the third order system, the cylinder and the inertial load are presented. We start from the structural feedback dictated by the method of linearization, by flow, then additional feedback to improve the control algorithm, variants of the system with two options of state regulators (models) to the final variants of the structure with internal and external feedback, cascade structure. Structures in space state are compared with a cascade structure.*

**Keywords:** Hydraulic actuator, mathematical model, structural modeling

## 1. INTRODUCTION

Structural modeling does not often appear in the literature as a special technology for modeling dynamic systems. In modeling of electrohydraulic systems, this technique of mathematical modeling implies connecting blocks which represent autonomous parts of the mathematical model, and it has a special use value in modeling of electrohydraulic because they are characterized by additional simplicity for structural modeling. It is a fact that they have their so-called unchangeable and changeable part in their structure. The invariable part is certainly the mathematical model of the distributor and the hydraulic cylinder with the load. The interchangeable parts are: the algorithmic part and the related approach to how and which feedback and filter blocks will be used in the mathematical model of the electrohydraulic system. This is also related to the fact whether the mathematical model will be worked in the input-output space or in the state space. But not only that, the main question we ask in this paper is when it makes and when it does not make sense to use a cascade structure. The cascade structure of the model has internal and external feedback. In other words, if the actuation system is intended for position controlled, should force be controlled or just monitor its change in order to ensure the best possible quality of position control. Electro-hydraulic proportional distributors can conditionally control both position and force.

## 2. P-Q ELECTROHYDRAULIC DISTRIBUTORS

The analysis of structural modeling options should begin primarily by clarifying the term P-Q distributors. These are proportional distributors produced by several specialized distributor manufacturers in the world. The distributor, the mechanical part is identical to any other 4/3

proportional distributor. The difference is in the electronic amplifier. These are most often digital options, which work with two modes. One is that in one period of time we control by position and in another period of time we control by force. This means that we must have reference values for both position and force. Another option is to use information from the pressure transmitter and position sensor, so that we control by position when our actual force is less than the allowed (reference) force, and to control the force when the change in force is greater than allowed. It is clear from Figure 1 that when we have only inertial load, the control will usually be by position, but when we have a combination of inertial and positional load reduced to the end of the cylinder rod, then both options can be in the choice of control. We do not usually see the previously described in the structural diagram because these are the options implemented in the digital electronic amplifier for the proportional distributor. But if we define a criterion in the basic control algorithm for example according to the rate of change of position and force in one sample period, the group of equations in model (1), where we neglect the changes of acceleration and viscous friction as no-fast, we can define the control signal so that we control by the size that changes faster. Then we get a structural block, which we define as part of the structural model, Figure 2.

It is clear from the above that if we know the structural stiffness,  $K$  of the load on the cylinder in advance or we can measure it, it is clear that we can improve the control algorithm because it can be defined when to position by position and when by force. This structure allows adaptability to the actual stiffness in online or in on-off mode. This is a very useful option especially when we have a high intensity of load stiffness change.

$$\begin{aligned}
 A_1 p_{t-1} A_1 p_{t-1} &= m a_{t-1} + B_p v_{t-1} + K x_{t-1} + F_L \\
 A_1 p_t &= m a_t + B_p v_t + K x_t + F_L \\
 \frac{A_1 (p_t - p_{t-1})}{K (x_t - x_{t-1})} &= \frac{m (a_t - a_{t-1}) + B_p (v_t - v_{t-1}) + 1}{K (x_t - x_{t-1})} \\
 \frac{(p_t - p_{t-1})}{(x_t - x_{t-1})} &= \frac{A_1}{K}
 \end{aligned}
 \tag{1}$$

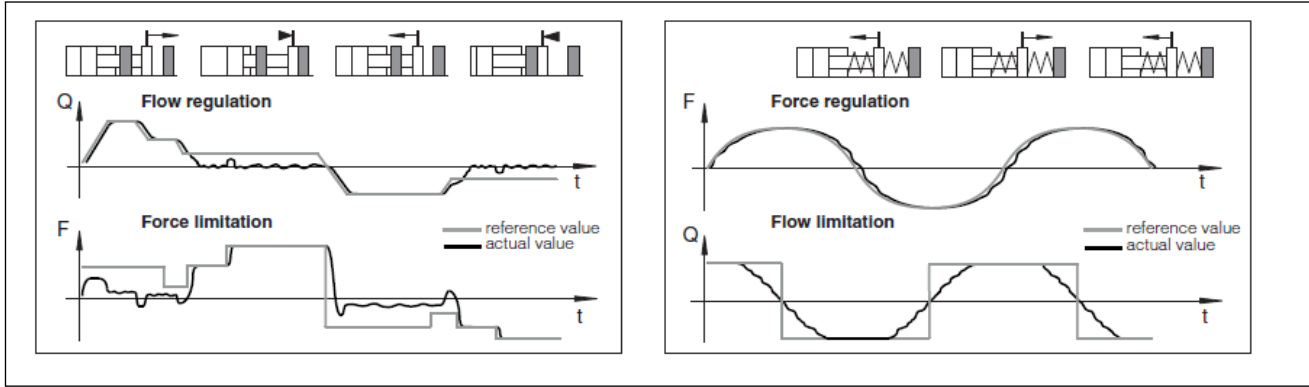


Figure 1: Application of proportional P-Q distributors [1]

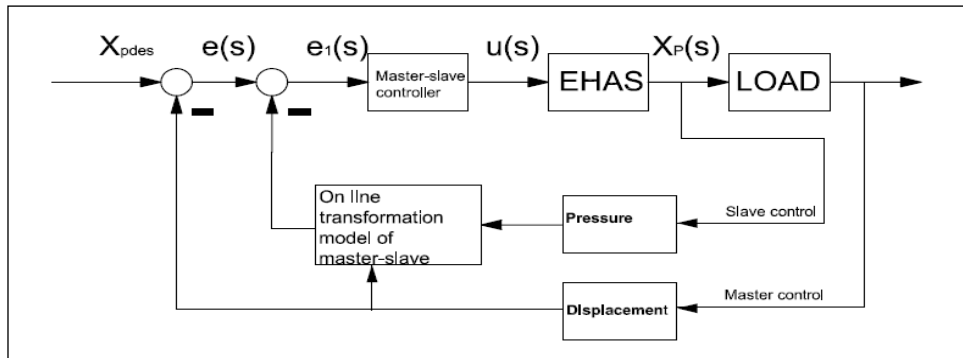


Figure 2: Control algorithm with option for selection position (master)-force (slave) control [2]

### 3. BASIC STRUCTURAL MODEL OF ELECTROHYDRAULIC ACTUATION SYSTEMS

The basic structural model is linear because it is obtained by linearization of a simplified nonlinear model that included only the mathematical nonlinearity of the square root type that defines the flow through the distributor. In this model, we have one flow feedback that

we do not physically define through the adequate sensor, But it is the internal implicit feedback. Depending on the magnitude of the flow change under load conditions, this feedback can sometimes be structurally neglected, Figure 3.

The basic model of the electrohydraulic actuation system can be defined as a model of the first, second or most often third order, depending on what we want to include in the model and what we want

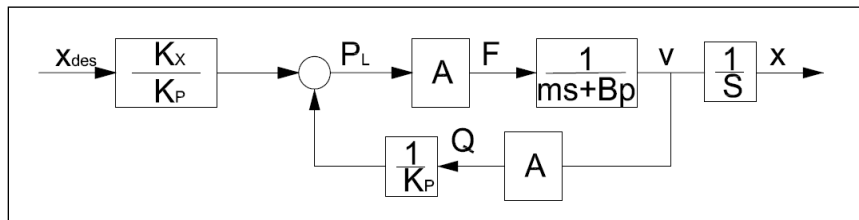


Figure 3: Basic structure of mathematical model of EHAS

$$\sum F = m \frac{d^2x}{dt^2} = P_L A - B_p \frac{dx}{dt}$$

$$p_L = \frac{K_x}{K_p} x + \frac{1}{K_p} Q \tag{2}$$

$$Q = K_x x - K_p p_L = A \frac{dx}{dt}$$

to leave in un-modeled dynamics. This question is further related to the verification of the mathematical model, the experimental verification of the actual system and model as well as the verification through the technique of mathematical identification. If we design a mathematical model of an electrohydraulic system whose bandwidth does not exceed 50 Hz and where the control algorithms are based on PID algorithmic options with various

additions, from previous practice we can consider that a linear mathematical model of the third order is sufficient.

#### 4. SIGNAL FILTER AS AN ELEMENT OF STRUCTURAL MODELING

Very often when additional feedback is introduced, either by simple addition when the mathematical model is done in the input-output space or when the feedback is the result of modeling in the state space, especially when feedback by load pressure, it is necessary to provide signal filtering, Figure 4, and the transfer function of the filter is directly introduced into the structure of the mathematical model.

$$W_F = \frac{s}{s + \omega_F} \tag{3}$$

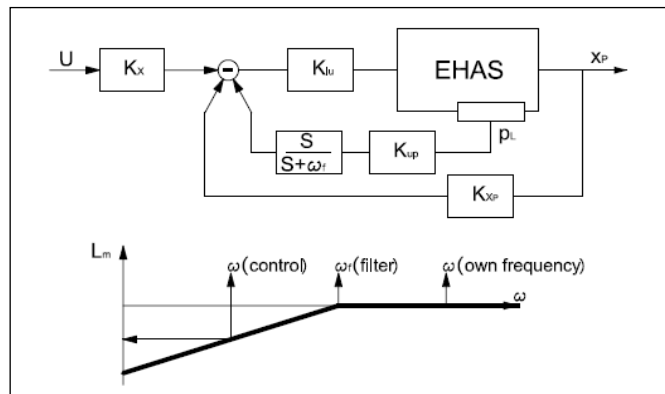


Figure 4: Filtering of pressure feedback signal before this signal go in control calculation [3]

#### 5. MATHEMATICAL MODEL OF THE ELECTROHYDRAULIC ACTUATION SYSTEM IN THE STATE SPACE

Figure 5 shows the structure options of the mathematical model in the state space. Within this

structural option, there are most special algorithmic solutions. It is clear from Figure 5 that we have two basic options in the state space. One when we use phase state variables and the other when we do not use phase state variables.

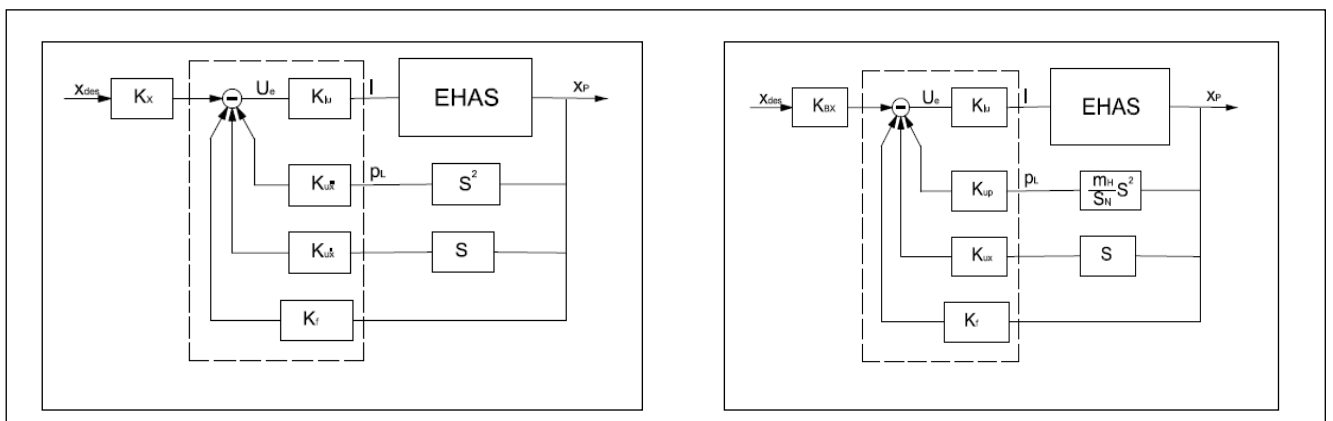


Figure 5: Structural mathematic model in space state of EHAS (two options) [3]

6. CASCADE STRUCTURE OF EHAS MATHEMATICAL MODEL

Certain criteria have been defined before when to control a position and when to control a force. The question remains which criterion to use to select the cascade structure of the electrohydraulic actuating positioning system during modeling. The empirical criterion says when one variable, in this case changes force much faster than the position. It is clear that this depends on the type (stiffness) of the load, but in any case, in order to control the position in the case of complex position loads, it is useful to use a cascade structure. In addition, the important fact is whether the desired value is variable in time (tracking) and how the intensity of the tracking error of the given trajectory for the electrohydraulic positional actuation system changes. This approach can be transferred from the analogy with electromechanical actuation systems where the active control torque depending on current and flux changes much faster than the position (angle), which would be transferred to electrohydraulic systems would mean that in

electrohydraulic systems the pressure changes much faster than position. This is also shown by certain analyzes of structural loads with finite elements. In any case, the general approach can be, in order to obtain a strictly aperiodic response when controlling the position, it is necessary that the change of force occurs aperiodically, because if it changes oscillatory, then the aperiodic response of the position cannot be provided. So, as a criterion for choosing the cascade structure of the mathematical model, there can be a requirement for a strictly aperiodic positional response. The cascade structure is shown in Figure 6. It is clear that there are two control algorithms, one for position and the other for force. It should be mentioned here that there is a certain problem when the system is structurally displayed in digital form, because the Zero Order Hold make delay between two sample periods. Practically keeps the pressure change at a constant value, regardless of the fact that the change in order of magnitude is faster than the position. This is solved in practice in several ways and this issue is not the subject of further consideration in this paper.

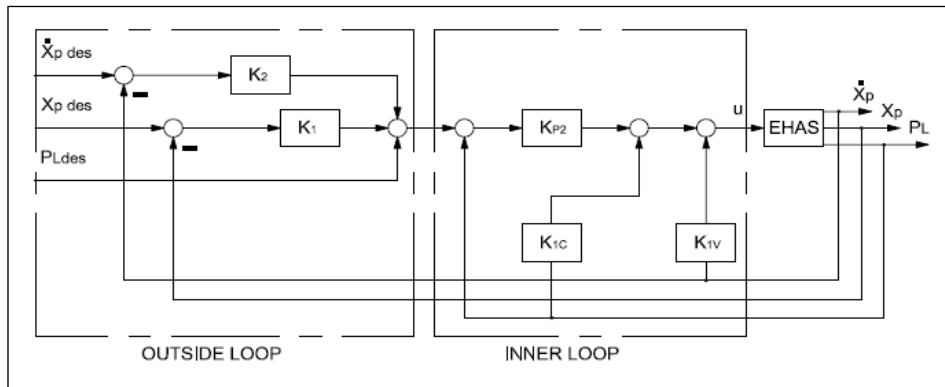


Figure 6: Cascade structure of EHAS mathematical modeling [4]

The mathematical apparatus that follows based on Figure 6 shows the difference in the final model of the electrohydraulic actuation system when it is shown in the

state space and in the cascade structure. (the first three members in the second row, are feedbacks in the state space)

$$\begin{aligned}
 u &= K_{vc}\dot{x} + K_{pL} \left[ K_1(x_{ref} - x) + K_2(\dot{x}_{ref} - \dot{x}) - (p_{Lref} - p_L) \right] + K_{1c}p_L \\
 &= K_p(x_{ref} - x) + K_{\dot{x}}(\dot{x}_{ref} - \dot{x}) + K_{pL}(p_{Lref} - p_L) + K_{vc}\dot{x} + K_{1c}p_L
 \end{aligned}
 \tag{4}$$

This difference is reflected in two additional members, one is as seen from the second row (4), the feedforward member for speed and the other is the member for leakage compensation. On this basis, the cascade structure tends to the "ideal" part of the algorithmic structure based on Figure 7.

Figure 7 conditionally shows one of the possible optimal or ideal structures of the electrohydraulic actuation system. Neither in theory nor in practice is not defined what is ideal structure of the mathematical model EHAS. It is clear that the model shown here is based on a third or 4th order model. The elements of an ideal model in any case are that it is shown in the state space, that it

has its own stabilization part and a part that should guarantee the accuracy of positioning.

The model in Figure 7 may be better called an ideal base structure that can be upgraded with another part of the control algorithm, such as a tracking part, a fuzzy part or an adaptable part, and of course an upgrade with filter blocks. It is clear that this is necessary with EHAS with very complex control requirements.

The improvement of linear models is in the first step the inclusion of static nonlinearities. This technique has proven to be effective and this has been quite well researched in practice.

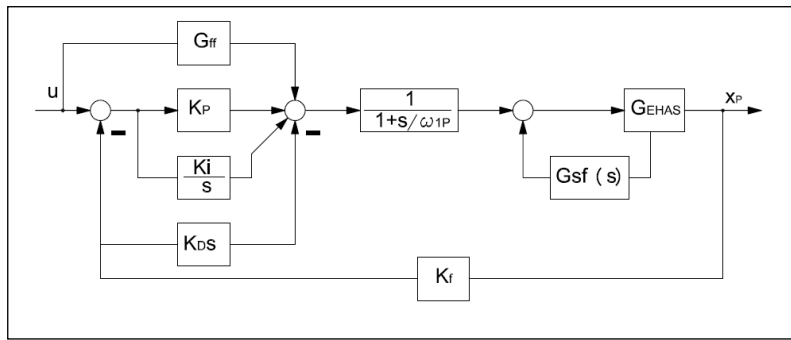


Figure 7: One of options for ideal structure of EHAS mathematical model [5]

7. ALGORITHM STRUCTURE WITH DIRECT COMPENSATION

This is a special type of structural modeling. The starting point is the principle that any electrohydraulic actuation system can be represented by equivalent nonlinearity and first order transfer function, Figure 8. Since the equivalent nonlinearity is usually of static type with insensitivity (dead) zone and saturation, it is concluded that compensation can be done by simple relay

nonlinearity which is added to the structural model (diagram) of the electrohydraulic actuation system. In practice, it is often an offset to proportional control intensity. This is the simplest way of structural modeling. This method of modeling also requires partial identification of system parameters, time constant for the transfer function of the first order (linear part) and the size of the insensitivity zone or saturation in equivalent nonlinearity. [6]

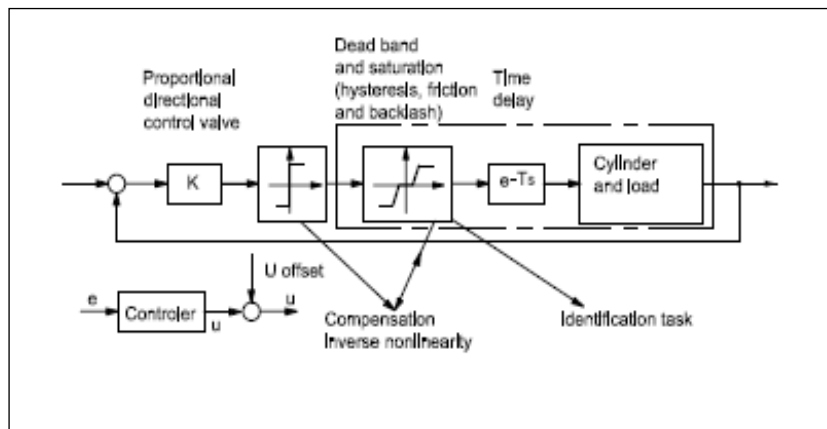


Figure 8: Structural model of EHAS with direct compensation [6]

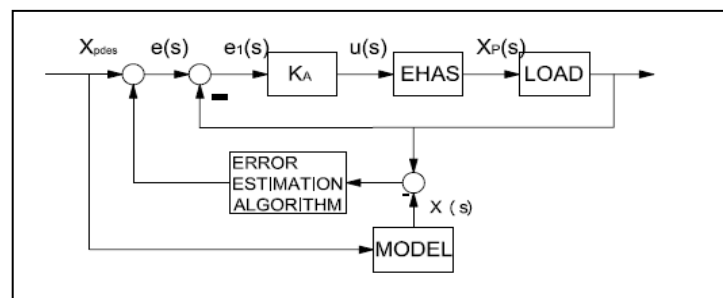


Figure 9: Shows the structure of the actuation system where the mathematical model of EHAS must be attached in the form of a system of differential ones

## 8. CONCLUSION

Based on the above, the options of structural mathematical modeling of the electrohydraulic actuation system with a hydraulic cylinder as an executive device are presented. Structural modeling is relatively simple when certain parts of the model is well known. (distributor and cylinder) A special option of structural modeling is a cascade structure, for which a criterion is defined when it should be used. Integrated position and force control is also analyzed at the level of the distributor or control algorithm and criteria are given when position is controlled and when force. These options are in certain cases possible alternatives to the cascading structure of the mathematical model. The option of structural modeling with direct compensation is also presented. One type of optimal structure of the mathematical model is shown in Figure 7. It can be reference model for structural modeling, especially the introduction of filters into the structure of the mathematical model. Structural modeling is suitable for fast simulation checks of the selected control algorithm and check the usefulness of the use of additional feedbacks. It is not suitable when the control algorithm requires a mathematical model of the actuation system, as shown in Figure 9.

The advantages of the cascade structure are much more pronounced in electromechanical actuators with rotational motion, because the load moments can be significantly less than the impulse active moments that depend on current and flux so that the friction moments are two orders of magnitude smaller than the active moment. Based on the previously described, the friction is not modeled separately, it is enough to add to the load only according to the value of intensity.

In this case, there is no one very complex nonlinearity in the mathematical model. The aim is to see in further research for the cascade structure whether the nonlinearity of friction can be compensated in this way in the case of EHAS as well. Structural modeling is one of the useful options that can be successfully applied in the synthesis of control systems for EHAS where the

load is a combination of inertial and positional. [7], [8]

## REFERENCES

- [1] Basic digital proportional with P/Q control, GS002-O/E-Atos, Italy
- [2] H.Han, Y.Liu, L.Mam, Z.Liu, L.Quan, "Analyze the characteristics of electro-hydraulic servo system's position-pressure master-slave control", *Advances in Mechanical Engineering*, Vol. 10(6), pp. 1-9, (2018)
- [3] Е.Федосов, "Машиностроение энциклопедия, Автоматическое управление теория", Том I-4, Машиностроение, Москва, (2000).
- [4] M.Jelali, A.Kroll, "Hydraulic Servo-systems, Modeling, Identification and Control", Springer, (2002)
- [5] K.E.Rydberg, "Feedbacks in Hydraulic Servo Systems", Linkopings university, (2008).
- [6] D.Nauparac, "Contribution to the theory of design of actuator for TVC by flexible nozzle", PhD Thesis, Faculty of Mechanical Engineering, Belgrade, Serbia, (2016)
- [7] D.Nauparac, D.Prsic, M.Milos, "Design criterion to select adequate control algorithm for electro-hydraulic actuator applied to rocket engine flexible nozzle thrust vector control under specific load", *FME Transaction*, Belgrade, Accepted for printing, Vol. 41, No 1, March 2013, pp. 31-37, (2013)
- [8] D.Nauparac, D.Prsic, M.Milos, "Electro-hydraulic system for the Simulation of Dynamic Behaviour of Rocket Engine Flexible Nozzle Thrust Vector Control", 2<sup>nd</sup> International conference Manufacturing Engineering & Management 2012, Presov, Slovak Republic, 5-7 (2012)

## Tribological test devices as heavy machinery

Vito Tič<sup>1\*</sup>, Darko Lovrec<sup>1</sup>

<sup>1</sup>Faculty of Mechanical Engineering, University of Maribor, Maribor (Slovenia)

*Testing of the lubricating ability of hydraulic fluid is carried out in a variety of test approaches. In certain types of tests, the physicochemical properties of the fluid related to its lubricating properties are at the forefront. In other tests, the emphasis is on determining the durability of the fluid and its service life, or it is an emphasis on hydraulic component degradation. Among the latter, are the very wellknown tribological tests, based on the use of hydraulic pumps – the so-called tribological pump tests. The aim of all these tests is to determine the wear of a hydraulic pump and its vital parts using the tested hydraulic fluid. Such tests involve the use of different types and sizes of pumps, varying amounts of tested hydraulic fluid and different operating conditions, as well as different pump loads and load profiles. Most of these tests are performed on special test devices, which can be, according to their design, scale and installed drive power, classified as heavy machinery.*

*In the context of tribological tests with a hydraulic pump is a pump load carried out in different ways. At the forefront of the discussion are the study and comparison of all such tests, both in terms of the type of pump used, the operating load type, operating parameters, scale of the test device and installed power.*

**Keywords: Tribological pump tests, Test devices and conditions, Energy consumption**

### 1. INTRODUCTION

With laboratory tribological tests of hydraulic fluids, which are usually performed under atmospheric pressure (e.g. the pin-on-disc test, Brugger test, Reichert test, Falex test, Timken test, FZG test...) it is difficult to model or recreate the pressure and flow conditions accurately, as they occur during the operation of hydraulic pumps. Thus, e.g., no wear or damage can be observed due to cavitation. Corrosive processes or material fatigue processes due to rolling contact also take a long time, so these tests take tens of hours, days, or even months. In short-term tests, there is simply not enough time for them to occur, even under tighten-up or accelerated testing conditions (and for the most part, they are not designed for this). In addition, the conditions of accelerated wear may also be accompanied by a change in the wear mechanism; for example, from abrasion defect to adhesion. [1], [2], [3]

There are a number of other issues and concerns, for example:

- It is necessary to know the degradation mechanisms of the fluid over a wide range of operating conditions,
- It must be taken into account that the materials of the test pieces are identical or equivalent to those in the actual component; the same applies to combinations of materials,
- In order to evaluate the wear properties of hydraulic fluids successfully, it is necessary and reasonable to perform a wear test in a hydraulic pump,
- It is necessary to lay down test conditions which ensure similar conditions as during operation...

All of the above, as well as many other concerns, are the reason for performing tests with real hydraulic pumps, on a real hydraulic device and under real operating conditions. These tests include and enable:

- Comparison of differences in equipment performance,
- Gaining knowledge (and experience) with new fluids,
- Obtaining comparative data on the lubricating properties of different types of hydraulic fluids,

different manufacturers and different types of hydraulic pump.

In addition to the above, the process of pump degradation and consequent failure is usually accompanied by increased noise, change in the noise profile, vibration and, of course, by gradual decrease in volumetric efficiency. Knowing these values, and especially the process of changing them, allows us to assess the current condition of the pump and its remaining service life later in industrial operation. Therefore, during the course of the test with the pump to determine the rate and the subsequent cause of its degradation, it is necessary to determine the range of those quantities that will be monitored in more detail.

Testing should be performed in approximately the same environmental conditions as in actual use: Temperature conditions, the presence of contamination and the presence of water or humidity, different types of metal, alternating pressure changes. In certain cases, testing can also take place under harsh operating conditions, such as elevated temperature, pulsating pressure change or higher circulation number.

With tests carried out with hydraulic pumps, we want to check the influence of the lubricating properties of the tested hydraulic fluid on the conditions that occur inside the pump (components) during its operation. Thus, for example, the friction of the sliding vane against the running surface of the vane pump, the conditions when engaging the two teeth of the gear pump, the friction and the type of wear during the translational movement of the piston of the piston pump are in the foreground.

In the case of known and commonly used hydraulic fluid or (slightly) modified fluid (e.g. different base oil, different additive package), tests involving the use of real hydraulic components, usually hydraulic pumps, are used mainly. The pump is always a running component and is also the most loaded component of the hydraulic system.

Tests based on hydraulic pumps are very different. The tests are performed under different operating

\*Corresponding author: Smetanova ulica 17, Maribor, Slovenia, email: [vito.tic@um.si](mailto:vito.tic@um.si)

conditions, different amounts of test fluid are used, different types of pumps are used, and the tests take different lengths of time. The way the pump is loaded can also be different – either the pump is loaded with a constant pressure during the test, or the pressure changes. In addition, they are more or less energy consuming in terms of installed and consumed power during the test, and more or less expensive in terms of the equipment used.

In any case, it makes sense to test the influence of the lubricating properties of a certain hydraulic fluid on a certain hydraulic pump under real operating conditions. At first glance, this is inappropriate and impractical, given how many different types of pumps we have, and how many different types of hydraulic fluids and their formulations we use.

This becomes even more complicated when it comes to updating a known type of pump, either in terms of a design change or the use of different materials. To this must be added the possibility of using different types of hydraulic fluid, which can cause a different course of degradation in the same pump. This problem can be simplified by using one, or a limited number of "standard" hydraulic pump tests.

By "standard" test we often do not mean an actually standardised test, but certain, verified and, in practice, recommended, as well as established test procedures used by individual, especially established, pump manufacturers. Therefore, certain test procedures are usually named after them. When there is a change in the ownership of the brand, there is often a change in the already used test regarding the pump used and additions to the name of the test. Often this test is no longer the same, but comparable.

With development, the quality of pumps changes, new insights and materials are introduced, and hydraulic fluids are no longer the same. Only certain tests with hydraulic pumps have grown into standard tests, e.g., the ASTM Vickers test. All the mentioned and later introduced changes regarding the type of pump and the hydraulic fluid used already represent a deviation from the Standard. Also, changes based on development and application requirements change much faster than the Standards themselves. We need to be aware of this fact. In the case of testing the suitability of a hydraulic fluid, the dilemma is smaller if a well-known pump is used for the test. However, several dilemmas arise in the opposite direction – the new fluid type and the new pump type.

## 2. PUMP TESTS WITH A LARGE AMOUNT OF HYDRAULIC FLUID

The most established tests with pumps are performed with conventional industrial pumps of well-known manufacturers e.g. with a Denison pump, a Parker pump, an Eaton-Vickers vane pump, or with a Sundstrand (John Deere) piston pump or Rexroth piston pump... and are usually also named after the manufacturer. Hydraulic mineral-based oil is usually used as the tested fluid.

In the field of the profession, the mentioned tests are considered to be the most important tests performed with hydraulic pumps. Only the main features of certain tests will be summarised below. Other details on the conditions and method of performing each test are available e.g. in the ASTM Standards or test procedures of the individual manufacturer.

Regarding the pump type used and regarding the loading profile, the most important pump test can be divided into different groups.

Regarding the hydraulic pump (flow) type, into:

- Pump tests with constant pumps and constant flow.
- Pump tests with variable pumps and variable flow.

Regarding the hydraulic pump loading profile, into:

- Pump tests with pumps at constant load,
- Pump tests with pumps at variable load.

In the following, in the presentation of the most well-known and established tests, the emphasis will be mainly on the operating parameters, the operating pressure and flow rate of the pump, and, consequently, the installed power of the drive unit.

### 2.1. Tests with constant pumps

The first group of tests is represented by tests with constant hydraulic pumps. These emerged as the first tests with pumps. In these tests, the load profile of the pressure pump may be constant or variable.

Based on the Denison HF-0 test, we estimate the hydraulic fluid capacity based on flow, sediment, and wear in the Denison P46 axial piston constant pump and the Denison T5D vane pump. [2] Both pumps operate for 100 hours as part of the test, and are periodically (at specified test hours) disassembled for inspection, reassembled and used further. Denison's HF-0 test is recognised by experts as a comprehensive test, as it assesses all aspects of the hydraulic fluid. The basic test parameters are listed in Table 1. The Sundstrand and Eaton/Vickers test pumps were designed to determine the durability of the hydraulic fluid. The built-in power of the powertrain is 90 kW.

Table 1: Denison Vane Pump Test [2]

|                  |  |
|------------------|--|
| Fluid volume     | 189 L                                    |
| Test temperature | 71 °C for 60 hours<br>99 °C for 40 hours |
| Test duration    | 100 hours (4 days)                       |
|                  | cca. 172 bar                             |
| Pump speed       | cca. 2,400 rev/min                       |
| Flow rate        | 265 L/min                                |
| Power            | 90 kW                                    |

The layout of the test rig using the Denison HF-0 is shown in Figure 1.

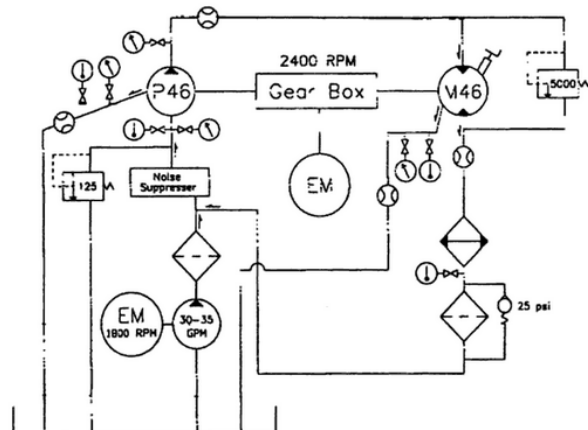


Figure 1: Schematic of the Denison P46 piston pump test according the HF-0 protocol [2]

The *Sundstrand piston pump test*, using constant piston pump Series 22 and 64 kW drive, was run initially under standard conditions, lasting 225 hours, with mineral-based hydraulic oil, with antiwear additives, and it passed all the criteria established for the test. A *second Sundstrand pump test* was run under the same test, extended to 450 hours, or double the length of the standard test, and it also passed (Table 2). All components are assessed visually for signs of wear and discolouration at the end of the test.

Table 2: Sundstrand Piston Pump – Series 22

|                           |                           |
|---------------------------|---------------------------|
| Fluid volume              | 45 L                      |
| Test temperature standard | 82 °C (1 % water content) |
| Test temperature elevated | 120 °C (no water)         |
| Test duration – standard  | 225 hours (9 days)        |
| Test duration – extended  | 450 hours (19 days)       |
| Pressure                  | cca. 345 bar              |
| Pump speed                | cca. 3,100 rev/min        |
| Flow rate                 | 95 L/min                  |
| Power                     | 64 kW                     |

The Sundstrand pump test included one percent of water contamination to stress the fluid further. Even with the added water, there was no evidence of any hydrolytic reactions that could cause the formation of precipitates. Contamination from precipitates leads to blocked valves and filter-plugging problems.

Another round of Sundstrand pump tests were run at an elevated temperature of 120 °C. Due to the higher temperature, no water was added to this test, and all other conditions remained the same. This round of tests showed that the hydraulic fluid with the premium hydraulic additive package had the endurance to exceed the performance parameters of the Sundstrand piston pump without difficulty, despite the higher temperature and the extended length of the test. The layout of a Sundstrand piston pump test stand is shown in Figure 2.

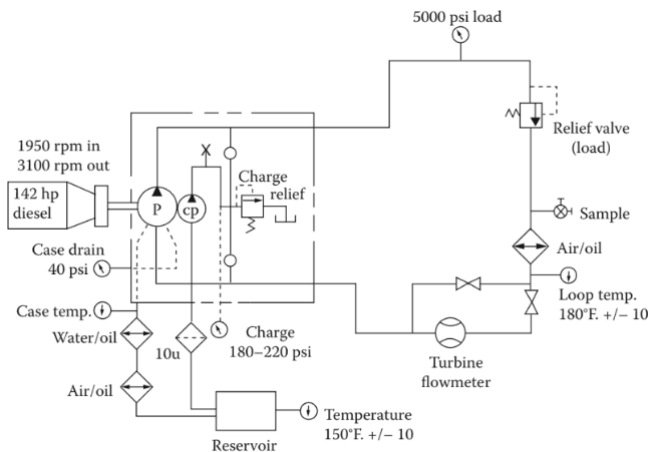


Figure 2: Schematic of a Sundstrand test circuit using a constant piston pump [2]

The next, very well-known test involves the use of an (Eaton-) Vickers type 35VQ-25 vane pump. [4] As is well known, vane pumps are tribologically very "vulnerable". [5] This type of standard test, generally called the Vickers test, is relatively short, and lasts 50 hours. The extended Vickers test takes much longer, 1,000 hours, and allows for more realistic conclusions regarding

the durability of the hydraulic oil contained in the anti-wear additive package. In the case of quality mineral oil, after 1,000 hours of testing the pump, the loss of total metal mass due to wear of the sliding ring and vanes is still below the limit provided by the test to ensure an adequate service life of the pump.

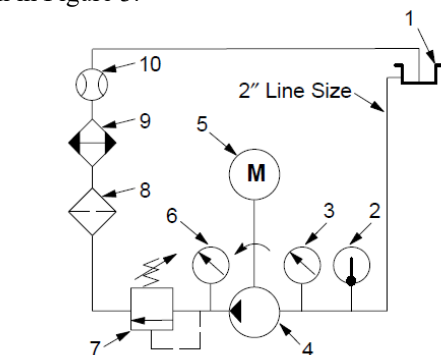
The older vane pump type, the V-104 pump, should be tested in accordance with the ASTM D2882 test protocol at an operating pressure of 2,000 psi (approx. 138 bar), which is outside the recommended operating pressure of this pump. The operating pressure of the 20VQ25 pump is 3,000 psi (approx. 207 bar), which is completely in line with the Standard. This type of data is even more important, as operating parameters such as speed and operating pressure affect the amount of wear greatly. The basic parameters of the Vickers test with the 35VQ-25 pump are summarised in Table 3.

The criterion for pump wear is weight loss, which is also a known capacity reserve – at known values for a known pump. Based on the loss of material mass of the pump after certain hours of testing and the maintained capacity of the pump until its failure, we determine the remaining service life of the pump. [6], [7], [8]

Table 3: Vickers test with Eaton-Vickers 35VQ-25 pump - ASTM D6973 [9]

|                          |  |
|--------------------------|--|
| Fluid volume             | min. 196 L   |
| Test temperature         | 93 °C  |
| Test duration – standard | 50 hours (2 days)                                    |
| Test duration – extended | 1,000 hours (42 days) with inspections at 300 hours) |
| Pressure                 | cca. 207 bar   |
| Pump speed               | cca. 2,400 rev/min                                   |
| Flow rate                | 144 L/min  |
| Power                    | 91 kW  |

The scheme of the test rig for performing the Vickers test, which assumes the use of a 35VQ25A vane pump with the basic building blocks of the test site, is shown in Figure 3.



- 1- Hydraulic tank, min. 190 L (50 gallon)
- 2- Temperature gauge
- 3- Suction pressure gauge
- 4- Pump 35VQ25A-11\*20
- 5- Electromotor 91 kW
- 6- Operational pressure gauge
- 7- Pressure relief valve
- 8- Filter 10 µm
- 9- Cooler
- 10- Pump flow meter

Figure 3: Test facility structure for the Vickers test with a 35VQ25A constant pump [10]

2.2. Constant and variable operating conditions

One of the most important aspects of testing are definitely the operating conditions used in testing, especially the way the test pump is loaded. Certain tests are performed at a constant pressure, although it is elevated or the maximum allowed for a given pump, while for others the load profile changes cyclically. According to experts, the latter tests, tests with the so-called variable operating conditions or variable load, are closer to real operating conditions and, thus, are more realistic test results.

When performing tests with pumps, the height of the operating pressure and the rotational speed of the pump are the most important operating parameters. The speed of movement of the vital components of the pump is related to the latter, and the load on the surface is related to the height of the operating pressure. Thus, in tests with pumps carried out at a constant pressure, pressure is constant, but differently high. There may also be different drive speeds and, thus, pump flow. In most of these tests, constant-displacement pumps are used, and the pump is loaded at a higher or lower constant pressure. In the second group of tests, the load profile of the pressure pump changes cyclically – the load of the pump with a constant but differently high pressure in each phase of the test cycle. Pressure change is achieved in the simplest way with pressure relief valves. [1], [2], [11]

One of these tests, where the pressure is changed via differently set safety valves, is the Wanke test with three gear pumps [12]. In this test, the study of the influence of the degree of purity on gear wear was at the

forefront. In the case of this test, the load is cyclic – cyclically changing pressure, and the electric motor is 150 kW. The structure of the test facility for performing this test is shown in Figure 4.

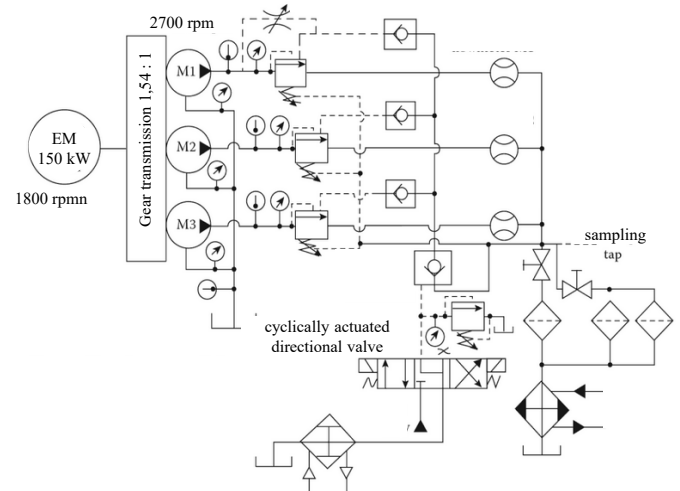


Figure 4: Test station for tribological tests with gear pumps – Wanke [12]

A very well-known and established test with variable pump load is also the already presented Eaton-Vickers test with vane pumps type V-104 and 20VQ5. A comparison of the operating parameters during the test, including the operating pressure heights and flow rates of both pumps, is shown in Table 4.

Table 4: Comparison of Eaton-Vickers tests with variable operating parameters [1]

| Parameter                       | Eaton-Vickers V-104 |       | Eaton-Vickers 20VQ5 |       |       |
|---------------------------------|---------------------|-------|---------------------|-------|-------|
|                                 | Pump flow (L/min)   | 30    | 38                  | 19    | 38    |
| Pressure (bar)                  | 138                 | 103   | 207                 | 207   | 207   |
| Revolution (min <sup>-1</sup> ) | 1,200               | 1,500 | 1,200               | 2,400 | 2,700 |
| Power (kW)                      | 69                  | 65    | 65                  | 130   | 147   |

It is similar in the case of tests with piston pumps. Several types of wear occur within piston pumps. In addition to sliding wear, which occurs when the piston moves in the hole, there is also combined wear (in combination with rolling and rotation of the pump elements), as well as wear due to corrosion and cavitation. Testing using a piston pump refers to, e.g., also ASTM Standard D6813-02a. [13]

The Sauer-Danfoss test procedure is often used to determine the effect of water contamination, where the operating pressure varies according to a certain profile – different long maintenance of different high operating pressures: 345 bar for up to 2 hours, 207 bar during the 3rd to 25th hours, 34 bar from 25 to 26 hours and 380 bar from 26 to 225 hours – so-called cyclic loading. As this test is intended to determine the effect of the presence of water, phases without the presence of water (first 25 hours) are observed at different periods of operating pressure, and 1 % water contamination is maintained at different operating pressures until the end of the test. In addition to checking for signs of wear, corrosion and cavitation, a further test criterion is a drop in pump flow – a 10 % drop in flow is considered a pump failure. [1]

An example of cyclic loading of a pump is also a performance test for HFC hydraulic fluids, where the use of a Sauer-Danfoss axial piston pump in swash plate design is envisaged, driven by a Sauer-Danfoss Series 20 hydraulic motor of the same design. The duration of individual periods for a total of 600 s of the long loading cycle and the associated pressures are given in Table 2. The complete cyclic loading test lasts 500 hours. Upon completion of the test, all rotary components of the pump are inspected for signs of wear. An axial piston variable pump is used in the case of this 500 hour Sauer-Danfoss test.

Table 5: Cyclic loading phases Sauer-Danfoss 500 hour pump test [1]

| Duration of load period (s) | Pressure in individual load period (bar) |
|-----------------------------|--|
| 130                         | 214                                      |
| 325                         | 172                                      |
| 60                          | 310                                      |
| 85                          | 172                                      |

2.3. Tests with variable pumps

A cyclic load test with the variable pump is also the Bosch test – Bosch Racine test (or Bosch-Rexroth test with vane pump). This test involves the use of a cyclic load of an SV-10 type vane pump driven by an electric motor of approximately 5.5 kW, with a tank size of 70 litres. The duration of the pressure change phases, as well as the scheme of the test device, is given in Figure 5. The pressure varies from the pressure relief state to a pressure of 10 bar and onwards to 40 bar, each phase lasting 10 s. Compared to the tests described so far, in this case the power of the electric drive motor is lower.

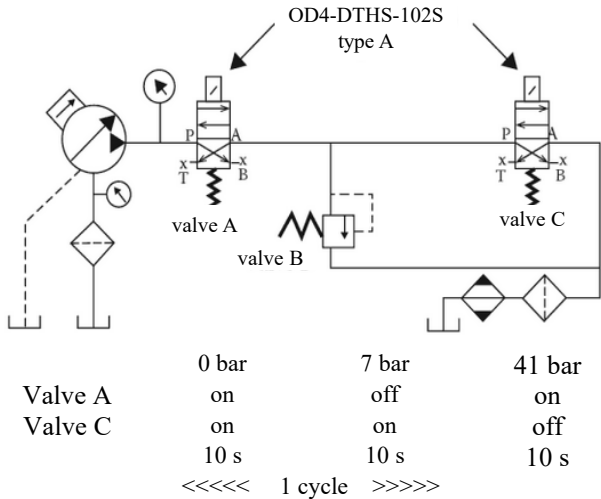


Figure 5: Bosch-Rexroth (Racine) test with cyclic loading of the SV-10 variable vane pump

Changing the load on the pump is achieved by switching on the directional valves and the pressure relief valve. Due to the pressure peaks that occur when the directional valves switch, their effect on the operation and wear of the pump and on the operation of the entire hydraulic system is much better recreated than in the case of tests with constant load pressure. Also, in this case, after the test is completed, the weight loss of the ring and vanes is measured and other damage to the contact surface and the pump bearings is observed (similar to the Eaton-Vickers test).

The next variable pump test is the well-known 500-hour test using the Komatsu HPV35 + 35 twin-piston pump, which is intended primarily for testing biodegradable hydraulic oils and for the field of Mobile Hydraulics [14]. The testing takes place at a cyclically variable pressure (from 10 bar to about 410 bar) and a flow between 60 L/min and 20 L/min, with a cycle duration of 5 s, a tank size of approximately 75 litres and the installed power amount is about 22 kW. This test monitors changes in pump efficiency, friction and surface roughness, the formation of varnish products and slurries and, of course, the deterioration of the physico-chemical state of the oil. The test is known today as the Komatsu test. The test site for the Komatsu test and the load profile of the piston pump are shown in Figure 6.

Unlike the Bosch-Rexroth test with a vane pump, the further Rexroth test determines the use of two adjustable piston pumps (tandem) type AA4VSO-71DR and takes place in three stages. Driving power is 45 kW

(regenerative power of 100 kW), the size of the tank is from 150 to 200 litres.

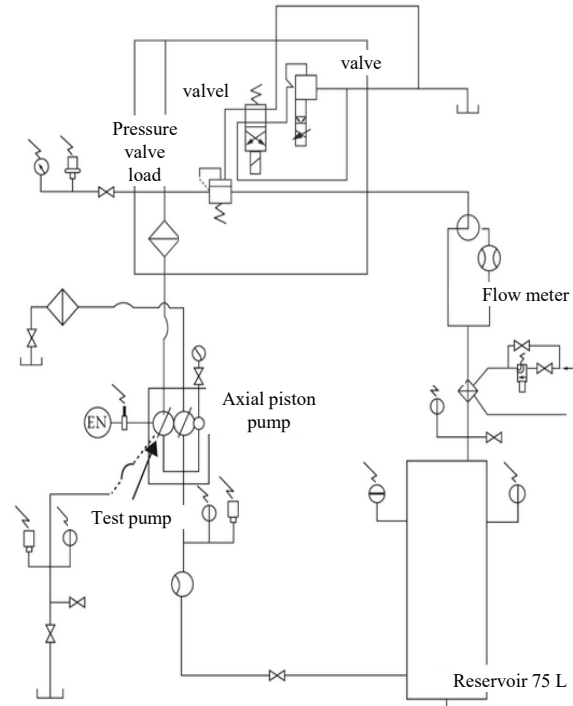
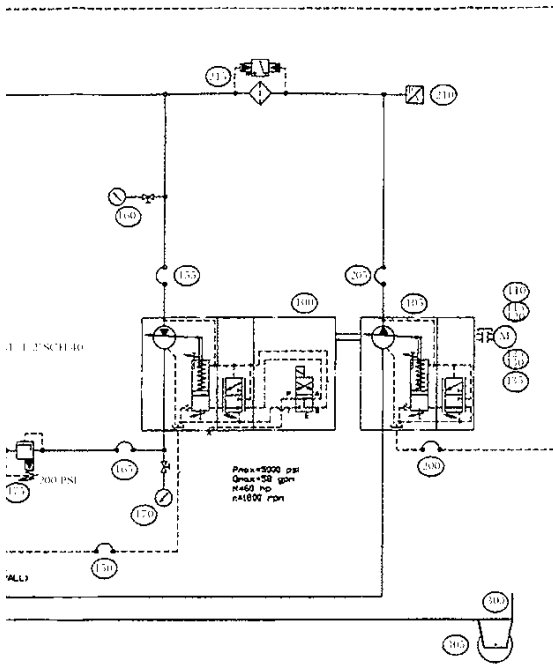


Figure 6: Komatsu test facility HPV35 + 35 with twin-piston variable pumps

The first stage of the test (250 hours) is carried out at a maximum pressure and maximum temperature, and, thus, the minimum allowable viscosity of the fluid. The second stage of the test is carried out at pulsating pressure by altering the maximum setting of the pump, from the lowest pressure to the maximum pressure and the maximum temperature defined by the specification of the liquid and the duration of 1 million cycles, with a frequency of the change in pressure of 2 to 3 Hz (about 140 to 93 hours). In the third phase of testing, which lasts 280 hours, testing is carried out at variable flow, from minimum to maximum, at maximum pressure and temperature and minimum viscosity.

A part of the Bosch-Rexroth combined test facility with variable dynamic load is shown in Figure 7.

The updated Bosch-Rexroth test is performed in accordance with the requirements given in the Rexroth RDE 90235 data sheet, which focuses on the interaction between the fluid and the vital components of the components under actual operating conditions [15]. The standardised procedure was initially developed and adopted for the axial-piston hydraulic pumps of the A4VG series, and for the A6VM series hydraulic motors operating in closed hydraulic circuits. After the first phase of constant loading, the components are subjected to dynamic cyclic loading under high pressure for 300 hours: 450 bar, 4,000 rpm and a temperature of 100 °C. The test continues in the ultimate performance test to check the load-bearing capacity of the components at maximum pressure and speed for 200 hours: 500 bar, 4,000 rpm and 100 °C. Both parts of the test as a whole are used to determine the resistance to shear loads, protection against wear and compatibility of materials with the tested liquid, etc.



Part of a test bench for the Bosch-Rexroth test with dynamic piston pump loading [16]

The descriptions of the most commonly used test procedures with pumps have so far been given in a very indicative way: The basic scheme of the test site and the operating conditions and parameters. Many more details about the test performance itself and the test conditions are given in the Standards, but these also leave certain details of the test performance to the test provider. The Standards specify only the main parameters of the test. In our case, the parameters of the test and the size of the test device are more important than the test procedure itself.

In much more detail, the test is described by the so-called performance testing protocol. The test protocols give a very precise hydraulic scheme of the test site, with the exact location of certain components with appropriate dimensions, as well as the exact procedure of rinsing the entire hydraulic system before testing. Unfortunately, detailed protocols are more or less internal in nature, as they are written down by the test performer of an individual test based on the experience of previous tests.

### 3. COMPARISON OF TEST CHARACTERISTICS

All of the aforementioned pump tests involve relatively large systems, with a large amount of hydraulic fluid, usually greater than 100 litres: Except in the case of the Komatsu test, where the amount is slightly smaller, as the test is intended for the field of Mobile Hydraulics, where slightly higher pumping numbers are characteristic. These are also high operating pressures, either constant values or variable, high flows and, consequently, large installed power of the test device.

The main characteristics of the presented and similar mechanical tests:

- a) Mainly different types of mineral based hydraulic oils are used.
- b) Wear/impact on the component – pump: Only observing the changes in wear or weighting the loss of mass, or any observation of the effect on components – only the changes of physical-chemical parameters of lubricant.
- c) Operating pressure while testing: Constant operating pressure during the test or, in some cases, alternating pressure. Pressure value up to 450 bar
- d) Pump flow rate: Up to 300 L/min.
- e) Fluid volume: Standard test (45 L to 200 L), small volume test up to 20 L.
- f) Circulation number  $Q_{Tank}/Q_{Pump}$  for example:
  - Denison test: 1 : 1,4
  - Sundstrand test: 1 : 2,11
  - Eaton/Vickers test: 1 : 1,36
- g) Installed power of the drive train to power the system and the cooling energy: Standard test: Up to 130 kW; in the case of a small volume pump test: Up to 7 kW.

An overview of the pump tests and classification regarding pump type used and load type, are summarised in Tables 6 and 7. Table 6 gives the comparison of the basic characteristics of the test related to the type of pump used (constant / variable) and the method of loading the pump with pressure (constant / variable). For some of the more important and most commonly used tests, however, values for flows, pressures, and installed power are given in Table 7 for energy comparison purposes.

Table 6: Pump tests type overview

| Test type               | Pump type | Pump flow |          | Pump load |          |
|-------------------------|-----------|-----------|----------|-----------|----------|
|                         |           | constant  | variable | constant  | variable |
| Denison P46             | piston    | x         |          | x         |          |
| Denison T5D             | vane      | x         |          | x         |          |
| Sundstrand Series 22    | piston    | x         |          | x         |          |
| Bosch Rexroth A2F010    | piston    | x         |          | x         |          |
| Wanke test              | gear      | x         |          |           | x        |
| Eaton-Vickers V-104     | vane      | x         |          |           | x        |
| Eaton-Vickers 20VQ5     | vane      | x         |          | x         |          |
| Eaton-Vickers 35VQ-25   | vane      | x         |          | x         |          |
| Sauer Danfoss 500 h     | piston    | x         |          |           | x        |
| Sauer Danfoss Series 20 | piston    |           | x        |           | x        |
| Bosch-Racine SV10       | vane      |           | x        |           | x        |
| Rexroth A4VSO           | piston    |           | x        |           | x        |
| Komatsu HV35+35         | piston    |           | x        |           | x        |

Table 7: Operating parameters of some pump tests

| Test type             | Pump type | Flow rate (L/min) | Pressure (bar) | Power (kW) |
|-----------------------|-----------|-------------------|----------------|------------|
| Denison T5D           | vane      | 265               | 172            | 90         |
| Sundstrand Series 22  | piston    | 95                | 345            | 64         |
| Eaton-Vickers V-104   | vane      | 38                | 138            | 69         |
| Eaton-Vickers 20VQ5   | vane      | 43                | 207            | 147        |
| Eaton-Vickers 35VQ-25 | vane      | 144               | 207            | 58         |
| Komatsu HV35+35       | piston    | 30                | 350            | 350 (415)  |

## CONCLUSION

The study provides an overview of various tests for testing the tribological properties of hydraulic fluids using hydraulic pumps with constant displacement, normally loaded with constant pressure. The emphasis is on the study of the basic characteristics of these types of tests, including the type of pumps used, the operating conditions of each test, the size of the installed power of the test device, the extent of the necessary equipment for execution of the test and the amount of fluid tested. The study served as a starting point for designing your own tight device.

All established tests with pumps have in common is that they most often use vane or piston pumps. In the case of the use of vane pumps, the load pressure of the pump is usually lower, and in the case of piston pumps is (significantly) higher. The pressure is usually constant, but it can also vary. In the latter case, it is the use of adjustable pumps.

All the briefly presented tests with pumps have in common is that they are implemented in large own testing – large test devices. For almost all tests a large amount of test fluid is used, a high flow pump is used, the operating pressures are realistic, which means high, suitable for the pump type used, and, consequently, a large drive power is required.

In addition, due to the long duration of the test a lot of heat is generated, which also requires a correspondingly large cooling power. Given this "energy dimension" of the tests, these tests are expensive, and everything is focused more or less solely on the degradation of the pump. Determining the degradation of other hydraulic components of the test device is not at the forefront.

These types of tests are less suitable or too expensive for completely new types of hydraulics, as there are too many unknowns. A new type of hydraulic fluid tested can damage all hydraulic components of the test device, not just the pump. In the case of the development of a new type of hydraulic fluid, the development takes place in several steps or levels of the stage of fluid development. Therefore, testing a fluid at a certain stage of fluid development, with the aforementioned established test procedures, can be very expensive, due to the large amount of fluid used and the possible negative effects on all components of the test device.

On the other hand, as already mentioned, in the case of testing a new type of fluid, we are also interested in the impact of the new fluid on other hydraulic components (valves, hydraulic cylinders, hydraulic tube motors, filters, sensors, cooling system). We are also interested in the compatibility of the new fluid with the materials of the hydraulic components under real operating

conditions (for example, in the presence of moisture, temperature, other types of movement of component components, cyclic loading). In the case of a new type of hydraulic fluid or a significantly changed formulation of an otherwise known fluid, it certainly makes much more sense, of course after extensive preliminary laboratory tests, to perform endurance tests under real conditions on a test device of smaller dimensions. Thus, the potential damage in the case of poor test results is much smaller.

The presented study served as a starting point for the design of a new test device of smaller dimensions, and a new test procedure that provides cost-effective testing of all characteristic components of the hydraulic system, under real operating conditions, suitable for new types of hydraulic fluids. [17], [18]

## REFERENCES

- [1] G.E. Totten, V.J. De Negri, "Handbook of Hydraulic Fluid Technology", CRC Press, Taylor & Francis Group, 2nd edition, ISBN 9781138077348, p. 983, (2012)
- [2] G.E. Totten, G.H. Kling, D.J. Smolenski, "Tribology of Hydraulic Pump Testing", Technology & Engineering, ASTM STP 1310, p.373, (1997)
- [3] G.E. Totten, R.J. Bishop, G.M. Gent, "Evaluation of Hydraulic Fluid Lubrication by Vickers Vane Pump Testing: Effect of Testing Conditions", NFPA, Presented at the International Exposition for Power Transmission and Technical Conference 4-6 April 2000, Technical paper series I00-9.7, (2000)
- [4] ASTM D2882: STP1310, Vickers' 35VQ25 Pump Test
- [5] ASTM D2882-00, "Standard Test Method for Indicating the Wear Characteristics of Petroleum and Non-Petroleum Hydraulic Fluids in Constant Volume Vane Pump", (Withdrawn 2003), (2003)
- [6] Light, D.: Hydraulic Fluids Meet Increasing Operating Demands, Machinery Lubrication, p. 9, 5/2005, (2005)
- [7] M. Evans, "Fluid technologies for a better world™ Durability and Retention of Performance In Hydraulic Fluids", Lubrizol, p. 24, <https://slideplayer.com/slide/4275253/>, (2015)
- [8] Oesterle, D., Profflet, R., Can Your Hydraulic Fluid Meet Today's Demands For Durability?, Hydraulics&Pneumatics 14, (2007)
- [9] ASTM D6973-14, "Standard Test Method for Indicating Wear Characteristics of Petroleum Hydraulic Fluids in a High Pressure Constant Volume Vane Pump", (2019)

- [10] N.N., Vickers, Eaton, "General Product Support – Hydraulic hints & Trouble Shooting Guide", Vickers company brochure No. 8/98, p. 29, (1998)
- [11] D. Lovrec, V. Tič, "Tribološki testi s hidravličnimi črpalkami ob konstantni obremenitvi", *Ventil : revija za fluidno tehniko in avtomatizacijo*, ISSN 1318-7279, april 2019, Vol. 25, No. 2, pp. 132-139, (2019)
- [12] T. Wanke, "A Comparative Study of Accelerated Life Test Methods on Hydraulic Fluid Power Gear Pumps", Proceedings of 37<sup>th</sup> National Conference Fluid Power, National Fluid Power Association, Milwaukee, Vol. 35, pp. 231-243, (1985)
- [13] ASTM D6813-02a, "Standard Guide for Performance Evaluation of Hydraulic Fluids for Piston Pumps", (2013)
- [14] A. Ohkawa, et. all., "Oxidation and Corrosion Characteristics of Vegetable-Base Biodegradable Hydraulic Oils", SAE Technical Paper Series, Paper No. 951038, ISSN: 0148-7191, (1995)
- [15] K. Korane, "Hydraulic fluid test matches real-world conditions, Sealing&Contamination Tips", 12-2016, <https://www.sealingandcontaminationtips.com/hydraulic-fluid-test-matches-real-world-conditions/>,(2016)
- [16] G.E Totten, M.H. Melief, J.R. Bishop, "Hydraulic Fluid Qualification Using the Rexroth High-Pressure Piston Pump Test", International Exposition for Power Transmission and Technical Conference, April, 2000, I00-9.2, pp. 241-248, (2000)
- [17] V. Tič, D. Lovrec, "Test device and automated test procedures for measuring valve characteristics", Conference proceedings, International Conference Fluid Power 2019, 1<sup>st</sup> ed. Maribor: University of Maribor Press, Faculty of Mechanical Engineering, pp. 145-158, (2019)
- [18] D. Lovrec, V. Tič, "A New Approach for Long-Term Testing of New Hydraulic Fluids", New Technologies, Development and Application IV, NT 2021, Lecture Notes in Networks and Systems, Vol. 233, Springer, Cham., pp 788-801 [https://doi.org/10.1007/978-3-030-75275-0\\_87](https://doi.org/10.1007/978-3-030-75275-0_87), (2021)

# The analysis of a sustained oscillation in the heat pump system with buffer tank

Dragan Pršić<sup>1\*</sup>, Aleksandar Vičovac<sup>2</sup>, Marko Nešković<sup>3</sup>

<sup>1</sup>Faculty of Mechanical and Civil Engineering in Kraljevo, University of Kragujevac (Serbia)

<sup>2</sup>SM Engineering, Beograd (Serbia)

<sup>3</sup>Gymnasium, Kraljevo (Serbia)

The most of domestic scale heat pumps with fixed speed compressors are thermostatic controlled. Control units with a relay characteristic are used to control these pumps. Such pumps operate in the mode of sustainable oscillations. To overcome short cycling, i.e. switching on and off of heat pumps, as this reduce energy efficiency and pump life cycle, buffer tanks are installed with the task of absorbing the excess heat delivered by the pump. The paper analyzes how the properties of a heat accumulator and a heat pump affect the oscillations parameters. The buffer tank is described by the FOPDT model while the pump is approximated by relay nonlinearity with symmetric hysteresis. A relay feedback technique with a describing function was used for the analysis. The results were confirmed by simulation in Simulink / Matlab environment.

**Keywords:** Heat pump, Relay with hysteresis, Sustainable oscillations, Describing function

## 1. INTRODUCTION

In the European domestic sector, water-to-water heat pumps (HP) with fixed-speed compressors are most commonly used [1,2]. Control units with a relay characteristic are used to control these pumps [3]. To overcome short cycling, i.e. fast switching on and off, as this reduce energy efficiency and pump life cycle, buffer tanks (BT) are installed with the task of absorbing the excess heat delivered by the pump. The use of heat accumulators affects both the dynamics of the pump itself and the accuracy of the controlled temperature. Energy flow through heat pump with BT is shown in Fig. 1.

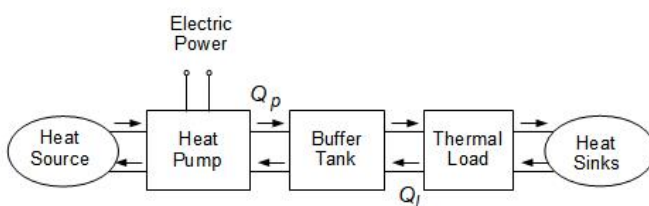


Figure 1: Heat pump system with buffer tank

In this paper we are primarily interested in buffer dynamics. The environment influence on BT is considered through heat flow  $\dot{Q}_p$  (between HP and BT) and heat flow  $\dot{Q}_l$  (between BT and thermal load).

From control point of view the system can be described by block diagram shown in Fig. 2. The dynamics of the heat pump is neglected in relation to the dynamics of the buffer. The combined impact of the HP and the thermal load on the buffer is modeled as nonlinearity (NL) of relay type with non symmetric hysteresis (Fig. 3). Manipulated variable  $u$  represent resulting heat flow ( $\dot{Q}_p - \dot{Q}_l$ ) in to the BT.

It should be noted that this characteristic corresponds to the heating mode of of a pump. In cooling mode, the nonlinearity changes phase by  $\pi$ .

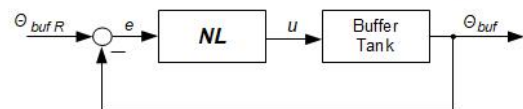


Figure 2: Block diagram of a heat pump + buffer tank

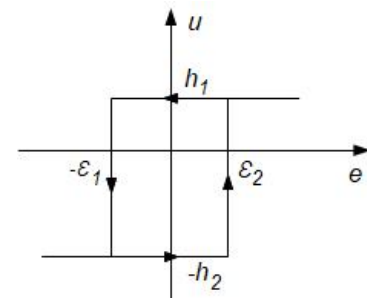


Figure 3: Asymmetric relay with hysteresis

In steady state there are sustainable oscillations at the output of BT. Our intention is to establish a quality relationship between the period of these oscillations and the parameters of the NL and the buffer tank itself.

## 2. DESCRIBING FUNCTION OF ASYMMETRIC RELAY WITH HYSTERESIS

In order for the describing function to accurately approximate the periodic function at the output of the nonlinearity in the relay feedback loop (Fig.2) it is necessary that BT has the characteristics of the low pass filter [4]. Actual changes in real buffer temperature is shown in Fig.4 [3].

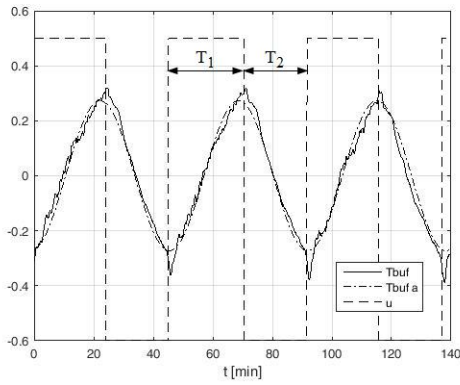


Figure 4: Buffer tank temperature

If the Fourier analysis of the temperature signal is performed with a series of order 10, the values of the coefficients shown in Fig.5 are obtained.

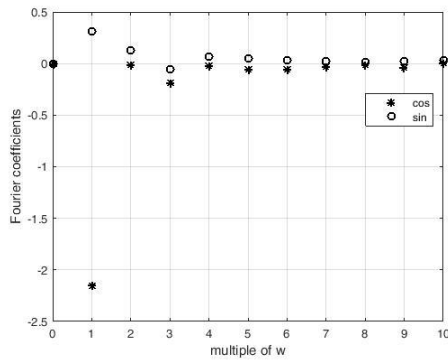


Figure 5: Fourier coefficients of buffer tank temperature

It can be seen that the first harmonic is dominant. For example, the ratio of the amplitudes of the first and second harmonics is 18.16. This means that the buffer can be viewed as a low pass filter. Fig.4 shows actual temperature approximation with first harmonic ( $T_{buf.a}$ ).

If the analysis of the manipulated variable (Fig.4-u) is performed with a Fourier series of order 10, the values of the coefficients is shown in Fig. 6.

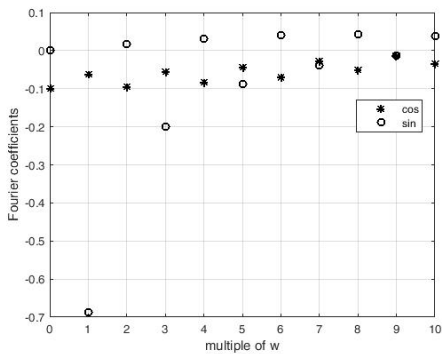


Figure 6: Fourier coefficients of manipulated variable

It can be noticed that the complex member of the first harmonic has a dominant importance. However, higher harmonics also have an effect on the output signal of nonlinearity. Ignoring higher harmonics can lead to a significant error if the approximation is performed only with a first-order harmonic. Figure 7 shows the actual value of the output magnitude of the nonlinearity ( $u$ ) and its approximation ( $u_a$ ).

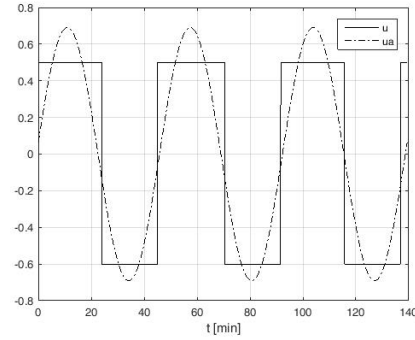


Figure 7: Manipulated variable and its approximation

The justification for approximating the output signal using the first harmonic lies in the fact that the buffer tank behaves like a low pass filter. In other words, it nullifies the influence of higher harmonics.

Due to this approximation, an error may occur in determining the position of the critical point on the Nyquist curve of a plant from a realy feedback experiment [5]. Nevertheless, such an approximation can help us in a qualitative analysis of the process.

The nonlinearity from Fig. 3 can be described by equation (1):

$$u = \begin{cases} h_1 & e > \varepsilon_2 \vee e \leq \varepsilon_2 \wedge e^- = h_1 \\ -h_2 & e < -\varepsilon_1 \vee e \geq -\varepsilon_1 \wedge e^- = -h_2 \end{cases} \quad (1)$$

If the error is of the form:

$$e(t) = e_0 + e_A \sin(\omega t) \quad (2)$$

where  $e_0$  is DC component,  $e_A$  magnitude and  $\omega$  error radial frequency ( $e$ ), then output signal of the nonlinearity can be approximated by harmonic of the first order. If the relation:

$$e_A \geq \max(\varepsilon_1, \varepsilon_2) \quad (3)$$

is fulfilled, then it is valid:

$$u = \frac{a_0}{2} + a_1 \cos(\omega t) + b_1 \sin(\omega t) \quad (4a)$$

where is

$$a_0 = (h_1 - h_2) + \frac{1}{\pi} (h_1 + h_2) (\theta_2 - \theta_1) \quad (4b)$$

$$a_1 = -\frac{(h_1 + h_2) (\varepsilon_1 + \varepsilon_2)}{\pi e_A} \quad (4c)$$

$$b_1 = \frac{(h_1 + h_2)}{\pi} (\cos(\theta_1) + \cos(\theta_2)) \quad (4d)$$

$$\theta_1 = \text{asin}\left(\frac{\varepsilon_1 + e_0}{e_A}\right) \quad (4e)$$

$$\theta_2 = \text{asin}\left(\frac{\varepsilon_2 - e_0}{e_A}\right) \quad (4f)$$

For a describing function we can write:

$$DF = \frac{b_1}{e_A} + j \frac{a_1}{e_A} \quad (5)$$

If the condition:

$$\dot{Q}_P = 2 \dot{Q}_I \quad (6)$$

is met, i.e. if the heat flow from the pump is equal to twice the value of the heat flow going out to the thermal load, then:

$$h_1 = h_2 = h \tag{7a}$$

$$\varepsilon_1 = \varepsilon_2 = \varepsilon \tag{7b}$$

$$e_0 = 0 \tag{7c}$$

we get:

$$DF = \frac{4h}{\pi e_A} \left\{ \sqrt{1 - \left(\frac{\varepsilon}{e_A}\right)^2} - j \frac{\varepsilon}{e_A} \right\} \tag{8a}$$

or

$$DF = \frac{4h}{\pi e_A} \angle -\arcsin\left(\frac{\varepsilon}{e_A}\right) \tag{8b}$$

If  $\varepsilon = 0$  then equations (8) represents DF of realy without hysteresis with magnitude  $h$ :

$$DF = \frac{4h}{\pi e_A} \tag{9}$$

It should be noted that DF does not depend on the frequency of the output signal but only on its amplitude. The hysteresis in the relay characteristic in Fig. 3 does not affect the change in amplitude but introduces the phase shift of the signal  $u$  in relation to  $e$ . The phase lag depends on the width of the hysteresis and the amplitude of the output signal.

From (8a) we can find the negative reciprocal of the DF:

$$-\frac{1}{DF} = -\frac{\pi e_A}{4h} \sqrt{1 - \left(\frac{\varepsilon}{e_A}\right)^2} - j \frac{\pi \varepsilon}{4h} \tag{10a}$$

where is:

$$Re(-1/DF) = -\frac{\pi e_A}{4h} \sqrt{1 - \left(\frac{\varepsilon}{e_A}\right)^2} \tag{10b}$$

$$Im(-1/DF) = -\frac{\pi \varepsilon}{4h} \tag{10b}$$

The complex functions (10) determine the position of the critical points of Nyquist plot for the buffer tank. It can be noticed that for a given nonlinearity with a fixed  $(\varepsilon, h)$  the imaginary part  $Im(-1/DF)$  has a constant value and does not depend on the properties of the plant. On the other hand, the absolute value of real part grows with increasing amplitude of the output signal.

### 3. THE PERIOD OF SUSTAINED OSCILLATION

We assume that the buffer dynamics can be described by first-order-plus-dead-time (FOPDT) model [3]:

$$G_P(s) = \frac{K_P}{\tau_P s + 1} e^{-T_d s} \tag{11}$$

where is:  $K_P$  - plant static gain,  $\tau_P$ - plant time constant,  $T_d$ - plant dead time.

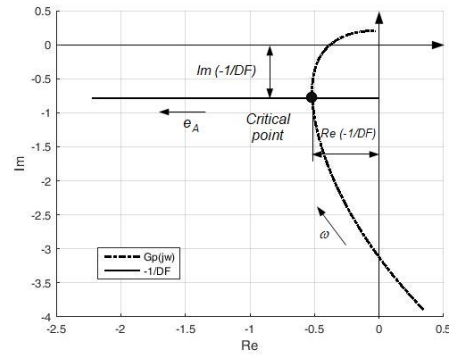


Figure 8: DF analysis of heat pump+buffer tank

Then the critical point in the frequency plane can be found in the cross section of  $G_P(j\omega)$  and  $-1/DF$  as shown in Fig. 8.

Bearing in mind (10), for a given buffer tank, the period of sustained oscillation can be influenced in the following way:

- with increasing hysteresis width ( $\varepsilon$ ) we increase the period of oscillation,
- by changing the width of the hysteresis ( $\varepsilon$ ) we can influence the amplitude of the oscillations. For example. by increasing the hysteresis we can reduce the amplitude of the oscillations. But  $e_A \geq \varepsilon$  must always be valid,
- a change in thermal load can affect the period of oscillation. The increase in load reduces the period of oscillation (provided that it is valid (6)). If the load decreases (less  $h$ ) the period of oscillation increases.

If the width of the hysteresis increases beyond some limit value, at some point the system can go out of the mode of its own oscillations. For example. if the heat flow from the pump is not sufficient to exceed the shut-off threshold then the pump runs continuously.

In addition to the nonlinearity, the parameters of the buffer itself affect the period of oscillation of self-sustaining oscillations. Fig. 9 shows the dependence of the amplitude and the period of the limit cycle for different values of plant static gain ( $K_P$ ).

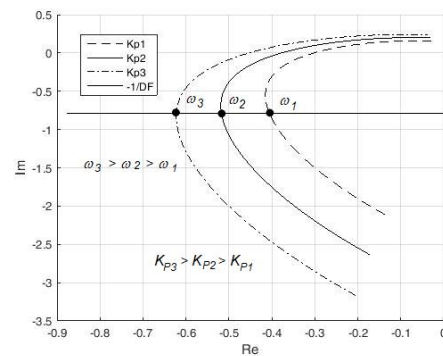


Figure 9: DF analysis for diferent values of  $K_P$

As the gain increases, the amplitude of oscillation increases and the period decreases.

Figure 10 shows the dependence of the amplitude and period of the limit cycle for different plant time constant values ( $\tau_p$ ).

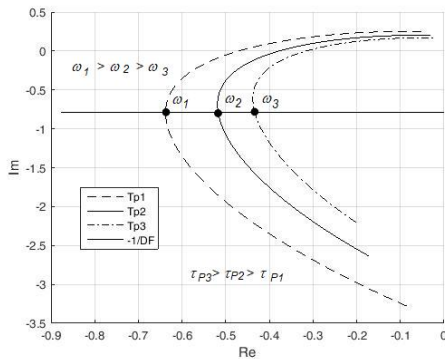


Figure 10: DF analysis for different values of  $\tau_p$

As the time constant increases, the oscillation amplitude decreases and the period increases.

Figure 11 shows dependence of the amplitude and period of limit cycle for different plant dead time ( $T_d$ ).

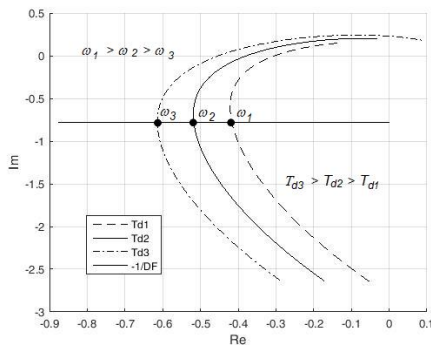


Figure 11: DF analysis for different values of  $T_d$

As the dead time increases, both the oscillation amplitude and the period increases.

Prethodna analiza je sprovedena uz pretpostavku da važi uslov (6). U tom slučaju nelinearnost se modeluje pomoću simetričnog histerezisa. Kao rezultat vaze relacije (7). U odzivu sistema ne postoji DC komponenta i  $T_1 = T_2$  (Fig. 12).

The previous analysis was performed assuming that condition (6) holds. In this case, the nonlinearity is modeled using symmetric hysteresis. As a result, relationships (7) apply. There are no DC components in the system response and  $T_1 = T_2$  (Fig. 12).

We have introduced this simplification to make it easier to conduct a qualitative analysis. In practice, this is a rare case and usually applies:

$$\dot{Q}_p \neq 2 \dot{Q}_l \tag{12a}$$

As a consequence, we have:

$$T_1 \neq T_2 \tag{12b}$$

and a DC component appears in the system response.

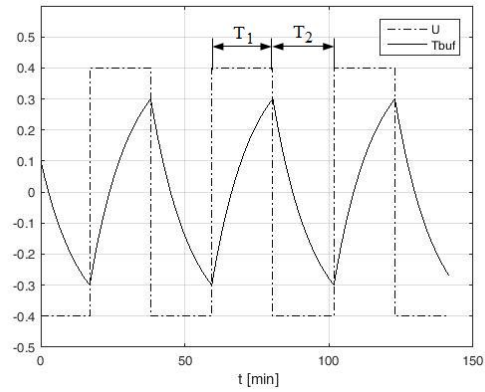


Figure 12: Output for symmetric hysteresis (Simulation)

#### 4. CONCLUSION

Heat pump with on/off control operate in the mode of sustainable oscillations. Relay feedback technique with describing function is a natural way to analyze such systems. Fourier analysis of the experimental data shows that the buffer tank can be viewed as a low pass filter in relation to the remaining parts of the heat pump system. Thanks to this, hard nonlinearity such as the relay with hysteresis can be approximated using the describing function. The paper uses symmetric hysteresis to describe relay nonlinearity. Even such a simplified model analytically confirms our intuitive knowledge about oscillations in the system.

#### ACKNOWLEDGEMENTS

This research has been supported by the Serbian Ministry of Education, Science and Technological Development under grant No. 451-03-9/2021-14/200108

#### REFERENCES

[1] R.Green, “The Effects of Cycling on Heat Pump Performance”, Confidential Report, Project No: 46640, (2012), Available online at: [https://assets.publishing.service.gov.uk/government/uploads/system/uploads/attachment\\_data/file/65695/7389-effects-cycling-heat-pump-performance.pdf](https://assets.publishing.service.gov.uk/government/uploads/system/uploads/attachment_data/file/65695/7389-effects-cycling-heat-pump-performance.pdf), (Accessed 01.05.21).

[2] R. Curtis, T. Pine, “Effects of cycling on domestic GSHPs, Supporting analysis to EA Technology Simulation /Modelling”, Mimer GeoEnergy, Report No: C207-R2, (2012), Available online at: <https://www.gov.uk/government/publications/modelling-and-simulation-of-cycling-of-ground-source-heat-pumps-mimergeoreport2> (Accessed 01.05.21)

[3] A. Vičovac, D. Pršić, V. Stojanović, “Analysis of Dynamic Characteristics of Heat Pump With Thermal Accumulator”, Proceedings of 5<sup>th</sup> International Scientific Conference, “COMETA 2020”, Jahorina, Republic of Srpska, pp. 383-388, (2020)

[4] J.H. Taylor, “Describing functions”, in Electrical Engineering Encyclopedia, John Wiley & Sons, New York, NY, USA, 1999.

C.C. Yu, “Autotuning of PID Controllers”, Springer-Verlag, London, (1999)

# Offline Robot Programming Using ABB RobotStudio

Vojislav Vujičić <sup>1\*</sup>, Ivan Milićević <sup>1</sup>, Milan Marjanović <sup>1</sup>,  
Nedeljko Dučić <sup>1</sup>, Aleksandar Jovičić <sup>1</sup>, Snežana Dragičević <sup>1</sup>

<sup>1</sup> Faculty of Technical Sciences Čačak, Department of Mechatronics and Department of Mechanical Engineering, University of Kragujevac, Čačak (Serbia)

*During the regular teaching syllabus in the subject of Robotics at the Faculty of technical sciences in Čačak, a new laboratory exercises in which the programming of industrial robots using ABB RobotStudio have recently been introduced. An offline way of programming in a mentioned software tool and needed steps for creating a program for one robotic cell are presented in this paper. Robot setup and programming was performed on an ABB IRB 120 robot cell controlled by an IRC5 controller. After programming and simulation, the program is switched from RAPID to a real robot controller, where fine-tuning and commissioning is performed.*

**Keywords:** Robot; ABB; RobotStudio; Programming.

## 1. INTRODUCTION

A series of industrial and technological revolutions, which have occurred throughout history and which still occur daily, have led to significant changes in the way we live today. The fact is that today's way of life is very fast and dynamic. Therefore, there is a need for the development of autonomous systems that would be able to replace human labour in certain areas of work. Systems that can replace humans in certain jobs in a very reliable and efficient way are called *robotic systems* or *robots* for short. Thanks to the rapid development of modern industry, robots have become an irreplaceable part of modern industrial production, but the present moment and the recent past are characterized by a rapid expansion of the development of robotic systems that are also widely used in other spheres of life. [1]

Robotic systems achieved significant improvements in recent years, which reflects the growing capabilities of these systems. Despite their increased complexity compared to older systems, their programming needs to be simplified as much as possible. To achieve this, constant improvements are needed in the field of robotics. Since robotics is a multidisciplinary technology field, its development is directly affected by the development of individual fields of technology, such as mechanics, electrical engineering, electronics, computer technology, etc.

One of the fields of technology that has the biggest impact on the development of robotics is computer technology. The development of sensor systems, computers and computer softwares enables easier control of robotic systems. Creating models and simulations of the entire system enables easier implementation of robotic systems in the production process. In addition to these advantages, the development of computer software has led to the simplification of robot programming software, and thus facilitates the programming of robots, which is very important from the end user's point of view.

The first part of this paper describes the characteristics of the laboratory setup installed in the laboratory of the Science and technology park in Čačak.

The second part describes the application of the ABB RobotStudio software package in robot programming and performing laboratory exercises with students. The third part of this paper shows a part of the code regarding the robot movement, while the fourth part will discuss the realized program.

## 2. LABORATORY SETUP

Thanks to the funds provided by the Ministry of Education, Science and Technological Development of the Republic of Serbia, A new research laboratory in the field of robotics has been established within the Science and Technology Park in Čačak. Two robotic cells were installed and put into operation in this laboratory, one of which is an industrial robot ABB IRB 120.

This robot is a multi-purpose industrial robot with six degrees of freedom, which can perform various tasks in a large number of industries, including electronic, food, machine, solar, pharmaceutical, medical, etc. Due to its small size, it is extremely convenient for use in research purposes. This robot is controlled by an IRC5 controller that has input and output modules as well as communication modules. The main features of this robot are: reach 580 mm, six degrees of freedom, load capacity up to 3 kg, acceleration from 0 to 1 m / s in 0.07 s, and position repeatability of 0.01 mm. [2]

The second robotic cell is a collaborative type of robot, the ABB IRB 14000 YuMi.

This robot is the first two-handed collaborative robot made for operations in which man and robot work together. It is designed to meet the flexible and agile production and assembly needs of small electronic parts. It is also suitable for other work environments that require high precision, such as the production of watches, toys, and the assembly of automotive components. The main features of this robot are: reach 559 mm, load capacity 500 g per hand, seven degrees of freedom per hand, maximum speed 1.5 m/s, maximum acceleration 39.1 m/s<sup>2</sup>, and position repeatability of 0.02 mm. [3]

Both of these robotic cells are placed in a common work environment which is also a safety zone for robots. A working area on which working elements, sensors,

\*Corresponding author: vojislav.vujcic@ftn.kg.ac.rs

supports, etc. can be placed, is made from construction profiles and placed within the safety zone. Next to the safety zone, a standing desk with commands for starting the robot is placed with a PLC controller and an HMI panel that can be programmed to define a work process. The laboratory setup with robots, safety zone and control desk is shown in Figure 1.



Figure 1. Laboratory setup with ABB robots.

### 3. CREATING A ROBOT MOVEMENT PATH USING ABB ROBOTSTUDIO SOFTWARE

ABB RobotStudio is software support for ABB robots offline programming.

Offline programming is the best way to increase return on investment for robotic systems. ABB's offline simulation and programming software, RobotStudio, allows the programming of robots on a computer without interruption in production. This allows performing tasks such as training, programming and optimization without disrupting production. [4]

The program is built on the ABB Virtual Controller, an exact copy of the real software that runs robots in production. This allows very realistic simulations to be performed, using robot programs and configuration files identical to those used in industry. [4]

RobotStudio comes with a complete package of features and add-ons that enable offline simulation thus reducing risks, speeding up system startup, shortening the transition time from one product to another and increasing productivity. [4]

The first step in programming the robot is to start the software, select the *Empty Station* option and confirm by pressing *Create* button. After this step, software opens the working environment. In the next step, it is necessary to insert a work bench (safety zone) on which the robot will be placed and the object that needs to be processed. RobotStudio allows to import various 3D models created in one of the 3D modeling softwares. In this step, it is necessary to import a previously created 3D model. This can be achieved using the *Import Geometry* option. Before this procedure, the 3D model file that you want to import needs to be copied into a folder with the following path: This PC>Documents>RobotStudio>Geometry.

After inserting the working bench, it is necessary to adjust its position in the work environment. This is achieved by right-clicking on the body of the table model and then selecting *position/set position* option. This procedure opens a window as shown in Figure 2.



Figure 2. Adjusting the position of the work bench

The next step is to insert the ABB IRB 120 robot into the work environment. This is achieved by selecting an *ABB Library* option in the toolbar and selecting the desired robot from the drop-down list. The position of the robot is adjusted as follows (position (x,y,z): 680, 880, 753, orientation (x,y,z): 0,0,-90).

Then it is necessary to insert a 3D model of the part, in the same way as importing a 3D model of the work bench, i.e. by selecting the *Import Geometry* option, as well as the position and orientation of the part (position (x,y,z): 1162, 633, 795, orientation (x,y,z): 0,0,90).

The next step involves defining the working tool or end effector. The tool is selected using the *Import Library/Equipment* option. Many different types of tools, robot stands, parts suppliers, etc. are available for selection. In this case, the *PEN* training tool was chosen. The tool needs to be attached to the last axis of the robot. This can be done by right-clicking the selected tool and selecting *Attach tool* option. On the list that shows up, the name of the selected robot and the axis on which the tool needs to be placed can be selected.

After setting up the tool, all mechanical components are ready for operation. In this example, following the same procedure, a YuMi IRB 14000 robot was also added. The appearance of the work environment after performing the previous tasks is shown in Figure 3.



Figure 3. Appearance of a virtual work environment with robots

The next step is defining the coordinate systems for the workbench and the workpiece. This can be achieved with the *Frame* option located on the toolbar. It is first necessary to set the appropriate cursor *Snap* points (the ends of the line, the middle of the line, the center of the circle, etc.).

In this case the coordinate systems are set up as in Figure 4.

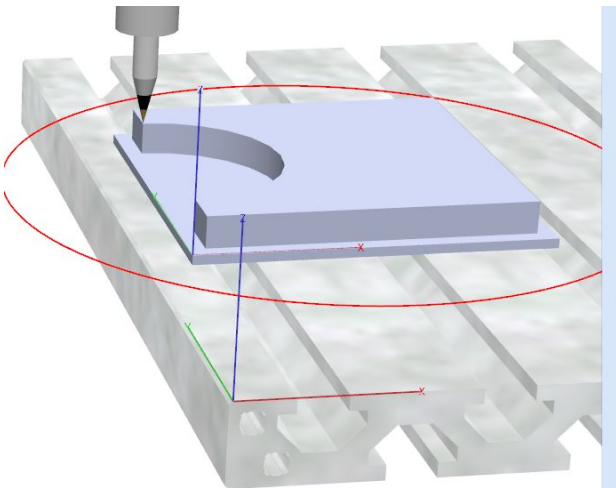


Figure 3. Selection of coordinate systems

After defining the coordinate systems, it is necessary to define the working object of the part that needs to be processed. This task is performed by selecting *Other/Create Workobject* option, after which it is necessary to define the object in a popup window.

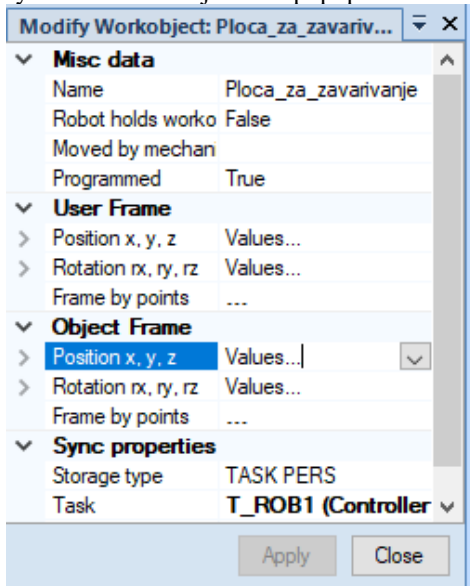


Figure 4. Creating a work object

In this window, the name of the work object and its coordinate system needs to be set up. Defining the coordinate system of the work object is done under *Object Frame/Position*. The coordinate system of the work object is the coordinate system of the work piece that was selected in the previous step. To select this coordinate system, *Snap* needs to be set up so that it can be captured by *Frame*.

In order for a robot to perform a specific task, it is necessary to implement a specific virtual controller that will control the robot. The virtual controller is inserted into the software by selecting the option *Virtual Controller/From Layout*, after which it goes through the procedure as in the Figure 5.

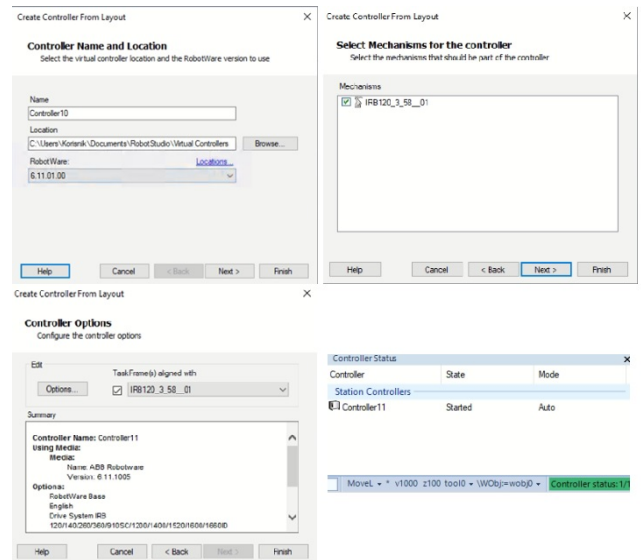


Figure 5. Creating a virtual controller

An important step that must be realized, in order for the robot to use its work tool to access the points that will be created later, is to define the active task, work object and tools. These parameters settings are shown in Figure 6.

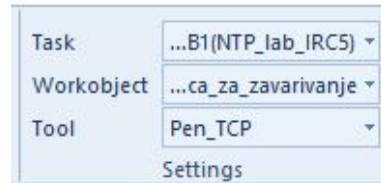


Figure 6. Selection of active task, work object and tool

After successfully completing the previous steps, the path can be created. This step can be realized by selecting *Path/AutoPath* option. The path is created by selecting characteristic points along the contour that the tool needs to follow. When the contour is selected, it is necessary to define the starting point of the robot (*Target*) by selecting *Target/Create Target* option. Setting up the starting point is shown in Figure 7.

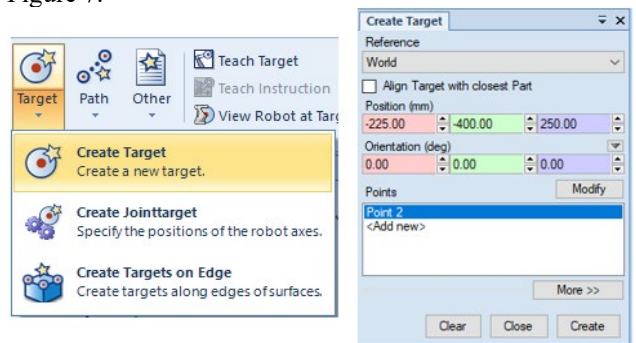


Figure 7. Setting up the starting point

The created path is shown in Figure 8. For each trajectory point, it is necessary to adjust the position of the tool in relation to the workpiece. This can be done by right-clicking on the desired target and selecting an *ModifyTarget/SetPosition* option. When adjusting the tool position, a programmer needs to make sure that the robot can physically be in desired position. The movement of the robot along the set path can be checked by right-clicking

on a created path and choosing the option *Move Along Path*.

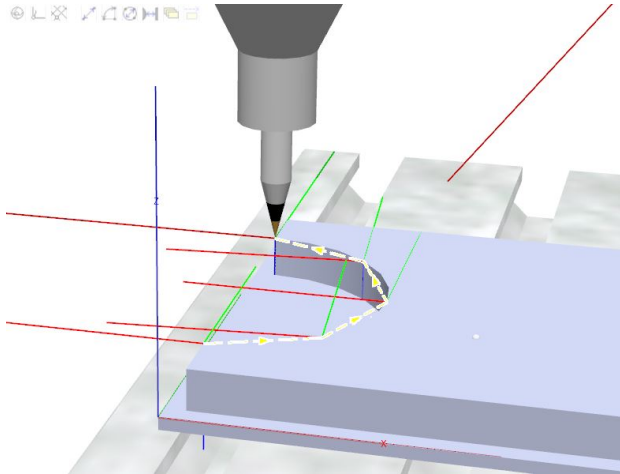


Figure 8. Created path

Starting the simulation is done by clicking on the *Run* button located in the *Simulation* tab. During the simulation, it is possible to check if the created path is satisfactory. Also, potential problems with the orientation of the tool can be examined and solved in this step. The simulated tool trajectory is presented by a red line shown in Figure 9.

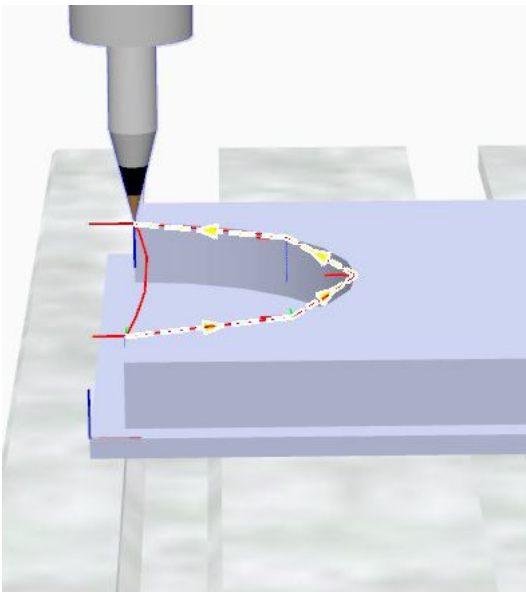


Figure 9. Simulated tool trajectory

#### 4. PROGRAM CODE „RAPID“

After generating the tool path and simulating the operation of the robot, it is necessary to transfer the program from the virtual station to the „RAPID“ program code. This can be done by selecting *Synchronize/Synchronize to RAPID* feature from the toolbar. Clicking on this feature opens up a window shown in Figure 10. A part of the virtual controller that needs to be synchronized with the RAPID program can be selected inside this window. By selecting the desired options, program synchronizes.

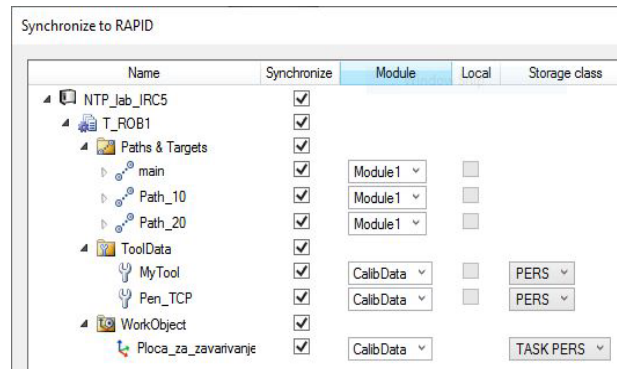


Figure 10. Synchronize the virtual controller with RAPID code

After synchronization is done, it is now possible to select the *RAPID* tab from the main menu. *Module 1* must be selected from the model tree. *Module 1* contains the code defined by previously created points and paths. Each target is defined by a following line of code:

```
CONST robotarget Target_Home:=
[[-477.392,-246.005,409.147],
[0,0.707106781,0.707106781,0],[-1,1,-2,0],
[9E+09,9E+09,9E+09,9E+09,9E+09,9E+09]];
```

where the first bracket is the position and the second is the orientation of the tool.

Each process is defined by a code:

```
PROC Path_20()
MoveJ Target_70,v1000,fine,Pen_TCP\WObj:=
Ploca_za_zavarivanje;
MoveJ Target_80,v1000,fine,Pen_TCP\WObj:=
Ploca_za_zavarivanje;
MoveJ Target_90,v1000,fine,Pen_TCP\WObj:=
Ploca_za_zavarivanje;
.
.
.
```

#### ENDPROC

where *Path\_20* is the path that consists of the functions for moving the robots joints *MoveJ*. Every *MoveJ* function has a defined *Target*, velocity (*v*), accuracy (*fine*), tool and workpiece.

In order to execute the program, it is necessary to bring up the executable path using the *Main* function.

The path activation is defined by a code:

```
PROC main()
Path_20;
ENDPROC
```

Any change in RAPID code or a change within a virtual station requires running a synchronization again. Therefore, the changes are visible on both the virtual controller and the workstation. After creating the final version of the RAPID code, all that remains is to transfer it to a real controller. This procedure is performed using *File Transfer feature* within the *Controller* tab in the software. After transferring the program to the robot controller, the robot starts by performing the program routine. Figure 11 shows the robot performing the specified path.



Figure 11. The robot executing the specified path

## 5. CONCLUSION

During the cooperation with the Science and technology park Čačak in the last few years, the Faculty of Technical Sciences in Čačak has been given the opportunity to use a laboratory with modern industrial robotic cells to perform practical laboratory exercises for students in the field of robotics. In addition to performing exercises, the Faculty also uses the laboratory for research purposes.

Through specific subject, students of master studies perform calculations of robot kinematics and dynamics. After that, using the software package ABB RobotStudio, students create the working environment of the robot, add the necessary components, working area, robot, tool, workpiece. Then the characteristic points and trajectories of the robot are defined. The simulation validates the path, after which the program code RAPID is transferred to the physical controller of the robot. After the program is inserted into the robot controller, fine adjustments of the robot are carried out and its robot can be started.

In this way, students become fully introduced to robotic systems, from theory to practice. This type of teaching develops the engineering way of thinking in students, connecting theory and practice. This type of teaching enables the development of engineering way of thinking in students, connecting theory and practice, but also prepare and train them for future work in industry.

The following research will be focused on the creating of various laboratory exercises that could mimic the work of a production line by adding additional equipment to the work table, as well as the practical implementation of a collaborative robot.

## ACKNOWLEDGEMENTS

This study was supported by the Ministry of Education, Science and Technological Development of the Republic of Serbia, and these results are parts of the Grant No. 451-03-9/2021-14/200132 with University of Kragujevac - Faculty of Technical Sciences in Cacak.

## REFERENCES

- [1] Kunpeng, Xie. *Research on Industrial Robot Monitoring Technology Based on PC SDK*. International Journal of Engineering Research and. V7. 10.17577/IJERTV7IS100020. (2018).
- [2] IRB 120 ABB's 6 axis robot – for flexible and compact production, available at: [https://search.abb.com/library/Download.aspx?DocumentID=ROBO149EN\\_D&LanguageCode=en&DocumentPartId=2&Action=Launch](https://search.abb.com/library/Download.aspx?DocumentID=ROBO149EN_D&LanguageCode=en&DocumentPartId=2&Action=Launch)
- [3] YuMi® IRB 14000, available at: <https://search.abb.com/library/Download.aspx?DocumentID=9AKK106354A3254&LanguageCode=en&DocumentPartId=&Action=Launch>
- [4] RobotStudio, available at: <https://new.abb.com/products/robotics/robotstudio>



**SESSION D**

**APPLIED MECHANICS**



# Nonlinear oscillations of a pendulum wrapped around a cylinder

Anastas Ivanov Ivanov\*

Department Mechanics, Todor Kableshev University of Transport, Sofia (Bulgaria)

*The large oscillations of a pendulum are studied. The pendulum is a material point that is suspended on a elastic cord with nonlinear characteristics. The mass of the cord is accepted. It is wrapped around a perfectly rigid and fixed cylinder. The system has two degrees of freedom. Nonlinearity is due to a geometric and physical nature. A system of two differential nonlinear equations is derived. A numerical solution was performed with the mathematical package MatLab. The laws of motion, the generalized velocities and accelerations and the phase trajectories are obtained. In order to continue the task by preparing an actual model and conducting experimental research, the projections of the velocity and acceleration of the material point along the horizontal and vertical axes, as well as their magnitudes, are determined. The obtained results are presented graphically and analyzed in detail.*

**Keywords: Pendulum, Geometric and physical nonlinearity, Nonlinear oscillations**

## 1. INTRODUCTION

The pendulum has been the subject of researches from ancient times. During the Renaissance, the phenomenal periodic movements of the pendulum were studied by Leonardo da Vinci and Galileo Galilei, [1].

In 1656, the Dutch scientist Christiaan Huygens constructed a pendulum clock. Such clocks remained the most accurate instruments for measuring time until the 1930 year, [2].

In 1851, Jean-Bernard Leon Foucault constructed a mathematical pendulum to prove the rotation of the Earth around the North-South axis, [3].

Analytical solutions related to the study of small and large oscillations of the pendulum provide a field for the development of a number of branches of Mathematics. To this day, many scientists, when studying the large nonlinear oscillations of the pendulum, apply analytical solutions, [4].

In the work [5], a few terms of the Fourier series expansion of the elliptic function as a source of periodic solutions for the pendulum equation are studied.

The nonlinear oscillation of a pendulum wrapping and unwrapping on two cylindrical bases is studied in the article [6]. An analytical solution is obtained using the multiple scales method.

The nonlinear oscillations of a pendulum wrapping on two cylinders is studied by means of a new analytical technique, namely the optimal auxiliary function method are studied in the publication [7].

A detailed theoretical and computational analysis of the period, tension and centripetal forces are studied in the paper [8].

The dynamical behavior of rigid weightless rod and concentrated mass, sliding periodically along the axis of the rod is studied in the article [9].

The dynamical behavior of rigid weightless rod and concentrated mass, moving simultaneously along and across the axis of the rod, according to given periodical laws is studied in article [10].

Today, in the presence of powerful electronic computing equipment and modern mathematical packages, such as MatLab, MathCAD, Mathematica, and others, these solutions are made mainly numerically, [11, 12, 13, 14]. They are particularly suitable for optimizing some parameters, [15].

The present study complicates the classical dynamic model of the mathematical pendulum in two directions simultaneously.

The cord is wrapped around a stationary cylinder. This leads to the lack of a fixed center of rotation and determines a variable length of the cord at any moment of time. Therefore, there is a specific geometric nonlinearity.

The cord is considered to be elastic with a soft characteristic, unlike the classic models, where the cord is inextensible. This leads to the typical physical nonlinearity.

The main goals of this study are the following:

1. To obtain the differential equations that describe the big oscillations of the mathematical pendulum taking into account both the geometric and physical nonlinearity of the model.

2. To compile a program for numerical integration of the derived nonlinear differential equations in the area of the mathematical package MatLab, and after then, to perform a computer simulation.

3. The study should be a basis for continuing the task by preparing a real pendulum and conducting of experimental researches, [16, 17, 18, 19, 20].

## 2. MATHEMATICAL MODEL

The mathematical pendulum studied in this work is a material point  $M$  with concentrated mass  $m$ , which is connected by an elastic cord with distributed mass  $\bar{m}$ . The cord is wrapped around a fixed rigid cylinder with a radius  $R$ . In a stable equilibrium position and at rest, when the cord is vertical, its length is  $L$ . This is the distance between the points  $A$  and  $M_0$ , (Figure 1).



These expressions are the following:

$$v_x = (L + R \cdot \varphi + u) \cdot \dot{\varphi} \cdot \cos \varphi + \dot{u} \cdot \sin \varphi, \quad (12)$$

$$v_y = (L + R \cdot \varphi + u) \cdot \dot{\varphi} \cdot \sin \varphi - \dot{u} \cdot \cos \varphi, \quad (13)$$

$$a_x = (L + R \cdot \varphi + u) \cdot \ddot{\varphi} \cdot \cos \varphi - \left( (L + R \cdot \varphi + u) \cdot \dot{\varphi}^2 - \ddot{u} \right) \cdot \sin \varphi, \quad (14)$$

$$a_y = (L + R \cdot \varphi + u) \cdot \ddot{\varphi} \cdot \sin \varphi + \left( (L + R \cdot \varphi + u) \cdot \dot{\varphi}^2 - \ddot{u} \right) \cdot \cos \varphi. \quad (15)$$

The magnitudes of the velocity and acceleration of point  $M$  are as follows:

$$v = \sqrt{(L + R \cdot \varphi + u)^2 \cdot \dot{\varphi}^2 + \dot{u}^2}, \quad (16)$$

$$a = \left( (L + R \cdot \varphi + u)^2 \cdot \ddot{\varphi}^2 + \left( (L + R \cdot \varphi + u) \cdot \dot{\varphi}^2 - \ddot{u} \right)^2 \right)^{0.5}. \quad (17)$$

It can be seen from the derived formulas that the main purpose of the study is to determine both laws  $\varphi = \varphi(t)$  and  $u = u(t)$ .

The elastic cord is an one-way connection. This means that it can function only if it is tensioned at any time during the movement of the pendulum. The condition for the cord to be tensioned is as follows:

$$S = m \cdot (g \cdot \cos \varphi - \ddot{u} + (L + R \cdot \varphi + u) \cdot \dot{\varphi}^2) > 0. \quad (18)$$

Therefore, the initial conditions must be set inappropriate values that they take into account the elastic characteristics of the cord.

#### 4. NUMERICAL SOLUTIONS

The numerical integration of the system of differential equations (10) and (11) is performed with the solver ode45 of MatLab, based on the explicit Runge-Kuta method of 4th and 5th order. This is a one-step algorithm with a chosen fixed-step  $\Delta t = 0.001 \text{ s}$ . This method calculates the value of function  $f(t_n)$  using only one previous value of function  $f(t_{n-1})$ .

The solver ode45 is the most used in such studies and guarantees relative accuracy  $\varepsilon_r = 1.10^{-6}$  and absolute accuracy  $\varepsilon_a = 1.10^{-8}$ .

The parameters with which the calculations were performed are:  $m = 1.50 \text{ kg}$ ,  $R = 0.50 \text{ m}$ ,  $L = 2 \text{ m}$ ,  $c = 250 \text{ N/m}$ , and  $c_1 = 20 \text{ N/m}^3$ ,  $\bar{m} = 0.10 \text{ kg/m}$ .

The following initial conditions are accepted:

$$\varphi_0 = \pi/4 \text{ rad}, \quad \dot{\varphi}_0 = 0 \text{ s}^{-1}, \quad u_0 = 0.05 \text{ m} \quad \text{and} \quad \dot{u}_0 = 0 \text{ m/s}.$$

In order to ignore the transient processes, a longer integration time was adopted, namely  $t = 10 \text{ s}$ .

The following kinematic characteristics were obtained:

a.) Laws of the first generalized coordinate,  $\varphi(t)$ ,  $\dot{\varphi}(t)$ ,  $\ddot{\varphi}(t)$ , (Figures 2, 3 and 4);

b.) Laws of the second generalized coordinate,  $u(t)$ ,  $\dot{u}(t)$ ,  $\ddot{u}(t)$ , (Figures 5, 6 and 7);

c.) Velocity of point  $M$ ,  $v_x(t)$ ,  $v_y(t)$ ,  $v(t)$ , (Figures 8, 9 and 10);

d.) Acceleration of point  $M$ ,  $a_x(t)$ ,  $a_y(t)$ ,  $a(t)$ , (Figures 11, 12 and 13);

e.) Phase trajectories of point,  $M$ ,  $\dot{\varphi} = \dot{\varphi}(\varphi)$  and  $\dot{u} = \dot{u}(u)$ , (Figures 14 and 15);

f.) Tensile force in the cord,  $S = S(t)$ , (Figure 16).

The law  $\varphi(t)$  is a periodic function with period

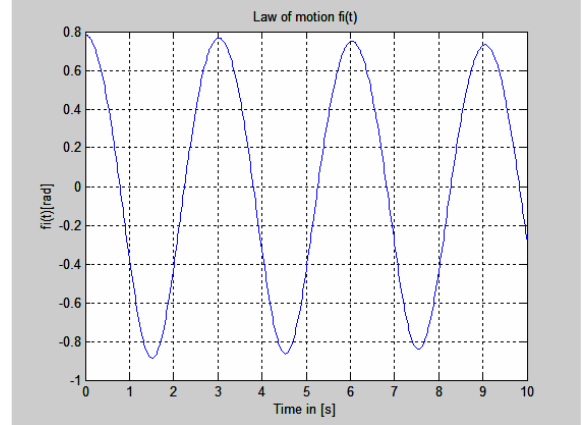


Figure 2: Law of angle function,  $\varphi = \varphi(t) \text{ rad}$

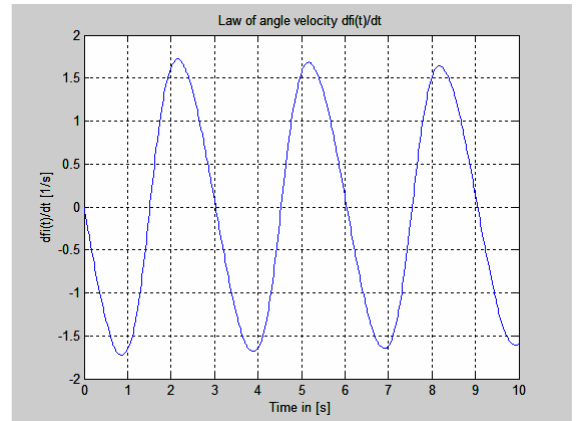


Figure 3: Law of angle velocity,  $\dot{\varphi} = \dot{\varphi}(t) \text{ s}^{-1}$

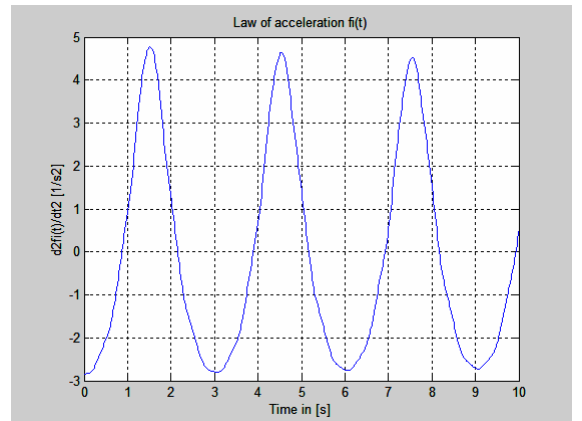


Figure 4: Law of angle acceleration,  $\ddot{\varphi} = \ddot{\varphi}(t) \text{ s}^{-2}$

$T = 3.025 \text{ s}$ , natural frequency  $f = 0.331 \text{ Hz}$ , and circular frequency  $\omega = 2.077 \text{ s}^{-1}$

The maximum angular velocity is  $\max|\dot{\varphi}| = 1.7227 \text{ s}^{-1}$ . The extreme values of the angular acceleration are  $\max|\ddot{\varphi}| = 4.8207 \text{ s}^{-2}$  and  $\min|\ddot{\varphi}| = 2.8569 \text{ s}^{-2}$ .

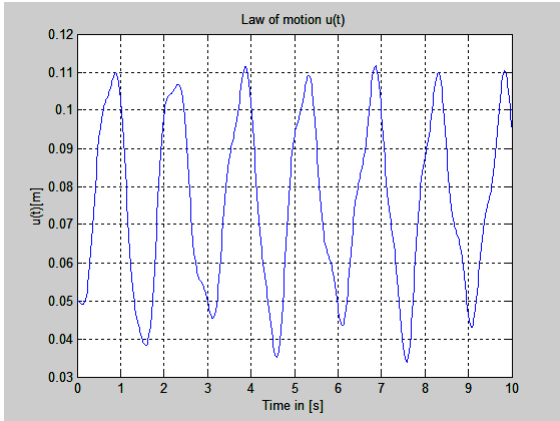


Figure 5: Law of motion  $u = u(t) \text{ m}$

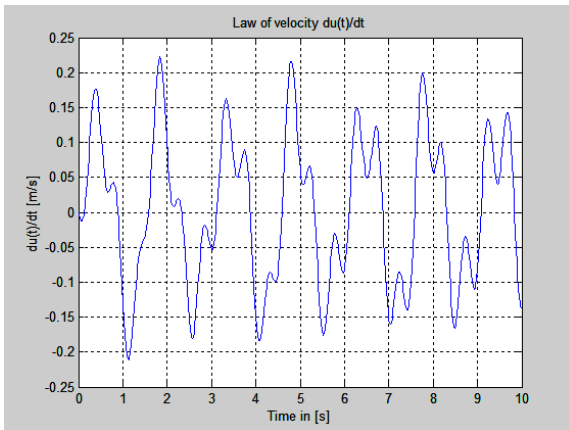


Figure 6: Law of velocity  $\dot{u} = \dot{u}(t) \text{ m/s}$

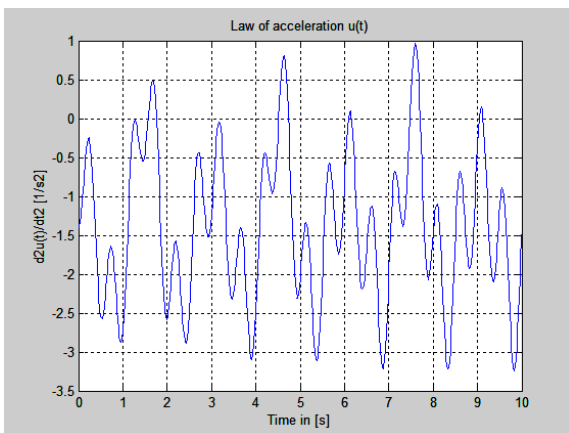


Figure 7: Law of acceleration  $\ddot{u} = \ddot{u}(t) \text{ m/s}^2$

The laws  $u(t)$ ,  $\dot{u}(t)$  and  $\ddot{u}(t)$  are periodic indeterminate functions of time. The extreme values are  $0.0340 \text{ m} \leq u(t) \leq 0.1115 \text{ m}$ ,  $\max|\dot{u}| = 0.2231 \text{ m/s}$  and  $\max|\ddot{u}| = 1.6205 \text{ m/s}^2$ .

The laws of velocity  $v_x(t)$ ,  $v_y(t)$  and  $v(t)$  are periodic functions with maximum values  $\max|v_x| = 3.5610 \text{ m/s}$ ,  $\max|v_y| = 1.6010 \text{ m/s}$  and  $0.0320 \text{ m/s} \leq v(t) \leq 3.6020 \text{ m/s}$ .

The laws of acceleration  $a_x(t)$ ,  $a_y(t)$  and  $a(t)$  are periodic functions with values, namely  $-6.9034 \text{ m/s}^2 \leq a_x \leq 6.0740 \text{ m/s}^2$ ,  $-5.4295 \text{ m/s}^2 \leq a_y \leq 3.5482 \text{ m/s}^2$ ,

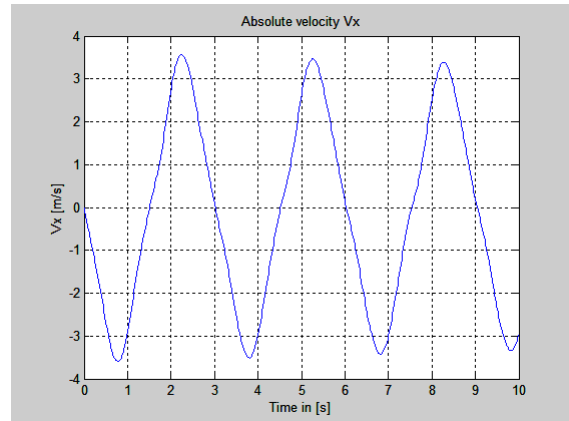


Figure 8: Velocity  $v_x$  of point  $M$  :

$$v_x = v_x(t) \text{ m/s}$$

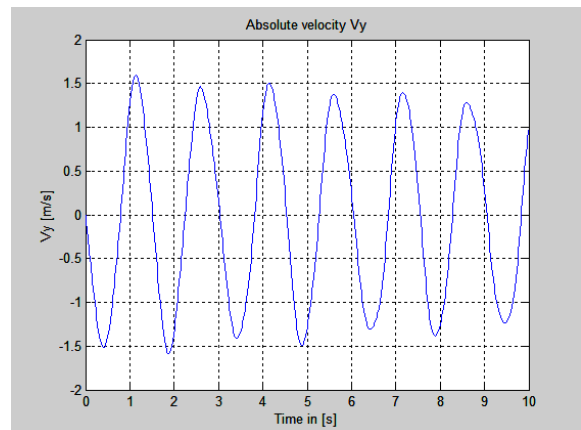


Figure 9: Velocity  $v_y$  of point  $M$  :

$$v_y = v_y(t) \text{ m/s}$$

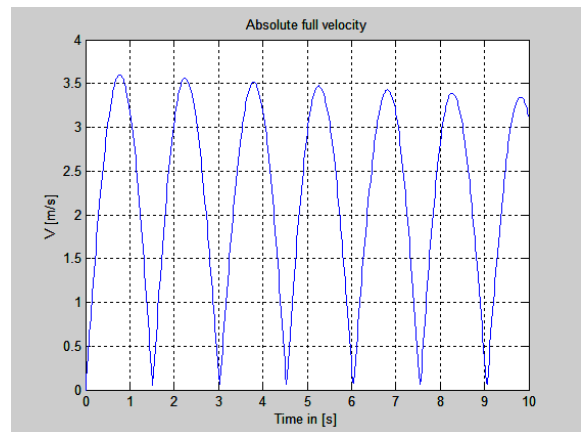


Figure 9: Velocity  $v$  of point  $M$  :

$$v = v(t) \text{ m/s}$$

$$4.7046 \text{ m/s}^2 \leq a \leq 7.6962 \text{ m/s}^2 .$$

The inner force  $S(t)$  in the cord has always a positive value, or in other words, the cord is always loaded with tensile force. This force is in the range  $7.4519 \text{ N} \leq S(t) \leq 16.8625 \text{ N}$  .

The phase trajectories of Figure 14 and Figure 15 fully correspond to the obtained laws  $\varphi(t)$ ,  $\dot{\varphi}(t)$ ,  $u(t)$  and  $\dot{u}(t)$  .

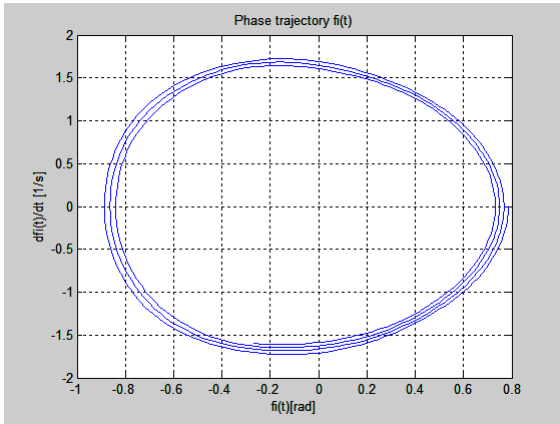


Figure 14: Phase trajectory of point  $M$  :  
 $\dot{\varphi} = \dot{\varphi}(\varphi)$

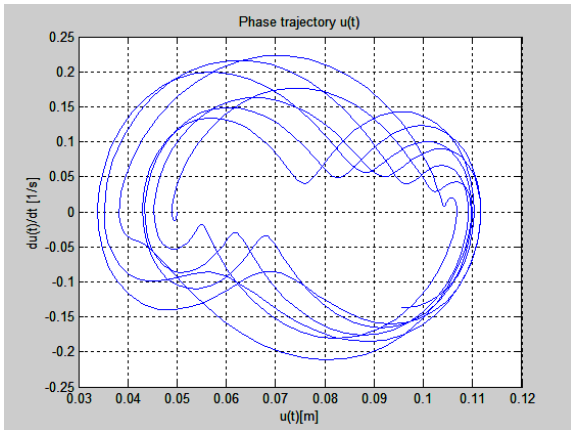


Figure 15: Phase trajectory of point  $M$  :  
 $\dot{u} = \dot{u}(u)$

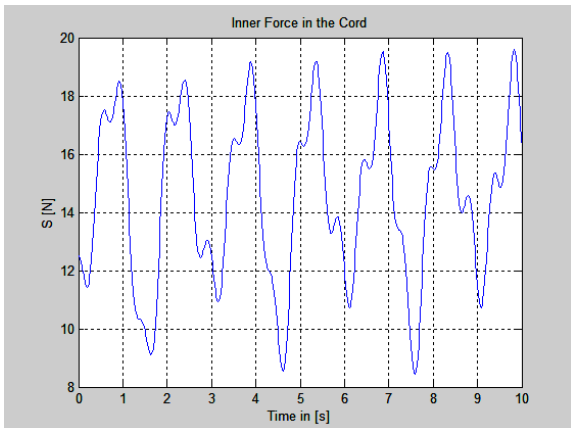


Figure 16: Tensile force in the cord:  
 $S = S(t) \text{ N}$

If an analysis of the phase trajectory  $\dot{\varphi} = \dot{\varphi}(\varphi)$  of Figure 14 is made, it will be seen that the distributed mass  $\bar{m}$  causes a gradual attenuation of the oscillations. To demonstrate this, two calculations are made.

Figure 17 shows the phase trajectory  $\dot{\varphi} = \dot{\varphi}(\varphi)$  at  $\bar{m} = 0 \text{ kg/m}$  and  $c_1 = 0 \text{ N/m}^3$  . Moreover, the integration time is increased to  $t = 25 \text{ s}$  .

Figure 18 shows the phase trajectory  $\dot{\varphi} = \dot{\varphi}(\varphi)$  at  $\bar{m} = 0.50 \text{ kg/m}$ ,  $c_1 = 0 \text{ N/m}^3$  and integration time is  $t = 25 \text{ s}$  .

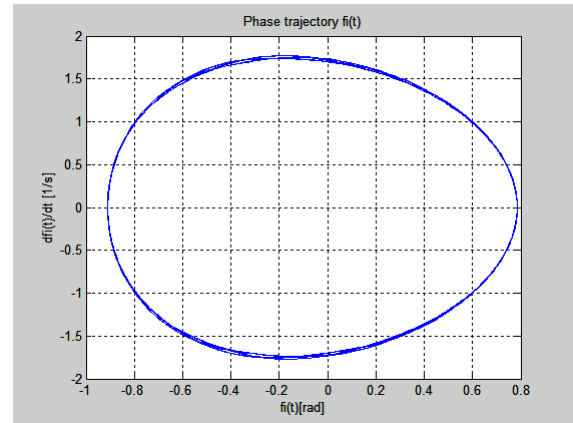


Figure 17: Phase trajectory of point  $M$  :  
 $\dot{\varphi} = \dot{\varphi}(\varphi)$ ,  $\bar{m} = 0 \text{ kg/m}$ ,  $c_1 = 0 \text{ N/m}^3$

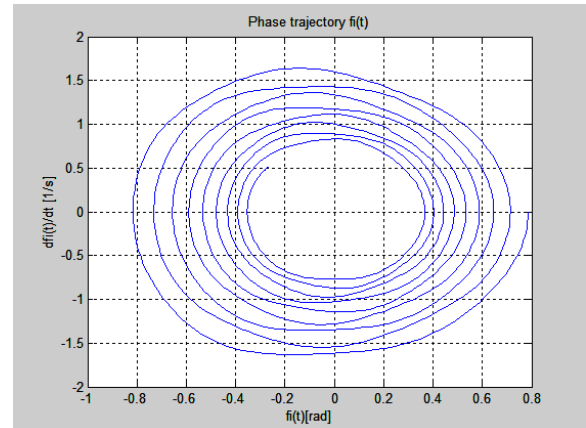


Figure 18: Phase trajectory of point  $M$  :  
 $\dot{\varphi} = \dot{\varphi}(\varphi)$ ,  $\bar{m} = 0.50 \text{ kg/m}$ ,  $c_1 = 0 \text{ N/m}^3$

The analysis of the phase trajectory  $\dot{u} = \dot{u}(u)$  for two states is made.

At the first state, it is accepted  $\bar{m} = 0 \text{ kg/m}$  and  $c_1 = 0 \text{ N/m}^3$  . The integration time is increased to  $t = 60 \text{ s}$  . The obtained phase trajectory is shown in Figure 19.

At the second state, it is accepted  $\bar{m} = 0.50 \text{ kg/m}$ , and  $c_1 = 0 \text{ N/m}^3$  . The integration is also  $t = 60 \text{ s}$  . The obtained phase trajectory is shown in Figure 20.

The analysis shows that if the distributed mass  $\bar{m}$  of the cord is increased, the longitudinal oscillations  $u(t)$  also decrease. They are moved to another zone and are established in some constant limits.

The case for the influence of the stiffness of the cord is also interesting. To establish this effect, two calculations for  $\bar{m} = 0.10 \text{ kg/m}$ ,  $c_1 = 50 \text{ N/m}^3$  and integration time  $t = 60 \text{ s}$  were performed.

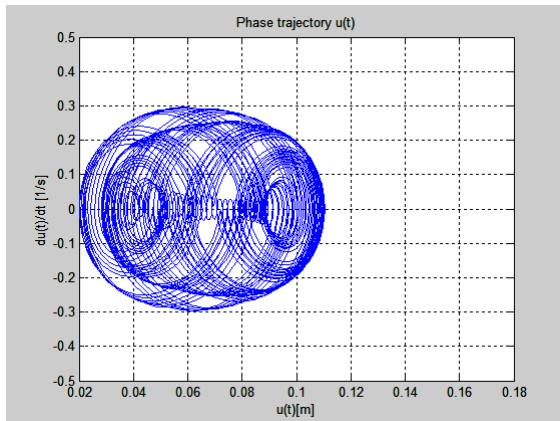


Figure 19: Phase trajectory of point  $M$  :  
 $\dot{u} = \dot{u}(u)$ ,  $\bar{m} = 0 \text{ kg/m}$ ,  $c_1 = 0 \text{ N/m}^3$

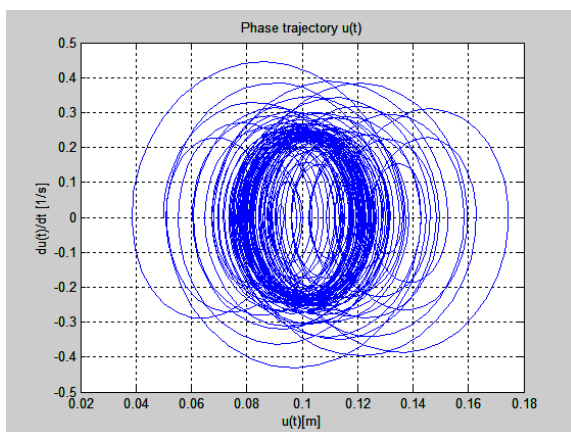


Figure 20: Phase trajectory of point  $M$  :  
 $\dot{u} = \dot{u}(u)$ ,  $\bar{m} = 0.50 \text{ kg/m}$ ,  $c_1 = 0 \text{ N/m}^3$

The first calculation is made with the coefficient of elasticity  $c = 300 \text{ N/m}$ , and the second calculation is made with the coefficient of elasticity  $c = 900 \text{ N/m}$ .

The phase trajectories  $\dot{u} = \dot{u}(u)$  for the two states are shown in Figures 21 and 22.

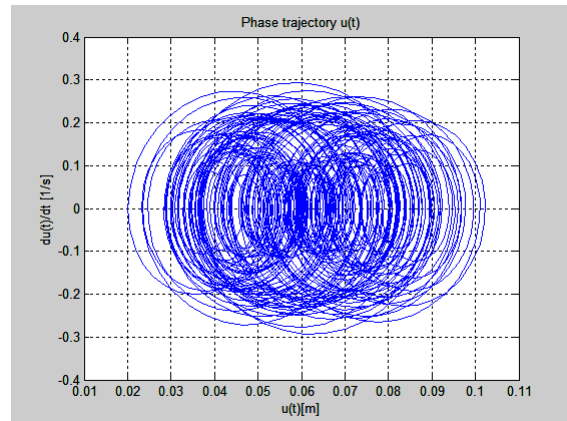


Figure 21: Phase trajectory of point  $M$  :  
 $\dot{u} = \dot{u}(u)$ ,  $\bar{m} = 0.10 \text{ kg/m}$ ,  $c = 300 \text{ N/m}$

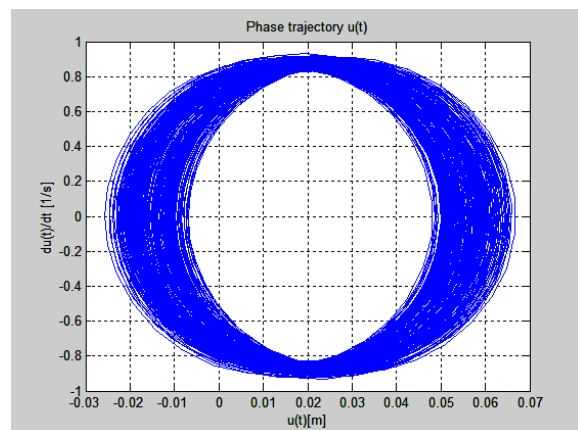


Figure 22: Phase trajectory of point  $M$  :  
 $\dot{u} = \dot{u}(u)$ ,  $\bar{m} = 0.10 \text{ kg/m}$ ,  $c = 900 \text{ N/m}$

From the phase trajectories, shown in Figures 21 and 22, it can be seen that as the coefficient of elasticity of the cord increases, the amplitudes of the longitudinal oscillations decrease, but the velocity increases. The phenomenon "beating" is observed on both phase trajectories, which is more pronounced in Figure 21 in comparison with Figure 22.

## 5. CONCLUSION

A mathematical model of a pendulum is created. It consists of a concentrated mass and an elastic mass cord, which is wrapped around a fixed cylinder.

Nonlinear differential equations are derived, which describe the oscillations of the pendulum and the oscillations of the material point in the longitudinal direction of the cord.

A program was compiled in the area of the MatLab mathematical package, with the help of which all kinematical characteristics were obtained, namely: laws of motion, velocities and accelerations for the two generalized coordinates, linear velocities and accelerations of the concentrated mass, as well as the inner force of the elastic cord.

The phase characteristics for the two generalized coordinates are obtained. They conducted a study with variation of some parameters, such as distributed mass of the thread, coefficients of elasticity and integration time.

This study has a theoretical and methodological nature and contributes to the enrichment of knowledge in the field of nonlinear mechanics, as well as computational mathematics.

## ACKNOWLEDGEMENTS

The author of this conference paper expresses his gratitude to Prof. Daniela Todorova, Rector of Todor Kableskov University of Transport, Sofia, and Vice-Rectors, Prof. Petar Kolev and Prof. Krassimir Krastanov, for their support in the procedure for obtaining the scientific degree "Doctor of Science".

## REFERENCES

- [1] P. Palmieri, "A phenomenology of Galileo's experiments with pendulums," *British Society for the History of Science*, Vol. 42(4), pp. 479-513, doi: 10.1017/S0007087409990033, (2009)
- [2] C.D. Andriessse, "Huygens: The Man Behind the Principle," Cambridge University Press, ISBN 978-0-521-85090-2, p. 134, (2005)
- [3] W. Tobin, "The life and science of Léon Foucault: The man who proved the earth rotates," Cambridge University Press, ISBN 9780521808552, p. 272, (2003)
- [4] P. Amore, A. Aranda, "Improved Linstedt-Poincare method for the solution of nonlinear problems," *Jour. Sound Vib*, Vol. 283(3-5), pp. 1115-1136, (2005)
- [5] F.M.S. Lima, "Simple but accurate periodic solutions for the nonlinear pendulum equation," *Revista Brasileira de Ensino de Fisica*, Vol. 41(1), pp. 1-6, doi: <http://dx.doi.org/10.1590/1806-9126-RBEF-2018-0202>, (2019)
- [6] H. Mazaheri, A. Hosseinzadeh, M.T. Ahmadian, "Nonlinear oscillation analysis of a pendulum wrapping on a cylinder," *Scientia Iranica*, Vol. 19(2), pp. 335-340, doi: 10.1016/j.scient.2012.02.014, (2012)
- [7] V. Marinca, N. Herisanu, "Optimal auxiliary functions method for a pendulum wrapping on two cylinders," *Mathematics*, Vol. 8(1364), doi:10.3390/math8081364, pp. 2-18, (2020)
- [8] K. Dean, "Conical Pendulum: Part 2. A detailed theoretical and computational analysis of the period, tension and centripetal forces," *European J Physics Education*, Vol. 8(1), pp. 11-30, (2017)
- [9] P. Djou, V. Bozduganva, V. Vitliemov, "Dynamics of a pendulum with variable length and dry friction," *Jour. Mechanics of machines*, TU-Varna, Year XVII, Book 3, ISSN 0861-9727, pp. 41-44, (2009)
- [10] V. Bozduganva, V. Vitliemov, "Dynamics of pendulum with variable length and dry friction as a simulator of a swing," *Jour. Mechanics of machines*, TU-Varna, Year XVII, Book 3, ISSN 0861-9727, pp. 45-48, (2009)
- [11] D.N. Nikolov, M.B. Marinov, B.T. Ganev, T.S. Djamijkov, "Nonintrusive Measurement of Elevator Velocity Based on Inertial and Barometric Sensors in Autonomous Node," *Proceedings of the International Spring Seminar on Electronics Technology*, doi: 10.1109/ISSE49702.2020.9121077, (2020)
- [12] M. Marinov, D. Nikolov, B. Ganev, G. Nikolov, "Environmental noise monitoring and mapping," *Proceedings of the International Spring Seminar on Electronics Technology*, doi: 10.1109/ISSE.2017.8000992, (2017)
- [13] B. Ganev, D. Nikolov, M.B. Marinov, "Performance evaluation of MEMS pressure sensors," *Proceedings of 11th National Conference with International Participation, ELECTRONICA 2020*, doi: 10.1109/ELECTRONICA50406.2020.9305140, (2020)
- [14] Iliev IT, Ganev BT, Kanev IK. Study of the audio characteristics of mobile phones in the context of transmission of biomedical signals converted into sound. *11th National Conference with International Participation, ELECTRONICA 2020*; doi: 10.1109/ELECTRONICA50406.2020.9305147, (2020)
- [15] V. Vitliemov, I. Ivanov, "Robust-trajectory optimal synthesis of spread macro-particles," *Jour. Mechanics of machines*, TU-Varna, Year XXII, Book 2, ISSN 0861-9727, pp. 3-7, (2014)
- [16] S. Hensel, M.B. Marinov, C. Kehret, M. Stefanova-Pavlova, "Experimental Set-up for Evaluation of Algorithms for Simultaneous Localization and Mapping," *Communications in Computer and Information Science*, Springer, Cham, Vol. 1251, [https://doi.org/10.1007/978-3-030-56441-4\\_32](https://doi.org/10.1007/978-3-030-56441-4_32), (2020)
- [17] S. Hensel, M.B. Marinov, M. Schmitt, "System Setup for Synchronized Visual-Inertial Localization and Mapping", *XXIX International Scientific Conference Electronics (ET)*, Sozopol, (Bulgaria), pp. 1-4, (2020)
- [18] Sergeev Y.S., Sergeev S.V., D'yakonov A.A., Kononistov A.V., Karpov G.E., Mikryukov A.A., *Automated Monitoring System for Self-Synchronizing Vibrational Drives*. *Russian Eng. Research*, 38(2), pp. 86-90, doi:10.3103/S1068798X18020168, (2018).
- [19] Sergeev S.V., Sergeev Y.S., Kononistov A.V., *Self-Synchronized Controlled Vibration Drive with Automated Oscillation Parameters Monitoring System for High-Tech Equipment*. *Proceeding of the 40<sup>th</sup> Int. Conf. on Industrial Engineering , Lecture Notes in Mechanical Engineering*, Springer Nature Switzerland AG 2019, pp. 367-374, [https://doi.org/10.1007/978-3-319-95630-5\\_40](https://doi.org/10.1007/978-3-319-95630-5_40), (2019)
- [20] Marinov MB, Ganev B, Djermanova N, Tashev TD. Analysis of sensors noise performance using allan deviation. In: *2019 28th International Scientific Conference Electronics, ET 2019*, doi: 10.1109/ET.2019.8878552, (2019)



# Analysis of Centrifugal Compressor Testing Capabilities

Stojko Biočanin<sup>1\*</sup>, Milica Timotijević<sup>2</sup>

<sup>1</sup>Technical College of Professional Studies, Belgrade (Serbia)

<sup>2</sup>"Šinvoz" d.o.o, Zrenjanin (Serbia)

*The work shows examining of the centrifugal compressor for which there are no technical conditions by which the compressor manufacturer defines the form and important characteristics of the measuring installation. In the absence of the necessary data, a table for testing of centrifugal compressors was designed, where the pipeline measures and other details are freely defined in accordance with the available possibilities.*

**Keywords: Welding, Centrifugal compressor, Functional testing**

## 1. INTRODUCTION

The work showed an examining of the centrifuge compressor of a motor vehicle. The compressor lid had damages in the shape of cracks. The damaged lid was regenerated by welding. The mentioned procedure was necessary because there were no compressors nor their parts on the market. The lid is made of aluminum alloy. TIG procedure was used to weld the crack. There was no manufacturer's documentation for the compressor on the shape and characteristics of the measuring installation. Nevertheless, the compressor should have been examined for function after the welding procedure was carried out. For this reason, a table for functional testing of compressors was designed.

## 2. DESCRIPTION OF THE SUBJECT OF THE WORK

The centrifugal compressor (Figure 1) is used to increase air pressure entering the engine cylinders. It consists of a flowing part and a multiplier. The flow part consists of: rotor (7), diffuser (4), disc (5) and pre-compressor pipe (6). The body (19) and lid (3) are made of Aluminum alloy. In the body there are: gears of two-stage reduction, elastic and two frictional joints [3].

From the gears on the engine's collet shaft, the rotation is transferred to the gear block and further across the gears (24), small (34) and large (25) gears on the gear (33) of the rotor shaft. The gear block consists of: gear vein (22), vaudeville (21) and connected gear with it using a screw (18). In the gear block, an elastic coupling is placed. It consists of six packages, with two springs (17) with clamps (15 and 16). The packages are placed in a wreath and guide tray. The elastic coupling is designed to reduce the dynamic load of the compressor drive. The axle (20) of the block and the axle of the inter-cogs (24) are immobile, and their support is in the body and the lid.

The large gear (25) moves freely on a bronze nail, placed on the sleeve of the small gear. It contains a frictional compressor coupling, consisting of six weights (28) with a cap (27), a cleaner (30) and a spring (32). Weights are started, over caps and springs, with a attachment tightly connected to a small gear. Under the presence of centrifugal forces, weights settle on the conical surfaces of the large gear. When increasing and reducing rotations, weights slightly connect or separate the gear vein of a large gear, thus relieving the compressor drive from inertia loads.

The diffuser has 23 arrow shaped spatulas. The pre-compressor pipe disk is placed with a central air entrance into the compressor. In the opening of the pre-compressor pipe (6) is a cop (1) with a torque port (2), from where the air is taken through the pipe to create super pressure in exhaust compound compensators, for better sealing of the compensator's rings.

The rotor (7) of the compressor relies, over coasters, on a cocoon (13), and is tightened to the shaft (29) by the rolling (11) over coasters (12). Not to get oil into the air-passing area, they are placed in groove shells (13) of two rings (14), which perform sealing with a cocoon in the compressor lid.

Lubrication of the rotor shaft tray and the gear tray the is under pressure. The gears are oiled with oil that passes through the trays. The oil, which performed lubrication, flows into the engine carter.

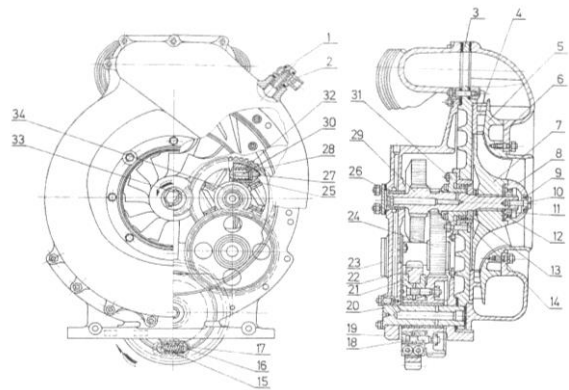


Figure 1: Centrifugal Compressor [1]

## 3. WELDING OF CRACKS

The compressor lid is made by casting under pressure from Al-alloy quality AlSi12.

During the general overhaul of the engine, damage of the compressor lid was found in the form of an irregularly shaped opening, dimensions of 30x30 mm minimum to 70x70 mm maximum (Figure 8). Lid damage is due to an improper handling and maintenance or hidden errors in the lid material was made of. The basic material of the lid is iron-cast under the pressure of AlSand12 quality. The chemical composition of the alloy is in Table 1.

Table 1: Chemical composition of the alloy [2]

| Required |      |                       | Permitted impurities, % |      |      |     |     |      |     | Density,<br>kg/dm <sup>3</sup> |
|----------|------|-----------------------|-------------------------|------|------|-----|-----|------|-----|--------------------------------|
| Mn       | Si   | Al                    | Ni                      | Fe   | Zn   | Cu  | Mg  | Ti   | Pb  |                                |
| 0.1      | 11.2 | complement<br>to 100% | 0.08                    | 0.45 | 0.12 | 0.1 | 0.1 | 0.15 | 0.1 | 2.65                           |

Welding of aluminum and aluminum alloys is generally feasible to all conventional welding procedures. Bearing in mind the fact that it is individual production, welding of the lid with electrolyte procedure with non-melting electrode in the protection of inert gas (Wolfram Inert Gas-TIG procedure) is accepted.

The thickness of the lid wall at the spot of the damage is 4 mm. Al 99.5%, 4 mm thick sheet was selected for the patch, because AlSi12 sheet is not being produced. Choosing some other alloy would create additional problems of welding ability.

The characteristics and application of aluminum depend on its purity. Increasing impurities in Aluminum reduces corrosion resistance, electrical conductivity, and above all strength.

99.8% or above pure Aluminum, is applied for the production of chemical equipment, which functions in very aggressive environments. A very important feature of Aluminum is to build  $Al_2O_3$  oxide on its surface in the form of a 0,01  $\mu\text{m}$  layer. This layer occurs at higher temperatures and in conditions of increased humidity, and reaches thickness of 0,03  $\mu\text{m}$  to 0,1  $\mu\text{m}$ . The layer has high density and prevents further Aluminum oxidation. Cast Aluminum alloys are applied for complex mechanical strains and often contain higher percentage presence of alloy elements.

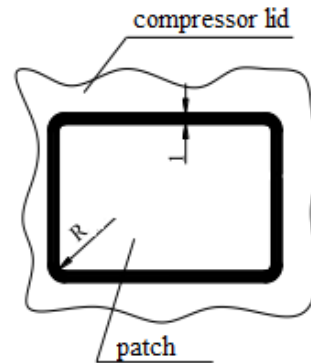
Since the basic materials of different chemical composition (the lid is from AlSi12 and the patch of Al 99.5), as well as on the basis of recommendations for selecting additional materials, the accepted wire is S-AlSi5,  $\phi$ 0,3 mm. [3]

With this quality of the wire, obtained seam had composition between Al 99,5 and AlSi12.

Protective gas was used from auxiliary (expendable) material. The protective gas was aimed at protecting basic and additional material while in melted state, as well as during the period after hardening as protection from the effects of oxidation, so as not to create undesirable oxides. Also, in addition to this basic role, the protective gas was partly to cool Wolfram's electrode. When welding, argon and helium could be used as pure gases or gas mix: argon and helium, argon and hydrogen, argon and oxygen.

Due to the good supply of argon on the market as well as the lower purchase price than helium, argon was accepted as a protective gas of higher purity of 99.96%. On the milling machine the edges of the opening are processed in order to obtain the regular geometric shapes (rectangle, square, circle...). After processing the lid opening, the sheet was made - patch. The junction of the patch and the lid is given in Figure 2.

Figure 2: The patch and lid junction



For the sheet thickness of 4 mm, according to table 6 it is accepted [3]:

- Two-sided  $\Gamma$  joint,
- Space between parts  $s=1$  mm,
- One weld on both sides.

Based on the recommended parameters for welding Aluminum and Aluminum alloys, the following welding parameters were [3]:

- Current power  $I = 180\text{A}$ ,
- Number of cycles  $i = 2$ ,
- Argon flow  $Q = 9 \text{ l/min}$ ,
- Diameter of extra material  $d_2 = 3 \text{ mm}$ .

Preheating of Aluminum is often performed when it is necessary to avoid the appearance of porosity in the metal seam.

Since the welded lid patch junction must ensure impenetrability, the appearance of porosity in the metal seam is not permitted.

Due to the above, the overheating of the lid and the patch in the chamber furnace at a temperature of 150°C was applied.

Based on the data presented and after the preheating was performed, welding was performed in the following order (Figure 3):

- Patch joining in four places,
- Welding the patch by a welding plan, according to figure 3, on the inside of the lid in one aisle,
- Welding the patch by a welding plan, according to figure 3, on the outside of the lid in one aisle.

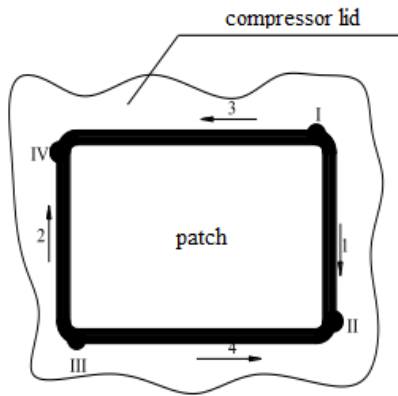


Figure 3: Welding plan

4. COMPRESSOR TESTING

After welding compressor lid regeneration carried out, a functional compressor test was performed. The initial problem was the lack of data on the basic characteristics of the measurement installation:

- Diameter and length of suction and thyme platoon,
- Exact locations and types of regulatory valves,
- Presence of expansion container for calming and slowing down of electricity on the thyme pipeline,
- Types and positions of temperature probes,
- Presence of laminators for air current regulation in front of measuring sites.

In the absence of the necessary data, a test table was designed to test centrifugal compressors (Figure 4). The installation is complemented by an oil preheating device, with a control thermometer.

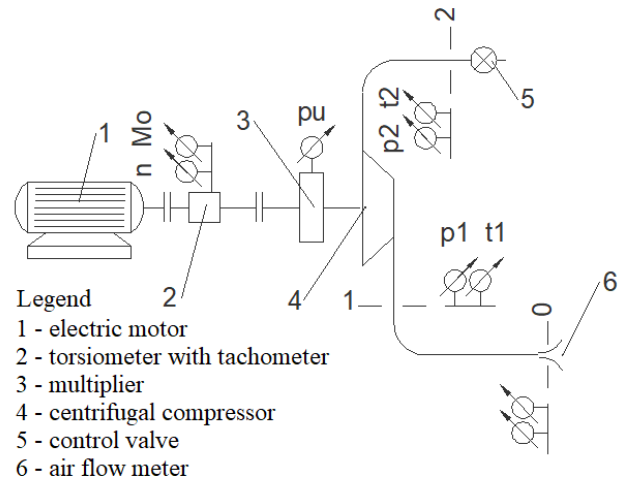


Figure 4: Test table for testing centrifugal compressor

Compressor quality is checked at work points corresponding to engine speed modes  $n = 1300 \text{ min}^{-1}$ ,  $n = 1800 \text{ min}^{-1}$  and  $n = 2000 \text{ min}^{-1}$  at full power. The quality rating process is all about forming compressor characteristics at constant rev numbers, corresponding to the specified rev speeds. Characteristics are determined by four work points. The boundaries on the maximum flow line correspond to a fully open dampener valve [4,5]. The accuracy of the method increases as the number of points through which the curve forms increases.

Based on the relative position of reference points in relation to the recorded characteristics, a rating is given on whether the compressor meets the prescribed requirements.

The values of the control parameters that were taken from the Technical Conditions for compressor testing on handover, are in Table 2.

Table 2: Values of the control parameters[4]

|                           | $\Delta P_{TOT}$ , kPa | $\Delta T_{TOT}$ , K | $P_k$ , kW | $m_{KOR}$ , kg/s |
|---------------------------|------------------------|----------------------|------------|------------------|
| $n=1300 \text{ min}^{-1}$ | 32.35                  | 38                   | 0.7        | 27.96            |
| $n=1800 \text{ min}^{-1}$ | 69.63                  | 67                   | 1.1        | 80.93            |
| $n=2000 \text{ min}^{-1}$ | 88.24                  | 82                   | 1.3        | 117.72           |

Technical conditions for handover compressor testing [4] define the correcting of mass air flow to standard conditions, ( $T_{ref} = 288,152K$  i  $p_{ref} = 101,3kPa$ ). Correction factor is calculated according to the form:

$$k = \sqrt{\frac{T_{tot}}{T_{ref}} \cdot \frac{p_{ref}}{p_{tot}[1]}} \quad (1)$$

The bringing to normal atmospheric conditions is also predicted for differences in pressure values  $\Delta p_{tot}$ , and temperature values  $\Delta T_{tot}$ , as well as for the engaged strength P. Since the technical conditions for the handover compressor tests do not contain a correction procedure, these sizes are not being brought to normal.

The test table in the current configuration does not have an expansion container on the thyme pipeline, whose presence would allow for measurements of pressure and temperature in low-speed air currents. In such conditions, the measured pressure, i.e. temperature, would be approximately equal to total or static sizes ( $P_{mer} \approx P_{tot} \approx p_{stat}$ ,  $t_j$ ,  $t_{mer} \approx t_{tot} \approx t_{stat}$ ). Since the reference sections on the installation occur at speeds of over 100m/s, the calculation process of determining total and static sizes from measured pressure and temperature values has been applied. Since no probes were used to measure the stop temperature, an assumption was made as recommended by literature that standard probes register 50% dynamic temperature.

Table 3 presents the results of the examination. The table contains data on mass flow, air flow rates in reference sections, static and total sizes of the states in

measuring sections 1 and 2. The recommended values for the isentropic and actual current work, isentropic, total and mechanical level of usefulness, as well as the degree of increase in compressor pressure were also given.

Also, the data are listed on engaged torque, propulsion engine power and pressure and temperature

differences at front and back of the compressor. The sizes specified in the last sentence are used, along with data for mass flow, as reference control parameters, through which the quality of the tested compressor is checked.

Table 3: Results of the examination

(First part of the Table 3)

| Serial number        | Compressor NO 12AT5347 |          |          |          |          |          |          |          |          |
|----------------------|------------------------|----------|----------|----------|----------|----------|----------|----------|----------|
|                      | Testing results        |          |          |          |          |          |          |          |          |
|                      | 1                      | 2        | 3        | 4        | 5        | 6        | 7        | 8        | 9        |
| $\rho_{i0} (kg/m^3)$ | 1.21                   | 1.21     | 1.21     | 1.21     | 1.21     | 1.21     | 1.21     | 1.21     | 1.21     |
| $k$                  | 1.02                   | 1.03     | 1.04     | 1.04     | 1.03     | 1.03     | 1.05     | 1.05     | 1.06     |
| $m_k (kg/s)$         | 0.51                   | 0.86     | 1.09     | 0.98     | 0.83     | 0.65     | 1.16     | 1.30     | 1.42     |
| $m_{kor} (kg/s)$     | 0.52                   | 0.89     | 1.14     | 1.02     | 0.86     | 0.66     | 1.22     | 1.37     | 1.50     |
| $p_1 (Pa)$           | -931.63                | -2471.28 | -3795.15 | -3167.55 | -2333.98 | -1421.96 | -4511.06 | -5442.69 | -6815.62 |
| $p_2 (Pa)$           | 1461.23                | 2922.46  | 6641.96  | 20324.39 | 28294.73 | 32279.91 | 8900.22  | 10892.81 | 14612.30 |
| $p_{1tot} (Pa)$      | 98068.37               | 96528.72 | 95204.83 | 95823.45 | 96666.02 | 97578.04 | 94488.94 | 93557.31 | 92184.38 |
| $p_{2tot} (Pa)$      | 100451.2               | 101922.5 | 105642.0 | 119324.4 | 127294.4 | 131279.9 | 107900.2 | 109892.8 | 113612.3 |
| $T_{1s} (K)$         | 284.57                 | 284.10   | 283.33   | 283.77   | 283.93   | 284.69   | 283.52   | 283.30   | 282.88   |
| $c_1 (m/s)$          | 24.17                  | 40.96    | 52.83    | 47.12    | 39.83    | 30.67    | 56.70    | 63.98    | 70.53    |
| $\rho_{v1} (kg/m^3)$ | 1.20                   | 1.18     | 1.17     | 1.18     | 1.19     | 1.19     | 1.16     | 1.15     | 1.14     |
| $p_{1tot} (Pa)$      | 98419.09               | 97521.83 | 96838.55 | 97138.82 | 97606.80 | 98139.83 | 96355.19 | 95912.55 | 95008.29 |
| $T_{1tot} (K)$       | 284.87                 | 284.94   | 284.71   | 284.87   | 284.71   | 285.15   | 285.12   | 285.34   | 285.36   |
| $T_{2s} (K)$         | 292.41                 | 301.36   | 312.84   | 315.40   | 317.34   | 319.36   | 318.25   | 328.10   | 339.85   |
| $c_2 (m/s)$          | 45.08                  | 76.52    | 97.75    | 78.22    | 62.86    | 47.56    | 103.63   | 117.31   | 127.85   |
| $\rho_{v2} (kg/m^3)$ | 1.20                   | 1.18     | 1.18     | 1.32     | 1.40     | 1.43     | 1.18     | 1.17     | 1.16     |
| $p_{2tot} (Pa)$      | 101677.7               | 105372.2 | 111263.2 | 123356.6 | 130055.7 | 132899.6 | 114243.3 | 117922.3 | 123130.7 |
| $Dp_{2tot} (Pa)$     | 3258.6                 | 7850.4   | 14424.7  | 26217.7  | 32448.9  | 34759.8  | 17888.2  | 22009.8  | 28122.4  |
| $DT_{1tot} (K)$      | 8.6                    | 19.3     | 32.9     | 33.6     | 34.6     | 35.3     | 38.5     | 49.6     | 62.6     |
| $T_{2tot} (K)$       | 293.43                 | 304.28   | 317.60   | 318.44   | 319.30   | 320.48   | 323.59   | 334.94   | 347.99   |
| $\pi_{ks}$           | 1.02                   | 1.06     | 1.11     | 1.25     | 1.32     | 1.35     | 1.14     | 1.17     | 1.23     |
| $\pi_{kt}$           | 1.03                   | 1.08     | 1.15     | 1.27     | 1.33     | 1.35     | 1.19     | 1.23     | 1.30     |
| $Yik (J/kg)$         | 2674.30                | 6393.03  | 11546.80 | 20179.63 | 24409.23 | 25900.75 | 14240.18 | 17366.33 | 21946.84 |
| $h (J/kg)$           | 8599.55                | 19428.00 | 33033.80 | 33723.35 | 34746.60 | 35490.19 | 38648.53 | 49832.56 | 62915.79 |
| $\eta_{isk}$         | 0.31                   | 0.33     | 0.35     | 0.60     | 0.70     | 0.73     | 0.37     | 0.35     | 0.35     |
| $P_s (W)$            | 1371.49                | 5478.05  | 12620.28 | 19772.08 | 20378.17 | 16765.88 | 16566.47 | 22592.90 | 31056.66 |
| $P_k (W)$            | 4876.4                 | 19575.3  | 39996.2  | 36325.7  | 31850.7  | 25829.8  | 47987.8  | 70591.6  | 96132.7  |
| $\eta_{uk}$          | 0.28                   | 0.28     | .32      | 0.54     | 0.64     | 0.65     | 0.35     | 0.32     | 0.32     |
| $\eta_m$             | 0.90                   | 0.85     | 0.90     | 0.91     | 0.91     | 0.89     | 0.94     | 0.92     | 0.93     |
| $n_k (min^{-1})$     | 7958.01                | 13396.65 | 17435.64 | 17448.97 | 17475.63 | 17488.96 | 18795.30 | 21394.65 | 23994.00 |

(Second part of the Table 3)

| Serial number        | Compressor NO 12AT5347 |          |          |          |          |          |          |          |  |
|----------------------|------------------------|----------|----------|----------|----------|----------|----------|----------|--|
|                      | Testing results        |          |          |          |          |          |          |          |  |
|                      | 10                     | 11       | 12       | 13       | 14       | 15       | 16       | 17       |  |
| $\rho_{i0} (kg/m^3)$ | 1.21                   | 1.21     | 1.20     | 1.20     | 1.20     | 1.20     | 1.20     | 1.20     |  |
| $k$                  | 1.06                   | 1.05     | 1.04     | 1.07     | 1.07     | 1.07     | 1.06     | 1.05     |  |
| $m_k (kg/s)$         | 1.37                   | 1.16     | 0.96     | 1.46     | 1.47     | 1.44     | 1.32     | 1.15     |  |
| $m_{kor} (kg/s)$     | 1.145                  | 1.22     | 0.99     | 1.56     | 1.57     | 1.53     | 1.39     | 1.21     |  |
| $p_1 (Pa)$           | -6942.00               | -4756.23 | -2991.03 | -7404.02 | -7502.09 | -7207.89 | -6129.16 | -4756.23 |  |
| $p_2 (Pa)$           | 34006.81               | 59511.93 | 65356.85 | 16472.05 | 37859.15 | 56456.63 | 74788.42 | 81696.06 |  |
| $p_{1tot} (Pa)$      | 92508.00               | 94243.77 | 96008.97 | 91596.0  | 91497.91 | 91792.11 | 92870.84 | 94243.77 |  |
| $p_{2tot} (Pa)$      | 133006.8               | 158511.9 | 164356.8 | 115472.1 | 136859.1 | 155456.6 | 173788.4 | 180696.1 |  |
| $T_{1s} (K)$         | 283.16                 | 284.21   | 285.19   | 283.67   | 283.65   | 284.12   | 284.65   | 285.62   |  |
| $c_1 (m/s)$          | 68.26                  | 56.95    | 46.11    | 73.58    | 74.23    | 72.17    | 65.49    | 56.71    |  |
| $\rho_{v1} (kg/m^3)$ | 1.14                   | 1.16     | 1.17     | 1.12     | 1.12     | 1.13     | 1.14     | 1.15     |  |

| Serial number          | 10       | 11       | 12       | 13       | 14       | 15       | 16       | 17       |
|------------------------|----------|----------|----------|----------|----------|----------|----------|----------|
| $p_{1TOT} (Pa)$        | 95159.44 | 96117.51 | 97255.92 | 94641.0  | 94594.07 | 94723.23 | 95308.60 | 96092.28 |
| $T_{1TOT} (K)$         | 285.48   | 285.83   | 286.25   | 286.37   | 286.39   | 286.72   | 286.79   | 287.22   |
| $T_{2s} (K)$           | 343.47   | 347.54   | 351.07   | 348.11   | 385.53   | 361.79   | 363.50   | 366.88   |
| $c_2 (m/s)$            | 107.88   | 77.00    | 61.66    | 133.18   | 116.64   | 100.90   | 83.11    | 70.65    |
| $\rho_{v2} (kg/m^3)$   | 1.35     | 1.59     | 1.63     | 1.16     | 1.33     | 1.50     | 1.67     | 1.72     |
| $p_{2TOT} (Pa)$        | 140741.3 | 163222.4 | 167456.3 | 125720.9 | 145906.2 | 163076.9 | 179540.6 | 184978.6 |
| $\Delta p_{2TOT} (Pa)$ | 45581.9  | 67104.8  | 70201.4  | 31079.9  | 51312.1  | 68353.6  | 84232.0  | 88885.8  |
| $\Delta T_{TOT} (K)$   | 63.7     | 64.7     | 66.7     | 70.6     | 78.9     | 80.1     | 80.2     | 82.1     |
| $T_{2TOT} (K)$         | 349.17   | 350.50   | 352.97   | 356.93   | 365.31   | 366.85   | 366.94   | 369.36   |
| $\pi_{ks}$             | 1.44     | 1.68     | 1.71     | 1.26     | 1.50     | 1.69     | 1.87     | 1.92     |
| $\pi_{kt}$             | 1.48     | 1.70     | 1.72     | 1.33     | 1.54     | 1.72     | 1.88     | 1.93     |
| $Y_{ik} (J/kg)$        | 33792.06 | 46768.76 | 48206.69 | 24199.33 | 37740.67 | 48144.56 | 56928.79 | 59207.40 |
| $h (J/kg)$             | 63984.96 | 64963.70 | 67021.86 | 70889.09 | 79275.27 | 80503.59 | 80517.67 | 82517.09 |
| $\eta_{isk}$           | 0.53     | 0.72     | 0.72     | 0.34     | 0.48     | 0.60     | 0.71     | 0.72     |
| $P_s (W)$              | 46393.82 | 54380.85 | 46073.47 | 35396.30 | 55637.52 | 69110.44 | 74892.90 | 68210.21 |
| $P_k (W)$              | 93305.3  | 80676.1  | 69144.9  | 109547.3 | 123878.2 | 120098.9 | 111700.4 | 99732.5  |
| $\eta_{uk}$            | 0.50     | 0.67     | 0.67     | 0.32     | 0.45     | 0.58     | 0.67     | 0.68     |
| $\eta_m$               | 0.94     | 0.94     | 0.93     | 0.95     | 0.94     | 0.96     | 0.95     | 0.95     |
| $n_k (min^{-1})$       | 23994.00 | 23994.00 | 24113.97 | 25353.66 | 26726.65 | 26726.65 | 26726.65 | 26726.65 |

5. TESTING RESULTS

Table 4 has a comparative overview of referenced and measured sizes. Measured sizes are displayed at two

points. These points on the top and down side limit the area. which contain reference sizes.

Table 4: Comparative overview of referenced and measured sizes

|                           |       | $\Delta P_{2TOT}$ . kPa |       |       | $\Delta T_{TOT}$ . K |        | Pk. kW |      | $m_{KOR}$ . kg/s |  |
|---------------------------|-------|-------------------------|-------|-------|----------------------|--------|--------|------|------------------|--|
| 1300<br>min <sup>-1</sup> | Ref.  | 32.35                   |       |       | 38.00                |        | 27.96  |      | 0.70             |  |
|                           | Meas. | 32.45                   | 34.76 | 35.17 | 36.21                | 32.85  | 25.83  | 0.84 | 0.64             |  |
| 1800<br>min <sup>-1</sup> | Ref.  | 69.53                   |       |       | 67.00                |        | 80.93  |      | 1.10             |  |
|                           | Meas. | 67.10                   | 70.20 | 66.35 | 68.20                | 80.68  | 69.14  | 1.20 | 0.97             |  |
| 2000<br>min <sup>-1</sup> | Ref.  | 88.24                   |       |       | 82.00                |        | 117.2  |      | 1.3              |  |
|                           | Meas. | 84.23                   | 88.89 | 81.62 | 83.10                | 111.70 | 99.73  | 1.46 | 1.18             |  |

In addition to the above mentioned test results, the following was noted:

- There's no oil leak registered on the body and lid of the multiplier,
- There's no oil marks on the compressor wheel shovels,
- No excessive heating of the base in the zones of deposited shells of multipliers,
- No increased noise levels have been registered in the compressor.

6. CONCLUSION

The results of the test unequivocally indicate that an adequate process of welding the compressor cover was chosen. Based on the results of the test, it can be noted that the compressor meets the prescribed requests in terms of achieving the reference characteristics. This means that the

test compressor can, as correct and reliable, be used on a motor vehicle.

REFERENCES

[1] Compressor description and operation TU -I. Technical repair institute – Čačak (1982)

[2] T. Lipinski "Mechanical properties of als12 alloy with aluminium bronze", University of Warmia and Mazury in Olsztyn. Engineering for rural development, Poland (2017)

[3] B. Delić. „Tungsten electrode welding - TIG“. DUZS – Belgrade (1987)

[4] "Technical requirements for handover tests of compressors". SS-55-5MP (1986)

[5] Compressor maintenance TU – II.- Technical repair institute – Čačak (1982)



# Application of Denavit-Hartenberg method to robot model KUKA IR 161/15.0

Đorđe Jovanović<sup>1\*</sup>, Branislav Milenković<sup>1</sup>

<sup>1</sup>Mathematical Institute of Serbian Academy of Sciences and Arts, Belgrade (Serbia)

*In modern times, robots have achieved great expansion and found wide application in nearly every field of research, such as: science, education, medicine, industry, information technology. This paper deals with studying the kinematics of a type KUKA IR 161/15.0 robot. For describing the kinematics of the fore mentioned robot, the analytical Denavit-Hartenberg approach was used.*

**Keywords:** DH parameters, Robot, Kinematic, KUKA IR 161/15.0

## 1. INTRODUCTION

A robot can be modelled as a chain of solid bodies connected with joints. The front of this chain is the stationary base of the robot, while the back contains a tool which the robot holds. In order for the robot to move in three-dimensional space, while performing certain tasks, controlling the position and orientation of the tool is crucial. For this reason, determining the relation between the joint parameters of the robot and the position of orientation of the tool.

On Figure 1, various types of robots are shown.



Figure 1: Various types of robots

As for the kinematics of robots, there are two major approaches found in literature:

- Denavit-Hartenberg, a representative of analytic approaches
- Rodrigues' formula, a representative of numerical approaches

These two approaches are identical in terms of complexity, in the case when the main axes of inertia coincide with the joint axes and the common perpendicular axis, which is commonplace in the area of industrial robots.

The Denavit-Hartenberg approach is more convenient when the kinematic equations of the robot are already formed, and the Rodrigues' formula approach is more appropriate in forming the dynamical equations of the robot.

In the paper by Tonetto et al. [1], a novel approach for kinematics programming of a system composed of two robots is demonstrated. A well-structured procedure is presented, using screw theory, Davies' method and Assur virtual chains. This approach was taken due to the fact that the Denavit-Hartenberg method does not include multi-robot computation. The screw approach allows the use of optimization techniques and to perform tasks in a full cooperative way, taking profit from the redundancy of the cooperative system.

In the paper by Abdel-Malek and Othman [2], the use of the DH formulation for multiple sweeps, through examples, is demonstrated. It was shown that the Denavit-Hartenberg representation method adopted from kinematics is well suited for the representation of solid models that are created as a result of multiple of sweep (combination of revolve and extrude) operations. The DH formulation also can relate multiple sweeps using a small number of parameters, simplifying the computations.

In the paper by Aamir et al. [3], the Denavit-Hartenberg parameters for a serial robot were identified. The performance of the proposed methodology was tested by changing the range of motion given to the joints and evaluating the DH parameters again. This proposed method showed that a small range of the end-effector did not change the identified results for the DH parameters, proving the robustness of the algorithm.

In the remainder of the paper, the Denavit-Hartenberg analytical approach will be described in detail.

## 2. DENAVIT-HARTENBERG PARAMETERS

The DH parameters first appeared in 1955 (Denavit and Hartenberg, 1955) to represent a directed line which is nothing but the axis of a lower pair joint.

The D-H parameters are:

- $a_i$  - the distance between the fixed coordinated systems to the robot links ( $O_i$  and  $O_{i0}$ );
- $d_i$  - the direction of the coordinate axis from  $O_{i0}$  through  $z_{i-1}$ ;
- $\alpha_i$  - the angle between the  $z_{i-1}$  and  $z_i$  axes related to the  $x_i$  axis;
- $v_i$  - the angle between the  $x_{i-1}$  and  $x_i$  axes related to the  $z_{i-1}$  axis;

The distances  $a_i$  and the angles  $\alpha_i$  are always constant, depending only of the geometry of the consecutive joints of link  $i$ . In particular, if the  $i$  joint is revolute,  $v_i$  is variable, while if  $i$  joint is prismatic,  $d_i$  is variable.

Also, an example of how to calculate D-H parameters is shown in Figure 2.

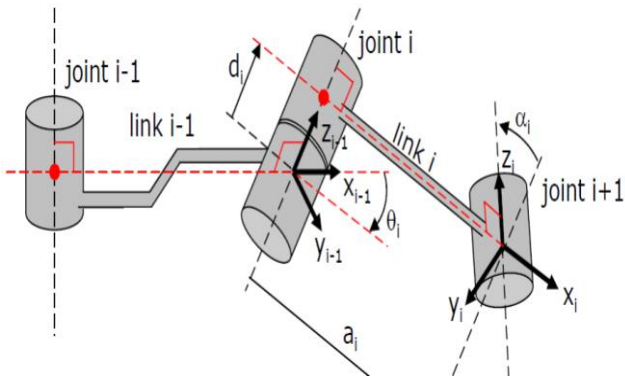


Figure 2: Example of D-H parameters

The transformation matrix for the coordinates system between the robot's joints  $i$  and  $i - 1$  is given by:

$$A_i^{i-1}(q_i) = \begin{bmatrix} c_{q_i} & -s_{q_i}c_{\alpha_i} & c_{q_i}s_{\alpha_i} & a_i c_{q_i} \\ s_{q_i} & c_{q_i}c_{\alpha_i} & -c_{q_i}s_{\alpha_i} & a_i s_{q_i} \\ 0 & s_{\alpha_i} & c_{\alpha_i} & d_i \\ 0 & 0 & 0 & 1 \end{bmatrix} \quad (1)$$

The transformation matrix for the coordinates system from the base to the end-effector is given by a net of the transformation matrices:

$$T_n^0(q) = A_1^0 A_2^1 \dots A_n^{n-1} = \begin{bmatrix} R(q) & pq \\ 0 & 1 \end{bmatrix} \quad (2)$$

in which  $R(q)$  is a submatrix with elements in the first to the third rows, and from the first to the third column of the  $T_n^0$  matrix and represent a rotation between coordinates system,  $p(q)$  is the submatrix containing elements from the first to the third rows of the fourth column of  $T_n^0$  and represents the translation between coordinates system, and  $q$  is the vector containing the joints variables.

The equation (3) allows to compute the Jacobian systematically, in the direct kinematics programming [4]. The direct kinematics relations are given by:

$$\begin{bmatrix} J_{P_i} \\ J_{O_i} \end{bmatrix} = \begin{cases} \begin{bmatrix} z_{i-1} \\ 0 \end{bmatrix} \\ \begin{bmatrix} z_{i-1} \times (p - p_{i-1}) \\ z_{i-1} \end{bmatrix} \end{cases} \quad (3)$$

in which  $z_{i-1}$  is the third column elements of the rotation matrix  $R_{i-1}^0$ ,  $p$  is given by the first three elements of the fourth column of the  $T_n^0$  and  $p_{i-1}$  is given by the first three elements of the fourth column of the  $T_{n-1}^0$  matrix.

## 3. SOLVING THE DIRECT KINEMATICS PROBLEM FOR THE ROBOT MODEL KUKA IR 161/15.0

Base on the DH parameters for the robot model KUKA IR 161/15.0, given in Table 1, its kinematics model schematics according to Denavit-Hartenberg model was shown (Figure 3).

Table 1: DH parameters for the robot model IR 161/15.0

| JOINT | $q_i$ | $\alpha_i$ (mm) | $a_i$ (mm) | $\theta_i$ | $d_i$ (mm) | $\sin \alpha_i$ | $\cos \alpha_i$ |
|-------|-------|-----------------|------------|------------|------------|-----------------|-----------------|
| 1     | $q_1$ | 90,000          | 0,000      | 0,000      | 775,000    | 1               | 0               |
| 2     | $q_2$ | 0,000           | 799,953    | 50,000     | 0,000      | 0               | 1               |
| 3     | $q_3$ | 90,000          | -0,034     | 220,000    | 0,000      | 1               | 0               |
| 4     | $q_4$ | 90,000          | 0,000      | 180,000    | 799,970    | 1               | 0               |
| 5     | $q_5$ | 90,000          | 0,000      | 180,000    | 0,000      | 1               | 0               |
| 6     | $q_6$ | 0,000           | 0,000      | 0,000      | 140,000    | 0               | 1               |

Based on the parameters in Table 1 for the coordinate systems of robot's kinematics model, the matrices of homogenous transformations according to DH method can be calculated.

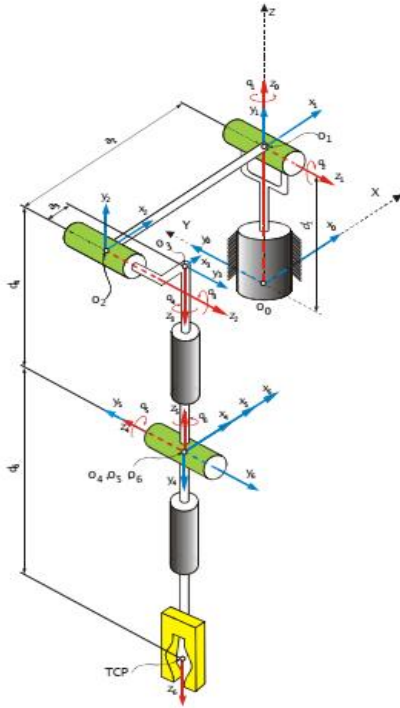


Figure 3: Kinematic model of the robot KUKA IR 161/15.0

The matrices of homogenous transformations for parameters given in Table 1 for coordinate systems of robot's kinematics model are calculated based on the matrix, taking the following shape:

$${}^0_1[D] = \begin{bmatrix} \cos q_1 & 0 & \sin q_1 & 0 \\ \sin q_1 & 0 & -\cos q_1 & 0 \\ 0 & 1 & 0 & d_1 \\ 0 & 0 & 0 & 1 \end{bmatrix}, \quad \begin{aligned} \sin \alpha_1 &= 1 \\ \cos \alpha_1 &= 0 \\ a_1 &= 0 \\ d_1 &= 775 \text{ mm} \end{aligned}$$

$${}^1_2[D] = \begin{bmatrix} \cos q_2 & -\sin q_2 & 0 & a_2 \cos q_2 \\ \sin q_2 & \cos q_2 & 0 & a_2 \sin q_2 \\ 0 & 0 & 1 & 0 \\ 0 & 0 & 0 & 1 \end{bmatrix}, \quad \begin{aligned} \sin \alpha_2 &= 0 \\ \cos \alpha_2 &= 1 \\ a_2 &= 799,953 \text{ mm} \\ d_2 &= 0 \end{aligned}$$

$${}^2_3[D] = \begin{bmatrix} \cos q_3 & 0 & \sin q_3 & a_3 \cos q_3 \\ \sin q_3 & 0 & -\cos q_3 & a_3 \sin q_3 \\ 0 & 1 & 0 & 0 \\ 0 & 0 & 0 & 1 \end{bmatrix}, \quad \begin{aligned} \sin \alpha_3 &= 1 \\ \cos \alpha_3 &= 0 \\ a_3 &= -0,034 \text{ mm} \\ d_3 &= 0 \end{aligned}$$

$${}^3_4[D] = \begin{bmatrix} \cos q_4 & 0 & \sin q_4 & 0 \\ \sin q_4 & 0 & -\cos q_4 & 0 \\ 0 & 1 & 0 & d_4 \\ 0 & 0 & 0 & 1 \end{bmatrix}, \quad \begin{aligned} \sin \alpha_4 &= 1 \\ \cos \alpha_4 &= 0 \\ a_4 &= 0 \\ d_4 &= 799,970 \text{ mm} \end{aligned}$$

$${}^4_5[D] = \begin{bmatrix} \cos q_5 & 0 & \sin q_5 & 0 \\ \sin q_5 & 0 & -\cos q_5 & 0 \\ 0 & 1 & 0 & 0 \\ 0 & 0 & 0 & 1 \end{bmatrix}, \quad \begin{aligned} \sin \alpha_5 &= 1 \\ \cos \alpha_5 &= 0 \\ a_5 &= 0 \\ d_5 &= 0 \end{aligned}$$

$${}^5_6[D] = \begin{bmatrix} \cos q_6 & -\sin q_6 & 0 & 0 \\ \sin q_6 & \cos q_6 & 0 & 0 \\ 0 & 0 & 1 & d_6 \\ 0 & 0 & 0 & 1 \end{bmatrix}, \quad \begin{aligned} \sin \alpha_6 &= 0 \\ \cos \alpha_6 &= 1 \\ a_6 &= 0 \\ d_6 &= 140 \text{ mm} \end{aligned}$$

By multiplying all six matrices, the following matrix is obtained:

$${}^0_6[W] = {}^0_1[D] \cdot {}^1_2[D] \cdot {}^2_3[D] \cdot {}^3_4[D] \cdot {}^4_5[D] \cdot {}^5_6[D], \quad (4)$$

Representing the total robot movement.

After matrix multiplication and applying the following substitutions:

$$\begin{aligned} s_i &= \sin q_i & i & & c_i &= \cos q_i \\ \cos(q_i + q_j) &= c_{ij} & \cos(q_i - q_j) &= c_{i-j} \\ \sin(q_i + q_j) &= s_{ij} & \sin(q_i - q_j) &= s_{i-j} \end{aligned}$$

And based on following trigonometrical identities:

$$\sin(\alpha \pm \beta) = \sin \alpha \cos \beta \pm \cos \alpha \sin \beta,$$

$$\cos(\alpha \pm \beta) = \cos \alpha \cos \beta \mp \sin \alpha \sin \beta,$$

$$c_1 c_2 c_3 - c_1 s_2 s_3 = c_1 (c_2 c_3 - s_2 s_3) = c_1 c_{23};$$

$$c_{23} = \cos(q_2 + q_3),$$

$$s_1 c_2 c_3 - s_1 s_2 s_3 = s_1 (c_2 c_3 - s_2 s_3) = s_1 c_{23},$$

$$c_1 c_2 s_3 + c_1 s_2 c_3 = c_1 (c_2 s_3 + s_2 c_3) = c_1 s_{23},$$

$$s_{23} = \sin(q_2 + q_3),$$

$$s_1 c_2 s_3 + s_1 s_2 c_3 = s_1 (c_2 s_3 + s_2 c_3) = s_1 s_{23},$$

$$s_2 c_3 + c_2 s_3 = s_{23},$$

$$s_2 c_3 - c_2 s_3 = s_{2-3}; \quad s_{2-3} = \sin(q_2 - q_3),$$

$$s_2 s_3 - c_2 c_3 = -(c_2 c_3 - s_2 s_3) = -c_{23},$$

$$a_3 c_1 c_2 c_3 - a_3 c_1 s_2 s_3 + a_2 c_1 c_2 = c_1 (a_3 c_{23} + a_2 c_2),$$

$$a_3 s_1 c_2 c_3 - a_3 s_1 s_2 s_3 + a_2 s_1 c_2 = s_1 (a_3 c_{23} + a_2 c_2),$$

$$a_3 s_2 c_3 - a_3 s_3 c_2 + a_2 s_2 + d_1 = a_3 s_{2-3} + a_2 s_2 + d_1$$

The matrix (4) takes the following shape:



# Application of Grasshopper Algorithm for Solving Optimization Problems in Engineering

Branislav Milenković<sup>1\*</sup>, Radovan Bulatović<sup>2</sup>, Ivana Atanasovska<sup>1</sup>

<sup>1</sup>Mathematical Institute of Serbian Academy of Sciences and Arts, Belgrade (Serbia)

<sup>2</sup>Faculty of Mechanical and Civil Engineering Kraljevo, University of Kragujevac, Kraljevo (Serbia)

*Today, there is increasing use of optimization methods in order to achieve acceptable performance. In this paper we will demonstrate how Grasshopper Optimization Algorithm (GOA for short) can be used for solving certain optimization problems in engineering. In the first part, biological fundamentals, as well as method explanation are given. Afterwards, the GOA algorithm and its' applicability is explained in detail. The pseudo code for this algorithm was written using Matlab R2018a software suite. This algorithm can be used for optimization of engineering problems, such as: helical spring optimization, car side impact optimization, cone clutch optimization and speed reducer optimization. In the end, all the results for the fore mentioned problems, as well as a result comparison with other methods are shown.*

**Keywords: Optimization, Grasshopper algorithm, Helical spring, Car side impact, Cone clutch, Speed reducer**

## 1. INTRODUCTION

In the past two decades, a set of methods that proved to be highly efficient in solving difficult optimization problems appeared. These methods are named metaheuristic algorithms and are oft-times inspired by natural phenomena, since they mimic behaviors and patterns found in nature. For this reason, this class of algorithms is also called naturally-inspired or biological metaheuristic algorithms.

The surge in popularity of these algorithms gathers great attention from engineers and industry professionals. One of the reasons of this popularity is their adaptability and efficiency. Also, albeit simple in nature, these algorithms solve complex optimization problems with ease. Metaheuristic algorithms comprise an important part of contemporary optimization algorithms, artificial intelligence and computer science.

Many metaheuristic algorithms have the trait that they attain global optimum convergence in a fairly small number of iterations. Algorithms that belong to this class are: Differential Evolution algorithm, Genetic algorithm, Bat algorithm, Grey Wolf Optimization algorithm, Firefly algorithm, Particle Swarm Optimization algorithm, and many others.

Many of authors for the application in engineering design optimization have used different metaheuristic algorithms which are nature-inspired.

Differential Evolution algorithm (DE) was applied by Gašić, Abderazek for solving structural optimization problems[1-2]. In the paper by Gašić et al. [1], the trapezoidal cross section of the truck crane boom was optimized by using Lagrange's multipliers and the

Evolution Algorithm (DE) methods. The results of these two methods were compared to the numerical example for an existing solution. The results have shown that Evolution algorithm gives better solutions for the existing problem. In the paper by Hammoudi and Djeddou [2], a modified version of DE, called Composite Differential Evolution (CoDE) was presented and used to optimize the dimensions of a helical spring. The results have proven to be better than those obtained by the Firefly Algorithm, Particle Swarm Optimization and Genetic Algorithm.

Grasshopper Optimization Algorithm (GOA) has been applied by: Saremi [3], Jovanović and Milenković [4] for solving constrained engineering optimization problems. In [5], authors used a improved grasshopper algorithm to solve a pressure vessel design problem.

In paper by Zhang et al. [6], a multi-objective problem was solved by the modified PSO algorithm, called Niche PSO. The problem involved mapping virtual networks to substrate networks, in terms of revenue and energy cost. The Niche PSO has shown better results for both objective functions, while having a slightly larger execution time. Manickavelu and Vaidyanathan [7] used the PSO algorithm to make predictions about route route rediscovery during route failures in mobile networks. The network consisted of nodes, whose status was decided upon by fuzzified parameters. This method was tested on a randomized network, while the packet size and node speed were varied. The PSO has shown better results in all the test cases.

In the paper by Long et al. [8], an improved version of GWO with modified augmented Lagrangian was used. The modified augmented Lagrangian is used to remove constraints by integrating them into the objective function. GWO is modified in such a manner so that the global

\*Corresponding author: Branislav Milenković, Kneza Mihaila 36, Belgrade, bmilenkovic@mi.sanu.ac.rs

optimum exploration factor is decreasing sub linearly. In this paper, a set of 24 optimization problems was selected as a testbench for GWO. Also, a comparison between the standard and improved GWO was drawn, with the conclusion being that the improved GWO yields better solutions for most problems. For the first 13 problems, a comparison between other p-based optimization algorithms and GWO was drawn. In most cases, an equal or better result was yielded by GWO.

In this paper, GOA is used for solving several engineering design problems.

The first problem [9] consists of minimization of spring weight subject to constraints on minimum deflection, shear stress, surge frequency, limits on the outside diameter and design variables. The design variables are: coil diameter  $D$ , wire diameter  $d$  and number of active coils  $N$ .

The second problem is automobile side impact optimization problem, with the aim of minimizing total vehicle weight, using eleven design variables. This problem was first subjected in a paper by Gu [10].

The third engineering problem that will be considered in this paper is optimization of a cone clutch. The goal of this optimization is to minimize clutch volume. This example was defined in [11].

The last problem to be solved is speed reducer optimization, having the goal of minimizing reducer weight in accordance with bending stress constraints of gear teeth, surface stresses, transverse deflections of shafts and stresses in shafts. This problem was first analyzed and solved by Coello using GA[12].

## 2. GRASSHOPPER OPTIMIZATION ALGORITHM (GOA)

Grasshoppers (Figure 1) can be the most noticeable and damaging insects to yards and fields. They also are among those most difficult to control, since they are highly mobile. For many reasons, grasshopper populations fluctuate greatly from year to year, and may cause serious damage during periodic outbreaks.



Figure 1: Real grasshopper

Grasshopper Optimization Algorithm (GOA) is a p-type optimization algorithm inspired by movement of grasshopper swarms [21]. The grasshopper life cycle has three phases: larva, nymph and adult, with the grasshopper

movement becoming quicker with each phase. The life cycle of grasshopper is shown in Figure 2.

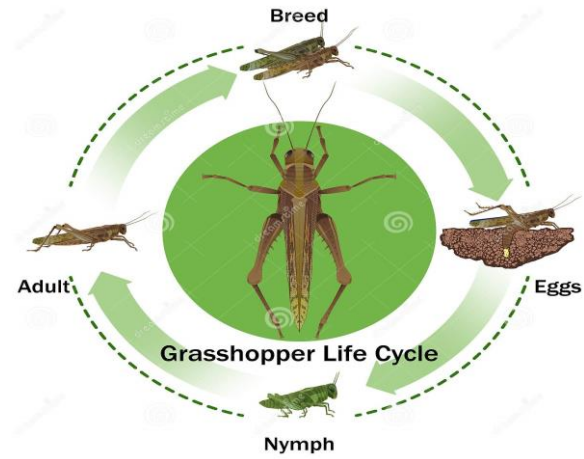


Figure 2: Life cycle of grasshopper

The mathematical model used to simulate grasshopper movement is given by the following equations:

$$X_i = S_i + G_i + A_i \quad (1)$$

$$S_i = \sum_{\substack{j=1 \\ j \neq i}}^N s(d_{ij}) \cdot \hat{d}_{ij} \quad (2)$$

$$s(r) = f \cdot e^{-\frac{r}{l}} - e^{-r} \quad (3)$$

$$G_i = -g \cdot \hat{e}_g \quad (4)$$

$$A_i = u \cdot \hat{e}_w \quad (5)$$

Where  $X_i$  is the grasshopper position,  $S_i$  are the social interaction forces,  $G_i$  the gravitational force, and  $A_i$  wind advection.  $s(r)$  represents the social force between two grasshoppers. The equation for grasshopper movement can be modified as such. Since both the gravitational force and the wind advection have essentially the same mathematical form, they can be represented by one term,  $\overline{T}_d$ . As the problem space has  $d$  dimensions, and each one of them has their upper and lower bounds,  $ub_d$  and  $lb_d$ , by substituting into the movement equation, we get the following form:

$$X_i^d = c \cdot \left( \sum_{\substack{j=1 \\ j \neq i}}^N c \cdot \frac{u \cdot b_d - l \cdot b_d}{2} \cdot s(|x_j^d - x_i^d|) \cdot \frac{x_j - x_i}{d_{ij}} \right) + \overline{T}_d \quad (6)$$

The algorithm consists of three phases:

1. Constant initialization
2. Initial population creation and calculating their fitness values
3. Main loop, having  $L$  iterations

- a) Recalculating the parameter values for all grasshoppers, using the movement equation
- b) Search for the best solution

The complete pseudocode for the algorithm is given below.

```

Swarm initialization Xi (i = 1, 2, ..., n)
Initialize cmax, cmin, and maximum number of iterations
Calculate the fitness value for each grasshopper
T = current best search agent
while (current iteration < maximum number of iterations)
    Update c
    for each search agent
        Normalize the distances between grasshoppers as
to fit the interval
        Update the current search agent position
        Reposition the search agent if it goes out of
bounds
    end for
    Update T if there is a better solution
    Increment the iteration counter
end while
return T
    
```

### 3. EXPERIMENTAL ENGINEERING EXAMPLES FOR OPTIMIZATION

This chapter will present certain examples of engineering problems, such as: optimization of helical spring, car side impact, cone clutch and speed reducer. The basis of the problem, the objective function, variable parameters that should be found as well as the constraints that should be respected will be shown. Then the results obtained by the GOA method (Chapter 2) will be presented and they will be compared to the optimum results for these four examples obtained and published so far. Analysis and obtaining of results by GOA were performed in the code written in Matlab R2018a.

Results of the Grasshopper optimization algorithm (GOA) will be compared to results obtained by the modified ant colony algorithm (MACA), genetic algorithm (GA), cuckoo search (CS), improved cuckoo search (ICS), water cycle algorithm (WCA), whale optimization algorithm (WOA), grey wolf optimization (GWO), moth flame optimization (MFO), firefly algorithm (FA) depending of solutions found in literature.

In Figure 3, a schematic view of helical spring, along with all the project variables, is shown.

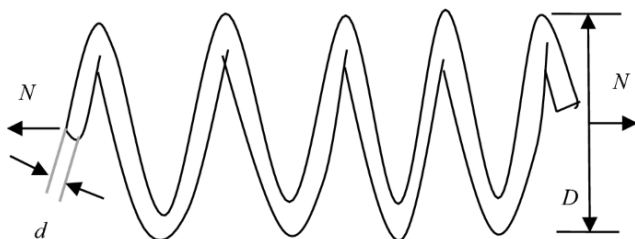


Figure 3: Schematic view of helical spring with variable parameters

This problem consists of three continual variables, two linear constraints, and five nonlinear constraints, given in inequality form. The goal of this optimization is minimizing the weight of the spring.

There are three variables that should be optimized:

- the wire diameter (d)
- the coil diameter (D)
- the number of active coils (N)

Goal function to be minimized is defined as:

$$f(x) = (x_3 + 2)x_2x_1^2$$

subject to the following constraints:

$$g_1(x) = 1 - \frac{x_2^3x_3}{71785x_1^4} \leq 0;$$

$$g_2(x) = \frac{4x_2^2 - x_1x_2}{12566(x_2x_1^3 - x_1^4)} + \frac{1}{5108x_1^2} - 1 \leq 0;$$

$$g_3(x) = 1 - \frac{140,45x_1}{x_2^2x_3} \leq 0;$$

$$g_4(x) = \frac{x_1 + x_2}{1,5} \leq 0;$$

$$0,05 \leq x_1 \leq 2;$$

$$0,25 \leq x_2 \leq 1,3;$$

$$2 \leq x_3 \leq 15;$$

The car (Figure 4) is exposed to a side impact on the foundation of the European Enhanced Vehicle-Safety Committee (EEVC) procedures. The aim is to minimise the total weight of the car using eleven mixed variables.

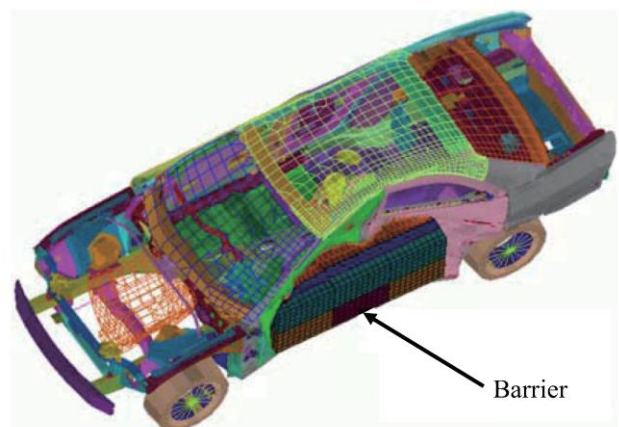


Figure 4: Finite element model utilized in the car side impact problem

There are eleven variables that should be optimized:

- the thickness of the B-Pillar inner ( $x_1$ )

- the thickness of the B-Pillar reinforcement ( $x_2$ )
- the thickness of the floor side inner ( $x_3$ )
- the thickness of the cross members ( $x_4$ )
- the thickness of the door beam ( $x_5$ )
- the thickness of the door belt line reinforcement ( $x_6$ )
- the thickness of the roof rail ( $x_7$ )
- the thickness of the materials of B-pillar inner ( $x_8$ )
- the thickness of the materials of floor side inner ( $x_9$ )
- barrier height ( $x_{10}$ ) and
- hitting position ( $x_{11}$ )

The problem is reduced to minimization of the function:

$$f(x) = 1.98 + 4.90x_1 + 6.67x_2 + 6.98x_3 + 4.01x_4 + 1.78x_5 + 2.73x_7$$

subject to:

$$g_1(x) = F_a \leq 1(kN)$$

$$g_2(x) := VC_u \leq 0.32(m/s)$$

$$g_3(x) := VC_m \leq 0.32(m/s)$$

$$g_4(x) := VC_1 \leq 0.32(m/s)$$

$$g_5(x) := \Delta_{ur} \leq 32(mm)$$

$$g_6(x) := \Delta_{mr} \leq 32(mm)$$

$$g_7(x) := \Delta_{lr} \leq 32(mm)$$

$$g_8(x) := F_p \leq 4(kN)$$

$$g_9(x) := V_{MBP} \leq 9.9(mm/ms)$$

$$g_{10}(x) := V_{FD} \leq 15.7(mm/ms)$$

$$0.5 \leq x_1, x_2, x_3, x_4, x_5, x_6, x_7 \leq 1.5$$

$$-30 \leq x_{10}, x_{11} \leq 30$$

$$x_8, x_9 \in \{0.192, 0.345\}$$

Variables  $F_a, VC_u, VC_m, VC_1, \Delta_{ur}, \Delta_{mr}, \Delta_{lr}, F_p, V_{MBP}, V_{FD}$  are mathematical described in the paper [13].

The cone clutch problem (Figure 5) must be designed for minimum volume coupling to two constraints.

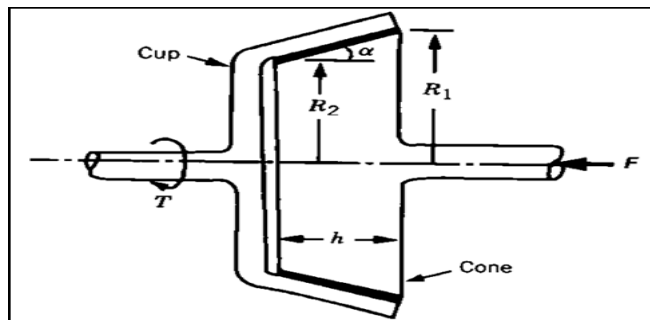


Figure 5: Schematic view of cone clutch with variable parameters

Problem variables are:

- inner radius of the clutch  $R_1 \equiv x_1$  and
- outer radius of the clutch  $R_2 \equiv x_2$ .

Goal function to be minimized is defined as:

$$f(X) = (x_1^3 - x_2^3)$$

Whilst the conditions to be met are:

$$g_1(X) = \frac{x_1}{x_2} \geq 2$$

$$g_2(X) = \frac{(x_1^2 + x_1x_2 + x_2^2)}{(x_1 + x_2)} \geq 5$$

$$X = (x_1, x_2)$$

$$1 \leq x_1, x_2 \leq 10$$

The goal of speed reducer optimization is minimizing the reducer weight whilst fulfilling all the defined constraints.

In Figure 6 a schematic view of speed reducer is shown.

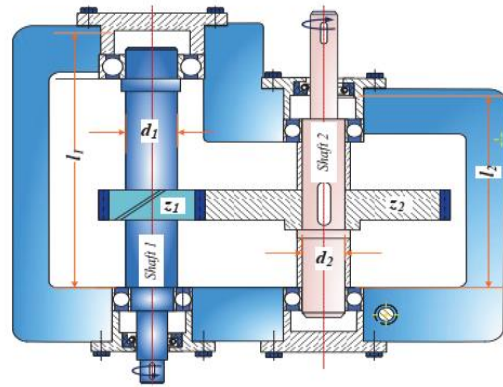


Figure 6: Schematic view of speed reducer with variable parameters

There are seven variables:

- the width between the shafts ( $b$ )
- the module of the teeth ( $m$ )
- the number of teeth in the pinion ( $z$ )
- the length of the first shaft between the bearings ( $l_1$ )
- the length of the second shaft between the bearings ( $l_2$ )
- the diameter of the first shaft ( $d_1$ )

- the diameter of the second shaf ( $d_2$ )

The problem can be expressed as minimization of the function:

$$f(x) = 0,7854x_1x_2^2(3,3333x_3^2 + 14,933x_3 - 43,0934) - 1,508x_1(x_6^2 + x_7^2) + 7,4777(x_6^3 + x_7^3) + 0,7854(x_4x_6^2 + x_5x_7^2)$$

subject to the following constraints:

$$g_1(x) = \frac{27}{x_1x_2^2x_3} - 1 \leq 0$$

$$g_2(x) = \frac{397.5}{x_1x_2^2x_3^2} - 1 \leq 0$$

$$g_3(x) = \frac{1.93x_5^3}{x_2x_3x_7^4} - 1 \leq 0$$

$$g_4(x) = \frac{1.93x_5^3}{x_2x_3x_7^4} - 1 \leq 0$$

$$g_5(x) = \frac{\left(\left(\frac{475x_4}{x_2x_3}\right)^2 + 16.9 \times 10^6\right)^{1/2}}{110x_6^3} - 1 \leq 0$$

$$g_6(x) = \frac{\left(\left(\frac{475x_4}{x_2x_3}\right)^2 + 157.5 \times 10^6\right)^{1/2}}{85x_7^3} - 1 \leq 0$$

$$g_7(x) = \frac{x_2x_3}{40} - 1 \leq 0$$

$$g_8(x) = \frac{5x_2}{x_1} - 1 \leq 0$$

$$g_9(x) = \frac{x_1}{12x_2} - 1 \leq 0$$

$$g_{10}(x) = \frac{15x_6 + 1.9}{x_4} - 1 \leq 0$$

$$g_{11}(x) = \frac{1.1x_7 + 1.9}{x_5} - 1 \leq 0$$

$$2,6 \leq x_1 \leq 3,6 ; 0,7 \leq x_2 \leq 0,8 ; 17 \leq x_3 \leq 28$$

$$7,3 \leq x_4 \leq 8,3 ; 7,3 \leq x_5 \leq 8,3 ; 2,9 \leq x_6 \leq 3,9$$

$$5,0 \leq x_7 \leq 5,5$$

Experimental research was performed for the helical spring problem, and the results of GOA algorithm, along with the results for MACA, FSO, and WCA algorithms, are given in Table 1.

Table 1. Comparison of results for the helical spring

| Variables | MACA[14] | ICS[15] | WCA[16] | GOA            |
|-----------|----------|---------|---------|----------------|
| $x_1$     | 0.0523   | 0.0517  | 0.0516  | <b>0.0524</b>  |
| $x_2$     | 0.3722   | 0.3570  | 0.3562  | <b>0.3750</b>  |
| $x_3$     | 10.4141  | 11.2699 | 11.3004 | <b>10.3038</b> |
| $f(x)$    | 0.0128   | 0.0126  | 0.0126  | <b>0.0126</b>  |

In the case of helical spring optimization, GOA gives the same result as WCA and ICS, while MACA give a slightly worse result.

A detailed display of the results obtained by GOA and a comparison with several results obtained by other methods, for the problem of car side impact, are shown in Table 2.

Table 2. Comparison of results for the car side impact

| Variables | MFO[17] | GWO[18] | WOA[19] | GOA            |
|-----------|---------|---------|---------|----------------|
| $x_1$     | 0.5     | 0.5     | 0.5     | <b>0.5</b>     |
| $x_2$     | 1.116   | 1.14    | 1.108   | <b>1.115</b>   |
| $x_3$     | 0.5     | 0.5     | 0.534   | <b>0.5</b>     |
| $x_4$     | 1.301   | 1.268   | 1.305   | <b>1.303</b>   |
| $x_5$     | 0.5     | 0.5     | 0.5     | <b>0.5</b>     |
| $x_6$     | 1.5     | 1.5     | 1.473   | <b>1.5</b>     |
| $x_7$     | 0.5     | 0.5     | 0.5     | <b>0.5</b>     |
| $x_8$     | 0.345   | 0.345   | 0.345   | <b>0.345</b>   |
| $x_9$     | 0.345   | 0.192   | 0.192   | <b>0.286</b>   |
| $x_{10}$  | -19.530 | -20.605 | -19.699 | <b>-19.715</b> |
| $x_{11}$  | 0.0000  | 0.5     | 3.481   | <b>0.320</b>   |
| $f(x)$    | 22.842  | 22.878  | 23.042  | <b>22.878</b>  |

In the case of car side impact optimization, GOA gives the same result as GWO, WOA give a slightly worse result, while MFO gave better results.

For the cone clutch design problem, the results shown in Table 3, along with the results obtained by FA, CS and GWO methods.

Table 3. Comparison of results for the cone clutch

| Variables | FA[20]  | CS[20] | GWO[18] | GOA            |
|-----------|---------|--------|---------|----------------|
| $x_1$     | 4.2987  | 4.2858 | 4.286   | <b>4.2861</b>  |
| $x_2$     | 2.1405  | 2.1428 | 2.142   | <b>2.143</b>   |
| $f(x)$    | 69.6278 | 68.887 | 68.893  | <b>68.8948</b> |

In this case, the GOA gives the near same result as the CS and GWO algorithm, while FA gave worse results.

A detailed display of the results obtained by GOA and a comparison with several results obtained by other methods, for the problem of speed reducer, are shown in Table 4.

Table 4. Comparison of results for the speed reducer

| Variables | ICS[15]  | GWO[18]  | WCA[16]  | GOA              |
|-----------|----------|----------|----------|------------------|
| $x_1$     | 3.499    | 3.502    | 3.5      | <b>3.5</b>       |
| $x_2$     | 0.700    | 0.7      | 0.7      | <b>0.7</b>       |
| $x_3$     | 17       | 17       | 17       | <b>17</b>        |
| $x_4$     | 7.300    | 7.333    | 7.3      | <b>7.3</b>       |
| $x_5$     | 7.800    | 7.8      | 7.715    | <b>7.8</b>       |
| $x_6$     | 3.350    | 3.351    | 3.350    | <b>3.35022</b>   |
| $x_7$     | 5.287    | 5.288    | 5.286    | <b>5.28762</b>   |
| $f(x)$    | 2997.058 | 2998.299 | 2994.471 | <b>2996.9641</b> |

In the case of the speed reducer problem, the GOA algorithm gave better results than ICS and GWO, while WCA results are better.

#### 4. CONCLUSION

This paper deals with the GOA optimization algorithm and applies it to a few engineering design examples: speed reducer, helical spring, side impact of a car, and cone clutch.

In the introduction, a brief overview of literature was given. In Section 2, the inspiration, the mathematical model, and the pseudo code for the GOA algorithm was presented. In Section 3, the engineering design examples, which are common benchmarks for optimization methods, were solved by using the GOA algorithm. For this algorithm, 30 search agents and 1000 iterations were chosen as input parameters. The mathematical formulation, graphical representation, and the results were shown.

The obtained results were compared to latest papers published in SCI list journals.

This algorithm was used to obtain optimal or near-optimal results, as shown in the examples. Further developing of this algorithm can be used to redefine and upgrade this method, as to gain better results.

#### ACKNOWLEDGEMENT

This work was supported by the Serbian Ministry of Education, Science and Technological Development through Mathematical Institute of the Serbian Academy of Sciences and Arts.

#### REFERENCES

[1] M.Gašić, M.Savković, R.Bulatović, "Optimization of Trapezoidal Cross Section of the Truck Crane Boom by Lagrange Multipliers and by Differential Evolution Algorithm (DE)", Journal of Mechanical Engineering 57(2011)4, 304-312.

[2] A. Hammoudi, F. Djeddou, "Composite Differential Evolution Algorithm: Mixed Variable Structural Optimization Problem", Journal of Chemistry and Materials Research Vol. 3, 2015, 3–8.

[3] Shahrzad S, Seyedali Mirjalili and Andrew Lewis, "Grasshopper Optimisation Algorithm: Theory and Application" Advances in Engineering Software, Volume 105, March 2017, pp 30-47.

[4] Dj.Jovanović, B.Milenković, M.Krstić, "Application of Grasshopper Algorithm in Mechanical Engineering", YOURS 2020, pp.1-6.

[5] S.Guo, J.Wang, W.Xie, M.Guo, L.Zhu, "Improved Grasshopper Algorithm Based on Gravity Search Operator and Pigeon Colony Landmark Operator", IEEE Access Vol 8, February 2020, pp 1-22.

[6] P.Zhang, H.Yao, C.Fang and Y.Lui, "Multi-objective enhanced particle swarm optimization in virtual network embedding", EURASIP Journal on Wireless Communications and Networking (2016) 2016:167.

[7] D.Manickavelu, R.Vaidyanathan, "Particle swarm optimization (PSO)-based node and link lifetime prediction algorithm for route recovery in MANET", EURASIP Journal on Wireless Communications and Networking 2014, 2014:107.

[8] X. L. S. C. J. J. W. Z. Wen Long, "A modified augmented Lagrangian with improved grey wolf optimization to constrained optimization problems," Neural Computing & Applications.

[9] Arora JS. Introduction to optimum design. New York: McGraw-Hill; 1989.

[10] Gu, L., Yang, R., Tho, C., Makowskit, M., Faruquet, O. and Y.Li, Y. (2001) 'Optimisation and robustness for crashworthiness of side impact', International Journal of Vehicle Design, Vol. 26, No. 4, pp.348–360.

[11] R.V.J..Savsani, Mechanical Design Optimization Using Advanced Optimization Techniques, Springer-Verlag London, 2012.

[12] Carlos A. Coello Coello: Constraint-handling in genetic algorithms through the use of dominance based tournament selection, Advanced Engineering Informatics, 16 (2002):193–203.

[13] T.Kim, M.Cho, S.Shin, "Constrained Mixed Variable Design Optimization Based on Particle Swarm Optimizer with a Diversity Classifier for Cyclically Neighboring Subpopulations" Mathematics 2020, 8, 2016, pp.1-29.

[14] V.Grčković, R.Bulatović, Modified Ant Colony Algorithm for Solving Engineering Optimization Problems, IMK-14-Research and Development 18(2012)4.

[15] Bulatović, R. R., Bošković, G., Savković, M. M., & Gašić, M. M. (2014). Improved Cuckoo Search (ICS) algorithm for constrained optimization problems. /Latin American Journal of Solids and Structures/, /11/(8), 1349-1362.

[16] H.Eskandar, A. Sadollah, A. Bahreininejad, M.Hamdi: Water cycle algorithm – A novel metaheuristic optimization method for solving constrained engineering optimization problems, Computers and Structures, 2012.

- [17] Mirjalili S (2015) Moth-flame optimization algorithm: a novel nature-inspired heuristic paradigm. *Knowl Based Syst* 89:228–249.
- [18] B.Milenković,M.Krstić,Đ.Jovanović:Primena algoritma sivog vuka za rešavanje inženjerskih optimizacionih problema, *Tehnika*, 2021.,Vol.76, Br.1. str.50-57, ISSN 0040-2176.
- [19] S.Mirjalili, A.Lewis, ,“The Whale Optimization Algorithm” *Advances in Engineering Software*, Volume 95, March 2016, pp 51-67.
- [20] G.Miodragović,Advanced bio-inspired algorithms development for solving optimization problems in applied mechanics, doctoral thesis, Faculty of Mechanical and Civil Engineering Kraljevo, University of Kragujevac (2015).
- [21] Saremi, S., Mirjalili, S., & Lewis, A. (2017). Grasshopper optimisation algorithm: theory and application. *Advances in Engineering Software*, /105/, 30-47.



# Contribution to the problem of in-plane vibration of circular arches with varying cross-sections

Slaviša Šalinić<sup>1\*</sup>, Aleksandar Obradović<sup>2</sup>

<sup>1</sup>Faculty of Mechanical and Civil Engineering/Department, University of Kragujevac, Kraljevo (Serbia)

<sup>2</sup>Faculty of Mechanical Engineering /Mechanics, University of Belgrade, Belgrade (Serbia)

*Free in-plane vibration analysis of circular arches with varying cross-sections is studied by means of the symbolic-numeric method of initial parameters. The effects of axial extension, transverse shear deformation and rotatory inertia are considered. For various boundary conditions, natural frequencies of free in-plane vibration of circular arches with varying cross-sections are obtained. By comparing obtained results with previous ones available in the literature the effectiveness of application of the symbolic-numeric method of initial parameters to the problem considered is proven.*

**Keywords:** Circular arch, Free vibration, Varying cross-section, Natural frequencies

## 1. INTRODUCTION

The circular arches represent important components of engineering structures. The vibration analysis of circular arches is one of important aspect of dynamic analysis of these structural components. The review of papers on this topic can be found in [1-4]. In the literature, the three principal dynamical models of circular arches were considered: the model with included the effects of axial extensibility, shear deformation and rotary inertia [5-11] (the so-called Timoshenko circular arches); the model with neglected the effects of both shear deformation and rotary inertia [12-15]; the model without the effects of axial extensibility, shear deformation and rotary inertia [16,17] (the so-called Euler-Bernoulli circular arches). The exact solution of the vibration problem of uniform Timoshenko circular arches was given in [6] and for stepped ones in [7]. Based on these solutions the approximate approach for vibration analysis of tapered Timoshenko circular arches was presented in [9]. Note that the similar idea is used in the approach for vibration analysis of tapered Euler-Bernoulli circular arches was given in [16]. The papers [10, 19-23] are interesting in that they consider the influence of functionally graded material on the vibration characteristics of circular arches.

The aim of this paper is to evaluate a method for the vibration analysis of tapered circular Timoshenko arches. The method is based on the use of the symbolic-numeric method of initial parameters [24]. To the authors' best knowledge of the literature, the method presented was not considered so far in scientific papers.

## 2. FORMULATION OF GOVERNING EQUATIONS

Figure 1 shows a thin elastic circular arch with varying cross-section in its undeformed configuration. Without loss of generality, it is assumed that the arch has a rectangular cross-section of constant width  $b$  and variable height  $h$  which is a function of the angular coordinate  $\theta$ .

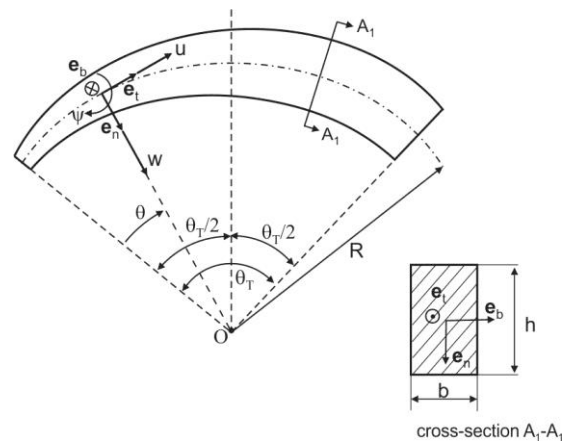


Figure 1: The geometry of a circular arch with varying cross-section

By the angle  $\theta$  a point on the arch centroidal curve is defined. Also, the following quantities are shown in Figure 1:  $\mathbf{e}_t$ ,  $\mathbf{e}_n$ , and  $\mathbf{e}_b$  are the unite vectors of tangent, principal normal, and binormal of the arch centroidal curve, respectively;  $R$  is the radius of the undeformed centroidal curve of the arch;  $\theta_T$  is the opening angle of the arch,  $w$  represents the radial displacement of a point of the centroidal curve in the  $\mathbf{e}_n$  direction;  $u$  represents the tangential displacement of a point of the centroidal curve in the  $\mathbf{e}_t$  direction;  $\psi$  is the angle of rotation of the arch cross-section due to bending. The circular arch is made of a homogeneous material of the modulus of elasticity  $E$ , the mass density  $\rho$ , and the shear modulus  $G$ . It is taken that  $\theta = 0$  at the arch left end.

The corresponding governing differential equations of the free in-plane vibrations of the circular arch considered read [9]:

\*Corresponding author: Slaviša Šalinić, Dositejeva 19, Kraljevo, salinic.s@mfv.kg.ac.rs

$$\frac{dU}{d\theta} = W + \frac{R}{EA(\theta)} N, \quad (1)$$

$$\frac{dW}{d\theta} = -U + \frac{R}{GA(\theta)k} Q + R\Psi, \quad (2)$$

$$\frac{d\Psi}{d\theta} = \frac{R}{EI_b(\theta)} M_b, \quad (3)$$

$$\frac{dM_b}{d\theta} = -RQ - R\rho\omega^2 I_b(\theta)\Psi, \quad (4)$$

$$\frac{dN}{d\theta} = Q - R\rho A(\theta)\omega^2 U, \quad (5)$$

$$\frac{dQ}{d\theta} = -N - R\rho A(\theta)\omega^2 W. \quad (6)$$

where  $W$  and  $U$  are the mode shape functions corresponding to the radial and tangential displacements,  $w$  and  $u$ , respectively,  $N$ ,  $Q$ , and  $M_b$  are the mode shape functions of axial forces, shear forces, and bending moments at an arch cross-section, respectively,  $k$  is the shear correction factor, and  $\omega$  is the natural angular frequency of free in-plane vibration of the circular arch. In this paper, it is taken  $k = 5/6$  for the rectangular cross-sections. The other expressions for the coefficient  $k$  may be found in [25].

For the purpose of further exposition, let us introduce the following dimensionless quantities:

$$\xi = \frac{\theta}{\theta_r}, \quad \bar{U} = \frac{U}{R}, \quad \bar{W} = \frac{W}{R}, \quad (7)$$

$$r = \frac{I_{br}}{A_r R^2}, \quad \bar{A}(\xi) = \frac{A(\theta)}{A_r}, \quad \bar{I}_b(\xi) = \frac{I_b(\theta)}{I_{br}}, \quad (8)$$

$$\mu = \frac{E}{Gk} = \frac{2(1+\nu)}{k}, \quad \bar{N} = \frac{N}{EA_r}, \quad \bar{Q} = \frac{QR^2}{EI_{br}}, \quad (9)$$

$$\bar{M}_b = \frac{M_b R}{EI_{br}}, \quad \frac{d}{d\theta} = \frac{1}{\theta_r} \frac{d}{d\xi}, \quad (10)$$

where  $\nu$  is the Poisson's ratio and  $A_r$  and  $I_{br}$  are the cross-sectional area and the cross-sectional area moment of inertia about axis  $e_b$ , respectively, at a reference cross-section.

Using (7)-(10) the equation system (1)-(6) can be written in the following dimensionless form:

$$\frac{d\bar{U}}{d\xi} = \theta_r \bar{W} + \frac{\theta_r}{\bar{A}(\xi)} \bar{N}, \quad (11)$$

$$\frac{d\bar{W}}{d\xi} = -\bar{U}\theta_r + \frac{\theta_r r \mu}{\bar{A}(\xi)} \bar{Q} + \theta_r \Psi, \quad (12)$$

$$\frac{d\Psi}{d\xi} = \frac{\theta_r}{\bar{I}_b(\xi)} \bar{M}_b, \quad (13)$$

$$\frac{d\bar{M}_b}{d\xi} = -\theta_r \bar{Q} - r\theta_r \bar{I}_b(\xi)\omega^2 \Psi, \quad (14)$$

$$\frac{d\bar{N}}{d\xi} = r\theta_r \bar{Q} - r\theta_r \bar{A}(\xi)\omega^2 \bar{U}, \quad (15)$$

$$\frac{d\bar{Q}}{d\xi} = -\frac{\theta_r}{r} \bar{N} - \theta_r \bar{A}(\xi)\omega^2 \bar{W}, \quad (16)$$

where

$$\bar{\omega} = \omega \sqrt{\frac{R^4 \rho A_r}{EI_{br}}} \quad (17)$$

is the dimensionless natural frequency. This differential equation system can be shown in the matrix form as follows:

$$\frac{d\bar{\mathbf{X}}(\xi)}{d\xi} = \mathbf{B}\bar{\mathbf{X}}(\xi) \quad (18)$$

where

$$\bar{\mathbf{X}}(\xi) = [\bar{U}(\xi), \bar{W}(\xi), \Psi(\xi), \bar{N}(\xi), \bar{Q}(\xi), \bar{M}_b(\xi)]^T \quad (19)$$

and

$$\mathbf{B} = \begin{bmatrix} 0 & \theta_r & 0 \\ -\theta_r & 0 & \theta_r \\ 0 & 0 & 0 \\ -r\theta_r \bar{A}(\xi)\omega^2 & 0 & 0 \\ 0 & -\theta_r \bar{A}(\xi)\omega^2 & 0 \\ 0 & 0 & -r\theta_r \bar{I}_b(\xi)\omega^2 \\ \theta_r / \bar{A}(\xi) & 0 & 0 \\ 0 & \theta_r r \mu / \bar{A}(\xi) & 0 \\ 0 & 0 & \theta_r / \bar{I}_b(\xi) \\ 0 & r\theta_r & 0 \\ -\theta_r / r & 0 & 0 \\ 0 & -\theta_r & 0 \end{bmatrix}. \quad (20)$$

The corresponding boundary conditions are:

- clamped left arch end  $\bar{U}(0) = 0, \bar{W}(0) = 0, \Psi(0) = 0,$  (21)

- hinged left arch end  $\bar{U}(0) = 0, \bar{W}(0) = 0, \bar{M}_b(0) = 0,$  (22)

- clamped right arch end  $\bar{U}(1) = 0, \bar{W}(1) = 0, \Psi(1) = 0,$  (23)

- hinged right arch end  $\bar{U}(1) = 0, \bar{W}(1) = 0, \bar{M}_b(1) = 0,$  (24)

- free right arch end  $\bar{N}(1) = 0, \bar{Q}(1) = 0, \bar{M}_b(1) = 0.$  (25)

The differential equation system (18) and the relations (21)-(25) form a two-point boundary value problem of the free in-plane vibration of the circular arch with varying cross-section. The equations system (11)-(16) covers some special cases. Namely if the assumption of inextensibility of the arch centroidal line is used then the equation (11) should be replaced with:

$$\frac{d\bar{U}}{d\zeta} = \theta_T \bar{W} . \quad (26)$$

Also, if rotatory inertia effect is ignored then the equation (14) should be replaced with:

$$\frac{d\bar{M}_b}{d\zeta} = -\theta_T \bar{Q} . \quad (27)$$

Finally, if transverse shear effect is not considered then the equation (12) should be replaced with:

$$\frac{d\bar{W}}{d\zeta} = -\bar{U}\theta_T + \theta_T \Psi . \quad (28)$$

### 3. SOLUTION PROCEDURE

In this paper the two-point boundary value problem formulated will be solved by using the symbolic-numeric method of initial parameters [24]. Since (18) represents a linear system of differential equations then its solution can be represented as:

$$\bar{\mathbf{X}}(\zeta) = C_1 \bar{\mathbf{X}}_1(\zeta, \bar{\omega}) + C_2 \bar{\mathbf{X}}_2(\zeta, \bar{\omega}) + C_3 \bar{\mathbf{X}}_3(\zeta, \bar{\omega}) \quad (29)$$

where  $C_1, C_2,$  and  $C_3$  are the integration constants and

$$\bar{\mathbf{X}}_1(\zeta, \bar{\omega}) = \left[ \bar{U}_1(\zeta, \bar{\omega}), \bar{W}_1(\zeta, \bar{\omega}), \Psi_1(\zeta, \bar{\omega}), \bar{N}_1(\zeta, \bar{\omega}), \bar{Q}_1(\zeta, \bar{\omega}), \bar{M}_{b1}(\zeta, \bar{\omega}) \right]^T , \quad (30)$$

$$\bar{\mathbf{X}}_2(\zeta, \bar{\omega}) = \left[ \bar{U}_2(\zeta, \bar{\omega}), \bar{W}_2(\zeta, \bar{\omega}), \Psi_2(\zeta, \bar{\omega}), \bar{N}_2(\zeta, \bar{\omega}), \bar{Q}_2(\zeta, \bar{\omega}), \bar{M}_{b2}(\zeta, \bar{\omega}) \right]^T , \quad (31)$$

and

$$\bar{\mathbf{X}}_3(\zeta, \bar{\omega}) = \left[ \bar{U}_3(\zeta, \bar{\omega}), \bar{W}_3(\zeta, \bar{\omega}), \Psi_3(\zeta, \bar{\omega}), \bar{N}_3(\zeta, \bar{\omega}), \bar{Q}_3(\zeta, \bar{\omega}), \bar{M}_{b3}(\zeta, \bar{\omega}) \right]^T \quad (32)$$

are the particular solutions obtained by integrating the differential equations system (18) using the built-in function **ParametricNDSolve[]** in Mathematica programming package with the following initial conditions, respectively:

$$\begin{aligned} \bar{U}(0) = 0, \bar{W}(0) = 0, \Psi(0) = 0, \\ \bar{N}(0) = 1, \bar{Q}(0) = 0, M_b(0) = 0 \end{aligned} , \quad (33)$$

$$\begin{aligned} \bar{U}(0) = 0, \bar{W}(0) = 0, \Psi(0) = 0, \\ \bar{N}(0) = 0, \bar{Q}(0) = 1, M_b(0) = 0 \end{aligned} , \quad (34)$$

and

$$\begin{aligned} \bar{U}(0) = 0, \bar{W}(0) = 0, \Psi(0) = 0, \\ \bar{N}(0) = 0, \bar{Q}(0) = 0, M_b(0) = 1 \end{aligned} , \quad (35)$$

for the clamped left arch end, whereas for the hinged left arch end the following corresponding initial conditions are used:

$$\begin{aligned} \bar{U}(0) = 0, \bar{W}(0) = 0, \Psi(0) = 1, \\ \bar{N}(0) = 0, \bar{Q}(0) = 0, M_b(0) = 0 \end{aligned} , \quad (36)$$

$$\begin{aligned} \bar{U}(0) = 0, \bar{W}(0) = 0, \Psi(0) = 0, \\ \bar{N}(0) = 1, \bar{Q}(0) = 0, M_b(0) = 0 \end{aligned} , \quad (37)$$

and

$$\begin{aligned} \bar{U}(0) = 0, \bar{W}(0) = 0, \Psi(0) = 0, \\ \bar{N}(0) = 0, \bar{Q}(0) = 1, M_b(0) = 0 \end{aligned} . \quad (38)$$

From the condition that the solution (29) satisfies the boundary conditions (23)-(25) it follows that for clamped arch right end one has:

$$\begin{aligned} C_1 \bar{U}_1(1, \bar{\omega}) + C_2 \bar{U}_2(1, \bar{\omega}) + C_3 \bar{U}_3(1, \bar{\omega}) = 0, \\ C_1 \bar{W}_1(1, \bar{\omega}) + C_2 \bar{W}_2(1, \bar{\omega}) + C_3 \bar{W}_3(1, \bar{\omega}) = 0, \\ C_1 \Psi_1(1, \bar{\omega}) + C_2 \Psi_2(1, \bar{\omega}) + C_3 \Psi_3(1, \bar{\omega}) = 0 \end{aligned} \quad (39)$$

whereas for hinged right arch end one has:

$$\begin{aligned} C_1 \bar{U}_1(1, \bar{\omega}) + C_2 \bar{U}_2(1, \bar{\omega}) + C_3 \bar{U}_3(1, \bar{\omega}) = 0, \\ C_1 \bar{W}_1(1, \bar{\omega}) + C_2 \bar{W}_2(1, \bar{\omega}) + C_3 \bar{W}_3(1, \bar{\omega}) = 0, \\ C_1 \bar{M}_{b1}(1, \bar{\omega}) + C_2 \bar{M}_{b2}(1, \bar{\omega}) + C_3 \bar{M}_{b3}(1, \bar{\omega}) = 0 \end{aligned} \quad (40)$$

and finally for the free arch right end it holds that:

$$\begin{aligned} C_1 \bar{N}_1(1, \bar{\omega}) + C_2 \bar{N}_2(1, \bar{\omega}) + C_3 \bar{N}_3(1, \bar{\omega}) = 0, \\ C_1 \bar{Q}_1(1, \bar{\omega}) + C_2 \bar{Q}_2(1, \bar{\omega}) + C_3 \bar{Q}_3(1, \bar{\omega}) = 0, \\ C_1 \bar{M}_{b1}(1, \bar{\omega}) + C_2 \bar{M}_{b2}(1, \bar{\omega}) + C_3 \bar{M}_{b3}(1, \bar{\omega}) = 0 \end{aligned} \quad (41)$$

The equations systems (39)-(41) represent homogeneous systems of equations in unknowns  $C_1, C_2,$  and  $C_3$ . In order that these systems can have non-trivial solutions for  $C_1, C_2,$  and  $C_3$ , the determinants of their corresponding coefficients matrix must be equal to zero, that is:

$$f_C(\bar{\omega}) \equiv \det \begin{bmatrix} \bar{U}_1(1, \bar{\omega}) & \bar{U}_2(1, \bar{\omega}) & \bar{U}_3(1, \bar{\omega}) \\ \bar{W}_1(1, \bar{\omega}) & \bar{W}_2(1, \bar{\omega}) & \bar{W}_3(1, \bar{\omega}) \\ \Psi_1(1, \bar{\omega}) & \Psi_2(1, \bar{\omega}) & \Psi_3(1, \bar{\omega}) \end{bmatrix} = 0 , \quad (42)$$

$$f_H(\bar{\omega}) \equiv \det \begin{bmatrix} \bar{U}_1(1, \bar{\omega}) & \bar{U}_2(1, \bar{\omega}) & \bar{U}_3(1, \bar{\omega}) \\ \bar{W}_1(1, \bar{\omega}) & \bar{W}_2(1, \bar{\omega}) & \bar{W}_3(1, \bar{\omega}) \\ \bar{M}_{b1}(1, \bar{\omega}) & \bar{M}_{b2}(1, \bar{\omega}) & \bar{M}_{b3}(1, \bar{\omega}) \end{bmatrix} = 0, \quad (43)$$

$$f_F(\bar{\omega}) \equiv \det \begin{bmatrix} \bar{N}_1(1, \bar{\omega}) & \bar{N}_2(1, \bar{\omega}) & \bar{N}_3(1, \bar{\omega}) \\ \bar{Q}_1(1, \bar{\omega}) & \bar{Q}_2(1, \bar{\omega}) & \bar{Q}_3(1, \bar{\omega}) \\ \bar{M}_{b1}(1, \bar{\omega}) & \bar{M}_{b2}(1, \bar{\omega}) & \bar{M}_{b3}(1, \bar{\omega}) \end{bmatrix} = 0 . \quad (44)$$

The relations (42)-(44) represent the corresponding form of frequency equations for, respectively, clamped, hinged and free right arch ends. For easier evaluation of roots of the equations (42), (43), and (44), the graphs of the functions  $f_C(\bar{\omega})$ ,  $f_H(\bar{\omega})$ , and  $f_F(\bar{\omega})$  obtained by using the built-in function **Plot[]** in Mathematica programming package may be used. The values of the natural frequencies can be obtained by means of the Mathematica built-in function **FindRoot[]**.

#### 4. NUMERICAL EXAMPLES

##### 4.1. Uniform Euler-Bernoulli circular arches

In this section, the accuracy of the proposed approach in the case of the effects of axial extension, transverse shear deformation and rotatory inertia ignored is examined. For both clamped-clamped and hinged-hinged boundary conditions values of the dimensionless frequency coefficient  $c = \theta_T^2 \bar{\omega}$  are calculated for various values of the opening angle  $\theta_T$ . These values are shown in Tables 1 and 2.

Table 1: The lowest five dimensionless frequency coefficients  $c_i = \theta_T^2 \bar{\omega}_i$  ( $i = 1, \dots, 5$ ) of clamped-clamped uniform Euler-Bernoulli circular arches for  $r = 1/2500$  and various values of the opening angle  $\theta_T$ .

| $\theta_T$ [rad] | Mode | [6]      | This study |
|------------------|------|----------|------------|
| $\pi/2$          | 1    | 55.82523 | 55.82521   |
|                  | 2    | 106.7301 | 106.7304   |
|                  | 3    | 193.0345 | 193.0354   |
|                  | 4    | 284.8229 | 284.8374   |
|                  | 5    | 376.6113 | 376.6258   |
| $2\pi/3$         | 1    | 51.96935 | 51.96931   |
|                  | 2    | 103.5760 | 103.5765   |
|                  | 3    | 188.3591 | 188.3597   |
|                  | 4    | 281.2906 | 281.2913   |
|                  | 5    | 374.2221 | 374.2228   |
| $\pi$            | 1    | 43.27259 | 43.27257   |
|                  | 2    | 95.26028 | 95.26036   |
|                  | 3    | 176.8800 | 176.8810   |
|                  | 4    | 271.6560 | 271.6495   |
|                  | 5    | 366.4320 | 366.4255   |

Table 2: The lowest five dimensionless frequency coefficients  $c_i = \theta_T^2 \bar{\omega}_i$  ( $i = 1, \dots, 5$ ) of hinged-hinged uniform Euler-Bernoulli circular arches for  $r = 1/2500$  and various values of the opening angle  $\theta_T$ .

| $\theta_T$ [rad] | Mode | [6]      | This study |
|------------------|------|----------|------------|
| $\pi/2$          | 1    | 33.96053 | 33.96054   |
|                  | 2    | 79.95263 | 79.95272   |
|                  | 3    | 152.1706 | 152.1712   |
|                  | 4    | 237.9724 | 237.9718   |
|                  | 5    | 323.7742 | 323.7736   |
| $2\pi/3$         | 1    | 30.38416 | 30.38415   |
|                  | 2    | 76.74733 | 76.74741   |
|                  | 3    | 148.1494 | 148.1496   |
|                  | 4    | 234.5716 | 234.5713   |
|                  | 5    | 320.9938 | 320.9931   |
| $\pi$            | 1    | 22.37183 | 22.37184   |
|                  | 2    | 68.33021 | 68.33020   |
|                  | 3    | 137.9534 | 137.9541   |
|                  | 4    | 225.2190 | 225.2200   |
|                  | 5    | 312.4846 | 312.4856   |

##### 4.2. Uniform Timoshenko circular arches

In this section, the accuracy of the proposed approach in the case when the effects of axial extension, transverse shear deformation and rotatory inertia are taken into account. For both clamped-clamped and hinged-hinged boundary conditions values of the frequency coefficient  $c = \theta_T^2 \bar{\omega}$  are calculated for  $r = 1/2500$  and various values of the opening angle  $\theta_T$ . These values are shown in Tables 3 and 4.

Table 3: The lowest five dimensionless frequency coefficients  $c_i = \theta_T^2 \bar{\omega}_i$  ( $i = 1, \dots, 5$ ) of clamped-clamped uniform Timoshenko circular arches for  $r = 1/2500$  and various values of the opening angle  $\theta_T$ .

| $\theta_T$ [rad] | Mode | [6]      | This study |
|------------------|------|----------|------------|
| $\pi/2$          | 1    | 53.96596 | 53.96698   |
|                  | 2    | 86.19077 | 86.19724   |
|                  | 3    | 132.7272 | 132.7371   |
|                  | 4    | 175.8392 | 175.8474   |
|                  | 5    | 265.8141 | 265.8130   |
| $2\pi/3$         | 1    | 50.93224 | 50.93284   |
|                  | 2    | 96.85173 | 96.85474   |
|                  | 3    | 178.1998 | 178.2048   |
|                  | 4    | 198.0489 | 198.0699   |
|                  | 5    | 282.9555 | 282.9633   |
| $\pi$            | 1    | 42.86968 | 42.86991   |
|                  | 2    | 93.26808 | 93.26909   |
|                  | 3    | 172.2951 | 172.2978   |
|                  | 4    | 258.4766 | 258.4856   |
|                  | 5    | 372.7893 | 372.5899   |

Table 4: The lowest five dimensionless frequency coefficients  $c_i = \theta_T^2 \bar{\omega}_i$  ( $i = 1, \dots, 5$ ) of hinged-hinged uniform Timoshenko circular arches for  $r = 1/2500$  and various values of the opening angle  $\theta_T$ .

| $\theta_T$ [rad] | Mode | [6]      | This study |
|------------------|------|----------|------------|
| $\pi/2$          | 1    | 33.46323 | 33.46350   |
|                  | 2    | 74.34122 | 74.34354   |
|                  | 3    | 121.4958 | 121.5088   |
|                  | 4    | 144.0231 | 144.0274   |
|                  | 5    | 226.3381 | 226.3465   |
| $2\pi/3$         | 1    | 30.12124 | 30.12138   |
|                  | 2    | 74.69487 | 74.69574   |
|                  | 3    | 143.4124 | 143.4163   |
|                  | 4    | 197.2652 | 197.2830   |
|                  | 5    | 242.4045 | 242.4115   |
| $\pi$            | 1    | 22.28359 | 22.28363   |
|                  | 2    | 67.67219 | 67.67259   |
|                  | 3    | 135.8837 | 135.8850   |
|                  | 4    | 219.2887 | 219.2796   |
|                  | 5    | 323.9065 | 323.8902   |

4.3. Timoshenko circular arches with varying cross-sections

In this section, the accuracy of our approach in the case of Timoshenko circular arches with varying cross-sections is analysed. Both unsymmetric arches with varying cross-section height defined as:

$$h(\theta) = h_c(1 - \eta + 2\eta\theta / \theta_T), \quad 0 \leq \theta \leq \theta_T \quad (45)$$

and symmetric arches with varying cross-section height prescribed as:

$$h(\theta) = \begin{cases} h_c(1 + \eta - 2\eta\theta / \theta_T), & 0 \leq \theta \leq \theta_T / 2 \\ h_c(1 - \eta + 2\eta\theta / \theta_T), & \theta_T / 2 \leq \theta \leq \theta_T \end{cases} \quad (46)$$

are considered where  $h_c$  represents the cross-section height at the arch crown and  $\eta$  is the taper ratio. Note that here, the cross-section width  $b$  is constant. Also, the reference cross-section is placed at the arch crown which means that:

$$A_r = bh_c, \quad (47)$$

$$I_{br} = \frac{bh_c^3}{12}. \quad (48)$$

For both clamped-clamped and hinged-hinged boundary conditions, the corresponding values of dimensionless natural frequencies  $\bar{\omega}_i (i = 1, \dots, 4)$  are calculated for  $r = 1/2500$ ,  $\eta = 0.1$ , and various values of the opening angle  $\theta_T$ . These values are shown in Tables 5 and 6.

Table 5: The lowest four dimensionless natural frequencies  $\bar{\omega}_i (i = 1, \dots, 2)$  of tapered clamped-clamped Timoshenko symmetric circular arches for  $r = 1/2500$ ,  $\eta = 0.1$ , and various values of the opening angle  $\theta_T$

| $\theta_T$ [rad] | Mode | [9]        | This study |
|------------------|------|------------|------------|
| $\pi/18$         | 1    | 433.46730  | 433.46807  |
|                  | 2    | 848.3639   | 848.3653   |
| $\pi/9$          | 1    | 161.500908 | 161.502319 |
|                  | 2    | 346.5162   | 346.5176   |
| $\pi/6$          | 1    | 88.1269568 | 88.1275550 |
|                  | 2    | 185.2505   | 185.2518   |
| $2\pi/9$         | 1    | 61.7200715 | 61.7203672 |
|                  | 2    | 113.0604   | 113.0616   |
| $5\pi/18$        | 1    | 50.8647280 | 50.8648687 |
|                  | 2    | 75.13195   | 75.13295   |

Table 6: The lowest four dimensionless natural frequencies  $\bar{\omega}_i (i = 1, \dots, 4)$  of tapered hinged-hinged Timoshenko unsymmetric circular arches for  $r = 1/2500$ ,  $\eta = 0.1$ , and various values of the opening angle  $\theta_T$

| $\theta_T$ [rad] | Mode | [9]         | This study |
|------------------|------|-------------|------------|
| $2\pi/9$         | 1    | 48.6310055  | 48.6310041 |
|                  | 2    | -           | 73.5871226 |
|                  | 3    | -           | 159.537886 |
|                  | 4    | -           | 227.199368 |
| $5\pi/18$        | 1    | 45.66166116 | 45.6616819 |
|                  | 2    | -           | 47.5315845 |
|                  | 3    | -           | 106.612136 |
|                  | 4    | -           | 172.488529 |
| $\pi/3$          | 1    | 32.51755826 | 32.5176282 |
|                  | 2    | -           | 44.1841916 |
|                  | 3    | -           | 76.7889457 |
|                  | 4    | -           | 125.924402 |
| $4\pi/9$         | 1    | 17.59579627 | 17.5958086 |
|                  | 2    | -           | 36.3558497 |
|                  | 3    | -           | 52.0315664 |
|                  | 4    | -           | 73.3148923 |

5. CONCLUSIONS

In this paper the symbolic-numeric method of initial parameters developed in [24] has been applied to the problem of in-plane vibration of circular arches with varying cross-sections. Through the numerical examples shown in Section 4 the effectiveness of application of the symbolic-numeric method of initial parameters to the vibration problems considered has been proved. The proposed approach allows also the vibration analysis in the case when the effects of axial extension, transverse shear deformation and rotatory inertia are ignored as well as in the case when the effects of transverse shear deformation and rotatory inertia are not included in the arch model. It is the goal of future work to expand the symbolic-numeric method of initial parameters to vibration analysis of circular arches made of functionally graded materials [10, 18-23], noncircular curved beams [3] (such as parabolic, sinusoidal, and elliptical arches) as well as arches carrying concentrated masses [26,27].

ACKNOWLEDGEMENTS

Support for this research was provided by the Ministry of Education, Science and Technological Development of the Republic of Serbia under Grant Nos. 451-03-9/2021-14/200108 and 451-03-9/2021-14/200105. This support is gratefully acknowledged.

REFERENCES

[1] P.A.A. Laura and M.J. Maurizi, “Recent Research on Vibration of Arch-Type Structures,” Shock Vib. Dig, Vol. 19(1), pp. 6-9, (1987)

[2] N.M. Auciello and M.A. De Rosa, “Free Vibrations of Circular Arches: A review,” J. Sound Vib, Vol. 176(4), pp. 433–458, (1994)

- [3] F. Yang, R. Sedaghati and E. Esmailzadeh, "Free In-Plane Vibration of Curved Beam Structures: A Tutorial and the State of the Art," *J. Vib. Control*, Vol. 24(12), pp. 2400–2417, (2018)
- [4] P. Chidamparam and A.W. Leissa, "Vibrations of a Planar Curved Beams, Rings and Arches," *Appl. Mech. Rev.*, Vol. 46, pp. 467–483, (1993)
- [5] M.S. Issa, T.M. Wang and B.T. Hsiao, "Extensional Vibrations of Continuous Circular Curved Beams with Rotary Inertia and Shear Deformation 1: Free vibration," *J. Sound Vib.*, Vol. 114, pp. 297-308, (1987)
- [6] E. Tufekci and A. Arpacı, "Exact Solution of In-Plane Vibrations of Circular Arches with Account Taken of Axial Extension, Transverse Shear and Rotatory Inertia Effects," *J. Sound Vib.*, Vol. 209(5), pp. 845–856, (1998)
- [7] E. Tufekci and O. Ozdemirci, "Exact Solution of Free In-Plane Vibration of a Stepped Circular Arch," *J. Sound Vib.*, Vol. 295, pp. 725–738, (2006)
- [8] F. Yang, R. Sedaghati and E. Esmailzadeh, "Free In-Plane Vibration of General Curved Beams using Finite Element Method," *J. Sound Vib.*, Vol. 318(4-5), pp. 850-867, (2008)
- [9] E. Tufekci and O.O. Yigit, "In-Plane Vibration of Circular Arches with Varying Cross-Sections," *Int. J. Struct. Stab. Dyn.*, Vol. 13(1), pp. 1350003, (2013)
- [10] S. Rajasekaran, "Static, Stability and Free Vibration Analysis of Arches Using a New Differential Transformation-Based Arch Element," *Int. J. Mech. Sci.*, Vol. 77, pp. 82-97, (2013)
- [11] U. Eroglu and E. Tufekci, "A New Finite Element Formulation for Free Vibrations of Planar Curved Beams," *Mech. Based Des. Struct. Mach.*, Vol. 46(6), pp. 730-750, (2018)
- [12] T.M. Wang and M.P. Guilbert, "Effects of rotary inertia and shear on natural frequencies of continuous circular curved beams," *Int. J. Solids Struct.*, Vol. 17, pp. 281-289, (1981)
- [13] S.Y. Lee and J.Y. Hsiao, "Free in-plane vibrations of curved non-uniform beams," *Acta Mech.*, Vol. 155, pp. 173-189, (2002)
- [14] B. Kang, C.H. Riedel and C.A. Tan, "Free vibration analysis of planar curved beams by wave propagation," *J. Sound Vib.*, Vol. 260(1), pp. 19-44, (2003)
- [15] C.H. Riedel and B. Kang, "Free vibration of elastically coupled dual-span curved beams," *J. Sound Vib.*, Vol. 290, pp. 820-838, (2006)
- [16] X. Tong, N. Mrad and B. Tabarrok, "In-Plane Vibration of Circular Arches with Variable Cross-Sections," *J. Sound Vib.*, Vol. 212(1), pp. 121–140, (1998)
- [17] G. R. Liu and T.Y. Wu, "In-Plane Vibration Analyses of Circular Arches by the Generalized Differential Quadrature Rule," *Int. J. Mech. Sci.*, Vol. 43, pp. 2597–2611, (2001)
- [18] P. Malekzadeh, "Two-Dimensional In-Plane Free Vibrations of Functionally Graded Circular Arches with Temperature-Dependent Properties," *Compos. Struct.*, Vol. 91, pp. 38-47, (2009)
- [19] S. Rajasekaran, "Free vibration of tapered arches made of axially functionally graded materials," *Struct. Eng. Mech.*, Vol. 45(4), pp. 569–594, (2013)
- [20] A.R. Noori, T.A. Aslan and B. Temel, "An Efficient Approach for In-Plane Free and Forced Vibrations of Axially Functionally Graded Parabolic Arches with Nonuniform Cross Section," *Compos. Struct.*, Vol. 200, pp. 701-710, (2018)
- [21] J.K. Lee and B.K. Lee, "In-Plane Free Vibration of Uniform Circular Arches Made of Axially Functionally Graded Materials," *Int. J. Struct. Stab. Dyn.*, Vol. 19(8), pp. 1950084, (2019)
- [22] J.K. Lee and B.K. Lee, "Free Vibration of AFG Circular Arch with Symmetric and Anti-symmetric Boundary Conditions at Mid-Arc," *Symmetry*, Vol. 12, pp. 417, (2020)
- [23] G.S. Kim, S.J. Oh, T.E. Lee and B.K. Lee, "Free vibrations of axially functionally graded horseshoe arch," *Engineering Solid Mechanics*, Vol. 9, pp. 251-262, (2021)
- [24] S. Šalinić, A. Obradović and A. Tomović, "Free Vibration Analysis of Axially Functionally Graded Tapered, Stepped, and Continuously Segmented Rods and Beams," *Compos. B. Eng.*, Vol. 150, pp. 135-143, (2018)
- [25] J-G. Kim, J-K. Lee and H.J. Yoon, "On the Effect of Shear Coefficients in Free Vibration Analysis of Curved Beams," *J. Mech. Sci. Technol.*, Vol. 28(8), pp. 3181–3187, (2014)
- [26] J.S. Wu, F.T. Lin and H.J. Shaw, "Free In-Plane Vibration Analysis of a Curved Beam (arch) with Arbitrary Various Concentrated Elements," *Appl. Math. Model.*, Vol. 37, pp. 7588-7610, (2013)
- [27] A. Babahammou and R. Benamarb, "Semi-Analytical Solution of In-Plane Vibrations of Circular Arches Carrying Added Point Masses," *Procedia Manuf.*, Vol. 44, pp. 465-472, (2020)

# The influence of spatial aliasing to experimental determination of dispersion relationship of flexural waves in beams by correlation method

Vladimir Sindelić<sup>1</sup>, Snežana Ćirić Kostić<sup>1</sup>, Branko Radičević<sup>1</sup>, Zlatan Šoškić<sup>1\*</sup>

<sup>1</sup>The Faculty of Mechanical and Civil Engineering in Kraljevo, University of Kragujevac, Kraljevo (Serbia)

*The experimental determination of a dispersion relation by measurements of wave properties in different points in space meets the challenge of spatial aliasing, which is a consequence of description of continuous wave by a discrete set of measurement points. The paper presents an analysis of the phenomenon and derives a relationship between the average distance between the measurement points and the frequency range for experimental determination of dispersion relationship of flexural waves in beams by correlation method. The results of the analysis are verified by experiments that comprised determination of the dispersion relationship with variable average distance between the measurement points.*

**Keywords:** Mechanical waves, Dispersion relationship, Frequency range, Spatial aliasing

## 1. INTRODUCTION

Dispersion relationship (abbreviated as “DR” in the following text) is defined as the relationship between the wavevector of a periodic wave  $k$  and its angular frequency  $\omega$ . Due to the simple linear dependencies, DR also represents, and is sometimes even defined as, the relationship between the wavelength  $\lambda$  ( $\lambda = 2\pi/k$ ) or the wavenumber  $\kappa$  ( $\kappa = k/2\pi$ ) of the wave, on one side, and the period  $T$  ( $T = 2\pi/\omega$ ) or the frequency  $f$  ( $f = \omega/2\pi$ ) of the wave on the other side of DR. Since the phase velocity  $c$  of a wave may be expressed as  $c = \omega/k$ , and the group velocity of a wave  $v$  may be expressed as  $v = d\omega/dk$ , the DR enables calculation of both phase and group velocity of the wave, thus representing an important tool for wave propagation studies. DR of mechanical waves depend on viscoelastic (such as elastic moduli and material loss factors) and inertial (such as density) properties of the medium through which the waves propagate.

The usual applications of DR are theoretical and numerical studies of wave propagation in structures, and the recent interest of the Laboratory for advanced design methodologies “3D Impulse” and Laboratory for acoustics of the Faculty of Mechanical and Civil Engineering in Kraljevo for experimental determination of DR [1][2] is raised by studies of dynamic behaviour of 3D printed periodic and aperiodic structures [3]. Besides, DRs are sometimes also used for calculation of elastic properties of viscoelastic properties of matter [4][5].

The DRs may be theoretically derived from partial differential equations of motion, and may be expressed in explicit form only for the cases of wave propagation through media with simple geometries and high symmetry. As a particularly simple geometry, which confines the wave propagation to one dimension, thin beams represent the most convenient object for studies of various applications of DRs. The simplest mechanical waves for excitation and detection are flexural waves, which have a parabolic form of DR [6]:

$$\omega = \sqrt{\frac{EI}{\rho A}} k^2 \quad (1)$$

with  $I$  standing for the area moment of inertia, and  $A$  for the area, of the cross-section of the beam.

The main concept for experimental determination of the DR in thin beams consists in measurement of the response (usually acceleration) to an excitation (usually impulse or harmonic) in multiple points along the beam. The responses at these points at a particular excitation frequency (obtained by direct measurement or spectral decomposition) are then used to construct wave fields with known wavevectors that have minimal deviation from the measured responses. There are two main groups of methods for construction of the wavefields with minimal deviation from the measured responses, and they differ in accuracy, mathematical complexity and range of applicability. The first group of methods are based on Prony method for decomposition of a function into a series of damped sinusoids, an idea analogous to use of sinusoids in Fourier analysis [7]-[9]. These methods are computationally efficient, but they have two serious disadvantages: first, their application is limited only to evenly spaced measurement points, and second, they require a large number of measurement points. The other group of methods are based on systematic repetitive testing of different wavefields in search for a set of parameters that provide the best fit between a wavefield and the experimental data. The applicability of the second group of methods is substantially wider, but their drawback is the related substantially longer computation time. Different methods that belong to the second group use different forms of the test wavefields, different criteria selected as measure of the quality of the fit, and the different procedures for finding the optimal wavefield parameters [4][5][10].

The method that is the subject of this paper is the correlation method [10], which uses sets of progressive waves as the test wavefields, and the simple sequential search of wavevector space to find the wavevector value that provides maximum of correlation between the measured data and the test wavefield at certain frequency, which is used as the measure of deviation of the test wavefield from experimental data. In its simplest form, used to study the waves propagating along a beam, the correlation method for experimental determination of DR (in further

\*Corresponding author: Zlatan Šoškić, Dositejeva 19, Kraljevo, soskic.z@mfkv.kg.ac.rs

text just "correlation method") uses wavefields constructed on the basis of a harmonic progressive waves with selected test wavevector  $k_t$  and angular frequency  $\omega$ , and the longitudinal axis of the beam as the  $x$ -axis. If a harmonic progressive wave is generated by force acting at one end of the beam, expressed in a complex form as  $\underline{F}(t) = \underline{F}_\omega \cdot \exp(-\omega t)$ , the accelerations of beam points due to the wavefield may be expressed as  $\underline{a}_t(x, t) = \underline{a}_\omega \exp(k_t x - \omega t)$ , and the wavefield of the response, the accelerances  $\underline{w}_t(x, t) = \underline{a}_t(x, t)/F(t)$  may be described by its complex amplitudes:

$$\underline{w}_t(x, \omega) = \underline{w}_{t\omega} \cdot \exp(k_t x), \quad (2)$$

which represent the *frequency response function* (FRF) of the measurement system represented by the experiment. The complex amplitudes of the accelerances of the wavefield for a selected wavevector  $k_t$  are compared to complex amplitudes of accelerances  $\underline{w}(x, \omega)$  measured in  $L$  measurement points  $x_l$  ( $l = 1, 2, \dots, L$ ) along the beam, and the measure of the fit between two datasets is their correlation defined in the form:

$$\begin{aligned} \underline{W}_\omega(k_t) &= \int_{-\infty}^{+\infty} \underline{w}(x, \omega) \underline{w}_t^*(x, \omega) dx = \\ &= \underline{w}_\omega^* \int_{-\infty}^{+\infty} \underline{w}(x, \omega) e^{-ik_t x} dx \end{aligned} \quad (3)$$

which is, due to the discrete nature of input data, estimated as:

$$\hat{W}_\omega(k_t) = \underline{w}_\omega^* \sum_{l=1}^L \underline{w}(x_l, \omega) e^{-ik_t x_l} \Delta x_l = \underline{w}_{l\omega}^* \sum_{l=1}^L \underline{w}_{l\omega} e^{-ik_t x_l} \Delta x_l \quad (4)$$

where  $\Delta x_l$  represents the space interval around the point  $x_l$ , and introducing the notation  $\underline{w}(x_l, \omega) = \underline{w}_{l\omega}$ . The expression for correlation between the two datasets given by (3) leads to the conclusion that, if the wave propagating along the beam is a progressive harmonic wave, then the modulus of the estimated correlation will have maximal value when the wavevector of the test wavefield  $k_t$  is equal to the wavevector of the propagating wave  $k$ . In order to determine the DR of waves propagating along the beam, the wavevector space is scanned in the range  $k_{min} < k_t < k_{max}$  for each angular frequency  $\omega$ , and the value of  $k_t$  that leads to maximal modulus of the estimated correlation is assumed to be the wavevector that corresponds to the angular frequency  $\omega$ , denoted as  $k(\omega)$ . Since the correlation is proportional to the complex amplitude factor  $\underline{w}_{l\omega}^*$ , which does not affect the position of the maxima of the estimated correlation (3), and the DR may be determined by finding the wavevectors that maximize the expression:

$$Y_\omega = \left| \sum_{l=1}^L \underline{w}_{l\omega} \exp(-ik_t x_l) \Delta x_l \right|, \quad (5)$$

which will be called "the correlation function" in further text, for each of the angular frequencies  $\omega$  in the range  $\omega^{min} < \omega < \omega^{max}$  where DR is determined. As it may be seen, the correlation method does not make any assumption, nor imposes any limitation, on the number and the positions of data measurement points  $x_l$ , which, together with its simplicity, represents the fundamental advantage of the method. In the case of equidistant measurement points  $x_l = l \cdot d$ , the correlation function takes the form

$$Y_\omega = \left| \sum_{l=1}^L \underline{w}_{l\omega} \exp(-i \cdot l \cdot d \cdot k_t) \right|, \quad (6)$$

with  $d$  being the distance between the measurement points.

The method was successfully used for determination of DR in steel and composite plates [10], and a later modification of the method [11], which uses damped plane waves for construction of the test wavefields, was successfully used for materials with high material losses.

## 2. THEORY

The key conceptual problems of the implementation of the correlation method lie in the fact that the concept of the method is based on the **existence of a unique value of test wavevector  $k_t$  that maximizes the correlation, given by the integral (3)**. There are two aspects of the concept that represent the problem for implementation:

A1: An integral is a mathematical operator defined for a continuous function as an integrand, so calculation of the integral in (3) requires knowledge of a continuous FRF  $\underline{w}(x, t)$ ;

A2: The correlation  $\underline{W}_\omega(k_t)$ , as defined in (3), is a continuous function of the test wavenumber  $k_t$ ;

However, the discrete nature of the digital computer calculations prevents complete implementation of the concept of continuity of mathematical functions, reducing the continuous functions to a representation by discrete arrays of pairs of arguments and values of functions in the process known as *discretization of continuous mathematical functions*.

The discretization of FRF in space is made by its measurement in finite number of measurement points measurement points  $x_l$  ( $l = 1, 2, \dots, L$ ), and its further implementation using the equations (4)-(6) leads to "picket-fence" effect, the well-known phenomenon that two signals become indistinguishable if they are sampled in a finite number of measurement points where they have equal values. Omnipresent in discrete data analysis [12], the "picket-fence" effect is best known as the cause of the *temporal aliasing* in frequency analysis, while in this case, since the discretized variable is space, it causes *spatial aliasing*. The spatial aliasing arises because for any given value of wavevector  $k_t$ , there is an infinite number of wavevectors  $k_t' \neq k_t$  such that for each measurement point  $x_l$  holds:

$$\exp(-ik_t' x_l) = \exp(-ik_t x_l) \quad (l = 1, 2, \dots, L), \quad (7)$$

As a consequence, the wavefields with complex amplitudes given by equation (2), constructed using wavevectors  $k_t$  and  $k_t'$  are indistinguishable in the measurement points, and, therefore, they have equal estimations for correlation with experimental data. It further means that in an interval  $k_t^{min} < k_t < k_t^{max}$  there may be several wavevector values with equal correlation with the measurement data as any selected  $k_t$ , and, in particular, that **there may exist more than one value of test wavevector  $k_t$  that maximizes the correlation function given by (5)**, which opposes to the concept of the method expressed at the beginning of the chapter.

When the measurement points are equidistant, hence when  $x_l = l \cdot d$ , then the condition of indistinguishability of two test wavefields, expressed by the equation (7), reduces to

$$\exp(-ik_t' l d) = \exp(-ik_t l d) \quad (l = 1, 2, \dots, L), \quad (9)$$

which may be expressed as

$$\exp(i[k_i' - k_i]d) = 1, \quad (10)$$

resulting in

$$k_i' - k_i = z \frac{2\pi}{d}. \quad (11)$$

Therefore, if the measurement data are equidistant, with the distance between the measurement points being  $d$ , then the correlation function (5) is periodic, with the period  $2\pi/d$ , as it is shown in Figure 1.

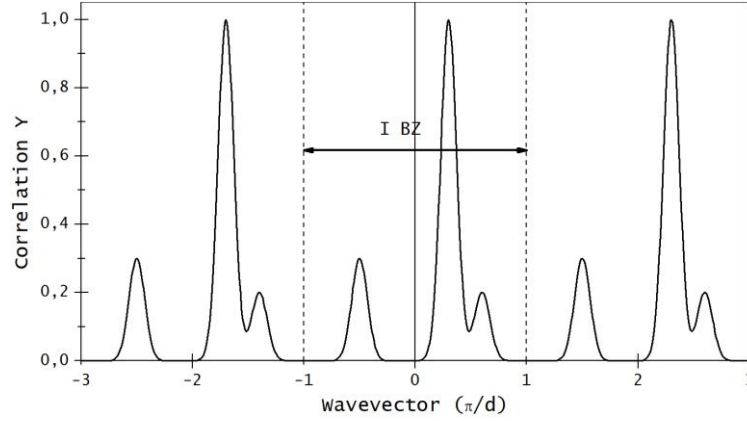


Figure 1: Periodic correlation function in the case of equidistant measurement points and the limits of the IBZ

One way to ensure that the correlation method leads to correct results is to reduce the scanned wavevector range  $k_{min} < k_i < k_{max}$  to one period of the correlation function (5). In its famous treatise of propagation of waves in periodic structures [14], Leon Brillouin has shown that two one-dimensional progression waves with wavevectors  $k_i$  and  $k_i'$ , which propagate through periodic structures with period  $d$ , cannot be distinguished by both amplitude and direction if the wavevectors satisfy the equation (11). For those reasons, he argued that the periodic structures act as low-frequency filters that enable propagation of waves in both directions, so that only the waves with wavevectors in the range  $-\pi/d < k < +\pi/d$  may propagate through such structures. The wavevector range is called *the first Brillouin zone* (abbreviated as IBZ) and it is of fundamental importance in quantum mechanics of solids. While the theoretical model used to study the flexural waves propagation in thin beams, and for derivation of the equation (1), considers a thin beam to be a continuous medium, so that the periodicity of the correlation function (5) is only an artefact introduced by the finite number of measurement points  $L$ , the obtained experimental data are exactly the same as they would be in the case of a periodic structure, so that the obtained results may be properly interpreted only by limiting to the wavevectors within the first Brillouin zone.

The limitation of the wavevectors range for experimental determination of DR to

$$|k| < k_{BZ} = \frac{\pi}{d} \quad (12)$$

means, according to the equation (1), the respective reduction of the frequency range where the DR is determined to

$$f < f_{BZ} = \frac{1}{2\pi} \sqrt{\frac{EI}{\rho A}} \left( \frac{\pi}{d} \right)^2 = \frac{\pi}{2d^2} \sqrt{\frac{EI}{\rho A}} \quad (13)$$

This relationship between the frequency range for experimental determination of the DR and the average

If the measurement points are not equidistant, then the correlation function is not periodic in wavevector space, but the system of equations (7) still has an infinite number of solutions for any selected value of  $k_i$ , and the average difference between the solutions is close to  $(2\pi/d)$ , where  $d$  is the average distance between the measurement points [13].

distance between the measurement points may be used to determine the maximal distance  $d_{max}$  between the measurement points that may be used to determine DR by correlation method in a frequency range  $f < f_{max}$ ,

$$d_{max} = \sqrt[4]{\frac{EI}{\rho A}} \cdot \sqrt{\frac{\pi}{2f_{max}}} \quad (14)$$

### 3. EXPERIMENT

In order to experimentally verify the derived relationship (14), two experiments were carried out. The average distance between the measurement points in one experiment was satisfying the condition (14), while in the other experiment the condition (14) was not met. Each of the experiments comprised a series of subsequent measurements of time history of acceleration  $a_x(t)$  at a single point of a beam excited by impact hammer.

The measurement object was a steel rod with length  $D \approx 1,65$  m, and roughly square cross-section with side  $b \approx 1$  cm. Therefore, the area of the cross-section of the rod was  $A = b^2 \approx 1 \cdot 10^{-4}$  m<sup>2</sup>, while the moment of inertia of the cross-section of the rod for flexion was  $I = b^4/12 \approx 8,33 \cdot 10^{-10}$  m<sup>4</sup>.

The vibrations were excited by the impact hammer B&K 8204 with sensitivity 30.89 mV/N, and the excitation was measured by the B&K Pulse system with CCLD input with range  $\pm 10$ V, so that force measurement range was around 300 N. The impact hammer is light and small, and it is equipped with a light and hard impact head, so that the bandwidth of the impact hammer is broad, up to 10 kHz.

Automatic double-hit detection was not provided, so that each excitation hit was monitored by inspecting the time history of impacting force  $F(t)$ , and the double-hits were discarded.

The rod was hit close to one of its ends, at the area  $x = 0-1$  cm from the beginning of the rod. The hitting area was covered by a piece of scotch-tape that provided a bit of dampening to the hit with the aim to reduce excessive accelerations, which prevented recording of the response

by the software used for data acquisition, but it also reduced the bandwidth to around 6 kHz. The maximal impact force was in the range 8-12 N.

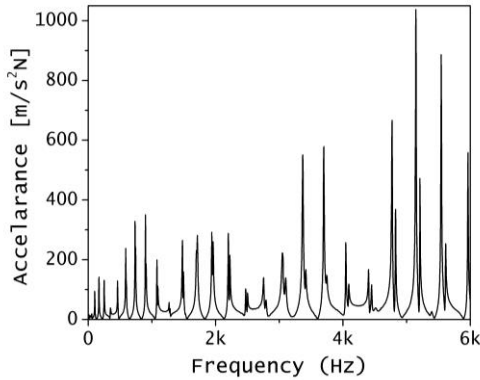


Figure 3: FRF of acceleration at point  $x = 90$  cm from beginning of the rod

The response was measured using the accelerometer B&K 4507Bx with sensitivity  $10.055 \text{ mV/ms}^{-2}$  and B&K Pulse system with CCLD input with range  $\pm 10\text{V}$ , so that so that acceleration measurement range was around  $\pm 1000 \text{ m/s}^2$ .

For each of the measurement points the measurements of acceleration were taken 10 times. During each of the measurements were recorded time histories of excitation force and acceleration. After each of the measurements, the data acquisition software calculated power spectral density of force and acceleration, FRF of acceleration, and the respective coherence.

The measurements were organized in two series – experiments, with the aim to test both the case when the average distance between the measurement points satisfy the equation (14) and the case when they do not satisfy it. Since the frequency range determined by the experimental setup is limited to  $f_{\max} = 6 \text{ kHz}$ , the maximal average distance between the measurement points that would, by the equation (14), allow to experimentally determine DR in the range  $f < f_{\max}$  is  $d_{\max} \approx 6,1 \text{ cm}$ , which is calculated using the values  $E = 200 \text{ GPa}$  and  $\rho = 7800 \text{ kg/m}^3$  for Young modulus and density of steel.

In the first experiment, the measurement points were uniformly distributed at 10 equidistant positions with distances  $d \approx 15 \text{ cm}$ , so that  $d > d_{\max}$ , and the corresponding frequency of the border of the IBZ was  $f_{\text{BZ}} \approx 1010 \text{ Hz}$ .

In the second experiment, 31 non-equidistant measurement points were selected to have the distances to the beginning of the rod (the excited end) being 7.5 cm, 8.7 cm, 11.1 cm, 13.5 cm, 18.3 cm, 20.7 cm, 25.5 cm, 27.9 cm, 32.7 cm, 39.9 cm, 42.3 cm, 49.5 cm, 54.3 cm, 56.7 cm, 61.5 cm, 68.7 cm, 75.9 cm, 78.3 cm, 85.5 cm, 90.3 cm, 92.7 cm, 99.9 cm, 104.7 cm, 111.9 cm, 121.5 cm, 126.3 cm, 128.7 cm, 133.5 cm, 135.9 cm, 140.7 cm and 157.5 cm, which is proportional to the first 31 prime numbers sequence 2, 3, 5, 7, 11, 13, 17, 19, 23, 29, 31, 37, 41, 43, 47, 53, 59, 61, 67, 71, 73, 79, 83, 89, 97, 101, 103, 107, 109, 113 and 127. The average distance between the points was  $d \approx 5 \text{ cm}$ , so that  $d < d_{\max}$ , and the corresponding frequency of the border of the IBZ was  $f_{\text{BZ}} \approx 9090 \text{ Hz}$ .

## 4. RESULTS

### 4.1. Frequency response spectra

The acceleration amplitude spectra revealed the expected resonant behaviour (Figure 3). The resonant frequencies present in all spectra are the same, but the amplitudes of the FRFs at different resonant points show different behaviours at different points. The frequency with maximal amplitude shows dependence on the measurement point. The resonant peaks at low frequencies (14 Hz – 590 Hz) are singlets, while at higher frequencies the resonant peaks appear to be doublets, with the frequency split of the doublets increasing with resonant frequency.

### 4.2. Correlation function

The calculated correlation functions show the predicted behaviour. In the first case, with equidistant measurement points, the correlation function is periodic, with period  $2\pi/d \approx 21 \text{ m}^{-1}$ . In Figure 4 are shown correlation function values calculated for the case of equidistant measurement points at frequency  $f = 200 \text{ Hz}$ . The theoretical equation (1) for that frequency predicts the corresponding value of wavevector to be  $k_0 \approx 9,3 \text{ m}^{-1} \approx 0,44 (\pi/d)$ . Figure 4 shows that, as explained, not only values  $\pm k_0$ , but also other values that satisfy condition (11) represent strong local maxima of the correlation function, requiring limitation of the wavevectors to the IBZ for experimental detection of the DR.

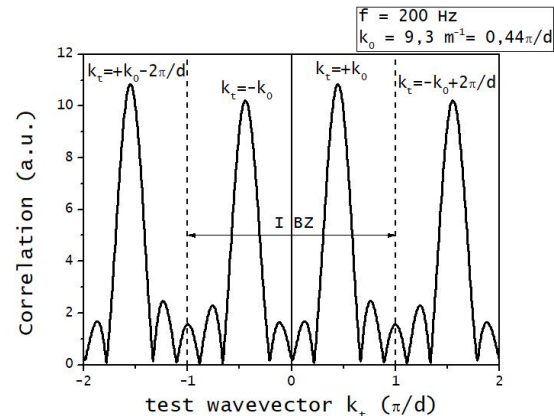


Figure 4: Correlation function for the case of equidistant measurement points

### 4.3. Dispersion relationships

In this section are presented results of the application of the correlation method for experimental calculation of the DR.

#### 4.3.1. Average distance larger than $d_{\max}$

The results of the application of the correlation method to the measurements taken in equidistant measurement points with distance  $d \approx 15 \text{ cm}$ , with the correlation function calculated for test values of wavevectors in the range  $(0, +5\pi/d)$ , are shown in Figure 7. The pairs of corresponding wavevector–frequency values that represent the experimentally determined DR are presented with full circles. The line that passes through origin represent the DR theoretically predicted by (1). The other lines represent the aliases, i.e., the wavevector values that satisfy condition (11) with respect to the theoretically predicted DR. There are two kinds of aliases, the increasing aliases

that have positive slope, and the decreasing aliases, which have negative slope. The positive slope (positive group velocity  $d\omega/dk$ ) of increasing aliases indicates energy transfer in the direction of  $x$ -axis, which means that increasing aliases represent aliases of the waves propagating in the direction of incidence of the excited waves. Conversely, the decreasing aliases represent aliases of the waves propagating in the opposite direction. It should be noted that the decreasing aliases have positive phase velocities ( $\omega/k > 0$ ) and negative group velocities ( $d\omega/dk < 0$ ) because they represent aliases of the negative solutions of equation (1) for wavenumbers.

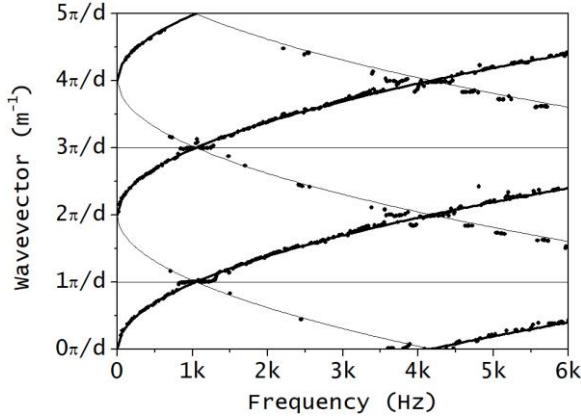


Figure 7: Wavevectors detected by the straightforward implementation of correlation method to equidistant measurements with  $d \approx 15$  cm ( $\pi/d \approx 21$  m<sup>-1</sup>)

The Figure 7 clearly shows that the detected values of wavevectors corresponding to frequencies used in the experiment belong to different aliases of wavevector values with respect to the values predicted by (1), and that the correlation method is not capable of distinguishing them. Majority of the wavevectors calculated by correlation method describe waves propagating in the direction of  $x$ -axis, but some of them describe waves propagating in the opposite direction, so that correlation method is not capable of detecting even the direction of propagation of the wave, as explained by Brillouin [14].

However, if the range of test wavevectors is reduced to the IBZ according to the equation (12), the obtained results are shown in the Figure 8. The circles and lines have the same meanings as in the Figure 7. The first feature of the obtained results is that, with reduction to  $|k| < \pi/d$ , the correlation method, as predicted, leads to correct determination of DR within the frequency range  $f < f_{BZ}$ . The lines in that frequency range represent theoretical predictions given by (1). Furthermore, almost all detected wavenumbers represent the waves propagating in the direction of  $x$ -axis, with the only exception occurring for a frequency where doublet resonances are observed. The mere existence of the doublets, otherwise not predicted by the theory, indicates that, under resonant conditions, the experimental setup does not satisfy the assumptions requested by the theoretical model that leads to (1). The existence of the doublets is still not properly explained and is worthy of further research.

The application of the correlation method for frequencies above  $f_{BZ}$  leads to aliasing, as the waves with wavevectors  $|k| > \pi/d$  have the same accelerations in measurement points as the waves with corresponding wavevec-

tor values in the IBZ. The lines in the frequency range  $f > f_{BZ}$  represent the aliases of the theoretical predictions given by (1). It may be noted that the majority of the waves experimentally detected by the correlation method have positive group velocities, and that the sign of experimentally determined phase velocity depends on the wavenumber so that phase velocity is positive if the wavenumber is between even and odd multiples of  $\pi/d$  (hence between  $(2z)\pi/d$  and  $(2z+1)\pi/d$ ), while phase velocity is negative if the wavenumber is between odd and even multiples of  $\pi/d$  (hence between  $(2z+1)\pi/d$  and  $(2z)\pi/d$ ). Therefore, the group velocity may be correctly determined by correlation method even for frequencies higher than above  $f_{BZ}$ , but the phase velocity cannot.

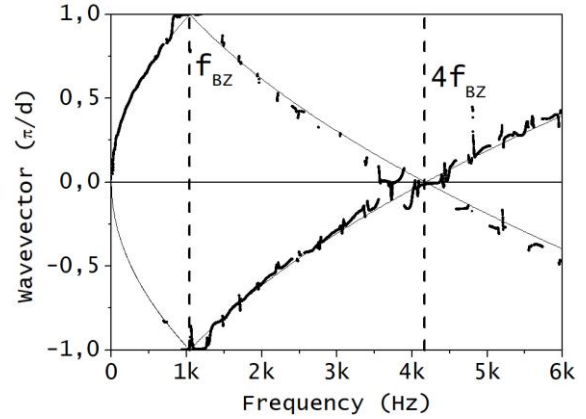


Figure 8: Dispersion relationship from Fig.7 reduced to the first Brillouin zone ( $\pi/d \approx 21$  m<sup>-1</sup>)

A notable deviation from the theoretical predictions is observed in vicinity of borders of the Brillouin zones, where  $k = z\pi/d = z \cdot k_{BZ}$  and, according to the equation (1),  $f = z^2 \cdot f_{BZ}$ . The borders of the Brillouin zones are marked by the thick vertical dotted lines in the Figure 8, and experimentally detected wavevectors are almost independent of the frequency in the frequency ranges around the borders. Since the Brillouin zones are only the consequence of equidistant spatial distribution of measurement points, the observed departure from monotonicity has also to be an artefact introduced by the experimental setup. The explanation of the observed behaviour represents a different phenomenon related to the experimental technique of measuring DRs, and it will be discussed in a separate paper [15].

#### 4.4. Average distance smaller than $d_{max}$

Figure 10 presents the results of application of the correlation method to the measurements taken in the second experiment, with non-equidistant measurement points, and with average distance  $d = 5$  cm being smaller than the maximal distance  $d_{max}$  corresponding to the frequency range  $f < 6$  kHz.

The figure shows that the experimentally obtained DR agrees with the theoretical predictions in the whole frequency range used in the experiment. As it was the case with the measurements with  $d > d_{max}$ , almost all detected wavevectors describe the waves propagating in the direction of  $x$ -axis, with the exceptions for frequencies that correspond to the observed doublet resonances.

## 5. CONCLUSIONS

The paper presented an analysis of the concept for determination of dispersion relationship of flexural waves in beams using correlation method. It was shown that the spatial aliasing restricts applicability of correlation method in experiments with equidistant measurements to the first Brillouin zone of wavevector space, which reflects in reduction of the frequency range for application of the correlation method. The derived analytical expression (14) determines the maximal average distance between the measurement points  $d_{max}$  that enables application of the correlation method for experimental determination of DR in thin beams in the selected frequency range  $f < f_{max}$ .

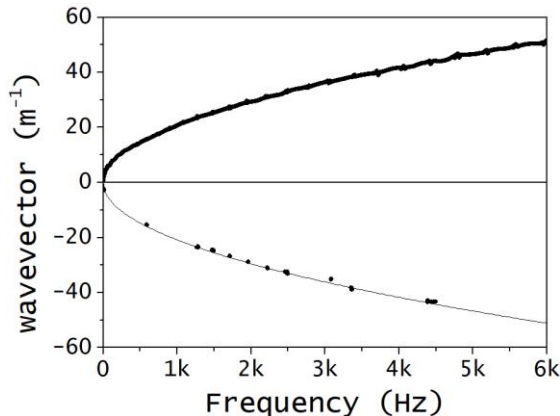


Fig. 9: Wavevectors detected by the correlation method with the average distance between the measurements  $d \approx 5 \text{ cm} < d_{max}$

Two experiments that were carried out confirmed the validity of application of the expression (14). The results of the experiment with  $d < d_{max}$  were in perfect agreement with the theoretical predictions (1), while the results of the experiment with  $d > d_{max}$  agreed with the theoretical predictions only in the limited frequency range where  $f < f_{BZ}$ . Therefore, the obtained results may be useful for planning the experiments for determination of the DR of flexural waves in thin beams, but may also be used as a starting point for experimental determination of other waves in other mechanical structures.

## ACKNOWLEDGEMENTS

The authors wish to express their gratitude to prof. Neil Fergusson from Institute of Sound and Vibration of University of Southampton for inspiration and support to this research effort.

The authors also wish to acknowledge the support of Ministry of Education, Science and Technology Development of Republic of Serbia through Grant 451-03-9/2021-14/200108.

## REFERENCES

- [1] V. Sindelić, S. Ćirić-Kostić, A. Nikolić and Z. Šoškić, "Extension of the frequency range for experimental determination of dispersion relationship of flexural waves in beams by correlation method", *IMK-14 – Research & Development in Heavy Machinery* Vol. 26(4), pp. 95-107 (2020) doi:10.5937/IMK2004095S
- [2] J. Tomić, V. Sindelić, S. Ćirić Kostić, N. Bogojević and Z. Šoškić, "Artificial neural network approach to extension of the frequency range for experimental determination of dispersion relationship using sparse spatial data", *Proceedings of the 16<sup>th</sup> International Conference „Acoustics & Vibration of Mechanical Structures AVMS 2021”*, Timișoara (Romania), May 28-29, 2021 (to be published)
- [3] F. Lucklum and M.J. Vellekoop, "Bandgap engineering of three-dimensional phononic crystals in a simple cubic lattice", *Applied Physics Letters*, Vol. 113(20), p.201902 (2018)
- [4] J. G. McDaniel, P. Dupont, and L. Salvino, "A wave approach to estimating frequency-dependent damping under transient loading", *Journal of Sound and Vibration*, Vol. 231(2), 433-449 (2000)
- [5] J.G. McDaniel and W.S. Shepard Jr, "Estimation of structural wave numbers from spatially sparse response measurements", *The Journal of the Acoustical Society of America*, Vol. 108(4), 1674-1682 (2000)
- [6] C.F. Beard, "Structural Vibrations – Analysis and Damping", Elsevier, Oxford, (UK) (1996)
- [7] W.M. Steedly, C-H. J. Ying, and R.L. Moses, "Statistical analysis of TLS-based Prony techniques", *Automatica*, Vol. 30(1), pp.115-129 (1994)
- [8] D.W. Tufts, and R. Kumaresan, "Estimation of frequencies of multiple sinusoids: Making linear prediction perform like maximum likelihood", *Proceedings of the IEEE* Vol.70(9), pp. 975-989 (1982)
- [9] K. Grosh and E.G. Williams. "Complex wave-number decomposition of structural vibrations", *The Journal of the Acoustical Society of America* Vol. 93(2), pp. 836-848 (1993)
- [10] Ferguson, N.S., Halkyard, C.R., Mace, B.R. and Heron, K.H, "The estimation of wavevectors in two-dimensional structures", *Proceedings of ISMA2002: International Conference on Noise and Vibration Engineering*, Leuven (Belgium) 16 - 18 Sep 2002. pp.799-806 (2002)
- [11] O. Bareille, M. Ichchou, J. Berthaut, and L. Jezequel. "Numerical extraction of dispersion curves from experimental data", *The Second Conference on Noise and Vibration Emerging Methods - NOVEM 2005*, St. Raphael, France (2005).
- [12] D. Havelock, K. Sonoko, and M. Vorländer, eds. *Handbook of signal processing in acoustics*. Springer Science & Business Media, (2008)
- [13] M.W. Maciejewski, H.Z. Qui, I. Rujan, M. Mobli and J.C. Hoch, "Nonuniform sampling and spectral aliasing." *Journal of Magnetic Resonance* Vol. 199 (1) pp. 88-93
- [14] L. Brillouin, "Wave Propagation in Periodic Structures", McGraw-Hill, New York and London (1946)
- [15] V. Sindelić, S. Ćirić Kostić, B. Radičević and Z. Šoškić, "Spatial aliasing and false detection of standing waves in experimental determination of dispersion relationship by correlation method", *Proceedings of the 27<sup>th</sup> International Conference „Noise & Vibration 2021”*, Niš (Serbia), October 27-29, 2021 (to be published)

# Experimental determination of dispersion relationship of polyamide thin beams

Jelena Tomić<sup>1\*</sup>, Vladimir Sindelić<sup>1</sup>, Aleksandar Nikolić<sup>1</sup>, Nebojša Bogojević<sup>1</sup>

<sup>1</sup>Faculty of Mechanical and Civil Engineering, University of Kragujevac, Kraljevo (Serbia)

*Due to its superior mechanical properties, polyamide represents the most frequently used polymer material for additive manufacturing of automotive and aerospace components. With the perspectives of future use for on-site production in space, the field of application is extending to larger structures, raising interest for dynamic behavior of polyamide structures. The paper presents experimental study of dynamic response of thin beams made of three different types of polyamide: polyamide PA6, composite polyamide PA6 with 30% of glass fibers and polyamide PA12 obtained by selective laser sintering of polyamide powder PA2200. The results show that the dynamic response of polyamide beams is similar to metal beams.*

**Keywords: Polyamide, Additive manufacturing, Mechanical waves, Dispersion relationship**

## 1. INTRODUCTION

The global demands for increasing energy efficiency through reduction in weight of motor vehicles and aircrafts and, consequently, reduction of energy consumption lead to increased use of polymers for industrial production [1]. In the past few years, the emergence of new types of polymers with different spectrum of mechanical and thermal characteristics resulted in a significant increase of polymer applications in all spheres of industry production and manufacturing. The application of modern tools for analysis of polymers impact on the environment and decision support for the manufacturing process, such as eco-efficiency assessment model (EEAM), life cycle assessment (LCA) and life cycle cost analysis (LCCA), has shown that the carbon footprint of manufacturing and environmental pollution can be notably reduced [2]. Furthermore, increased attention must be paid to the proper end-of-life disposal of parts made of polymers.

In addition to standard polymers, nowadays the interest for the application of biodegradable polymers in the industrial production has been increasing. Several studies have been conducted in order to determine if biopolyamides as well as PLA (polylactic acid) may replace thermoplastics reinforced by natural fibers that are mainly used in the automotive industry [3].

The aerospace industry usually uses composites - a combination of two or more materials with different physical or chemical properties designed to have specific characteristics, such as added strength, efficiency or durability. With the aim of improving the mechanical properties of parts, composite material most often represents a combination of basic plastics such as polyamide, polypropylene, polyester and carbon fibers [4].

According to the latest analyzes, the automotive industry uses approximately 130 kg of different plastics for the production of one average middle-class passenger vehicle. During the exploitation, the polymer parts embedded in different types of systems are exposed to both mechanical loads and thermal influences.

Since the polyamide usually represents the basic polymer mass for the technical applications, transmission

of vibrations through this material is the subject of study presented in the scope of this paper.

Polyamide (Nylon) is any polymer in which the repeating units in the molecular chain are linked by amide bonds. They are classified into various categories depending on the arrangement and chemical nature of monomers. Nowadays, imperative types of polyamides for technical application are PA6, PA6.6, PA 11, PA 12. Their properties, manufacture, processing and use are covered in the scope of paper [5].

With the development of new production processes, in addition to casting and injection molding, polyamide parts can also be made with additive manufacturing (AM). Due to main advantages of AM technology, such as material costs and waste reduction, production speed and efficiency, as well as the possibility of topology optimization, the aerospace became an early adopter of additive manufacturing. In aerospace industry, these manufacturing processes often use polyamide as a basic polymer for parts production.

Due to the difference in the structure of parts produced by conventional methods of manufacturing and parts produced by AM technology, this paper presents a comparative analysis of dispersion relationships of polyamide beam produced by AM (selective laser sintering) and polyamide beams produced by cutting the extruded plate.

## 2. DISPERSION RELATIONSHIP

Dispersion relationship (abbreviated as "DR" in the following text) expresses the relation between the wavenumber of a wave  $k$  and its angular frequency  $\omega$ . Since it enables calculation of the phase and group velocities of the wave, the DR represents an important tool for wave propagation studies.

Thin beams represent the most convenient object for experimental determination of dispersion relationship. Depending on location and direction of the excitation, different types of mechanical waves may propagate through beams, such as longitudinal compression waves or torsional waves. The simplest mechanical waves for excitation and detection are flexural waves, which have

\*Corresponding author: Jelena Tomić, Dositejeva 19, Kraljevo, tomic.j@mfkv.kg.ac.rs

parabolic form of dispersion relationship **Error! Reference source not found.**

$$\omega = \sqrt{\frac{EI}{\rho A}} k^2 \quad (1)$$

In the equation (1),  $\rho$  stands for density,  $E$  represents Young's modulus of the beam material,  $I$  is the area moment of inertia, while  $A$  represents the area of the cross-section of the beam.

According to the Euler-Bernoulli beam theory for flexural waves in a free-free elastic beam [7], resonances occur when the wavenumber of wave  $k_m$  is equal to  $(2m+1) \cdot k_0$ , where  $k_0 = \pi/(2L)$ , while  $L$  [m] represents the length of the beam's longest dimension. Resonant frequencies can be expressed with  $f_m = (2m+1)^2 \cdot f_0$  with  $f_0 = k_0^2 \cdot (EI)^{1/2} / (\rho A)^{1/2} / (2\pi)$ .

### 2.1. Experimental determination of the DR

Experimental determination of dispersion relationship consists in measurement of the response (usually acceleration) to an excitation (usually impulse or harmonic) in multiple points along the beam. The responses at these points at a particular excitation frequency  $f$  are then used to construct wavefields with wavenumbers that have minimal deviation from the measured responses. There are several methods for wavefield construction and they differ in accuracy, mathematical complexity and range of applicability. The method that is the subject of this paper, so-called correlation method [8], uses a simple form of the wavefield and the sequential search of the wavenumber space in order to find the wavenumber value that provides maximum of correlation between the wavefield and measured response.

In its simplest one-dimensional form, which is used to study the waves propagating along a beam, the correlation method for experimental determination of DR (in further text just "*correlation method*") uses test wavefields constructed on the basis of harmonic progressive waves with angular frequency  $\omega$  and different test wavenumbers  $k_t$ . When the wave propagating along the beam is a progressive harmonic wave with wavenumber  $k$ , then the correlation between the wavefield of the wave and the test wavefield

$$W_\omega(k_t) = \int_{-\infty}^{\infty} \underline{w}(x, \omega) \underline{w}_t^*(x, \omega) dx \quad (2)$$

will have the highest value when  $k_t = k$ . In the expression (2),  $x$ -axis is adopted as the direction of the wave propagation,  $\underline{w}(x, \omega)$  and  $\underline{w}_t(x, \omega)$  represent complex amplitudes of the progressive harmonic wave with wavenumber  $k$  and the constructed wavefield with the wavenumber  $k_t$ , respectively. In order to determine the DR of a wave in a frequency range  $f_{min} < f < f_{max}$ , the correlation method scans the wavenumber space in the range  $k_{min} < k_t < k_{max}$  for each of the frequencies  $f$ , and assumes that the value of  $k_t$  that leads to the highest value of the correlation between the wavefield of the wave and the test wavefield is equal to the wavenumber that corresponds to the frequency  $f$ , denoted as  $k(f)$ .

Due to the discrete nature of input data (amplitudes of accelerances  $\underline{w}(x_l, \omega) = \underline{w}_{l\omega}$  measured in  $L$  measurement points  $x_l$ ,  $l=1, 2, \dots, L$ , along the beam), the correlation (2) may be expressed as the following *correlation function*  $Y_\omega$ :

$$Y_\omega(k_t) = \left| \sum_{l=1}^L \underline{w}_{l\omega} \exp(-ik_t x_l) \Delta x_l \right| \quad (3)$$

The scanning of the wavenumber space in the range  $k_t^{min} < k_t < k_t^{max}$  consists in calculation of  $Y_\omega$  values using equation (3) in a sufficiently large, but still finite number of points within the wavenumber range  $k_t^{(j)}$  ( $j = 1, 2, \dots, J$ ). In the following text, the obtained array of points  $Y_\omega^{(j)} = Y_\omega(k_t^{(j)})$  ( $j = 1, 2, \dots, J$ ) will be called "*the correlation array*". The test wavenumber  $k_t$  that corresponds to the largest member of the correlation array is assumed to be the wavenumber that corresponds to the frequency  $f$ .

The implementation of the correlation method meets the challenges caused by a) the finite number of wavenumber test points; b) the finite number of measurement points.

The finite number of wavenumber test points may lead to omission of the actual wavenumber value that maximizes the correlation function, which results in misidentification of the wavenumber that corresponds to a frequency  $f$ .

On the other hand, due to the finite number of measurement points, for any wavenumber value  $k_t$ , there is an infinite number of wavenumbers  $k_t' \neq k_t$  such that for each measurement point  $x_l$  holds:

$$\exp(-ik_t' x_l) = \exp(-ik_t x_l) \quad (l = 1, 2, \dots, L), \quad (5)$$

As a consequence, there may be several local maxima with the same correlation function value within the wavenumber range  $k_t^{min} < k_t < k_t^{max}$ .

In the case of equidistant measurement points the equality (4) is satisfied for each measurement point if  $k_t' - k_t = z(2\pi/d)$ , where  $z$  is an integer. Therefore, within the wavenumber range  $k_t^{min} < k_t < k_t^{max}$ , the number of equal local maxima of the correlation function is  $(k_t^{max} - k_t^{min})d/2\pi$ . Direct application of the correlation method is thus reduced to the wavenumber range  $-\pi/d < k_t < +\pi/d$ , which is known as the first Brillouin zone (abbreviated as BZ). In the case of non-equidistant measurement points, the system of equations (4) still has an infinite number of solutions and the average difference between the solutions is close to  $(2\pi/d)$ , where  $d$  is the average distance between the measurement points **Error! Reference source not found.**

The restriction of the wavenumbers range to the first BZ reduces the frequency range for the experimental determination of the DR to

$$f < f_{BZ} = \frac{\pi}{2d^2} \sqrt{\frac{EI}{\rho A}} \quad (6)$$

In order to extend the frequency range for experimental determination of dispersion relationship of flexural waves in beams, artificial neural network (ANN) approach presented in the paper [10] has been used. A recurrent neural network (Fig. 1) is developed as a sequence prediction tool for estimation of the wavenumber corresponding to a frequency  $f$  using the wavenumbers of the previously determined points of the dispersion relationship. By implementing the sliding window technique, wavenumber values of the five previous DR points are used as neural network input data, while the difference  $\Delta k$  between two the current and the previous wavenumber values represents the target value at the network output layer. Developed neural network contains one hidden layer with five nodes and one output layer

containing one node. Bipolar sigmoid function and linear function are used as transfer functions of the hidden layer and the output layer, respectively.

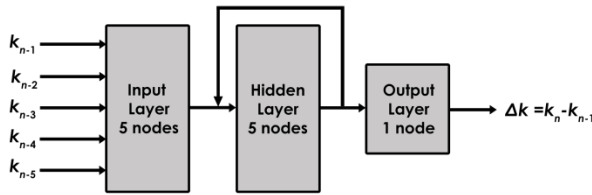


Figure 1: ANN network architecture

In order to define a neural network training data set, the straightforward correlation method has been applied for determination of the DR in a frequency range  $f < f_{BZ}/2$ . Resulted sequence of the wavenumbers has been used for the neural network training process.

For each frequency  $f_n > f_{BZ}/2$ , the wavenumber value is determined using the following steps:

- by using the wavenumbers of five previous points of dispersion relationship as neural network inputs, the wavenumber value  $k_{est}$  corresponding to frequency  $f_n$  is estimated by adding the output of developed ANN to the wavenumber of previous DR point
- the correlation array  $Y_{\omega}^{(j)}$  ( $j=1,2,\dots,J$ ) is calculated using the equation (3) and  $\omega = 2\pi f_n$  for all test wavenumber points  $k^{(j)}$  ( $j = 1, 2, \dots, J$ );
- after finding the local maxima in the obtained correlation array, the candidate array is created by selecting the wavenumbers corresponding to the local maxima such that relative difference between their correlation value and maximal correlation value is smaller than predefined value  $\varepsilon_Y$ ;
- the element of the candidate array closest to the  $k_{est}$  value is selected as the final candidate  $k_{final}$  and its proximity rate is calculated by applying equation:

$$r(k_{final}) = \frac{|k_{final} - k_{est}|}{k_{est}}, \quad (7)$$

- if the proximity ratio of the final candidate is lower than the proximity limit  $\varepsilon_k$ , then the final candidate  $k_{final}$  is accepted as the wavenumber corresponding to the frequency  $f_n$ ; However, if the proximity ratio of the final candidate is higher than the proximity limit, the value  $k_{est}$  is accepted as the wavenumber corresponding to the frequency  $f_n$

### 3. EXPERIMENT

For the purpose of experimental determination of dispersion relationship of mechanical waves propagating through polyamide thin beams, series of subsequent measurements of time history of acceleration  $a_x(t)$  at a single point of a beam excited by impact hammer have been conducted.

#### 3.1. Measurement objects

The experiment has been carried out on the following beams:

- polyamide beam produced by cutting from the plate (PA6 in the following text);
- glass filled polyamide beam produced by cutting from the plate (PA6GF in the following text);
- polyamide beam produced by selective laser sintering (PA3D in the following text);

Characteristics of the measurement objects are given in the Table 1.

Table 1: Properties of the measurement objects

| beam  | Length [cm] | Width [cm] | Height [cm] | $E$ [GPa] | $\rho$ [g/cm <sup>3</sup> ] |
|-------|-------------|------------|-------------|-----------|-----------------------------|
| PA6   | 104         | 1.5        | 1           | 2.9       | 1.13                        |
| PA6GF | 63.8        | 2.3        | 2           | 6         | 1.49                        |
| PA3D  | 30          | 1          | 1           | 1.65      | 8.67                        |

With the aim to emulate a beam with free ends, the end parts of the beams were resting on soft sponges.

#### 3.2. Excitation

The vibrations were excited by the impact hammer B&K 8204 with sensitivity 30.89 mV/N and the bandwidth up to 10 kHz. The excitation was measured by the B&K Pulse system with CCLD input with range  $\pm 10V$ . The force measurement range was around 300 N.

Automatic double-hit detection was not provided. In order to discard the double-hits, each excitation hit was monitored by inspecting the time history of impacting force  $F(t)$ .

The beam was hit at the area 0-1 cm from the beam's beginning. In order to reduce excessive accelerations that prevented recording by the data acquisition software, the hitting area was covered by a piece of scotch-tape which provided a bit of dampening to the hit, but also reduced the bandwidth to around 6 kHz. The maximal impact force was in the range 10-25 N.

#### 3.3. Response

The accelerometer B&K 4507Bx with sensitivity 10.055 mV/ms<sup>-2</sup> and B&K Pulse system with CCLD input with range  $\pm 10V$  were used for measuring the response. Acceleration measurement range was around  $\pm 1000$  m/s<sup>2</sup>.

#### 3.4. Experimental procedure

For each of the beams, the measurements of acceleration were carried out ten times for each of the measurement points. Time histories of excitation force and acceleration were recorded during each of the measurements. After each of the measurements, the data acquisition software calculated power spectral density of force and acceleration, frequency response function (FRF) of acceleration and the respective coherence.

#### 3.5. Measurement points

The measurement points were distributed along the rod's largest dimension at positions with following distances from the beginning of the beam (the excited end):

- PA6 beam: 7.5 cm, 8.7 cm, 11.1 cm, 13.5 cm, 18.3 cm, 20.7 cm, 25.5 cm, 27.9 cm, 32.7 cm, 39.9 cm, 42.3 cm, 49.5 cm, 54.3 cm, 56.7 cm, 61.5 cm, 68.7 cm, 75.9 cm, 78.3 cm, 85.5 cm, 90.3 cm, 92.7 cm and 99.9 cm;

- PA6GF beam: 7.5 cm, 8.7 cm, 11.1 cm, 13.5 cm, 18.3 cm, 20.7 cm, 25.5 cm, 27.9 cm, 32.7 cm, 39.9 cm, 42.3 cm, 49.5 cm, 54.3 cm, 56.7 cm, 61.5 cm;
- PA3D beam: 7.5 cm, 8.7 cm, 11.1 cm, 13.5 cm, 18.3 cm, 20.7 cm, 25.5 cm, 27.9 cm;

The numbers of measurement points for PA6, PA6GF and PA3D beams are 22, 15 and 8, respectively. The distances are derived from the following sequence of prime numbers: 2, 3, 5, 7, 11, 13, 17, 19, 23, 29, 31, 37, 41, 43, 47, 53, 59, 61, 67, 71, 73 and 79. The proportionality of the distances to the prime numbers reduces (practically eliminates) the influence of the aliasing due to the finite length of the measurement points array.

#### 4. RESULTS

For each of the polyamide beams, on the basis of the experimental results and applied correlation method with ANN approach to extension of frequency range, the following graphs have been created:

- a graph of the dispersion relationship between the wavenumber of a wave  $k$  and its frequency  $f$ ,
- a comparison graph of the theoretical and experimental values for the resonant frequencies in the frequency range between 0 Hz to 6 kHz,
- a comparison graph of the theoretical and experimental values for the wavenumbers corresponding to the resonant frequencies in the frequency range between 0 Hz to 6 kHz,
- experimental values of wavenumbers corresponding to resonant frequencies in the frequency range between 0 Hz to 6 kHz for the purpose of visualization of values scattering around the line  $k_m=(2m+1) \cdot k_0$  (theoretically these wavenumbers should lie on the line  $k_m=(2m+1) \cdot k_0$ ).

Comparisons of theoretical and experimental values of fundamental frequency  $f_0$ , corresponding wavenumber  $k_0$  and  $b_{kf}$  parameter ( $b_{kf}=k/f^{1/2}$ ) are represented tabular for each of the polyamide beams. Theoretical values are calculated based on the values of density and Young's modulus of elasticity obtained from the manufacturer's specification.

##### 4.1. PA6 beam

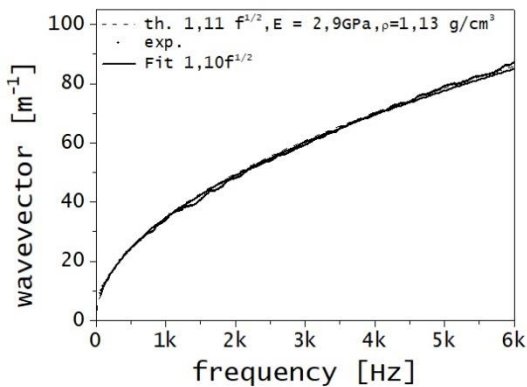


Figure 2: Dispersion relationship for PA6 beam

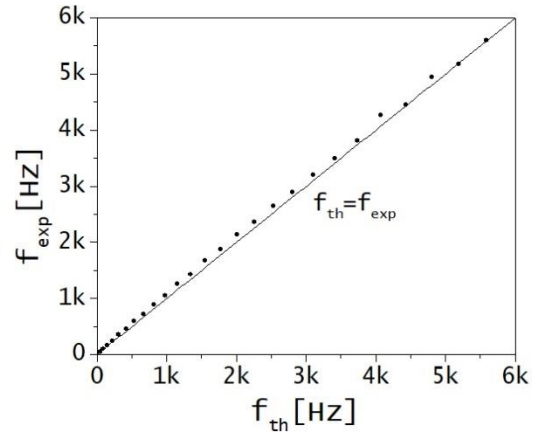


Figure 3: Comparison between theoretical and experimental values of resonant frequencies for PA6 beam

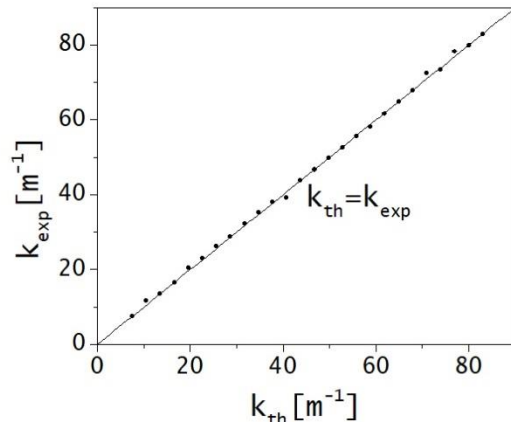


Figure 4: Comparison between theoretical and experimental values of wavenumbers corresponding to the resonant frequencies for PA6 beam

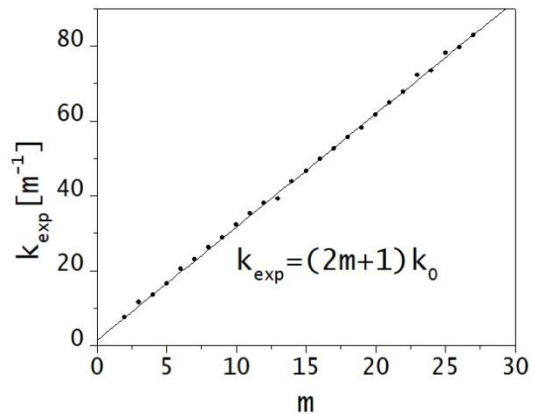


Figure 5: Experimental values of wavenumbers corresponding to resonant frequencies for PA6 beam

Table 2: Comparisons of theoretical and experimental values of  $f_0$ ,  $k_0$  and  $b_{kf}$  parameters for PA6 beam

|          | Theory | Experiment | Relative diff |
|----------|--------|------------|---------------|
| $k_0$    | 1.51   | 1.52       | 1%            |
| $f_0$    | 1.85   | 1.96       | 6%            |
| $b_{kf}$ | 1.11   | 1.09       | -2%           |

4.2. PA6GF beam

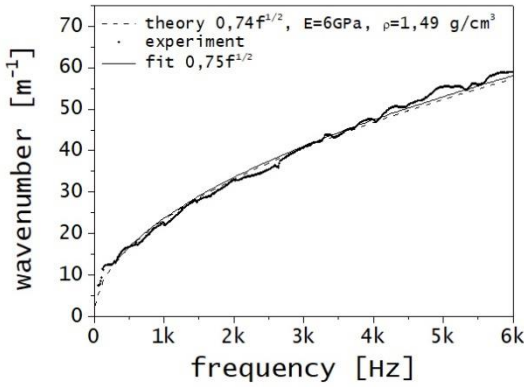


Figure 6: Dispersion relationship for PA6GF beam

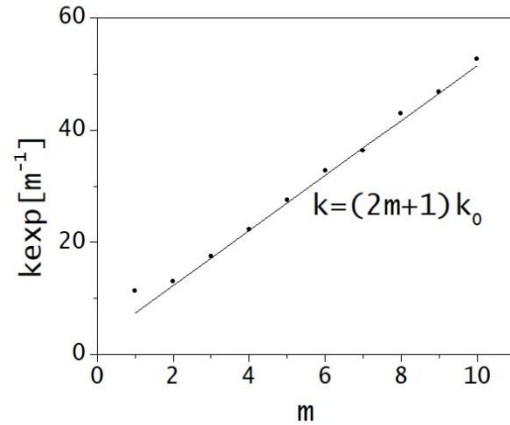


Figure 9: Experimental values of wavenumbers corresponding to resonant frequencies for PA6GF beam

Table 3: Comparisons of theoretical and experimental values of  $f_0$ ,  $k_0$  and  $b_{kf}$  parameters for PA6GF beam

|          | Theory | Experiment | Relative diff |
|----------|--------|------------|---------------|
| $k_0$    | 5.24   | 5.15       | -2%           |
| $f_0$    | 11.12  | 11.80      | 6%            |
| $b_{kf}$ | 0.74   | 0.73       | -1%           |

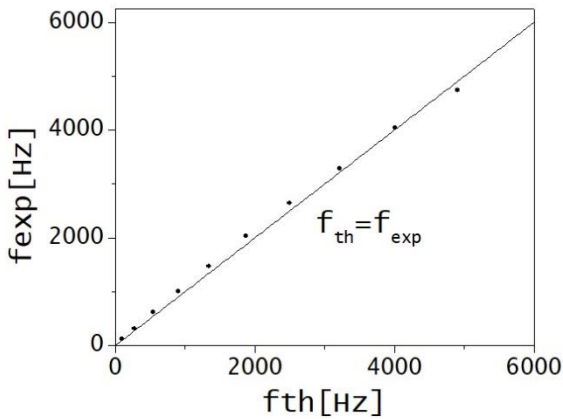


Figure 7: Comparison between theoretical and experimental values of resonant frequencies for PA6GF beam

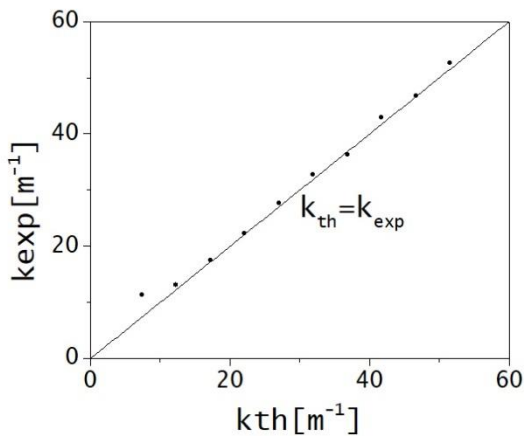


Figure 8: Comparison between theoretical and experimental values of wavenumbers corresponding to the resonant frequencies for PA6GF beam

4.3. PA3D beam

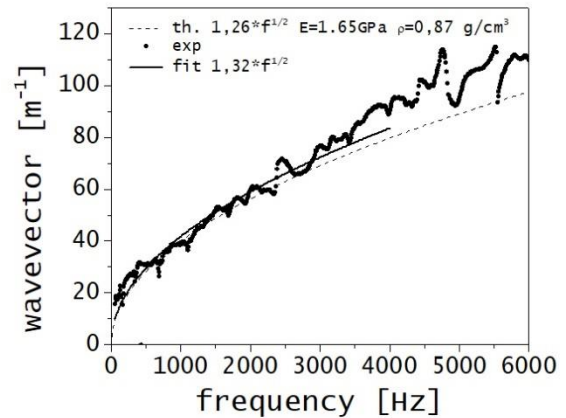


Figure 10: Dispersion relationship for PA3D beam

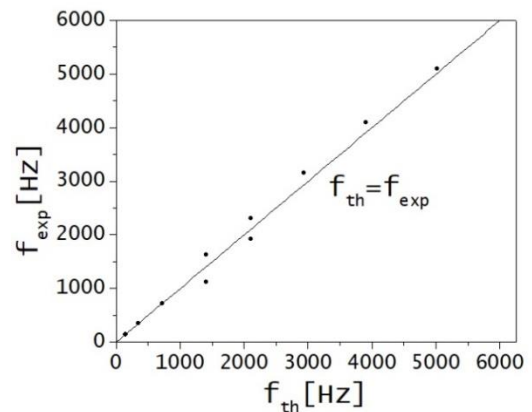


Figure 11: Comparison between theoretical and experimental values of resonant frequencies for PA3D beam

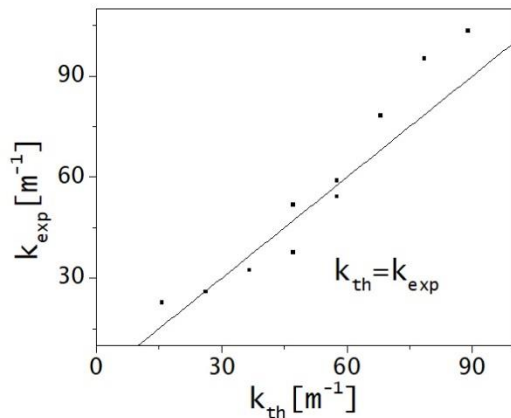


Figure 12: Comparison between theoretical and experimental values of wavenumbers corresponding to the resonant frequencies for PA3D beam

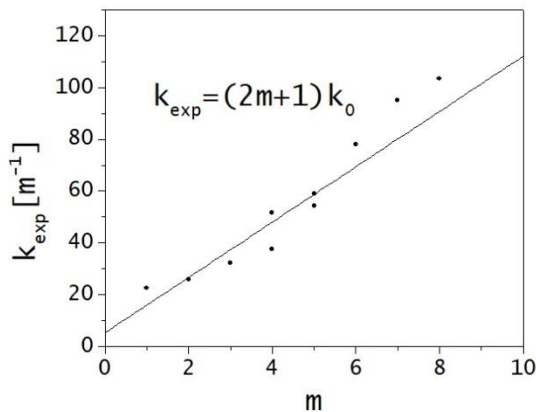


Figure 13: Experimental values of wavenumbers corresponding to resonant frequencies for PA3D beam

Table 4: Comparisons of theoretical and experimental values of  $f_0$ ,  $k_0$  and  $b_{kf}$  parameters for PA3D beam

|          | Theory | Experiment | Relative diff |
|----------|--------|------------|---------------|
| $k_0$    | 5.24   | 5.15       | -2%           |
| $f_0$    | 17.38  | 17.04      | -2%           |
| $b_{kf}$ | 1.26   | 1.25       | -1%           |

The obtained results show good agreement between the experimental and theoretical values for all three polyamide beams which were the objects of conducted analysis.

For the polyamide beam produced by selective laser sintering, slightly larger deviations between theoretical and experimental results (as shown in the Figures 10 to 13 and the Table 4) are due to the relatively short beam's length compared to the lengths of the other two beams and, consequently, fewer measurement points and smaller amount of experimental data for the further analysis. Furthermore, the cross-sectional area of the rod produced by selective laser sintering is 1.5 and 4.6 times smaller than the cross-sectional areas of the other two polyamide rods cut from extruded plates, and, therefore, the mass of this rod is significantly smaller.

## 5. CONCLUSION

This paper presents a methodology for the experimental determination of the dispersion relationship of polyamide thin beams. The experiments were conducted on polyamide rods produced by cutting the extruded plates and polyamide rod produced by additive manufacturing (the process of selective laser sintering).

The obtained results show good agreement between the theoretical and experimentally obtained dispersion relationship for all three polyamide rods.

The slightly larger differences between theoretical and experimental values obtained for the rod made by selective laser sintering are due to its smaller dimensions and mass (compared to the dimensions and mass of rods produced by traditional cutting method), which directly affects the number of measurement points and measurement accuracy. Therefore, in further research, appropriate attention should be given to selecting dimensions and mass of the specimens.

## ACKNOWLEDGEMENTS

The authors wish to express their gratitude to prof. Neil Fergusson from Institute of Sound and Vibration of University of Southampton for inspiration and support to this research effort.

The authors also wish to acknowledge the support of Ministry of Education, Science and Technology Development of Republic of Serbia through Grant 451-03-9/2021-14/200108.

## REFERENCES

- [1] Muhammad, A., Rahman, M. R., Bains, R., & Bakri, M. K. B. (2021). Applications of sustainable polymer composites in automobile and aerospace industry. In *Advances in Sustainable Polymer Composites* (pp. 185-207). Woodhead Publishing.
- [2] Al-Lami, A., Hilmer, P., & Sinapius, M. (2018). Eco-efficiency assessment of manufacturing carbon fiber reinforced polymers (CFRP) in aerospace industry. *Aerospace Science and Technology*, 79, 669-678.
- [3] Bodros, E., Pillin, I., Montrelay, N., & Baley, C. (2007). Could biopolymers reinforced by randomly scattered flax fibre be used in structural applications?. *Composites Science and Technology*, 67(3-4), 462-470.
- [4] Toozandehjani, M., Kamarudin, N., Dashtizadeh, Z., Lim, E. Y., Gomes, A., & Gomes, C. (2018). Conventional and advanced composites in aerospace industry: Technologies revisited. *Am. J. Aerosp. Eng.*, 5, 9-15.
- [5] Palmer, R. J. (2001). Polyamides, *Plastics*. Encyclopaedia of Polymer Science and Technology. doi:10.1002/0471440264.pst251
- [6] Beards, C. (1996). *Structural vibration: analysis and damping*. Elsevier.
- [7] Rao, S.S. (2019). *Vibration of continuous systems*. John Wiley & Sons.
- [8] Ferguson, N. S., Halkyard, C. R., Mace, B. R., & Heron, K. H. (2002). The estimation of wavenumbers in two-dimensional structures. *Proceedings of ISMA2002: International Conference on Noise and Vibration Engineering*, Leuven (Belgium), 799-806

- [9] Maciejewski, M. W., Qui, H. Z., Rujan, I., Mobli, M., & Hoch, J. C. (2009). Nonuniform sampling and spectral aliasing. *Journal of Magnetic Resonance*, 199(1), 88-93.
- [10] Tomić, J., Sinđelić, V., Ćirić Kostić, S., Bogojević, N., Šoškić, Z. (2021). Artificial neural network approach to extension of the frequency range for experimental determination of dispersion relationship using sparse spatial data. *Acoustics and Vibration of Mechanical Structures*. Timisoara (Romania)



# Free vibration of double-cracked uniform beam

Aleksandar Nikolić\*

Faculty of Mechanical and Civil Engineering in Kraljevo, University of Kragujevac

*This paper considers free vibration analysis of double-cracked uniform beam under various boundary conditions. It is supposed that cracks stay opened due to vibrations. The Euler-Bernoulli beam model was considered by using the rigid segment method. Satisfactory agreement of the obtained results with the results of other was achieved. In the case of occurrence of larger errors, it was noticed that there is a problem of closing the crack, which deviates from the initial assumption.*

**Keywords:** Double-cracked beam, Free vibration, Uniform beam

## 1. INTRODUCTION

The appearance of cracks leads to a change in the dynamic characteristics of the beam. More precisely, with the appearance of a crack, the stiffness of the beam decreases, which leads to decreasing of natural frequencies of free beam vibrations. The literature dealing with this topic is rich, so its review will not be given here.

This paper is based on the previous research of the author that is published the paper [1], where the rigid segment method was used for free vibration analysis of uniform beam with one open crack under the various boundary conditions.

Here, the usage of the rigid segment method is extended to the double-cracked beam. The position of the cracks and their depths differ from each other in a general case. The case of the free-free beam will be analysed first. All other beam boundary conditions will be provided as a special case of free-free beam.

## 2. APPROXIMATE MODEL OF DOUBLE-CRACKED BEAM

Figure 1(a) shows the double-cracked uniform beam that is analysed in this paper. The beam cross-section is rectangular with dimensions  $b \times h$ . The total beam length is  $L$ , whereas two open cracks of depth  $a_1$  and  $a_2$  are placed at the distances  $L_1$  and  $L_2$ , respectively, measured from the left end of the beam.

In the first step of modelling, the cracked beam was divided into the three beams (*I*, *II* and *III*) of the following lengths:

$$L_I = L_1, L_{II} = L_2 - L_1, L_{III} = L - L_2. \quad (1)$$

The first and the second beam (*I* and *II*), as well as the second and the third beam (*II* and *III*) are connected mutually by the crack elastic joints  $J_{c_1}$  and  $J_{c_2}$ , respectively, as shown in Fig. 1(b).

In the second step of modelling, each of three introduced beams was divided into the  $n_I$ ,  $n_{II}$  and  $n_{III}$  elastic segments, respectively, whereas this numbers are chosen by using the following formula:

$$n_i = \frac{L_i}{L} n, \quad (i = I, II, III). \quad (2)$$

The number  $n$  represents the total number of elastic segments in all of the three introduced beams. The number  $n$  should be chosen so that each of numbers  $n_i$  must be an integer.

The third modeling step involves replacing each of the introduced elastic segments with two rigid segments, interconnected by joint element  $J_i$  with three degrees of freedom, as shown in Figs. 1(c) and (d).

The joint element  $J_i$  has three degrees of freedom: axial, translational and rotational. An appropriate springs are placed in the directions of the introduced degrees of freedom. The rigidity of introduced springs is defined as [1]:

$$k_{p_i} = n \frac{AE}{L}, \quad k_{q_i} = n \frac{EI_z}{L}, \quad k_{r_i} = n^3 \frac{12EI_z}{L^3}, \quad (3)$$

for all values of  $i$  except for  $i=n_1+1$  or  $i=n_1+n_2+2$ , for which, based on the references [2,3] holds that:

$$k_{p_i} = \frac{Eb}{(1-\nu^2)F_{1,j}}, \quad k_{q_i} = \frac{Eb}{(1-\nu^2)F_{2,j}}, \quad (4)$$

$$k_{r_i} = \frac{Eb}{(1-\nu^2)F_{3,j}},$$

where:

$$F_{k,j} = e^{\frac{1-\xi_j}{1-\xi_j} \sum_{i=1}^{10} a_{k,i} \xi_j^i}, \quad \xi_j = a_j / h, \quad (5)$$

$$j = \begin{cases} 1, & i = n_1 + 1, \\ 2, & i = n_1 + n_2 + 2. \end{cases}$$

Note that the parameters  $a_{k,i}$  are listed in the Table 1.

### 2.1 Kinetic energy

Kinetic energy of the approximate model of the double-cracked uniform beam model should be obtained as the positive definite quadratic form [1]:

$$T = \frac{1}{2} \dot{\mathbf{v}}^T \mathbf{M} \dot{\mathbf{v}}, \quad (6)$$

where:

\*Corresponding author: Aleksandar Nikolić, Dositejeva 19, Kraljevo, nikolic.a@mfv.kg.ac.rs

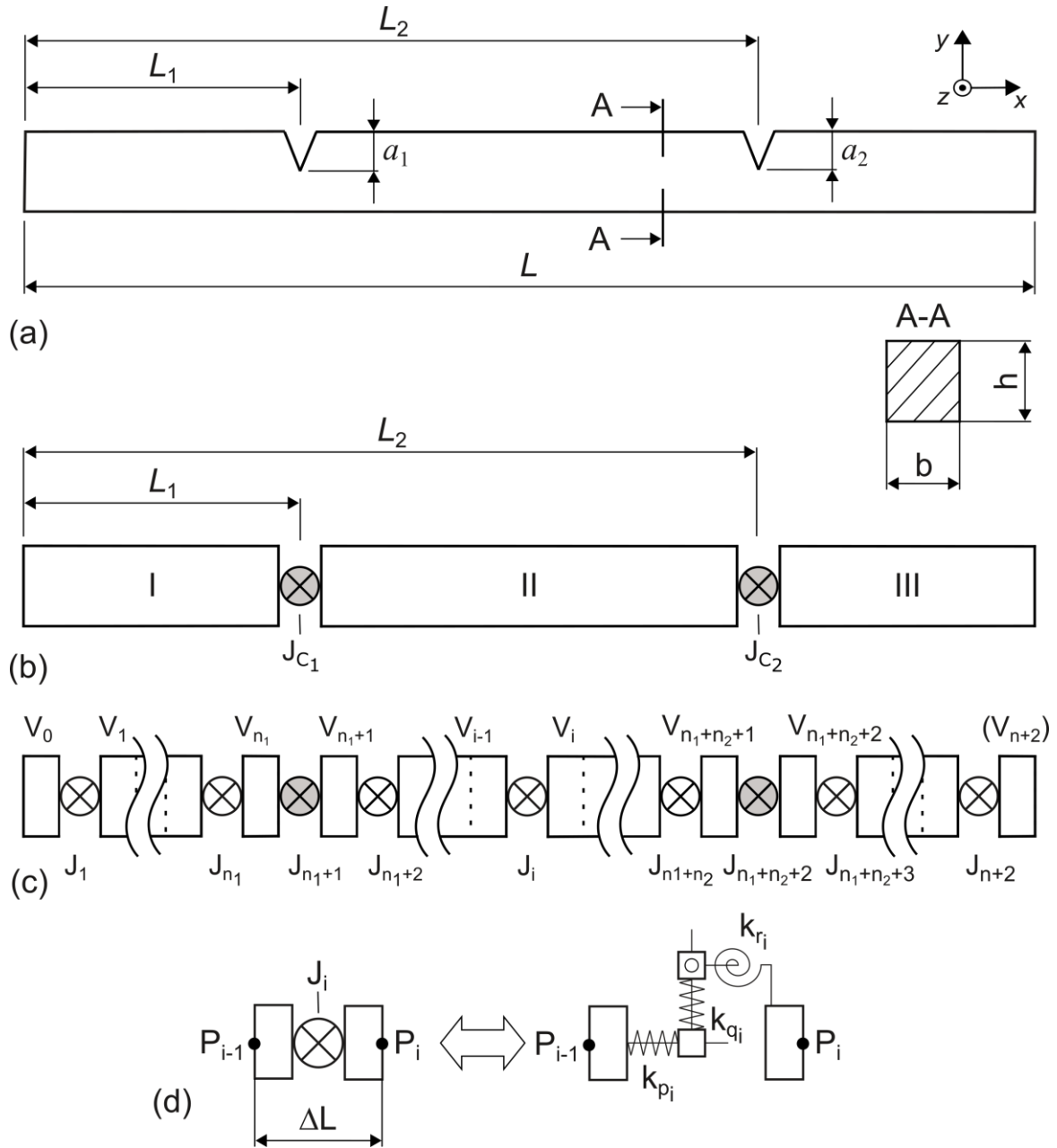


Figure 1 : Double-cracked uniform beam: (a) exact shape, (b) equivalent beam model, (c) rigid segment beam model, (d) joint element  $J_i$

$$\dot{\mathbf{v}} = [\dot{\mathbf{v}}_0^T \quad \dots \quad \dot{\mathbf{v}}_i^T \quad \dots \quad \dot{\mathbf{v}}_{n+2}^T]^T \in R^{3(n+3) \times 1}, \quad (7)$$

$$\mathbf{M} = \text{diag}(\mathbf{M}_0, \dots, \mathbf{M}_i, \dots, \mathbf{M}_{n+2}) \in R^{3(n+3) \times 3(n+3)}, \quad (8)$$

$$\mathbf{M}_i = [m_{jk,i}] \in R^{3 \times 3}, \quad (9)$$

$$m_{11,i} = m_{22,i} = m_i,$$

$$m_{33,i} = J_{C_i \zeta_i} + m_i \left( \overline{PC}_{i, \xi_i}^2 + \overline{PC}_{i, \eta_i}^2 \right),$$

$$m_{12,i} = m_{21,i} = 0,$$

$$m_{13,i} = m_{31,i} = -m_i \overline{PC}_{i, \eta_i},$$

$$m_{23,i} = m_{32,i} = m_i \overline{PC}_{i, \xi_i}, \quad (10)$$

$$m_i = \rho A l_i, \quad J_{C_i \zeta_i} = \frac{1}{12} m_i l_i^2, \quad (11)$$

$$l_i = \begin{cases} \frac{1}{2} \frac{L}{n}, & i = k, \\ \frac{L}{n}, & i \neq k. \end{cases}$$

$$k = n_1 \vee n_1 + 1 \vee n_1 + n_2 + 1 \vee n_1 + n_2 + 2 \vee n + 2, \quad (12)$$

$$\overline{P_i C_i} = \begin{cases} [l_i / 2 & 0 & 0]^T, & i = 0 \vee n_1 + 1 \vee n_1 + n_2 + 2, \\ [-l_i / 2 & 0 & 0]^T, & i = n_1 \vee n_1 + n_2 + 1 \vee n + 2, \\ [0 & 0 & 0]^T, & i \neq k. \end{cases} \quad (13)$$

 Table 1: Coefficients  $a_{k,i}$  of functions  $F_k$ 

| $k \backslash i$ | 1                            | 2                            | 3                            |
|------------------|------------------------------|------------------------------|------------------------------|
| 1                | -0.326584 · 10 <sup>-5</sup> | -0.326018 · 10 <sup>-6</sup> | -0.219628 · 10 <sup>-4</sup> |
| 2                | 1.455190                     | 1.454954                     | 52.37903                     |
| 3                | -0.984690                    | -1.455784                    | -130.2483                    |
| 4                | 4.895396                     | -0.421981                    | 308.442769                   |
| 5                | -6.501832                    | -0.279522                    | -602.445544                  |
| 6                | 12.792091                    | 0.455399                     | 939.044538                   |
| 7                | -26.723556                   | -2.432830                    | -1310.95029                  |
| 8                | 35.073593                    | 5.427219                     | 1406.52368                   |
| 9                | -34.954632                   | -6.643057                    | 1067.4998                    |
| 10               | 9.054062                     | 4.466758                     | 391.536356                   |

## 2.2 Potential energy

Potential energy of the approximate model of the double-cracked uniform beam model should be obtained as the positive definite quadratic form [1]:

$$\Pi = \frac{1}{2} \mathbf{v}^T \mathbf{K} \mathbf{v}, \quad (14)$$

where:

$$\mathbf{v} = [\mathbf{v}_0^T \quad \dots \quad \mathbf{v}_i^T \quad \dots \quad \mathbf{v}_{n+2}^T]^T \in R^{3(n+3) \times 1}, \quad (15)$$

$$\mathbf{K} = \text{diag}(\mathbf{K}_0, \dots, \mathbf{K}_i, \dots, \mathbf{K}_{n+2}) \in R^{3(n+3) \times 3(n+3)}, \quad (16)$$

$$\mathbf{K}_i = \text{diag}(k_{p_i}, k_{q_i}, k_{r_i}) \in R^{3 \times 3}. \quad (17)$$

## 2.3 Eigenvalue analysis

Differential equations of motion should be obtained as [1]:

$$\mathbf{M} \ddot{\mathbf{v}} + \mathbf{K} \mathbf{v} = \mathbf{0} \in R^{3(n+3) \times 1}, \quad (18)$$

which implies the eigenvalue problem in the following form:

$$(\mathbf{K} - \omega_r^2 \mathbf{M}) \mathbf{u}_r = \mathbf{0}, \quad (r = 1, \dots, 3(n+3) \times 1), \quad (19)$$

where  $\mathbf{u}_r$  represents the eigenvector which corresponds to natural frequency  $\omega_k$ . In order to obtain the natural frequencies and their corresponding eigenvectors under different boundary conditions, it is necessary to remove the columns and vectors of the matrices  $\mathbf{M}$  and  $\mathbf{K}$  which correspond to the restricted displacements.

In addition, the proposed model of a double-cracked beam can be adjusted for the analysis of beams with one crack, as well as for beams without cracks. In the case of beam with one crack it is necessary to put into the

proposed algorithm that  $\mathbf{v}_{n_1+n_2+1} \equiv \mathbf{v}_{n_1+n_2+2}$ , as well as in the case of uncracked beam it holds that  $\mathbf{v}_{n_1} \equiv \mathbf{v}_{n_1+1}$  and  $\mathbf{v}_{n_1+n_2+1} \equiv \mathbf{v}_{n_1+n_2+2}$ .

## 3. NUMERICAL EXAMPLES

### 3.1. Beam with one crack

Let's consider here the pinned-pinned (P-P) beam with one crack of the following characteristics:  $L=0.4$  [m],  $b=h=0.01$  [m],  $E=2.16 \cdot 10^{11}$  [N/m<sup>2</sup>],  $\rho=7650$  [kg/m<sup>3</sup>],  $a_1/h=0.5$ ,  $L_1/L=0.5$ .

Results obtained by using the proposed approach, experiment [4], and FEM are given in Table 2. Note that the FEM results are obtained by using Ansys software, whereas 2628 elements of type Solid 185 were used. The results obtained by the proposed approach are very close to the results of the experiment [4] as well as to the FEM results obtained by using Ansys. However, it can be noticed that the relative error increases with increasing order of the required frequency. Thus in the case of the third frequency, the relative error between the results of the proposed approach and FEM is 2.31 [%].

Table 2: Comparison of the first three natural frequencies of the P-P beam with one crack

| Methods                | Natural frequencies [Hz] |                    |                    |
|------------------------|--------------------------|--------------------|--------------------|
|                        | $f_1$                    | $f_2$              | $f_3$              |
| This study ( $n=100$ ) | 140.18                   | 602.24             | 1271.04            |
| FEM                    | 138.96<br>(0.88 %)       | 596.05<br>(1.04 %) | 1242.3<br>(2.31 %) |
| Experiment [4]         | 139.2<br>(0.7 %)         | 593.0<br>(1.56 %)  | -                  |

If we take a closer look at Figure 2, which shows the first three mode shapes of considered beam, it can be seen that the crack is closed in the third mode shape. This is contrary to the main assumption of this paper, that the crack is open all the time of beam vibration. So this fact is a possible reason for a slightly larger deviation of the obtained results in the case of the third frequency.

At this point, it is interesting to comment the influence of the position of the crack on the deviation in the value of the frequencies of the uncracked beam. Figure 3 (a) - (d) shows the change of the first three frequencies of the beam in relation to the corresponding values of the uncracked beam at different positions of the crack, for the most commonly used boundary conditions. The depth of the crack ( $a_1/h$ ) in all considered cases is equal to 0.5. Only in the case of the first frequency of C-F beam, with increasing distance of the crack  $L_1$ , the difference between the frequency of the cracked and uncracked beam decreases. In all other cases of beam boundary conditions, the dependence of the obtained frequencies on the distance of the crack  $L_1$  has an oscillatory character. Also, under symmetrical boundary conditions (P-P, C-C, and F-F), the obtained diagrams are symmetrical with respect to the center of the beam.

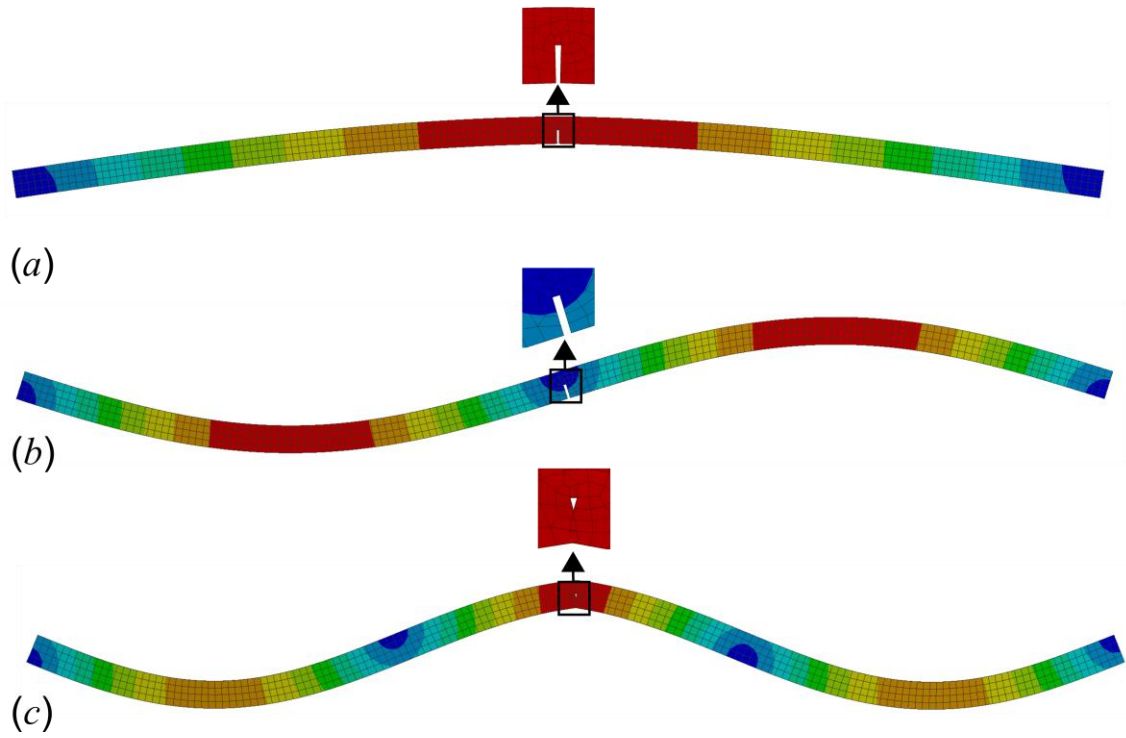


Figure 2: The first three mode shapes of the P-P beam with one crack

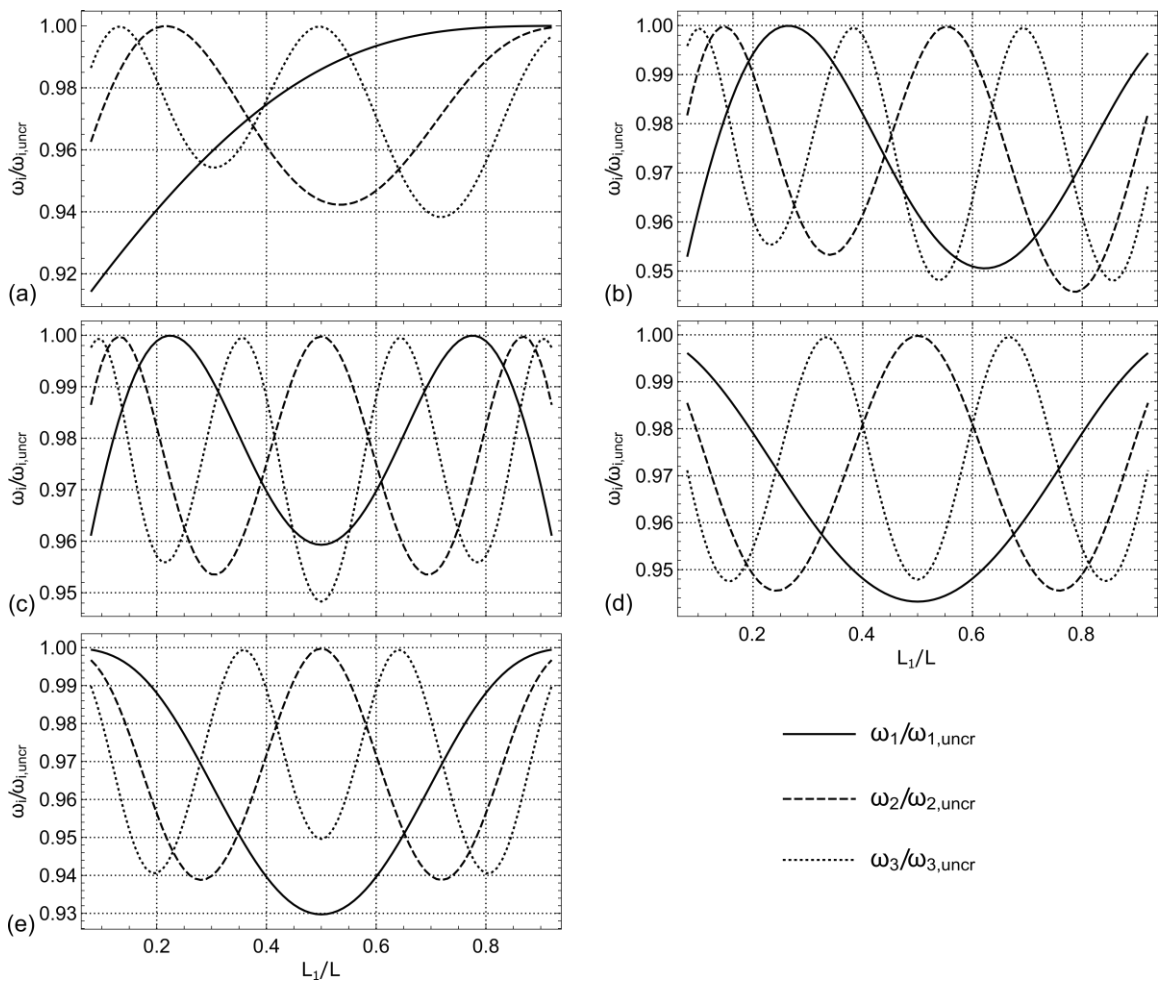


Figure 3: Influence of the crack position to first three natural frequencies of the beam with one crack:

a) clamped-free (C-F), b) clamped-pinned (C-P), c) clamped-clamped (C-C), d) pinned-pinned (P-P), e) free-free (F-F).

### 3.2. Double-cracked beam

Here will be considered double-cracked beam with the cracks depth  $a_1/h = a_2/h = 0.5$ . The distances of the cracks from the left end are  $L_1/L=0.3$  and  $L_2/L=0.7$ . All other beam parameters are the same as in the previous example. Table 2 shows the comparison of the results of this study and FEM at various boundary conditions.

The best results of this study are achieved in the C-F case, where the minimal error is equal to 1.01 % for the first frequency, and maximum error is in the case of third frequency and it is equal to 2.88 %. The worst results are in the case of P-P beam, where errors range from 2.48 % for the first frequency to 3.96 % for the third frequency. These are unexpectedly poor results compared to the previously achieved results of the rigid segment method [1] in the case of a single-cracked beam.

However, if we look at the first three mode shapes of the P-P double-cracked beam, obtained by using Ansys, then it can be seen that in the second mode shape the crack closes. It is obvious that the open crack model used here does not give sufficient accuracy in this case.

Table 2: Comparison of the first three natural frequencies of double-cracked beam at various boundary conditions

| Boundary condition | Methods            | Natural frequencies [Hz] |                 |                  |
|--------------------|--------------------|--------------------------|-----------------|------------------|
|                    |                    | $f_1$                    | $f_2$           | $f_3$            |
| C-F                | This study (n=100) | 50.84 (1.01 %)           | 318.60 (1.10 %) | 826.22 (2.88 %)  |
|                    | FEM                | 50.33                    | 315.14          | 803.09           |
| C-P                | This study (n=100) | 223.21 (1.6 %)           | 692.87 (2.74 %) | 1547.37 (2.31 %) |
|                    | FEM                | 219.7                    | 674.35          | 1512.4           |
| C-C                | This study (n=100) | 334.45 (0.02 %)          | 840.28 (2.35 %) | 1774.87 (1.63 %) |
|                    | FEM                | 334.51                   | 820.97          | 1746.4           |
| P-P                | This study (n=100) | 137.96 (2.48 %)          | 535.22 (3.87 %) | 1345.9 (3.96 %)  |
|                    | FEM                | 134.62                   | 515.26          | 1294.6           |
| F-F                | This study (n=100) | 313.15 (1.87 %)          | 810.03 (3.34 %) | 1762.32 (2.37 %) |
|                    | FEM                | 307.39                   | 783.81          | 1721.6           |

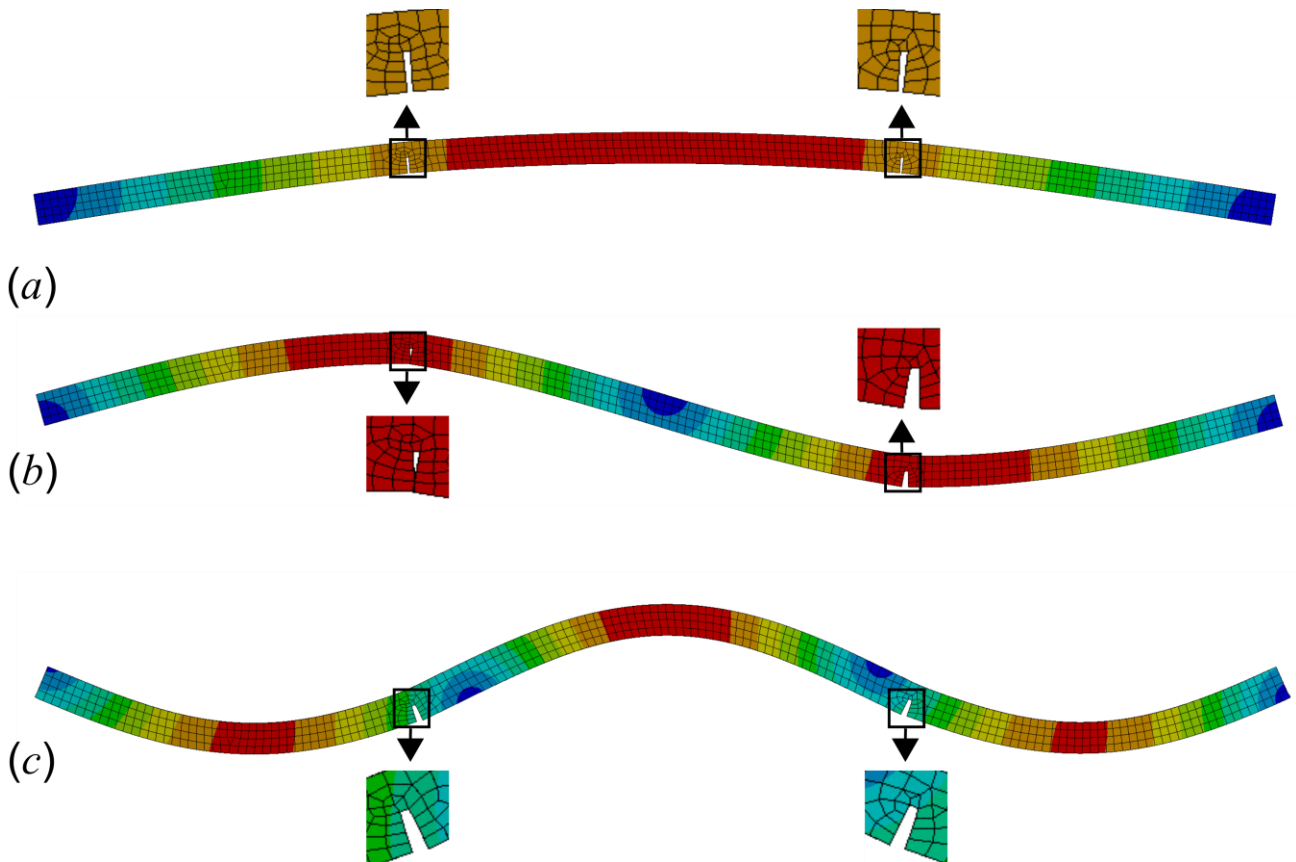


Figure 4: The first three mode shapes of P-P double-cracked beam

#### 4. CONCLUSION

In this paper, the extension of the use of method of rigid segments to beams with two cracks is presented. Although at first glance it seems that the method will be just as effective in the case of the beam with two cracks, as it was the case with the beam with one crack, it is not so. It has been observed that a significantly larger error occurs when the crack closure is observed in one of vibration modes during vibration. Note only that the case where the depth of both cracks is equal to half of the cross-section height is analysed here. It is possible that at smaller crack depths this problem will be less pronounced. This would allow further use of this approach for the case of a beam with an arbitrary number of cracks, which will be the subject of further research by the author.

#### ACKNOWLEDGEMENTS

This research was supported under grant no. 451-03-9/2021-14/200108 by the Ministry of Education, Science and Technological Development of the Republic of Serbia. This support is gratefully acknowledged.

#### REFERENCES

- [1] A. Nikolić and S. Šalinić, "Free vibration analysis of cracked beams by using rigid segment method", *Appl. Math. Model.*, Vol. 84, pp. 158-172, (2020)
- [2] D.Y.Zheng and N.J. Kessissoglou, "Free vibration analysis of a cracked beam by finite element method", *J. Sound Vib.*, vol. 273(3), pp. 457-475, (2004)
- [3] J. Banerjee, S. Guo, "On the dynamics of a cracked beam", *Proceedings of the Fiftieth AIAA/ASME/ASCE /AHS/ASC Structural Dynamics and Materials*, Palm Springs (California), 4–7 May 2009, pp. 1-11.
- [4] H.I. Yoon, I.S. Son and S.J. Ahn, "Free vibration analysis of Euler-Bernoulli beam with double cracks", *J. Mech. Sci. Technol.*, vol. 21(3), pp. 476-485, (2007)

**SESSION E**

**RAILWAY ENGINEERING**



# A method for transformation of between the criteria against derailment of rail vehicles of various class

Dobrinka Atmadzhova<sup>1\*</sup>

<sup>1</sup>Machinery and Construction Technologies in Transport/Transport Equipment, Todor Kableskov University of Transport, Sofia (Bulgaria)

*The international regulations used to assess the dynamic behaviour of railway vehicles – UIC code 518 and EN 14363 – define a set of testing conditions. Under these regulations, the so-called normal method of assessing the movement safety is based on the measurement of forces horizontal-crosswise and vertical of the attacking wheel-rail contact. In the methodology developed is introduced as an initial (given) real criterion, so-called "nominal criterion" with participation of a horizontal nominal force called "frame" or "axial". The vertical load on the two wheels of a wheel-axle and the geometric position of nominal force are taken into consideration. Entering the "wheel load" parameter as a diagnostic parameter in the system leads to improvement. A complete cycle for seamless and high precision mutual transformation between the criteria for derailment of different classes is applied. The parameters are analyzed - safety factor and/or risk of derailment*

**Keywords – Railway, rail vehicle, wheel-rail contact, derailment.**

## 1. INTRODUCTION

Incidents and accidents in railway transport caused by derailment of railway rolling stock have always and everywhere in the world accounted for the highest share of all railway accidents - in any case over 50% and up to 80-90%. It is no coincidence that derailment is considered a typical (even popular) accident for railway rolling stock.

Although the problems of ensuring safety against derailment of railway rolling stock have existed since its inception (i.e. approximately two centuries ago), the first theoretical dependencies on these problems were given by Eng. Poshe in 1882. Later these dependencies are further developed by Marie G., Nadal MJ and others, and form the basis of modern theory of resistance to derailment in rail transport. Extremely significant is the contribution of Nadal M. J. [1, 2, 3], who in 1908 proposed the current and to this day working formula:

$$\frac{Y}{Q} = \frac{tg\gamma - \mu}{1 + \mu.tg\gamma} = tg(\lambda - \rho) \quad (1)$$

where: Y and Q are the horizontal transverse force and the vertical load, respectively, transmitted by the attacking wheel on the rail at the contact point;  $\gamma$  the angle of inclination of the flange generator in its right part or in the inflection point (if there is no right part);  $\mu$  and  $\rho$  - respectively coefficient of friction and angle of friction between the flange and the rail.

Nadal's task deals with a single wheel and does not require the fact that in the process of derailing the wheelset is moves on the rails, and not just off the rails. It is assumed that all the forces acting on the wheel act at one point, which is not really the case.

Taking into account the forces of interaction of the second wheel (non-attacking) from the axle with the rail leads to a modification of the derailment condition. In the 1930s, Marie G. [4] made a correction to Nadal's formula

taking into account the frictional force of the non-attacking wheel  $\mu'Q'$  and it took the form:

$$\frac{Y}{Q} = \frac{tg\gamma - \mu}{1 + \mu.tg\gamma} - \mu' \frac{Q'}{Q} \quad (2)$$

where: Q' and  $\mu'$  respectively are the vertical load on the rail and the coefficient of friction with the same on the non-attacking wheel.

It is noted that in case of a positive angle of attack it is necessary to make a correction of Marie G., taking into account the action of the friction force of the non-attacking wheel, which helps to raise the wheel above the rail. However, Marie G.'s formula is derived without taking into account the rotation of the wheels and the friction of the flange with the head-rail, due to which the friction force is used to move the wheels along the line of traction, as shown in [5].

It is worth noting that the experimental determination under operating conditions of the horizontal and vertical forces (Y, Q and Q') in the above formulas was not possible at the time of their creation, as well as for many years there after.

In [6, 7, 8, 9] the authors consider a whole wheelbase, but under specified conditions [10] and propose a derailment criterion representing the ratio of the shoulder force  $Y_p$  to the vertical force  $Q_1$  applied to the axial in wheelset on the side of the attacking wheel.

Elkins J.'s paper [11] compares the criteria for assessing North American, British and European standards for the interaction between rolling stock and rail, with the North American accepting the static vertical static load on the road and the European standards as the maximum horizontal and vertical loads transmitted by the railway vehicles to the track.

In [12] Weistock H. proposed that the relationship between horizontal and vertical force be accepted for both wheels (attacking and non-attacking, when measured

\*Corresponding author: Assoc. Prof. Dobrinka Atmadzhova, 158 Geo Milev Str. 1574 Sofia, Bulgaria, atmadzhova@abv.bg

simultaneously) as a criterion for evaluation against derailment. Characteristic of this method is the reduction of the influence on the final result of the value of the coefficient of friction  $\mu_1$ , which is always controversial due to its difficult and inaccurate determination.

In [13], the influence of the inertial force of the wheelset on the safety against derailment was studied and it was proved that this influence is negligibly weak in freight wagons in the loaded state. In the work of Blokhin EP [7] it is proved that the influence of the mass of the wheelset can be neglected not only when loaded, but also when the empty (unloaded) state of the freight cars.

In [14] it is proposed to use the ratio between the transverse component of the creep forces and the normal reaction at the contact point of the attacking wheel instead of the coefficient of friction. This method is usually combined with measuring and recording the lifting of the attacking wheel above the rail head and is difficult to perform in routine tests.

In [15] it is proposed to bring the initial system of forces acting on the attacking wheelset to the mass center of the wheelset and to treat only the main vector and the main moment of this system.

In [16], a method for assessing safety against derailment was proposed, based on a normalization factor, representing the ratio between the transverse component of the creep force and the normal response at the point of contact of the attacking wheel. This normalizing factor is used instead of the coefficient of friction between the rounded edge of the rail head and the working surface of the flange.

In [17] a method for safety assessment against derailment was developed, based on a sufficient condition for the stability of the wheel on the rail in the probabilistic aspect.

In papers [18, 19, 20, 21, 22] a comparison of the safety criteria against derailment is made, in which reduced vertical and transverse-horizontal forces are used in the "wheel-rail" contact or a system of forces acting on the wheelset by of the bogie frame, or forces acting in the

$$\frac{Y}{Q} = \frac{-t_x \cdot \mu \cdot \sin \alpha \cdot \frac{\cos \zeta}{\cos \gamma} - t_y \cdot \mu (\cos \alpha - \sin \alpha \cdot \sin \zeta \cdot \operatorname{tg} \gamma) + \operatorname{tg} \gamma \cdot \cos \alpha + \sin \alpha \cdot \sin \zeta}{(1 + t_y \cdot \mu \cdot \operatorname{tg} \gamma) \cos \zeta + t_x \cdot \mu \cdot \frac{\sin \zeta}{\cos \gamma}} \quad (3)$$

where:  $\mu$  - coefficient of friction;  $\gamma$  angle of inclination of the flange;  $\alpha$  - angle of attack;  $\zeta$  - angle of the contact point when climbing the flange on the head-rail;  $t_x$  and  $t_y$  coefficients determined by the ratios of the components of the tangential forces, respectively by the axes "x" and "y", the creep [25, 26, 27] and the tangential forces at the point of contact ( $t_x = T_x/T$  and  $t_y = T_y/T$ , as  $(t_x^2 + t_y^2)^{1/2} = 1$ ).

In numerical simulations performed with software products EXCEL, MATHCAD and UMLAB, when the coefficient varies  $\mu$ , the angles  $\alpha$  and  $\zeta$ , with the accepted angle of inclination of the flange -  $\gamma$  S1002 - 70°, it is established that the critical values of the derailment criterion for straight movement do not depend on the difference in the vertical load of the two wheels from one wheelset, but when driving in a curve it is necessary to take into account the angle of attack.

The angle of attack between the wheels and the rails is one of the quantities characterizing the mutual position

direction of movement of the wheel relative to the rail head, specifying in [19, 23] the safety criterion against derailment taking into account the angle of inclination of the rolling surface of the non-attacking wheel and the height of application of frame force.

In our country, respectively in the Research Institute of Transport at the Ministry of Transport/Bulgarian State Railways (NIIT - BDZ), the method for assessing safety against derailment from the beginning (1965) was based on the criterion representing the relationship between the axial H or frame force  $Y_p$  and the vertical force  $P_1$  on the axle in wheelset to the attacking wheel. The force measuring instruments for the vertical and horizontal (frame) force are designed and manufactured by the Institute and are strain gages. When the UIC method was introduced after 1969, the horizontal frame (axial) force was corrected with the inertial addition (-  $m \cdot \ddot{x}$ ) for which purpose the transverse (along the y-axis) acceleration of the axle was registered, which is assumed to be identical to that of the wheelset.

After 1969, a unified UIC method was introduced to experimentally determine the safety criterion against derailment as well as the safety factor against derailment of rolling stock.

Derailment mechanisms, according to their causes [28], can be classified into the following categories:

- climbing a flange;
- displacement of the track;
- widening of the track gauge and unloading of the wheels.

Each of these derailment mechanisms must be controlled, using appropriate safety criteria at the design stage and tests to demonstrate the site's compliance with approved regulations at the "prototype" stage.

The criterion used to assess the danger associated with climbing the flange on the head-rail and derailing the wheel is the dependence obtained on the basis of the analysis of the force ratio at the contact point "wheel-rail" - Y/Q, according to the dependence [24]:

and interaction between the railway crew and the track in a curve [29, 30, 31]. The general statement, taking into account all possible horizontal displacements in the system "frame - wheelset - rails" the angle of attack for the j - th axle ( $j = 1, 2, \dots, n$ ) of a multi - axle crew with n - axles can be represented by the following expression:

$$\alpha_j = \frac{\ell_D - \ell_j}{R} + \frac{\delta_{Sn} - \delta_{S1}}{2\ell_D} + \frac{\sigma_n - \sigma_1}{2\ell_D} + \frac{y_n - y_1}{2\ell_D} - \frac{x_{jk} - x_{jk\pm 1}}{2b} - \xi \quad (4)$$

where:  $\ell_D$  is half of the base (wheelbase) of the crew;  $\ell_j$  is the distance from the first wheelset to the considered random wheelset with № j ( $j = 1, 2, \dots, n$ ); R - the radius of the curve;  $\delta_{Sn}$  and  $\delta_{S1}$  - the total horizontal irregularities of the track in the places of the "n" and the first wheelset;  $\sigma_n$  and  $\sigma_1$  - transverse displacements (distances or clearances) between the flanges and the outer rail;  $y_n$  and  $y_1$  - the

transverse displacements of the bogie frame relative to the wheelsets;  $x_{jk}$  and  $x_{jk\pm 1}$  - the longitudinal displacements of the axles box at a transverse distance of  $2b$ , relative to the frame and  $\xi$  - horizontal oblique deformation of the bogie frame.

The models for experimental determination of the angle of attack of the wheel axle are a direct experimental method, a direct experimental-theoretical model and an indirect experimental-theoretical model.

With significant contributions of our country to the research on the problems of improving the driving qualities and safety against derailment of the rolling stock, three Bulgarian scientific and technical achievements stand out, developed theoretically by NIIT - BDZ and VTU "T. Kableshkov", massively implemented in the production and operation and defended as dissertations, under the following titles:

- "Studies on torsion vibrations of wagon structures"- to the problem of ORE/ERRI B-55 (to increase safety against derailment) [32];
- "Studies of the axle box connections with the bogie frame of the passenger cars" - to the problem of ORE/ERRI C-138, for the creation of a bogie for passenger cars with radial entry in curves [33];
- "Interactions in the system" locomotive - railway "- problem areas and modern solutions", contributing to the creation and implementation in all locomotive repair companies system for measuring the load of the wheels on the rails" [34].

With the implementation of the developments, the cases of derailment have been drastically reduced.

The normative documents EN 14363 and UIC 518 define a virtual derailment criterion considering only the attacking wheel (Nadal  $Y/Q$  criterion). Благодарение на разработките случайте на дерайлиране са намалени драстично.

ORE B10/RP12/D defines a nominal criterion ( $Y_p/Q'_1$ ), determined by experimental results and not taking into account all force and other characteristics of the "wheel-rail" interaction related to derailment safety.

There are no dependencies and methodology for determining the conditional criterion  $Y_1/Q_1$ , taking into account the specifics of the force interaction "wheelset-rail track".

One of the groups of unresolved issues / problems is the lack of theoretical (computational) interpretation of derailment problems according to EN 14363 and UIC cod. 518 based on a instrumented wheelset; and in particular, in the first place - the impossibility to determine visually and convincingly in a theoretical way (by real calculations by an established method) the criterion against derailment  $Y/Q$ , as well as any force and other characteristics and computational results of the wheel-rail interaction Relating to safety against derailment.

The problem comes down to the fact that the determination of the  $Y/Q$  criterion approved by the European standards and UIC is possible only experimentally and with the help of a special instrumented wheelset with the appropriate equipment and personnel [39-40] provided for use by the owner. Under certain conditions; or - which is even more unprofitable for our country - full outsourcing of testing activities to Western companies. This state of affairs inevitably gives rise to the

alternative of seeking another solution, at least for the most common cases of low liability - for example, according to the aim set here - the theoretical determination of the criterion against derailment  $Y_1/Q_1$  and  $Y/Q$  respectively, but not by a direct method (which is impossible!), but indirectly by theoretical or experimental determination of the nominal criterion against derailment  $Y_p/Q'_1$  (or, possibly, another suitable criterion) and its subsequent adjustment to the conditional criterion  $Y_1/Q_1$  which is practically equivalent or in a certain dependence to the approved criterion  $Y / Q$  according to EN and UIC. And the conversion from  $Y_p/Q'_1$  to  $Y_1/Q_1$  is done on the basis of revealed methodological compatibility with the analogy and the drive (transforming) functions between the criteria  $Y_p/Q'_1$  and  $Y_1/Q_1$ .

## 2. DEPENDENCES OF CRITERIA SUBJECT TO MUTUAL TRANSFORMATION

As a starting (set) real criterion, subject to adjustment to the internationally approved  $Y/Q$  according to EN 14363 and UIC 518, the so-called "Nominal" criterion  $Y_p/Q'_1$  involving the horizontal nominal force  $Y_p$ , called "frame" or "axial", transmitted between the axle and the frame [12]; and the vertical  $Q'_1$  representing the resultant force at the point of contact of the attacking wheel:

$$\frac{Y_p}{Q'_1} = \frac{1 - \frac{\mu_1}{\sin \gamma_1 (\cos \gamma_1 + \mu_1 \sin \gamma_1)} - \frac{Q'_2}{Q'_1} \frac{\mu_2}{\text{tg} \gamma_1}}{\cot \gamma_1 - \frac{h}{c} + \frac{\mu_1 h/c}{\sin \gamma_1 (\cos \gamma_1 + \mu_1 \sin \gamma_1)} - \frac{\mu_2 h/c}{\text{tg} \gamma_1}} \quad (5)$$

where:  $\gamma_1$  and  $\mu_1$  - respectively the angle of the flange and the coefficient of friction at the contact point "flange-rail" of the attacking wheel;  $\mu_2$  - the coefficient of friction at the contact point "rebord-rail" of the non-attacking wheel;  $Q'_2$  and  $Q'_1$  - vertical load on both wheels of the axle and  $h/c$  - parameter taking into account the geometric location of the nominal force  $Y_p$ ;

The internationally approved Nadal criterion  $Y/Q = Y_1/Q_1$  (and respectively system) according to EN 14363 and UIC 518, formula (1) and with Marie G. correction - formula (2), is temporarily replaced by the so-called "conditional transforming "criterion (and respectively system) against derailment  $Y_1/Q_1$ , which is closer to reality, is characterized by actually acting reduced (reduced) forces  $Y_1$  and  $Q_1$  at the contact point of the attacking wheel, helps to achieve methodological compatibility with the initial criterion, being taken temporarily with a practical tolerance of  $Y_1/Q_1 \approx Y/Q$ ; the other more important features of the conditional transforming criterion and the respective system (model) are:

- The conditional transforming system has 2 wheels (attacking and non-attacking), as the forces and parameters of the bandage profile have indices "1" and "2" for the attacking and non-attacking wheels, respectively;
- The forces are actually acting and contain the "additives" due to the action of the frame force  $Y_p$ ;
- The parameter  $Q'_2/Q'_1$  takes into account the influence of the unevenness of the wheel load and is an indirect measure of the safety against derailment and an important identifying factor.

3. TRANSFORMATION BETWEEN THE CRITERIA "NOMINAL" -  $Y_p/Q'_1$  AND "CONDITIONAL" -  $Y_1/Q_1$ .

The present problem is usually set as follows: at the input of the system (Fig. 1) a nominal criterion  $Y_p/Q'_1$  is set, which is transformed (converted) into a conditional criterion  $Y_1/Q_1$  and it is output as such. Of course, the transformation is possible in reverse order - from conditional to nominal criterion. The transformation itself is performed under two initial mandatory requirements:

first - the transformable criterion of input and output, ie. before and after the transformation, have the same values of the parameters at the primary level  $\gamma_1$  and  $\mu_1$ ;

second - the transformable criterion of input and output, ie. before and after the transformation, to have the same values of the indicator "safety factor against derailment  $\eta$ ", ie. to fulfill the condition  $\eta_{nom} = \eta_{con}$ .

These two initial requirements serve as "reference points" in the transformation and the forthcoming research, because they are always actually fulfilled: the first - because at the primary level the ongoing processes are exactly the same for both criteria, due to the angle of the flange  $\gamma_1$  friction  $\mu_1$  of the same with the rail; and the second - because in all processes for transformation in

Nature the condition for preservation of the characterizing substance is obligatory - energy, matter, etc.

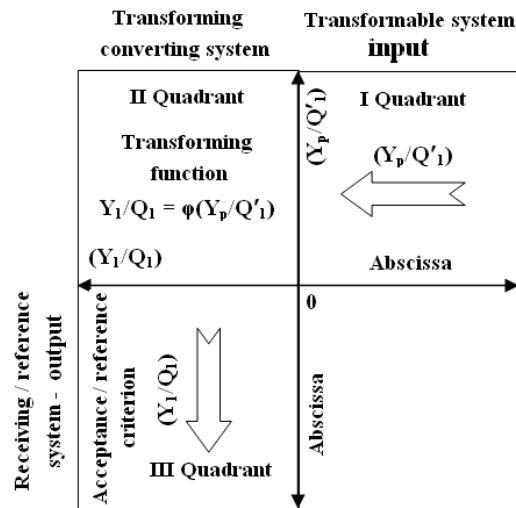


Figure 1. Plan-scheme for transformation (transformation) of the criteria  $Y_p/Q'_1 \leftrightarrow Y_1/Q_1$ .

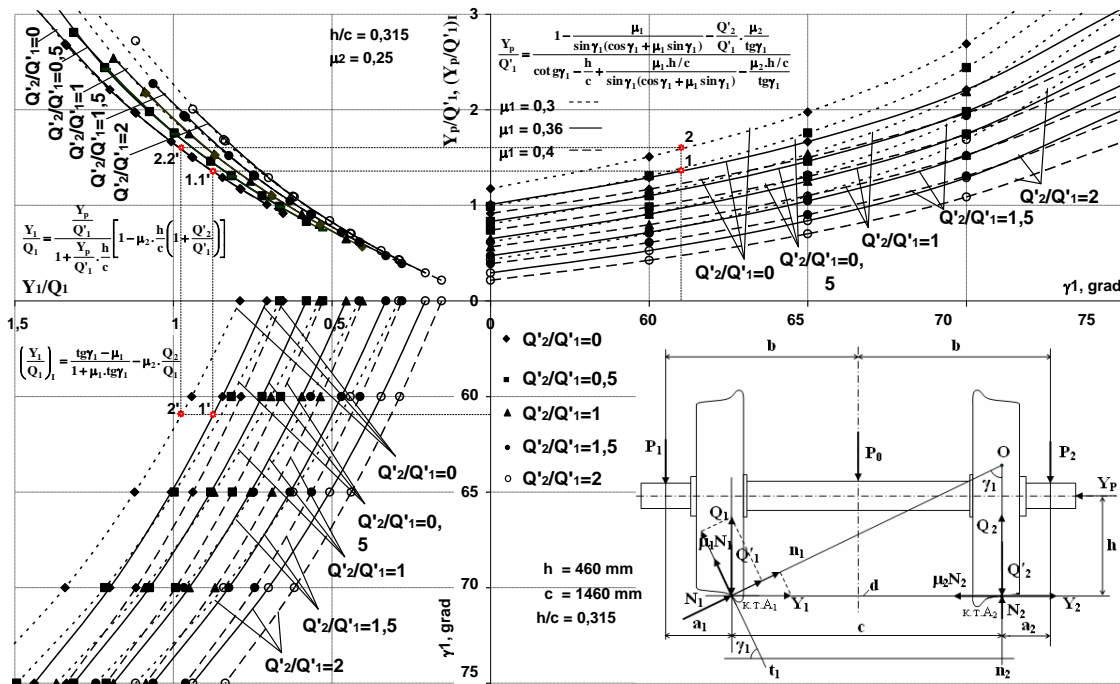


Figure 2. Nomogram with methodical combination of criteria against derailment  $Y_p/Q'_1$  and  $Y_1/Q_1$  for standard wagon wheelsets  $\phi 920$  mm,  $h = \phi/2 = 460$  mm,  $c = 1460$  mm.

The accepted and introduced prerequisites and criteria in different ways help to increase their methodological compatibility - starting from their initial level to reaching the state of complete analogy, which can be seen visually from the nomogram (Fig. 2). There in I and III quadrants are given the graphs of the criteria against derailment  $Y_p/Q'_1$  and  $Y_1/Q_1$  at abscissas  $\gamma_1$  (edge of the flange) and parameters  $Q_2/Q'_1$  ( $Q_2/Q_1$ ) and  $\mu_1$  (friction-rail coefficient), and in the II quadrant the graphically transforming function of these criteria is presented.

On the other hand, based on the primary force dependences of the transforming systems can be written 
$$\frac{Y_1}{Q_1} = \frac{Y_p/Q'_1 \pm \mu_2 \cdot Q_2/Q'_1 - \mu_2 \cdot (h/c) Y_p/Q'_1}{1 + (h/c) Y_p/Q'_1} \quad (6)$$
 where: the sign " $\pm$ " - reflects the presence of "invalid" decisions (decisions inconsistent with reality), and for other indications - see figure 2.

The dependence (6) at a value of the parameter  $Q_2/Q_1 = 0$  becomes a basic dependence:

$$\frac{Y_1}{Q_1} = \frac{Y_p/Q'_1}{1 + (h/c) Y_p/Q'_1} \left( 1 - \mu_2 \frac{h}{c} \right), \quad (7)$$

whose graph is presented on a large scale in fig. 2 (nomogram, second quadrant).

In addition to the above-mentioned analogy between the diagrams of the transforming criteria, it also exists between separate zones (sections) of these diagrams, as well as between separate points or states; for example, analog points are item 1 of quadrant I and item 1' of quadrant III, item 2 and item 2', etc. - figure 2. Thus, the condition for the existence of analog points is that they have the same values of the parameters  $\mu_1$ ,  $\gamma_1$  and  $Q_2/Q_1$  ( $Q_2/Q_1$ ).

An important property of the analogous points is: through them, using the analogy, the dependence between the transforming criteria can be outlined. For example, the ordinates of the analogous points 1 and 1' with parameter  $Q_2/Q_1$  ( $= Q_2/Q_1$ ) = 0, located in the I and III quadrants respectively and representing the criteria  $Y_p/Q_1$  and  $Y_1/Q_1$ , respectively, are "transferred" to the II quadrant by rays parallel to the respective abscissas, which with their intersection points, for example item 1.1', there (in the second quadrant) outline the dependence between the same criteria.

The dependence thus outlined on the basis of the analogy completely coincides with the dependence (2), which is derived in an analytical way.

The dependence (6) is determined only by the parameter  $Q_2/Q_1 = Q_2/Q_1 = 0$ , at all possible values, of the parameters  $\mu_1$  and  $\gamma_1$ . For example, if besides the analogous points 1 and 1' at  $\mu_1 = 0,36$  we take other analogous points for example 2 and 2' at another value of  $\mu_1 = 0,3$  (the top thin dashed line) at the same value of the parameter  $Q_2/Q_1 = Q_2/Q_1 = 0$ , then the intersection point 2.2' between the rays also falls on the curve on formula (7) - the basic transforming function; the same hit (on a curve of formula (5)) will be obtained at  $\mu_1 = 0,4$  (thick dashed line located at the top), as well as at any other value of  $\mu_1$ , not indicated in the nomogram, if  $Q_2/Q_1 = Q_2/Q_1 = 0$ .

#### 4. UNIVERSAL TRANSFORMING FUNCTION

The universal transform function (UTF) in comparison with the basic one refers to a significantly wider area with a larger number of parameters and at any possible values of the same, due to which the task of determining this function is significantly more complicated. Because there is an analogy between the transforming criteria, thanks to its use with a procedure similar to the previous case, a successful solution is obtained, because the "transferred" in the second quadrant analog points outline curves (more precisely, family curves), which within the "experiment" with a given construction are separated only by the value of the parameter  $Q_2/Q_1 = Q_2/Q_1$  without any influence of the other parameters -  $\mu_1$  and  $\gamma_1$  for the attacking wheel. The influence of the construction in the required transforming function is adequately expressed by entering in it the parameters  $h/c$  and  $\mu_2$ , in the same way as in the previous case with the basic transforming function.

Regarding the analytical substantiation of the required function, here mainly due to the increased influence of the invalid decisions, the obtained results can be unreservedly accepted not in their entirety, but partially by selection, i.e. they can only serve as landmarks.

And when using the "landmarks" thus obtained, relying entirely on the above-revealed connections and when applying the Gaussian method with the "least squares" (according to the program), the so-called "universal" transforming function is derived:

$$\frac{Y_1}{Q_1} = \frac{Y_p/Q_1}{1 + (h/c)Y_p/Q_1} \left[ 1 - \mu_2 \frac{h}{c} \left( 1 + \frac{Q_2}{Q_1} \right) \right], \quad (8)$$

which includes and replaces formula (2).

The inverse transformation formula, i. from the criterion  $Y_1/Q_1$  to the criterion  $Y_p/Q_1$ , we get the dependence:

$$\frac{Y_p}{Q_1} = \frac{Y_1/Q_1}{1 - \mu_2 \frac{h}{c} - \mu_2 \frac{h}{c} \frac{Q_2}{Q_1} - \frac{Y_1}{Q_1} \frac{h}{c}}, \quad (9)$$

which is in condition for practical use at  $Q_2/Q_1 = Q_2/Q_1$ .

For cases where the value of the wheel load parameter  $Q_2/Q_1$  and/or  $Q_2/Q_1$  must be precisely determined, respectively, as follows:

$$\frac{Q_2}{Q_1} = \left\{ \frac{Y_p}{Q_1} \left[ \frac{h}{c} - 1 - \frac{\mu_1 h/c}{\cos \gamma_1 (\cos \gamma_1 + \mu_1 \sin \gamma_1)} + \mu_2 \frac{h}{c} \right] + \right. \\ \left. + \operatorname{tg} \gamma_1 - \frac{\mu_1}{\cos \gamma_1 (\cos \gamma_1 + \mu_1 \sin \gamma_1)} \right\} \frac{1}{\mu_2}; \quad (10)$$

$$\frac{Q_2}{Q_1} = \frac{\operatorname{tg}(\gamma_1 - \rho_1) - Y_1/Q_1}{\operatorname{tg}(\gamma_2 + \rho_2)} \quad (11)$$

As can be seen, in UTF the parameter of the wheel load can occupy different positive values, i.e.  $P_{wl} \geq 0$  ( $P_{wl} = Q_2/Q_1$ ), while for the basic transform function (BTF) the same parameter has only zero value. All other signs and properties of BTF are also valid for UTF.

For the current variables (parameters)  $\gamma_1$  and  $\mu_1$ , precisely defined values are set, corresponding to the standardized, set, etc. values of the criteria or possibly other indicators.

Therefore, three main ways to transform the values of the so-called nominal criterion against derailment  $Y_p/Q_1$  to the conditional transform criterion  $Y_1/Q_1 \approx Y/Q$ , as follows:

- graphic, with nomogram (fig.2);
- analytical, with classical procedure;
- analytical, with software products.

The main methods recommended for use in practice are unconditionally the analytical methods, and the graphical one is given rather for the purpose of illustration, more convincing substantiation of the methodology and even, including deriving through it of basic analytical dependences.

#### 5. ON THE SECURITY COURSE AGAINST DERIALIZATION

In any case, and especially when comparing and evaluating different criteria against derailment, the question of the safety factor as a "measure" of their effectiveness is at the forefront. And as this indicator is inextricably linked to the parameter of the wheel load  $Q_2/Q_1 = Q_2/Q_1$ , it is appropriate to make some further explanations about it here.

The wheel load parameter  $Q_2/Q_1$  respectively  $Q_2/Q_1$  is initially a measure of the unevenness of the wheel load on the rails, but it also makes sense to

characterize the load on the running gear in relation to the unused (reserve, in reserve) anti-derailment ability, and in the most general aspect characterizes the safety against derailment. Because the maximum (or full) usability of the anti-derailment ability or the lack of reserve would be realized at  $Q_2/Q_1$  (respectively  $Q'_2/Q'_1$ ) = 0, i.e. when all the wheel load would be concentrated in the attacking wheel; and this in the diagrams corresponds to the highest level of the lines  $Q_2/Q_1$  (respectively  $Q'_2/Q'_1$ ), from which state when increasing the value of this ratio (i.e. when approaching the lines in question to the abscissa axis  $\gamma_1$ ) unused (reserve) anti-derailment capacity increases, which from a different point of view means an increase in the safety factor against derailment.

In any case, and especially when comparing and evaluating different criteria against derailment, the question of the safety factor as a "measure" of their effectiveness is at the forefront.

For the identical equality between the values of the coefficient of safety against derailment for the two criteria (i.e.  $\eta_{nom} \equiv \eta_{con}$ ) we have:

$$\frac{1}{\eta_{nom}} = 1 - \frac{Q'_2}{Q'_1} \cdot \frac{\mu_2}{tg\gamma_1} \left( 1 - \frac{\mu_1}{\sin\gamma_1(\cos\gamma_1 + \mu_1 \sin\gamma_1)} \right) \quad (12)$$

$$\frac{1}{\eta_{con}} = 1 - \mu_2 \cdot \frac{Q_2}{Q_1} \cdot \frac{1}{\left[ \frac{tg\gamma_1 - \mu_1}{1 + \mu_1 \cdot tg\gamma_1} \right]} \quad (13)$$

(Graphically presented in Fig.3, a and Fig.3, b)

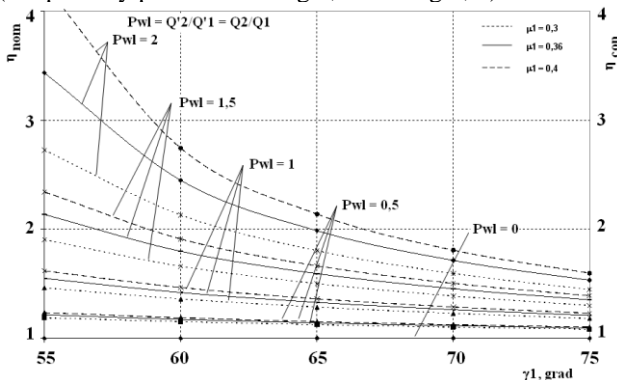


Figure 3a Dependence of  $\eta_{nom}$  and  $\eta_{con}$  of  $\gamma_1$ , at different values of the parameters  $\mu_1$  and  $Q'_2/Q'_1 = Q_2/Q_1$ , (according to dependences (12) and (13).

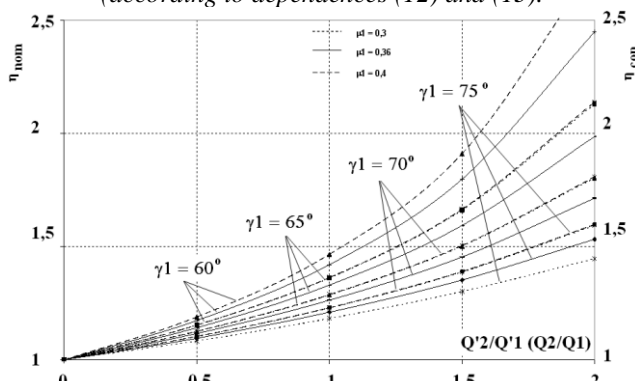


Figure 3b Dependence of  $\eta_{nom}$  and  $\eta_{con}$  on  $Q'_2/Q'_1 (= Q_2/Q_1)$  at different values of  $\mu_1$  and  $\gamma_1$ , (according to dependences (12) and (13).

6. ANALYTICAL REPRESENTATION OF TRANSFORMING FUNCTIONS BETWEEN THE

CRITERIA ( $Y_p/Q'_1$ ) AND ( $Y_1/Q_1$ ) WITH IDENTIFYING PARAMETER  $\eta = \eta_{nom} = \eta_{con}$

In order to transform into an analytical form the graphs of the transforming functions obtained through the nomogram matrix, the first and most important condition is to determine or choose the type of the functions, their "construction". Despite the existing variety of different types of functions, choosing the most suitable to meet the requirements is actually a complex and responsible task; To solve it, the so-called "guidelines" are used here, representing, first of all, mathematical dependencies and individual expressions from them, obtained from the theoretical research on the problem conducted here. In addition, an important "guideline" is the existing and revealed analogy with other problems or tasks that have been successfully solved here, such as the task of analytical representation of the graphs of transforming functions with identifying parameter  $Pwl = Q'_2/Q'_1 (= Q_2/Q_1)$ , resp. BTF, UTF and mainly formula (14). Because the revealed complete "overlap" between formula (14) and the graphs of the transforming functions in the same range allows for the concentration of attention and efforts to the second part of the formula, while inspiring confidence in the correctness of the chosen direction of research; moreover, bearing in mind that formula (14) in the form:

$$\left( \frac{Y_1}{Q_1} \right)_I = \frac{(Y_p/Q'_1)_I}{1 + \frac{h}{c} \cdot (Y_p/Q'_1)_I} \left( 1 - \mu_2 \cdot \frac{h}{c} \right) \quad (14)$$

And going back to the reasoning about the role and meaning of the landmarks, if we consider even just the first expression of the formula -  $(Y_p/Q'_1)/[1+(h/c) \cdot (Y_p/Q'_1)]$ , it is not difficult to be convinced that it is practically impossible to reach the same kind if there was no landmark; and there are other expressions, physical quantities and numbers in the formula, and the possible combinations between them are also extremely important.

The above-mentioned factors, rather "benchmarks", if well defined, contribute significantly to the successful solution of the present task, as well as to its alleviation, although it still remains extremely difficult and complex, related not only to routine recruitment operations. , but also with extra systems based on intuition, deduction, etc. works that cannot be described and at the same time - plus the simplest logic.

Based on the above considerations, the exposition of the present works on the transformation into an analytical form of the transforming functions with an identifying parameter  $\eta = \eta_{nom} = \eta_{con}$  condition is omitted here and the same are presented in summary as follows –

$$\frac{Y_1}{Q_1} = \frac{Y_p/Q'_1}{1 + \frac{h}{c} \cdot Y_p/Q'_1} \left[ 1 - \mu_2 \cdot \frac{h}{c} - \frac{1}{\mu_2} \cdot \left( \frac{h}{c} \right)^2 \cdot \left( 1 - \frac{1}{\eta} \right) \right] \quad (15)$$

where:  $Y_1/Q_1$  is a conditional criterion against derailment;  $Y_p/Q'_1$  - nominal criterion against derailment;  $\eta = \eta_{nom} = \eta_{con}$  - coefficient of safety against derailment;  $h = r$  (usually!) - radius of the attacking wheel:  $r = 460$  mm - for wagon wheels;  $r = 600$  mm - for locomotive wheels;  $c$  - distance between the contact points of the wheel ( $c = 1460$  mm = const);  $\mu_2$  - coefficient of friction between the

rolling surface of the non-attacking wheel and the rail head ( $\mu_2 = 0,25 = \text{const}$ ).

The validity of formula (15) as presented herein has not been confirmed to date at a value of  $\mu_2 \neq 0,25$ ; to prove it, a complete revision (basic examination, examination) of the nomogram matrix, through which the formula is derived, is required.

Solution of (15) with respect to the coefficient of safety against derailment  $\eta = \eta_{\text{nom}} = \eta_{\text{con}}$  we obtain the dependence:

$$\eta = \frac{\frac{Y_p/Q'_1}{1+(h/c)(Y_p/Q'_1)} \left(\frac{h}{c}\right)^2 \cdot \frac{1}{\mu_2}}{\frac{Y_l}{Q_l} - \frac{Y_p/Q'_1}{1+(h/c)(Y_p/Q'_1)} \left[ 1 - \mu_2 \cdot \frac{h}{c} - \frac{1}{\mu_2} \left(\frac{h}{c}\right)^2 \right]} \quad (16)$$

which can be used to directly determine the value of  $\eta$  depending on the limit values of the mutually transformed input and output criteria.

The results of the conducted research show that the transforming functions between the criteria  $Y_p/Q'_1$  and  $Y_l/Q_l$ , depending on the number of identifying parameters can be:

- one-parameter, with parameter -  $Pwl = Q'_2/Q'_1 = Q_2/Q_1$  or  $\eta = \eta_{\text{nom}} = \eta_{\text{con}}$ ;
- two-parameter, with parameters -  $\gamma_1$  and  $\mu_1$ .

In the first case, the transforming functions are determined either by the wheel load parameter  $Pwl = Q'_2/Q'_1 = Q_2/Q_1$ , or by the derailment safety factor  $\eta$  ( $\eta_{\text{nom}} = \eta_{\text{con}}$ ), at all possible values of  $\gamma_1$  and  $\mu_1$ .

In the second case, the transforming functions are determined only by the parameters  $\gamma_1$  and  $\mu_1$ , whose fixed quantitative values in the form of degrees form different combinations for the different functions, the influence of the parameters  $Pwl$  and  $\eta$  is completely excluded.

In many cases of practice, the coefficient of safety against derailment is of paramount importance, which is why it is of interest to present the dependences related to the parameters  $\eta_{\text{nom}}$  and  $\eta_{\text{con}}$  conditions.

Fig.4 shows an nomogram matrices for transforming and outputting the transform functions between criteria  $Y_p/Q'_1$  and  $Y_l/Q_l$  with identifying parameter  $\eta = \eta_{\text{nom}} = \eta_{\text{con}}$ , standard wagon wheelsets.

The idea arose to combine the nomogram matrix, some details for this type of nomogram matrix for wagon wheels are shown in Fig.5a, b.

In addition, the parameters introduced in this paper - the coefficient of safety against derailment ( $\eta$ ) and the parameter of wheel load  $Pwl$  - complicate the approved method according to EN 14363 and UIC-518, but allows to accurately determine the value of even the criterion ( $Y/Q$ ) and showing the extent (or value) of the reserve until it is completely depleted and reaches its limit state [41].

The border state according to international normative documents (IND), in turn, is also a source of contradictions and controversies, caused mainly by its virtuality; whereas the limit state of the derailment criterion, determined by Nadal's formula, is the only theoretically justified state; and at the same time, it is accepted as a standard operating state or in other words - for a normal (standard) operating mode, which, however, is virtual. Other operating modes (not only standard) can obviously correspond to the same limit state, but they are all unrealizable in practice, because otherwise the vertical load of the non-attacking wheel would have to be zero (something unrealizable, of course se!).

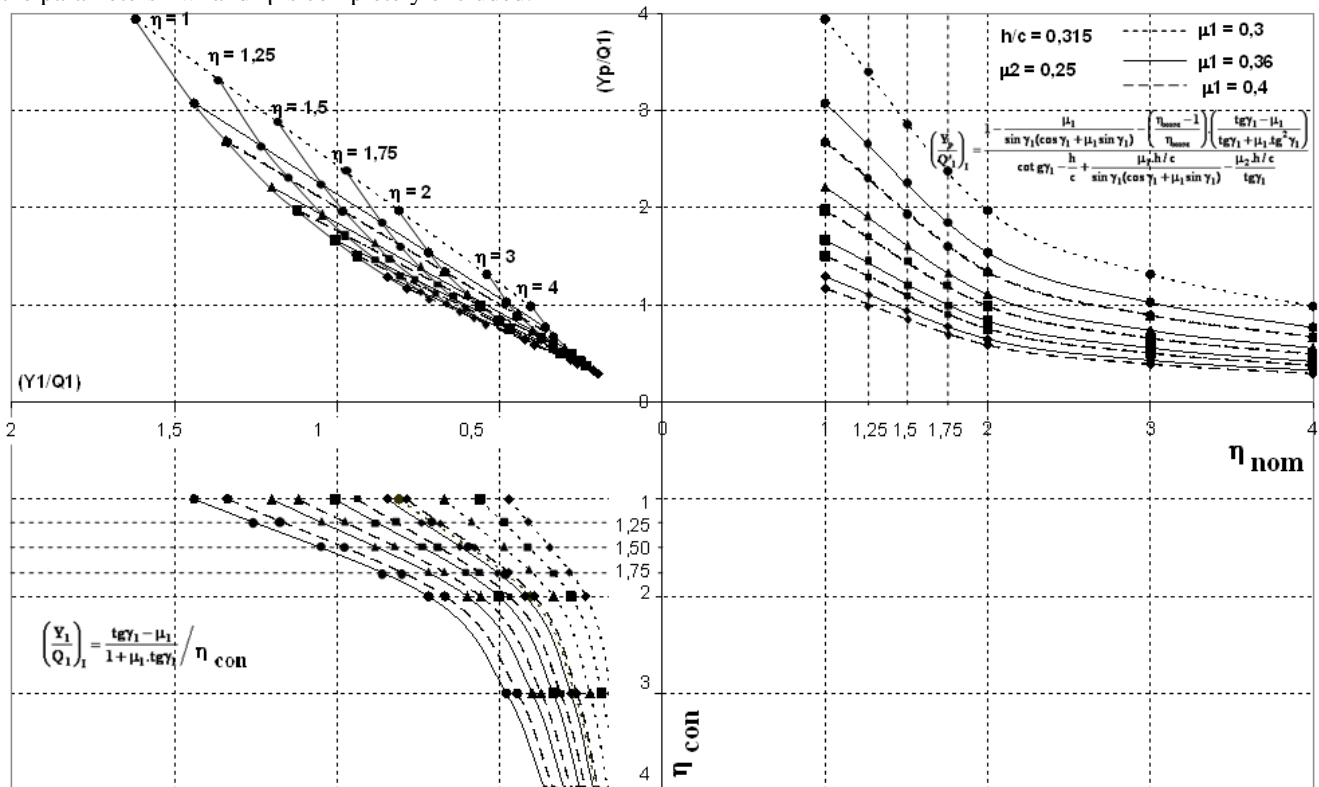


Figure 4. Nomogram matrix for transformation and creation of transforming functions between the criteria  $Y_p/Q'_1$  and  $Y_1/Q_1$  with identifying parameter  $\eta = \eta_{nom} = \eta_{con}$  for standard UIC wagon wheelsets  $\phi 920\text{mm}$ .

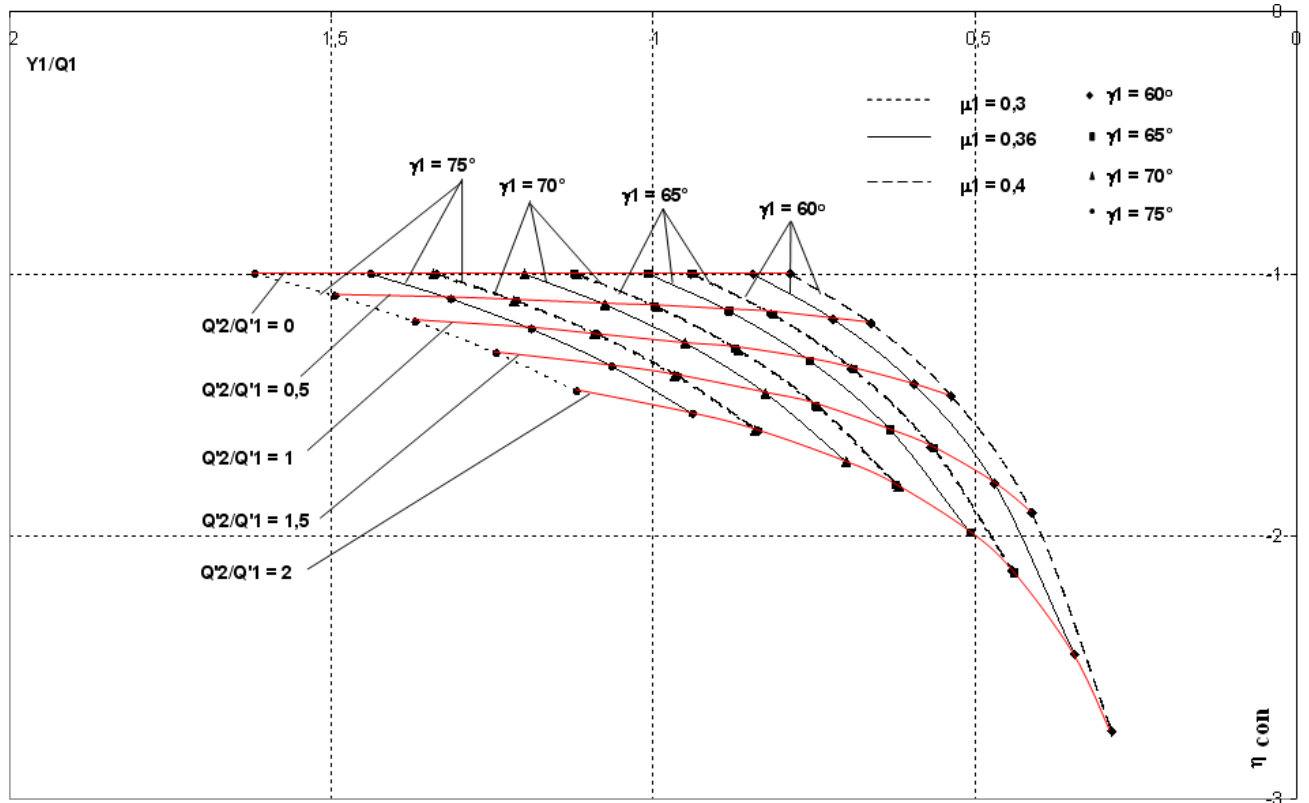
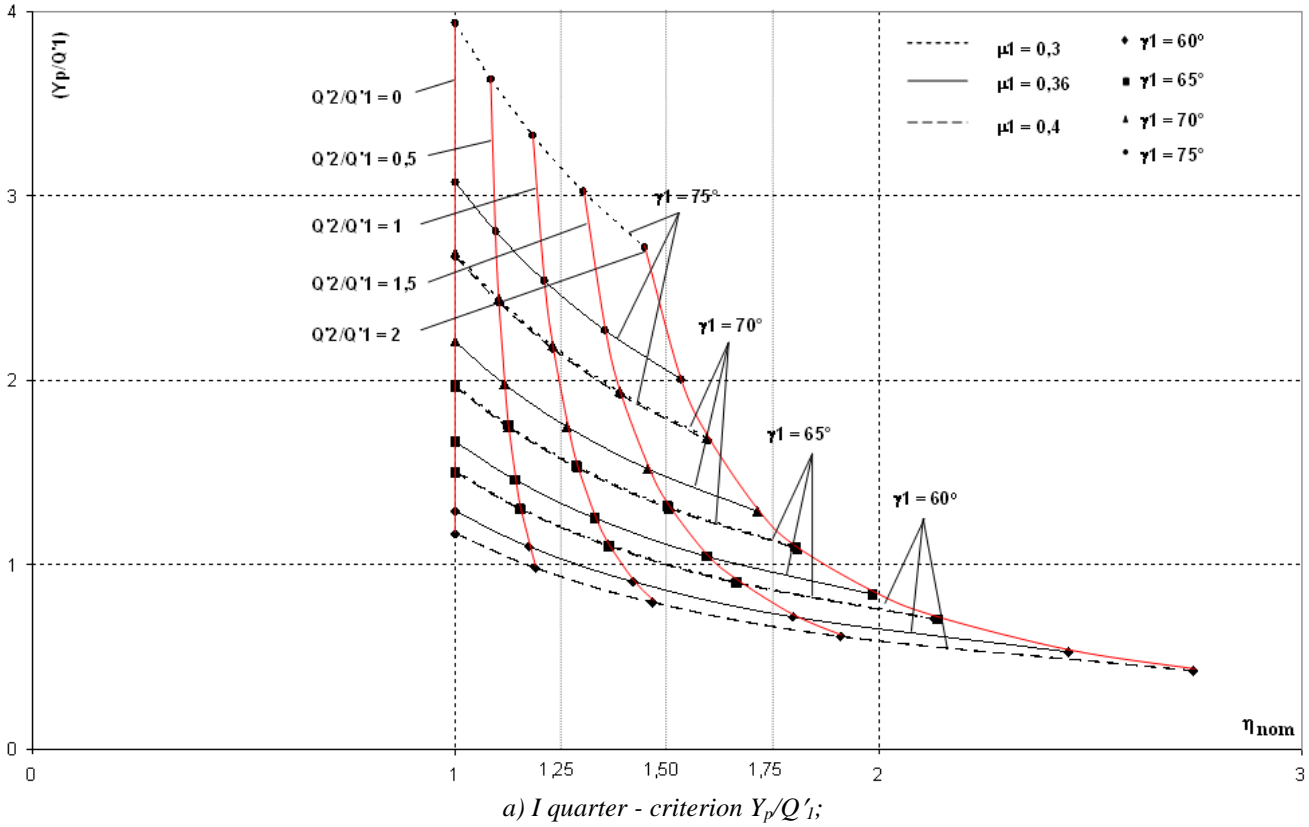


Figure 5. Details of a combined nomogram matrix with identification parameter  $\eta$  or  $Pwl$ .

## CONCLUSION

1. The article presents an overview of existing research on theoretical grounds and promising special safety trends against derailment in railway transport. The experience, research and contributions and inconsistencies of various developments are presented.

2. A mathematical function and respectively a method for mutual transformation of criteria against derailment of different class, namely the nominal criterion  $Y_p/Q'_1$ , transformed into virtual (conditional)  $Y_1/Q_1$  (equal to the internationally approved by EN 14363 and UIC) - 518 criterion  $Y/Q$ , as well as inverse transformation.

3. A method has been developed for theoretical determination of the internationally approved by EN and UIC criterion against indirect derailment by transforming the nominal criterion  $Y_p/Q'_1$  predetermined by known methods and its subsequent transformation to a conditional criterion.

4. A nomogram matrix with a method for transformation and derivation (creation) of transforming functions between the criteria against derailment of different class - nominal and virtual in graphical form, which matrix is recommended and can be used for other criteria and any type of functions within various organizations and companies, including the International Railway Union UIC.

5. The criteria against derailment of different class have been adapted, thus achieving the necessary methodological compatibility between them and a complete analogy, expressed by equality between the values of the variable parameters of the criteria at primary level  $\gamma_1$  and  $\mu_1$  and the safety factor (or hazard) against derailment  $\eta$  ( $\xi$ ) and the wheel load parameter  $P_{wl}$ .

6. In the dependences determining the criteria against derailment of different class new additional parameters have been introduced - the safety factor  $\eta$  (which is a basic, unconditionally mandatory indicator for all technical objects and processes) and the parameter for uneven wheel load  $P_{wl}$  (which gives only true and unambiguous answer regarding the limit value of the derailment criterion). The introduction of additional parameters in the system will contribute to its improvement, which is expressed in the ability to avoid borderline risk regimes in operation, reduce the scattering of results, increase sensitivity, improve system manageability, etc.

7. Different transforming functions between the criteria of different class are revealed, which depending on the number of identifying parameters are classified as: - one-parameter, with one identifying parameter - wheel load  $P_{wl}$  or safety factor  $\eta$  and - two-parameter, with two identifying parameters - primary level criteria  $\gamma_1$  and  $\mu_1$  (flange angle and friction coefficient at the wheel-rail contact).

## REFERENCES

- [1] Nadal, J. Locomotives a vapeur, Collection Encyclopédie Scientifique, Bibliothèque de Mécanique Appliquée et Génie, Vol.186, Paris, France, (1908)
- [2] EN 14363: Railway applications - testing for the acceptance of running characteristics of railway vehicles - Testing of running behaviour and stationary tests. ISBN 83-243-8546-0 (2005)
- [3] UIC Code 518. Testing and approval of railway vehicles from the point of view of their dynamic behavior – Safety – Track fatigue – Ride quality. 3-d ed. October (2009).
- [4] Марье Г. Взаимодействие пути и подвижного состава/ М.: Госжелдориздат,– 338 с. (1933)
- [5] Коротенко Григорий, Коротенко Леонид, Клименко Ирина, International Book Market Service Ltd., Member of Omni Scriptor Publishing Group ISBN: 978-3-659-884001-6, 275. (2019),
- [6] Азовский А. П., Котуранов В. Н., Овечников М. Н., Плотников И. В. Об оценке запаса устойчивости колеса от выкатывания на головку рельса // Безопасность движения поездов: сб. ст. междунар. конф. Москва, С. VI-1–VI-2 (2007).
- [7] Блохин, Е. П. Усовершенствование конструкции тягового привода класса II локомотива / Проблемы та перспективи розвитку залізничного транспорту: тезиы Междунар. научно-практ. конф./ Днепрпетр. нац. ун-т ж.-д. тр-та им. акад. В. Лазаряна. – Д.: ДНУЖТ,– С. 6-7. (2007).
- [8] Вериго М., Взаимодействие пути и подвижного состава- М., Транспорт,– 559 с. (1986)
- [9] Вершински С., Данилов С., Целноков И., Динамика вагонов, Издательство Транспорт, Москва, (1978)
- [10] Галеев, А. У. К вопросу теории схода колес с рельсов/ Труды МИИТ– № 55– С. 179-191. (1948)
- [11] Elkins, J. New Criteria for Flange Climb Derailment – 2000 ASME/IEEE Joint Railroad Conference, April 4-6, P. 1-7 (2000).
- [12] Weistock, H. Whell Climb Derailment Criteria for Evaluation of Rail Vehicle Safety// Paper no. 84 – WA/RT – 1, ASME– P. 34-42 (1984).
- [13] Ромен, Ю. С. Определение устойчивости от всползания колеса на рельс при испытаниях подвижного состава/ Вестник ВНИИЖТ. – № 4. – С. 45-47. (1986).
- [14] Погорелов, Д. Ю. Показатель для оценки опасности схода подвижного состава путем вкатывания колеса на головку рельса/ Вісник Східноукраїнського національного університету ім. В. Даля. – № 5 (147) I. – С. 64-70. (2010).
- [15] Кондратьев, В. Ф. О сходе колеса с рельса/ Вестник ВНИИЖТ № 6. – С. 23-25 (1980).
- [16] Черкашин, Ю. М. Сравнение некоторых критериев, оценивающих опасность схода путем всползания колеса на рельс/ Вісник Східноукраїнського національного університету ім. В. Даля –№ 8 (90) I– С. 98-103 (2005).
- [17] Коган, А. Я. Оценка достаточного условия устойчивости колеса на рельсе с учетом вероятностного характера влияющего на нее

- некоторых факторов/ Вестник ВНИИЖТ. – № 2. – С. 36-41. (2008)
- [18] Клименко, И. В., Развитие теоретических основ и методов оценки и повышения безопасности движения подвижного состава железных дорог, Днепропетровск – (2015)
- [19] Коротенко Григорий, Коротенко Леонид, Клименко Ирина, Информационные технологии и безопасность на транспорте, 2019 International Book Market Service Ltd., (2019).
- [20] Кузишин А. Я., А. В. Батіг, Анализ существующих подходов к расчету критериев безопасности движения на железнодорожном транспорте, Innovative technologies and scientific solutions for industries. ISSN 2522-9818 No.4(6) 50-56 (2018).
- [21] Михайлов Е.В., Семенов С.А., Полупан Е.В., ОЦЕНКА БЕЗОПАСНОСТИ ДВИЖЕНИЯ ПО СХОДУ С РЕЛЬСА КОЛЕСА ПЕРСПЕКТИВНОЙ КОНСТРУКТИВНОЙ СХЕМЫ, ВІСНИК СХІДНОУКРАЇНСЬКОГО НАЦІОНАЛЬНОГО УНІВЕРСИТЕТУ імені Володимира Даля № 3 (233) с.120-124 (2017)
- [22] Смольянинов Александр Васильевич, Сравнительный анализ методик расчета устойчивости колесной пары от схода с рельсов, Транспорт Урала/ № 2 (49) стр. 48-54 (2016)
- [23] Бромберг Е.М., Вериго М.Ф., Данилов В.Н., Фришман М.А., Взаимодействие пути и подвижного состава. М., Трансжелдориздат (1956)
- [24] White R. C., Limbert D. A., Hedrick J. K., Cooperrider N. K. Guideway-Suspension Tradeoffs in Rail Vehicle Systems.- Report DOTOS-50107, Washington, Department of Transportation, (1978)
- [25] Gavrilovic Branislav, "A Mechatronic Approach for the Detection of Wheel Slip/Slide and Antislip Control of Locomotive with AC Traction Motors", American Journal of Mechanics and Applications, Vol. 5, No. 6, pp. 47-52, ISSN: 2376-6115. (2017)
- [26] Branislav Gavrilovic, Zoran Bundalo: "USAGE OF THE INTERNAL OPTICAL ENCODER FOR THE DETECTION OF WHEEL SLIP/SLIDE AND ANTISLIP CONTROL IN RAILWAY TRACTION SYSTEMSPROCESS", 3<sup>rd</sup> International Conference „NEW TECHNOLOGIES NT-2016“ Development and Application, pp. 338-347, ISSN 2303-5668 (2016)
- [27] Gavrilović S. Branislav, Bundalo Zoran, Vukadinovic Radisav: „THE RAILWAY VEHICLES OF „SERBIAN RAILWAYS“ WITH WHEEL SLIP CONTROL“, Academic jurnal: Mechanics Transport Communications, Transport Equipment: Per. No. 0414, VI-1, issue 3, ISSN 1312-3823, 19th International Scientific Conference „Transport 2009“, Sofia, Bulgaria. (2009)
- [28] Popovič Z., Lazerevič L., Vatin N. Analysis of Track Gauge Widening in Curves with Small Radius, Applied Mechanics and Materials ISSN: 1662-7482, Vols. 725-726, pp 967-973 (2015)
- [29] Barbosa, R.S.: A 3D contact safety criteria for flange climb derailment of a railway wheel. Vehicle System Dynamics 42 (5), pp. 289–300 (2004)
- [30] Barbosa R. S., Safety of a railway wheelset – derailment simulation with increasing lateral force, Vehicle System Dynamics, Vol. 47, No. 12, 1493–1510 (2009)
- [31] Guan Qinghua, Jing Zeng and Xuesong Jin, An angle of attack-based derailment criterion for wheel flange climbing Proc IMechE Part F: J Rail and Rapid Transit, Vol. 228(7) 719–729 (2014)
- [32] Пенчев Ц., Исследования по крутильным колебаниям вагонных конструкций. Диссертация, ЛИИЖТ, Л., (1974)
- [33] Atmadzhova, D. Methods for determinations of characteristic an bush tie with frame for pushcart an coaches, Thesis VTU "T. Kableshkov", S., (2001)
- [34] Nenov N., Interactions in the system "locomotive - railway" - problem areas and modern solutions, dissertation for awarding the scientific degree "Doctor of Technical Sciences" Sofia, VTU, (2007)
- [35] Bižić Milan, Dragan Petrović, Dušan Stamenković Basics of experimental determination of wheel-rail contact forces using instrumented wheelsets, FACTA UNIVERSITATIS SERIES: Mechanical Engineering Vol. 1, N° 10, (2003).
- [36] Bižić Milan, Dragan Petrović, Methodologies of experimental determination of wheel-rail contact forces., The XVI Conference RAILCON'14, Niš, Serbia, (2014)
- [37] Bizic M. Research of influential parameters in wheel-rail interaction on running stability of railway vehicles Doctoral Dissertation, University of Kragujevac, Faculty of Mechanical and Civil Engineering in Kraljevo, Serbia (2015)
- [38] Bižić Milan, Dragan Z Petrović, Miloš C Tomić and Zoran V Djinović Development of method for experimental determination of wheel–rail contact forces and contact point position by using instrumented wheelset, Measurement Science and Technology, Vol. 28, No 7, (2018)
- [39] Petrovic Dragan, Milan Bižić, Development of Measurement Equipment for Testing of Dynamic Behavior of Railway Vehicles at Faculty of Mechanical Engineering Kraljevo, Workshop on Rail Vehicle Dynamics Kraljevo (2011)
- [40] Bižić M., Petrović D., Stamenković D., Basic aspects of problem of continuous measurement of wheel-rail contact forces, XVII Scientific – expert conference on railways, RAILCON'16, Faculty of Mechanical Engineering, Niš, Serbia, (2016).
- [41] Atmadzhova D. Study on Theoretical Fundamentals of Criteria against Rolling Stock Derailment, Dissertation for Doctor of Science, (2021).

# Research and analysis of electricity quality parameters for traction of trains with multisystem locomotive "Siemens Vectron X4-E-LOC-AB, A26"

Branislav S. Gavrilović<sup>1</sup>\*, Zoran Bundalo<sup>1</sup>, Aleksandar B. Blagojević<sup>1</sup>

<sup>1</sup> Academy of Technical and Artistic Professional Studies Belgrade, Section: College of Railway Engineering, Belgrade, Serbia

The paper presents the results of research on the parameters of electricity quality measured in the output 25 kV field of the Indjija electric traction substation when moving the locomotive "Siemens Vectron X4-E-LOC-AB, A26" on the section of railway from Golubinci station on the right track to the neutral section at Ruma Station (approx. 20 km long). The results of the measurements are significant for undertaking further activities in order to eliminate the observed irregularities.

**Keywords:** Multisystem locomotive, Electric traction substation, Quality parameters

## 1. INTRODUCTION

During 2019, „Serbia Cargo” acquired a total of 16 multi-system locomotives (“Siemens Vectron X4-E-LOC-AB, A26”), which represent the first new electric locomotives in Serbia after a full 38 years. These locomotives are intended for traffic on Corridor 10 (covering the Republic of Austria, Hungary, Slovenia, Croatia, Serbia and Bulgaria) and are equipped with the European Train Control System "ETCS" [8].

The Siemens Vectron X4-E-LOC-AB, A26 multisystem locomotive (Figure 1) is a traction vehicle designed to tow freight and passenger trains capable of being powered by three electric traction systems:

- one DC: 3 kV;
- two AC 15kV/16,7 Hz and 25kV/50 Hz.



Figure 1: Siemens Vectron X4-E-LOC-AB, A26

The technical characteristics of the locomotive are given in Table 1.

Table 1: Technical characteristics of the locomotive "Siemens Vectron X4-E-LOC-AB, A26"

|                                       |                 |
|---------------------------------------|-----------------|
| The total weight of the locomotive    | max. 90 t       |
| Locomotive body weight without bogies | max. 50 t       |
| Overall weight of the bogie           | 17,5 t (+0/-2%) |
| Weight of one wheelset                | 3,1 t           |

|   |   |
|---|---|
| (including gearbox and brake discs)   |   |
| Voltage system  | AC 15AC kV, 16,7 Hz<br>AC 25AC kV, 50 Hz<br>DC 3 DC kV  |
| Layout of wheelset  | Bo'Bo'  |
| Wheel spacing   | 1435 mm   |
| Vehicle length (length above bumper)  | 18980 mm  |
| Vehicle width (above the handlebar)   | 3012 mm   |
| Vehicle height (above train driver's cab)                                     | 3860 mm   |
| Mean distance of the bogies   | 9500 mm   |
| Distance between axles in the bogie   | 3000 mm   |
| Nominal accumulator voltage   | 24DC V  |
| Ambient temperature   | -30 to +40 °C   |
| Maximum application height  | 1400 m beyond normal altitude zero  |
| The smallest coupe radius that can be driven                                  | 250 m   |
| The smallest radius of the trough that can be driven                          | 250 m   |
| Smallest arch radius to drive (open line)                                     | 150 m   |
| Smallest arc radius that can be driven (depot) without dismantling components | 80 m ( $v \leq 5$ km/h, single vehicle)   |
| Maximum traction force  | 300 kN  |
| Maximum electric braking force  | 150 kN  |
| Wheel power (maximum)   | AC 15 KV, 6400 kW (driving and recuperative braking)<br>AC 25 KV, 6400 kW (driving and recuperative braking)<br>DC 3 KV, 6000 kW (driving and recuperative braking)<br>AC 3 KV, 2600 kW (resistive braking) |

The main circuit of the locomotive is realized with three-phase asynchronous motors and indirect vector speed control with the possibility of recuperative electrical braking (Figure 2).

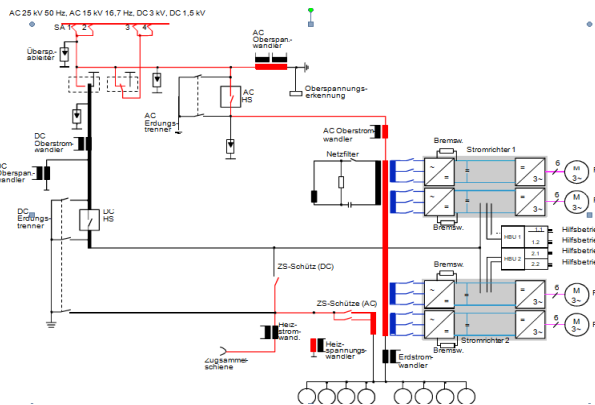


Figure 2: Main circuit of the "Siemens Vectron X4-E-LOK-AB, A26"

The technical characteristics of three-phase asynchronous short-rotor traction motors are:  $U_n = 2675$  V,  $U_{max} = 3353$  V,  $I_n = 384$  A,  $I_{max} = 570$  A,  $P_n = 1480$ ,  $n_n = 1810$  1/min,  $n_{max} = 4300$  1/min,  $f_n = 60,8$  Hz

## 2. POWER QUALITY STANDARDS FOR LOCOMOTIVE POWER SUPPLY

Different standards are used in the world to define the quality of electricity [1, 2, 3]:

- IEEE 1159-1995 (America and some other countries);
- EN 50160- 1994 (Europe);
- IEC 61000-4-30-2000 (International standard).

The European standard EN 50160 processes and determines, among other things, the basic requirements for the quality of electricity at the points of connection of the observed locomotives through the contact line to the electric traction substations (ETS). In these places, the waveform, amplitude, and voltage constancy depend primarily on the strength of the three-phase power grid to which the electric traction substations are connected, ie. on short-circuit power at the ETS connection point, electromagnetic interference in the contact line caused by other locomotives, nonlinearities of the elements of the electric traction system and on the operating characteristics of all electric locomotives. The purpose of the standard EN 50160 is to prescribe the voltage characteristics of the locomotive in relation to the waveform, height, frequency, voltage decays and interruptions. Table 2 gives the limit values of the voltage parameters according to the recommendations of EN 50160.

Table 2: Limit values of voltage parameters as recommended by EN 50160

| Parameters         | Averaging time | Limit values during 95% of the time in one week (160 hours) | Limit values throughout the week (160 hours) |
|--------------------|----------------|---|--|
| Voltage variations | 10 min         | +/- 10%   |  |

| Flickers                  | Pst-10 min<br>Piz- 120 min. | Plt <1                                      |           |
|---------------------------|-----------------------------|---|-----------|
| Total harmonic distortion | 10 min                      | < 8   |           |
| Frequency                 | 10 s                        | +/- 1%                                      | -4% / -6% |
| Voltage decay             | 10 ms                       | It is not defined exactly but descriptively |           |
| Interruptions             | 10 ms                       | It is not defined exactly but descriptively |           |

The specified voltage supply characteristics change during normal operation due to changes in locomotive loads, interferences or malfunctions caused by external events. EN 50160 does not set actual limit values, but sets those values which must not be exceeded during 95% of the observation period of one week (160 hours).

However, the actual voltage and frequency values on the busbars in 110/25 kV electrical substations are defined in the SRPS EN 50163 standard and are given in Table 3.

Table 3: Supply voltages on ETS output busbars

| Minimum voltage of limited duration between $U_{min1}$ and $U_{min2}$ must not exceed 2 minutes $U_{min2}$ | Minimum continuous voltage $U_{min1}$ | Rated voltage $U_n$ | Maximum continuous voltage $U_{max1}$ | Maximal voltage of limited duration between $U_{max1}$ i $U_{max2}$ must not exceed 5 minutes $U_{max2}$ |
|--|---------------------------------------|---------------------|---------------------------------------|--|
| 17 500 V   | 19 000 V                              | 25 000              | 27 500 V                              | 29 000 V   |
| Voltage frequency $f_n$  | 49 (Hz) - 51(Hz)                      |                     |                                       |  |

In the 25 kV, 50 Hz electric traction system, it is of particular interest to consider the time changes of active and reactive power as well as power factors. EN 50388 point 6 provides that the inductive power factor at power greater than 2MW shall not be less than 0,95 and at lesser power not less than 0,85.

EN 50388 clause 12.1.1 provides that trains may not perform energy regeneration if the voltage on the contact line exceeds 29 kV, or if the contact network cannot receive the returned energy.

## 3. DESCRIPTION AND MEASUREMENT RESULTS

On 16.04.2019 at the time from 10:49h to 11:08h the locomotive "Siemens Vectron VECTRON X4-E-LOK-AB, A26" was tested, with serial number 91 80 6193 903-2 during movement on the section of railway from Golubinci station on the right track. to the neutral section at Ruma Station, approx. 20 km in length [4]:.

Measurement was performed by C.A 8352 power quality analyzer manufactured by Chauvin Arnoux. The recording device was connected to the secondary terminals of a voltage measuring transformer that measures voltage at 25 kV busbars in the ETS of Indjija and a current

measuring transformer (measuring core) that measures the current at the circuit breaker that feeds the contact line on the right track of a section from the neutral section Indjija Selo (km 43 + 415) to the neutral section of Ruma (km 66 + 215). The observed locomotive was alone on the feeder arm, so that all measurements refer to the influence of this locomotive exclusively (Figure 3).

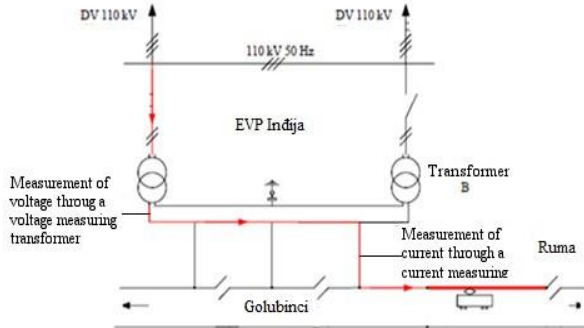


Figure 3: Connection location of C.A 8352 power quality analyzer, Chauvin Arnoux

In the period when measurements were made, that is, by the time the locomotive passed the neutral section of Ruma (from 10:49 h to 11:08 h), slight variations in voltage were observed (Fig. 4):  $U_{min} = 24,45$  kV and  $U_{max} = 24.94$  kV.

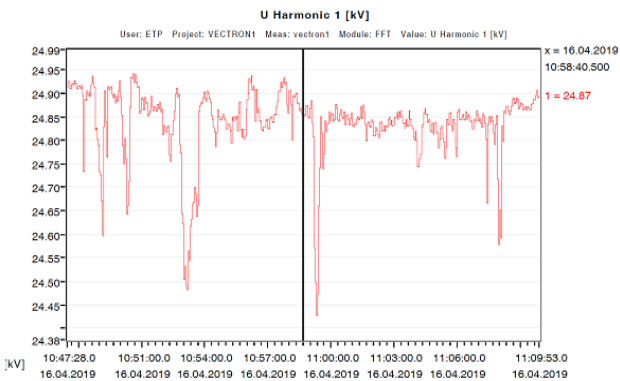


Figure 4: Measured voltage values

At 10:58:40 at maximum voltage  $U = 4.87$  kV and acceleration of the locomotive, a maximum value of traction current of  $I_{maxu} = 123.2$  A was registered (Figure 5).

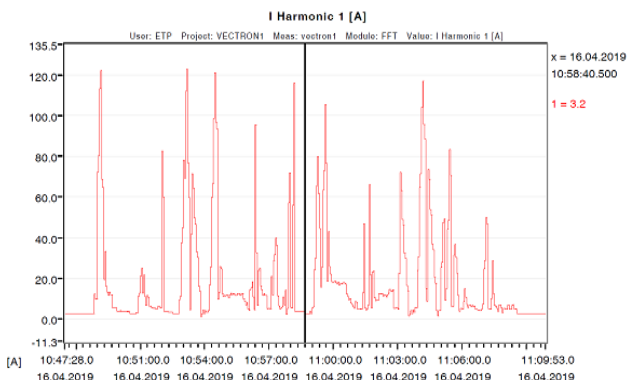


Figure 5: Measured current values

When using recuperative braking at 10:53:09 the maximum braking current was measured:  $I_{maxk} = 73.6$  A (Figure 6). No abnormal increase in the voltage on the contact network was observed during this brake.

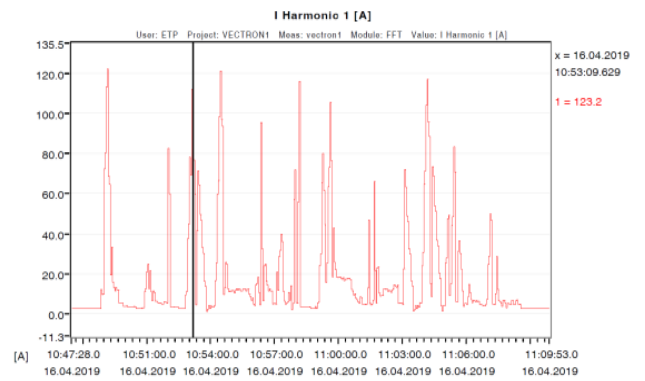


Figure 6: Measured value of current in recuperative braking

When accelerating the locomotive at the maximum traction current value of  $I_{maxu} = 123.2$  A (10:58:40), the highest active power of  $P_{max} = 3,017$  MW and reactive power  $Q_{max} = 0.215$  MVar were recorded, and at regenerative braking, the active power of:

$P_{kočmax} = 1.825$  MW (Figures 7 and 8).

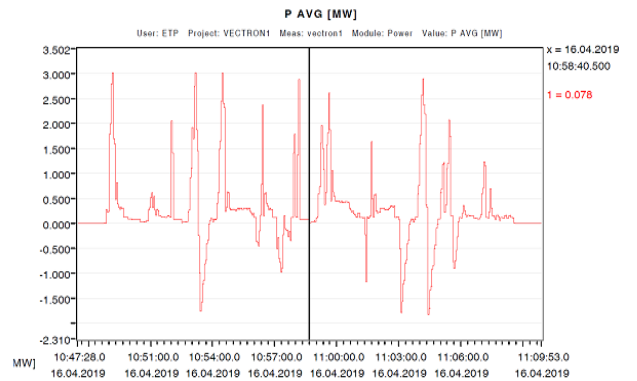


Figure 7: Measured values of active power

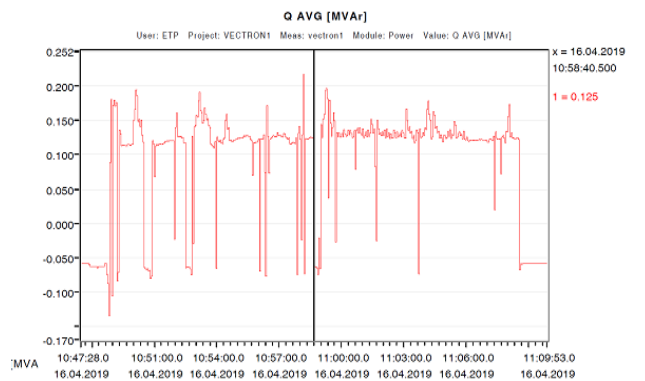


Figure 8: Measured reactive power values

The measured power factor when moving the first locomotive in the period from 10:54:26 to 10:54:34, when the power was greater than 2 MW, was on average 0,999, and during the regenerative braking in the period from 10:53:21 to 10:53:41 averaged 0.998.

The minimum power factor of 0.35 was achieved when controlling the speed of the locomotive in traction mode and at the time interval 10:52:00 to 10:52:20 (Figure 9).

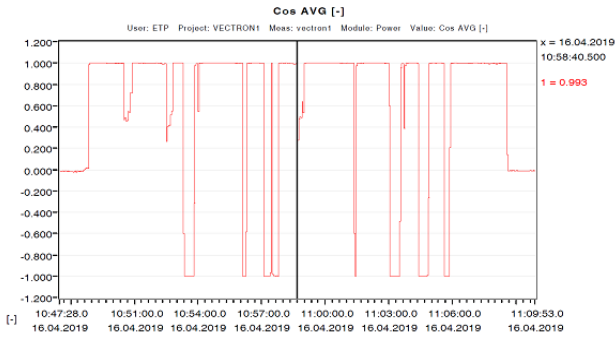


Figure 9: Measured power factor values

The measured values of the higher harmonics of voltage and current as well as their total distortions are given in Figures 10, 11, 12 and 13 respectively. From these figures, it can be seen that the locomotive under study, as a nonlinear consumer, causes only odd harmonics in the waveform of voltages and currents. The measured maximal values of total voltage and current distortion are:  $THD U = 6.395\%$  and  $THD I = 139.792\%$ .  $THD U$  is below the permissible values ( $<8\%$ ) and  $THD I$  is not defined according to EN 50160. However, according to IEEE 1159-1995  $THD I$  is limited to 5%.

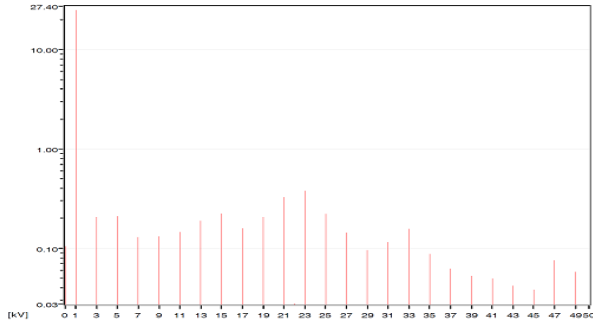


Figure 10: Measured values of higher harmonics of voltage

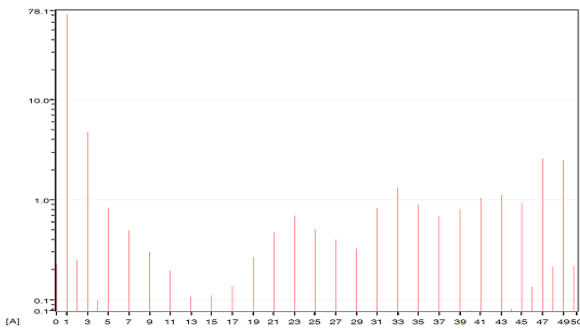


Figure 11: Measured values of higher harmonics of current

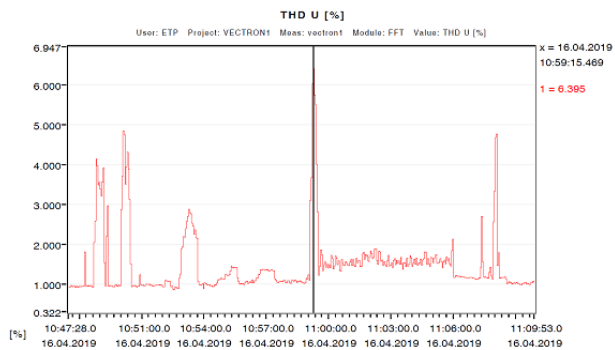


Figure 12: Measured values of Total voltage distortion ( $THD U$ )

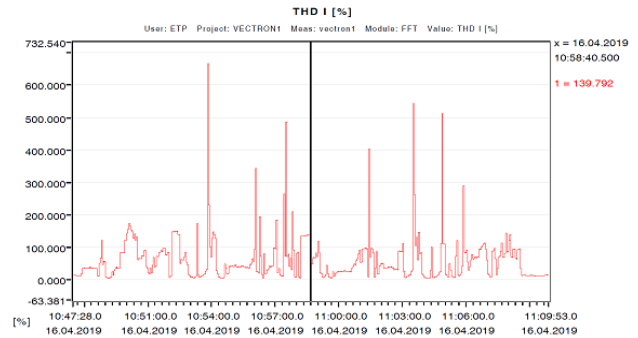


Figure 13: Measured values of total current distortion ( $THD I$ )

Figure 14 shows the time change of the active energy consumed during locomotive movement (for the observed time interval from 10: 47.28 to 11: 09.53 a total of 0.69 MWh), and figure 15 shows the time change of active energy returned to the contact line during the regenerative braking of the locomotive. and via ETS to the three-phase 110 kV transmission network of Serbia (for the observed time interval from 10:47.28 to 11:09.53 a total of 0.19 MWh).

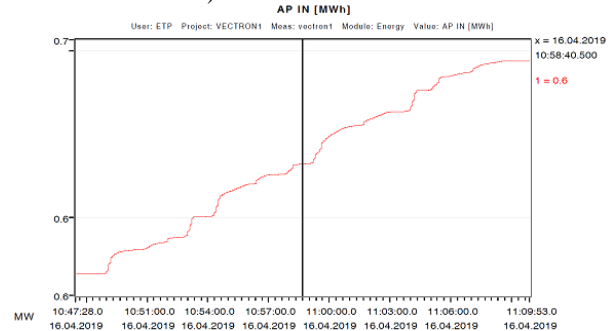


Figure 14: Measured time change of active energy consumption spent for locomotive traction

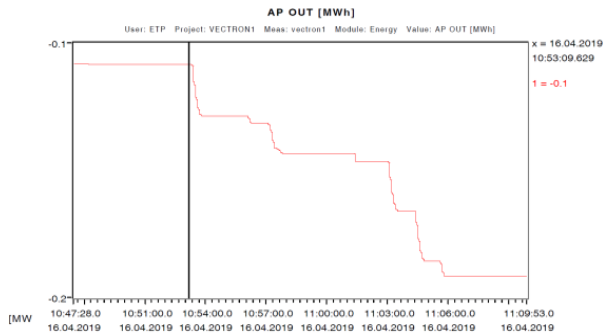


Figure 15: Measured time change of active energy returned to the contact line during locomotive regenerative braking

#### 4. CONCLUSION

Based on the performed measurements and analysis of the parameters of electricity quality on the 25 kV side of ETS Indjija when powering three-system locomotives “Simens Vectron X4-E-LOK-AB, A26” it is concluded:

- Harmonic voltage distortion and corresponding THD are within the permissible limits.
- The change in voltage in the contact line during locomotive regenerative braking is insignificant.
- Harmonic current distortions and corresponding THD are above the prescribed values.

- Only odd higher harmonics with dominant first harmonics are present in the voltage and current waveform.
- Harmonic current distortion and the corresponding *THD* should be reduced by incorporating appropriate active filters into the ETS.
- The power factor is within the prescribed limits both in the electric traction mode and in the regenerative braking of the locomotive.
- The reactive power flows during traction and recuperative braking of the locomotive are considerable ( $Q_{max} = 215$  kVAr)

#### REFERENCES

- [1] Janda Žarko: Review of Standards and Recommendations for the Control of Higher Harmonics in Power Grids, Proceedings, Electrical Engineering Institute "Nikola Tesla", (2004)
- [2] P. Giesbertz P., Petrov K., Quality of Supply in the Regulatory Control", BPC Proceedings, Belgrade, 19-21 June 2002, (2002)
- [3] M. Romero M., Pardo R., Gallego L., Developing a PQ Monitoring System for Assessing Power Quality and Critical Areas Detection, Revista Ingeniería e Investigación, Vol. 31, No. 2, pp. 102-109, (2011)
- [4] P. Urošević, M. Dražić: Report on tests and measurements of electricity quality at the voltage level 25kV while driving and regenerative (recuperative) braking of the VECTRON X4-E-LOK-AB locomotive, variant A26, Serbian Railway Infrastructure, joint-stock company, Electrical Engineering Sector, (2019)
- [5] Ž.R. Đurišić, M.B. Đurić, Description of measurement and acquisition system for control of electricity quality in the distribution system, 27th Consultation JUKO CIGRE, Zlatibor, May 29th - June 3rd 2005, (2005)
- [6] M. Karimi-Ghartemani and M. R. Iravani, Measurement of harmonics/inter-harmonics of time-varying frequencies, IEEE Trans. Power Del., vol. 20, no. 1, pp. 23–31, January (2005)
- [7] M. Romero M., Pardo R., Gallego L., Developing a PQ Monitoring System for Assessing Power Quality and Critical Areas Detection, Revista Ingeniería e Investigación, Vol. 31, No. 2, pp. 102-109, (2011)
- [8] <https://press.siemens.com/global/en/feature/vectron-vehicle-concept>



# Determination of optimal layout, number and way of connection of strain gauges on instrumented railway wheelsets

Milan Bižić\*, Dragan Petrović

Faculty of Mechanical and Civil Engineering in Kraljevo, University of Kragujevac, Serbia

*The instrumented wheelsets are unavoidable measurement equipment in experimental testing of derailment risk of the railway vehicles in accordance to the international regulations. There is no universal technical solution of instrumented wheelsets. There are a lot of different approaches when it comes to the solution of the problems of the determination of locations for placement of strain gauges, as well as their layout, number and way of connection into Wheatstone bridges. The main aim in solving these problems and the design of instrumented wheelsets is achieving the highest possible sensitivity and measurement accuracy. As a continuation of the previous author's researches, this paper analyses mentioned problems and proposes one methodology for their optimal solution. The content of the paper may be useful for all those who are dealing with the problems of development or usage of instrumented railway wheelsets or similar measurement equipment.*

**Keywords: Instrumented wheelset, Strain gauges, Wheel-rail contact forces, Derailment risk.**

## 1. INTRODUCTION

In the processes of certification of newly-designed or modified railway vehicles the international regulations, in a large number of cases, prescribing the usage of the instrumented wheelsets [1, 2]. They are primarily used for continuous indirect measurement of vertical force  $Q$  and lateral force  $Y$  in wheel-rail contact (Fig. 1). The ratio of these two forces  $Y/Q$  is the main parameter for assessment of the derailment risk of tested railway vehicle [3].

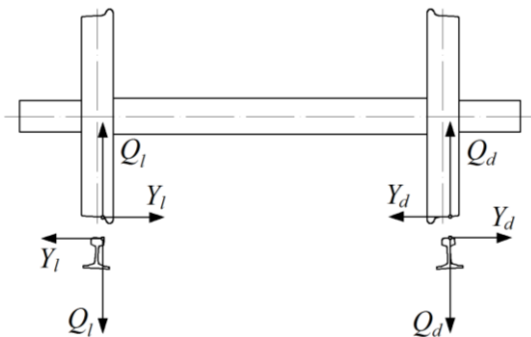


Figure 1: Wheel-rail contact forces

Although they define obligatory usage of instrumented wheelsets, international regulations don't provide more details related to their design and technical solution, measurement accuracy, sensitivity, etc. As a consequence, there are a lot of different approaches and technical solutions of instrumented wheelsets from one test centre or manufacturer to another. The approaches significantly varies when it comes to the solution of the problems of the determination of locations for placement of strain gauges, as well as their layout, number and way of connection into Wheatstone bridges [4]. Success in solving all these problems directly affects the accomplishment of the main aim in development of instrumented wheelsets - high measurement accuracy.

As a continuation of the previous author's researches in this field, this paper, in a gradual and systematic way, analyses the problems of determination of optimal layout, number and way of connection of strain

gauges in the phase of design of instrumented wheelsets. Given in mind the lack of literature and publication with this thematic, the content of the paper may be very useful for all those who are dealing with the problems of development or usage of instrumented railway wheelsets or similar measurement equipment.

## 2. PRINCIPLE OF OPERATION OF STRAIN GAUGE AND WHEATSTONE BRIDGE

Knowledge of the principle of operation of strain gauge and Wheatstone bridge is the basis for solving the problem of experimental determination of unknown parameters in wheel-rail contact and determining the optimal layout, number and way of connection of strain gauges on the wheel of instrumented wheelset, with the aim of achieving high measurement accuracy. The strain gauges in their present form were found and patented in the middle of the last century in USA. From then, strain gauges have been using as one of the most common transducers in experimental tests of mechanical and other structures. Their primary purpose is measurement of strains, but they can also be indirectly used to measure stresses, forces, moments, as well as other quantities that can be related to the strains.

The principle of operation of strain gauge is based on the resistance effect, i.e., on the change of the electrical resistance of the wire during its loading. In general, each strain gauge consists of two flat insulating strips between which a thin conductive wire is placed which is bent several times in order to increase its length (Fig. 2).

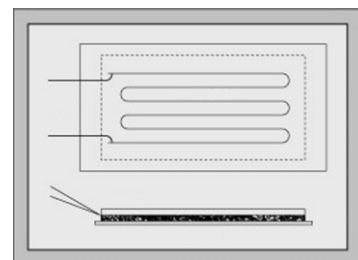


Figure 2: Construction of strain gauge

\*Corresponding author: Milan Bižić, Dositejeva 19, 36000 Kraljevo, Serbia, bizic.m@mfkv.kg.ac.rs

The strain gauge is glued to the surface of the tested object, and when the object is deformed, it simultaneously deforms and changes electrical resistance of the strain gauge. In the general case, there is the following mathematical connection between the change in the electrical resistance of the strain gauge and the measured strain of the object:

$$\frac{\Delta R}{R} = k\varepsilon \quad (1)$$

where:  $\varepsilon$  – measured strain of the object,  $R$  – nominal resistance of strain gauge,  $\Delta R$  – change of resistance of strain gauge,  $k$  – strain gauge factor.

Bearing in mind that the values of strains  $\varepsilon$  measured during testing of structures are very small, it can be concluded that the change in resistance  $\Delta R$  also will be very small. Precisely for that reason, direct resistance measurements are not performed in the practise, but Wheatstone bridges are used.

Wheatstone Bridge is defined as an electrical circuit designed to accurately and precisely measure of electrical resistance. It consists of 4 resistors (in this case the resistors are strain gauges of nominal resistances  $R_i$ ,  $i=1\div 4$ ), power supply and measuring instrument (Fig. 3). The electrical voltage  $U_E$  is supplied to one diagonal of the bridge, while the measuring instrument measures the output electrical voltage  $U_A$  that occurs between the ends of the other diagonal of the bridge.

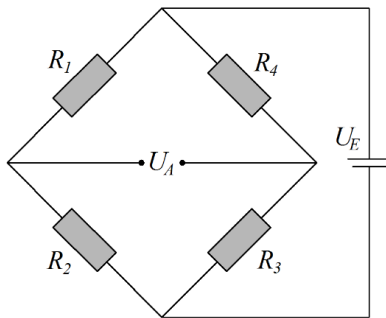


Figure 3: Wheatstone bridge

The output voltage of the Wheatstone bridge  $U_A$  can be calculated according to the following expression:

$$U_A = U_E \frac{R_1 R_3 - R_2 R_4}{(R_1 + R_3)(R_2 + R_4)} \quad (2)$$

If the bridge is composed of 4 strain gauges of identical resistances and is in equilibrium, the change of resistance of each strain gauge  $\Delta R_i$  ( $i=1\div 4$ ) leads to the occurrence of bridge imbalance, where the output voltage  $U_A$  can be determined according to the following expression:

$$U_A = U_E \frac{\frac{\Delta R_1}{R} + \frac{\Delta R_3}{R} - \frac{\Delta R_2}{R} - \frac{\Delta R_4}{R}}{4} \quad (3)$$

By replacing expression (1) into the previous expression, a connection is established between the strains registered by each of the four strain gauges  $\varepsilon_i$  ( $i=1\div 4$ ) and the output voltage of the Wheatstone bridge  $U_A$ :

$$U_A = U_E \frac{k(\varepsilon_1 + \varepsilon_3 - \varepsilon_2 - \varepsilon_4)}{4} \quad (4)$$

By combining active strain gauges (glued to the tested object), passive strain gauges (not glued to the test object) and resistors that are an integral part of the measuring instrument, in the general case, it is possible to realize three types of configurations of Wheatstone bridges: full-bridge configuration, half-bridge configuration and quarter-bridge configuration.

Given in mind that the output voltage of the Wheatstone bridge  $U_A$  is proportional to the supply voltage  $U_E$ , the influence of changes in resistance or strains of strain gauges on the output voltage of the bridge is usually described by  $U_A/U_E$  ratio which is dimensionless, and according to expression (4) can be defined as:

$$\frac{U_A}{U_E} = \frac{k}{4} (\varepsilon_1 + \varepsilon_3 - \varepsilon_2 - \varepsilon_4) \quad (5)$$

Since at a supply voltage of several [V], the output voltage is usually of the order of several [mV], then the  $U_A/U_E$  ratio, i.e., signal from measuring – Wheatstone bridge is usually expressed in [mV/V] units.

### 3. SIGNALS FROM MEASURING BRIDGES AT MEASUREMENT OF PARAMETERS IN WHEEL-RAIL CONTACT

In experimental determination of unknown parameters in wheel-rail contact using an instrumented wheelset, only those discrete values of mixed signals from measuring bridges that appear at the moments when each strain gauge passes above the contact point between wheel and rail, are relevant (Fig. 4).

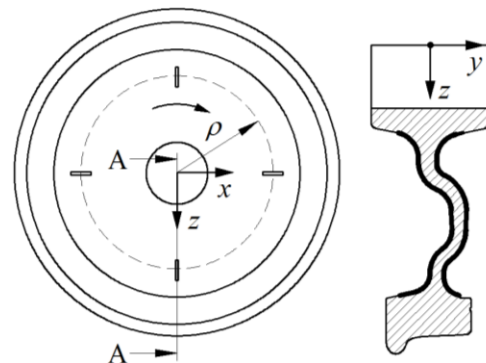


Figure 4: Section A-A relevant for determination of unknown parameters in wheel-rail contact

In order to analyse the signals in more detail, one specific case is considered. It implies that at each optimal radial distance on the wheel there is one full measuring bridge which is formed by connecting of 4 strain gauges, arranged at angles of  $90^\circ$  (Fig. 5).

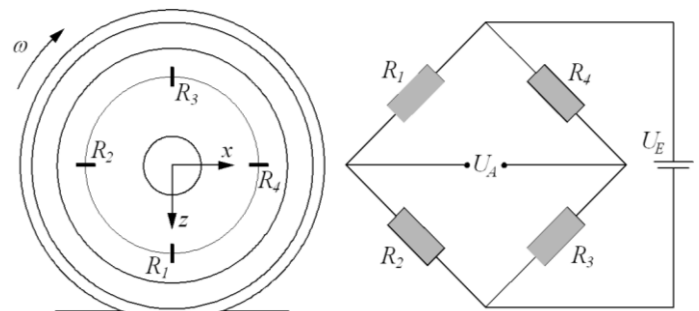


Figure 5: Full measuring bridge at wheel formed by connecting of 4 strain gauges arranged at  $90^\circ$

During wheel rotation, a measuring signal is obtained from each bridge, which changes as a function of the change of parameters in the wheel-rail contact, speed of movement and angular position of the wheel. The maximum values of the measuring signals appear at the moments when the strain gauges pass above the contact point, i.e., 4 times during one rotation of the wheel (Fig. 6). The intensity of these maximum values depends on the intensity of wheel-rail contact forces and the position of contact point, while the time between their occurrence  $t_p$  depends on the running speed of the tested vehicle. Therefore, when there are 4 strain gauges at a given optimal radial distance, the discrete values of the measurement signals relevant for determining the unknown parameters in the wheel-rail contact are obtained at each 1/4 of the wheel circumference. All other values of measuring signals, in periods when strain gauges are not above the contact point, have no significance for measuring. Thus, in the inverse identification algorithm, during one wheel revolution, maximum discrete values of each of the measuring signals are introduced, which arise as a consequence of mixing the influence of the parameters to be measured. By solving the inverse identification problem and determining individual influences based on the values of the mixed input signals, output signals of the unknown parameters are obtained (Fig. 7) [3, 5]. These output signals represent discrete values whose intensity changes during the time, i.e., movement along the track, where the time  $t_p$  depends on the running speed of the tested railway vehicle.

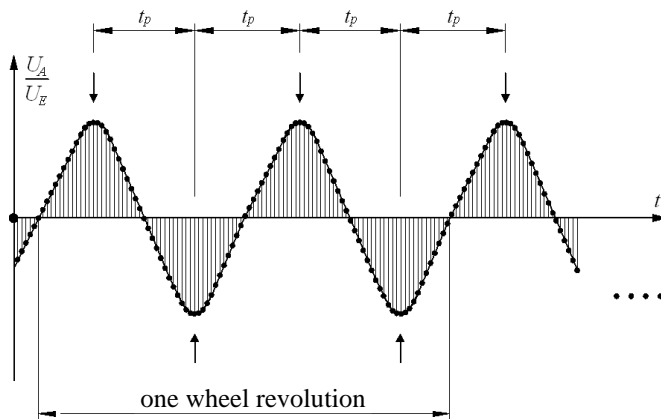


Figure 6: Appearance of measuring mixed input signals obtained during one wheel revolution

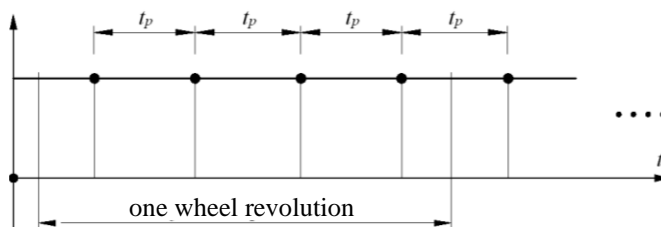


Figure 7: Appearance of the output signal of parameters in the wheel-rail contact

#### 4. DIFFERENT SOLUTIONS OF LAYOUT, NUMBER AND WAY OF CONNECTION OF STRAIN GAUGES

In accordance with the previous considerations, different variants of layout, number and way of connection of strain gauges are analysed in this chapter, which should

lead to the definition of the optimal solution. For each solution, the following characteristics are determined, which are extremely important for the analysis of its acceptability as well as assessment of measurement quality: time elapsed between two adjacent representative values of the measuring signal ( $t_{rv}$ ); distance travelled between two adjacent representative values of the measuring signal ( $s_{rv}$ ); frequency of strain gauges crossing above the wheel-rail contact point ( $f$ ).

A special attention is paid to the analysis of whether the given solution enables compensation of the influence of centrifugal acceleration due to wheel rotation, as well as the influence of ambient temperature and temperature due to braking. All solutions were analysed for three different running speeds of 50, 100 and 150 km/h. The basic parameters related to the wheel running with specified speeds are given in Table 1.

Table 1: Parameters of wheel running with speeds of 50, 100 and 150 km/h

| Parameters of wheel running             |                    | Running speed $v$ [km/h] |       |       |
|---|--------------------|--------------------------|-------|-------|
|   |                    | 50                       | 100   | 150   |
| Angular speed of wheel                  | $\omega_o$ [rad/s] | 30.19                    | 60.39 | 90.58 |
| Number of revolutions per sec           | $n_o$ [o/s]        | 4.81                     | 9.62  | 14.42 |
| Duration of one revolution              | $t_o$ [s]          | 0.21                     | 0.10  | 0.07  |
| Distance traveled during one revolution | $s_o$ [m]          | 2.89                     | 2.89  | 2.89  |

#### 4.1. One strain gauge

If at a certain radial distance there is one strain gauge connected in quarter-bridge (Fig. 8), only one representative discrete value of measuring signal relevant for determining unknown parameters in wheel-rail contact is obtained during one wheel rotation. The basic characteristics of solution with one strain gauge are given in Table 2.

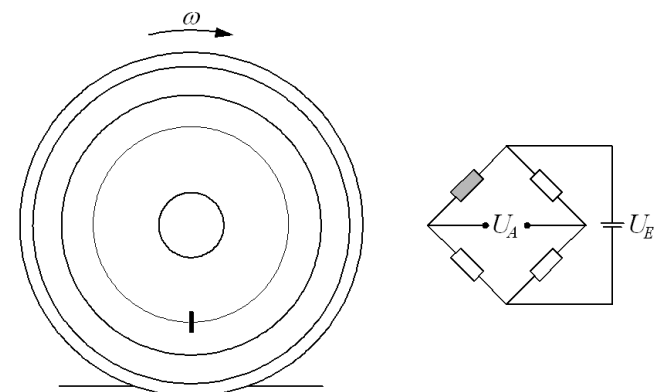


Figure 8: One strain gauge connected in quarter-bridge

Table 2: Characteristics of solution with one strain gauge

| Characteristics | Running speed $v$ [km/h] |      |       |
|-----------------|--------------------------|------|-------|
|                 | 50                       | 100  | 150   |
| $t_{rv}$ [ms]   | 210                      | 100  | 70    |
| $s_{rv}$ [m]    | 2.89                     | 2.89 | 2.89  |
| $f$ [Hz]        | 4.76                     | 10   | 14.28 |

It can be seen that, regardless of the speed  $v$ , the distance travelled between two adjacent representative

discrete values of the measuring signal  $s_{rv}$  is 2.89 m. Given that international standards require the measurement of forces in the wheel-rail contact and the  $Y/Q$  ratio per 2 m of distance travelled, it can be concluded that a solution with one strain gauge is unacceptable. In addition, the quarter-bridge solution does not provide the necessary compensation for the effects of centrifugal acceleration due to wheel rotation and the effects of ambient temperature and temperature due to braking.

4.2. 2 strain gauges at 180°

If at a certain radial distance there are 2 strain gauges arranged at 180° and connected in half-bridge (Fig. 9a), two representative discrete values of measuring signal relevant for determining unknown parameters in wheel-rail contact are obtained during one wheel rotation. The basic characteristics of this solution are given in Table 3.

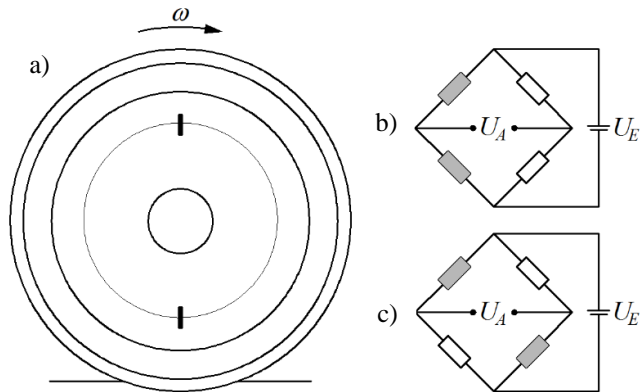


Figure 9: 2 strain gauges arranged at 180°

Table 3: Characteristics of solution with 2 strain gauges

| Characteristics | Running speed $v$ [km/h] |       |       |
|-----------------|--------------------------|-------|-------|
|                 | 50                       | 100   | 150   |
| $t_{rv}$ [ms]   | 105                      | 50    | 35    |
| $s_{rv}$ [m]    | 1.445                    | 1.445 | 1.445 |
| $f$ [Hz]        | 9.52                     | 20    | 28.57 |

In this solution, the distance travelled between two adjacent representative values of the measuring signal is 1.445 m, i.e., it is twice smaller in relation to the solution with one strain gauge. Discrete values of signal relevant for determining the parameters in the wheel-rail contact would be obtained for every 1.445 m of distance travelled, which is insufficient from the aspect of measurement reliability. Solution with 2 strain gauges connected in a half-bridge configuration enables compensation of the influence of centrifugal acceleration and temperature, if strain gauges are connected in adjacent branches of the bridge (Fig. 9b). If strain gauges are connected in opposite branches of the bridge (Fig. 9c), the mentioned undesirable influences are duplicated.

4.3. 4 strain gauges at 90°

If at a certain radial distance there are 4 strain gauges arranged at 90° and connected in full-bridge (Fig. 5), four representative discrete values of measuring signal relevant for determining unknown parameters in wheel-rail contact are obtained during one wheel rotation. The basic characteristics of this solution are given in Table 4.

In this solution, the distance travelled between two adjacent representative values of the measuring signal is

0.7225 m. Discrete values of signal relevant for determining the parameters in the wheel-rail contact would be obtained for every 0.72 m of distance travelled, which is on the very edge of acceptability from the aspect of measurement reliability and quality. Solution with 4 strain gauges connected in a full-bridge enables compensation of the influence of centrifugal acceleration and temperature.

Table 4: Characteristics of solution with 4 strain gauges

| Characteristics | Running speed $v$ [km/h] |        |        |
|-----------------|--------------------------|--------|--------|
|                 | 50                       | 100    | 150    |
| $t_{rv}$ [ms]   | 52.5                     | 25     | 17.5   |
| $s_{rv}$ [m]    | 0.7225                   | 0.7225 | 0.7225 |
| $f$ [Hz]        | 19.05                    | 40     | 57.14  |

4.4. 8 strain gauges at 45°

If at a certain radial distance there are 8 strain gauges arranged at 45° and connected in full-bridge (Fig. 10a), 8 representative discrete values of measuring signal relevant for determining unknown parameters in wheel-rail contact are obtained during one wheel rotation. The basic characteristics of this solution are given in Table 5.

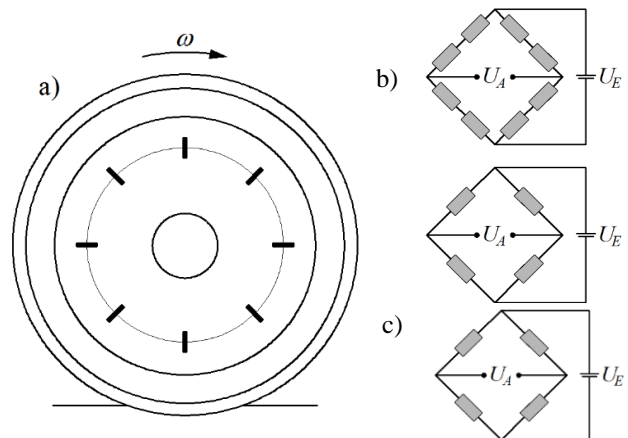


Figure 10: 8 strain gauges arranged at 45°

Table 5: Characteristics of solution with 8 strain gauges

| Characteristics | Running speed $v$ [km/h] |         |         |
|-----------------|--------------------------|---------|---------|
|                 | 50                       | 100     | 150     |
| $t_{rv}$ [ms]   | 26.25                    | 12.5    | 8.75    |
| $s_{rv}$ [m]    | 0.36125                  | 0.36125 | 0.36125 |
| $f$ [Hz]        | 38.09                    | 80      | 114.28  |

With this solution of layout and number of strain gauges, the discrete values of the measuring signal relevant for determining the parameters in the wheel-rail contact would be obtained approximately every 36 cm of distance travelled, which is two times larger than the solution with 4 strain gauges. The strain gauges can be connected in one full-bridge (Fig. 10b), or in two independent full-bridges (Fig. 10c). Both ways enable compensation of the influence of centrifugal acceleration and temperature.

4.5. 12 strain gauges at 30°

If at a certain radial distance there are 12 strain gauges arranged at angles of 30° (Fig. 11a), which are connected in one or three full-bridges (Fig. 10b,c), 12 representative discrete values of measuring signal are obtained during one wheel rotation. The basic characteristics of this solution are given in Table 6.

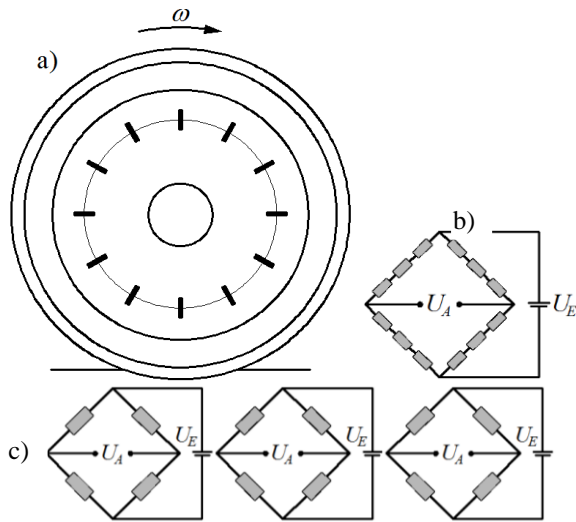


Figure 11: 12 strain gauges arranged at 30°

Table 6: Characteristics of solution with 12 strain gauges

| Characteristics | Running speed $v$ [km/h] |         |         |
|-----------------|--------------------------|---------|---------|
|                 | 50                       | 100     | 150     |
| $t_{rv}$ [ms]   | 17.5                     | 8.33    | 5.83    |
| $s_{rv}$ [m]    | 0.24083                  | 0.24083 | 0.24083 |
| $f$ [Hz]        | 57.14                    | 120.05  | 171.53  |

With this solution of layout and number of strain gauges, the discrete values of the measuring signal relevant for determining the parameters in the wheel-rail contact would be obtained approximately every 24 cm of distance travelled. The strain gauges can be connected in one full-bridge (Fig. 11b), or in 3 independent full-bridges (Fig. 11c). Both ways enable compensation of the influence of centrifugal acceleration and temperature.

4.6. 16 strain gauges at 22.5°

If at a certain radial distance there are 16 strain gauges arranged at angles of 22.5° (Fig. 12a), which are connected in 1, 2 or 4 full-bridges (Fig. 12b,c,d), 16 representative discrete values of measuring signal are obtained during one wheel rotation.

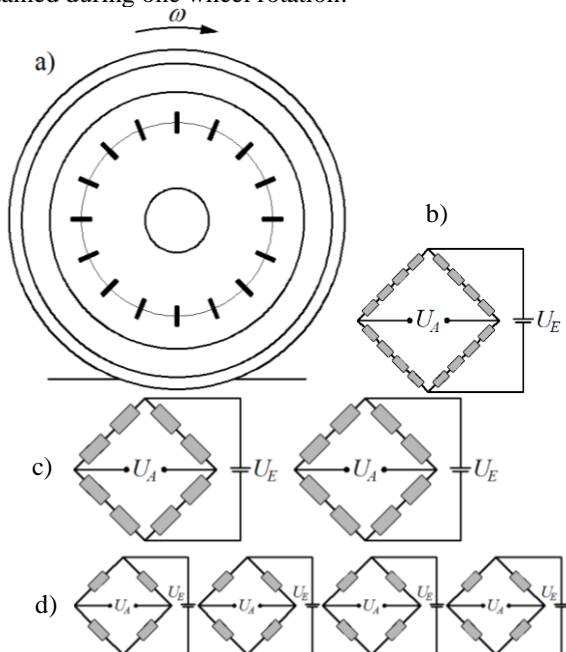


Figure 12: 16 strain gauges arranged at 22.5°

The basic characteristics of the solution with 16 strain gauges are given in Table 7. With this solution, the discrete values of the measuring signal relevant for determining the parameters in the wheel-rail contact would be obtained approximately every 18 cm of distance travelled. The strain gauges can be connected in one full-bridge (Fig. 12b), 2 independent full-bridges (Fig. 12c) or 4 independent full-bridges (Fig. 12d). All three ways enable compensation of the influence of centrifugal acceleration and temperature.

Table 7: Characteristics of solution with 16 strain gauges

| Characteristics | Running speed $v$ [km/h] |          |          |
|-----------------|--------------------------|----------|----------|
|                 | 50                       | 100      | 150      |
| $t_{rv}$ [ms]   | 13.125                   | 6.25     | 4.375    |
| $s_{rv}$ [m]    | 0.180625                 | 0.180625 | 0.180625 |
| $f$ [Hz]        | 76.19                    | 160      | 228.57   |

5. SELECTION OF OPTIMAL LAYOUT AND NUMBER OF STRAIN GAUGES

When choosing the optimal layout and number of strain gauges, several mutually contradict criteria should be taken into account. First of all, the criterion of reliability of measurements must be taken into account. It should be taken into account that international standards prescribe determination of wheel-rail contact forces at 2 m of the distance travelled. Thus, the first criterion that should be taken into account is the distance travelled between two adjacent representative discrete values of the measurement signal  $s_{rv}$ , authoritative for determination of the unknown parameters in the wheel-rail contact. If the choice of layout and number of strain gauges were made according to this criterion, then the optimal solution would involve a large number of strain gauges. However, such solutions are unacceptable from the aspect of the possibility of technical realization of the measuring system and its cost price. Therefore, when choosing the optimal solution, the criteria of the number of strain gauges at one wheel  $n_{sgw}$  and the number of strain gauges on the instrumented wheelset  $n_{ws}$ , must also be taken into account. In order to select the optimal solution, Table 8 is formed, which gives a comparative overview of the values of previously defined parameters relevant for the selection of the optimal layout and number of strain gauges.

Table 8: Comparative overview of parameters relevant for the selection of the optimal solution

| Criterion | Number of strain gauges at one radial distance |        |       |       |       |       |
|-----------|--|--------|-------|-------|-------|-------|
|           | 1  | 2      | 4     | 8     | 12    | 16    |
| $s_{rv}$  | 289 cm   | 144 cm | 72 cm | 36 cm | 24 cm | 18 cm |
| $n_{sgw}$ | 4  | 8      | 16    | 32    | 48    | 64    |
| $n_{ws}$  | 8  | 16     | 32    | 64    | 96    | 128   |

It can be seen that according to the criterion of the distance travelled between two adjacent representative values of the measuring signal, the most favourable solution is with 16 strain gauges. However, that means that one wheel would be equipped with 64, and one instrumented wheelsets with 128 strain gauges. In addition to the high production costs, such a solution would be extremely difficult for technical implementation due to the presence of a large number of strain gauges, cables and

other equipment in a very limited space. Somewhat smaller, but similar problems exist with the solution with 12 strain gauges, which is also not favourable. On the other hand, solutions with one and two strain gauges are not acceptable from the aspect of measurement reliability, and the solution with 4 measuring tapes is at the very limit of acceptability. Based on all this, it can be concluded that the optimal solution is with 8 strain gauges that provides sufficient reliability of measurement, and at the same time it is acceptable from the aspect of technical realization and cost price of the measuring system. The finally determined optimal layout and number of strain gauges per wheel is shown in Fig. 13.



Figure 13: Finally determined optimal layout and number of strain gauges per wheel [5]

6. SELECTION OF OPTIMAL WAY OF CONNECTION OF STRAIN GAUGES

By analysing the output signals from the measuring bridges  $U_A/U_E$ , and based on the values of strains obtained from the wheel FEM model [3], it was concluded that the most favorable solution is to connect all eight strain gauges at one radial distance into one full measuring bridge. The highest values of the output signals  $U_A/U_E$  for different load combinations are obtained when two adjacent strain gauges at a given radial distance are connected in series, in the same branch of the measuring bridge. This solution ensures that, in the case of constant values of the wheel-rail contact forces, the given bridge shows identical discrete values of the measuring signal at passing the strain gauges over the contact point. The defined optimal way of connection of strain gauges at four optimal radial distances according to Fig. 13, is shown in Fig. 14.

It is very important to emphasize that the defined way of connection of strain gauges enables compensation of the influence of centrifugal acceleration due to wheel rotation, as well as the influence of ambient temperature and temperature due to braking. In the general case, the output signals from the measuring bridges shown in Fig. 13 can be determined based on the following expression:

$$\left(\frac{U_A}{U_E}\right) = \frac{k}{4} (\varepsilon_1 + \varepsilon_2 - \varepsilon_3 - \varepsilon_4 + \varepsilon_5 + \varepsilon_6 - \varepsilon_7 - \varepsilon_8) \quad (6)$$

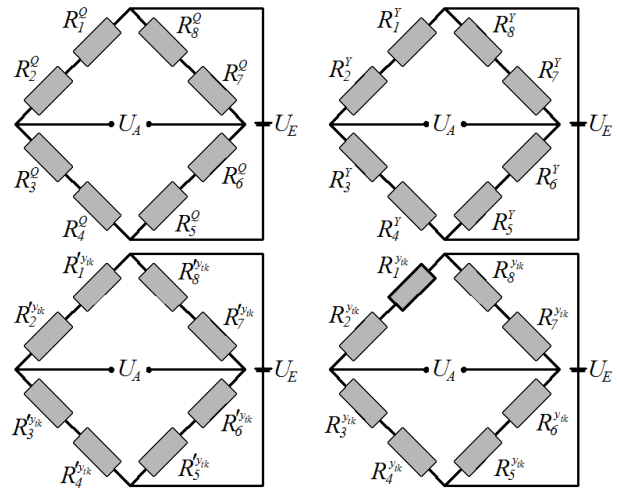


Figure 14: Defined optimal way of connection of strain gauges at four optimal radial distances

7. CONCLUSION

Obtained optimal solutions of layout, number and way of connection of strain gauges, with determination of their optimal locations - radial distances, provide good basis for development of instrumented wheelsets of high performance and measurement accuracy. These results have a high practical significance, bearing in mind that the instrumented wheelsets will certainly be used for a long time for testing the dynamic behaviour of railway vehicles. Further researches in this field should be directed toward the testing of eventual convenience of usage of fiber-optic sensors instead the strain gauges.

ACKNOWLEDGEMENTS

The authors wish to express their gratitude to Serbian Ministry of Education, Science and Technological Development for supporting this research (contract no. 451-03-9/2021-14/200108).

REFERENCES

[1] EN 14363:2016+A1:2018, Railway applications – Testing and Simulation for the acceptance of running characteristics of railway vehicles – Running Behaviour and stationary tests, (2018)

[2] UIC CODE 518 OR, Testing and approval of Railway vehicles from the point of view of their dynamic behaviour – Safety – Track fatigue – Running behaviour. 4th edition, (2009)

[3] M. Bižić, Research of influential parameters in wheel–rail interaction on running stability of railway vehicles, PhD Thesis, University of Kragujevac, Faculty of Mechanical and Civil Engineering in Kraljevo, Serbia, (in Serbian), (2015)

[4] M. Bižić, D. Petrović, Methodologies of experimental determination of wheel-rail contact forces, Proceedings of XVI International Scientific-Expert Conference on Railways – RAILCON 2014, pp. 157-160, (2014)

[5] Bižić, M., Petrović, D., Tomić, M., Djinović, Z., Development of method for experimental determination of wheel–rail contact forces and contact point position by using instrumented wheelset, Measurement Science and Technology, Vol. 28, No. 7; 25 pp., (2017)

# Failure analysis in passenger bogies from the railway system of the Republic of Bulgaria

Vanio Ralev<sup>1</sup>, Dobrinka Atmadzhova<sup>2</sup>

<sup>1,2</sup> Machinery and Construction Technologies in Transport/Transport Equipment, Todor Kableskov University of Transport, Sofia (Bulgaria)

*This paper is based on a review of a study of damage to passenger bogies on railway vehicles. The results of the research of the reliability of the passenger bogies from the park of the Bulgarian State Railways (BDZ) are analyzed. The constructions of passenger bogies type swing in the operation of the Republic of Bulgaria are presented - YT72, Görlitz V and GP200. The most common faults of the passenger bogies are indicated. The general failures, the probable causes of failures and the ways to minimize them have been successfully identified.*

**Keywords – Railway vehicles, passenger cars, bogies.**

## 1. INTRODUCTION

All modern passenger wagons are with bogies. Passenger wagons are subject to greater requirements in terms of smoothness, the size of the accelerations of the body car and the dynamic forces, and for movement at much higher speeds [1, 2]. This imposes a number of requirements on the construction of passenger wagons, namely:

- a) a small total mass of the bogies and especially of the unsprung parts;
- b) providing a large static sag (especially in the range of 200-300 mm) of spring suspension in two degrees;
- c) realization of an elastic connection in the transverse direction between the basket (respectively the spring beam) and the bogie frame by means of a rocking device in the central spring stage, working on the pendulum principle, or by using horizontal transverse deformation of the central springs;
- d) an effective system for damping all types of oscillations;
- e) the distance between the spring sets, measured transversely to the wagon, shall be as large as possible and the side bearer on the bogies shall lie closer to the plane passing through the axles of the wheels in order to increase the lateral stability and reduce the intensity of the lateral oscillations of the carbody;
- f) the braking system to be with high efficiency, etc.

## 2. THE CONSTRUCTION TYPE SWING BOGIE

The first Bulgarian passenger bogie, produced in our country for the VKAZH-57 wagons, is similar to the carriages of the Görlitz IV family (Germany). The second Bulgarian construction used in the non-compartment and part of the compartment cars manufactured in our country after 1964 is the T-65 bogie.

Frequent damages in primary suspension require structural changes, after which the bogie receives the designation T 65-2. On its basis in 1972 the bogie YT-72 was created [3].

The Görlitz-V bogie is used in most of the wagons imported from Germany, and the imported couchette wagons have GP 200 bogies.

The object of this article are bogies type YT-72, Görlitz-V/Va/DVJ and GP 200.

### 2.1. Bogie YT-72 and YT-72 A

The bogie YT-72 (fig.1) is intended for wagons type B4-68 and 70.

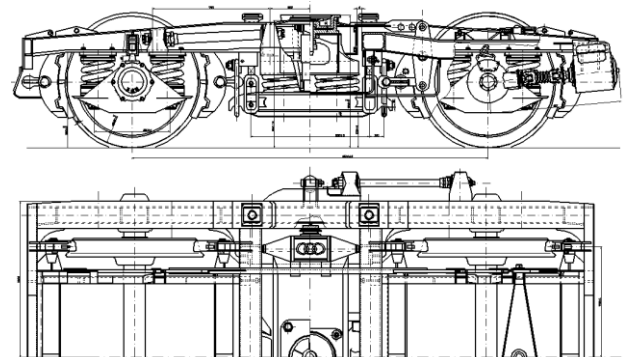


Figure 1. General view of the bogie type YT-72.

The base of the bogie is 2.5 m, the wheel axles in the rolling circle for the bogie YT-72 are 1000mm, and for the bogie YT-72A are 920mm. Design speed - 160 km/h.

The frame is a welded construction, closed type, consisting of two side longitudinal beams, front beams, cross beams and inner beams.

The spring suspension is made of springs.

The axle boxes are spindle driven. The primary suspension consists of two sets of double coil springs and a friction vibration damper, consisting of a conical sleeve and 6 conical segments pressed by the inner axle spring.

The secondary spring suspension consists of 4 sets - double coil springs, two vertical hydraulic dampers with a stroke of 150 mm, mounted externally and two transverse horizontal hydraulic dampers with a stroke of 100 mm, mounted internally between the bolster and the internal crossbeams of the frame. The transverse elastic mobility

\*Corresponding authors: Vanio Ralev, 158 Geo Milev Str. 1574 Sofia, Bulgaria, vanio.ralev@gmail.com

Dobrinka Atmadzhova, 158 Geo Milev Str. 1574 Sofia, Bulgaria, atmadzhova@abv.bg

between the carbody, respectively the bolster of the bogie and its frame, is realized by a swing device in the secondary suspension (as in the bogie T-65). The bogie has two linkers for longitudinal guidance of the spring beam and a generator for lighting.

The vertical load from the carbody is transmitted to the bogie only by the side bearers. The central pivot is a traditional type (cylindrical flat), but its upper part is raised by 10 mm, so it transmits only horizontal loads.

### 2.2 Bogie type Görlitz V

The Görlitz V bogie [3] is a modern construction (Fig. 2) with a two-stage suspension of cylindrical coil springs only.

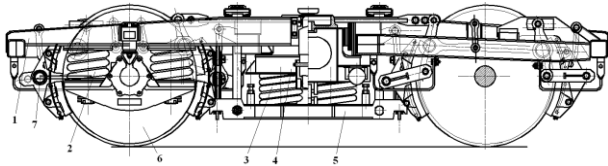


Figure 2. Bogie Görlitz V 1-frame; 2- primary suspension; 3-secondary suspension; 4-bolster; 5-spring beam; 6-wheelset; 7- braking system.

The secondary suspension is a swing, made of four sets of coil springs lying on two beams, which are suspended in a pendulum in the frame of the bogie. The spring beam is suspended to the bogie frame by means of balancing bolts (swing supports). The adjustment of the distance "buffers-head rail" is carried out by means of a balancing nut on the frame of the bogie and a screw thread of the balancing bolts. The movement of the swing in space amounts to 25mm in the transverse direction and 5mm in the longitudinal direction. The transverse and longitudinal clearances of the swing are limited by metal-rubber supports. The damping is in the secondary suspension and is carried out by two vertical and two horizontal dampers.

The primary suspension consists of two coil springs located on both sides of the axle on its wings. The axle wings are guided by spindles and bushings located between them.

The bogie frame consists of two longitudinal beams, two transverse beams forming the cradle space and two front beams.

The carbody rests on the side bearer by a center pivot of flat type, and the lateral support of the carbody is done by height-adjustable hinged sliders. There is a small gap between the bogie sliders and the carbody, so that the vertical and horizontal loads from the carbody on the frame are transmitted through the center pivot, and only the additional vertical loads from the centrifugal and wind force of the carbody are transmitted through the sliders.

The base of the bogie is 2.5 m. Mass of the bogie - 6103 kg.

### 2.3 Bogie type Görlitz Va/DVJ

This bogie (Fig. 3) has been reconstructed in order to provide good ride quality, noise reduction by installing additional rubber elements, and also by installing disc brakes to achieve a better braking effect. This bogie (Fig. 3) has been reconstructed in order to provide good ride quality, noise reduction by installing additional rubber

elements, and also by installing disc brakes to achieve a better braking effect. This bogie (Fig. 3) has been reconstructed in order to provide good ride quality, noise reduction by installing additional rubber elements, and also by installing disc brakes to achieve a better braking effect.

The new bogies are equipped with a disc brake system, modified spring suspension, and modified bearing, additional rubber elements for sound insulation, grounding of the axle ends and at the same time electronic traction protection.

The guide of the axle box has been changed using a new development of DVJ, namely tight-elastic guide of the axle boxes.

The guide elements (spindles) have retained their old dimensions and are mounted on the machined surfaces of the bogie frame.

The rubber ring, ensuring the elasticity of the axle box connection, is placed in a tubular construction.

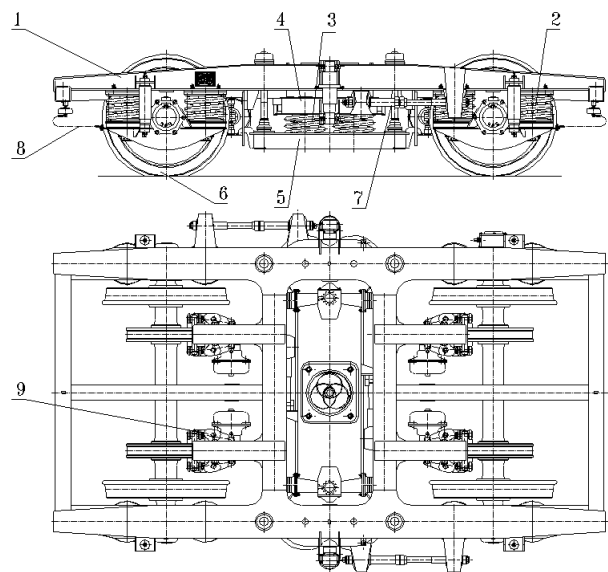


Figure 3. General view of the Görlitz Va/DVJ bogie 1-frame; 2- primary suspension; 3- secondary suspension; 4- bolster; 5- spring beam; 6- wheelset; 7- linker; 8- earthing device; 9- braking system.

The secondary suspension (Fig. 4) is made of four sets of cylindrical coil springs that lie on newly manufactured spring beams (bathtubs). The double spring set also has a rubber pad, which in case of overload or larger dynamic thrusts, is like a third spring element and helps to absorb the load.

The damping is performed with two hydraulic dampers in vertical and horizontal direction, the over sprung beam is connected to the bogie frame. The damping characteristic is progressive.

The connection between the bolster and the central bolt beam of the wagon is made by means of a central pivot of flat type. Between the upper and lower part of the camp there is a so-called "Central bolt".

When tilted transversely, the side bearers stabilize the carbody. The side bearers are adjustable and can be adjusted without play.

When tilted transversely, the side bearers stabilize the carbody. The side bearers are adjustable and can be adjusted without play.

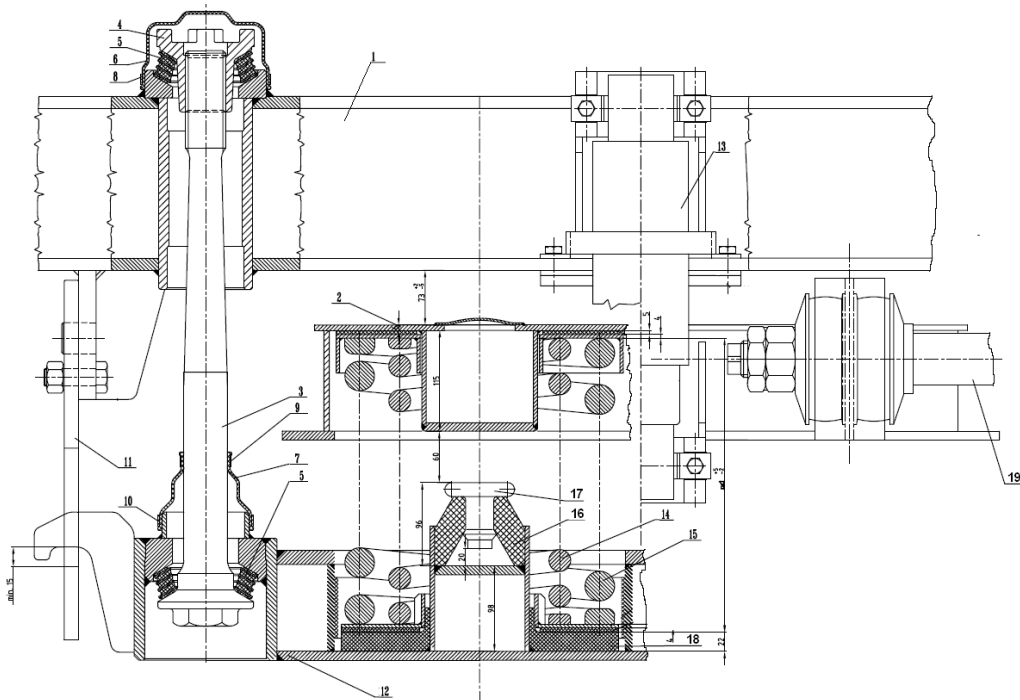


Figure 4. Secondary suspension (SS) of the Görlitz Va/DVJ bogie  
 1-frame; 2- bolster; 3- balancing bolt; 4- nut; 5 – rubber-metal package; 6 - cap; 7 - casing; 8, 9, 10 - washer; 11 - insurer; 12 - spring beam; 13 - damper; 14 - internal spring from SS; 15 - outer spring from the SS; 16-bumper rubber; 17 - beater; 18 - rubber support; 19 - linker.

When tilted transversely, the side bearers stabilize the carbody. The side bearers are adjustable and can be adjusted without play.

The braking system is disc and two brake kits (disc + cylinder) are mounted on each axle.

#### 2.4 Bogie type GP200

The GP 200 bogie (Fig. 5) was developed by the VÚKV Institute for Railway Vehicle Research as an international project developed by VÚKV together with Vagonka in Görlitz, Germany, with the name GP 200, meaning the maximum possible design speed using an electromagnetic rail brake.

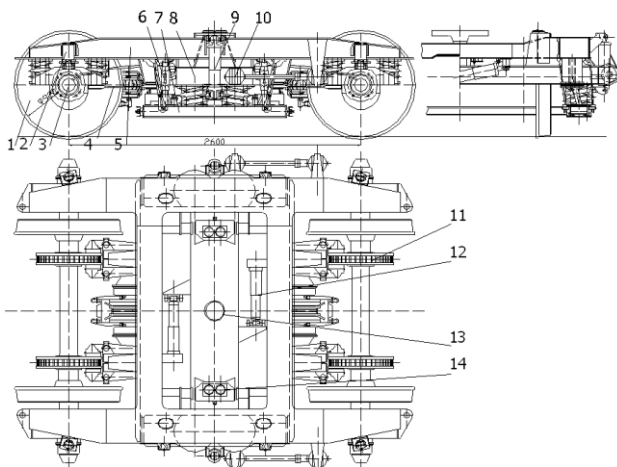


Figure 5. Bogie GP-200

1-wheelsets; 2-friction damper; 3-axle box; 4-guides; 5- frame; 6-swing pendants; 7-spring beam; 8-bolster; 9- vertical hydraulic damper; 10-linker; 11-sided disc; 12- horizontal hydraulic damper; 13 – center pivot; 14 – slide bearer.

The GP 200 bogies are two-axle with a two-stage spring cradle suspension for light railway vehicles. Base 2600 mm. Carriage weight - 5400 ÷ 6035 kg. Year of production 1984 and 1990.

The bogie frame is a welded construction.

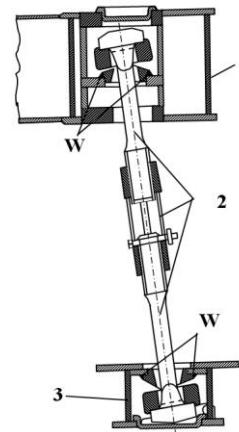


Figure 6. Inclined outwards at an angle of about 10° swing pendants  
 1 - bogie frame; 2- swing pendants (upper stabilizer, connecting nut, lower stabilizer); 3- spring beam (bathtub); W- welding.

The frame consists of two longitudinal and two transverse elements.

The secondary suspension is swung by means of swing pendants inclined outwards at an angle of about 10° (Fig. 6).

The guide axle box is guided by an elastic fiberglass connection, fixedly connected to the wing of the axle box body by a bolted connection, and on the other side to the bracket of the bogie frame (Fig. 7). The

detachable axle box body allows disassembly of the axles without disassembly of the axle spring suspension. The axle box body consists of three parts.

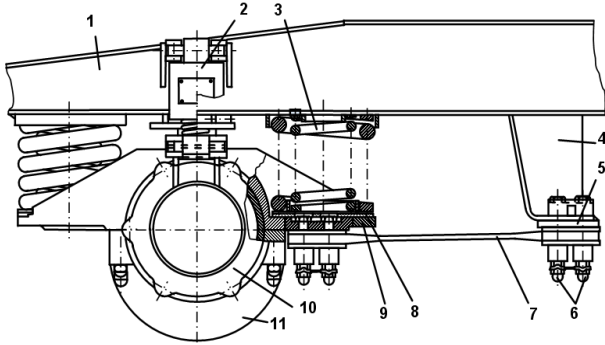


Figure 7. Primary suspension

1-frame; 2-friction damper; 3-springs from the primary suspension; 4-support; 5-slot connection; 6-bolt connection; 7- elastic fiberglass flat connection; 8-pad; 9- axle body - upper part; 10- axle body - middle part; 11- axle body - lower part.

Bearings, safety and labyrinth rings are mounted in the cylindrical sleeve of the axle box body. The axle box cover is mounted to the cylindrical part

The bolster has a closed section made of steel sheets. The center pivot, the side bearer, the baffles and hinges for horizontal and vertical dampers and the linker connection are mounted on the over sprung beam.

### 3. FAILURE IN PASSENGER BOGIES TYPE SWING OF THE RAILWAY SYSTEM OF THE REPUBLIC OF BULGARIA

The importance of the problems related to the strength condition and especially the durability of the bogies of the passenger wagons can be judged by the fact that they are decisive for the safety of the movement. Indeed, all failures of passenger wagons of a strong nature, ie. all destruction leads directly to severe accidents and catastrophes related to the lives of passengers.

Of course, in the framework of the present work not all cases of failures can be found, but only those of them will be affected, which are related to mass defects and are mainly due to design deficiencies and mass deviations from technological requirements [4]. Wheelset and braking systems failures will not be treated because they are subject to separate regulations and special attention, although they can be said to have problems [5, 6, 7].

We will note in advance that due to the dynamic nature of the loads on the passenger wagons and due to the presence of a certain level of technical literacy of the staff in the railways, the destruction is in all cases caused by fatigue of the material, ie. from cyclic rather than one-time loads. This assessment for the specific cases is confirmed by the characteristic features - lack of neck (thinning of the section) at the site of destruction and the presence of visible to the naked eye different areas of fracture, characteristic of different stages of crack development. It should be noted that these stages are not short-lived and it is good that it is so, because there is a possibility to detect the crack before the actual loss of performance, ie. before the demolition itself took place, characterized by the

division of the part into two parts. Ways and means to detect cracks is the subject of another topic.

Unfortunately, fatigue damage is almost always widespread [4]; they are characteristic and do not appear as single cases, but for whole series and production batches. Because this type of destruction requires a large number of load cycles (hundreds of thousands and millions - usually up to 10 million for steel), which can not be obtained either in factory tests and test trips, or in institute tests, but accumulate over time. of a relatively long period of operation.

It can be said that such mass damages did not occur after the institute tests, which actually started from 1964 to 1965, were introduced for serial productions after 1970, because in these tests, also called "determinants", , in addition to the dynamic-running indicators, also the strength properties, the stresses that precisely cause the cracks.

However, even with this approach (by performing definitive tests) there is no complete guarantee for cracks and damage.

Here will be considered only those of the elements and units of the bogie that require close attention.

A) *In the first place* - are the object of close attention - The joints between the sides and crossbeams. Very low stressess were obtained in these places during the static bench tests, according to UIC 515 [8], but during the train tests in the conditions of movement in curves the stressess are significantly higher. From the analysis of the records and from the additional stationary tests performed by simulating the loads in curves, it was found that these high stressess are due to the pair of longitudinal shoulder forces caused by the longitudinal components of the creep forces when entering a curve. Due to the high responsibility of this unit in the subsequent strength vibration tests of fatigue [9] an additional cyclic load was realized (which is not prescribed by UIS slip 515 [8]), trying to cause horizontal oblique deformation of the frame, turning it from a rectangle into rhomboid (seen in plan!). In addition, the requirements of the Transport Research Institute (NITIZHT) include the requirement for mandatory defectoscopy of the welds in this unit. Unfortunately, however, data were later found showing that this unit was not implemented for all bogies of the required quality. This is the main reason for placing this unit among those that should be the subject of close attention during operation and repair.

B) *Secondly* - are the object of attention to the brackets (ears), through which the longitudinal linkers are connected to the bolster and the sides of the bogie frame, in and around the joints. To reduce the high stressess resulting from different train conditions, it is recommended to increase the radius of curvature at the base of the brackets and improve the quality of the welds connecting the latter to the bolster or the side. In addition, there are recommendations regarding the linker rubber "hinges", because the stressess in the specified places strongly depend on the serviceability of these "hinges" or on the extent to which they act as such, ie. without generating a bending moment of tension or with the lowest possible value of the same. This factor depends on the quality of the tire, the degree of its tension, etc., which does not

exclude striking faults associated with leaning "hard" and locking.

Therefore, along with the checks for cracks in the indicated places of the linker consoles, it is necessary in case of factory repair (and if possible in case of depot) to check the force for the necessary vertical and horizontal deviation of the lantern at one end, free from metal package, provided that the other end is connected to the corresponding metal package.

*C) Thirdly, cracks can be expected under certain conditions in the lower sheet of the spring beam around the places near the edges of the brackets, perceiving the transverse forces as reactions of the elastic bumpers. In these places cracks occur in bench fatigue tests at 6 million cycles, in connection with which recommendations are given with welding of external or internal ribs. After the implementation of the recommendations, the structures are tested on a multi-cycle load and they can withstand the prescribed loads according to EN 13749 [10] and EN 14363 [11], calculated with a large reserve for the depreciation period of the wagons.*

### 3. NECESSARY CONDITIONS FOR PUTTING INTO SERVICE OF BASIC ELEMENTS OF PASSENGER BOGIES

When putting railway carriages into operation according to the European normative documents, obligatory stages are:

- Development of constructive and technological documentation;
- Conducting strength-strain analysis;
- Testing of a prototype.

The normative documents of the European Union and the UIC allow the commissioning to take place only on the basis of strength-strain analysis. The necessary conditions for this are:

- The manufacturer has received a bogie certificate with similar design, technological and operational characteristics;
- To perform the full volume of theoretical research with verified computational and simulation models.

The normative documents related to the testing and theoretical examination of railway bogies (including the study of fatigue of the material in the welds in the metal structure) are EN 15827: 2011 [9], EN 13749: 2011 [10], UIC 510- 3 [13], UIC 615-4 [14] UIC 515-4 [15], TSI [16], ERRI B 12 / RP 17 [17], ERRI B 12 / RP 60 [18], EN 12663-1: 2010 [19], DVS 1612: 2014 [20] and Eurocode 3 [21]. Their analysis shows that the forces of loading, the places of their application, the combinations under the different regimes (groups of loads) are clearly and unambiguously defined [10].

The analysis of the normative documents regarding the study of the fatigue of the material in the area of the welds in theoretical and experimental way shows some differences. The reason for this is that the theoretical assessment is performed by quantitative indicators (allowable stresses), and in the experimental - by qualitative (presence or absence of cracks).

The German national welding standard DVS 1612: 2014 [20] is preferred by most European manufacturers of railway equipment and complex machine-building products due to the very good results regarding the

reliability of the welds. The standard is based on curves Moore-Kommers-Jasper (MKJ) diagram.

Depending on the type of welded structure, the type of weld, the control technology and the type of applied load, a diagram is selected to determine the allowable stresses. In the general case for the study of complex machine-building products under complex loading, the assessment is performed by four consecutive criteria, three by components and one complex [21, 22, 23, 24], formulas:

$$\frac{\sigma_{II}}{\sigma_{IIlim}} \leq 1; \quad \frac{\sigma_{\perp}}{\sigma_{\perp lim}} \leq 1; \quad \frac{\tau}{\tau_{lim}} \leq 1; \\ \left( \frac{\sigma_{II}}{\sigma_{IIlim}} \right)^2 + \left( \frac{\sigma_{\perp}}{\sigma_{\perp lim}} \right)^2 - \frac{\sigma_{II}\sigma_{\perp}}{\sigma_{IIlim}\sigma_{\perp lim}} + \left( \frac{\tau}{\tau_{lim}} \right)^2 \leq 1,1 \quad (1)$$

where  $\sigma_{II}$  are the normal stresses longitudinally of the weld;  $\sigma_{\perp}$  - normal stresses transverse to the weld;  $\tau$  - tangential stresses longitudinally at the weld;  $\sigma_{IIlim}$  - normal allowable stresses along the seam;  $\sigma_{\perp lim}$  - normal allowable stresses;  $\tau_{lim}$  - tangential allowable stresses longitudinally at the weld.

The allowable stresses  $\sigma_{lim}(R_{\sigma})$  are a function of the cyclic load asymmetry coefficient, which is calculated according to the formula:

$$\sigma_{lim}(R_{\sigma}) = 150 \cdot (1,04^{-x}) \left[ \frac{2 \cdot (1 - 0,3R_{\sigma})}{1,3 \cdot (1 - R_{\sigma})} \right] \quad (2)$$

where x is the exponent depending on the selected curve corresponding to the respective weld and load.

### 4. TESTING OF FATIGUE STRENGTH OF PASSENGER BOGIES

According to the requirements of the International Railway Union – UIC 510 [13] and UIC 515-4 [15] - bench tests of wagon bogies are of two types and are conducted in two stages in the following sequence, usually on the same sample:

- first stage - static (for static strength);
- second stage - dynamic (for fatigue strength).

In addition, there are the conditions: a) dynamic bench tests (which are more lengthy and expensive) to be conducted if the respective sample (construction) has successfully "passed" the static tests at the 1st stage; (b) bench tests of wagon bogies must be carried out on: new or modified structures; new or changed technologies; material replacement; new company-manufacturer and new place (workshop, factory) for production.

#### 4.1. Dynamic fatigue strength tests

The loads (forces) on the test bogie acting in the vertical transverse plane through the central bearing are first grouped [3, 25] (see Fig. 8) in:

- system of vertical forces  $F_{z1}$  and  $F_{z2}$ , applied on the right and left side beams in the plane of the central bearing;
- a system of horizontal forces  $\pm F_{y1}$  and  $\pm F_{y2}$ , also applied to the right and left side beams in the plane of the center bearing, usually assuming:  $F_{y1} = F_{y2} = F_y$ .

The vertical forces  $F_{z1}$  and  $F_{z2}$  are different from each other in time t, and are considered to be composed of 3 components - one constant and two periodically changing (see Fig. 12), as follows:

- vertical static component  $F_{zs} = \text{const}$ ;
- vertical quasi-static components  $\pm F_{zq}$ ;
- vertical dynamic component  $\pm F_{zd}$ .

It is customary for the right and left curves to have the same parameters and to alternate without straight lines. The period  $T_q$  of the periodic function thus obtained (component  $F_{zq}$ ) in the tests must be significantly longer than the period  $T_{dq}$  of the dynamic component (according to UIC-510 and 515).

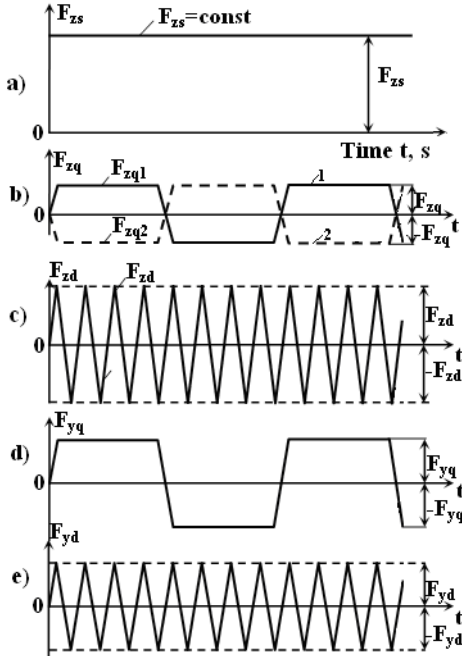


Figure 8. Loads applied to the side beams of the passenger bogie frame [4, 22] according to code. UIC - 515 [13]: a, b, c - vertical: static  $F_{zs}$ , quasi-static  $F_{zq}$  and dynamic  $F_{zd}$ ; d, e - horizontal-transverse; quasi-static  $F_{yq}$  and dynamic  $F_{yd}$ . 1- right side beam; 2- left side beam.

The horizontal forces  $F_u$  of each side beam, which are equal in size and direction, are composed of two periodically changing components over time (see Fig. 8, d, e), as follows:

- horizontal quasi-static component  $\pm F_{yq}$ ;
- horizontal dynamic component  $\pm F_{yd}$ .

With the mandatory UIC-510 and 515 phase correspondences between  $F_{zq}$  and  $F_{yq}$  and between  $F_{zd}$  and  $F_{yd}$ , the aim is clearly to test the most unfavorable operational combinations that can be obtained, albeit for a short time.

To determine the value of the vertical static component  $F_{zs}(t) = \text{const}$  and the amplitude values of the periodically changing components  $F_{zq}$ ,  $F_{zd}$ ,  $F_{yq}$  and  $F_{yd}$ , defined above, UIC-510 and 515, respectively for bogies of freight and passenger wagons - are suitable in different ways, although there is an analogy between them.

According to this approach, the values of the 5 load components in question in the bench tests are determined as follows:

- 1) The vertical static component  $F_{zs}$

$$F_{zs} = \frac{1}{4} \cdot (m_{VON} + 1,2 \cdot m_{CN} - 2m^+) \cdot g \quad (3)$$

where:  $m_{VOM}$  is the curb weight of the wagon;  $m_{CN}$  - payload;  $m^+$  - bogie mass.

- 2) The vertical quasistatic components  $F_{zq}$

$$F_{zq} = \pm \alpha \cdot F_{zs} \quad (4)$$

where:  $\alpha$  is the coefficient for the influence of road condition ( $\alpha = 0.10$  for normal and  $\alpha = 0.15$  for bad).

- 3) The vertical dynamic component  $F_{zd}$ ,

$$F_{zd} = \pm \beta \cdot F_{zs} \quad (5)$$

where:  $\beta$  is the coefficient of dynamism ( $\beta = 0.2$  for normal road condition;  $\beta = 0.3$  for bad road)

4) The horizontal quasistatic component  $F_{yq}$  and the horizontal dynamic component  $F_{yd}$  to each side beam are determined by the formula

$$F_{yq} = F_{yd} = \pm 0,125 (F_{zs} + 0,5 m^+ \cdot g) \quad (6)$$

The normal duration of fatigue tests is  $6 \cdot 10^6$  pcs. cycles, which is stage I. At the end of the first stage, at  $6 \cdot 10^6$  pcs. cycles the elements of the bogie structure (bogie frame) must not have cracks, even in the embryo. The stage ends with an intermediate qualitative and quantitative assessment. Quality assessment is mandatory and requires full control of welds. The criterion is the absence of cracks. Quantitative evaluation is most often performed with Goodman-Smith diagrams [4]. It allows exceeding the stressess above the normalized in a limited number of controlled points. The condition of these areas is closely monitored in the next two stages. This is the condition for putting the bogie into regular production. However, in order to evaluate the construction and with a view to greater safety, the tests are continued in stage II, which contains  $2 \cdot 10^6$  pieces. cycles with 20% increased dynamic and quasi-static loads  $F_{zq}$ ,  $F_{zd}$ ,  $F_{yq}$  and  $F_{yd}$  while maintaining the vertical static load  $F_{zs}$ . In order to give a positive assessment of stage II, namely that the structure is "durable", it should not have cracks, but germs of cracks up to 2-3mm are allowed. Provided that they have successfully passed the tests of stage II, another continuation is undertaken - stage III -  $2 \cdot 10^6$  pcs. cycles and by 40% increased compared to stage I quasi-static and dynamic loads while maintaining the static. The condition for successfully passing stage III is the same as for the previous one.

During the tests, the condition of the tested structure is constantly monitored in parallel with the operation of the stand, as in the event of unusual noises, shocks (crashes), deformations, etc. the work is stopped to clarify the condition. It is recommended that work be interrupted every 1 million cycles to perform a basic inspection - primarily for cracks. There are international requirements for documenting test regimes and results obtained.

#### 4.2. Static bench tests (static strength tests)

The loads in the static bench tests simulate the dynamic ones in character and size; the difference is that here they are applied in static mode with stresses measurement.

Based on the fact that for each point of the structure at any time  $t$  (more precisely peak moment), the stress is determined by the vertical and horizontal forces applied in the considered places (right or left side beams - with indices 1 and 2), it is obtained:

- for vertical forces  $F_{z1}$  and  $F_{z2}$ :

$$F_{z1}(t) = F_{zs} + F_{zq}(t) + F_{zd}(t) \quad F_{z2}(t) = F_{zs} + F_{zq}(t) + F_{zd}(t) \quad (7)$$

or taking into account only the peak (amplitude) values  $F_{zq}$  and  $F_{zd}$ , according to (4) and (5) we get:

$$F_{z1}(t) = F_{zs}(1 \pm \alpha \pm \beta) \quad F_{z2}(t) = F_{zs}(1 \pm \alpha \pm \beta) \quad (8)$$

- for horizontal loads

$$F_{y1} = \pm F_{yq1} \pm F_{yd1} \quad F_{y2} = \pm F_{yq2} \pm F_{yd2} \quad (9)$$

or, in the case of an even distribution between the two side beams, i. for  $F_{y1} = F_{y2} = F_y$  and taking into account, according to (6), the equality between the amplitude values of the quasi-static and dynamic components (ie  $F_{yq}$  and  $F_{yd}$ ), the maximum and minimum values of the total horizontal force of the bogie are obtained, for the tense state

$$\max/\min 2F_y = \pm 0,5(F_{zs} + 0,5.m^+.g) \quad (10)$$

When the bogie is loaded with different combinations between the vertical forces  $F_{z1}$  and  $F_{z2}$  taken from formula (8) and the horizontal force from (10), code. UIC-515 and EN 13749 [7] prescribe mandatory 9 combinations of loads, shown in Table 1 and with the corresponding values for the tested bogie, confirmed by [4].

From these combinations, the stresses from two of them must be taken, namely the largest and the smallest values for each point of the structure, which represent the simulated maximum  $\sigma_{\max}$  and minimum  $\sigma_{\min}$  stresses at these loads; when plotting them in the Goodman diagram on the ordinate, for abscissas  $\sigma_m = (\sigma_{\max} + \sigma_{\min})/2$ , the obtained points must be inscribed in its contours.

Table 1. Load combinations for static bench test of passenger bogie at operating loads

| Combination № | Vertical loads               |                              | Horizontal transverse load |
|---------------|------------------------------|------------------------------|----------------------------|
|               | $F_{z1}$                     | $F_{z2}$                     | $F_y$                      |
| 1.            | $F_{zs}$                     | $F_{zs}$                     | 0                          |
| 2.            | $F_{zs}(1 + \alpha - \beta)$ | $F_{zs}(1 - \alpha - \beta)$ | 0                          |
| 3.            | $F_{zs}(1 + \alpha - \beta)$ | $F_{zs}(1 - \alpha - \beta)$ | +2 $F_y$                   |
| 4.            | $F_{zs}(1 + \alpha + \beta)$ | $F_{zs}(1 - \alpha + \beta)$ | 0                          |
| 5.            | $F_{zs}(1 + \alpha + \beta)$ | $F_{zs}(1 - \alpha + \beta)$ | +2 $F_y$                   |
| 6.            | $F_{zs}(1 - \alpha - \beta)$ | $F_{zs}(1 + \alpha - \beta)$ | 0                          |
| 7.            | $F_{zs}(1 - \alpha - \beta)$ | $F_{zs}(1 + \alpha - \beta)$ | - 2 $F_y$                  |
| 8.            | $F_{zs}(1 - \alpha + \beta)$ | $F_{zs}(1 + \alpha + \beta)$ | 0                          |
| 9.            | $F_{zs}(1 - \alpha + \beta)$ | $F_{zs}(1 + \alpha + \beta)$ | - 2 $F_y$                  |

It is recommended that the loads in combinations №№ 3, 5, 7, and 9 (Table 1) be repeated because they are extreme and most likely are the stresses generated by them. The above method is known as the "operating load method".

A static bench test is prescribed by the method of extreme loads, which is applied with a single static load at higher values of vertical and horizontal forces - respectively  $F_{z1\max}$ ,  $F_{z2\max}$ ,  $2F_{y\max}$  - determined by the formulas:

$$F_{z1\max} = F_{z2\max} = (m_{VCE} - 2m^+).g \quad (11)$$

$$m_{VCE} = (m_{VOM} + 2.n.80) \quad (12)$$

$$2F_{y\max} = 2.(10 + m_{VCE}), kN \quad (13)$$

where:  $m_{VCE}$  is the gross mass of the wagon under extreme load;  $m_{VOM}$  - the own weight (tare) of the wagon;  $m^+$  - mass of the bogie;  $n$  - the number of seats in the car;  $F_{z1\max}$  and  $F_{z2\max}$  - maximum (exclusive) vertical forces applied to the right resp. left side beams;  $2F_{y\max}$  - maximum (exclusive) horizontal effort of the bogie.

The conditions for admissibility in the test with extreme loads are: 1) the stresses at any point of the structure do not exceed the limit of proportionality of the

material; 2) no residual deformations in the structure after its release from the loads.

### 5. CALCULATION OF BASIC LOAD-BEARING ELEMENTS OF A PASSENGER BOGIE OPERATED BY BDZ PASSENGER TRANSPORT EOOD

The calculation of the bogies is realized through an engineering package of software products. The bogies are 3D modeled in the middle of Soidworks in accordance with their original design documentation, and the welds are created in a uniform shape by the existing modeler in the computer system (CAD). The models thus created are statically loaded by the extreme forces defined above in accordance with UIC-515 and EN 13749, using the finite element method (FEA). For this purpose, the models are divided into elements with dimensions from 2 to 4.4 mm, which makes a compromise decision in order to obtain a numerical solution within a reasonable time interval. At the same time, the sensitivity of the numerical process to the existing stress concentrations in the welded joints is limited, and admissible imperfections in the welded seam are not taken into account [26, 27]. Results were obtained for the stress state and for the deformations of the calculated elements.

#### 5.1. Calculation of main load-bearing elements of Görlitz Va/DVJ type bogie

For the construction of a Görlitz Va/DVJ passenger bogie, the load values for the different combinations are given in Table 2.

Table 2. Load combinations for static bench test of passenger bogie type Görlitz Va/DVJ at operating loads (at accepted  $\alpha = 0.15$  and  $\beta = 0.3$  for poor road condition)

| Combination № | Vertical loads |          | Horizontal transverse load |
|---------------|----------------|----------|----------------------------|
|               | $F_{z1}$       | $F_{z2}$ | $2F_y$                     |
| 1.            | 88,275         | 88,275   | 0                          |
| 2.            | 75,034         | 48,551   | 0                          |
| 3.            | 75,034         | 48,551   | 59,105                     |
| 4.            | 127,999        | 101,517  | 0                          |
| 5.            | 127,999        | 101,517  | 59,105                     |
| 6.            | 48,551         | 75,034   | 0                          |
| 7.            | 48,551         | 75,034   | -59,105                    |
| 8.            | 101,517        | 127,999  | 0                          |
| 9.            | 101,517        | 127,999  | -59,105                    |

The generalized scheme of the forces on the frame of the bogie type Görlitz Va/DVJ, applied from the side of the carbody is given in Fig.9.

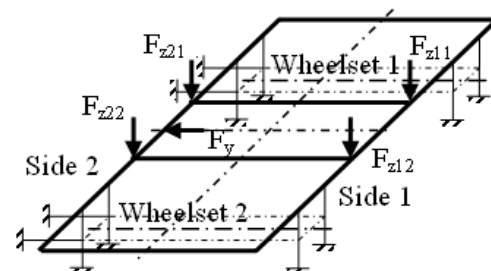


Figure 9. Loads of bogie type Görlitz Va/DVJ.

The vertical load is transmitted in the supports of the suspension from the SS and  $F_{z11} = F_{z12} = F_{z1}/2$ , and the horizontal-transverse load is in the support between a page of the frame and the overhang beam.

The maximum values for determining the stresses in the structure of the frame of the considered passenger bogie are in combination № 5.

The values of the loads are:  $F_{z11} = F_{z12} = F_{z1}/2 = 64$  kN;  $F_{z21} = F_{z22} = F_{z2}/2 = 50.76$  kN and  $F_y = 29.55$  kN shown in figure 6.

The results of the SolidWorks program in the calculation of the bogie frame type Görlitz Va/DVJ are given in Table 3.

Table 3. Study Results for bogie frame type Görlitz Va/DVJ

| Name          | Type                         | Max                       | Location                          |
|---------------|------------------------------|---------------------------|-----------------------------------|
| Stress1       | VON: von Mises Stress        | 66,87 MPa<br>Node: 43     | (0 mm, 152 mm, -924.8 mm)         |
| Displacement1 | URES: Resultant Displacement | 0.388 mm<br>Node: 11330   | (6.4373e-006 mm, 190 mm, -878 mm) |
| Strain1       | ESTRN: Equivalent Strain     | 0.000194<br>Element: 9439 | (-877.625 mm, -4 mm, -1052.94 mm) |

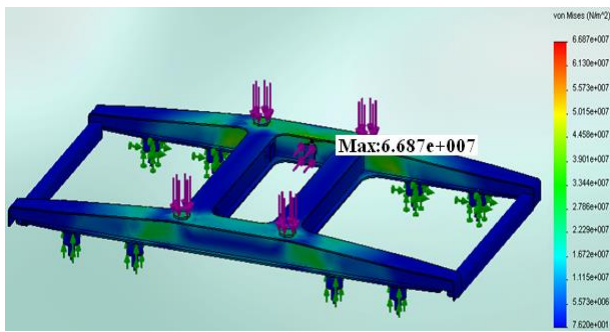


Figure 10. Stress condition of the bogie frame type Görlitz Va/DVJ.

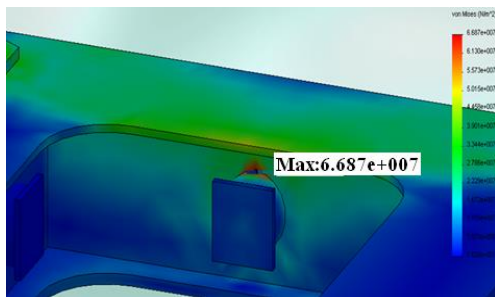


Figure 11. Stress state with maximum value.

In figure 10 shows the stress state of the bogie frame, the maximum value being 66.87 MPa obtained in the middle of the beam in the area of the weld of the lateral bump (Fig. 11). In other areas, maxima have been reported, which are 15-30% lower stresses values.

The displacements shown in the table are within normal limits, in accordance with the regulations.

5.2. Calculation of main load-bearing elements of GP200 type bogie

For the construction of a GP200 passenger bogie, the load values for the different combinations are given in Table 4.

The generalized scheme of the loads on the frame of the bogie type GP200, applied from the side of the carbody is given in fig.12.

Table 4. Load combinations for static bench test of passenger bogie type GP200 at operating loads (at accepted  $\alpha = 0.15$  and  $\beta = 0.3$  for poor road condition)

| Combination № | Vertical loads |          | Horizontal transverse load |
|---------------|----------------|----------|----------------------------|
|               | $F_{z1}$       | $F_{z2}$ | $2F_y$                     |
| 1.            | 98,1           | 98,1     | 0                          |
| 2.            | 83,385         | 53,955   | 0                          |
| 3.            | 83,385         | 53,955   | 62,784                     |
| 4.            | 142,245        | 112,815  | 0                          |
| 5.            | 142,245        | 112,815  | 62,784                     |
| 6.            | 53,955         | 83,385   | 0                          |
| 7.            | 53,955         | 83,385   | -62,784                    |
| 8.            | 112,815        | 142,245  | 0                          |
| 9.            | 112,815        | 142,245  | -62,784                    |

The vertical load is transmitted in the supports of the suspension from the SS and  $F_{z11} = F_{z12} = F_{z1}/2$ , and the horizontal-transverse load is in the support between a page of the frame and the overhang beam.

The maximum values for determining the stresses in the structure of the frame of the considered passenger bogie are in combination № 5.

The values of the loads are:  $F_{z11} = F_{z12} = F_{z1}/2 = 71,12$  kN;  $F_{z21} = F_{z22} = F_{z2}/2 = 56,41$  kN and  $F_y = 31,39$  kN shown in figure 12.

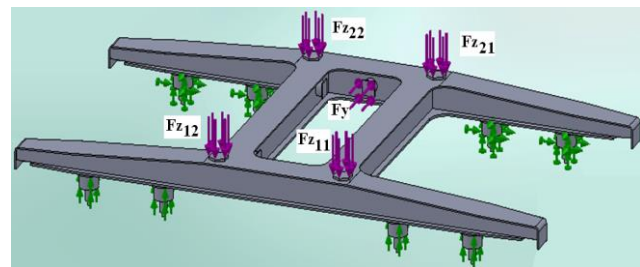


Figure 12. Load and supports for bogie type GP200.

The results of the SolidWorks program in the calculation of the bogie frame type GP200 are given in Table 5.

In figure 13 shows the stress state of the bogie frame, the maximum value being 72.39 MPa obtained in the middle of the beam in the area of the weld of the lateral bump. In other areas, maxima have been reported, which are 10-30% lower stresses values.

Table 5. Study Results for bogie frame type GP200

| Name          | Type                         | Max                       | Location                          |
|---------------|------------------------------|---------------------------|-----------------------------------|
| Stress1       | VON: von Mises Stress        | 72.39 MPa<br>Node: 43     | (0 mm, 152 mm, -924.8 mm)         |
| Displacement1 | URES: Resultant Displacement | 0.5612 mm<br>Node: 11330  | (6.4373e-006 mm, 190 mm, -878 mm) |
| Strain1       | ESTRN: Equivalent Strain     | 0.000229<br>Element: 9439 | (-877.625 mm, -4 mm, -1052.94 mm) |

The displacements shown in the table are within normal limits, in accordance with the regulations.

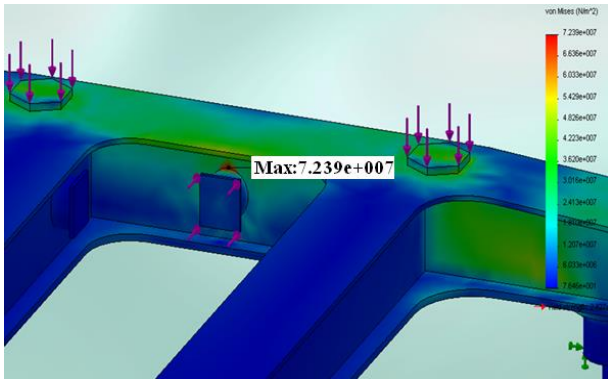


Figure 13. Stress state with maximum value.

In total for both bogies it can be concluded that the maximum stresses are in the area of the bumper, assuming that the reason is in the prevailing local stresses of pressure from the lateral forces  $F_y$ . The maximum stresses are in the T weld of the bumpers, and the formation of tired micro cracks in tests confirms this.

5.3. Goodman diagram for Görlitz Va/DVJ and GP200 passenger bogies frame.

Drawing the theoretically and experimentally obtained Goodman diagram, we determine the position of the endangered stresses for the sections of the frames of the two bogies.

For passenger bogie type Gorlitz Va/DVJ:

$$\sigma_m = 66,87 \text{ MPa and } \sigma_{max} = 80,244 \text{ MPa;}$$

For passenger bogie type GP200:

$$\sigma_m = 72,39 \text{ MPa and } \sigma_{max} = 86,868 \text{ MPa.}$$

The obtained values plotted in the Goodman diagram are shown in Fig.14.

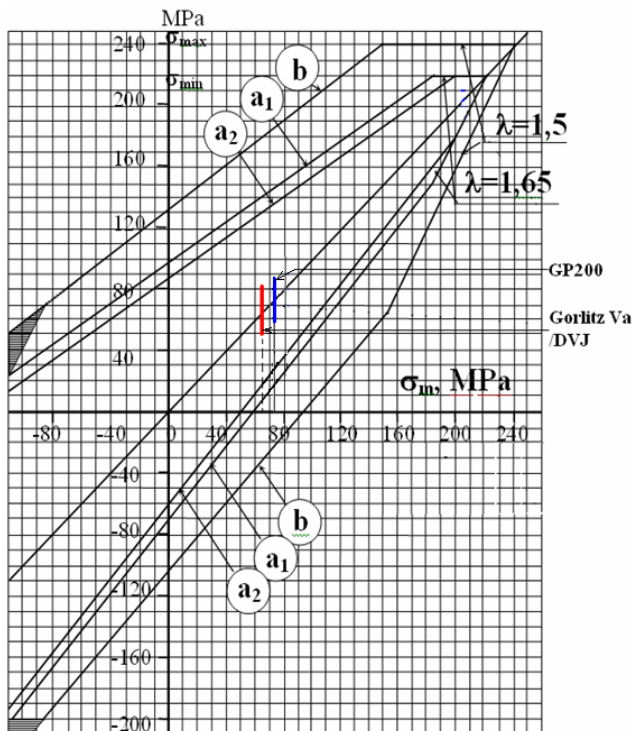


Figure 14. Goodman diagram with plotted stresses values.

The values of stresses for the frame of passenger bogies type Görlitz Va/DVJ and GP200 are in the outline  $a_2$ , which gives grounds for the necessary strength of the structure, but we still recommend strict control of welds and determining the coefficient of accumulation of damage [4, 28].

CONCLUSION

In the present article the constructions of passenger carriages in operation of BDZ "Passenger Transport" EOOD are considered. Cases of failures that are related to mass defects and are mainly due to design deficiencies and mass deviations from technological requirements are analyzed. Particular attention is paid to the problems in the construction of passenger carriages type YT-72, Görlitz-V/Va /DVJ and GP 200. The weak points in the constructions of the indicated bogies and the conditions for the occurrence of cracks have been determined. The article examines the strength of the frames of the specified passenger bogies. The loads are in accordance with the requirements of UIC-515 and EN 13749. The various fatigue strength tests of the passenger bogie are indicated. It is calculated that the construction of the frame has the necessary fatigue strength, but nevertheless it is recommended to strictly control the welds and determine the coefficient of accumulation of damage.

REFERENCES

- [1] Petrovic D., Rakanovic R., Zeleznicka vozila Praktikum., Kraljevo, (2006)
- [2] Petrovic D., Aleksandrov V., Jeleznicka vozila. Osnove, MF Kraljevo, ISBN 978-86-82631-66-8 p.223, (2013)
- [3] Penchev Ts., Atmadzhova D. Issues from operation, repair and recycling of passenger cars from the park of BDZ, VTU "T. Kableshkov", Sofia, (2003)
- [4] Penchev Ts., Atmadzhova D. Strength and durability of automobile and railway technology, VTU, "T. Kableshkov", Sofia, (2007).
- [5] Nikolov V., MODELLING AND STRENGT ANALYSIS OF THE WHEELSETS OF LOCOMOTIVES OF TYPE 86 Scientific Journal "Mechanics of Transport Communications" Volume 16, Issue 3/3, No 1678 pp.VI-48 - VI-53, ISSN 1312-3823, (2018)
- [6] Nikolov V., Reliability indicators of the brake distributors KE 1 for rolling stock in operation, IX International Conference "Heavy Machinery-HM 2017", Zlatibor, (2017)
- [7] NIKOLOV V., MODELING AND STRENGTH ANALYSIS OF THE AXLES OF BOGIE WITH VARIABLE-GAUGE WHEELSETS, The Fourth International Symposium for Students CPMA 2015, (2015)
- [8] UIC 515-4, PASSENGER ROLLING STOCK - TRAILER BOGIES - RUNNING GEAR - BOGIE RUNNING GEAR - BOGIE FRAME STRUCTURE STRENGTH TESTS, (1993)
- [9] Ivanov A.I, Structural Dynamics. publ. "Avangard Prima", ISBN 978-954-323-684-8, Sofia, (2010).

- [10] EN 13749:2011 – Railway applications. Wheelsets and bogies. Method of specifying the structural requirements of bogie frames, (2021)
- [11] EN 14363:2016 Railway applications - Testing for the acceptance of running characteristics of railway vehicles - Testing of running behaviour and stationary tests, June, (2016).
- [12] EN 15827:2011 Railway applications - Requirements for bogies and running gears, Brussels: EUROPEAN COMMITTEE FOR STANDARDIZATION, (2011)
- [13] UIC 510-3, WAGONS - STRENGTH TESTING OF 2 AND 3-AXLE BOGIES ON TEST RIG, International Union of Railways (UIC), (1989)
- [14] UIC 615-4, "Movie power units bogies and running gear bogie frame structure strength tests," International Union of Railway, (1994)
- [15] UIC 515-4 (E), 1st Edition, January 1, 1993 - PASSENGER ROLLING STOCK - TRAILER BOGIES - RUNNING GEAR - BOGIE RUNNING GEAR - BOGIE FRAME STRUCTURE STRENGTH TESTS, (1993)
- [16] Technical specification for interoperability of the rolling stock - freight wagons subsystem of the trans-European conventional rail system, (2006)
- [17] ERRI B12/RP17-8th Edition, Programme of tests to be carried out on wagons with steel underframe and body structure (suitable for being fitted with the automatic buffing and draw coupler) and on their cast steel frame bogies, Utrecht, April, (1997)
- [18] ERRI B 12/RP 60, 2nd Edition, regulation for proof tests and maximum permissible stresses, Utrecht, (1998).
- [19] EN 12663-1:2010 Railway applications - Structural requirements of railway vehicle bodies - Part 1: Locomotives and passenger rolling stock (and alternative method for freight wagons), (2010).
- [20] DVS 1612:2014 Design and endurance strength analysis of steel welded joints in rail-vehicle construction, (2014)
- [21] Eurocode 3: Design of steel structures – (2005)
- [22] Svetoslav SLAVCHEV, Vladislav MAZNICHKI, Valeri STOILOV, Stanislav ENEV, Sanel PURGIC. METHODOLOGY FOR THE EVALUATION OF MATERIAL FATIGUE IN THE AREA OF WELDED SEAMS OF RAILWAY BOGIES ON THEORY WAY. Materials Science and Engineering, VOL. 618 ISSN: 1757-899X, (2019)
- [23] P. Štastniak, M. Moravčík, P. Baran и L. Smetanka, „Computer aided structural analysis of newly developed railway bogie frame,“ MATEC Web of Conferences, том 157, № 157, (2018).
- [24] H. Dannbauer, C. Gaier и K. Hofwimmer, „Fatigue Analysis of Welding Seams and Spot Joints in Automotive Structures“, ARABIAN JOURNAL FOR SCIENCE AND ENGINEERING, (2005).
- [25] Atmadzhova D., Determining the strength of elements of passenger carriage type Y32, International Scientific Forum "Engineering and Construction Technologies in Transport - 2014" Banya, Razlog, September 18-19, 2014, Article 1046, vol. 12, issue 3/3, pp VI-1-VI-10, (2014)
- [26] Kolarov I. Concentration in welding joints due to the presence of pores in the seam. Scientific Journal "Mechanics of Transport Communications", Volume 18, Issue 3/1, XIII-21 - 26, ISSN 1312-3823, (2020)
- [27] Kolarov I. Stress state in a weld with a linear and point concentrator. Scientific Journal "Mechanics of Transport Communications" Volume 18, Issue 3/1, XIII - 14 - 19, ISSN 1312-3823, (2020)
- [28] Jankovic Miodrag D., Malociklusni zamor, Msinski Fakultet, Beograd, (2001).

# Braking – precondition for faster movement of railway vehicles

Dragan Petrović\*, Milan Bižić

Faculty of Mechanical and Civil Engineering in Kraljevo, University of Kragujevac, Serbia

*The paper gives a brief review of development of the braking system of railway vehicles. At the end of the nineteenth and the beginning of the twentieth century, the development of the concept of the drive of the railway vehicles has completed. After the steam, both electric and diesel traction have developed. For further development of railway traffic, it was necessary to develop a more efficient braking system. After the official start of railway traffic, it took almost a hundred years to development the braking system that allows faster and safer movement of railway vehicles. The credit for that belongs Serbian inventor, Eng. Dobrivoje Božić. In an original way, he constructed the brake which solved many problems that until then had been a limiting factor for faster and safer movement of railway vehicles. The aim of this paper is to bring the ingenious technical achievements of Dobrivoje Božić in the field of braking of railway vehicles closer to the scientific and professional public.*

**Keywords: Serbian inventors, Dobrivoje Božić, Railway traffic, Train braking.**

## 1. INTRODUCTION

People always try to overcome the distance between two places as easily and quickly as possible. The discovery of the wheel had led to a revolutionary transformation of land transport. The development of the technology in that period was mostly contributed by the exploitation of ore. Wooden wagons loaded with ore had moved more easily on rails than on macadam roads. With the invention of the steam engine in 1782, the Scottish inventor James Watt had started the new era in industrialization, especially in the development of transport.

During the nineteenth century, almost all over the world, railways rapidly replaced existing stagecoach networks. The railway traffic, in that period of great geographical discoveries and industrial revolutions, became crucial for the development of the economy and society of the whole world. The first railway for public transport was built in 1825. In addition to participating in the construction of the railway, George Stephenson built a steam engine in the same year, which he called "Locomotion". Stephenson personally drove this machine, which was not equipped with a cabin or a place for a machine operator. Due to great successes in development, the year 1825 is considered to be the beginning of organized railway traffic, and the name "Locomotive" came into official use [1].

The first regular railway line Liverpool – Manchester for passenger transport was opened in 1830. Since then, rail traffic has been expanding at high speed all over the world. The limiting factor for further, even faster, development of railway traffic was the unsolved problem of braking.

Along with the development and improvement of railway constructions, the standardization of technical solutions of vehicles, as well as infrastructure and the entire railway traffic took place. This was necessary because rail traffic connected distant cities and states, and even continents.

In addition to many good and useful characteristics, railway traffic enabled exploitation and occupation of certain territories in hitherto unimaginable proportions.

That is why some countries, in accordance with their interests (primarily military) - deliberately hindered the free flow of railway traffic and deviated from some established dimensions, such as e.g. track width.

## 2. THE BEGINNING OF THE DEVELOPMENT OF RAILWAY TRAFFIC IN SERBIA

By signing the Congress of Berlin in 1878, Serbia undertook to build a railway on the route Belgrade - Niš - Vranje. However, even more significant is that the Belgrade - Nis railway was a section of the planned Berlin - Baghdad railway. This would allow Germany access to significant oil deposits, which did not suit other major world countries. The finishing the section Belgrade - Nis marks the beginning of the existence of Serbian railways. The first train passed on this line on October 4, 1884.

For the construction of Belgrade - Niš railway, the so-called Bontu's concession was agreed. In the first contact with large western capital, one of the biggest money scandals in Serbian history occurred. The collapse of the Bontu's General Union was caused the fall of the French government. Regarding this concession, prof. Slobodan Jovanović wrote: "The spoilage of our political natures began immediately under the influence of foreign gold" [2, 3].

## 3. BRAKING OF RAILWAY VEHICLES

The braking system of railway vehicles regulates the running speed, as well as deceleration and stopping of train. A known joke that trains can move faster uphill than downhill speaks of the greatness of the technical problem of safe braking of variable mass (empty - loaded) of several thousand tons. As in the case of construction of locomotives, wagons and tracks, at the end of the nineteenth century, a race arose in the construction of the brakes of railway vehicles.

At the beginning of the development of railway vehicles, the braking force was changing manually. After that, at the end of the nineteenth century, the American George Westinghouse constructed an air (pneumatic) brake with direct action. During braking, air was released into the main line, and in the unlocked position,

\*Corresponding author: Dragan Petrović, Dositejeva 19, 36000 Kraljevo, petrovic.d@mfkv.kg.ac.rs

atmospheric pressure prevailed in the line. When the train was interrupted, there was not possibility for automatic braking, and with other shortcomings, this brake did not meet the basic requirements of a good and safe brake. In addition to Westinghouse's brake, four other technical solutions of the brake competed in America. This competition led to the certain improvements and spreading the Westinghouse's brake both in America and in Europe. In Europe, the Westinghouse's brake was used only for passenger trains. Until the First World War, freight trains in Europe were braked exclusively manually. Each wagon had to have one or two brake operators, which took care of the safe braking of the train.

In addition to Westinghouse in America was also Smith, as well as Hardy in Europe, who designed brakes with diluted air - vacuum brakes. After Westinghouse's brake, several brake variants appeared in Germany, such as Kunze-Knor, Hildebrand-Knor and in Switzerland Drolshamer. All these brakes operated on the principle of a standard two-pressure distributor and did not satisfactorily solve the observed shortcomings.

The idea of brakes with distributor with three pressures was patented in 1892 by the Englishman Humpfrey. The idea remained only on the paper and was never practically realized.

While Watt, Trevithick, Stephenson, Diesel and other inventors set trains in motion with their inventions, Westinghouse, Smith, Hardy, Kunce, Knorr, and many others, have been developing the brakes of railway vehicles which had huge deficiencies until the occurrence of Dobrivoje Božić.

The main shortcomings of the then brakes of the railway vehicles were reflected in the following:

The main shortcomings of the then brakes of the railway vehicles were reflected in the following:

- when the train was interrupted, both parts of the train were not automatically braked;
- the brake was exhausting on longer track falls, i.e., the brake was losing its power;
- there was no automation of braking force depending on the degree of loading of the train;
- there was no automation of braking force depending on the speed of the train;
- the brake transmission speed of the braking system was unacceptably low (maximum 80 m/s);
- wheel blocking was very often.

These shortcomings limited the running speed and made it difficult to use the railway on a larger scale. Due to the imperfection of the brakes, frequent accidents and railway traffic interruptions were occurring. Due to the blocking of the wheels during the braking many problems were occurring such as: sliding the wheels on the track; extension of the train stopping distance; formation of flat places on the wheels; damages to both the vehicle and the track etc.

Until the appearance of Božić's invention, the braking of railway vehicles was initially performed manually, and later pneumatically but non-automatically (directly) according to the scheme shown in Fig. 1.

In the case of direct - nonautomatic - exhaustive brakes, the air is fed directly from the main tank through the air line into the brake cylinder. The big disadvantage of these brakes is that in the event of a train break, there

will be no automatic braking of any disassembled part of the train.

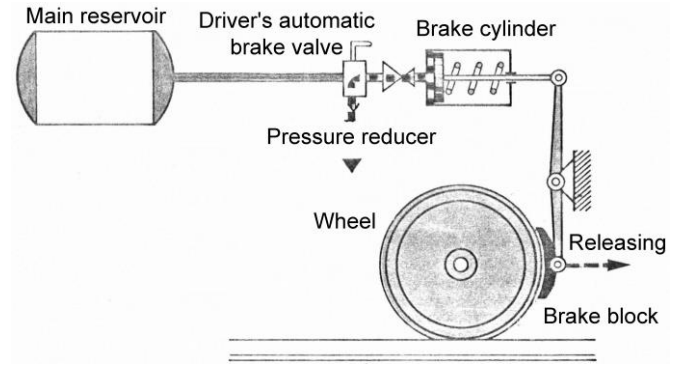


Figure 1: Principle of operation of direct (non-automatic - exhaustive) brake

The exhaustive brakes have a single-stage release, i.e., once started release cannot be interrupted. In this case, the brake distributor has two distribution pressures: the main line - the brake cylinder. If the train is braked to any degree, as soon as the main line is slightly charged, the brakes will fully release. The brake cylinder will not be completely charged because the pressure in the main line did not reach its maximum value. If the braking-releasing process is repeated several times, the pressure in the brake cylinder will decrease more and more, i.e., the amount of compressed air is exhausted, and thus the braking force will decrease more and more (Figs. 2 and 3).

In addition, the huge disadvantage of exhaustive brakes is that they do not have regulation of the magnitude of braking force depending on the weight of the vehicle (with and without load) and running speed. Also, they do not have synchronization of braking (low brake transmission speed) from locomotive to rear wagon, so it often happened that when changing the movement regime (start, acceleration, deceleration) there is a collision between individual vehicles of the composition or the rupture of connections between vehicles.

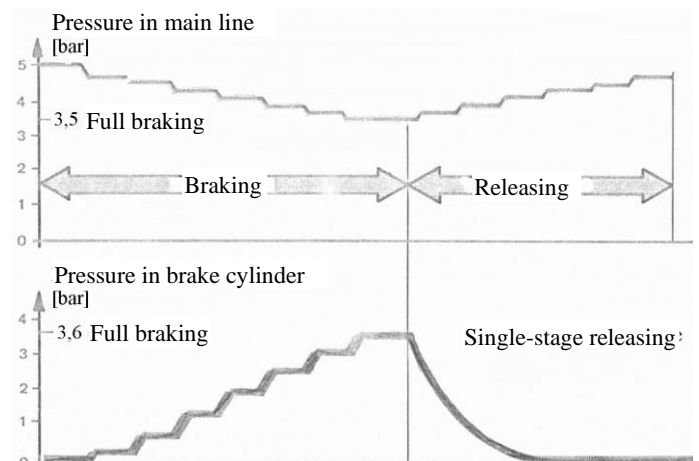


Figure 2: The change of pressure in the main line during braking and releasing at exhaustive brakes

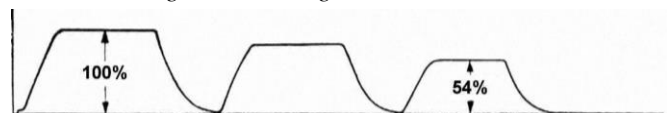


Figure 3: The change the air pressure in the brake cylinder at exhaustive brakes

Although this method of braking had great shortcomings and although many researchers around the world worked on solving this problem, after several decades of attempts, better braking system wasn't successfully developed. The impression is that there was no way out of that vicious circle. The main topic of discussions in the circles of scientists and engineers who developed the brake was whether the braking of railway vehicles should be done with diluted air or compressed air. After many tests with diluted air, no significant progress was made.

#### 4. CONTRIBUTION OF DOBRIVOJE BOŽIĆ TO DEVELOPMENT OF BRAKES OF RAILWAY VEHICLES

In the beginning, English, French, German, and American engineers contributed to the development of the railway. However, the braking of railway vehicles was not resolved in an appropriate way. Further development of the railway (increase of running speeds and weight of transported cargo) was not possible without a quality solution to all previously mentioned problems.

Dobrivoje Božić (Fig. 4) was born, according to the then valid calendar, on December 23, 1885 in Raška, Serbia. Due to the later state transition to the new calendar, some sources state that he was born at the beginning of 1886. After finishing primary and secondary school in Kraljevo and Kragujevac, he was studying at the Technical High School in Karlsruhe and Dresden - Germany, where one of his professors was Rudolf Diesel. After completing his studies, he returned to Serbia. In 1911 he employed in the state railway workshop in Niš where he faced with problems with braking railway vehicles. He developed his invention in the period 1911-1914. He designed and patented the braking system of railway vehicles in which a brake and distributor with three pressures were applied for the first time (Fig. 5). According to Božić's solution, the role of the new braking system is to distribute the air not in two, but in three parts of the braking system - the main air line, the brake cylinder and the auxiliary reservoir [4].



Figure 4: Dobrivoje Božić

In 1922, the American Patent Office accepted his solution of the braking system called "System of continuous braking of passenger and freight trains with compressed air". That was just the beginning because there was still a long way to go before International Railway Union (IUC) approved and recommended Božić's patent for use on railway vehicles.

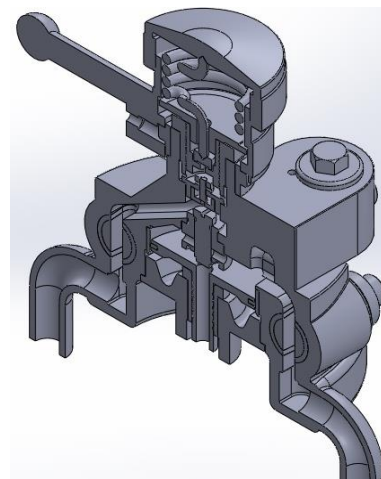


Figure 5: Božić's three-pressure distributor

At the conference of the victorious countries of the First World War, in 1923, France submitted a proposal in which it recommended the use of the direct, exhaustive Westinghouse's brake for braking railway vehicles. Since the Knorr's brake came from a country that was a loser of the Great World War, it did not have a great chance next to the Westinghouse's brake in that period. The Knorr's brake was just one of the modifications of the Westinghouse's brake. In that time, these brakes used a standard two-pressure distributor. At the same conference, the representative of the Kingdom of Serbs, Croats and Slovenes recommended the general reception of the Božić's brake, as a better and more perfect solution. The great success of that representative is that the French proposal, i.e. Westinghouse's brake, was not automatically accepted. Instead, a certain period of time was left for Božić and other constructors to practically prove the quality of their solutions to the International Railway Union.

In 1923, Božić also applied for a patent called "Quick-reacting triple valve", which was recognized in 1926. His solution of brake of railway vehicles, Dobrivoje Božić officially submitted via the railway of the Kingdom of Serbs, Croats and Slovenes in 1925. The third patent "Distributor for brake systems with pressurized fluid" was adopted in 1928.

Since they represented a completely new, revolutionary solution, these patents initially faced with a lot of resistance, but after numerous tests on the Zagreb-Rijeka line, they were accepted by the International Union

of Railways in 1928. The complete solution is registered as a Božić brake.

With Božić's automatic - indirect - inexhaustible brakes, there are three pressures: constant pressure in the working chamber of the main reservoir, variable pressure in the main line (1) and variable pressure in the brake cylinder (3). The air from the main reservoir, through the main line (1) is indirectly via the distributor and the auxiliary reservoir (2) introducing into the brake cylinder (3). Conversely to direct brakes, at the Božić brake in the unlocked position, the main line is under pressure and the brake shoes (4) are not in contact with the vehicle's wheel (Fig. 6a). In case of braking or rupture of the railway composition, the main line is emptied, atmospheric pressure prevails in it then, so the pressure from the auxiliary reservoir acts on the brake cylinder and braking occurs automatically (Fig. 6b).

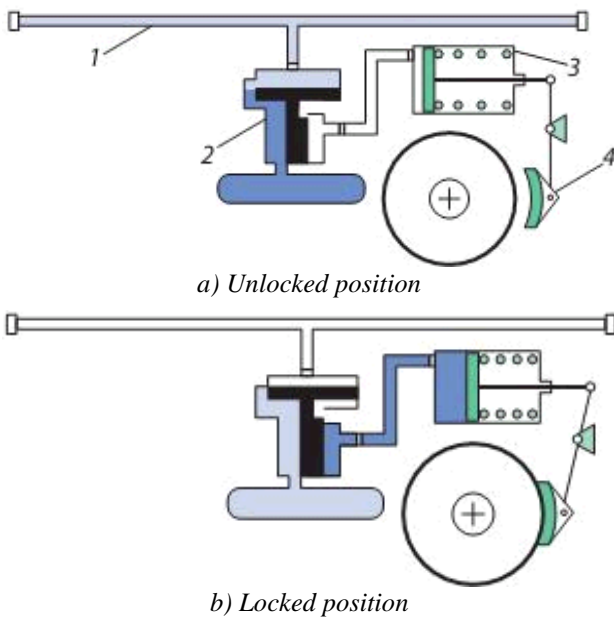


Figure 6. Simplified scheme of operation of Božić automatic - indirect - inexhaustible brake

The role of the distributor is to distribute the air into the parts of the braking system such as: the main air line, the brake cylinder and the auxiliary reservoir. Božić's three-pressure distributor was designed in a such way that it solved the issue of gradual unlocking of railway vehicles for the first time in the world (Fig. 7). Also, it eliminated the danger existed at the previous brakes with two pressures, that due to the emptying (exhausting) of the auxiliary reservoir on the long falls of the railway track, the necessary braking force will not be realized (Fig. 8).

Unlike the hauled vehicles, traction vehicles (locomotives) also have a braking control device which is the central device of the train braking system. The Božić's braking control device gives commands for:

- braking and unlocking all brakes in the train
- filling the brake system with compressed air
- compensation of losses due to unsealed brake devices, i.e. maintaining the working pressure in the main line
- discharging of the main line into the atmosphere and rapid braking.

Before the Serbian inventor Božić, no braking control device could automatically maintain a constant air

pressure in the main line during the braking. Compared to earlier solutions, Božić designed the pressure adjustment in the relay chamber in an original way. Guided by the same principles according to which Božić designed his braking control device (Fig. 5), all modern braking control devices have the property of maintaining the working pressure in the main line during the braking and unlocking. In this way, brake exhausting is avoided, i.e., no matter how many times braking is performed, the braking force will have approximately the same value.

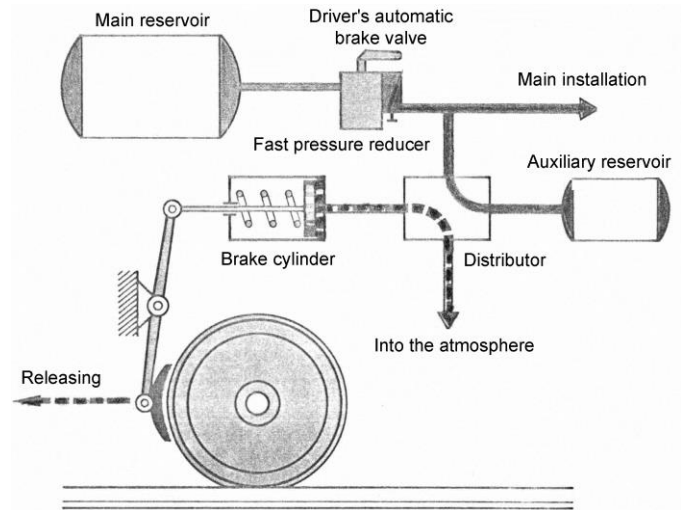


Figure 7. Principle of operation of indirect (automatic, inexhaustible) - Božić brake

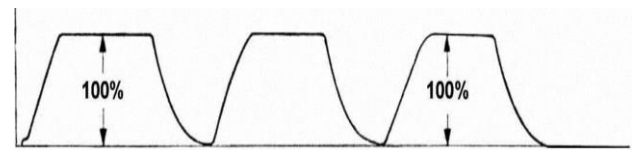


Figure 8. Change of the air pressure in the brake cylinder of Božić brake

These brakes are also called inexhaustible, because the auxiliary reservoirs are filled for all the time of braking and unlocking, so that the pressure in the brake cylinder remains constant. With Božić brakes, the reduction in the braking force can be done gradually. Gradual unlocking is enabled by a distributor with three distribution pressures: main air line - working (auxiliary) chamber (reservoir) - brake cylinder.

Therefore, brakes at which gradual braking and gradual unlocking are possible, i.e., in which the auxiliary reservoirs are replenished for the entire time of braking and unlocking, while maintaining the maximum value of the braking force at any time, regardless of the repeated braking, are called inexhaustible (Fig. 9).

The Božić distributor is designed so that it automatically adjusts the pressure in the brake cylinder for each load. This was achieved with special device that changed the value of the braking force depending on the deflection of the vehicle suspension. In this way, empty or lightly loaded railway vehicles are braked with smaller, and more loaded with greater braking force. Other countries at the time were developing brakes with two brake cylinders. In the case of an empty wagon, only one brake cylinder would work, and in the case of a loaded wagon, both brake cylinders would work.

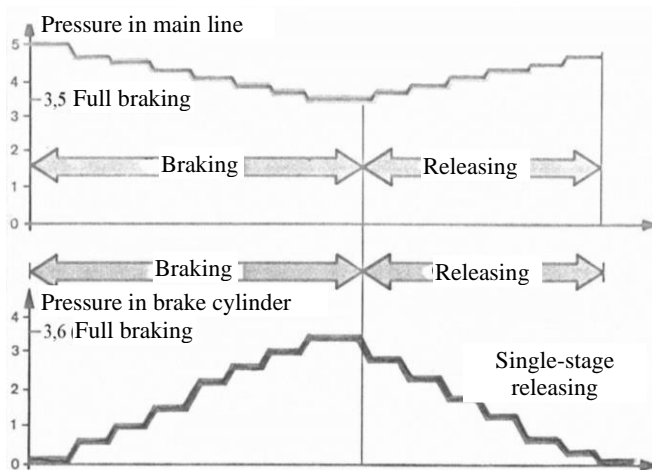


Figure 9: The change of the pressure in the main line of Božić brake

Because of their interests, large companies tried to criticize Božić's patents through their representatives. Despite, all later constructions of the braking system are based on Božić's (simpler, safer and cheaper) solution. Božić's brake system of railway vehicles have remained in an essentially unchanged form until today. In this way, the genius and superiority of Božić's solution was proven, and all the criticism "fell into the water" over time, because they were technically unfounded and encouraged only by the desire for profit and fame.

In addition to previously realized and internationally accepted patents, Božić designed and proposed a device based on the principle of a centrifugal regulator which, at lower train speeds, would reduce the pressure in the brake cylinder to an appropriate measure and thus reduce braking force. This solution would prevent blocking the vehicle wheels during braking. In this way, the problem of changing the braking force depending on the speed of railway vehicles is solved [5]. Although Božić's solution preventing blocking the wheels, forming a "flat place" on the wheel and significantly shortening the stopping distance of railway vehicles, his proposal was not accepted at the time.

This Božić's attitude was understood and accepted by science and profession only many years later and is used in modern railway brakes. Božić sold the license for his patent to the Czech company "Skoda". After the Second World War, Božić was unjustifiably declared as an enemy of the state by the new authorities and arrested on charges of collaborating with the occupier. He was released from the prison at the insistence of the Russians. Fearing that, in those troubled times, he would be arrested again and shot, and that he would be prevented from further work on perfecting the brakes of railway vehicles, with his family he secretly left Yugoslavia in 1948.

In 1954, a special commission of the General Directorate of the Yugoslavian Railways considered the issue of the type of brakes that should be approved for use. Even then, the "Metalski zavod Tito" in Skopje had purchased a license of the brake from the then little-known Swiss company Oerlikon and was just waiting for the decision of the commission to start production. Of course, the Collegium of the General Directorate, ignoring Božić's results, adopted the Commission's view that the Oerlikon brake is most suitable for Yugoslavian Railways and made

the decision that in the future only that brake will be installed on all railway vehicles on Yugoslavian Railways. By unnecessarily spending money on a license, any further serious development of the brake of railway vehicles in Serbia was also prevented.

## 5. CONCLUSION

With his inventions, Dobrovoje S. Božić solved the hitherto unsolvable problems of braking of railway vehicles: he was the first who constructed and applied a distributor with three working pressures. He constructed the most efficient braking control device. Božić's designs of braking control devices and distributors solved the problems of automatic keeping of constant air pressure in the main air line during braking and unlocking, and at the same time increased the brake transmission speed of air in the main line from 80 to 150 m/s. His braking control device enabled the gradual braking and unlocking of the train and solved the problem of inexhaustibility of the train brake during braking. For modern brakes, the UIC prescribed a mandatory examination of the inexhaustibility of the brake, which was not obligatory in previous regulations. With his inventions, Božić solved the problem of overcrowding of the working chamber, as well as the problem of automatic change of braking force depending on the load of the railway vehicle. He was the first who solved and proposed the automation of passenger train braking as a function of speed, and for that he constructed a centrifugal regulator. Although this solution was not accepted at that time, today it is used in all (both passenger and freight) railway vehicles.

In a completely new way, Božić significantly increased the degree of automation of the braking process and prevented frequent blocking and the formation of "flat" places on the wheels of railway vehicles. Božić's inventions enabled safer, better quality and more economical braking of railway vehicles. It was no longer necessary to employ a large number of braking operators who, in addition to train drivers, were obligatory participants in the movement of railway compositions. After Božić's discoveries, concept of diluted air brakes was definitely abandoned and it was decided to use brakes with compressed air. Also, the issue of two-distributed and three-distributed brakes has been resolved. The three-distributed concept has been adopted as a more perfect, which enables gradual unlocking and ensures the inexhaustibility of the brake. Increasing the brake transmission speed enabled calmer and safer braking. Automation of braking depending on the load and speed of movement also contributed to more efficient and safer braking. This influenced the further, even faster, development of railway traffic in the whole world. The best judge of these conclusions is always immutable and impartial time, because all other developed systems of braking of railway vehicles have long been out of use. All later solutions of air brakes in the world are just improvements of Božić's inventions. His braking principle is unsurpassed and is the basis for all types of air brakes used to date.

From all the above, we conclude that Božić's contribution to the development of brakes of railway vehicles is of planetary proportions, and in many cases, he was far ahead of the time in which he created [6]. We can

rightly say that Dobrivoje Božić was even a forerunner of the development of the ABS (anti-lock braking system) with which road vehicles are equipped today.

After the Second World War, Dobrivoje Božić was unjustly accused for cooperating with the enemy. All his property was confiscated, and he, fearing further and more drastic measures, emigrated with his family from Yugoslavia to the North America. He remained in exile until 1961, when, without a family, he returned to Belgrade permanently with a great desire to start the production of the most perfect brake of railway vehicles in the world. Having been left without a family and without property, he failed to fulfil this wish in the new state system, exposed to huge obstruction. The state government of that time, for reasons known only to them, was not ready to accept this invaluable gift. He died in Belgrade on October 13, 1967, at the age of eighty-two.

As an illustration of the positive influence of Božić, the words of Josip Švigel from Zagreb should be cited, who in the preface of his book "Brakes of railway vehicles" points out [7]: "... I should especially emphasize my gratitude to Mr. Dobrivoje Božić, who interested me in this important branch of railway technology with his brakes and personal influence, and is thus the real initiator of this book." "The extraordinary development of conduction brakes in the last decade, the great success in that field of our compatriot Eng. Božić, is looking for its interpreter."

In the end, it can be concluded that the development of railway traffic is not the merit of one man, but it is the continuous improvement of many inventions of several generations of engineers and technicians of several countries, among which Serbia has a significant place thanks to mechanical engineer Dobrivoje S. Božić. Studying his work and life, it can be seen that Dobrivoje Božić is an example of a world inventor - a sufferer, although he did everything to enable everyone a safer, easier and better life.

The life destiny of inventors like Dobrivoje S. Božić should not discourage future researchers. The greatest Serbian inventor Nikola Tesla also spoke about this in 1919, emphasizing [8]: "It is a difficult task for the inventor, who is often misinterpreted and not rewarded. However, he finds enormous compensation in the satisfaction that comes from his powers and the cognitions that he belongs to the class of extremely privileged people without whom humanity would have long ago disappeared in the difficult struggle against the ruthless forces of nature".

Among other, in an interview with Nikola Karanović in 1963 in Belgrade, Dobrivoje Božić said:

- "... all foreign copies of my brake are very complicated and therefore unreliable, and at the same time very expensive. For example, while my distributor has 70 parts, foreign copies have even 200 parts."
- "Until recently, my brake was the only one with automatic adjustment of braking power according to the load of the wagon, which was done with a single

part, while all similar brake systems had only manual adjustment, and even very limited - only for empty or partially loaded wagon".

- "Only when UIC prescribed my automatic adjustment of braking power according to the load of the wagon as obligatory in 1953, an attempt was made to apply it to foreign copies, but the device was incredibly complicated. That's why it works poorly on the one hand, and on the other - it's very expensive."
- "The production of my last universal type of brake is obstructed in our country ... it was not enough for them that foreigners earned billions by copying, but they want foreigners to sell licenses for making those bad and expensive copies to my homeland." The Swiss company Oerlikon already succeeded in that several years ago, and now the West German company Knorr-Bremse is also trying to do that. "(Price Božić - 330000 dinars, Erlikon - 530000 dinars).
- "So my country, instead to use my brake, which is why I came here and whose improvement I am now working on, has already issued a billion foreign currency dinars to buy a license to produce a bad and expensive copy of my brake!"

#### ACKNOWLEDGEMENTS

The authors wish to express their gratitude to Serbian Ministry of Education, Science and Technological Development for supporting this research (contract no. 451-03-9/2021-14/200108).

#### REFERENCES

- [1] D. Veličković, "Stivenson", Tehnička knjiga, Beograd, (1949)
- [2] S. Jovanović, "Vlada Milana Obrenovića 1878-1889", knjiga druga, BIGZ, Jugoslavija public, SKZ, Beograd (1990)
- [3] R. Kalabić, "Grofovsko vremena", drugo dopunjeno izdanje, Grafiprof, ISBN 978-86-903027-1-0, Beograd, (2015)
- [4] V. Vainhal, "Kočnice i kočenje vozova", Preduzeće za železničku izdavačko-novinsku delatnost, Beograd, (1991)
- [5] D. Petrović, M. Bižić, "Influence of Božić brake on development of rail traffic", Proceedings of XVII Scientific-Expert conference on Railways, RAILCON 16, 13-14 October 2016. Niš, Serbia, (2016)
- [6] D. Petrović, V. Aleksandrov, "Železnička vozila – osnove", Fakultet za mašinstvo i građevinarstvo u Kraljevu, ISBN 978-86-82631-66-8, Kraljevo (2013)
- [7] J. Švigel, "Kočnice na železničkim vozilima", Preduzeće za železničku izdavačko-novinsku delatnost, Beograd, (1962)
- [8] Muzej Nikole Tesle, "Stalna izložbena postavka o Nikoli Tesli", Krunska ulica br. 51, Beograd, (2016)

# Numerical analysis of wagon leaf spring using Ansys software package

Mladen Krstić<sup>1\*</sup>, Branislav Milenković<sup>2</sup>, Đorđe Jovanović<sup>2</sup>

<sup>1</sup>Faculty of Mechanical and Civil Engineering Kraljevo, University of Kragujevac, Kraljevo (Serbia)

<sup>2</sup>Mathematical Institute of Serbian Academy of Sciences and Arts, Belgrade (Serbia)

*Leaf spring are widely used for the suspension system in trains and commercial vehicles to absorb vibrations and shocks. This paper deals with the methodology of analysis of the leaf springs of the freight railway wagons by using software package Ansys 14.5. The methodology is applied in a concrete example of leaf spring for axle load of 225 kN. The procedure of forming the CAD model of the leaf spring using AutoCad and Autodesk Inventor is exposed, as well as the development of numerical model in Ansys software package. The results of the static analysis of given leaf spring are presented and commented.*

**Keywords:** Leaf spring, FEM analysis, Wagon, Ansys

## 1. INTRODUCTION

A leaf spring is a type of spring made by a number of plates (leaves) stacked upon each other in descending order of size. It is used to absorb shocks and vibrations in heavy commercial vehicles like trucks, trains, buses, etc.

The leaf spring provides quite a few major advantages. Below, we have mentioned a few of the main benefits:

- Leaf springs are simple in design
- Leaf springs are light in weight and strong
- Leaf springs provides good damping action
- Leaf springs provides good support to the axle and the chassis
- Leaf springs can withstand a large amount of load when compared to helical springs

However, leaf springs have a series of shortcomings: manufacturing process and their maintenance is more expensive than other types of springs, their mass is larger, leaves are exposed to damage, friction force between the leaves depends upon the state of contact surfaces, and they are not convenient for horizontal impact amortization. Besides, they are not resistant to small forces, transmitting them to the solid body, thus leading to vibration and noise. It is for this reason that the contemporary passenger cars do not possess leaf springs. They can however be found only in older models of passenger cars.

There are five different types of leaf springs:

- Transverse
- Eliptic
- Semi-eliptic
- Quarter-eliptic
- Three quarter eliptic

Different types of leaf springs are shown in Figure 1.

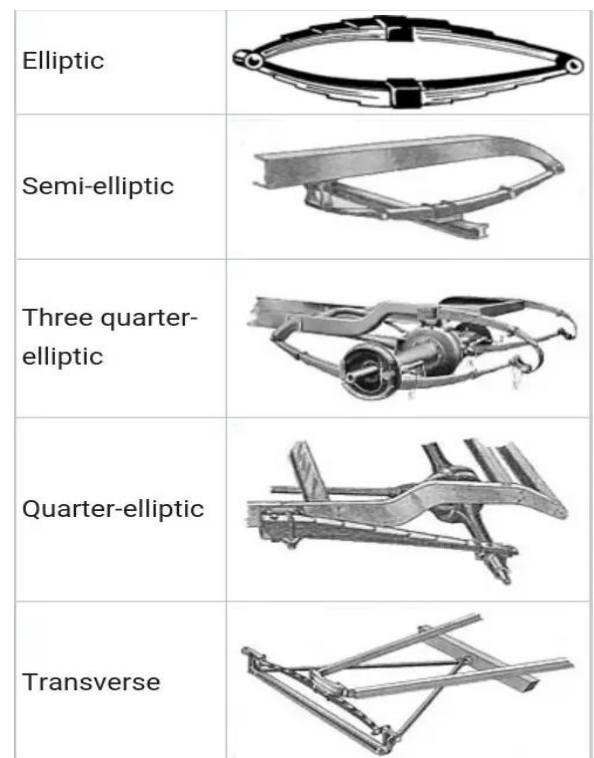


Figure 1: Types of leaf spring

The material used for leaf springs is usually a plain carbon steel having 0.90 to 1.0% carbon. The leaves are heat treated after the forming process. The heat treatment of spring steel produces greater strength and therefore greater load capacity, greater range of deflection and better fatigue properties.

The complete of leaf spring is composed of the main leaf (with eyes), other leaves, spring buckle and wedge.

Leafs are made of steel tapes which are bend in certain radius and subjected to the thermal treatment. Every leaf has on its upper side the longitudinal groove and on bottom side the appropriate longitudinal rib, which prevents mutual lateral movement of the leafs. The main leaf has on its ends the eyes for connection with the wagon underframe or bogie frame.

The characteristic construction and dimensions of the leaf spring are shown in Figure 2.

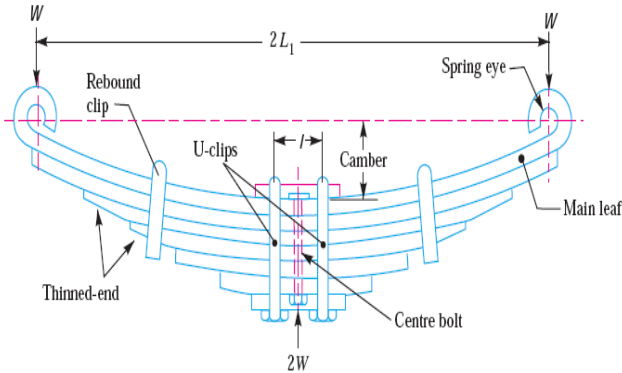


Figure 2: The characteristic construction of the leaf spring

In this paper we use FME analysis to solve static analysis of the leaf spring using modern software packages Ansys 14.5 [1,3].

2. LOAD CASES FOR LEAF SPRING CALCULATION

In this Section, a leaf spring on a 4-axle tank wagon with the following parameters was analysed:

- $G_k = 210 \text{ kN}$  -mass of the empty wagon
- $G_{os} = 14,5 \text{ kN}$  - mass of the wheelset
- $G_g = 1,2 \text{ kN}$  -mass of the leaf spring
- $n_{os} = 4$  - number of axles
- $n_g = 8$  - number of leaf spring
- $P_{os} = 225 \text{ kN}$  - maximum axle load

For leaf spring for axle load of 225 kN considered in this paper, the specific load cases are calculated in [2], and those are:

Load case 1: The load of the leaf spring under empty wagon

$$F_k = \frac{G_k - n_{os} \cdot G_{os} - n_g \cdot G_g}{n_g} = \frac{210 - 4 \cdot 14,5 - 8 \cdot 1,2}{8} = 17,8 \text{ kN}$$

Load case 2: The load of the leaf spring under fully loaded wagon

$$F_t = F_k + \frac{G_t}{n_g} = 17,8 + \frac{690}{8} = 104,05 \text{ kN}$$

Load case 3: The load of the leaf spring under fully loaded wagon in the dynamic regime

$$F_{max} = k_d \cdot F_t = 1,3 \cdot 104,05 = 135,265 \text{ kN}$$

The required stiffness, dimensions, number of leafs, stresses and safety factor, are determined. The defined geometry and the previous load cases are used for

demonstration of procedure of analytical calculation of the leaf spring, as shown in the next chapters.

3. FORMING CAD AND FEM MODEL

The first step is modelling the main leaf in 2D surrounding, for which AutoCAD is the most favourable, and it is used in this case.

In next phase, formed dwg or dxf file with sketch is imported in software for 3D modelling - in this case Autodesk Inventor is used. After this, it is very simple to obtain 3D geometry of main leaf, as shown in Figure 3.

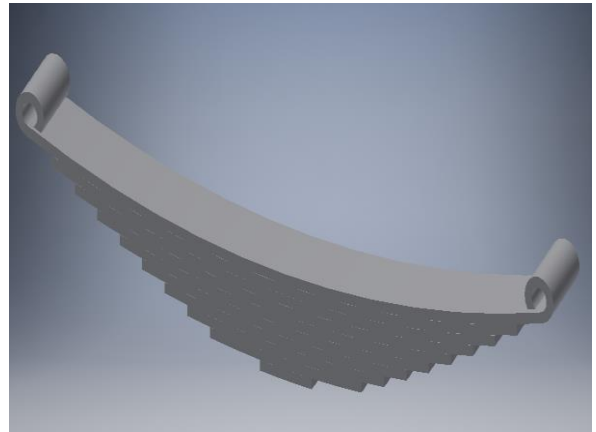


Figure 3: The 3D geometry of leaf spring formed in Autodesk Inventor

The basis for forming the FEM model is previously formed CAD geometry which is imported in Ansys in form of IGES or STEP file.

The values of parameters of the leaf spring material (spring steel 51Si7) are put in Ansys 14.5. (Figure 4).

| Chart : Alternating Stress Outline Row 3: Structural Steel |   |                       |         |     |
|--|---|-----------------------|---------|-----|
|  | A   | B                     | C       | D E |
| 1  | Property  | Value                 | Unit    |     |
| 2  | Density   | 7850                  | kg m^-3 |     |
| 3  | Isotropic Secant Coefficient of Thermal Expansion |                       |         |     |
| 4  | Coefficient of Thermal Expansion                  | 1.2E-05               | C^-1    |     |
| 5  | Reference Temperature                             | 22                    | C       |     |
| 6  | Isotropic Elasticity                              |                       |         |     |
| 7  | Derive from                                       | Young's Modulus an... |         |     |
| 8  | Young's Modulus                                   | 2E+11                 | Pa      |     |
| 9  | Poisson's Ratio                                   | 0.3                   |         |     |
| 10   | Bulk Modulus                                      | 1.6667E+11            | Pa      |     |
| 11   | Shear Modulus                                     | 7.6923E+10            | Pa      |     |
| 12   | Alternating Stress Mean Stress                    | Tabular               |         |     |
| 13   | Interpolation                                     | Log-Log               |         |     |
| 14   | Scale   | 1                     |         |     |
| 15   | Offset  | 0                     | MPa     |     |
| 16   | Strain-Life Parameters                            |                       |         |     |
| 17   | Display Curve Type                                | Strain-Life           |         |     |
| 18   | Strength Coefficient                              | 2063                  | MPa     |     |
| 19   | Strength Exponent                                 | -0.08                 |         |     |
| 20   | Ductility Coefficient                             | 9.56                  |         |     |
| 21   | Ductility Exponent                                | -1.05                 |         |     |
| 22   | Cyclic Strength Coefficient                       | 2432                  | Pa      |     |
| 23   | Cyclic Strain Hardening Exponent                  | 0.13                  |         |     |
| 24   | Tensile Yield Strength                            | 1100                  | MPa     |     |
| 25   | Compressive Yield Strength                        | 1100                  | MPa     |     |
| 26   | Tensile Ultimate Strength                         | 1300                  | MPa     |     |

Figure 4: Values of parameters of the leaf spring material

In the next phase, supports are adjusted, as shown in Figures 5-7.

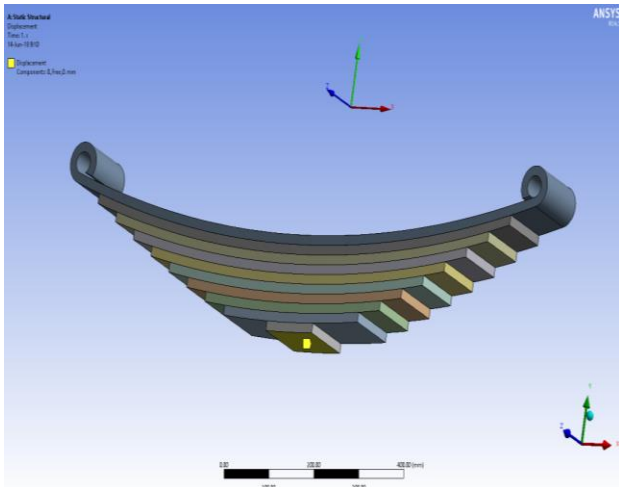


Figure 5: Support 1. – only vertical translation allowed

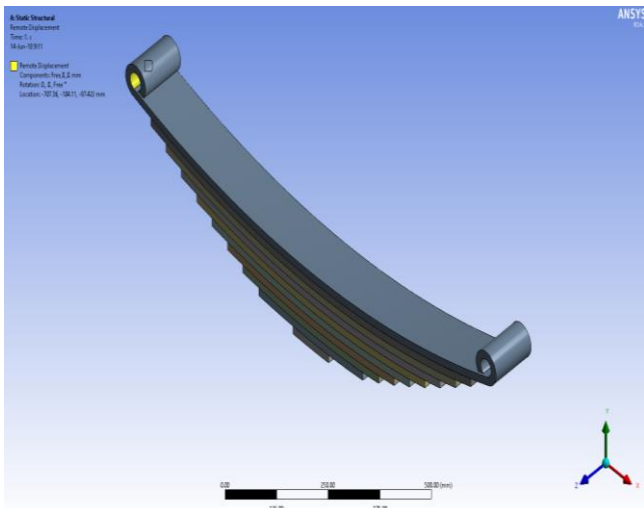


Figure 6: Support 2. – rotation and horizontal translation allowed

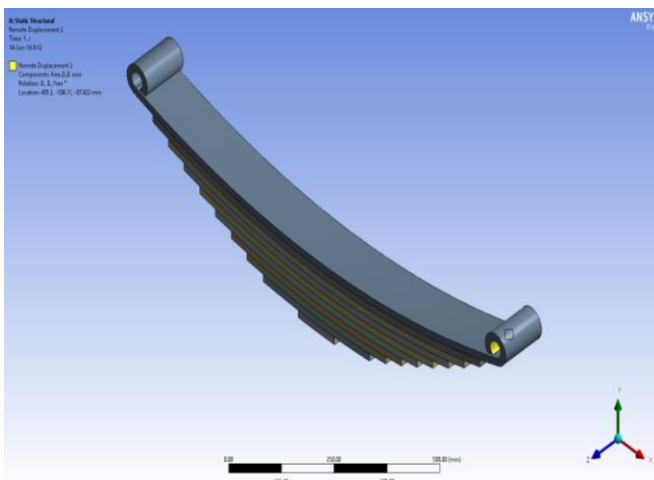


Figure 7: Support 3. – rotation and horizontal translation allowed

The finally generated FEM model is composed of 28158 finite elements and 109598 joints (Figure 8).

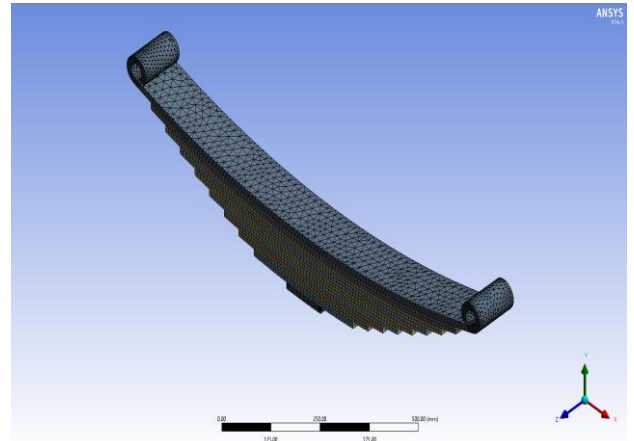


Figure 8: The finally formed FEM model of the leaf spring in Ansys 14.5

The applied force for third load case is shown in Figure 9.

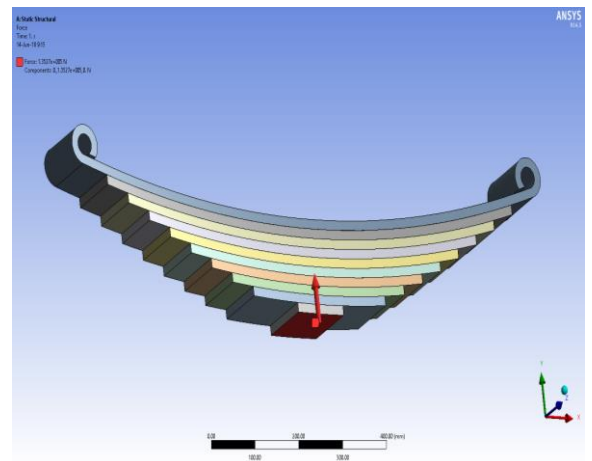


Figure 9: The applied force for third load case

#### 4. NUMERICAL RESULTS

The obtained results for given load cases are shown in Figures 10-15.

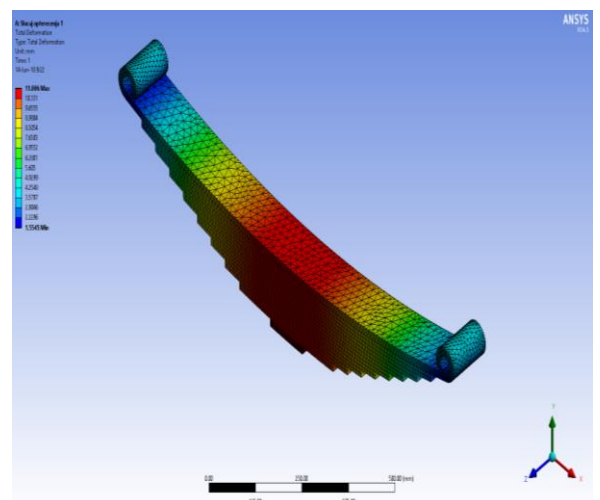


Figure 10: The deflection for load case 1

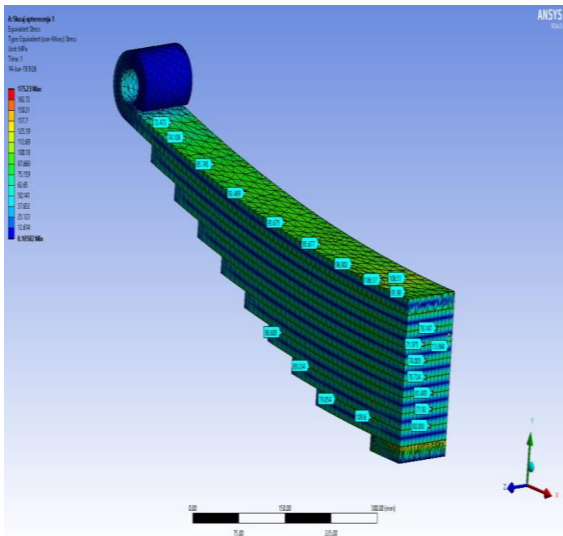


Figure 11: The equivalent stress for load case 1

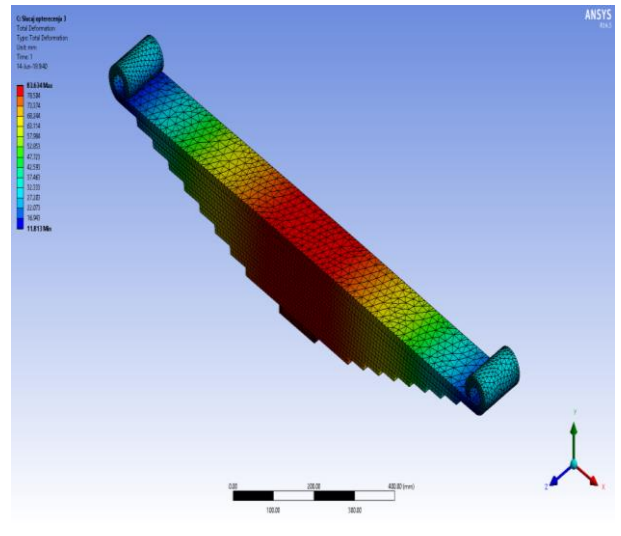


Figure 14: The deflection for load case 3

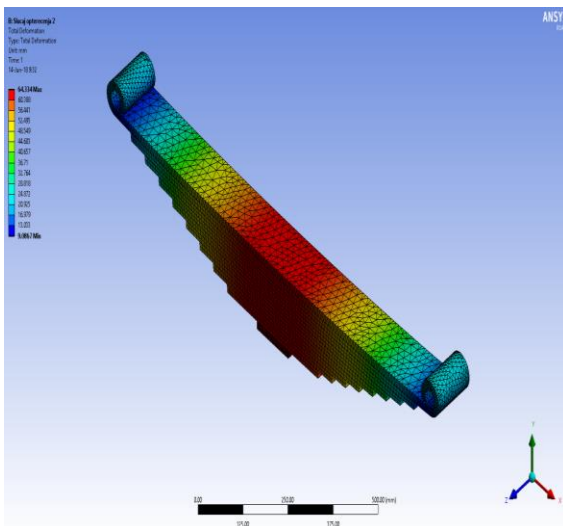


Figure 12: The deflection for load case 2

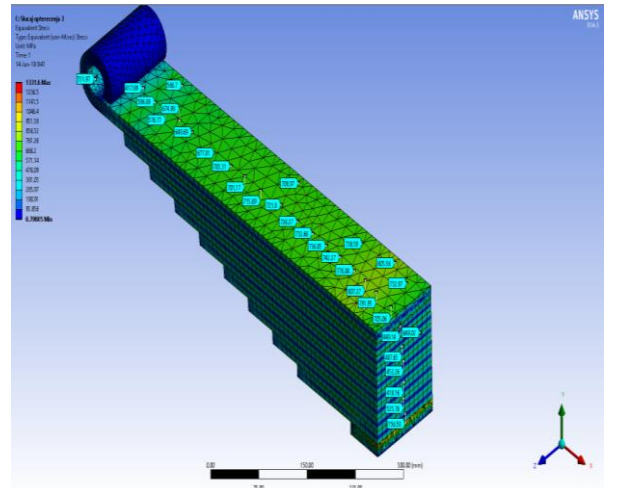


Figure 15: The equivalent stress for load case 3

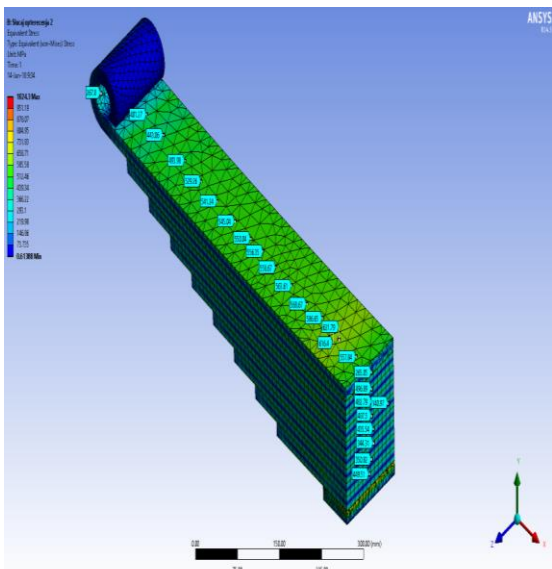


Figure 13: The equivalent stress for load case 2

In the final stage, the results obtained by the numerical calculation are compared with the results of analytical calculation (exposed in literature [2]).

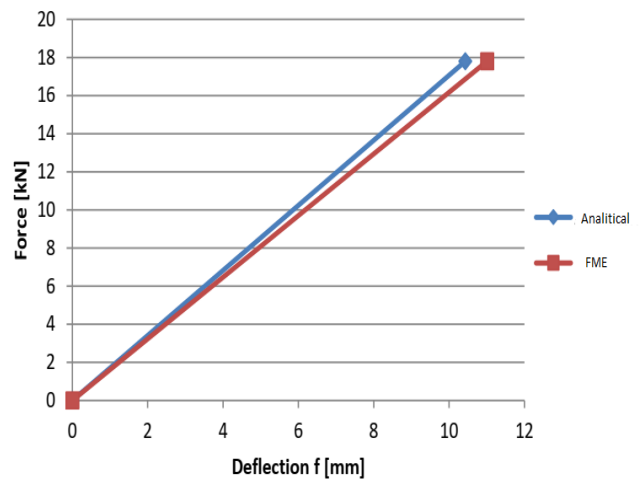


Figure 16: The comparative diagram of leaf spring deflection obtained by the FEM and analytical way for load case 1

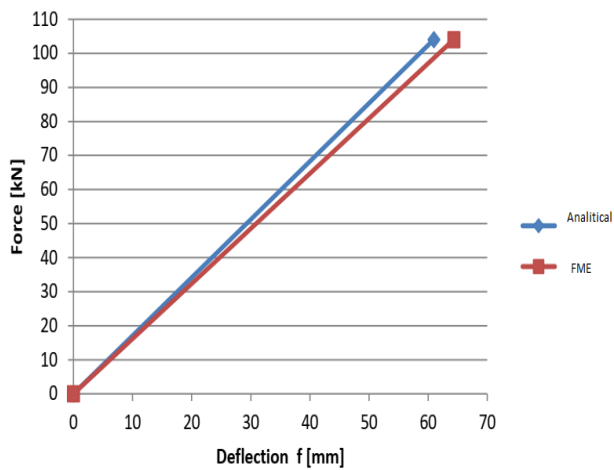


Figure 17: The comparative diagram of leaf spring deflection obtained by the FEM and analytical way for load case 2

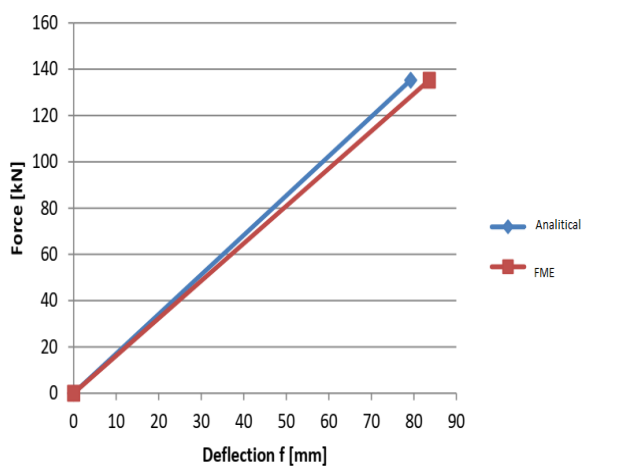


Figure 18: The comparative diagram of leaf spring deflection obtained by the FEM and analytical way for load case 3

## 5. CONCLUSION

This paper uses analytic and numeric (FME) methods for constructing a leaf spring of a passenger car (rail). Save for the analytic method, the finite element method – FME was used. The 3D model of the leaf spring was developed in Autodesk Inventor Professional software suite, while the FME analysis was performed using Ansys 14.5 software suite.

Based on calculation results given by FME, a significant conclusion about the state of analyzed leaf spring construction can be drawn. In the first case, considering an empty wagon under the influence of a force of 17,8 kN, the deflection of the spring is 1,04cm, a characteristic result for such a force. In the second case, considering the full wagon under the influence of a force of 104,05 kN, the deflection of the spring is 6,09cm. This result was expected, and the value represents a difference of the arrow length between the empty and full wagon. In the third case, considering spring behavior under the influence of the maximum force of 135,26kN, the deflection is 7,92cm, which is an expected result.

Based on obtained results, the following conclusion can be drawn: the analyzed construction of the leaf spring

does satisfy all of the criteria, and it can be installed on the passenger car (rail).

## ACKNOWLEDGEMENTS

This work was supported by the Serbian Ministry of Education, Science and Technological Development through Mathematical Institute of the Serbian Academy of Sciences and Arts.

## REFERENCES

- [1] Bižić.M,Petrović.D “Numerical analysis of wagon leaf spring”, XIX Scientific-Expert Conference on Railways RAILCON 2020, 15-16 October, Serbia, Niš, pp.21-24.
- [2] Petrović, D., *Železnička vozila – Praktikum*, Mašinski fakultet Kraljevo, Kraljevo, 2006.
- [3] Gowd, H., Static Analysis of Leaf Spring, International Journal of Engineering Science and Technology, Vol. 4, No. 08, pp. 3794-3803, 2012.
- [4] Милосав Огњановић, *Машински елементи*, Машински факултет Београд, Београд,2013.
- [5] <http://www.tatravagonkabrastvo.rs/>



# Experimental and numerical strength analysis of freight wagon type SHIMMNS intended for the transportation of the sheet coils

Vladimir Milovanović<sup>1\*</sup>, Miroslav Živković<sup>1</sup>, Snežana Vulović<sup>2</sup>, Aleksandar Dišić<sup>2†</sup>, Marko Topalović<sup>2</sup>

<sup>1</sup>Faculty of Engineering, University of Kragujevac, Kragujevac (Serbia)

<sup>2</sup>Institute for Information Technologies, University of Kragujevac, Kragujevac (Serbia)

*Shimmns wagons are very common type of freight wagons that are used for transportation of heavy steel sheet coils, which are further used as an initial material in automotive and other industries. Due to frequent usage, and heavy loading, these wagons are prone to fatigue cracks, which, if not identified it time, could cause catastrophic failures. Therefore, these wagons must satisfy rigorous standards, and must be thoroughly analysed and tested. In this paper, we will present a methodology that combines experimental testing and Finite Element Analysis according to TSI standard and norm EN 12663-2:2010. Measurements with strain gauges and stresses obtained by FEM calculation gives good agreement. FEM model is created in FEMAP software, and analysis was done using NX Nastran solver. Based on the agreement between numerical and experimental results, it can be concluded that the FEM analysis can be reliably applied during the designing of new wagons, or analysis of failures in existing ones. FEM analysis can be used to perform several design cycles virtually, thus reducing the number of the prototypes required for experimental testing. This can lead to great savings in time and money during the design of new wagons.*

**Keywords:** Finite Element Method, Freight wagon, Sheet coils, Fatigue strength analysis, Stress field

## 1. INTRODUCTION

Finite Element Method (FEM) simulations are widely used for solving various problems in the heavy machinery industry because they reduce the time and cost of developing the new products [1]. FEM analysis results provide very useful information about the product and can indicate the potential problems that can be eliminated in the virtual environment. The second step in the design cycle is making a prototype, based on the results obtained using FEM. The strain gauges are placed where FEM analysis predicts the high stress concentration, and measurements are carried out for required load cases. When the prototype testing is finished, in a third step a comparative analysis of the results obtained by FEM calculation and experimental measurements on a prototype is performed. Measurement results and results obtained by FEM calculation must satisfy all requirements defined in the standards.

In the case of SHIMMNS freight wagon analysis, presented in this paper, strength validation is done according to TSI standard [2] and norm BS EN 12663-2:2010 [3].

The paper is organized as follows. In the Chapter 2, the FEM model of the SHIMMNS freight wagon is described. This chapter also contains descriptions of analysed load case, standard requirements, safety factor and permissible stress. In the Chapter 3, we will present measuring procedure, positioning of the strain gauges and obtained experimental stress values. Chapter 4 features FEM results and their comparison with experimental data. In the conclusion, FEM analysis results and experimental data are discussed, and based on these results, we can conclude that analysed SHIMMNS wagon satisfy all of the safety requirements defined by standards [2], [3].

## 2. FEM MODEL OF SHIMMNS WAGON

The SHIMMNS freight wagons are used for the transportation of sheet metal coils, placed on five wagon saddles as shown in the Fig. 1.



Figure 1: SHIMMNS wagon

These coils can have different diameter, length, mass, and different saddle placement. Wagon must be able to withstand a wide range of load cases set by the International Union of Railways (UIC).

FEM analysis, according to standards [2] and [3] was performed using the NX Nastran solver, which is built in FEMAP pre and post-processor [4]. FEMAP is used to create a finite element mesh, that primarily consists of shell elements, which have appropriate thicknesses in accordance with the part of construction. Some 3D elements were also used for modelling of support plates, relief ring, traction device. The construction is modelled in detail with 153420 elements and 151650 nodes, and the system of about 900 thousand equations is solved during the calculation. The average size of the element is 40 mm. Full FEM model is shown in the Fig. 2.

\* Corresponding author: Vladimir Milovanović, Sestre Janjić 6 34000 Kragujevac, vladicka@kg.ac.rs



Figure 2: FEA model of SHIMMNS wagon

In the most of the load cases, due to symmetry, we were able to use one quarter of the model, shown in the Fig. 3, which saved us a lot of computational time.

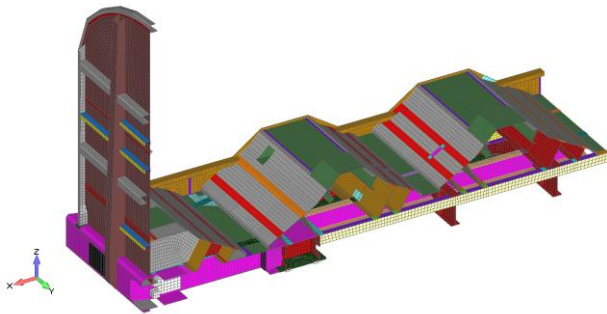


Figure 3: One quarter FEA model of SHIMMNS wagon

The main characteristics of the SHIMMNS wagon, according to [5] are given in Tab. 1.

Table 1: Technical data of wagon type SHIMMNS

|                                    |                       |
|------------------------------------|-----------------------|
| Track width                        | 1435mm                |
| Gauge                              | G1                    |
| Length over buffers                | 12240mm               |
| Length without buffers             | 10800mm               |
| Distance between the central bolts | 7200mm                |
| Load opening width                 | 2400mm                |
| Max. axle load                     | 20t                   |
| Buffer height                      | $1.060_{-5}^{+10}$ mm |
| Tare weight                        | 23t±3%                |
| Max. cargo weight                  | 57 t                  |
| Max. speed (empty/loaded)          | 120/100km/h           |
| Bogie type                         | Y25 Cst               |
| The smallest curve radius          | 70m                   |

The wagon is made of steel S355J2+N, with the following characteristics, shown in Tab. 2. [5].

Table 2: Material characteristics of S355J2+N

| Physical Characteristics         |                                  |       |
|----------------------------------|----------------------------------|-------|
| E N/mm <sup>2</sup>              | $\rho$ kg/mm <sup>3</sup>        | $\nu$ |
| $2.10 \cdot 10^5$                | $7.85 \cdot 10^{-6}$             | 0.3   |
| Mechanical Characteristics       |                                  |       |
| R <sub>e</sub> N/mm <sup>2</sup> | R <sub>m</sub> N/mm <sup>2</sup> | KV J  |
| 355                              | 510                              | 27    |

According to UIC 577 and BS EN 12663-2: 2010 [3], Clause 5.2.3.1 Tab. 6, the analysis is performed in the case of maximum load of the wagon. Here, the value of the maximum load is increased 1.3 times (30%) in relation to the nominal load, in order to take the dynamics into the account.

The maximum weight of steel coils that this wagon can carry is 57 tons, as shown in Tab. 1, and this weight

can include the combination of different diameters and widths of the coils shown in Tab. 3.

Table 3: Maximum loading of the cradle and dimensions of the steel coils

| Cradle number | Coil diameter mm | Load t |
|---------------|------------------|--------|
| 1             | 1000 – 2250      | 28     |
| 2             | 800 – 1700       | 17     |
| 3             | 1000 – 2250      | 33     |
| 4             | 800 – 1700       | 17     |
| 5             | 1000 – 2250      | 28     |

In accordance with EN 12663-2:2010 [2], clause 6.2.2.1 Tab. 18 and Tab. 19, and based on the material characteristics given in Tab. 2, in this paper, we can calculate permissible stress in parent material, and in the welded joints, shown in Tab. 4.

Table 4: Safety factors and permissible stress in parent material and welded joints

| Material  | Safety factor S <sub>1</sub> | $\sigma_{cmax}$ MPa |
|---|------------------------------|---------------------|
| S355J2+N  | 1.0                          | 355                 |
| Parent material in the immediate vicinity of welds (S355J2+N) | 1.1                          | 323                 |

Safety factors specified in Tab. 4. cover static load cases defined in EN 12663-2:2010 [3]. Also, in accordance with EN 12663-2:2010, Clause 6.2.2.1, the maximum deflection on the underframe should not exceed 3‰ of the wheelbase from the initial position. In accordance with the data given in the Tab. 1, the maximum deflection at half the distance between wheelbase must not exceed 21.6mm.

Horizontal, vertical load cases, load combinations and lifting load cases were analyzed using FEM. Vertical load cases cause the highest stress values in the significant loaded zones and unfavorable vertical load case is used for comparative analysis of experimental and numerical results.

According to the technical characteristics of four-axle bogie wagon type SHIMMNS for transporting sheet metal coils [5], given in Tab.1, the maximum vertical load of the wagon is 57t. Accordingly, and respecting the limitations regarding the maximum load of cradles given in Tab 3, six cases were performed within the analysis of the vertical load.

In the first load case the second and fourth cradles are loaded with 12t each, with medium sized coils that have a diameter of 1700mm, and width 1000mm, while the middle cradle is loaded with the maximum size coil that according to Tab. 3, has a diameter of 2250mm, width 1000mm and weight of 33t. This combination corresponds to the maximum load capacity of the wagon, which is 57t.

In this paper, we will present experimental testing of the wagon according to the first vertical load case [2] (unfavorable vertical load case) which is shown in the Fig. 4, and afterwards we will show the additional FEM analysis which is used to replicate experimental conditions and to verify calculated stress.

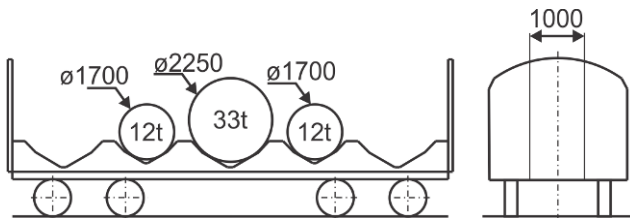


Figure 4: First load case for SHIMMNS wagon analysis

### 3. EXPERIMENTAL MEASURING OF STRESS IN SHIMMNS WAGON

Analysed model has two main subassemblies: underframe and superstructure. Based on the initial FEA results, strain gauges are placed on the wagon structure, their positions are given in the technical drawings shown in the Fig. 5. (position of strain gauges on underframe) and Fig. 6 (position of strain gauges on superstructure and cradles).

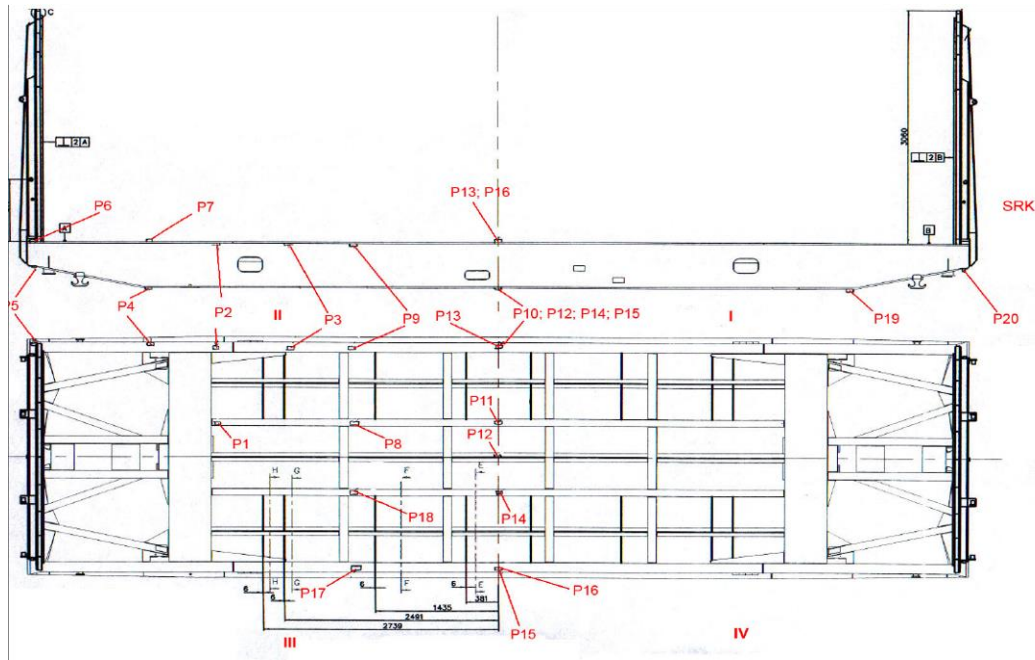


Figure 5: Underframe technical drawings with strain gauge positions

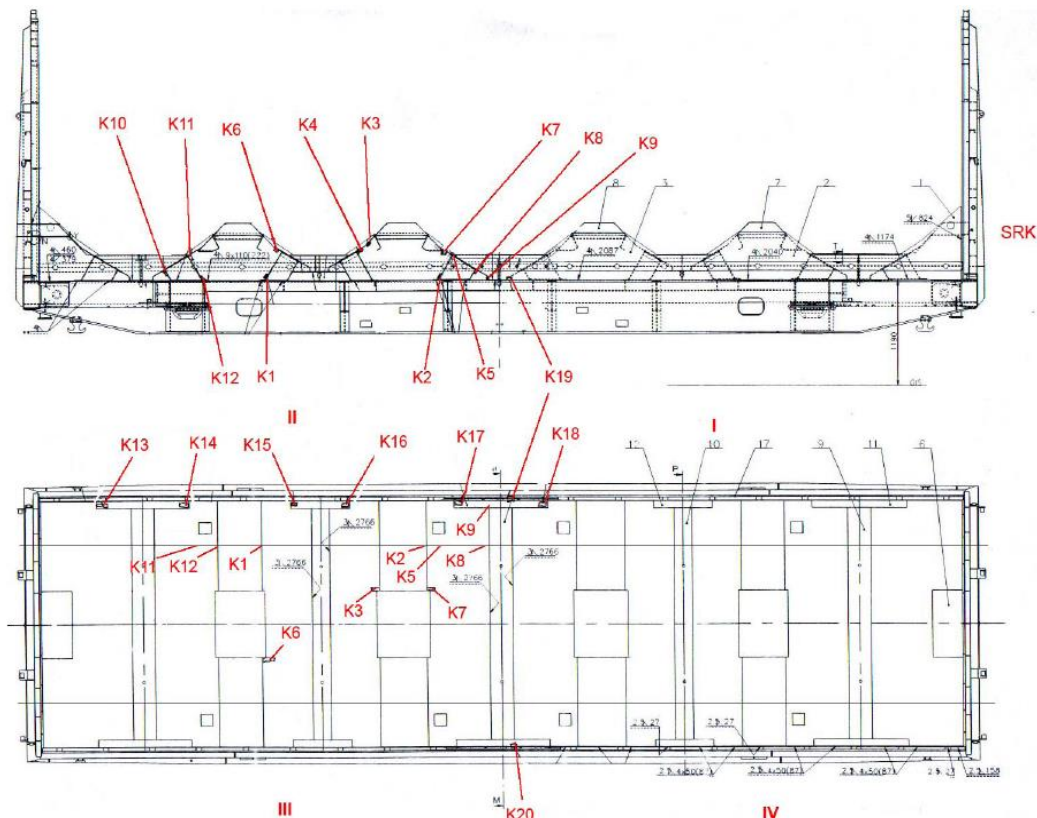


Figure 6: Superstructure technical drawings with strain gauge positions

Unfortunately, coils with the exact dimensions given in the Fig. 3. were not available for testing, so the closest ones at hand were placed on cradles 2 and 4, and the largest coil in the middle cradle is substituted with a combination of 3 coils. Dimensions of the experimental coils are given in Tab. 5, and their placement on SHIMMNS wagon cradles is shown in the Fig. 7.

Table 5: Experimental setup for the first load case

| Cradle number | Coil dimensions mm | Load t     |
|---------------|--------------------|------------|
| 2             | $\phi$ 1400x1500   | 11.66      |
| 3             | $\phi$ 1400x1500   | 11,8+0,85+ |
|               | $\phi$ 1400x1500   | 7,26+9+1,6 |
|               | $\phi$ 1400x1500   | =30,51     |
| 4             | $\phi$ 1400x1500   | 11.66      |



Figure 7: Experimental setup for the first load case

Strain gauges are shown in the Fig. 8. and Fig. 9.

Data acquisition equipment is shown in the Fig. 10.



Figure 8: Strain gauge P16



Figure 9: Strain gauge P13



Figure 10: Data acquisition equipment

Stress obtained experimentally by gradual, incremental loading are shown in Tab. 6.

Table 6: Experimental measurements results

| Stress MPa   |         |         |        |               |
|--------------|---------|---------|--------|---------------|
| Strain gauge | Load t  |         |        |               |
|              | 11,05   | 23,32   | 35,12  | 53,83         |
| P1           | -14,960 | -27,271 | -40,36 | <b>-63,2</b>  |
| P2           | 0,954   | -1,28   | -1,116 | 0,173         |
| P3           | 0,211   | -4,337  | -6,759 | -10,42        |
| P4           | 1,972   | 1,703   | 2,745  | 3,401         |
| P5           | 1,857   | -0,102  | 0,159  | 0,078         |
| P6           | -0,448  | -0,341  | -0,177 | -0,074        |
| P7           | 0,547   | 0,315   | 1,178  | 2,934         |
| P8           | 1,000   | 13,006  | 14,821 | 17,337        |
| P9           | -1,514  | -1,498  | -4,129 | -7,918        |
| P10          | 14,658  | 24,691  | 50,972 | <b>91,693</b> |
| P11          | 3,336   | 2,122   | 19,283 | <b>46,619</b> |
| P12          | -4,702  | -3,714  | 3,333  | 13,743        |
| P13          | -4,939  | -10,201 | -20,63 | <b>-37,33</b> |
| P14          | 0,157   | 2,05    | 16,031 | <b>37,004</b> |
| P15          | 10,816  | 23,13   | 45,091 | <b>78,301</b> |
| P16          | 0,626   | -10,624 | -21,24 | <b>-36,68</b> |
| P17          | -1,642  | -1,909  | -3,829 | -6,931        |
| P18          | 3,631   | 12,989  | 13,539 | 14,083        |
| P19          | -       | -       | -      | -             |
| P20          | 0,793   | -0,176  | -0,253 | -0,19         |
| K1           | -2,713  | -7,73   | -8,485 | -10,17        |
| K2           | -0,618  | 0,169   | -1,137 | -5,437        |

|     |        |         |        |               |
|-----|--------|---------|--------|---------------|
| K3  | 16,985 | -21,188 | -19,52 | -17,61        |
| K4  | -2,399 | 55,958  | 74,489 | <b>80,549</b> |
| K5  | 15,301 | 10,026  | 31,578 | <b>66,241</b> |
| K6  | -4,483 | -34,452 | -34,91 | <b>-35,64</b> |
| K7  | 10,448 | 3,479   | 1,982  | 1,603         |
| K8  | -0,784 | -0,615  | -2,347 | -5,737        |
| K9  | 7,166  | -2,389  | -25,66 | <b>-59,14</b> |
| K10 | -1,681 | -4,556  | -6,625 | -9,733        |
| K11 | -0,651 | 9,28    | -14,92 | <b>-25,2</b>  |
| K12 | 0,919  | -3,405  | -4,487 | -6,581        |
| K13 | 2,546  | 3,373   | 5,528  | 10,768        |
| K14 | -2,283 | 0,286   | 0,726  | 1,327         |
| K15 | -9,789 | -23,434 | -33,40 | <b>-45,55</b> |
| K16 | 0,043  | -29,033 | -45,91 | <b>-71,45</b> |
| K17 | -0,495 | -7,521  | -14,97 | <b>-26,74</b> |
| K18 | -2,115 | 6,388   | 19,147 | <b>38,035</b> |
| K19 | 3,041  | -3,79   | -8,158 | -14,52        |
| K20 | -3,527 | -4,002  | -8,235 | -13,94        |

For subsequent comparison with FEM results, we considered only stress greater than 20 MPa which are emphasized in Tab. 6.

#### 4. FEM RESULTS AND COMPARISON WITH EXPERIMENTAL DATA

Subsequent FEM analysis was done for the realistic experimental load case defined in Tab 5, which slightly different from the initial load case shown in the Fig. 4. Von Mises stress field in one quarter model is shown in the Fig. 11. to Fig.16, for different viewing angles, and zoomed in areas with high stress values.

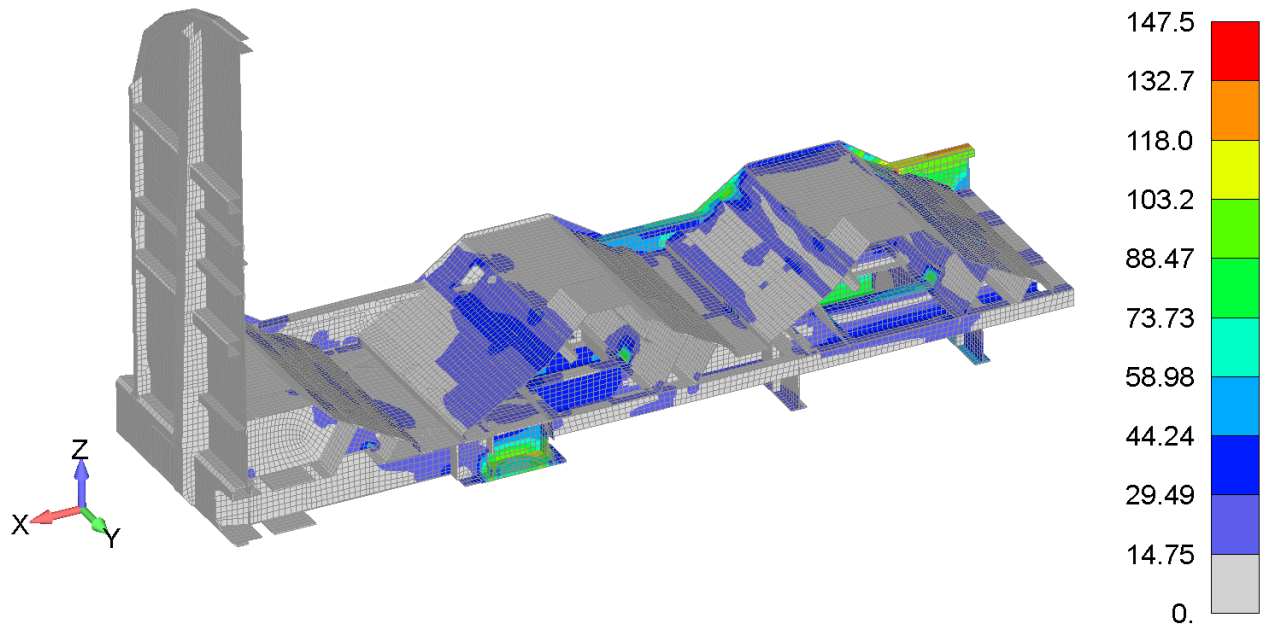


Figure 11: Von Mises equivalent stress field, view 1

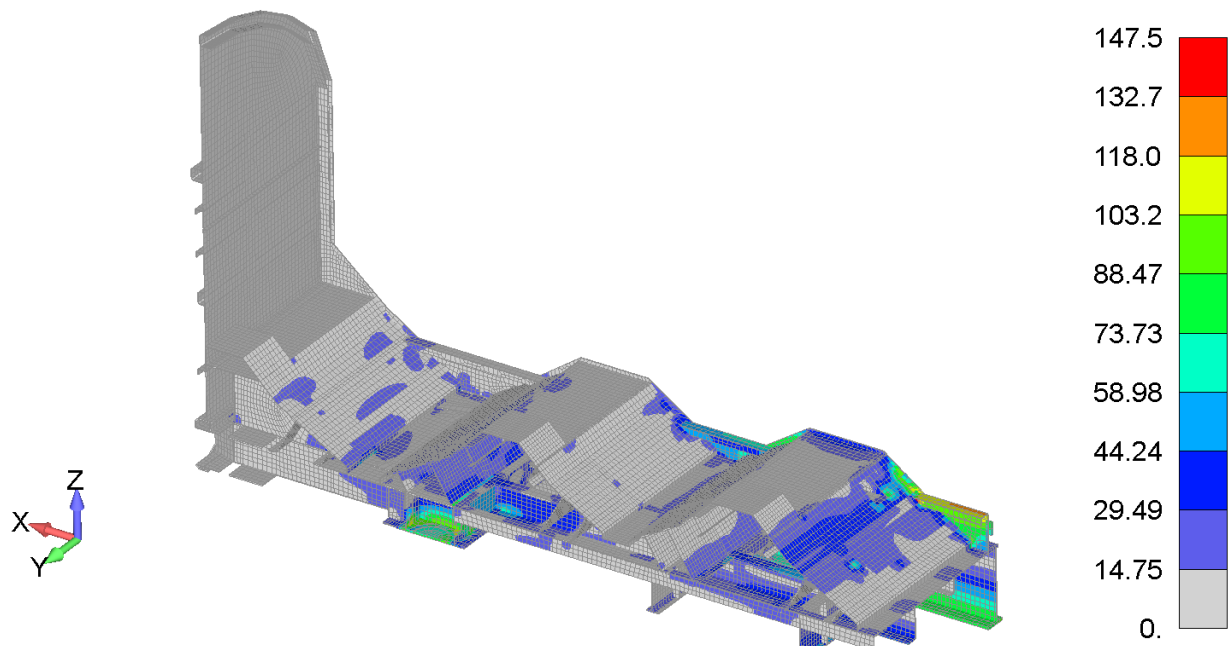


Figure 12: Von Mises equivalent stress field, view 2

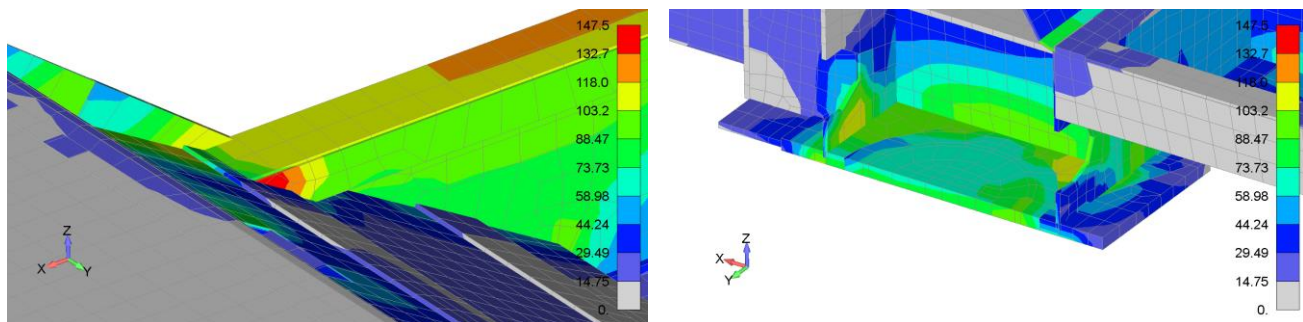


Figure 13: Significant loaded zones, view 3,4

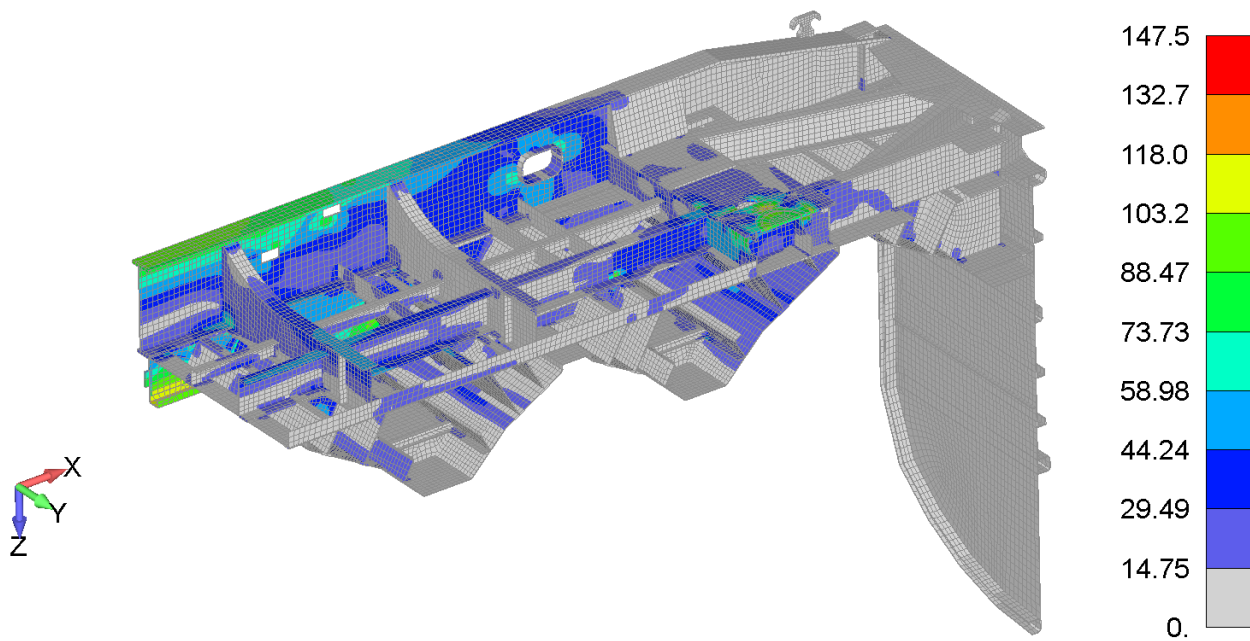


Figure 14: Von Mises equivalent stress field, view 5

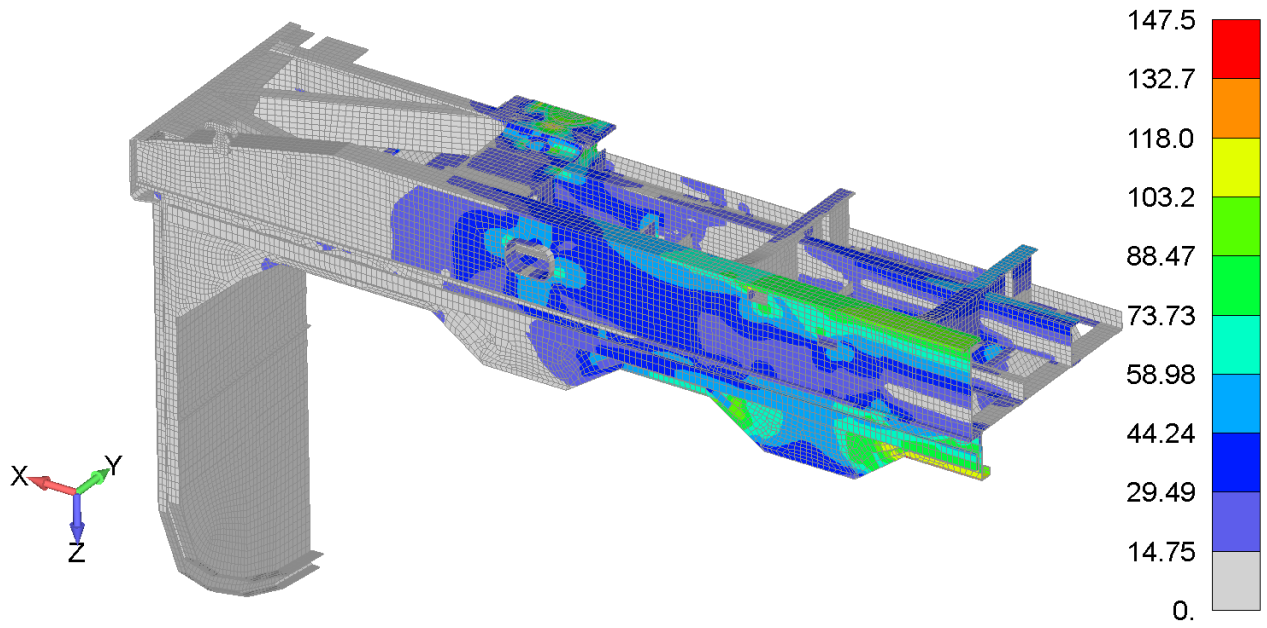


Figure 15: Von Mises equivalent stress field, view 6

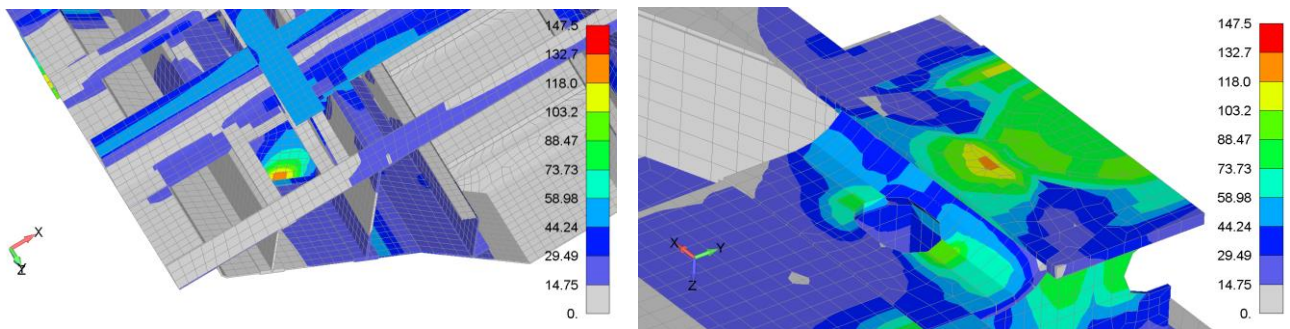


Figure 16: Significant loaded zones, view 7,8

Longitudinal displacement is shown in the Fig. 17.

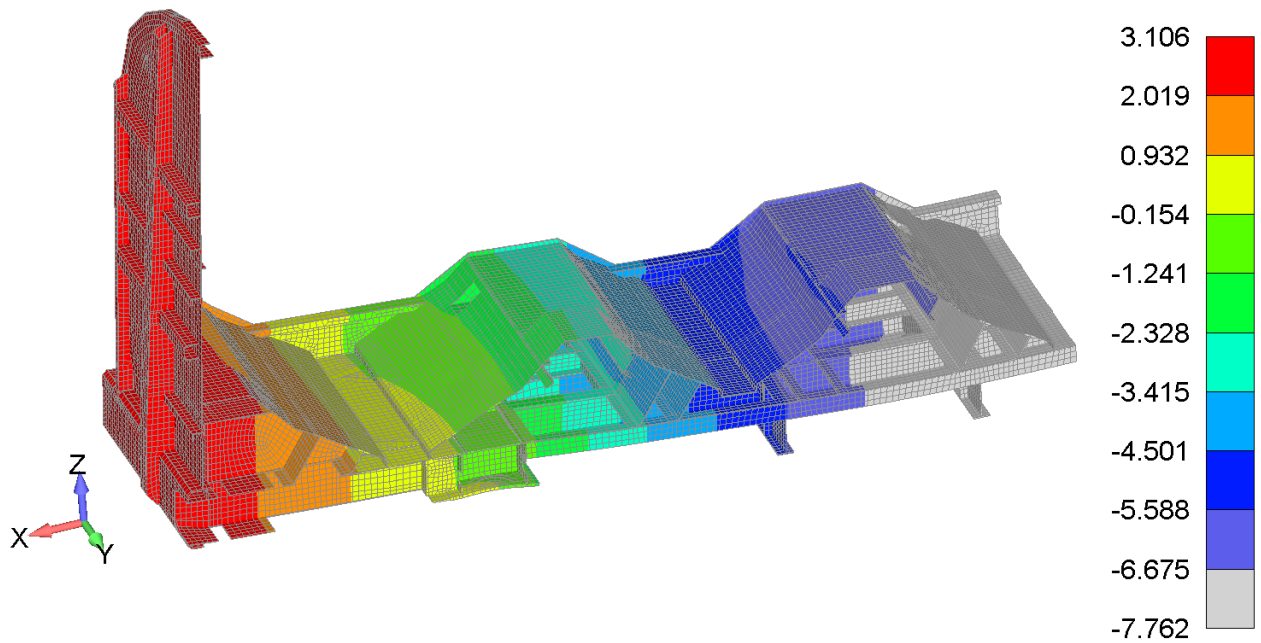


Figure 17: Longitudinal displacement field –  $U_z$

The FEM results show good agreement with experimental data, and that Von Mises equivalent stress in

both parent material and welded joints [6] is far less than permissible stress, as can be seen in Tab. 7.

Table 7: Comparison between experimental and FEM results

| Stress MPa   |                |              |                    |
|--------------|----------------|--------------|--------------------|
| Strain gauge | Measured value | FEM analysis | Permissible stress |
| P1           | -63,2          | -64.88       | 216                |
| P10          | 91,639         | 92.23        | 238                |
| P11          | 46,619         | 46.11        | 238                |
| P13          | -37,33         | -36.42       | 216                |
| P14          | 37,004         | 46.11        | 238                |
| P15          | 78,301         | 92.23        | 238                |
| P16          | -36,68         | -36.42       | 216                |
| K4           | 80,549         | 60.09        | 216                |
| K5           | 66,241         | 65.66        | 216                |
| K6           | -35,64         | -34.55       | 216                |
| K9           | -59,14         | -62.61       | 238                |
| K11          | -25,2          | -25.93       | 238                |
| K15          | -45,55         | -47.74       | 216                |
| K16          | -71,45         | -62.3        | 216                |
| K17          | -26,74         | -44.77       | 216                |
| K18          | 38,035         | -44.77       | 216                |

Due to the lack of appropriate measuring equipment, the maximum deflection at half the distance between wheelbase is not experimentally confirmed, but based on stress agreement between FEM and experimental testing, we can vouch that this condition is satisfied as well, as shown in Tab. 8.

Table 8: Maximum deflection at the middle of the wagon

| Measured deflection | FEM result | Permissible deflection |
|---------------------|------------|------------------------|
| -                   | 7.152      | 21.6                   |

## 5. CONCLUSIONS

In this paper numerical analysis of SHIMMNS type wagon is presented along with the experimental verification. According to standards [2] and [3], this type of wagon must be certified to withstand numerous loading conditions that can occur during its exploitation. However, experimental validation can be difficult, impractical and expensive, so FEM analysis is used to refine wagon design before the first prototype for testing is constructed. Six vertical load cases are analysed using FEM according to wagon specifications, and in this paper only the first load case is presented. Exact loading of wagon cradles was

impossible to experimentally recreate due to the lack of sheet coils with specific dimensions and weight, however, the deviation from the targeted values can be neglected having in mind the difference between stress calculated using FEM and experimental values on one side, and permissible stress on the other side.

Analysed wagon satisfies all safety criteria defined in the standards [2] and [3], but its tare weight/cargo weight ratio makes it inferior to the competition, so optimization of wagon is required in order to reduce tare weight and to increase its cargo capacity, which will require multiple repetition of design changes and FEM analysis cycles.

## ACKNOWLEDGEMENTS

This research is supported by the Ministry of Education, Science and Technological Development, Republic of Serbia, Grant TR32036 and 451-03-9/2021-14/200378.

One of the authors, Aleksandar Disic, deceased due to COVID-19 complications after this research was done. We would like to keep him on the author list, because his contribution has great impact on this paper

## REFERENCES

- [1] M. Kojić, R. Slavković, M. Živković and N. Grujović, "Finite Element Method I - Linear Analysis", Faculty of Mechanical Engineering, University of Kragujevac, (Serbia), (1998).
- [2] TSI Standard - Commission Regulation (EU) No 321/2013 of 13 March 2013 concerning the technical specification for interoperability relating to the subsystem 'rolling stock — freight wagons' of the rail system in the European Union and repealing Decision 2006/861/EC; including amendment Commission Regulation (EU) No 1236/2013 of 2 December 2013.
- [3] BS EN 12663-2:2010 - Railway applications – Structural requirements of railway vehicle bodies, Part 2: Freight wagons, European Standard.
- [4] Femap with NX Nastran user manual.
- [5] Technical description of the SHIMMNS wagon.pdf
- [6] V. Milovanović, V. Dunić, D. Rakić, M. Živković, "Identification causes of cracking on the underframe of wagon for containers transportation - Fatigue strength assessment of wagon welded joints", Eng. Fail. Anal, Vol. 31, pp. 118-131, (2013)

# Influence of the traction force and the speed of movement on the strength characteristics of the locomotive axles

Vasko Nikolov<sup>1\*</sup>

<sup>1</sup> Department Transport Equipment, Todor Kableshev Transport University, Sofia, Bulgaria

*The article presents the dependencies obtained when researching the load on the locomotive axles, depending on the traction force and the speed of movement of the locomotive. The traction characteristic of the locomotive is the relationship between the traction force achieved by the traction motors and the speed of movement, and it is different under different driving conditions. Different modes of operation of locomotive axles are considered. A simulation of the axles' behaviour has been developed. The strength and deformation characteristics of the locomotive axles under different loading modes are calculated. A comparative analysis of the strength characteristics of locomotives with different classes of transmission mechanisms has been made.*

**Keywords:** locomotive axles, strength characteristic, comparative analysis, traction characteristic, strength analysis, simulation, traction force

## 1. INTRODUCTION

Locomotive axles are subjected to heavy and variable loads during their operation. As a result, they accumulate fatigue of the material, leading to unacceptable failures in them. These failures are unacceptable because locomotive axles have a direct impact on the safety of trains and rail transport in general. The change in the load of the locomotive axles depends mainly on the magnitude of the torque with which they are loaded during the realization of the traction forces of the locomotive. Since the traction force is not constant, the load on them is variable. The traction force of a locomotive is a function of the current in the traction motors and the gear ratio of its axle gearbox and varies for the different power transmitted by the locomotive at different speeds. The present study aims to determine specific quantitative values of the strength characteristics of the locomotive axles depending on the traction force realized by the locomotive and its speed.

In the study, electric locomotives with individual drive of the axles with the help of a traction motor and a single-speed gear of the transmission mechanism were observed.

## 2. TRACTION FORCE AND TRACTION CHARACTERISTICS OF LOCOMOTIVES

The movement of trains on the track is considered to be translational, i.e., as if all its points have the same velocities in both direction and magnitude. In other words, the train is seen as a material point. The accepted assumption does not affect in any way the results of the train running calculations.

The study used the data and designs of the transmission mechanisms of several series of locomotives used in railway transport in Bulgaria: type of 43, 44, 45, which have the same design parameters of the transmission mechanism, types of 46 and 86.

The first two types of locomotives (43-45 and 46) are constructed with transmission mechanisms – support-

frame suspended traction motor and support-axle suspended wheel axle reducer (Fig. 1). In the considered

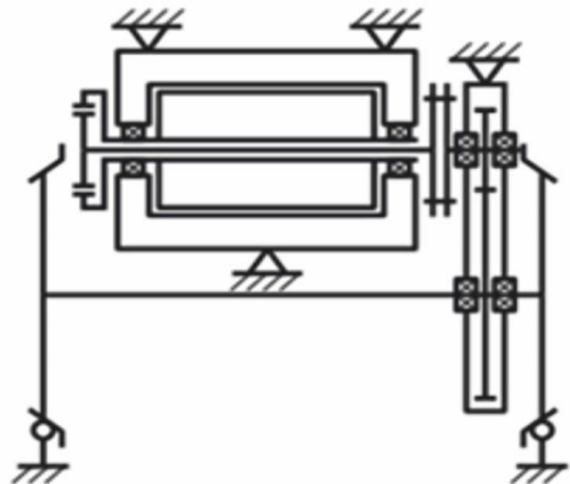


Figure 1

locomotives the transmission of the torque is carried out by means of a cardan shaft, placed in the hollow shaft of the traction motor, as in locomotives 43, 44 and 45 this is carried out by a cardan shaft and hinged connections at both ends, and in locomotives 46 - with using a shaft with gear clutches at both ends.

Locomotives of type of 86 have a transmission mechanism of the third kind - support-frame suspended traction motor and wheel axle reducer and one-sided transmission of torque with a hollow shaft placed on the axis of the wheel axle (Fig. 2). The transmission of the torque from the traction motor to the motor wheel is carried out by means of a gear, as the big gear is attached to the hollow shaft by means of elastic (rubber-metal) joints. In turn, the hollow shaft mounted on the drive wheel is connected to one of the wheels in the same way - by means of an elastic connection.

\* Corresponding author: Vasko Nikolov, Todor Kableshev Transport University, Geo Milev str, va\_r\_nikolov@abv.bg

All this leads to a different distribution of the load on the motor wheel, as well as a different distribution of forces along it.

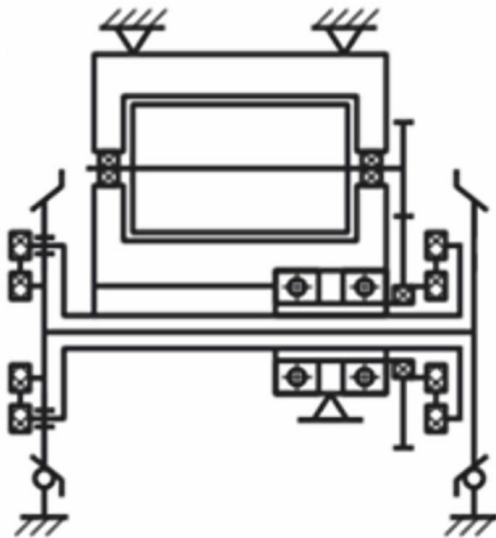


Figure 2

The formation of the traction force in the considered types of locomotives (with individual drive of the axles by traction electric motors) is carried out by the following mechanism:

When the current enters the traction motor of its armature, a torque  $M_1$  occurs, which is then transmitted to the locomotive of the locomotive by means of the gear. The moment  $M_1$  can also be represented as a pair of forces, one of which  $Z_1$  is applied at the point of contact of the teeth of the gears, and the other  $Z_2$  is applied in the centre of the engine (Fig. 3). Therefore,

$$M_1 = Z_1 r_1$$

From where:

$$Z_1 = \frac{M_1}{r_1}$$

But the force  $Z_1$ , acting on the large gear, generates torque:

$$M_2 = Z_1 r_2 \eta_z$$

Substituting the force  $Z_1$  with its value, we obtain:

$$M_2 = \frac{M_1 r_2}{r_1} \eta_z$$

In the above dependencies:

$M_1$  - torque created by the traction motor armature;

$M_2$  - torque acting on the large gear;

$Z_1$  - force applied at the point of contact of the two gears;

$Z_2$  - force applied in the centre of the rotor of the traction motor;

$r_1$  - radius of the small gear pressed on the shaft of the traction motor;

$r_2$  - radius of the large gear pressed on the axis of the motor wheel;

$l$  - length of the arm from the centre of the rotor of the traction engine to its jet support;

$R$  - radius of the wheel of the motor wheel on its rolling surface;

$A_1$  - point of contact of the teeth of the gears;

$A_2$  - centre of rotation of the rotor of the traction motor;

$A_3$  - centre of rotation of the motor wheel;

$A_4$  - point of suspension of the reaction;

$P$  - part of the weight of the locomotive, falling on the respective motor wheel (axle load);

$V$  - direction of movement of the crew.

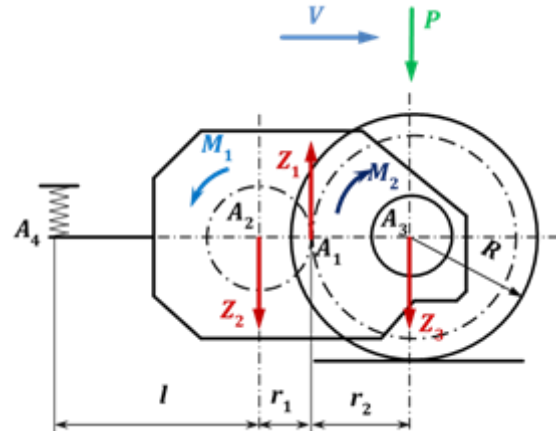


Figure 3

The proposed considerations apply to locomotives with second-class transmission mechanisms. With small additions to the above dependencies, they can also be adapted for locomotives with third-generation gears.

The traction characteristic of the locomotive is a graphical relationship between the tangential traction force  $F_k$  and the speed of the train  $V$  at different modes of operation of the locomotive power system and within the limits of reliability, stability, and safety.

To assess the impact of the torque created on the drive wheel in order to realize the traction force of the locomotive, it is necessary to take into account both the values of traction force and the speed at which they are realized, i.e., to analyze the traction characteristics of each type of locomotive in order to calculate the load on the motor axles at each operating mode.

### 3. WHEELSET LOAD

The forces to be taken into account in the design calculations of the axle shall be determined so as to represent a constant fatigue load applied over the entire service life of the element, which is equivalent to the full sum of the various loads occurring during operation (Fig. 3).

The forces acting on the locomotive axles are caused by:

- The mass of the locomotive:

- o  $Q_1$  and  $Q_2$  - vertical forces applied in the axle necks arising from the mass of the locomotive together with the mass of the bogies in which the respective axles are located, N;

- o  $Z_1$  and  $Z_2$  - vertical reactions occurring at the contact points between the wheels and the rails due to the mass of the locomotive, N;

- $Y_1$  and  $Y_2$  - horizontal reactions occurring at the contact points between the wheels and the rails due to the movement of the locomotive in a curve, N;

- $F_i$  - force generated by the unsprung masses pressed on the axis between the necks. This force exists only in

locomotives whose transmission mechanisms are of the second kind with axially suspended axle gearboxes. In this case these are locomotives 43, 44, 45 and locomotives 46, N;

$F'_{iz}$  - vertical component of the traction force realized by the locomotive. This force exists only in locomotives whose transmission mechanisms are of the second kind with axially suspended axle gearboxes. In this case these are locomotives 43, 44, 45 and locomotives 46, N;

The braking process - in the present study these forces will not be considered;

The traction forces that the locomotive realizes:

$X'_1$  and  $X'_2$  - horizontal reactions arising from the traction forces and applied at the points of bearing of the axle with the axles, N;

$Z'_1$  and  $Z'_2$  - vertical reactions arising from the traction forces and applied at the points of bearing of the axle with the axles, N;

$F'_{iz}$  - vertical component of the force  $F'_i$ , generated by the torque of the traction motor, N;

In addition to the listed forces, the main role in the load of the locomotive wheel is played by the torque generated by the current in the traction motor, which is the primary reason for creating the traction forces realized by the locomotive. In the case of second gears (locomotives 43, 44, 45 and 46) this is done with the help of the axle mounted on the axle (Figs. 4 and 5), and in the case of locomotives with third gear (locomotive 86) - by means of a hollow shaft mounted on the axle of the axle, which is an intermediate element between the large gear and one of the driving wheels of the axle, connected to each other by elastic metal-rubber elements (Fig. 6).

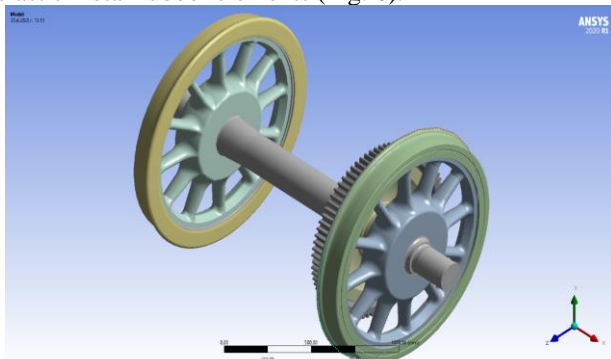


Figure 4

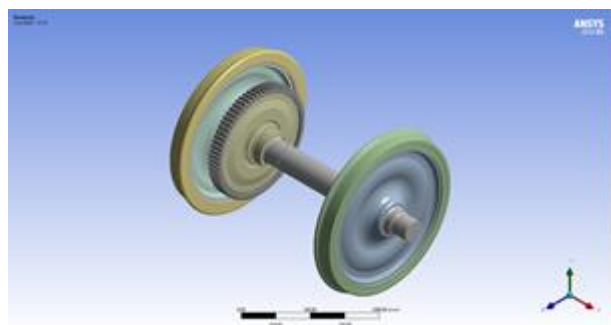


Figure 5

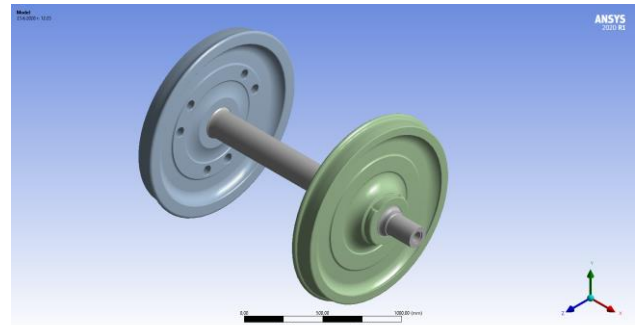


Figure 6

#### 4. MODELING AND STRENGTH ANALYSIS OF THE WHEELSETS

The strength analysis of the wheelsets was performed using the finite element method (FEM).

For the successful analysis of the considered nodes the accuracy of the chosen model is of special importance. It should be as close as possible to the actual design, while being simple enough and not complicating the calculations unnecessarily. The loads in the selected model must also correspond as much as possible to the actual ones in terms of size, location and direction, and the selected supports must sufficiently provide the necessary degrees of freedom of the considered elements.

The three-dimensional model of the axles of the various locomotives is made with the help of a computer program and is integrated into the software product ANSYS Workbench, with the help of which the strength-strain analysis is made.

In the analysis, the results for the following parameters were examined:

- Equivalent stress;
- Equivalent elastic strain;
- Total deformation;
- Safety factor under static load;
- Fatigue tool safety factor;
- Fatigue tool, Life;

#### 5. RESULTS OF THE CONDUCTED SIMULATIONS

The simulations were performed at a certain speed (respectively, rotation at a certain angular speed), varying from rest at the moment of departure (0 km / h) to the design speed at the maximum torque corresponding to the set speed according to the traction power of the locomotive in question.

##### 5.1. Wheelsets of locomotives 43-45

##### 5.1.1. Equivalent stress acting on the wheelset.

In fig. 7 shows the results obtained during the simulation for the equivalent stress acting in the axle of locomotives 43-45, and two graphs are formed: for the maximum effective stress obtained in the holker (the transition between the two subhead parts - the wheel and the gear - fig. 8) and for the average for the axle stress in the whole range of speeds. The maximum stress takes values from 108.43 MPa at start-up to 103.43 MPa at maximum speed and decreases by 4.83%. The tendency of the values of the maximum stress is towards continuous decrease. At the average value of the stress acting on the wheel, the maximum value initially assumes a value of

3.92 MPa, with an increase in speed there is a slight tendency to decrease to 3.78 MPa at 30 km / h. This trend intensifies and the minimum value reaches the average equivalent stress at 70 km / h - 3.35 MPa, after which the values begin to increase and the highest value of 5.195 MPa it reaches at a maximum speed - 130 km / h. The average equivalent stress between 0 and 30 km / h tends to decrease by 3.8% (between 3.92 and 3.78 MPa), and between its minimum value at 70 (3.35 MPa) and the maximum at 130 km / h (5.195 MPa) increased by 35.5%.



Figure 7

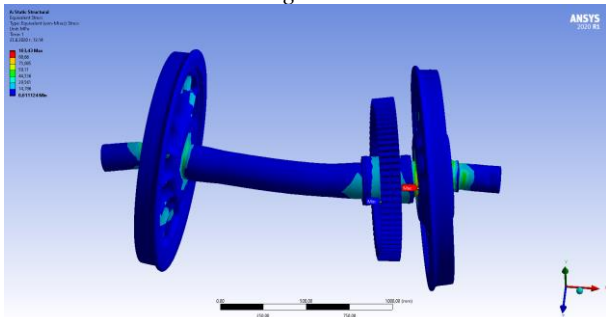


Figure 8

5.1.2. Equivalent elastic strain

The maximum value of the equivalent elastic strain of the wheel is observed in the holker and decreases with increasing speed, the decrease being 4.82% (Fig. 9).



Figure 9

5.1.3. Total deformation

The total deformation of the wheelset illustrates its deformation under load in operating conditions from rest

to movement at the maximum allowable speed for the locomotive (Fig. 10). The change in deformation along the wheel itself under different operating conditions increases from 0.206 mm when starting to 0.219 mm at a maximum speed in the range of 5.95%.

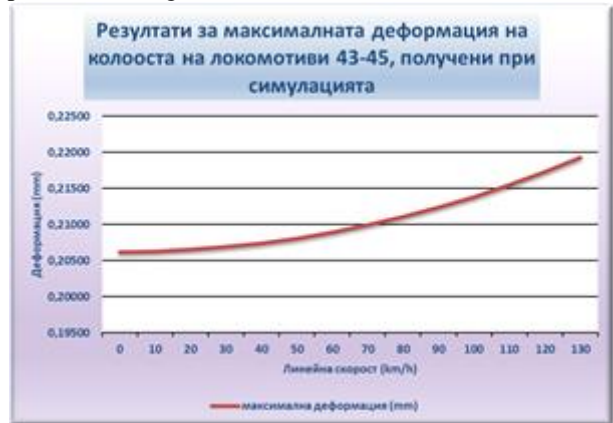


Figure 10

5.1.4. Safety factor under static load

The distribution of this indicator in the different operating modes is shown in fig. 11. The trend is towards continuous growth. Its values increase from 2.3 at the time of departure to 2.717 at maximum speed, i.e., with 4.6%.



Figure 11

5.1.5. Fatigue tool safety factor

The change in the fatigue safety factor is illustrated in fig. 12. Its value increases at different loads in the whole speed range by 4.61%, as the minimum is 0.795 when starting, and the maximum - when driving at maximum speed - 0.833.



Figure 12

5.1.6. Fatigue tool, Life



Figure 13

The change in the longevity indicator of the wheel is illustrated in fig. 13. This indicator varies in the range from 266890 cycles when starting to 350130 when driving at maximum speed, i.e., it increased by 23.77%. The maximum is at the weakest point of the wheel - the holker between the two subheadings - the wheel and the gear.

5.2. Wheelsets of locomotives 46

5.2.1. Equivalent stress acting on the wheelset.

In fig. 14 shows the results obtained during the simulation for the equivalent stress acting in the axle of locomotives 46, and two graphs are formed: for the maximum effective stress obtained in the holker (the transition between the head parts of the wheel and the gear - Fig. 15) and the average for the axle stress over the entire speed range. The maximum stress takes values from 239.22 MPa at start-up to 238.16 MPa at maximum speed and decreases by 0.45%. The tendency of the values of the maximum stress is towards continuous decrease. At the average value of the stress acting on the rim, the maximum value initially assumes a value of 4.00 MPa, where with increasing speed there is a slight tendency to decrease to 30 km / h. This trend is slightly intensifying, and the minimum value of the average equivalent stress is reached at 50 km / h - 3.76 MPa, after which the values begin to increase and the highest value of 7.29 MPa it reaches at a maximum speed - 130 km / h. The average equivalent stress between 0 and 30 km / h tends to decrease by 1.88%, and from 50 to 130 km / h increases by 48.43%.

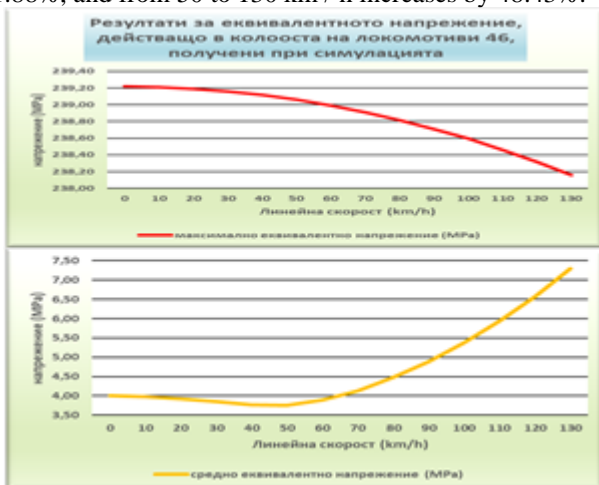


Figure 14

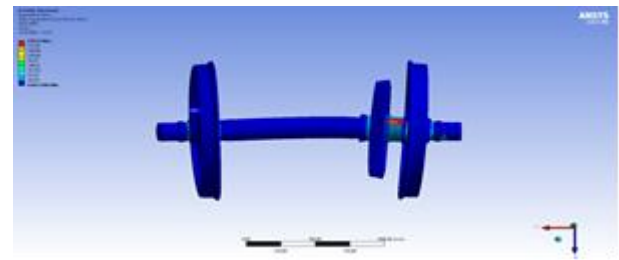


Figure 15

5.2.2. Equivalent elastic strain

The values of the equivalent elastic strain of the wheel are shown in fig. 16. The maximum value of the equivalent elastic elongation of the wheel is observed in the holker and decreases with increasing speed, the decrease is 0.48%.

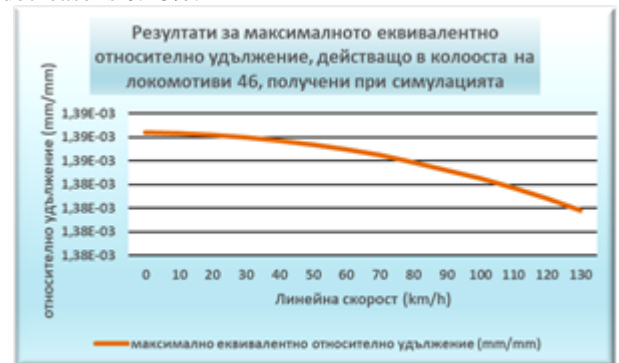


Figure 16

5.2.3. Total deformation

The total deformation of the wheelset under load in operating conditions from rest to movement at the maximum allowable speed for the locomotive (Fig. 17). The change in deformation along the wheel under different operating conditions increases from 0.135 mm when starting to 0.167 mm at a maximum speed in the range of 19.03%.

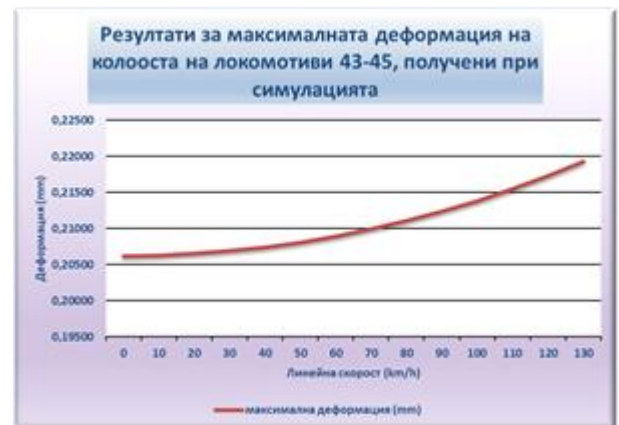


Figure 17

5.2.4. Safety factor under static load

The change of this indicator for the wheel axles of locomotives 46 is illustrated in fig. 18. The trend is towards continuous growth. Its values increase slightly from 1.045 at the time of departure to 1.049 at maximum speed, i.e., with 0.44%.



Figure 18

5.2.5. Fatigue tool safety factor

The change in the fatigue safety factor in the axles of locomotives 46 is illustrated in fig. 19. Its value increases at different loads in the whole speed range by 0.44%, as the minimum is 0.3603 when starting, and the maximum - when driving at maximum speed - 0.3619.



Figure 19

5.2.6. Fatigue tool, Life

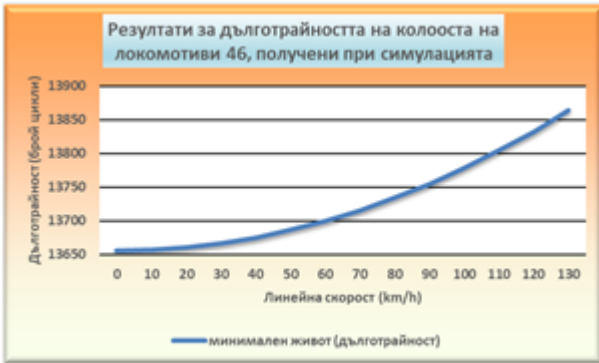


Figure 20

The change in the durability index for the axles of locomotives 46 is illustrated in fig. 20. This indicator varies in the range from 13655 cycles when starting to 13864 cycles when driving at maximum speed, ie. it increases by only 1.51%.

5.3. Wheelsets of locomotives 86

5.3.1. Equivalent stress acting on the wheelset.

In fig. 21 shows the results obtained during the simulation for the equivalent stress acting in the axle of locomotives 86, and two graphs are formed: for the maximum effective stress obtained in the transition between the pre-head and sub-head part of the axle at the wheel-clamping point and for the mean for the axle stress in the whole range of speeds. The maximum stress takes

values from 969,790 MPa at start-up to 969,470 MPa at maximum speed and decreases by 0.03%. The tendency of the values of the maximum stress is towards continuous decrease. At the average value of the stress acting on the wheel, the maximum value initially assumes a value of 11,883 MPa, with an increase in speed there is a slight tendency to decrease to 80 km/h. This is the minimum value of the average stress, after which the values begin to increase and the highest value of 14,293 MPa it reaches at a maximum speed - 170 km/h. The average equivalent stress between 0 and 80 km/h tends to decrease by 0.79%, and from 80 to 170 km/h increases by 17.03%.



Figure 21

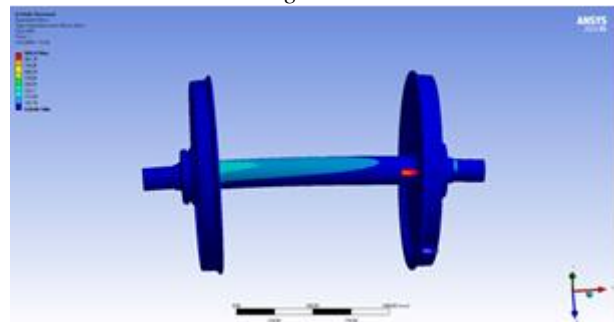


Figure 22

5.3.2. Equivalent elastic strain

The values of the equivalent elastic strain of the wheel are shown in fig. 23. The maximum value of the equivalent elastic elongation of the axle is observed in the transition between the pre-head and sub-head part of the axis and decreases with increasing speed of movement, as the decrease is by 0.48%.

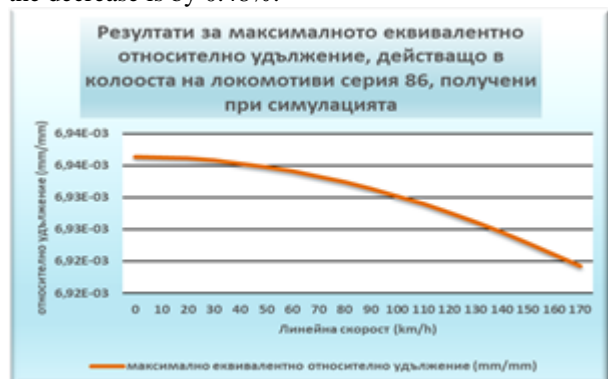


Figure 23

5.3.3. Total deformation

The total deformation of the rim illustrates its deformation under load in operating conditions from rest to movement at the maximum allowable speed for the locomotive (Fig. 24). The change in deformation along the wheel itself for the entire speed range remains constant.



Figure 24

5.3.4. Safety factor under static load

The change of this indicator for the wheel axles of locomotives 86 is illustrated in fig. 25. The trend is towards continuous growth. Its values increase slightly from 0.25779 at the time of departure to 0.25787 at maximum speed, i.e., with 0.03%.



Figure 25

5.3.5. Fatigue tool safety factor

The change in the fatigue safety factor in the locomotives of locomotives 86 is illustrated in fig. 26. Its value increases at different loads in the whole speed range by 0.03%, as the minimum is 0,08889 when starting, and the maximum - when driving at maximum speed - 0,08891.



Figure 26

5.3.6. Fatigue tool, Life

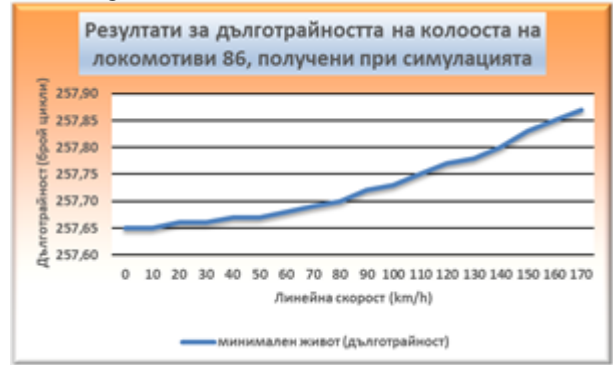


Figure 27

The change in the durability index for the axles of locomotives 46 is illustrated in fig. 27. This indicator varies in the range from 3881200 cycles when starting to 3877900 cycles when driving at maximum speed, i.e. it decreased by 0.08%. The minimum value is marked in the transition between the pre-head and sub-head parts of the axle on the side of the wheel, which is not connected to the driving hollow axle.

6. ANALYSIS OF THE OBTAINED RESULTS

From the obtained results it can be concluded that the strength characteristics of the axles of the considered locomotives in most cases show dependence on both the change of the torque and the change of the speed of the locomotive. This dependence is dominated by two factors to varying degrees: at low speeds torque dominates due to the nature of the traction characteristics of locomotives, then the main factor is the speed due to its increased values on the one hand and on the other due to reduced values of torque, again due to the nature of the traction characteristics of the locomotives.

Another characteristic feature of the change in the strength characteristics of the axles is that no characteristic bend is observed in their graphs when the design speed of the locomotives is exceeded, regardless of the type of their transmission mechanism. This, in turn, once again proves the influence of the speed of the locomotive, respectively the speed of rotation of the axle.

The maximum equivalent stress obtained in the heaviest loaded sections of the wheelsets of all three locomotives shows a tendency to decrease with increasing speed. The decrease is most noticeable for locomotives 43-45 - 4.83%, for locomotives 46 - 0.45% and most imperceptible for locomotives 86 - 0.03%. This shows that the places where the highest values of stresses are obtained remain potentially dangerous throughout the entire wheelset load range, respectively over the entire speed range of the locomotive. On the other hand, the almost constant high stress obtained in the most endangered sections of the axles gives sufficient reason for designers to think of new ways and methods to strengthen these potentially most dangerous in terms of strength, without applying the same methods to others. sections where the loads are not so high.

An interesting picture is presented by the graphs of change of the average equivalent stress acting on the axles, which show a change of its values in both directions: to increase and to decrease, depending on the change of torque and speed of movement. In the three cases there is

an initial retention of the values around the initial one obtained when starting the locomotive, followed by a decrease in the range from  $\frac{1}{2}$  to  $\frac{1}{3}$  of the maximum speed, after which the stress increases rapidly and reaches a maximum value between 1.2 and 1.8 times -higher than when starting, obtained at maximum speed of the locomotive. This shows that at the values of the average equivalent stress acting on the axles, the speed of movement has a greater influence than the torque applied to them.

The maximum equivalent relative strain of the axles shows a steady downward trend with increasing speed, which is a clear sign of the predominant influence of speed before torque on the condition of the axles. The largest difference in the values of this indicator is observed for locomotives 43-45 – 4.82%, while for the other two types of locomotives it is 1.48% (for locomotives 46) and 0, 23% (for locomotives 86). This can be explained both by the structural features of the axle and, in particular, by the choice of material for its manufacture, which for these locomotives is high-carbon steel with greater elasticity.

The total axle deformation in locomotives 43-45 and 46 also shows a tendency to increase the values with increasing speed, as for locomotives 43-45 it is 5.95%, and for locomotives 46 - 19.03%. The latter can be explained by the particularly high values of traction force, respectively torque, at the maximum speed of the locomotive (9.79 kNm for locomotives 46 at 6.18 kNm for locomotives 43-45 and 6.98 kNm for locomotives 86). Unlike the other two types of locomotives, in locomotives 86 there is a complete invariability of the results of the total deformation - it remains the same for the entire speed range of the locomotive. This proves the advantages of this type of transmission mechanism, which subjects the axle to the same operating conditions during operation, regardless of its operating modes.

Safety factors are parameters that show the reserve of axle strength, providing them with the ability to withstand loads greater than the nominal in different operating modes. The general trend observed is that both the static load safety factor and the fatigue safety factor have the lowest values when starting – a fact that proves once again that at the time of start and at low speed and high torques the reserve of axle strength is the smallest. As the speed increases, both coefficients increase their values (respectively 4.6% and 4.61% for locomotives 43-45, 0.44% for both coefficients for locomotives 46 and 0.03% for both coefficients for locomotives 86), as in locomotives 43-45 and 46 this happens smoothly for both coefficients, and in locomotives 86 the increase is stepped, as this is more pronounced for the coefficient of safety under static load and not so much at the safety factor against fatigue. The analysis of the results for the safety factors proves the connection between the values of the maximum equivalent voltage acting in the axis and those of the safety factors, as well as the fact that when designing a locomotive axle special attention should be paid to the sections in which receive the highest stresses because they determine the values of the safety factors. Another characteristic feature is that the nature of the change in the safety factors does not depend on the type of transmission mechanism – in the three types of locomotives considered there is a clear trend towards

increasing the safety factors when increasing the speed, i.e., on the values of these parameters the torque before the speed prevails, regardless of the way of transmitting the traction force to the axle itself.

Despite the same tendency of change of safety coefficients, it should be noted that for locomotives 43-45 the difference between the minimum and maximum values of their values is many times greater as a function of speed (4.6% and 4.61 %), while for the other two types of locomotives the differences are less than 1% - especially pronounced for locomotives 86. From the point of view of the loads received in the axles, it can be said that for locomotives 46 and 86 they are constructed more correctly, but from the results obtained in operation, it can be seen that the cases of fractures and cracks in the dangerous sections of the axles are the rarest in locomotives 43-45, from which the following conclusions can be drawn: the axle strength of locomotives 46 and 86 are designed to be in a hazardous area over the entire load range; locomotives 46 and 86 are operated with loads that do not correspond to the strength qualities of their axles; the axles of locomotives 43-45 are designed so that the stresses obtained in the dangerous sections are far from the maximum allowable for the respective material.

The parameter axle life shows the minimum resource that the locomotive axles have and is indicative based on the results obtained for the other studied parameters. To a large extent, its values overlap as a trend with the values for the safety factors and confirm the obtained results.

## CONCLUSIONS AND RECOMMENDATIONS

The conducted research and the made analyses of the obtained results give grounds to make the following conclusions:

- The load of the locomotive axles is not constant in the different modes of operation of the locomotives and is constantly changing in operation;
- The load on the locomotive axles during operation depends on both the torque applied to them by the traction motor and the instantaneous speed of the locomotive;
- Different axle strengths are affected to varying degrees by applied loads: some of them depend more on the applied torque, others are more affected by the instantaneous speed;
- The type of transmission used in the different locomotives has a significant effect on the values of individual indicators and must always be taken into account when designing locomotive axles.

Locomotive axles, as one of the main elements of the running gear and the propulsion of locomotives, on which the safety of traffic in railway transport directly depends, are constantly in the focus of researchers and designers in this field. In their design and construction must be taken into account not only all the parameters that affect their strength and durability, but also their change in all modes to which they will be subjected in operation.

## REFERENCES

- [1] Atmadzhova D., Mihaylov E., Iontchev E., „Study of the interaction "wheelset-track" of the attacking wheelset of tram bogie type T81 in exploitation in Sofia”, IX

International Scientific Conference Heavy Machinery HM 2017, Златибор, Сърбия, 2017 г. pp. E33-E40, 2017г.

[2] EN 13261:2009 UIC Code 515-3. Rolling stock. Bogies – Running gear. Axle design calculation method. 2009.

[3] Николов, В. Изследване на факторите, влияещи на дълготрайността на локомотивните колооси, С. ТУ, 2008.

[4] Николов, В., Влияние на спирачните усилия върху якостните качества на локомотивните оси, Научна конференция с международно участие по авиационна, автомобилна и железопътна техника и технологии, Созопол, 2009.

[5] Николов, В., Тяга на влаковете – ръководство за упражнения и курсово проектиране, С., ВТУ, 2012.

[6] Ружеков, Т., Ж. Димитров, Д. Стоянов, Г. Стайков, А. Стефанов. Конструкция, теория и проектиране на локомотиви. С., ТУ - София, 1987.



# Research and analysis of the wearing of the elements of axle roller bearings

Lyudmil Paskalev<sup>1\*</sup>

<sup>1</sup>Machinery and Construction Technologies in Transport/Transport Equipment, Todor Kableshev University of Transport, Sofia (Bulgaria)

*One of the main tasks facing the rolling stock of the Bulgarian State Railways is to increase operational reliability. Rolling bearings largely determine the performance of rolling stock. Currently at the entrance of the wagons for scheduled repairs, no detailed inspection of the axle roller bearings is carried out to establish their current technical condition. Only a visual inspection is performed to detect visible defects in their elements. The actual radial clearance of the axle roller bearings as an assembled unit is also not checked. The report shows the results of the measurements that were performed on the elements of the axle bearings and the analysis performed.*

**Keywords: Railway stock, wagons, axle roller bearings, reliability.**

## 1. INTRODUCTION

One of the main tasks in regards with the rolling stock of the Bulgarian State Railways is to increase operational reliability [1, 2, 3, 4]. The aim is to ensure train safety, improve performance, increase axle load and speed.

The current practice is after a certain period of time, the wagons to undergo routine repair, without taking into account their actual technical condition. This does not allow the further operation of the wagons prior to entry for routine repairs, although they may still have a resource. Increasing the cost-effectiveness of rolling stock operation can be achieved by using the method of replacing and repairing the units and the aggregates depending on their current technical condition. This method will allow the respective units and aggregates to remain in service, if their current technical condition allows it.

The performance of the rolling bearings largely determines the performance of rolling stock. It is well known their failures lead to emergencies. The technical condition of a unit depends on many factors that characterize the quality of its bearings, their normal lubrication, conditions and regime of operation [5, 6].

Currently, during the dispatch of the wagons for routine repairs, no detailed inspection of the axle roller bearings is carried out to determine their current technical condition [7]. Only a visual inspection is performed to detect visible malfunctions on their elements. Also, the actual radial looseness of the axle roller bearings as an assembled unit is not checked.

This report shows the results of the measurements that were made on the elements of the axle bearings and the respective analyzes.

## 2. MEASUREMENT OF THE ROLLERS.

The device, which is designed and manufactured to measure the rollers of the axle roller bearing, has been developed using the two-point scheme and the relative measurement method. This was performed by measuring

the element (roll) in a prism with an angle of  $90^{\circ}$  (there were prisms with angles of  $60^{\circ}$  and  $108^{\circ}$  respectively). Two indicator clocks with a measurement accuracy of  $0.001\text{mm}$  were used. for greater accuracy. The indicator clocks were positioned at an angle of  $90^{\circ}$  relative to each other in such a way that their axes were perpendicular to both of the base surfaces of the prism respectively. /Figure 1/

For the sake of greater reliability of the results, measurements were made of 450 rolls, disassembled from 30 roller bearings, installed as new in the rolling stock axle units in the same calendar year. Roller bearings were removed from rolling stock during routine repairs. The rollers were pre-washed and dried before starting the measurements.



Figure1

- The measurements of the rollers were made in three sections - one in the middle of the roller and the other two at 5mm. from the heads of the rollers;
- The measuring clocks were reset by a calibrated measuring roll in each of the measured sections. The deviations of the tested rollers were measured. As a final result, the maximum deviations were taken in two

\* Corresponding author: Lyudmil Paskalev, 158 Geo Milev Str. 1574 Sofia, Bulgaria, lyudmil\_paskalev@abv.bg

mutually perpendicular sections -  $d_{horizontal}$  and  $d_{vertical}$ . These measurements were made in all three sections of the rollers.

### 3. MEASUREMENT OF OUTER RINGS

The device, which is designed and manufactured to perform measurements on the outer rings of the axle roller bearings, has been developed using the three-point scheme and the relative measurement method. The measured element (outer ring) is based on two supports simulating basing in the prism with an angle of  $90^{\circ}$ . The contact between the outer ring edges and the supports is pointwise. For better measurement accuracy, a retainer is used at the base, which supports the measured outer ring at the rear end. The indicator clock is accurate to 0,001mm. It is placed on a stand located at the bottom of the stand. The stand on which the indicator clock is mounted has the ability to move parallel to the axis of the outer ring so that measurements can be made in several sections. /Figure 2/



Figure 2

For the sake of greater reliability, measurements were made on 100 outer rings dismantled by roller bearings, fitted as new to the rolling stock axle units in the same calendar year.

Roller bearings were removed from rolling stock during routine repairs. Before starting the measurements, the outer rings were washed and dried.

- The measurements of the outer rings were made in three sections - one in the middle of the outer ring and the other two at 5mm. from the faces of the outer ring edges;
- The measurement clocks were reset by a calibrated outer ring for measurements in each of the measured sections. The deviations of the checked outer rings were measured. These measurements were made in all three sections of the outer rings.

### 4. MEASUREMENT OF INNER RINGS

The device, which is designed and manufactured to measure the inner rings of the axle roller bearings, has been developed using the two-point scheme and the relative measurement method. The measurement was carried out by measuring the element (inner ring) in a prism with angle  $90^{\circ}$  (there were prisms with angles of  $60^{\circ}$  and  $108^{\circ}$  respectively) /Figure 3/. Two indicator clocks with a measurement accuracy of 0.001mm were used. for greater accuracy.



Figure 3

## ROLLERS

### Dispersion of dimensions

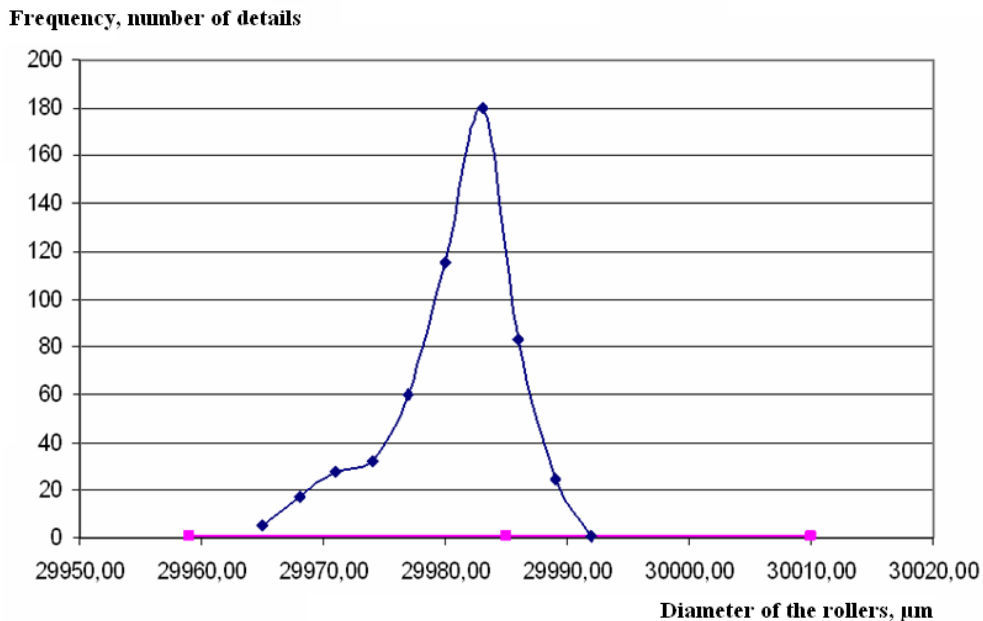


Figure 4 a)

### OUTER RINGS Dispersion of dimensions

**Frequency, number of details**

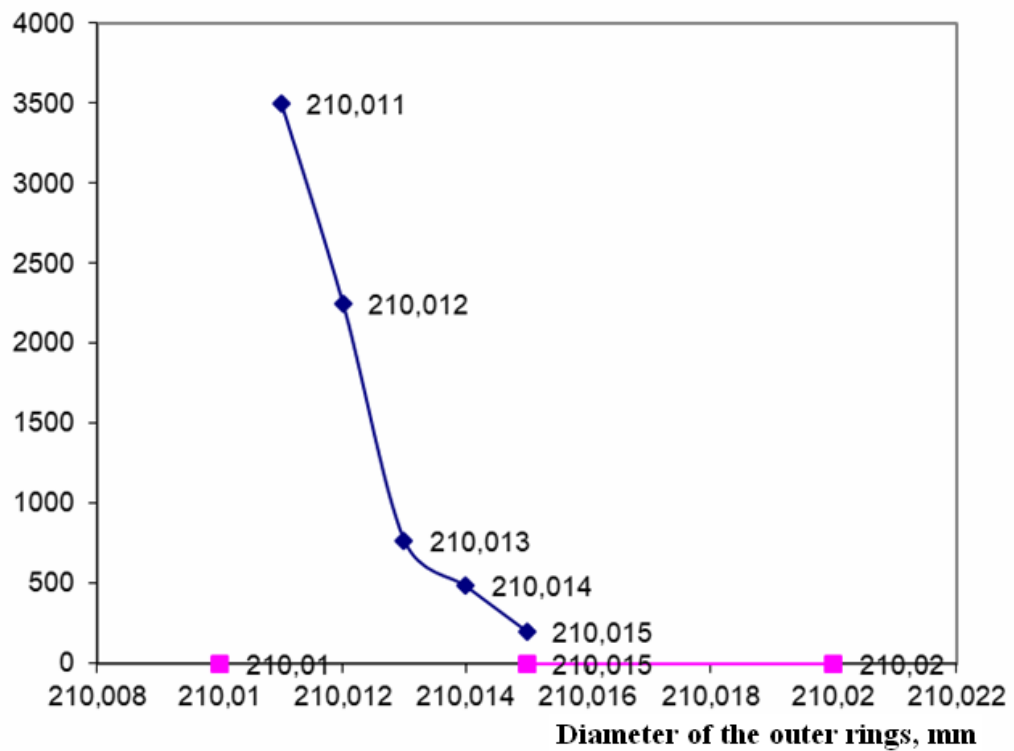


Figure 4 b)

### INNER RINGS Dispersion of dimensions

**Frequency, number of details**

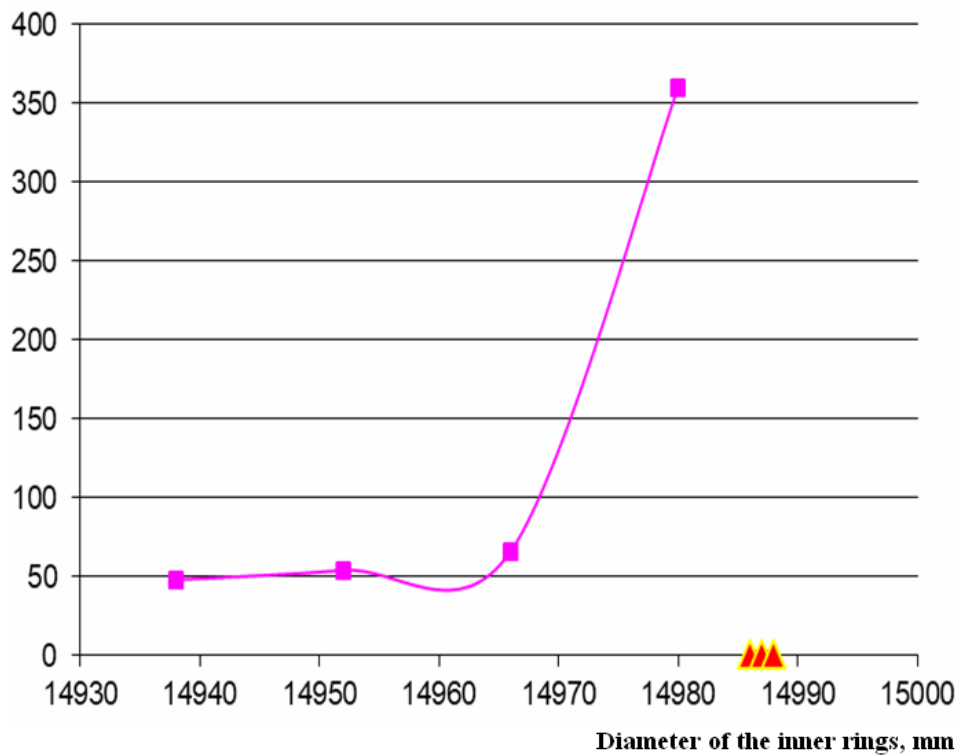


Figure 4 c)

The indicator clocks were positioned at an angle of  $90^{\circ}$  relative to each other such that their axes were placed perpendicular to each other and the base surfaces of the prism respectively.

For the sake of greater reliability, measurements were made of 99 inner rings dismantled by roller bearings, fitted as new to the rolling stock axle units in the same calendar year. Roller bearings were removed from rolling stock during routine repairs. Before starting the measurements, the inner rings were pre-washed and dried.

- The measurements of the inner rings were made in three sections - one in the middle of the inner ring and the other two at 5mm. from the front of the inner ring;

- The measurement clocks were reset by a calibrated inner ring for measurements in each of the measured sections. The deviations of the checked inner rings were measured. The maximum deviations in two mutually perpendicular sections  $d_{\text{horizontal}}$  and  $d_{\text{vertical}}$  were considered as final result. These measurements were made in all three sections of the inner rings.

After processing the obtained values from the measurements, the results were summarized, indicating the relationship between the number of measurements and the specific values in microns. /Figure. 4 a, b,c/

Based on the results we made the

### CONCLUSION

- For roller bearing roller bearings:
  - about 80% of the measured roller diameters of the axle roller bearings were grouped around the average tolerance field value -  $\phi 30^{-0.015}$  mm.
  - about 20% of the measured roller diameters of the axle roller bearings were in the area of the average tolerance field value of  $\phi 30^{-0.015}$  mm. and a lower boundary of the tolerance field of  $\phi 30^{-0.041}$  mm.
  - about 9% of the measured roller diameters of the axle roller bearings were located in the area relatively close to the lower boundary of the tolerance field -  $\phi 30^{-0.041}$  mm.
- For the inner rings of the axle roller bearings:

- All measured diameters of the inner rings of the axle roller bearings were outside the lower limit of the tolerance field -  $\phi 150^{-0.140}$  mm.
- about 61% of the measured diameters of the inner rings of the axle roller bearings were in the area of 0.010 mm. below the lower limit of the tolerance field -  $\phi 150^{-0.140}$  mm.
- For the outer rings of the axle roller bearings:
  - all the measured diameters of the outer rings of the axle roller bearings were in the area between the mean value of the tolerance field  $\phi 210^{+0.015}$  mm. and the lower boundary of the tolerance field  $\phi 210^{+0.010}$  mm.
  - about 48% of the measured diameters of the outer rings of the axle roller bearings were in the area close to the lower boundary of the tolerance field  $\phi 210^{+0.010}$  mm.

### REFERENCES

- [1] Petrovic D., Rakanovic R., Zeleznicka vozila Praktikum., Kraljevo, 2006.
- [2] Petrovic D., Aleksandrov V., Zeleznicka vozila. Osnove, MF Kraljevo, 2013, ISBN 978-86-82631-66-8 p.223.
- [3] Мијанац Рајко, Железничка кола, Београд, ISBN 86-7307-102-X, 2000.
- [4] Stoilov V., Slavchev S., Vagoni, Ed. TU-Sofia, 2014, ISBN 978-619-167-135-9, Sofia, 2014, p.222.
- [5] Kolarov IG Dimchev. Machine components. Textbook. VTU, "T. Kableskov", 2018.
- [6] Ivanov A.I, Structural Dynamics. publ. "Avangard Prima", ISBN 978-954-323-684-8, Sofia, 2010, pp. 324.
- [7] Ristic Marko, Uticaj kontaminirajućih čestica na smanjenje radnog veka kotrljajnih ležaja pregled istraživanja, University of Niš, Faculty of Mechanical Engineering, Business Jul. 01, 2011 <https://www.slideshare.net/MarkoRistic83/uticaj-kontaminirajuih-estica-na-smanjenje-radnog-veka-kotrljajnih-leaja-pregled-istraivanja>.

# Regarding requirements for the design and installation of elements for passive safety of passenger trains operated by the Bulgarian State Railways

Venelin Pavlov<sup>1\*</sup>

<sup>1</sup>Machinery and Construction Technologies in Transport/Transport Equipment, Todor Kableshkov University of Transport, Sofia (Bulgaria)

When designing a new generation passenger train, it is necessary to provide for the existence of a passive safety system (PSS) integrated in its construction, which should ensure the protection of passengers and service personnel in the event of the most probable emergency collisions. The article provides an excerpt from statistics of accidents and incidents related to railway transport for the Bulgarian State Railways, which show the need to improve safety. The aim of the study is to develop energy absorption devices included in the PSS of high-speed passenger trains of a new generation. The article discusses the requirements for the harmonization of European safety standards and regulations in force in Russia and the United States. The main concepts of passive safety equipment and possibilities for application in the construction of passenger trains in operation of the Bulgarian State Railways (Holding BDZ EAD - BDZ - Passenger Transport EOOD) are indicated.

**Keywords:** Railway stock, passenger trains, passive safety.

## 1. INTRODUCTION

In 1991 the UIC made appropriate adjustments in Leaflet 526 to comply with the new trends in railway transport and ensure traffic safety [1, 2, 3]. The most important change is aimed at increasing the energy absorption of draw gear equipment. Its minimum value is recommended to be 30 kJ, which is a double increase of current standards.

The compressive forces are absorbed by buffers, which also maintain a certain distance between wagons [4]. The requirements for the structure of buffers are reflected in UIC Leaflets 526-1; 526-2 and 526-3.

The development of transport industry is always associated with accidents. The causes of accidents are many, including damage or breakage of parts, physical and moral aging of equipment, human factor, track poor condition, unfavourable weather conditions.

If we take into account the statistics of accidents, then it will be possible to trace a trend – the higher the speed, the more accidents happen in different modes of transport. Rail transport is no exception.

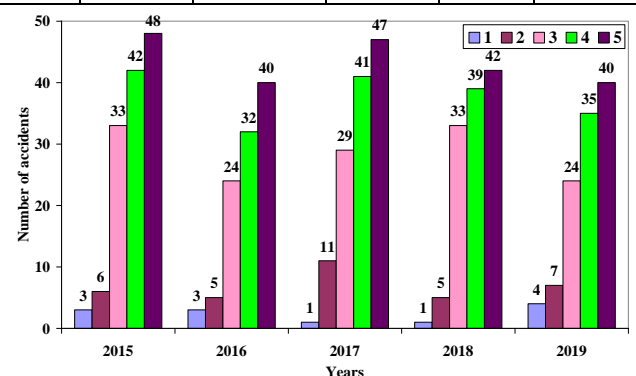
Since the management teams of railway companies have set a goal to increase the volume of high-speed transport by 20% by 2030, it is necessary to urgently improve the level of freight and passenger rail transport safety, especially of high-speed trains. Table 1 and Fig. 1 provide an excerpt of statistics of accidents and incidents [5] related to railway transport carried out by BDZ EOOD that shows the need to increase its safety.

The largest value of relative share of:

- collisions between trains in relation to the total number of accidents is 10% in 2019;
- collisions with a car at level crossings is 23.4% in 2017;
- all collision-related accidents are 92.9% in 2018.

Table 1 Collision-related accidents.

| Year | Number of collisions between trains | Number of collisions with cars at level crossings | Number of collisions with people | Total number of collisions | Total number of accidents |
|------|-------------------------------------|---|----------------------------------|----------------------------|---------------------------|
| 2015 | 3                                   | 6   | 33                               | 42                         | 48                        |
| 2016 | 3                                   | 5   | 24                               | 32                         | 40                        |
| 2017 | 1                                   | 11  | 29                               | 41                         | 47                        |
| 2018 | 1                                   | 5   | 33                               | 39                         | 42                        |
| 2019 | 4                                   | 7   | 24                               | 35                         | 40                        |



1 - Collision of a train with railway vehicle; 2 - Collisions with a car at railway crossings; 3 - Accident with people; 4 - Total collisions; 5 - Total accidents.

Figure 1- Diagram of railway stock accidents related to collisions.

In order to reduce railway accidents, it is necessary to improve the two main safety systems:

- active safety system;
- passive safety system.

The main focus should be put on improving the passive safety system, which consists of developing a set

of measures and technical solutions aimed at reducing the level of injuries caused to passengers and minimizing the damage to rail stock in cases where it is not possible to avoid collisions with obstacles.

Since the beginning of the 21<sup>st</sup> century, global manufacturers of railway vehicles have begun to use passive safety elements in their projects, including emergency crash systems. In principle, they are similar to those used in cars but are adapted to the rail track conditions.

Crash emergency systems are designed to reduce the risk of severe accidents, injuries of passengers and train staff as well as to protect the load-bearing parts of wagon structure in case of train collision with an obstacle, particularly with another train. In this case the absorption of kinetic energy is due to irreversible controlled deformation of crash elements.

Modern passive safety systems are based on a number of international research programs. As a result passive safety requirements have been proposed for all types of rolling stock, including urban rail vehicles. The requirements for emergency systems have been included in European standard EN 15227 [6].

It is increasingly necessary to introduce emergency crash elements in the structure of rail vehicle to provide protection against serious accidents, such as the accident in Hitrino in 2016 [5]. As a result of train derailment, the tank of the tenth tank wagon was drilled, which caused leakage of transported cargo (propylene) that subsequently ignited. The explosion followed by fire killed 7 and seriously injured 29 residents of the village of Hitrino. The blast affected an area of about 535,000 m<sup>2</sup>, partially destroying 50 residential and public buildings, the railway infrastructure and rolling stock.

As a result of the investigation carried out, the Special Unit for Investigation of Accidents and Incidents in Railway Transport with Ministry of Transport, Information Technology and Communications prepared "Final Report on Technical Investigation of the Railway Accident" giving the following recommendation to prevent accidents cause by the same reasons: Tank cars transporting liquefied hydrocarbons have to be equipped with draw gear with crash elements according to the requirements of BDS EN 15227: 2008 + A1: 2010 and shall possess a safety certificate.

## 2. OVERVIEW OF THE REGULATORY REQUIREMENTS FOR RAILWAY STOCK EMERGENCY CRASH SYSTEMS

In 1997 SAFETRAN (Safe Train), a research project for railway safety, was launched in Europe [7], involving more than 10 European railway companies and rolling stock manufacturers such as Deutsche Balm, SNCF, Alstom, Siemens, Bombardier, etc. [8]. A great number of studies on vehicle passive safety were conducted under the project including human behaviour modelling in the event of train collision, nonlinear dynamic analysis of rail vehicle structure through the finite element method and field tests on rail vehicle collision.

The research results have contributed to the development of a regulatory document for ensuring passive safety of railways: EN 15227:2020 "Railway applications. Crashworthiness requirements for rail

vehicles". In accordance with the principles of passive safety included in EN 15227, the emergency crash system have to limit the acceleration of rail vehicles, ensure the integrity of the body structure in the passenger area and reduce the derailment risk of rail vehicles.

It is not possible to provide absolute protection to people in all possible cases of collisions, therefore the regulatory documents introduce the concept of an emergency collision scenario as a specific design case where the fulfilment of emergency crash system requirements are monitored. The collision scenarios were developed using the data taken from investigations of 500 accidents in 12 railway companies in Europe from 1991 to 1995. The data analysis made it possible to determine the most common cases of collisions of railway stock according to "Railway applications. Crashworthiness requirements for rail vehicles". Thus, when checking the requirements to crash system of a train running in regional European railway networks, it is necessary to use the following collision scenarios: head-on collision with identical rolling stock, collision with a freight wagon and collision with a freight vehicle at a level crossing.

According to the requirements of standard EN 15227, the crash system efficiency is evaluated by the following criteria:

- by the values of rolling stock longitudinal accelerations;
- by the values of the residual deformation of rolling stock body;
- by the condition wheel-rail contact maintenance (for assessment of derailment risk).

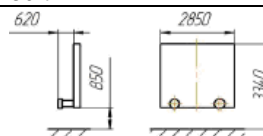
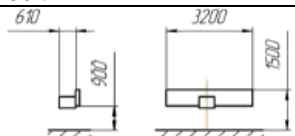
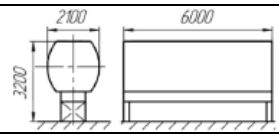
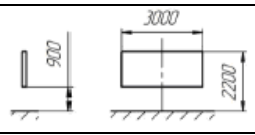
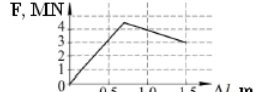
Comparing the basic provisions of EN 15227 with GOST 32410-2013 "Emergency systems for emergency rolling stock for passenger transport. Technical requirements and control methods" [9], it can be noticed that the Russian standard is not equivalent to the European one because of the differences in railway stock structure and in the statistics of collision accidents in the CIS countries and the European Union. The performance of the crash system in this standard is checked by the values of rolling stock longitudinal accelerations and the values of the residual deformations of car bodies, without checking the maintenance condition of wheel-rail contact. Similar to the European standard, the control on fulfilment of emergency crash system requirements is carried out according to the design scenarios: emergency collision with a car at a level crossing and collision with a freight wagon.

Analyzing the existing differences in the conditions of collision scenarios, the following can be distinguished:

- GOST 32410-2013 does not have a scenario of collision with identical rolling stock;
- in the collision scenario established by EN15227 the freight wagon has buffers with a given energy absorption while according to GOST 32410 the freight wagon shall not be equipped with buffers as they do not exist in the wagons operated in Russia;
- in European standard EN15227 the scenario of collision with a car provides irreversible obstacle deformation while according to GOST 32410-2013 the obstacle is given as an absolutely rigid body.

Table 2 presents a comparison of crash scenarios.

Table 2 – Comparison of crash scenarios

| Scenarios   | Scenario parameters                         | EN 15227-2008 [6]   | GOST 32410-2013 [9]   |
|---|---|---|---|
| Crash scenario with a freight wagon               | Crash speed                                 | 36 km/h   | 36 km/h   |
|   | Obstacle mass                               | 80 t  | 80 t  |
|   | Obstacle geometry                           |  |  |
|   | Obstacle stiffness                          | Absolutely solid body*  | Absolutely solid body   |
|   | Acceleration limit per unit of rail vehicle | 5 g **  | 50 m/s <sup>2</sup>   |
| Crash scenario with a vehicle at a level crossing | Crash speed                                 | 110 km/h  | 72 km/h (110 km/h)***   |
|   | Obstacle mass                               | 15 t  | 10 t  |
|   | Obstacle geometry                           |  |  |
|   | Obstacle stiffness                          |  | Absolutely solid body   |
|   | Acceleration limit per unit of rail vehicle | 7,5 g   | 50 m/s <sup>2</sup>   |

\* - in the freight car collision scenario. EN 15227 defines the power features of buffer devices whose total energy capacity is 62 kJ;

\*\* - g – ground acceleration;

\*\*\* - a collision speed of 110 km/h is set for a vehicle with a design speed over 160 km/h.

The collision scenario with a car in GOST 32410-2013 is of particular interest because the obstacle is assumed as an absolutely rigid body.



a) - damage to the electric train; b) - damage to the car.

Figure 2 - Consequences of the emergency collision of "Swallow" electric train

Under real conditions, the car has a relatively low strength, therefore in a collision it will suffer significant damage and thus will affect the processes of accident. This is confirmed by the collision of "Swallow" electric train at a speed of 90 km/h with an MAZ car [10]. The consequences of this collision are shown in Fig. 2.

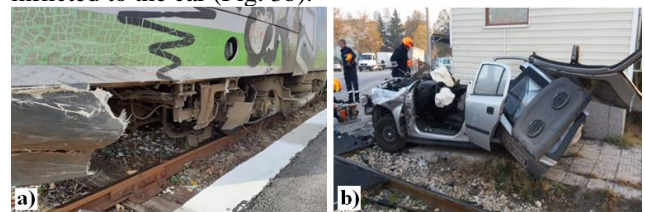
This collision corresponds to the conditions of a collision scenario with a truck: the collision speed and the mass of obstacle were identical to the design conditions: the check of electric train damage revealed that the emergency energy absorption device of the emergency system had not worked because there were no residual deformations, while at the same time the first bogie derailed.

Thus, in a real emergency situation, the car absorbed part of the energy of collision due to its own destruction. At the same time to model a car in the form of an absolutely rigid body does not allow to take into account this effect that can lead to a strong discrepancy between the calculation results and the actual consequences of collision.

On November 12, 2019, 19205 passenger train (PT) consisting of an electric multiple unit (EMU) series 31-

005/006 with four wagons was moving in direction Plovdiv - Asenovgrad - Plovdiv. At 06:42 the traffic manager on duty at Krumovo station ordered the departure of 19205 passenger train (PT) with a telephone message to the guards of the level crossings at kilometer 3<sup>+784</sup> and at kilometer 8<sup>+830</sup>. After the train left Krumovo station at 06:44, the on-duty traffic manager verbally informed the level-crossing guards about the train departure. Although the guard of level-crossing at km 8<sup>+830</sup> had recorded the telephone message, he did not activate the barrier mechanisms before passing of 9205 passenger train. Approaching the level crossing, the engine driver gave a "Warning" signal with the whistle of the EMU having seen that the barriers are raised and the crossing guard is standing next to the barrier control mechanism. At that moment, a vehicle – an Opel (ASTRA) car, approached the level crossing to the left in direction of the train running and entered the danger zone [11]. That resulted in a collision, the car was turned and thrown to the left of railway track and the train continued to run without stopping.

One of the passengers travelling next to the driver died. The engine driver was not injured. The left side of the EMU was damaged (Fig. 3a) and severe damage was inflicted to the car (Fig. 3b).



a) – damage caused to the EMU; b) – damage caused to the car.

Figure 3 - Consequences of the emergency collision of an EMU with a car at a level crossing [11].

It is not only in the European countries, but also in the United States experts have been actively involved in the passive safety issues in railway transport for more than 20 years, so a significant number of different designs of energy-absorbing devices have been already available. That is why regulatory documents have appeared and based on them modern public standards have been developed. Both Western European and US regulatory agencies are making significant efforts to rapidly update rail stock safety requirements. The modern rail stock operating on the European railways shall meet the following standards EN 12663: 2000 [12] and EN 15227: 2008; in the United States railways shall keep the Code of Federal Regulation 49 CFR [13].

In terms of harmonization, European standard EN 15227 is closer to the safety standards, which are in force in Russia. The development of TT SPB and GOST 32410-2013 has taken into account the peculiarities of rail stock (structure, design, production, testing, operation) in Russia, as well as statistics of rail stock emergency collisions with obstacles that differ from the European ones. Tables 3 and 4 show the main differences between the European, American and Russian standards [14].

Table 3 – Maximum values of accelerations in strength calculations of wagon equipment and interior

| Standard        | Acceleration values by axes |                |                               |                    |
|-----------------|-----------------------------|----------------|-------------------------------|--------------------|
|                 | X (longitudinally)          | Y (vertically) | Z (transversally) to the body |                    |
|                 |                             |                | In the front part             | In the middle part |
| EN 12663, 15227 | ± 5 g                       | ± 1 g          | ± 3 g                         | ± 1,5 g            |
| 49CFR           | ± 8 g                       | ± 4 g          | ± 4 g                         |                    |
| TT SPB          | ± 7,5 g                     | ± 1 g          | ± 3 g                         | ± 1,5 g            |
| Gost 32410-2013 | ± 5 g                       | *              | *                             |                    |

\* It is not regulated

Table 4 – Main crash scenarios of wagons and locomotives

| Speed V, km/h   | Crash scenarios |      |       |      |     |
|-----------------|-----------------|------|-------|------|-----|
|                 | No1             | No 2 | No3   | No4  | No5 |
| Standard        |                 |      |       |      |     |
| EN 12663, 15227 | 36              | 36   | -     | 110  | -   |
| TT SPB          | -               | -    | 18 36 | - 72 | 110 |
| Gost 32410-2013 | -               | -    | 36 -  | 72   | 110 |

No 1 - collision with an identical train; No 2 - with a freight wagon of 80 t equipped with buffers; No 3 - with freight wagon with mass 80 t without buffers; No 4 - with a freight vehicle (truck) with a mass of 15 t; No 5 - with a freight vehicle (truck) with a mass of 10 t.

The mentioned distinctive features of main regulatory documents setting the requirements for passive protective devices show that the existing collision scenarios do not fully take into account all possible cases of emergency collisions.

Based on the statistics of railway accidents and the operating conditions of rail stock, it is necessary to significantly expand the list of possible collision scenarios.

In order to fully cover all possible collision scenarios, based on statistics, the main types of obstacles must be taken as follows:

- obstacle No 1 - a large animal with a mass of 1 t;
- obstacle No 2 - a vehicle with mass of 2 t;
- obstacle No 3 - a truck with mass of 15 t;
- obstacle No 4 - a heavy truck of 30 t;
- obstacle No 5 - a freight wagon of 80 t without buffers;
- obstacle No 6 - a similar fixed train with different mass.

The study of emergency collisions with the indicated types of obstacles will allow to determine the area of effective operation of energy absorption devices (EOD) and to design energy-absorbing structures that meet the requirements of regulations.

### 3. COLLISION SCENARIOS

Collision scenarios have been developed taking into account statistical analyzes of railway accidents in Europe and the CIS [14].

Collision scenarios (Fig. 4 ÷ 7) are characterized by a set of conditions for emergency collision of passenger cars/trains with an obstacle (values of masses, initial speeds and other parameters of the objects of collision).

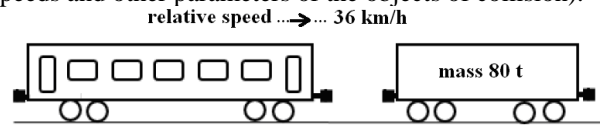
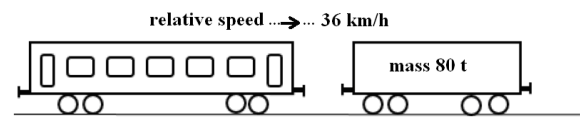
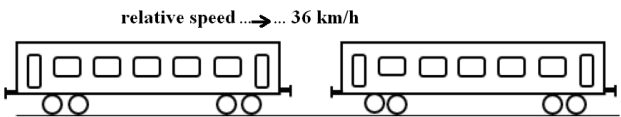


Fig. 4. Collision scenario (4a, 4b) of a passenger car equipped with side buffers for 1435 mm gauge



On a track gauge of 1520 mm – a collision at a speed of 36 km h with a freight wagon of 80 t.

Fig. 5. Collision scenario of a passenger carriage equipped with auto-coupler for 1520 mm track gauge

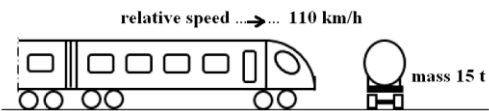
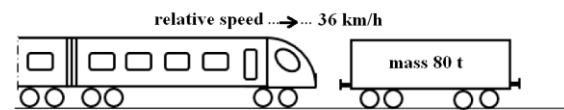


Fig. 6. Collision scenario (1a, 1b, 2) of a multiple unit equipped with auto-coupler for 1435 mm track gauge

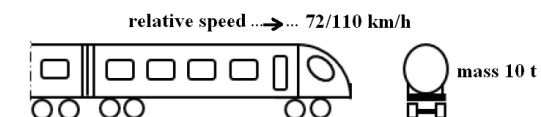
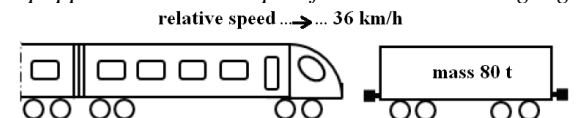


Fig. 7. Collision scenario (1b, 2) of a multiple rail unit equipped with auto coupling for 1520 mm track gauge

To determine the power and energy features of the crash system devices, the following collision scenarios have been assumed:

- scenario 1a simulates an emergency collision of with passenger cars/trains of one and the same type (only for 1435 mm gauge track);
- scenario 1b simulates an emergency collision with a freight wagon of 80 t;
- scenario 2 simulates an emergency collision at a level crossing with a vehicle of 15 t for a track gauge of 1435 mm and of 10 t for a track gauge of 1520 mm.

The following collision scenarios are foreseen for passenger carriages with locomotive traction:

On a track gauge of 1435 mm:

- collision at a speed of 36 km/h with the same type of passenger cars;
- a collision at a speed of 36 km/h with a freight wagon of 80 t equipped with a side buffer set.

The following collision scenarios are provided multiple units (connected trains).

For track gauge of 1435 mm:

- collision at a speed of 36 km/h with a train of the same type;
- collision at a speed of 36 km/h with a freight wagon of 80 t equipped with a side buffer set;
- collision with a speed of 110 km/h at a level crossing with a truck weighing 15 t.

For track gauge of 1520 mm:

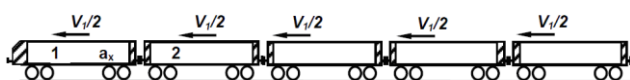
- collision at a speed of 36 km/h with a freight wagon of 80 t;
- a collision at a speed of 72 km/h at a level crossing with a vehicle weighing 10 t at a design train speed not exceeding 160 km/h;
- collision at a speed of 110 km/h at a level crossing with a vehicle weighing 10 t at a design train speed exceeding 160 km/h.

#### 4. TESTS OF PASSENGER CARRIAGES UNDER COLLISION SCENARIOS

The passenger carriages participate in collision scenarios in a reference train, which includes a locomotive and four passenger carriages of one and the same structure.

A four-axle locomotive with an axle load of 19 t, having a rigid (non-deformable) body, equipped with an auto-coupler with a locking contour in compliance with GOST 21447 [15] and absorbers of T2 class with energy absorption from 100 kJ at a full stroke of 120 mm in compliance with GOST 32913 [16], equipped with crash elements in the front locomotive parts.

The crash elements of this locomotive must provide an average value of its longitudinal acceleration equal to the absolute value of 50 m/s<sup>2</sup> in emergency collision with an obstacle of the locomotive without wagons in a collision scenario 1.



▣ - crash elements in locomotives and wagons fronts.

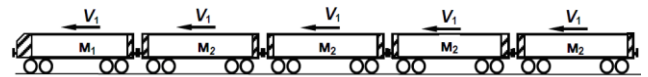
Fig.8. Reference train composition for testing passenger carriages.

where: 1 - front unit of the train (locomotive), 2 – a passenger carriages under evaluation,  $a_x$  is the amount of delay in the longitudinal direction of the leading train unit;

$a_x = 5,0$  g according to point 7.1 of GOST 32410-2013 or point 6.4 of EN 15227,  $V_{i/2}$  - half of the collision speed according to scenario 1.

While testing a multiple unit, the composition shown in Fig. 9 is used. In the case of operation of fewer wagons, tests with the same minimum train composition are admitted.

The minimum number of wagons in the train is 1 wagon (e.g. a rail bus), but the abovementioned does not exclude such a case.



▣ - crash elements at the front of the wagons.

Fig. 9. Testing of multiple unit rail stock.

where:  $M_1$  is the mass of a multiple unit wagon;  $M_2$  is the average mass of an intermediate wagon.

In order to clarify the state of force factors in the collision of two vehicles and to be able to specify the efficiency of the energy-absorbing elements, it is necessary to analyze relative movement of the two vehicles, which subsequently interact with their draw gear equipment.

Using the Lagrange equation and taking into account the kinetic energy and the total system energy absorption, an equation is obtained, which determines the maximum value of impact force from collision between two vehicles [17]:

$$F = \sqrt{2((2i)^{-1} \cdot M \cdot V_0^2 - E_0)} \cdot k \quad (1)$$

where:  $F$  - force acting on the buffers;

$M$  - reduced mass;  $M = (m_1 \cdot m_2) / (m_1 + m_2)$ , where  $m_1, m_2$  - masses of the first and second vehicles;  $E$  - energy absorption of the buffers;  $k$  - stiffness of the wagon structure;  $i$  - coefficient obtained from experimental data and reflecting the inertial characteristic of the system under the conditions of impact, taking into account the influence of spring suspension, the shocking wagons and track superstructure of the railway, the energy absorption of load, etc.

Analyzing the formula given above and taking into account the high value of wagon structure stiffness; we can see the crucial importance of energy absorption of buffers to prevent impact forces of inadmissible values.

#### 5. OVERVIEW OF STRUCTURAL FEATURES OF "CRASH" ENERGY ABSORPTION DEVICES

Thin-walled metal tubes are widely used to manufacture energy absorption devices. The absorption features of tubes are influenced by the type of metal, geometric parameters and given deformation mode. The following deformation modes can be distinguished for thin-walled metal tubes:

- axial deformation. The deformation mode is characterized with load directed along the longitudinal axis of the tube that leads to a local plastic loss of stability of the tube walls with formation of annular folds;
- transverse deformation. The pressure load in this mode of deformation is perpendicularly directed to the tube longitudinal axis;
- deformation with inversion of walls. In this mode,

energy is absorbed when the tube is pressed into a punch with a special shape, which leads to radial plastic deformation and inversion of tube walls;

- deformation with expansion of walls. The deformation mode is carried out by pressing the “sacrifice” tube into a harder tube with a conical contact surface, while the energy is being absorbed due to radial plastic deformation and due to friction on the walls of tubes;
- deformation with tearing the walls of tubes. The deformation mode is accompanied by the formation of multiple longitudinal cracks along the deformed tube and the accompanying division of its wall into strips.

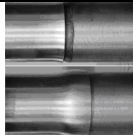
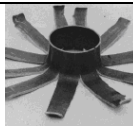
Based on the analysis of references [18, 19], Table 5 shows the energy absorption features of steel tubes depending on deformation modes.

Table 5 – Energy absorption features for steel tubes depending on deformation modes

| Features of energy absorption | Axial deformation | Transverse deformation | Inversion of walls | Widening walls | Tearing walls |
|-------------------------------|-------------------|------------------------|--------------------|----------------|---------------|
| CF                            | 0,3               | 0,9                    | 0,8                | 0,8            | 0,6           |
| SE, kJ/kg                     | 8 ÷ 30            | 2 ÷ 8                  | 6 ÷ 12             | 9 ÷ 24         | 6 ÷ 20        |

Table 6 shows a comparison of deformation modes according to load patterns, deformation diagrams and forms of plastic deformation.

Table 6 – Tube deformation modes

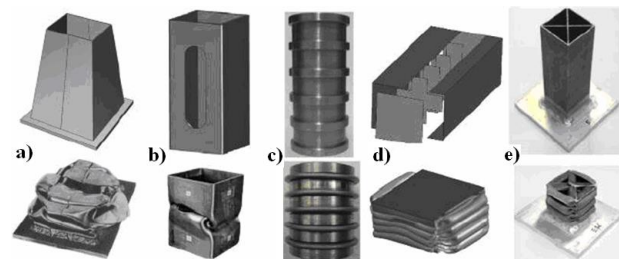
| Mode                   | Deformation form  | Comment   |
|------------------------|---|---|
| Axial deformation      |  | <b>Advantages:</b> high energy absorption.<br><b>Disadvantages:</b> low coefficient of deformation force; unstable deformation force. |
| Transverse deformation |  | <b>Advantages:</b> high coefficient of deformation force; stable deformation force<br><b>Disadvantages:</b> low energy absorption.    |
| Inversion of walls     |  | <b>Advantages:</b> high coefficient of deformation force; stable deformation force.<br><b>Disadvantages:</b> complex structure.       |
| Widening walls         |  | <b>Advantages:</b> high coefficient of deformation force; stable deformation force.<br><b>Disadvantages:</b> complex structure.       |
| Tearing walls          |  | <b>Advantages:</b> stable deformation force.<br><b>Disadvantages:</b> complex structure.  |

Energy absorbing devices are most often made of thin-walled metal structures that absorb energy by analogy with the axial deformation of tubes. Such devices have high energy absorption and very simple design but there are also disadvantages expressed in big triggering force and unstable axial deformation force.

In order to reduce the triggering force, it is

necessary to reduce the local hardness of energy absorption device, e.g. by reducing the wall thickness in a certain area of device structure. Another method involves the development of an energy absorption device with inclination of its walls relative to the longitudinal axis (in the form of a truncated pyramid) [18] as shown in Fig. 10-a. It is also possible to reduce the triggering force by introducing special zones of stress concentration, particularly by creating perforations in the energy absorption device structure [19] as shown in Fig. 10-b.

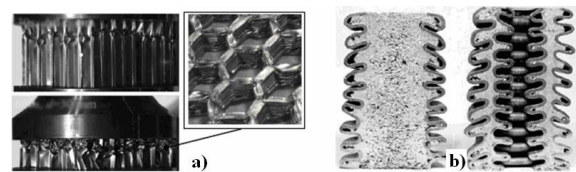
Thick-walled tubes with belts in the form of wide cylinders on the outer surface possess good energy absorption features during axial deformation: as it is shown in Fig. 10-c, the thick sections provide stable destruction of the entire structure. As a result such transformation reduces the sensitivity to deviations in the angle of loading as well as to triggering force and stabilizes the axial deformation force.



a) – design of sloping walls; b) – creation of perforations; c) – creation of belts; (d) – introduction of diaphragms; e) – introduction of auxiliary cells

Fig.10 – Technical solutions for improving energy absorption features [18,19].

Another way to ensure a stable deformation force is to incorporate metal diaphragms into the energy absorption device as shown in Fig. 10-d [18,19]. It is possible to achieve an energy consumption increase of the energy absorption device with unchanged dimensions introducing auxiliary tube cellular energy capacity from 11.21 to 35.00 kJ / kg. An example of such structures is shown in Fig.10-e.



(a) honeycomb structures; b) metal tubes filled with aluminium foam

Fig. 11 – Energy absorber structural elements [18,19]

Honeycomb structures made of aluminium are an array structure of hollow cells formed of thin vertical walls (Fig. 11-a). They have good absorption features thanks to their high strength combined with small weight.

According to the study results, it was found that the absorption features of metal tubes filled with aluminium foam are influenced by the ratio between the wall thickness and the diameter of inscribed cell circle and the angle of branching of cells (Fig. 11-b).

Based on the review, a classification of technical solutions for improving the features of energy absorption devices operating in axial deformation mode has been developed and presented in Fig.12.

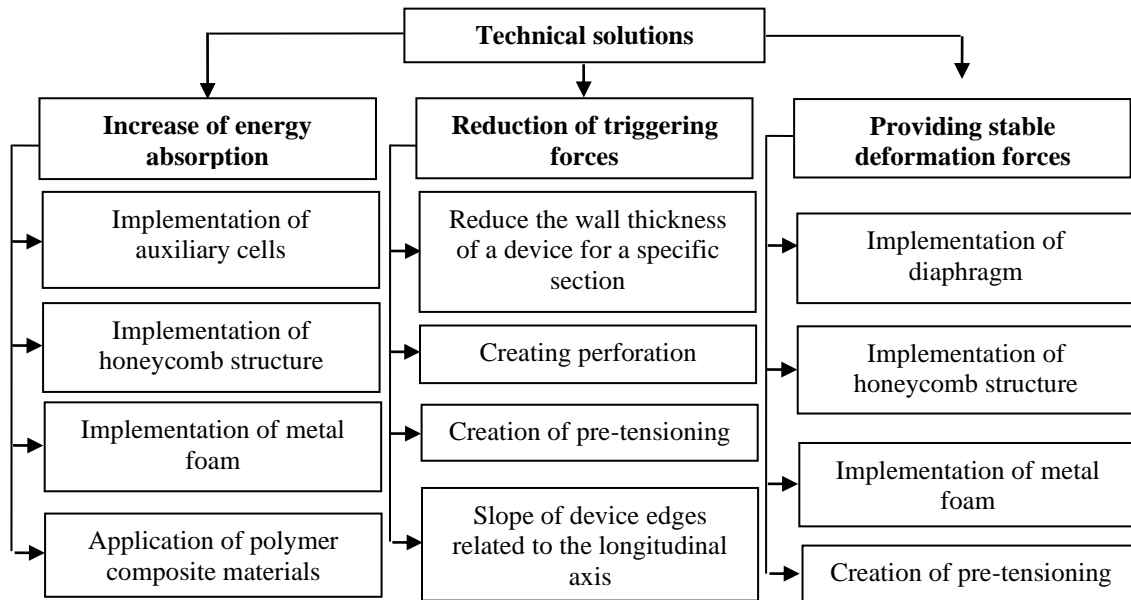
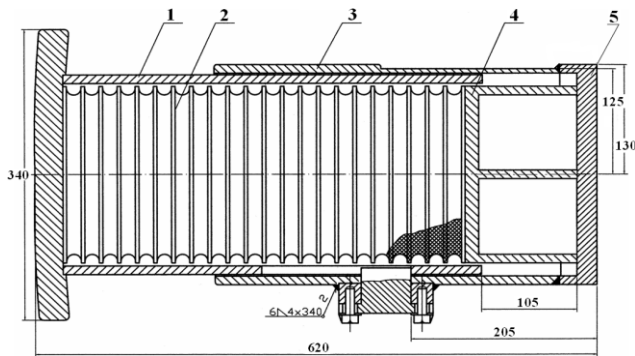


Fig. 12 – Technical solutions to improve the performance of energy absorbing devices.

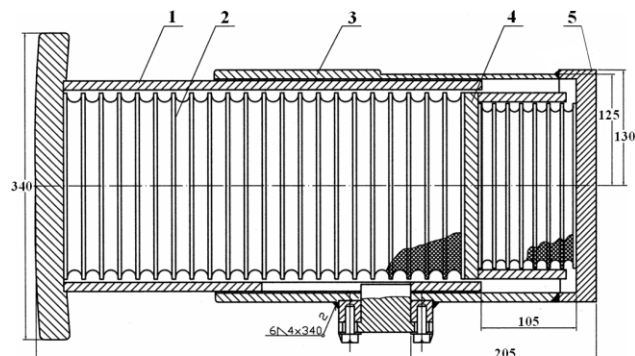
6. BUFFER STRUCTURES IN OPERATION OF BDZ HOLDING "PASSENGER TRANSPORT"

The structures of buffers for passenger carriages in operation of BDZ holding "Passenger Transport" are buffers with metal-rubber absorbers and buffers with absorbers made of elastomeric or hydraulic capsules.



1- plate with a bushing; 2- rubber-metal package; 3- outer cylinder; 4 – support; 5- supporting plate.

Fig. 13 Buffer with a metal-rubber package [20].



1- plate with a bushing; 2- rubber-metal package; 3- outer cylinder; 4 – support with a metal-torsion plate; 5- supporting plate.

Fig. 14 Buffer with two metal-rubber packages [20].

At present the most widespread devices in the Bulgarian railways are draw gear ones based on rubber-metal packages (Fig.13 and Fig.14).

There are two types of *buffers with rubber-metal packages* used in operation. The older device is with a stroke of 105 mm and one rubber-metal package (Fig. 13). The latest buffer, which is with increased energy absorption and the same stroke of 105 mm, has two rubber-metal packages: the smaller package is behind the bigger one (Fig. 14).

The elastic element in both types is a metal-rubber package made of metal plates and rubber discs, which are glued together by vulcanization.

The smaller rubber-metal package of buffer with increased energy absorption is placed on the rear part of support plate and it serves to absorb smaller forces during the train movement (120 ÷ 150 kN); with the increase of force acting on the buffer, the bigger rubber-metal package is also included in energy absorption. In this way the power characteristic of buffer with increased energy absorption becomes softer than the one of the buffer produced with one bigger rubber package. In its turn that helps the vehicle to run at a higher speed in rail track curved sections.

These were the prerequisites that imposed the development of rubber-metal packages with high energy absorption at the Research Institute for Transport jointly with the Research Institute for Rubber and Plastics Industry.

The tests for establishing a suitable rubber composition for the rubber elements of rubber-metal packages for buffers were carried out on the basis of the rubber requirements in compliance with the approved methodology for conducting type tests as well as on the specific operating conditions under which rubber works.

Based on the abovementioned, the rubber for a metal package must have:

- Good resistance to thermal aging, expressed in changes of the basic strength indicators after 7-day aging at 70° C within the range of up to 20% and hardness up to 10 units.
- Small residual deformation under pressure combined with high elasticity.
- Preservation of its qualities and performance at low temperatures.

To meet these requirements to rubber, which serves as an elastic element in buffers with rubber-metal packages, a recipe has been developed and adopted.

The use of elastomer SKD leads to a decrease of the abovementioned indicators but at the same time to a significant improvement of their elasticity and residual deformation under pressure.

The application of elastomer SKD up to 10% in the of natural rubber composition leads to a decrease of their brittleness temperature by 5° C. The percentage changes of values of physicochemical parameters of vulcanizates in the mixtures under examination after thermal aging at 70° C for 72 h, 168 h are very small and within the requirements. The obtained negative values for the change of tensile strength in some vulcanizates are due to the increase of this indicator after aging, which is characteristic of synthetic rubber. Based on the abovementioned, it follows that all tested rubber compositions have very good resistance to thermal aging. The small change in the hardness of vulcanizates after thermal aging of most tested compositions up to 2 units will have a favourable effect on the characteristics of buffer in the process of operation.

In general, the buffer with a rubber-metal package is tested in Research and Technology Institute of Railway Transport (НИТИЖТ) [2] - the first stage of the tests was intended to take down the static characteristics. The buffer was tested as a set, in the kind it would be mounted on the wagon for operation. The ambient temperature was 15° C.

The buffer was loaded using a laboratory press at a speed not exceeding 0.05 m/s. The buffer was unloaded immediately after loading, continuously reporting about the deformation obtained.

The maximum force of 1000 kN was obtained at a maximum deformation stroke of 105 mm. The pre-tensioning was ~ 20 kN.

The total energy absorption of buffer  $We = 23500$  J, which is significantly higher than the determined limit of 12500 J, the irreversible energy absorption  $We = 12500$  J, which represents 53%.

There are also strength requirements to buffers, as they are subjected to axial loading with force  $F > 2500$  kN and transverse force  $F_2 > 200$  kN ( $F_2$  is applied to the buffer casing).

It was found that the buffer continues to function normally, with no residual deformations. Also, no residual deformations were found after loading the support plate with a force of 2500 kN. It should be noted that regulations allow residual deformations after loading, commensurable with the established deviations in dimensions during their production, which should not be greater than 0.2%.

The buffer dynamic tests were performed on an crash test bench at different speeds. The maximum energy absorption of 30 kJ was obtained at a maximum force of 1000 kN.

Conclusion: Buffers with metal-rubber GUM-METSL packages are a relatively reasonable compromise between cost and efficiency of draw gear. With maximum use of the bushing internal space and the correct choice of rubber mixture, it is possible to implement a buffer that meets the requirements of UIC Leaflet 526-1 and UIC Leaflet 528 [22].

Their main advantages are relatively low price and satisfactory reliability. In addition, these buffers have a number of *disadvantages*, the most important of which are:

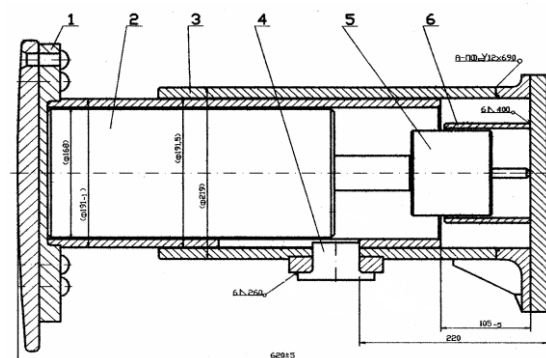
1. Accumulated and especially absorbed energy have small values. According to these indicators, they are on the border of what is allowed by the UIC, which calls into question their efficiency and possibility to perform domestic and especially international transport. The metal-rubber package qualities are extremely dependent on the composition of rubber mixture and manufacturing technology. Even small deviations from the established recipe or production technology lead to significant differences in the buffer strength features. This is the main reason why it cannot be claimed that the Bulgarian freight wagons are equipped with draw gear corresponding to Leaflet 526-1 and Leaflet 528.

3. The buffers with rubber-metal packages (RMP) have a relatively low durability, which is incommensurable with the durability of the wagon body. The main reason for this is aging of rubber due to oxidation and variable temperatures during operation.

4. This type of elastic elements have a nonlinear parabolically increasing characteristic. Therefore, at the end of stroke the force acting on the buffer is approximately equal to the maximum admissible for both the draw gear and wagon metal body.

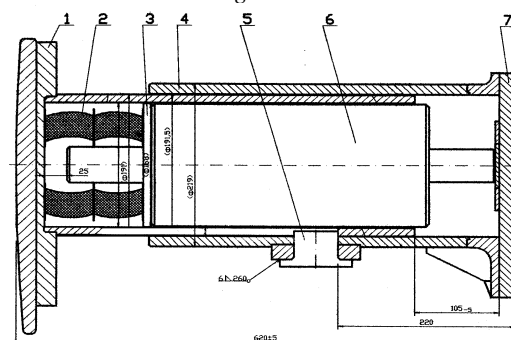
This leads to extremely unfavorable consequences related to the strength of front beam and other load-bearing elements, the safety of cargo or comfort of passengers in passenger cars.

The *elastomeric buffers* in Fig. 15 most often consist of metal part and a set of two energy absorption elements.



1 - plate; 2 - large elastomeric capsule; 3 - outer cylinder; 4 - trigger; 5 - small elastomeric capsule; 6 - guide bushing.

Figure 15



1 - plate; 2 - rubber-metal package; 3 - ring; 4 - outer cylinder; 5 - trigger; 6 - elastomeric capsule; 7 - support.

Figure 16

The latter is known in three versions: a small and large hydraulic capsule, metal-rubber package and large hydraulic capsule – Fig. 16, rubber package and large hydraulic capsule.

In order to obtain the indicated features of energy absorption, metal foam is used.

The small energy absorption element (i.e. a small hydraulic capsule, rubber package or Belleville spring) provides buffer pre-tensioning and works up to a stroke of 25-30 mm from the complete deformation of the draw gear. The purpose of this solution is as follows:

(a) According to statistics, 90-95% of crashes between wagons cause relative displacements in the buffers up to 25 mm. Therefore, in normal operation of railway vehicles, it is only the small energy absorption element that works in practice.

(b) Regulations do not require a relatively gradual increase of force to a stroke of 25 mm for freight wagons and 30 mm for passenger carriages and abruptly after the specified values.

In all three variants, the main energy absorption element is the large hydraulic capsule. It operates effectively at significant values of compressive force, providing dissipation of 70-90% of the accumulated energy under the shock load. The capsule is single-chambered. It is filled with an elastomeric substance with high viscosity and significant compressibility.

The conversion of the impact energy into heat is carried out at the expense of operating fluid throttling with relative displacement of the piston to the capsule body.

There is a trend in railway car manufacturing to apply buffers of "C" category with "crash" devices for energy absorption. The buffer with "crash" technology acts as a device absorbing much of the impact energy in an irreversible process.

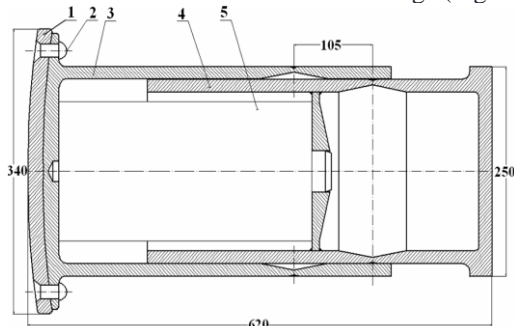
### 7. SAMPLE SOLUTIONS FOR PASSENGER CARRIAGE BUFFERS WITH "CRASH" ENERGY ABSORPTION DEVICES

Two proposals for a buffer of passenger carriages with a "crash" element have been developed:

- with breakable inner and outer bushings;
- with inner "crash" element on tube-in-tube principle.

#### 7.1 Buffer for a passenger carriage with a "crash" element – breakable inner and outer bushings

The proposed design of a buffer with a "crash" element – breakable inner and outer bushings (Fig. 18).



1 – plate; 2 – rivets; 3 – outer bushing; 4 – inner bushing; 5 – absorption device.

Figure 17. Scheme of a buffer for a passenger carriage with a "crash" element – breakable inner and outer bushings

The structure of the buffer consists of a plate, inner and outer bushings building the casing and an absorber, which can be built of various energy absorption elements.

The proposed casing structure consists of a plate and inner and outer bushings, which are "crash" elements. Upon crash into the buffer, an elastic stroke is performed by the absorber contraction, the stroke being 105 or 110 mm.

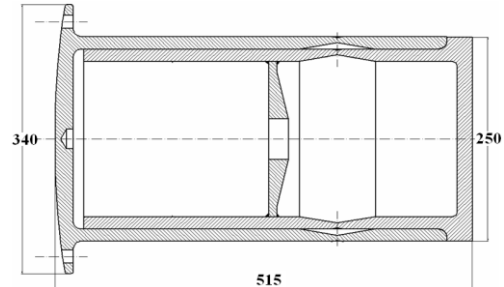


Figure 18. "Crash" elements with exhausting the elastic stroke of 105 mm.

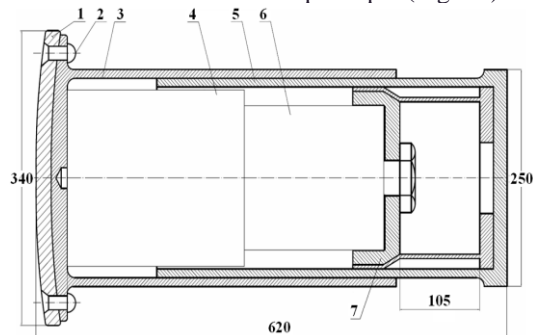
When the elastic stroke is exhausted, the weakened sections of the two bushings coincide and are plastically deformed (Fig. 18).

The proposed structure is a buffer with 7 DURAL packages and "crash" elements.

**Technical specifications for the proposed "crash" buffer (Fig. 18):** Length: UIC classification: category 6 (UIC 526-1); Reversible spring travel: 105 mm; Energy absorption reversible (dyn.): approx. 40 kJ; Typ. trigger force per buffer: 1500 kN; Typ. mean deformation force per buffer: 1112 kN; Maximum axial deformation: approx. 200 mm; Total energy absorption capacity per vehicle end (dynamic): approx. 600 kJ; Weight per buffer: 127 kg

#### 7.2. Buffer for a passenger car with an inner "crash" element on tube-in-tube principle

The proposed structure of a buffer with an inner "crash" element on tube-in-tube principle (Fig. 19).



1 – plate; 2 – rivets; 3 – outer bushing; 4, 6 – absorption device; 5 – inner bushing, 7 - "crash" element.

Figure 19. Scheme of a buffer for a passenger carriage with an inner "crash" element on tube-in-tube principle.

The full buffer length does not differ from the typical design. The incomparable advantage of this model is the possibility for block replacement of deformable elements in case of emergency collisions of rail stock with all obstacles. It is assumed that the buffer will work in three stages: Stage 1 - the operation of the first energy absorption element (element with stiffness  $k = 44.29$  N/mm and a stroke of 25 mm).

Stage 1 ensures light crashes of wagons during shunting operations.

Stage 2 – is operation of a set of elastic elements. When the second stage of buffer and absorber operate together, maximum crash absorption is achieved and the smoothest auto-coupler is ensured as a result of shunting operation. In addition, as a result of train movement, the second stage of buffer makes it possible to minimize the negative dynamic accelerations acting on the wagon body.

Stage 3 – is operation of the buffer in case of collision of railway stock themselves (of wagons with each other) or with any obstacle. As a result, the deformable element, which operates on the principle of a deformable tube, comes into action due to the plastic deformation of metal and maximum crash energy absorption is achieved.

The body of proposed buffer with the elastic stroke exhausted is shown in Fig. 21.

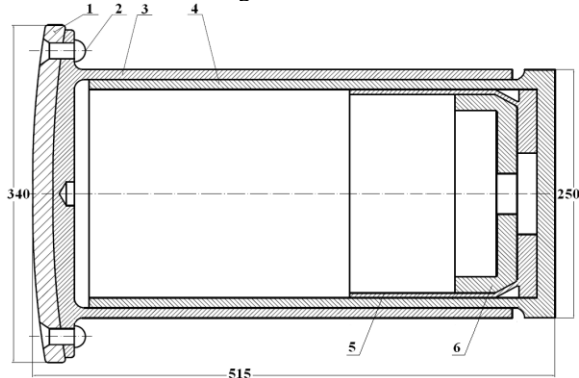


Figure 21. Buffer with inner "crash" element on the tube-in-tube principle of when the elastic stroke of 105 mm is exhausted.

**Technical specifications for the proposed "crash" buffer with 7 DUREL packages (Fig.19):** Energy absorption reversible (dyn.): approx. 74.09 kJ; Total energy absorption capacity per vehicle end (dynamic): approx. 954 kJ; Weight per buffer: 130 kg.

## 8. CONCLUSION

Based on the presented analysis, the following more important conclusions can be drawn:

1. At present the buffers with rubber-metal packages RMP have the greatest application in BDZ.

2. From the analysis performed, the buffers with elastomeric capsules can be preferably considered as well as their variants in set with RMP or Belleville spring.

3. From the analysis made, considering the value of irreversible absorption coefficient and the low value of buffer capsules, in this paper to build-in elastomeric elements of TecsPak or DUREL types in the buffer and draw gear absorber.

4. It is necessary to construct a buffer with "crash" elements. These "crash" elements should be destroyed in a crash between wagons with a shock speed above 12 km/h and force > 1.5 MN.

5. Two structures for buffers with increased energy absorption and "crash" elements are proposed.

## REFERENCES

- [1] 526-1 Wagons - buffers with a stroke of 105 mm, ed.3, July (2008)
- [2] UIC 526-2 Wagons - buffers with a stroke of 75 mm and a stroke of 150 mm, ed.2, October (2008)
- [3] UIC 526-3 Wagons – buffers with a stroke of 130 mm and a stroke of 150 mm, ed.3, October (2008)
- [4] Petrovic D., Aleksandrov V., *Jelesnicka vozila. Osnove*, MF Kraljevo, 2013, ISBN 978-86-82631-66-8 p.223 (2013)
- [5] Annual reports on the investigation of railway accident: <https://www.mtitc.government.bg>
- [6] EN 15227-2020 Railway applications - Crashworthiness requirements for rail vehicles (2020)
- [7] SAFETRAIN project <http://www.safetrain.com>
- [8] Мировой лидер технологий поглощения энергии. <http://sdrives.ru/files/Rail-series-brochure-RU.pdf>;
- [9] ГОСТ 32410-2013 Крэш-системы аварийные железнодорожного подвижного состава для пассажирских перевозок. Технические требования и методы контроля (2013)
- [10] Оганьян, Э.С. Критерии несущей способности конструкций локомотивов в экстремальных условиях нагружения: дис. М.: МИИТ, (2004)
- [11] FINAL REPORT on the investigation of a railway accident – collision of 19205 passenger train with a car at the guarded level crossing between the stations Krumovo, <https://www.mtitc.government.bg> (2019)
- [12] EN 12663-1:2015, Railway Applications - Structural Requirements of Railway Vehicle Bodies (2015).
- [13] CFR Current approach in 49 CFR Part 238 focuses on force resistance of key structural members, 2018
- [14] Барышников, А.В. Целесообразность применения устройств поглощения энергии при различных скоростях соударения подвижного состава с препятствием / Наука и техника транспорта. — 2019. № 1 С. 78-84.
- [15] ГОСТ 21447-75 Зацепления автосцепки (1975).
- [16] ГОСТ 32913-2014 Аппараты поглощающие сцепных и автосцепных устройств железнодорожного подвижного состава. Технические требования и правила приемки.
- [17] Perovic D., *Dinamika sudara vagona*, Biblioteka DISSERTATIO, Beograd, (2001)
- [18] Барышников, А. В. Выбор конструкционного решения энергопоглощающего устройства и обоснование его эффективности / Наука и техника транспорта. - № 2 — С. 52-58; (2019)
- [19] Азарченков, А.А. Разработка методики оценки аварийной нагруженности пассажирских вагонов при продольных соударениях: дис. ... канд. тех. наук: 05.22.07 / Брянск,-113 с; (2005)
- [20] Stoilov V., Slavchev S., *Vagoni*, Ed. TU-Sofia, 2014, ISBN 978-619-167-135-9, Sofia, 2014, p.222 (2014).
- [21] Tests of energy absorption elements for buffers by RTIRT, (2010)
- [22] UIC 528 Buffer gear for coaches, ed.8, (2007).

## Determining the longitudinal force in collision of two wagons

Milica Timotijević<sup>1\*</sup>

<sup>1</sup>Faculty of Mechanical and Civil Engineering in Kraljevo, University in Kragujevac, Kraljevo (Serbia)

*This paper defines the load that appears collision of two wagons and longitudinal oscillations which are caused by these striking loads. Because of the complexity of the system, which has many degrees of freedom and not knowing the forces that affect the wagon in a short time, when forming a mathematic model, certain limitations have been introduced.*

**Keywords: Longitudinal force, Longitudinal oscillations, Restitution coefficient**

### 1. INTRODUCTION

There are various attempts in literature [1,2,3,4] to define longitudinal force in the collision of wagons. However, with testing [5,6,7] there was conclusion that given equations do not measure influence of moving the load to the total amount of force in collision, the loss of energy in friction that happens under collision in the set of the wagon, influence on energy loss with the oscillations of the wagon etc.

Beside this, with these equations the force that exists under stiff collision cannot be precisely determined- when buffers use their strokes. To be able to determine the influences already mentioned on the value of the force in buffers, a more complex model will be formed.

### 2. ESTIMATING THE LONGITUDINAL FORCE IN THE COLLISION OF TWO TRAIN WAGONS

Let us consider the collision of two wagons (Figure 1) and the wagon with its mass  $m_1$  moves with the speed of

$v_2$  and hits wagon with mass  $m_2$  and speed  $v_2$ . Velocities of the wagons before and after the collision have the same direction and therefore, can be written without vector marks. We will examine the movement of the entire system starting from the moment of collision. Movement of the wagons in the direction of collision is  $x_1$  and  $x_2$ . Wagons have the weight of the mass  $m_3$  and  $m_4$ , and, in the collision there is a relative shift of the mass in the wagon for  $x_3$ , or  $x_4$ . And we have elastic construction stiffness' for the wagon and the load  $c_3$  and  $c_4$ . Besides, dry friction forces and forces of viscous friction are opposed to the masses  $m_3$  and  $m_4$  and they are proportional to the first degree of the relative movement of the load. And the friction rolling force is opposed to movement of the first and second wagon.

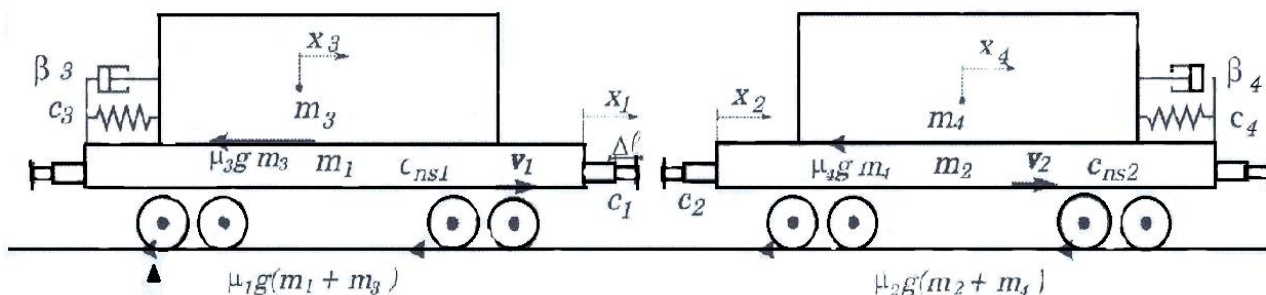


Figure 1. Collision of wagons where shift of load is possible[7]

Formulas for kinetic ( $E_k$ ) i potential ( $E_p$ ) energy of the system shown on the Figure 1:

$$E_k = \frac{1}{2}(m_1 + m_3)\dot{x}_1^2 + \frac{1}{2}(m_2 + m_4)\dot{x}_2^2 + \frac{1}{2}m_3\dot{x}_3^2 + \frac{1}{2}m_4\dot{x}_4^2 + m_3\dot{x}_1 \dot{x}_3 + m_4\dot{x}_2 \dot{x}_4 \quad (1)$$

$$E_p = \frac{1}{2}c_s x_1^2 + \frac{1}{2}c_s x_2^2 + \frac{1}{2}c_3 x_3^2 + \frac{1}{2}c_4 x_4^2 - c_s x_1 x_2 \quad (2)$$

Dissipation function  $\Phi_r$

$$\Phi_r = (m_1 + m_3)g|\dot{x}_1| + \mu_2(m_2 + m_4)g|\dot{x}_2| + \mu_3 m_3 g|\dot{x}_3| + \mu_4 m_4 g|\dot{x}_4| + \frac{1}{2}\beta_3 \dot{x}_3^2 + \frac{1}{2}\beta_4 \dot{x}_4^2 \quad (3)$$

Where these are:

$c_s$  - stiffness of the system during collision/impact,

$\mu_1, \mu_2, \mu_3$  i  $\mu_4$  - Coefficient of dry friction,

$\beta_3$  i  $\beta_4$  - dynamic viscosity that characterize medium resistance,

$g$  - force of gravity.

As this system is under the conservative and dissipative forces, we have Lagrange's equations of the second kind:

\* Corresponding author: Milica Timotijević: Dositejeva 19, timotijevic.milica93@gmail.com

$$\frac{d}{dt} \frac{\partial E_k}{\partial \dot{q}_i} + \frac{\partial \phi_r}{\partial \dot{q}_i} + \frac{\partial E_p}{\partial \dot{q}_i} = 0 \quad (4)$$

When we change the equation for kinetic and potential energy from the previous equation, and the

$$y_1 = x_1, y_2 = x_1, y_3 = x_2, y_4 = x_2, y_5 = x_3, y_6 = x_3, y_7 = x_4, y_8 = x_4 \quad (5)$$

And we get the final differential equations of the collision of two train wagons:

$$\ddot{x}_1 = a_1(y_3 - y_1) + a_2 y_5 + a_9 y_6 - a_{10} \sin y_2 + a_{13} \sin y_4$$

$$\ddot{x}_2 = a_3(y_1 - y_3) + a_4 y_7 + a_5 y_8 - a_{11} \sin y_4 + a_{14} \sin y_8$$

$$\ddot{x}_3 = a_1(y_1 - y_3) - (a_2 + a_{12})y_5 - (a_7 + a_9)y_6 + a_{10} \sin y_2 - (a_{13} + a_{15}) \sin y_6$$

$$\ddot{x}_4 = a_3(y_3 - y_1) - (a_4 + a_8)y_7 - (a_5 + a_6)y_8 + a_{11} \sin y_4 - (a_{14} + a_{16}) \sin y_8 \quad (6)$$

Constants used in Formula 6 ( $a_1 \dots a_{16}$ ) are given in the Table 1.

Table 1. Constants  $a_1 \dots a_{16}$

|                           |                                 |                                 |           |
|---------------------------|---------------------------------|---------------------------------|-----------|
| $a_1$                     | $a_2$                           | $a_3$                           | $a_4$     |
| $c_s/m_1$                 | $c_3/m_1$                       | $c_s/m_2$                       | $c_4/m_2$ |
| $a_5$                     | $a_6$                           | $a_7$                           | $a_8$     |
| $\beta_4/m_2$             | $\beta_4/m_4$                   | $\beta_3/m_3$                   | $c_4/m_4$ |
| $a_9$                     | $a_{10}$                        | $a_{11}$                        | $a_{12}$  |
| $\beta_3/m_1$             | $\mu_1 \frac{m_1 + m_3}{m_1} g$ | $\mu_2 \frac{m_2 + m_4}{m_2} g$ | $c_3/m_3$ |
| $a_{13}$                  | $a_{14}$                        | $a_{15}$                        | $a_{16}$  |
| $\mu_3 \frac{m_3}{m_1} g$ | $\mu_4 \frac{m_4}{m_1} g$       | $\mu_3 g$                       | $\mu_4 g$ |

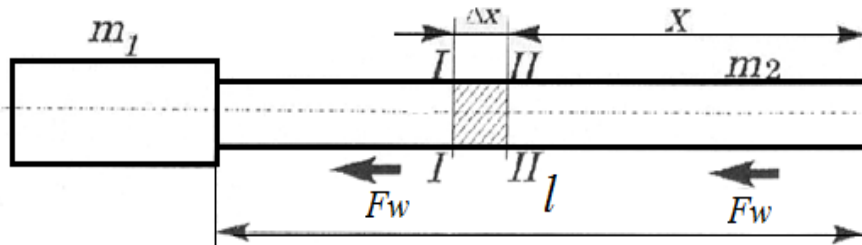
equation for dissipation function and include these spatial vectors we get:

This way defined system of differential equations takes into account shift of the load in the collision and it is good for solving it numerically.

In solving this system, Runge-Kutta formula of order 4 was used.

### 2.1. LONGITUDINAL OSCILLATIONS IN THE COLLISION OF TWO WAGONS

Train wagons in collisions act like elastic beams. In the moment of collision, the wagon with mass  $m_2$  is hit by a load (locomotive or a second wagon) of the mass  $m_1$ . Therefore, the scheme of the collision of the wagons that is shown on the Figure 1 (in the case of longitudinal oscillations) can be exchanged with the scheme on the Figure 2.



$$c_{II} \left( \frac{\partial u_1}{\partial x} + \frac{\partial u}{\partial x} \right) \leftarrow \blacksquare \rightarrow c_{II} \left( \frac{\partial u_1}{\partial x} + \frac{\partial^2 u_2}{\partial x^2} dx \right) + c_{II} \left( \frac{\partial u}{\partial x} + \frac{\partial^2 u}{\partial x^2} dx \right)$$

Figure 2. Scheme of the collision of the wagons[7]

Using D’Alambert’s principle, the differential equation for the basic movement of the part  $dx$  will be like this:

$$\left( \frac{d^2 u_0}{dt^2} + \frac{\partial^2 u}{\partial t^2} dx \right) \rho dx = c_s \left( \frac{d^2 u_1}{dx} + \frac{\partial^2 u}{\partial x^2} dx \right) - F_w dx \quad (7)$$

And these are:

$F_w$  - friction forces,

$$\rho = \frac{m_2}{l} - \text{mass of the longitude of the wagon,} \quad (8)$$

$u$  - deformity of the wagon as an elastic beam,

$c_s$  - the overall stiffness of the system in the collision.

If we take into consideration that part of the force is used for friction force, that the size of  $\frac{d^2 u_0}{dt^2}$  can be defined from considering the differential equation of the movement of the system of the mass and that there is no coercive force  $F$ , the equation 7 becomes:

$$\frac{\partial^2 u}{\partial t^2} - c^2 \frac{\partial^2 u}{\partial x^2} = 0 \quad (9)$$

where:

$$c = \sqrt{\frac{c_s}{\rho}} - \text{speed of elastic waves.} \quad (10)$$

Since the forces in buffers are equal to zero in any time at the free end of the beam, and since oscillations are in harmonic law, we get:

$$u_i = A_{ix} \cos \left( \frac{\omega_i}{c} \right) x \cdot (A_{it} \cos \omega_i t + B_{it} \sin \omega_i t) \quad (11)$$

And these will be:

$A_{ix}, A_{it}, B_{it}$  - constant of oscillation,

$\omega_i$  - frequency of oscillation.

Using the equations from (8) and (10) you will get:

$$tg \frac{\omega}{c} l = -m_1 \frac{\omega^2 c}{\omega c^2 \rho} i$$

$$tg \frac{\omega}{c} l = -\frac{m}{m_2} \frac{\omega}{c} l. \quad (12)$$

Finally it is:

$$tg \lambda = -k \lambda \quad (13)$$

Where this is:

$$\lambda = \frac{\omega}{c} l. \quad (14)$$

Using this equation (13) the frequency of wagon oscillations in the collision can be determined. And the wagon is observed as an elastic beam with the load at only one end.

### 3. INFLUENCE OF THE ENERGY WAGON OSCILLATION TO THE LONGITUDINAL FORCE IN THE COLLISION

Considering the fact that in the collision, the each force are weaker than the combined forces of the wagons, it can be deduced that this collision happens in the isolated system with the conservation laws (quantity of movement, energy etc.).

$$\frac{m_1 v_1}{2} + \frac{m_2 v_2}{2} = \int_{x=0}^{2\Delta l} F_0(x) dx + \frac{(m_1+m_2)v_{cm}^2}{2} + \sum_{i=0}^n \int_0^{x_i} b_i \dot{x}_i dx_i + E_{asc} \quad (17)$$

On the right side of equation:

$\int_{x=0}^{2\Delta l} F_0(x) dx$  - the absorbed energy of springs of the buffers in both wagons,

$\frac{(m_1+m_2)v_{cm}^2}{2}$  - kinethic energy of the system during collision,

$\sum_{i=0}^n \int_0^{x_i} b_i \dot{x}_i dx_i$  - thermal energy, or the work of all the fringe forces (thermal energy is a result of movement of wagons, shift of load, etc),

$E_{asc}$  - oscillating energy of both wagons and the load.

Here are:

$x = x_1 - x_2 = 0 \div 2\Delta l$  - stroke in compression of buffers of wagons ni case where buffers have the same stiffness, in general case, this would be:  $x = \Delta l_1 + \Delta l_2$

$F_0(x)$  – Force in the buffers,

$b_i$  – of proportion that characterize medium resistance,

$x_i, \dot{x}_i$  - move and speed of masses.

From the equation (17) it can be concluded that the overall kinetic energy of the system before the collision transforms into energy of the springs in the buffers, kinetic energy of the system after the impact (collision), the lost „energy” which is used for the overcoming of the friction (due to the shift of the wagon, shift of the load and the energy of the system oscillation.

We can disregard the energy lost on the overcoming friction and mark the lost mechanical energy with  $E_i$  - that is lost on the oscillation of the wagon that takes part in the collision. This energy is hard to define analytically, because it depends not just from the velocity and the mass of wagon and the load that take part in the collision, it depends on the other factors among which the most important is dynamic stiffness of the wagon. In the first period of the impact we will mark this lost energy with  $E_{i,1}$ .

Now the equation (17) can be written like this:

$$\frac{m_1 v_1}{2} + \frac{m_2 v_2}{2} = \int_{x=0}^{2\Delta l} F_0(x) dx + \frac{(m_1+m_2)v_{cm}^2}{2} + E_{i,1} \quad (18)$$

Taking (16) into consideration for the central mass velocity  $v_{cm}$  from the previous equation, the energy

During the collision, the centre of the masses of the connected wagons is moving with the constant speed  $v_{cm}$ , and based on the Conservation law of movement it is:

$$m_1 v_1 + m_2 v_2 = (m_1 + m_2) v_{cm} = const. \quad (15)$$

It can be concluded that the velocity of the mass  $v_{cm}$  during the collision is constant and equal:

$$v_{cm} = \frac{m_1 v_1 + m_2 v_2}{m_1 + m_2} \quad (16)$$

The collision of two wagons can be divided into the period of compressing buffers to reaching the maximum stroke and the period when buffers use all of their strokes, and then we have a case of stiff collision of the wagon.

In the period that lasts from the moment of touching the buffer to the maximum compression of springs ( $2\Delta l$ ), the center of the wagon masses is moving with the constant velocity of  $v_{cm}$ - which is defined in the previous equation.

In general case, kinetic energy of the wagon movement, during the collision is:

of the impact that corresponds to the work of wagon buffers:

$$\int_{x=0}^{2\Delta l} F_0(x) dx = (v_1 - v_2)^2 \frac{m_1 m_2}{2(m_1 + m_2)} - E_{i,1} \quad (19)$$

Let's assume that in a general case, force in the buffers  $F_0(x)$  does not linear depend on the hod of the springs, and is given in relation:

$$F_0(x) = c_1 x^n + F_{st} \quad (20)$$

Because:

$c_1$  - equivalent stiffness,

$x = 0 \div 2\Delta l$  - stroke of the springs,

$n$  - pring coefficient characteristic, for the linear dependency  $n=1$ ,

$F_{st}$  - Static force of pre stressing the spring.

If:

$c_{o1}$  - stiffness of one spring of the first wagon,

$c_{o2}$  – stiffness of one spring of the second wagon,

$c_1$  - stiffness of parallel springs on the first wagon,

$c_2$  – stiffness of parallel springs on the second wagon, then stiffness of parallel springs of the first and second wagon is:

$$c_1 = 2c_{o1}$$

$$c_2 = 2c_{o2}$$

In general case, stiffness in the system during the first period of impact ( $C_1$ ) of two wagons equals:

$$\frac{1}{c_1} = \frac{1}{c_1} + \frac{1}{c_2} + \frac{1}{c_{ns1}} + \frac{1}{c_{ns2}} \quad (21)$$

Where:

$c_{ns1}$  – stiffness of the base structure of first wagon,

$c_{ns2}$  – stiffness of the base structure of second wagon.

To be precize, during the first period of collision, stiffness of system consists of lineary connected stiffness of springs and stiffness of the base springs that are in collision. However, stiffness of base wagon structures is much bigger from the stiffness of spring buffers ( $c_{ns} \gg c_{1,2}$ ), and if we omit the last two equasions (18) it can be written:

$$c_1 \cong \frac{c_1 c_2}{c_1 + c_2} \quad (22)$$

Let's also mention that stiffness of the spring changes depending on the speed of reaction to the load. If the spring, when statically tested, had a linear dependency between force and stroke, in dynamics it is possible that this characteristic is not linear any more.

Assuming that force in the buffers  $F_0(x)$  does not only linearly depend on the spring stroke replacing the spring static force and also replacing (20) equation into (19) equation and we get, after intergraljenje (pise da je to na hrvatskom, nije mi poznato) integration, we get mathematical expression for the maximum spring stroke:

$$F_0 = \sqrt[n+1]{c_1(n+1)^n \left[ \frac{(v_1 - v_2)m_1 m_2}{2(m_1 + m_2)} - E_{i,1} \right]^n}, \quad (23)$$

for  $|v_1 - v_2| \leq |v_0|$

So, the previous expression for the force in the buffers to the velocity  $|v_0|$  under which the maximum stroke of the buffer springs is made.

From the equation (19), taking into consideration the force in the buffers (20), we get the expression for the speed in the moment of the spring max usage stroke:

$$v_0 = \sqrt{\frac{2(m_1 + m_2)}{m_1 m_2} \left[ c_1 \frac{(2\Delta l)^{n+1}}{n+1} + E_{i,1} \right]} \quad (24)$$

#### 4. COLLISION OF TWO WAGONS WHEN SPRING STROKE IS OVERUSED

In the end of the first period of collision, the force in the wagon buffers  $F_0$  reaches the result given by the

$$\int_0^x F(x) dx = \frac{F_0 2\Delta l}{2} + \frac{F_0 + F_{max}}{2} (x - 2\Delta l) = \frac{F_0^2}{2c_1} + \frac{F_{max}^2 - F_0^2}{2c_n} \quad (25)$$

The work of these forces has to be equal to the energy of impact:

$$\int_0^x F(x) dx = (v_1 - v_2)^2 \frac{m_1 m_2}{2(m_1 + m_2)} - E_i \quad (26)$$

Equalizing two previous math expressions, we get:

$$\frac{F_0^2}{2c_1} + \frac{F_{max}^2 - F_0^2}{2c_n} = (v_1 - v_2)^2 \frac{m_1 m_2}{2(m_1 + m_2)} - E_i \quad (27)$$

Expression for max. force during collision:

$$F_{max} = \sqrt{F_0^2 \left( 1 - \frac{c_n}{c_1} \right) + c_n (v_1 - v_2)^2 \frac{m_1 m_2}{m_1 + m_2} - 2c_n E_i} \quad (28)$$

If the collision is not entirely elastic, the part of kinetic energy that objects had on the beginning of the collision is wasted on deformation and the warming of the objects. We saw that wagon with the mass  $m_1$  moves with velocity of  $v_1$  and collides with wagon which mass is  $m_2$  and speed is  $v_2$ .

The relation between the speed of an object under the steering collision in the end and the beginning of the object, Newton named The coefficient of restitution or coefficient of impact and is defined as in [2,3]:

$$k_r = \frac{v'_i}{v_i} \quad (29)$$

Where:

$v'_i$  - velocity of  $i$  mass after the impact,

$v_i$  - velocity of  $i$  mass before the impact.

In the previous expression  $k_r$  represents coefficient of restitution or coefficient of the impact by which elastic traits of the objects are analyzed. The value

expression (23) for the stroke  $x=2\Delta l$ . In the end of the second period of collision, the force reaches its maximum- $F_{max}$ . The result of this force will be determined with equalization of the surface of the diagram (Figure 3), that represents the work of forces on the certain path and the energy of the impact.

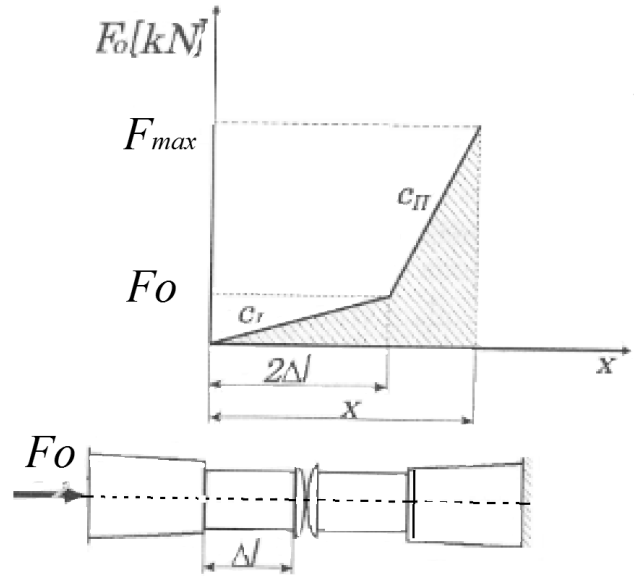


Figure 3. Work of forces in the wagon collision [7]

of the restitution coefficient is defined experimentally for different materials. The loss of energy is equal to zero in the impact of perfect elastic objects, and then it is  $k_r=1$ . In the collision of ideally plastic objects it is  $k_r=0$ .

Using the expression for the velocity of the centre of masses, the equation (16), you get:

$$k_r = \frac{m_1(v_1 - v'_1) + m_2(v_2 - v'_2)}{m_2(v_1 - v_2)}, \text{ or} \quad (30)$$

$$k_r = \frac{m_1(v_2 - v_1) + m_2(v_2 - v'_2)}{m_2(v_1 - v_2)}$$

The previous expression can calculate restitution coefficient for the each impact under known initial and final speeds of the given objects, under the condition that there is no relative shift of the weight over the wagon construction during the collision. Experimental research shows that restitution coefficient depends on elastic traits and shapes of object that collide, and it is said in general that restitution coefficient is a function:

$$k_r = f \left\{ \begin{array}{l} \text{elastic traits and shapes of objects, masses } (m_i) \text{ and} \\ \text{velocity of object } (v_i) \text{ in collision} \end{array} \right\}$$

Using equations (30), with the well-known value of the restitution coefficient it is possible to determine speed of the wagons after collision:

$$v'_1 = v_1 - (1 + k_r) \frac{m_2}{m_1 + m_2} (v_1 - v_2),$$

$$v'_2 = v_2 + (1 + k_r) \frac{m_2}{m_1 + m_2} (v_1 - v_2) \quad (31)$$

### 5. LOSS OF KINETIC ENERGY IN THE COLLISION

In these examinations we will limit ourselves to the case of collision of two wagons, when there is no relative shift of the load to the construction of wagon. If we mark with  $E_{k0}$  kinetic energy of two wagons before

$$E_i = \Delta E_k = E_{k0} - E_k = \frac{1}{2}[m_1(v_1^2 - v_1'^2) + m_2(v_2^2 - v_2'^2)] \quad (32)$$

Changing the expression for the velocity of wagon after collision (31) in the previous equation and arranging it, you will get that the loss of kinetic energy in the collision equals to:

$$E_i = (1 - k_r^2) \frac{m_1 m_2 (v_1 - v_2)^2}{2(m_1 + m_2)} \quad (33)$$

This expression represents the complete Karnot theorem which says that the loss of kinetic energy in straight central non-elastic collision of two objects is equal to kinetic energy the system would have if it was moving in lost speed[3].

In the first period of collision, the lost energy is marked with  $E_{i,l}$ , and for it, we have coefficient of restitution  $k_{r,l}$ . This coefficient changes with the increase of collision speed.

If we know the coefficient of restitution, it is easy to determine the value of the lost energy, and with its maximum force value created in the collision. This is important for the further dynamic estimate of wagon.

Coefficient of restitution can be determined another way, using results that are given experimentally.

Intensity of force on the buffers, in the collision, changes from zero to maximum in the very short period of time, and then, under a certain law, it comes back to zero. If the time interval of how much the collision lasts is  $\tau$ , the impact impuls will be equal to:

$$\vec{I} = \int_{t_0}^{t_0+\tau} \vec{F}_0 dt \quad (34)$$

The impact impuls  $I$ , for the time interval  $\tau \rightarrow 0$  will be final number.

The change in quantity of moving the bodies during collision is equal to impact impulse, and in case of collision of more than one object it can be written like this:

$$\sum_{i=1}^n m_i \vec{v}'_i - \sum_{i=1}^n m_i \vec{v}_i = \sum_{i=1}^n \vec{I}_i \quad (35)$$

here:

$\sum_{i=1}^n m_i \vec{v}'_i$  - quantity of moving of material system in the end of impact,

$\sum_{i=1}^n m_i \vec{v}_i$  - of material system in the beginning of impact,

And we get:

$$\vec{K} - \vec{K}' = \sum_{i=1}^n \vec{I}_i \quad (36)$$

Using equations (30) and Law of changing the quantity of material system in collision, coefficient of restitution can be defined in another way. If we have  $I_r$  for force impulse for the unload period, and  $I_o$  for the load of construction, we will have:

$$\vec{I}_r = m_1(\vec{v}_{cm} - \vec{v}'_1) = m_2(\vec{v}'_2 - \vec{v}_{cm}) \quad (37)$$

collision, with  $E_k$  kinetic energy after collision, and loss of kinetic energy is  $\Delta E_k = E_i = E_{OSC}$  under straight, non-elastic collision of two wagons, when there is no relative shift of the load, will be equal to:

and coefficient of restitution is equal to relation of two impulses:

$$k_r = \frac{I_r}{I_o} \quad (38)$$

On the Figure 4, you can see the change of force in buffers in the time of the collision.

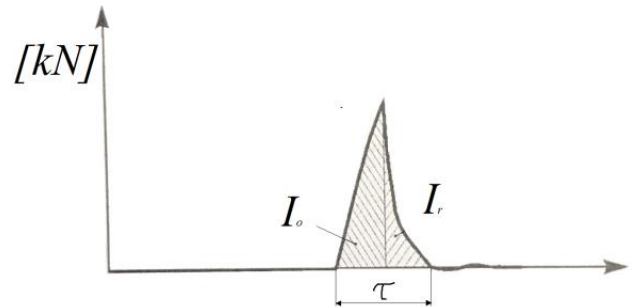


Figure 4. Change of force in buffers during time in the impact of wagons[7]

Impulses  $I_o$  and  $I_r$  are equal to the appropriate surfaces on the diagram (Figure 4). Experimental assessment diagram of impulse force in the function of time, as well as the appropriate surfaces in the exact testing of wagons, is done and it is given by professor Petrović [7]

### CONCLUSION

The basis of dynamic research of collision of two wagons represents determining of longitudinal oscillations and the coefficient of restitution.

In today's experimental studies of wagons, which are defined by international regulations of UIC and the recommendations of ERRI, not enough attention was given to estimating the coefficient of restitution. Namely, in those regulations the way how to load and the type of load on the wagons (for the experiment) are defined up to a point, but they do not give the value of the restitution coefficient is allowed to be for a certain type of wagon.

Coefficient of restitution is in the function of the speed of collision, outside of experiments become irregular. Of course, this would take vast research on all the types of wagons and systematizing of the given results.

### REFERENCES

- [1] С. Вершинский, В. Данилов, Н. Челноков, *Динамика вагона*, Издательство „Транспорт“, Москва 1978.
- [2] N. Goldsmith, *Impact, Theory and physical behaviour of colliding solids*, London 1965.
- [3] В. Лазарян, *Динамика вагонов- Устойчивость движения и колебания*, Издательство „Транспорт“, Москва 1964
- [4] L. Rusov, *Mehanika - Dinamika*, Naučna knjiga, Beograd, 1975.

[5] А. Смехов, и др., *Грузоведение, сохранность и крепление грузов*, „Транспорт“, Москва 1989.

[6] V. Rakanovic, *Dinamičko ponašanje šinskih vozila pri programiranom sudaru*, Doktorska disertacija, Mašinski fakultet Beograd, 1981.

[7] D. Petrović, "Dinamika sudara vagona", Zadužbina Andrejević, Beograd, Srbija 2001.

# **SESSION F**

## **THERMAL TECHNIQUE AND ENVIRONMENT PROTECTION**



# The importance and benefit of the energy management standard implementation

Andjela Lazarevic<sup>1\*</sup>, Ivana Marinovic Matovic<sup>2</sup>

<sup>1</sup> Faculty of Mechanical Engineering, University of Nis (Serbia)

<sup>2</sup> Glenfield Training and Consulting, Belgrade (Serbia)

*Although certification to ISO 50001 standard can contribute to companies' social responsibility visibility, the solely implementation of energy management system in accordance to this standard could be performed only for the benefits it provides. Energy management system requirements for an organization lead toward better understanding of its purpose, support setting targets and objectives, and the development of sustainable approach to the efficient use of energy, establishing and enhancing contribution of all organizational levels. This paper investigates how methodology developed and introduced under this standard contributes to the energy efficiency improvements in organization. The precondition is the commitment of the top level management in organization, that should enable organization to recognize risk and opportunities in its energy performance, support identification of measures and actions in energy management plans and contribute to the overall improvement of its organizational energy performance. If the expected results are effective and measurable, the plan-do-check-act framework proposed by ISO standards will provide continuous, effective, data-driven energy efficiency improvement.*

**Keywords:** Energy Management System, ISO 50001 standard, Energy efficiency

## 1. INTRODUCTION

One of the preconditions for EU accession is the alignment of Serbian legislation with EU legislation. In the scope of organizational, legal and political reforms in different sectors in Serbia, energy sector is subject to very intense changes. The awareness of efficient and rational use of energy was increased during past decade, while the establishment of energy management systems was considered as crucial to the long-term, responsible behaviour toward the environment. To contribute this objective, the Law on energy efficiency and rational use of energy [1] provided the introduction and implementation of the energy management system in Serbia, defining main actors in this system, as well as their responsibilities and obligations, and scope of their activities and competences. The activities and regulatory, technical, organizational measures set by this Law contribute to the energy efficiency objectives which belong to the wider range of energy policy objectives. The establishment of the energy management system was also recognized by the Energy Sector Development Strategy of the Republic of Serbia until 2025, with projections until 2030 [2] as a strategic direction of actions, within the strategic priority of energy efficiency increasing in all consumption sectors. Also, within this strategic direction, the implementation of energy management system in public sector was conceived as the priority activity.

In accordance with the Law on energy efficiency and rational use of energy, the subjects of the energy management system are: the Government of the Republic of Serbia, Ministry on charge for the energy issues, designated parties of the energy management system, energy managers and energy auditors.

The introduction and implementation of the energy management system is obligatory for designated parties including: companies whose dominant economic activity is production, if they consume more energy than the

quantity prescribed by the Government, companies whose dominant economic activity is trade and services, if they consume more energy than the quantity prescribed by the Government, bodies of local self-government and cities/municipalities with populations exceeding 20,000 and bodies of the state governance, other bodies and organizations of the Republic of Serbia, bodies and organizations of the autonomous province and organization of the obligatory social insurance.

The Law on energy efficiency and rational use of energy is a result of alignment procedure of Serbian legislation in the energy sector with EU directives. The energy audit as a measure of energy performance, and the establishment of energy management systems in EU legislation was primary prescribed in the Energy Services Directive [3]. However, under Energy Efficiency Directive [4] the obligatory nature of energy audits is stronger, especially in a case of larger enterprises, where the undertaking of energy audits is compulsory. This paper highlights the importance of energy management systems for energy savings, explores how it fits within the existing strategic and regulatory framework in Serbia and interrelates with EU legislation and guidelines. Finally, this paper investigates how methodology developed and introduced under ISO standard for energy management system contributes to the energy efficiency improvements in the organization, since this standard is also recognized by Energy Efficiency Directive as a useful tool to undertake energy audits and monitor energy performance.

## 2. EUROPEAN UNION AND ENERGY UNION – PERSPECTIVES FOR THE FUTURE

The EU set and regularly update comprehensive framework to manage its energy policy, taking into account its long-term perspectives and reflecting new circumstances in the energy sector. In this scope, each Member State is recognized by its own specificities: different energy mixes, economic wealth and capacity to

\* Corresponding author: Andjela Lazarevic: Aleksandra Medvedeva 14, 18.000 Nis and andjela.lazarevic@gmail.com

act, having different contribution to the EU's energy policy targets in the field of greenhouse gases emission reductions, promotion of renewable energy and energy savings. Although the energy regulation was set to be common for all Member States at the European level, until 2015, it could not be said that an integrated energy market produced the expected effects. European energy security strategy from 2014 [5] stated that EU imports 53% of its energy consumption, which makes it the largest energy importer in the world. The import dependency related almost 90% to crude oil, 66 % to natural gas, 42% to solid fuels and 40 % to nuclear fuel.

When in 2015 concerns were raised about the existence of inconsistencies between national energy regulatory frameworks of individual Member States and energy rules set at the European level, EU wanted to reset its energy policy in the right direction – all ideas, thoughts and beliefs were focused on the establishment of Energy Union, as an effective way to support sustainable, low-carbon and climate-friendly economy, designed to last. Therefore, the Energy Union was founded out of the EU effort to build the resilience to all energy supplies shocks

and disruptions and to reduce dependences on particular suppliers, fuels and energy routes (avoiding supply-side approach). They also realized that the way of communicating energy priorities and possibilities to each energy consumer need to be changed in order to create flexibility to manage the energy demand, so that the consumers can have a control over their energy costs and the choice of the energy suppliers [6].

Energy Union relies on the Energy Security Strategy [5] and has five "closely related and mutually reinforcing dimensions", that are designed to bring greater energy security, sustainability and competitiveness [6]: energy security, solidarity and trust; fully integrated energy market; energy efficiency contributing to moderation of demand; decarbonizing the economy and research innovation and competitiveness. Figure 1 summarize the objectives and interconnections of these five dimensions. It could be observed that Energy Union mostly relies on the documentation and events that happened in 2014 and 2015. The most important event was Paris climate conference (COP21) in December 2015.

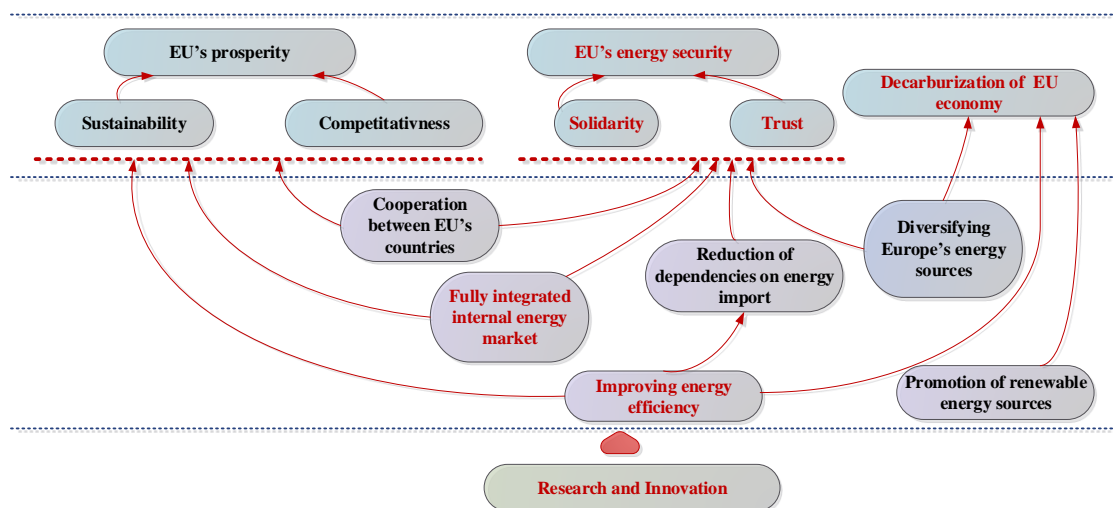


Figure 1: Structured dimensions and objectives of the Energy Union

In previous decades, EU also faced challenges related to the climate change and environmental protection, especially related to the energy demand and supply. Therefore, one of the EU priorities for next five years is to become the first climate-neutral continent, meaning that reach net zero greenhouse gas emissions by 2050, while remaining and economic growth by efficient use of resources, restoring biodiversity, protecting ecosystems and cut pollution. This objective was set in line with the objectives from the legally binding international treaty on climate change - Paris Agreement, taking into account its importance for setting a global framework to avoid dangerous climate change by limiting global warming below 2 °C [7]. Reaching climate neutrality implies serious transformations of the economy, encompassing its recoupling from resource use, adjustments of all relevant EU legislation and policies and significant public and private investments. The most important instrument to reach this optimistic target is European Climate Law [8], which established a framework

for irreversible and gradual reduction of greenhouse gasses. This regulation is also consistent with the Regulation on the Governance of the Energy Union and it builds the monitoring and reporting process on the ones included in the Energy union regulation, reducing the administrative burden of the Member States.

The response to the newest concerns related to the climate and environmental-related challenges (atmosphere warming, climate changes, many species under risk of being lost, oceans and forests pollution and destruction etc.) is the European Green Deal, which is a new growth strategy that should lead EU's economy transformation toward sustainable future: fair and prosperous society, modern, resource-efficient and competitive economy, and economic growth decoupled from resource use [9].

### 3. ENERGY POLICY AND POLICY ON ENERGY EFFICIENCY AND RATIONAL USE OF ENERGY IN SERBIA

Serbia, together with other five Western Balkans countries, is in the process of accession to the EU, which implies the acceptance of EU's values, requirements and standards, especially in terms of its legislation alignments with the EU legislation and to use its best practices, especially of the countries with transitional economies.

The first Energy Law in Serbia was adopted by the Parliament of the Republic of Serbia in 2004. Currently actual Energy Law was adopted in 2014, and it already passed many changes so far. However, the objectives of the Serbian energy policy and method of its implementation, as prescribed by this law, did not change. Further on, the details of the national energy policy are implemented through three basic documents: Energy Sector Development Strategy of the Republic of Serbia until 2025, with projections until 2030 [2], Program for Realization of Energy Sector Development Strategy of the Republic of Serbia until 2025, with projections until 2030 for the period from 2017 to 2023 [10] and Energy Balance (to be prepared and adopted each year) [11].

Energy law determined energy policy objectives, taking into account the potential impact of some energy policy options. Similarly, as with the EU's energy priorities and objectives, the objectives of the Serbian energy policy could be grouped into three priority areas: security of supply, environmental protection and economic competitiveness. Figure 2 visualizes the energy policy objectives with respect to this grouping. The top objective is the promotion of environmental protection, while it is followed by the objective which relates to the reliable, safe and quality energy supply. Other energy policy objectives should contribute to this objective, and through this objective to the environmental protection. The graphical representations of the energy policy objectives should be considered only as a mosaic part, whose approach is in close interrelationship with other state policy areas. Comparing EU's and Serbian documents related to the energy policy, it could be concluded that the economy is dominant subject in all issues related to the environmental protection and provision of security of energy supply, tailored to the EU's energy consumers while the objectives of Serbian energy policy are more generic.

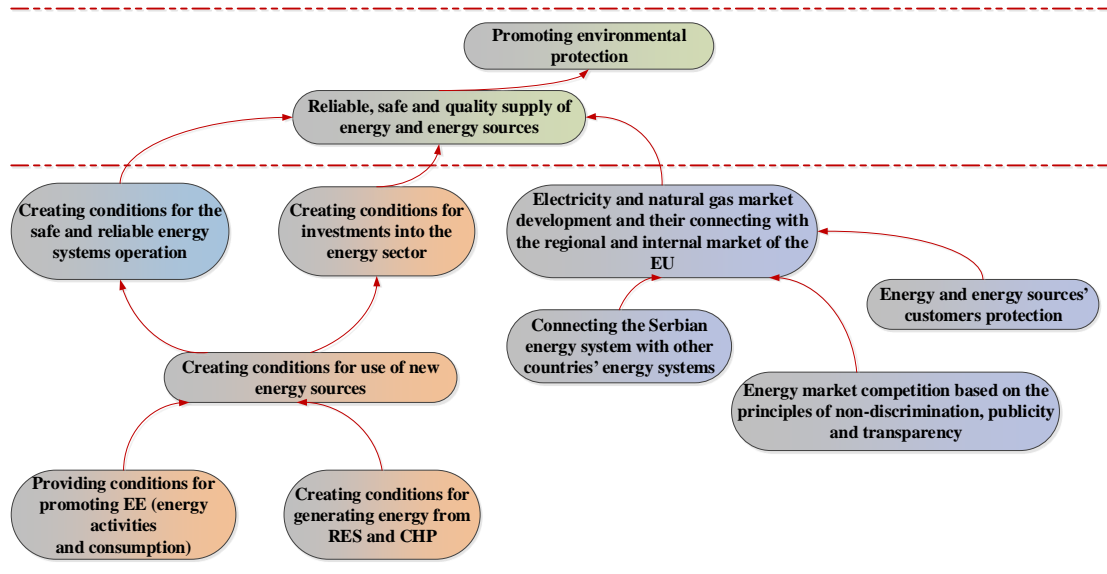


Figure 2: Energy policy objectives

Law on efficient energy and rational use of energy [1] was adopted early this year regulating the conditions and manners of efficient energy-use in different production and consumption sectors, efficient energy-use policy and energy management system, term that was for the first time introduced in the Serbian legislation in the previous Law on efficiency energy-use [12]. Figure 3 visualizes how the creation of conditions for the rational use of energy and improvement of energy efficiency, can be supported by the energy policy objectives. Basically, this should present how the rational use of energy and implementation of the energy efficiency objectives relate to the energy policy objectives. As it could be observed red-marked objectives are the objectives of the Law on efficient energy and rational use of energy and are very

general. This means that those objectives have been realized through the implementation of the lower level objectives, which are more specific. Comparing to the previous figure seven additional objectives occur: Security of energy supply, achieving of energy savings, sustainable use of natural and other resources, reducing energy poverty, reducing the impact of energy sector on environment and climate change, increasing economic competitiveness and improving conditions for economic development, each of them can be contributed by achieving one of the energy policy objectives. The representations at Figure 2 and 3 could be a base for identification of certain clear actions, targets and timeframes to meet these interlinked objectives.

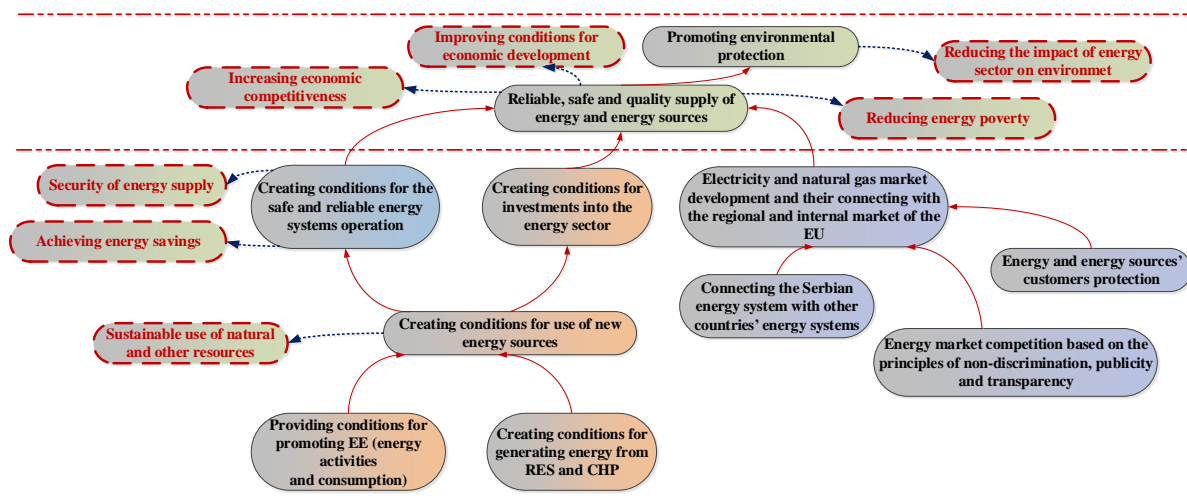


Figure 3: Efficient energy-use policy objectives

Law on efficient energy and rational use of energy was a result of alignment procedure of the Serbian legislation in the energy sector with EU rules and directives. Under the European Green Deal framework, new Energy Efficiency Directive is in preparation. However, the previous versions of this directive contained enough information about the energy management system, identifying energy audits as essential tool to achieve energy savings, by obtaining enough knowledge about the energy consumption of any subject under consideration, so that its energy saving opportunities could be quantified [4]. Each Member State was responsible to promote the availability of high quality and cost-effective energy audits to all final consumers, to determine minimum criteria for energy audit and to ensure compulsory and regular (every four years) audits for large enterprises fulfilling these minimum criteria. They were also obliged to ensure the development of programs to encourage energy audit in those organizations where it was not mandatory, such as small and medium enterprises, as well as to raise awareness among households about the benefits of energy audit, in order to enable as much as possible energy savings through energy management system [13].

Under the Energy Efficiency Directive, there is Annex VI which represent a basis for establishment of transparent and non-discriminatory minimum criteria for energy audits, including those carried out as part of energy management systems [14]. The requirements set into this Annex VI are "not more far reaching than the requirements of the relevant European or International Standards" [13]. Among others, standard EN ISO 50001 was named as standard that can provide guidelines in developing national minimum criteria for energy audits on the basis of Annex VI. Also, the large enterprises are exempted from the obligation to carry out regular energy audits if they are implementing and have formalized energy and/or environmental management system certified by an independent accreditation body according to the relevant ISO standard.

#### 4. ENERGY MANAGEMENT SYSTEM IN ISO STANDARDS

Many International Organization for Standardization (ISO) standards are aimed to support

organizations in managing various performances, defined as measurable values. Among others, there is environmental performance, asset performance, quality performance and finally energy performance that is subject of this study.

The standard EN ISO 50001:2018 Energy Management System – Requirements with Guideline for Use, has been developed and prepared by ISO Technical Committees, and it superseded the standard EN ISO 50001:2011. In Serbia, Institute for Standardization of Serbia (ISS) is in charge of the standardization process at national level. Therefore, in our country, this international standard was adopted as SRPS EN ISO 50001:2018, without any modification comparing to the original one. This Standard specifies the energy management system requirements for any organization, regardless of its type, size, complexity, or products or services it provides. What is more important, this standard is applicable to any organization, regardless type and quantity of energy consumed. The most important issue related to the implementation of standard EN ISO 50001:2018 is the commitment of all actors and levels of the organization, especially in supporting energy performance improvements. The commitment of top management is certainly essential, since it establishes energy policy, and delegate the responsibilities and authorities for relevant roles to the members that are assigned to the energy management team.

The structure of this standard is mostly the same as other standards related to the different management systems: environmental, quality, information security, business continuity etc. (context of the organization, leadership, planning, support, operation, performance evaluation and improvement). Also, like in other management systems this standard follows the "Plan-Do-Check-Act" process for continual improvement, which makes incorporation of energy management into existing systems easier. Therefore, this standard can be applied independently or as an integrated management system.

According to EN ISO 50001:2018, energy management system represents useful management tool that helps organizations to better manage its energy consumption, improving the productivity. Energy Efficiency Directive also defines energy management

system as a set of interrelated or interacting elements of a plan which sets an energy efficiency objective and a strategy to achieve that objective. Standard EN ISO 50001:2018 provides a framework to manage and improve their energy performance, providing guidelines for establishing, implementing, maintaining and improving an energy management system. Similarly, as at the state and local level, the introduction and implementation of the energy management system in any entity and organization begins with energy policy determination, defining its objectives and directions to achieve these objectives, establishing a system for monitoring energy performance, and implementing procedures for a continuous improvement of the energy performance [15,16]

As with other ISO standards, EN ISO 50001:2018 standard does not consist of a specific energy performance measures related to energy consumption and energy performance. It sets final energy objectives and targets and enables organization to achieve them but does not provide the exact set of actions and measures on how to reach those energy objectives and targets. Each organization that is willing to certifies to EN ISO 50001:2018 applies its own manner to establish, implement, maintain and continually improve an energy management system. However, standard proposes a management model that contributes to the development and implementation of the energy policy in order to achieve the defined energy objectives and targets, taking into account legal requirements and information resulting from the analysis and energy consumption data [17]. It also requires a systematic, data-driven and facts-based process, focused on continually improving energy performance, an concept related to the energy efficiency, energy use and energy consumption [15].

## 5. CONCLUSION

The establishment of energy management system has many benefits for the organization in terms of optimizing its energy consumption, costs reduction and diminishing or mitigating negative impact on the environment. It can also improve the image of one organization and contribute to increase its corporate responsibility.

The importance of energy management system is well recognized and wide accepted as useful tool (instrument) that can significantly contribute to the energy savings and environmental protection. This can be confirmed also by the status that ISO and other standards have in Energy Efficiency Directive and other EU's Directives related to the energy savings.

In the context of standard application and usage for the development of national minimum criteria for energy audits, as prescribed by Annex VI of Energy Efficiency Directive, it could be said that standard EN ISO 50001:2018 represents useful guidance for the definition of the scope and level of detail of an energy audit. Also this standard may provide useful guidance for the planning the audit, proposing the content of the audit report, ways to collect data, specific checklists to evaluate actual energy performance, typical energy and financial saving opportunities etc.

Although the energy management system does not have to be established for the certification purposes, the

application of the management model and energy management methodology set by EN ISO 50001:2018 has multiple benefits for the organization and its energy performance. It leads organization to save money by using energy as efficient as possible, while protecting the environment and reducing greenhouse gases by improving energy performance and providing energy savings. This is the reason why the application of this standard methodology itself, significantly contributes to the organization energy performance regardless of whether the organization is certified to EN ISO 50001:2018. If the organization decide to certify to EN ISO 50001:2018, it needs to carefully consider the business benefits of this process and the total cost of the energy management system establishment and maintenance.

Another ISO standards can be useful for the energy management system operation lifetime: EN ISO 50002:2014 Energy audits — Requirements with guidance for use, defines minimum set of requirements leading to the identification of opportunities for energy performance improvements. Practical guidelines for the implementation of the energy management system requirements are prescribed by EN ISO 50004:2020 Energy Management System - Guidance for the implementation, maintenance and improvement of an ISO 50001 energy management system.

## REFERENCES

- [1] Law on Energy Efficiency and Rational Use of Energy, Official Gazette for the Republic of Serbia, No. 40/2021
- [2] Energy Sector Development Strategy of the Republic of Serbia until 2025, with projections until 2030, Official Gazette for the Republic of Serbia, No. 101/2015
- [3] Directive 2006/32/EC of the European Parliament and of the Council of 5 April 2006 on energy end-use efficiency and energy services
- [4] Directive 2012/27/EC of the European Parliament and of the Council of 25 October 2012 on energy efficiency, amending Directives 2009/125/EC and 2010/30/EU and repealing Directives 2004/8/EC and 2006/32/EC
- [5] European Energy Security Strategy, COM (2014) 330
- [6] A Framework Strategy for a Resilient Energy Union with a Forward-Looking Climate Change Policy, COM (2015) 080
- [7] Paris agreement to the United Nations Framework Convention on Climate Change, United Nations (2015)
- [8] European Climate Law, COM (2020) 80 final
- [9] The European Green Deal, COM (2019) 640 final
- [10] Program for Realization of Energy Sector Development Strategy of the Republic of Serbia until 2025, with projections until 2030 for the period from 2017 to 2023
- [11] Energy Law, Official Gazette for the Republic of Serbia, No. 145/2014, 95/2018 – other law, and 40/2021
- [12] Law on Efficiency Energy-Use, Official Gazette for the Republic of Serbia, No. 25/2013, and 40/2021 – other law)

[13] Guidance note on Directive 2012/27/EU on energy efficiency, amending Directives 2009/125/EC and 2010/30/EC, and repealing Directives 2004/8/EC and 2006/32/EC, Article 8: Energy audits and energy management systems, SWD (2013) 447 final

[14] Guidance note on Directive 2012/27/EU on energy efficiency, amending Directives 2009/125/EC and 2010/30/EC, and repealing Directives 2004/8/EC and 2006/32/EC, Annex VI "Minimum criteria for energy audits including those carried out as part of energy management systems"

[15] ISO 50001:2018. (2018). Energy Management Systems – Requirements with Guideline for Use. International Organization for Standardization. Geneva.

[16] M. Rajic, R. Maksimovic, P. Milosavljevic and D. Pavlovic, "Energy management system application for sustainable development in wood industry enterprises," Sustainability, Vol. 12, Issue 1, (2019), doi:10.3390/su12010076

[17] M. Rajic, R. Maksimovic, P. Milosavljevic and D. Pavlovic, "Energy Management System Application in Healthcare", Proceedings on "15th International Conference on Accomplishments in Mechanical and Industrial Engineering", Banja Luka, 28–29 May 2021, (2021)

# Some Aspects of the Implementation of Actions Plans for Noise Prevention and Reduction in Urban Areas

Vasile Bacria<sup>1</sup>, Nicolae Herisanu<sup>1\*</sup>

<sup>1</sup>Faculty of Mechanics/Department of Mechanics and Strength of Materials, University Politehnica Timisoara, Timisoara (Romania)

*Following the analysis of noise maps for road, rail and industrial traffic on Lden and Ln as well as the corresponding conflict maps, action plans were prepared to prevent and reduce noise in the mentioned areas of the urban environment. They set out the measures to be taken, the completion dates and the number of people benefiting from the noise reduction. Measures to reduce urban noise have also been established for the long-term strategy. These were performed with an application to the Timișoara city. Subsequently, the administrative bodies of the municipality proceeded to implement the measures provided in the action plans. The paper refers to some considerations on their implementation highlighting the resulting effects.*

**Keywords: Noise protection, Action plans, Noise reduction**

## 1. INTRODUCTION

The main sources of noise in the urban environment are the means of transport participating in the naval, air, rail, road traffic and industrial activities. The noise generated by these sources affect the life and health of members of the urban community. In this sense, research on noise and vibration pollution produced by road traffic has been carried out in Timisoara since 1996 [5]. On the other hand, the European Parliament and the Council of the European Union, of which Romania is a member, are concerned with ensuring a high level of health and environmental protection for the inhabitants of all Union countries, and Directive 2002/49/EC was adopted on 25 June 2002 [6], its main task being to create a common basis for all European Union states for the urban management of environmental noise.

Some important aspects are provided, among which:

a) Monitoring environmental issues by involving the competent authorities of the member states in the creation of strategic noise maps for roads, railways, airports, industrial areas and important agglomerations using harmonized noise indicators Lden and Ln. These maps will be used to assess the number of people affected by noise throughout the European Union

b) Informing and consulting the public on exposure to noise, its effects and the measures that can be taken to combat it.

c) Development of noise management action plans to prevent and reduce environmental noise in order to protect human health and conserve quiet areas

d) Ensuring the effective participation of the authorities in the whole process of planning activities. In this regard, all Member States of the European Union have been concerned with the development by 30 June 2007 of strategic noise maps for all urban areas with more than 250000 inhabitants and for all major areas with more than 6 million vehicles in traffic per year, major railways with

over 60000 trains in traffic per year and major airports located on their territory.

On the basis of the noise maps drawn up by 18 July 2008, the competent bodies drew up the action plans on noise prevention and reduction in the city of Timișoara, for which the acoustic map was drawn up [10]. According to Directive 2002/49/EC, the strategic noise map and action plans on the prevention and reduction of ambient noise for those agglomerations must be reviewed every 5 years. For the city of Timișoara, the strategic noise and conflict map were updated in 2013 [14]. Following the analysis of these acoustic maps, the authors of this paper have drawn up action plans on preventing and reducing environmental noise in Timisoara.

The action plans have been drawn up on the basis of the requirements of Directive 2002/49/EC [6]. In this sense, we will illustrate the reflection of these requirements in the action plans prepared for the city of Timișoara, presenting considerations on their implementation and highlighting the resulting effects.

## 2. INFORMATION OBTAINED BY NOISE MAPPING

The authority responsible for the implementation of noise mapping and action plans for the prevention and reduction of ambient noise in the city of Timișoara is the City Hall. Timișoara is the residence of Timiș County, the largest city in western Romania, a very important economic, historical, social and cultural centre covering an area of 130 square km and having on January 1, 2020 a population of 306466 inhabitants. Also, Timisoara is a strong economic and industrial pole of the country, being crossed by the main national and European roads and railways, with an international airport. The strategic noise map and the action plans for the prevention and reduction of noise in urban areas, specifically in the city of Timișoara, were prepared taking into account all legislative regulations contained in the following normative acts: H.G. 321/2005 republished on environmental noise assessment and management; O.M.

\*Corresponding author: <Bd.M.Viteazu, no.1, Timisoara, Romania> and <nicolae.herisanu@upt.ro>

no. 1830/2007 on the approval of the guide on the development, analysis and evaluation of strategic noise maps; O.M. 152/558/1119/532/2008 for the approval of the guide on the adoption of limit values and their application when drawing up action plans for the  $L_{den}$  and  $L_n$  indicators for road, rail and air traffic noise and noise of industrial activities.

The indicators  $L_{den}$  and  $L_n$  are used to characterize the permissible limit values of ambient noise. The  $L_{den}$  indicator is defined by

$$L_{den} = 10 \lg \frac{1}{24} \left[ 12 \cdot 10^{\frac{L_d}{10}} + 4 \cdot 10^{\frac{L_{e+5}}{10}} + 8 \cdot 10^{\frac{L_{n+10}}{10}} \right] \quad (1)$$

where  $L_d$  is the long-term noise existing on a 12-hour day during a year between 07.00-19.00,  $L_e$  is the long-term noise level measured in a four-hour evening during a year between 19.00- 23.00,  $L_n$  is the long-term noise level for an 8-hour night between 23.00 and 7.00.

Based on the order of the Minister of Environment and Sustainable Development number 152/13.02.2008, the maximum allowed values for the indicators  $L_{den}$  and  $L_n$  target values to be reached are those presented in table 1.

Table 1: Admissible limits for noise indicators

| Lden [dB(A)]    |        |            | Ln [dB(A)]      |        |            |
|-----------------|--------|------------|-----------------|--------|------------|
| Source of noise | Target | Max. value | Source of noise | Target | Max. value |
| Roads           | 65     | 70         | Roads           | 50     | 60         |
| Railways        | 65     | 70         | Railways        | 50     | 60         |
| Airports        | 65     | 70         | Airports        | 50     | 60         |
| Industry        | 60     | 65         | Industry        | 50     | 55         |

For the elaboration of the action plans were used the data highlighted by the strategic noise maps and conflict maps prepared in 2013 regarding the noise produced by road traffic, rail traffic (train, tram), air traffic and industrial activities, all in  $L_{den}$  and  $L_n$  regime. [14]. The analysis of these data showed that there were a number of 24294 people exposed to noise above the allowable limit of 65 dB for the  $L_z$  indicator, respectively 45562 people exposed to a level of over 50 dB for the  $L_n$  indicator due to road traffic, five people exposed to noise level above the limit of 65 dB for the  $L_{den}$  indicator and 535 persons exposed at the level of over 50 dB for the  $L_n$  indicator due to rail traffic (tram), as well as 10 people exposed to the noise level above the limit of 60 dB for the  $L_{den}$  indicator, respectively 99 people exposed to noise level over 50 dB for the  $L_n$  indicator due to industrial activities.

It also turned out that there are no people exposed to a noise level above the 65 dB limit for  $L_{den}$  and over 50 dB for  $L_n$  due to rail traffic (tram) and air traffic. At the same time, the arteries of road traffic with the most pronounced impact on the exposure of the population to noise were identified. Thus, on 24 of them, the  $L_{den}$  noise level exceeded 70 dB, on 29 it reached 70-75 dB, and on 19 it reached values of 65-70 dB. From the presented data results that the noise pollution in Timișoara city was in a relatively good situation. This is also due to the fact that the local administration has been concerned with reducing noise in the city since 1996, when based on research contracts he collaborated with the research team in the department of mechanics and vibrations at the Faculty of

Mechanics of the Polytechnic University of Timișoara (a group that includes the authors of the paper) in the issue of identifying noise sources on the territory of the city and reducing its level. In this sense, since 2006 the research team has prepared by measurements the first noise map of Timișoara, this having priority character in Romania.

According to Directive 2002/49/EC [6], action plans must be drawn up with the participation of the public and the public should be informed on their implementation. For this, in the first phase the public opinion was consulted through a questionnaire that was filled in individually by various persons residing in the city of Timișoara, including questions related to the position of housing in relation to the traffic artery, if disturbed by street noise, whether the noise affected his health and in what way, as well as proposals to reduce the noise produced by means of transport and other sources. From the synthesis of the answers, one obtained the following:

- 72.4% of dwellings are located in the front area and 27.6% in screened buildings
- while traveling in the city, 34.5% of Timișoara residents are disturbed, 24.1% in homes, 34.5% in the city and housing and 6.9% are disturbed
- the noise affected the health of 17.2% of those surveyed, causing them a state of stress and headache.

The respondents made proposals to reduce the noise produced by means of transport and other sources in the urban environment. Among these:

- public transport should be made free of charge, to discourage individual transport
- construction of city bypasses
- elimination of heavy vehicles from urban traffic
- reducing traffic intensity
- construction of noise-proof panels and manufacture of absorbent asphalt
- creation of green areas consisting of ornamental trees
- the purchase of new, quiet means of public transport

These proposals, together with the data resulting from the elaboration of the strategic noise and conflict maps were used for the elaboration of the action plans, which for the information of the inhabitants were posted on the official website of the Timișoara City Hall ensuring the conditions to appear also observations of public opinion.

It should be mentioned that prior to drawing up the action plans, the local administration of Timișoara being concerned with reducing noise in the city since 1996, implemented some reduction measures such as: restoring the infrastructure and superstructure of the tramway on a large part of it, largely improving the road traffic in the city and modernizing the intersections, equipping the public transport base with quieter means of transport, limiting the speed on certain traffic arteries and using speed bumps, limiting the access of large vehicles in the central area, restricting the access of certain vehicles in some areas of the city, introducing one-way on some of the traffic arteries, streamlining traffic, making green protective curtains, making an antiphonal screen on one of the traffic arteries, investigating the absorbent effects of rubber asphalt in order to implement as a solution to reduce traffic noise, the construction of the bypass in the north-eastern part of the city, the encouragement and

support of the tenants for the use of thermal and sound insulation system, etc.

Following the values presented above, it results that although these measures have been implemented, there are still areas in the city where the permissible noise level limits mentioned in table 1 are exceeded. In this sense, it was necessary to identify and investigate the causes of this condition and to establish measures to normalize them.

### 3. NOISE GENERATING SOURCES IN URBAN AREAS

The state of noise pollution of the urban environment is due to the noise generated by urban, railway, air traffic and industrial activities. Each of them highlights specific sources.

At the means of road transport, the propulsion engine, the transmission system, the braking system, the running and the air resistance to advance generate noise. The resulting noise level depends on the composition and intensity of the traffic, the speed of the vehicles, their operating condition, as well as the nature and condition of the road.

For rail vehicles, the causes of noise are bumps, curves and road elasticity, play at the ends of the rails, jerking and braking, variations in speed, etc. In aircraft, the main sources of noise are internal combustion engines, propeller jet engines, turbo engines.

Noise and vibration in the means of shipping are generated by main and auxiliary engines, generators and electric motors, propellers, cooling pumps, oil, fuel, turbochargers, current converters, fans, wave blows, etc.

In the case of industrial activities, noises are produced by collision phenomena in the case of body interaction, friction on contact surfaces, aerodynamic turbulence, forced oscillations of solid bodies, the action of variable electromagnetic forces, vibration of membrane-shaped parts and pulsating pressure in hydrostatic operating installations during mechanical, electromagnetic, aerodynamic and hydrostatic processes.

The noise generated by these sources bothers a large part of the population. It is enough to have a noise with the equivalent level of 75 dB per day to disturb 80% of the population [4]. In addition, it causes damage to the human auditory organ and various organs and apparatus of the body. Noise is very harmful to the human nervous system producing psychophysiological changes, for blood circulation, produces sleep disorders, negatively affects the visual function and endocrine glands producing biochemical disorders.

Due to the noise, hearing fatigue, sound trauma and general fatigue of the body occur. Noise also has a negative influence on physical and intellectual work that requires a focus of attention, reduces work productivity and speech intelligibility [1], [2]. In order to prevent these harmful effects of noise, the characteristic noise indicators  $L_{den}$  and  $L_n$  must not exceed in the urban environment the values presented in Table 1. If values exceeding these permissible limits are obtained, then noise reduction methods must be established and implemented.

### 4. NOISE REDUCTION METHODS

In establishing the specific methods in this case, we start from the fact that measures can be taken to reduce noise directly at the source or on the transmission route. have a quiet operation, proper technical condition and correct handling. Taking into account that the noise is influenced by the number and nature of the sources, restrictions are indicated for the intensity and composition of the traffic as well as the reduction of the maximum speed limit of the vehicles. Some elements of detail that highlight how these parameters influence the level of noise generated by the means of transport participating in road traffic can be traced in [4].

To reduce running noise, one can use the replacement of ordinary asphalt with rubberized asphalt. This helps to reduce noise by 1 to 6 dB depending on the speed of the vehicles. A more pronounced reduction is made for sounds whose frequencies are in the bands with a centre frequency of 1 Hz and 2 Hz in the case of higher vehicle speeds [15]. As a significant contribution to the generation of a high-level noise in the urban environment has the means of transport in transit, it is necessary to eliminate their presence by building bypasses for the city.

The noise produced by trams can be actively reduced by ensuring their proper technical and functional condition as well as by creating paths according to advanced technologies, installing between the runway and sleepers an effective insulating layer and planting grass in the space between the lines. The noise level produced by the trams is also influenced by the way the driving manoeuvres are performed, which must be as appropriate as possible.

With regard to the reduction directly to the source of the noise produced by the means of railway transport, this can be achieved by ensuring the use of means with good technical condition running on roads in perfect condition, they must be checked permanently and the defects remedied.

The reduction of the noise produced by the industrial activities directly at the source implies the realization within each industrial unit of the diminution of the noise produced by the main machine parts, by the aggregates of the machine tools and industrial equipment and by the technological processes. Inside the industrial halls, the soundproofing of the workplaces, the rational location of the noise sources, their casing and shielding, as well as the acoustic arrangement of the interior of the halls must be performed. At the same time, a rational location of the industrial rooms inside the industrial units and of them within the urban complexes must be made.

To reduce the noise produced by cars, trams, trains, planes at airports and passive industrial activities in the urban environment, acoustic screens and protection areas (green areas) can be created between residential neighbourhoods and roads, airports and industrial units, as well as increasing the distances between them. Some elements of correlation between the geometric characteristics of acoustic screens, their positioning as well as the source and receiver and the attenuation achieved can be traced in [1], [2], [3], [4]. The methods presented in this

section can be used to choose solutions for drawing up action plans.

## 5. ACTION PLANS

Although measures were taken in the city of Timișoara to reduce the noise produced by road traffic before the adoption of the European Directive 2002/49/EC, the noise problem was still not solved. An important achievement is the construction of the bypass in the north-eastern part of the city. However, this must be continued with the construction of the bypass in the south-eastern part. In this way, the vehicles in transit would be eliminated from the urban traffic. At the same time, the development of urban traffic in Timișoara is greatly influenced by the street configuration of the city which is of radial ring type, better structured at north of the Bega canal and less outlined in the south, to which is added the fact that the city is crossed from east to west by the railway line. Outside the central area there is an insufficient number of crossings, which does not allow the closure of the ring links between the areas on either side of the two obstacles. This makes the existing bridges over the Bega, the underpass viaducts and the corrective traffic arteries very crowded. In fact, the Bega canal and the railway are the two important obstacles that affect the continuity of the road network due to the insufficient number of bridges and passages. This is proved by the values recorded by the indicators Lden and Ln on the 24 traffic arteries on which the first indicator exceeded 75 dB.

The configuration of the road network in Timișoara city presents some deficiencies in its structuring, the absence of collector arteries with four traffic lanes, as well as the inadequate capacity of some intersections and stationary traffic. The development of traffic in Timișoara can be done by building bypasses that would take over transit traffic, the development of public transport, parking networks, ensuring quiet means of transport, extending sidewalks in the central area, etc. The measures proposed to reduce the noise on the traffic arteries on which the limit values of the indicators Lden and Ln were exceeded were established in accordance with the traffic study for the city of Timișoara [13]. It contains the analysis of the current traffic, the elaboration of the proposals to improve the traffic and the plan of organization of the traffic. The traffic organization plan is identified by the road network plan, zoning, the graph associated with the major traffic network, traffic regulations, traffic light intersections, routes of transport lines, general orientation signalling, signalled routes for freight traffic and passengers and the classification of streets into categories.

This plan was improved in accordance with the traffic forecast and with the inclusion of the changes brought by the traffic regulations adopted by the Timișoara City Hall. In order to reduce the ambient noise, the strategic noise and conflict maps of the city of Timișoara corresponding to the indicators Lden and Ln were studied. After analysing these maps and taking into account the noise reduction methods in the urban environment presented above, 6 action plans for reducing road traffic noise, an action plan for reducing noise from rail traffic and an action plan to reduce noise generated by industrial activities were drawn up. They provided for:

- a) modernization of 4 intersections of traffic arteries
- b) location of acoustic screens between road traffic arteries and residential areas on 14 traffic arteries
- c) construction of the bypass in the southern part of the city
- d) opening of traffic ring 4 from the traffic organization plan in Timișoara city
- e) replacement of ordinary asphalt with rubberized asphalt on six traffic arteries
- f) creation of green protection areas between the traffic arteries and the blocks of flats on 60 traffic arteries
- g) implementation of the building envelope program and installation of soundproof doors and windows
- h) Location of acoustic screens between the train track and the blocks of flats in the area of three streets
- i) reduction of the noise level inside the industrial premises and on the transmission route from the arteries to the inhabited areas

Based on the estimates, it resulted that following the application of the elaborated action plans, 14459 people benefit from the reduction of the noise level in the regime of Lden and in the regime of Ln 18892 persons. The action plans also contained the delimitation of the quiet areas of the city as well as the actions that the authorities intend to undertake in the next five years.

## 6. ESTABLISHING A LONG-TERM STRATEGY

The action plans foreseen for a period of 5 years from the date of elaboration had to be complemented with the long-term strategy which includes the long-term vision of noise reduction. However, this requires good planning. Based on the noise maps prepared, the urban plans can be adjusted so as to ensure that no new buildings are built in areas with a high noise impact and no new industrial noise-generating units are located near residential or quiet areas. Also, the planning of activities for noise prevention and conservation of quiet areas is feasible to be drawn up in the long-term strategy point according to the development strategy "Vision Timisoara 2030 - support for the development of a sustainable concept for the infrastructure of Timisoara", developed by Timișoara City Hall in collaboration with the Polytechnic University of Timișoara and the Fraunhofer Stuttgart Institute considered that environmental aspects should be integrated into other areas as much as possible.

The Vision 2030 concept must ensure in the city of Timișoara and in its peri-urban area an integrated transport system with additional services and increased comfort. The conditions of solid connections with the surrounding areas will be created, respectively the premises of a sustainable economic and social development will be generated. Regarding the objectives of the projects provided in the long-term strategy, the noise reduction measures can be highlighted as follows: construction of a closed bypass of Timișoara, closure of road rings, construction of uneven traffic jams, construction of 5 bridges over the Bega canal, the development of the network for non-motorized transport, the application of a layer of rubber asphalt on a significant number of traffic

arteries in the penetration areas and inside the city of Timișoara, the installation of acoustic screens between traffic arteries and residential neighbourhoods, schools, hospitals, kindergartens, universities, further rehabilitation of traffic arteries, traffic flow obtained by traffic lights, one-way streets, new arteries, car and pedestrian walkways, establishment and increase of the density of alignment plantations, conservation and expansion of public green spaces and preserving the green character of existing areas individual targets, elimination of the surface railway transport line between Timișoara Nord and Timișoara Est stations, replacement of surface transport by underground by building metro lines with connections between important areas of the city, refurbishment and economic conversion for existing industrial areas, increasing competitiveness based on the promotion of new, creative and ecological industries, the realization of massive tree plantations in residential areas and residential neighbourhoods, the completion of the program of thermal rehabilitation and sound insulation of buildings by enveloping and installation of windows and soundproof doors, North Station arrangement, elimination of stationary traffic by creating underground and above-ground parking lots, redevelopment of the Bega canal, rehabilitation of tramway lines, replacement of new means of transport with the purchase of 100 trams and 100 electric buses, complex rehabilitation and modernization of all neighbourhoods at the level of roads, sidewalks, parking lots, bike lanes, green spaces, play trains, sports venues, construction of a new tram line between Gara de Nord and Children's Hospital, transformation of the Metropolitan Cathedral area into a pedestrian space by underpass, construction of new car passages and widening of existing ones, refurbishment of the traffic ring 1 and the construction of Traffic Rings 2, 3 and 4, the construction of two above-ground parking lots, the construction of a park of 5000 square meters, etc. Completion deadlines have been set for these objectives. At the same time, the local public authorities had to take care of preserving the quiet areas on the territory of the city by applying and extending the appropriate measures. It was estimated that by implementing the long-term strategy, 8349 people will benefit from the reduction of the noise level  $L_n$  and 15288 people will benefit from the reduction of the noise level  $L_{den}$ .

#### 7. CONSIDERATIONS REGARDING THE IMPLEMENTATION OF ACTION PLANS

After drawing up the action plans and the long-term strategy, the key issue was their implementation. In this sense, in order to reduce the noise produced by road traffic, four important intersections of traffic arteries located in the central area of Timișoara were rearranged, the South East belt of the city with a length of 27 km will be completed by the end of 2022, the usual asphalt was also replaced on a significant number of traffic arteries, the program of enveloping buildings and the installation of sound-absorbing doors and windows was continued, as well as the creation of green protection areas between traffic arteries and apartment blocks. In order to streamline the road traffic between the southern and northern part of Timișoara, over the Bega canal and the railway, crossing

passages and bridges were widened. In order to reduce the noise level produced by the means of transport, the pedestrian traffic was arranged, the use of bicycles and scooters by restoring the sidewalks on the side of the streets and especially the bicycle tracks. The creation of a green protection zone between the railway and the neighbouring inhabited areas contributes to their protection against the noise generated by the railway traffic. Regarding the noise generated by industrial activities to reduce the acoustic effects on people in inhabited buildings, it was ensured that the industrial units were not located near them, had an environmental permit, and green protection areas were planted between industrial and inhabited units.

In order to obtain a new quiet area, it started to implement noise reduction measures in the respective area: modernization of the neighbouring street, imposing speed restrictions, complementing the existing living degree with a curtain of vegetation in several steps. Given the condition and improper operation of a large number of trams and noise-generating buses, it was proceeded to purchase 100 new trams and 100 new electric buses to be received. In order to eliminate the stationary traffic, underground car parks have been built and two above-ground car parks are to be built. The Bega canal was redeveloped in order to capitalize on its naval potential, which will contribute to the decongestion of road and rail traffic and thus to the reduction of noise levels in urban areas. For a large number of streets, the one-way street was introduced, which allowed, in addition to a good organization of road traffic also obtaining parking spaces. The implementation of these measures contributes to reducing the level of urban noise, their efficiency will be highlighted by new measurements and experimental determinations in the near future.

#### REFERENCES

- [1] M. Grumăzescu, A. Stan and N. Wegener, "Combaterea zgomotului și vibrațiilor", Editura Tehnică, București (Romania), (1964)
- [2] E.Ia Iudin, "Izolarea împotriva zgomotului", Editura Tehnică, București (Romania), (1968)
- [3] \*\*\* Stadtbauliche Lärmfild. Hinweise für die Bauleitplanung, Baden Württemberg, Innenministerium, (Germany), (1991)
- [4] \*\*\* Lärmbekämpfung in Wien. Entwicklung Stand Tendenzen Magistratsabteilung 22 Umweltschutz
- [5] Gh. Sila, L. Brindeu, M. Toader, V. Bacria, N. Herisanu, M. Suci, "Cercetari privind poluarea prin zgomote și vibrații produse de traficul rutier în municipiul Timișoara", Ses. Comunicari de Acustica a Academiei Romane, Caiet 26, Bucuresti, (Romania), 15-16 October 1996, pp.81-84 (1996)
- [6] \*\*\* Directive 2002/49/EC of European Parliament and European Council
- [7] N. Herisanu, V. Bacria, M. Toader, S. Popa Radovan, "Investigation of noise pollution in an urban area", WSEAS Transaction on Systems, Vol. 7(5), pp.1648-1653, (2006)

- [8] N. Herisanu, V. Bacria, M. Toader, S. Popa Radovan, "Investigation and reduction of ambient noise in urban area", Proceedings of 7-th WSEAS Int. Conference on Acoustics. Theory and Applications, Cavtat, (Croatia), pp. 48-53, (2006)
- [9] V. Bacria, M. Toader, N. Herisanu, C. Opritescu, V. Ciupa, C. Fiat, "Considerations concerning noise attenuation in urban environment", Proceedings of the IX-th Symposium AVMS Timisoara (Romania), 31 May 2007, pp.7-12, (2007)
- [10] \*\*\* Harta strategica de zgomot a Timisoarei", Primaria Municipiului Timisoara, (2008)
- [11] \*\*\* Vision 2030 Timisoara metropola europeana, Ed. Brumar, (Romania), (2009)
- [12] V. Bacria and N. Herisanu, "Phonic attenuation due to screen barriers", Analele Univ. Resita, pp.35-42, (2011)
- [13] \*\*\* Studiu de circulatie pentru municipiul Timisoara", Primaria Timisoara, (2012)
- [14] \*\*\* Protocol privind actualizarea hartii strategice de zgomot a municipiului Timisoara", Primaria Timisoara, (2013)
- [15] N. Herisanu, V. Bacria, "The effect of rubberized asphalt on decreasing the phonic pollution", Appl. Mechanics and Materials, Vol. 430, pp.257-261, (2013)
- [16] V. Bacria, N. Herisanu, "Noise control in an industrial hall", Appl. Mechanics and Materials, Vol.430, pp. 251-256, (2013)
- [17] V. Bacria and N. Herisanu, "Action plans for noise prevention and reduction in the city of Timisoara", Facta Universitatis. Series Working and Living Environmental Protection, Vol.12(2), pp.139-149, (2015)

# Application of Biologically Inspired Algorithms for Determining the Coefficients of Empirical Models for Determining Sound Absorption

Kolarević Milan<sup>1</sup>, Radičević Branko<sup>1</sup>, Mišo Bjelić<sup>1</sup>, Tanja Miodragović<sup>1\*</sup>, Goran Miodragović<sup>2</sup>

<sup>1</sup>Faculty of Mechanical and Civil Engineering in Kraljevo, University of Kragujevac, Kraljevo (Serbia)

<sup>2</sup>Academy of Applied Study Šumadija, Department Trstenik, Trstenik (Serbia)

*The paper investigates the possibility of applying biologically inspired algorithms for determining the optimal values of the coefficients in known empirical models for acoustic impedance. To solve this problem, a gray wolf algorithm was used, for cases of infinite and deterministic search space. Using the gray wolf algorithm, new values of the coefficients in the empirical model for the impedance of foam materials were determined. The new model provides satisfactory predictions of the sound absorption coefficient of open-cell polyurethane foams, compared to the experimental results obtained in an impedance tube. Known empirical models for impedance in which the constants are determined by the method of linear regression, give slightly better predictions of the coefficient of sound absorption of polyurethane foams compared to the new model in which the constants are determined using the gray wolf algorithm. The presented method of determining the coefficients of empirical models for impedance provides a basis for the application of other biologically oriented algorithms, as well as for their hybridization.*

**Keywords:** Gray wolf algorithm, Empirical models for impedance, Sound absorption coefficient, Polyurethane foams

## 1. INTRODUCTION

Noise can affect human health, directly to the sense of hearing, but also to other organs, causing various symptoms and diseases. Due to the rapid industrialization and the fact that the standard of living in modern times is based on mechanization that directly affects noise pollution, noise is a hazard to human health. In order to improve the quality of life and protect the working and living environment, especially in densely populated areas, protection from noise and the struggle against its harmful effects is one of the main solutions.

The application of absorption materials is very useful in noise control, because they reduce noise by expanding the wavefront of sound energy and converting it into heat. Absorption materials are characterized by a sound absorption coefficient that defines the ability of a material to absorb and transform part of the energy of sound into another form of energy [1]. The sound absorption coefficient of porous materials depends on several parameters, and some of them are: sound frequency, porosity of the material, thickness of the material layer, resistance to air flow. The absorption coefficient is a useful concept when using geometrical acoustic theory, especially to evaluate the decline and growth of sound energy in a room [2]. When sound is considered as a wave, it is necessary to use the concept of acoustic impedance. The values of the absorption coefficient are usually in range from 0-1.

Empirical acoustic models in combination with measurement results are used to determine the dependence of absorption coefficients as a function of frequency and material thickness. To determine the coefficients in the empirical model for impedance, numerical methods can be used, such as the method of least squares or methods of statistical data processing, respectively regression analysis.

In this paper, the application of a biologically inspired algorithm is presented, namely the gray wolf

algorithm for determining the coefficients in the empirical model for acoustic impedance. The model for determining the characteristic acoustic impedance was performed on the basis of known dependences defined by Delany and Bazley [3]. The regression constants in this empirical model were determined in a new way, using a biologically inspired gray wolf algorithm. The accuracy of the new model was determined by comparing the predicted and experimental values for one type of polyurethane foam with open cells.

## 2. EMPIRICAL MODELS FOR DETERMINATION OF CHARACTERISTIC ACOUSTIC IMPEDANCE

Empirical models are commonly used to evaluate the acoustic properties of porous materials. Empirical models are used to estimate acoustic properties, namely complex propagation constants and characteristic impedances, using physical parameters or material properties.

The best known and one of the first empirical models is a Delany-Bazley model [4], for the determination of the acoustic impedance and the propagation coefficient of the fibrous absorption material. In this model, air flow resistivity is used as the only input parameter. The model is based on numerous impedance tube measurements and is good for determining the group of acoustic properties at frequencies higher than 250 Hz, but not at low frequencies [5].

Qunli [6] later verified the Delany-Bazley model, using a large amount of experimental data for plastic foams, which cover a wider range of longitudinal airflow resistance values. Following the Delany-Bazley model Dunn & Davern [7] calculated new values of regression constants for polyurethane foams.

Voronina [8] model is a simple model based on the porosity of the material. This model uses the average pore diameter, frequency and porosity of the material to define the acoustic characteristics of the material.

\*Corresponding author: Tanja Miodragović, Dositejeva 19, miodragovic.t@mfkv.kg.ac.rs

Empirical models are very useful because they use only one input parameter, flow resistivity, which is easily measurable. However, they are only suitable for one type of material and the certain frequency ranges.

### 2.1. MODEL FOR CHARACTERISTIC ACOUSTIC IMPEDANCE

In this paper, in order to prove the validity of the application of a biologically inspired algorithm to determine the characteristic acoustic impedance, the model defined by Delany-Bazley was used [3].

The dependencies in this model are given in the equations (1) – (4), [9].

$$Z_{CR} = \rho_0 c_0 \left[ 1 + C_1 \left( \frac{\sigma}{\rho_0 f} \right)^{C_2} \right] \quad (1)$$

$$Z_{CI} = -\rho_0 c_0 \left[ C_3 \left( \frac{\sigma}{\rho_0 f} \right)^{C_4} \right] \quad (2)$$

$$\alpha = \left( \frac{2\pi f}{c_0} \right) \left[ C_5 \left( \frac{\sigma}{\rho_0 f} \right)^{C_6} \right] \quad (3)$$

$$\beta = \left( \frac{2\pi f}{c_0} \right) \left[ 1 + C_7 \left( \frac{\sigma}{\rho_0 f} \right)^{C_8} \right] \quad (4)$$

Where are:

$Z_{CR}$  and  $Z_{CI}$  – real and imaginary part of characteristic acoustic impedance,  $Z_C$ ,

$\alpha$  and  $\beta$  – real and imaginary parts of the propagation constant,  $\Gamma$ ,

$\sigma$  – airflow resistivity,

$f$  – frequency,

$\rho_0$  – air density and

$c_0$  – sound speed in air.

The sound absorption coefficient at normal incidence,  $\alpha_n$ , for a firmly supported layer of material of thickness  $d$ , can be obtained using well - know expressions (5) and (6), with knowledge of the characteristic acoustic impedance and propagation constants  $\Gamma$ .

$$ZS = Z_C \coth \Gamma d \quad (5)$$

$$\alpha_n = 1 - \left| \frac{Z_S - \rho_0 c_0}{Z_S + \rho_0 c_0} \right|^2 \quad (6)$$

The values of the sound absorption coefficient, which will be used to check the proposed algorithm, are given in the Table 1 [4]. These values were obtained by measuring in an impedance tube by using the transfer function method between two microphones, described in the SRPS EN ISO 10534-2 standard [10]. This method is based on the decomposition of a standing wave which is formed in a tube by recording signals from two microphones and calculating their transfer function. The reflection coefficient is calculated from the transfer function and then the absorption coefficient is calculated. This method results in obtaining the value of the absorption coefficient at normal incidence, in the

frequency range defined by the physical dimensions of the tube and the distance between the microphones.

### 3. MODEL

Since the middle of the XX, and especially with the beginning of the XXI century, methods have appeared that effectively solve complex optimization problems. The main characteristic of these methods is that they are inspired by phenomena in nature. For that reason, they are called biologically inspired methods. Among the best known, most popular, methods are: genetic algorithms (Genetic Algorithm - GA, John Holland, 1962), differential evolution (Differential Evolution - DE, R. Storn and K. Price 1996), particle swarm optimization (Particle Swarm Optimization - PSO, J. Kennedy and R. Eberhart in 1995), ant colony optimization (ACO M. Dorigo in the late 1990s), cuckoo search (CS - Xin-She Yang and Suash Deb, 2007), firefly algorithm (FA - Xin-She Yang, 2008), bat algorithm (Bat Algorithm - BA - Xin-She Yang, 2010), krill herd algorithm - (KHA - Amir H Gandomi and Amir H Alavi, 2012), gray wolf algorithm (Gray Wolf Optimizer, Seyedali Mirjalili, Seyed Mohammad Mirjalili, Andrew Lewis, 2014).

Table 1: Absorption coefficient values for foam HR 3744 [4]

| f <sub>c</sub> (Hz) | Material thickness (cm) |          |          |          |          |          |         |         |         |         |
|---------------------|-------------------------|----------|----------|----------|----------|----------|---------|---------|---------|---------|
|                     | 1                       | 2        | 3        | 4        | 5        | 6        | 7       | 8       | 9       | 10      |
| 125                 | 0.078945                | 0.052273 | 0.078038 | 0.091768 | 0.095615 | 0.099378 | 0.14166 | 0.14739 | 0.1988  | 0.23425 |
| 160                 | 0.07159                 | 0.064579 | 0.088787 | 0.095501 | 0.1163   | 0.13339  | 0.17142 | 0.1915  | 0.23306 | 0.28444 |
| 200                 | 0.067147                | 0.071539 | 0.095544 | 0.1082   | 0.13866  | 0.16303  | 0.21552 | 0.26369 | 0.29383 | 0.36679 |
| 250                 | 0.062784                | 0.081199 | 0.10469  | 0.12844  | 0.16959  | 0.20025  | 0.26771 | 0.3208  | 0.37254 | 0.47083 |
| 315                 | 0.060061                | 0.082818 | 0.11674  | 0.15397  | 0.20809  | 0.24824  | 0.34862 | 0.41372 | 0.44536 | 0.56428 |
| 400                 | 0.061533                | 0.088451 | 0.13883  | 0.19781  | 0.26972  | 0.31781  | 0.44411 | 0.49926 | 0.59604 | 0.73095 |
| 500                 | 0.062915                | 0.10462  | 0.17202  | 0.25435  | 0.324    | 0.38727  | 0.55493 | 0.66397 | 0.75279 | 0.88024 |
| 630                 | 0.07125                 | 0.12535  | 0.22696  | 0.3171   | 0.44179  | 0.52143  | 0.74253 | 0.82768 | 0.8864  | 0.96609 |
| 800                 | 0.086209                | 0.15796  | 0.29957  | 0.44704  | 0.59085  | 0.67178  | 0.88578 | 0.93204 | 0.94498 | 0.9434  |
| 1000                | 0.089769                | 0.19083  | 0.40787  | 0.5967   | 0.74673  | 0.80233  | 0.92326 | 0.92662 | 0.90819 | 0.8601  |
| 1250                | 0.1146                  | 0.24294  | 0.56195  | 0.75699  | 0.84916  | 0.8587   | 0.86797 | 0.85938 | 0.83806 | 0.82517 |
| 1600                | 0.073466                | 0.30496  | 0.74481  | 0.86448  | 0.85371  | 0.84389  | 0.77397 | 0.80167 | 0.80959 | 0.90507 |
| $\alpha_w$          | 0.05                    | 0.15     | 0.25     | 0.3(M)   | 0.35(M)  | 0.4(M)   | 0.55(M) | 0.6(M)  | 0.65    | 0.75    |

| f <sub>c</sub> (Hz) | $\alpha_p$ |          |          |          |          |          |          |          |          |          |
|---------------------|------------|----------|----------|----------|----------|----------|----------|----------|----------|----------|
|                     | 250        | 0.063331 | 0.078519 | 0.105658 | 0.130203 | 0.172113 | 0.20384  | 0.277283 | 0.33257  | 0.370577 |
| 500                 | 0.065233   | 0.10614  | 0.17927  | 0.25642  | 0.34517  | 0.408837 | 0.580523 | 0.663637 | 0.745077 | 0.859093 |
| 1000                | 0.096859   | 0.197243 | 0.42313  | 0.600243 | 0.728913 | 0.77603  | 0.892337 | 0.906013 | 0.897077 | 0.876223 |

The advantage of these algorithms is that they can be applied to a large number of optimization problems, as well as their adaptability to the optimization problem. Also, these methods do not require experience in determining the initial values of variables, because it is possible to set a wide range for the initial values of variables. It is important to note here that the function optimized by these methods does not have to be differentiable and continuous, and that there is no limit to the number of variables to be optimized. However, perhaps the most important advantage of these methods is that they are all algorithmically designed and, as such, can be improved by simple modifications, thus achieving greater efficiency in finding the optimal solution.

#### 3.1. GREY WOLF ALGORITHM

The Gray Wolf algorithm (The Gray Wolf Optimizer - GWO) was proposed by [11] Seyedali Mirjalili, Seyed Mohammad Mirjalil, Andrew Lewis and is based on the behavior of gray wolves during the search, pursuit of prey and the hunt itself. Gray wolves are social animals, living in packs, respecting a strict, social, hierarchy. The pack leaders are the dominant male (alpha

male) and the dominant female (alpha female), which are called by the one name alpha,  $\alpha$ . Alphas make the most important decisions for the pack. The second in the hierarchy of gray wolves are the so-called beta,  $\beta$ . The beta individual assists the alpha in organizing the pack when making decisions. Beta can be either male or female and they are the best candidates to inherit alpha. The lowest in the pack hierarchy are omegas,  $\omega$  and they are subordinate to everyone in the pack. There are also so-called deltas in the pack,  $\delta$ , which carry out the orders of alpha and beta, and are superior to omegas. This category includes sentinels, hunters and caretakers.

In addition to the characteristics of social organization and strict hierarchy in the pack, another very important characteristic of gray wolves is organized behavior during hunting. The main phases of gray wolf hunting [11] are:

- tracking and approaching,
- pursuing, encircling, and harassing the prey until it stops moving,
- attack.

Precisely these two mentioned characteristics of gray wolves, hierarchical organization and hunting technique are mathematically modeled in order to design an optimization algorithm [11].

Considering the hierarchy of gray wolves, when optimizing, the best solution will be alpha ( $\alpha$ ), while the second and third best solution will be beta ( $\beta$ ) or delta ( $\delta$ ). Candidates for other good solutions will, of course, be omega ( $\omega$ ).

As mentioned above, grey wolves encircle prey during the hunt. The mathematical model of this behavior is given by equations (7) to (10), [11].

$$\vec{D} = \left| \vec{C} \cdot \vec{X}_p(t) - \vec{X}(t) \right| \quad (7)$$

$$\vec{X}(t+1) = \vec{X}_p(t) - \vec{A} \cdot \vec{D} \quad (8)$$

$$\vec{A} = 2\vec{a} \cdot \vec{r}_1 - \vec{a} \quad (9)$$

$$\vec{C} = 2 \cdot \vec{r}_2 \quad (10)$$

Where are:

- $\vec{D}$  – alpha position in the iterative process,
- $t$  – current iteration,
- $\vec{X}_p$  – a vector indicates the position of the prey in the iteration  $t$ ,
- $\vec{X}$  – a vector indicates the position of the grey wolf in the iteration  $t$ ,
- $\vec{A}, \vec{C}$  – coefficient vectors, which are calculated by equations (3) и (4),
- $\vec{a}$  – vector of elements that are linearly decreased from 2 to 0 and
- $\vec{r}_1, \vec{r}_2$  – random vectors whose components take (random) values in the interval [0, 1].

The advantage of gray wolves, in hunting, is that they can recognize "easy" prey. As mentioned, the alpha is the one leading the hunt. The beta and delta might also participate in hunting. It is innate for wolves to find prey, but the very application of possible solutions to the search for space is difficult because, usually, the position of the

optimal or best solution is not known. Therefore, in the proposed algorithm [11], it is assumed that alpha, beta and delta have better knowledge about the potential location of prey - their positions give the best solution. For this reason, the first three best solutions (alpha;  $\vec{D}_\alpha$ , beta;  $\vec{D}_\beta$  and delta;  $\vec{D}_\delta$  search agents) obtained, in an iterative process, oblige the other search agents (including the omegas) to update their positions according to them, Figure 1, [11]. This process in the algorithm is defined by equations (11), (12) and (13).

$$\vec{D}_\alpha = \left| \vec{C}_1 \cdot \vec{X}_\alpha - \vec{X} \right|, \quad \vec{D}_\beta = \left| \vec{C}_2 \cdot \vec{X}_\beta - \vec{X} \right|, \quad \vec{D}_\delta = \left| \vec{C}_3 \cdot \vec{X}_\delta - \vec{X} \right| \quad (11)$$

$$\vec{X}_1 = \vec{X}_\alpha - \vec{A}_1 \cdot \left( \vec{D}_\alpha \right), \quad \vec{X}_2 = \vec{X}_\beta - \vec{A}_2 \cdot \left( \vec{D}_\beta \right), \quad \vec{X}_3 = \vec{X}_\delta - \vec{A}_3 \cdot \left( \vec{D}_\delta \right) \quad (12)$$

$$\vec{X}(t+1) = \frac{\vec{X}_1 + \vec{X}_2 + \vec{X}_3}{3} \quad (13)$$

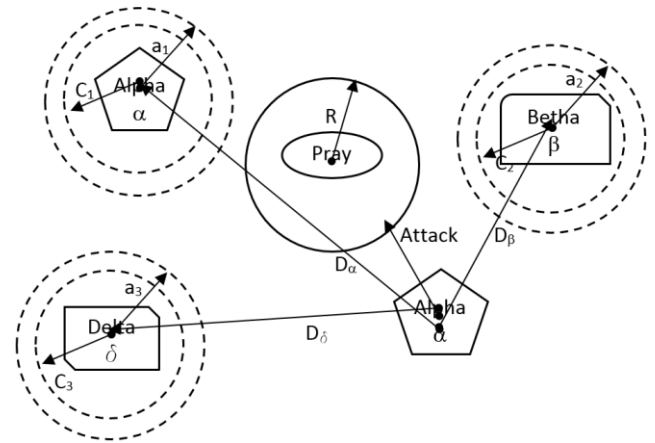


Figure 1: Illustration of updating search agent positions in the GWO algorithm

Respecting the proposed mathematical models, which mimic a pack of gray wolves in hunting, the following approximations were made, [11], in order to form a theoretical algorithm for gray wolves:

- Pack hierarchy assists GWO to save the best solutions obtained during iterative process
- The prey encirclement mechanism, defines a circle-shaped neighborhood around the solutions which can extend to a larger radius as a hyper-sphere.
- The random parameters  $\vec{A}$  and  $\vec{C}$  assist other candidates, varying the radius of the hypersphere, in finding the best solutions.
- The proposed hunting method allows candidate to locate the probable position of the prey.
- Exploration and exploitation are guaranteed by the adaptive values of  $\vec{a}$  and  $\vec{A}$ .
- The adaptive values of parameters  $\vec{a}$  and  $\vec{A}$  allow GWO algorithm a smooth transition between exploration and exploitation.
- With decreasing  $\vec{A}$ , one half of the iterations refers to exploration, and the other half are dedicated to exploitation.

- The GWO has only two main parameters that need to be adjusted ( $a$  and  $C$ ).

Based on all given mathematical models and the stated approximations, the proposed GWO algorithm is given in the form of pseudo code in A -1, [11].

A.1 Pseudo code of the gray wolf algorithm GWO

```

1: begin
2:   Objective function  $f(X), X = (x_1, x_2, \dots, x_d)^T$ 
3:   Initialization of the gray wolf population,  $X_i (i = 1, 2, 3, \dots, n)$ 
4:   Initialization  $a, A, C$ 
5:   The calculation of the objective function for each of the agents search
6:    $X_\alpha$  The best search agent
7:    $X_\beta$  The second ranked agent search
8:    $X_\delta$  The third ranked search agent
9:   while ( $t < \text{Number of iterations}$ )
10:    for For each search agent
11:      Update positions for each agent
12:    end for
13:    Update  $a, A, C$ 
14:    The calculation of the objective function for each agent search
15:    Update  $X_\alpha, X_\beta, X_\delta$ 
16:     $t = t + 1$ 
17:  end while
18:  Processing and displaying results
19: end
    
```

4. 5. RESULTS AND DISCUSSION

The application of optimization algorithms, ie algorithms that seek the best solutions, implies setting certain boundaries of the search space, Figure 2. These boundaries, in fact, represent the boundary conditions that must be met during the iterative process of searching the space for a possible solution.

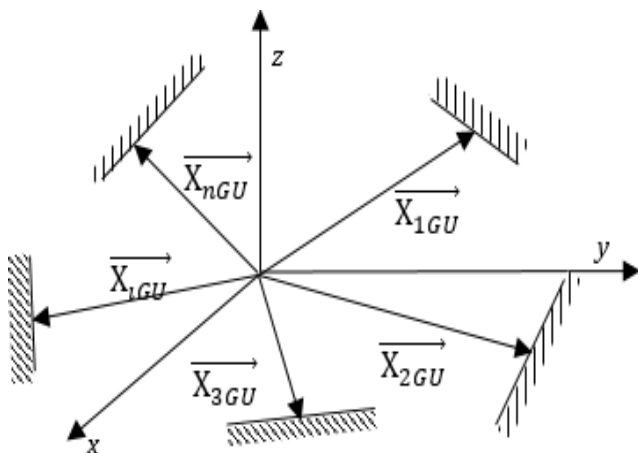


Figure 2: Search space constrained by boundary conditions ( $X_{iGU}$ ) for each of the variables whose values are sought

In the case of determining the sound absorption coefficient equation for a particular type of material, the objective function should calculate the coefficients,  $C_1 \dots C_8$  from equation (6), which will give the closest results to the results obtained by measurement, [4], given in Table 1:  $T(i)$ , (8).

$$\Delta = \alpha_n(i) - T(i) \rightarrow 0 \tag{14}$$

The only limitation in this problem is that the value  $\alpha_n$  must be in the range from 0 to 1, [2], (9).

$$0 < \alpha_n \leq 1 \tag{15}$$

The values of the coefficients can have values from  $-\infty$  to  $+\infty$ , that is:  $-\infty \leq C_i \leq +\infty, i=1, \dots, 8$ . In other

words, in this problem, it is not possible, explicitly, to define the boundaries within which to look for coefficients, that is, the search space is infinite, Figure 3.

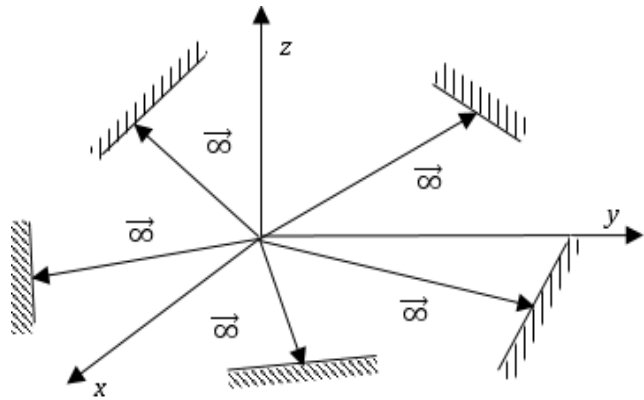


Figure 3: Infinite search space

No matter how experienced the researcher is in defining boundary value problems, it cannot avoid entering the space of the local minimum. This danger may lead the researcher to come up with a "best" solution at some point, when in fact a local minimum has been found.

In the GWO algorithm, which was applied in this case, the following algorithm parameters were applied:

- Number of search agents: 50
- The maximum number of iterations 1000,  $t=1, \dots, 1000$

The algorithm is implemented in the MatLab software package.

The application of the GWO algorithm went in two directions:

- P1. Defining fixed search boundaries  
The boundaries are set in the form of:
  - a)  $l = [-\infty \ -\infty \ -\infty \ -\infty \ -\infty \ -\infty \ -\infty \ -\infty]$ ; - lower boundaries values  
 $h = [\infty \ \infty \ \infty \ \infty \ \infty \ \infty \ \infty \ \infty]$ ; - upper boundaries values
  - b)  $l = [-l_1 \ -l_2 \ -l_3 \ -l_4 \ -l_5 \ -l_6 \ -l_7 \ -l_8]$ ; - lower boundaries values  
 $h = [h_1 \ h_2 \ h_3 \ h_4 \ h_5 \ h_6 \ h_7 \ h_8]$ ; - upper boundaries values
 where  $-l_i$  и  $h_i$  are random chosen values

P2. Reducing the scope of the limits search

In this case, a certain modification of the original algorithm was performed by modifying the search space for possible solutions based on the variables that gave the best solution, equations (10) and (11).

$$l(i) = TheBestPos(i) * (-1) - r_z; \tag{16}$$

$$h(i) = TheBestPos(i) + r_z; \tag{17}$$

where  $r_z$  - a random number that is randomly selected depending on the best solution given in the vector *TheBestPos*.

The following paper provides comparative results for different search space boundaries.

4.1. Infinite search space P1.a

In the case of infinite search space (P1.a), the results were obtained, shown below, and illustrated in Figure 4 and Table 2, respectively:

Search time = 704.1551 sec

C1 = 3.4172; C2 = -0.7412;  
 C3 = 0.77532; C4 = 0.6189;  
 C5 = 0.25774; C6 = 3124.0577;  
 C7 = 14.4902; C8 = 0.92315;  
 Best value: **6.0679**  
 Mean value: 6.1925  
 Worst value: 54.4117  
 SD: 1.8996 - standard deviation

Figure 5 and shown in Table 3, are:  
 Search time = 611.1237 sec  
 C1 = 1.0154; C2 = -0.0039128;  
 C3 = 0.89559; C4 = -0.040922 ;  
 C5 = 0.54164; C6 = 0.19802;  
 C7 = 0.15113; C8 = 0.3144;  
 Best value: **0.1043**  
 Mean value: 0.47815  
 Worst value: 30.5376  
 SD: 2.153

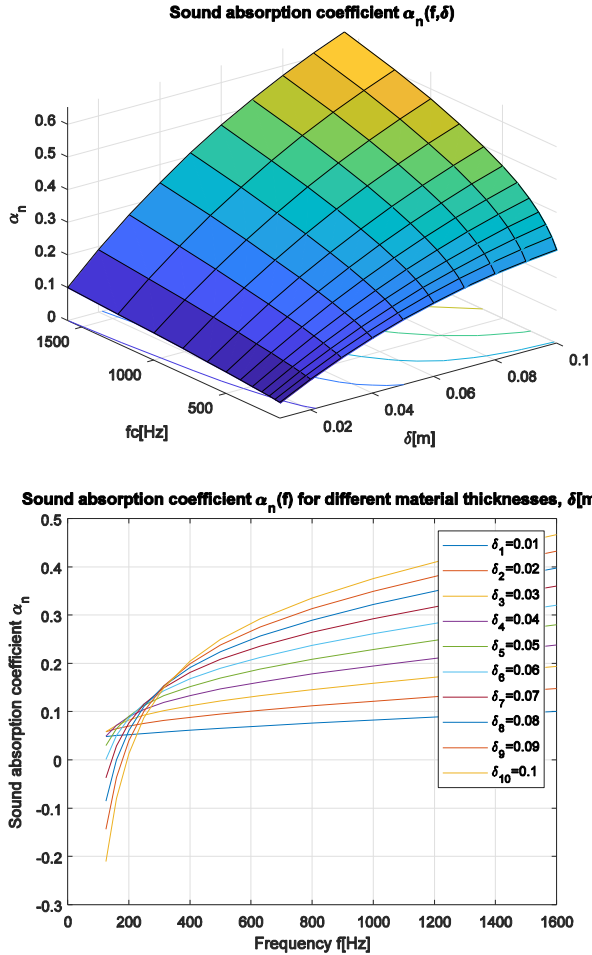


Figure 4: Graphical representation of the sound absorption coefficient  $\alpha_n = F(f, \delta)$ , at infinite search space

Table 2: Obtained values of  $\alpha_n$ , for at infinite search space

| $f_c$ [Hz] | Material thickness $\delta$ [cm] |        |        |        |        |        |        |        |        |        |
|------------|----------------------------------|--------|--------|--------|--------|--------|--------|--------|--------|--------|
|            | 1                                | 2      | 3      | 4      | 5      | 6      | 7      | 8      | 9      | 10     |
| 125        | 0.0485                           | 0.0933 | 0.1337 | 0.1693 | 0.1998 | 0.2254 | 0.2464 | 0.2631 | 0.2761 | 0.2859 |
| 160        | 0.0504                           | 0.0973 | 0.1401 | 0.1785 | 0.2123 | 0.2415 | 0.2665 | 0.2873 | 0.3045 | 0.3183 |
| 200        | 0.0525                           | 0.1014 | 0.1465 | 0.1873 | 0.2239 | 0.2562 | 0.2845 | 0.3088 | 0.3296 | 0.3470 |
| 250        | 0.0549                           | 0.1062 | 0.1536 | 0.1969 | 0.2362 | 0.2715 | 0.3028 | 0.3304 | 0.3545 | 0.3754 |
| 315        | 0.0578                           | 0.1119 | 0.1619 | 0.2080 | 0.2501 | 0.2882 | 0.3226 | 0.3533 | 0.3807 | 0.4048 |
| 400        | 0.0614                           | 0.1187 | 0.1719 | 0.2209 | 0.2659 | 0.3070 | 0.3443 | 0.3781 | 0.4085 | 0.4358 |
| 500        | 0.0654                           | 0.1263 | 0.1826 | 0.2347 | 0.2825 | 0.3264 | 0.3664 | 0.4028 | 0.4358 | 0.4657 |
| 630        | 0.0702                           | 0.1353 | 0.1955 | 0.2510 | 0.3019 | 0.3487 | 0.3914 | 0.4304 | 0.4660 | 0.4983 |
| 800        | 0.0762                           | 0.1464 | 0.2110 | 0.2703 | 0.3247 | 0.3746 | 0.4201 | 0.4617 | 0.4996 | 0.5340 |
| 1000       | 0.0827                           | 0.1584 | 0.2277 | 0.2911 | 0.3489 | 0.4017 | 0.4498 | 0.4937 | 0.5335 | 0.5697 |
| 1250       | 0.0903                           | 0.1724 | 0.2469 | 0.3147 | 0.3762 | 0.4320 | 0.4827 | 0.5286 | 0.5701 | 0.6077 |
| 1600       | 0.1002                           | 0.1904 | 0.2715 | 0.3446 | 0.4104 | 0.4695 | 0.5228 | 0.5707 | 0.6138 | 0.6525 |

From Table T-2, it can be seen that each value of  $\alpha_n$ , in the range from 0 to 1. However, the error is quite large,  $\Delta = 6.0679$ , as is the search time (704.1551 sec).

4.2. Randomly selected search space, P1.b.

Obtained results for arbitrarily selected search space::  $l_i = -20$ ;  $h_i = 20$ ,  $i = 1, \dots, 8$ , which are illustrated in

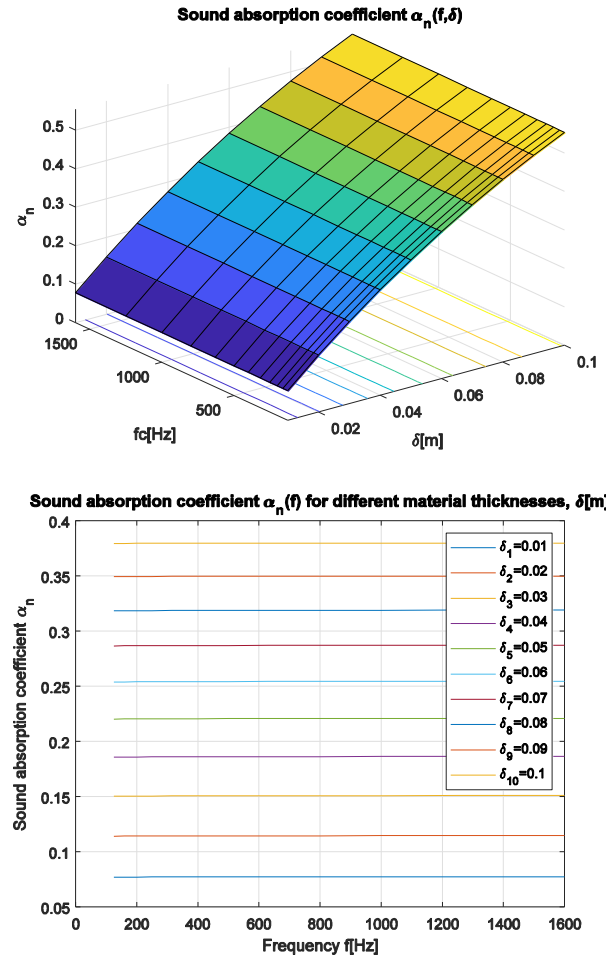


Figure 5: Graphical representation of the sound absorption coefficient  $\alpha_n = F(f, \delta)$ , in a determined search space

Table 3: Obtained values of  $\alpha_n$ , for determined search space

| $f_c$ [Hz] | Material thickness $\delta$ [cm] |        |        |        |        |        |        |        |        |        |
|------------|----------------------------------|--------|--------|--------|--------|--------|--------|--------|--------|--------|
|            | 1                                | 2      | 3      | 4      | 5      | 6      | 7      | 8      | 9      | 10     |
| 125        | 0.0769                           | 0.1480 | 0.2136 | 0.2743 | 0.3304 | 0.3822 | 0.4302 | 0.4745 | 0.5156 | 0.5535 |
| 160        | 0.0770                           | 0.1481 | 0.2137 | 0.2744 | 0.3305 | 0.3823 | 0.4303 | 0.4747 | 0.5157 | 0.5536 |
| 200        | 0.0770                           | 0.1481 | 0.2138 | 0.2745 | 0.3306 | 0.3825 | 0.4304 | 0.4748 | 0.5158 | 0.5538 |
| 250        | 0.0770                           | 0.1482 | 0.2139 | 0.2746 | 0.3307 | 0.3826 | 0.4305 | 0.4749 | 0.5159 | 0.5539 |
| 315        | 0.0771                           | 0.1482 | 0.2140 | 0.2747 | 0.3308 | 0.3827 | 0.4307 | 0.4750 | 0.5161 | 0.5540 |
| 400        | 0.0771                           | 0.1483 | 0.2141 | 0.2748 | 0.3309 | 0.3828 | 0.4308 | 0.4752 | 0.5162 | 0.5541 |
| 500        | 0.0771                           | 0.1484 | 0.2141 | 0.2749 | 0.3310 | 0.3829 | 0.4309 | 0.4753 | 0.5163 | 0.5542 |
| 630        | 0.0772                           | 0.1484 | 0.2142 | 0.2750 | 0.3312 | 0.3831 | 0.4311 | 0.4754 | 0.5164 | 0.5544 |
| 800        | 0.0772                           | 0.1485 | 0.2143 | 0.2751 | 0.3313 | 0.3832 | 0.4312 | 0.4755 | 0.5166 | 0.5545 |
| 1000       | 0.0772                           | 0.1485 | 0.2144 | 0.2752 | 0.3314 | 0.3833 | 0.4313 | 0.4757 | 0.5167 | 0.5546 |
| 1250       | 0.0773                           | 0.1486 | 0.2145 | 0.2753 | 0.3315 | 0.3834 | 0.4314 | 0.4758 | 0.5168 | 0.5547 |
| 1600       | 0.0773                           | 0.1487 | 0.2146 | 0.2754 | 0.3316 | 0.3836 | 0.4316 | 0.4759 | 0.5169 | 0.5540 |

As in the previous example, each value of  $\alpha_n$  is in the range from 0 to 1, Table 3. Error,  $\Delta = 0.1043$ ; is significantly less than the error obtained in infinite search space, and the search time is shorter (611.1237 sec).

4.3. Reducing the scope of the limits search P2

In the case of an infinite search space, and when it narrows in each iteration, equations (10) and (11), in relation to the values of the obtained variables, which at that time give the best solution, the results illustrated in Figure 6 and Table 4 are obtained:

Search time = 628.5198sec  
 C1 = 0.44309; C2 = 0.00512;  
 C3 = 0.15295; C4 = -0.02567;  
 C5 = 0.22699; C6 = 0.23031;  
 C7 = 0.30494; C8 = 0.26245;  
 Best value: **0.0862138277**  
 Mean value: 0.6912305913  
 Worst value: 30.5388861113  
 SD: 2.4624322978

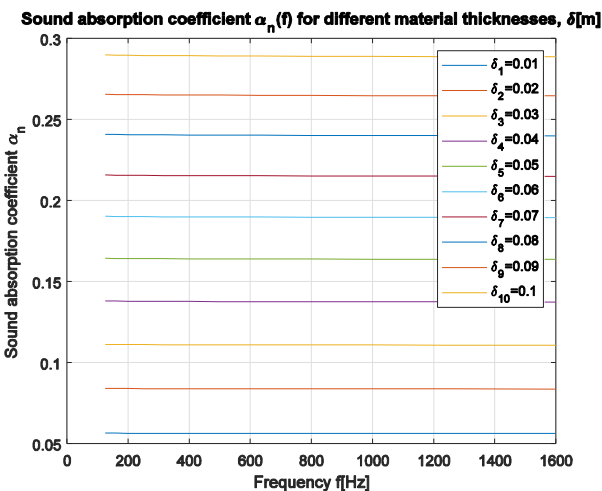
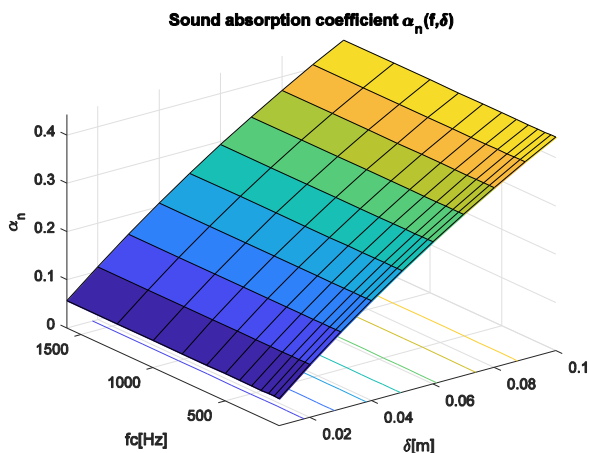


Figure 6: Graphical representation of the sound absorption coefficient  $\alpha_n = F(f, \delta)$ , when narrowing the search space

Table 4 shows that there is any value of  $\alpha_n$  in the range from 0 to 1. This can get even less error than in the previous case:  $\Delta = 0.0862138277$ . Search time: 628.5198sec, is approximately the same.

Figure 7 shows the course of the iterative process in determining the coefficients  $C_i, i=1, \dots, 8$ . From the diagram it can be seen that the convergence is very good, because already after some 30 steps comes to approaching the best values.

Table 4: Obtained values of  $\alpha_n$ , in infinite search space, but in narrowing search space

| $f_c$ [Hz] | Material thicknesses $\delta$ [cm] |        |        |        |        |        |        |        |        |        |
|------------|------------------------------------|--------|--------|--------|--------|--------|--------|--------|--------|--------|
|            | 1                                  | 2      | 3      | 4      | 5      | 6      | 7      | 8      | 9      | 10     |
| 125        | 0.0564                             | 0.1096 | 0.1599 | 0.2074 | 0.2523 | 0.2947 | 0.3348 | 0.3728 | 0.4087 | 0.4426 |
| 160        | 0.0564                             | 0.1096 | 0.1599 | 0.2073 | 0.2522 | 0.2946 | 0.3347 | 0.3726 | 0.4085 | 0.4425 |
| 200        | 0.0564                             | 0.1096 | 0.1598 | 0.2073 | 0.2521 | 0.2945 | 0.3346 | 0.3725 | 0.4084 | 0.4424 |
| 250        | 0.0563                             | 0.1095 | 0.1598 | 0.2072 | 0.2520 | 0.2944 | 0.3345 | 0.3724 | 0.4083 | 0.4422 |
| 315        | 0.0563                             | 0.1095 | 0.1597 | 0.2071 | 0.2520 | 0.2943 | 0.3344 | 0.3723 | 0.4082 | 0.4421 |
| 400        | 0.0563                             | 0.1094 | 0.1596 | 0.2071 | 0.2519 | 0.2943 | 0.3343 | 0.3722 | 0.4081 | 0.4420 |
| 500        | 0.0563                             | 0.1094 | 0.1596 | 0.2070 | 0.2518 | 0.2942 | 0.3342 | 0.3721 | 0.4080 | 0.4419 |
| 630        | 0.0563                             | 0.1094 | 0.1595 | 0.2069 | 0.2517 | 0.2941 | 0.3341 | 0.3720 | 0.4078 | 0.4418 |
| 800        | 0.0562                             | 0.1093 | 0.1595 | 0.2069 | 0.2516 | 0.2940 | 0.3340 | 0.3719 | 0.4077 | 0.4416 |
| 1000       | 0.0562                             | 0.1093 | 0.1594 | 0.2068 | 0.2516 | 0.2939 | 0.3339 | 0.3718 | 0.4076 | 0.4415 |
| 1250       | 0.0562                             | 0.1093 | 0.1594 | 0.2067 | 0.2515 | 0.2938 | 0.3338 | 0.3717 | 0.4075 | 0.4414 |
| 1600       | 0.0562                             | 0.1092 | 0.1593 | 0.2067 | 0.2514 | 0.2937 | 0.3337 | 0.3716 | 0.4074 | 0.4413 |

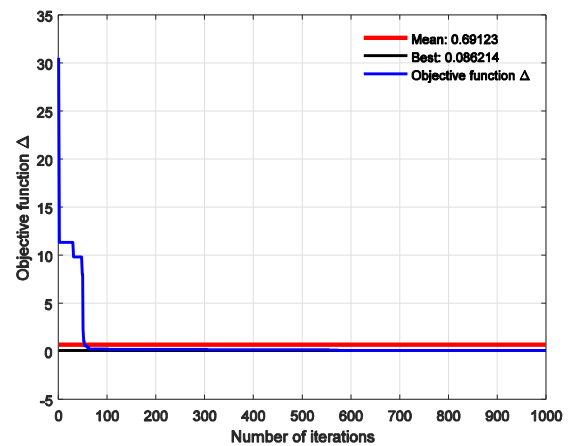


Figure 7: The course of the iterative process in determining the coefficients  $C_i, i = 1, \dots, 8$ , by narrowing the search space

The result obtained by this procedure is slightly worse than the results obtained using the empirical Dunn-Davern model, which is known in the literature as the most commonly used model for foam materials, and especially for polyurethane foams, for which it was formed. Using the Dunn-Davern model, absolute error values of 4.7% and relative error of 14.21% were obtained [9] in relation to the experimental values of the sound absorption coefficient for polyurethane foam (HR 3744).

This indicates the fact that it is necessary to investigate modifications of the proposed algorithm or a combination with other biological algorithms - hybridization, in order to obtain better solutions.

Table 5: Coefficients in empirical models

| Model           | Coefficients |         |         |          |         |         |         |         |
|-----------------|--------------|---------|---------|----------|---------|---------|---------|---------|
|                 | $C_1$        | $C_2$   | $C_3$   | $C_4$    | $C_5$   | $C_6$   | $C_7$   | $C_8$   |
| Dunn-Davern [7] | 0.114        | 0.369   | 0.0985  | 0.758    | 0.168   | 0.715   | 0.136   | 0.491   |
| GWO             | 0.44309      | 0.00512 | 0.15295 | -0.02567 | 0.22699 | 0.23031 | 0.30494 | 0.26245 |

This indicates that it is necessary to investigate modifications of the proposed algorithm or a combination with other biological algorithms - hybridization, in order to obtain better solutions.

5. CONCLUSION

The paper presents the possibility of using biologically inspired algorithms for determining the coefficients in empirical models for acoustic impedance, which are usually determined using regression analysis and the least squares method. The gray wolf algorithm was applied for cases of infinite and determined search space. As with other biologically inspired algorithms, local minimum spaces need to be avoided. Using a

modifications, the infinite space is corrected and narrowed, whereby an optimal solution is obtained with good convergence of results. The results of the research showed that biologically inspired algorithms are a suitable tool for determining constants in empirical models for determining acoustic impedance. A further direction of research in order to increase the accuracy of empirical models for impedance whose coefficients are determined using biologically inspired algorithms is to hybridize the gray wolf algorithm with some other biologically inspired algorithms.

#### ACKNOWLEDGEMENTS

This work is co-financed by the Ministry of Education, Science and Technological Development of the Republic of Serbia on the base of the contract whose record number is 451-03-9/2021-14/200108. The authors thank the Ministry of Education, Science and Technological Development of the Republic of Serbia for supporting this research..

#### REFERENCES

- [1] M. Prašćević, D. Cvetković, "Buka u životnoj sredini", Univerzitet u Nišu, Fakultet zaštite na radu, Vol. 1, (2005),
- [2] Md R. Rahman, S. Hamdan, E. Jayamani, M. Khusairy B. Bakri and Md S. Islam, "Biocomposite Materials and Its Applications in Acoustical Comfort and Noise Control", Green Biocomposites, Green Energy and Technology, pp. 247-259, DOI:10.1007/978-3-319-49382-4\_11,
- [3] Delany M.E., Bazley E.N., Acoustical properties of fibrous absorbent materials, Appl. Acoust., Vol. 3, № 2, p. 105–116, DOI:10.1016/0003-682X(70)90031-9, (1970),
- [4] Prof. dr Milan Kolarević, Mr Branko Radičević, Vladan Grković, AKUSTIČKA SVOJSTVA POLIURETANSKIH PENA MALE GUSTINE, PROJEKAT 37020, Elaborat 1/2016, Kraljevo, januar 2016. god,
- [5] R. Rey, J. Alba, J.P. Arenas, V.J. Sanchis, "An empirical modeling of porous sound absorbing materials made of recycled foam", Applied Acoustics, Vol. 73, Nos. 6-7, pp. 604-609, (2012),
- [6] W. Qunli, "Empirical relations between acoustical properties and flow resistivity of porous plastic open cell foam", Applied Acoustics, Vol. 25, pp. 141-148, (1988),
- [7] Dunn I.P., Davern W.A., Calculation of acoustic impedance of multi-layer absorbers, Appl. Acoust., Vol. 19, № 5, p. 321–334, DOI:10.1016/0003-682X(86)90044-7, (1986),
- [8] Voronina N., Acoustic properties of fibrous materials, Appl. Acoust., 1994, Vol. 42, № 2, pr .165–174, DOI:10.1016/0003-682X(94)90005-1,
- [9] B. Radičević, "Razvoj modela odlučivanja za izbor optimalne smeše zvučno apsorcionih materijala", Doktorska disertacija, Fakultet za mašinstvo i građevinarstvo u Kraljevu, Univerzitet u Kragujevcu, Kraljevo, Srbija, (2016),
- [10] SRPS EN ISO 354:2008, Akustika - Merenje zvučne apsorpcije u reverberacionoj komori,
- [11] S. Mirjalili, S. M. Mirjalil, A. Lewis, "Grey Wolf Optimizer", Advances in Engineering Software, Vol. 69, pp. 46–6, (2014)



## Composite Materials that are Good Sound Absorbers

Tanja Miodragović<sup>1\*</sup>, Olivera Erić-Cekić<sup>1</sup>, Branko Radičević<sup>1</sup>, Vladan Grković<sup>1</sup>

<sup>1</sup>Faculty of Mechanical and Civil Engineering in Kraljevo, University of Kragujevac, Kraljevo (Serbia)

*As a consequence of the accelerated development of science and technology, noise pollution is one of the biggest problems of modern society. The most common method for reducing noise pollution is the use of sound - absorbing materials, sound insulation materials, and noise damping materials. This paper aims to provide a review of composite materials that have been shown to be good sound absorbers. Which include composites made of synthetic, natural and recycled materials. The advantages and disadvantages of synthetic fibres and natural fibres were also studied. The influence of individual components, such as porosity, density, thickness, in composite materials on the sound absorption characteristic is also shown.*

**Keywords: composite materials, noise control, sound absorption, recycled materials**

### 1. INTRODUCTION

In recent decades, we have witnessed a scientific and technical revolution. Due to this revolution, there are various factors that have a strong influence on everyday human life. As a result, environmental pollution is one of the biggest problems of modern society. Noise pollution poses a real threat to the health and welfare of people.

Under pollution, noise means any unwanted sound. Noise, although it has the same physical characteristics as sound, differs from sound in that it causes different psychophysiological effects and harmful effects on human health. The effect of noise can be an auditory effect, limited to the hearing organ and extra charge effect, an effect on other organs and functions of the human body [1]. The sound volume of 120 to 150 dB causes severe disturbances, but even 70 dB sound can cause side effects. Frequent noise exposure affects stress and emotional stability. Noise also affects the living world, sound is important in the communication of animal species and has a significant place in the balance of ecosystems.

Environmental pollution with noise is a common problem in urban areas, and is caused by a wide range of noise sources, from vehicles in traffic, through restaurants, concert halls, all the way to factory plants and means of work. The biggest noise comes from machines and traffic, especially cars, trucks, planes. Construction, mining, agricultural machines and machines in factories create noise. Noise cannot be eliminated, but it can be reduced by traffic regulation, insulated walls, application of personal protective equipment, etc. Due to the extreme harmfulness of exposure to excessive noise, it is necessary to control noise and apply appropriate protection measures. Noise control can be performed at the noise source (active noise control), on the transmission routes and at the place of reception (passive noise control). From the population of sound propagation, there are materials that transmit, absorb or reflect sound. This is important when choosing materials for the construction of plants, machines, devices.

The use of sound-absorbing materials is one of the effective noise control technologies. Sound-absorbing materials absorb most of the sound energy while reflecting a very small part of the sound energy. They are used in various locations: near noise sources, on various

transmission routes, and sometimes near receivers. There is a wide range of sound-absorbing materials; which provide absorption properties that depend on frequency, composition, thickness and surface area. However, materials that have a high value of the sound absorption coefficient are usually porous. Composite materials are an important part of noise protection solutions due to the properties that make them suitable for use in passive noise control devices. The properties of composite materials can be controlled and optimized based on the application of interest by adding reinforcing materials. In the rapidly growing technological world, composite materials are a unique promising material.

### 2. SOUND ABSORBING MATERIALS

Sound-absorbing materials are materials that reduce the acoustic energy of a sound wave as the wave passes through the material. Sound absorptive materials typically have a soft, porous structure, offer only low resistance to a sound wave, and reduce the acoustic energy of a sound wave as the wave passes through it by the phenomenon of absorption. To be an efficient sound absorber, a material usually will convert acoustic energy to some other form of energy, usually heat. The main reasons for the acoustic energy losses when sound passes through the sound - absorbing materials are due to momentum losses, frictional losses, and temperature fluctuations. According to the mode of sound absorbers, they can be divided into porous, resonator and panel absorbers.

A porous absorbent material is a solid that contains cavities, channels, or interstices, so that sound waves can enter through them. According to the macroscopic configurations, sound absorbing materials can be classified into two types, the first type is called 'closed pores' and the second type is called 'open pores'. Closed pores are substantially less efficient than open pores in absorbing sound energy, but they have an effect on some macroscopic properties of the material such as its bulk density, mechanical strength and thermal conductivity. Open pores have a continuous channel of communication with the external surface of the body, and they have a great influence on the absorption of the sound [2]. Porous sound - absorbing materials can also be classified based on their microscopic configurations as cellular, fibrous, or

\*Corresponding author: <The Faculty of Mechanical and Civil Engineering in Kraljevo of the University in Kragujevac, Dositejeva 19, 36000 Kraljevo > and <miodragovic.t@mfkv.kg.ac.rs>

granular. In these materials, absorption occurs by causing the sound waves to activate the motion of the fibres, membranes and the air in the spaces surrounding the fibres or voids. Frictional energy losses generate heat, which is dissipated, thereby reducing the acoustic energy [2]. It is known that there are several parameters that may influence the sound losses, such as thickness, density, porosity or flow resistance, coefficient of elasticity.

Absorption materials are characterized by a sound absorption coefficient that defines the ability of a material to absorb and transform part of the energy of sound into another form [1]. The absorption coefficient is a useful concept when using geometrical acoustic theory, especially to evaluate the decay and growth of sound energy in a room. However, when sound is considered as a wave motion, it is necessary to use the concept of acoustic impedance.

### 3. COMPOSITES THAT ARE GOOD SOUND ABSORBERS

The application of composite materials in noise control is of great importance, because the properties of composite materials can be controlled and optimized based on the application of interest by adding reinforcement. Each composite material absorbs sound at a certain frequency which is characteristic of the properties of that material [3]. Natural, synthetic and recycled materials can be used as sound absorbers. Hemp, bamboo, coconut, cotton, kenaf, rice, wheat fibres are examples of natural sound absorbers. Synthetic materials such as ceramics, mineral fibres glass wool are used in noise control as absorption materials. Composite material technology provides the possibility of using hazardous waste materials in useful materials that can be used in noise control.

Composite absorption materials are a good solution to the noise problem. Therefore, these composites play a crucial role in the automotive and aerospace industries, medicine and other areas where noise pollution significantly affects human health. With the different types of composite materials currently available, it is possible to cover a wide frequency range [3].

#### 3.1. Synthetic composite materials

Synthetic composite materials have proven to be effective sound absorbers. Availability of materials of known properties, low production cost make synthetic materials suitable for passive noise control. The most commonly used sound absorbers and insulation materials are glass wool, polyurethane foam, mineral wool and their composites, but although they have good sound insulation properties, they have disadvantages such as risks to health and pollution of the workplace and environment [4]. The sound absorption characteristics of glass fibre materials, in the norm, are excellent, but increasing density may improve barrier characteristics, but will also decrease absorption. The acoustic properties of many composites are tested, such as composites based on aluminium, cement, ceramics.

Different types of aluminium composites are used in noise control. Aluminium foam, the material of the future, has modified properties obtained by combining the properties of the metal and the cell structure [5]. Such modified properties cannot be achieved by any of the

conventional properties of aluminium. Aluminium foam is a metal with a cellular structure that contains more than 70% of pores. The pores can be closed (closed cell foam) or interconnected (open cell foam). Aluminium foams, especially those with interconnected pores, absorb sound very efficiently, incoming sound is mixed between the pores inside the foam, the pore surfaces vibrate, resulting in the transformation of sound energy into heat. Fero Simancik et al. [5] examined the absorption properties of aluminium foam of different densities in relation to the absorption properties of PU foam and fiberglass mats. Lower density aluminium foam showed better sound absorption in the frequency range below 1000 MHz, while higher density aluminium foam showed better performance in the 4000-5000 MHz range. Low-density aluminium foam has a better effect in sound absorption. The advantages of using aluminium foam are reflected in the fact that it is not flammable, does not erode under air currents and vibrations and can be easily cleaned if it is contaminated with dust, it is also more environmentally friendly compared to glass wool, polyurethane foam.

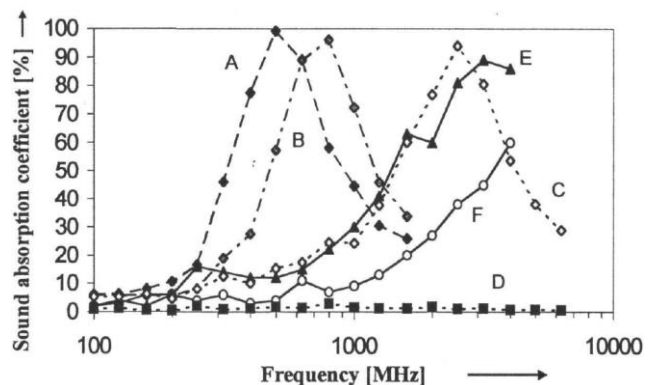


Figure 1: Sound absorption coefficient of aluminium foam at various thickness of the air gap between the sample and the solid background (A = 40 mm, B = 20 mm, C = 0 mm), compared with bulk aluminium (D) and glass fibre mat (F) [5]

Porous ceramics have a wide range of applications, including the fabrication of filters, membranes, sensors, supports, biomedical and building materials. Microstructures such as porosity and pore size distribution are very important factors for many potential applications of porous ceramics. The development of porous ceramics as external building materials will provide ceramic tiles not only with the production of light constructions but also with other functions such as insulation, workability and sound absorption. In the field of acoustic absorption, porous ceramic-absorbent structures can have other important properties in addition to sound absorption, such as resistance to high temperature, resistance to chemicals. Zhang et al., examined the acoustic properties of porous ceramics obtained by gel casting production. In this process, a precipitate of ceramic powder and N<sub>2</sub> bubbles, formed from a separate canister containing a surfactant before the precipitate forms is mixed in a spiral mixer [6]. They compared the sound absorption of porous ceramics obtained by the new method and the conventional method with a dense ceramic tile. The results showed that porous ceramics obtained by the new method have the highest degree of absorption, while purchased dense ceramics

have a low coefficient of absorption. Porous ceramics obtained by the new and conventional method showed good sound absorption, in the frequency range between 5000-6000 Hz, where porous ceramics obtained by the new method have an absorption coefficient of 0.7, while conventional porous ceramics have an absorption coefficient of 0.5. Porous ceramics produced by the new method show a higher total porosity, which results in the expected increase in the sound absorption coefficient [6]. Giese et al. [7] obtained porous ceramics by freeze gelation process, they also used expanded perlite as a melting phase to form pores. Expanded perlite is a great example of inorganic glass fillers that create pores and at the same time act as a reinforcing material. Compared to traditional dense ceramics, porous ceramics showed a high absorption coefficient. Porous ceramics showed better acoustic performance in the range of 400-800 Hz, with an absorption coefficient greater than 0.6. Porous ceramics have good acoustic performance due to low resistance to airflow [7]. Because airflow resistance can be adjusted over a wide range, the material is useful for many applications.

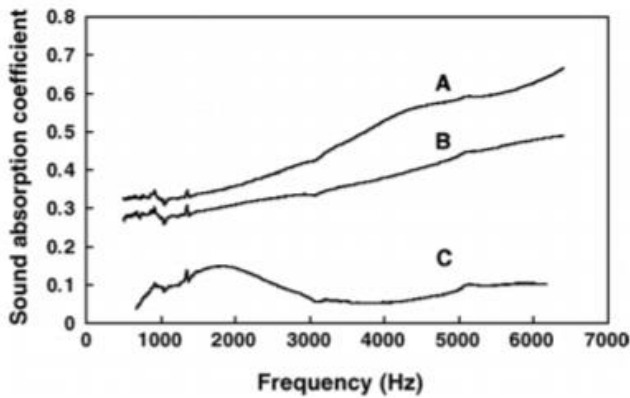


Figure 2: Sound absorption as a function of frequency for the porous ceramics fabricated by the new method (A) and the conventional method (B), and the dense ceramic tile bought from the market (C) [6]

Aerogel is one of the lightest known hard materials. It is a silicate solid that contains 99.8% air. Aerogels are also known as frozen smoke and for them, it is claimed to be the best thermal insulators ever made, as they are 40 times better than conventional fibreglass insulation materials [8]. Several raw materials have been used to produce aerogels, but silica aerogels are the most common. Recent research has focused on the use of aerogels in granular form as sound-absorbing materials. Donga et al. [9] investigated the acoustic properties of composite aerogel with different concentrations of silicon dioxide and polydimethylsiloxane, which reduce the rigidity of the material. Such composite aerogels have pore sizes between 5-20 nm, and experimental results have shown that these materials show better sound absorption properties than commercial fibreglass. Silicon aerogel composites with 40% polydimethylsiloxane showed a high absorption coefficient in the range of 800-1000 Hz. Unfortunately, aerogel production is still expensive, but it is very likely that advances in materials science will reduce the cost of aerogel production, which could lead to their widespread use in the construction and automotive industries in the near future.

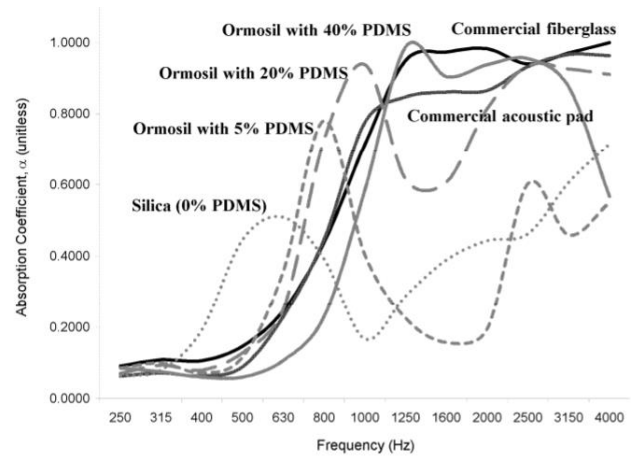


Figure 3: Adsorption coefficient as a function of the acoustic frequency. Silica/PDMS ormolus (with varying concentrations of PDMS) are compared with commercially available acoustic insulators [9]

Although the production of metal foams, ceramics and aerogels can contribute to greenhouse gas emissions, these materials simultaneously have high structural strength and reduced structural weight, and their use in the aerospace industry has the potential to reduce fuel consumption and save energy. Although harmful to human health and the environment, the advantages of using synthetic materials over natural fibres are reflected in better mechanical properties and the fact that synthetic fibres have a low resistance to moisture absorption [4].

### 3.2. Natural composite materials

Natural fibre composites are increasingly used in the construction and automotive industries. The wide application of natural materials is reflected in their minimal impact on human health and the environment. Although it is often emphasized that the mechanical properties of natural materials are inferior to synthetic materials, composites based on natural fibres compensate for these shortcomings in other aspects. Natural fibre composites are renewable, non-abrasive, cheaper, more numerous and do not present a great risk to human health and are safer during handling and processing [4]. The acoustic properties of different types of natural fibres such as: cotton, kenaf, hemp, flax, bamboo, rice, coconut, etc. are examined.

Kenaf is the name of the hibiscus plant related to fibres of jute and cotton and shows similar characteristics. Stems produce two types of fibres, coarser in the "bast", and finer in the "core". Bast fibres (about 35%) are suitable for making paper, textiles and rope; the core (about 65%) is usually used as biomass or can be reduced to particles and bonded into panels similar to particleboard. D'Alessandro and Pispola [10] examined the acoustic properties of a kenaf sample. Kenaf samples show an average absorption coefficient of 0.85 in the range 500-5000 Hz and 0.65 in the range 100 - 5000 Hz. Although their performance appears to be slightly lower than that of traditional fibre absorbers, these materials can be considered a valid alternative to traditional mineral wool covers for thermoacoustic applications, given their low environmental and human impact [10]. The sound and

mechanical properties of kenaf can be improved using composite technology. This acoustic material provides the possibility to be used as a sound absorber covering a wide frequency range when incorporated into other composites [4].

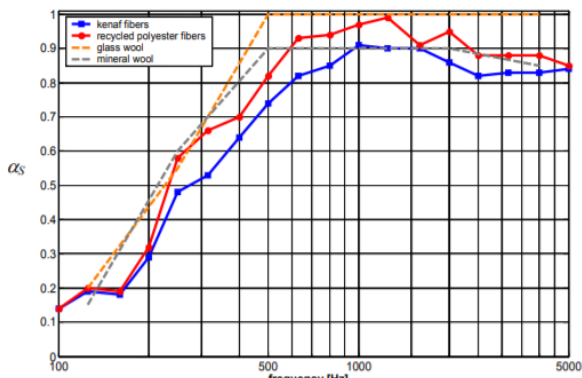


Figure 4: Third-octave band sound absorption coefficient of kenaf in comparison with traditional fibrous absorber [10]

Hemp is a significant source of fibre for both the textile and many other industries. Hemp is used to making ropes, bags, paper, such as filter, cigarette, painting paper, etc. Hemp fibres are also used to treat wastewater and soil. Lukić et al. [11] examined the acoustic properties of hemp composites with different polypropylene content. The composite was formed by alternating layers of hemp and polypropylene, where the amount of polypropylene ranged from 10 to 40% of the total mass. The best result was achieved for a composite with 20% polypropylene, where the absorption coefficient of 82% was measured in the frequency range of 2000-4000 Hz. Composites with a higher polypropylene content should be used to attenuate lower frequencies [11]. Markiewicz et al. [12] also examined the acoustic properties of hemp and polypropylene composites. By measuring in an impedance tube, they concluded that pure polypropylene composites without the presence of hemp show very poor sound absorption in the frequency range from 0 to 7000 Hz. Hemp composites showed good absorption properties in the frequency range of 3000 to 6000 Hz, while in the region below 3000 Hz there is no improvement compared to pure polypropylene composites [12]. The produced composites have good acoustic properties thanks to their porous structure. Hemp-based composites show good absorption properties at frequencies higher than 1500 Hz, which is why they have found application in the automotive industry.

Apart from the production of conventional textile products, flax is also used for the production of technical textiles. Flax fibre is used in automotive industry, paper industry, production of protective textiles, construction industry and in the production of composites. Namely, flax fibre has all the desirable properties required for the manufacture of composite materials: relatively high heat resistance and hardness, low tendency to deformation, low density. Yang and Yan [13] examined the acoustic properties of flax and its epoxy composites and compared the results with synthetic fibres. At frequencies above 1000 Hz the absorption coefficient of flax is 0.8 while the values for glass and carbon fibres are generally lower than

the values of natural fibres. Flax fibres have superior sound absorption properties than synthetic fibres such as glass and carbon fibres due to their unique porous and multiple structures [13]. Flax fibre reinforced composites also had better sound absorption behaviour than synthetic fibre reinforced composites, especially at high frequencies, which could be very useful for aerospace applications. Lee et al. [14] compared the sound absorption behaviour of flax/epoxy composites compared to glass/epoxy composites. Sound absorption is small at frequencies below 500 Hz, while absorption gradually increases at higher frequencies and is relatively constant at frequencies from 3150 to 6300 Hz, with an absorption coefficient of 0.3 [14]. The absorption values of the flax/epoxy composite compared to the results of Yang and Yan [13], where the woven flax fibers had a high absorption coefficient, are low. Due to the production process of composite samples, the density increases, which results in a decrease in the free space between the flax fibres, while the sound absorption performance of epoxy is generally poor. The results show that flax/epoxy composites have good acoustic properties and that there are ways to improve their acoustic properties, for example by adding additives such as calcium carbonate, which would increase the stiffness of the composites and provide better absorption of sound waves [14].

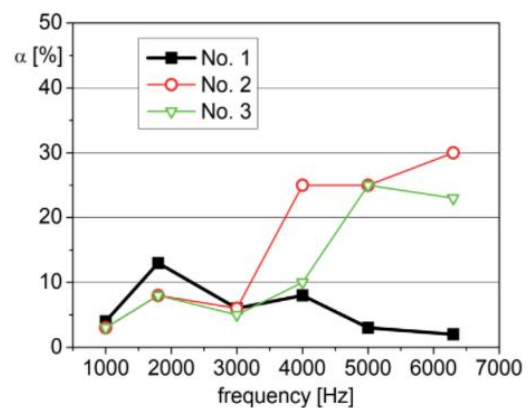


Figure 5: Frequency dependences of sound absorption coefficient for the different samples [12]

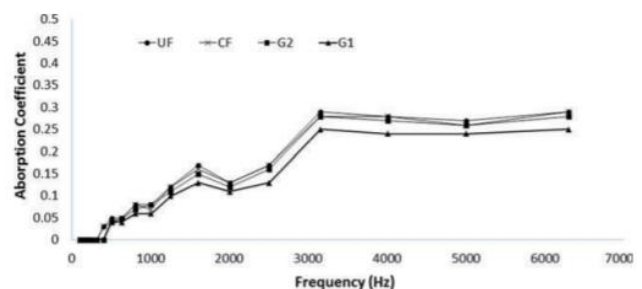


Figure 6: Sound absorption coefficients of samples at different frequencies [14]

In addition to various applications in everyday life, coconut fibre has proven to be one of the strongest lingocellulosic material in sound absorption [4]. With the help of composite technology, coconut fibers can be processed into efficient sound absorbers for various industrial applications. Researchers examined the effects of porous layer backing and perforated plates on the sound absorption coefficient using coconut fibres [15]. Coconut

fibre thickness of 20 mm without porous substrate has a maximum value of noise absorption coefficient in the frequency range 3680-3860 Hz. The porous layer backing can improve the noise absorption coefficient at low and high frequencies. A 20 mm thick coconut fiber layer with a porous layer backing shows the maximum noise absorption values in the frequency range with an absorption coefficient of 0.97. Coconut fibre with a perforated plate gives a higher value for lower frequencies in the range of 600-2400 Hz. The absorption coefficient of noise coconut fibres was increased with the backing with a woven cotton cloth. This is because the substrate of the porous layer has a higher flow resistance than coconut fibres, so that sound can be significantly dissipated as it travels through the material [15]. Mahzan et al. [16] used coconut fiber composites for reinforcement, recycled rubber as secondary material and polyurethane as a bonding material for acoustic panels. The sample with the maximum porosity value showed an absorption coefficient of 0.9 in the frequency range close to 1500 Hz [16]. The acoustic absorption of this composite is improved as a result of the increase in porosity when coconut fibres are used as a reinforcing element in this composite. All these results lead to the need for further development of coconut fibre materials for industrial applications in a wide range of frequencies.

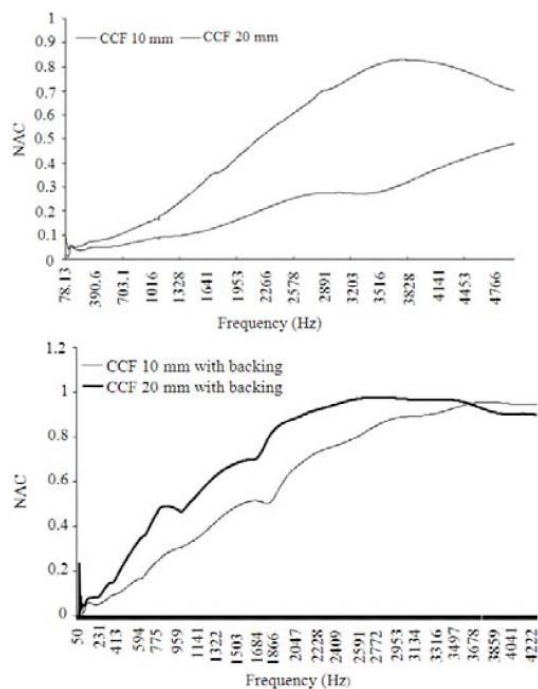


Figure 7: The noise absorption coefficient of coconut fiber without/with porous layer [15]

Natural fibres have great potential to be used as a sound-absorbing material. Due to the increasing pollution of the environment, there is increasing use of environmentally friendly, natural materials. Therefore, manufacturers of sound-absorbing materials tend to change their main components of products containing asbestos-based materials with natural fibres. These new fibres are much safer and pose fewer problems for human health and the environment. With the development of the industry, there are questions related to global warming caused by the emission of greenhouse gases into the atmosphere. The materials industry and the manufacturing

industry can have a lot of influence on the change of course in the market of acoustic materials. Therefore, research on acoustic materials is important and should be increased, especially those based on renewable resources that can lead to sustainable alternatives to conventional materials for future and current applications. These achievements include the use of natural fibres, recycled polymers and bio-based polymers, porous metals, new composites and smart materials.

### 3.3. Recycled composite materials

Continuous increase in pollution and considering environmental protection tends to the need to develop alternative materials for sound attenuation. In order to protect the environment and mitigate noise from industry and urban transport, many new noise control materials have been developed as alternatives to traditional (glass or stone wool); these materials can be made from recycled materials such as rubber, plastics, agricultural waste, recycled textile fibres, etc.

In the case of industrial waste in the last few years, the disposal of used car tires has become one of the main environmental problems. The amount of waste tires is increasing due to the high demand for tires and their short service life. Therefore, it is necessary to improve or develop a certain procedure for the application of recycled waste tires. Nowadays, many ways of waste rubber management have been proposed and it is classified into three groups, i.e. energy reuse, recycling, remodelling and recovery. In countries where the problem of used tires is solved in a safe way, part of the used tires is processed into semi-finished and finished products and used as an energy source. The use of recycled rubber to produce sound absorbers or resilient substrates can solve two environmental problems, noise and environmental pollution. Hong et al. examined the acoustic properties of a recycled rubber composite material. The composite absorber has a layer upon layer structure with the rubber particles as the bottom layer, on the top of which is a single or multiple layers of polymer porous foam or perforated panel [17]. It was found that the layer of recycled rubber particles has a higher sound absorption coefficient than porous materials that absorb the sound of the same thickness in the low-frequency range. In the rubber particle layer, two main mechanisms affect the reduction of sound energy: viscous losses due to friction between air and particles, and the friction between particles. It should be understood that the functional area of sound absorption shifts to the high-frequency side as the layer of PU foam becomes thicker and the sound absorption at higher frequencies is relatively small [17]. Radičević and Ristanović [18] presented the initial results of research on the absorption properties of materials made on the basis of recycled rubber granules. Samples of red and black rubber, different thicknesses and different granule structures were examined. The red rubber material has a higher absorption coefficient in the frequency range below 1000 Hz, while the maximum absorption coefficient of 0.9 has a black rubber at a frequency of 1000 Hz. Based on the measurement of the absorption coefficient of recycled rubber materials, it has been determined that these materials have a high level of absorption in the medium frequency range [18]. As such, they have a wide

range of applications, thus solving environmental pollution with rubber waste by converting rubber waste products into sound absorbers to reduce noise.

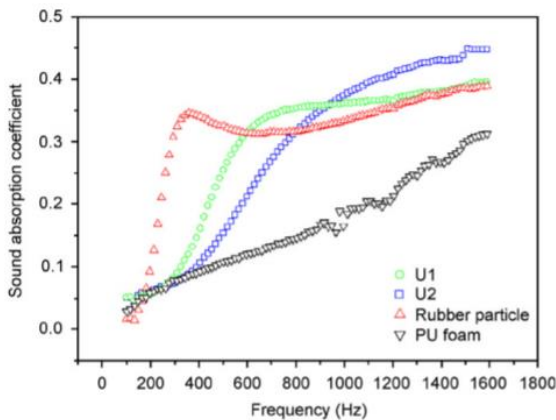


Figure 8: The absorption spectra for double-layer structures of rubber particles with porous foam materials [17]

Foams are widely used as sound-absorbing materials in noise control engineering. These sound-absorbing materials are used to control noise and vibration in many mechanical systems, including industrial machinery, household appliances, vehicles and buildings. Foam is a solid substance that contains cavities, channels or interstices so that sound waves can enter through them. One of the residues of production processes in the textile industry is polyurethane foam, so the recycling of these residues prevents the foam from going to a landfill, which is a serious environmental risk. Recycled polyurethane foam is often used in the production of carpet mats, cushion inserts for footwear, furniture, packaging materials, thermal insulation boards and automotive parts. Rey et al [19] modelled the acoustic behaviour of recycled polyurethane foam from two different points of view. First, the airflow resistivity was used as a simple parameter to describe the properties of the recycled foam material, on the other hand, the porosity and the average pore diameter of the recycled foam were considered as two simple parameters [19]. Both models provide good predictions of sound absorption of recycled foam. It is noted that these recycled materials have good sound absorption properties and could be a viable alternative to conventional materials for current and future applications.

Among various agricultural wastes, rice straw can be a very interesting material to be used as a filler in biodegradable polymers due to its high thermal stability compared to other agricultural wastes. Rice straw is used for thermal insulation, like fuel, for the production of toothpaste, etc. Rice husk is used as a reinforcement in a composite to improve the sound absorption property of a particular composite [4]. Wang and co-workers incorporated rice husk as a reinforcement in the polyurethane composite. Rice husk improved the physical, mechanical and acoustic properties of the material [20]. This environmentally friendly composite has proven to be an excellent sound absorber in the frequency range below 500 Hz compared to pure polyurethane foam. Thus, the presence of rice husk in this composite shifts its sound frequency response range above 1200 Hz to the lower frequency range. Due to these properties, it finds

application in the automotive industry, packaging industry and even in the aircraft industry.

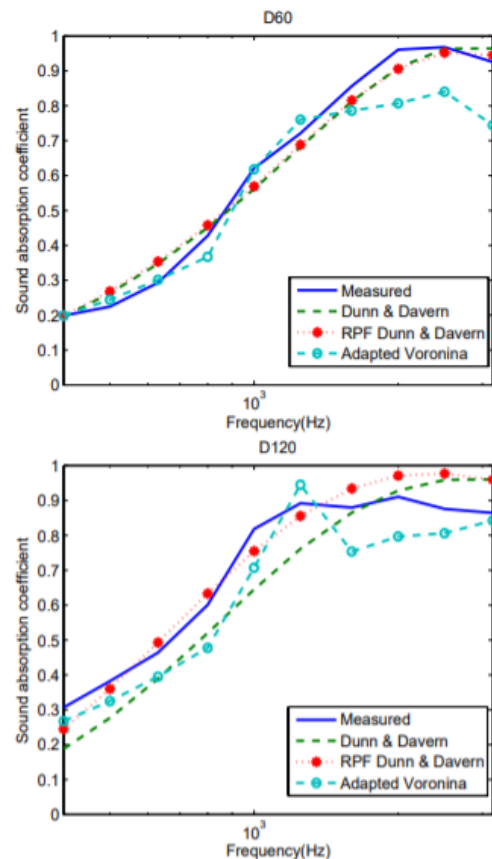


Figure 9: Results of sound absorption coefficient for the different samples of recycled polyurethane foam as a function of frequency [19]

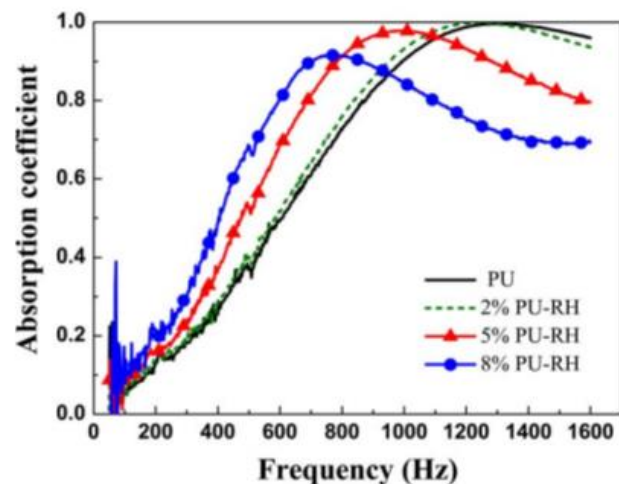


Figure 10: The sound absorption coefficient of various foams [20]

Wood fibre waste such as wood chips is mainly used in the thermoplastic industry. Waste wood is obtained for species of a certain purity and is usually based on certain particle size distributions. The use of composite materials based on textile residues and wood chips to reduce noise has two main advantages, low production costs and low specific weight. Stanciu et al [21] evaluated the acoustic properties of composite structures based on sawdust and textile waste linked by common ecological bonds. Different samples were tested, the differences

between samples consist of the quantities of raw materials or the type of binders, which conduct more or less to the compaction of the particles. The composition of the binder has a great influence on the acoustic properties of the sample, ie on the absorption coefficient, the impedance ratio and the reflection coefficient. The absorption coefficient is also affected by the density of the material, increasing the density of the material leads to a decrease in the absorption coefficient [21]. As some of the samples had constant absorption, with high values of absorption coefficients, at different frequencies, it can be concluded that these composites can find application for sound panels for highways, airports and railways.

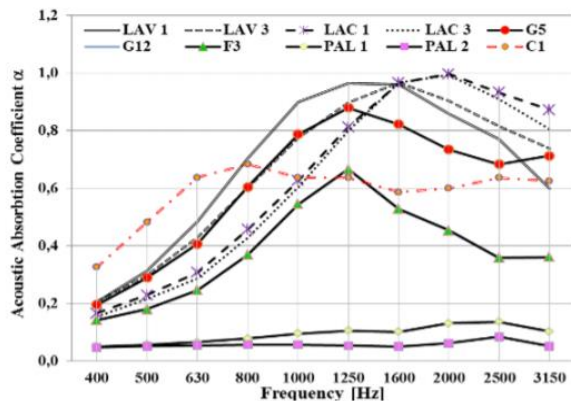


Figure 11: The effect of type of binders on sound absorption coefficient [21]

#### 4. CONCLUSION

The use of composites has developed rapidly in recent years primarily due to the problem of the lack of frequently used sound-absorbing material. This review indicates the importance of research and development undertaken in the field of composite materials that have proven to be good sound absorbers. The three general classifications of this group of materials include composites made from synthetic, natural, and recycled materials.

Materials obtained from synthetic fibre are commonly used for thermal and sound insulation, because of their good performances and low cost. It seems that environmentally friendly, degradable, recycled and green produced noise absorbers will play an important role in the noise absorbers market in the future.

Composites made of natural materials are cost-effective, renewable material, low density, environmentally friendly and reduces CO<sub>2</sub> emissions. Natural fibre materials have internal porosity which is suitable for sound absorption, as it provides more airflow resistivity. The performance of natural material in the acoustic field can change by varying its composition, porosity, thickness and other properties.

The research indicated that recycled materials hold promise for use as a raw material for sound-absorbing, being low cost, thanks to the use of wastes derived from other production cycles, lightweight and biodegradability. Recycled materials are becoming an interesting alternative to synthetic materials due to their good acoustic behaviour similar to the traditional porous material. As more research is conducted, and production increases and material-

making technology advances, we anticipate that the number of new noise-absorbing materials will increase in the coming years. In this regard, composite materials are particularly suitable because of their ease of manufacture and properties comparable to other materials used for sound absorption

Due to the different application of the absorbent material, researchers should consider the environmental constraints and acoustic characteristics of the sound-absorbing material. Therefore, when choosing sound-absorbing materials, effective noise absorption factors such as fibre size (in fibrous absorbents), air resistance, porosity, placement or position of sound absorbers, compression, thickness and density of absorbents should be taken into account.

#### ACKNOWLEDGEMENTS

This work is co-financed by the Ministry of Education, Science and Technological Development of the Republic of Serbia on the base of the contract whose record number is 451-03-9/2021-14/200108. The authors thank the Ministry of Education, Science and Technological Development of the Republic of Serbia for supporting this research.

#### REFERENCES

- [1] M. Prašević, D. Cvetković, "Buka u životnoj sredini", Univerzitet u Nišu, Fakultet zaštite na radu, Vol. 1, (2005)
- [2] D. A. Harris, "Noise control manual: Guidelines for Problem-Solving in the Industrial / Commercial Acoustical Environment", Springer Science & Business Media, New York, (1991)
- [3] S. Rajappan, P. Bhaskaran and P. Ravindran, "An insight into the composite materials for passive sound absorption", Journal of Applied Sciences, Vol. 17, issue 7, pp. 339-356, (2017)
- [4] Md R. Rahman, S. Hamdan, E. Jayamani, M. Khusairy B. Bakri and Md S. Islam, "Biocomposite Materials and Its Applications in Acoustical Comfort and Noise Control", Green Biocomposites, Green Energy and Technology, pp. 247-259, DOI:10.1007/978-3-319-49382-4\_11,
- [5] F. Simancik, J. Jerz, J. Kováčik, P. Minár, "Aluminium foam - A new light-weight structural material", Kovové Materiály/Metallic Materials, Vol. 35, pp. 265-277, (1997),
- [6] Fa-Zhi Zhang, T. Kato, M. Fuji, M. Takahashi, "Gelcasting fabrication of porous ceramics using a continuous process", Journal of the European Ceramic Society, Vol. 26, pp. 667-671, (2006),
- [7] F. Giese, C. Eigenbrod, and D. Koch, "A Novel Production Method for Porous Sound-Absorbing Ceramic Material for High-Temperature Applications", International Journal of Applied Ceramic Technology, Vol. 8, pp. 646-652 DOI:10.1111/j.1744-7402.2009.02479.x, (2011),
- [8] Arenas, J.P. and M.J. Crocker, "Recent trends in porous sound-absorbing materials", J. Sound Vibr., Vol. 44, pp. 12-18, (2010),

- [9] W. Dong, T. Faltens, M. Pantell, D. Simon, T. Thompson, and W. Don, "Acoustic Properties of Organic/Inorganic Composite Aerogels", *Materials Research Society Symposium Proceedings*, Vol. 1188, Warrendale, PA, (2009),
- [10] F. D'Alessandro, G. Pispola, "Sound absorption properties of sustainable fibrous materials in an enhanced reverberation room", *Proc. of Internoise 2005*, Rio de Janeiro, Brazil, (2005),
- [11] S. Lukić, M. Vojinović, A. Milutinović-Nikolić, "Akustična svojstva kompozita na bazi konoplje", *Konf za ETRAN*, Čačak, (2004),
- [12] E. Markiewicz, D. Paukszta and S. Borysiak, "Acoustic and Dielectric Properties of Polypropylene-Lignocellulosic Materials Composites", In: *Polypropylene*, Dogan, F. (Ed.). Intech, USA, pp: 193-218, (2012),
- [13] W. Yang and Y. Li, "Sound absorption performance of natural fibers and their composites", *Science China Technological Sciences*, Vol. 55(8), pp. 2278–2283. doi:10.1007/s11431-012-4943-1 (2012),
- [14] H. P. Lee, B. M. Pun Ng, A. V. Rammohan and Le Q. N. Tran, "An Investigation of the Sound Absorption Properties of Flax/Epoxy Composites Compared with Glass/Epoxy Composites", *Journal of Natural Fibers*, Vol. 14, pp. 71-77, DOI: 10.1080/15440478.2016.1146643, (2017),
- [15] R. Zulkifli, Zulkarnain and M .J. M. Nor, "Noise Control Using Coconut Coir Fiber Sound Absorber with Porous Layer Backing and Perforated Panel", *American Journal of Applied Sciences*, Vol. 7, pp. 260-264, ISSN 1546-9239, (2010),
- [16] S. Mahzan, A.M. Ahmad Zaidi, N. Arsat, M.N. Yahya, M.N. Mohamed-Hatta, M.I. Ghazali and S.R. Mohideen, "Study on sound absorption properties of coconut coir fibre reinforced composite with added recycle rubber", *Int. J. Integr. Eng.*, Vol. 2, pp. 29-34, (2010),
- [17] Z. Hong, L. Bo, H. Guangsu, H. Jia, "A novel composite sound absorber with recycled rubber particles", *Journal of Sound and Vibration*, Vol. 304, pp. 400–406, (2007),
- [18] B. Radičević, I. Ristanović, "Koeficijent apsorpcije materijala od recikliranog gumenog otpada", *Zbornik 58. konferencije za elektorniku, telekomunikacije, računarstvo, automatiku i nuklearnu tehniku ETRAN 2014*, Vrnjačka Banja, 2-5 juna 2014. godine, ISBN 978-86-80509-70-9, (2014),
- [19] Rey, Romina and Fernandez, Jesús and Arenas, Jorge and Sanchis, "Sound absorbing materials made of recycled polyurethane foam", *40th International Congress and Exposition on Noise Control Engineering 2011, INTER-NOISE 2011*, Vol. 3, pp. 2058-2063, (2011),
- [20] Y. Wang, C. Zhang, L. Ren, M. Ichchou, M.A. Gall and O. Bareille, "Influences of rice hull in polyurethane foam on its sound absorption characteristics", *Polym. Compos.*, Vol 34, pp. 1847-1855, (2013),
- [21] D. Stanciu, I. Curtu, C. Cosereanu, D. Lica and S. Nastac, "Research regarding acoustical properties of recycled composites", *8th International DAAAM Baltic Conference "INDUSTRIAL ENGINEERING "*, pp. 19-21 April 2012, Tallinn, Estonia, (2012).

## Non-Exhaust PM Emissions from Heavy-Duty Vehicles

Jasna Glišović<sup>1\*</sup>, Saša Vasiljević<sup>2</sup>, Nenad Miloradović<sup>1</sup>, Nadica Stojanović<sup>1</sup>, Ivan Grujić<sup>1</sup>

<sup>1</sup>Faculty of Engineering/Department for Motor Vehicles and Motors, University of Kragujevac, Kragujevac (Serbia)

<sup>2</sup>High Technical School of Professional Studies, Kragujevac (Serbia)

*The important technological improvements have been made for reducing particulate matter (PM) emissions from exhaust sources, but no actions are currently in place to reduce the non-exhaust part of emissions such as those from brake wear, road wear, tyre wear and road dust resuspension. In the future these emissions will become increasingly important in relative terms. However, as exhaust emissions are set to steadily decline, in 2030, total non-exhaust emissions will be an estimated 1.6 times greater than total exhaust emissions. Non-exhaust emissions are more difficult to quantify than exhaust emissions owing to the strong influence of not only the type of vehicle and traffic conditions, but also the material properties and meteorological factors. Most studies indicate that emission factors for PM from brake wear are significantly larger from heavy-duty vehicles (HDVs) than from light-duty vehicles (LDVs). This would be due to the larger number or size of brakes on heavy-duty vehicles and the fact that the larger vehicle weight releases more kinetic energy in the process of slowing the vehicle down. HDVs contributed five to ten times more resuspended road dust than LDVs. One of the objectives of this paper is to overcome significant gaps still exist in our understanding of the participation of HDVs in total non-exhaust emissions.*

**Keywords: Heavy-Duty Vehicles, Non-Exhaust Emission, Particle Matter, Road Traffic**

### 1. INTRODUCTION

Whilst exhaust emissions of PM are becoming heavily regulated, non-exhaust sources of PM emissions remain largely uncontrolled. Manufacturers have strict emission standards to adhere to and the majority of diesel vehicles on roads are now equipped with a particulate traps. Therefore attention is now focussing on emission sources such as non-exhaust emissions (NEE), which have been found to contribute significantly to particulate concentrations. Non-exhaust emissions are generated through the resuspension of road dust or road surface wear as the vehicle travels over the road surface, corrosion of vehicle components or during the mechanical friction processes associated with driving, such as brake, clutch or tyre wear (Table 1) [1]. Grigorators and Martini [2] noted that as exhaust emissions controls become stricter, relative contributions of non-exhaust sources to traffic related emissions will become more significant.

*Table 1: Mechanisms for non-exhaust particle emission*

| Emission type | Mechanism   | Includes                          |
|---------------|---|-----------------------------------|
| Direct        | Abrasion and wear and tear                                    | Tyre, brake, clutch, road surface |
|               | Corrosion   | Vehicle, street furniture         |
| Indirect      | Resuspension (due to tyre shear, wind and vehicle turbulence) |                                   |

Key reasons for needing to understand non-exhaust emissions include their inherent toxicity including their tendency to act as carriers of heavy metals and carcinogenic components [4] and their contribution to exceedances of air quality guidelines and standards [5]. Many studies have aimed to distinguish between the different non-exhaust particulate emissions by identifying particular chemical components. While the constituents of brake material may vary among manufacturers, iron, copper, antimony, and barium have been associated with

the particulate matter released from brake operation. Road surfaces are generally composed of either concrete or aggregate with a bituminous binder and abrasion of such a surface is likely to result in particulate matter of mineral origin. Tyre wear is likely to result in predominantly carbonaceous particles, although small quantities of metals, in particular zinc which is used as a vulcanization activator, may be present. Material resuspended from the road surface may include all types of vehicle abrasion debris, in addition to material from non-road sources which has been deposited on the road surface. This may include mineral dust from the local environment, typically including silicon, aluminium, calcium, and iron particularly in arid locations [6].

Most countries follow the methodology for estimating emissions from tyre and brake wear and road surface wear given in the 2016 version of the EMEP/EEA Air Pollutant Emissions Inventory Guidebook [7]. This provides a fairly simple approach which combines PM emission factors in milligrams emitted per kilometre (mg/km) for passenger cars, light goods vehicles, heavy-duty vehicles (HDVs and buses) and two-wheelers, with vehicle kilometres travelled per year. The method and emission factors in the Guidebook [7] have not been updated for nearly 15 years and are based on the information available at the time, mostly on wear rates, and a number of assumptions.

Some countries have used emission factors based on their own literature search (e.g. the Netherlands) or have used evidence from country-specific information and research. These are generally based on the total mass loss of tyre or brake material resulting from the wear process and estimates on the amount that remain airborne in the PM<sub>10</sub> and PM<sub>2.5</sub> range. The Scandinavian countries have been particularly active in this area and, for example, have taken account of the effect of studded tyres resulting in higher emissions from road wear.

\* Corresponding author: Jasna Glišović: 6 Sestre Janjic Str., Kragujevac, jaca@kg.ac.rs

The UK's National Atmospheric Emissions Inventory (NAEI) for tyre and brake wear and road abrasion uses the Tier 2 inventory method and emission factors in the EMEP/EEA Emissions Inventory Guidebook [7]. This approach provides mg/km emission factors for Total Suspended Particulates (TSP) for passenger cars, LDVs, HDVs and two-wheeled vehicles, together with PM<sub>10</sub> and PM<sub>2.5</sub> mass fractions to combine with the TSP factors. The TSP factors for tyre and brake wear are used with an average speed correction factor which implies higher emission factors at lower speeds, on the basis of greater braking and cornering per km at lower speeds. For heavy-duty vehicles, a further correction factor is applied to take account of the load carried by the truck and in the case of tyre wear on the number of wheel axles. No such speed and load correction factors are provided for road surface wear emissions [8].

Nearly one-third of the traffic-related source contributions were associated with non-exhaust emissions from brake and tyre wear and road dust resuspension in the urban environment. Elevated levels of non-exhaust sources were correlated with the number of heavy-duty vehicles, rather than total traffic volume.

There are 6.6 million trucks on the EU's roads. With more than 1.1 million trucks, Poland has the largest truck fleet, followed closely by Germany (946,541) and Italy (904,308).

Table 2: Medium and heavy commercial vehicles [10]

|                | 2014       | 2015       | 2016       | 2017       | 2018       |
|----------------|------------|------------|------------|------------|------------|
| European Union | 6,103,698  | 6,214,936  | 6,337,504  | 6,472,374  | 6,621,641  |
| Norway         | 89,746     | 88,659     | 86,757     | 86,154     | 85,661     |
| Switzerland    | 60,602     | 60,076     | 58,507     | 60,438     | 61,989     |
| EFTA           | 150,348    | 148,735    | 145,264    | 146,592    | 147,650    |
| Russia         | 3,738,145  | 3,690,032  | 3,703,635  | 3,733,711  | 3,759,152  |
| Turkey         | 814,459    | 850,051    | 876,152    | 898,817    | 908,821    |
| EUROPE         | 10,806,650 | 10,903,754 | 11,062,555 | 11,251,494 | 11,437,264 |

The EU motor vehicle fleet is getting older year-on-year. Passenger cars are now on average 11.1 years old, vans 11 years and heavy commercial vehicles 12 years. Trucks are on average 12.4 years old in the European Union. Among the EU's five major markets, Spain has the oldest truck fleet (14.4 years), followed closely by Italy (14.0 years).

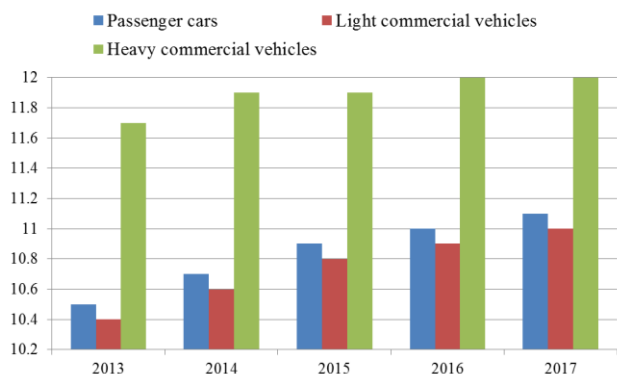


Figure 1: Average age of the EU fleet by vehicle type [10]

Emissions of heavy metals vary with the fleet composition, with higher emissions reported for some of the elements for heavy-duty vehicles (HDVs) so the aim of

this paper is to highlight the share of this category in non-exhaust emission.

## 2. NON-EXHAUST EMISSION

Different non-exhaust particle sources contribute to both fine and coarse particles as well as ultrafine particles. Figure 2 presents an overview of the processes (flows) and deposits of road dust particles as a system diagram. It also summarizes factors affecting the processes and flows.

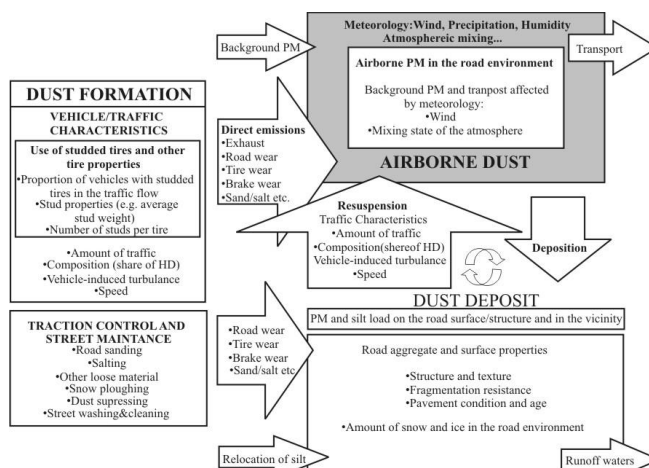


Figure 2: Material flows of road dust particles, with the main factors affecting the source strengths [11]

Particulate matter is present in a range of sizes in the atmosphere. Combustion processes generally result in smaller particles, which over time will agglomerate into the accumulation mode. Abrasive processes result in particles with aerodynamic diameters larger than the accumulation mode which are lost from the atmosphere largely by sedimentation. Size distribution of the particles measured by Harrison et al. [6] at the Marylebone Road site in London is shown in Figure 3. The red line shows brake wear, the purple line shows tyre wear, and the green line shows resuspension.

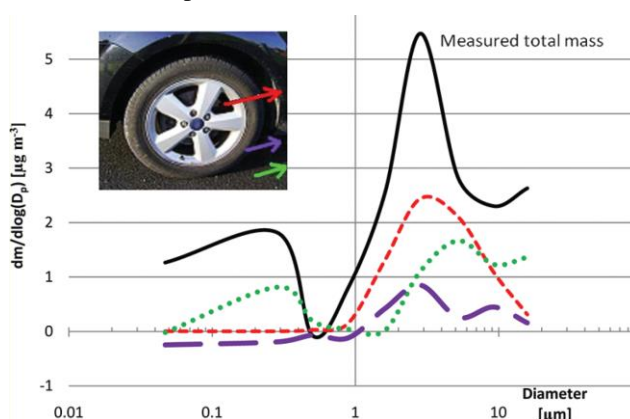


Figure 3: Size distribution of the particles measured at the Marylebone Road site in London [6]

However, emissions of trace metal markers are reported to vary with the fleet composition, with higher emissions reported for some of the elements for heavy-duty vehicles (HDVs). In addition, the profile of trace metal concentrations in non-exhaust particulate matter is unique for every region and varies based on parameters such as traffic volume and pattern, vehicle fleet characteristics, driving and traffic patterns and climate and geology of the. Another important aspect is the variability

of tyre and brake composition depending on the manufacturer which makes it very difficult to ascertain fleet-wide composition other than from environmental measurements. Several factors are reported to affect non-exhaust emissions including increase in vehicle speed reported a non-linear relationship between traffic volume and non-exhaust emissions. Metal emissions due to road dust show a low correlation to metal emissions due to abrasion/brake wear and combustion. One of the major problems in analysis of non-exhaust PM using field data has been the difficulty in distinguishing between wear and tear emissions and road dust since the chemical composition is often very similar [12]. This may, in any case, not be a clear distinction as wear emissions may deposit to the road surface, only to be resuspended subsequently [3].

The factors in Table 3 are averages for different road types and can be seen to be greater on urban roads, followed by rural roads and then motorways. This reflects the greater amount of braking done on urban roads, although this may be partially offset by the fact that the intensity of braking when it does occur would be higher on motorways where the vehicles are slowing down from greater velocities [9].

Table 3: Emission factors for PM<sub>10</sub> from tyre and brake wear for road transport vehicles as used in the UK's National Atmospheric Emissions Inventory [7,9]

| mg PM <sub>10</sub> /km |          | Tyre | Brake |
|-------------------------|----------|------|-------|
| Cars                    | Urban    | 8.7  | 11.7  |
|                         | Rural    | 6.8  | 5.5   |
|                         | Motorway | 5.8  | 1.4   |
| LDVs                    | Urban    | 13.8 | 18.2  |
|                         | Rural    | 10.7 | 8.6   |
|                         | Motorway | 9.2  | 2.1   |
| Rigid HDVs              | Urban    | 20.7 | 51.0  |
|                         | Rural    | 17.4 | 27.1  |
|                         | Motorway | 14.0 | 8.4   |
| Artic HDVs              | Urban    | 47.1 | 51.0  |
|                         | Rural    | 38.2 | 27.1  |
|                         | Motorway | 31.5 | 8.4   |
| Buses                   | Urban    | 21.2 | 53.6  |
|                         | Rural    | 17.4 | 27.1  |
|                         | Motorway | 14.0 | 8.4   |
| Motorcycles             | Urban    | 3.7  | 5.8   |
|                         | Rural    | 2.9  | 2.8   |
|                         | Motorway | 2.5  | 0.7   |

Table 4 shows the average PM<sub>10</sub> emission factors for road abrasion taken from the Guidebook [7] for all road types and speeds.

Table 4: Emission factors for PM<sub>10</sub> from road abrasion [8]

| mg PM <sub>10</sub> /km | Road abrasion |
|-------------------------|---------------|
| Cars                    | 7.5           |
| LDVs                    | 7.5           |
| HDVs                    | 38.0          |
| Buses                   | 38.0          |
| Motorcycles             | 3.0           |

There are two general approaches for determining emission factors (EFs) from non-exhaust sources:

i. Direct measurements from the sources, either under real world test conditions or in the laboratory.

ii. Receptor modelling where ambient pollutant concentration data are sub-divided according to its different sources and EFs are derived using mass-balance techniques.

Both methods have advantages and limitations. In particular, the first method provides emission factors of a relatively small number of vehicles, but for very well controlled conditions. However, tyre, brake and road surface wear are difficult to simulate in controlled tests. Speed, acceleration/deceleration, tyre material, temperature and parameters such a road surface construction and curvature are all important considerations. Sampling problems have also been noted. Further, resuspension fluxes are difficult to measure directly because the space around a vehicle does not form a "closed" system with obvious air inlets and outlets. Receptor modelling method requires knowledge of source composition and assumes that the sources specified are responsible of the species measure at the receptor. Beyond that source apportionment and quantification of airborne PM measured in the vicinity of roads is a rather complex task, road traffic contribution can be small compared with the background concentrations. Measurements in tunnels tend to overestimate pollutant concentrations due to limited dispersion and dilution, not to mention that influences of meteorology are reduced.

Non-exhaust EFs included in the database corresponds to tyre, brake, road wear and resuspension component is given for Heavy-Duty Vehicles in Table 5 and 6.

Table 5: EC (Elemental Carbon) Non-exhaust Emission Factors for Euro 7 diesel Heavy-Duty Vehicles [11]

| Vehicle            | Urban | Rural | Highway |
|--------------------|-------|-------|---------|
| HDV Rigid<=7.5t    | 0.008 | 0.005 | 0.003   |
| HDV Rigid 7.5-12t  | 0.008 | 0.005 | 0.003   |
| HDV Rigid 12-14t   | 0.008 | 0.005 | 0.003   |
| HDV Rigid 14-20t   | 0.008 | 0.005 | 0.003   |
| HDV Rigid 20-26t   | 0.009 | 0.006 | 0.004   |
| HDV Rigid 26-28t   | 0.009 | 0.006 | 0.004   |
| HDV Rigid 28-32t   | 0.009 | 0.006 | 0.004   |
| HDV Rigid >32t     | 0.009 | 0.006 | 0.004   |
| Articulated 20-28t | 0.010 | 0.007 | 0.004   |
| Articulated 28-34t | 0.010 | 0.007 | 0.004   |
| Articulated 34-40t | 0.011 | 0.007 | 0.005   |

Table 6: OM (Organic Matter) Non-exhaust Emission Factors for Euro 7 diesel Heavy-Duty Vehicles [11]

| Vehicle            | Urban | Rural | Highway |
|--------------------|-------|-------|---------|
| HDV Rigid<=7.5t    | 0.018 | 0.012 | 0.007   |
| HDV Rigid 7.5-12t  | 0.018 | 0.012 | 0.007   |
| HDV Rigid 12-14t   | 0.018 | 0.012 | 0.007   |
| HDV Rigid 14-20t   | 0.018 | 0.012 | 0.007   |
| HDV Rigid 20-26t   | 0.021 | 0.014 | 0.009   |
| HDV Rigid 26-28t   | 0.021 | 0.014 | 0.009   |
| HDV Rigid 28-32t   | 0.021 | 0.014 | 0.009   |
| HDV Rigid >32t     | 0.021 | 0.014 | 0.009   |
| Articulated 20-28t | 0.023 | 0.016 | 0.010   |
| Articulated 28-34t | 0.023 | 0.016 | 0.010   |
| Articulated 34-40t | 0.023 | 0.016 | 0.010   |

### 2.1. Tyre Wear

The surface of a tyre when in contact with the road is steadily abraded by contact with the road surface. This leads to release of large quantities of small rubber particles which cover a wide range of sizes. The larger particles will typically remain on the road surface until washed off in drainage water. However, the size range extends into sizes

below 10 micrometres diameter and hence contributes to  $PM_{10}$  (and to  $PM_{2.5}$ ). The smaller abraded particles are liable to become airborne contributing to non-exhaust particles in the atmosphere [8].

It is estimated that an average passenger vehicle tyre lasts for 40,000-50,000 km before it is worn out, with approximately 10-30% of its tread rubber emitted into the environment. The wear factor (defined as the total amount of material lost per kilometre) varies enormously depending on several parameters such as: a) *tyre characteristics* with the most important being size (radius/width/depth), tread depth, construction, pressure and temperature, contact patch area, chemical composition, accumulated mileage and set-up; b) *vehicle characteristics* such as weight, distribution of load, location of driving wheels, engine power, electronic braking systems, suspension type and state of maintenance; c) *road surface characteristics* with the most important being material (bitumen/concrete), texture pattern and wavelength, porosity, condition, wetness and surface dressing; d) *vehicle operation* such as speed, linear acceleration, radial acceleration, frequency and extend of braking and cornering [14]. For instance, heavy-duty vehicles have been reported to emit approximately ten times higher tyre wear particles compared to light duty vehicles and passenger cars, while concrete pavements have been shown to produce lower wear emissions to  $PM_{10}$  compared to other types of pavements [15].

Tyre wear factors are substantially higher for HDVs than for LDVs. The wear factor per vkm will be dependent on the vehicle configuration, such as the number of axles and the load, and so a wide range of values is to be expected [13].

## 2.2. Brake Wear

There are two main brake system configurations in current use: disc brakes, in which flat brake pads are forced against a rotating metal disc, and drum brakes, in which curved pads are forced against the inner surface of a rotating cylinder. The frictional process causes abrasion both of the brake pad and of the surface of the disc or drum leading to the release of particles, a substantial fraction of which become airborne [8]. Drum brakes tend to be a more enclosed system than disc brakes, which means that a greater proportion of the particles released do not get emitted to the atmosphere, instead, becoming trapped within the drum brake system. For this reason, emissions to the atmosphere from drum brakes tend to be lower than from disc brakes. Historically, drum brakes have tended to be more widely used in heavy-duty vehicles (HDVs), relative to light duty vehicles (LDVs), although HDVs are using disc brakes more now [7].

The effect on wear rate of the relative position of brakes on a vehicle is even more important than it is for tyres. With heavy trucks, the braking energy is more evenly distributed between the axles because of lower deceleration rates and the heavy load at the back of the vehicle. Wear rates also depend on brake actuation mechanism (pneumatic, electric), and hence it is more difficult to estimate lifetime of linings. It is expected that for trucks and coaches, the lifetime of brake linings is of the order of 60 000 km [13].

Abu-Allaban et al. [18] employed chemical mass balance receptor modelling and SEM techniques in order to determine brake wear EFs of light and heavy-duty vehicles at roadside locations in the U.S.A. They found  $PM_{10}$  EFs of 0-80 mg/km per vehicle for LDVs and 0-610 mg/km per vehicle for HDVs. The corresponding  $PM_{2.5}$  EFs were 0-5 and 0-15 mg/km per vehicle. In general, high brake wear EFs were observed at freeway exit sites, while brake wear emissions in highways and tunnels were negligible.

There is very little literature on direct heavy-duty brake emissions measurements. To decelerate, heavy-duty vehicles employ technologies such as disc and drum as well as other braking methods including downshifting and engine (or "jake") braking. Due to the difficulty of differentiating a small brake emissions signal from the much larger signal coming from tailpipe, tire wear and road dust combined, there is much uncertainty in these measurements-yet another reason why adjusted laboratory measurements were favoured above [16].

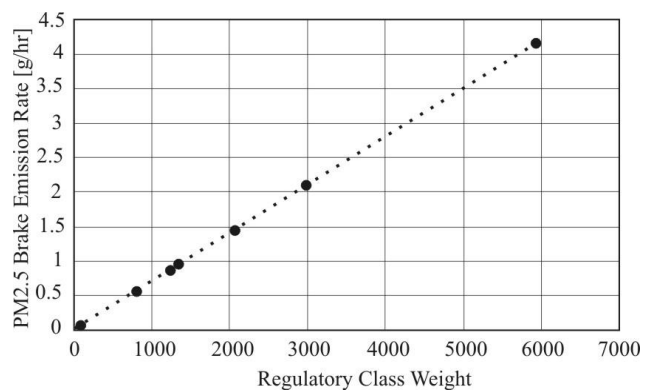


Figure 4: Interpolated Brake  $PM_{2.5}$  Emission Rate by Regulatory Class Weight. Passenger Cars and Combination Heavy-duty Trucks Define the Slope [16]

Figure 5 presents the  $PM_{2.5}$  emissions from brake wear in the UK split by vehicle type and road type. The emissions at this level of detail are derived by combining the vehicle and road type specific emission factors with vehicle kilometre data available for different vehicle and road types, as provided for the UK inventory by the UK Department for Transport (DfT). These data come from DfT's traffic census and traffic forecasts available at this level of detail. Note that the points of the lines are offset slightly to avoid overlapping (e.g. as occurs for Heavy-Duty Vehicles and Passenger cars on Motorways). It is clearly apparent from this figure how emissions from brake wear are more dominant on urban roads than on motorways and how emissions from passenger cars dominate over other vehicle types on urban roads. The dominance of passenger cars is less on rural roads and on motorways, passenger cars and heavy-duty vehicles make a similar small contribution [9].

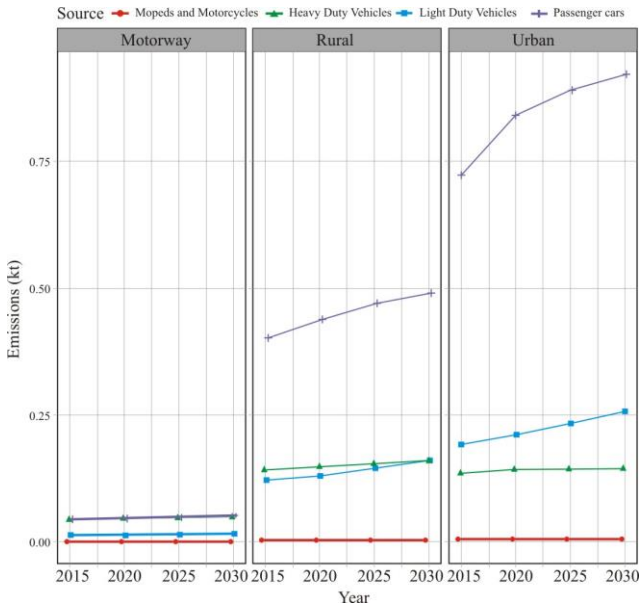


Figure 5: PM<sub>2.5</sub> emissions from brake wear in the UK split by vehicle type (coloured legend lines) and road type [9]

Most studies indicate that emission factors for PM from brake wear are significantly larger from HDVs than from LDVs [12] and [7]. This would be due to the larger number or size of brakes on heavy-duty vehicles and the fact that the larger vehicle weight releases more kinetic energy in the process of slowing the vehicle down. Garg et al. [19] also found a positive relationship between the weight of vehicles considered and the associated brake wear emission factors. Table 3 shows the emission factors for tyre wear and brake wear of road vehicles as used in the UK’s National Atmospheric Emissions Inventory, submitted in 2017 [9]. These emission factors were developed based on a method Table in the EMEP/EEA Emissions Inventory Guidebook [7], a Guidebook for national emissions inventory compilation. This shows, amongst other things, that the brake wear emission factors for HDVs are around 5 times higher than those from passenger cars [9].

Figure 6 shows the average fractional size distribution of the LDV and HDV emission factors. The similar distribution for most of the considered elements suggests that these elements origin from the same source, i.e., from individual brake wear particles. Brake wear particles from light duty vehicles were distributed in the entire size range larger than 1 μm, while the contribution from the submicrometer mode was very low.

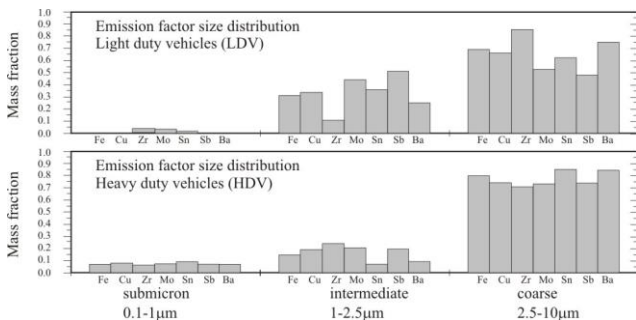


Figure 6: Fractional size contribution for LDV and HDV EF determined for brake wear related trace elements [12]

In contrast, more than 75% of the brake wear emissions from heavy-duty vehicles were found in the coarse mode (2.5-10 μm). An explanation of these different size distributions remains difficult, but is likely due to the different design and operating conditions of LDV and HDV brake systems [12].

Total brake wear for light-duty vehicles appears to be around 10 to 20 mg/vkm, and around 50 to 80 mg/vkm for heavy goods vehicles. Typically 50% of brake wear debris from LDVs escapes the vehicle and enters the atmosphere, and more than 80% of airborne brake wear particles can be classified as PM<sub>10</sub>. A substantial amount of the PM<sub>10</sub> can also be present as PM<sub>2.5</sub>. There is considerable uncertainty regarding the amount of material which is lost from the brake linings, and the amount which is lost from the disc or drum [14].

### 2.3. Road surface wear

The friction between the tyre surface and the road surface which leads to tyre abrasion is also liable to abrade the road surface, especially where this is already fragmenting. Hence, road surface wear particles are also released to the atmosphere. Some studies have suggested that road wear particles are internally mixed with tyre rubber in the particles generated through this abrasion process [8].

With the increasing demands on road surfaces due to heavy traffic loads and extreme weather conditions, a range of modifiers are incorporated into the bituminous binder or asphalt mix. All serve to enhance the properties of the road surface material such that it is fit for its application and to consolidate the bonding between the binder and the mineral aggregate components. Various fillers and fibres may be added to reinforce binder-aggregate bonding. Glass, coal fly ash, and rubber tyres have been used as fillers, the latter becoming increasingly popular owing to problems relating to the disposal of used tyres. In order to harden the binder, sulphur may be added. An array of polymers, epoxy resins, and metal complexes have also been utilised as modifiers. Concrete road materials are a mixture of mineral aggregate, sand, and cement. There is little information in the literature on the precise chemical composition of the bulk road surface materials or PM generated by the wear of the road surface material, presumably due to the complexity of its composition and the range of different surface materials in use. Consequently, there exists no definitive molecular marker for road surface wear [20].

Some authors reported wear factors for LDVs and HDVs of 7.9 and 38 mg/vkm respectively, although these values also included tyre and brake wear. For New Zealand, Kennedy et al. [21] calculated a wear factor of 0.44 g/vkm for a road surface containing 50 % bitumen. In a situation where the bitumen comprises only 10 % of the worn surface, this figure would be reduced to 0.09 g/vkm. However, in areas where there is extensive use of studded tyres during the winter, the wear of the road surface, and the resulting PM concentrations due to resuspension, are considerably higher. Indeed, the wear when non-studded tyres are used is insignificant compared to when studded tyres are used. Winter maintenance procedures in cold climates, such as traction sanding (the dispersion of sand aggregate on the road surface) and the use of studded

tyres, have been associated with high airborne particle concentrations through a formation process known as the "sandpaper effect". The wear of the road surface increases with moisture level, and is 2 to 6 times larger for a wet road than for a dry one. It also increases after salting of the road, since the surface remains wet for longer periods. Vehicle speed, tyre pressure and air temperature also affect road wear. As the temperature decreases the tyres become less elastic, with the result that the road surface wear rates increase [13].

#### 2.4. Resuspension

Dusts from a number of sources accumulate on road surfaces. These originate from dry and wet deposition of airborne particles, especially coarser particles such as those deriving from soil. Additionally, abrasion products from the vehicle may deposit on the road contributing to the road surface dusts. Some of this material is in the PM<sub>10</sub> size range when depositing to the road surface and the action of tyres on surface dusts may also cause some grinding leading to the creation of smaller particles from the coarser dusts. Studies of road surface dusts have shown a substantial fraction to be within the PM<sub>2.5</sub> and PM<sub>10</sub> size ranges. Such particles are rather easily suspended from the road surface, both by shear forces at the tyre-road interface and by atmospheric turbulence in the wake of the vehicle. There is also evidence that elevated wind speeds contribute to the resuspension of surface dusts [8].

Heavy-duty vehicles (HDVs) are expected to contribute significantly more to road wear than light duty vehicles (LDV). In the literature the enhancement of road wear by HDV can be from 5 to 100 [14], though in many studies it is often difficult to distinguish between suspended and direct road wear. All LDV wear rates ( $v=li$ ) have been enhanced by a factor of 5 to specify HDV wear rates ( $v=he$ ). It is also worth noting that the percentage of studded tyres on HDV is often quite low, or none at all, and so the studded tyre contribution from HDV's may not be significant [17].

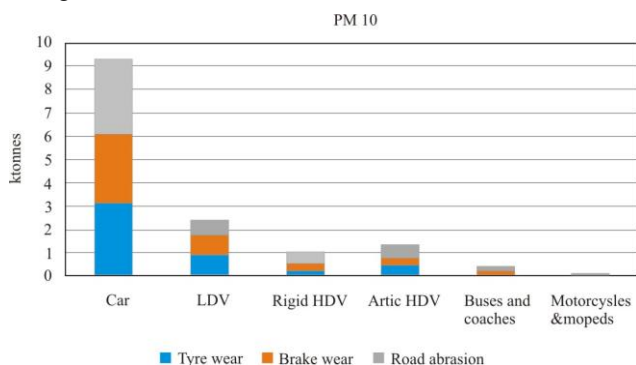


Figure 7: UK emissions of PM<sub>10</sub> from road transport in 2016 by vehicle type [8]

### 3. FUTURE TRENDS IN NON-EXHAUST EMISSIONS OF PARTICULATE MATTER

The magnitude of non-exhaust emissions of PM as currently estimated has important implications for future PM emissions and air quality, because although current policies on exhaust emissions suggest that emissions of PM per vehicle, both light- and heavy-duty, will decrease significantly, as legislation and policy currently stand this is not necessarily the case for non-exhaust emissions.

Three important issues determine the level and importance of non-exhaust emissions in future years, namely (i) the effect of future vehicle technology, in particular the effect of electric and hybrid vehicles on non-exhaust emissions, (ii) future trends in vehicle activity and (iii) the effect of any future legislation which could affect the level and chemical composition of non-exhaust emissions [8].

Using the Guidebook emission factors and vehicle activity data, the NAEI reports the trends in UK tyre wear, brake wear and road abrasion emissions of PM<sub>10</sub> and PM<sub>2.5</sub> shown in Figure 8 and Figure 9. For comparison, emissions from vehicle exhausts are also shown. The emissions shown from 2000-2016 are from the latest version of the reported UK inventory representing actual vehicle activities, while emissions from 2017-2030 are projections in emissions based on DfT's traffic growth assumptions and in the case of exhaust emissions reflect the turnover in the vehicle fleet with the penetration of new vehicles meeting tighter Euro standards for PM emissions. Figures show how as vehicle exhaust emissions have declined, the non-exhaust emissions have been slowly increasing with increasing traffic levels and are becoming a much larger share of overall PM<sub>10</sub> and PM<sub>2.5</sub> traffic emissions. The proportion of total NEE from brake wear, tyre wear, road surface wear has increased from 39% of total UK road transport emissions of PM<sub>10</sub> in 2000 to 73% in 2016; for PM<sub>2.5</sub> the proportion of NEE has increased from 26% in 2000 to 60% in 2016.

Without any NEE abatement this trend is predicted to continue so that by 2030, the non-exhaust sources will contribute to 94% of total UK road transport emissions of PM<sub>10</sub> and 90% of PM<sub>2.5</sub> [8].

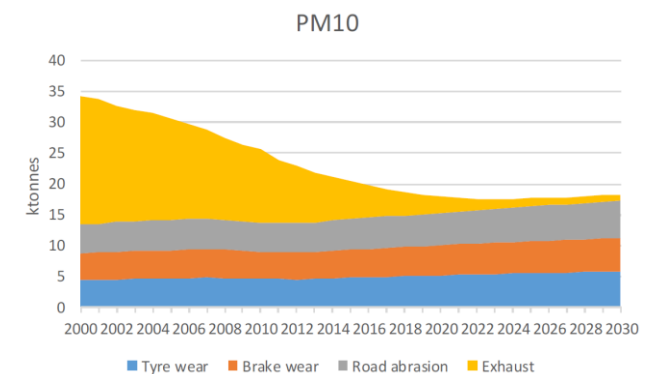


Figure 8: UK emissions of PM<sub>10</sub> from road transport [8]

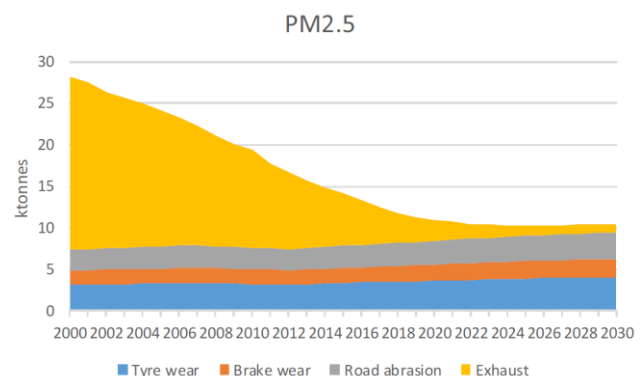


Figure 9: UK emissions of PM<sub>2.5</sub> from road transport [8]

#### 4. CONSLUSIONS

Non-exhaust emissions from mobile sources make significant contributions to total PM emissions in the world today. The importance of this source will grow in the future since effective control programs are in place to reduce exhaust emission from transport.

In case of urban street canyon, the percentage of HDVs is lower than on the highway (10 compare to 15%). Compared to light duty vehicles, the absolute emission factors for heavy-duty vehicles were 15 times higher for total PM<sub>10</sub> and 10 times higher for brake wear and the exhaust emissions. In contrast to light duty vehicles, the road dust resuspension capability of an individual heavy-duty vehicle was estimated to be substantial. More than half of the PM<sub>10</sub> emissions of an individual heavy-duty vehicle were attributed to road dust resuspension and minor contributions of road wear and tire wear.

The average PM<sub>10</sub> emission factor for highway was caused by exhaust emissions (≈40%) and very low contributions from brake wear emissions (3%). The remaining percentage of the traffic emissions were not directly identified, but probably represented contributions from road dust resuspension (and minor contributions from tire wear and road wear).

Significant gaps still exist in our understanding of traffic emissions, particularly:

1. Characterization and quantification of different non-exhaust sources.

2. Impacts of non-exhaust emissions upon human health: While there are many studies reporting links between exposure to air pollution and adverse health impacts, detailed information on the components that contribute to toxicity is missing.

3. Aerosol chemistry in high traffic environments, and the evolution of particles emitted from vehicles. Further, most of the reported analyses have been carried out in the USA or Europe, and there is a lack of reliable information on traffic emissions in areas with high population density in Africa, Asia and South America. The field offers much scope for future research, including the development of enhanced methods for quantification of non-exhaust contributions to airborne concentrations.

#### ACKNOWLEDGEMENTS

This paper was realized within the researching project "The research of vehicle safety as part of a cybernetic system: Driver-Vehicle-Environment" ref. no. TR35041, funded by Ministry of Education, Science and Technological Development of the Republic of Serbia.

#### REFERENCES

- [1] S. Lawrence, R. Sokhi and K. Ravindra, "Quantification of vehicle fleet PM<sub>10</sub> particulate matter emission factors from exhaust and non-exhaust sources using tunnel measurement techniques", *Environmental Pollution*, Vol. 210, pp. 419-428, (2016)
- [2] T. Grigoratos and G. Martini, "Brake wear particle emissions: a review" *J. Environ. Sci. Poll. Res.* pp.1-14, (2014)
- [3] P. Pant and R.M. Harrison, "Estimation of the contribution of road traffic emissions to particulate matter concentrations from field measurements: A review", *Atmospheric Environment*, Vol 77, 78-97, (2013)
- [4] K. Adachi, Y. Tainosho, "Characterization of heavy metal particles embedded in tire dust", *Environment International* Vol.30 (8), pp. 1009-1017, (2004)
- [5] F. Amato, M. Pandolfi, M. Viana, X. Querol, A. Alastuey, T. Moreno, "Spatial and chemical patterns of PM<sub>10</sub> in road dust deposited in urban environment", *Atmospheric Environment*, Vol.43 (9), pp. 1650-1659, (2009)
- [6] R. M. Harrison, A. M. Jones, J. Gietl, J. Yin, D. C. Green, "Estimation of the contributions of brake dust, tire wear, and resuspension to nonexhaust traffic particles derived from atmospheric measurements", *Environmental Science & Technology* Vol.46, pp. 6523-6529, (2012)
- [7] EMEP/EEA, Air Pollutant Emissions Inventory Guidebook, available at <https://www.eea.europa.eu/publications/emep-eea-guidebook-2016>, (2016)
- [8] Non-Exhaust Emissions from Road Traffic, Air Quality Expert Group, Crown copyright (2019)
- [9] D. Wakeling, T. Murrells, D. Carslaw, J. Norris, L. Jones, "The Contribution of Brake Wear Emissions to Particulate Matter in Ambient Air", FORSCHUNGSVEREINIGUNG AUTOMOBIL TECHNIK E.V. FAT-SCHRIFTENREIHE
- [10] ACEA Report Vehicles in use Europe 2019
- [11] I. Vouitsis, L. Ntziachristos, Z. Samaras, "TRANSPHORM Report, Transport related Air Pollution and Health impacts-Integrated Methodologies for Assessing Particulate Matter, Methodology for the quantification of non-exhaust road transport PM emissions", (2013)
- [12] N. Bukowiecki, R. Gehrig, P. Lienemann, M. Hill, R. Figi, B. Buchmann, M. Furger, A. Richard, C. Mohr, S. Weimer, A. Prévôt, and U. Baltensperger, "PM<sub>10</sub> emission factors of abrasion particles from road traffic (APART)". Swiss Association of Road and Transportation Experts (VSS), (2009)
- [13] L. Ntziachristos and P. Boulter, "EMEP/EEA emission inventory guidebook 2009, Road vehicle tyre and brake wear; Road surface wear", (2009)
- [14] P.G. Boulter, "A review of emission factors and models for road vehicle non-exhaust particulate matter, TRL Report PPR065. TRL Limited, Wokingham (2006)
- [15] F. Amato, M. Pandolfi, T. Moreno, M. Furger, J. Pey, A. Alastuey, N. Bukowiecki, A.S.H. Prevot, U. Baltensberger, and X. Querol, "Sources and variability of inhalable road dust particles in three European cities", *Atmospheric Environment* Vol. 45, pp. 6777-6787, (2011)
- [16] Brake and Tire Wear Emissions from On-road Vehicles in MOVES2014, Assessment and Standards Division Office of Transportation and Air Quality U.S. Environmental Protection Agency, (2014)
- [17] B.R. Denby, I. Sundvor, C. Johansson, L. Pirjola, M. Ketzler, M. Norman, K. Kupiainen, M. Gustafsson, G. Blomqvist, G. Omstedt, "A coupled road dust and surface

moisture model to predict non-exhaust road traffic induced particle emissions (NORTRIP). Part 1: Road dust loading and suspension modelling", *Atmospheric Environment*, Vol. 77, pp. 283-300, (2013)

[18] M. Abu-Allaban, J.A. Gillies, A.W. Gertler, R. Clayton and D. Proffitt, "Tailpipe, resuspended road dust, and brake-wear emission factors from on-road vehicles", *Atmospheric Environment* Vol. 37, pp.5283–5293 (2003)

[19] B. D. Garg, S.H. Cadle, P.A. Mulawa and P.J. Groblicki, "Brake wear particulate matter emissions",

*Environmental Science and Technology* Vol. 34, pp.4463-4469, (2000)

[20] A. Thorpe and R. M. Harrison, "Sources and properties of non-exhaust particulate matter from road traffic: A review", *Science of the total environment*, Vol 400, pp. 270–282, (2008)

[21] K. Kennedy, J. Gadd, I. Moncrieff, "Emission factors for contaminants released by motor vehicles in New Zealand". Prepared for the New Zealand Ministry of Transport and Infrastructure Auckland. (2002)

# Standards, Regulations and Legislation of Used Motor Oil Management and Disposal – A Review

Jelena Mihajlović<sup>1\*</sup>, Nevena Marković<sup>2</sup>, Goran Petrović<sup>1</sup>, Danijel Marković<sup>1</sup>, Žarko Čojbašić<sup>1</sup>

<sup>1</sup>Faculty of Mechanical Engineering, University of Niš, Niš (Serbia)

<sup>2</sup>Ministry of Defense, Niš (Serbia)

*Constant satisfaction of human needs, which are rapidly increasing, led by science and technologies, has created a vast amount of different waste types. Inventions of new, artificial based materials caused the presence of the dangerous waste type – hazardous waste. One type of hazardous waste is lubricants and especially, used motor oil. Uncontrolled and inadequate disposal of used oil is equally hazardous for humans and the whole living world. This state is unfortunately widely spread in undeveloped countries, where negative effects are severe. Given the danger that inadequate disposal of used motor oil may cause on the environment, proper standards and regulations have been developed to define the proper system for managing and controlling the used motor oil disposal and storage. The Republic of Serbia as a developing country has in recent years adopted World's and European's standards and regulations to deal with problems as such. This paper introduces the standards and regulations that have been implemented.*

**Keywords: Standards, regulations and legislations; used motor oil; hazardous waste.**

## 1. INTRODUCTION

The daily increase in human needs, the unhindered satisfaction of which has been made possible by science and technologies that are in constant and intensive development, has led to the production of significant quantities of different types of waste. Initially, the characteristics of all types of waste were unknown, and on the other hand, the discovery of a large number of new, artificial materials lead to the emergence of a special type of waste - hazardous waste.

One of the most hazardous wastes with inadequate disposal represents a great danger for people, as well as for the entire living world, i.e. lubricants. Even if humans began to use lubricants before the new era, the danger which they oppose to humans was increased only after the spread of oil use, and especially in the second half of the 20th century when synthetic lubricant uses were developed (such as motor oil). Lubricating oil finds several applications in a technologically advanced economy. Particularly, according to the estimates of Europalub, the Association in charge to harmonize and publish European lubricants statistics, 49% is used in the automotive sector, 37% is used by industry, while the remaining 14% is represented by base oils used as raw materials [1].

Management of used motor oils is a growing concern, particularly in industrial and urban areas. The generation of waste oils is closely linked with an increase in the population of automobiles and industries. When additives and foreign substances, such as metal powder, chips, and other particles, are mixed with lubricating oil, aging, degrading, and failure will likely occur, leading to mechanical fault and degraded performance [2, 3]. In such cases, the oil is replaced to improve the performance. The used, spent, or waste oils should be collected and recycled not only to prevent environmental pollution but also to preserve natural resources [3].

Given the above-mentioned, it was necessary to observe the whole problem of used motor oils, to get to know its characteristics, its behaviour in nature because in

undeveloped countries it is still uncontrollably disposed of with no regard to consequences. Developed industrial countries, which have first encountered the problem of the used motor oil, due to the rapid industrialization, first initialled detailed researches that created rules and principles that in form of legally defined standards regulate the functioning of management systems. For the adequate functioning of each phase and the behaviour of participants in this complex system, it was necessary to apply the approval of legislative, institutional, and planning frameworks, as well as mechanisms for their implementation, which reduces the potential risks of negative effects.

However, developing countries, including the Republic of Serbia, have only recently become involved in the solution to the problem of uncontrolled waste disposal in nature. In order to indulge in European and world trends, the state is artificially imposed to implement drastic changes that aimed at establishing a sustainable and functional system of management of used motor oil. At that moment, it is necessary to make great efforts in order to raise the environmental awareness of the widest circle of the population.

## 2. LAW REGULATIONS IN MANAGEMENT OF USED MOTOR OIL

Lubricating oils are certainly necessary for everyday life and enable the operation of many complex and less complex systems.

Modern or conventional lubricants in most cases consist of base oil, which usually makes up 90% of a certain lubricant, and the remaining 10% are additives.

When looking at the base oil, it can be said that it is a component that together with additives serves for the production of various lubricants.

By origin, the base oil can be [4]:

- Mineral - consist of mineral base oil and additives. The largest amount (approximately 95%) of modern lubricants is represented by mineral oils obtained by oil refining.

\*Corresponding author: Jelena Mihajlović: Sl.Oraovica, Leskovac, jelena.mihajlovic@masfak.ni.ac.rs

- Synthetic - produced as a replacement for mineral lubricants. The basic feature of synthetic lubricating oils is that the required and desired lubricating properties can be determined in advance by the composition of raw materials as well as the conditions under which the synthesis is performed, i.e. the combination of all raw materials.
- Natural - based on plants and animals' fat.

Today, experts in the field of lubrication have come to several practical findings on reducing wear and saving energy to run individual assemblies, and scientists and researchers are trying to answer questions about how to improve lubrication in the broader sense of the field. Such a practice is positive for everyone because the experts try to apply the available knowledge of researchers as soon as possible and in full in everyday practice.

However, in recent years, much has been said about the topic of lubricants. Especially after their use, they become waste oils and at the same time a type of hazardous waste.

According to the Regulation on the conditions, manner, and procedure of waste oil management, waste oils are defined as:

“Waste oils are all mineral or synthetic oils or lubricants that are unusable for the purpose for which they were originally intended, such as hydraulic oils, motor oils, turbine oils or other lubricants, marine oils, oils or fluids for insulation or heat transfer, other mineral or synthetic oils, as well as oil residues from tanks, oil-water mixtures, and emulsions, under the law governing waste management” [4,5].

In order to minimize the negative impacts or possible consequences that waste oils can lead to, it was necessary to regulate by law certain rules of conduct for all persons who use lubricating oils, whether they are producers or direct users.

Today, this segment is regulated by numerous regulations, which are defined for producers and users, and also define the rights, obligations, responsibilities at the international and national level. International regulations were created before national ones, so they also served as a model for the adoption of national regulations.

### 2.1. Law Regulations and Practises in European Union

The history of the European Union's environmental policy begins with the waste policy in general after the major incidents have occurred during the seventies and eighties of the last century. Because those incidents were caused by industrial plants (It is noticeable that industrial plants have always had a significant impact on environmental pollution.) it is easy to conclude why the laws of the European Union were first aimed at hazardous waste management.

The beginnings of European Union legislation on hazardous waste management began in 1975, when the Waste Framework Directive was adopted, which aimed to reduce pollution, improve the natural and urban environment, and take the necessary measures to raise awareness of environmental problems.

These activities influenced the undertaking of more active measures in the preparation and adoption of certain regulations in the field of environment. Member states

began to take measures at the national level by controlling and managing hazardous waste, so in 1975 the Directive on Hazardous Waste was adopted, and later the Regulation on Waste Disposal. It can be said that the above three legal provisions have established the foundations of the regulatory structure related to hazardous waste. It is clear that these three documents which define waste and other key concepts, ensuring that waste is managed without harmful consequences for the environment or human health.

However, the first directives adopted in the European Union did not specify the parameters of emissions of harmful effects on the environment that are considered acceptable. Most of these imperfections have been remedied by the adoption of the Landfill and Disposal Directive in 2001, as well as the 2000 Waste Incineration Directive [5]. In addition to the previous regulations, numerous other directives regulating waste streams have been introduced, and one of them is the regulation related to waste motor oils.

As presented on the Figure 1 one of the first regulations of European Union legislation governing waste management, which regulated waste streams, was the 1975 Waste Oils Directive. Thus, the mid-1970s were considered the beginning of the introduction of waste oil management into the practice of European legislation (Council Directive 75/439 / EEC). The mentioned directive regulated the uncontrolled disposal of waste oils until then, but at the same time, it was focused only on waste lubricating oils. The basic requirement set before the Member States was to give priority to the regeneration of waste oils over other disposal methods, as regeneration is considered the most energy-efficient option. Otherwise, Member States should have burned waste oils, but under acceptable conditions that would not harm the environment. The directive also prohibits the dumping of used oils into surface and groundwater and sewage, as well as on land. Due to the limitations that were noticed, the directive was amended three times [5].

It underwent the first amendments to the 1975 directives after twelve years when a new amended directive (87/101 / EEC) was adopted in 1987. The first changes were mainly focused on the level of permitted concentrations of harmful products that occur during the incineration of waste oils. On that occasion, the permitted concentrations of harmful products were reduced compared to those defined by the 1975 Directive, Member States were invited to strive to remain below the permitted harmful concentrations, and the Commission was invited to consider all the facts and to entry into force of the said directive comes out with new proposals, in order to minimize the harmful impact of waste oil incineration. The other two changes that occurred with the adoption of the directives in 1991 and 2000 concerned the standardization and rationalization of reports on the implementation of certain directives relating to the environment (91/692 / EEC), as well as waste incineration and adverse effects that occur during the process (2000/76 / EC). The last changes regarding the management of waste oils in the European Union were made in 2008 when Directive 2008/98 of the European Parliament concerning waste, in general, came into the act and repeals certain directives that regulated this area in the years before [5].

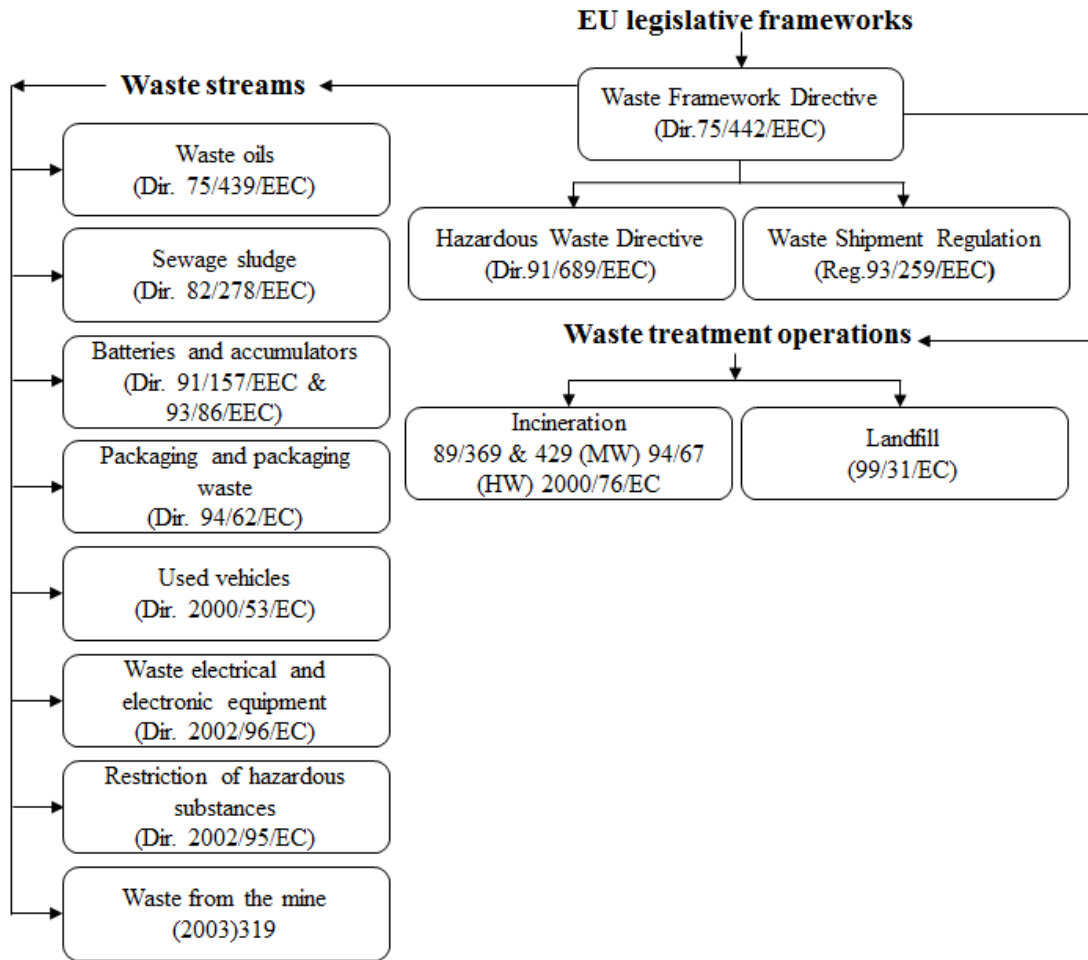


Figure 1. Review of European Union regulations regarding the waste management[5]

2.2. Law Regulations and Practises in the Republic of Serbia

Legislation and practice of the Republic of Serbia in terms of environmental protection and waste management has always had some delays concerning laws and their implementation within the European Union. The period of the seventies and eighties of the last century was marked as a period of the awakening of environmental awareness among the inhabitants throughout Europe. In the same period, there was an intensive and turbulent industrial development in Serbia, but also a complete absence of environmental awareness. The generated waste in that period was mostly disposed of in the factory circle of industrial plants because it was considered that the same waste could be used as secondary raw material in some industrial processes. Therefore, there was no tendency to define or enable the development of some other treatment option or adequate final waste disposal.

When observing and comparing the period of the 1990s, it can be concluded that Europe is in constant and increasing progress in terms of environmental protection and waste disposal by adopting new regulations, while the same cannot be said for Serbia. Due to the problems and wars that shook Serbia during the 1990s, the country began to weaken economically, industrial production was less and less dominant, and in such conditions, it was impossible to correct the existing state of relations towards waste disposal. The whole decade was marked by the absence of an adequate legislative, institutional, and

planning framework, so the entire environment protection was to a greater or lesser extent based on the decisions and conscience of the individuals.

After 2000, when the political and economic situation in Serbia stabilized to some extent, serious work began on regulating waste management, and thus regulating the flow of used oil. The creation of environmental protection policy and legal regulation in this field becomes an important topic for the Republic of Serbia at the moment of the beginning of harmonization of Serbian legislation with the legislation of the European Union, as part of the obligation to join the European Union. Starting from the Stabilization and Association Process, which began in 2000, to officially gaining European Union candidate status, Serbia has taken serious steps towards transforming its legal system. In order to meet all the requirements and thus enable the closure of Chapter 27, which focuses on the environmental protection sector, serious transformations of the state system had to be made in order to reach the level characteristic of developed countries. The biggest step was made in 2009 when the National Assembly of the Republic of Serbia adopted sixteen laws, which make up the so-called "green package". The set of the mentioned laws primarily regulated the area of hazardous waste management and the already existing Law on Environmental Protection was improved.

One of the sixteen laws from the set of so-called "green package" of laws adopted in 2009 is the Law on

Waste Management ("Official Gazette of RS" No. 36/09-115, 88/10-170, 14/16-17 and 95/18-267) [6]. Like the Law on Environmental Protection and the Law on Waste Management, it has undergone several changes, the last of which was adopted in 2016. The Law on Waste Management is the basic document based on which several bylaws have been adopted that are crucial for defining and regulating procedures with waste oils [6].

According to the Law on Waste Management, the Waste Management Strategy for the period 2010-2019 (Official Gazette of the RS No. 29/10-13 of 2 May 2010) was also issued. One of the points in the Waste Management Strategy for the period 2010-2019, is also an analysis of the existing situation, within which the used motor oil management was analysed [7].

The Decree on products that after use become special waste streams, the form of daily records on the quantity and type of manufactured and imported products and the annual report, the manner and deadlines for submitting the annual report, fee bonds, calculation criteria, amount and method of calculation and payment of fees from the regulations adopted in 2010 based on the Law on Waste Management ("Official Gazette of RS" No. 54/10, 86/11, 15/12, 41/13, 03/14, 81/15, 31/15, 44/16, 43/17, 45/18, 67/18, 95/18) [8]. The third article of the mentioned regulation defines six products that, after use, become special waste streams, and one of those products is all waste oils and lubricants that are not suitable for the original purpose. The significance of this decree is also in the fact that it defines the obligations of taxpayers, i.e. producers and importers of products that after use become special waste streams, reports that are obliged to submit to the Environmental Protection Agency, fees, and penalties if do not abide by the law. Thus, it is possible to form records and monitor statistics on the quantities of products that become special waste streams, so now the state has somewhat realistic data, which was not the case before 2010 [8].

Another regulation that was adopted in 2010, and which also resulted from the Law on Waste Management, is the Rulebook on conditions, manner, and procedure of waste oil management ("Official Gazette of RS" No. 71/10-40 of 4 October 2010) [9]. If we look at the regulations of the European Union, it cannot be overlooked that the management and treatment of waste oils were regulated in 1975, which concerning the regulations of the Republic of Serbia represents a difference of 35 years of delay. The mentioned rulebook is the most important normative document that defines the management of waste oils on the territory of the Republic of Serbia. A total of sixteen articles of this rulebook define what waste oils are, what are the obligations of producers, owners, and collectors of waste oils, as well as persons who transport them. The ordinance also regulates the storage of waste oils and the treatment of waste oils, i.e. regeneration, thermal treatment, and disposal of products resulting from thermal treatment. It is important to emphasize that the rulebook forecast keeping daily records on the quantities generated, handing over waste oils to the collector, the person performing storage, or the person performing waste oil treatment, but only for quantities of waste oils that amount to more than 500 litres per year [9].

### 3. USED MOTOR OIL MANAGEMENT AND DISPOSAL IN SERBIA

The Waste Management Strategy for the period from 2010 to 2019 presents the activities that should be obligated to when it comes to used motor oils. First of all, used motor oils must not be discharged to land, surface and groundwater and sewage. Also, it is forbidden to mix used motor oils during collection and storage with substances other than waste oils or mixing them with hazardous waste.

The presented Strategy states that used motor oil treatment processes for reuse, such as regeneration and refraining, have priority overuse for energy purposes or other appropriate treatment procedures. Also, it is stated that the treatment of used motor oils can be performed only in the treatment plant in a way that does not endanger the environment and human health.

Another fact whose application is projected for the period from 2010 to 2019, and is already applied in the Europe, is the introduction of the payment of a fee whose payers are producers and importers of fresh-unused oil, and which after use becomes waste. According to projections, the money from the fees would be used for the collection and treatment of all waste oils.

Also, the person who collects stores and treats waste oils must have a permit, keep the records of used motor oils and the quantities which have been collected, stored or treated, as well as the final disposal of the residue after treatment. That information needs to be submitted to the Agency for environmental protection.

By adopting the Rule book on conditions, manner and procedure of waste oil management (Figure 2), persons who collect, store and treat waste oils are obliged to do so in the exact manner provided by the rule book [10]. Given to that it is obligatory to [5]:

- Have adequate space,
- Handle used motor oil in the prescribed manner,
- Keep proper documentation on the amount that has been collected, stored or treated, as well as on the final disposal of residues after treatment and submit the data to the Ministry.

The obligation of the manufacturer/ owner of used motor oils must ensure the collection and temporary storage of used motor oils generated by his activity. The owner of waste oils is obliged to hand over the used motor oils to an authorized collector and to provide him with conditions for its uninterrupted collection. Also, the owner can directly hand over the collected waste oil to the transfer station or collection centre, which is located at the waste management plant.

The authorized waste oil collector must have a warehouse, i.e. transfer station, for the temporary storage of the collected waste oils. Used motor oil treatment is not allowed in the warehouse or transfer station. The used motor oil must be stored at that place in the accordance with the regulations governing the treatment of waste materials and environmental impact assessments. The authorized waste oil collector is obliged to take over the waste oils from the owner of the waste oils free of charge and to hand over the waste oils to the authorized treatment operator and/or the authorized person for waste oil disposal.

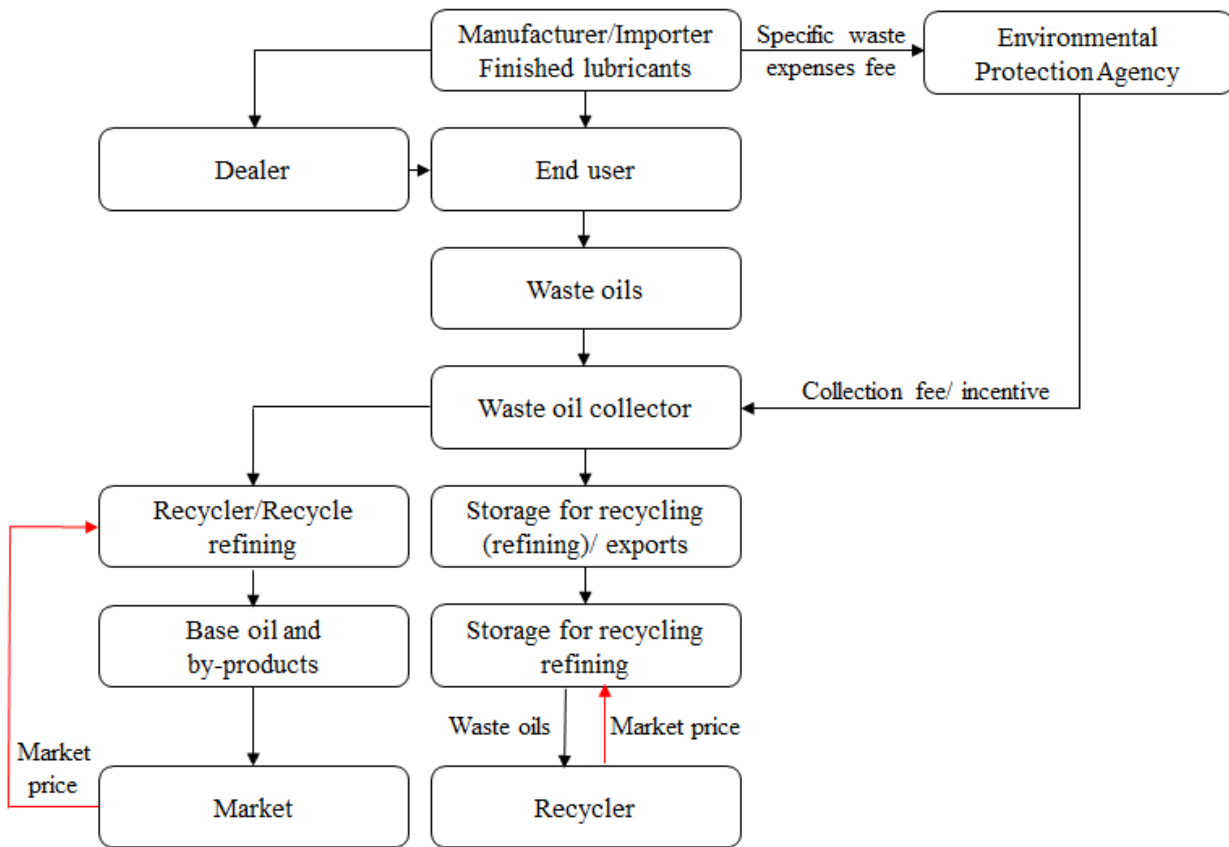


Figure 2. Sustainable used motor oil management system [10]

Table 1. Imported oils that become special waste streams after use [10]

| Years | Total amount (l) | Total amount (t) | SUM 2011-2019 (t) | Potential fee amount for special waste streams (RSD) |
|-------|------------------|------------------|-------------------|--|
| 2011  | 23968490.49      | 14617.28         | 36188.92          | 434267057.29   |
| 2012  | 19527292.53      | 16502.64         | 34077.20          | 408926439.32   |
| 2013  | 19092040.74      | 18320.48         | 35503.32          | 426039799.99   |
| 2014  | 17029009.90      | 20767.05         | 36093.16          | 433117906.92   |
| 2015  | 21495817.06      | 20768.33         | 40114.57          | 481374784.25   |
| 2016  | 21926658.80      | 16971.30         | 36705.29          | 440463515.04   |
| 2017  | 20492853.70      | 17699.10         | 36142.67          | 433712019.96   |
| 2018  | 21093163.30      | 19097.90         | 38081.75          | 456980963.64   |
| 2019  | *                | 38706.20         | 38706.20          | 464474400.00   |

Table 2. Used motor oil management on the territory of the Republic of Serbia [10]

| Years | Disposed waste (t) | Treated waste (t) | Exported waste (t) | SUM 2011-2019 (t) |
|-------|--------------------|-------------------|--------------------|-------------------|
| 2011  | /                  | 5304.00           | 5.00               | 5309.00           |
| 2012  | /                  | 3411.00           | 1304.00            | 4715.00           |
| 2013  | /                  | 8245.00           | 79.00              | 8324.00           |
| 2014  | /                  | 10136.00          | 0.00               | 10136.00          |
| 2015  | /                  | 3042.00           | 245.00             | 3287.00           |
| 2016  | /                  | 4343.00           | 116.00             | 4459.00           |
| 2017  | /                  | 5967.00           | 41.00              | 6008.00           |
| 2018  | /                  | 5042.00           | 186.00             | 5228.00           |
| 2019  | /                  | 2348.00           | 44.00              | 2392.00           |

The authorized recycler must have a regulated warehouse, i.e. a collection centre for storage of collected used motor oils, as well as waste (hazardous and non-hazardous) generated by processing of used motor oils, by regulations governing waste management and environmental impact assessment. The authorized recycler

is obliged to ensure that the amount of collected used motor oils corresponds to the amount of regular procession. The authorized recycler is obliged to take over the collected waste oil from the authorized collector.

Based on the data presented in the reports of the Environmental Protection Agency from 2019 [10], and

showed in Table 1, about 55,000 tons of finished lubricants are placed on the Serbian market annually, which, according to the current legislation, are subject to payment of fees for products that become potential fee amount for special waste streams after use. Bearing in mind that between 50% and 60% of used motor oils can be collected from the quantity placed on the market means that the amount of used motor oil generated is between 26,000 and 33,000 tons per year [10].

This amount will grow in line with the projected growth of industrial production (approx. 4% per year).

According to the Environmental Protection Agency, in 2019, and presented in Table 2, 2348.00 tons of waste mineral and synthetic oils were treated in treatment plants (combustion and preparation for combustion) and 44.00 tons were exported, which represents a total of about 6.18% of the total quantities placed on the market [10].

It is alarming that in 2019, fewer used motor oils were collected in Serbia than in any other year in the period 2011-2019!

#### 4. CONCLUSIONS

Unlike other types of waste, used motor oils also have hazardous properties (both physical and chemical), and consequently, negative consequences in the case of inadequate disposal can have a larger impact on the entire environment. Because of the characteristics of used motor oils, in order to reduce the probability of an accident and the magnitude of the consequences, it is necessary to manage the entire cycle through which lubricating oils pass from production to end of use when they become waste oils. As in the case of other waste types, the used motor oil management system is an organized approach of guidance and control from the moment of its generation, collection, storage, treatment to final disposal or disposal. One of the key guidelines that can properly manage the risk of this type of waste is the responsibility of all entities of the system or the responsibility of society as a whole.

However, complete protection against lubricating oils that become used motor oils at the end of their life cycle does not actually exist. This would only be possible if they were not produced and used. Therefore, everyone, from manufacturers to end-users, must have maximum responsibility when using lubricating oil. Only in this way, the application of appropriate measures and procedures can reduce the risk of harmful effects to a minimum, and thus protect the health of living beings, as well as the preservation of material goods and natural resources, i.e. the environment.

The practice of developing countries, including the Republic of Serbia, when it comes to waste management in general in previous years, was assessed as poor. It was pointed out through serious problems that require a special approach when comes to solving them, so it became clear that big changes are necessary if Serbia wants to get closer to European trends. Building a new legislative system that is fully in line with European Union standards is one of the steps that have been taken. On the other hand, an institutional framework has been established that should enable the implementation of all prescribed provisions and planning bases that set short-term and long-term goals. However, one gets the impression that adequate education

of responsible persons and the public has not been performed, but also that constant and complete control is not performed, which is why the implementation of the established principles is not fully realized.

Although the legislation is today adjusted to the regulations of the European Union, another problem should be singled out, and that is the lack of an appropriate network of waste oil management plants, i.e. the absence of plants for self-collection and some types of used motor oil treatment.

As a result, finding the best possible location of such a facility applied in the regional center of Southern and Eastern Serbia – the city of Niš regarding the multi-criteria decision-making (MCDM) methodology would be the future step in our research.

#### ACKNOWLEDGEMENTS

This research was financially supported by the Ministry of Education, Science and Technological Development of the Republic of Serbia (Contract No. 451-03-9/2021-14/200109).

#### REFERENCES

- [1] Y. L. Hsu, C. H. Lee, and V. B. Kreng, "Analysis and Comparison of Regenerative Technologies of Waste," WSEAS Transactions on Environment and Development, issue 3, Vol. 5, pp. 295-309, (2009)
- [2] M. J. Diphare, E. Muyenda, T. J. Pilusa, and M. Mollagee, "A Comparison of Waste Lubricating Oil Treatment Techniques," 2nd International Conference on Environment, Agriculture and Food Sciences ICEAFS 2013, Kuala Lumpur (Malaysia), 25-26 August, pp. 107-109, (2013)
- [3] F. D. Giovanna, O. Khlebinskaia, A. Lodolo, and S. Mertus, "Compendium of Used Oil Regeneration Technologies," International Centre for Science and High Technology, Trieste, (2003)
- [4] Đ. Šilić, V. Stojković, D. Mikulić, "Goriva i maziva," Veleučilište, Velika Gorica, (Velika Gorica), (2012)
- [5] N. Marković, "Analiza problema upravljanja otpadnim uljima na teritoriji grada Niša (in Serbian)," Master thesis, The Faculty of Mechanical Engineering, University of Nišu, (Serbia), (2018)
- [6] Zakon o upravljanju otpadom, Sl. glasnik RS. 36/2009-115, 88/2010-170, 14/2016-17, 95/2018-267
- [7] Strategija upravljanja otpadom za period 2010.-2019., Sl. glasnik RS. 29/2010-13
- [8] Uredba o proizvodima koji posle upotrebe postaju posebni tokovi otpada, obrascu dnevne evidencije o količini i vrsti proizvedenih i uvezenih proizvoda i godišnjeg izveštaja, obveznicima plaćanja naknade, kriterijuma za obračun, visinu i način obračunavanja i plaćanja naknade. Sl. glasnik RS, br. 54/2010, 86/2011, 15/2012, 41/2013, 3/2014, 81/2014, 31/2015, 44/2016, 43/2017, 45/2018, 67/2018, 95/2018
- [9] Pravilnik o uslovima, načinu i postupku upravljanja otpadnim uljima. Sl. glasnik RS, 71/2010-40
- [10] <https://reciklaza.biz/rec-struke/otpadna-ulja-najopasniji-zagadjivac/>, last accessed 20.05.2021.

# The usage of shallow groundwater heat by heat pumps in a high-temperature district heating system

Dragiša Šimunović<sup>1\*</sup>, Rade Karamarković<sup>1</sup>, Miloš Nikolić<sup>1</sup>, Đorđe Novčić<sup>1</sup>, Anđela Lazarević<sup>2</sup>

<sup>1</sup>Faculty of Mechanical and Civil Engineering in Kraljevo/Department for Thermal Technique and Environment Protection, University of Kragujevac, Kraljevo (Serbia)

<sup>2</sup> Faculty of Mechanical Engineering/Department of Management in Mechanical Engineering, University of Niš, Niš (Serbia)

*The general tendency in district heating (DH) is the lowering of grid temperatures. To achieve this, heat pumps (HPs) are necessary technology that has an important role in very low (below 60 °C) and ultra-low (below 45 °C) DH supply temperatures. A significant variation in outdoor temperatures during the heating season in the climate of Serbia makes the implementation of HPs in the high-temperature DH systems possible. The goal of the paper is to analyze the implementation of HPs that extract heat from the shallow groundwater to satisfy a part of heat requirements in a boiler room of a DH system. This is a superheated water system with a nominal capacity of 37.728 MW and a nominal temperature regime 130/75°C that belongs to the PUC Toplana in Kraljevo. The city is placed at an alluvial plane rich with shallow groundwater with temperatures in the range of 12 to 18°C. The analysis is carried with two operating modes: (i) present, with an everyday stoppage between 9 PM and 5 AM, and (ii) continuous operation with limited overnight heating. Not to endanger the inflow, the maximal extraction of the heat from groundwater of 755 kW was assumed. The present operating mode would have seasonal COP 3.87 and negative economic indicators, whereas the continuous operation would lead to a sustainable project with a financial rate of return of 10.5%, benefit-cost ratio of 1.192, and the reduction of CO<sub>2</sub> emissions of 201 t/year. The seasonal COP of the HPs would be 4.29.*

**Keywords:** district heating, water source heat pumps, shallow groundwater, cost-benefit analysis

## 1. INTRODUCTION

In the second decade of the XXI century, Lund et al. [1] defined the 4<sup>th</sup> generation of the DH systems. The tendency in the development of the DH systems is the lowering of supply and return temperatures and integration of cogeneration and trigeneration systems, renewable energy sources, and heat pumps (HPs). Actually, from the beginning of the DH development, the general tendency is the lowering of supply and return temperatures. This is in accordance with the 2<sup>nd</sup> law of thermodynamics. In the past few years, a new concept of the development of DH systems emerged. It is called the 5<sup>th</sup> generation of DH systems and represents a thermal energy supply grid that uses water or brine as a carrier medium and hybrid substations with water source heat pumps (WSHP) [2]. These systems use ultra-low temperature regimes. In these emerging DH systems HPs are the key technologies because [3]:

- they can act as a balancing technology when electrical production fluctuates.
- HPs phase out fossil fuels from the energy system.
- HPs make it possible to use very low (below 60 °C) and ultra-low (below 45°C) temperatures in the district heating grid.
- HPs make it possible to minimize grid losses in the district heating grid.

The subject of the paper is an existing DH system with superheated water with a nominal temperature regime 130/75°C and a nominal capacity of 37.728 MW in the "Nova kolonija" boiler room. For this class of the systems,

the analyzed DH system is very efficient and belongs to the PUC Toplana in Kraljevo, Serbia. Although the temperature regime does not favor WSHPs, their usage is possible because of a significant variation in outdoor temperatures during the heating season. The climate is characterized by several cold waves during the winter, whereas during the rest of the heating season mild weather suitable for the implementation of WSHPs prevails.

The goal of the paper is to analyze the implementation of WSHPs that extract heat from the shallow groundwater to satisfy a part of heat requirements in a boiler room of a DH system. The paper should answer: (i) what should be the capacity of the WSHPs, (ii) should the DH company change its operational schedule, and (iii) is the implementation of the WSHPs economically beneficial for the DH company? The city is placed at an alluvial plane rich with shallow groundwater [4] with temperatures in the range of 12 to 18°C. The boiler room "Nova kolonija" has an excellent position suitable for shallow groundwater usage.

To investigate the impact of the temperature regimes and the electricity tariff system, the analysis is carried with two operating modes: (i) present, with an everyday stoppage between 9 PM and 5 AM, and (ii) continuous operation with limited overnight heating. In the second operational mode, only 15% of the nominal load is supplied in the period between 9 PM and 5 AM and the supply temperatures do not exceed 50 °C. Low electricity tariffs in this period as well as low temperatures should support the usage of HPs. As a basis for decision-making, a cost-benefit analysis (CBA) of the analyzed system is performed.

\*Corresponding author: Dragiša Šimunović, Dositejeva 19, 36000 Kraljevo, Serbia, simunovic.d@mfkv.kg.ac.rs

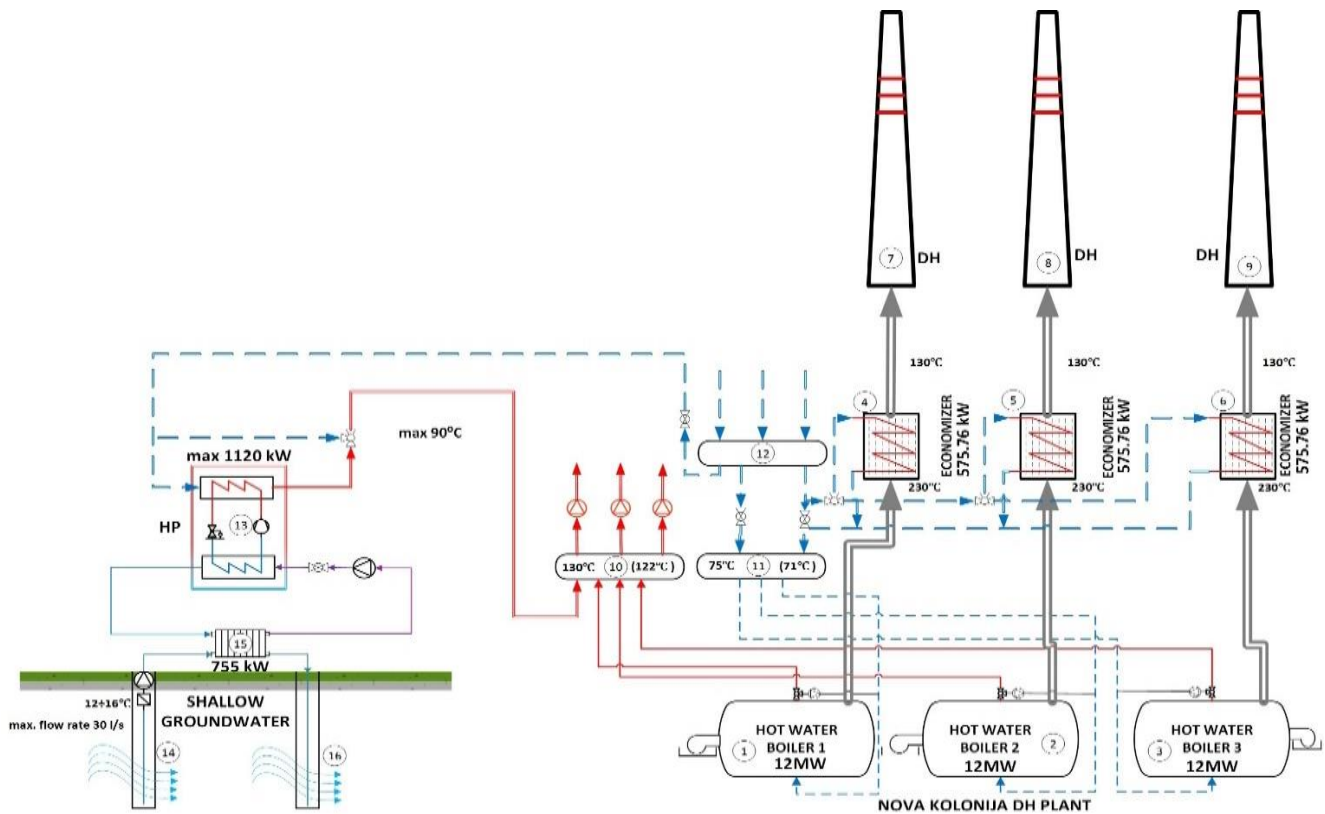


Figure 1: Integration of the groundwater HPs (13) into the “Nova kolonija” plant. Shallow groundwater (14÷16) is the heat source for HPs (13), which work in parallel with the boilers (1÷3) whenever their work is financially profitable. In the figure: 1 ÷ 3- hot water (superheated water) boilers, 4÷6 economizers, 7÷9 – each boiler has its chimney, 10 - supply manifold, 11- return manifold (2nd stage), 12 – return manifold (1st stage), 13 – heat pump(s), 14 – supply well, 15 – plate heat exchanger, 16 – return well.

Figure 1 shows a simplified scheme of the analyzed system. The system utilizes shallow groundwater (14÷16 in Fig. 1) as the heat source for the HPs (13) to supply a part of the required heat in the DH plant “Nova kolonija”. The figure is simplified and shows the parallel connection of the boilers and the HPs. In practice, by a proper design, both series and parallel connections would be used. Additionally, safety and expansion equipment as well as many other details regarding valves, air separators, etc., are omitted from the figure. The analyzed system is dimensioned to limit the maximal flow of groundwater to 30 l/s. The system has the following features:

- Kraljevo is situated at an alluvial plane rich with shallow groundwaters [4]. The position of the plant suits the exploitation of the shallow groundwater. Based on the study and several conversations with geological engineers a modest flow rate of 30 l/s for the location is taken in the analysis. Figure 2. shows the location of the DH plant as well as the potential area for the wells.
- The system should work only when the plant operates, i.e., 180 days per year.
- Depending on the water quality, which has not been analyzed, the direct heat exchange in HPs (13) or with an indirect circuit (as in Figure 1.) would be used.

- Two variants (case studies) are analyzed. They depend on the operational mode of the DH company and are: 1. operation as usual, i.e., from 5 AM to 9 PM, and 2. continuous operation with limited overnight heating.
- The HPs have been implemented in many DH companies, especially in Scandinavian countries because of the low-temperature regimes [5].



Figure 2: The locations of the “Nova kolonija” DH plant together with the potential locations for the wells.

## 2. METHODOLOGY

The main points of the methodology sequentially applied are:

- Meteorological data. The energy calculations in the study were performed for the average

meteorological days during the heating season. The data were taken from the Republic Hydrometeorological Service of Serbia for the period 1990-2010 [6].

- Heat requirement and production. The heat produced in the “Nova kolonija” plant was simulated on the average meteorological days for each month during the heating season [6]. The daily variation of temperature was obtained by the average temperatures at 7 AM, 2 PM, and 9 PM. The data regarding the performance of the DH system were provided by the company PUC Toplana. It was assumed that the temperature of the shallow groundwater changes in the range from 13°C during the winter to 15°C during the summer months.
- Sizing and performance of the HP(s). The HP efficiency is averaged from the available data provided by the manufacturers and was determined based on the previously explained temperature profiles. Constant heat extraction from the groundwater of 755 kW and the maximum heat delivery to the DH system at 85°C of 1120 kW were assumed [7].
- Cost-benefit analysis is carried by the Guide to Cost-Benefit Analysis of Investment Projects [8].
- The same methodology is applied to two variants. The continuous work was taken because it favors the electricity usage by HPs during the low electricity tariffs.

### 3. METEOROLOGICAL DATA AND PERFORMANCE OF THE DH SYSTEM

#### 3.1 Meteorological data and heating requirements

The energy calculations in the study were performed for the average meteorological days during the heating season [6]. The average monthly days with their temperature profiles that are shown in Figure 3 were used in the study.

The temperature profiles were then used to calculate supply and return temperatures in the DH system. Figure 4. shows the temperature profiles for the DH system for the present mode of operation whereas Figure 5 shows the daily temperature profiles for the continuous mode of operation with limited overnight heating obtained by the usage of data provided by Todorović [9]. The continuous mode of operation estimates around a 5% reduction in the energy usage for DH heating. The average overnight supply and return temperatures are shown in Table . Based on measurements provided by the PUC Toplana, and by assuming linear dependence between the heating requirements and outdoor temperature the required thermal energy necessary to fulfill the requirements of all consumers of the “Nova kolonija” plant is:

$$Q[kW] = -555.5 \cdot t + 11110, \quad (1)$$

where t is the outdoor temperature [°C].

For the average meteorological data, the previous equations give the thermal energy needs that are shown in Table 1.

Table 1: Heating requirements for the hospital and the DH company.

| The energy required for DH heating in the “Nova kolonija” plant [kWh/day] – with an overnight stoppage of operation |          |        |       |         |          |          |
|---|----------|--------|-------|---------|----------|----------|
| January   | February | March  | April | October | November | December |
| 165283  | 146427   | 92259  | 40637 | 37386   | 112714   | 155834   |
| The energy required for DH heating in the “Nova kolonija” plant [kWh/day] – continuous heating                      |          |        |       |         |          |          |
| 05-20   | 136318   | 120089 | 72352 | 29551   | 27654    | 128977   |
| 20-05   | 19882    | 18291  | 14837 | 8853    | 7677     | 14585    |
|   |          |        |       |         |          | 18293    |

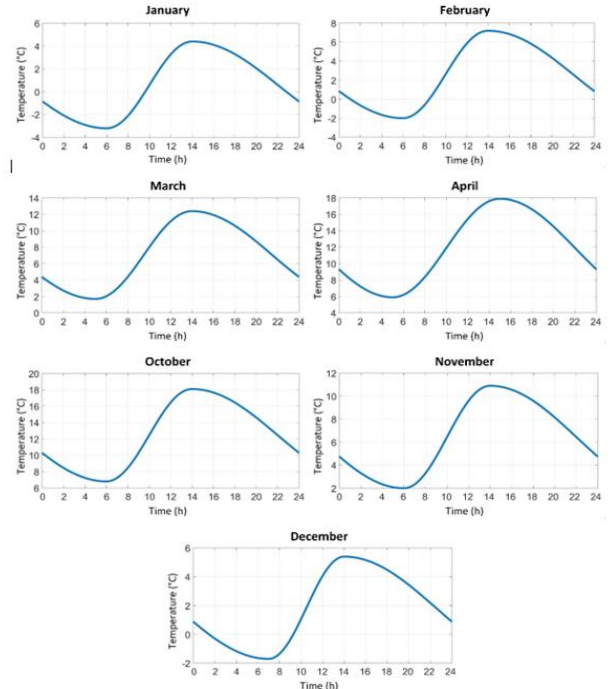


Figure 3: Temperature profiles for the average days during the heating season in Kraljevo.

Figures 4 and 5 show the temperature profiles that fulfill heating requirements on the average days in the DH company from the “Nova kolonija” plant.

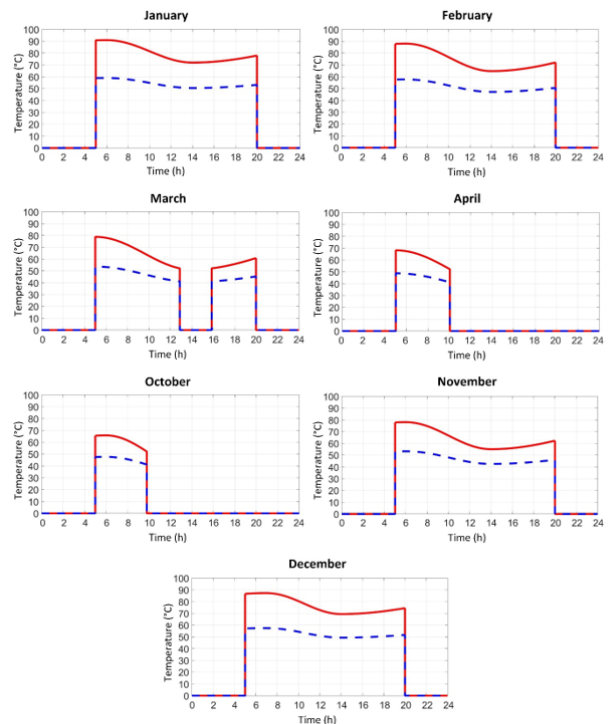


Figure 4: Temperature profiles (supply and return lines) in the DH system for the average month days. The present mode of operation (overnight stoppage).

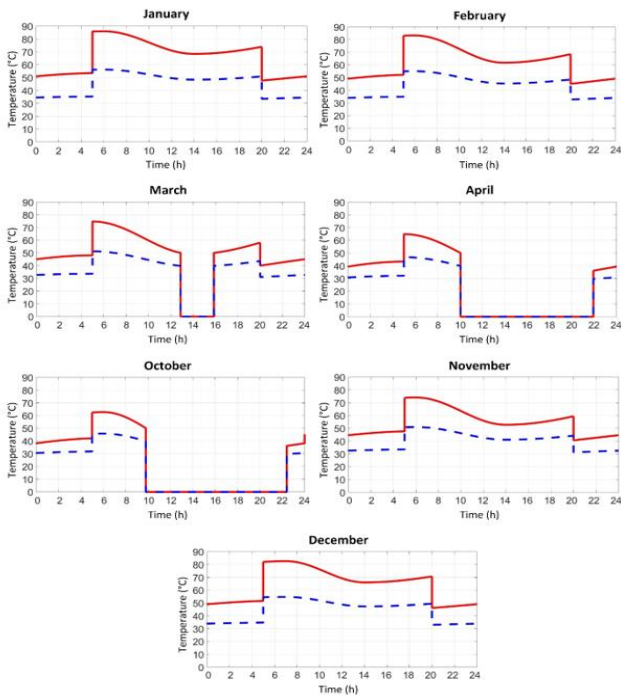


Figure 5: The daily temperature profiles (supply and return lines) in the DH system for the average month days for the continuous mode of operation with limited overnight heating.

### 3.2 HP efficiency

The efficiency of the HP was calculated based on the data provided by HP manufacturers [10] and the fact that the HP efficiency is between 0.5 and 0.6 of the Carnot cycle [11]. The HP efficiency was determined by:

$$COP = 0.618 \cdot \frac{(T_{H-SINK} + 5)}{(T_{H-SINK} - T_{EVAPORATION} + 10)} \quad (2)$$

where: COP [-] is the heat pump efficiency,  $T_{H-SINK}$  in [K] the highest temperature of the heat sink at an instant, in this case, DH water,  $T_{EVAPORATION}$  in [K] is the temperature of evaporation. In our case, the temperature is in the range of 306 to 310 K.

## 4. ENERGY BALANCES

Table 2. shows the basic data for the energy and CBA analyses, whereas in the rest of the heading energy balances are presented for both variants of the project. All calculations in this section were done based on the average monthly temperatures.

Table 2: The basic data for the study.

|  |                |                       |
|--|----------------|-----------------------|
| The average emissions of CO <sub>2</sub> from the natural gas combustion | 1.9            | [kg/m <sup>3</sup> ]  |
| The average emissions of CO <sub>2</sub> from the natural gas combustion | 9.564          | [kWh/m <sup>3</sup> ] |
| Fuel unit cost for the DH company  | 0.344          | [€/m <sup>3</sup> ]   |
| Fuel unit cost for the DH company  | 0.036          | [€/kWh]               |
| Higher daily tariff for electricity                                      | 0.0899         | [€/kWh]               |
| Lower night tariff for electricity                                       | 0.0517         | [€/kWh]               |
| Thermal energy cost from DH system                                       | 0.04           | [€/kWh]               |
| Thermal power of NG fired hot water boilers in "Nova kolonija" plant     | 3 x (12+0.575) | [MW]                  |
| The efficiency of the DH boilers   | 95.13%         | [%]                   |

In Table 2, the values for average emissions of CO<sub>2</sub> are taken from the literature [13], fuel unit cost was provided by PUC Toplana, Kraljevo. The electricity price for the higher daily tariff was calculated from the electricity bill for January 2021. All prices exclude VAT and the taxes for overconsumption and renewable energy. Similarly, the electricity price for the lower night tariff was calculated. The thermal power of natural-gas-fired hot water boilers in the "Nova kolonija" plant and their efficiencies were based on the data provided by the manufacturer Buderus.

### 4.1 Variant 1 – the present mode of operation (overnight stoppage).

Tables 3 and 4 show the energy balance and the main outcomes of the proposed project.

Table 3: Energy balance of the analyzed system in the present mode of operation (overnight stoppage).

| Month    | Temperature regime [°C] | Groundwater temperature [°C] | COP | Thermal power from underground water P <sub>SGW</sub> [kW] | Heat delivered to DH [kW] | Electricity consumption HP [kWh] | Electricity consumption circulation pumps [kWh] | Total electricity consumption [kWh] |
|----------|-------------------------|------------------------------|-----|--|---------------------------|----------------------------------|---|-------------------------------------|
| January  | 82.3/55.3               | 12.5                         | 2.8 | 755  | 508653                    | 134173                           | 9123  | 143296                              |
| February | 77.3/53.1               | 12                           | 2.9 | 755  | 454192                    | 115952                           | 8240  | 124192                              |
| March    | 65.8/47.8               | 12                           | 3.3 | 755  | 486902                    | 112422                           | 9123  | 121546                              |
| April    | 52.7/41.3               | 12                           | 4.0 | 755  | 301506                    | 59906                            | 5886  | 65792                               |
| October  | 52.7/41.3               | 14                           | 4.2 | 755  | 164529                    | 31649                            | 3237  | 34886                               |
| November | 67.9/48.7               | 13.5                         | 3.3 | 755  | 471503                    | 109103                           | 8829  | 117932                              |
| December | 79.1/53.9               | 12.5                         | 2.9 | 755  | 504360                    | 129880                           | 9123  | 139004                              |
| TOTAL    |                         |                              |     |  | 2891645                   | 693085                           |   | 746648                              |
|          |                         |                              |     |  | COPs                      |                                  | 4.17  | 3.87                                |

The temperature regime shown in Table 3 is the average value from Figure 4. COP is determined by Eq. (4), and the heat delivered by the HP  $Q_{delivered}$  [kWh] is calculated by

$$Q_{delivered} = Q_{SGW} + \frac{Q_{SGW}}{COP}, \quad (3)$$

where  $Q_{SGW}$  in [kWh] is the heat extracted from shallow groundwater, and COP is calculated based on the temperature regimes and Eq. (2).

Electricity consumption is used for HPs and water circulation. Electricity consumption by HPs is  $Q_{delivered}/COP$ . The electricity consumption by water circulation pumps was calculated based on the following data:

- volume flow rate 30 l/s,
- total head 30 m,
- pump efficiency 48% (motor + impeller),
- 16 hours per day.

The electricity consumption for water pumping is not negligible as it accounts for 7.2% of the total electricity consumption. The energy required for water circulation reduces the seasonal COP by 0.3.

Table 4 shows that the majority of electricity is consumed during the high tariffs (between 7 AM and 10 PM).

Table 4: Electricity consumption and cost.

|              | Tariff | Electricity for the HPs [kWh] | Electricity cost [€] |
|--------------|--------|-------------------------------|----------------------|
| January      | HT     | 125384                        | 11274                |
|              | LT     | 17912                         | 926                  |
| February     | HT     | 108668                        | 9771                 |
|              | LT     | 15524                         | 802                  |
| March        | HT     | 106352                        | 9563                 |
|              | LT     | 15193                         | 785                  |
| April        | HT     | 57568                         | 5176                 |
|              | LT     | 8224                          | 425                  |
| October      | HT     | 30525                         | 2745                 |
|              | LT     | 4361                          | 225                  |
| November     | HT     | 103191                        | 9279                 |
|              | LT     | 14742                         | 762                  |
| December     | HT     | 121628                        | 10937                |
|              | LT     | 17375                         | 898                  |
| <b>TOTAL</b> |        | <b>746648</b>                 | <b>63569</b>         |

Table 7: Electricity consumption and cost for variant 2.

|              | Tariff | Electricity for the HPs [kWh] | Electricity cost [€] |
|--------------|--------|-------------------------------|----------------------|
| January      | HT     | 126450                        | 11370                |
|              | LT     | 59621                         | 3082                 |
| February     | HT     | 109757                        | 9869                 |
|              | LT     | 52172                         | 2697                 |
| March        | HT     | 107797                        | 9693                 |
|              | LT     | 52187                         | 2698                 |
| April        | HT     | 58763                         | 5284                 |
|              | LT     | 29401                         | 1520                 |
| October      | HT     | 31090                         | 2796                 |
|              | LT     | 15409                         | 797                  |
| November     | HT     | 104347                        | 9383                 |
|              | LT     | 49969                         | 2583                 |
| December     | HT     | 122740                        | 11036                |
|              | LT     | 58085                         | 3003                 |
| <b>TOTAL</b> |        | <b>977788</b>                 | <b>75809</b>         |

The following table shows the financial and ecological benefits of the project, which improves energy efficiency, reduces natural gas (NG) consumption, and increases electricity consumption. The increase in electricity consumption and the cost of electricity reduce the benefits of the project.

Table 5: The outcomes of the project.

|  |           |                      |
|--|-----------|----------------------|
| NG reduction due to the use of HPs                                     | 317825    | m <sup>3</sup> /year |
| Cost reduction due to the decrease in NG consumption                   | 109213    | €/year               |
| Increase in electricity consumption                                    | 746648    | kWh/year             |
| Cost of the additional electricity                                     | 63569     | €/year               |
| CO <sub>2</sub> reduction due to the NG reduction                      | 604       | t/year               |
| CO <sub>2</sub> increase due to the additional electricity consumption | 515       | t/year               |
| <b>Net CO<sub>2</sub> reduction</b>                                    | <b>89</b> | <b>t/year</b>        |

The following table shows the financial and ecological benefits of variant 2 of the project. Compared with variant 1, the NG reduction is almost 50% larger, whereas the electricity cost is only 19.2% larger.

Table 8: The outcomes of variant 2 of the project.

|  |            |                      |
|--|------------|----------------------|
| NG reduction due to the use of HPs                                     | 460913     | m <sup>3</sup> /year |
| Cost reduction due to the decrease in NG consumption                   | 158381     | €/year               |
| Increase in electricity consumption                                    | 977788     | kWh/year             |
| Cost of the additional electricity                                     | 75809      | €/year               |
| CO <sub>2</sub> reduction due to the NG reduction                      | 876        | t/year               |
| CO <sub>2</sub> increase due to the additional electricity consumption | 675        | t/year               |
| <b>Net CO<sub>2</sub> reduction</b>                                    | <b>201</b> | <b>t/year</b>        |

#### 4.2 Variant 2 – the continuous operation with limited overnight heating.

Tables 5-8 show the main outcomes for this variant. Compared with variant 1, the DH system operates in a lower temperature regime. In addition, overnight temperature regimes are lower and suitable for HP usage. Compared with variant 1: (i) the seasonal COP is larger because of the lower temperature regimes, (ii) water pumping is more influential to the seasonal COP, and (iii) there is substantial electricity usage during the low tariffs.

Table 6: Energy balance of variant 2 of the project.

| Month        | Temp. regime [°C] | Groundwater temperature [°C] | COP | Thermal power from underground water P <sub>HP</sub> [kW] | Heat delivered to DH [kW] | Electricity consumption by HP [kWh] | Electricity consumption circulation pumps [kWh] | Total electricity consumption [kWh] |
|--------------|-------------------|------------------------------|-----|---|---------------------------|-------------------------------------|---|-------------------------------------|
| January      | 78/52.8           | 12.5                         | 2.9 | 755.0   | 502944                    | 128464                              | 9123  | 137588                              |
|              | 49.7/34.2         | 12.5                         | 4.3 | 755.0   | 230858                    | 43618                               | 4866  | 48483                               |
| February     | 73.4/50.8         | 12                           | 3.0 | 755.0   | 449354                    | 111114                              | 8240  | 119355                              |
|              | 47.4/33.5         | 12                           | 4.4 | 755.0   | 207299                    | 38179                               | 4395  | 42574                               |
| March        | 62.7/45.9         | 12                           | 3.5 | 755.0   | 482422                    | 107942                              | 9123  | 117065                              |
|              | 42.2/31.8         | 12                           | 4.9 | 755.0   | 225294                    | 38054                               | 4866  | 42919                               |
| April        | 50.6/39.9         | 12                           | 4.2 | 755.0   | 299371                    | 57771                               | 5886  | 63657                               |
|              | 36.4/29.8         | 12                           | 5.7 | 755.0   | 142168                    | 21368                               | 3139  | 24507                               |
| October      | 50.6/39.9         | 14                           | 4.4 | 755.0   | 163346                    | 30466                               | 3237  | 33703                               |
|              | 36.4/29.8         | 14                           | 6.0 | 755.0   | 77509                     | 11069                               | 1727  | 12795                               |
| November     | 64.6/46.8         | 13.5                         | 3.5 | 755.0   | 466982                    | 104582                              | 8829  | 113411                              |
|              | 433.2/32.1        | 13.5                         | 5.0 | 755.0   | 217397                    | 36197                               | 4709  | 40906                               |
| December     | 75/51.5           | 12.5                         | 3.0 | 755.0   | 498872                    | 124392                              | 9123  | 133515                              |
|              | 48.2/33.7         | 12.5                         | 4.4 | 755.0   | 229684                    | 42444                               | 4866  | 47309                               |
| <b>TOTAL</b> |                   |                              |     |   | <b>4193408</b>            | <b>895658</b>                       |   | <b>977788</b>                       |
|              |                   |                              |     |   | <b>COPs</b>               | <b>4.68</b>                         |   | <b>4.29</b>                         |

## 5. CBA ANALYSIS

The economic advantages and disadvantages of the proposed project were assessed by the CBA carried out following the Guide to Cost-Benefit Analysis of Investment Projects [8].

The main points in the CBA analysis are:

- For this scenario, projections were made of all cash flows related to the operations in the project area for each year during the project lifetime, which was supposed to be 15 years.
- A counterfactual baseline scenario for the project would be the so-called “business as usual”, i.e., the usage of hot water (superheated water) boilers with economizers in the DH systems.
- A long-term loan, under the following conditions, is assumed: (i) tenor of up to 12 years including the grace period of 2 years, and (ii) an upfront fee of 1%.
- Analysis was prepared and expressed in EUR, and all figures exclude VAT.
- A 4 % discount rate in real terms is used in the financial calculations, whereas a 2.5 % interest rate is used in the economic analysis.

Two variants of the project were analyzed:

1. present operation mode, i.e., from 5 AM to 9 PM.

2. continuous operation mode with limited overnight heating. Period with limited heating from 9 PM to 5 AM.
  - The cost of NG was taken to be as in the heating season 2019/2020. Additionally, the benefit due to the reduced NG cost should rise at a rate of 1.2% per year.
  - Unite price for the electricity was assumed to be as in January 2021 and that the price would rise with a 2% rate yearly.
  - The depreciation rate of 8% per annum was supposed to calculate the residual value for the equipment.
  - The maintenance cost was assumed to be 1.5% of the total investment.
  - Environment and climate change considerations were included in the economic analysis.
  - The HP costs were obtained by an offer from Viessmann doo Belgrade [7].

Table 9 shows the investment cost of the project. The HPs are the most expensive item that makes 70% of the budget. In this phase of the project, a contingency of 10% was assumed.

Table 9. The investment cost for both variants of the project.

| Project investment cost [€]  | 1                | 2-14 | 15                 |
|--|------------------|------|--------------------|
| Planning/design fees   | 20000            | 0    |                    |
| Land purchase  | 0                | 0    |                    |
| Machinery and construction:  |                  | 0    |                    |
| Heat pumps   | 403050           | 0    |                    |
| Heat exchanger 755 kW  | 13479            |      |                    |
| Wells for shallow underground water+pump+pipelines   | 22813            | 0    |                    |
| Electrical equipment in DH boiler room   | 12092            | 0    |                    |
| Pumps, valves, piping, regulating equipment, automatic control, measuring equipment in the boiler room | 30229            | 0    |                    |
| Supervision during construction and implementation   | 16000            | 0    |                    |
| Contingency  | 51776            | 0    |                    |
| Residual value   |                  | 0    | -137899            |
| <b>TOTAL</b>   | <b>569,428 €</b> |      | <b>(137,899) €</b> |

The financial net present value of investment (FNPV(C)) and the financial rate of return of the investment (FRR(C)) compare investment costs to net revenues and measure the extent to which the project net revenues can repay the investment, regardless of the sources or methods of financing [8]. Table 10 shows their values for both variants of the project. Compared with variant 1, variant 2 has positive financial indicators.

Table 10: The outcome of the CBA analysis for both variants

|                      | Variant 1 | Variant 2 |
|----------------------|-----------|-----------|
| Discount rate        | 4%        | 4%        |
| FNPV(C)              | -105176   | 290962    |
| FRR(C)               | 1.4%      | 10.5%     |
| B/C ratio            | 0.923     | 1.192     |
| Social discount rate | 5%        | 5%        |
| ENPV                 | 99,532 €  | 362,584 € |
| ERR                  | 2%        | 14%       |
| B/C ratio            | 0.92      | 1.26      |

Variant 2 of the project is financially sustainable. According to the assumptions made for the analysis, this variant of the project does not have the risk of running out of cash in the future, both during the investment and the

operational stages. The cumulated net cash flow is negative only during the construction phase for all other considered years it is greater than zero.

The economic analysis is carried out to appraise the project's contribution to the welfare [8]. This is the project that improves the energy efficiency of the DH system. The direct benefit of the project is the increase in energy efficiency. This induces two economic benefits and two costs. The two benefits are: (i) lower greenhouse gas emissions due to the reduced usage of natural gas, and (ii) substitution of the natural gas import. Consequently, the two costs are: (i) the usage of HP requires a larger domestic electricity production, which subsequently increases the greenhouse gas emissions.

The benefit from reduced CO<sub>2</sub> emissions is calculated as the net reduction of CO<sub>2</sub> emissions (see **Error! Reference source not found.** and 7) multiplied by the unit cost of GHG emissions. The net reduction of CO<sub>2</sub> emissions is calculated as the difference between the decrease in natural gas consumption and the increase in electricity consumption. The equivalent CO<sub>2</sub> emissions for NG are 1.9 kg/mN<sup>3</sup> whereas the equivalent emissions for the electricity production in the Republic of Serbia are 690 g/kWh. The unit cost of GHG emissions is taken from the Guide to Cost-Benefit Analysis of Investment Projects [8]. The central cost of 25 €/t-CO<sub>2e</sub> was adopted with an annual adder of 1.

The benefit from the substitution of natural gas import is calculated by the use of the border price for the fuel of 155 \$/1000m<sup>3</sup>. The economic cost of additional electricity usage is calculated by assuming that the production and distribution cost of electricity is 4.8 c€/kWh. The electricity consumptions are shown in is shown in Tables 4 and 6.

Table 10 shows that compared to the financial indicators, the economic indicators are not substantially better because of the additional electricity usage that increases carbon dioxide CO<sub>2</sub> emission and electricity production cost.

## 6. SENSITIVITY ANALYSIS

To identify the crucial variables of the project, sensitivity analysis was carried out for the implementation of the HPs in the DH plant "Nova kolonija". Both variants are covered with the analysis. Figure 6 and Figure 7 show the sensitivity analysis for variant 1 of the project. This project is the least sensitive to the variation of the investment cost, whereas it is the most sensitive to the total inflows. Consequently, it is the most sensitive to the number of working hours and the COP of the HPs.

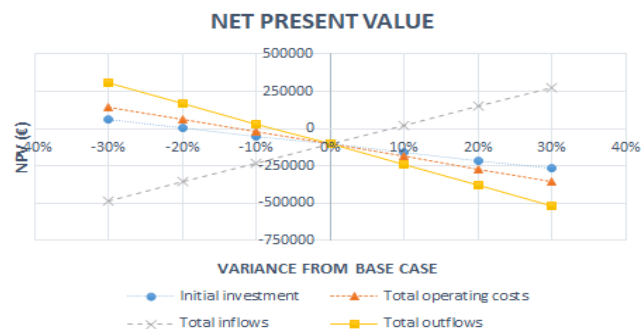


Figure 6: The sensitivity analysis of the net present value for variant 1 of the project.

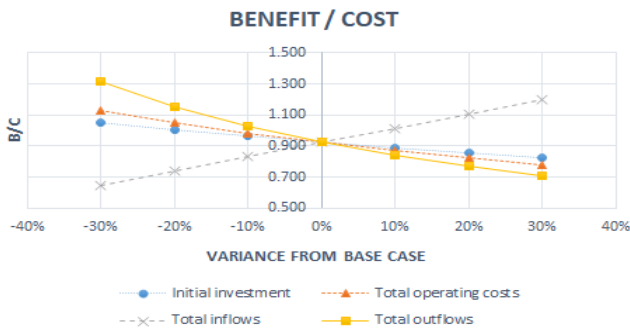


Figure 7: The sensitivity analysis of the BC ratio for variant 1 of the project.

Compared to variant 1, variant 2 of the project has equal sensitivity to the basic project parameters. However, financial and economic indicators for this variant are positive. The project is the most sensitive to total inflows, and consequently to the working hours and COP of the HPs. The second most important parameter of the project is the total outflows and consequently electricity and maintenance cost. The project can tolerate an increase in total outflows of 20%, an increase in the investment cost of over 30%, and a decrease in total outflows of less than 17%.

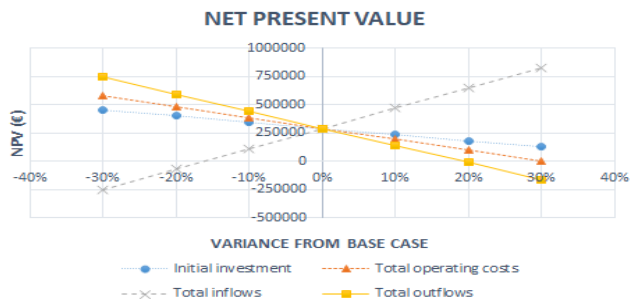


Figure 8: The sensitivity analysis of the net present value for variant 2 of the project.

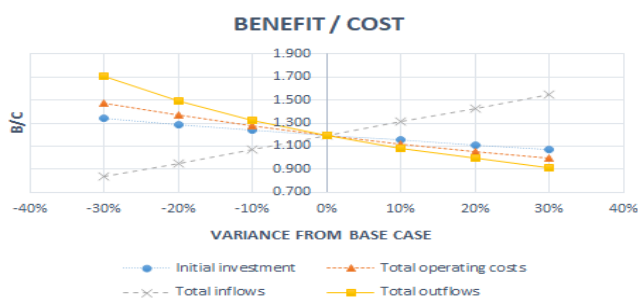


Figure 9: The sensitivity analysis of the BC ratio for variant 2 of the project.

## 7. CONCLUSIONS

The main conclusions of the study are:

- The analyzed HP system is financially and economically beneficial if the DH system works continuously with limited overnight heating. If the DH system works as in the present mode of operation with the overnight stoppage, it is not financially nor economically beneficial to implement the analyzed HPs.

- The stable operation of the analyzed system requires groundwater flow rates larger than 18 l/s.
- Assuming that the pumping power decreases the COP of the system by 0.3, and with the unit costs of electricity and NG as in Table 2, the HPs should work in the system if the COP is larger than 2.8 and 1.74 during higher and lower electricity tariffs, respectively.
- The project is the most sensitive to the total inflows and outflows during its realization. Compared with them, the project is less dependent on the variations of the total investment cost. Consequently, the operating hours, COP, and electricity cost are the most important variables in the project.
- To be implemented the project requires the transformation from the present to the continuous work with limited overnight heating. Additionally, it requires hydrological examinations and adequate placement of the wells.

## ACKNOWLEDGEMENTS

This research was supported by the Ministry of Education, Science and Technological Development of the Republic of Serbia (Grant No. 451-03-9/2021-14/200108).

## REFERENCES

- [1] H. Lund et al., 4th Generation District Heating (4GDH): Integrating smart thermal grids into future sustainable energy systems, *Energy*, 68, 2014, pp. 1-11
- [2] Buffa S. et al, 5th generation district heating and cooling systems: A review of existing cases in Europe, *Renewable and Sustainable Energy Reviews*, 104, 2019, pp. 504-522
- [3] Marguerite C. et al., Heat Pumps in District Heating and Cooling Systems, Task 3: Review of concepts and solutions of heat pump integration, International Energy Agency, 2019, pp.56
- [4] Dejan Milenić et al., Evaluation of resources and possibilities for the usage of underground water in the municipality of Kraljevo, Faculty of Forestry Belgrade 2007 (in Serbian)
- [5] <https://heatpumpingtechnologies.org/publications> (accessed in April 2021).
- [6] [http://www.hidmet.gov.rs/ciril/meteorologija/stanica\\_sr.php?moss\\_id=13376](http://www.hidmet.gov.rs/ciril/meteorologija/stanica_sr.php?moss_id=13376) (accessed in April 2021).
- [7] <https://www.viessmann.rs/> (accessed in April 2021).
- [8] [https://ec.europa.eu/regional\\_policy/sources/docgener/studies/pdf/cba\\_guide.pdf](https://ec.europa.eu/regional_policy/sources/docgener/studies/pdf/cba_guide.pdf) (accessed in April 2021).
- [9] B. Todorović. The design of the central heating systems. Faculty of Mechanical Engineering in Belgrade, Belgrade 2010. (In Serbian).
- [10] [https://webapps.viessmann.com/vibooks/api-internal/file/resources/technical\\_documents/GB/en/MDS/9443294MDS00001\\_1.PDF](https://webapps.viessmann.com/vibooks/api-internal/file/resources/technical_documents/GB/en/MDS/9443294MDS00001_1.PDF) (accessed in April 2021).
- [11] <https://heatpumpingtechnologies.org/market-technology/efficiency-heat-pumps/> (accessed in April 2021).

[12] European Investment Bank, Methodologies for the Assessment of Project GHG Emissions and Emission Variations, 2020 (accessed in April 2021).

[13] [IFI Dataset of Default Grid Factors 27.06.19 for Publication \(unfccc.int\)](#) (accessed in April 2021).

## Optimization of compact heat exchangers

Miljan Marašević<sup>1</sup>, Nebojša Bogojević<sup>1</sup>, Nenad Stojić<sup>1</sup>, Stefan Adžić<sup>1</sup>, Dragiša Šimunović<sup>1</sup>,  
Faculty of Mechanical and Civil Engineering in Kraljevo/Department for Thermal Technique and Environment Protection,  
University of Kragujevac, Kraljevo (Serbia)

*The need to develop heat exchangers of small dimensions, high efficiency and relatively low cost has led to the emergence of compact exchangers. These exchangers are made of thin sheets, different materials and are designed for gas-gas systems, where some constructions can also be used for gas-liquid systems. In this paper, the shape and dimensions of compact exchangers are optimized in order to evenly distribute the flow in the apparatus itself. Fluid flow analysis in a compact exchanger was performed for different sheet metal constructions in current channels. The construction of a compact exchanger with external dimensions of 400x400x400mm was adopted. The optimization was performed in the software package "Solidworks", for several variant solutions.*

**Keywords:** compact heat exchanger, fluid flow, optimization

### 1. INTRODUCTION

Along with the development of industry and technology, there are increased demands for miniaturization - reducing the dimensions of the device, increasing the efficiency while, if it possible, the cost of production should be same or reduced. This trend permeates both the energy segments and the heat exchanger field.

The field of application of heat exchangers is very wide and includes a very large number of industry branches. It would be very difficult to list all the examples of heat exchangers, they are used wherever it is necessary to perform some energy exchange. During technological processes, it is necessary to transfer a certain amount of energy (generated in that process) to another carrier (fluid) in the most efficient way possible in order to minimize energy losses.

Heat exchangers can be divided and classified into different groups and the established division is reduced to the division according to: purpose, functional and technological solutions and operating temperature regime. According to the purpose, heat exchangers are used in industrial applications as: refrigerators and heaters, condensers and evaporators, crystallizers, freezers and defrosters, chemical and biochemical reactors. The most used classification of heat exchangers is according to the method of heat transfer from one fluid to another: recuperative heat exchangers, regenerative heat exchangers, heat exchangers with indirect heat exchanger and contact heat exchangers [1].

This paper presents an analysis of the fluid flow and operation of a compact heat exchanger with defined geometric characteristics, known inlet and outlet temperatures of fluid 1 (combustion products), known inlet temperature of fluid 2 (air) as well as known mass flows of both fluids. The number of channels for both fluids is equal and amounts to seven, whereby the sheets in the channels are bent so as to form an equilateral triangle, as it is shown in Fig. 1. and Fig. 2 Based on the previously mentioned data, the power of a compact heat exchanger of 30 kW was determined. The exchanger is installed in a wood

processing plant. During the operation of the compact exchanger, a problem was noticed in the construction, in the way of introducing fluid into the apparatus, which results in uneven fluid flow. In the further part of the paper, modeling and optimization were performed in order to achieve uniformity of fluid flow in the heat exchanger [2], [3].

### 2. COMPACT HEAT EXCHANGER

The compact heat exchangers are the type of the recuperative exchanger, in the which heat is exchanged between cooled fluid (warmer fluid) and the heated fluid (colder fluid) through a flat surface. The need to develop heat exchangers with high compactness, simple construction and of course the lowest possible price, have led to the development of a compact heat exchangers. These exchangers are made of thin sheets whose thickness ranges from 0.7 mm to 15 mm. The channels are shaped in such a way that the flow of fluid is usually done cocurrent or in countercurrent direction. They are most often used in cases when both fluids are gases, and they can also be used in cases when one fluid is a gas and the other is a liquid. Working pressures in the compact heat exchanger can be up to 16 bar and the fluid temperature range is up to 400°C.

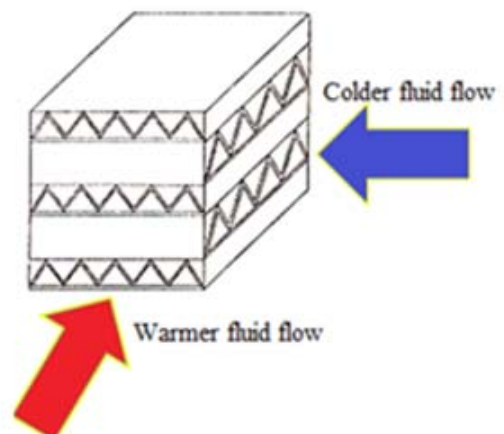


Fig.1 Construction of the compact heat exchanger

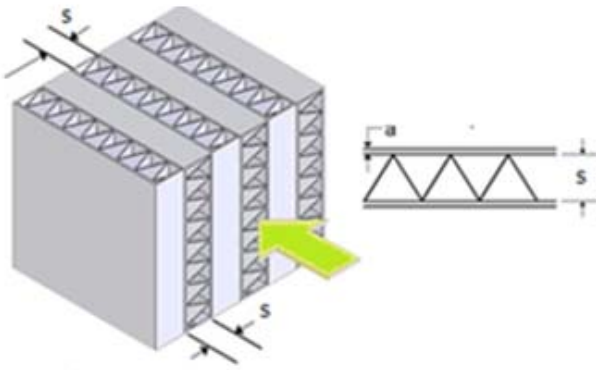


Fig.2 Construction of the compact heat exchanger

$$Q = \dot{m}_1 \cdot c_{p1} \cdot (t_{1in} - t_{1out}) = \dot{m}_2 \cdot c_{p2} \cdot (t_{2out} - t_{2in}) = k \cdot A_{exch} \cdot \Delta t_m \quad (1)$$

where are:  $\dot{m}_1$ -mass flow rate of the combustion products,  $c_{p1}$ -specific heat capacity of the combustion products,  $t_{1in}$ -temperature of the combustion products at the inlet of the heat exchanger,  $t_{1out}$ - temperature of the combustion products at the outlet of the heat exchanger,  $\dot{m}_2$ -mass flow rate of air,  $c_{p2}$ -specific heat capacity of air,  $t_{2in}$ -temperature of air at the second inlet of heat exchanger.

The mean logarithmic temperature difference is determined from equation (2) for a heat exchanger with countercurrent flow, taking into account correction factor  $\varepsilon$  taken from [6], [7] and [8]:

$$\Delta t_m = \varepsilon \cdot \frac{(t_{1in} - t_{2out}) - (t_{1out} - t_{2in})}{\ln\left(\frac{t_{1in} - t_{2out}}{t_{1out} - t_{2in}}\right)} \quad (2)$$

Based on known geometry of the compact heat exchanger and on the basis of the known inlet and outlet temperature of the both fluids obtained from (1), the heat transfer coefficient is calculated:

$$\frac{1}{k} = \left(\frac{1}{\alpha_1} + R_1\right) \frac{1}{\eta_1} + \frac{\delta_z}{\lambda_z} \cdot \frac{1}{1 - \frac{\delta_z}{s}} + \left(\frac{1}{\alpha_2} + R_2\right) \frac{1}{\eta_2}, \quad (3)$$

The heat resistance coefficients due to contamination were adopted from [8]:

$$R_1 = 0,2 \cdot 10^{-3} \frac{m^2K}{W} \text{ и } R_2 = 0,1 \cdot 10^{-3} \frac{m^2K}{W}. \quad (4)$$

Convective heat transfer coefficient is obtained by the formula:

$$\alpha_i = \frac{Nu_i \cdot \lambda_i}{d_{e,i}} \quad (5)$$

where are:  $\lambda_i$  – the coefficient of the conduction,  $d_{e,i}$  – the equivalent diameter,  $Nu_i$  – Nusselt number.

In this paper, a compact heat exchanger is considered, in which combustion products are used to heat the air as a colder fluid, with special attention paid to the flow of fluid through the exchanger.

### 3. MODELING

The design of this type of exchanger is based on the calculation of heat exchange between two fluids taking into account the construction of the exchanger, mass flows and inlet temperature of both fluids, as well as the outlet temperature of one of the fluids.

The energy balance of a heat exchanger is determined from the equation:

Dimensionless numbers, required for determination of the heat transfer coefficient, were calculate from (5) and (6).

$$Nu_i = 0,21 \cdot Re_i^{0,6} \cdot Pr_i^{\frac{1}{3}} \quad (5)$$

$$Re_i = \frac{w_i \cdot d_{e,i} \cdot \rho_i}{\mu_i} \quad (6)$$

where are:  $w_i$  – the fluid velocity,  $\rho_i$  – the fluid density,  $\mu_i$  – the coefficient of dynamic viscosity of the fluids,  $Pr_i$  – Prandtl number, where is  $i=1$  - for combustion product,  $i=2$  – for air.

Efficiency of the ribbed surface is calculated based on expressions (8), (9), (10) and (11), taking into account that  $\lambda_r = \lambda_p = 20W/mK$  is the coefficient of the conduction for stainless steel plate:

$$\eta_i = 1 - \frac{S_r}{s} (1 - \theta_i) \quad (7)$$

$$\theta_i = \frac{\tan h(\sqrt{Bi_i})}{\sqrt{Bi_i}} \quad (8)$$

$$Bi_i = \frac{\alpha_i \cdot l_r^*}{\lambda_r} \quad (9)$$

$$l_r^* = l_r \cdot \frac{h_r^2}{A_r} \quad (10)$$

where are:  $h_r = \frac{s}{2}$  -the rib height,  $s=25mm$  – the distance between main plates,  $l_r = 2h_r + \delta_r$  – the rib circumference,  $\delta_r = 1mm$  – the rib thickness,  $A_r = h_r \cdot \delta_r$  – the rib area.

Based on previous, the outlet air temperature and heat transfer coefficient were determined for the given input parameters.

Table 1. Parameters of the basic compact heat exchanger

| $\dot{m}_1$ [kg/s] | $t_{1in}$ [°C] | $t_{1out}$ [°C] | $c_{p1}$ [J/kg°C] | $\Delta t_m$ [°C] |
|--------------------|----------------|-----------------|-------------------|-------------------|
| 0,712              | 159            | 120             | 1079,5            | 107.4             |
| $\dot{m}_2$ [kg/s] | $t_{2in}$ [°C] | $t_{2out}$ [°C] | $c_{p2}$ [J/kg°C] | $k$ [W/m²K]       |
| 0.634              | 10             | 57              | 1007              | 64                |

The parameters that define the operation of the existing heat exchanger, the mass flow rates of the fluid, the inlet temperature of both fluids and the outlet temperature of the fluid 2 were measured in the operating conditions in

which the exchanger was installed. The specific heat capacities of the fleece were adopted on the basis of certain mean temperatures from [6], [7] and [8].

#### 4. FLOW ANALYSIS USING SOLIDWORKS FLOW SIMULATION

Based on obtained data, a „digital twin” was formed using SolidWorks software package in which, after defining of the geometry, a Flow analysis of fluid flow through a compact heat exchanger was performed [4], [5].

The data obtained from analytical model were taken as input parameters for the designed digital twin, where the following parameters were taken into account:

- Heat exchange by conduction between fluids,
- Heat exchange by convection between plates and heated fluid (air),

- Model is adiabatic isolated,
- Heat exchanger is made of stainless steel,
- It is adopted that the fluids before entering the exchanger have a fully developed flow,
- The flow of the fluids in the heat exchanger is countercurrent,
- The number of passes of both fluids is equal (seven passes).

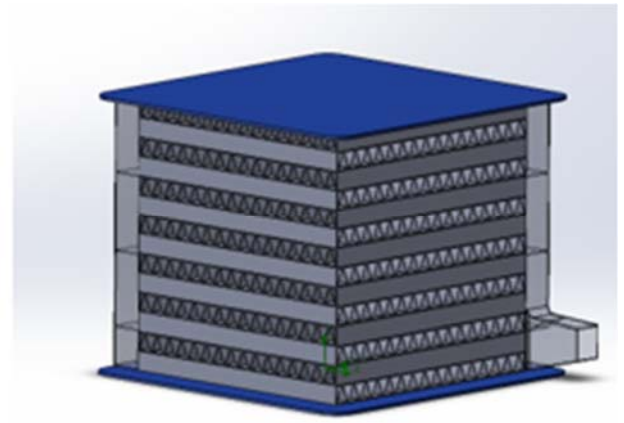
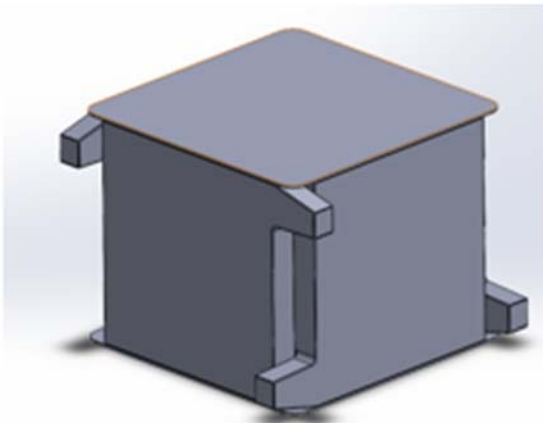


Fig.3. 3D model of the compact heat exchanger

The flow of the fluids inside of heat exchanger is analyzed by Flow Simulation where the results of the simulations are shown on the Fig. 3. Despite the fact that it is assumed that at the entrance in heat exchanger was the fully development flow, fluids tend to go to the first

obstacle, which in this case is the back wall of the inlet channel and then are directed through passes of heat exchanger (see Fig. 3.). This flow of the fluids leads to low efficiency of the exchanger, because the fluids do not pass through the entire surfaces, as shown in Fig. 3.

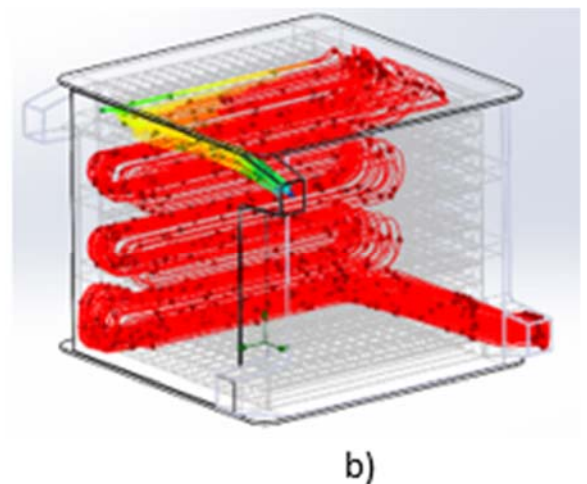
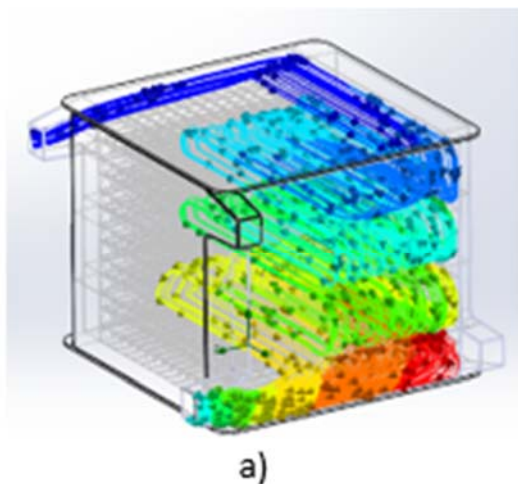


Fig.4. The flow of both fluids thought the heat exchanger, a) air, b) combustion products

In order to better routing the fluid through the exchanger and improve the efficiency, in the inlet channels of the exchanger baffles are placed (See Fig.4.). The height

of the first baffle is 1/3 of the height of the inlet channel while the height of the second baffle is 2/3 of the height of the channel, as shown at the right side of Fig. 4.

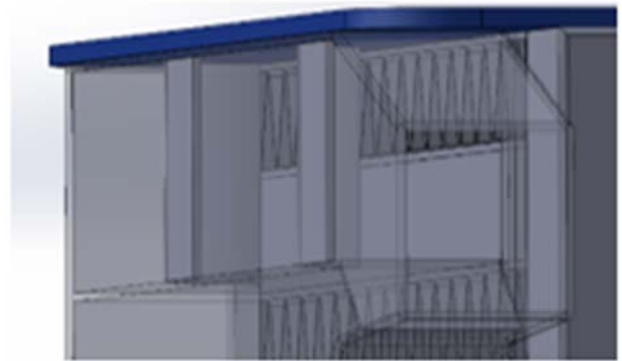
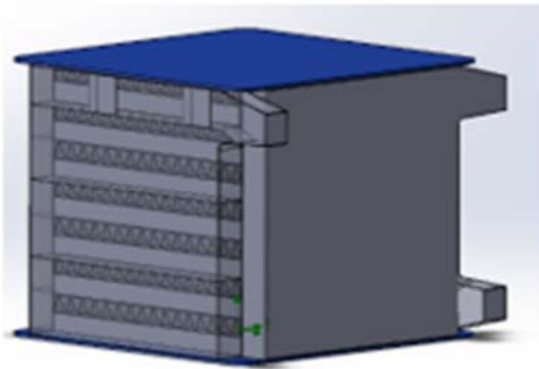
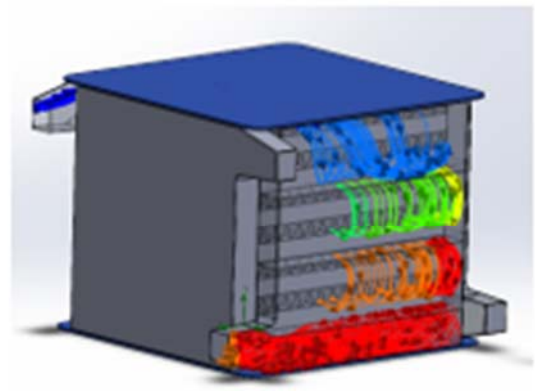
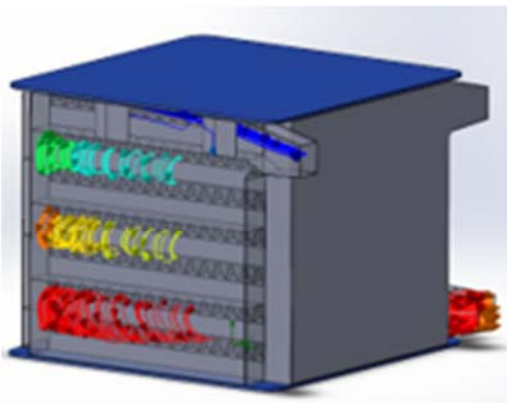


Fig.5. The position of the baffles at the inlet channel of heat exchanger

After obtained analysis of this solution, it can be concluded that in this case there has been improvement in fluid flow but there are still parts of exchanger in which we

have very little or no fluid flow at all, as shown in Fig. 5. In this case the efficiency is improved in comparison with the basic construction of the heat exchanger given in Fig.3.



a)

b)

Fig. 6. Simulation of the fluid flow through heat exchanger with baffles, a) air, b) combustion products

Despite the added baffles, the flow analysis shows that the flow of both fluids in heat exchanger can be improved and that we still have a large part of the exchanger through which there is almost no fluid flow, and therefore no heat exchange between fluids, as shown in Fig.6.

In order to further improve the flow of fluids in the exchanger, a constructive change was made on the fluid inlets and outlets of the exchanger where the entrance and exit of the fluid is given along the entire sidewalls, as shown in Fig. 7. The assumption during flow simulation is that the flow at the inlet is fully developed. This assumption requires that the fluids be fed to the exchanger at a constant flow rate through a corresponding cross-section of a channel of similar geometry as inlet ports [4], [5].

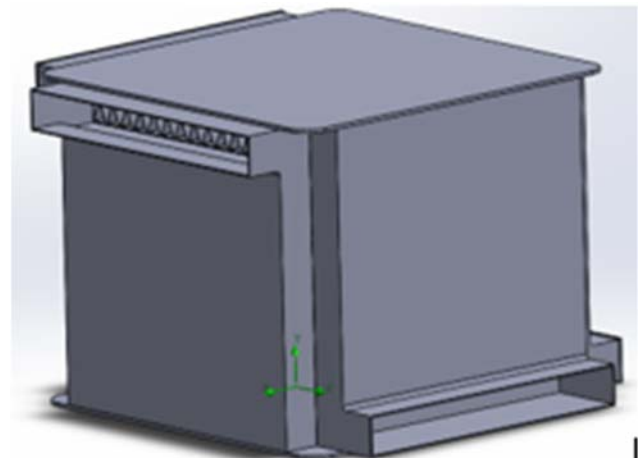


Fig.7. Compact heat exchanger with redesign inlet and outlet ports

After the flow analysis of fluid flow through redesigned heat exchanger, efficiency is improved due to better fluid flow along the entire surfaces of the exchanger, as shown in Fig 8.

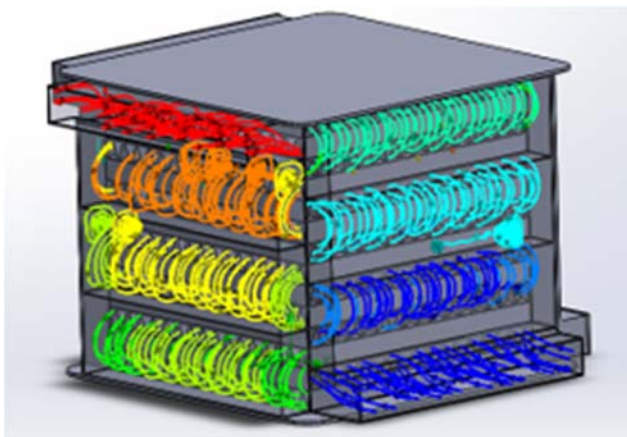


Fig.8. Simulation of the fluid flow through heat exchanger with redesign inlet and outlet ports

### 5. RESULTS

Based on the performed analyzes of all models and shown fluid output temperatures, it can be seen that in the case of exchanger with redesigned inlet and outlet ports, the highest degree of heat transfer from one fluid to another is achieved. In all cases the input parameters were the same. The obtained results for all models are given in the Tab.2

Table 2. Inlet and outlet temperatures depending of type construction

| Fluid                       | Fluid 1 -combustion product |                 | Fluid 2 -air    |                 |
|-----------------------------|-----------------------------|-----------------|-----------------|-----------------|
| Type of construction        | $t_{1\in}$ [°C]             | $t_{1out}$ [°C] | $t_{2\in}$ [°C] | $t_{2out}$ [°C] |
| basic                       | 159                         | 120             | 10              | 57              |
| basic with baffles          | 159                         | 118             | 10              | 60              |
| basic with redesigned ports | 159                         | 114             | 10              | 64              |

The modification of the inlet and outlet ports on the heat exchanger leads to the higher amount of the exchanged heat, which can be seen from lower temperature of the combustion products and higher temperature of the air at the outlet ports. With reconstruction of the inlet ports, both fluids have better flow over plates, which directly means better efficiency of heat exchanger.

In all three analyses, the mass flow of the combustion products and the air on the inlet ports has the same value. Due to different surface area for exchange, it is clear that in first two analysis the velocity of the air and combustion products has higher values compared to the velocities in the third analysis. This change of the velocity of the fluids on inlet ports may have significant influence on the fluids flow inside the heat exchanger. Regarding that, the future analyses should take into account and fluid velocity in the heat exchanger, in order to increase the amount of the exchanged heat and increase the efficiency of the heat exchanger.

### 6. CONCLUSION

In this paper optimization of the compact heat exchanger is performed, for defined geometry, mass and energy parameters in order to achieve uniformity of fluid flow in the heat exchanger. The modeling and fluid flow simulation of the existing (basic) heat exchanger is performed. Based on obtained results, optimization of the heat exchanger construction in order to achieved uniformity of the fluids over the entire surfaces was performed. The obtained solution does not require a change in the arrangement of the plates in the exchanger, but a correction is needed in the part where the fluids are introduced into the apparatus.

The analytical design process of the exchanger does not take into account the fluid flow inside the exchanger and does not consider the actual efficiency. Most often, when design, degree of security is taken into account, which leads to oversizing of the required power of the heat exchanger.

Using Flow simulation, as shown in this paper, it is possible to analyze the fluid flow inside the exchanger and perform optimizations of operation, or increase the efficiency of the exchanger. When designing new types of exchangers, the dimensions of the exchanger can be significantly reduced and the efficiency can be increased using this type of analysis.

### ACKNOWLEDGEMENT

This research was supported by the Ministry of Education, Science and Technological Development of the Republic of Serbia (Grant No. 451-03-9/2021-14/200108).

### REFERENCE

[1] *Optimization of compact heat exchangers by a genetic algorithm*, G. N. Xie, Sunden B., Q. W. Wang. Applied Thermal Engineering, Volume 28, Issues 8–9, June 2008, Pages 895-906.

[2] *Thermohydraulic engineering of plate-fin surfaces for heat exchangers subject to required dimensions*. Jorge L. García-Castillo, Fidel Vizcaino-García, Martín Picón-Núñez. Process Integration and Optimization for Sustainability volume 4, pages135–147 (2020).

[3] *A review on heat exchanger*. Shambhu Kumar Rai, Parmeshwar Dubey. IJARIE-ISSN(O)-2395-4396. Vol-3 Issue-1 2017.

[4] *Laminar flow and heat transfer in plate-fin triangular ducts in thermally developing entry region*. Li-ZhiZhang. International Journal of Heat and Mass Transfer. Volume 50, Issues 7–8, April 2007, Pages 1637-1640.

[5] *Microchannel heat exchangers – present and perspectives*. Traian POPESCU, Mircea MARINESCU, Horațiu POP, Gheorghe POPESCU, Michel FEIDT. U.P.B. Sci. Bull., ISSN 1454-2358, Series D, Vol. 74, Iss. 3, 2012.

[6] Jaćimović, B., Genić, S., Toplotne operacije i aparati – Deo 1: Rekuperativni razmenjivači toplote, Mašinski fakultet, Beograd, 2016.

[7] Genić S., Jaćimović B., Jarić M., Budimir N., Svojstva procesnih fluida, Savez mašinskih i elektrotehničkih inženjera i tehničara Srbije, Beograd, 2014.

[8] Jaćimović, B., Genić, S., Nagi, M., Laza, J., Problemi iz toplotnih operacija i aparata, SMEITS i Mašinski fakultet, Beograd, 1996.

## Gradual combustion of wood logs by the use of preheated air

Đorđe Novčić<sup>1\*</sup>, Miloš Nikolić<sup>1</sup>, Rade Karamarković<sup>1</sup>, Dragiša Šimunović<sup>1</sup>

<sup>1</sup>Faculty of Mechanical and Civil Engineering/Department of Energetics and Environmental Protection, University of Kragujevac, Kraljevo (Serbia)

*The tendency to automate operation and minimize human involvement in small-scale biomass boilers has led to an increase in pellet usage. Standardized biomass-derived solid fuels are getting a bigger share in the market. In this battle, traditional firewood is not yet ready to give in. Compared with the standardized fuels, the processing of firewood is cheaper, emits smaller amounts of parasite emissions whereas complete combustion and automation require further development. To achieve these requirements, wood log gasification is a promising intermediate step. The paper aims to design gasification and combustion chambers for a 25-kW wood-log-fired water boiler. For both processes, preheated air is used. Its appropriate distribution and preheating are the main tasks that are realized by the use of a CFD model. In the gasification chamber, the oxidation should take place at least 20 cm before the introduction of the secondary (combustion) air, which is introduced by the use of many openings. Their numbers and positions are envisaged to achieve as complete as possible combustion in a larger area and to divert the flame. A gradual introduction of air in a larger area should reduce carbon monoxide (CO), nitrogen oxides (NO<sub>x</sub>), and the emissions of volatile organic compounds (VOC), whereas the diversion of the flame should reduce the emissions of particulate matter.*

**Keywords:** Combustion, Small-scale biomass boiler, CFD, Gasification, Air distribution

### 1. INTRODUCTION

To achieve sustainable development, mankind envisaged the need for energy systems to be renewable and sustainable, efficient and cost-effective, convenient and safe [1]. To meet these requirements, biomass is seen as one of the most promising energy sources. Moreover, the use of biomass as fuel leads to the mitigation of greenhouse gas emissions [2].

Biomass is the first fuel, which has been used for millennia. More than half of all biomass is nowadays used as a fuel for household heating and cooking. In developing countries, that usage leads to a major cause of serious indoor pollution, particularly to women, small children, and the elderly [3]. Biomass is renewable organic material that comes from plants (including algae, trees, and crops) and animals in which the energy of sunlight is stored in chemical bonds [4,5]. The use of biomass reduces the need for fossil fuels, such as coal, oil, and natural gas, which have taken millions of years to evolve.

In small-scale biomass boilers, except for pellets and briquettes and in rare situations wood chips, firewood is still the dominant biomass fuel for traditional use. Although firewood is an ecological fuel and a renewable energy source, its combustion emits large amounts of pollutants into the atmosphere. The importance and the impact of these emissions are best illustrated by the increased concentrations of pollutants in urban and suburban areas with a large number of individual boilers, stoves, and furnaces in many cities in the Republic of Serbia. This problem is particularly accentuated during winter weather inversion. Solid biomass boilers emit numerous pollutants, of which the most attention is paid to carbon monoxide (CO), nitrogen oxides (NO<sub>x</sub>), and volatile organic compounds (VOC). In the Republic of Serbia, wood biomass is currently used annually with 1.021 Mtoe, while its annual untapped potential is 0.509 Mtoe [6].

### 2. AN OVERVIEW OF THE FIREBOX DESIGN IN SMALL-SCALE BIOMASS BOILERS

Manufacturers of wood biomass stoves and boilers are making significant efforts to increase efficiency and reduce pollutant emissions. Compared with derived fuels such as wood pellets, briquettes, and chips, firewood is the most economically acceptable fuel. Except for the price, the advantage of firewood is lower emissions of indirect pollutants due to shorter transport and less need for processing during production. Oppositely, the main disadvantages of firewood are: difficult control of the combustion process and higher pollutant emissions into the atmosphere. To reduce emissions, wood is burned in multi-stages or boilers and stoves are paired with heat accumulators to establish a stationary combustion regime [7,8].

When it comes to multi-stage combustion, in the first stage the wood is incompletely burned (gasified), while in the second stage the combustible gas is burned. Gasification and combustion zones are physically separated in gasification boilers. The basic schemes of the most commonly used constructions are shown in Figure 1. Only DC (direct current) gasification of wood (air and combustible gas flow in the same direction) was applied to them, and in all shown designs the gasification chamber (which is also a fuel bunker) is usually above the combustion chamber of the combustible gas (boiler firebox). In addition to the shown designs, there are designs with transverse and opposite gasification [9], as well as in the case of a fixed bed gasification reactor. The presented constructions dominate the market due to reliability, elaborated principle (manufacturers most easily accept successfully elaborated principles), the possibility of burning wood with larger moisture content, and stable air and gas flow through the gasification zone. The construction shown in Figure 1.A is technically the simplest, but also the most environmentally unacceptable. Its deficiency is caused by the flue gas loaded with a large

\*Corresponding author: Đorđe Novčić: Dositejeva 19, Kraljevo, novcic.d@mfkv.kg.ac.rs

concentration of particulates. These particles fall to the bottom of the firebox, cool very quickly, and cause higher emissions of carbon monoxide (CO), a higher amount of unburned carbon in the ash, and a higher amount of particles in the flue gas. This problem is more pronounced when reducing the amount of fuel in the gasification chamber (position 1 in Figure 1) because then the resistance of air and gas flow decreases. Therefore, most of the firebox space is covered with refractory ceramics as in the design shown in Figure 1.B, which is found in references [10,11,12].

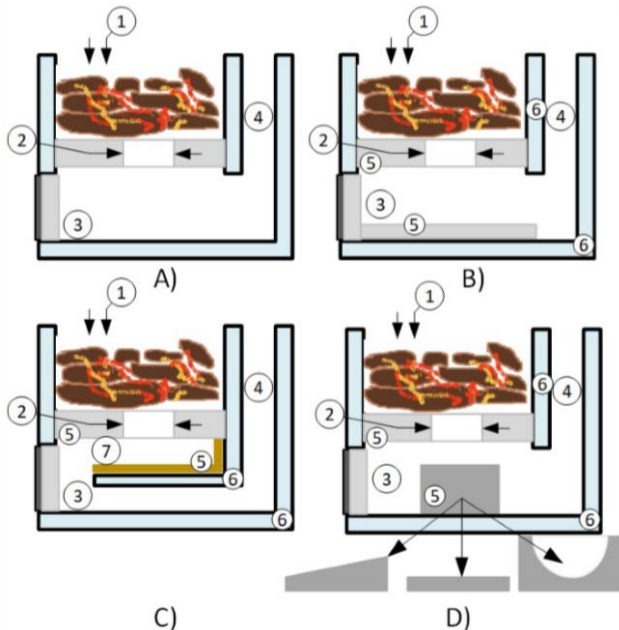


Figure 1: Analyzed designs of gasification boilers with direct current gasification of firewood. 1 – primary air (for gasification) and gasification chamber, 2 – secondary air (for combustion of combustible gas), 3 – combustion chamber, 4 – convective part of the boiler, 5 – refractory ceramic elements, 6 – water flow channels, 7 – intermediate chamber [13]

The design shown in Figure 1.C is often applied as can be seen in the reference [14]. This is a reliable design with some shortcomings. In the gasification chamber (position 1 in Figure 1), the airflow in one direction and burns incompletely the firewood. After leaving the gasification zone, the gas burns in the intermediate chamber (position 7 in Figure 1). The gasification zone and the intermediate chamber are divided by a plate of refractory ceramics (position 5 in Figure 1), whose role is to: limit the gasification zone and the firebox, keep the fuel being burned, enable the introduction and preheating of secondary air, and provide adequate mixing of producer gas from the gasification zone and combustion air. Figure 1.D shows the principle of design with a refractory insert. This type of design is found in references [15,16].

To achieve complete burnout and high efficiencies in small-scale combustion, downdraft boilers with the inverse flow have been introduced, which apply the two-stage combustion principle which is found in reference [17] and shown in Figure 2.

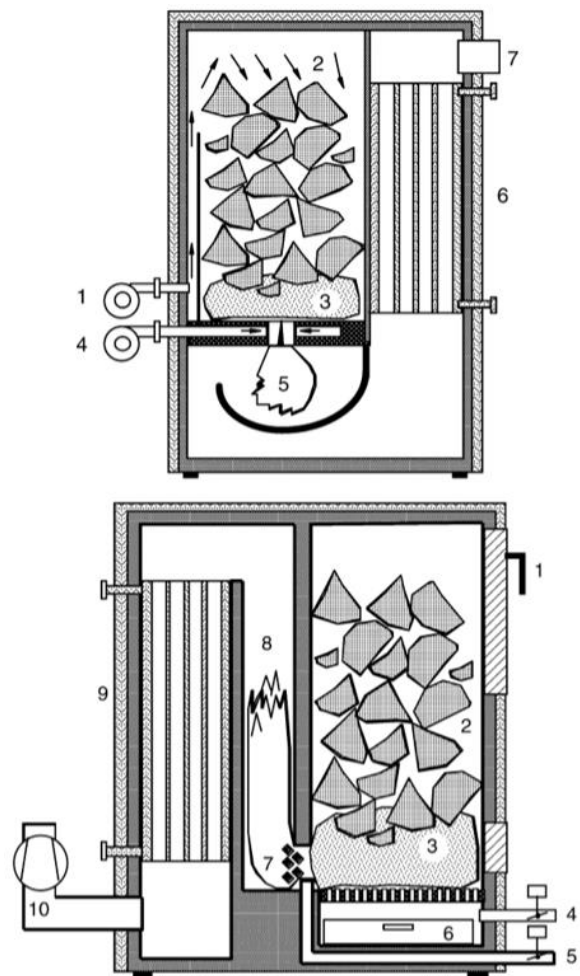


Figure 2: Downdraft boilers with inverse combustion of logwood and with enforced airflow and air supply with primary and secondary air. Above: 1 – primary air, 2 – fuel hopper, 3 – glow bed, 4 – secondary air, 5 – post-combustion chamber, 6 – heat exchanger, 7 – chimney. Below: 1 – fuel inlet, 2 – fuel hopper, 3 – glow bed, 4 – primary air, 5 – secondary air, 6 – ash bin, 7 – mixing zone, 8 – post-combustion chamber, 9 – heat exchanger, 10 – chimney [17]

### 3. INITIAL DESIGN OF SMALL-SCALE GASIFICATION BOILER

Figure 3 shows the initial design of a small-scale gasification boiler. In the design, wood logs are adequately gasified. However, the problem arises during the combustion of the product gas. High levels, i.e., high emissions of carbon monoxide (CO) were measured. In two weeks of testing, the carbon monoxide CO emissions were in the range of 2500 to 3000 ppm. Two reasons caused the problem. These are unstable control of primary and secondary air and relatively large distance between the gasification and combustion zones. When a small amount of fuel remains in the gasification zone, the primary air flows with ease through the gasification chamber. Due to a lower flow resistance, the amount of primary (gasification) air increases. That causes a more intense uncomplete oxidation in the gasification zone. At that point, the control of the secondary (combustion) air becomes a problem. The flow through the fuel bed and the design of air canals cause a large difference between flow resistances of the primary and secondary air. The primary

air is used for oxidation in the gasification zone, whereas, the secondary air is introduced for the complete combustion of the gas phase. The huge difference in the resistances causes the unstable control of two electro motors, which control two valves that regulate the amounts of the primary and secondary air. The other problem is caused by the rapid cooling of the incompletely oxidized gas phase. The cooling prevents the total burnout of the gas phase. The low residence time and the low temperature make unfavoured conditions for the complete oxidation of the gas phase. The subcooling happens because the gas path is too long from the gasification zone to the zone where the secondary air is introduced. Because of the decrease in temperature and inadequate gas flow, incomplete combustion and increased CO emissions occur.

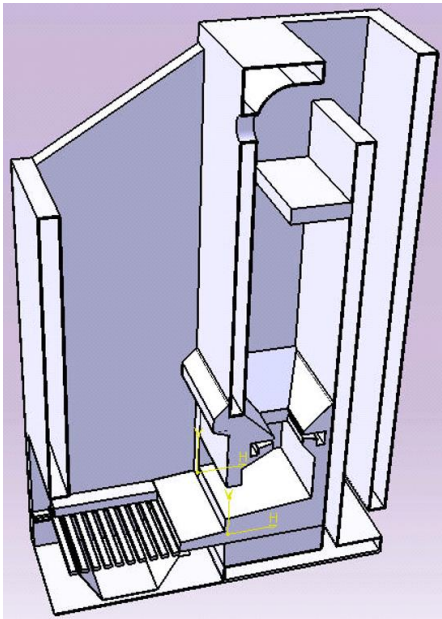


Figure 3: A cross-section view of the initial design of a small-scale gasification boiler

#### 4. CFD MODELLING

This paper aims to present a CFD (Computational Fluid Dynamics) simulation of a 25 kW wood-log-fired water boiler with the use of preheated air. The new design should solve the problem presented in the previous heading. The appropriate distribution of the primary and secondary air and adequate air preheating are the main tasks that are tested by the use of the CFD model. The tool used for the CFD simulation was based on the commercially available software, ANSYS CFX 18.1.

Based on the reference [18], the entire domain of the wood-log-fired water boiler can be divided into gasification and combustion zone.

This heading also describes the boiler geometry, the used mesh, fuel properties, boundary conditions, and air staging configurations.

##### 4.1. Description of the boiler geometry and mesh

For the CFD simulation, the design of the wood-log-fired water boiler shown in Figure 4 was simulated. The ANSYS Design Modeler software and ANSYS Meshing software were used for the wood-log-fired water boiler geometry simulation and numerical grid generation [19].

To improve the shortcomings of the initial design, a new air introduction system has been designed. The new concept of the boiler uses preheated primary and secondary air. Primary air flows through the hottest zone, cools the hearth (position 3 in Figure 4), and is introduced from the opposite sides (9) of the combustion chamber (2). The secondary air (8) is introduced through a large number of orifices (10). The concept is used in the present 25 kW wood-log-fired water boiler. The dimensions of the gasification chamber (1) are: 400x520x145 mm (length, width, and height). The influence of the position and size of the deflector plate (position 4 in Figure 4) affects the emissions of pollutants and leads to higher/lower velocities of the flue gas, which is found in reference [20]. After the initial oxidation reactions, the obtained gas should be immediately in the contact with preheated airflow (secondary air). As the gas is at this stage laden with particulates, their and combustibles in the gas phase burning together should happen from position 10 to position 3 in Figure 4. The intention is to elongate the flame, reduce its temperature and consequently decrease the NO<sub>x</sub> emissions.

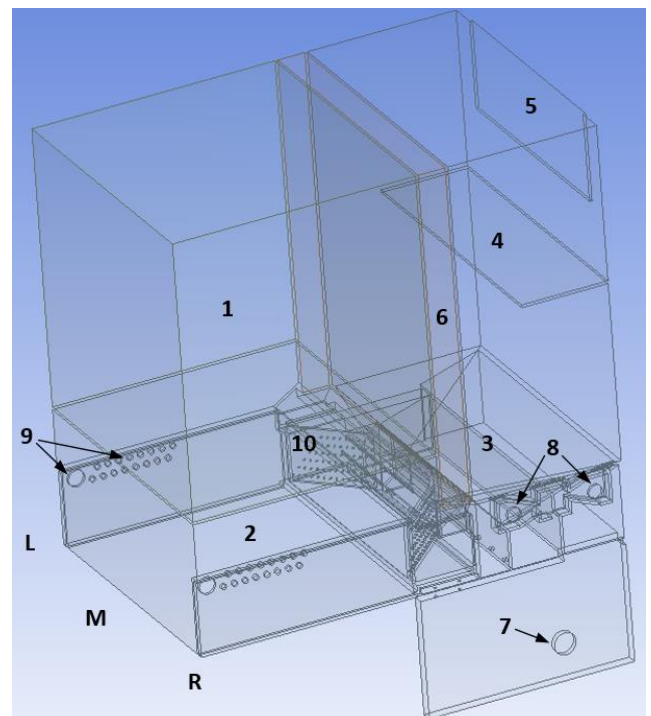


Figure 4: Individual parts of the wood-log-fired water boiler. 1 – fuel import area, 2 – gasification chamber, 3 – combustion chamber, 4 – deflector plate, 5 – flue gas exit, 6 – water channel, 7 – primary air inlet, 8 – secondary air inlets, 9 – primary air inlets to the gasification zone, 10 – secondary air inlets to the combustion zone

Figure 5 shows a detailed 3D fine mesh grid that was used for the numerical simulation. The number of elements is approximately slightly larger than 15 million.

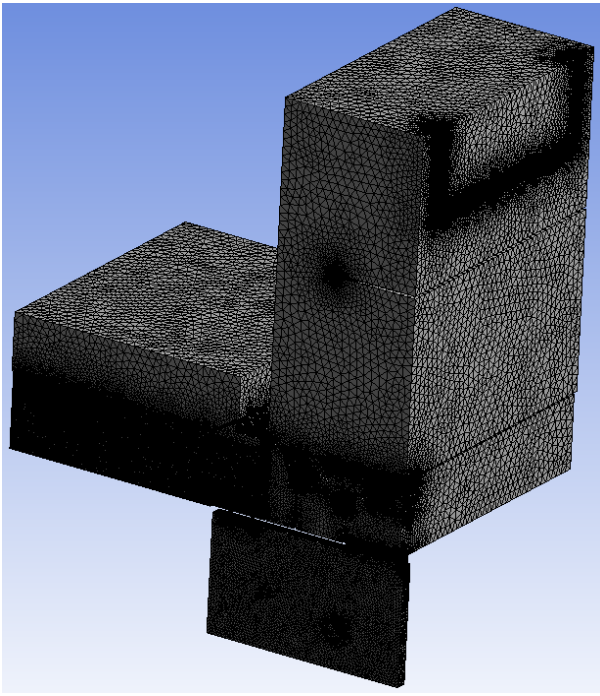


Figure 5: Representation of the 3D fine mesh grid

Table 1 shows the details of the mesh.

Table 1: Details of the mesh

| Statistics         |          |
|--------------------|----------|
| Nodes              | 2799678  |
| Elements           | 15137173 |
| Mesh Metric        | Average  |
| Element Quality    | 0.84241  |
| Aspect Ratio       | 1.8268   |
| Orthogonal Quality | 0.86365  |

#### 4.2. Fuel properties

The most important fuel properties which give the first impression of a certain fuel are given by proximate and ultimate analysis, heating value, and ash fusion point [2]. Beechwood of different lengths was used as the test fuel. Their proximate and ultimate analyses were not done, but the composition of dry beech wood was taken from the database Phyllis2 [21] and is shown in Table 2. The average moisture content of 19.3 wt.% in fuel was measured using Testo 606-1 device and was determined as the arithmetic mean of at least 50 measured values.

Table 2: Properties of the fuel used [21]

| Proximate analysis                  |       |
|-------------------------------------|-------|
| Moisture content [wt.%]             | 19.3  |
| Ash content [wt.%]                  | 0.49  |
| Ultimate analysis                   |       |
| Carbon [wt.%]                       | 48.35 |
| Hydrogen [wt.%]                     | 5.86  |
| Oxygen [wt.%]                       | 44.98 |
| Nitrogen [wt.%]                     | 0.31  |
| Sulphur [wt.%]                      | 0.02  |
| Heating value                       |       |
| Net calorific value (LHV) [MJ/kg]   | 19.07 |
| Gross calorific value (HHV) [MJ/kg] | 20.25 |

#### 4.3. Boundary conditions

The excess air  $\lambda$  is determined using the following equation [22]:

$$\lambda = \frac{20.9}{20.9 - O_2} \quad (1)$$

The excess air of 1.5 was used. With this excess air, the oxygen content in the flue gas of 7% is obtained. This is a typical value for this kind of boilers. Based on the reference [17], the primary air ratio ( $\lambda_{prim}$ ) of 0.8, and the secondary air ratio ( $\lambda_{sec}$ ) of 0.7 were chosen.

The burning rate of the fuel of 0.001457 kg/s was calculated based on the nominal power of the boiler 25 kW, the LHV of the fuel, and assumed efficiency of 90 % [23]:

$$\dot{B} = \frac{Q}{LHV \cdot \eta} \quad (2)$$

Based on the air ratios and the fuel-burning rate, the airflows at 293 K are: 0.002304 kg/s and 0.001249 kg/s for the primary and secondary air, respectively. These were calculated by [24]:

$$\dot{m} = \rho \cdot A \cdot v = \rho \cdot \pi \cdot \left(\frac{d}{2}\right)^2 \cdot v \quad (3)$$

In Eq. (3), the air density is taken to be 1.2041 kg/m<sup>3</sup>. The geometry of the openings for the primary and secondary air was calculated based on the assumed velocities: 1.5 m/s for the primary and 2 m/s for the secondary air.

#### 4.4. Air staging configurations

The required primary air for the gasification process is introduced into the gasification chamber through 34 holes (2 larger ones with a diameter of 30 mm, and 32 smaller holes that are 10 mm in diameter) located laterally on both sides of the chamber (Figure 6). The trajectory of the primary air around and below the combustion chamber is shown in Figure 6. The goal was to preheat the primary air before it enters the gasification chamber. The amount of primary air is controlled by a control valve driven by an electric motor.

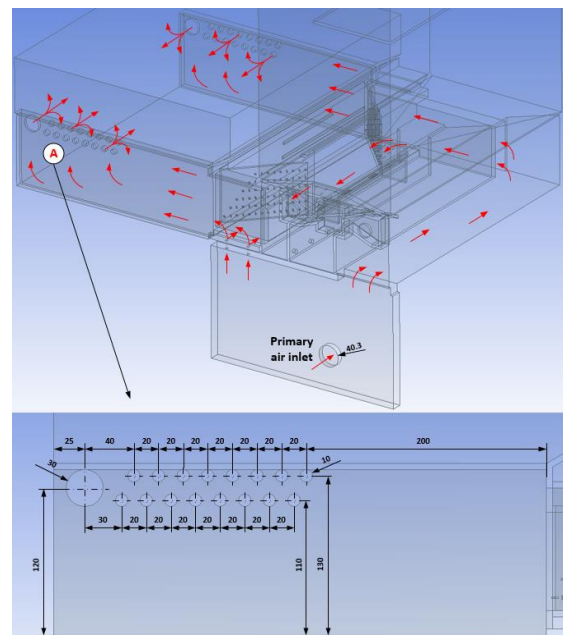


Figure 6: The primary air distribution to the gasification chamber

The shortest distance between the primary and secondary openings is 20 cm. The secondary air is introduced by an array of openings that are shown in Figure 7.

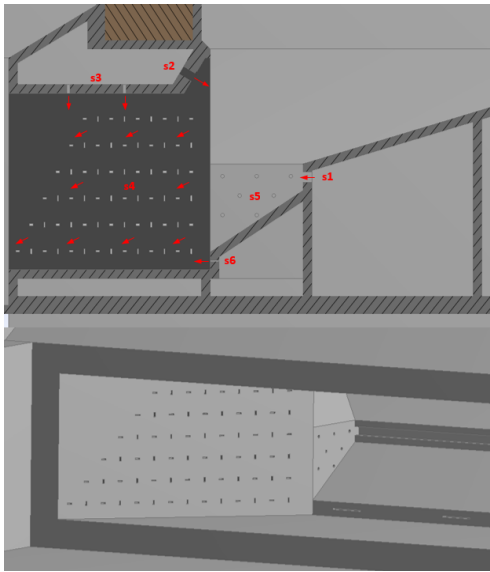


Figure 7: The secondary air distribution to the combustion chamber through the many openings

5. RESULTS AND DISCUSSION

Numerical simulations have been performed on the design shown in Figures 4 and 7. to investigate the influence of air staging on the distribution of the primary and secondary air. Figure 8. shows the simulation results.

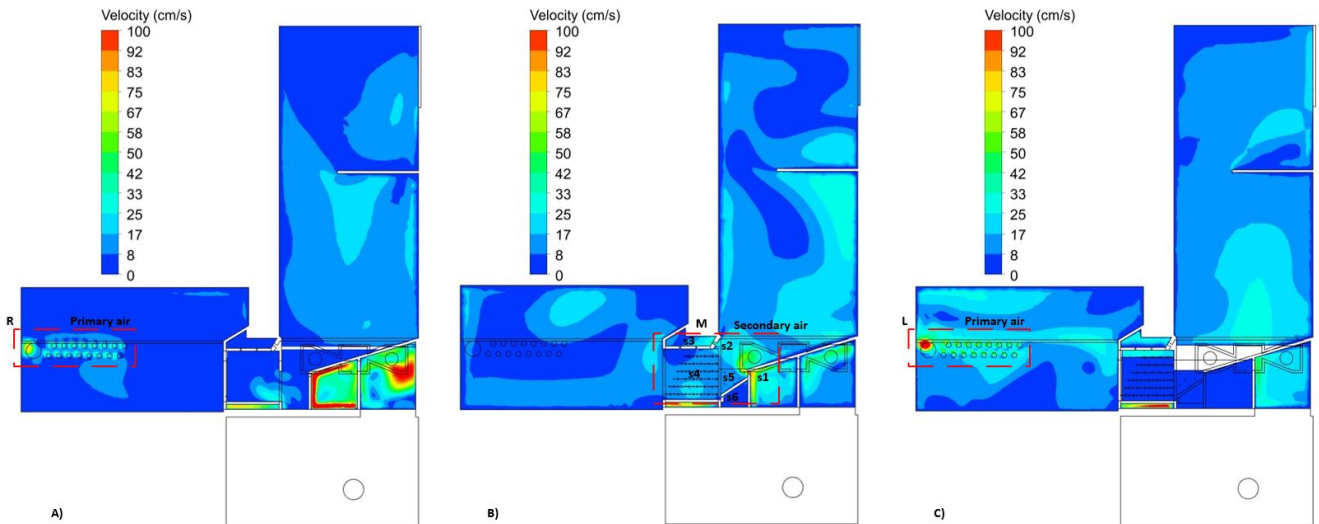


Figure 8: Air velocity field. A – primary air velocity (R), B – secondary air velocity (M), and C – primary air velocity (L)

In the presentation of the results in Figure 8., the priority is given to the velocity fields of the primary and secondary air. The numerical simulation was modeled with the help of 2,799,678 nodes and 15,137,173 elements. The k-epsilon model was used in the Ansys CFX software assuming a pressure of 1 bar in the firebox.

The primary air path (Figure 6.) favors the side (position 9 in Figure 4.) opposite to the primary air inlet (position 7 in Figure 4.). Based on the simulation, it was noticed that there is an uneven velocity field in the chamber that is located in the gasification zone. Figure 8. C shows the primary air (L) velocities (framed by a red dashed line) in the range from 0.67-1.2 m/s, whereas Figure 8. A shows the primary air (R) velocities (framed by a red dashed line) in the range from 0.6-0.8 m/s. The numerical simulation shows that the obtained results differ from the expected for the primary air. Compared with the desired air velocity of 1.5 m/s, the simulated values are lower. In both cases, the highest velocities were achieved through the 2 larger holes that are 30 mm in diameter.

These holes are placed at the end opposite the air entrance (see Figure 8. A)

Figure 8.B shows the velocity field for the secondary air (M). In this case, also, the obtained results are contrary to the expected ones of 2 m/s. As can be seen, the secondary air favors the air curtain (position s1 in Figure 8.B) located in the combustion zone with velocities in the range from 0.6-1.1 m/s. The aim of the air curtain (position s2 in Figure 8.B) was to divert the flame and the velocities were in the range of 0.6-0.67 m/s. The secondary air velocities (positions s3, s4, s5, and s6 in Figure 8.B) were in the range from 0.08-0.25 m/s. It can also be seen that the velocity field is less favorable because there is a "short circuit" to the convective part of the boiler on the underside of the deflector plate. Also, in the combustion zone, the secondary air velocity field shows that the highest flow velocities were at the air curtain (position s1 in Figure 8.B), which is good because it favors the uplift of ash and unburned particles towards the convective part of the boiler.

## 6. CONCLUSION

The initial design of the small-scale gasification boiler had large carbon monoxide (CO) emissions, which were in the range of 2500 to 3000 ppm with a flue gas oxygen content of 7 %. Incomplete combustion of gas due to its rapid cooling has been identified as a cause of excessive emissions of pollutants. The paper aimed to answer the question of how to improve the second stage of the combustion process in the boiler. Multi-stage combustion of wood logs by the use of preheated air was envisaged. The preheating of the primary air by passing around and under the combustion chamber, before entering into the gasification chamber through a total of 34 holes. The primary air ratio is 0.8 and it should be maintained close to 0.7-0.8, which is found in reference [17]. It has also been proposed to preheat the secondary air and introduce it into the combustion chamber through the many openings. The goal was to improve the mixing of the secondary air and the gas that is coming from the gasification chamber. It is important to note that the flow resistances of the primary and secondary air should be on the same order of magnitude because the low resistance of the secondary compared with the primary air can lead to a negative impact on the control of the combustion process in such types of boilers. The numerical simulation showed that the primary and secondary air streams enter the chambers at slower than desired velocities. This problem should be solved by an additional redesign of the hearth. A gradual introduction of air in a larger area should reduce carbon monoxide (CO), nitrogen oxides (NO<sub>x</sub>), and the emissions of volatile organic compounds (VOC), whereas the diversion of the flame should reduce the emissions of particulate matter.

## ACKNOWLEDGEMENTS

This research was supported by the Ministry of Education, Science and Technological Development of the Republic of Serbia (Grant No. 451-03-9/2021-14/200108).

## REFERENCES

- [1] H.L. Chum and R.P. Overend, "Biomass and renewable fuels," *Fuel Processing Technology*, Vol. 71, pp. 187–195, (2001)
- [2] A.A. Khan, W. de Jong, P.J. Jansens and H. Spliethoff, "Biomass combustion in fluidized bed boilers: Potential problems and remedies," *Fuel Processing Technology*, Vol. 90, pp. 21–50, (2009)
- [3] J. Goldemberg and S.T. Coelho, "Renewable energy – traditional biomass vs. modern biomass," *Energy Policy*, Vol. 32, pp. 711–714, (2004)
- [4] P. McKendry, "Energy production from biomass (part 1): overview of biomass," *Bioresource Technology*, Vol. 83, pp. 37–46, (2002)
- [5] <https://www.eia.gov/energyexplained/biomass/> (accessed June 2021)
- [6] <https://www.pravno-informacioni-sistem.rs/SlGlasnikPortal/eli/rep/sgrs/skupstina/ostalo/2015/101/1/r> (accessed June 2021)
- [7] L.S. Johansson, B. Leckner, L. Gustavsson, D. Cooper, C. Tullin and A. Potter "Emission characteristics of modern and old-type residential boilers fired with wood logs and wood pellets," *Atmospheric Environment*, Vol. 38, pp. 4183–4195, (2004)
- [8] L. Deng, D. Torres-Rojas, M. Burford, T.H. Whitlow, J. Lehmann and E.M. Fisher "Fuel sensitivity of biomass cookstove performance," *Applied Energy*, Vol. 215, pp. 13–20, (2018)
- [9] <https://www.viessmann.de/de/wohngbaeude/festbrennstoffkessel/stueckholzheizung/vitoligno-250-s.html> (accessed June 2021)
- [10] US 9,273,861 B1 (2016)
- [11] US 2013/0186313 A1 (2013)
- [12] US 2016/0290747 A1 (2016)
- [13] R. Karamarković, Đ. Novčić, M. Nikolić, M. Karamarković and D. Šimunović "Eksperimentalno ispitivanje gasifikacionog kotla: dizajn komore za sagorevanje," *Procesna tehnika*, Vol. 30, pp. 20–26, (2018)
- [14] <https://www.solarbayer.com/Wood-boiler-HVS-E-LC.html> (accessed June 2021)
- [15] US 8,640,655 B2 (2014)
- [16] [https://luuma-energy.de/wp-content/uploads/2018/07/PRO\\_SH18\\_SH27\\_20180112\\_w eb.pdf](https://luuma-energy.de/wp-content/uploads/2018/07/PRO_SH18_SH27_20180112_w eb.pdf) (accessed June 2021)
- [17] T. Nussbaumer "Combustion and Co-combustion of Biomass: Fundamentals, Technologies, and Primary Measures for Emission Reduction," *Energy & Fuels*, Vol. 17, pp. 1510–1521, (2003)
- [18] M.A. Gomez, R. Comesana, M.A. Alvarez Feijoo and P. Eguia "Simulation of the Effect of Water Temperature on Domestic Biomass Boiler Performance," *Energies*, Vol. 5, pp. 1044–1061, (2012)
- [19] P. Drosatos, A. Nesiadis, N. Nikolopoulos, N. Margaritis, P. Grammelis and E. Kakaras "CFD Simulation of Domestic Gasification Boiler," *Journal of Energy Engineering*, Vol. 143, (2016)
- [20] R. Buczynski, R. Weber and A. Szlek "Innovative design solutions or small-scale domestic boilers: Combustion improvements using a CFD-based mathematical model," *Journal of the Energy Institute*, Vol. 88, pp. 53–63, (2015)
- [21] <https://phyllis.nl/Biomass/View/62> (accessed June 2021)
- [22] PCA 3 Portable Combustion Analyzer – Operation and Maintenance Manual. 2011
- [23] P. Motyl, D. Krol, S. Poskrobko and M. Juszcak "Numerical Modelling and Experimental Verification of the Low-Emission Biomass Combustion Process in a Domestic Boiler with Flue Gas Flow around the Combustion Chamber," *Energies*, Vol. 13, pp. 1–16, (2020)
- [24] <https://www.omnicalculator.com/physics/flow-rate#how-to-calculate-flow-rate-flow-rate-formulas> (accessed June 2021)

**SESSION G**

**CIVIL ENGINEERING**



## Interaction diagrams in limit and shakedown analysis

Bojan Milošević<sup>1\*</sup>, Žarko Petrović<sup>2</sup>, Saša Marinković<sup>1</sup>

<sup>1</sup>Faculty of Mechanical and Civil Engineering in Kraljevo, University of Kragujevac, Kraljevo (Serbia)

<sup>2</sup> Faculty of Civil Engineering and Architecture, University of Niš, Niš, Serbia

*In the case when the load acting on the structure is multi-parameter, it is not possible to determine the value of the limit load, but only the safe area, which can be most simply shown by an interaction diagram. Depending on whether the load is proportional or variable (low cyclic or alternative), static and kinematic theorems of limit and shakedown analysis are used to determine the safe area. The paper presents the procedure for determining interaction diagrams in continuous and frame girders exposed to the action of proportional and variable repeated load. The parameters that are varied in the paper are: the character of load and the beam span value of the continuous girder, i.e., the character of load, degree of static indeterminacy and ratio of height and width of frame girders.*

**Keywords:** Safe limit load, Continuous girders, Frame girders, Interaction diagrams

### 1. INTRODUCTION

Many engineering structures or some of their parts are exposed to different types of loads, some of which can act completely independently of each other, so some of these loads are constant while others are not defined over time and belong to the group of variable repeated loads. In a large number of cases, only the area to which the variable repeated load belongs can be defined.

By applying the limit analysis of structures, the maximum load parameter or load increase parameter that one elasto-plastic structure can carry is determined. If the structure is exposed to the action of a gradually increasing load, at some point it can reach a certain critical value, which leads to a plastic failure of the structure, after which the structure is no longer able to receive further increase of load. This state is called the limit state of the structure, and the load that causes is called the limit load. Determining the load-bearing capacity of the structure, as well as the assessment of the failure of the structure is valuable not only as a simple control of the load-bearing capacity of the girder, but also as a significant base and factor in the design of structures. The limit load determined by the application of the limit analysis is one of the indicators of the bearing capacity of the structure exposed to the action of proportional load.

When a structure is exposed to the effect of a variable repeated load, it breaks under the effect of a load that is less than the load obtained by applying the limit analysis of the structures. The application of shakedown analysis in assessing the safety of structures exposed to variable, repeated loads is important, and often unavoidable. The structure in this case experiences a failure due to one or both types of failure, called incremental collapse and alternative plasticity. Shakedown analysis is a method in which it is not necessary to monitor the entire flow of the structure response (stress and strain) under the action of a variable repeated load, and it represents a significant generalization of the limit analysis theorems.

Limit analysis is more recent, although some ideas emerged in the 18th century. The static theorem was first proposed by Kist (1917) [1], as an intuitive axiom, but it is considered that the basic theorems of limit analysis were

first presented by Gvozdev in 1936. Limit analysis theorems were independently derived by Hill in 1951, for rigid perfectly plastic material [2], as well as Drucker et al. in 1952 [3,4], for elastic perfectly plastic material. Formal proof of these theorems for beams and frames was performed by Horne (1949) [5], as well as Greenberg and Prager (1949) [6]. The concept and method of structural design using shakedown analysis was originally developed in 1930, although it has been expanding since 1950. The first papers in this field were presented by Bleich 1932, Melan 1938 [7] and Koiter 1956 [8]. They proved two basic shakedown theorems: the static shakedown theorem (Melan's theorem), i.e., the lower shakedown load limit, and the dynamic shakedown theorem (Koiter's theorem), i.e., the upper shakedown load limit, which are the basis of the shakedown theory of elasto-plastic structures.

In recent years, shakedown analysis has become increasingly used in the analysis of engineering problems due to the growing demands of modern technologies. Thus, it has successfully found application in solving many engineering problems, such as the construction of nuclear reactors, railways, space and aeronautical facilities or over ocean oil platforms, which places great demands on the assessment of structural safety and reliability of facilities.

The aim of this paper is to apply the static and kinematic theorem of limit analysis, as well as the application of the shakedown theorem to perform the analysis of the bearing capacity of line girders depending on the degree of static indeterminacy, as well as the character of the load. Using the limit analysis theorem, the bearing capacity analysis was performed when the beam was exposed to a load that grows proportionally, while in the case of a variable repeated load, the analysis was performed using the shakedown theorem. On the basis of the obtained expressions, the construction of interaction diagrams was performed, by means of which the change in the magnitude of the limit and incremental failure forces was presented. Interaction diagrams make it possible to define a safe area of the girder in which no failure mechanism is formed. Based on the conducted analysis, a conclusion is reached on the justification of the construction of interaction diagrams and determination of

\*Corresponding author: Bojan Milošević, Veljka Dugoševića 44, 1100 Beograd, milosevic.b@mfkv.kg.ac.rs

the safe area of the girder, when it is exposed to a load whose character is unknown.

## 2. BASIC POSTULATES OF LIMIT AND SHAKEDOWN ANALYSIS

The analysis of the girders using the theory of plasticity, i.e., limit analysis allows the plasticization of the material.

In the area of elastic behaviour of the girder, stresses and strains are proportionally dependent. Due to the increase in load, the stresses gradually increase, until the value of the stress in the most loaded fibre reaches the value of the yield stress. Further increase of the load leads to plasticization of the cross section, i.e., increase of the plasticity zone, which gradually expands both in height and length of the girder, until the entire cross section is plasticized, and thus the formation of a plastic hinge [9].

It is known that, in the case of statically determined girders, complete plasticization of one cross section of the girder (formation of a plastic hinge at the place of maximum bending moment) and transition of the girder into the failure mechanism results in loss of load bearing capacity. In statically indeterminate girders, the formation of one plastic hinge does not lead to the formation of a failure mechanism, and the load-bearing capacity of one  $n$  times statically indeterminate girder is completely exhausted when  $n+1$  plastic hinge is formed in the girder.

It can be said that the girder is in the state of limit equilibrium when the bearing capacity of the girder is completely exhausted, and in a sufficient number of sections the girder behaves completely plastic [10]. The moment immediately preceding the formation of the failure mechanism represents the moment of the limit equilibrium of the girder.

In order to determine the limit bearing capacity of one girder by applying limit analysis, it should first be proved that the relevant limit state for it will be created by the formation of the failure mechanism, i.e., the occurrence of any other limit state condition should be eliminated. It is necessary to exclude the occurrence of fatigue due to the action of variable load, then the possibility of local instability before reaching full plasticization and to exclude the occurrence of any effect that would lead to failure of the girder before forming a sufficient number of plastic hinges and its transition to failure mechanism [39].

If the girder is unloaded before the formation of the failure mechanism, permanent (plastic) deformations occur, which cause the appearance of residual bending moments. By applying the limit analysis, it is not possible to introduce into the calculation of the remaining bending moments, in the case of reloading of the girder. This is possible by applying the shakedown theorems. In shakedown analysis, all the assumptions that are introduced in the limit analysis method are valid, whereby this method enables the analysis of the behaviour of the girder that is exposed to repeated loading.

The basic theorems of the limit analysis can be applied to all types of static systems, both statically determinate and statically indeterminate, and they are:

- static theorem or lower load limit theorem and
- kinematic theorem or upper load limit theorem.

The static theorem is based on the static equilibrium of the observed system. For a statically indeterminate system, a large number of distributions of bending moments can be assumed, which satisfy the equilibrium conditions due to a given external load. Greenberg and Prager (1952) called this distribution statically permissible. If such a system satisfies the condition of plasticity, i.e., the bending moment in any section did not exceed the appropriate value, it is said that it is safe. A necessary condition is that there must be at least one safe distribution of moments in the construction, which is also statically permissible. According to the static theorem, this is a sufficient condition for providing bearing capacity.

The static theorem can be expressed as follows: If there is any distribution of bending moments in a static system that is both safe and statically permissible due to the load  $\lambda P$ , then the value of  $\lambda$  must be less than or equal to the failure load factor  $\lambda_c$ , ( $\lambda_c > \lambda$ ). The actual limit load ( $\lambda_c P \geq P_p$ ) can be equal to or greater than the set one.

In the case when the failure mechanism is known, the failure load factor  $\lambda_c$ , i.e., the ultimate load ( $\lambda_c P$ ), is determined by equalizing the work of external forces with the work absorbed in plastic hinges. When the failure mechanism corresponding to the limit load is not known, the equation of work can be written for each assumed failure mechanism, whereby values ( $\lambda P$ ) corresponding to the assumed failure mechanisms are obtained.

The kinematic theorem can be expressed as follows: For a given static system, which is exposed to an external load  $\lambda P$ , the value  $\lambda$  corresponding to any assumed failure mechanism must be greater than or equal to the failure load factor  $\lambda_c$  or  $\lambda_c \geq \lambda$ .

Shakedown theorems have the role of setting the main conditions under which plastic yielding in a structure finally ceases, no matter how often and in what order the load is applied [11].

The bending moment of the observed cross section  $j$  can be represented as:

$$M_j = m_j + (M_e)_j \quad (1)$$

where:

$M_j$  – is the actual bending moment of the cross section,

$(M_e)_j$  – is elastic bending moment of cross section,

$m_j$  – is the residual bending moment of the cross section.

Any distribution of residual bending moments, defined in this way, must be statically possible in the case when the structure is unloaded, because the moments  $M_j$  and  $(M_e)_j$  must be in equilibrium with the external load [12]. The construction is adapted to the action of a variable repeated load, if at some point condition (1) is satisfied, and all subsequent loads cause only an elastic change in bending moments.

Based on condition (1), the static adaptation theorem can be expressed in the following form: If there is any distribution of residual bending moments  $m_j$  in the structure, and that the distribution is statically possible in the case when the structure is not loaded and satisfied for each cross-section  $j$ , is to meet one of the conditions:

$$m_j + \lambda M_j^{\max} \leq (M_{pl})_j \quad (2)$$

$$m_j + \lambda M_j^{\min} \geq -(M_{pl})_j \quad (3)$$

$$\lambda (M_j^{\max} - M_j^{\min}) \leq 2(M_e)_j \quad (4)$$

the value of  $\lambda$  will be equal to or less than the factor of safe limit load  $\lambda_s$ .

Each girder tends to adapt to the action of a variable repeated load. Thus, if  $\lambda$  exceeds the value of  $\lambda_s$ , unlimited plastic yield occurs and in that case any distribution of residual moments is not possible, which is a necessary condition for determining a safe limit load. Depending on the calculated load factor  $\lambda$ , it is possible to determine a safe limit load, which depends on the type of variable repeated load, based on satisfying some of equations (2) and (3), as incremental conditions of plasticity and equation (4), as conditions of alternative plasticity.

Assuming that the observed failure mechanism is known, rotations of formed plastic hinges can be observed in a number of characteristic cross sections  $\theta$  [13]. If the rotation in any section is positive, then it can be said that the total bending moment in that section tends to reach the value  $+M_{pl}$ , and if the rotation of the formed plastic hinge is negative, the bending moment tends to reach the value  $-M_{pl}$ . Based on the introduced assumptions, equations (2) and (3) can be written in the form:

$$m_j + \lambda M_j^{\max} = (M_{pl})_j \quad \text{for} \quad \theta_j^+ \quad (5)$$

$$m_j + \lambda M_j^{\max} = -(M_{pl})_j \quad \text{for} \quad \theta_j^- \quad (6)$$

If the equations (5) and (6) are multiplied by the corresponding rotation of the formed plastic hinge in the cross-section  $j$ , then they have the form:

$$m_j \theta_j + \lambda M_j^{\max} \theta_j^+ = (M_{pl})_j |\theta_j| \quad (7)$$

$$m_j \theta_j - \lambda M_j^{\max} \theta_j^- = (M_{pl})_j |\theta_j| \quad (8)$$

Adding equations (7) and (8), of all the plastic hinges which have been formed on the observed failure, give the following:

$$\sum m_j \theta_j + \lambda \left[ \sum M_j^{\max} \theta_j^+ + \sum M_j^{\max} \theta_j^- \right] = \sum (M_{pl})_j |\theta_j| \quad (9)$$

As the distribution of residual bending moments is in equilibrium when the structure is unloaded, and the  $\theta$  is rotation of the cross section where plastic hinge has been formed, the equation of the principle of the virtual work can be written in the following form  $\sum m_j \theta_j = 0$ , thus (9) becomes:

$$\lambda \left[ \sum M_j^{\max} \theta_j^+ + \sum M_j^{\max} \theta_j^- \right] = \sum (M_{pl})_j |\theta_j| \quad (10)$$

which represents the basic equation of incremental failure.

Based on equation (10), the kinematic adaptation theorem can be expressed as follows: The value of the parameter  $\lambda$ , which corresponds to any assumed failure mechanism (alternative  $\lambda_a$  or incremental  $\lambda_i$ ), must be greater than or equal to the value of the safe limit load parameter  $\lambda_s$ .

The kinematic theorem of adaptation in this form was first set by Koiter (1956, 1960), although it can be said that he did it on the basis of the work of P.S. Symonds

and B.G. Neal [14], which was published at the first National Congress of Applied Mechanics in Chicago, in 1951. They started from the assumption that the work of all residual moments on a possible failure mechanism is equal to zero. In this paper, the incremental failure load will be calculated using the Symonds and Neal method.

### 3. INTERACTION DIAGRAMS

There are two ways to calculate the failure load (limit and shakedown failure load), and these are the step-by-step method (incremental elasto-plastic analysis) and the direct method. The step-by-step method is based on a gradual, detailed calculation of the failure load, which requires an extensive calculation. The direct method is based on determining the failure load on a possible failure mechanism without gradually monitoring the development and formation of plastic hinges, which is simpler for practical application.

When a structure is exposed to a variable repeated load, failure can occur due to the development of excessive plastic yielding in some part of the structure, even if no applied load is large enough to lead to the formation of a failure mechanism. If the load is of alternating character, in the cross section there is a repetition of plastic deformations of the opposite sign (without accumulation of plastic deformations), thus causing the phenomenon of low-cycle fatigue. The load that leads to the failure of the girder is called the alternative limit load. Another type of failure can occur if several critical load combinations are repeated during the action of a variable load, and they follow each other in certain cycles. The formation of the failure mechanism occurs due to the accumulation of plastic deformations during each load cycle (progressive deformation), causing a decrease in the durability of the structure. In this case, it is an incremental limit load. If the limit load is determined as two-parameter, the interdependence of the loads acting on the observed structure can be represented by an interaction diagram.

Sometimes it is convenient to show all possible ways of failure of the structure on one interaction diagram. The goal of the construction of interaction diagrams is reflected in the definition of the safe area of the observed static system [15]. Based on interaction diagrams, it is possible to speed up the process of dimensioning structures, and greater safety is achieved in the design phase because the problem can be seen and better understood in the whole area of combinations of simultaneous load effects on the structure.

Interaction diagrams in the limit analysis of structures are usually defined for the ultimate load-bearing capacity of the cross-section of the girder. The safe area is defined on the basis of safety according to the failure of the cross section of the girder. Thus, for a particular cross-sectional shape of the girder, the diagrams represent the interaction between the limit failure forces acting on the observed girder. As usual, the diagrams are shown two-dimensionally as a function of the limit loads of the girders. Such a diagram will usually not be of much help in the analysis of complex constructions, but here the opportunity can be used to illustrate the behaviour of some simpler static systems.

3.1. Analysis of the bearing capacity of continuous beam depending on the load character

By applying an adequate method, and depending on the load character, the analysis of the ultimate load-bearing capacity of the girder shown in Figure 1 was performed. In the example of a continuous girder, the procedure of calculating the magnitude of the failure force depending on the change of the span of the girder field was carried out, which is defined by the coefficients  $\alpha$  and  $\beta$ .

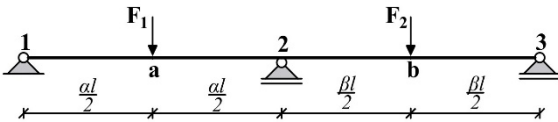


Figure 1: Continuous two-span beam loaded by concentrated forces in the middle of span

The ultimate failure load can also be determined by applying the kinematic theorem when it is necessary to equate the virtual work of all external forces on the assumed failure mechanism with the works absorbed in the cross sections in which the plastic hinges are assumed. For each of the possible failure mechanisms, one limit failure force is obtained, of which the one that is the smallest at the same time and the force that leads to the formation of the relevant failure mechanism.

For the observed carrier (Figure 1), three failure mechanisms can be formed, two independent (Figure 2a and Figure 2b) and one combined (Figure 2c).

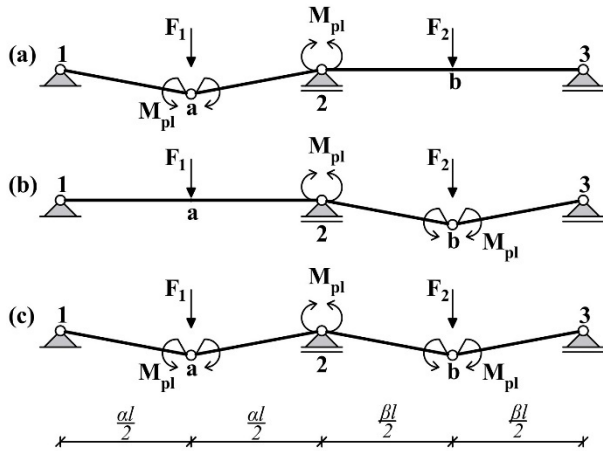


Figure 2: (a) Failure mechanism of the first span, (b) Failure mechanism of the second span, (c) Combined failure mechanism

For each of the possible failure mechanisms, by applying the kinematic theorem, the limit failure forces are obtained:

$$F_1 = \frac{6M_{pl}}{\alpha l} \tag{11}$$

$$F_2 = \frac{6M_{pl}}{\beta l} \tag{12}$$

$$12M_{pl} = l(F_1\alpha + F_2\beta) \tag{13}$$

When the fields are of the same length ( $\alpha=\beta=l$ ), and the girder is simultaneously acted upon by two independent load systems  $F_1$  and  $F_2$ , which are in an arbitrary relationship, the analysis of the ultimate bearing

capacity and defining the area in which the girder is safe for failure can be performed based on the interaction diagram. In the interaction diagram, the interrelationship of the failure mechanism and the mutual relationship of the load is best observed.

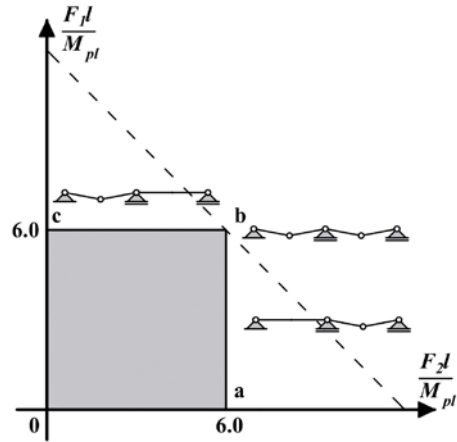


Figure 3: Interaction diagram in the case of proportional loading

From the interaction diagram (Figure 3) it can be concluded that the formation of the failure mechanism in the second field occurs when the  $F_1 \leq F_2$ , while the formation of the failure mechanism in the first field occurs when the  $F_1 \geq F_2$ . For any load ratio located within the range  $0abc0$ , no failure mechanism will occur, and thus no failure of the girder. If the load ratio is such that it is defined by one of the lines, the failure mechanism that defines that line is formed.

When the girder (Figure 1) is exposed to the effect of a variable repeated load, the area in which the load acts is in the following range:  $0 \leq F_1 \leq F_1, 0 \leq F_2 \leq F_2$ . Figure 4a shows a diagram of bending moments when only the force  $F_1$  acts on the beam, and Figure 4b shows a diagram of bending moments when only the force  $F_2$  acts on the beam. The values of the elastic bending moments are shown in Table 1.

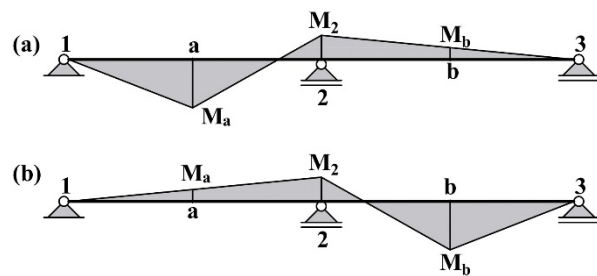


Figure 4: Elastic bending moment diagrams of continuous two-span beam

Table 1: Elastic bending moments of continuous two-span beam

|       | $F_1 = F_1, F_2 = 0$   | $F_1 = 0, F_2 = F_2$                        |
|-------|--|---|
| $M_a$ | $\frac{F_1 l \alpha (5\alpha + 8\beta)}{32(\alpha + \beta)}$ | $\frac{3F_2 l \beta^2}{32(\alpha + \beta)}$ |
| $M_b$ | $\frac{6F_1 l \alpha^2}{32(\alpha + \beta)}$                 | $\frac{6F_2 l \beta^2}{32(\alpha + \beta)}$ |

|       |   |   |
|-------|---|---|
| $M_b$ | $\frac{3F_1\alpha^2}{32(\alpha+\beta)}$ | $\frac{F_2\beta(8\alpha+5\beta)}{32(\alpha+\beta)}$ |
|-------|---|---|

The analysis of the ultimate load-bearing capacity of the girder when exposed to the effect of a variable repeated load will be performed by applying the shakedown theorem. To apply the static shakedown theorem, it is necessary to know the possible distribution of the residual bending moment (Figure 5).

By applying the static shakedown theorem on the basis of equations (2) and (3), as incremental conditions of plasticity and equation (4) as an alternative condition, the values of the forces leading to the failure of the girder are obtained.

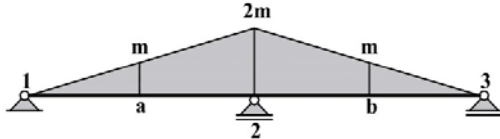


Figure 5: Possible distribution of residual bending moment

The relevant failure limit load depends on the ratio of the coefficients  $\alpha$  and  $\beta$ . Thus, if  $\alpha \geq \beta$ , the failure mechanism is formed in the first field, and the magnitude of the incremental failure force and the residual bending moment are defined by expressions (14) and (15):

$$8F_1 \alpha (\alpha + \beta) + 3F_2 \beta^2 = \frac{48M_{pl} (\alpha + \beta)}{l} \quad (14)$$

$$m = \frac{F_1 \alpha l (8\beta - \alpha) - 6F_2 \beta^2 l}{96(\alpha + \beta)} \quad (15)$$

while in the case when  $\beta \geq \alpha$ , the failure mechanism is formed in the second field, and the magnitude of the incremental failure force and the residual bending moment are defined by expressions (16) and (17):

$$8F_2 \beta (\alpha + \beta) + 3F_1 \alpha^2 = \frac{48M_{pl} (\alpha + \beta)}{l} \quad (16)$$

$$m = \frac{F_2 \beta l (8\alpha - \beta) - 6F_1 \alpha^2 l}{96(\alpha + \beta)} \quad (17)$$

On the basis of the alternating plasticity conditions (4) for the cross sections a, 2 and b is obtained:

$$F_1 l \alpha (5\alpha + 8\beta) + 3F_2 l \beta^2 = 64M_e (\alpha + \beta) \quad (18)$$

$$3F_1 l \alpha^2 + 3F_2 l \beta^2 = 32M_e (\alpha + \beta) \quad (19)$$

$$F_2 l \beta (8\alpha + 5\beta) + 3F_1 l \alpha^2 = 64M_e (\alpha + \beta) \quad (20)$$

As  $M_e = M_{pl}/\alpha_{form}$ , it is concluded that the value of alternating failure force depends on the coefficient of cross section form. Here the rectangular cross section is adopted whose form coefficient is  $\alpha_{form} = 1,50$ .

Interaction diagram (Figure 6.) is constructed for the case when the beam spans are equal ( $\alpha = \beta = 1$ ), on the basis of expressions (14), (16), (18), (19) and (20).

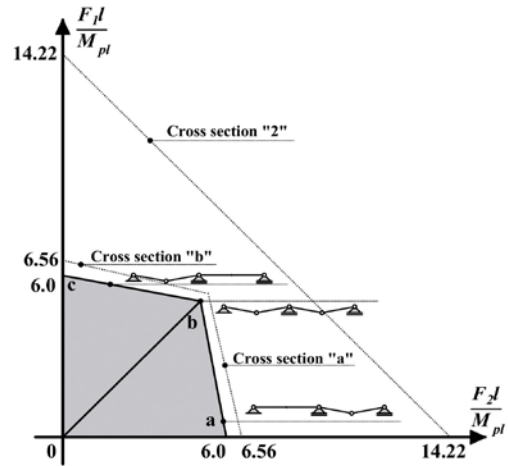


Figure 6: Interaction diagram in the case of variable repeated loading

From the diagrams, it is observed that the safe area **0abc0** is defined on the basis of incremental failure condition.

In further analysis of the limit bearing capacity of beams it is assumed that the force in the first span of the alternating character ( $-F_1 \leq F_1 \leq F_1$ ), while the force acting in the second span is in the range  $0 \leq F_2 \leq F_2$ . Applying the static shakedown theorem and failure conditions (2) and (3), when  $\alpha \geq \beta$ , the value of the failure force is defined on the basis of the expression:

$$8F_1 \alpha l (\alpha + \beta) + 3F_2 \beta^2 l = 48M_{pl} (\alpha + \beta) \quad (21)$$

and the value of the residual bending moment is:

$$m = \frac{F_1 \alpha l (8\beta - \alpha) - 6F_2 \beta^2 l}{96(\alpha + \beta)} \quad (22)$$

that is, in the case when  $\alpha \leq \beta$ , the following is obtained:

$$3F_1 \alpha^2 l + 4F_2 \beta l (\alpha + \beta) = 24M_{pl} (\alpha + \beta) \quad (23)$$

$$m = \frac{F_2 \beta l (8\alpha - \beta) - 3F_1 \alpha^2 l}{96(\alpha + \beta)} \quad (24)$$

For the cross sections a, 2 and b the following expressions are obtained on the basis of alternating condition of plasticity (4) of the static shakedown theorem:

$$F_1 \alpha l (10\alpha + 16\beta) + 3F_2 \beta^2 l = 64M_e (\alpha + \beta) \quad (25)$$

$$3l (2\alpha^2 F_1 + \beta^2 F_2) = 32M_e (\alpha + \beta) \quad (26)$$

$$6F_1 \alpha^2 l + F_2 \beta l (8\alpha + 5\beta) = 64M_e (\alpha + \beta) \quad (27)$$

Applying the kinematic theorem, when in the first span of the beam a force of alternating character is acting, for possible failure mechanisms, the following expressions are formed:

$$8F_1 \alpha l (\alpha + \beta) + 3F_2 \beta^2 l = 48M_{pl} (\alpha + \beta) \quad (28)$$

$$3\alpha^2 l F_1 + 4F_2 \beta l (\alpha + \beta) = 24M_{pl} (\alpha + \beta) \quad (29)$$

$$F_1 \alpha l (14\alpha + 8\beta) + F_2 \beta l (8\alpha + 11\beta) = 96M_{pl} (\alpha + \beta) \quad (30)$$

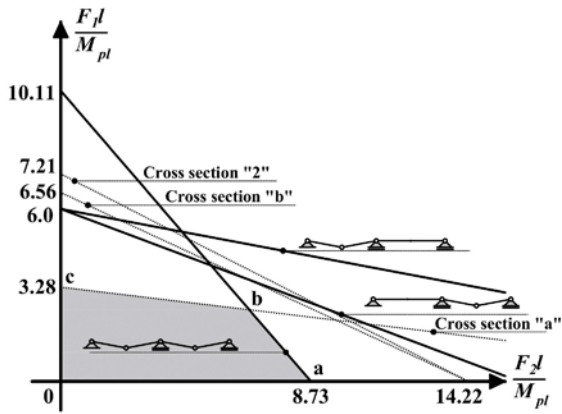


Figure 7: Interaction diagram when the force in action in the middle of the first field of alternating character

On the basis of the expressions (25), (26) (27) as well as of the expressions (28), (29), (30) the interaction diagram was constructed (Figure 7.) on which it can be observed that inside the area **0abc0** the beam is safe against the onset of failure. This area is defined by the alternating failure condition corresponding to the formation of the second field failure mechanism.

3.2. Analysis of the bearing capacity of frame structures depending on the load character and degree of static indeterminacy

Applying the adequate method depending on the character of the load, the analysis of limit bearing capacity of the frames displayed in Figure 8. was performed. The procedure of failure force calculation depending on the change of the coefficient representing the ratio of height and width of the frame  $\alpha = h/l$  was performed. Depending on the coefficient  $\alpha$  the distribution of internal forces changes, which leads to the change of failure force value.

The limit load analysis was performed using limit and shakedown theorems depending on the character of the load.

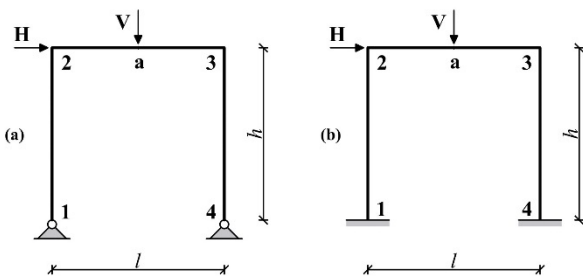


Figure 8: (a) Frame 1; (b) Frame 2.

There are two possible failure mechanisms for the frame in Figure 8a, which are displayed in Figure 9.

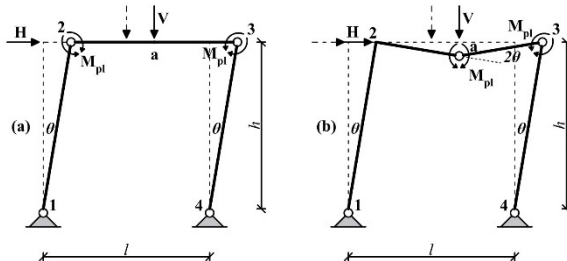


Figure 9: (a) Sway failure mechanism; (b) Combined failure mechanism.

while there are three possible mechanisms for the frame in Figure 8b, which are displayed in Figure 10.

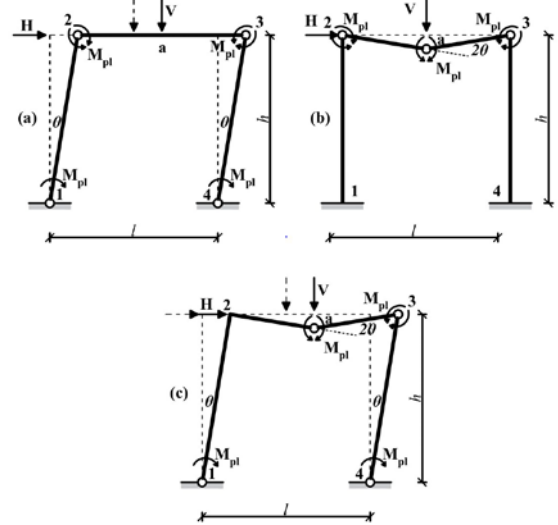


Figure 10: (a) Sway failure mechanism, (b) Beam failure mechanism, (c) Combined failure mechanism.

3.2.1. Frame 1 limit bearing capacity analysis

In case the Frame 1 is exposed to the proportionally increasing load, the failure force can be determined by some of the limit analysis theorems. For the sway failure mechanism (Figure 9a), applying kinematic theorem, the failure force is:

$$H = \frac{2M_{pl}}{h} \tag{31}$$

while for the combined failure mechanism (Figure 9b) the following expression is obtained:

$$2hH + Vl = 8M_{pl} \tag{32}$$

If Frame 1 is exposed to the action of variable repeated load acting in the range:  $0 \leq H \leq H$ ,  $0 \leq V \leq V$  failure load (incremental failure force) is determined by applying the kinematic shakedown theorem.

Elastic distribution of bending moments if only V force acts on the frame, that is, only the force H, is presented in Figure 11. The values of the elastic bending moments are shown in Table 2.

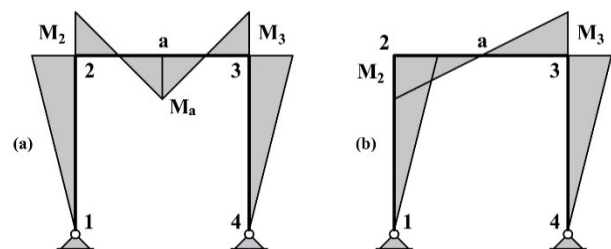


Figure 11: (a) Elastic distribution of bending moments due to V, (b) elastic distribution of bending moments due to H.

Table 2: Elastic bending moments of Frame 1

|       | V  | H              |
|-------|--|----------------|
| $M_2$ | $\frac{-3Vl}{16\alpha + 24}$             | $\frac{Hh}{2}$ |
| $M_a$ | $\frac{Vl(4\alpha + 3)}{8(2\alpha + 3)}$ | /              |

|       |                              |                |
|-------|------------------------------|----------------|
| $M_3$ | $\frac{-3Vl}{16\alpha + 24}$ | $\frac{Hh}{2}$ |
|-------|------------------------------|----------------|

On the basis of the condition that residual bending moments on the potential failure mechanisms are in equilibrium the following equations can be written:

$$m_2(\theta) + m_4(-\theta) = 0 \quad (33)$$

$$m_3(2\theta) + m_4(-2\theta) = 0 \quad (34)$$

By solving the equations (33) and (34) the following expressions are obtained:

$$3Vl + 24H\alpha l + 16Hl\alpha^2 = 16M_{pl}(3 + 2\alpha) \quad (35)$$

$$Vl + 2Hl\alpha = 8M_{pl} \quad (36)$$

In further analysis of the limit analysis of Frame 1, it is assumed that the horizontal force has alternate character ( $-H \leq H \leq H$ ), while vertical force is in the range  $0 \leq V \leq V$ . When the frame is exposed to the action of alternate load, the alternative failure force is determined applying conditions () of the static shakedown theorem.

For the cross sections 2 and 3, as well as the cross-section *a*, on the basis of alternative plasticity condition (4) of the static shakedown theorem the following equations can be written:

$$\left( \frac{Hh}{2} + \frac{3Vl}{16\alpha + 24} + \frac{Hh}{2} \right) \leq \frac{2M_{pl}}{\alpha_{form}} \quad (37)$$

$$\frac{Vl(4\alpha + 3)}{8(2\alpha + 3)} \leq \frac{2M_{pl}}{\alpha_{form}} \quad (38)$$

On the basis of conducted bearing capacity analysis depending on the load character, it is possible to perform the comparative analysis of Frame 1. When two independent load systems *H* and *V* simultaneously act on the frame, which are in the random relationship, it is possible to perform the analysis of limit bearing capacity and define the domain within the frame is safe to occurrence of failure by use of interaction diagram on whose basis connectedness of failure mechanisms and relations of load is best identified. For Frame 1, in case when  $h=l$  ( $\alpha=1$ ), the interaction diagram is presented in Figure 12. It can be concluded that for the load ratio which is defined on the basis of **ab** segment the sway failure mechanism is formed when load ratio is  $V/H \leq 1$ , while for the segment **bcdef** the load ratio is  $V/H \geq 1$  and the combined mechanism is formed.

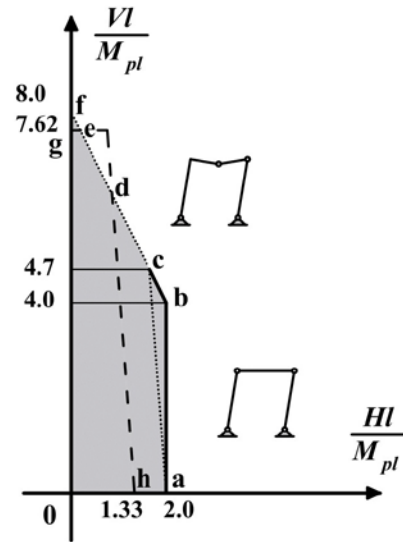


Figure 12: Interaction diagram of limit bearing capacity of Frame 1

For any ratio of load inside the **0abcdef0** area there will be no failure mechanism, therefore, no frame failure will occur when the load gradually increases. If the ratio of load is defined by some of the segments, then the failure mechanism defined by some segments, then the failure mechanism defined by the segment is formed. The frame is safe from the occurrence of failure when it is exposed to the action of variable repeated load, when the ratio of *H* and *V* load is within **0acdef0** area. When the ratio of *H* and *V* load is defined on the basis of the **cdef** segment, the combined failure mechanism occurs at the same value of limit and incremental failure force. Area **0hdeg0** is defined on the basis of the alternative failure conditions, whereby on the basis of the segments **hd** and **fg** formation of plastic hinges in the cross sections 1 and 4 is defined, while on the basis of the segment **ed** the ratio of forces bringing about combined failure mechanism is defined.

### 3.2.2. Frame 2 limit bearing capacity analysis

Depending on the load character, Frame 2 limit bearing capacity was analysed, by the analogous procedure as for Frame 1. The following limit failure forces are obtained for the possible failure mechanism displayed in Figure 10.

$$4M_{pl} = Hh \quad (39)$$

$$8M_{pl} = Vl \quad (40)$$

$$12M_{pl} = 2Hh + Vl \quad (41)$$

When a variable repeated load acts on the frame, the limit load is determined by applying the method of adaptation. If the Frame 2 is exposed to the action of a variable repeated load acting in the range:  $0 \leq H \leq H$ ,  $0 \leq V \leq V$  the failure load (incremental failure force) is determined by applying the kinematic shakedown theorem.

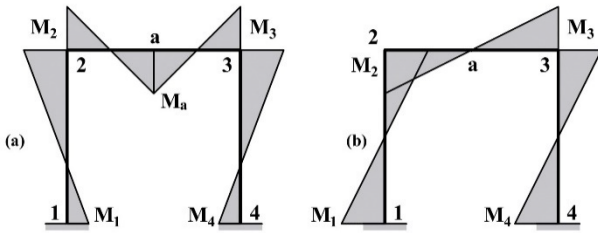


Figure 13: (a) Elastic distribution of bending moments due to V, (b) elastic distribution of bending moments due to H.

Figure 13 shows diagrams of bending moments due to each force individually, when the frame is in the elastic region. The values of the elastic bending moments are shown in Table 3.

Table 3: Elastic bending moments of Frame 2

|       | V                                | H  |
|-------|----------------------------------|--|
| $M_1$ | $\frac{Vl}{8\alpha+16}$          | $\frac{Hh}{2} \frac{3\alpha+1}{6\alpha+1}$ |
| $M_2$ | $\frac{Vl}{4\alpha+8}$           | $\frac{Hh}{2} \frac{3\alpha+1}{6\alpha+1}$ |
| $M_a$ | $\frac{Vl(\alpha+1)}{4\alpha+8}$ | /  |
| $M_3$ | $\frac{Vl}{4\alpha+8}$           | $\frac{Hh}{2} \frac{3\alpha+1}{6\alpha+1}$ |
| $M_4$ | $\frac{Vl}{8\alpha+16}$          | $\frac{Hh}{2} \frac{3\alpha+1}{6\alpha+1}$ |

Based on the procedure for determining the incremental failure force for possible failure mechanisms (Figure 10), the following equations can be written:

$$m_1(-\theta) + m_2(\theta) + m_4(-\theta) + m_5(\theta) = 0 \quad (42)$$

$$m_2(-\theta) + m_3(2\theta) + m_4(-\theta) = 0 \quad (43)$$

$$m_1(-\theta) + m_3(2\theta) + m_4(-2\theta) + m_5(\theta) = 0 \quad (44)$$

If in these equations the values of the bending moments in characteristic sections are replaced, the following equations are obtained:

$$3Vl + 16Hl\alpha + 8Hl\alpha^2 = 32M_{pl}(2 + \alpha) \quad (45)$$

$$Vl + 6Vl\alpha + 3Hl\alpha^2 = 8M_{pl}(1 + 6\alpha) \quad (46)$$

$$9Vl + 16Hl\alpha + 4Vl\alpha + 8Hl\alpha^2 = 48M_{pl}(2 + \alpha) \quad (47)$$

When determining the safe limit load, it is necessary to examine the condition of alternative plasticity (4). The following equations can be written for the observed frame for the sections 1 and 4, respectively 2 and 3, and section a:

$$\left( \frac{Vl}{8\alpha+16} + \frac{Hl}{2} \frac{3\alpha+1}{6\alpha+1} \right) \leq \frac{2M_{pl}}{\alpha_{form}} \quad (48)$$

$$\left( \frac{Vl}{4\alpha+8} + \frac{Hl}{2} \frac{3\alpha}{6\alpha+1} \right) \leq \frac{2M_{pl}}{\alpha_{form}} \quad (49)$$

$$\frac{Vl(\alpha+1)}{4\alpha+8} \leq \frac{2M_{pl}}{\alpha_{form}} \quad (50)$$

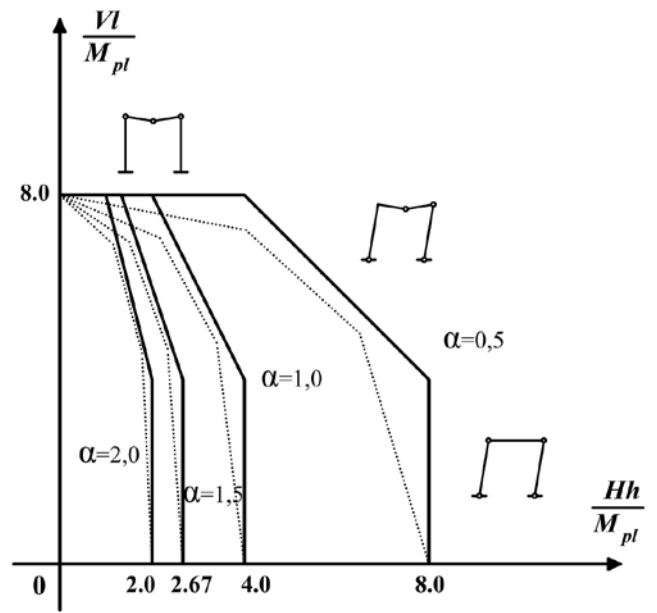


Figure 14: Interaction diagrams depending  $\alpha$

In the further analysis of the ultimate bearing capacity of Frame 2, it is assumed that the horizontal force is of alternating character ( $-H \leq H \leq H$ ), while the vertical force is in the range  $0 \leq V \leq V$ . When the girder is exposed to an alternating load, the alternative failure force is determined by applying condition (4) of the static shakedown theorem.

These conditions for the characteristic sections 1 and 4, respectively 2 and 3, and section a are:

$$\left( \frac{Vl}{8\alpha+16} + \frac{Hl}{2} \frac{3\alpha+1}{6\alpha+1} + \frac{Hl}{2} \frac{3\alpha+1}{6\alpha+1} \right) \leq \frac{2M_{pl}}{\alpha_{form}} \quad (51)$$

$$\left( \frac{Vl}{4\alpha+8} + \frac{Hl}{2} \frac{3\alpha}{6\alpha+1} + \frac{Hl}{2} \frac{3\alpha}{6\alpha+1} \right) \leq \frac{2M_{pl}}{\alpha_{form}} \quad (52)$$

$$\frac{Vl(\alpha+1)}{4\alpha+8} \leq \frac{2M_{pl}}{\alpha_{form}} \quad (53)$$

Based on the incremental failure condition for the sway and combined failure mechanism, equations of the same shape as (45) and (47) are obtained, while for the failure beam mechanism, the failure equation is obtained in the form:

$$Vl + 6Vl\alpha + 6Hl\alpha^2 = 8M_{pl}(1 + 6\alpha) \quad (54)$$

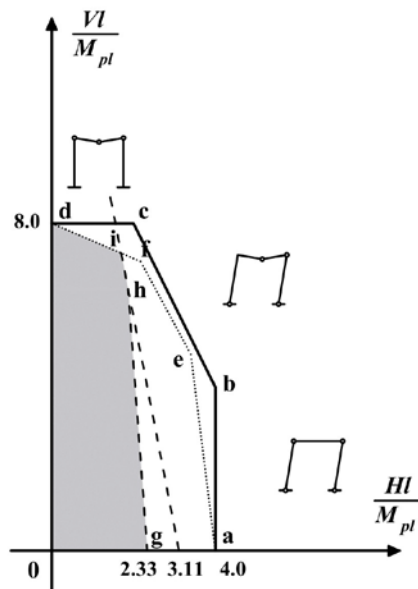


Figure 15: Interaction diagram

For Frame 2, in the case when ( $\alpha=1$ ), i.e.,  $h=1$ , the interaction diagram is shown in Figure 15. For any load ratio within the range **0abcd0**, there will be no occurrence of the failure mechanism, and thus the failure of the girder when the load gradually increases. If the load ratio is defined by one of the longer ones, then the failure mechanism that defines that length is formed. The frame is safe to failure when exposed to a variable repeated load, when the load ratio of  $H$  and  $V$  is within the range **0aefd0**. The region **0ghid0** is defined on the basis of an alternative failure condition, whereby the formation of plastic hinges in sections 1 and 4, that is in 2 and 3 is defined on the basis of lines **gh** and **hi**, while the relation of forces leading to the formation of a combined failure mechanism is defined on the basis of the line **id**.

#### 4. CONCLUSION

The analysis of the ultimate bearing capacity and the determination of the bearing capacity of linear girders depending on the character of the load can be performed by applying the limit and shakedown theorems, the basic assumptions of which are presented in the introduction to this paper. The main advantage of the methods of limit analysis based on limit and shakedown theorems is reflected in the simplicity and very fast determination of the limit load. When the limit load is determined as two-parameter one, the dependence of the load on possible failure mechanism is presented on the interaction diagram which differs from the case when the limit load is defined as one-parameter one.

Analysis of the behaviour of girders exposed to variable repeated load whose intensity lies in the previously defined range is presented on the example of the continuous beam with two spans as well as on the example of the frame girder.

Based on the performed analysis, it is possible to conclude that from the point of view of designing safe and secure structures, it is important to know the safe area shown through the interaction diagram.

#### REFERENCES

- [1] N.C. Kist, "Leidt een Sterkteberekening, die Uitgaat van de Evenredigheid van Kracht en Vormverandering, tot een goede Constructie van Ijzeren Bruggen en gebouwen", Inaugural Dissertation, Polytechnic Institute, Delft, (1917)
- [2] R. Hill., On the state of stress in a plastic rigid body at the yield point, *Phi. Mag.* Vol. 42, pp. 868-875, (1951)
- [3] D.C. Druker, W. Prager, H.J. Greenberg, „Extended limit design theorems for continuous media“ *Quart. Appl. Math.*, Vol. 9, pp. 381-392, (1952)
- [4] D.C. Druker, W. Prager, "Soil mechanics and plastic analysis for limit design", *Quart. Appl. Math.*, Vol.10, pp. 157-165, (1952)
- [5] M.R. Horne, "Fundamental propositions in the plastic theory of structures" *J. Inst. Civil Engrs*, Vol. 34, p. 174, (1950)
- [6] H.J. Greenberg, W. Prager, "On limit design of beams and frames" *Trans. Am. Soc. Civil Engrs*, 117, p. 447. (First published as Tech. Rep. A18-1, Brown Univ., 1949), (1952)
- [7] E. Melan, "Theorie Statisch Unbestimmter Tragwerke aus idealplas-tischem Baustoff" *Sitzungsberichtder Akademieder Wissenschaften (Wien) Abt. II A* 195, pp.145–195. (1938)
- [8] W.T. Koiter, "A new general theorem on shakedown of elastic-plastic structures" *Proceedings of the Koninklijke Nederlandse Akademie van Wetenschappen B.59*, pp. 24–34, (1956)
- [9] B.G. Neal, "The Plastic Methods of Structural Analysis" Chapman and Hall, 1977, London
- [10] S. Stevanović, B. Popović, D. Petković "Granična analiza konstrukcija", Građevinski fakultet Univerziteta u Nišu, Niš, (1994)
- [11] J. Heyman, "Plastic Design of Frames" Vol. 2, Cambridge University Press, Cambridge, (1971)
- [12] J. Chakrabarty "Theory of plasticity" Elsevier Butterworth-Heinemann, (2006)
- [13] J. Baker, J. Heyman, "Plastic Design of Frames" Vol 1. Fundamentals, Cambridge University Press, London (1969)
- [14] B.G. Neal, P.S. Symonds, "A method for calculating the failure load for a framed structures subjected to fluctuating load" *J.Inst.Civil Engrs*. Vol. 35 pp. 186-197 (1951)
- [15] B. Milošević, "Analiza granične nosivosti linijskih nosača primenom metode adaptacije" magistarski rad, Građevinsko-arhitektonski fakultet u Nišu, (2010)



# The Influence of Different type of aggregate, Fly ash and Fiber Reinforced Polymer on Splitting resistance in Pretensioned Concrete Railroad Ties

Adrijana Savic<sup>1\*</sup>, Robert J. Peterman<sup>2</sup>

<sup>1</sup>Department of Civil Engineering, Kansas State University, Manhattan (Kansas, USA)

<sup>2</sup>Department of Civil Engineering, Kansas State University, Manhattan (Kansas, USA)

**Keywords:** Prestressed Concrete, Fly Ash, Civil engineering, Fiber Reinforced Polymer

*This research evaluates the influence of the different types of concrete mixture, using a shallow type of indentation of wire, having the different edge distance and compressive strength of concrete on splitting resistance in pre-tensioned concrete railroad sleepers. The investigated compressive strength of concrete was 4500psi. The research was experimental, and the part of this research was formally adapted in Arema Standards for Railway Engineering Chapter 30 section 4.2.4.*

## 1. INTRODUCTION

This research is focused on longitudinal splitting which occurs in prestressed concrete members due to different variables such as concrete mixture, wire type, and release strength of concrete. The goal is to find the best possible design parameters to diminish longitudinal splitting in prestressed concrete members. Different prestressed concrete prisms were examined having different cross-sections using different concrete mixture and compressive strength. The examined wire type which will be described in this paper is denoted as "WB" wire type, which belongs to the chevron type of wire. The research which was conducted at Kansas State University used this wire type having 1in edge distance and experiments with this wire were successful without longitudinal splitting in prestressed concrete members. The influence of variables was presented in the research of Bodapati [1], Savic et al [2-6]. They investigated the influence of edge distance and wire type indentation on longitudinal splitting. According to their research, the minimum edge distance depends on the wire type and for shallow wire type, it will be 0.75in.

## 2. METHODOLOGY

### 2.1. Splitting Crack Evaluation

Three prisms having different cross-sections were cast at a time. The values of edge distances were 3/4in, 5/8in, and 1/2in. Different concrete mixes were designed so that the most effective factors were included. These factors are angularity, coarseness, the volume of coarse aggregate, class F fly ash, and w/cm ratio. In addition, 5 mixes were designed to assess the effect of transverse reinforcement on splitting cracks. The compressive strength of concrete was 4500psi for each prism and the water/cement ratio was 0.32. Adva Cast 530 was used as a water reducer.

### 2.2 WB Wire Type

WB wire Type belongs to chevron type of wires, but during this research and after all experimental investigation this wire had performance remarkably similar to wires which belong to deep chevron wire type. The physics behind this splitting is still unknown and the VOLPE center is working on a numerical approach to find the reason for such behavior. The geometry of the prestressing wire indents is a significant variable in the formation of longitudinal splitting cracks in pre-tensioned concrete members. Longitudinal splitting along prestressing tendons can result in severe splitting and complete tie failure in the field under normal train loading over time. Features of interest for each wire type are indent depth, indent volume, indent sidewall area, indent sidewall angle, indent length, indent pitch period, indent width, indent distance, and indent orientation angle. Figure 1 shows graphically the indent features of wires [2].

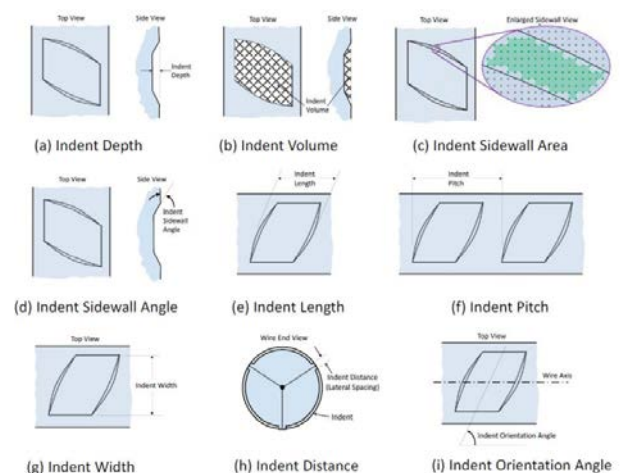


Figure 1: The indent Features of wires

Table 1: Indented wire Measurements

|    | Average depth (mm) | Edge Wall angle (degree) | Side Wall Area (mm <sup>2</sup> ) | Volume (mm <sup>3</sup> ) |
|----|--------------------|--------------------------|-----------------------------------|---------------------------|
| WB | 0.119              | 16.45                    | 2.92                              | 1.696                     |

Figure 2 presents WB Wire Type Microscope Image and 3D Model [8].



Figure 2: WB Wire Type- Microscope Image and 3D Model (8)

2.3 Sample preparation

Three prisms having different edge distances were cast at a time. The edge distance is defined as a distance from the tendon center to the edge of the prism. Four prisms were embedded into each cross-section having a common distance of 2in. Three different values of edge distances were examined 3/4in, 5/8in, and 1/2in.

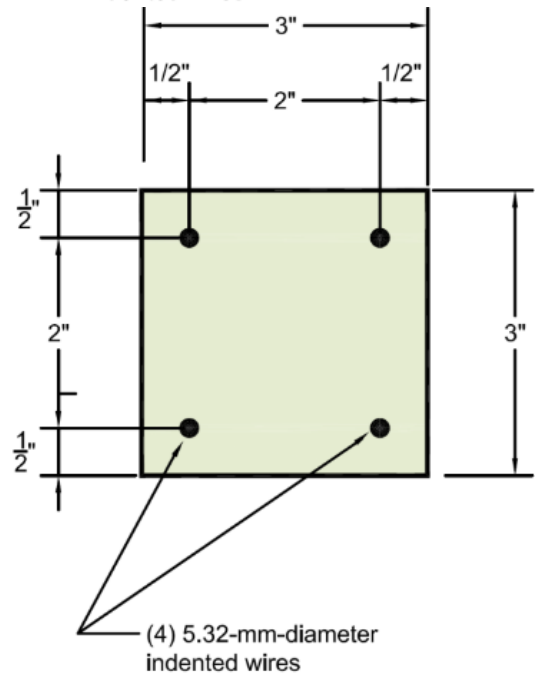
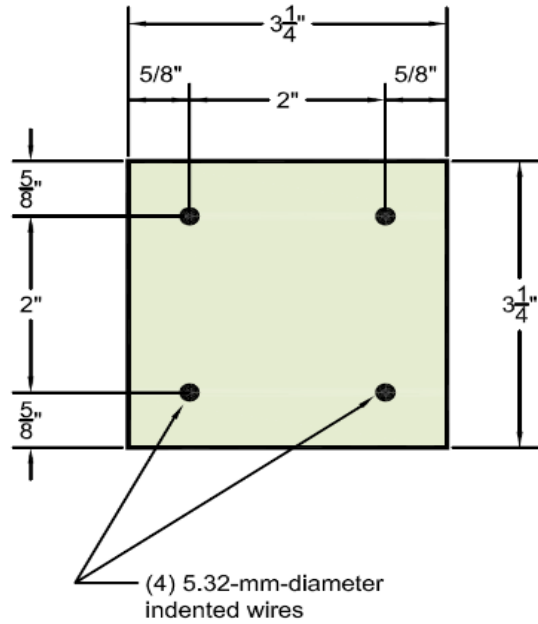
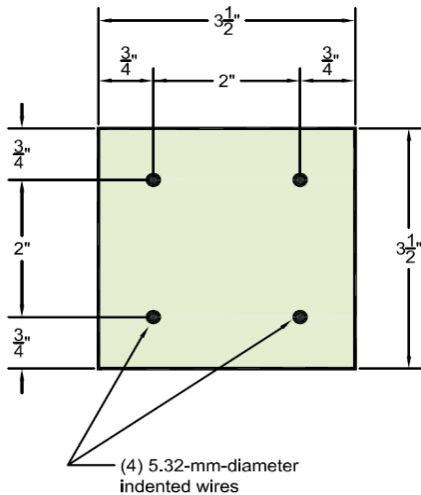


Figure 3: Cross-section of three prisms for each set of prisms

Before the casting procedure, each wire was pulled to 7000lbs. The average initial compressive stress for edge distance 3/4 in was equal to  $28000 \text{ lb.}/(3.5 \text{ in})^2 = 2285 \text{ psi}$ . For prisms with a 5/8 in edge distance, the value of stress was:  $28000 \text{ lb.}/(3.25 \text{ in})^2 = 2650 \text{ psi}$  which was 59% of the 4500-psi concrete release strength. For prisms with 1/2 in edge distance, the average initial compressive stress was it was 3110psi, which was approximately 89% of the 4500psi concrete release strength. This value is significantly into the nonlinear range of the concrete. In the pre-tensioning frame, wires within each prism were tensioned between two abutments before the casting of concrete. A jacking assembly was created at Kansas State University and used for this study. The mechanical gear jack was attached to the metal frame which allowed

gradual tensioning and release operations. Jacking of the steel prestressing wires occurred at the end of the steel frame referred to as the "Live End" as shown in Figure 4. Figure 5 shows a prestressed concrete bed with three sets of prisms having different edge distances.



Figure 4: Prestressed Jacking Arrangement at the Live End

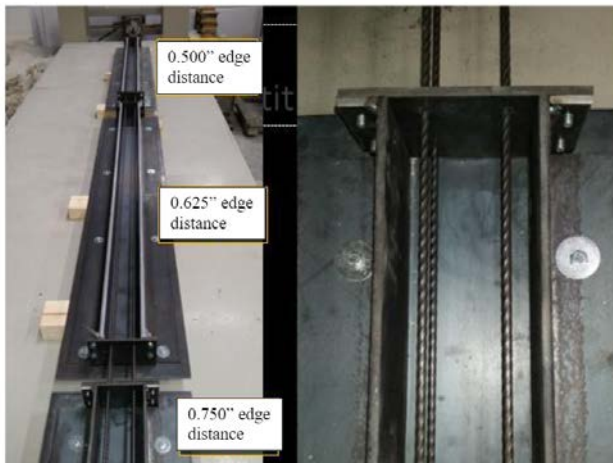


Figure 5: Prestressed Concrete Bed

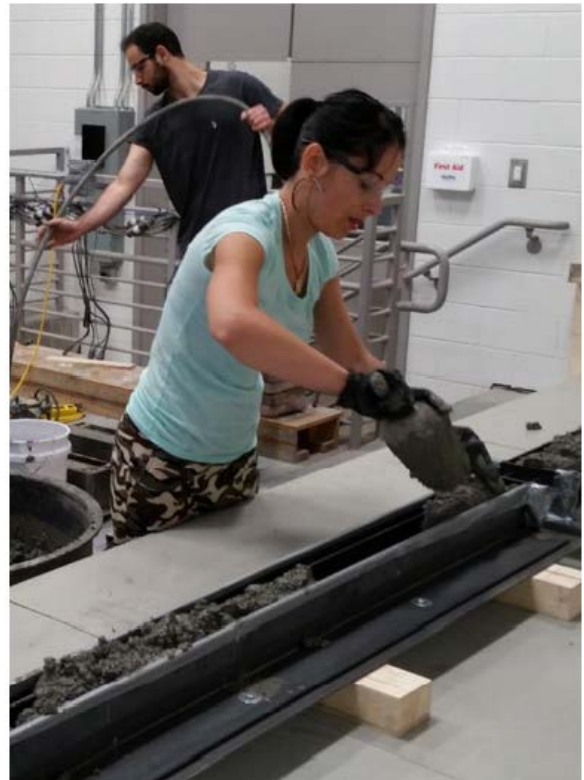


Figure 6: Casting the Prestressed Concrete Prisms

#### 2.4. Test Procedure

After casting specimens, temperature-match cured cylinders were tested at periodic intervals to determine the compressive strength. As soon as the cylinders reached 4500psi (approximately after eight hours, depending on the lab temperature), the prisms were gradually de-tensioned. For prestressed concrete railroad ties to function sufficiently in the field, and to guarantee safety, the prestressing force must be fully introduced into the railroad tie at a location well before the rail load is applied. The length needed to transfer the prestress force into the concrete member is well known as the "Transfer length". The laser-speckle device was used to scan the top surface of a concrete prism before and after de-tensioning, and automatically plot the strain profile and determine the transfer length using a least-squares algorithm [9].



Figure 7. Measuring the Transfer Lengths

Two scans are required for transfer length measurement one before de-tensioning and one after the

cutting operation after the de-tensioning procedure. The surface strain was calculated and plotted automatically after the raw images are captured.

Each prism provided two measurements of transfer lengths (live and dead-end) and provided approximately eight independent splitting tests of edge distance (four-wire cover tests on each end) for a given release strength [2].

The length and width of cracks were measured using a ruler and concrete crack comparator respectively, after 90 days. This time delay was used to evaluate long term creep behavior of splitting cracks. In some cases, the longitudinal splitting occurred immediately after the de-tensioning procedure but due to lateral sustained stresses, some cracks appeared after several weeks. All cracks were marked using a permanent red marker. For further investigations crack length for each prism was determined along with the values of Crack Areas. The crack area was defined as crack width multiplied with crack length. In the case where spalling occurred the arbitrary value of crack width was used as 2in.

3. RESULTS

3.1. WB wire type 4500psi using Crushed Gravel as aggregate.

WB wire type which belongs to the chevron type of wire was examined using different concrete mixtures to understand which variable is most important in transferring the stresses between steel and concrete. Mix#1 used Crushed Gravel as aggregate, Adva Cast 530 as High Range Water Reducer, and water/cement ratio was 0.32 for all set of prisms. Table 2 shows the concrete mix ingredients.

Table 2: Concrete Mix Design Using Crushed Gravel as Aggregate

| Material             | Weight (lbs./yd <sup>3</sup> ) |
|----------------------|--------------------------------|
| Cement               | 813.8                          |
| Water                | 260.4                          |
| Large Crushed Gravel | 897.8                          |
| Small Crushed Gravel | 538.7                          |
| Sand                 | 1436.5                         |
| Adva Cast 530        | 81 fl.oz./yd <sup>3</sup>      |

Figure 8 shows a set of prisms after the de-tensioning procedure on the dead-end of the prestressed bed (Dead end stress operations did not occur). Spalling was noticed on the prism having 1/2in edge distance.



Figure 8: Observed Cracking

Figures 9 and 10 present Crack Area and Crack Length respectively as a function of the edge distance of the prisms. With reducing the values of edge distance more cracks appeared, and crack lengths are higher.

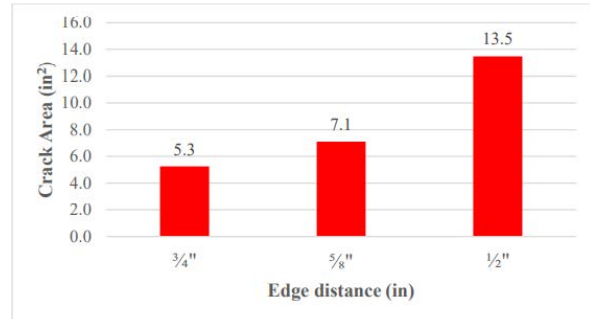


Figure 8: Crack Area (in<sup>2</sup>)

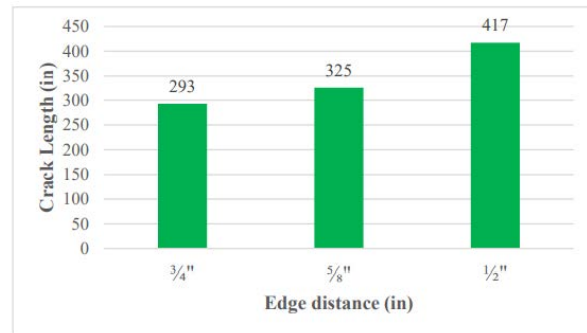


Figure 9: Crack Length

3.2. WB wire Type using Mix#2

Mix design number 2 used Granite as aggregate and Table 3 shows the mix properties.

Table 3: Concrete Mix Design Used Granite as Aggregate

| Material        | Weight Lbs/yd <sup>3</sup> |
|-----------------|----------------------------|
| Cement          | 813.8                      |
| Water           | 260.4                      |
| Crushed Granite | 1447                       |
| Sand            | 1447                       |
| Adva Cast 530   | 81 fl.oz/yd <sup>3</sup>   |

Figure 11 shows the longitudinal strain profile for the prism having 3/4 in edge distance. The values for transfer lengths are enormous. This results from the large magnitudes of longitudinal surface strain that go along with longitudinal splitting of the prism. The values of transfer lengths imply that wire type WB exhibits poor performance.

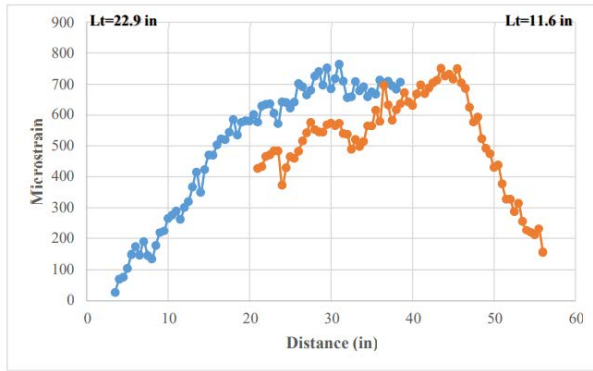


Figure 11: Longitudinal Strain Profile

The average crack width was 0.02in and the average crack length was approximately 15in.

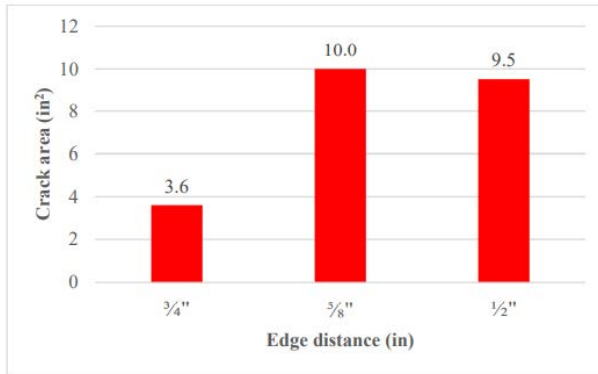


Figure 12: Crack Area

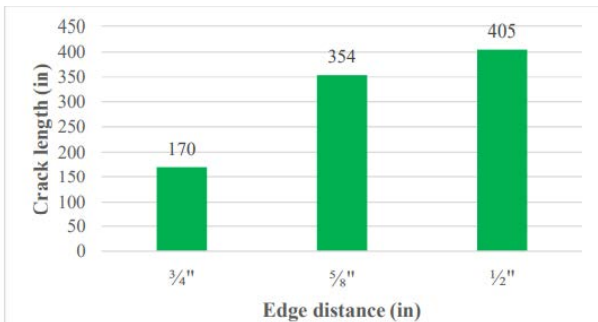


Figure 13: Crack length

According to Figures 12 and 13 WB wire type performed better using Granite in comparison to crushed gravel.

3.3. WB wire Type using Mix #3

Mix Design #3 had uncrushed local Pea Gravel and had poor performance resulting in high values of crack areas and crack lengths as shown in Figures 14 and 15.

Table 4: Concrete Mix Design #3

| Material         | Weight (lbs./yd <sup>3</sup> ) |
|------------------|--------------------------------|
| Cement           | 780                            |
| Water            | 249.6                          |
| Uncrushed Gravel | 1526                           |
| Sand             | 1526                           |
| Adva Cast 530    | 81 fl.oz/yd <sup>3</sup>       |

The maximum crack width on the live end of the prism with a 3/4in edge distance was 0.05in and the maximum crack length was 32in. On the other side, the maximum crack width was 0.04in and the maximum crack length was 27in.

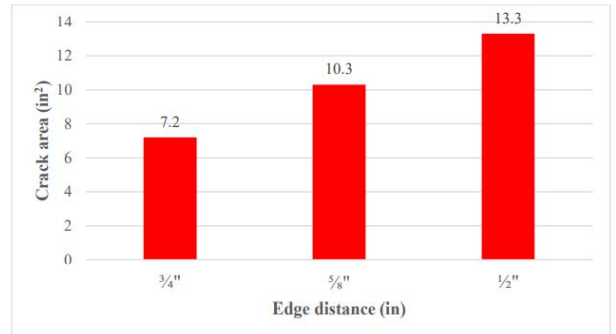


Figure 14: Crack Area

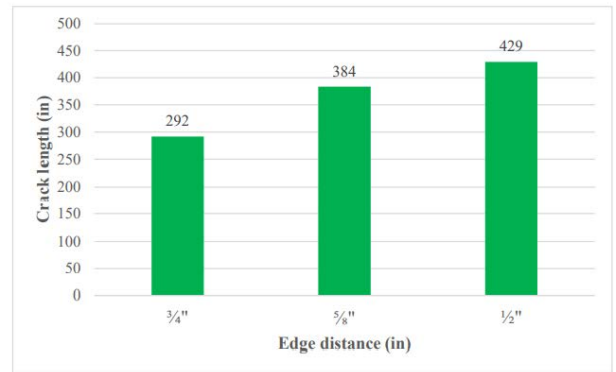


Figure 15: Crack Length

3.4. WB wire Type using Mix #4

To diminish the crack lengths and crack areas in prisms using WB wire type in Mix#1 25% fly ash replacement was added. According to the results shown in Figure 16, adding fly ash into the mixture has a slight effect on 3/4in.-edge distance prisms. Overall, the substitution of fly ash negatively affects prisms in terms of splitting cracks.

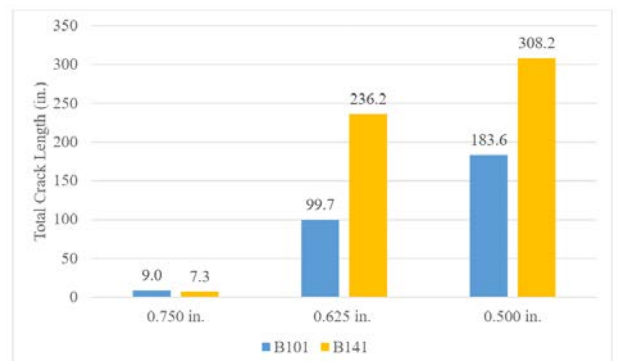


Figure 16: Crack length measurements for prisms with 0 and 25% Fly ash

### 3.5. Effect of Fiber Reinforcement

During the years of research, it was well-established that reinforcing concrete can lead to a greater crack resistance [10-11]. To improve the mechanical properties of concrete material, polymer fibers have been widely used with different percentages.

To increase the mechanical properties of the concrete a monofilament polypropylene micro-fiber was also added to the concrete of a select number of prestressed prisms. This Fiber complied with ASTM C 1116, Standard Specification for Fiber Reinforced Concrete and Shotcrete.



Figure 17: Polymer Fiber [10]

Polymer Fiber of 5% was added to Mix#3 and according to experimental investigation, it was concluded that better results were achieved. The number of detectable cracks declined by more than 30% when polymer fiber was used. However, the number of splitting cracks was reduced at 1/2-in. edge distance.

There is a significant improvement in crack propagation resistance when polymer fiber is used.

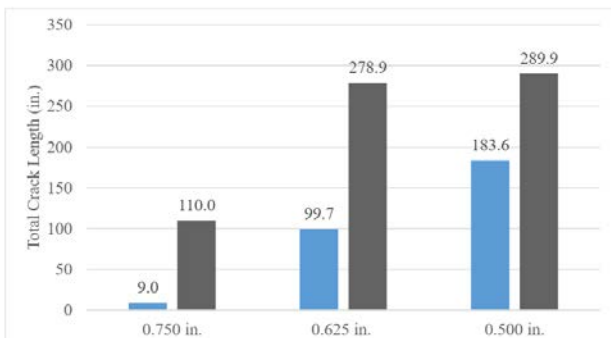


Figure 18: Crack length measurements for prisms with 0% and 5% polymer fiber

Figure 18 shows the crack length measurements using WB wire type and concrete mixture #3 with fiber polymer.

### 4. CONCLUSIONS AND RECOMMENDATIONS

Based on the results of this study, the following four primary conclusions are drawn.

- The edge distance is the most significant parameter to prevent longitudinal splitting in prestressed concrete members. According to previous research conducted at Kansas State University by Naga Bodapati, WB wire type did not split having 1in tendon edge distance.
- The second significant parameter is the wire indent characteristics. According to research conducted by A. Savic [3-5] the shallow chevron type of wires did not split on the prisms having 3/4in edge distance. The indent wire type affects the edge distance, according to all results the minimum edge distance for WB wire type and deep chevron wire types is 1.25in.
- The third important parameter which affects longitudinal splitting is a concrete mixture. Concrete mix using fiber polymer showed the best performance and increase splitting resistance. Fly ash in concrete mixture had a negative impact on splitting resistance.
- The fourth important parameter is concrete maturity at the time of the de-tensioning procedure. In this research 4500psi compressive strength was examined since that all prestressed concrete tie manufacturers de-tensioning procedure commenced at that time. Higher compressive strengths at the transfer of prestressing also correspond to a higher Modulus of Elasticity (MOE). The higher MOE causes increased lateral stresses and serve to diminish much of the benefit aspect of the increased tensile strength.

## REFERENCES

- [1] Bodapati, N. B., Peterman, R. J., Zhao, W., Wu, C.-H. J., Beck, B. T., Haynes, M., & Holste, J. (2013). Influence of Indented Wire Geometry and Concrete Parameters on the Transfer Length in Prestressed Concrete Crossties. 2013 Joint Rail Conference. Knoxville, TN: American Society of Mechanical Engineers.
- [2] Savic, Adrijana, "Developing a prism qualification test to ensure adequate splitting resistance in pretensioned concrete railroad ties" Thesis, Kansas State University
- [3] Savic, A, Beck, BT, Robertson, AA, Peterman, RJ, Clark, J, & Wu, C(. "Effects of Cover, Compressive Strength, and Wire Type on Bond Performance in Prismatic Prestressed Concrete Members." Proceedings of the 2018 Joint Rail Conference. 2018 Joint Rail Conference. Pittsburgh, Pennsylvania, USA. April 18–20, 2018. V001T01A007. ASME.  
<https://doi.org/10.1115/JRC2018-6153>
- [4] Savic, A, Beck, BT, Shafiei Dastgerdi, A, Peterman, RJ, Riding, K, & Robertson, AA. "The Effect of Wire Type on Cracking Propensity in Prestressed Concrete Prisms." Proceedings of the 2019 Joint Rail Conference. 2019 Joint Rail Conference. Snowbird, Utah, USA. April 9–12, 2019. V001T01A002. ASME.  
<https://doi.org/10.1115/JRC2019-1234>
- [5] Beck, BT, Robertson, AA, Peterman, RJ, Savic, A, Wu, CJ, Riding, KA, & Bloomfield, J. "A High Resolution Automated Prestressing Wire Indent Profiling System for Verification of Wire-Concrete Mix Compatibility." Proceedings of the 2019 Joint Rail Conference. 2019 Joint Rail Conference. Snowbird, Utah, USA. April 9–12, 2019. V001T01A009. ASME.  
<https://doi.org/10.1115/JRC2019-1269>
- [6] Shafiei Dastgerdi, A, Savic, A, Peterman, RJ, Riding, K, & Beck, BT. "Evaluation of Splitting Crack Propagation in Pre-Stressed Concrete Ties Made With Different Types of Coarse Aggregate." Proceedings of the 2019 Joint Rail Conference. 2019 Joint Rail Conference. Snowbird, Utah, USA. April 9–12, 2019. V001T01A015. ASME.  
<https://doi.org/10.1115/JRC2019-1280>
- [7] Aref Shafiei Dastgerdi, Robert J. Peterman, Adrijana Savic, Kyle Riding, B. Terry Beck, Prediction of splitting crack growth in prestressed concrete members using fracture toughness and concrete mix design" Elsevier Construction and Building Materials, 20 June 2020
- [8] Savić A, Dastgerdi AS, Beck T, Peterman RJ, Robertson A. The Influence of Concrete Cover, Type of Wire Indentation and Concrete Mix on Bond between Steel and Concrete in Prismatic Prestressed Concrete Members. AEF 2021;39:103–26.
- [9] Shafiei Dastgerdi, A, Savic, A, Peterman, RJ, Riding, K, & Beck, BT. "Evaluation of Splitting Crack Propagation in Pre-Stressed Concrete Ties Made With Different Types of Coarse Aggregate." Proceedings of the 2019 Joint Rail Conference. 2019 Joint Rail Conference. Snowbird, Utah, USA. April 9–12, 2019. V001T01A015. ASME.  
<https://doi.org/10.1115/JRC2019-1280>
- [10] Aref Shafiei, "Effect of concrete composition on splitting-cracks in prestressed concrete railroad ties: Application of fracture mechanics", Thesis, Kansas State University
- [11] Mustafa M. Raheem et al. "Development of an objective model to predict shear capacity of FRP U-wrap anchors" Composite Structures Volume 265, 1 June 2021, 113762  
<https://doi.org/10.1016/j.compstruct.2021.113762>
- [12] Shafiei, A, Riding, KA, Peterman, RJ, Christensen, C, Beck, BT, Robertson, AA, & Wu, CJ. "Suitability and Variability of Non-Destructive Testing Methods for Concrete Railroad Tie Inspection." Proceedings of the 2016 Joint Rail Conference. 2016 Joint Rail Conference. Columbia, South Carolina, USA. April 12–15, 2016. V001T01A020. ASME.  
<https://doi.org/10.1115/JRC2016-5776>



# Load-bearing Capacity and Thermal Conductivity of Axially Loaded Walls in Accordance with EC6

Iva Despotović<sup>1,2\*</sup>, Bojan Milošević<sup>1,2</sup>, Marina Nikolić – Topalović<sup>2</sup>, Vladimir Mandić<sup>1</sup>, Stefan Mihajlović<sup>1</sup>

<sup>1</sup>The Faculty of Mechanical and Civil Engineering in Kraljevo, University of Kragujevac, Serbia

<sup>2</sup>Academy of Technical and Art Applied Studies, Belgrade, Serbia

*Since 2019 the application of European technical norms of Eurocodes has been mandatory. The issue of energy efficiency of buildings, with the aim of saving energy, is more topical than ever. As for masonry structures, there is a large choice of different masonry materials on the market. By choosing the proper material, we influence both the load-bearing capacity and energy efficiency of the wall.*

*The aim of the paper is to show the method of calculating load-bearing capacity of the wall, which is connected to the slab floor of reinforced concrete at the top and bottom and is not laterally supported, depending on the chosen masonry material and binder, all according to Eurocode 6., as well as the calculation of the heat transfer coefficient, according to the policy on energy efficiency of buildings.*

**Keywords: masonry structures, load-bearing capacity, heat transfer coefficient**

## 1. INTRODUCTION

In December 2019, the implementation of European technical standards, Eurocodes 0-9, became mandatory in the territory of the Republic of Serbia, while a large number of regulations in force until then were withdrawn.

The issue of energy efficiency of buildings was brought up in order to save energy and to reduce CO<sub>2</sub> emissions into the atmosphere, which is one of the main causes of global warming. In September 2012 the Ordinance of the energy efficiency of buildings entered into force, and it prescribed in more detail energy properties and the method of calculating thermal properties of buildings, as well as energy requirements for new and old buildings.

Within this paper, load-bearing capacity of the wall, that is connected at the top and bottom with the reinforced concrete slab floor structures and is not laterally supported, was considered. Frequently used materials were used for the masonry: solid bricks, gutter blocks, as well as Porotherm blocks 25 N+F, Porotherm 25 profi and Porotherm 25-38 IZO profi blocks by professional manufacturer Wienerberger. The thickness of all walls was 25 cm, in the first three cases mortar was used as a binder and professional glue was used for blocks Porotherm 25 ptofi and Porotherm 25-38 IZO profi. In addition to the load-bearing capacity, for each type of wall, it was checked whether the value of the heat transfer coefficient, U, met the requirements of the Ordinance on energy efficiency of buildings.

## 2. THERMAL CONDUCTIVITY CALCULATION

There are three basic ways of heat transfer:

1) During heat transfer by conducting, heat is transferred from one body to another without noticeable movement of body particles, in the direction of heat flux, i.

e. from a place of higher temperature to a place of lower temperature. The condition for heat to be transferred exclusively in this way is that bodies, or part of the body, are in direct contact.

2) Heat transfer by convection occurs through the movement of individual parts of the body and under the effect of temperature differences.

3) Heat transfer by radiation is a form of heat transfer from one body to another through the movement of electromagnetic waves in the space between these two bodies (bodies are not in direct contact).

All three mentioned ways of heat transfer can take place simultaneously, but one of them is always dominant.

Heat transfer by flow (convection) is characteristic of fluids (gases and liquids). For buildings, the process in which thermal energy is transferred from the liquid to the solid and vice versa, is important. The size that characterizes the heat transfer from solid to fluid medium and vice versa, is called the heat transfer coefficient.

Through solids heat is transferred by conduction. This process essentially represents the exchange of kinetic energy. The amount of heat transferred by conducting through a flat homogeneous wall depends on the transfer surface, the coefficient of thermal conductivity, the temperature difference, the time and the thickness of the wall. The value of the thermal conductivity coefficient has been experimentally determined for all types of building materials and depends on the type and structure of the material, bulk density of the material (porosity) and moisture. The ratio of wall thickness (d) and thermal conductivity coefficient ( $\lambda$ ),  $d/\lambda$  represents the resistance to heat conduction (R). Total resistance to heat conduction ( $R_0$ ) includes both resistances at the air and wall boundaries, expressed by transition coefficients for the outer and inner side of the wall. Reciprocal value of total resistance  $R_0$  represents the heat transfer coefficient U

\*Corresponding author: Iva Despotović, Dositejeva 19, 36000 Kraljevo, [despotovic.i@mfkv.kg.ac.rs](mailto:despotovic.i@mfkv.kg.ac.rs)

whose maximum values are defined by the Ordinance on energy efficiency of buildings [1].

### 3. LOAD-BEARING CAPACITY OF WALLS EXPOSED TO VERTICAL LOADING

According to production control, masonry elements are divided into two categories. Category I wall elements are those for which the manufacturer has provided constant quality control and which, within delivery, have a defined compressive strength that does not deviate from the mean value of more than 5% (5% fractil). Category II elements are those whose average value of compressive strength is equal to the declared value, so the elements of natural stone are classified in category II. To determine the load-bearing capacity of walls, it is necessary to know the mechanical properties of masonry elements and binder material [2].

The most reliable data on the characteristic compressive strength of the wall are certainly obtained directly, experimentally, when it is necessary to use materials that are applied to a specific wall in practice, In the absence of concrete experimental results of wall compressive strength, the current legislation in the field of wall constructions, Eurocode 6, allows the characteristic wall compressive strength to be defined on the basis of the expression [3,4]:

$$f_k = K \cdot f_b^\alpha \cdot f_m^\beta \quad [\text{MPa}] \quad (1)$$

where:

$f_k$  – characteristic value of compressive strength of the masonry structure [N/mm<sup>2</sup>],

$K$  - constant that depends on the characteristic of the elements used for masonry,

$\alpha, \beta$  – constants,

$f_b$  – normalized mean value of compressive strength of masonry elements in the direction of the applied load [N/mm<sup>2</sup>],

$f_m$  – mortar compressive strength [N/mm<sup>2</sup>].

Relationship between characteristic value of the compressive strength of the masonry structure  $f_k$ , the normalized mean value of the compressive strength of masonry elements  $f_b$  and mortar strength, can be determined depending on the type of mortar used.

- for masonry construction made with the use of general purpose mortar and light aggregate mortar

$$f_k = K \cdot f_b^{0,7} \cdot f_m^{0,3} \quad (2)$$

- for masonry construction made with the use of thin-layer mortar, when the horizontal joints are 0.5 mm to 3.0 mm thick, and with the use of clay elements from group 1 and group 4, calcium silicate elements, concrete elements and autoclaved aerated concrete elements

$$f_k = K \cdot f_b^{0,85} \quad (3)$$

- for masonry construction made with the use of thin-layer mortar, when the horizontal joints are 0.5 mm to 3.0 mm, and with the use of clay elements of group 2 and group 3

$$f_k = K \cdot f_b^{0,7} \quad (4)$$

In order to adequately calculate the load-bearing capacity of elements of the masonry structure exposed to vertical load, in accordance with Eurocode 6, it is necessary to first define the effective height of the wall

and to determine the effective wall thickness. Effective (calculated) wall height should be taken as:

$$h_{ef} = \rho_n h \quad (5)$$

where:

$h_{ef}$  – effective wall height,

$h$  – effective wall height,

$\rho_n$  – reduction factor, where  $n = 2, 3$  or  $4$ , depending on the number of stiffened edges of the wall.

For the reduction factor, ( $\rho_n$ ) the following can be assumed:

- For walls at the top and at the bottom connected with reinforced concrete mezzanine structures or with roof structures that are load-bearing in both directions or with reinforced concrete mezzanine structures that are load-bearing in one direction and rely on at least 2/3 of the wall thickness, the size of the reduction factor is:

$$\rho_2 = 0,75 \quad (6)$$

- For walls connected at the top and at the bottom, stiffened only along one vertical edge (the other vertical edge is free):

when  $h \leq 3,5l$  the reduction factor is:

$$\rho_3 = \frac{1}{1 + \left[ \frac{\rho_2 h}{3l} \right]^2} \rho_2 \quad (7)$$

when  $h > 3,5l$  the reduction factor is:

$$\rho_3 = \frac{1,5l}{h} \geq 0,3 \quad (8)$$

where  $l$  is the length of the wall.

- For walls connected at the top and bottom and stiffened along the vertical edge:

when  $h \leq 1,15l$

$$\rho_4 = \frac{1}{1 + \left[ \frac{\rho_2 h}{l} \right]^2} \rho_2 \quad (9)$$

when  $h > 1,15l$  the reduction factor is:

$$\rho_4 = \frac{0,5l}{h} \quad (10)$$

Effective wall thickness ( $t_{ef}$ ) of a single wall, double wall, face wall, facade wall, wall with horizontal joints, filled two-layer wall, should be taken as the actual wall thickness  $t$ :

$$t_{ef} = \rho_t t \quad (11)$$

where:

$t_{ef}$  – effective thickness,

$t$  – wall thickness,

$\rho_t$  – stiffness coefficient.

For the calculation of masonry walls exposed to vertical load, as well as for the stability of the wall, it is important to determine the wall slenderness coefficient. The value of the slenderness coefficient of the wall exposed to

predominantly vertical load, must meet the following condition:

$$\frac{h_{ef}}{t_{ef}} \leq 27 \quad (12)$$

Calculated load-bearing capacity of the non-reinforced wall ( $N_{Rd}$ ), per unit length of single-layer wall, on the effect of vertical load, is defined on the basis of the expression:

$$N_{Rd} = \frac{\Phi_{i,m} \cdot t \cdot f_k}{\gamma_M} = \Phi_{i,m} \cdot t \cdot f_d \quad (13)$$

where:

$\Phi_{i,m}$  – load reduction coefficient ( $\Phi_i$  and/or  $\Phi_m$ ) which takes into account the effect of slenderness and load eccentricity,

$\gamma_M$  – partial safety factor for the material.

Based on Eurocode 6, for the ultimate limit state, partial safety coefficients are defined, depending on the material properties. The value of the partial safety factor depends on the masonry category, A, B and C. Thus, category A includes facilities that are under constant supervision and quality control during construction, carried out by the supervisory authority, category B includes periodic supervision and control, while category C includes facilities that are built without a supervisory body and the only control is carried out by the construction contractor.

Table 1: Partial safety coefficients for material properties (EC 1)

| $\gamma_M$ |                           | category of control during constructions | category of control during constructions |     |     |
|------------|---------------------------|--|--|-----|-----|
|            |                           |  | A  | B   | C   |
| wall       | category of wall elements | I  | 1,7                                      | 2,2 | 2,7 |
|            | production control        | II                                       | 2,0                                      | 2,5 | 3,0 |

Value of the buckling coefficient which takes into account slenderness and eccentricity is based on a stress diagram of rectangular shape and at the top and bottom of the wall ( $\Phi_i$ ), is obtained on the basis of the expression:

$$\Phi_i = 1 - 2 \frac{e_i}{t} \quad (14)$$

where:

$e_i$  – eccentricity at the top or bottom of the wall, depending on the case under consideration, calculated on the basis of the expression:

$$e_i = \frac{M_{id}}{N_{id}} + e_{he} + e_{init} \geq 0,05t \quad (15)$$

$M_{id}$  – calculated value of the bending moment at the top or bottom of the wall, which is the result of the vertical load eccentricity from the mezzanine structure on its support,

$N_{id}$  – calculated value of the vertical load at the top or bottom of the wall,

$e_{he}$  – eccentricity at the top or bottom of the wall due to the action of a horizontal load (wind), if any,

$e_{init}$  – initial eccentricity with a sign that increases the absolute value  $e$ ; (the initial eccentricity must be adopted along the entire height of the wall, in order to take into account the imperfections when performing, adopted as  $h_{ef}/450$ ).

Value of the buckling coefficient which takes into account slenderness and eccentricity in the middle height of the wall ( $\Phi_m$ ), can be determined using  $e_{mk}$ , where:

$$e_{mk} = e_m + e_k \geq 0,05t \quad (16)$$

where:

$$e_m = \frac{M_{md}}{N_{md}} + e_{hm} + e_{init} \quad (17)$$

$e_m$  – eccentricity due to load-bearing,

$M_{md}$  – calculated value of the maximum bending moment in the middle of the wall height, which is the result of the moment at the top and bottom of the wall, including any load eccentricity placed in relation to the face of the wall (e. g. holders),

$N_{md}$  – calculated value of the vertical load in the middle of the wall height, including any load eccentricity placed in relation to the face of the wall,

$e_{hm}$  – eccentricity in the middle of the wall height due to the action of a horizontal load (e. g. wind) if any, (the inclusion of member  $e_{hm}$  depends on the combination of loads used for verification, where it is necessary to take it with the appropriate sign in relation to  $M_{md}/N_{md}$ ),

$e_{init}$  – initial eccentricity which means the increase of the absolute value  $e_m$ ,

$e_k$  – eccentricity due to flow is determined on the basis of the expression:

$$e_k = 0,002\phi_\infty \frac{h_{ef}}{t_{ef}} \sqrt{t \cdot e_m} \quad (18)$$

$\phi_\infty$  - final value of the flow coefficient.

Eccentricity due to creeping has a value of zero for all walls made of baked clay or natural stone and for all walls of other masonry elements with a slenderness of up to 15.

## 4. EXAMPLES OF WALLS

### 4.1. Material Properties

For the purposes of this paper, from masonry elements offered on the market, the elements of the following groups were used [5]:

- elements of baked clay: bricks, blocks (EN 771-1) whose durability is achieved by firing shaped element of raw clay at high temperatures,
- elements are of the second group, except the brick which is of the first group,
- all elements are of the first category,
- depending on the masonry element, suitable binders were used: general purpose mortar brand 10 and appropriate adhesives (Table 2).

#### 4.2. Wall Thermal Conductivity Calculation

Table 3 shows values of total resistance  $R_u$  and heat transfer coefficient  $U$  for walls of different materials and cases when the wall is in a heated or unheated space.  $U_{max}$

is the maximum allowable value of the heat transfer coefficient, defined by the Ordinance on energy efficiency of buildings for old and newly constructed facilities.

Table 2: Characteristics of masonry elements

| Masonry element           | Dimensions  | Medium compressive strength | Applied binder | $\lambda$ |
|---------------------------|-------------|-----------------------------|----------------|-----------|
| Brick                     | 250/120/65  | 10                          | M 10           | 0,76      |
| Gutter                    | 250/190/190 | 10                          | M 10           | 0,52      |
| Porotherm 25N+F           | 375/250/238 | 10                          | M 10           | 0,26      |
| Porotherm 25 Profi        | 375/250/249 | 10                          | glue           | 0,143     |
| Porotherm 25-38 IZO Profi | 375/250/249 | 12,5                        | glue           | 0,072     |

Table 3: Thermal conductivity parameters

|                           | Wall towards an unheated space |       |           | Wall in a heated space |       |           |
|---------------------------|--------------------------------|-------|-----------|------------------------|-------|-----------|
|                           | $R_u$                          | $U$   | $U_{max}$ | $R_u$                  | $U$   | $U_{max}$ |
| Brick M10                 | 0,610                          | 1,64  | 0,55/0,40 | 0,56                   | 1,786 | 0,90/0,90 |
| Gutter M10                | 0,762                          | 1,312 | 0,55/0,40 | 0,712                  | 1,404 | 0,90/0,90 |
| Porotherm 25 N+F          | 1,242                          | 0,80  | 0,55/0,40 | 1,192                  | 0,839 | 0,90/0,90 |
| Porotherm 25 Profi        | 2,030                          | 0,49  | 0,55/0,40 | 1,980                  | 0,505 | 0,90/0,90 |
| Porotherm 25-38 IZO Profi | 3,754                          | 0,266 | 0,55/0,40 | 3,704                  | 0,270 | 0,90/0,90 |

#### 4.3. Calculation of the Load-bearing Capacity of the Wall Exposed to Vertical Load

Depending on the dimensions of the applied masonry elements, based on EC 6, the shape coefficient of the wall element is defined, while depending on the group of applied elements and the binder, the characteristic compressive strength of the wall is defined (Figure 1, Table 4), [6]:

Table 4: Shape coefficient and characteristic wall compressive strength

| Masonry element           | Shape coefficient | Characteristic compressive strength |
|---------------------------|-------------------|-------------------------------------|
| Brick                     | 0,81              | 3,88                                |
| Gutter                    | 1,14              | 4,93                                |
| Porotherm 25N+F           | 1,138             | 4,93                                |
| Porotherm 25 Profi        | 1,149             | 3,86                                |
| Porotherm 25-38 IZO Profi | 1,149             | 4,52                                |

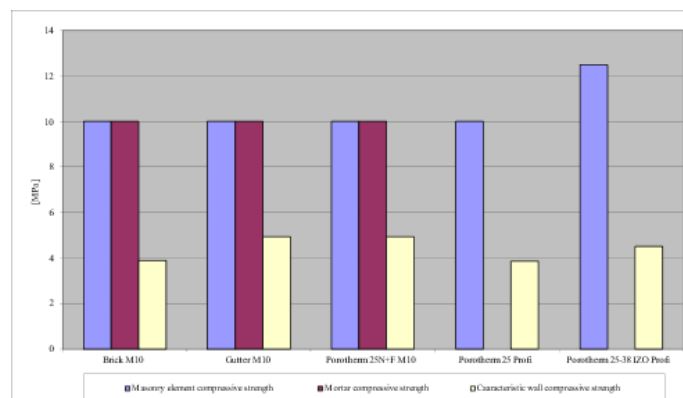


Figure 1: Mechanical properties of the masonry element, applied binder and wall

Within this paper, the load-bearing capacity of a wall that is connected at the top and bottom with slab floor structures of reinforced concrete and is not laterally supported, was considered. For a wall height of 2.75 m the initial eccentricity is less than the minimum eccentricity value of 1.25 cm so that for the calculation of load-bearing capacity in the bottom and middle of the wall, the minimum value of initial eccentricity is adopted.

Calculated load-bearing capacity of a non-reinforced wall per unit length of a single-layer wall, under the effect of vertical load, is defined in the bottom and middle of the wall, for elements of the first group and the partial safety factor for material properties depends on masonry category, A, B or C (Figure 2,3)

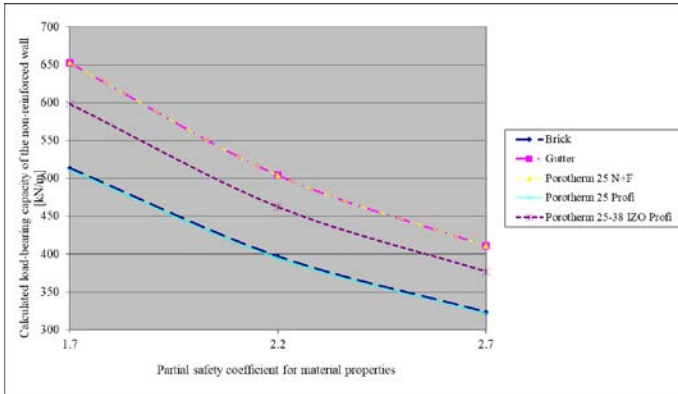


Figure 2: Calculated load-bearing capacity at the bottom of the wall as a function of the safety coefficient for material properties

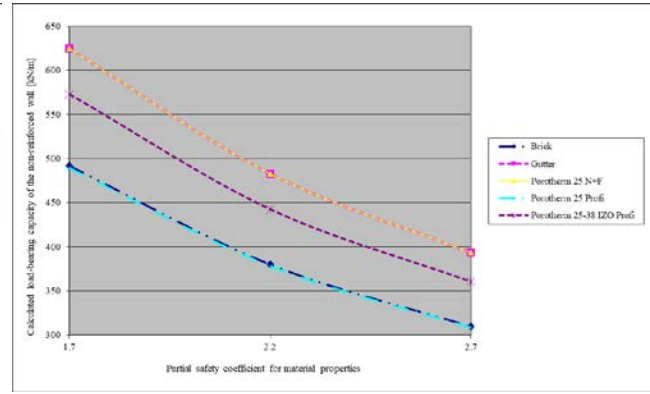


Figure 3: Calculated load-bearing capacity in the middle of the wall height as a function of the safety coefficient for material purposes

Table 5: Calculated load-bearing capacity of the wall in the bottom and middle of the wall

|                            |     |                    | Brick M10 | Gutter M10 | Porotherm 25 N+F | Porotherm 25 Profi | Porotherm 25-38 IZO Profi |
|----------------------------|-----|--------------------|-----------|------------|------------------|--------------------|---------------------------|
| Partial safety coefficient | 1,7 | Bottom of the wall | 513,52    | 652,5      | 652,5            | 510,88             | 598,28                    |
|                            |     | Middle of the wall | 491,58    | 624,62     | 624,62           | 489,05             | 572,67                    |
|                            | 2,2 | Bottom of the wall | 396,81    | 504,2      | 504,2            | 394,77             | 462,27                    |
|                            |     | Middle of the wall | 379,86    | 482,66     | 482,66           | 377,90             | 442,52                    |
|                            | 2,7 | Bottom of the wall | 323,33    | 410,83     | 410,83           | 321,67             | 376,67                    |
|                            |     | Middle of the wall | 309,51    | 393,28     | 393,28           | 307,92             | 360,57                    |

### 5. RESULT ANALYSIS

Heat transfer coefficient calculation shows that in the case of a wall in an unheated space, the requirements of the Ordinance on the energy efficiency of buildings are met by walls built with Porotherm 25 Profi and Porotherm 25-38 IZO Profi blocks. In the case of a wall in a heated space, the requirement of the Ordinance ( $U_{max} = 0.90/0.90$ ) is met by walls built with Porotherm 25 N+F, Porotherm 25 Profi and Porotherm 25-38 IZO Profi blocks. In both cases, walls built of bricks and Gutter blocks without insulation, do not meet the requirements of the Ordinance.

Based on the conducted analysis, it was concluded that the highest calculated load bearing capacity had the wall made of masonry elements Gutter block and Porotherm 25 N+F, where masonry was done with mortar grade 10, while the wall of Porotherm 25-38 IZO Profi elements where masonry was done with glue, had a slightly lower load-bearing capacity. Although Porotherm 25-38 IZO Profi had a higher initial mean value of compressive strength of the masonry element, due to the use of glue, its characteristic compressive strength changed and therefore the calculated load-bearing capacity of the wall was lower (Figure 4).

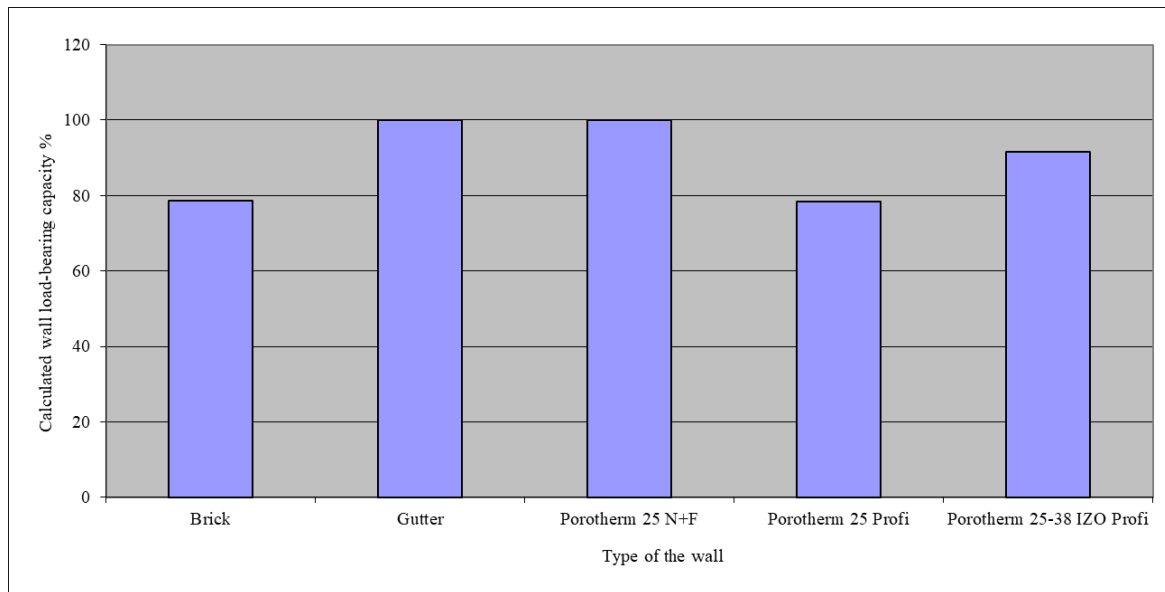


Figure 4: Ratio of the calculated wall load-bearing capacity to the applied masonry element

Compared to a wall made of Gutter blocks and of Porotherm 25 N+F blocks, a wall made of Porotherm 25-38 IZO Profi elements has a lower load bearing capacity by 9%, while a wall made of bricks and Porotherm 25 Profi elements has a 22% lower load bearing capacity. When the wall is one-sided or two-sided, the reduction factor changes depending on the number of stiffened edges of the wall, as follows:

- when the wall is one-sided, its length must be within  $1,0 \leq l \leq 3,8$
- when the wall is double-sided, its length must be within  $2,30 \leq l \leq 11,25$ .

## 6. CONCLUSION

Choice of masonry material significantly affects the wall physical and mechanical properties. Considering that the issue of energy efficiency of buildings is very topical, it is necessary to check the parameters of thermal conductivity, all according to the Ordinance on energy efficiency of buildings, in order to apply appropriate insulation and reduce heat loss. Load-bearing analysis, conducted in all respects according to Eurocode 6, shows a variation of up to 20%, depending on the applied masonry element and binder.

## REFERENCES

- [1] Pravilnik o energetskej efikasnosti zgrada, Službeni glasnik RS, br.61/2011, Beograd, (2011)
- [2] Z. Sorić, „Zidane konstrukcije I, Hrvatski savez građevinskih inženjera“, Zagreb, (1999)
- [3] SRPS EN 1996-2, Evrokod 6 – Projektovanje zidanih konstrukcija – Deo 2: Razmatranje tokom projektovanja, izbor materijala i izvođenje zidanih konstrukcija, Institut za standardizaciju Srbije, 2016
- [4] SRPS EN 1996-1-1, Evrokod 6 – Projektovanje zidanih konstrukcija – Deo 1-1: Opšta pravila za armirane i nearmirane konstrukcije, Institut za standardizaciju Srbije, 2016
- [5] B. Milošević, „Zbirka rešenih zadataka iz zidanih konstrukcija prema Evrokodu 6“, Visoka građevinsko-geodetska škola strukovnih studija, Beograd, (2019)
- [6] M. Muravljev, B. Stevanović, „Zidane i drvene konstrukcije zgrada“, Građevinski fakultet Univerziteta u Beogradu, Beograd, (2003)

## Analysis of cost and time required for the construction of RC diaphragms depending on the method of execution

Stefan Mihajlović<sup>1\*</sup>, Saša Marinković<sup>1</sup>, Vladimir Mandić<sup>1</sup>, Iva Despotović<sup>1</sup>, Marijana Jančićević<sup>1</sup>

<sup>1</sup>Faculty of Mechanical and Civil Engineering, University of Kragujevac, Kraljevo (Republic of Serbia)

*Load in deep massive foundations is transferred to the substrate through surface elements called the diaphragms. For the last ten years, reinforced concrete diaphragms has been used as a deep foundation cover in a pit for underground levels of buildings in urban areas. On an example of a multi-storey building with a basement level in urban environment, construction of monolithic reinforced concrete diaphragms is planned in several phases. Analysis was conducted of cost and time required to construct two different variants of diaphragms for the purpose of obtaining an optimal construction method. The first variant is with construction of every second lamella (even and odd) and the second variant is with construction of every third lamella. Due to the proximity of surrounding buildings and impossibility of making a wide excavation, analysed reinforced concrete diaphragms are used as protection of the pit for the foundation slab, and at the same time as the walls of the basement level.*

**Keywords:** reinforced concrete diaphragm, construction cost analysis, construction machinery

### 1. INTRODUCTION

In the last ten years, there has been a need for construction of residential and commercial buildings in urban areas. Due to deficiency location for building, the future building is most often constructed in a small area that is bordered by the adjacent buildings. For the area planned for the construction of the facility to be used to the maximum, it is planned to build basements. Deep massive foundations which are used to protect the vertical excavations of the basement level and to transfer the load to the deeper layers of the soil of higher bearing capacity are reinforced surface elements called the diaphragms.

In addition to diaphragms, deep founding is also made up of foundations that are built in deep supported excavations or foundations that are built with walls and caissons. The characteristic of a deep foundation is that the foundations transfer loads over the overlying horizontal surface to deeper soil layers that have less compressibility and higher bearing capacity.

The beginning of the use of reinforced concrete diaphragms (RC diaphragms) is related to the sixties of the last century, and for the needs of building construction in urban environment, can see the rapid development [1] and improvement both in the design phase and in technologies and methods of execution. RC diaphragms are used if it is not possible to perform a wide excavation due to the nearness of the adjacent building. Wide excavation is excavation with sides at an angle that provides slope stability [2], which is a characteristic in cases when the building is built in urban areas. Excavations for deep foundation pits, which are most often used for basement level, are mostly performed in complex geotechnical conditions with a high groundwater level. Complex geotechnical conditions include the foundation on gravelly, sandy, and dusty-clay soils with a high level of groundwater [3]. In these conditions, before the appearance of the RC diaphragm, the foundation was performed using caisson,

wells and piles, which are methods with a more complex procedure of execution and design. These problems at the deep foundation are effectively solved by using a RC diaphragm. The use of RC diaphragms avoids wide excavations and expansion, whereby these surface elements protect the foundation pit from collapsing the surrounding soil. In addition to this form of application, which is the most common, diaphragms can also be used to solve a variety of problems, as load-bearing elements of engineering structures, as supporting structures on roads, as antifiltration curtains under hydraulic structures, as elements in specific drainages, for waterproof cores embankment bodies, etc. The appearance of the RC diaphragm build from the segments is given in Figure 1.

RC diaphragms are made in several phases. It is first necessary to protect the parts around the diaphragm (on both sides of the diaphragm) during excavation from soil collapse, which is most often performed using a special solution of high-value clay - bentonite in water, the so-called clay suspensions as shown in Figure 2 and Figure 3. This special solution of high-value clay is used during excavation as a protection deep slit in which the reinforcement is put down after excavation (if the projected diaphragm is from reinforced concrete), which is shown in Figure 4. After putting down the reinforcement, this deep slit is filled with concrete while extruding the solution of high-value clay, forming a surface element - the RC diaphragm.

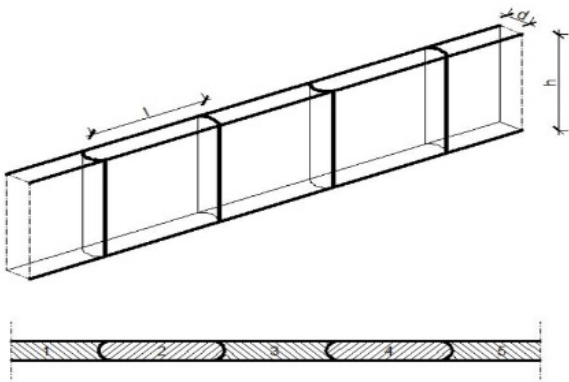


Figure 1: The appearance of the segments that form the RC diaphragm



Figure 2: Excavation of the diaphragm trench



Figure 3: Excavation of the diaphragm trench



Figure 4: Installation of a reinforcing skeleton in a trench of a RC diaphragm

## 2. TECHNICAL CHARACTERISTICS OF THE BUILDING AND RC DIAPHRAGMS

Reinforced concrete diaphragms are used in multi-storey buildings during construction to protect foundation pits, and later during the exploitation of the building in the function of deep foundations, they transfer loads from the structure to the soil layers of higher load capacity. The construction of a multi-storey building is planned in an urban environment, with neighbouring buildings in the immediate vicinity on both sides of the future building, and on the remaining two sides is the road, as shown in Figure 5.

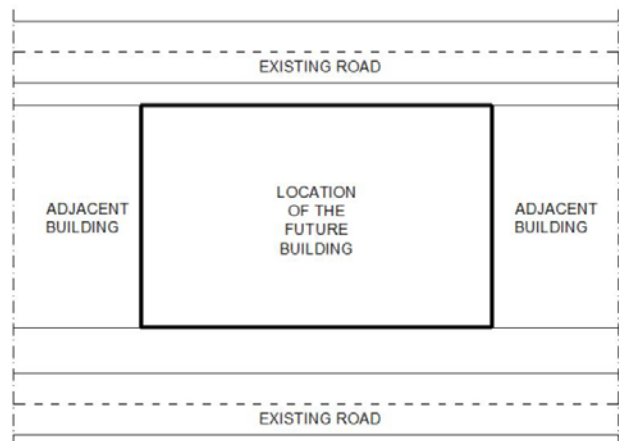


Figure 5: Location of the future building

Since the geotechnical study determined that the soil at the location of the building is sandy and gravelly with a certain content clay with low load capacity, it is necessary to foundation the building using foundation slabs. Due to the proximity of surrounding buildings and impossibility of making a wide excavation, analysed RC diaphragms are used as protection of the pit for the foundation slab, and at the same time as the walls of the basement level. On an example of a multi-storey building with a basement level in

urban environment, construction of monolithic RC diaphragms is planned in several phases. Analysis was conducted of cost and time required to construct two different variants of diaphragms for the purpose of obtaining an optimal construction method. The first variant is with construction of every second lamella (even and odd) and the second variant is with construction of every third lamella. For both variants, the construction phases and the analysis of the time required are described for the building of RC diaphragms. The first phase includes preparatory work, followed by the work necessary to make the diaphragm trench. When the excavation of the trench is completed, it is necessary to form a reinforcing skeleton which is embedded in the trench of a certain thickness, and then is performed concreting by a special procedure. Since the monolithic RC diaphragm is built from segments - lamellas, it is necessary to perform the RC connecting beam whose role is to connect all segments of the diaphragm into one whole.

2.1. Technical description of a multi-storey building

For the needs of collective housing, a residential and business building has been designed and its construction is planned. The building is planned to be a reinforced concrete multi-storey building consisting of a basement level, ground level, and six floors, which is shown in Figure 6.

According to the architectural project, it is planned to use the basement level for auxiliary and common rooms, the ground level with 11 shops as business space, and the floors for housing. The building has a rectangular base with dimension 18.5x29.5m. On the characteristic floor level, there are five apartments of different sizes. A solution in the form of a flat impassable roof is planned for the roof construction of the building.

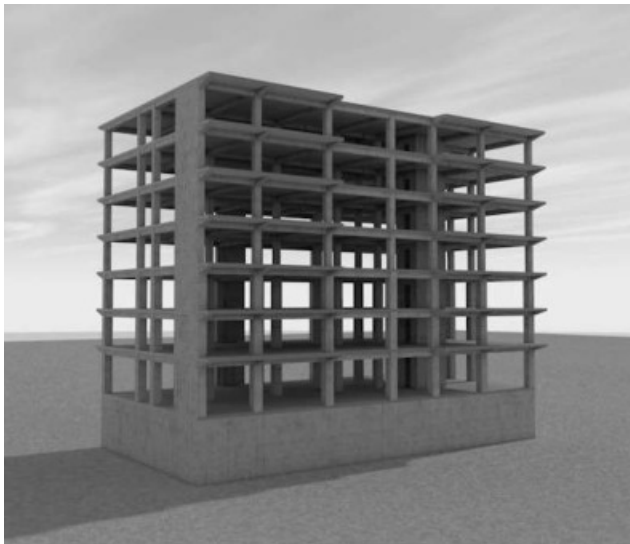


Figure 6: Appearance future building

The load is transferred from the roof over the floor to the soil across a foundation slab thick 80cm [4], whose strength increased is with reinforced concrete beams.

The analysis of all relevant loads that affect the construction and dimensioning of characteristic reinforced concrete elements was done according to European standards - Eurocodes.

2.2. Characteristics of soil and technical characteristic of diaphragm

The data obtained by geotechnical research performed at a given location show that the soil is sandy and gravelly with a certain percentage of clay [5]. The sand and gravel has a characteristic weight density  $\gamma=17\text{KN/m}^3$ , effective cohesion  $c=5\text{KPa}$  and angle of shearing resistance  $\varphi=32^\circ$ . Soil with that characteristics is to the depth of 3.2m, which was determined by geotechnical research. The soil at a depth of more than 3.2m has better characteristics and higher load capacity. According to the geotechnical report, the groundwater level is at a depth of 4.2m measured from the terrain surface, which does not affect the building of reinforced concrete diaphragms and structures.

The load is mostly transferred across line elements - columns of cross-sectional dimensions 60/60cm from higher to lower floors. Then the load is transferred across columns to a foundation slab thick 80cm which is building in underground level on soil lower load capacity. The primary role of RC diaphragms is to protect the pit for the foundation slab during the construction of the basement level, then they are used for the transfer load to the layers of soil better characteristics during the exploitation of the building.

Cantilever RC diaphragms are used to protect the foundation pit because the building of anchored RC diaphragms is impossible due to the proximity of the adjacent buildings [6]. The necessary length [7] of the cantilever part RC diaphragm is calculated using (1), for the soil of the described characteristics and the height of the basement level which amounts to  $H_c=2.6\text{m}$ , the necessary length  $h$  of the cantilever part RC diaphragm must be greater than 1.088m.

$$h \geq H_c - \frac{2 \cdot c_r}{\gamma_1} \cdot \left(1 + \frac{\pi}{2}\right) \quad (1)$$

According to (1) is being adopted length  $h$  of the cantilever part RC diaphragm of 1.2m. The total height of the 0.6m thick RC diaphragm is 3.8m. The dimensions of the RC diaphragm and the position when the diaphragm to build from the segments - lamellas are shown in Figure 7.

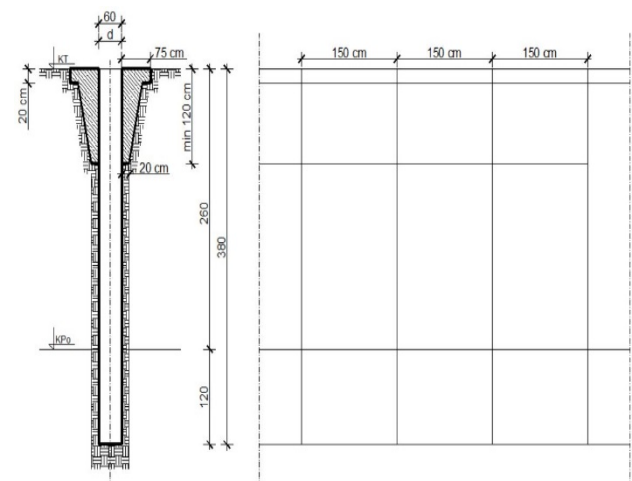


Figure 7: Dimensions of reinforced concrete diaphragm

The RC diaphragm is built of segments - lamellas to prevent changes in the equilibrium state in the soil [8]. A change in the equilibrium state in the soil can cause a loss of stability to the adjacent building. In the following, the times necessary to building the RC diaphragm are

considered for two variants: the first variant is with the construction of every second lamella (even and odd) and the second variant is with the construction of every third lamella. In both cases, the wall of the pit for the foundation slab consists of 66 lamellas of different widths.

The longer side of the diaphragm wall consists of 20 lamellas, of which the initial and final ones are 155 cm long, and the others are 150cm long. The shorter side consists of 13 lamellas, with the initial and final ones being 160cm long and the others 150cm long. The RC diaphragms are reinforced with ribbed reinforcement B500B in the vertical direction with bars with a diameter of 14mm at a distance of 10cm and the horizontal direction with bars with a diameter of 12mm at a distance of 20cm. Concreting is performed with concrete class C30/37. The division of the walls in the basement level into segments of the RC diaphragm is given in Figure 8.

Except concrete class C30/37, reinforcing skeletons are used to building diaphragms, which consist of vertical bars  $\varnothing 14/10\text{cm}$  and horizontal bars  $\varnothing 12/20\text{cm}$  of reinforcement B500B. The necessary reinforcement on the construction site arrives in the form of bars 12.0m long and of a determined diameter.

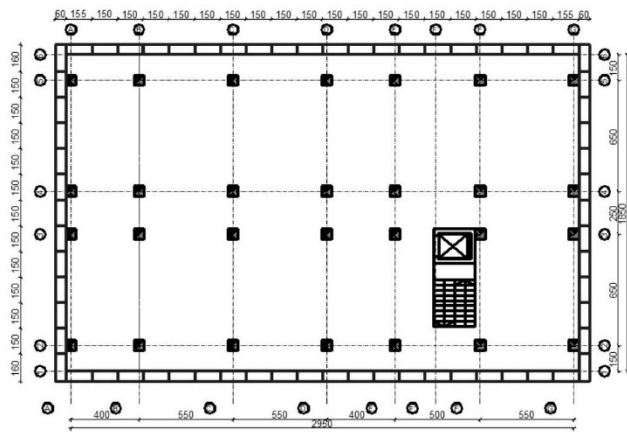


Figure 8: Partition of the diaphragm into segments - lamellas

On the construction site, the bars are cut and cambered, after which the workers form the skeleton. The reinforced concrete connecting beam that connects the segments into one whole in the upper zone is a dimension  $b/d=60/60\text{cm}$ . The beam is reinforced in the upper zone with 3 reinforcing bars with a diameter of  $\varnothing 16\text{mm}$ , in the lower zone with 7 reinforcing bars with a diameter of  $\varnothing 16\text{mm}$ , one bar with a diameter of  $\varnothing 12\text{mm}$  is adopted on both sides as constructive reinforcement and stirrups with a diameter of  $\varnothing 10/15\text{cm}$  along the entire length of the beam. Plans reinforcement diaphragm is given in Figure 9, plans reinforcement connecting beam is shown in Figure 10.

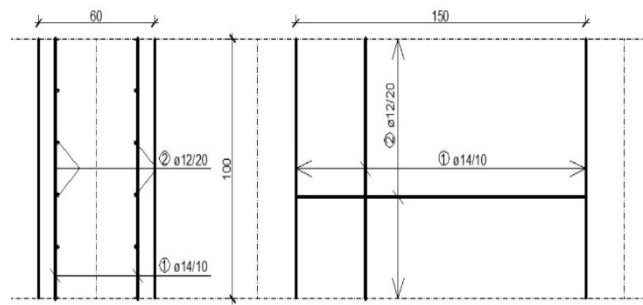


Figure 9: Diaphragm segment reinforcement plan

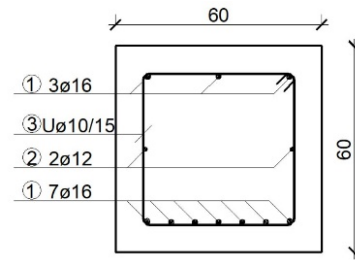


Figure 10: Connecting beam reinforcement plan

2.3. Phases of execution of reinforced concrete diaphragms when the building of every second lamella

Phases building of reinforced concrete diaphragms are: construction site preparation, earthworks of lamellas marked with number 1, reinforcement works of lamellas marked with number 1, concreting works of lamellas marked with number 1, earthworks of lamellas marked with number 2, reinforcement works of lamellas marked with number 2, concreting works of lamellas marked with number 2, finishing concrete works, in Table 4 numbered 1-8.

2.4. Phases of execution of reinforced concrete diaphragms when the building of every third lamella

Phases building of reinforced concrete diaphragms are: construction site preparation, earthworks of lamellas marked with number 1, reinforcement works of lamellas marked with number 1, concreting works of lamellas marked with number 1, earthworks of lamellas marked with number 2, reinforcement works of lamellas marked with number 2, concreting works of lamellas marked with number 2, earthworks of lamellas marked with number 3, reinforcement works of lamellas marked with number 3, concreting works of lamellas marked with number 3, finishing concrete works, in Table 5 numbered 1-11.

3. ANALYSIS OF COST AND TIME REQUIRED FOR THE CONSTRUCTION OF RC DIAPHRAGMS

For the analysis of the cost and planning of the time required for the execution of the reinforced concrete diaphragm, it is necessary to make a bill of quantities for the listed phases of execution. The bill of quantities for the excavation phase consists of calculating the quantity of soil to be excavated with a grapple excavator. Then for the next phase the quantity of reinforcement to be embedded should be determined, and after the reinforcement is embedded the quantity of concrete that is used for concreting.

3.1. Bill of quantities (BOQ) of construction works

For known dimensions of diaphragm segments and reinforcement steel plan, it is possible to determine the quantities of materials required for the execution. The required quantities of material are shown in Table 1 for the first variant of execution and in Table 2 for the second variant of execution.

Table 1: Bill of quantities (BOQ) for the first variant

| The phase of lamellas execution | The total length of lamellas [m] | Bill of quantities                |                                     |  |
|---------------------------------|----------------------------------|-----------------------------------|-------------------------------------|--|
|                                 |                                  | Excavation soil [m <sup>3</sup> ] | Quantity of reinforcement [kg]      | Quantity of concrete [m <sup>3</sup> ] |
| Even lamellas                   | 51.5                             | 117.42                            | Ø14:<br>5347.31<br>Ø12:<br>2139.39  | 117.42                                 |
| Odd lamellas                    | 48.1                             | 109.67                            | Ø14:<br>4994.28<br>Ø12:<br>1998.15  | 109.67                                 |
| Total                           | 99.6                             | 227.09                            | Ø14:<br>10341.59<br>Ø12:<br>4137.54 | 227.09                                 |

Table 2: Bill of quantities (BOQ) for the second variant

| The phase of lamellas execution                | The total length of lamellas [m] | Bill of quantities                |                                    |  |
|--|----------------------------------|-----------------------------------|------------------------------------|--|
|  |                                  | Excavation soil [m <sup>3</sup> ] | Quantity of reinforcement [kg]     | Quantity of concrete [m <sup>3</sup> ] |
| Lamellas which are building in the first phase | 36.5                             | 83.22                             | Ø14:<br>3789.84<br>Ø12:<br>1516.27 | 83.22                                  |
| Lamellas which are building in                 | 31.55                            | 71.93                             | Ø14:<br>3275.87                    | 71.93                                  |

|  |       |        |                                     |        |
|--|-------|--------|-------------------------------------|--------|
| the second phase                               |       |        | Ø12:<br>1310.64                     |        |
| Lamellas which are building in the third phase | 31.55 | 71.93  | Ø14:<br>3275.87<br>Ø12:<br>1310.64  | 71.93  |
| Total  | 99.6  | 227.09 | Ø14:<br>10341.59<br>Ø12:<br>4137.54 | 227.09 |

3.2. Practical performance of construction machinery

3.2.1. Performance of construction machinery for excavation soil - grapple excavator

A hydraulic excavator HITACHI ZX-350LC-5B is used to excavate the pit of the reinforced concrete diaphragm. Characteristics of a tracked excavator with a special bucket-grapple are: working part volume is 0,3m<sup>3</sup>, engine power is 202KW, weight is 346.17KN, length arm is 5,2m.

The practical performance of an excavator with a grapple is calculated using (2). The coefficients that appear in the given formula are chosen depending on the type of material from the geotechnical study and the conditions on the construction site where the excavation is performed, well as on the condition in which the excavating machine is located. When the values of these coefficients are included in the given formula, the practical performance of the construction machine is 20.36m<sup>3</sup>/h.

3.2.2. Performance of construction machinery for concreting - concrete pump

For the building of concrete elements, concrete is used which is produced in a concrete factory and delivered to the construction site as a ready product. A mobile pump MAN TGS SCHWING is used for concrete installation. The theoretical performance of a concrete pump is 30.0m<sup>3</sup>/h. The practical performance of a concrete pump is calculated using (3). The coefficients that appear in the given formula are chosen depending on the conditions on the construction site where the concreting is performed. When the values of these coefficients are included in the given formula, the practical performance of the construction machine is 21.80m<sup>3</sup>/h.

$$U_{pr} = \frac{T}{t_c} \cdot q \cdot k_{og} \cdot k_{rv} \cdot k_{ds} \cdot k_{vm} \cdot k_{rp} \cdot k_{uv} \cdot k_{kz} \cdot k_{pu} \tag{2}$$

$$U_{pr} = U_t \cdot k_v \cdot k_r \cdot k_p = \frac{T}{t_c} \cdot q \cdot k_v \cdot k_r \cdot k_p \tag{3}$$

### 3.3. Analysis of cost and time required for the construction of RC diaphragms

The times required to perform works on the construction site were analysed. According to the listed phases of construction, these works include earthworks - excavation of pits for the reinforced concrete diaphragm, reinforcement works - preparation and installation skeleton of reinforcement steel in excavated lamella pit and concrete works - concreting of diaphragm lamellas and concreting of the connecting beam. The cost of construction works is calculated by applying the formula (4).

$$C = M + R \cdot (K + 1) \quad (4)$$

In (4) [9], the price of the material is marked with M, the price of labor is marked with R, and the coefficient of non-uniformity is marked with K, the adopted value of which is 4. The cost required for the construction of a RC diaphragm is given in Table 3. The time required for the construction of a RC diaphragm is given in Table 4 and Table 5. The cost and time required for the construction of a RC diaphragm [10], for the first variant are given in table 4 and the cost and time required for the construction of a RC diaphragm for the second variant are given in table 5.

For analysis of cost and time required for the construction of RC diaphragms are used norms and standards of work in construction [11]: analysis of cost and time required for earthwork (machine excavation of soil category II with excavator - GN 200-507 5.1 025605), analysis of cost and time required for reinforcement works (machine cutting and bending, manual installation and binding of reinforcement ČBR, simple and medium complex, vertical crane transport, Ø12 - GN 400-106A 145601; machine cutting and bending, manual installation and binding of reinforcement ČBR, simple and medium complex, vertical crane transport, Ø14 - GN 400-106A 145604), analysis of costs and time required for concrete works (mechanical installation of concrete (without making) - GN 400-508 154504).

For the building phases given in the chapters 2.3. and 2.4. and bill of quantities for the two variants given in the tables 1 and 2, based on the calculated cost prices and the time required for building per unit of quantity, when these values are multiplied by the quantities from the bill of quantities, the time required for the execution and the total cost price for building reinforced diaphragm is obtained. It was adopted that the working day has one shift with duration of 8 hours.

Based on the calculated cost prices by phases of performed works, the cost values and the required number of days for building diaphragms using the first variant (when every second lamella is constructed) were calculated which is shown in Table 4, and the required number of days for building diaphragms using the second variant (when every third lamella is constructed) which is shown in Table 5.

Table 3: The cost required for the construction of a RC diaphragm

| The phase of lamellas execution | The cost of material [rsd/m <sup>3</sup> ] | The cost of labor [rsd/m <sup>3</sup> ] | The total cost [rsd/m <sup>3</sup> ] |
|---------------------------------|--|---|--------------------------------------|
| Earthwork                       | 36.76                                      | 35.00                                   | 211.76                               |
| Reinforcement works (Ø12)       | 1906.54                                    | 195.21                                  | 2882.59                              |
| Reinforcement works (Ø14)       | 4765.31                                    | 325.02                                  | 6390.41                              |
| Concrete works                  | 12000.00                                   | 725.50                                  | 15627.50                             |

Table 4: The cost and time required for the construction of a RC diaphragm for the first variant

| The phase of lamellas execution | Cost price [rsd] | Time required for the construction [day] |
|---------------------------------|------------------|--|
| 1                               | 24,865.09        | 2  |
| 2                               | 1,088,835.66     | 5  |
| 3                               | 1,834,981.00     | 4  |
| 4                               | 23,223.00        | 1  |
| 5                               | 1,016,969.91     | 5  |
| 6                               | 1,713,867.93     | 4  |
| 7                               | 528,800.70       | 3  |
| 8                               | 560,339.64       | 3  |
| Total                           | 6,791,883.92     | 27                                       |

Table 5: The cost required for the construction of a RC diaphragm for the second variant

| The phase of lamellas execution | Cost price [rsd] | Time required for the construction [day] |
|---------------------------------|------------------|--|
| 1                               | 17,622.83        | 1  |
| 2                               | 771,699.06       | 5  |
| 3                               | 1,378,658.05     | 4  |
| 4                               | 15,232.04        | 1  |
| 5                               | 667,006.89       | 4  |
| 6                               | 1,124,086.08     | 4  |

|       |              |    |
|-------|--------------|----|
| 7     | 15,232.04    | 1  |
| 8     | 667,006.89   | 4  |
| 9     | 1,124,086.08 | 4  |
| 10    | 528,800.70   | 3  |
| 11    | 560,339.64   | 3  |
| Total | 6,869,770.30 | 34 |

#### 4. ANALYSIS OF THE RESULTS

##### 4.1. Cost of performed works for the building of a RC diaphragm

The calculated values of the cost price of the performed works for the two execution variants can be shown graphically. The cost price for the first variant is 6,791,883.92rsd (when every second lamella is build), which is shown by the left bar on the diagram in Figure 11. The cost price for the second variant is 6,869,770.30rsd (when every third lamella is build), which is shown by the right bar on the diagram in Figure 11. These values are shown graphically because it is the easiest way to see the difference between the two described variants of building RC diaphragms.

##### 4.2. The time required for the building of a RC diaphragm

Time analysis was done for each phase of works individually. The phases of the works are described in chapters 2.3 and 2.4. For the first variant (when every second lamella is building) the phases are described in chapter 2.3 and the total time required for construction is given in Table 4. For the second variant (when every third lamella is building) the phases are described in chapter 2.4 and the total time required for construction is given in table 5. The time required to the building of a reinforced diaphragm according to the first variant is 27 days and is shown in the left bar of the diagram in Figure 12. The time required to the building of a reinforced diaphragm according to the second variant is 34 days and is shown in the right bar of the diagram in Figure 12.

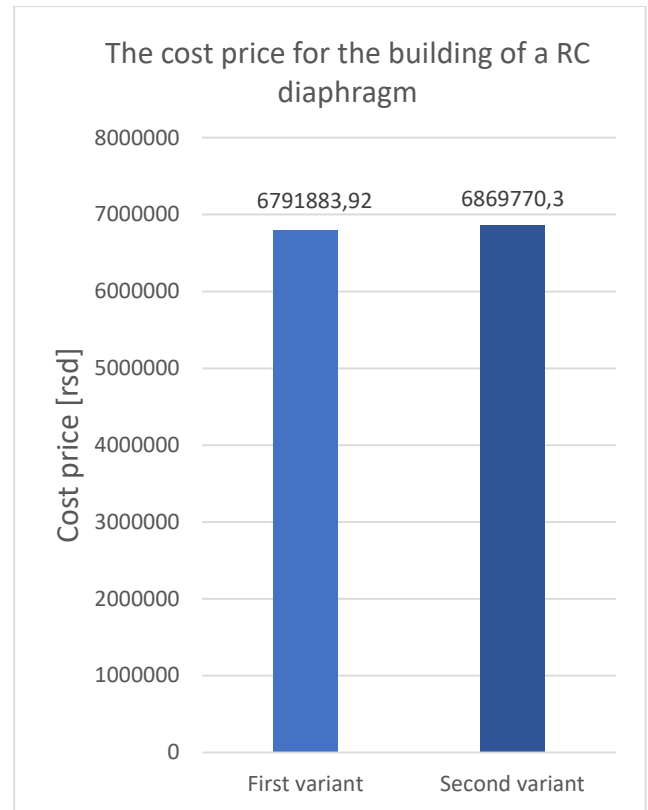


Figure 11: The cost required for the construction of a RC diaphragm

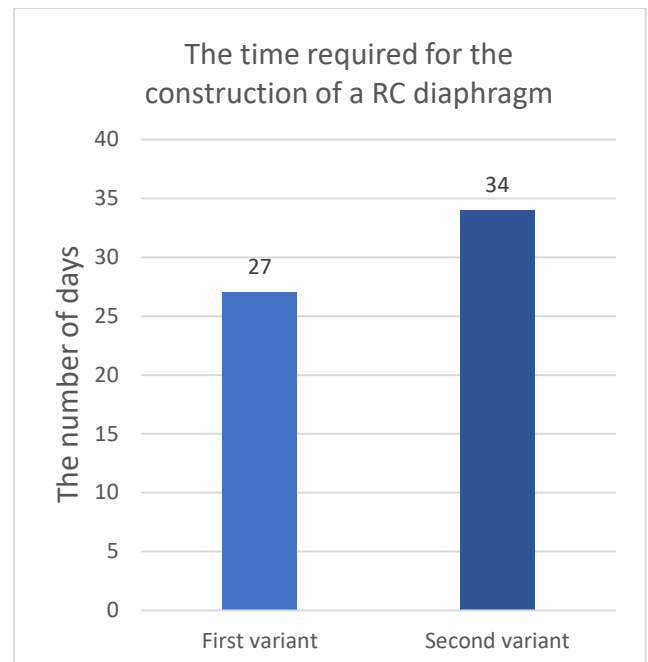


Figure 12: The time required for the construction of a RC diaphragm

##### 4.3. Discussion of the results

From the diagram shown in Figure 11, it can be seen that the cost values of building RC diaphragms are approximate. Since the cost values are approximate, the variant by which the RC diaphragms will be building is chosen based on other factors. The choice of variant usually depends on the security factor for the adjacent buildings. During the excavation of the pit for reinforced concrete

diaphragms, the stability of the adjacent buildings must not be endangered. The choice of the variant with which the reinforced diaphragms will be built also depends on the situation on the construction site, i.e., some characteristics that can be noticed only on the construction site. For the given example, the cost price of the second variant is higher by 1.13%, so the choice should not perform according to the cost required for the construction of RC diaphragms.

The opposite to the cost required for the building of RC diaphragms, the choice of variant could be defined by the required number of working days for the execution of RC diaphragms. A more complex execution procedure when every third lamella of the diaphragm is building results in the division of works into several positions, and because is required more time for building diaphragm. From the diagram shown in Figure 12, it can be seen that the number of days required to build a diaphragm according to the second variant is higher by 20.59%. With a good organization of works and comparatively building of diaphragm segments, this difference between two variants can be reduced, but in that case, a larger number of workers would be needed to build RC diaphragms.

## 5. CONCLUSION

For the given variants of execution of the RC diaphragm, the higher cost price and the time required for execution diaphragm is in the case when every third segment diaphragm is performed. Therefore, it is economically justified to building the RC diaphragms according to the first variant (when every second lamella is constructed). The building of the diaphragm according to the second variant is justified only in the case when the adjacent building is of great importance, so greater safety is required for the appearance of cracks and fissures. The building of the diaphragm according to the second variant is justified only in the case when the adjacent object is of great importance. This is justified because cracks are less probable to appear on an adjacent object during diaphragm building if every third segment of the diaphragm is performed. When reinforced concrete diaphragms are building according to the second variant, there is a smaller change in the equilibrium state in the soil, so the possibility of occurrence cracks on the adjacent building is smaller.

## REFERENCES

- [1] P. Pavlović, "Prilog analizi interakcije konstrukcija-tlo kod armirano-betonskih dijafragmi", Magistarski rad, Fakultet tehničkih nauka (Novi Sad), (1996)
- [2] M. Vasić, "Inženjerska geologija", Fakultet tehničkih nauka (Novi Sad), (2001)
- [3] S. Stevanović, "Fundiranje I", Naučna knjiga (Beograd), (2008)
- [4] S. Mihajlović, "Projekat fundiranja višespratne zgrade i analiza interakcije temeljne ploče i tla", Zbornik radova Fakulteta tehničkih nauka (Novi Sad), (2019)
- [5] D. Milović, "Mehanika tla", Univerzitet u Novom Sadu, Institut za industrijsku gradnju (Novi Sad), (1982)
- [6] J. E. Bowles, "Foundation Analysis and Design", McGraw-Hill Book Comp (New York), (1988)

- [7] M.I. Gorbunov-Pasadov and T.A. Malikova, "Rasčet konstrukcii na uprugom osnovanii", Strojizdat (Moskva), (1984)
- [8] D. Milović and M. Đogo, "Problemi interakcije tlo-temelj-konstrukcija", Fakultet tehničkih nauka (Novi Sad), (2009)
- [9] M. Trivunić and Z. Matijević, "Tehnologija i organizacija građenja", Fakultet tehničkih nauka (Novi Sad), (2006)
- [10] B. Trbojević, "Organizacija građevinskih radova", Građevinska knjiga (Beograd), (1985)
- [11] R. Mijatović, "Normativi i standardi rada u građevinarstvu", Građevinska knjiga (Beograd), (2008)

## Serviceability limit state analysis of a cracked cross-section in accordance with SRPS EN1992-1-1 and PBAB'87

Saša Marinković<sup>1\*</sup>, Bojan Milošević<sup>1</sup>, Stefan Mihajlović<sup>1</sup>, Marijana Jančićjević<sup>1</sup>, Žarko Petrović<sup>2</sup>

<sup>1</sup>Faculty of Mechanical and Civil Engineering, University of Kragujevac, Kraljevo (Republic of Serbia)

<sup>2</sup> Faculty of Civil Engineering and Architecture, University of Niš, Niš (Republic of Serbia)

*Serviceability limit state analysis is an important part of the design of reinforced concrete structures in order to meet the requirements of functionality, durability and aesthetics of the structure. The application of European standards (Eurocodes) in construction in the Republic of Serbia has started recently and there are still disagreements in the interpretation of certain provisions of the standards. On a simply supported reinforced concrete beam at an authoritative cracked cross-section was analyzed the applications of different combinations of permanent and variable actions for purpose of calculation characteristic crack width and deflections at the moment after inflicting load of a class S4 structure and at the end of service life. The results of the calculation according to Eurocode are compared with the results of the calculation according to the Standard for Concrete and Reinforced Concrete from 1987 for interpretation and selection of the relevant combination of actions.*

**Keywords: Serviceability limit state analysis, Reinforced concrete beam, cracked cross-section**

### 1. INTRODUCTION

Design of reinforced concrete (RC) structural elements by ultimate limit state (ULS) does not necessarily provide desired behaviour of structures and their elements in different moments during their service life, due to differences in actions intensity in regard to the intensity that provides equilibrium. Thus, serviceability limit state analysis (SLS) was introduced that evaluates the performance of structures during service life by taking into account criteria of functionality, durability and aesthetics.

SLS is actually an analysis of a stress-strain state of structures and their elements in which, under the combination of actions that occur during service life, some of the criteria for suitability of structures given in construction standards are met. In case of transgression of determined SLS criteria, structures or some of their elements are considered unsuitable for exploitation independently from their load bearing capacity.

These criteria of functionality, durability and aesthetics in SLS are evaluated by controlling parameters:

- Stress levels in materials – concrete and reinforcement steel,
- Width of cracks on RC structural elements,
- Displacement – usually deflection of RC structural elements,
- Vibrations.

In SLS analysis, when carrying out control of mentioned parameters, must be taken into account effects of creep and shrinkage of concrete during time as viscoelastoplastic material with the pronounced trait of aging. Creep and shrinkage of concrete are time dependent deformations. Due to the inhomogeneity of the structure of the concrete itself, the shrinkage cannot take place completely freely and it is uneven inside the concrete. Interferences to free shrinkage represent the

occurrence of reinforcement bars, as well as possible connections on the supports and contours of the elements. On the other hand, creep of hardened concrete is a phenomenon of gradual increase of elastic deformations of concrete that occur at the time of loading, under the further action of long-term loads. Differences in rheological properties, between concrete and steel which co-act under long term load, provide significant redistribution of stresses over time and changes stress-strain state in cross-sections of the RC elements. Thus, under long-term load occurs an increase of stress levels, concrete crack width and deflection.

SLS uses the usual calculation models for the characteristic stress-strain states: for the cross-section of structural element without cracks (state I) and the cross-section in element with cracks (state II), but must be used such stress and strain relations in concrete and steel, that as realistically as possible, show the actual behaviour of these materials in the conditions of service life of the RC structures.

The application of European standards in construction in the Republic of Serbia has started recently and there are still disagreements in the interpretation of certain provisions of the standards. The standard for Concrete and Reinforced Concrete from 1987 (PBAB87) that was used in the Republic of Serbia before the introduction of Eurocodes defined that SLS analysis was conducted into two steps:

- Step 1: control of stresses, crack width and deflection at the moment after inflicting load ( $t_0$ )
- Step 2: starting from the previous step, calculations of changes of stresses, crack width and deflection were conducted taking into account the effect of creep and shrinkage of concrete in a determined time interval ( $t_0-t_c$ ) under the constant intensity of actions on the

structure. Moment of time  $t_{\infty}$  was usually the end of service life of the concrete structure [1].

On the other hand, new standards for SLS analysis in concrete structures, European standard SRPS EN 1992-1-1:2015, does not give such specific guidelines as PBAB87, and according to it control of stresses, crack width and deflection at the moment after inflicting load ( $t_0$ ) is optional [2]. This regulation gives appropriate data for SLS analysis with short-term load, which is necessary for control at the moment after inflicting load ( $t_0$ ), and analysis with long-term load for control during the service life of the structure. The practice has shown that it is preferable to perform SLS analysis for both moments, for the beginning of service life  $t_0$  and for the end of service life  $t_{\infty}$ . This is especially true for purpose of service and revitalization of the existing concrete structures, in which analysis for these moments gives engineers better imaging of the development of stresses, cracks and deflection [3-4].

This paper shows SLS analyses (only crack width and deflection control) conducted for a simply supported reinforced concrete beam at an authoritative cracked cross-section conducted with different combinations of permanent and variable actions during the time from moment  $t_0$  to the end of service life, moment  $t_{\infty}$ . Different combinations of actions are from two different standards, PBAB87 and SRPS EN 1990:2012 which gives optional combinations for engineers based on the nature of actions and deformation state of the structural elements [5]. The results of the analysis according to Eurocode are compared with the results of the calculation according to the standard PBAB87 for interpretation and selection of the relevant combination of actions.

## 2. EXPERIMENTAL ANALYSIS

Ultimate limit state designs of the RC elements are conducted with the combination of actions formed by increasing values of permanent and variable actions with partial factors ( $\gamma$ ) for accounting model uncertainties, dimensional variations and the possibility of unfavourable deviations of the action values from the representative values. On the other hand, in the serviceability limit state analysis, actions are not increased with partial factors ( $\gamma=1$ ), because in the normal exploitation of the RC structures, the serviceability limit state can be achieved, but not exceeded.

SRPS EN 1990 for SLS analysis gives the following combinations of actions [5]:

- Characteristic combination for irreversible serviceability limit states:
 
$$\Sigma G_{k,j} + P + Q_{k,1} + \Sigma Q_{k,i} \cdot \psi_{0,i} \quad (j \geq 1, i > 1) \quad (1)$$
- Frequent combination for verification of reversible serviceability limit states involving accidental actions:
 
$$\Sigma G_{k,j} + P + Q_{k,1} \cdot \psi_{1,i} + \Sigma Q_{k,i} \cdot \psi_{2,i} \quad (j, i > 1) \quad (2)$$

- Quasi-permanent combination for verification of reversible serviceability limit states and calculation of the long-term effects:

$$\Sigma G_{k,j} + P + \Sigma Q_{k,i} \cdot \psi_{2,i} \quad (j, i \geq 1) \quad (3)$$

where are:

- $G_{k,j}$  – characteristic value of permanent action  $j$
- $P$  – relevant representative value of a prestressing action
- $Q_{k,1}$  – characteristic value of the leading variable action 1
- $Q_{k,i}$  – characteristic value of the accompanying variable action  $i$
- $\psi_0$  – factor for the characteristic value of a variable action
- $\psi_1$  – factor for the frequent value of a variable action
- $\psi_2$  – factor for the quasi-permanent value of a variable action

SLS analyses conducted in this paper based on SRPS EN 1992-1-1 includes permanent and imposed load for residential buildings as a variable load, thus only characteristic and quasi-permanent combinations were applicable on basis that cracked RC beam is in the irreversible limit state, and controls of crack width and deflection at the end of service life are calculated with the long-term effects.

Analyses based on PBAB87 are using a combination of loads without any factors [1]:

$$\Sigma G_{k,j} + P + \Sigma Q_{k,i} \quad (j, i \geq 1) \quad (4)$$

In total, four combination analysis were made:

- 1) K-K combination analysis with characteristic (1) combination of actions – load for crack width control and deflection volume control for moments  $t_0$  with short-term effects and  $t_{\infty}$  with long-term effects
- 2) K-QP combination analysis with characteristic (1) combination of actions – load for crack width control and deflection volume control for moment  $t_0$  with short-term effects and quasi-permanent combination (3) for moments  $t_{\infty}$  during and at the end of service life with long-term effects
- 3) QP-QP combination analysis with quasi-permanent (3) combination of actions – load for crack width control and deflection volume control for moments  $t_0$  with short-term effects and  $t_{\infty}$  with long-term effects
- 4) PBAB combination analysis with (4) combination of actions – load for crack width control and deflection volume control for moments  $t_0$  with short-term effects and  $t_{\infty}$  with long-term effects

These combination analyses were conducted to observe a change of crack width and deflection volume through time from moment  $t_0$  to moment  $t_{\infty}$  for a class S4 structure with a life service of 50 years. These SLS parameters are also calculated for moments of 1, 3, 5, 10, 15, 20, 30 and 40 years to complete the display of their change. Also, a change of crack width and deflection volume are observed with modification of characteristic compressive strength of concrete after 28 days of curing.

2.1. Crack width control

Crack width control is usually conducted by calculating the characteristic value of crack width at the specific moment of service life of the RC structure and comparing it with the limit value. Controls based on SRPS EN 1992-1-1 and PBAB87 have the same principles, and their general calculation algorithm is shown in Figure 1.

The calculation of characteristic crack width is based on experimental results and theoretical models. As in figure 1 protocol of calculation consists of:

- Determination of geometrical and mechanical characteristics of effective load bearing cross-section without creep effect for the moment after inflicting load  $t_0$ , and with creep effect for the moment  $t_\infty$  during and at the end of service life. Creep of concrete changes its modulus of elasticity, increase crack width over time and their propagation depth in an authoritative cracked cross-section, thus decreasing the effective area of a cross-section and decreasing

load bearing capacity of the observed RC element.

- Calculation of medium values of concrete strain  $\epsilon_{cm}$  and steel strain  $\epsilon_{sm}$ . Given that there is a co-act between concrete and steel in the tensile part of cross-section, concrete is tensed to a certain level which is lower than the strain level of reinforcement steel. The difference between these strains represents crack width.
- Calculation of distance between two successive cross-sections with formed cracks on the element.
- The characteristic value of the crack width represents a product of the difference between strains of concrete and steel and maximal distance between cracks. Crack with at the moment  $t_0$  is designated as  $w_{k(t_0)}$  and at the moment  $t_\infty$  as  $w_{k(t_\infty)}$ .

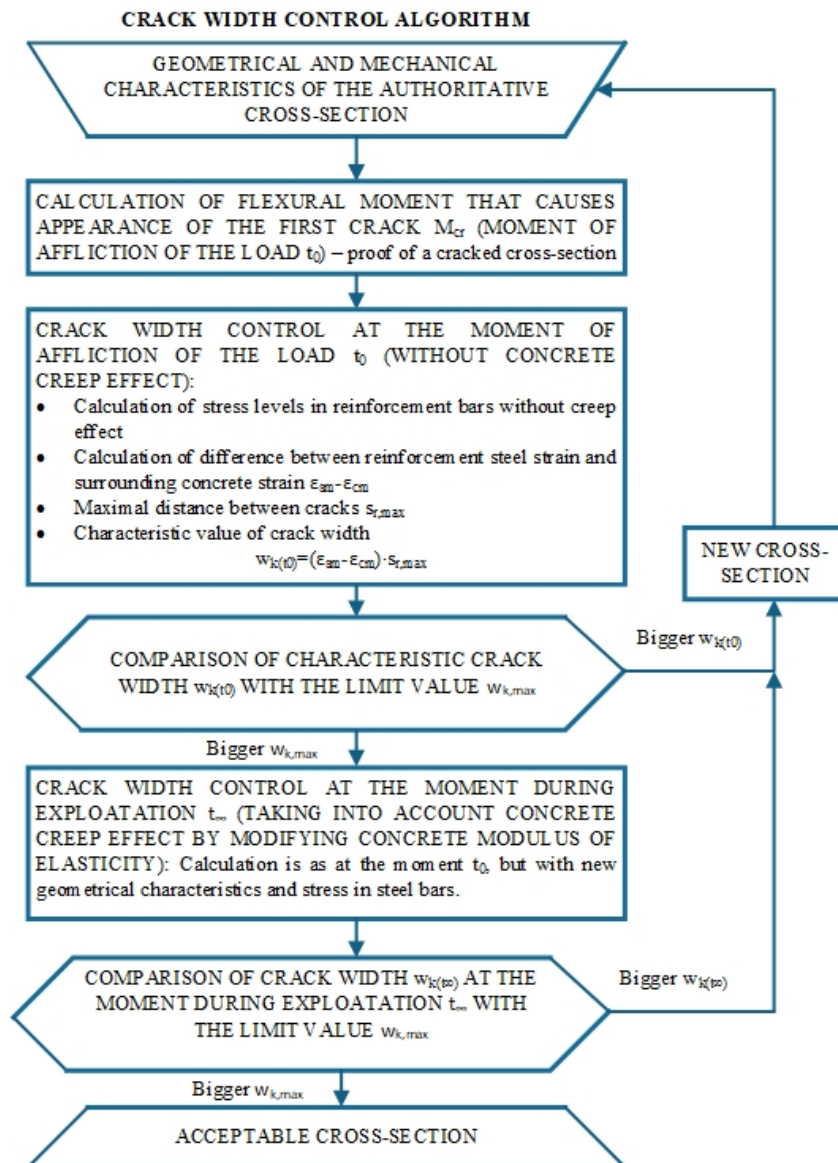


Figure 1: Crack width control algorithm

2.2. Deflection volume control

Independently from the type of their material, all structures under load are deformed. For engineering purposes, usually vertical and horizontal displacements are calculated. Vertical displacements (deflections) are mostly the result of gravitational pull and deformations from

flexural moments. Horizontal displacements are mostly the result of horizontal actions like earthquakes and wind.

Deflection with increased volume rarely endangers the stability and durability of structures. Reasons for its control and limitations are the functionality and aesthetics of the structure.

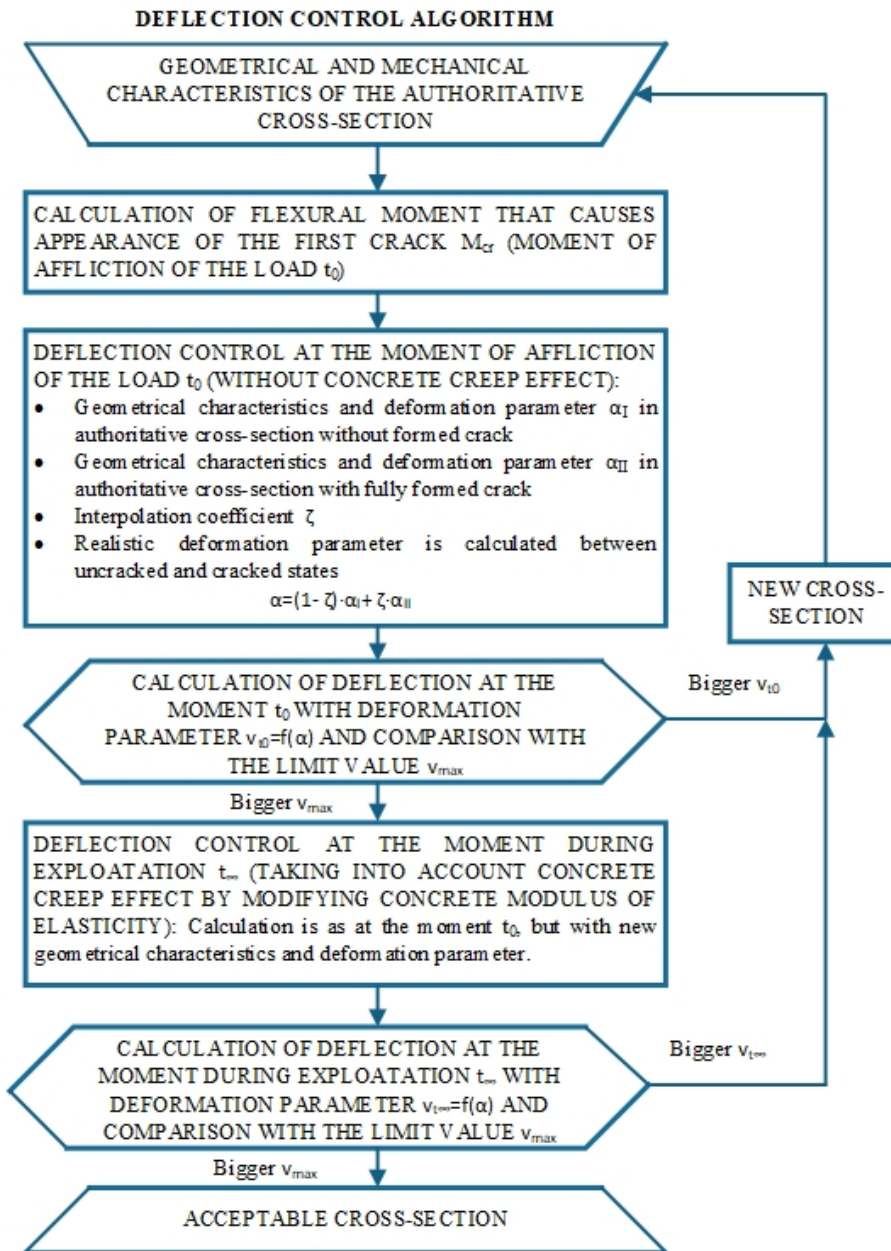


Figure 2: Deflection control algorithm

More than few procedures were developed for deflection volume control, and they are mostly based on a simple principle of determination with two limit values (Figure 2). It is considered that the realistic stress-strain state of the observed RC cracked beam for the SLS deflection control is between one with uncracked cross-section (state I) and one with fully formed crack (state II), thus two deformation parameters ( $\alpha_I$  and  $\alpha_{II}$ ) are calculated and combined with interpolation coefficient  $\zeta$  as in Figure 2. This is done because in a cracked beam there are cross-sections with cracks and between them cross-sections without cracks in which concrete in the tensile area participates in load bearing capacity of the beam, due to co-act with reinforcement steel bars. As a deformation

parameter for deflection control calculation, usually is chosen effective medium curve in a large number of relatively close sections of the RC element.

The characteristic value of deflection at moment  $t_0$  is calculated without creep and shrinkage effects and designated as  $v_{t_0}$ , and at the moment  $t_\infty$  characteristic value of deflection is calculated taking into account creep and shrinkage effects and it is designated as  $v_{t_\infty}$ .

3. RESULTS OF ANALYSIS

With mentioned four different SLS combination analyses, studies were made in which were observed changes of crack width and deflection over time and

changes concerning different values of characteristic compressive strength of concrete in two specific moments  $t_0$  and  $t_\infty$ .

3.1. Analysis in accordance with SRPS EN 1992-1-1

SLS analysis was conducted on a simply supported reinforced concrete beam with a span  $L=4.5m$ . Beam had uniformly distributed permanent and variable induced load (category A for residential buildings)  $g=q=10KN/m'$  for the first study - SLS parameters through time, and  $g=q=15KN/m'$  for the second study - SLS parameters concerning concrete strength. In accordance with the ULS design, the value of flexural moment in beams midspan (authoritative cross-section) was calculated by using appropriate partial factors for actions – loads ( $\gamma_G=1.35$  for permanent load and  $\gamma_Q=1.5$  for variable load) and partial factors for materials. Used concrete for the first study was with strength class C30/37 and for the second study four different strength classes were used: C20/25, C25/30, C30/37 and C35/45. Reinforcement steel class B500 was used for both studies. With this data was calculated required main tensile cross-sectional area of reinforcement. For the first study required reinforcement area was  $A_{a1,req}=10.32cm^2$  and for the second study value of the required reinforcement area changed with concrete strength ranging  $A_{a1,req}=10.03-11.91cm^2$ . For all calculated cross-sections were adopted four main reinforcement bars with diameter  $\varnothing 20mm$  with total cross-sectional area  $A_{a1,req}=12.57cm^2$ . Additional two bars with diameter  $\varnothing 12mm$  were adopted in corners of the cross-sectional compressed area and also were adopted stirrups U $\varnothing 8mm$ . The nominal value of the concrete cover layer was adopted  $c_{nom}=3cm$ . The adopted cross-section for analyses is shown in Figure 3 [2].

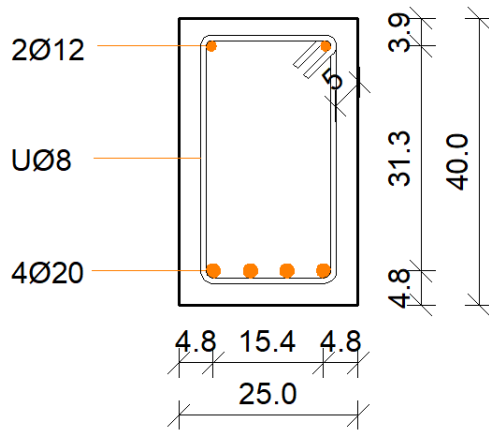


Figure 3: Authoritative cross-section of the observed beam in SLS analysis

For purpose of calculating linear creep coefficient and shrinkage adopted surrounding had a relative humidity of 50%. Concrete cured for 28 days at a temperature of 20°C and was cured for 7 days after casting.

After ULS design, SLS combination analyses were conducted by following protocols from Figures 1-2 with two different combinations of permanent and variable loads ( $\psi_0=0.7$  and  $\psi_2=0.3$  for category A) [2, 5]. Characteristic load value in accordance with (1) was  $q_K=g+q\cdot\psi_0=17KN/m'$  for the first study and  $q_K=g+q\cdot\psi_0=25.5KN/m'$  for the second study. Quasi-

permanent load value in accordance with (3) was  $q_{QP}=g+q\cdot\psi_2=16KN/m'$  for the first study and  $q_{QP}=g+q\cdot\psi_2=24KN/m'$  for the second study. These load values were used in three analyses, K-K, K-QP and QP-QP, as previously said [2].

3.2. Analysis in accordance with PBAB87

In order to make analyses with two different standards comparative, it was used same load values on the same RC beam with the same materials, steel with characteristic yield strength  $f_{yk}=500MPa$  and concrete with same characteristic compressive strength. While SRPS EN 1992-1-1 uses compressive strength of concrete measured on cylindrical specimens (the first number in designation in MPa) and cube specimens with edge length 15cm (the second number in designation in MPa), standard PBAB87 uses compressive strength measured on cube specimens with edge length 20cm, thus calibration of input parameters from SRPS EN 1992-1-1 analysis was required by multiplying strength with coefficient 0.95 to gain values similar to strength measured on cubes with edge 20cm. For example concrete class C30/37 ( $f_{ck,cube,15}=37MPa$ ) is equal to concrete class MB35 in PBAB 87 ( $f_{ck,cube,20}=37\cdot 0.95=35MPa$ ) [1]. An important difference between the two standards is the way that they trait reinforcement capacity and ductility of materials in cross-section. While PBAB87 allows strain in reinforcement up to  $\epsilon_{s,PBAB}\leq 10\%$ , SRPS EN 1992-1-1 allows higher strains in reinforcement ( $\epsilon_{s,SRPSEN}\leq 20\%$ ) by taking into account ductility. For this reason, ULS design in both studies is limited to strain  $\epsilon_{s,PBAB} = \epsilon_{s,SRPSEN}\leq 10\%$ .

Permanent and variable loads in PBAB87 analyses were multiplied with different partial factors ( $\gamma_G=1.6$  for permanent load and  $\gamma_Q=1.8$  for variable load) than those from SRPS EN 1992-1-1 analyses. ULS design in accordance with PBAB87 gave similar values of required reinforcement area,  $A_{a1,req}=10.43cm^2$  for the first study, and values ranging  $A_{a1,req}=10.19-11.34cm^2$  for the second study, thus the same authoritative cross-section was adopted (Figure 3).

SLS analyses was performed with principles shown in figures 1-2 in accordance with standard PBAB87 and with load combination (4) and values  $q_{PBAB}=g+q =20KN/m'$  for the first study and  $q_{PBAB}=g+q =30KN/m'$  for the second study.

3.3. Changes of crack width and deflection through time

Results for this study with four different combinations of loads in accordance with SRPS EN1992-1-1 and PBAB87 are shown in Figures 4-5, statistically processed with common logarithmic equations and presented as diagrams [6]. In Table 1 are given exact values of crack width and deflection, as well as calculated linear creep coefficient and shrinkage volume of concrete in specific moments of service life of the observed simply supported RC beam for S4 class structure (service life of 50 years). Calculations were conducted for time periods of  $t_0=28days$ , 1 year, 3 years, 5 years, 10 years, 15 years, 20 years, 30 years, 40 years and  $t_\infty=50years$ .

Table 1: Values of crack width, deflections, creep coefficients and shrinkage trough time for combination analyses K-K, K-QP, QP-QP and PBAB

| $t$                 | $t_0$ | 1     | 3     | 5     | 10    | 15    | 20    | 30    | 40    | 50    | [years] |
|---------------------|-------|-------|-------|-------|-------|-------|-------|-------|-------|-------|---------|
| $\varphi(t,\infty)$ | -     | 1.896 | 2.208 | 2.298 | 2.375 | 2.408 | 2.418 | 2.433 | 2.441 | 2.445 | -       |
| $\epsilon_{cs}$     | -     | 0.414 | 0.464 | 0.475 | 0.484 | 0.487 | 0.489 | 0.49  | 0.491 | 0.491 | [mm/m'] |
| $w_{K-K}$           | 0.208 | 0.229 | 0.23  | 0.231 | 0.231 | 0.231 | 0.232 | 0.232 | 0.232 | 0.232 | [mm]    |
| $w_{K-QP}$          | 0.208 | 0.149 | 0.151 | 0.152 | 0.152 | 0.152 | 0.152 | 0.152 | 0.152 | 0.152 | [mm]    |
| $w_{QP-QP}$         | 0.127 | 0.149 | 0.151 | 0.152 | 0.152 | 0.152 | 0.152 | 0.152 | 0.152 | 0.152 | [mm]    |
| $w_{PBAB}$          | 0.244 | 0.257 | 0.258 | 0.258 | 0.258 | 0.258 | 0.258 | 0.259 | 0.259 | 0.259 | [mm]    |
| $v_{K-K}$           | 1.613 | 2.041 | 2.137 | 2.162 | 2.183 | 2.19  | 2.194 | 2.197 | 2.199 | 2.201 | [cm]    |
| $v_{K-QP}$          | 1.613 | 1.411 | 1.487 | 1.506 | 1.521 | 1.527 | 1.53  | 1.533 | 1.534 | 1.535 | [cm]    |
| $v_{QP-QP}$         | 1.108 | 1.411 | 1.487 | 1.506 | 1.521 | 1.527 | 1.53  | 1.533 | 1.534 | 1.535 | [cm]    |
| $v_{PBAB}$          | 1.104 | 1.72  | 1.794 | 1.816 | 1.834 | 1.842 | 1.846 | 1.851 | 1.855 | 1.858 | [cm]    |

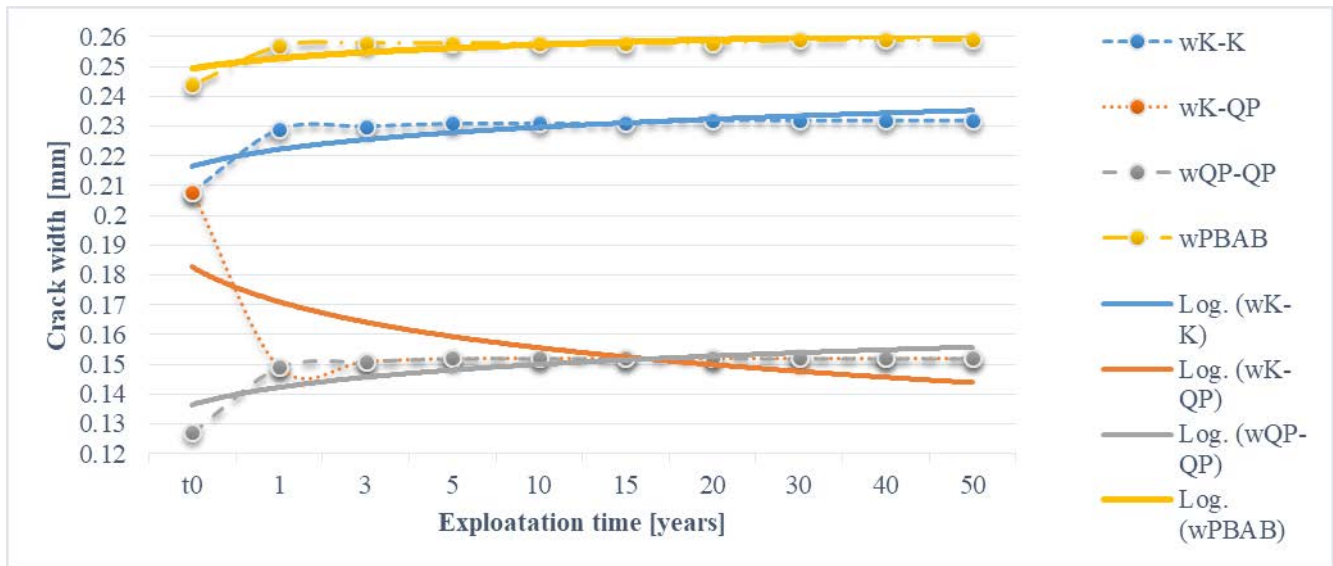


Figure 4: Change of crack width in concrete through time

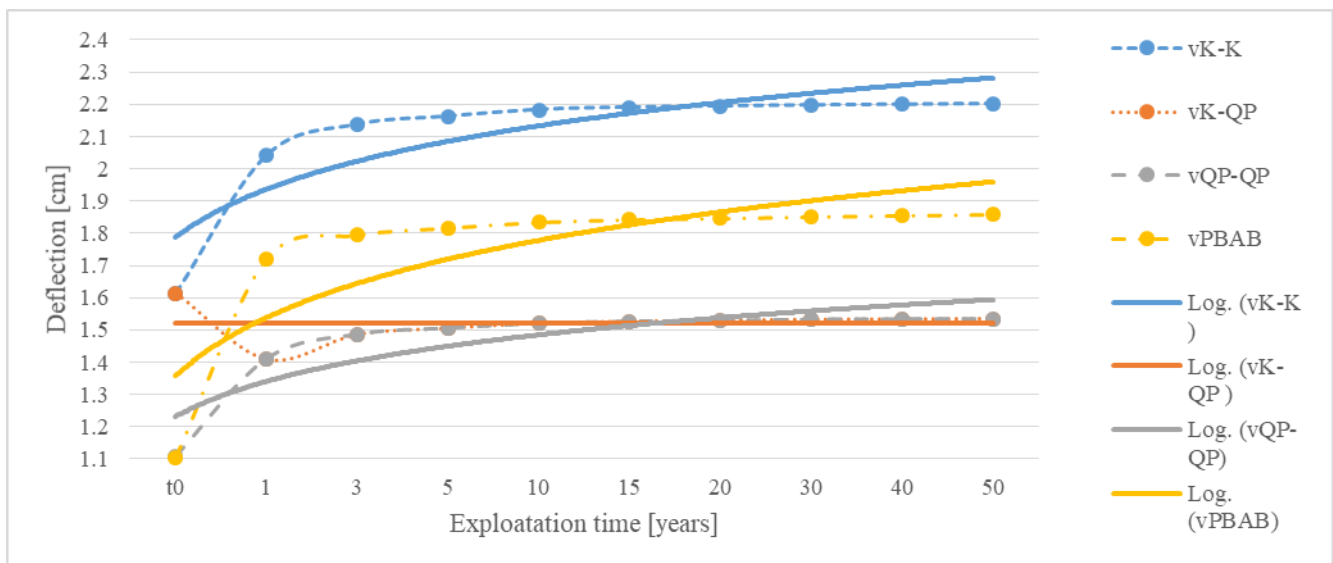


Figure 5: Change of deflection volume in concrete through time

### 3.4. Crack width and deflection with regard to different concrete compressive strengths

Results for this study with four different combinations of loads in accordance with SRPS EN1992-1-1 and PBAB87 are shown in Figures 6-7. Crack width and deflection were calculated for two moments,  $t_0=28$ days after inflicting loads and  $t_\infty=50$ years at the end of service life of the RC beam.

In Table 2 are given values of compressive strengths used in analyses from both standards ( $f_{ck,cube,15}$  from SRPS EN 1992-1-1 and  $f_{ck,cube,15}$  from PBAB), as well as steel strains calculated in ULS design and linear creep coefficients and shrinkage values for different strength classes of concrete.

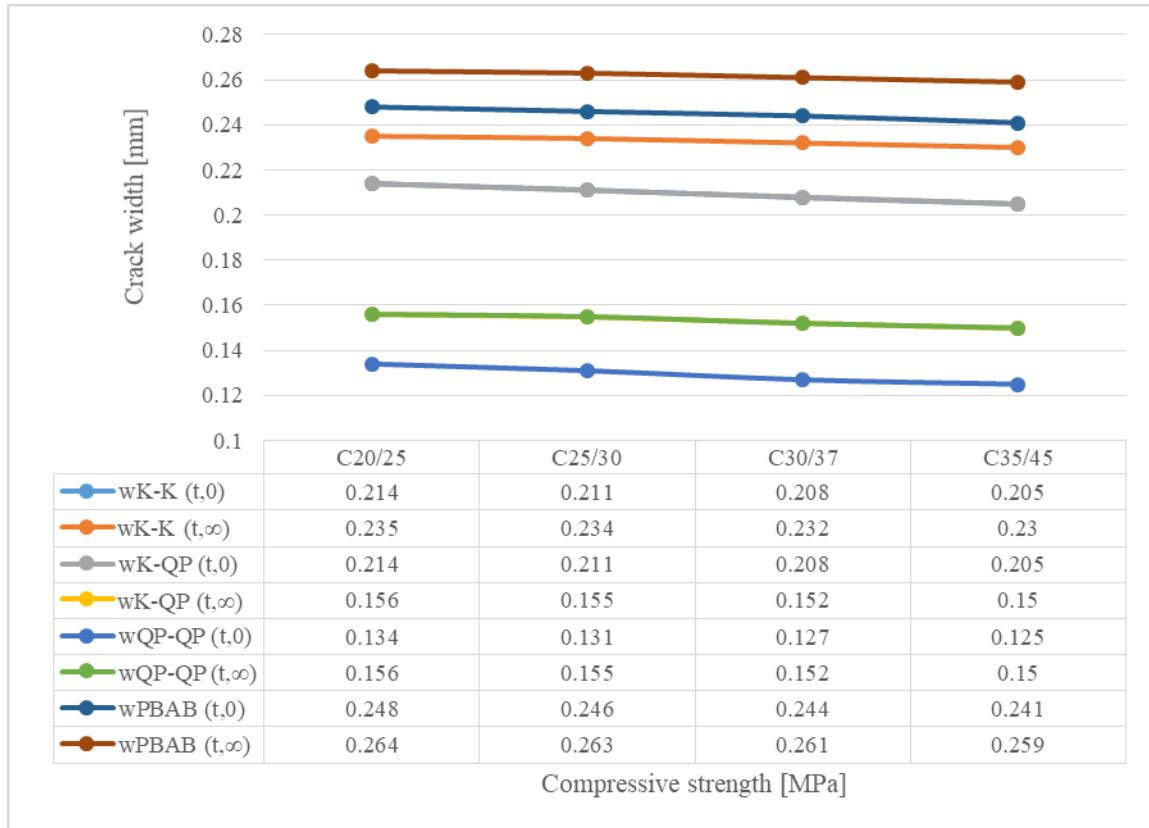


Figure 6: Change of crack width with regard to different concrete compressive strengths

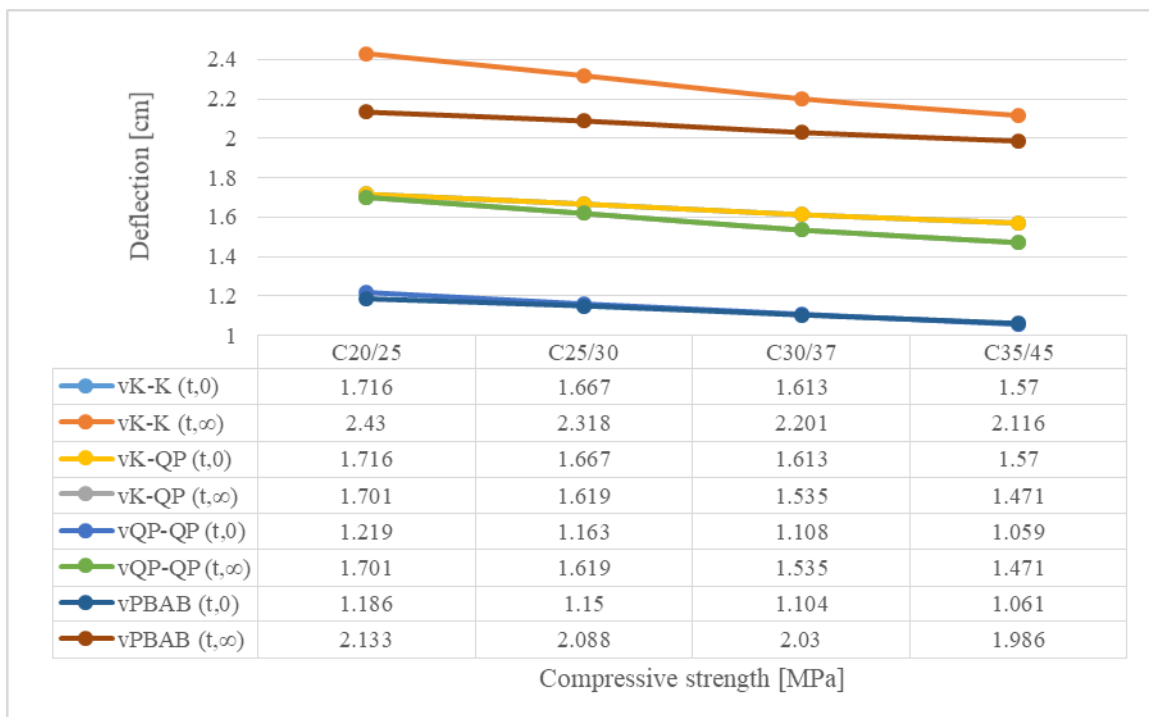


Figure 7: Change of deflection volume with regard to different concrete compressive strengths

Table 2: Values of characteristic compression strength of concrete, strains of reinforcement, creep coefficient and shrinkage for combination analyses K-K, K-QP, QP-QP and PBAB

| $f_{ck,cube,15}$      | C20/25 | C25/30 | C30/37 | C35/45 | [MPa]              |
|-----------------------|--------|--------|--------|--------|--------------------|
| $f_{ck,cube,20}$      | 23.75  | 28.5   | 35.15  | 42.75  | [MPa]              |
| $\varphi(t,\infty)$   | 3.218  | 2.797  | 2.445  | 2.156  | -                  |
| $\epsilon_{cs}$       | 0.523  | 0.506  | 0.491  | 0.478  | [mm/m]             |
| $A_{al}$              | 12.57  | 12.57  | 12.57  | 12.57  | [cm <sup>2</sup> ] |
| $\epsilon_{s,PBAB}$   | 3.73   | 5.513  | 7.534  | 9.583  | [‰]                |
| $\epsilon_{s,SRPSEN}$ | 1.96   | 3.999  | 5.946  | 7.859  | [‰]                |

#### 4. DISCUSSION OF THE RESULTS

##### 4.1. Changes of crack width and deflection through time

###### 4.1.1. Crack width

The highest value of crack width is 0.259mm, calculated at  $t_{\infty}$ =50years of the age, of the RC beam with PBAB combination of actions – loads, and the lowest value of crack width is 0.127mm, calculated at the moment after inflicting load  $t_0$ =28days with quasi-permanent combination analysis QP-QP.

Combination analyses PBAB, K-K and QP-QP have an increase in values from moment  $t_0$  to moment  $t_{\infty}$ =50years. This increase is more intense at the beginning of service life and through time it approaches constant values which are in accordance with theoretical knowledge and experimental data, and it follows an increase in creep and shrinkage of concrete, time dependent deformations. Crack width for combination analysis PBAB is in the range 0.244-0.259mm, for combination analysis K-K is in the range 0.208-0.232mm and for combination analysis QP-QP is in the range 0.127-0.152mm. Combination analysis K-QP has a decrease in crack width from moment  $t_0$  with a value of 0.208mm to moment  $t_{\infty}$  with a value of 0.152mm, due to calculation with two different load combinations used for moments  $t_0$  and  $t_{\infty}$  (a characteristic combination for moment at  $t_0$  gives higher values of crack width than those with quasi-permanent combination) [7-11].

###### 4.1.2. Deflection values

The highest value of deflection is 2.201cm, calculated at  $t_{\infty}$ =50years of the age of the RC beam with K-K characteristic combination of actions – loads, and the lowest value of deflection is 1.104cm, calculated at the moment after inflicting load  $t_0$ =28days with combination analysis PBAB.

Combination analyses PBAB, K-K and QP-QP have an increase in values from moment  $t_0$  to moment  $t_{\infty}$ =50years. This increase is more intense at the beginning of service life and through time it approaches constant values which are in accordance with theoretical knowledge and experimental data, and it follows an increase in creep and shrinkage of concrete. Deflection for combination analysis PBAB is in the range 1.104-1.858cm, for combination analysis K-K is in the range 1.613-2.201cm and for combination analysis QP-QP is in the range 1.108-

1.535cm. Combination analysis K-QP has a decrease in deflection volume from moment  $t_0$  with value 1.613cm to moment  $t_{\infty}$  with value 1.535cm, due to calculation with two different load combinations used for moments  $t_0$  and  $t_{\infty}$  [7-11].

##### 4.2. Crack width and deflection with regard to different concrete compressive strengths

###### 4.2.1. Crack width

The lowest calculated crack width at moment  $t_0$ =28days is 0.125mm for C35/45 with quasi-permanent load combination analysis QP-QP and the highest at the same moment is 0.248mm for C20/25 with combination analysis PBAB. The lowest calculated crack width at moment  $t_{\infty}$ =50years is 0.15mm for C35/45 with quasi-permanent load combination analysis QP-QP and the highest at the same moment is 0.264mm for C20/25 with combination analysis PBAB. All combination analyses for both moments of time have a decrease in crack width when increasing the compressive strength class of the concrete, due to an increase in tensile strength of concrete. Higher strength is followed by an appropriate decrease of creep and shrinkage and lower deformations [7-11].

###### 4.2.2. Deflection values

The lowest calculated deflection at moment  $t_0$ =28days is 1.059cm for C35/45 with quasi-permanent load combination analysis QP-QP and the highest at the same moment is 1.716cm for C20/25 with characteristic combination analysis K-K. The lowest calculated deflection at moment  $t_{\infty}$ =50years is 1.471cm for C35/45 with quasi-permanent load combination analysis QP-QP and the highest at the same moment is 2.43cm for C20/25 with characteristic combination analysis K-K. All combination analyses for both moments of time have a decrease in deflection when increasing the compressive strength class of the concrete and it is followed by an appropriate decrease of creep and shrinkage and lower deformations.

Standard PBAB87 comparing to Eurocodes was designed for use of materials with lower strengths. Previously for reinforcement bars was used steel with characteristic yield strength  $f_{yk}$ =240-400MPa instead of now commonly used reinforcement B500 with characteristic yield strength  $f_{yk}$ =500MPa. The use of concrete and steel with higher strengths allowed the design of smaller cross-sections and elements with larger spans.

Also, new materials kept a similar modulus of elasticity to older materials, thus the same ULS requirements are now met with elements with lower stiffness, but with a higher volume of deflections, thus shown results from PBAB87 combination analyses should be lower if reinforcement strains from SRPS EN 1992-1-1 are considered as more realistic [7-11].

## 5. CONCLUSION

The primary objective of this study was to evaluate referent load combination for moments  $t_0$  and  $t_\infty$  in SLS analysis. Results from the study indicate the following:

- It is not possible to use different combinations of actions – loads for different moments in one same SLS analysis,
- Crack width calculated with standard PBAB are higher in volume than crack width calculated with any possible combinations with standard SRPS EN 1992-1-1,
- Deflections calculated with standard PBAB are higher in volume than deflections calculated with quasi-permanent combination and lower than those calculated with characteristic combination in accordance with standard SRPS EN 1992-1-1.

This research has shown that, in comparison with standard PBAB87, a quasi-permanent combination of actions in standard SRPS EN 1992-1-1 is most adequate to use in SLS controls, but with reserve, due to incompatibility of two standards which is observed in strains of reinforcement steel.

## REFERENCES

- [1] Beton i armirani beton 1987 (Regulations for Concrete and Reinforced Concrete from 1987 - PBAB87), Official Gazette SFRJ 37/88, ISBN 86-80049-17-4
- [2] prSRPS EN 1992-1-1: 2015 Design of concrete structures Part 1-1: General rules – Rules for buildings, bridges and civil engineering structures, Institute for Standardization of Serbia, (2020)
- [3] A. Savic, N. Vatin, V. Murgul, "Complex Testing and Rehabilitation Measures of the Bridges (Example of Road Bridge Across the South Morava, Serbia)", *Applied Mechanics and Materials*, Vols. 725-726, pp 896-902, (2015), doi:10.4028/www.scientific.net/AMM.725-726.896
- [4] A. Savic, "Complex Testing of the Bridges", *MATEC Web of Conferences* 53, 01030, (2016), doi:10.1051/mateconf/20165301030
- [5] prSRPS EN 1990: 2012 Basis of structural and geotechnical design, Institute for Standardization of Serbia, (2019)
- [6] V. Mandic, M. Seslija, S.S. Kolakovic, S. Kolakovic, G. Jeftenic, S. Trajkovic, "Mountain Road-Culvert Maintenance Algorithm", *Water* 2021, vol. 13(4), pp 471, (2020), <https://doi.org/10.3390/w13040471>
- [7] A. Scanlon, P.H. Bischoff, "Shrinkage Restraint and Loading History Effects on Deflections of Flexural Members", *ACI Structural Journal*, vol. 105(4), pp 498-506, (2008)
- [8] N. Pecic, S. Marinkovic, "Design aspects of Eurocode 2 methods for deflection control", *Proceedings of 10th FIB symposium Prague 2011*, vol. 2
- [9] A. Starcev-Curcin, A. Raseta, M. Malesev, D. Kukaras, Dj. Ladjinovic, M. Seslija, "Strength Assessment of the Reinforced Concrete Wall Designed by Strut-and-Tie Method", 15. Symposium of the Association of Structural Engineers of Serbia – ASES, pp. 438-445, (2018), ISBN 978-86-6022-070-9
- [10] A. Starcev-Curcin, A. Raseta, M. Malesev, D. Kukaras, V. Radonjanin, M. Seslija, D. Zarkovic, "Experimental Testing of Reinforced Concrete Deep Beams Designed by Strut-And-Tie Method", *Applied Sciences MDPI*, vol. 10, 6217, (2020), doi:10.3390/app10186217
- [11] N. Pecic, S. Masovic, S. Stosic, "Verification of Deflection According to Eurocode 2", *Structural Concrete Journal of fib*, vol. 18 (6), pp.839-849, (2017), doi: doi.org/10.1002/suco.201600234



# Efficiency analysis of two spatial interpolation methods of precipitation on the Kolubara river basin

Vladimir Mandić<sup>1\*</sup>, Iva Despotović<sup>1</sup>, Miloš Šešlija<sup>2</sup>, Stefan Mihajlović<sup>1</sup>, Slobodan Kolaković<sup>2</sup>

<sup>1</sup>Faculty of mechanical and civil engineering in Kraljevo University of Kragujevac, Kraljevo (Serbia)

<sup>2</sup>Faculty of technical sciences University of Novi Sad, Novi Sad (Serbia)

*The efficiency comparison has been analyzed in this paper for the two spatial interpolation methods that have been most commonly used in the practice, for averaging precipitation data on the experimental catchment of the Kolubara river upstream of the Peštan river confluence, in the Republic of Serbia. The analyzed methods are most commonly used in engineering practice: the Thiessen polygon method and the Linear interpolation method based on the TIN network. The prediction efficiency of the average annual precipitation for a certain location, performed using the cross-validation method, showed that both analyzed methods have low efficiency of point data prediction and that both methods are very sensitive to the exclusion of at least one rain-gauge station. Sensitivity analysis of dependence spatially averaged value of annual precipitation for a given area and the number of precipitation stations, performed for four scenarios: S1 - only precipitation stations in the basin, S2 - precipitation stations up to 10 km from the basin boundary, S3 - precipitation stations up to 20 km from the basin boundary and S4 - precipitation station up to 30 km from the basin boundary, showed that for adequate application of both methods it is necessary to include the surrounding stations up to 20 km from the basin boundary.*

**Keywords: Spatial interpolation, Precipitation, Thiessen polygons, TIN interpolation, Kolubara**

## 1. INTRODUCTION

The average annual precipitation data are one of the most important input data for the design of many hydro-technical structures. Based on this data, the average annual volume of rainfall water in a basin is calculated, which is used in further hydrological studies required for complex hydro-technical analyses [1].

The measured data of precipitation at the locations of rain gauge stations represent spatially distributed "point" data. Therefore, the problem of spatial interpolation of precipitation data belongs to the group of problems of spatial interpolation of point data [2]. The need for interpolation of precipitation data occurs in the two most common cases: for a specific area (basin) and a specific location (point).

The precipitation data spatial interpolation problem has been actual in scientific circles for several decades [3]. For spatial interpolation of precipitation data, a large number of different methods have been developed [4], such as the Thiessen polygon method, the Inverse Distance Weighting, the Linear interpolation method, the Polynomial interpolation method, the Spline interpolation method, the Moving Window Regression method, and different variations of Kriging method. Despite the constant progress of spatial interpolation methods, the oldest methods are still most often used in practice..

This paper aims to check the efficiency of the two most commonly used methods in predicting the average annual precipitation for a particular location (point), as well as the sensitivity analysis of these methods in determining the average annual precipitation on a given area (basin) concerning the number of precipitation stations.

## 2. METHODS AND MATERIALS

### 2.1. The spatial interpolation methods

The relevance of the analyzed problem is represented in the existence of a large number of different spatial interpolation methods [4], but the practical application of most of these methods requires significant scientific knowledge, as well as extensive experience [5]. It is for this reason that methods that are significantly simpler to apply still have a high percentage of usage in practical application. The two most commonly used methods of spatial interpolation are the Thiessen polygons method and the Linear interpolation method based on the TIN network (TIN Linear interpolation).

The Thiessen polygon method is based on determining the area on which the value of a point measurement is representative [2]. With this method, the value of measured precipitation at one point is spatially distributed over a certain area near the measuring station. This method is also known as the Nearest neighbor method.

Determining the area on which the value of a point measurement will be spatially distributed is done by applying the half-distance method between the nearest neighboring stations. The half-distance method is based on the idea of splitting the distance between two points (two precipitation stations) with a line that is perpendicular to the length. By repeating this method for all points (precipitation stations) in the vicinity of the analyzed point, a polygon is formed, which represents the area on which the value of the point data will be spatially distributed.

The Figure 1 shows the basic principle of the method application.

\*Corresponding author: Vladimir Mandić, Dositejeva 19, 36000 Kraljevo, Serbia, mandic.v@mfv.kg.ac.rs

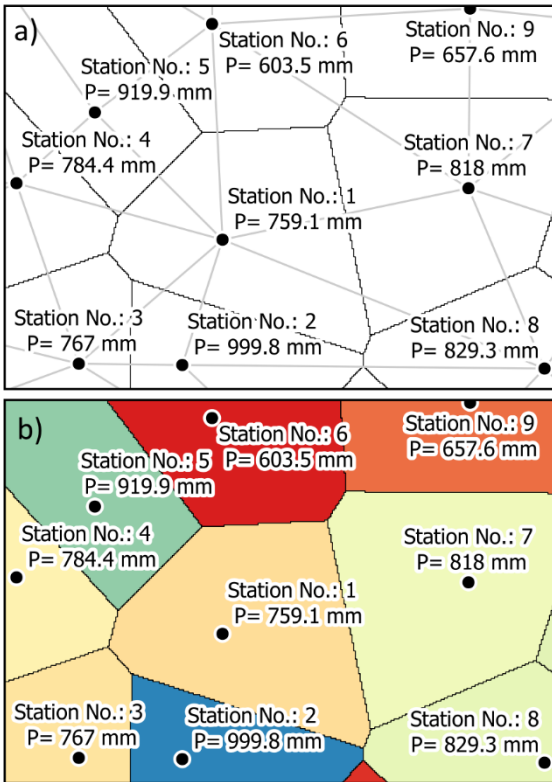


Figure 1: Thiessen interpolation method: a) making polygons with half-distance method and b) Thiessen polygons

The Thiessen polygons method performs a uniform distribution of the point data value on the polygon surface, ie it assumes that the value of the point data is constant for a certain surface (region of influence), defined for each point by half-distance method application. The above assumption on which this method is based has its limitations, which will be stated in Chapter 4 of this paper.

Determination of the average annual precipitation value for a particular basin by the Thiessen polygons method is based on the weighting method, where the weighting coefficients represent the area percentage of each polygon in the total catchment area, as shown in Figure 2, and according to (1).

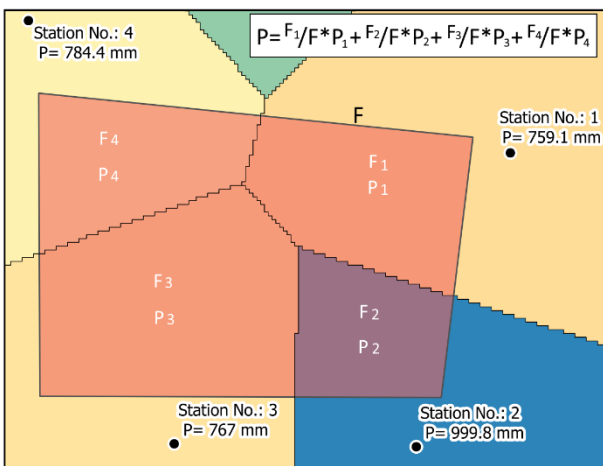


Figure 2: Exampe of spatial interpoaltion of rainfall over area F by Thiessen polygons method

$$P_{area} = \sum_{i=1}^n \left(\frac{F_i}{F}\right) P_i \quad (1)$$

where:

$P_{area}$  – is average value of precipitation over the analysed catchment,  $F$  – area of catchment,  $F_i$  – individual areas for each polygon and  $P_i$  – value of precipitation for each polygon.

The Thiessen method data prediction for a specific location (point), will determine the value which will be the same as the value of the nearest precipitation station. This type of point data prediction is a direct consequence of the Thiessen method basic assumption of the uniform distribution of point measurement data on a defined polygon.

Figure 3 shows an example of the Thiessen polygon method prediction of point data values, and according to (2).

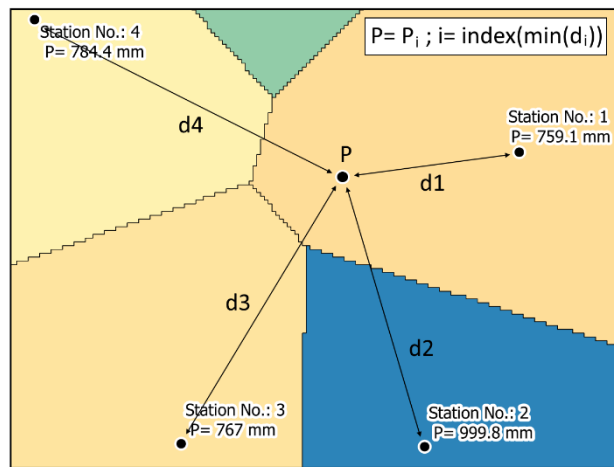


Figure 3: Example of Thiessen polygon method for point data prediction

$$P_{point} = P_i ; i = index (min(d_i)) \quad (2)$$

where:

$P_{point}$  – is point prediction of precipitation,  $d_i$  – Euclidean distances to nearest points (gauging stations) and  $i$  – is index of minimal distance.

The linear interpolation method is based on the formation of a Triangular Irregular Network (TIN) between point measurement data. The TIN network is formed based on the Dalanuy method and has great application in other scientific fields as well [6]. The values between every two connected points in the TIN network have been linearly interpolated, and the location of the integer values has been determined. By merging points with the same integer values, isolines of interpolated value are formed.

Unlike the Thiessen polygon method, the TIN linear interpolation method does not assume a uniform distribution of the measured values. The basic assumption of the Linear interpolation method is that the analyzed quantity is linearly distributed between the two measuring stations.

Figure 4 shows the formation of the TIN m and the determination of precipitation isolines based on linearly interpolated values between precipitation stations, as well as the result of applying the TIN linear interpolation method in the form of a map of precipitation contour lines.

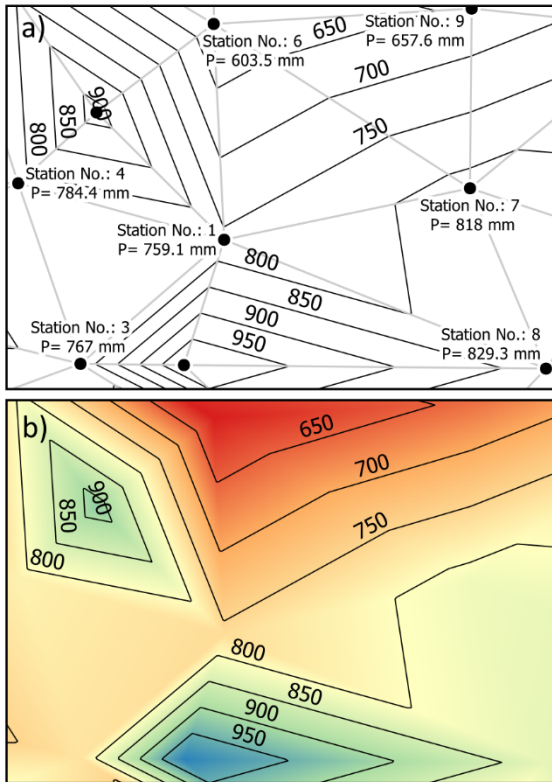


Figure 4: TIN Linear interpolation method: a) TIN mesh with interpolated values and b) map with contour lines.

Calculation of the average precipitation value on a surface (basin) based on the results of TIN linear interpolation of point precipitation data is done by the method of planimetry of surfaces and their corresponding values of precipitation from the map of precipitation contour lines. Figure 5 shows an example, which is based on the application of (3).

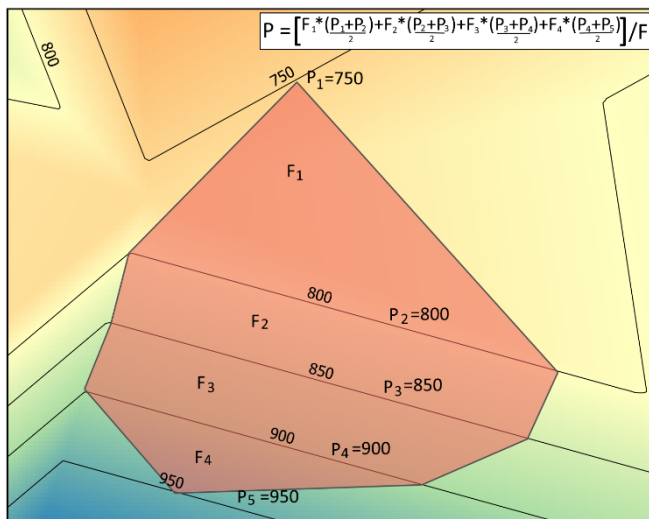


Figure 5: Example of TIN linear interpolation method results application for averaging rainfall over some area

$$P_{area} = \sum_{i=1}^n \left[ F_i \left( \frac{P_i + P_{i+1}}{2} \right) \right] / F \quad (3)$$

where:

$P_{area}$  – is average value of precipitation over the analysed area (catchment),  $F$  – area of catchment,  $F_i$  –

individual areas between two contour lines and  $P_i$  – value of precipitation for each contour line.

The result of spatial interpolation of point measurement data by the TIN linear interpolation is a map of isolines, based on which a prediction of precipitation can be made for a specific location (point). The precipitation value can be determined directly from the digital map in raster format, or it can be calculated by linear interpolation between two isolines.

Figure 6 shows an example of the point precipitation value determination by linear interpolation between two isolines, which is mathematically formulated by (4).

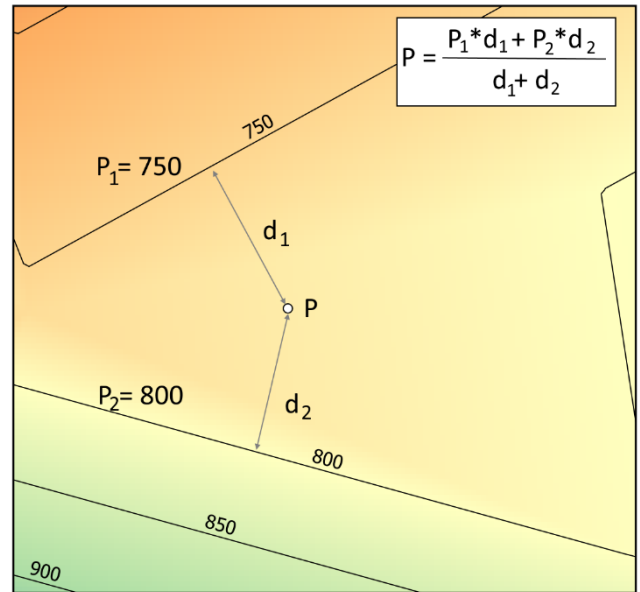


Figure 6: Example of point data prediction by linear interpolation between izolines

$$P_{point} = \frac{P_b * d_b + P_a * d_a}{d_b + d_a} \quad (4)$$

where:

$P_{point}$  – is point prediction of precipitation value,  $P_b$  – is precipitation value for izoline before piont,  $P_a$  – is precipitation value for izoline after piont,  $d_b$  and  $d_a$  – are Euclidean distances to nearest izolines before and after point.

## 2.2. Experimental basin for spatial interpolation over a specific area

For the sensitivity analysis between the number of precipitation stations and the results of average annual precipitation data spatial interpolation over a certain area, the basin of Kolubara river upstream of the Peštan river confluence was adopted as an experimental basin. The main advantage of the adopted experimental basin is the existence of the required number of precipitation stations, both in the basin and in the surrounding area.

The basin of the Kolubara river upstream of the Peštan river confluence is located in the central part of the Republic of Serbia. The experimental basin is almost rectangular in shape, with a very branched hydrographic network that collects water from the mountains on the southern basin boundary and leads it to the outlet profile in the north. Figure 7 shows the analyzed basin.

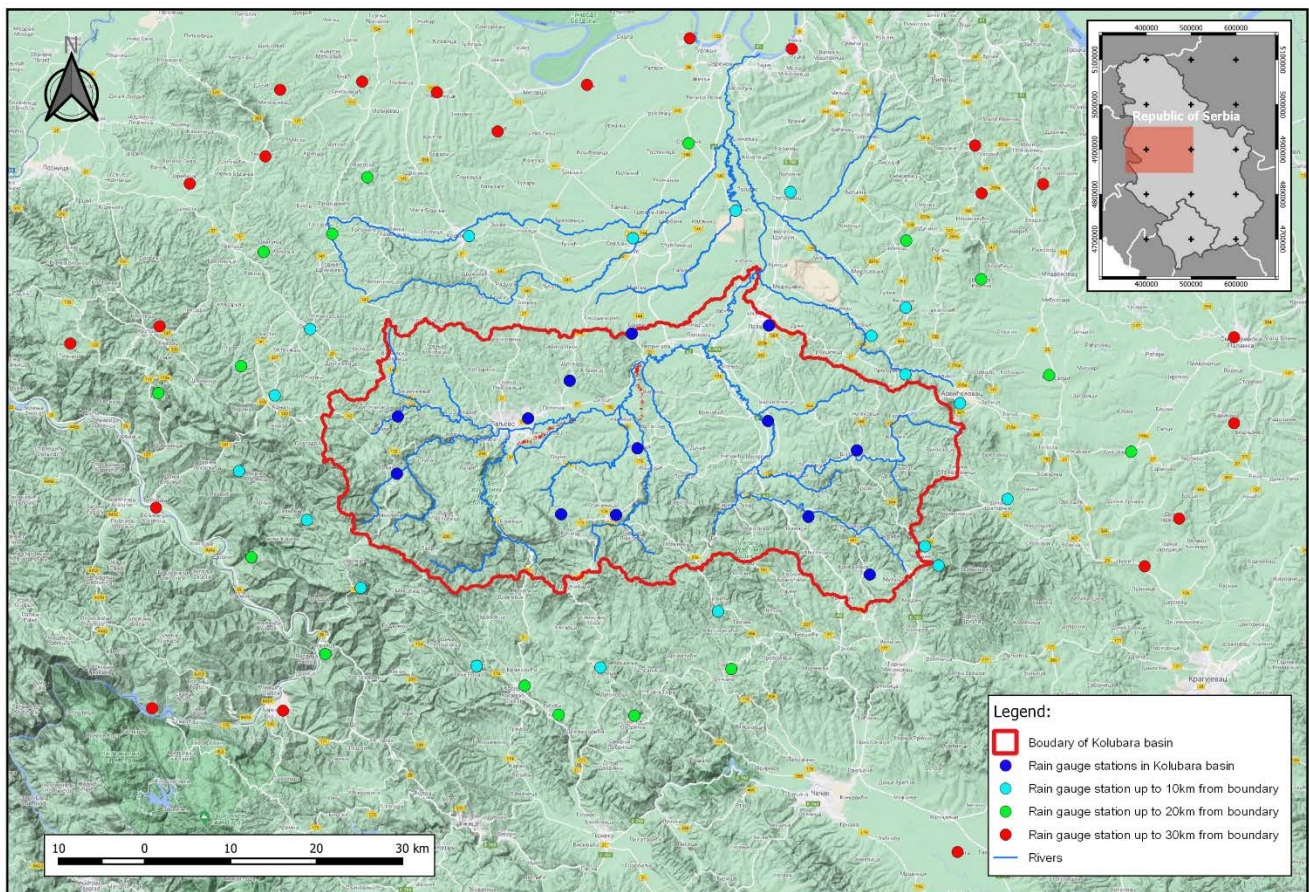


Figure 7: Location of Kolubara catchment with rain gauge stations

The southern border of the experimental basin extends over the large mountain massifs of central Serbia. The east and southeast border of the basin goes over the Rudnik mountain (Cvijićev vrh, 1132 m) and its slopes. The south border of the basin goes over the Suvobor mountain (Crni vrh 882 m), which continues to the massif of Divčibare mountain (Kraljev sto 1104 m). On the west side, the basin is bounded by the mountain range Jablanik (Jablanik 1274m).

The river flows in the basin have a dominant south-north direction so that they drain water from the mountains in the south in the direction of the northern Kolubara lowland. The lowest part of the Kolubara river basin was excluded from analysis due to it has been significantly altered by surface coal mines and has a small number of precipitation stations.

The analyzed part of the Kolubara river basin has a certain number of stations, which is sufficient for the application of chosen spatial interpolation methods, but for further analysis, the large number of precipitation stations in the vicinity of the analyzed basin is very important.

As shown in Figure 7, precipitation stations have been divided into four groups: precipitation stations located in the Kolubara river basin, precipitation stations located up to 10 km from the basin boundary, precipitation stations located up to 20 km from the basin boundary, and precipitation stations located up to 30 km from the basin boundary. The four sets of data were formed, on the basis of which the analysis of the influence of the number of stations on the results of the spatial interpolation of the

average annual precipitation on the experimental basin will be performed.

### 2.3. Methods for prediction efficiency evaluation

In addition to the analysis of the station number influence on the spatial interpolation results [7], the evaluation of the results of precipitation prediction at a certain point represents a significant assessment of the efficiency of a certain spatial interpolation method.

To evaluate the point prediction efficiency of some analyzed spatial interpolation method, the Cross-validation method was used, which can be found in the scientific literature under the names: Jack Knife validation, Leave-One-Out validation etc..

The basic problem of the validation of the results for spatial interpolation of point data is reflected in the question: in relation to which data to validate? The cross-validation method solves this problem very simply: validation is done in relation to one omitted station (one that is left out of the sample) in the spatial interpolation procedure. By repeating this procedure for each of the stations in the analyzed basin, two sets of precipitation data are obtained, one is the set of the observed or measured data, and the other is a set of predicted or simulated data. For the two obtained data sets, the correlation of the observed and simulated data was checked and a correlation coefficient was determined, which is often used in scientific researches as well [8].

3. RESULTS AND DISCUSSION

Spatial data interpolation methods are applied for the two most common cases: determining the mean value of the analyzed variable over a certain surface and determining the prediction of the point value of the analyzed variable.

In this paper, two methods of spatial interpolation of point data were applied, the Thiessen polygon method and the TIN linear interpolation method. These methods are applied to the problem of determining the average annual amount of precipitation based on measurement data from precipitation stations. These methods of spatial interpolation are very common in engineering practice due to their simplicity of application.

In hydrological practice, the problem of calculation of the average annual precipitation for a particular basin is very common. The value of average annual precipitation is very important data for various types of hydrological analyzes because it shows the average annual amount of

water that falls on the analyzed basin. To determine the mean value of annual precipitation in the experimental basin of the river Kolubara upstream of the Peštan river confluence, the two analyzed spatial interpolation methods were applied.

To analyze the influence of the precipitation station number on the results of spatial interpolation of the average annual precipitation in the basin, four scenarios were formed. The first scenario includes only precipitation stations located in the experimental basin. The second scenario includes all precipitation stations in the basin as well as precipitation stations that are up to 10 km away from the basin boundary. The third and fourth scenarios include all precipitation stations that are 20 and 30 km away from the basin border, respectively. Table 1 shows the data for each of the considered scenarios.

Figures 8 and 9 show the results of applying the Thiessen polygon and TIN linear interpolation methods for each of the above scenarios, respectively.

Table 1: Four scenarios with different data sets

| Scenario: | Number of rain gauge stations: N | min P <sub>station</sub> | max P <sub>station</sub> | Thiessen polygon method                            | TIN linear interpolation                           |
|-----------|----------------------------------|--------------------------|--------------------------|--|--|
|           |                                  |                          |                          | Average annual rainfall P <sub>kolubara</sub> [mm] | Average annual rainfall P <sub>kolubara</sub> [mm] |
| S1        | 13                               | 603.5                    | 999.8                    | 772.38   | 769.17   |
| S2        | 32                               | 586.8                    | 1017.7                   | 758.20   | 757.88   |
| S3        | 48                               | 586.8                    | 1056.2                   | 759.74   | 758.77   |
| S4        | 70                               | 548.6                    | 1056.2                   | 759.74   | 758.75   |

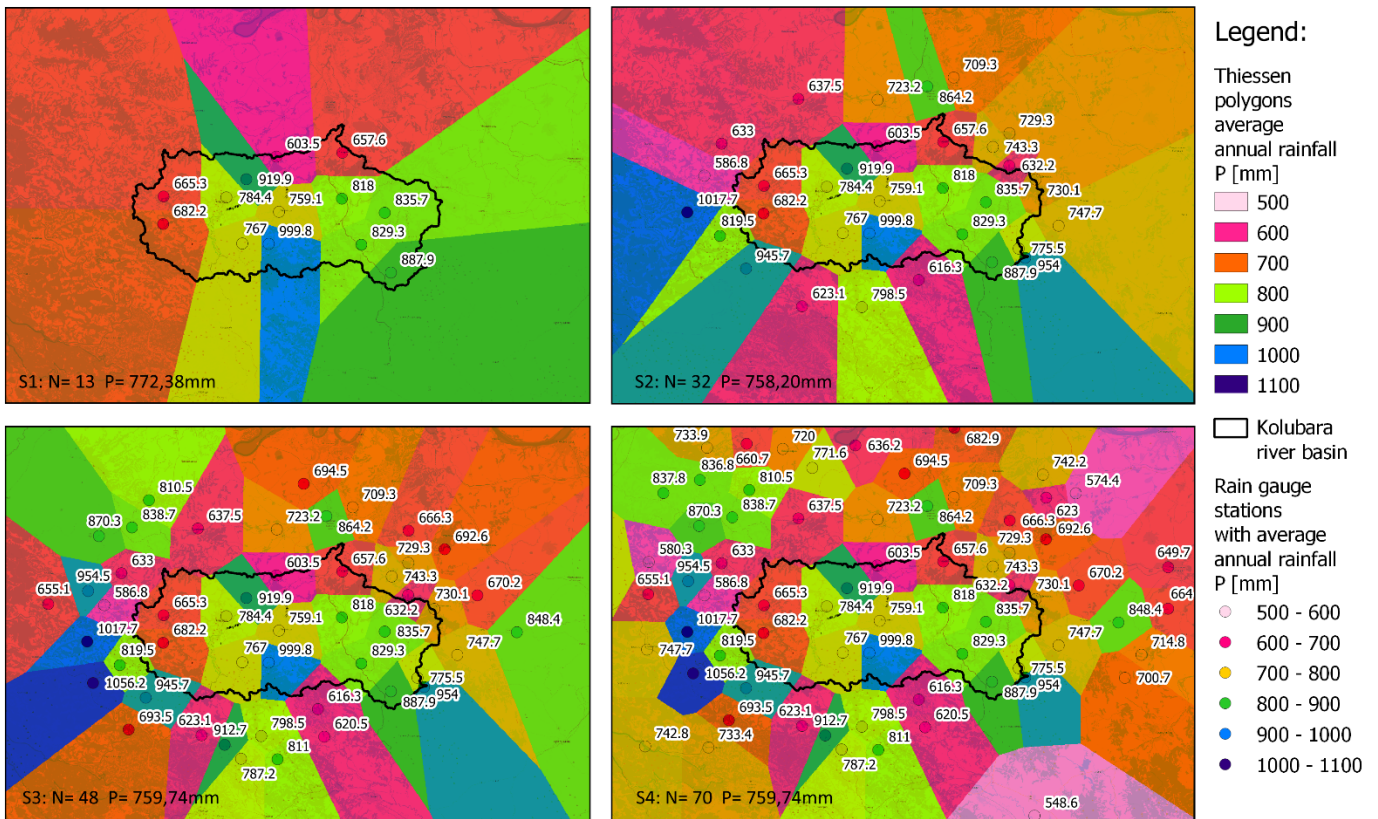


Figure 8: Results of Thiessen polygons method for calculation of average annual rainfall over the Kolubara river catchment for four scenarios

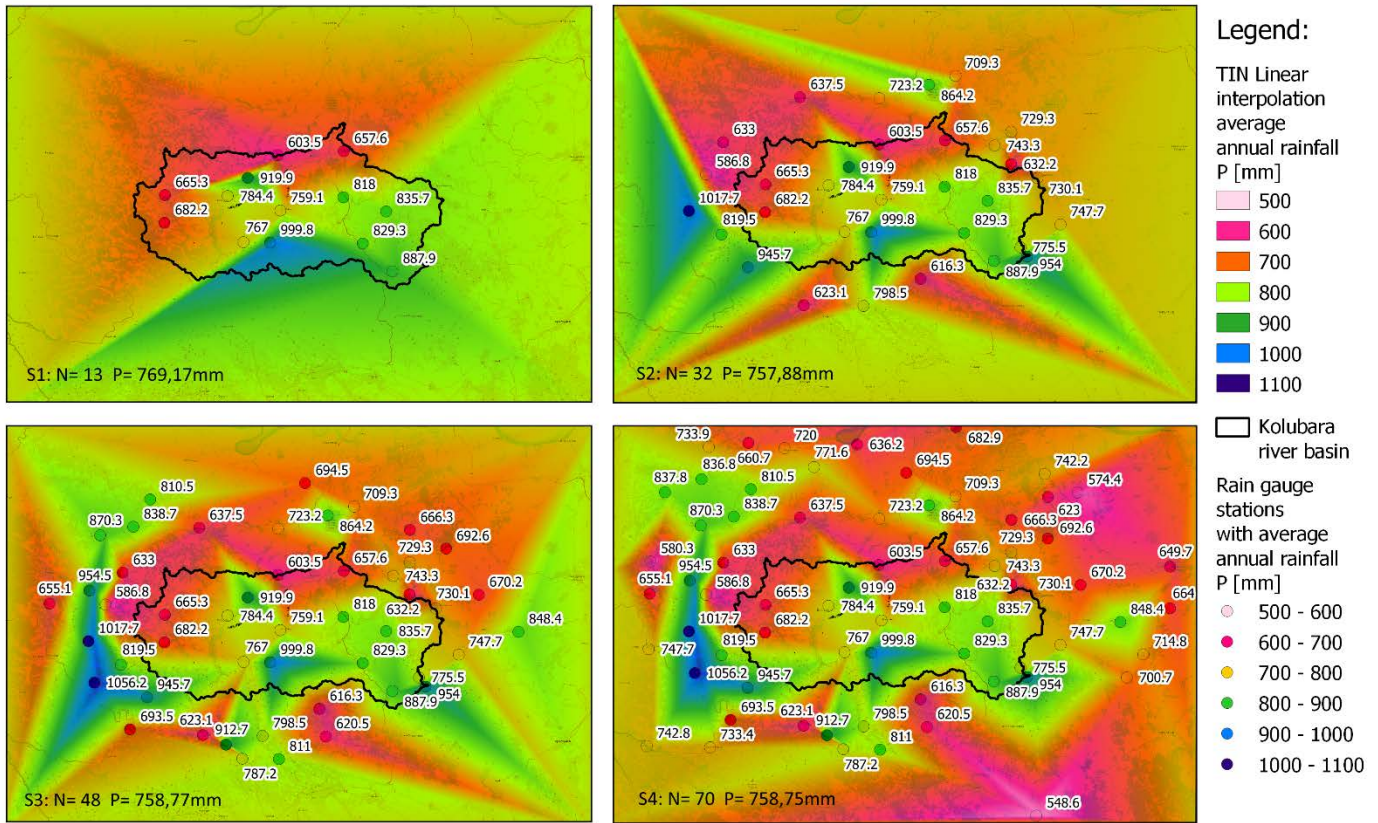


Figure 9: Results of TIN linear interpolation method for calculation of average annual rainfall over the Kolubara river catchment for four scenarios

As shown in the previous figures, both spatial interpolation methods were applied for each scenario, and then, based on the obtained results, the mean value of annual precipitation in the experimental Kolubara river basin was determined. A results comparison of the application of these two spatial interpolation methods concerning the number of precipitation stations used in each of the four scenarios is shown in Figure 10.

The results presented in Figure 10 show that both spatial interpolation methods are under the great influence of the number of input data, ie the number of precipitation stations in a particular case. Figure 10 shows the importance of including non-catchment rainfall stations when determining the mean annual rainfall for a catchment.

In engineering practice, very often in the analyzes, only precipitation stations in the considered basin are used, which, as Figure 10 shows, can give significantly different results. In this particular case, the results of determining the values of mean annual precipitation for the surface of the experimental basin were significantly higher for both methods. The reason for this is the fact that the basic data set (scenario S1) included one precipitation station with a very high value of mean annual precipitation of 999.8 mm (Table 1, Figures 8 and 9). The mentioned data is not an out-layer because it was determined that it is a rain station Brezdje with a large amount of precipitation per year. Both methods comparison for scenario S1 shows that the TIN linear interpolation method is less influenced by the extreme value data, ie that the TIN linear interpolation method performs greater averaging of interpolated data than the Thiessen polygon method.

Scenario S2 doubles the number of stations, and also included many stations with value of mean annual precipitation that is below the average for the experimental basin, resulting in a decreasing the value of mean annual precipitation for the experimental basin almost equally for both spatial interpolation methods.

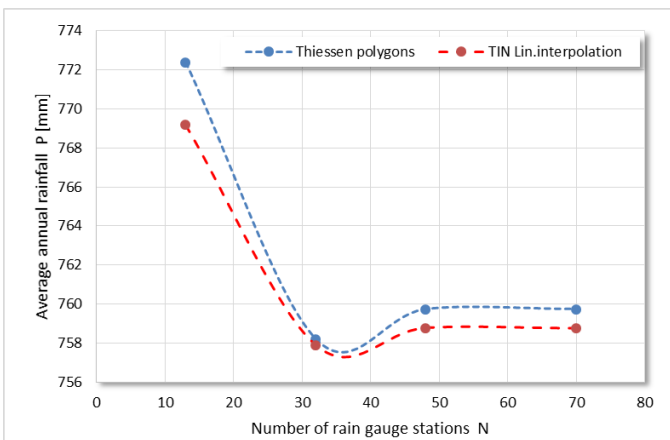


Figure 10: Dependence between number of rainfall stations and average annual rainfall value for experimental catchment

Scenarios S3 and S4 give the same results for both methods of spatial interpolation, respectively. The above result can be interpreted from two aspects: from the aspect of the number of stations and the aspect of the distance of the surrounding stations from the basin boundary.

The analysis of the results from the aspect of the number of stations gives the conclusion that for the calculation of average annual precipitation value for a certain basin it is necessary to include twice more precipitation stations in the vicinity of the basin than the number of precipitation stations in the analyzed basin. As shown in Table 2, scenario S3 included in the analysis 48 precipitation cells of which 13 cells were located on the surface of the experimental basin, which roughly corresponds to the ratio of 1/3 of the cells in the basin and 2/3 of the cells around the basin. The stated conclusion is equally valid for both analyzed methods of spatial interpolation.

The analysis of the results from the aspect of the distance of the stations from the basin border gives the conclusion that for the calculation of the average annual precipitation values for a certain basin it is necessary to include all stations located up to 20 km from the basin border. This conclusion is equally valid for both analyzed methods of spatial interpolation. It is very important to note that the stated conclusion directly depends on the physical characteristics of the analyzed basin, ie on the shape of the basin and the topography of the basin.

In order to generalize the two previously presented conclusions, it is necessary to repeat this experiment for a large number of basins with the same set of scenarios. This may be one of the directions of future research.

The results of the application of the TIN linear interpolation method for scenario S4 (the largest number of stations), Figure 9 - S4, show the directions of precipitation distribution in the considered area, ie the dominant directions of precipitation clouds. Based on the above results, Figure 9 clearly shows that the clouds that bring precipitation to this area come from the southwest, and that most precipitation is emitted in that part. It can also be seen that precipitation clouds move from there in two directions, in the direction of the east, along the southern border of the basin, in the direction of the mountain Rudnik, and in the northern direction, along the western border of the basin, very likely guided by air currents.

Figure 9, scenario S4, is a good basis for making general conclusions, but for a serious analysis of the direction of rain clouds movement in this area it would be necessary to have a data of the dominant directions wind speed and air masses movement.

These spatial interpolation methods have the ability to predict the analyzed value at points where there is no measurement data. Some scientists believe that the efficiency of a spatial interpolation method can be directly determined on the basis of the efficiency of prediction of that method, forgetting the importance of applying that spatial interpolation method in calculation of the mean value over a surface. In addition, it is indisputable that the ability to predict point data is one of the important indicators of the efficiency of a spatial interpolation method.

A large number of different methods can be found in the scientific literature to determine the efficiency of point

data prediction of a method, but cross-validation method is definitely the most common. As previously stated, the method is based on the principle of omitting one from the input data set, and determining the value for the omitted data based on the spatial interpolation of the remaining data from the set. By repeating the procedure for all data from the set, a correlation dependence can be determined between the observed data from the input data set and the values of the data determined by their omission, or the simulated values.

The diagram with the values of the observed data on the abscissa and the values of the simulated data on the ordinate, shows the prediction efficiency of the selected spatial interpolation method. The closer the data to the line (5) are, the more efficient the chosen prediction method is.

$$P_{obs} = P_{sim} \tag{5}$$

For the quantitative determination of the prediction efficiency of a spatial interpolation method, the correlation coefficient between sets of observed and simulated data is usually determined, according to (6):

$$R^2 = \frac{[\sum_{i=1}^n (P_{obs,i} - \overline{P_{obs}}) * (P_{sim,i} - \overline{P_{sim}})]^2}{\sum_{i=1}^n (P_{obs,i} - \overline{P_{obs}})^2 * (\overline{P_{sim}} - \overline{P_{sim}})^2} \tag{6}$$

where:

$P_{obs}$  – is observed value of average annual precipitation measured in rainfall gauging station,  $P_{sim}$  – is simulated value of average annual precipitation determined by application of spatial interpolation method,  $\overline{P_{obs}}$  – is average value of observed precipitation data and  $\overline{P_{sim}}$  – is average value of simulated precipitation data.

For scenario S4, cross-validation has been performed for both spatial interpolation methods, with leave out one by one the data from 13 precipitation stations located in the experimental basin. Figures 11 and 12 show the results of cross-validation for the Thiessen polygon method and the TIN linear interpolation method, respectively.

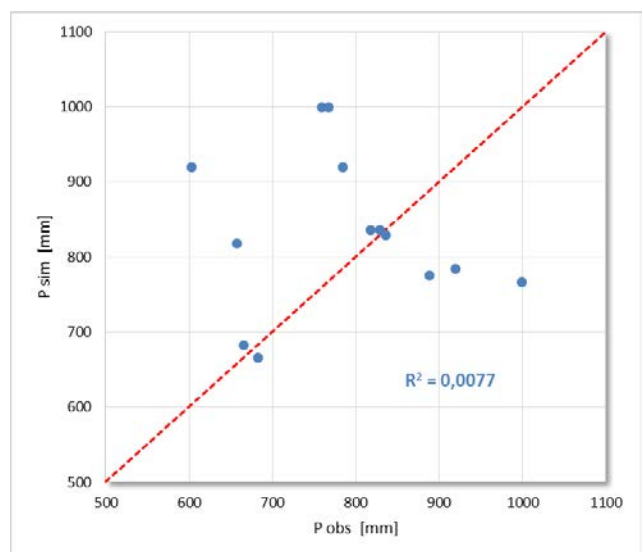


Figure 11: Results of cross-validation for Thiessen polygon method

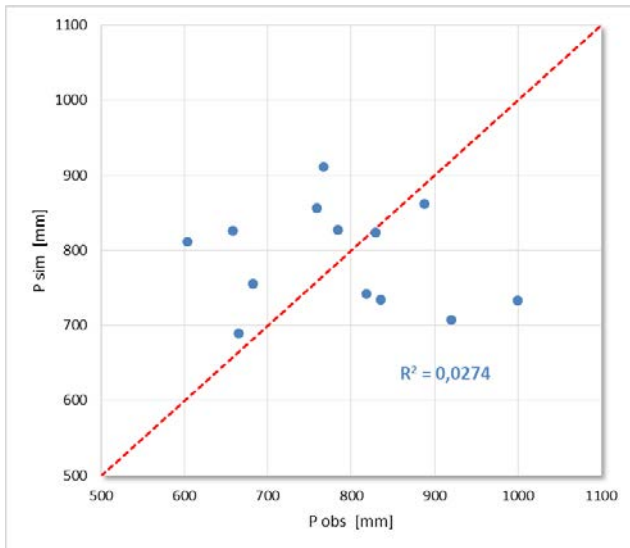


Figure 12: Results of cross-validation for TIN linear interpolation method

The results of cross-validation for the Thiessen polygon method, Figure 11, show a very low correlation coefficient, although as many as 5 of the 13 data are in close proximity to the correlation line given by (5). The consequence of the basic assumption of the Thiessen polygon method is uniform distribution of the measured value over the entire surface of the polygon. This assumption results in very large jumps in the value of the prediction of point data during relatively small changes in spacing, especially when the observed points are located on different sides of the polygon boundary.

The TIN linear interpolation method also has a very low correlation coefficient (Figure 12), although it is slightly higher than the correlation coefficient for the Thiessen polygon method. Figure 12 shows that all points on the diagram are grouped around a horizontal line that has the value  $\overline{P_{sim}}$ . The above conclusion supports the previously stated claim that the TIN linear interpolation method averages the values of the observed data significantly more than the Thiessen polygon method.

Based on the presented diagrams, it can be concluded that none of the analyzed methods has satisfactory efficiency in terms of prediction of point data, but that both methods are satisfactorily effective in terms of averaging data over a certain area.

#### 4. CONCLUSIONS

In this paper, the comparison of two spatial interpolation methods of point data, the method of Thiessen polygons and the method of TIN linear interpolation, has been made on the example of determining the values of mean annual precipitation for the experimental basin on the river Kolubara, analyzing the dependence of the results on the number of precipitation station, and the point data prediction efficiency using the cross-validation method. Based on the obtained results, the following conclusions were made:

- Both analyzed methods of spatial interpolation are highly dependent on the number of precipitation stations

involved in the calculation of the mean annual precipitation value for a basin.

- For the adequate application of both analyzed methods, it is necessary to include in the analysis twice the number of precipitation stations located around the basin than the number of precipitation stations located in the basin.

- The results of the calculation of the value of average annual precipitation for a basin converge to a constant value with the inclusion of all precipitation stations at a distance of 20 km from the basin boundaries.

- Both methods have very low efficiency in terms of prediction of point data, which is confirmed by low values of the correlation coefficient, but they both have satisfactorily effectiveness in terms of averaging data over a certain area.

#### ACKNOWLEDGEMENTS

This research paper has been supported by the Republic of Serbia, Ministry of Education, Science and Technological Development through the project 451-03-68/2020-14/200108.

#### REFERENCES

- [1] M. Keblouti, L. Ouerdachi, and H. Boutaghane, "Spatial Interpolation of Annual Precipitation in Annaba-Algeria - Comparison and Evaluation of Methods," *Energy Procedia*, Vol. 18, pp. 468–475, (2012)
- [2] P. D. Wagner, P. Fiener, F. Wilken, S. Kumar, and K. Schneider, "Comparison and evaluation of spatial interpolation schemes for daily rainfall in data scarce regions," *J. Hydrol.*, Vol. 464–465, pp. 388–400, (2012)
- [3] G. Q. Tabios and J. D. Salas, "A COMPARATIVE ANALYSIS OF TECHNIQUES FOR SPATIAL INTERPOLATION OF PRECIPITATION," *J. Am. Water Resour. Assoc.*, Vol. 21(3), pp. 365–380, (1985)
- [4] S. Ly, C. Charles, and A. Degré, "Different methods for spatial interpolation of rainfall data for operational hydrology and hydrological modeling at watershed scale: a review," *Biotechnol. Agron. Société Environ.*, Vol. 17( 2), pp. 392–406, (2013)
- [5] P. de A. Borges, J. Franke, Y. M. T. da Anunciação, H. Weiss, and C. Bernhofer, "Comparison of spatial interpolation methods for the estimation of precipitation distribution in Distrito Federal, Brazil," *Theor. Appl. Climatol.*, Vol. 123(1–2), pp. 335–348, (2016)
- [6] V. Mandić, M. Šešlija, S. Kolaković, S. Kolaković, G. Jeftenić, and S. Trajković, "Mountain Road-Culvert Maintenance Algorithm," *Water*, Vol. 13(4), p. 471, (2021)
- [7] A. Michelon, L. Benoit, H. Beria, N. Ceperley, and B. Schaeffli, "Benefits from high-density rain gauge observations for hydrological response analysis in a small alpine catchment," *Hydrology and Earth System Sciences*, Vol. 25(4), pp. 2301–2325, (2021)
- [8] S. Marinković, M. Protić, S. Paunović, I. Nešović, and J. Bijeljić, "Application of industrial by-products as mineral admixtures for self-compacting concrete," *J. Croat. Assoc. Civ. Eng.*, Vol. 70(1), pp. 31–38, (2018)





## IN MEMORIAM - PROF. MILOMIR GAŠIĆ (1950-2021)



On Friday, April 16, 2021, our esteemed Dr. Milomir Gašić, a retired full professor, academician of the Russian Federation, and the former chairman of the scientific board of the international scientific conference Heavy Machinery, suddenly passed away.

Milomir Gašić was born in the village of Rataje, near the small town of Aleksandrovac, in 1950. He graduated in 1974 at the Faculty of Mechanical Engineering in Belgrade at the Department of Mechanical Structures and Mechanization, where he also received his master's and doctor's degree in 1983 and 1989, respectively. He received a famous October Award of the City of Belgrade in 1974 for his bachelor's degree exam.

After graduation he worked for five years as a chief construction engineer in the factory IMK "14. Oktobar" Kruševac, and he worked for a year as a chief technology engineer at the Aviation Institute "Moma Stanojlović" in Batajnica. He completed his specialist studies in Coles-Sunderland, England in 1985 and in Caterpillar, University of Madison, the USA, in 1991.

He spent his entire academic career at the Faculty of Mechanical Engineering in Kraljevo. Being a full professor he published several university textbooks, workbooks and scientific monographs. He also published a large number of papers at international conferences, domestic conferences, foreign and domestic journals. He was an adviser on several master's and doctoral theses defended at the Faculty.

He made a professional contribution to the advancement and development of the Faculty of Mechanical Engineering in Kraljevo by performing functions at all organizational levels. He was the Head of the Department of Heavy Machinery as well as the Head of Department of Construction and Design in Mechanical Engineering. He was the Dean of the Faculty in five terms and the Vice Dean for Education in three terms. Professor Milomir Gašić was the founder and manager of the Centre for Construction and Transport Mechanization.

He participated in and managed several scientific and research projects financed by the Serbian Ministry of Science, as well as numerous projects for the needs of the Serbian economy. He was a regular member of the editorial board and a reviewer of the national journal called *IMK 14 - Research and Development in Heavy Machinery*. He was the chairman of the scientific board of the international scientific conference named *Heavy Machinery 2002*. He was also a member of many organizational and scientific committees of scientific and professional meetings in the country and abroad.

In 2005 professor Milomir Gašić became an Honorary Doctor of Technical Science at the State University in Voronjez, Russia. In 2009 he became a member of the National Educational Council of the Republic of Serbia and he was also a member of the Scientific Committee for Mechanical Engineering at the Ministry of Science and Technological Development. Finally, after a detailed evaluation of his entire scientific and professional work by the Council of Academics, Professor Milomir Gašić became a member of the Academy of the Russian Federation, Department of Quality.

CIP - Каталогизација у публикацији - Народна библиотека Србије, Београд

621(082)

621.86/.87(082)

629.3/.4(082)

622.6(082)

681.5(082)

INTERNATIONAL Triennial Conference Heavy Machinery (10 ; 2021 ; Vrnjačka Banja)

Proceedings / The Tenth International Triennial Conference Heavy Machinery HM 2021, Vrnjačka Banja, June 23-25, 2021 ; [editor Mile Savković]. - Kraljevo : Faculty of Mechanical and Civil Engineering University of Kragujevac, 2021 (Bor : Tercija). - 1 knj. (razl. pag.) : ilustr. ; 29 cm

Tekst štampan dvostubačno. - Tiraž 80. - Str. [7]: Predgovor / Mile Savković. - Bibliografija uz svaki rad.

ISBN 978-86-81412-09-1

a) Машиноградња - Зборници b) Транспортна средства - Зборници c) Производно машинство - Зборници d) Шинска возила - Зборници e) Аутоматско управљање - Зборници

COBISS.SR-ID 41166089



The Faculty of Mechanical  
and Civil Engineering in Kraljevo  
The University of Kragujevac  
Serbia, 36000 Kraljevo, Dositejeva 19  
Phone/fax +381 36 383 269, 383 377

E-mail: [office@mfkv.kg.ac.rs](mailto:office@mfkv.kg.ac.rs)  
[www.mfkv.kg.ac.rs](http://www.mfkv.kg.ac.rs)

